IntechOpen

Biomedical Engineering, Trends in Materials Science

Edited by Anthony N. Laskovski

WEB OF SCIENCE™

BIOMEDICAL ENGINEERING, TRENDS IN MATERIALS SCIENCE

Edited by **Anthony N. Laskovski**

Biomedical Engineering, Trends in Materials Science
http://dx.doi.org/10.5772/992
Edited by Anthony N. Laskovski

Contributors

Eberhard Burkel, Faming Zhang, Seda Kizilel, T. Ipek Ergenc, Valentyn Novosad, Elena Rozhkova, Mohammad E. Khosroshahi, Sigbritt Karlsson, Peter Kaali, Emma Strömberg, Anna Igual Muñoz, Carlos Valero Vidal, S.H. Choi, H.H. Cheung, James E. Kennedy, Laudemir Carlos Varanda, Miguel Jafelicci Jr., Watson Beck Jr., Ernesto Suaste-Gomez, Jose De Jesus Agustin Flores-Cuautle, Carlos Omar González Morán, Philippe Zinck, Nikita Bibinov, Dixon T. K. Kwok, Martin Schulz, Tao Hu, Chenglin Chu, Paul Chu, K. Zhang, Aswini Pradhan, J. Pradhan, M. Bahoura, G. T. Ramesh, P. Ravichandran, R. Gopikrishnan, Rui Yang, Yulin Hao, Shujun Li, Masayuki Kuzuya, Yasushi Sasai, Yukinori Yamauchi, Shin-ichi Kondo, Fengxiang Qin, Akihisa Inoue, Zhenhua Dan, Xinmin Wang, Guoqiang Xie, Nikolaj Gadegaard, Matthew Dalby, Rebecca McMurray, Hao-Ming Hsiao, Jolanta Kumirska, Mirko X. Weinhold, Małgorzata Czerwicka, Zbigniew Kaczyński, Anna Bychowska, Krzysztof Brzozowski, Jorg Thöming, Piotr Stepnowski, Anupam Srivastav, Fernando Seoane Martinez, Juan Carlos Marquez, Javier Ferreira, Ruben Buendia, Kaj Lindecrantz, Ziad O. Abu-Faraj, Hiroshi Tamura, Rangasamy Jayakumar, M. Prabaharan, Tetsuya Furuike, Shantikumar V. Nair

Notice

First published in Croatia, 2011 by INTECH d.o.o.
eBook (PDF) Published by IN TECH d.o.o.
Place and year of publication of eBook (PDF): Rijeka, 2019. IntechOpen is the global imprint of IN TECH d.o.o.
Printed in Croatia

Legal deposit, Croatia: National and University Library in Zagreb

Additional hard and PDF copies can be obtained from orders@intechopen.com

Biomedical Engineering, Trends in Materials Science
Edited by Anthony N. Laskovski
p. cm.
ISBN 978-953-307-513-6
eBook (PDF) ISBN 978-953-51-4533-2

Meet the editor

Anthony N. Laskovski completed his Bachelor of Engineering (Electrical) Degree at the University of Newcastle, Australia in 2006 on a UNISS industrial scholarship with the power distributer Energy Australia.
His research interests include RF electronics and implantable electronic devices for biomedical applications, with a particular focus on wireless power transmitters, inductive coils and implantable telemetry architecture. His publications include various conference and journal papers and book chapters.

Contents

Preface

Biological and medical phenomena are complex and intelligent. Our observations and understanding of some of these phenomena have inspired the development of creative theories and technologies in science. This process will continue to occur as new developments in our understanding and perception of natural phenomena continue. Given the complexity of our natural world this is not likely to end.

Over time several schools of specialisation have occurred in engineering, including electronics, computer science, materials science, structures, mechanics, control, chemistry and also genetics and bioengineering. This has led to the industrialised world of the 20th century and the information rich 21st century, all involving complex innovations that improve the quality and length of life.

Biomedical Engineering is a field that applies these specialised engineering technologies and design paradigms to the biomedical environment. It is an interesting field in that these established technologies and fields of research, many of which were inspired by nature, are now being developed to interact with naturally occurring phenomena in medicine. This completes a two-way information loop that will rapidly accelerate our understanding of biology and medical phenomena, solve medical problems and inspire the creation of new non-medical technologies.

This series of books will present recent developments and trends in biomedical engineering, spanning across several disciplines. I am honoured to be editing a book with such interesting and exciting content, written by a selected group of talented researchers. This book presents recent work involving materials science in biomedical engineering, including developments in metallic biomaterials, nanomaterials, polymers and other material technologies in biomedical engineering.

Anthony N. Laskovski

The University of Newcastle,
Australia

Part 1

Materials in Biomedical Engineering

1

Novel Chitin and Chitosan Materials in Wound Dressing

R. Jayakumar[1], M. Prabaharan[2], P. T. Sudheesh Kumar[1], S. V. Nair[1], T. Furuike[3] and H. Tamura[3]

[1]*Amrita Centre for Nanosciences and Molecular Medicine, Amrita Institute of Medical Sciences and Research Centre, Amrita Vishwa Vidhyapeetham University,*

[2]*Department of Chemistry, Faculty of Engineering and Technology, SRM University,*

[3]*Faculty of Chemistry, Materials and Bioengineering, Kansai University,*

[1,2]*India*

[3]*Japan*

1. Introduction

Chitin is the second most abundant natural polysaccharide after cellulose on earth. It is a high molecular weight linear homopolymer of β-(1, 4) linked N-acetylglucosamine (N-acetyl-2-amino-2-deoxy-D-glucopyranose) units. Chitosan, a copolymer of glucosamine and N-acetyl glucosamine units linked by 1-4 glucosidic bonds, is a cationic polysaccharide obtained by alkaline deacetylation of chitin. The role of chitin and chitosan as biomaterials are amazing as evidenced by the published scientific papers and patents. Chitin and chitosan are attracting increasingly more attention recently due to its biological and physicochemical characteristics. Chitin and chitosan with beneficial biological and antimicrobial properties and high valuable potential for wound healing are attractive for wound care. Healing restores integrity of the injured tissue and prevents organisms from deregulation of homeostasis. The treatment of the wounds has evolved from the ancient times. Initially, application of dressing material was aimed at inhibition of bleeding, protection of the wound from environmental irritants as well as water and electrolyte disturbances. Skin plays an important role in homeostasis and the prevention of invasion by microorganisms. Skin generally needs to be covered with a dressing immediately after it was damaged. At present, there are three categories of wound dressing: biologic, synthetic and biologic-synthetic. Alloskin and pigskin are biologic dressings commonly used clinically, but they have some disadvantages, such as limited supplies, high antigenicity, poor adhesiveness and risk of cross contamination. Synthetic dressings have long shelf life, induce minimal inflammatory reaction and carry almost no risk of pathogen transmission. In recent years, researchers have focused on biologic-synthetic dressings (Bruin et al., 1990; Suzuki et al., 1990), which are bilayered and consist of high polymer and biologic materials. These three categories of wound dressing are all used frequently in the clinical setting, but none is without disadvantages. An ideal dressing should maintain a moist environment at the wound interface, allow gaseous exchange, act as a barrier to microorganisms and remove excess exudates. It should also be non-toxic, non-allergenic, nonadherent and easily

removed without trauma, and it should be made from a readily available biomaterial that requires minimal processing, possesses antimicrobial properties and promotes wound healing. In recent years, a large number of research groups are dedicated to produce a new, improved wound dressing by synthesizing and modifying biocompatible materials (Shibata et al., 1997; Draye et al., 1998; Ulubayram et al., 2001).

Recent reports are also aiming on the acceleration of the wound repair by systematically designed dressing materials. In particular, efforts ware focused on the use of biologically derived materials such as, chitin and its derivatives, which are capable of accelerating the healing processes at molecular, cellular, and systemic levels. Chitin and its derivative, chitosan, are biocompatible, biodegradable, nontoxic, anti-microbial and hydrating agents. Due to these properties, they show good biocompatibility and positive effects on wound healing. Previous studies have shown that chitin-based dressings can accelerate the repair of different tissues and facilitates contraction of wounds and regulates secretion of the inflammatory mediators such as interleukin 8, prostaglandin E, interleukin 1 β, and others. Chitosan provides a non-protein matrix for 3D tissue growth and activates macrophages for tumoricidal activity. It stimulates cell proliferation and histoarchitectural tissue organization. Chitosan is a hemostat, which helps in natural blood clotting and blocks nerve endings and hence reducing pain. Chitosan will gradually depolymerize to release *N*-acetyl-*β*-D-glucosamine, which initiates fibroblast proliferation and helps in ordered collagen deposition and stimulates increased level of natural hyaluronic acid synthesis at the wound site. It helps in faster wound healing and scar prevention (Paul & Sharma, 2004). The advantage of chitin and chitosan is easily can processed into hydrogels (Nagahama et al., 2008a; Nagahama et al., 2008b; Tamura et al., 2010), membranes (Yosof, Wee, Lim & Khor, 2003; Marreco et al., 2004; Jayakumar et al., 2007; Jayakumar et al., 2008, Jayakumar et al., 2009; Madhumathi et al., 2009), nanofibers (Shalumon et al., 2009; Shalumon et al., 2010; Jayakumar et al., 2010), beads (Yosof, Lim & Khor, 2001; Jayakumar et al., 2006), micro/nanoparticles (Prabaharan & Mano, 2005; Prabaharan, 2008; Anitha et al., 2009; Anitha et al., 2010; Dev et al., 2010), scaffolds (Peter et al., 2009; Peter et al., 2010; Prabaharan & Jayakumar, 2009; Maeda et al., 2008) and sponges (Muramatsu, Masuda, Yoshihara & Fujisawa, 2003; Portero, 2007) for various types of biomedical applications such as drug and gene delivery (Prabaharan & Mano, 2005; Jayakumar et al., 2010a), wound healing (Jayakumar et al., 2005; Jayakumar et al., 2007; Jayakumar et al., 2010b; Jayakumar et al., 2010c; Tamura et al., 2010) and tissue engineering (Jayakumar et al., 2005; Jayakumar et al., 2010d; Tamura et al., 2010). Various forms of wound dressings materials based on chitin and chitosan derivatives are commercially available. The ordered regeneration of wounded tissues requires the use of chitin and chitosan in the form of non-wovens, nanofibrils, composites, films, scaffolds and sponges. So far a number of research works have been published on chitin and chitosan as wound dressing materials. However, only a few review articles have been reported about chitin and chitosan-based wound dressings with limited information (Ueno, Mori & Fujinaga, 2001; Ravi Kumar, 2000; Kim et al., 2008; Muzzarelli, 2009; Tamura et al., 2010). In this paper, we reviewed a recent development and applications on wound dressing materials based on chitin, chitosan and their derivatives.

2. Applications of chitin and chitosan materials in wound dressing

Chitin and chitosan have an accelerating effect on the wound healing process. A number of studies have demonstrated that chitin and chitosan accelerated wound healing. Chitin and

chitosan have been used as nanofibers, gels, scaffolds, membranes, filaments, powders, granules, sponges or as a composite. The main biochemical activities of chitin and chitosan-based materials in wound healing are polymorphonuclear cell activation, fibroblast activation, cytokine production, gaint cell migration and simulation of type IV collagen synthesis (Mezzana, 2008). Nanofiber matrices have shown tremendous promise as tissue engineering scaffolds for skin substitutes. The advantages of a scaffold composed of ultrafine, continuous fibers are oxygen-permeable high porosity, variable pore-size distribution, high surface to volume ratio and most importantly, morphological similarity to natural extracellular matrix (ECM) in skin, which promote cell adhesion migration and proliferation. Recent advances in process chemistry have made it possible to make chitin and chitosan nanofibril materials with more flexibility and useful for the development of new bio-related products (Mattioli-Belmonte et al., 2007). Dibutyrylchitin (DBC) is a water-soluble chitin derivative with confirmed biological properties. DBC is obtained in the reaction of shrimp chitin with butyric anhydride, under heterogeneous condition, in which perchloric acid was used as a catalyst. Recently, DBC fibrous materials were used for wound healing applications (Chilarski et al., 2007). In this study, DBC non-woven fabrics after γ-sterilisation were applied to a group of nine patients with different indications. Satisfactory results of wound healing were achieved in most cases, especially in cases of burn wounds and postoperative/posttraumatic wounds and various other conditions causing skin/epidermis loss (Chilarski et al., 2007). The effects of DBC on the repair processes and its mechanisms of action were studied by Blasinka & Drobnik (2007). The results showed that DBC implanted subcutaneous to the rats increased weight of the granulation tissue. Increased cell number isolated from the wound and cultured on the DBC films was also revealed. DBC elevates the glycosaminoglycans (GAG) level in the granulation tissue. This study documents the beneficial influence of DBC on the repair, which could be explained by the modification of the extracellular matrix and cell number (Blasinka & Drobnik, 2007). The effectiveness of three chitin nanofibril/chitosan glycolate-based preparations, a spray (Chit-A), a gel (Chit-B), and a gauze (Chit-C), in healing cutaneous lesions was assessed macroscopically and by light microscopy immunohistochemistry (Mattioli-Belmonte et al., 2007). These evaluations were compared to the results obtained using a laser co-treatment. The wound repair provided by these preparations are clearly evident even without the synergistic effect of the laser co-treatment. These results confirmed the effectiveness of chitin nanofibril/chitosan glycolate-based products in restoring subcutaneous architecture.

A biocompatible carboxyethyl chitosan/poly(vinyl alcohol) (CECS/PVA) nanofibers were prepared by electrospinning of aqueous CECS/PVA solution (Zhou et al., 2008) as wound dressing material. The potential use of the CECS/PVA electrospun fiber mats as scaffolding materials for skin regeneration was evaluated *in vitro* using mouse fibroblasts (L929) as reference cell line. Indirect cytotoxicity assessment of the fiber mats indicated that the CECS/PVA electrospun mat was non-toxic to the L929 cell. Cell culture results showed that fibrous mats were good in promoting the L929 cell attachment and proliferation (Zhou et al., 2008). This novel electrospun matrix would be used as potential wound dressing for skin regeneration. It is known that chitosan derivatives with quaternary ammonium groups possess high efficacy against bacteria and fungi. It is now widely accepted that the target site of these cationic polymers is the cytoplasmic membrane of bacterial cells (Tashiro, 2001). The photo cross-linked electrospun mats containing quaternary chitosan (QCS) were efficient in inhibiting growth of Gram-positive bacteria and Gram-negative bacteria (Ignatove et al., 2007). These results suggested that the cross-linked QCS/PVP electrospun

mats are promising materials for wound-dressing applications. Similarly, the photo-cross-linked electrospun nano-fibrous QCS/PVA mats had a good bactericidal activity against the Gram-negative bacteria *E. coli* and Gram-positive bacteria *S. aureus* (Ignatove et al., 2006). These characteristic features of the electrospun mats reveal their high potential for wound-dressing applications. A remarkable wet spun alginate composite containing 0.15-2.0% chitin nanofibrils was also characterized in view of its use as a wound dressing material (Turner et al., 1986; Watthanaphanit, Supaphol, Tamura, Tokura, & Rujiravanit, 2008). The result showed that the overall susceptibility to lysozyme was improved by the tiny amounts of chitin nanofibrils. Moreover, the release of chitin oligomers as a consequence of the enzymatic hydrolysis is a significant contribution to the efficacy of the calcium-alginate dressings. The best biomaterials for wound dressing should be biocompatible and promote the growth of dermis and epidermis layers. Chen et al. (2008) reported composite nanofibrous membrane of chitosan/collagen, which are known for their beneficial effects on wound healing. The membrane was found to promote wound healing and induce cell migration and proliferation. From animal studies, the nanofibrous membrane was found to be better than gauze and commercial collagen sponge in wound healing.

A wound dressing system with high liquid absorbing, biocompatibility, and antibacterial properties was designed based on chitosan/collagen (Wang, Su & Chen, 2008). Various solution weight ratios of collagen to chitosan were used to immobilize on the polypropylene nonwoven fabric, which were pre-grafted with acrylic acid (AA) or *N*-isopropyl acrylamide (NIPAAm) to construct a durable sandwich wound dressing membrane with high water absorbing, easy removal, and antibacterial activity. Swelling properties and antibacterial activity of the membranes were measured, and wound healing enhancement by skin full-thickness excision on animal model was examined. The results indicated that NIPAAm-grafted and collagen/chitosan-immobilized polypropylene nonwoven fabric (PP-NIPAAm-collagen-chitosan) showed a better healing effect than AA-grafted and collagen/chitosanimmobilized polypropylene nonwoven fabric (PP-AA-collagen-chitosan). The wound treated with PP-NIPAAm-collagen-chitosan demonstrated the excellent remodeling effect in histological examination with respect to the construction of vein, epidermis, and dermis at 21 days after skin injury. The values of water uptake and water diffusion coefficient for PP-NIPAAm-collagen-chitosan were higher than that for PP-AA-collagen-chitosan under a given solution weight ratio of collagen/chitosan. Both PP-NIPAAm-collagen-chitosan and PP-AA-collagen-chitosan demonstrated antibacterial activity (Wang, Su & Chen, 2008). A novel genipin cross-linked chitosan film, was prepared as a wound dressing material (Liu, Yao & Fang, 2008). This study examined the *in vitro* properties of the genipin-cross-linked chitosan film and the bi-layer composite. Furthermore, *in vivo* experiments were conducted to study wounds treated with the composite in a rat model. Experimental results showed that the degree of cross-linking and the *in vitro* degradation rate of the genipin-cross-linked chitosan films can be controlled by varying the genipin contents. In addition, the genipin contents should exceed 0.025 wt% of the chitosan-based material if complete cross-linking reactions between genipin and chitosan molecules are required. Water contact angle analysis shows that the genipin-cross-linked chitosan film is not highly hydrophilic; therefore, the genipin-cross-linked chitosan layer is not entangled with the soybean protein non-woven fabric, which forms an easily stripped interface layer between them. Furthermore, this wound dressing material provides adequate moisture, thereby minimizing the risk of wound dehydration and exhibits good mechanical properties. The in vivo histological assessment results revealed that

epithelialization and reconstruction of the wound are achieved by covering the wound with the composite, and the composite is easily stripped from the wound surface without damaging newly regenerated tissue (Liu, Yao & Fang, 2008).

Chitin and chitosan hydrogels are also used as wound dressing materials. Water-soluble chitin hydrogel was prepared with the desired deacetylation degree of 0.50 and molecular weight of 800 kDa as wound dressing material. The resulting hydrogel was found to be more susceptible to the action of lysozyme than chitosan. Full-thickness skin incisions were made on the backs of rats and then chitin, chitosan, chitin powders and the chitin hydrogel were embedded in the wounds. The chitin powder was found to be more efficient than chitin or chitosan as a wound healing accelerator: the wounds treated with chitin hydrogel were completely re-epithelialized, granulation tissues were nearly replaced by fibrosis and hair follicles were almost healed with in 7 days after initial wounding. Also, the chitin hydrogel treated skin had the highest tensile strength and the arrangement of collagen fibers in the skin was similar to normal skins. The chitin hydrogel was considered to be a suitable wound-healing agent due to its easy application and high effectiveness. It is likely that the superior enzymatic degradability and hydrophilicity of water-soluble chitin enhances its activity as a wound-healing accelerator (Cho et al., 1999). Topical formulations based on water soluble chitin were prepared and their effects on wound healing were evaluated on a rabbit ear model (Han, 2005). Full-thickness, open skins wound were made on the ears of rabbits and water soluble chitin ointments were embedded in the open wound. The application of water soluble chitin ointments significantly accelerated wound healing and wound contraction. The areas of epithelialization and granulation tissues in water soluble chitin ointment group were found to be remarkably larger than those in control group (no treatment) and in placebo group (treated with ointment-base materials). A large number of grown granulation tissues including dense fibroblast deposition were observed under the thickened epithelium of the wound treated with water soluble chitin ointments. The number of inflammatory cells in water soluble chitin ointment group was significantly decreased compared with those in control and placebo groups, indicating that water soluble chitin would give low stimuli to wounds and prevent excessive scar formation. Overall results demonstrated that the topical formulation based on water soluble chitin is considered to become an excellent dressing as a wound-healing assistant (Han, 2005).

Pietramaggiori et al. (2008) demonstrated that treatment of full-thickness cutaneous wounds in a diabetic mouse model with chitin-containing membranes results in an increased wound closure rate correlated with impressive rise of angiogenesis. Serum starved endothelial cells were treated with vascular endothelial growth factor (VEGF) or with different concentrations of chitin. As compared with the total number of cells plated (control), at 48 h after serum starvation, there was a twofold reduction of the number of cells, but this reduction was compensated upon addition of VEGF or chitin at either 5 or 10 mg/ml. These results indicate that like VEGF, chitin treatment prevents cell death induced by serum deprivation. However, chitin does not result in a higher metabolic rate (by MTT assays), suggesting that this polymeric material is not causing marked increases in cellular proliferation but is rescuing cells from dying by serum deprivation. To overcome current limitations in wound dressings for treating mustard-burn induced septic wound injuries, a non-adherent wound dressing with sustained anti-microbial capability has been developed (Loke et al., 2000). The wound dressing consists of two layers: the upper layer is a carboxymethyl chitin hydrogel material, while the lower layer is an anti-microbial impregnated biomaterial. The hydrogel layer acts as a mechanical and microbial barrier, and

is capable of absorbing wound exudate. In physiological fluid, the carboxymethylated chitin hydrogel swells considerably, imbibing up to 4 times its own weight of water and is also highly porous to water vapor. The moisture permeability of the dressing prevents the accumulation of fluid in heavily exudating wounds seen in second-degree burns. The lower layer, fabricated from chitosan acetate foam, is impregnated with chlorhexidine gluconate. From the in vitro release studies, the loading concentration was optimized to deliver sufficient anti-microbial drug into the wound area to sustain the anti-microbial activity for 24 h (Loke et al., 2000).

β-Chitin grafted poly(acrylic acid) (PAA) was prepared with the aim of obtaining a hydrogel suitable for wound dressing application. In this study, acrylic acid was first linked to chitin, via ester bonds between the chitin primary alcohol groups and the carboxyl groups of acrylic acid, as the active grafted moiety that was further polymerized upon addition of an initiator to form a network. The chitin-PAA films were synthesized at various acrylic acid contents: the degree of swelling of the chitin-PAA films was in the range of 30-60 times of their original weights depending upon the monomer feed content. The chitin-PAA film with 1:4 weight ratio of chitin: acrylate, possessed optimal physical properties. The cytocompatibility of the film was tested with L929 mouse fibroblasts that proliferated and adhered well onto the film. The morphology and behavior of the cells on the chitin-PAA film were found to be normal after 14 days of culture (Tanodekaew et al., 2004).

Skin repair is an important field of the tissue engineering, especially in the case of extended third-degree burns, where the current treatments are still insufficient in promoting satisfying skin regeneration. Bio-inspired bi-layered physical hydrogels only constituted of chitosan and water were processed and applied to the treatment of full-thickness burn injuries (Boucard et al., 2007). A first layer constituted of a rigid protective gel ensured good mechanical properties and gas exchanges. A second soft and flexible layer allowed the material to follow the geometry of the wound and ensured a good superficial contact. To compare, highly viscous solutions of chitosan were also considered. Veterinary experiments were performed on pig's skins and biopsies at days 9, 17, 22, 100 and 293, were analyzed by histology and immuno-histochemistry. Only one chitosan material was used for each time. All the results showed that chitosan materials were well tolerated and promoted a good tissue regeneration. They induced inflammatory cells migration and angiogenetic activity favouring a high vascularisation of the neo-tissue. At day 22, type I and IV collagens were synthesised under the granulation tissue and the formation of the dermal-epidermal junction was observed. After 100 days, the new tissue was quite similar to a native skin, especially by its aesthetic aspect and its great flexibility (Boucard et al., 2007). Ribeiro et al. (2009) developed chitosan hydrogel for wound dressing. In this study, fibroblast cells isolated from rat skin were used to assess the cytotoxicity of the hydrogel. The results showed that chitosan hydrogel was able to promote cell adhesion and proliferation. Cell viability studies showed that the hydrogel and its degradation by-products are non-cytotoxic. The evaluation of the applicability of chitosan in the treatment of dermal burns in Wistar rats was performed by induction of full-thickness transcutaneous dermal wounds. From macroscopic analysis, the wound beds of the animals treated with chitosan were considerably smaller than those of the controls. Histological analysis revealed lack of a reactive or a granulomatous inflammatory reaction in skin lesions with chitosan and the absence of pathological abnormalities in the organs obtained by necropsy, which supported the local and systemic histocompatibility of the biomaterial. This study suggested that chitosan hydrogel may aid the re-establishment of skin architecture (Ribeiro et al., 2009).

Application of ultraviolet light irradiation to a photocrosslinkable chitosan aqueous solution resulted in an insoluble and flexible hydrogel (Ishihara et al., 2001; 2002). In order to evaluate its accelerating effect on wound healing, full-thickness skin incisions were made on the backs of mice and subsequently a photocross-linkable chitosan aqueous solution was added into the wound and irradiated with ultraviolet light for 90 seconds. Application of the chitosan hydrogel significantly induced wound contraction and accelerated wound closure and healing compared with the untreated controls. Histological examination showed an advanced contraction rate on the first 2 days and tissue fill rate on days 2 to 4 in the chitosan hydrogel-treated wounds. Furthermore, in cell culture studies, chitosan hydrogel culture medium supplemented with 5% fetal-bovine serum was found to be chemo attractant for human dermal fibroblasts in an invasion chamber assay using filters coated with Matrigel and in a cell migration assay. Due to its ability to accelerate wound contraction and healing, chitosan hydrogel may become accepted as an occlusive dressing for wound management (Ishihara et al., 2001; 2002).

For effective wound healing accelerator, water-soluble chitosan/heparin complex was prepared using water-soluble chitosan with wound healing ability and heparin with ability to attract or bind growth factor related to wound healing process (Kweon, Song & Park, 2003). To study the wound healing effect, full thickness skin excision was performed on the backs of the rat and then water-soluble chitosan and water-soluble chitosan/heparin complex ointments were applied in the wound, respectively. After 15 days, gross and histologic examination was performed. Grossly, untreated control group revealed that the wound had well defined margin and was covered by crust. The second group treated with water-soluble chitosan ointment revealed small wound size with less amount of covering crust and ill-defined margin, which appeared to regenerate from margin. The third group treated with water-soluble chitosan/heparin complex ointment appeared to be nearly completely healed. The third group (water-soluble chitosan/heparin) showed nearly complete regeneration of appendage structure similar to normal in the dermis in contrast to control and second group with absence and less number of skin appendages, respectively (Kweon, Song & Park, 2003). For rapid wound healing, a hydrogel sheet composed of a blended powder of alginate, chitin/chitosan and fucoidan (ACF-HS; 60:20:2:4 w/w) has been developed as a functional wound dressing (Murakami et al., 2010). On application, ACF-HS was expected to effectively interact with and protect the wound in rats, providing a good moist healing environment with exudates. In addition, the wound dressing has properties such as ease of application and removal and good adherence. In this work, full-thickness skin defects were made on the backs of rats and mitomycin C solution (1 mg/ml in saline) was applied onto the wound for 10 min in order to prepare healing-impaired wounds. After thoroughly washing out the mitomycin C, ACF-HS was applied to the healing-impaired wounds. Although normal rat wound repair was not stimulated by the application of ACF-HS, healing-impaired wound repair was significantly stimulated. Histological examination demonstrated significantly advanced granulation tissue and capillary formation in the healing-impaired wounds treated with ACF-HS on day 7, as compared to those treated with calcium alginate fiber (Kaltostat; Convatec Ltd., Tokyo, Japan) and those left untreated (Murakami et al., 2010).

PVA, water-soluble chitosan and glycerol based hydrogel was made by irradiation followed by freeze-thawing was evaluated as wound dressing (Yang et al., 2010). MTT assay suggested that the extract of hydrogels was nontoxic towards L929 mouse fibroblasts. Compared to gauze dressing, the hydrogel based on PVA, water-soluble chitosan and

glycerol can accelerate the healing process of full-thickness wounds in a rat model. Wounds treated with hydrogel healed at 11th day postoperatively and histological observation showed that mature epidermal architecture was formed. These results indicate that it is a good wound dressing material (Yang et al., 2010). Sung et al. (2010) developed minocycline-loaded wound dressing with an enhanced healing effect. The cross-linked hydrogel films were prepared with PVA and chitosan using the freeze-drying method. Their gel properties, *in vitro* protein adsorption, release, *in vivo* wound healing effect and histopathology were then evaluated. Chitosan decreased the gel fraction, maximum strength and thermal stability of PVA hydrogel, while it increased the swelling ability, water vapour transmission rate, elasticity and porosity of PVA hydrogel. Incorporation of minocycline did not affect the gel properties, and chitosan hardly affected drug release and protein adsorption. Furthermore, the minocycline-loaded wound dressing composed of 5% PVA, 0.75% chitosan and 0.25% drug was more swellable, flexible and elastic than PVA alone because of relatively weak cross-linking interaction of chitosan with PVA. In wound healing test, this minocycline-loaded PVA-chitosan hydrogel showed faster healing of the wound made in rat dorsum than the conventional product or the control (sterile gauze) due to antifungal activity of chitosan. In particular, from the histological examination, the healing effect of minocycline-loaded hydrogel was greater than that of the drug-loaded hydrogel, indicating the potential healing effect of minocycline. Thus, the minocycline-loaded wound dressing composed of 5% PVA, 0.75% chitosan and 0.25% drug is a potential wound dressing with excellent forming and enhanced wound healing (Sung et al., 2010).

Hydrophilic biopolymeric membranes having a high swellability and permeability for water vapor and gases, good fluid transport via the membrane, and a high selectivity for the transport of polar substances. These properties in combination with an adequate mechanical strength make them highly desirable for the treatment of wounds as a coverage material. Flexibility, softness, transparency and conformability permit to use chitin films as occlusive, semi-permeable wound dressings. The chitin films are generally non-absorbent, exhibiting a total weight gain of only 120-160% in physiological fluid. Dry chitin films transpire water vapor at a rate of about 600 $g/m^2/24$ h, (similar to commercial polyurethane-based film dressings), that rises to 2400 $g/m^2/24$ h when wet (higher than the water vapor transmission rate of intact skin): the chitin films are non-toxic to human skin fibroblasts, maintaining 70-80% cell viability. Wound studies using a rat model showed no signs of allergenicity or inflammatory response. The chitin films displayed accelerated wound healing properties. Wound sites dressed with the chitin films healed faster and appeared stronger than those dressed with Opsite and gauze (Yusof, Wee, Lim, & Khor, 2003). Chitin accelerates macrophage migration and fibroblast proliferation, and promotes granulation and vascularization. While some chitin and chitosan derivatives have biochemical significance, some other is rather inert, as it is the case for dibutyryl chitin; in general, however, they are biocompatible. The high biocompatibility of dibutyryl chitin in the form of films and non-wovens has been demonstrated for human, chick and mouse fibroblasts by various methods: this water-insoluble modified chitin was also tested in full-thickness wounds in rats with good results (Muzzarelli et al., 2005). Traumatic wounds in a large number of patients were treated with chitosan glycolate dressings; in all cases they healed with satisfactory results (Muzzarelli et al., 2007).

Asymmetric chitosan membrane has been prepared by immersion precipitation phase-inversion method and evaluated as wound covering material (Mi et al., 2001). The top layer which contains skin surface and interconnected micropores was designed to prevent

bacterial penetration and dehydration of the wound surface but allows the drainage of wound exudate. The sponge-like sublayer was designed to achieve high adsorption capacity for fluids, drainage of the wound by capillary and enhancement of tissue regeneration. The thickness of the dense skin surface and porosity of sponge-like sublayer was controlled by the modification of phase-separation process using per-evaporation method. The asymmetric chitosan membrane showed controlled evaporative water loss, excellent oxygen permeability and promoted fluid drainage ability. Moreover, this material inhibited exogenous microorganisms invasion due to the dense skin layer and inherent antimicrobial property of chitosan. Wound covered with the asymmetric chitosan membrane was hemostatic and healed quickly. Histological examination confirmed that epithelialization rate was increased and the deposition of collagen in the dermis was well organized by covering the wound with this asymmetric chitosan membrane. The results in this study indicate that the asymmetric chitosan membrane could be adequately employed in the future as a wound dressing material (Mi et al., 2001). Chitosan membranes have been tested as wound dressing at the skin-graft donor site in patients (Azad et al., 2004). Bactigras, a commonly used impregnated tulle gras bandage, served as a control. Chitosan membrane, prepared with a 75% degree of deacetylation and a thickness of 10 μm, was used in non-mesh or mesh form. The progress in wound healing was compared by clinical and histological examination. Itching and pain sensitivity of the wound dressed area was scored with the use of a visual analogue scale. Mesh chitosan membrane in contrast to the nonmesh membrane allowed blood to ooze into the surrounding gauze. After 10 days, the chitosan-dressed area had been healed more promptly as compared with the Bactigras dressed area. Moreover, the chitosan mesh membrane showed a positive effect on the re-epithelialization and the regeneration of the granular layer. The data confirm that chitosan mesh membrane is a potential substitute for human wound dressing (Azad et al., 2004).

Fibroblast growth factor (bFGF) has been shown to stimulate wound healing (Mizuno et al., 2003). However, consistent delivery of bFGF has been problematic. Mizuno et al. (2003) studied the stability of bFGF incorporated into a chitosan film as a delivery vehicle for providing sustained release of bFGF. The therapeutic effect of this system on wound healing in genetically diabetic mice was determined as a model for treating clinically impaired wound healing. A chitosan film was prepared by freeze-drying hydroxypropyl chitosan in acetate buffer solution. Growth factor was incorporated into films before drying by mixing bFGF solution with the hydroxypropyl chitosan solution. bFGF activity remained stable for 21 days at 5 °C, and 86.2% of activity remained with storage at 25 °C. Full-thickness wound were created on the backs of diabetic mice, and chitosan film or bFGF-chitosan film was applied to the wound. The wound was smaller after 5 days in both groups, but the wound was smaller on day 20 only in the bFGF-chitosan group. Proliferation of fibroblasts and an increase in the number of capillaries were observed in both groups, but granulation tissue was more abundant in the bFGF-chitosan group. These results suggest that chitosan itself facilitates wound repair and that bFGF incorporated into chitosan film is a stabile delivery vehicle for accelerating wound healing (Mizuno et al., 2003).

Surface modification of biomaterials is another way to tailor cell responses whilst retaining the bulk properties. Silva et al. (2008) prepared chitosan membranes by solvent casting and treated with nitrogen or argon plasma at 20W for 10-40 min. Atomic Force Microscopy analysis (AFM) indicated an increase in the surface roughness as a result of the etching process. X-ray photoelectron spectroscopy (XPS) and contact angle measurements showed different surface elemental compositions and higher surface free energy on the surface

modified chitosan membrane. The MTS test and direct contact assays with an L929 fibroblast cell line indicated that the plasma treatment improved the cell adhesion and proliferation. Overall, the results demonstrated that such plasma treatments could significantly improve the biocompatibility of chitosan membranes and thus improve their potential in wound dressings and tissue engineering applications (Silva et al., 2008).

HemCon® bandage is an engineered chitosan acetate preparation designed as a hemostatic dressing, and is under investigation as a topical antimicrobial dressing (Burkatovskaya et al., 2008). The conflicting clamping and stimulating effects of chitosan acetate bandage on normal wounds were studied by removing the bandage from wounds at times after application ranging from 1 hour to 9 days. The results showed that three days application gave the earliest wound closure, and all application times gave a faster healing slope after removal compared with control wounds. Chitosan acetate bandage reduced the number of inflammatory cells in the wound at days 2 and 4, and had an overall beneficial effect on wound healing especially during the early period where its antimicrobial effect is most important (Burkatovskaya et al., 2008). The hydrophilic polymer membranes based on macromolecular chitosan networks have been synthesized and characterized (Clasen, Wilhelms & Kulicke, 2006). The structure of the membrane has been altered in several ways during the formation to adjust the properties, particularly with regard to the elasticity, tensile strength, permeability and surface structure. An alteration of the network structure was achieved by addition of flexibilizer, cross-linking with dialdehydes, simplex formation of the chitosan with the polyanion sulfoethyl cellulose, and the introduction of artificial pores on the micro- and nanometer scale into the chitosan matrix with silica particles or poly(ethylene glycol) (PEG). In this study, the impact of the network structures on physical properties of the membranes, the water vapor and gas permeability and the tensile strength was reported to evaluate possible application of the membranes as a wet wound dressing material with microbial barrier function that actively assists the healing process of problematic wounds (Clasen, Wilhelms & Kulicke, 2006).

Chitosan derivative sheets and pastes were evaluated *in vitro* for possible utilization in wound dressing applications (Rasad et al., 2010). In this study, the cytotoxicity of oligo chitosan, *N, O*-carboxymethyl-chitosan (*N, O*-CMC) and *N*-carboxymethyl-chitosan (*N*-CMC) derivatives in sheet like and paste forms were evaluated using primary normal human dermal fibroblast cultures and hypertrophic scars; a fibrotic conditions representing a model of altered wound healing with overproduction of extracellular matrix and fibroblast hyperproliferative activity. Cytotoxicities of these chitosan derivatives were assessed using MTT assay. The results indicated that both chitosan derivative sheets and pastes have appropriate cytocompatibility and appear promising as safe biomaterials with potential wound healing applications. *N, O*-CMC sheet exhibited highest cytocompatibility property and may be regulated by matrix metalloproteinase-13 (MMP-13) in controlling the cell growth and its expression level (Rasad et al., 2010).

In situ photopolymerized hydrogel dressings create minimally invasive methods that offer advantages over the use of preformed dressings such as conformability in any wound bed, convenience of application and improved patient compliance and comfort. An in situ-hydrogel membrane was prepared through ultraviolet cross-linking of a photocross-linkable azidobenzoic hydroxypropyl chitosan aqueous solution (Lu et al., 2010). The prepared hydrogel membrane is stable, flexible, and transparent, with a bulk network structure of smoothness, integrity, and density. The hydrogel membrane also exhibited barrier function, as it was impermeable to bacteria but permeable to oxygen. In vitro experiments using two

major skin cell types (dermal fibroblast and epidermal keratinocyte) revealed the hydrogel membrane have neither cytotoxicity nor an effect on cell proliferation. The in situ photocross-linked azidobenzoic hydroxypropyl chitosan hydrogel membrane has a great potential in the management of wound healing and skin burn (Lu et al., 2010). A wound dressings film composed of chitosan and minocycline hydrochloride was prepared using commercial polyurethane film (Tegaderm) as a backing (Aoyagi, Onishi & Machida, 2007). Various formulations were applied to severe burn wounds in rats in the early stage, and the wound status and change in the wound surface area were examined. The use of 10 mg of minocycline hydrochloride and complete sealing with Tegaderm had a negative effect. Minocycline hydrochloride ointment was not effective, but Geben cream was fairly effective. However, chitosan (83% degree of deacetylation) with a cutting of Tegaderm film containing 2mg of minocycline hydrochloride and chitosan (83% degree of deacetylation) films showed an excellent effect (Aoyagi, Onishi & Machida, 2007). To accelerate wound healing by stimulating the recruitment of fibroblasts and improve the mechanical properties of collagen matrixes, *N*, *O*-CMC was incorporated into the backbone of a collagen matrix without or with chondroitin sulfate or an acellular dermal matrix (Chen et al., 2006). The result of a cell migration study demonstrated that the migration of fibroblasts was significantly enhanced by *N*, *O*-CMC in a concentration-dependent manner. In the analysis with a dynamic mechanical analyzer, *N*, *O*-CMC-chondroitin sulfate/collagen matrixes presented higher tensile strengths than *N*, *O*-CMC/acellular dermal matrix/collagen matrixes. Skin fibroblasts cultured on the matrixes containing did *N*, *O*-CMC showed increased proliferation and secretion of three kinds of cytokines compared with the control. Results of the in vivo wound healing study showed that matrixes incorporating *N*, *O*-CMC showed markedly enhanced wound healing compared with the control. These results clearly suggest that *N*, *O*-CMC/collagen matrixes containing chondroitin sulfate or acellular dermal matrix can be used as potential wound dressings for clinical applications (Chen et al., 2006).

Biocompatible chitosan/polyethylene glycol diacrylate (PEGDA) blend films were successfully prepared by Michael addition reaction with different weight ratios as wound dressing materials (Zhang, Yang & Nie, 2008). The mechanical properties and the swelling property of chitosan were found to be enhanced after the chemical modification. Indirect cytotoxicity assessment of films with mouse fibroblasts (L929) indicated that the material showed no cytotoxicity toward growth of L929 cell and had good in vitro biocompatibility. SEM observation indicated that the microporous surface structure of the chitosan/PEGDA films was good to grow, proliferate, and differentiate of L929 cell. These chitosan/PEGDA films have the potential to be used as wound dressing material (Zhang, Yang & Nie, 2008).

To create a moist environment for rapid wound healing, a chitosan-PVA-alginate film with sustained antibacterial capacity had been developed by the casting/solvent evaporation method (Pei et al., 2008). This new type of chitosan-PVA-alginate film consists of a chitosan top layer and sodium alginate sublayer separated by an ornidazole (OD)-incorporated PVA layer, exhibited perfect binding characteristics among the three layers. Physical characterization of the chitosan-PVA-alginate film showed that the triple-layer film had excellent light transmittance, control of water vapor transmission rate and fluid drainage ability promotion, compared with the single-layer film. From the *in vitro* release studies, about 90% of OD was released from the composite films within 60 min, and no significant difference was observed in cumulative release percentage with increases in the drug content. The composite film at low concentration of OD (1.0 mg/cm^2) showed effective antimicrobial activity in the cultures of *Staphylococcus aureus* and *Escherichia coli* in agar

plates. The results indicated that chitosan-PVA-alginate composite film incorporated with OD has the potential for wound dressing application (Pei et al., 2008).
Chitosan/hyaluronic acid composite films with high transparency could be fabricated for wound dressing material on glass or poly(methyl methacrylate) substrates (Xu et al., 2007). Along with the increase of hyaluronic acid amount, the resulting films became rougher as detected by AFM. However, increase of the hyaluronic acid amount weakened the water vapor permeability, bovine albumin adsorption and fibroblast adhesion, which are desirable characteristics for wound dressing. *In vivo* animal test revealed that compared with the vaseline gauge the chitosan/ hyaluronic acid film could more effectively accelerate the wound healing and reduce the occurrence of re-injury when peeling off the dressing again. These results demonstrate that the chitosan mixed hyaluronic acid may produce inexpensive wound dressing with desired properties (Xu et al., 2007). Membranes made of chitosan in combination with alginates as polyelectrolyte complexes have also been prepared. They display greater stability to pH changes and are more effective as controlled release membranes than either the chitosan or alginate separately. The membranes based on chitosan/alginate could be used on highly exuding wounds and prevented the bacterial infections (Rodrigues, Sanchez, Da Costa, & Moraes, 2008).
A polyelectrolyte complex (PEC), which consists of chitosan as a cationic and γ-poly (glutamic acid) (γ-PGA) as an anionic polyelectrolyte, was developed as a wound dressing material (Tsao et al., 2010). The physical and chemical properties of the chitosan/γ-PGA PECs were fully investigated. Experimental results showed that the physical and chemical properties and the *in vitro* degradation of the chitosan/γ-PGA PECs directly reflect the degree of complex formation. In addition, chitosan/γ-PGA PECs provide suitable moisture content and exhibit good mechanical properties, both favorable for allowing dressing to be easily stripped off from the wound surface without damaging newly regenerated tissue. Histological examinations revealed that, more than 50% of re-epithelialization and regeneration of the wound are achieved by dressing it with the chitosan/γ-PGA PECs. On the basis of wound-healing efficacy, chitosan/γ-PGA PECs can be potentially applied as a wound dressing material (Tsao et al., 2010). A membrane composed of an alginate layer and a chitosan layer with sustained antimicrobial efficacy was prepared (Dong et al., 2010). In this study, ciprofloxacin HCl was incorporated into the alginate layer. Water uptake capacity, in vitro drug release, and in vitro antimicrobial activity were evaluated. The composite membrane exhibited perfect binding characteristic between the two layers. The water uptake capacity of all the membranes was above 800%. The ciprofloxacin HCl was found to be released from the composite membranes for 48 h. The membrane was found to control the bacterial growth persistently. The results suggested that this chitosan/alginate composite membrane incorporated with ciprofloxacin HCl had the potential for wound dressing application (Dong et al., 2010). The biocompatible and microbiologically safe composite membranes based on chitosan and 2-hydroxyethyl methacrylate (HEMA) have been prepared by gamma irradiation (Casimiro, Gil & Leal, 2010). The antimicrobial activity of obtained membranes against several reference strains was evaluated after inoculation. Sub-lethal gamma radiation doses were also applied in artificially contaminated membranes and the D values of microorganisms in use were determined in order to predict which radiation dose could guarantee membranes microbiological safety. *In vitro* haemolysis tests were performed using drug loaded membranes irradiated at different doses. Results point out that those membranes naturally exhibit antimicrobial properties. Also show that, over the studied range values, drug loaded irradiated membranes display a non-significant level of haemolysis (Casimiro, Gil & Leal, 2010).

Antibiotic resistance of microorganisms is one of the major problems faced in the field of wound care management resulting in complications such as infection and delayed wound healing. Currently a lot of research is focused on developing newer antimicrobials to treat wounds infected with antibiotic resistant microorganisms (Rai et al., 2009). Ag has been used as an antimicrobial agent for a long time in the form of metallic silver and silver sulfadiazine ointments. Recently Ag nanoparticles have come up as a potent antimicrobial agent and are finding diverse medical applications ranging from silver based dressings to silver coated medical devices (Rai et al., 2009). It is well known that membranes with asymmetric structures are of industrial importance. The top skin layer renders the membrane selectivity, whereas the porous support layer provides the membrane with mechanical strength. Ag sulfadiazine-incorporated asymmetric chitosan membranes with sustained antimicrobial capability have been developed by a dry/wet phase separation method to overcome current limitations in Ag sulfadiazine cream for treating acute burn wounds (Mi et al., 2003). The asymmetric chitosan membrane consists of a dense skin and sponge-like porous layer, which can fit the requirements (oxygen permeability, controlled water vapor evaporation and the drainage of wound exudates) for this membrane to be used as a wound dressing. Silver sulfadiazine cream is a traditionally-used antibacterial for the prevention of wound infection; however, it has raised concern of potential silver toxicity. The asymmetric chitosan membrane acts as a rate-controlling wound dressing to incorporate silver sulfadiazine, and release sulfadiazine and Ag ions in a sustained way. The release mechanism depends on the mass-transfer resistance for the release of sulfadiazine and silver ions from the dense and sponge-like porous layers, and the chemical resistance for the interaction of silver ions with chitosan polymeric chains, respectively. The bacteria-cultures (*Pseudomonas aeruginosa* and *Staphylococcus aureus*) and cell-culture (3T3 fibroblasts) assay of the Ag sulfadiazine-incorporated asymmetric chitosan membrane showed prolonged antibacterial activity and decreased potential silver toxicity (Mi et al., 2003).

Hemorrhage remains a leading cause of early death after trauma, and infectious complications in combat wounds continue to challenge caregivers. Although chitosan dressings have been developed to address these problems, they are not always effective in controlling bleeding or killing bacteria. Ong et al. (2008) aimed to refine the chitosan dressing by incorporating a procoagulant (polyphosphate) and silver. Chitosan containing different amounts and types of polyphosphate polymers was fabricated, and their hemostatic efficacies evaluated *in vitro*. The optimal chitosan-polyphosphate formulation accelerated blood clotting, increased platelet adhesion, generated thrombin faster, and absorbed more blood than chitosan. Silver-loaded chitosan-polyphosphate exhibited significantly greater bactericidal activity than chitosan-polyphosphate *in vitro*, achieving a complete kill of *Pseudomonas aeruginosa* and a >99.99% kill of *Staphylococcus aureus* consistently. The Ag dressing also significantly reduced mortality from 90% to 14.3% in a *P. aeruginosa* wound infection model in mice. This study demonstrated for the first time, the application of polyphosphate as a hemostatic adjuvant, and developed a new chitosan-based composite with potent hemostatic and antimicrobial properties (Ong et al., 2008). Wound dressing composed of nano Ag and chitosan was fabricated using chitosan films preliminarily sterilized by immersion in 75% alcohol solution overnight, exposed to ultraviolet light for 1h on each side and rinsed with sterile water (Lu, Gao, & Gu, 2008). Sterile chitosan films were immersed in nano Ag solution at 4 °C for 12 h for self-assembly of the nano- Ag chitosan films via Ag-N bonding and to obtain 0.35% w/w Ag in the dressing material. In this study, AFM was used to examine the dressing, and SEM identified

the nano Ag immobilized on the chitosan film. Sterility and pyrogen testing assessed biosafety, and efficacy was evaluated using Sprague-Dawley rats with deep partial-thickness wounds. Ag sulfadiazine and chitosan film dressings were used as controls. At day 13, the healing rate of the Ag-chitosan dressing group was higher than the rates of the control groups at 99% compared with 82% for the Ag sulfadiazine group. The healing time was 13.51 ± 4.56 days for the Ag-chitosan group, and 17.45 ± 6.23 days for the Ag sulfadiazine group, respectively. Observations made on the histological sections on day 9 indicated that in the nano Ag dressing group a continuous epithelial lamina was formed, together with some sebaceous glands. The Ag sulfadiazine group showed no epithelial laminae, whilst the chitosan film group exhibited patchy epithelial laminae with a few sebaceous glands. At 13 days the blood silver content was 5 times normal and on the 45th day post-operatively, the Ag content of liver, kidney and brain had increased in both nano-silver and Ag sulfadiazine groups but more so in the latter, where the liver silver content was 100 times greater than normal. Due to its distinct antimicrobial action towards a broad range of bacteria, yeast, fungi and viruses, the Sprague-Dawley rats of the nano- Ag group showed less post-operative infection than the control groups. The wound environment far less affects nano-Ag than the ionic form of Ag: therefore at the same concentration, the bactericidal activity of nano-Ag is greater than that of the ionic form (Lu, Gao, & Gu, 2008).

Thomas et al. (2009) developed chitosan/Ag nanoparticles films by a simple photochemical method of reduction of silver ions in an acidic solution of silver nitrate and chitosan. Chitosan used here is a natural polymer and acts as a very good chelating and stabilizing agent; thus, this approach of formation of chitosan/silver nanoparticle films is proved to be an excellent 'green approach' for the synthesis of metal nanoparticle composites. The developed chitosan-nano Ag films demonstrated excellent antibacterial action against model bacteria, *Escherichia coli* and *Bacillus*. These films can be used as antimicrobial packaging materials, as wound dressings and can also be grafted onto various implants (Thomas et al. 2009). Vimala et al. (2010) prepared porous chitosan-Ag nanocomposite films in view of their increasing areas of application in wound dressing, antibacterial application, and water purification. The entire process consists of three-steps including Ag ion-poly(ethylene glycol) (PEG) matrix preparation, addition of chitosan matrix, and removal of PEG from the film matrix. Chitosan films having uniform pores were impregnated with Ag nanoparticles were fabricated by this approach. The embedded silver nanoparticles were clearly observed throughout the film in SEM and the extracted Ag nanoparticles from the porous chitosan-Ag nanocomposite showed ~12nm in TEM. Improved mechanical properties were observed for porous chitosan-Ag nanocomposite than for chitosan blend and chitosan-Ag nanocomposite films. Further, the examined antibacterial activity results of these films revealed that porous chitosan-Ag nanocomposite films exhibited superior inhibition (Vimala et al. 2010).

ZnO has attracted wide interest because of its good photocatalytic activity, high stability, antibacterial property and non-toxicity (Cohen, 2000; Wang, 2004; Sharma et al., 1995). Novel chitosan/Ag/ZnO blend films were prepared via a new method of sol-cast transformation (Li et al., 2010). The results revealed that ZnO and Ag nanoparticles with spherical and granular morphology had uniform distribution within chitosan polymer. The product had excellent antimicrobial activities against *B. subtilis*, *E. coli*, *S. aureus*, *Penicillium*, *Aspergillus*, *Rhizopus* and *yeast*. Chitosan/Ag/ZnO blend films had higher antimicrobial activities than chitosan/Ag and chitosan/ZnO blend films. Moreover, the blend films almost maintained the initial color of chitosan, which have potential application as

antibacterial materials (Li et al., 2010). In another study ZnO nanoparticles were prepared by the Pechini method from polyester by reacting citric acid with ethylene glycol in which the metal ions are dissolved, and incorporated into blend films of chitosan and PVA with different concentrations of polyoxyethylene sorbitan monooleate, Tween 80 (Vicentini, Smania Jr & Laranjeira, 2010). The antibacterial activity of the films was tested, and the films containing ZnO nanoparticles showed antibacterial activity toward the bacterial species *S. aureus*. The observed antibacterial activity in the composite films prepared in this work suggests that they may be used as hydrophilic wound and burn dressings (Vicentini, Smania Jr & Laranjeira, 2010). The above studies indicated that ZnO nanoparticles incorporated with chitosan enhanced the antibacterial activity.

Collagen-chitosan spongy skin was developed as a scaffold for the reconstruction of skin *in vitro*: this artificial skin promoted the remodeling of an extracellular matrix similar to normal dermis (Berthod et al., 1996). Smad3 mediates the intracellular signaling of TGF-b1 superfamily and plays a critical role in the cellular proliferation, differentiation and elaboration of matrix pivotal to cutaneous wound healing. Smad3 antisense oligonucleotides (ASOs) impregnated polyelectrolyte complex scaffold containing chitosan and sodium alginate was prepared for accelerated wound healing (Hong et al., 2008). Physicochemical properties of polyelectrolyte complex were characterized by zeta potential, SEM and bioadhesive test. Full-thickness, excisional wounds were made on the dorsum of C57BL6 mice. Then, smad3 ASOs-polyelectrolyte complex, polyelectrolyte complex alone, smad3 ASOs and gauze dressing were applied to determine concentration of TGF-b1 and collagen in tissues. Zeta potentials and bioadhesive strengths of ASOs-polyelectrolyte complex were increased as the chitosan ratio in polyelectrolyte complex. In smad3 ASOs-polyelectrolyte complex, the healing process suggested by wound closure and histological observation was faster than other groups because collagen contents increased and level of TGF-b1 decreased. These results demonstrate that the smad3 ASOs-polyelectrolyte complex composed of chitosan and sodium alginate scaffold could be applied for accelerated wound healing (Hong et al., 2008). The gold colloid/chitosan film scaffold, accelerate proliferation of newborn mice keratinocytes, was fabricated by self-assembly technology (Zhang et al., 2009). In this study, the keratinocytes were cultured and observed on three different extracellular matrices: gold colloid/chitosan film scaffold, chitosan film and cell culture plastic (control groups). 6, 12 and 24 h after inoculation, the cell attached ratios were calculated respectively. In comparison to control groups, gold colloid/chitosan film scaffold could significantly increase the attached ratio of keratinocytes and promote their growth. Meanwhile, there were not any fusiform fibroblasts growing on this scaffold. The rapidly proliferating keratinocytes were indentified and characterized by immunohisto chemistry and TEM, which showed the cells maintain their biological activity well. The results indicated that gold colloid/chitosan film scaffold was nontoxic to keratinocytes, and was a good candidate for wound dressing in skin tissue engineering (Zhang et al., 2009).

Recently, a few studies have been reported on chitin scaffolds with Ag nanoparticles to treat patients with deep burns, wounds etc. Madhumathi et al. 2010 developed and characterized novel *α*-chitin/nano Ag composite scaffolds for wound healing applications. The antibacterial, blood clotting and cytotoxicity of the prepared composite scaffolds were studied. These *α*-chitin/nano Ag composite scaffolds were found to be bactericidal against *S.aureus* and *E.coli* with good blood clotting ability. Sudheesh Kumar et al. (2010) also reported about *β*-chitin/nano Ag composite scaffolds for wound healing applications using *β*-chitin hydrogel with Ag nanoparticles. The antibacterial, blood clotting, swelling, cell

attachment and cytotoxicity studies of the prepared composite scaffolds were evaluated. The prepared β-chitin/nano Ag composite scaffolds were found to be bactericidal against *Escherichia coli* and *Staphylococcus aureus* and they showed good blood-clotting ability as well. Cell attachment studies using vero (epithelial) cells showed that the cells were well attached on the β-chitin/nano Ag scaffolds. These results suggested that both *a* and β-chitin/nano Ag composite scaffolds could be a promising candidate for wound dressing applications.

A porous sponge-type wound dressing materials based on β-chitin were prepared (Lee et al., 2000). Oxygen permeabilities of the samples were found to be relatively good. These sponge-type samples contained antimicrobial agents, silver sulfadiazine, in order to prevent bacteria infection on a wound surface. Anti-microbacterial tests on agar plate were carried out to confirm the bactericidal capacity of wound dressing materials. These materials impregnating silver sulfadiazine had the complete bactericidal capacity against *Pseudomonas aeruginosa* up to 7 days. Finally, a wound healing effect of β-chitin-based semi-interpenetrating polymer networks was evaluated from the animal test using the wistar rat *in vivo*. Histological studies confirmed the proliferation of fibroblasts in the wound bed and a distinct reduction in infectious cells (Lee et al., 2000). Denkbas et al. (2004) prepared and characterized chitosan sponges encapsulated with a model antibiotic drug, norfloxacin, as wound dressing material. The cross-linked chitosan sponges were prepared by a solvent evaporation technique. The results indicated that the chitosan sponges were in the fibrillar structure. In this study, the swelling behavior, norfloxacin loading, *in vitro* release characteristics, and antibacterial activity were determined. The effects of cross-linker concentration, norfloxacin/chitosan ratio, chitosan molecular weight, and base concentration were also investigated. The most effective parameter was found to be the degree of neutralization. It was also observed that the equilibrium-swelling ratio decreased with increasing cross-linking density. The norfloxacin release was found to be swelling controlled initially and diffusion controlled at the extended release periods. It was found that the antibacterial activity was directly proportional to the release rate. These chitosan based sponges could be used for wound dressing applications (Denkbas et al., 2004).

3. Conclusions

From this review, chitin and chitosan seem to be excellent dressing materials for the wound healing. In this paper, we overviewed the recent progress of chitin and chitosan-based fibrous materials, hydrogels, membranes, scaffolds and sponges in wound dressing. In the area of wound management, the use of chitin, chitosan and its derivative is immense. Chitin and chitosan have excellent properties such as biodegradability, bio-compatibility, non-toxicity and have been shown to enhanced wound healing in animals and humans. To improve the potential of chitin and chitosan for wound dressing applications, further studies are needed.

4. Acknowledgements

One of the authors **R. Jayakumar** is grateful to SERC Division, Department of Science and Technology (DST), India, for providing the fund under the scheme of "Fast Track Scheme for Young Investigators" (Ref. No. SR/FT/CS-005/2008). The authors thankful to Department of Biotechnology (DBT), Government of India for providing financial support to

carried out research work. **Dr. S. V. Nair** is also grateful to DST, India, which partially supported this work, under a center grant of the Nanoscience and Nanotechnology Initiative program monitored by Dr. C. N. R. Rao.

5. References

Anitha A, Deepa N, Chennazhi KP, Nair SV, Tamura H, Jayakumar R. Development of mucoadhesive thiolated chitosan nanoparticles for biomedical applications. Carbohydr Polym 2011; 83: 66-73.

Anitha A, Divya Rani VV, Krishna R, Sreeja V, Selvamurugan N, Nair SV, Tamura H, Jayakumar R. Synthesis, characterization, cytotoxicity and antibacterial studies of chitosan, *O*-carboxymethyl and *N*, *O*-carboxymethyl chitosan nanoparticles. Carbohydr Polym 2009; 78: 672-677.

Aoyagi S, Onishi H, Machida Y. Novel chitosan wound dressing loaded with minocycline for the treatment of severe burn wounds. Int J Pharm 2007; 330: 138-145.

Azad AK, Sermsintham N, Chandrkrachang S, Stevens WF. Chitosan membrane as a wound-healing dressing: Characterization and clinical application. J Biomed Mater Res Appl Biomat 2004; 69B: 216-222.

Berthod F, Sahuc F, Hayek D, Damour O, Collombel, C. Deposition of collagen fibril bundles by long-term culture of fibroblasts in a collagen sponge. J Biomed Mater Res 1996; 32: 87.

Blasinska A, Drobnik J. Effects of nonwoven mats of di-*O*-butyrylchitin and related polymers on the process of wound healing. Biomacroloecules 2008; 9: 776-782.

Boucard N, Vitona C, Agayb D, Maric E, Rogerc T, Chancerelleb Y, Domard A. The use of physical hydrogels of chitosan for skin regeneration following third-degree burns. Biomaterials 2007; 28: 3478-3488.

Bruin P, Jonkman MF, Meijer HJ, Pennings AJ. A new porous polyetherurethane wound covering. J Biomed Mater Res 1990; 24: 217-226.

Burkatovskaya M, Castano, AP, Demidova-Rice TN, Tegos GP, Hamblin MR. Effect of chitosan acetate bandage on wound healing in infected and noninfected wounds in mice. Wound Rep Reg 2008; 16: 425-431.

Casimiro MH, Gil MH, Leal JP. Suitability of gamma irradiated chitosan based membranes as matrix in drug release system. Int J Pharmaceutics 2010; 395: 142-146.

Chen RN, Wang GM, Chen CH, Ho HO, Sheu MT. Development of *N*, *O*-(carboxymethyl)chitosan/collagen matrixes as a wound dressing. Biomacromolecules 2006; 7: 1058-1064.

Chen Z, Mo X, He C, Wang H. Intermolecular interactions in electrospun collagen-chitosan complex nanofibers. Carbohydr Polym 2008; 72: 410-418.

Chilarski A, Szosland L, Krucinska I, Kiekens P, Blasinska A, Schoukens G, Cislo R, Szumilewicz J. Novel dressing materials accelerating wound healing made from dibutyrylchitin. Fibers. Tex Eas Eur 2007; 15: 77-81.

Cho YW, Cho YN, Chung SH, Yoo G, Ko SW. Water-soluble chitin as a wound healing accelerator. Biomaterials 1999; 20: 2139-2145.

Clasen C, Wilhelms T, Kulicke WM. Formation and characterization of chitosan membranes. Biomacromolecules 2006; 7: 3210-3222.

Cohen ML. The theory of real materials. Annu Rev Mater Sci 2000; 30: 1-26.

Denkbas EB, Ozturk E, Ozdem N, Kecec K, Agalar C. Norfloxacin-loaded chitosan sponges as wound dressing material. J Biomat Appl 2004; 18: 291-303.

Dev A, Mohan JC, Sreeja V, Tamura H, Patzke GR, Nair SV, Jayakumar R. Novel carboxymethyl chitin nanoparticles for cancer drug delivery applications. Carbohydr Polym 2010; 79: 273-279.

Dong Y, Liu HZ, Xu L, Li G, Ma ZN, Han F, Yao HM, Sun YH, Li SM. A novel CHS/ALG bi-layer composite membrane with sustained antimicrobial efficacy used as wound dressing. Chinese Chem Lett 2010; 21: 1011-1014.

Draye JP, Delaey B, Van Den Voorde A, Van Den Bulcke A, De Reu B, Schacht E. In vitro and in vivo biocompatibility of dextran dialdehyde cross-linked gelatin hydrogel films. Biomaterials 1998; 19: 1677-1687.

Han SS. Topical formulations of water-soluble chitin as a wound healing assistant-evaluation on open wounds using a rabbit ear model. Fibers and Polymers 2005; 6: 219-223.

Hong HJ, Jin SE, Park JS, Ahn WS, Kim CK. Accelerated wound healing by smad3 antisense oligonucleotides-impregnated chitosan/alginate polyelectrolyte complex. Biomaterials 2008; 29: 4831-4837.

Ignatova M, Manolova N, Rashkov I. Novel antibacterial fibers of quaternized chitosan and poly(vinyl pyrrolidine) prepared by electrospinning. Eur Polym J 2007; 43: 1112-1122.

Ignatova M, Starbova K, Markova N, Manolova N, Rashkov I. Electrospun nano-fibre mats with antibacterial properties from quaternized chitosan and poly(vinyl alcohol), Carbohydr Res 2006; 341: 2098-2107.

Ishihara M, Nakanishi K, Ono K, Sato M, Kikuchi M, Saito Y, Yura H, Matsui T, Hattori H, Uenoyama M, Kurita A. Photocrosslinkable chitosan as a dressing for wound occlusion and accelerator in healing process. Biomaterials 2002; 23: 833-840.

Ishihara M, Ono K, Sato M, Nakanishi K, Saito Y, Yura H, Matsui T, Hattori H, Fujita M, Kikuchi M, Kurita A. Acceleration of wound contraction and healing with a photocrosslinkable chitosan hydrogel. Wound Rep Reg 2001; 9: 513-521.

Jayakumar R, Chennazhi KP, Muzzarelli RAA, Tamura H, Nair SV, Selvamurugan N. Chitosan conjugated DNA nanoparticles in gene therapy. Carbohydr Polym 2010a; 79: 1-8.

Jayakumar R, Divya Rani VV, Shalumon KT, Sudheesh Kumar PT, Nair SV, Furuike T, Tamura H. Bioactive and osteoblast cell attachement studies of novel *α*-, and *β*-chitin membranes for tissue engineering applications, Int J Biol Macromol 2009a; 45: 260-264.

Jayakumar R, Menon D, Manzoor K, Nair SV, Tamura H. Biomedical applications of chitin and chitosan nanomaterials-A short review. Carbohydr Polym 2010b; 82: 227-232.

Jayakumar R, Nwe N, Tokura S, Tamura H. Sulfated chitin and chitosan as novel biomaterials. Int J Biol Macromol 2007; 40: 175-181.

Jayakumar R, Prabaharan M, Nair SV, Tamura H. Novel chitin and chitosan nanofibers in biomedical applications. Biotech Adv 2010c; 28: 142-150.

Jayakumar R, Prabaharan M, Nair SV, Tokura S, Tamura H, Selvamurugan N. Novel carboxymethyl derivatives of chitin and chitosan materials and their biomedical applications. Prog Mater Sci 2010d; 55: 675-709.

Jayakumar R, Prabaharan M, Reis RL, Mano JF. Graft copolymerized chitosan-Present status and applications. Carbohydr Polym 2005; 62: 142-158.

Jayakumar R, Reis RL, Mano JF. Phosphorous containing chitosan beads for controlled oral drug delivery. J Bioact Compat Polym 2006; 21: 327-340.

Kim IY, Seo SJ, Moon HS, Yoo MK, Park IY, Kim BC, Cho CS. Chitosan and its derivatives for tissue engineering applications. Biotech Adv 2008; 26: 1-21.

Kweon DK, Song SB, Park YY. Preparation of water-soluble chitosan/heparin complex and its application as wound healing accelerator. Biomaterials 2003; 24: 1595-1601.

Lee YM, Kim SS, Park MH, Song KW, Sung YK, Kang IK. Beta-chitin-based wound dressing containing silver sulfurdiazine. J Mater Sci Mater Med 2000; 11: 817-823.

Li LH, Deng JC, Deng HR, Liu ZL, Li XL. Preparation, characterization and antimicrobial activities of chitosan/Ag/ZnO blend films. Chem Eng J 2010; 160: 378-382.

Liu BS, Yao CH, Fang SS. Evaluation of a non-woven fabric coated with a chitosan bi-layer composite for wound dressing. Macromol Biosci 2008; 8: 432-440.

Loke WK, Lau SK, Yong LL, Khor E, Sum CK. Wound dressing with sustained anti-microbial capability. J Biomed Mater Res Appl Biomater 2000; 53: 8-17.

Lu G, Ling K, Zhao P, Xu Z, Deng C, Zheng H, Huang J, Chen J. A novel in situ-formed hydrogel wound dressing by the photocross-linking of a chitosan derivative. Wound Rep Reg 2010; 18: 70-79.

Lu SY, Gao WJ, Gu HY. Construction, application and biosafety of silver nanocrystalline chitosan wound dressing. Burns 2008; 34: 623-628.

Madhumathi K, Binulal NS, Nagahama H, Tamura H, Shalumon KT, Selvamurugan N, et al. Preparation and characterization of novel_α-chitin-hydroxyapatite composite membranes for tissue engineering applications. Int J Biol Macromol 2009; 44: 1-5.

Madhumathi K, Sudheesh Kumar PT, Abilash S, Sreeja V, Tamura H, Manzoor K, Nair SV, Jayakumar R. Development of novel chitin/nanosilver composite scaffolds for wound dressing applications. J Mater Sci Mater Med 2010; 21: 807-813.

Maeda Y, Jayakumar R, Nagahama H, Furuike T, Tamura H. Synthesis, characterization and bioactivity studies of novel β-chitin scaffolds for tissue-engineering applications. Int J Biol Macromol 2008; 42: 463-467.

Marreco PR, Moreira PL, Genari SC, Moraes AM. Effects of different sterilization methods on the morphology, mechanical properties and cytotoxicity of chitosan membranes used as wound dressings. J Biomed Mater Res Part B: Appl Biomater 2004; 71B: 268-277.

Mattioli-Belmonte M, Zizzi A, Lucarini G, Giantomassi F, Biagini G, Tucci G, Orlando F, Provinciali M, Carezzi F, Morganti P. Chitin nanofibrils linked to chitosan glycolate as spray, gel and gauze preparations for wound repair. J Bioact Compat Polym 2007; 22: 525-553.

Mezzana P. Clinical efficacy of a new chitin nanofibrils-based gel in wound healing. Acta Chir Plast 2008; 50:81-84.

Mi FL, Shyu SS, Wu YB, Lee ST, Shyong JY, Huang RN. Fabrication and characterization of a sponge-like asymmetric chitosan membrane as a wound dressing. Biomaterials 2001; 22: 165-173.

Mi FL, Wu YB, Shyu SS, Chao AC, Lai JY, Su CC. Asymmetric chitosan membranes prepared by dry/wet phase separation: A new type of wound dressing for controlled antibacterial release. J Mem Sci 2003; 212: 237-254.

Mizuno K, Yamamura K, Yano K, Osada T, Saeki S, Takimoto N, Sakurai T, Nimura Y. Effect of chitosan film containing basic fibroblast growth factor on wound healing in genetically diabetic mice. J Biomed Mater Res 2003; 64A: 177-181.

Murakami K, Aoki H, Nakamura S, Nakamura SI, Takikawa M, Hanzawa M, Kishimoto S, Hattori H, Tanaka Y, Kiyosawa T, Sato Y, Ishihara M. Hydrogel blends of chitin/chitosan, fucoidan and alginate as healing-impaired wound dressings. Biomaterials 2010; 31:83-90.

Muramatsu K, Masuda S, Yoshihara Y, Fujisawa A. In vitro degradation behavior of freeze-dried carboxymethyl-chitin sponges processed by vacuum-heating and gamma irradiation. Polym Deg Stab 2003; 81: 327-332.

Muzzarelli RAA, Guerrieri M, Goteri G, Muzzarelli C, Armeni T, Ghiselli R, et al. The biocompatibility of dibutyryl chitin in the context of wound dressings. Biomaterials 2005; 26: 5844-5854.

Muzzarelli RAA, Morganti P, Morganti G, Palombo P, Palombo M, Biagini, G, et al. Chitin nanofibrils/chitosan glycolate composites as wound medicaments. Carbohydr Polym 2007; 70: 274-284.

Muzzarelli RAA. Chitin and chitosans for the repair of wounded skin, nerve, cartilage and bone. Carbohydr Polym. 2009; 76: 167-182.

Nagahama H, Kashiki T, Nwe N, Jayakumar R, Furuike T, Tamura H. Preparation of biodegradable chitin/gelatin membranes with GlcNAc for tissue engineering applications. Carbohydr Polym 2008b; 73: 456-463.

Nagahama H, Nwe N, Jayakumar R, Koiwa S, Furuike T, Tamura H. Novel biodegradable chitin membranes for tissue engineering applications. Carbohydr Polym 2008a; 73: 295-302.

Ong SY, Wu J, Shabbir M, Moochhala, Tan MH, Lu J. Development of a chitosan-based wound dressing with improved hemostatic and antimicrobial properties. Biomaterials 2008; 29: 4323-4332.

Paul W, Sharma CP. Chitin and alginates wound dressings: A short review. Trends Biomater. Artif. Organs. 2004; 18: 18-23.

Pei HN, Chen XG, Li Y, Zhou HY. Characterization and ornidazole release in vitro of a novel composite film prepared with chitosan/poly(vinyl alcohol)/alginate. J Biomed Mater Res 2008; 85A: 566-572.

Peter M, Binulal NS, Soumya S, Nair SV, Tamura H, Jayakumar R. Nanocomposite scaffolds of bioactive glass ceramic nanoparticles disseminated chitosan matrix for tissue engineering applications. Carbohydr Polym 2010; 79: 284-289.

Peter M, Sudheesh Kumar PT, Binulal NS, Nair SV, Tamura H, Jayakumar R. Development of novel chitin/nano bioactive glass ceramic nanocomposite scaffolds for tissue engineering applications. Carbohydr Polym 2009; 78: 926-931.

Pietramaggiori G, Yang HJ, Scherer SS, Kaipainen A, Chan RK, Alperovich M, et al. Effects of poly-N-acetyl glucosamine (pGlcNAc) patch on wound healing in db/db mouse. J Trauma, 2008; 64: 803-808.

Portero A, Teijeiro-Osorio D, Alonso MJ, Remunan-Lopez C. Development of chitosan sponges for buccal administration of insulin. Carbohydr Polym 2007; 68: 617-625.

Prabaharan M, Jayakumar R. Chitosan-graft-β-cyclodextrin scaffolds with controlled drug release capability for tissue engineering applications. Int J Biol Macromol 2009; 44: 320-325.

Prabaharan M, Mano JF. Chitosan-based particles as controlled drug delivery systems. Drug Deliv 2005; 12: 41-57.

Prabaharan M. Chitosan derivatives as promising materials for controlled drug delivery. J Biomat Appl 2008; 23: 5-36.

Rai M, Yadav A, Gade A. Silver nanoparticles as a new generation of antimicrobials. Biotechnol Adv 2009; 27: 76-83.

Rasad MSBA, Halim AS, Hashim K, Rashid AHA, Yusof N, Sahmsuddin S. *In vitro* evaluation of novel chitosan derivatives sheet and paste cytocompatibility on human dermal fibroblasts. Carbohydr Polym 2010; 79: 1094-1100.

Ravi Kumar MNV. A review of chitin and chitosan applications. Reac Func Polym 2000; 46: 1-27.

Ribeiro MP, Espiga A, Silva D, Baptista P, Henriques J, Ferreira C, Silva JC, Borges JP, Pires E, Chaves P, Correia IJ, Development of a new chitosan hydrogel for wound dressing. Wound Rep Reg 2009; 17: 817-824

Rodrigues AP, Sanchez EMS, daCosta, AC, Moraes AM. The influence of preparation conditions on the characteristics of chitosan-alginate dressings for skin lesions. J Appl Polym Sci 2008; 109: 2703-2710.

Shalumon KT, Binulal NS, Selvamurugan N, Nair SV, Menon D, Furuike T, Tamura H, Jayakumar R. Electrospinning of carboxymethyl chitin/poly(vinyl alcohol) nanofibrous scaffolds for tissue engineering applications. Carbohydr Polym 2009; 77: 863-869.

Sharma A, Rao P, Mathur RP, Ameta SC. Photocatalytic reactions of xylidine ponceau on semiconducting zinc oxide powder. J Photochem Photobiol 1995; A86: 197-200.

Shibata H, Shioya N, Kuroyangi Y. Development of new wound dressing composed of spongy collagen sheet containing dibutyryl cyclic AMP. J Biomater Sci Polym Ed 1997; 8: 601-621.

Silva SS, Luna SM, Gomes ME, Benesch J, Pashkuleva I, Mano JF, Reis RL. Plasma surface modification of chitosan membranes: Characterization and preliminary cell response studies. Macromol Biosci 2008; 8: 568-576.

Sudheesh Kumar PT, Abhilash S, Manzoor K, Nair SV, Tamura H, Jayakumar R. Preparation and characterization of novel β-chitin/nano silver composite scaffolds for wound dressing applications. Carbohydr. Polym., 2010; 80: 761-767.

Sung JH, Hwang MR, Kim JO, Lee JH, Kim YI, Sun JH, Chang W, Jin SG, Kim JA, Lyoo WS, Han SS, Ku SK, Yong CS, Choi HG. Gel characterization and in vivo evaluation of minocycline-loaded wound dressing with enhanced wound healing using polyvinyl alcohol and chitosan. Int J Pharmaceutics 2010; 392: 232-240.

Suzuki S, Matsuda K, Isshiki N, Tamada Y, Ikada Y. Experimental study of newly developed bilayer artificial skin. Biomaterials 1990; 11:356-360.

Tamura H, Furuike T, Nair SV, Jayakumar R. Biomedical applications of chitin hydrogel membranes and scaffolds. Carbohydr Polym (2010), doi:10.1016/j.carbpol.2010.06.001.

Tanodekaew S, Prasitsilp M, Swasdison S, Thavornyutikarn B, Pothsree T, Pateepasen R. Preparation of acrylic grafted chitin for wound dressing application. Biomaterials 2004; 25: 1453-1460.

Tashiro T. Antibacterial and bacterium adsorbing macromolecules. Macromol Mat Eng 2001; 286: 63-87.

Thomas V, Yallapu M, Mohan SB, Bajpai SK. Fabrication, characterization of chitosan/nanosilver film and its potential antibacterial application. J Biomat Sci Polym Ed 2009; 20: 2129-2144.

Tsao CT, Chang CH, Lin YY, Wu MF, Wang JL, Young TH, Han JL, Hsieh KH. Evaluation of chitosan/γ-poly(glutamic acid) polyelectrolyte complex for wound dressing materials. Carbohydr Polym (2010), doi:10.1016/j.carbpol.2010.04.034

Turner TD, Schmidt RJ, Harding KG. (Eds.). Advances in wound management. Chichester, UK: Wiley, 1986.

Ueno H, Mori T, Fujinaga T. Topical formulations and wound healing applications of chitosan. Adv Drug Deli Rev 2001; 52: 105-115.

Ulubayram K, Nur Cakar A, Korkusuz P, Ertan C, Hasirci N. EGF containing gelatin-based wound dressings. Biomaterials 2001; 22: 1345-1356.

Vicentini DS, Smania Jr A, Laranjeira MCM. Chitosan/poly (vinyl alcohol) films containing ZnO nanoparticles and plasticizers. Mat Sci Eng 2010; C30: 503-508.

Vimala K, Murali Mohan Y, Samba Sivudua K, Varaprasada K, Ravindra S, Narayana Reddy N, Padma Y, Sreedhar B, MohanaRaju K, Fabrication of porous chitosan films impregnated with silver nanoparticles: A facile approach for superior antibacterial application. Colloids Surf. B: Biointerfaces, 2010; 76: 248-258.

Wang CC, Su CH, Chen CC. Water absorbing and antibacterial properties of N-isopropyl acrylamide grafted and collagen/chitosan immobilized polypropylene nonwoven fabric and its application on wound healing enhancement. J Biomed Mater Res 2008; 84A: 1006-1017.

Wang ZL. Zinc oxide nanostructures: growth, properties and applications, J Phys: Condens Matter 2004; 16: R829-R858.

Watthanaphanit A, Supaphol P, Tamura H, Tokura S, Rujiravanit, R. Fabrication, structure, and properties of chitin whisker-reinforced alginate nanocomposite fibers. J Appl Polym Sci 2008; 110: 890-899.

Xu H, Ma L, Shi H, Gao C, Han C. Chitosan-hyaluronic acid hybrid film as a novel wound dressing: in vitro and in vivo studies. Polym Adv Technol 2007; 18: 869-875.

Yang X, Yang K, Wu S, Chen X, Yu F, Li J, Ma M, Zhu Z. Cytotoxicity and wound healing properties of PVA/ws-chitosan/glycerol hydrogels made by irradiation followed by freeze-thawing. Radiation Phys Chem 2010; 79: 606-611

Yusof NLBM, Lim LY, Khor E. Preparation and characterization of chitin beads as a wound dressing precursor Flexible chitin films as potential wound-dressing materials: Wound model studies. J Biomed Mater Res 2001; 54: 59-68.

Yusof NLBM, Wee A, Lim LY, Khor E. Flexible chitin films as potential wound-dressing materials: Wound model studies. J Biomed Mater Res 2003; 66A: 224-232.

Zhang Y, He H, Gao WJ, Lu SY, Liu Y, Gu HY, Rapid adhesion and proliferation of keratinocytes on the gold colloid/chitosan film scaffold. Mat Sci Eng 2009; C29: 908-912.

Zhang Z, Yang D, Nie J. Chitosan/polyethylene glycol diacrylate films as potential wound dressing material. Int J Biol Macromol 2008; 43: 456-462.

Zhou Y, Yang D, Chen X, Xu Q, Lu F, Nie J. Electrospun Water-soluble carboxyethyl chitosan/poly(vinyl alcohol) nanofibrous membrane as potential wound dressing for skin regeneration. Biomacromolecules 2008; 9: 349-354.

2

Influence of the Chemical Structure and Physicochemical Properties of Chitin- and Chitosan-Based Materials on Their Biomedical Activity

Jolanta Kumirska[1], Mirko X. Weinhold[2], Małgorzata Czerwicka[1], Zbigniew Kaczyński[1], Anna Bychowska[1], Krzysztof Brzozowski[1], Jorg Thöming[2], and Piotr Stepnowski[1]

[1]*Faculty of Chemistry, University of Gdansk, Sobieskiego 18/19, PL-80-952 Gdansk,*
[2]*UFT - Centre for Environmental Research and Sustainable Technology, University of Bremen, Leobener Straße UFT, D-28359 Bremen,*
[1]*Poland*
[2]*Germany*

1. Introduction

Chitin and chitosan are an important family of linear polysaccharides consisting of varying amounts of β-(1→4)-linked 2-acetamido-2-deoxy-β-D-glucopyranose (GlcNAc) and 2-amino-2-deoxy-β-D-glucopyranose (GlcN) units (Muzzarelli, 1973; Roberts, 1992). Chitin samples contain a high content of GlcNAc units; hence, they are insoluble in water and common organic solvents. On the other hand, they dissolve only in solvents such as *N*,*N*-dimethylacetamide, hexafluoroacetone or hexafluoro-2-propanol (Pillai et al., 2009; Austin, 1988; Kurita, 2001). When the degree of *N*-acetylation (defined as the average number of *N*-acetyl-D-glucosamine units per 100 monomers expressed as a percentage) is less than 50%, chitin becomes soluble in aqueous acidic solutions (pH < 6.0) and is called chitosan (Pillai et al., 2009). This means that the term "chitosan" represents a group of fully and partially deacetylated chitins, but a rigid nomenclature with respect to the degree of *N*-deacetylation between chitin and chitosan has not been established (Ravi Kumar, 2000). Some authors consider that chitosan is a polysaccharide containing at least 60% GlcN residues (Aiba, 1992). According to the nomenclature proposed by the European Chitin Society (EUCHIS) (Roberts, 2007), chitin and chitosan should be classified on the basis of their insolubility and solubility in 0.1 M acetic acid; the insoluble material is called chitin, whereas the soluble one is chitosan. The structures of "ideal" chitin and "ideal" chitosan, and the "real" structures of these compounds are presented in Figure 1.

Chitin is the second most abundant polysaccharide (next to cellulose) synthesized by a great number of living organisms, serving in many functions where reinforcement and strength are required (Muzzarelli et al., 1986). In nature, chitin is found as structural components in the exoskeleton of arthropods or in the cell walls of fungi and yeast. It is also produced by a number of other living organisms in the lower plant and animal kingdoms. It has been

estimated that 10^{10}–10^{12} tons of chitin are biosynthesized each year (Percot et al., 2003). Unlike chitin, chitosan is produced only by some fungi from the family *Mucoraceae* (Roberts, 1998). Industrially, chitosan is usually produced by de-*N*-acetylation of chitin. The various industrial sources of chitin (α-, β- and γ-chitin) (Roberts, 1992; Tolaimate et al., 2003; Synowiecki & Al-Khateeb, 2003), as well as the processes and conditions under which this polymer is prepared (Al Sagheer, 2009; Manni et al., 2010; Das & Ganesh, 2010; Chaussard & Domard, 2004), cause the physical and chemical properties of chitosan preparations to vary (Rinaudo, 2006; Tolaimate et al., 2003; Domard, 2010).

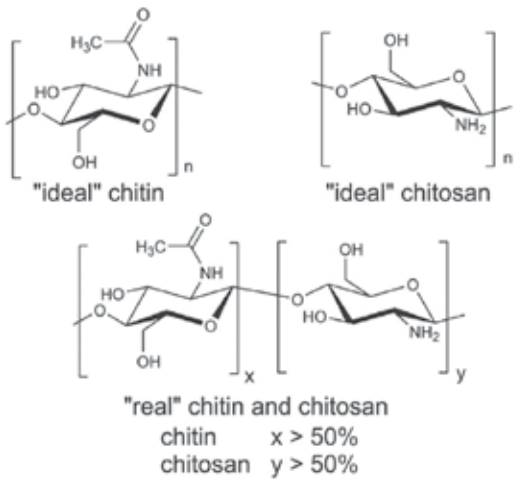

Fig. 1. The chemical structures of chitin and chitosan

Chitin and chitosan have great economic value because of their versatile biological activities such as biocompatibility, biodegradability, non-toxicity and adsorptive abilities, as well as chemical applications, mainly in the medical and pharmaceutical fields (Ravi Kumar, 2000; Rinaudo, 2006; Murugan & Ramakrishna, 2004; Yadav & Bhise, 2004; Aranaz et al., 2009; Ravi Kumar et al. 2004; Di Martino et al., 2005; Krajewska, 2004; Muzzarelli & Muzzarelli, 2005). The biological properties of these compounds depend closely on their physicochemical parameters, especially their solubility in water and other commonly used solvents. Most of the characteristic properties of chitosan are strictly related to its weight-averaged molecular weight (M_W) and the high content of glucosamine residues containing primary amino groups (Aranaz et al., 2009). In comparison to chitosan, chitin, being a highly insoluble and chemically rather unreactive material, has far fewer applications. By chemically modifying the primary amino and free hydroxyl groups of chitin and chitosan, their solubility in water and organic solvents can be improved (e.g. Zhong et al., 2007; Xie et al., 2007; Jeong et al. 2008), thereby increasing their range of biomedical applications (e.g. Kurita, 2001; Rinaudo, 2006; Alves & Mano, 2008).

Chitin/chitosan based materials with different structures show different biological activities, and not all the biological activities were found in one kind of chitin/chitosan material (Xia et al., 2010). Knowledge of the microstructure of chitin and chitosan samples is thus essential for an understanding of the structure–property–activity relationships, and special emphasis in this respect should be placed on the chitin/chitosans used in biomedical applications (Aranaz et al., 2009; Xia et al., 2010; Weinhold et al. 2009; ASTM. F2103-01, 2001;

ASTM. F2260-03, 2003; ASTM. WK965, 2003; Struszczyk & Struszczyk, 2007; Kean & Thanou, 2010).

The aim of this book chapter is to highlight the relationship between the chemical structure and physicochemical properties of chitin- /chitosan-based materials in the context of their biomedical activity. Special emphasis will be placed on the influence of the weight-averaged molecular weight, degree of *N*-acetylation and the types of chemical modification on the biomedical activity of chitin-/chitosan-based materials. A strategy for improving the characterization of chitosan for sustainable biomedical applications will also be presented.

2. Biomedical activity of chitin/chitosan samples differentiated on the basis of weight-averaged molecular weight (M_W)

The range of chitin/chitosan molecular weight is extensive (from several to more than thousands of kDa) and is thus divided into three categories: low-molecular-weight chitosan (LMWC), medium-molecular-weight chitosan (MMWC) and high-molecular-weight chitosan (HMWC) (Harish Prashanth & Tharanathan, 2007; Lin et al., 2009; Sun et al., 2009). As a consequence of increasing M_W, some physicochemical and biological properties of chitin/chitosan and its solutions change, which determines the bioactivity of the material (Table 1).

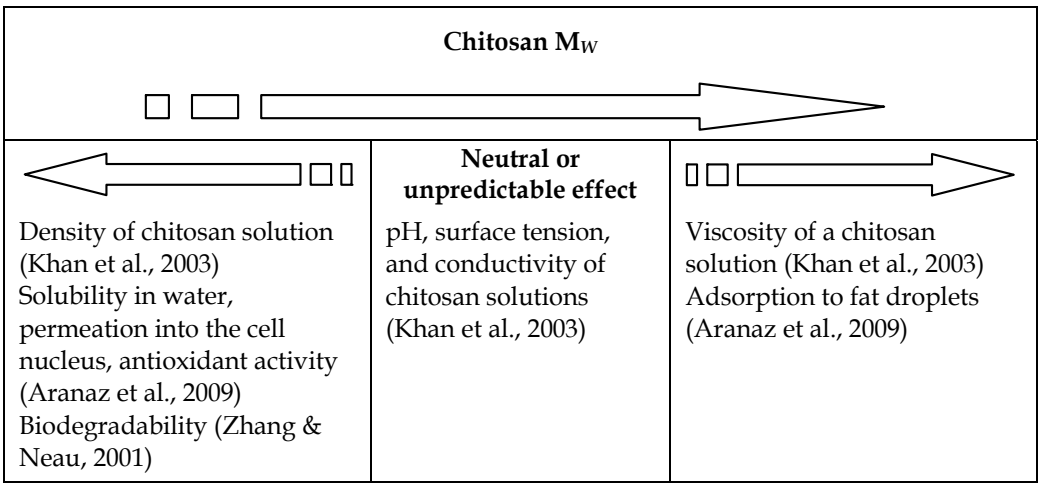

Table 1. The influence of molecular weight on some properties of chitosan and its solutions

Depending on the intended use, specific polymeric or oligomeric forms of chitin/chitosan are required. For some medical and pharmaceutical applications LMWC and chitooligosaccharides (COS) are more suitable. The exact product can be obtained by the enzymatic or chemical hydrolysis of polymer chains (Aranaz et al., 2009; Zhang et al., 2010b; Aam et al., 2010).

2.1 Drug delivery

One of the potential applications of chitin/chitosan products is a drug delivery system (nasal, oral, transdermal, etc.). Depending on the drug and its destination, a chitosan matrix can assume various forms: hydrogels, tablets, microspheres, films, nanoparticles, beads,

granules (Singh & Ray, 2000; Aranaz et al., 2009; Patel, 2006): everything serves a purpose to control drug release. Because they are better soluble in water, maintain a low viscosity with increasing concentration, and are derivatized more easily and faster, chitooligosaccharides appear to be more suitable as an injection material (Boesel et al., 2009). In the literature the expression "water-soluble chitosan" (WSC) is used to describe both LMWC and COS (Chae et al., 2005; Wang et al., 2007). WSC with a molecular weight range between 3.5 and 15.8 kDa was tested as a carrier for protein delivery (Wang et al., 2007). It was found that by increasing M_W, the loading efficiency of a model protein (bovine serum albumin BSA) increased from 8%to 48% for M_W from 3.5 to 6.3 kDa but only by a few percent for M_W = 15.8 kDa. The BSA release rate decreased very quickly up to 6.3 kDa, but then only slightly to 15.8 kDa. The results of this and other studies confirm that WSC nanoparticles are suitable for delivering protein drugs (Wang et al., 2007; Zhang et al., 2010a). There are also several studies relating the M_W effect to the characteristics of chitosan microspheres used as drug carriers (Nair et al., 2009; Sun et al., 2009). The aim of one of them was to test encapsulation with three different chitosans (40 kDa, 480 kDa, 850 kDa) for nasal methotrexate (MTX) administration (Sun et al., 2009). These authors concluded that MMWC microspheres have the best characteristics: the strongest mucoadhesive properties, as well as flowability and drug release in a controlled manner. In the case of LMWC drug release, control and mucoadhesion properties were poor. The disadvantages of HMWC microspheres were poor flowability and a tendency to aggregate. These results are in agreement with Gupta & Jabrail, who found that microspheres containing MMWC showed the best control of drug (nonsteroidal contraceptive - centchroman) release (Gupta & Jabrail, 2007). The effect of molecular weight on drug loading and drug release of drug-loaded chitosan microspheres was investigated using ketoprofen as a model drug (Genta et al., 1998). Comparing chitosans of 70 kDa, 750 kDa, and 2000 kDa, Genta et al. showed that a good ketoprofen content, an encapsulation efficiency independent of the polymer/drug ratio, and good control of drug release were achieved for microspheres composed of HMWC/LMWC (1:2 w/w). The main purpose of another study was to investigate the chitosan M_W effect on the formation and properties of pellets consisting of acetaminophen (model drug), chitosan, sodium alginate, dibasic calcium phosphate dehydrate and microcrystalline cellulose (Charoenthai et al., 2007). The influence of two samples of chitosans with different molecular weights (190 and 490 kDa) was compared. It was demonstrated that the characteristics of pellets, including shape, size, crushing force and speed of drug release, depend closely on chitosan M_W. Charoenthai et al. showed that LMWC had better pellet-forming properties (diameter, sphericity) and guaranteed drug release control. The effect of the molecular weight of four different samples of chitosan (160, 580, 1350, 1930 kDa) on the efficacy of two antibiotics (tobramycin and ofloxacin) used during external ocular infections was investigated over time by Felt et al. (Felt et al., 2001). The antibiotic content in tears was found to increase when HMWC was employed as compared to the controls and samples with a lower molecular weight of chitosan. The antibiotic efficacy of ofloxacin was also higher when HMWC was used, whereas tobramycin was independent of M_W.

The correlation between the molecular weight of chitosan and its interaction with different cell membranes was also tested (Yang et al., 2002; Chae et al. 2005). This information is very useful for the design of new drugs based on chitosan. Chae et al. investigated water soluble chitosan transport through a Caco-2 cell layer (in vitro) and intestinal absorption (in vivo) after the oral administration of fluorescence-labelled samples (Chae et al. 2005). It was

shown that intestinal absorption is molecular-weight-dependent and increases with decreasing chitosan M_W (more than 20 times, comparing WSC samples with molecular weights of 3.8 kDa and 230 kDa). The same tendency was observed with respect to permeation through a Caco-2 cell layer – the lower the M_W, the better the penetration. The interesting problem is the interaction of chitosan with the lipid bilayer. Yang et al. showed that LMWC (4.2 kDa) could destabilize a cell membrane at neutral pH (Yang et al., 2002).
Sometimes in order to increase human immunity, the lactic acid bacteria present in food can be helpful. They should be delivered to the colon, but the problem is not to kill these bacteria in extreme gastric conditions, or during the storage of food in the refrigerator. Microencapsulation offers a solution. Lee et al. investigated the survival of *Lactobacillus bulgaricus* KFRI 673 in alginate microparticles coated with chitosans of different molecular weights (Lee et al., 2004b). The experiment was carried out in simulated gastric and intestinal juices at 37°C, and in skimmed milk at 4° and 22°C. They demonstrated that with increasing chitosan M_W its protective ability towards gastric juices also increases. During storage at 4°C there was no difference between the stabilities of free and microencapsulated bacterial cells, but at 22°C the higher the molecular weight of the chitosan, the better the protection afforded. HMWC can be successfully used as a coating agent for alginate microparticles. Another example of the protection of the intestinal microbial flora is to deliver prebiotic agents. For this purpose chitooligosaccharides are much more useful (Lee et al., 2002). The influence of chitosan molecular weight on the minimum inhibitory concentration (MIC) was tested against bifidobacteria and lactic acid bacteria, and on the cell growth of the same microbes. It was shown that fully deacetyleted COS with a depolimerization degree of DP 2-8 exhibited a stimulatory effect on *Bifidobacterium bifidium* (0.1-0.5%) and *Lactobacillus casei*, and *Lactobacillus brevis* (0.1%), whereas chitosan in polymeric form displayed antimicrobial activity even at a very low concentration (0.078-0.31%).

2.2 Antimicrobial activity

In comparison to the prebiotic activity of chitin/chitosans, their antimicrobial properties are decidedly more often discussed. The antimicrobial activity of chitosans varies depending on their physical properties. These polymers can be used against a broad spectrum of target organisms like bacteria, fungi, viruses or algae (Chirkov, 2002; Rabea et al., 2003; Tikhonov et al., 2006; Visnova & Vavrikova, 2008; Goy et al., 2009). The significant influence of molecular weight on this activity has been demonstrated, but the type of microorganism also plays a significant role. For such investigations *Escherichia coli* (Gram-negative) and *Bacillus cereus* (Gram-positive) are often used (Babiker, 2002; Vishu Kumar et al., 2005; Kittur et al., 2005; Fernandes et al., 2009). Native chitosan, LMWC, COS, and monomers all displayed an inhibitory effect against them. Vishu Kumar et al. demonstrated the better activity of a chito-oligomeric-monomeric mixture (with high DP) compared with native chitosan and monomers (Vishu Kumar et al., 2005). Although *E. coli* is Gram-negative and *B. cereus* is Gram-positive, and the bactericidal mechanism is different in each case, the influence of chitosan molecular weight was similar. This concurred with the results obtained by Kittur et al. (Kittur et al., 2005). They found the COS-monomeric mixture more efficient against both bacteria than native chitosan, and that in the case of *B. cereus* this effect was stronger still. It was interesting in both studies that GlcN showed only slight bacterial growth inhibition, whereas GlcNAc did not display any activity. Among the chitooligomers,

the antibacterial effect increased from dimer to hexamer (Vishu Kumar et al., 2005; Kittur et al., 2005). Fernandes et al. investigated the mechanism of chitosan antibacterial activity against vegetative and resistant forms of *B. cereus* using atomic force microscopy imaging and nanoindentation (Fernandes et al., 2009). They found that HMWC surrounded the bacterial cells. The polymer layer that formed became a mechanical barrier preventing the uptake of nutrients, subsequently leading to the death of the vegetative form, whereas the spores remained unaffected. Chitooligosaccharides caused visible damage to vegetative cells, but were unable to destroy the spores. In another study, gluten peptides were conjugated with HMWC and LMWC, then tested for antibacterial activity against *E. coli* (Babiker, 2002). Bactericidal activity of the gluten peptide-chitosan conjugates was observed when both types of chitosan were used, but the presence of HMWC in a conjugate made this more active, especially at low temperatures. Atomic force spectroscopy was also used to investigate the molecular weight dependency of the antibacterial effect of chitosans, but this time against *Escherichia coli* and *Staphylococcus aureus* (Eaton et al., 2008). These studies also allowed the response strategies used by Gram-negative and Gram-positive bacteria to be compared. In the case of *E. coli* antibacterial activity was better with LMWC than with HMWC. This is the result of the ready penetration of the Gram-negative cell wall by oligomers. Gram-positive bacteria have an intrinsically different cell wall structure. In this case the formation of a chitosan polymer layer preventing nutrient absorption is preferred, and HMWC displayed better antibacterial activity against *S. aureus*. Lin et al. (Lin et al., 2009) reported similar observations: decreasing the chitosan molecular weight was conducive to growth inhibition of *E. coli*, but not of *S. aureus*. They also demonstrated the existence of an intraspecific diversity in sensitivity toward LMWC, which could explain the discrepancies appearing in some studies. They examined the different enzymes used to obtain LMWC, which significantly affects molecular size distribution. Comprehensive studies comparing antibacterial activity against many different microorganisms have also been carried out (Gerasimenko et al., 2004; Park et al., 2004a, Fernandes et al., 2010). Park et al. examined the antibacterial activity of hetero-chitosans (with different degrees of acetylation) and their oligosaccharides (5-10 kDa, 1-5 kDa, and <1 kDa) against three Gram-negative (*Escherichia coli, Salmonella typhimurium, Pseudomonas earuginosa*) and five Gram-positive bacteria (*Bacillus subtilis, Bacillus cereus, Staphylococcus epidermidis, Staphylococcus aureus, Micrococcus luteus*) (Park et al., 2004). Hetero-chitosans inhibited the growth of all bacteria, but the efficiency of this process additionally depended on the microorganism and DA. The inhibitory effect of hetero-COSs was lower in comparison to the activity of hetero-chitosans. The efficiency of inhibition was found to be higher for Gram-positive than for Gram-negative bacteria. The potential antimicrobial activities of chitosans with different molecular weights were tested in the context of their use in textile finishing so as to prevent (or treat) skin disorders (Fernandes et al., 2010). For these investigations six skin-borne miscroorganisms (three Gram-negative bacteria: *Escherichia coli*, *Klebsiella pneumoniae*, *Pseudomonas aeruginosa,* two Gram-positive bacteria: *Staphylococcus aureus*, *Staphylococcus epidermidids*, and the fungus *Candida albicans*), three chitosans (average 628, 591, and 107 kDa), and two mixtures of chitooligosaccharides (<5, <3 kDa) were chosen. The sensitivity of all Gram-negative bacteria increased with decreasing chitosan molecular weight. The opposite effect was observed with the fungus and the Gram-positive bacteria, although in the latter case the trend was not so distinct. The results of many investigations indicate that low molecular weight chitosans could be universal antimicrobial agents against all types of bacteria and fungi (Gerasimenko et al., 2004; Tikhonov et al., 2006).

2.3 Antitumour properties

In some medical applications of chitin/chitosan, as antitumour compounds, for example, their degradation products are preferred, as they have a lower viscosity and a better solubility in water. The antitumour activity of chitin/chitosan is manifested by the stimulation of the immune system (production of lymphokines, including interleukins 1 and 2, stimulation of NK, etc.) (Qin et al., 2002a; Jeon & Kim, 2002; Maeda & Kimura, 2004). Jeon & Kim tested the antitumour activity of three kinds of COSs (high molecular weight ranging from 6.5 to 12 kDa – HMWCOS, medium molecular weight ranging from 1.5 to 5.5 kDa - MMWCOS, and low molecular weight ranging from 0.5 to 1.4 kDa – LMWCOS) against Sarcoma 180 solid (S180) and Uterine cervix carcinoma No. 14 (U14) (Jeon & Kim, 2002). The efficiency of tumour growth inhibition for both types of tumour cells in mice was best in the case of MMWCOS. There are many reports of S180 tumour cells being used for testing the antitumour activity of chitosan (Qin et al., 2002a; Qin et al., 2004; Maeda & Kimura, 2004). Maeda & Kimura investigated the antitumour effect of three water-soluble low molecular weight chitosans (21 kDa, 46 kDa, 130 kDa) and various doses of 650 kDa chitosan in sarcoma 180-bearing mice (Maeda & Kimura, 2004). They found that LMWC (21 and 46 kDa) and also smaller oligosaccharides could activate the intestinal immune system of animals, thus preventing tumour growth. But no antitumour effect was observed after the oral administration of chitosan samples, even of low molecular weight (46 kDa). The same authors confirmed that high molecular weight chitosan (650 kDa) prevents the adverse reactions of some cancer chemotherapeutic drugs. Qin et al. also tested the antitumour activity of LMWC against sarcoma 180, but they came to the opposite conclusions. They noted that oral administration of LMW chitosan decreases the weight of the tumour (Qin et al., 2002a; Qin et al., 2004), although administration by intraperitoneal injection led to a higher inhibitory rate (Qin et al., 2004). It was reported the higher the M_W of LMWC, the better the inhibitory tumour effect (Qin et al., 2002a). The introduction of acidic groups as a result of chitosan oxidation has the opposite effect, and an increase in M_W decreases antitumour activity (Qin et al., 2002b). The influence of LMWC and COS (including the pentamer, hexamer, and higher oligomers) on the growth inhibition of Ehrlich ascites tumour (EAT) cells and tumour-induced neovascularization was investigated (Harish Prashanth & Tharanathan, 2005). Based on experimental results concerning the inhibition of angiogenesis and the induction of apoptosis, it was confirmed that COSs seem to be more potent angioinhibitory and antitumour compounds. Wang et al. reported that chitin oligosaccharides (DP 1-6) also reduced the number of K562 cells (human erythromyeloblastoid leukemia cell line) (Wang et al., 2006).

2.4 Gene delivery

Chitosan possesses many of the properties required of gene therapy material. It is suitable as a base polymer for a nonviral DNA delivery system. It is important to realize that molecular weight is a critical factor in cytotoxicity. Investigations into this problem have shown a reduction in cytotoxic effect with decreasing chitosan molecular weight (Richardson et al., 1999). For studying the relationship between structure and transfection efficiency five chitosans with molecular weights from 31 to 190 kDa were chosen. It was found that gene transfer efficacy was independent of chitosan molecular weight in the range of 31 to 170 kDa (Köping-Höggård et al., 2001). In another work the influence of the degree of polymerization in the 21-88 range (M_W 4.7-33 kDa) on transfection efficiency was tested

(Strand et al., 2010). The maximum level was achieved for DP from 31 to 42. With increasing chain length, gene expression was lower and delayed. Park et al. examined COSs with molecular weights from 3 to 45 kDa (Park et al., 2006). To compare transgene expression they used HEK 293 cells with pEGFP-N1 plasmid encoding green fluorescent protein. The best efficiency was found for COS of molecular weight 9 kDa. There are many reports concerning the design of chitosan/pDNA nanoparticles for gene delivery (Bozkir & Saka, 2004; de la Fuente et al., 2008; Centelles et al., 2008). The aim of Centelles et al. was to investigate the level of transgene expression mediated by three DNA-chitosan nanoparticle formulations differing in chitosan molecular weight (150 kDa, 400 kDa, 600kDa) (Centelles et al. 2008). They did not notice any effect of M_W of chitosan on the long term (105 days) expression. In another study, nanoparticles consisting of chitosan (CS) and hyaluronic acid (HA) were chosen to load with pDNA (de la Fuente et al., 2008). These nanoparticles differed in chitosan and chitooligosaccharide molecular weight (125 kDa, 10-12 kDA respectively), in HA molecular weight, and in HA:CS mass ratio. Taking into account only the influence of chitosan it could be concluded that a lower mass promoted a better transfection efficiency.

The chitosan–based delivery system is not limited to experiments with DNA. It has been used to transfer functionally active siRNA to HeLa cells (Techaarpornkul et al., 2010). For this study human cervical carcinoma cells with stable expression of enhanced green fluorescent protein (EGFP) were prepared. Then the gene-silencing effect of siRNA complexes with chitosans of different molecular weight (20, 45, 200, and 460 kDa) was examined. The best results were obtained with LMWC – 20 kDa. The molecular weight of chitosan did not affect the particle size of the CS/siRNA complex, but higher molecular weights did favour complex formation.

2.5 Tissue engineering

There is also a special place for chitin/chitosan in the field of tissue engineering. Nwe et al. reported that the mechanical properties of chitosan membranes deteriorated when the molecular weight of chitosan increased (New et al., 2009), whereas Hsu et al. maintained that it is precisely the high molecular weight of chitosan that gives the chitosan scaffold its better mechanical strength (Hsu et al., 2004a). The reduced proliferation of human skin fibroblast cells on a collagen/chitosan scaffold with increasing chitosan molecular weight was observed by Tangsadtkakun et al. (Tangsadtkakun et al., 2007), while Howling et al. reported that the M_W of chitin and chitosan samples had no appreciable influence on the proliferation of tissue fibroblasts or on keratinocytes (Howling et al., 2001). The major goal of another study was to measure the effects of chitin/chitosan with different molecular weights on wound healing (Minagawa et al., 2007). They concluded that both chitin and chitosan oligomers and monomers are better for the acceleration of wound healing than the polymeric forms. Additionally, it was found that collagenase activity was greater in the chitosan group (the highest for GlcN), whereas it was lower for chitin and remained at the same level for the whole chitin group. Shelma et al. used chitin and chitosan in their investigations, because both possess wound healing potential (Shelma et al., 2008). They found that introducing chitin nanofibres considerably increased the tensile strength of medium molecular weight (270 kDa) chitosan films, helping this complex to be a better accelerator of wound healing. This stands in agreement with results concerning the tensile strength and arrangement of collagen fibres in the skin, obtained previously by Cho et al.

(Cho et al., 1999). They demonstrated the better efficacy of water-soluble chitin in wound healing in comparison to chitin and chitosan samples.

2.6 The hypocholesterolemic effect

There are also studies concerning the role of chitosan in reducing the total cholesterol level, and the influence of molecular weight on this was tested. The purpose of one such study was to investigate the correlation between feeding chitosan (M_W 120 kDa) and lipid metabolism in hyperlipidemic rats (Xu et al., 2007). The cholesterol-lowering effect of chitosan was noted. The same results were achieved by Osman et al., although they used HMWC (Osman et al., 2010). The hypocholesterolemic effect of chitosan samples on human patients has also been recorded. Jaffer & Sampalis observed a lowering of serum cholesterol concentration after patients were treated with LMWC (40 kDa) (Jaffer & Sampalis, 2007). The results of other experiments did not testify to any statistically significant reductions in cholesterol levels (Tapola et al., 2008). It can be concluded that chitosans with different molecular weights are capable of lowering cholesterol levels, although the mechanisms of this effect are still not clear.

In summary, chitin/chitosan with different molecular weights have numerous potential applications in medicine and pharmacy. Nevertheless, taking into account the properties of chitin/chitosan such as toxicity, water solubility, low viscosity etc., low molecular weight chitosans and chitooligosaccharides would appear to be more useful for the majority of biomedical applications.

3. Biomedical activity of chitin/chitosan samples differentiated with respect to the degree of *N*-acetylation (DA)

As mentioned at the beginning of this review, chitin is insoluble in aqueous solvents whereas chitosan is soluble in acidic or even neutral conditions owing to the free protonable amino groups in the glucosamine residue. The degree of *N*-acetylation is therefore an important characteristic that influences the performance of chitin/chitosan in many of its applications.

The solubility, conformation and dimensions of chitosan chains in aqueous media have been extensively studied as a function of the degree of acetylation (DA) (Berth et al., 1998; Berth & Dautzenberg, 2002; Schatz et al., 2003). Schatz et al. have proposed general laws of chitosan behaviour in aqueous solutions (Schatz et al., 2003; Sorlier et al., 2001; Sorlier et al., 2002):

- at DA below 20%, chitosan exhibits the highest structural charge density. Chitosan displays polyelectrolyte behaviour related to long-distance intra- and intermolecular electrostatic interactions, which are responsible for chain expansion, high solubility and ionic condensation.
- for values of DA 20-50%, hydrophilic and hydrophobic interactions are progressively counterbalanced.
- for DA over 50% electrostatic interactions are essentially short-distance interactions. Then, hydrophobic interactions due to the increase in the acetyl group content become predominant.

It was confirmed that for biomedical applications chitosan with DA 0-30% is the most useful (Sandford, 1984; Aranaz et al., 2009).

The DA values of chitin/chitosan depend directly on the means of deacetylation and the conditions of the process. In general, chitosan is prepared by severe alkaline hydrolysis of

the chitin acetamide groups. Usually, sodium or potassium hydroxides are used at a concentration of 30-50% w/v at ~100°C. Sometimes the deacetylases isolated from certain bacteria and fungi are used. However, the activity of these enzymes is limited by the poor solubility of chitin (Martinou et al., 1998) – this is a major factor limiting its utilization. Most studies and applications have been carried out with chitosan because of its greater versatility and superior biological properties. In addition, Howling et al. demonstrated that highly deacetylated chitosan is biologically more active than chitin and less deacetylated chitosans (Howling et al., 2001). Since the majority of biological properties are related to the cationic behaviour of chitosan (the presence of free amino groups in the polymeric chain), all the below-mentioned properties depend significantly on the DA.

Biodegradability Chitin and chitosan can be degraded by several proteases (lysozyme, papain, pepsin) present in the human body (Vårum et al., 1997). Biodegradation yields non-toxic oligosaccharides that can be assimilated or excreted (Pangburn et al., 1982).

The rate of degradation of chitosan is very important because it affects the properties of the material. For example, scaffold degradation should be compatible with the rate of new tissue formation or be adequate for the controlled release of bioactive molecules. Degradation of chitosan has been shown to increase as the degree of deacetylation decreases (Hirano et al., 1989; Sashiwa et al., 1990; Kurita et al., 2000). Kofuji et al. investigated the enzymatic digestion of various chitosans by observing changes in the viscosity of a chitosan solution in the presence of lysozyme (Kofuji et al., 2005). They concluded that chitosan with a high DA tended to degrade more rapidly. However, the rates of enzymatic degradation of chitosan species differed, even in chitosan species with similar DA.

Aiba et al. and Shigemasa et al. suggested that the differences in degradation are due to variations in the distribution of acetamide groups in the chitosan molecule caused by differences in deacetylation conditions. Moreover, the absence of acetyl groups results in very low rates of enzymatic degradation (Aiba, 1992; Shigemasa et al, 1994). Therefore, it is impossible to estimate the biodegradation rate from the degree of deacetylation alone.

Finally, it should also be mentioned that the lability of chitin towards lysozyme also depends on its crystalline form. Kurita et al. showed that β-chitin was degraded much more readily than α-chitin owing to the weak intermolecular forces in the former (Kurita et al., 2000).

Biocompatibility This property depends on many parameters, although DA seems to be one of the most important. Orally administered chitin/chitosan can be regarded as not bioavailable, because they are not absorbed despite partial enzymatic degradation. The kinetics of enzymatic chitin/chitosan biodegradation, mentioned above, also affects biocompatibility. Very fast rates of degradation produce amino sugars, which can cause an inflammatory response. Therefore, chitosan samples with high DA can induce an acute inflammatory response, whereas samples with low DA can induce only a minimal response.

In the context of biocompatibility, the toxicity of chitin/chitosan should also be mentioned: it seems to depend on the DA. Schipper et al. reported that chitosans with DA lower than 35% displayed low toxicity, whereas DA above 35% caused dose-dependent toxicity (Schipper et al., 1996).

Mucoadhesion Mucus serves to protect epithelial cells in the gastrointestinal and respiratory systems in mammals. It is composed of mucin, which is negatively charged (the presence of sialic acid residues). In the stomach, chitosan is positively charged owing to the acidic condition and interacts with mucin by electrostatic forces.

It has been found that a lower DA leads to an increase in charge density of the molecule and the adhesive properties become more relevant (He et al., 1998). Mao et al. observed a direct correlation between the degree of deacetylation of chitosan and adhesion (Mao et al., 2004) The study revealed that the smaller the increases in DA, the stronger the cell adhesion.
Not only DA, but also the distribution of acetyl groups along the chain (random or blockwise) can affect the biomedical properties of chitin/chitosan as a result of changes in the solubility, inter-chain interactions due to H-bonds and the hydrophobic nature of the acetyl group (Zhang et al., 2010b).
Because of their considerable biocompatibility, quite easily controlled biodegradability and mucoadhesion, chitin and chitosan have been widely employed in drug and gene delivery, wound healing, tissue regeneration and some other biomedical applications.

3.1 Drug delivery

Owing to their controlled biodegradability and good biocompatibility chitin and chitosan are good candidates for drug delivery vehicles. The ability of chitosan to form drug delivery systems is due to its cationic charge and its ability to interact with negatively charged polyanions. Drug delivery systems using chitosan include microspheres, nanoparticles, hydrogels, solutions, films and tablets depend on the delivery route.
The selection of an ideal type of chitosan with certain properties is useful for developing efficient drug delivery systems, prolonging the duration of drug activity, improving therapeutic efficiency and reducing side effects (Aranaz et al., 2009). Kofuji et al. stated that the proper selection of physicochemical properties of chitosan is important for the choice of the appropriate chitosan as a drug delivery vehicle. Among several physicochemical properties, DA seems to be one of the most important (Kofuji et al., 2005).
Gupta & Jabrail observed the influence of DA and cross-linking on the physical characteristics, swelling and release of centchroman-loaded chitosan microspheres (Gupta & Jabrai, 2006). The authors concluded that since the hydrophobicity of chitosan depends on the numbers of *N*-acetyl groups, the loading and release characteristics of chitosan matrices depends closely on DA. Maximum loading capacity was observed at DA 38-52%, whereas very high DA can induce burst release. The degree of cross-linking in chitosans is controlled in a similar way. The larger numbers of free amino groups at lower DA increases the degree of covalent cross-linking. The authors also reported that the size and surface roughness of the microspheres decreased with a reduction in DA. Moreover, a lower DA in chitosan increases the compactness of matrices and its hydrophobicity, thus controlling the degree of swelling and diffusivity of the drug entrapped in chitosan matrices. The value of the diffusion coefficient for centchroman from microspheres decreased on reducing the DA of chitosan (Gupta & Jabrai, 2006).
Chiou et al. studied the influence of different chitosans on the initial burst and drug release from microspheres (Chiou et al., 2001). They observed that chitosans with higher DA reduce the initial burst of drug release more effectively.
Aranaz et al. summarized the relation between DA and the properties of microspheres, one of the most common drug delivery vehicles. A decrease in chitosan DA increases covalent crosslinking and the compactness and hydrophobicity of the matrices, whereas increasing DA reduces the size, surface roughness, swelling, loading capacity and burst release of the microspheres (Aranaz et al., 2009).

Kofuji et al. investigated the relationship between the DA and the ability of chitosan to form spherical gels (Kofuji et al., 2005). Chitosan with low DA was able to form a spherical gel by chelation with metal ions, unlike chitosan with high DA. This ability was explained by the larger numbers of amino groups available in polysaccharides.

3.2 Gene delivery

Discussed compounds forming complexes with DNA play an important role in gene therapy. Mumper et al. proposed a non-viral vector for a gene delivery system (Mumper et al., 1995). As a non-viral vector for gene delivery chitin and chitosan demonstrate some advantages compared to viral vectors. They do not produce endogenous recombination, oncogenic effects or immunological reactions (Ferber, 2001).

The M_W of chitosan and its DA are key parameters in the preparation of chitosan/pDNA complexes. Lavertu et al. studied several combinations of M_W and DA of chitosan. They selected two combinations of high transfection efficiency using a chitosan of 10 kDa and a DA of 8 and 20% (Lavertu et al., 2006).

Kiang et al. observed the effect of the degree of chitosan deacetylation on the efficiency of gene transfection in chitosan/DNA nanoparticles (Kiang et al., 2004). They suggested that the use of chitosan with a DA above 20% might accelerate chitosan degradation and DNA release, since highly deacetylated chitosan (above 80%) releases DNA very slowly.

3.3 Tissue engineering

Chitosan scaffolds are promising materials for the design of tissue engineered systems owing to their low immunogenic activity, controlled biodegradability and porous structure (Ho et al., 2005; Ma et al., 2003; Madihally & Howard 1999). The influence of DA on the structural and biological properties of chitosan scaffolds for cell culture and tissue engineering was studied by Tiğli & Gümüsderelioglu (Tiğli et al., 2007). These authors observed that the mechanical strength of chitosan was better with lower DA and that chitosan with lower DA favoured cell adhesion. They also observed that chitosan scaffolds with DA (15-25%) displayed a more regular structure in comparison to scaffolds with very low DA (<15%). Moreover, the lateral pore connectivity was much lower for chitosans DA 15-25% than for scaffolds with DA <15%. Both observations were very important, because it is very well known that the microstructure of the matrix has an important influence on cell intrusion, proliferation and functioning in tissue engineering.

Freier et al. prepared and characterized chitin and chitosan tubes for nerve regeneration (Freier et al., 2005). The compressive strength of these tubes was found to increase with decreasing of DA.

3.4 Wound healing

Both chitin and chitosan activate the complement system in polymorphonuclear cells, fibroblasts and vascular endothelial cells, thereby contributing to wound healing (Minagawa et al., 2007). Since all of these processes are related to the properties of the matrix (chitin/chitosan), they also depend on the DA (Ueno et al., 2001).

Minagawa et al. studied the influence of chitin and chitosan with different DA, as well as chitin oligomers and monomers (GlcN, GlcNAc) on wound healing (Minagawa et al., 2007). They observed that at lower DA wound break strength was greater and that fibroblasts were more highly activated.

3.5 Antimicrobial activity

Chitin and chitosan have been investigated as antimicrobial materials with respect to a wide range of target organisms like algae, bacteria, yeasts and fungi.

Chitin and chitosan with different DA were analyzed with respect to fungi (*Aspergillus fumigatus, Aspergillus parasiticus, Fusarium oxysporum, Candida albicans*), Gram-positive bacteria (*Staphylococcus aureus, Staphylococcus saprophyticus, Bacillus cereus, Listeria monocytogenes*) and Gram-negative bacteria (*Escherichia coli, Salmonella* Typhimurium*, Pseudomonas aeruginosa, Enterococcus faecalis, Aeromonas hydrophila, Shigella dysenteriae, Vibrio cholerae, Vibrio parahaemolyticus*). In all cases the antimicrobial activity increased with decreasing DA (Andres et al., 2007; Tipparat, H. & Riyaphan, 2008; Tsai et al., 2002).

Park et al. studied the antimicrobial activity of chitosans with different degrees of deacetylation against three Gram-negative bacteria and five Gram-positive bacteria and found that 75% deacetylated chitosan exhibited more effective antimicrobial activity than 90% or 50% deacetylated chitosan (Park et al., 2004a).

Three antibacterial mechanisms have been proposed:

- ionic surface interaction resulting in wall cell leakage;
- mRNA inhibition and protein synthesis via the penetration of chitosan into the nuclei of the microorganisms;
- the formation of an external barrier chelating metals and provoking the suppression of essential nutrients to microbial growth. It is likely that all events occur simultaneously but at different intensities (Goy et al., 2009; Helander et al., 2001; Liu et al., 2001; Roller, & Covill, 1999).

It should be mentioned that some authors have not found a clear relationship between DA and antimicrobial activity. They suggested that the antimicrobial activity of chitosan is dependent on both the chitosan and the microorganism used (Chien & Chou, 2006; Oh et al., 2001).

3.6 Antioxidative activity

Chitosan possesses a significant scavenging capacity against different radical species. Its antioxidant activity depends on the degree of deacetylation (Koryagin et al., 2006). Park et al. studied the abilities of chitosan samples with a DA of 50, 25 and 10% to scavenge 1,1-diphenyl-2-picrylhydrazyl (DPPH), hydroxyl, superoxide and alkyl radicals. The results indicated clearly that the radical scavenging activities of hetero-chitosans depend on their DA. Chitosan with the lowest DA exhibited the best scavenging activity (Park et al., 2004b; Je & Kim, 2006).

A similar study was performed with chitooligosaccharides. The oligosaccharide prepared from chitosan with DA 10% displayed the greatest radical scavenging activity (Je et al., 2004). It was concluded that the free amino groups in chitooligosaccharides can react with free radicals to form stable macromolecule radicals (Xie et al., 2001).

4. Biomedical activity of chitin-/chitosan-based materials differentiated with respect to chemical modification

They are a lot of chemical methods of modification which can generate completely new chitin-based biofunctional materials. The most common one is graft copolymerization, which allows the formation of applicative derivatives by the covalent binding of a molecule, the graft, onto the chitosan backbone (Alves & Mano, 2008). Chitosan can also be derivatized by introducing a small functional group such as alkyl or carboxymethyl into its structure. Other chemical modifications of chitin and chitosan include phosphorylation, combination

of chitosan derivatives with cyclodextrins, and thiolation. In this section the most important applications of such modified chitin and chitosan-based materials in biomedical fields such as drug delivery, tissue engineering and antimicrobial agents will be discussed.

4.1 Drug delivery

Drug delivery has been one of the major applications of chitin and chitosan derivatives in recent years. The main factors that allow the use of chitin and chitosan as drug delivery vehicles is their biodegradability and the fact that they can be easily metabolized by certain human enzymes, especially lysozyme (Muzzarelli, 1997).

There are several chitosan-based drug delivery systems prepared by different methods (Agnihotri et al., 2004). The usual ones are:

- tablets – prepared by coating - sodium diclofenac, pentoxyphylline, salicylic acid;
- capsules – prepared by capsule shell - insulin, 5-aminosalicylic acid;
- microspheres/microparticles -prepared by emulsion cross-linking – progesterone, aspirin, theophylline;
- nanoparticles – prepared by ionic gelation – ricin, bovin serum albumin;
- beads – prepared by coacervation/precipitation – riboflavin, adriamycin;
- films – prepared by solution casting – trypsin, testosterone, beta-oestradiol;
- gel – prepared by cross-linking – hydrocortisone acetate, caffeine, 5-fluorouracil.

In general, drug delivery materials can be supported via various routes, like nasal, ocular, oral, parenteral and transdermal. Some important applications of organ-specific drug delivery using chitosan derivatives are presented below.

4.1.1 Colon-targeted drug delivery

A chitosan-based delivery system can efficiently protect therapeutic agents from the hostile conditions of the upper gastrointestinal tract and release the entrapped agents, especially in the colon, through degradation of the glycosidic linkages of chitosan by colonic microflora (Hejazi & Amiji, 2003). In 1998 Lorenzo-Lamosa et al. designed microencapsulated chitosan microspheres for colonic drug delivery (Lorenzo-Lamosa et.al., 1998). Sodium diclofenac (SD), an anti-inflamantory drug, was efficiently entrapped in chitosan cores and then microencapsulated into EudragitL-100 and Eudragit S-100 to form a multireservoir system. *In vitro* release studies revealed that no SD was released at the gastric pH; when the microsphere reached the colonic environment, however, continuous release was observed for a variable time (8-12 h). Other derivatives – chitosan succinate and chitosan phthalate – were synthesized and assessed as potential matrices for colon-specific orally administered drug delivery applications (Aiedeh & Taha, 1999). These matrices resisted dissolution under acidic conditions. More recently, Jain A. and Jain S.K. reported a nanoparticular system for the colon-specific delivery of 5-fluorouracil (Jain & Jain, 2008). They prepared hyaluronic acid-coupled chitosan nanoparticles bearing 5-fluorouracil using ionotropic gelation. These derivatives showed enhanced cellular uptake by HT-29 colon cancer cells compared to uncoupled nanoparticles. Wang et al. also presented some fresh chitosan derivatives useful as drug delivery materials (Wang et al., 2009), e.g. a polyelectrolyte complex formed by sodium cellulose sulphate and chitosan as a drug carrier for colon-specific delivery.

4.1.2 Mucosal drug delivery

Ocular, nasal, peroral, vaginal and pulmonary mucosal surfaces are receving a great deal of attention as alternative routes of systemic administration. It has been shown in many

publications that *N*-trimethyl chitosan and *N*-carboxymethyl chitosan have a special feature enabling them to adhere to mucosal surfaces, which has made them some of the most useful chitosan derivatives for mucosal drug delivery (Lueben et al., 1996; Thanou et al., 2001; Jayakumar et al., 2006). More recently PEG-g-chitosan nanoparticles have been proposed as promising vehicles for insulin transport through the nasal mucosa (Zhang et al., 2009). Also not long ago, Perioli et al. prepared vaginal mucoadhesive tablets containing the bioadhesive polymers chitosan and polyvinylpyrrolidone in a ratio of 1:1 (Perioli et al., 2009). Several chitosan-based nanosystems, resulting in innovative ocular nanomedicines with a significant impact on clinical practice, have been described by Paolicelli et al. (Paolicelli et al., 2009). In turn, van der Lubben et al. in a review article presented the details of a chitosan-based delivery system for the transmucosal administration of drugs (van der Lubben et al., 2001).

4.1.3 Cancer therapy

The concept of polymer-drug conjugates for delivering hydrophobic, small molecular drugs to their site of action was first propounded by Ringsdorf in 1975 (Ringsdorf, 1975). Based on this strategy several chitosan-anticancer drug conjugates have recently been investigated and successfully applied in cancer therapy. A representative example is doxorubicin-conjugated glycol chitosan (DOX-GC) with a *cis*-aconityl spacer (Son et al., 2003). When these chitosan-based nanoparticles were systemically administered to mice they preferentially accumulated in the tumour tissue – this was ascribed to the EPR (enhanced permeability and retention) effect. *n*-Lauryl-carboxymethylchitosan is another example of a useful carrier for hydrophobic cancer drugs, developed by Miwa et al. (Miwa et al., 1998). These chitosan derivatives have the ability to form micelles that solubilize taxol, making it therapeutically more effective. More recently, Zhang et al. examined another chitosan-based polymeric micelle for taxol delivery in cancer therapy (Zhang et al., 2003). The results show that this new *N*-alkyl-*O*-sulphated chitosan can be effectively used as an potential drug carrier for taxol. Good antitumour activities were also exhibited by *N*-succinyl-chitosan derivatives conjugated with mitomycin C (MMC) (Kato et al., 2004). These chitosan-based conjugates are active against various tumours such as murine leukaemias (L1210 and P338), B16 melanoma, Sarcoma 180 solid tumour, murine liver metastatic tumour (M5076) and murine hepatic cell carcinoma (MH134). Further interesting examples of chitosan-anticancer drug conjugates are discussed in Tan et al. (Tan et al., 2009).

4.1.4 Gene delivery

Chitosan has the ability to interact ionically with negatively charged DNA to form polyelectrolyte complexes, which results in better DNA protection against nuclease degradation (Agnihotri et al. 2004). Several interesting studies describing the potential use of chemically modified chitosan in gene delivery have been reported. Quite a lot of them were focused on alkylated chitosan, mostly because of its high transfection efficiency. Among this class of derivatives dodecyl-chitosan has the most important application in DNA delivery (Liu et al., 2001a). Another example of chitosan-based gene delivery was studied by Mao et al. (Mao et al., 2001). They produced modified chitosan nanospheres with transferrin and poly (ethylene glycol) (PEG) but did not observe any significant enhancement in transfection. PEGylation of chitosan was also used by Zhang et al. to prepare chitosan-DNA complexes conjugated with alpha-methoxy-omega-succinimidyl

poly (ethylene glycol) (Zhang et al., 2007). As a result the gene expression was improved in comparison with the chitosan-DNA complex both *in vitro* and *in vivo*. More recently, Sajomsang et al. examined a methylated chitosan derivative/DNA complex containing different aromatic moieties (Sajomsang et al., 2009a). Of all the derivatives tested, *N*-(4-pyridinylmethyl) chitosan (MPyMeChX) exhibited the highest transfection efficiency in human hepatoma cells (Huh 7 cells). Many more examples of chemically modified chitosan used as potential gene delivery vehicels have recently been reported by Jaykakumar (Jayakumar et al., 2010).

4.1.5 Other ways of delivery

There are many publications showing that chitin and chitosan derivatives could also be used for liver-, kidney- and lung-targeted delivery. For example, Kato et al. evaluated the potential of lactosaminated *N*-succinyl-chitosan (Lac-Suc) as a liver-specific drug carrier (Kato et al., 2001). More recently, Yang et al. prepared polyion complex micelles (PIC micelles), also for liver-targeted delivery (Yang et al., 2009a). These micelles were based on methoxy poly (ethylene glycol)-graft-chitosan and lactose-conjugated poly (ethylene glycol)-graft-chitosan, and was prepared for the delivery of diammonium glycyrrhizinate (DG). The experiments showed that the lactose-conjugated PIC delivered more DG to the liver than conventional PIC micelles. As mentioned above, chitosan derivatives could also be used for lung-targeted delivery. For this purpose Yang et al. prepared chitosan-modified poly (lactic-coglycolic acid) nanoparticles containing paclitaxel (Yang et al., 2009). The results demonstrated that *in vitro* uptake of the nanoparticles by a lung cancer cell line (A549) was significantly increased by chitosan modification.

4.2 Tissue engineering

The present generation of tissue engineering research is based on seeding cells onto a porous biodegradable polymer matrix. The most recently published studies in this field have suggested the use of scaffolds to support and organize damaged tissue. Because of their controlled biodegradability and porous structure, chitosan and its derivatives have been reported as attractive candidates for scaffolding materials. Extensive studies on the use of chitosan-based materials in tissue engineering were described by Kim et al. in their recent review paper (Kim et al., 2008). Here we present just a few examples of the various types of chitosan derivatives modified for these applications. The strategies for using these derivatives in different kinds of organs such as skin, bone cartilage, liver, nerves and blood vessels will also be discussed.

4.2.1 Chitosan derivatives as tissue supporting materials

One of the most important groups of chitosan modification used for these applications involves the specific recognition of cells by sugars. For example, Li et al. reported that chitosan bound to D- and L-fucose showed specific interactions with lectin and cells (Li et al., 2000). Other chitosan derivatives prepared from lactobionic acid and chitosan with different activating agents, such as 1-ethyl-3-(3-dimethylaminopropyl)-carbodiimide (EDC) and *N*-hydroxysuccinimide (NHS), demonstrated the possibility of a synthetic extracellular matrix for hepatocyte attachment (Park et al., 2003). More recently, Kim et al. prepared mannosylated chitosan with a specific recognition for antigen-presenting cells such as B-cells, dendritic cells and macrophages (Kim et al., 2006).

The devlopment of the chemical grafting of chitosan has produced a series of practically useful tissue supporting materials. For example, chitosan graft-polymerized onto a poly (L-lactide) surface can be used to control the morphology and function of cells (Ding et al., 2004). Prabaharan et al. proposed a novel poly (L-lactide)-chitosan hybrid scaffold as a tissue engineering material that is simultaneously a drug release carrier (Prabaharan et al., 2006). These hybrid foams exhibit a much greater rigidity than pure chitosan foams, indicating that this strategy may allow for the use of chitosan-based structures in tissue engineering applications.

Another approach regarding the chemical modification of chitosan for tissue engineering applications has been to use electrospinning to create polymeric nanofibres. These materials have several useful properties such as a large specific surface area and extensive porosity. Chitin and chitosan nanofibres were produced, for example, by Min et al. (Min et al., 2004). Further investigations found that these chitosan-based nanofibres promoted the adhesion of chondrocyte and osteoblast cells and maintained characteristic cell morphology (Bhattarai et al., 2005).

Tissue	Types of derivatives	References
Skin	chitosan in combination with alginate polyelectrolyte complex chitosan/collagen porous scaffold made by cross-linking with glutaraldehyde	Yan et al., 2000; Ma et al., 2003
Bone	chitosan-calcium phosphate composites such as beta-tricalcium phosphate) hydroxyapatite/chitosan materials	Zhang & Zhang, 2002; Kawakami et al., 1992
Cartilage	chitosan-alginate hyaluronan scaffold attachment with RGD-containing protein porous collagen/chitosan/glycosaminoglycan scaffold loaded with transforming growth factor TGF-β1	Hsu et al., 2004b; Lee et al., 2004a
Liver	chitosan complex with glycosaminoglycans (GAG) chitosan/collagen/heparin matrix	Chupa et al., 2000; Wang et al., 2005
Nerve	hydroxyapatite-coated chitosan tubes with adsorbed laminin-1 and laminin peptides chitosan/gelatin composites	Itoh et al., 2003; Cheng et al., 2003
Blood vessel	heparin-chitosan scaffolds	Kratz et al., 1997

Table 2. Different tissue engineering applications of chitosan derivatives

The combination of chitosan with other materials seems to be a good opportunity for tissue engineering applications. Chung et al. prepared a galactosylated chitosan-based scaffold

combined with alginate to improve mechanical properties and biocompatibility (Chung et al., 2002). Sarasam & Madigally reported the effect of blending chitosan with poly(ε-caprolactone) (Sarasam & Madihally, 2005). Chitosan matrices were also modified by γ-poly (glutamic acid), which enabled the maximum strength to be increased in tissue engineering applications (Hsieh et al., 2005).

4.2.2 Applications of chitosan derivatives for different organs

Various types of chitosan derivatives have been used in different tissue engineering applications, namely, skin, bone, cartilage, liver, nerve and blood vessel tissue. Some of them are summarized in Table 2.

4.3 Antimicrobial agents

The antimicrobial activity of chitin, chitosan and their derivatives against different groups of microorganism, such as bacteria, yeast and fungi is considered to be one of the most important properties in recent years. These activities were first developed by Allan and Hadwiger in 1979, since then many interesting studies have been reported in this field (Allan & Hadwiger, 1979). Several mechanisms have been suggested as the cause of the inhibition of microbial cells by chitosan. One mechanism involves interaction with predominantly anionic components, such as lipopolysaccharides and microorganism surface proteins, resulting in changes in permeability, which causes cell death by inducing leakage of intracellular components (Helander et al., 2001). A second mechanism involves the inhibition of RNA and protein synthesis following permeation of the cell nucleus (Liu et al., 2001b). Yet another option is that chitosan on the surface of the cell can form a polymer membrane, which prevents nutrients from entering the cell (Liu et al., 2004). In this section we focus on the antibacterial and antifungal activities of some chitin and chitosan derivatives.

4.3.1 Antibacterial activity of chitosan derivatives

Many chitosan derivatives inhibit the growth of a wide range of bacteria. For example, Papineau et al. showed that chitosan lactate and chitosan glutamate are antagonistic towards *Escherichia coli* and *Staphylococcus aureus* (Papineau et al., 1991). Quaternary ammonium salts of chitosan, such as *N*,*N*,*N*-trimethylchitosan, *N*-propyl-*N*,*N*-dimethylchitosan and *N*-furfuryl-*N,N*-dimethylchitosan, were also shown to be effective in inhibiting the growth and development of *Escherichia coli,* especially in acidic media (Jia et al., 2001). Again, Xie et al. prepared multiple-derivatized chitosan (HPCTS-*g*-MAS) by the etherification of chitosan with propylene epoxide followed by the graft copolymerization of sodium malate and tested its antimicrobial activities against *Staphylococcus aureus* and *Escherichia coli* (Xie et al., 2002). Compared with chitosan, these derivatives exhibited a better inhibitory effect against these two bacterial species. The antibacterial activities of water-soluble *N*-alkylated disaccharide chitosan derivatives against *E. coli* and *S. aureus* were also investigated by Yang et al. (Yang et al., 2005). These bacteria were the most susceptible to cellobiose-chitosan derivatives and maltose-chitosan derivatives. More recently, Sajomsang et al. synthesized 17 derivatives of chitosan consisting of a variety of *N*-aryl substituents bearing either electron-donating or electron-withdrawing groups (Sajomsang et al., 2009b). Each of the derivatives was further quaternized using *N*-(3-chloro-2-hydroxypropyl)

trimethylammonium chloride and studied for their antibacterial activities. All the quaternized derivatives of chitosan displayed antibacterial activity against *E. coli* and *S. aureus*, as observed using the minimum inhibitory concentration (MIC) method.

4.3.2 Antifungal activity of chitosan derivatives

Chitosan is able to induce the *in vitro* growth of a number of fungi except Zygomycytes, which have chitosan as a component of their cell walls (Allan & Hadwiger, 1979). In 1996 Chen et al. reported that chitosan films made in dilute acetic acid solutions are able to inhibit the growth of *Rhodotorula rubra* and *Penicillium notatum* by direct applications of the film to the colony-forming organism (Chen et al., 1996). The antimicrobial activity of chitosan graft copolymers against *Candida albicans*, *Trichophyton rubrum* and *Trichophyton violaceum* was also observed (Jung et al., 1999). It was shown that the number and type of grafted chains, as well as the pH, substantially influenced the activities examined. Very extensive studies investigating the antifungal activity of chitosan derivatives were carried out by Rabea et al. (Rabea et al., 2005). They used a radial hyphal growth bioassay of *B. cinerea* and *P. grisea* to assess the fungicidal activity of 24 new derivatives of chitosan (i.e., *N*-alkyl, *N*-benzylchitosans). The results showed that all the derivatives are better fungicides than native chitosan. *N*-dodecylchitosan, *N*-(*p*-isopropylbenzyl) chitosan and *N*-(2,6-dichlorobenzyl) chitosan were the most active against *B. cinerea*, and *N*-(*m*-nitrobenzyl) chitosan likewise against *P. grisea*. Zhong et al. prepared 12 kinds of new hydroxylbenzenesulphonilanide derivatives of chitosan (CS), carboxymethyl chitosan (CMCS) and chitosan sulphated (CSS) and evaluated their antimicrobial activities against five pathogenic fungi: *P. asparagi*, *A. solani*, *F. oxysporum f. sp. vasinfectum* and *C. gloeosporioides* (Zhong et al., 2009). All these derivatives displayed stronger antifungal properties than the original materials (CS, CSS and CMCS). Palma-Guerrero et al. demonstrated that chitosan can permeabilize the plasma membrane of *Neurospora crassa* and kills the cells in an energy-dependent manner (Vruggink, 1970).

4.4 Other biomedical properties of chitin and chitosan derivatives

Chitin and chitosan derivatives have a great potential to be used in other biomedical applications. For example, chitin and chitosan sulphates display blood anticoagulant activity (Whistler & Kosik, 1971; Horton & Just, 1973). Substitution of a carboxyl group at position 6 in *N*-sulphonated chitosan yields a product with 23 % of the activity of heparin, and its *O*-sulphonated form exhibited 45 % activity *in vitro*. It has also been reported that the anticoagulant activity of sulphonated chitosan increases with rising sulphur content in chitosan. These derivatives could be useful as heparinoids for artificial blood dialysis. Grafted chitosan materials exhibited similar properties (Li et al., 2003). It has been demonstrated that the permeability of chitosan membranes grafted with HEMA can be controlled through plasma-treatment with the potential to be used in dialysis. Another very important biomedical activity of chitosan derivatives was investigated by Sosa et al. (Sosa et al., 1991), who demonstrated that *N*-carboxymethylchitosan *N*,*O*-sulphate inhibits HIV-1 replication and viral binding with CD4. Selective sulphation at *O*-2 and/or *O*-3 affords potent antiretroviral agents showing a much higher inhibitory effect against infection with the AIDS virus than that by the known 6-*O*-sulphated derivative (Nishimura et al., 1998). It was also shown that *N*-hexanoyl and *N*-octanoyl chitosan fibres can be used as haemostatic and anti-thrombogenic materials (Hirano, 1999). More recently, Huang et al. developed a

nanofibrous chitosan/PVA membrane for lipase immobilization (Huang et al. 2007). The results showed that this system can be used for biosensor applications.

5. Suitable strategy for the characterization of chitin-/chitosan-based materials used in biomedical applications

5.1 Standardization of M_W and DA determination

During recent decades of chitosan research, many methods have been proposed to determine the degree of acetylation (DA) and the weight-averaged molecular weight (M_W). Although these are two of the most important parameters of chitosan, no standard technique could be established. This is due mainly to some typical drawbacks of chitosan: poor solubility, polyelectrolyte behaviour and its polymeric character. As a consequence of the lack of a standard technique, many alternative methods have been put forward to determine these parameters. However, their accuracy and reliability are sometimes questionable and often depend on sample composition. DA and M_W values determined by different methods are sometimes scarcely comparable, and interpretation or comparison of these data must be done carefully. To inform the reader about the methods that can be applied, we will briefly discuss and summarize the techniques used and described in the literature.

5.2 M_W determination

In linear polymers the polymer chains rarely have the same degree of polymerization and molar mass, and there is always a distribution around an average value especially in natural polymers (except proteins and DNA). Different average values can be defined depending on the statistical method that is applied. Four values, such as the number-averaged molecular weight M_N, the weight-averaged molecular weight M_W, the viscosity-averaged molecular weight M_V, and the z-averaged molecular weight M_Z are in use; one of these, M_W, is the most important. The polydispersity of a polymer sample is defined as M_W divided by M_N and gives an indication of just how narrow the distribution is. Several techniques have been used over the years, often measuring just one of the values mentioned above. In modern times the most common technique has become size-exclusion chromatography (SEC). Apart from batch methods such as batch viscosity measurements (Nah & Jang, 2002), batch static light-scattering (SLS) measurements (Berth & Dautzenberg, 2002; Cölfen et al., 2001; Lamarque et al., 2005; Pa & Yu, 2001), or batch multi-angle light-scattering (MALS) measurements (Anthonsen et al., 1994; Chen & Tsaih, 1998; Tsaih & Chen, 1997), chromatography has the advantage of determining the polydispersity of the sample. The width of the molecular weight distribution is often the key parameter of a chitosan sample. The higher this distribution, the less conclusive is the observed effect of one sample due to the presence of several thousand different molecular weights at the same time. The reliable determination of the polydispersity of a sample is therefore an important requirement for pharmaceutical and scientific observations.

- SEC-RI (pullulan calibration) (Hasegawa et al., 1994; Knill et al., 2005; Lin & Lin, 2003)
- SEC-LALS (Kubota et al., 2000; Ottøy et al., 1996, 1995)
- SEC-MALS (Tømmeraas et al., 2002; Sorlier et al., 2001; Sorlier, 2002; Berth et al., 1998; Lamarque et al., 2004, 2005; Schatz et al., 2003; Brugnerotto et al., 2001)
- SEC-LALS-Vis (Weinhold et al., 2009)
- SEC-MALS-Vis (Christensen et al., 2008)

Since the use of size-exclusion chromatography is commonly agreed upon, more controversy is present about surrounds the different detectors used online for chromatography. Nowadays, all the old bench methods can be applied to a chromatography setup such as a refractive index detector (RI), viscosity detector (Vis) and light-scattering detectors (single-90°, low-angle and 90° (LALS), or multi-angle with 3, 5, or up to 18 angles (MALS). But using only refractive index or viscosity detectors M_W can only be obtained with reference to some standard samples (often pullulan or dextran). These values differ significantly from the "real" molecular weight because chitosan coils differ in solution in comparison to pullulan and dextran. Absolute values can be obtained by light-scattering, but sample composition determines the type of light-scattering device to be used. If the sample is below roughly 100 000 g/mol, a single-90° is sufficient to give reliable M_W values. If the the sample weight is much higher, scattered light underlies the angular dependence and a significant decrease of laser intensity is observable at a detection angle of 90°. To overcome this problem laser light is also detected at rather low angles (LALS) (where the decrease becomes negligible) or at many angles (MALS). Additionally, light-scattering detectors can be combined with a viscosity detector to increase information about sample composition as a result of the simultaneous observation of conformation (via the Mark-Houwink plot) and branching behaviour. However, the type of light scattering device to be used in chitosan science (low angle vs. multi angle vs. triple detection) is still a matter of discussion and may be based mainly on the use of different parameters in light-scattering experiments in chitosan research. For a light-scattering experiment, values such as dn/dc (refractive index increment) and R_θ (Rayleigh ratio) must be known for the molecular weight analysis. If only one value is changed, for example, for an interlab comparison, the resulting M_W values will be significantly different even for identical samples.

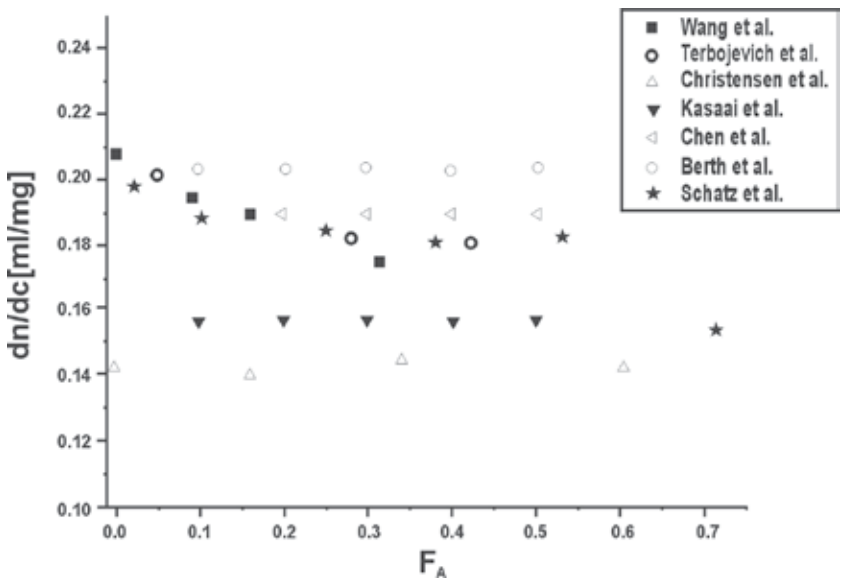

Fig. 2. Variation of the dn/dc values.

In different studies of chitosan different dn/dc values were used. The diagram (Fig. 2) presents values obtained at 436 nm (Wang et al. 1991) and values obtained at 633 nm

(Terbojevich et al., 1991; Christensen et al., 2008; Kasaai et al., 2000; Chen & Tsaih, 1998; Berth et al., 1998; Schatz et al., 2003) for different chitosan preparations with changing FA(DA).

The reason for this change is that dn/dc enters the molecular weight calculation quadratically. Using, for example, dn/dc = 0.142 (Christensen et al., 2008) for calculating the M_W of a high molecular weight chitosan sample, we obtain a molecular weight of 1098 kg/mol. Changing the dn/dc value to 0.208 (Berth et al., 1998) for the same chromatography data, the M_W decreases to 750 kg/mol. The use of published dn/dc values on identical data therefore leads to a drastic change in the molecular weight of up to 32%! Thus, comparison of molecular weight data obtained by light-scattering must include information about the dn/dc value; otherwise, a comparison will never show conformity when two different dn/dc's are used.

A similar effect can be seen by changes of R_θ. To make a light scattering detector into an absolute measurement device the equipment needs to be calibrated once after manufacturing to ensure its accuracy and functionality. This is a typical procedure and is often done by the manufacturer. For this calibration, a pure organic solvent with known Rayleigh ratio, e.g. toluene (Wyatt, 1993; Santos & Castanho, 1996) is used. Nowadays, a R_θ of 1.402 x $10^5 cm^{-1}$ obtained at 90° using 632.8 nm laser light (Kaye & McDaniel, 1974) should be used; this is stipulated by the Federal Institute for Materials Research and Testing (BAM, Bundesanstalt für Materialforschung und -prüfung). However, there are still other values in use such as 1.3522 x $10^{-5} cm^{-1}$ and 1.340 x $10^{-5} cm^{-1}$ (Itakura et al., 2005). Again, to obtain comparable molecular weight data for interlab comparisons, information about the Rayleigh ratio used must be included.

Despite these difficult conditions, it has been shown that a reliable determination of molar masses with acceptable deviations is possible, according to a round-robin test with four different polymer reference materials (Just et al., 2005). In this test, different detector devices were applied (low-angle and multi-angle light scattering detectors), indicating negligible dependencies on different instruments (especially LALS vs. MALS), different cell geometries, or different wavelengths of laser light. Dependencies on dn/dc values, inappropriate solvents and the Rayleigh ratio of toluene $R_{\theta,toluene}$ were excluded as they were prescribed by the regulations. This indicates how difficult it is to initiate a standardization of molecular weight determination of chitosan, even for light-scattering devices, as long as different dn/dc and $R_{\theta,toluene}$ values are being used. But it also shows that standardization in chitosan research might be possible in the future.

5.3 DA determination

For the determination of DA, up to 17 different methods have been applied in the literature. Considering the solubility issue of some chitin/chitosan samples, some of these methods are inapplicable to insoluble samples. In several methods, the samples have to be carefully purified to avoid any interference with the measurements. Moreover, most methods have several drawbacks with respect to analysis time, cost or accuracy.

To present the problem more clearly, we will summarize these methods in two bullet lists. The first one contains the methods that were proposed some time ago but are hardly used regularly as the procedures they require are time-consuming. All the methods have the determination of non-absolute DA values in common. The second bullet list contains the more accurate methods for DA determination; thus they are used more regularly. We will

also indicate whether the method is suitable only for chitosan, highlighted by "soluble material", or whether it is also applicable to chitin, highlighted by "solid material".

- conductometric titration (Raymond et al., 1993) (soluble material)
- UV-VIS (Muzzarelli, 1985) (soluble material)
- circular dichroism (Domard, 1987) (soluble material)
- thermal analysis (Alonso et al., 1983) (solid material)
- enzymatic hydrolysis (Nanjo et al., 1991) (soluble material)
- picric acid assay (Neugebauer et al., 1989) (soluble material)
- pyrolysis GC (Lal & Hayes,1984) (solid material)
- acid hydrolysis GC (Holan et al., 1980) (solid material)
- acid hydrolysis HPLC (Niola et al., 1993) (solid material)
- ninhydrin test (Curotto & Aros, 1993; Prochazkova et al., 1999) (soluble material)
- X-ray deffraction (Zhang et al., 2005) (solid material)

Since chitosan is a natural product it may contain certain residues (protein, alkali, salt, astaxanthin), depending on the quality of the chitin source and the reaction conditions. Problems with sample contamination may arise with several methods. Residual salts may interfere with conductometric titration by influencing the endpoint of the titration and therefore shift the measured DA value. Other residues like proteins display UV activity and may interfere with the UV-VIS and the circular dichroism method. In 2002, the European Pharmacopeia proposed the UV method as a standard method for characterizing chitosan hydrochloride. However, Aiba et al. (Aiba, 1986) found changes in the DA values (30%, strong) in comparison to IR spectroscopy and colloid titration, which reflects the vulnerability of this method. Enzymatic hydrolysis requires non-standard enzymes, the activity of which must be checked beforehand, and the overall procedure is relatively time-consuming. Together with pyrolysis, acid hydrolysis GC and acid hydrolysis HPLC need a 100% rate for the preceding hydrolysis reaction, which cannot be checked easily. Furthermore, the measurement time including sample preparation is very long. The ninhydrin method is non-quantitative and depends on different molecular weights and therefore needs a calibration curve determined by a second method (Prochazkova et al., 1999). The XRD method is affected by the lyophilization of the samples, which changes the original crystalline properties. In summary, the overall accuracy of the above methods may be directly dependent on the purity of the samples investigated, and their applicability is limited. Thus, they do not qualify as standard methods for DA determination.

Let us now focus on the more important methods used for DA determination. To illustrate the impact in the scientific community, the number of citations is shown after each method (determined via Web of Science (ISI Web of Knowledge) 20th July 2010).

- IR spectroscopy (Miya et al., 1980) (solid samples) cited 117 times.
- ^{1}H-NMR (Hirai et al., 1991; Vårum et al., 1991a) (soluble material) cited 176 and 203 times, respectively.
- ^{13}C-NMR (Vårum et al., 1991b) (soluble material) cited 84 times.
- solid state ^{13}C-NMR (Saito et al., 1987; Raymond et al., 1993) (solid samples) cited 76 times.
- ^{15}N-NMR (Heux et al., 2000) (soluble material) cited 49 times.
- colloid titration (Broussignac, 1968) (soluble material) .

The IR spectroscopy method has two main advantages: it is rather quick and can also be used for chitin samples as the measurement requires solid material. However, there are

uncertainties about the best baseline setting and the selection of peaks for analysis (amide, amino, hydroxyl) (de Velde & Kiekens, 2004), which results in different DA values for the same spectrum. This shortcoming of IR spectroscopy is shown up by very highly deacetylated samples, in the spectra of which the amide band is scarcely distinguishable. On the other hand, it gives good results with very slightly deacetylated samples, which cannot be measured by many other methods. A serious problem is that it does not give absolute values and needs to be calibrated with a direct method such as NMR (de Velde & Kiekens, 2004). Given the number of citations, it is obvious that ^{1}H-NMR is the favourite among the scientific community. With up to 200 citations, the leading position of liquid state ^{1}H-NMR is reflected by the best accuracy in combination with very quick results (Fernandez-Megia et al., 2005). Both the Hirai method and the Vårum method yield comparable DA values (deviation no greater than 1 or 2% of the DA value); in addition, the Vårum method is more accurate as it incorporates the H1 and H2 signals. However, these authors prefer Hirai's method because the Vårum method requires measurements at high temperatures and extends the measuring time, whereas the Hirai method can be performed at room temperature. The main advantage of the NMR method is the generation of absolute values through the simultaneous detection of deacetylated and acetylated signals. The ratio of the one to the other reveals the DA value without any calibration or assumptions. In contrast, liquid state ^{1}H-NMR cannot be used for chitin because this technique is limited to soluble material and the equipment is extremely costly. Similar results can be obtained by ^{13}C-NMR, solid state ^{13}C-NMR and ^{15}N-NMR, but these techniques extend the measurement time to more than one hour per sample at the least (depending on the device and conditions) and are, despite the good accuracy, far from becoming standard methods. Exceptionally, solid state ^{13}C-NMR shows greater potential because it covers the range of 0% to 100% deacetylated samples. Nevertheless, NMR has become the most reliable technique for DA determination in recent years (Domard, 2007). It shows good repeatability and reproducibility of results, not only for interoperator comparisons but also for interlab comparisons on different NMR devices (at least, this is our experience). Beyond the scientific research community, the simple colloid titration method enjoys great popularity mainly due to its unbeatable costs. Small chitosan producing facilities typically do not have access to NMR equipment or simply want to avoid their expense. Although it is prone to impurities (alkali residues), it can be performed very quickly in even the simplest lab. Like the above-mentioned methods it does not give absolute values and needs to be calibrated or should first be performed with samples of known DA.

6. Conclusions

Chitin and chitosan are natural aminopolysaccharides with unique structures, multidimensional properties, highly sophisticated functions and wide ranging applications, especially in the biomedical and pharmaceutical fields. Moreover, the chemical modification of these polymers improves their solubility in water or organic solvents, which in turn enhances their biological activities and raises the number of potential biomedical applications. Chitin and chitosan have an intrinsic structural and physicochemical variability because of their natural origin and the manufacturing process. Furthermore, the poor physicochemical characterization of the chitin-/chitosan-based products used in biomedical experiments makes it very difficult to compare results and to establish relationships between the physiological behaviour of these compounds and their properties.

At present, the accurate study of the properties of chitin/chitosan requires the use of well-characterized, high-quality products. Knowledge of the microstructure of these compounds is essential for an understanding of structure–property–activity relationships. On the basis of literature data it has been possible to present in this chapter important information about the influence of the chemical structure and physicochemical properties of chitin-/chitosan-based materials on their biomedical activity. This knowledge is especially important for biotech companies. In each of these uses, it is necessary to control the different parameters which influence the characteristics of chitin/chitosan so as to produce it according to the characteristics desired by companies. The proper adjustment of the process conditions will make it possible to produce chitins very similar to their native form, and to prepare chitosans and their derivatives with well-controlled characteristics. An understanding of these molecular-level details provides insights into the unknown biochemical functions of chitin-/chitosan-based products and helps to accelerate their future applications.

7. Acknowledgements

The authors express their gratitude for the financial support provided by the Polish Ministry of Research and Higher Education under grant DS/8200-4-0085-10 and the German Academic Exchange Service (DAAD).

8. References

Aam, B.B.; Heggset, E.B.; Norberg, A.L.; Sørlie, M.; Vårum, K.M. & Eijsink, V.G.H. (2010). Production of Chitooligosaccharides and Their Potential Applications in Medicine. *Mar. Drugs*, 8, 1482-1517, ISSN 1660-3397

Agnihotri, S.A.; Mallikarjuna, N.N. & Aminabhavi T.M. (2004). Recent advances on chitosan-based micro- and nanoparticles in drug delivery. *J. Control. Release*, 100, 5–28, pISSN 0168-3659

Aiba, S. (1986). Studies on chitosan: 1. Determination of the degree of *N*-acetylation of chitosan by ultraviolet spectrophotometry and gel-permeation chromatography *Int. J. Biol. Macromol.*, 8, 173–176, pISSN 0141-8130

Aiba, S. (1992). Studies on chitosan: 4. Lysozymic hydrolysis of partially *N*-acetylated chitosans. *Int. J. Biol. Macromol.*, 14, 225-228, pISSN 0141-8130

Aiedeh, K. & Taha, M.O. (1999). Synthesis of chitosan succinate and chitosan phthalate and their evaluation as suggested matrices in orally administered, colon-specific drug delivery systems. *Arch. Pharm.*, 332, 103–107, pISSN 0365-6233

Al Sagheer, F.A. Al-Sughayer, M.A. Muslim, S. & Elsabee, M.Z. (2009). Extraction and characterization of chitin and chitosan from marine sources in Arabian Gulf. *Carbohydr. Polym.*, 77, 410–419, ISSN 0144-8617

Allan, C. & Hadwiger, L.A. (1979). The fungicidal effect of chitosan on fungi of varying cell wall composition. *Exp. Mycol.*, 3, 285–287, ISSN 0147-5975

Alonso, I.; Corvas, C.R. & Nieto, J. (1983). Determination of the degree of acetylation of chitin and chitosan by thermal analysis. *J. Therm. Anal. Calorim.*, 28, 189–195, ISSN 1388-6150

Alves, N.M. & Mano, J.F. (2008). Chitosan derivatives obtained by chemical modifications for biomedical and environmental applications. *Int. J. Biol. Macromol.*, 43, 401–414, ISSN 0141-8130

Andres, Y.; Giraud, L.; Gerente, C. & Le Cloirec, P. (2007). *Environ. Techno*l., 28, 1357-1363, pISSN 0959-3330

Anthonsen, M.; Vårum, K.; Hermansson, A.; Smidsrød, O. & Brant, D. (1994). Aggregates in acidic solutions of chitosans detected by static laser light scattering. *Carbohydr. Polym.*, 25, 13–23, ISSN 0144-8617

Aranaz, I.; Mengíbar, M.; Harris, R.; Paños, I.; Miralles, B.; Acosta, N.; Galed, G. & Heras Á. (2009). Characterization of Chitin and Chitosan. *Curr. Chem. Biol.*, 3, 203–230, pISSN 1872-3136

ASTM. F2103-01 (2001). Standard guide for characterization and testing of chitosan salts as starting materials intended for use in biomedical and tissue-engineered medical product applications

ASTM. F2260-03 (2003). Standard Test Method for Determining Degree of Deacetylation in Chitosan Salts by Proton Nuclear Magnetic Resonance (1H NMR) Spectroscopy

ASTM. WK965 (2003). New Test Method for Determining the Molar Mass of Chitosan and Chitosan Salts by Size Exclusion Chromatography with Multi-angle Light Scattering Detection (SEC-MALS)

Austin, P.R. (1988). Chitin solutions and purification of chitin. *Methods Enzymol*., 161, 403–407, pISSN 0076-6879

Babiker, E.E. (2002). Effect of chitosan conjugation on the functional properties and bactericidal activity of gluten peptides. *Food Chem*., 79, 367-372, ISSN 0308-8146

Berth, G. & Dautzenberg, H. (2002). The degree of acetylation of chitosans and its effect on the chain conformation in aqueous solution *Carbohydr. Polym.,* 47, 39–51, ISSN 0144-8617

Berth, G.; Dautzenberg H. & Peter, M.G. (1998). Physico-chemical characterization of chitosans varying in degree of acetylation. *Carbohydr. Polym.,* 36, 205-216, ISSN 0144-8617

Bhattarai, N.; Edmondson, D.; Veiseh, O.; Matsen F.A. & Zhang, M. (2005). Electrospun chitosan-based nanofibers and their cellular compatibility. *Biomaterials,* 26, 6176–6184, pISSN 0142-9612

Boesel, L.F.; Reis, R.L. & Román, J.S. (2009). Innovative Approach for Producing Injectable, Biodegradable Materials Using Chitooligosaccharides and Green Chemistry. *Biomacromolecules*, 10, 465-470, pISSN 1525-7797

Bozkir, A. & Saka, O.M. (2004). Chitosan Nanoparticles for Plasmid DANN Delivery: Effect of Chitosan Molecular Structure on Formulation and Release Characteristics. *Drug deliv.*, 11, 107-112, pISSN 1071-7544

Broussignac, P. (1968). Haut Polymère Naturel Connu dans I'Industrie: Le Chitosane. *Chim. Ind. Genie Chim*., 99, 1241–1247

Brugnerotto, J.; Desbrières, J.; Heux, L.; Mazeau, K. & Rinaudo, M. (2001). Overview on structural characterization of chitosan molecules in relation with their behavior in solution. *Macromol. Symp.*, 168, 1–20, ISSN 1022-1360

Centelles, M.N; Qian, C.; Campanero, M.A. & Irache, J.M. (2008). New methodologies to characterize the effectiveness of the gene transfer mediated by DNA-chitosan nanoparticles. *Int. J. Nanomedicine*, 3, 451–460, pISSN 1176-9114

Chae, S.Y.; Jang, M.-K. & Nah, J.-W. (2005). Influence of molecular weight on oral absorption of water soluble chitosans. *J. Control. Release*, 102, 383-394, pISSN 0168-3659

Charoenthai, N.; Kleinebudde, P. & Puttipipatkhachorn, S. (2007). Influence of Chitosan Type on the Properties of Extruded Pellets With Low Amount of Microcrystalline Cellulose. *AAPS Pharm. Sci. Tech*., 8, Article 64, ISSN 1530-9932

Chaussard, G. & Domard, A. (2004). New Aspects of the Extraction of Chitin from Squid Pens. *Biomacromolecules*, 5, 559-564, ISSN 1525-7797

Chen, M.C.; Yeh, G.H.C. & Chiang, B.H. (1996). Antimicrobial and physicochemical properties of methylcellulose and chitosan films containing a preservative. *J. Food Process Preserv.*, 20, 379-390, ISSN 01458892

Chen, R. & Tsaih, M. (1998). Effect of temperature on the intrinsic viscosity and conformation of chitosans in dilute HCl solution. *Int. J. Biol. Macromol.*, 23, 135–141, pISSN 0141-8130

Cheng, M.; Deng, J.; Yang, F.; Gong, Y.; Zhao N. & Zhang, X. (2003). Study on physical properties and nerve cell affinity of composite films from chitosan and gelatin solutions. *Biomaterials,* 24, 2871–2880, pISSN 0142-9612

Chien, P. & Chou, C. (2006). Antifungal activity of chitosan and its application to control post-harvest quality and fungal rotting of Tankan citrus fruit (Citrus tankan Hayata). *J. Sci. Food Agric*., 86, 1964-1969, pISSN 0022-5142

Chiou, S.H.; Wu, W.T.; Huang, Y.Y. & Chung, T,W. (2001). Effects of the characteristics of chitosan on controlling drug release of chitosan coated PLLA microspheres. *J. Microencapsul*., 18, 613-625, pISSN 0265-2048

Chirkov, S.N. (2002). The Antiviral Activity of Chitosan (Review). *Appl. Biochem. Microbiol*., 38, 1-8, pISSN 0003-6838

Cho, Y.-W.; Cho, Y.-N.; Chung, S.-H.; Yoo, G. & Ko, S.-W. (1999). Water soluble chitin as a wound healing accelerator. *Biomaterials*, 20, 2139-2145, pISSN 0142-9612

Christensen, B.; Vold, I. & Vårum, K. (2008). Chain stiffness and extension of chitosans and periodate oxidised chitosans studied by size-exclusion chromatography combined with light scattering and viscosity detectors. *Carbohydr. Polym*., 74, 559–565, ISSN 0144-8617

Chung, T.W.; Yang, J.; Akaike, T.; Cho, K.Y.; Nah, J.W.; Kim, S.I. & Cho, C.S. (2002). Preparation of alginate/galactosylated chitosan scaffold for hepatocyte attachment. *Biomaterials,* 23, 2827–2834, pISSN 0142-9612

Chupa, J.M.; Foster, A.M.; Sumner, S.R.; Madihally, S.V. & Matthew, H.W. (2000). Vascular cell responses to polysaccharide materials: in vitro and in vivo evaluations. *Biomaterials,* 21, 2315–2322, pISSN 0142-9612

Cölfen, H.; Berth, G.& Dautzenberg, H. (2001). Hydrodynamic studies on chitosans in aqueous solution. *Carbohydr. Polym*., 45, 373–383, ISSN 0144-8617

Curotto, E. & Aros, F. (1993). Quantitative determination of chitosan and the percentage of free amino groups. *Anal. Biochem*., 211, 40–241, pISSN 0003-2697

Das, S. & Ganesh, E.A. (2010). Extraction of Chitin from Trash Crabs (*Podophthalmus vigil*) by an Eccentric Method. *Curr Res. J. Biol. Sci*., 2, 72-75, pISSN 2041-076X

de la Fuente, M.; Seijo, B. & Alonso, M.J. (2008). Design of novel polysaccharidic nanostructures for gene delivery. *Nanotechnology*, 19, 075105 (9pp) doi:10.1088/0957-4484/19/7/075105 pISSN 0957-4484, ISSN 1361-6528 (online)

De Velde, K.V. & Kiekens, P. (2004). Structure analysis and degree of substitution of chitin, chitosan and dibutyrylchitin by FT-IR spectroscopy and solid state ^{13}C-NMR. *Carbohydr. Polym*., 58, 409–416, ISSN 0144-8617

Di Martino, A.; Sittinger, M. & Risbud, M.V. (2005). Chitosan: A versatile biopolymer for orthopaedic tissue-engineering, *Biomaterials,* 26, 5983–5990, pISSN 0142-9612

Ding, Z.; Chen, J.; Gao, S.; Chang, J.; Zhang, J. & Kang, E.T. (2004). Immobilization of chitosan onto poly-l-lactic acid film surface by plasma graft polymerization to

control the morphology of fibroblast and liver cells. *Biomaterials,* 25, 1059–1067, pISSN 0142-9612

Domard, A. (2007). Recent concepts regarding the physical chemistry of chitosan and their applications, plenary lecture held on the 8th International Conference of the European Chitin Society, Antalya, Turkey

Domard, A. (2010). A perspective on 30 years research on chitin and chitosan. *Carbohydr. Polym.*, doi:10.1016/j.carbpol.2010.04.083, ISSN 0144-8617

Domard, A.(1987). Determination of *N*-acetyl content in chitosan samples by c.d. measurements. *Int. J. Biol. Macromol.*, 9, 333–336, pISSN 0141-8130

Eaton, P.; Fernandes, J.C.; Pereira, E.; Pintado, M.E. & Malcata, F.X. (2008). Atomic force microscopy study of the antimicrobial effects of chitosans on *Escherichia coli* and *Staphylococcus aureus*. *Ultramicroscopy*, 108, 1128-1134, pISSN 0304-3991

Felt, O.; Baeyens, V.; Buri, P. & Gurny, R. (2001). Delivery of Antibiotics to the Eye Using a Positively Charged Polysaccharide as Vehicle. *AAPS Pharm. Sci.*, 3, Article 34, DOI: 10.1208/ps030434, eISSN 1522-1059

Ferber, D. (2001). Gene therapy: safer and virus-free? *Science*, 294, 1638-1642, pISSN 0036-8075

Fernandes, J.C.; Eaton, P.; Gomes, A.M.; Pintado, M.E. & Malcata, F.X. (2009). Study of the antibacterial effects of chitosans on *Bacillus cereus* (and ist spores) by atomic force microscopy imaging and nanoindentation. *Ultramicroscopy*, 109, 854-860, pISSN 0304-3991

Fernandes, J.C.; Tavaria, F.K.; Fonseca, S.C.; Ramos, Ó.S.; Pintado, M.E. & Malcata, F.X. (2010). In Vitro Screening for Antimicrobial Activity of Chitosans and Chitooligosaccharides, Aiming at Potential Uses in Functional Textiles. *J. Microbiol. Biotechnol.*, 20, 311–318, pISSN 1017-7825

Fernandez-Megia, E.; Novoa-Carballal, Quiñoá, R.E. & Riguera, R. (2005). Optimal routine conditions for the determination of the degree of acetylation of chitosan by 1H-NMR. *Carbohydr. Polym.*, 61, 55–161, ISSN 0144-8617

Freier, T.; Montenegro, R.; Koh, H..S. & Shoichet, M.S. (2005). Chitin-based tubes for tissue engineering in the nervous system. *Biomaterials*, 26, 4624-32, pISSN 0142-9612

Genta, I.; Perugini, P. & Pavanetto, F. (1998). Different molecular weight chitosan microspheres: influence on drug loading and drug release. *Drug Dev. Ind. Pharm.*, 24, 779-784, pISSN 0363-9045

Gerasimenko, D.V.; Avdienko, I.D.; Bannikova, G.E.; Zueva, O.Yu. & Varlamov V.P. (2004). Antibacterial Effects of Water-Soluble Low-Molecular-Weight Chitosans on Different Microorganisms. *Appl. Biochem. Microbiol.*, 40, 253-257, pISSN 0003-6838

Goy, R.C.; de Britto, D. & Assis, O.B.G. (2009). A Review of the Antimicrobial Activity of Chitosan. *Polímeros: Ciência e Tecnologia*, 19, 241-247, ISSN 0104-1428

Gupta, K.C. & Jabrail, F.H. (2006). Effects of degree of deacetylation and crosslinking on physical characteristics, swelling and release behavior of chitosan microspheres. *Carbohydr. Polym.*, 66, 43-54, ISSN 0144-8617

Gupta, K.C. & Jabrail, F.H. (2007). Glutaraldehyde cross-linked chitosan microspheres for controlled release of centchroman. *Carbohydr. Res.*, 342, 2244-2252, pISSN 0008-6215

Harish Prashanth, K.V. & Tharanathan, R.N. (2005). Depolymerized products of chitosan as potent inhibitors of tumor-induced angiogenesis. *Biochim. Biophys. Acta*, 1722, 22-29, ISSN 0006-3002

Harish Prashanth, K.V. & Tharanathan, R.N. (2007). Chitin/chitosan:modifications and their unlimited application potential – an overview. *Trends Food Sci. Technol*., 18, 117-131, pISSN 0924-2244

Hasegawa, M.; Isogai, A. & Onabe, F. (1994). Molecular mass distribution of chitin and chitosan. *Carbohydr. Res.,* 262, 161–166, pISSN 0008-6215

He, P.; Davis, S.S. & Illum, L. (1998). In vitro evaluation of the mucoadhesive properties of chitosan microspheres. *Int. J. Pharm*., 166, 75-88, pISSN 0378-5173

Hejazi, R.& Amiji, M. (2003). Chitosan-based gastrointestinal delivery systems. *J. Control Release,* 89, 151–165, pISSN 0168-3659

Helander, I.M.; Nurmiaho-Lassila, E.L.; Ahvenainen, R.; Rhoades, J. & Roller, S. (2001). Chitosan disrupts the barrier properties of the outer membrane of gram-negative bacteria. *Int. J. Food Microbiol.,* 71, 235–244, pISSN 0168-1605

Heux, L.; Brugnerotto, J.; Desbrières, J.; Versali, M.F. & Rinaudo, M. (2000). Solid state NMR for determination of degree of acetylation of chitin and chitosan. *Biomacromolecules*, 1, 746–751, pISSN 1525-7797

Hirai, A.; Odani, H. & Nakajima, A. (1991). Determination of degree of deacetylation of chitosan by ^{1}H-NMR spectroscopy. *Polym. Bull*., 26, 87-94, pISSN 0170-0839

Hirano, S. (1999). Chitin and chitosan as novel biotechnological materials. *Polym. Int.*, 48, 732-734, pISSN 0959-8103

Hirano, S.; Tsuchida, H. & Nagao, N. (1989). *N*-acetylation in chitosan and the rate of its enzymic hydrolysis. *Biomaterials*, 10, 574-576, pISSN 0142-9612

Ho, M.H.; Wang, D.M.; Hsieh, H.J.; Liub, H.C.; Hsienc, T. Y. ; Laid, J.Y. & Hou, L.T. (2005) Preparation and characterization of RGD-immobilized chitosan scaffolds. *Biomaterials*, 26, 3197-3206, pISSN 0142-9612

Holan, Z.; Votruba, J. & Vlasalova, V. (1980) New method of chitin determination based on deacylation and gas-liquid chromatographic assay of liberated acetic acid. *J. Chromatogr*., 190, 67-76, pISSN 0021-9673

Horton, D. & Just, E.K. (1973). Preparation from chitin of (1→4)-2-amino-2-deoxy-β-D-glucopyranuronan and its 2-sulfoamino analog having blood-anticoagulant properties. *Carbohydr. Res.,* 28, 173–179, pISSN 0008-6215

Howling, G.I.; Dettmar, P.W.; Goddard, P.A.; Hampson, F.C.; Dornish, M. & Wood, E.J. (2001). The effect of chitin and chitosan on the proliferation of human skin fibroblasts and keratinocytes in vitro. *Biomaterials*, 22, 2959-2966, pISSN 0142-9612

Hsieh, C.Y.; Tsai, S.P.; Wang, D.M.; Chang Y.N. & Hsieh, H.J. (2005). Preparation of gamma-PGA/chitosan composite tissue engineering matrices. *Biomaterials,* 26, 5617–5623, pISSN 0142-9612

Hsu, S.; Whu, S.W.; Tsai, C.-L.; Wu, Y.-H.; Chen, H.-W. & Hsieh, K.-H. (2004a). Chitosan as Scaffold Materials: Effects of Molecular Weight and Degree of Deacetylation. *J. Polym. Res.*, 11, 141-147, ISSN 1022-9760

Hsu, S.H.; Whu, S.W.; Hsieh, S.C.; Tsai, C.L.; Chen D.C. & Tan, T.S. (2004b). Evaluation of chitosan–alginate–hyaluronate complexes modified by an RGD-containing protein as tissue-engineering scaffolds for cartilage regeneration. *Artif. Organs,* 28, 693–703, pISSN 0160-564X

Huang, X.J.; Ge, D. & Zu, C.K. (2007). Preparation and characterization of stable chitosan nanofibrous membrane for lipase immobilization. *Eur. Polym.* J., 43, 3710-3718, ISSN 0014-3057

Itakura, M.; Shimada, K.; Matsuyama, S.; Saito, T. & Kinugasa, S. (2005). A convenient method to determine the rayleigh ratio with uniform polystyrene oligomers. *J. Appl. Polym. Sci.,* 99, 1953–1959, ISSN 1097-4628

Itoh, S.; Yamaguchi, I.; Suzuki, M.; Ichinose, S.; Takakuda, K.; Kobayashi, H. Shinomiya, K. & Tanaka, J. (2003). Hydroxyapatite-coated tendon chitosan tubes with adsorbed laminin peptides facilitate nerve regeneration in vivo. *Brain Res.,* 993, 111–123, pISSN 0006-8993

Jaffer, S. & Sampalis, J.S. (2007). Efficacy and safety of chitosan HEP-40™ in the management of hypercholesterolemia: a randomized, multicenter, placebo-controlled trial. *Altern. Med. Rev.*, 12, 265-273, ISSN 1089-5159

Jain, A. & Jain, S.K. (2008). In vitro and cell uptake studies for targeting of ligand anchored nanoparticles for colon tumors. *Eur. J. Pharm. Sci.* , 35, 404–416, pISSN 0928-0987

Jayakumar, R.; Chennazhi, K.P.; Muzzarelli, R.A.A.; Tamura, H.; Nair, S.V. & Selvamurugan, N. (2010). Chitosan conjugated DNA nanoparticles in gene therapy. *Carbohydr. Polym.*, 79, 1–8, ISSN 0144-8617

Jayakumar, R.; Reis, R.L. & Mano, J.F. (2006). Synthesis of *N*-carboxymethyl chitosan beads for controlled drug delivery applications. *Mater. Sci. Forum.,* 514–516, 1015–1019, ISSN 0255-5476

Je, J.Y. & Kim, S.K. (2006). Reactive oxygen species scavenging activity of aminoderivatized chitosan with different degree of deacetylation. *Bioorg. Med. Chem*., 14, 5989-5994, pISSN 0968-0896

Je, J.Y.; Park, P.J. & Kim, S.K. (2004). Free radical scavenging properties of hetero-chitooligosaccharides using an ESR spectroscopy. *Food Chem. Toxicol*., 42, 381-387, pISSN 0278-6915

Jeon, Y.-J. & Kim, S.-K. (2002). Antitumor Activity of Chitosan Oligosaccharides Produced In Ultrafiltration Membrane Reactor System. *J. Microbiol. Biotechnol.*, 12, 503-507, pISSN 1017-7825

Jeong, Y.-I.; Kim, D.-G.; Jang, M.-K. & Nah, J.-W. (2008). Preparation and spectroscopic characterization of methoxy poly(ethylene glycol)-grafted water-soluble Chitosan. *Carbohydr. Res*., 343, 282–289, ISSN 0008-6215

Jia, Z.; Shen, D. & Xu, W. (2001). Synthesis and antibacterial activities of quaternary ammonium salt of chitosan. *Carbohydr. Res*., 333, 1–6, ISSN 0008-6215

Jung, B.O.; Kim, C.H.; Choi, K.S.; Lee, Y.M. & Kim, J.J. (1999). Preparation of Amphiphilic Chitosan and Their Antimicrobial Activities. *J. Appl. Polym. Sci.,* 72, 1713–1719, ISSN 1097-4628

Just, U.; Weidner, S.; Kilz, P. & Hofe, T. (2005). Polymer reference materials: Round-robin tests for the determination of molar masses. *Int. J. Polym. Anal. Charact*., 10, 225–243, pISSN 1023-666X

Kasaai, M.; Arul, J. & Charlet, G. (2000). Intrinsic viscosity-molecular weight relationship for chitosan. *J. Polym. Sci. B Polym. Phys*., 38, 2591–2598, ISSN 0887-6266

Kato, Y.; Onishi, H. & Machida, Y. (2001). Biological characteristics of lactosaminated N-succinyl-chitosan as a liver-specific drug carrier in mice. *J. Control Release,* 70, 295–307, pISSN 0168-3659

Kato, Y.; Onishi, H. & Machida, Y. (2004). *N*-succinyl-chitosan as a drug carrier: waterinsoluble and water-soluble conjugates. *Biomaterials,* 25, 907–915, pISSN 0142-9612

Kawakami, T.; Antoh, M.; Hasegawa, H.; Yamagishi, T.; Ito M. & Eda, S. (1992). Experimental study on osteoconductive properties of a chitosan-bonded hydroxyapatite self-hardening paste. *Biomaterials,* 13, 759–763, pISSN 0142-9612

Kaye, W. & McDaniel, J. (1974). Low-angle laser light scattering: Rayleigh factors and depolarization ratios. *Appl. Opt*., 13, 1934–1937, ISSN 0003-6935

Kean, T. & Thanou, M. (2010). Biodegradation, biodistribution and toxicity of chitosan. *Adv Drug Deliv Rev*., 62, 3–11, ISSN 0169-409X

Khan, T.A. & Peh, K.K. (2003). Influence of chitosan molecular weight on its physical properties. *The International Medical Journal*, 2, 1, ISSN 1823-4631

Kiang, T.; Wen, J.; Lim, H.W.; Leong, K.W. & Kam, K.W. (2004). The effect of the degree of chitosan deacetylation on the efficiency of gene transfection. *Biomaterials*, 25, 5293-301, pISSN 0142-9612

Kim, I.Y.; Seo, S.J.; Moon, H.S.; Yoo, M.K.; Park, I.Y.; Kim, B.C. & Cho, C.S. (2008). Chitosan and its derivatives for tissue engineering applications. *Biotechnol. Adv.,* 26, 1–21, pISSN 0734-9750

Kim, T.H.; Nah, J.W.; Cho, M.H.; Park, T.G. & Cho, C.S. (2006). Receptor-mediated gene delivery into antigen presenting cells using mannosylated chitosan/DNA nanoparticles. *J. Nanosci. Nanotechnol.,* 6, 2796–2803, pISSN 1533-4880

Kittur, F.S.; Vishu Kumar, A.B.; Varadaraj, M.C. & Tharanathan, R.N. (2005). Chitoologosaccharides-preparation with the aid of pectinase isozyme from *Aspergillus niger* and their antibacterial activity. *Carbohydr. Res.*, 340, 1239-1245, pISSN 0008-6215

Knill, C.; Kennedy, J.; Mistry, J.; Miraftab, M.; Smart, G.; Groocock, M. & Williams, H. (2005). Acid hydrolysis of commercial chitosans. *J. Chem. Technol. Biotechnol.,* 80, 1291–1296, ISSN 0268-2575

Kofuji, K.; Qian, C.J.; Nishimura, M.; Sugiyama, I.; Murata, Y. & Kawashima, S. (2005). Relationship between physicochemical characteristics and functional properties of chitosan. *Eur. Polym. J.*, 41, 2784-91, ISSN 0014-3057

Köping-Höggård, M.; Tubulekas, I.; Guan, H.; Edwards, K.; Nilsson, M.; Vårum, K.M.; & Artursson, P. (2001). Chitosan as a nonviral gene delivery system. Structure-property relationships and characteristics compared with polyethylenimine in vitro and after lung administration in vivo. *Gene Ther*., 8, 1108-1121, pISSN 0969-7128

Koryagin, A.S.; Erofeeva, E.A.; Yakimovich, N.O.; Aleksandrova, E.A.; Smirnova, L.A. & Malkov, A.V. (2006). Analysis of antioxidant properties of chitosan and its oligomers. *Bull. Exp. Biol. Med*., 142, 461-463, ISSN0007-4888

Krajewska, B. (2004). Application of chitin- and chitosan-based materials for enzyme immobilizations: a review, *Enzyme Microb. Technol.,* 35, 126–139, pISSN 0141-0229

Kratz, G.; Arnander, C.; Swedenborg, J.; Back, M.; Falk, C.; Gouda I. & Larm, O. (1997). Heparin–chitosan complexes stimulate wound healing in human skin. *Scand. J. Plast. Reconstr. Surg. Hand Surg.,* 31, 119–123, pISSN 0284-4311

Kubota, N.; Tatsumoto, N.; Sano, T. & Toya, K. (2000). A simple preparation of half *N*-acetylated chitosan highly soluble in water and aqueous organic solvents. *Carbohydr. Res.*, 324, 268–274, pISSN 0008-6215

Kurita, K. (2001). Controlled functionalization of the polysaccharide chitin. *Progr. Polym. Sci*., 26, 1921–1971, pISSN 0079-6700

Kurita, K.; Kaji, Y.; Mori, T. & Nishiyama, Y. (2000). Enzymatic degradation of [beta]-chitin: susceptibility and the influence of deacetylation. *Carbohydr. Polym*., 42, 19-21, ISSN 0144-8617

Lal, G. & Hayes, E. (1984). Determination of the amine content of chitosan by pyrolysis-gas chromatography. *J. Anal. Appl. Pyrolysis*, 6, 183–193, ISSN 0165-2370

Lamarque, G.; Cretenet, M.; Viton, C. & Domard, A. (2005). New route of deacetylation of *a*- and *β*-chitins by means of freeze-pump out-thaw cycles. *Biomacromolecules*, 6, 1380–1388, pISSN 1525-7797

Lamarque, G.; Viton, C. & Domard, A. (2004). Comparative study of the second and third heterogeneous deacetylations of *a*-and *β*-chitins in a multi step process. *Biomacromolecules*, 5, 1899–1907, pISSN 1525-7797

Lavertu, M.; Methot, S.; Tran-Khanh, N. & Buschmann, M.D. (2006). High efficiency gene transfer using chitosan/DNA nanoparticles with specific combinations of molecular weight and degree of deacetylation. *Biomaterials*, 27, 4815-4824, pISSN 0142-9612

Lee, H.G.; Park, Y.-S.; Jung, J.-S. & Shin, W.-S. (2002). Chitosan oligosaccharide, dp 2-8, have prebiotic effect on the *Bifidobacterium bifidium* and *Lactobacillus* sp. *Anaerobe*, 8, 319-324, pISSN 1075-9964

Lee, J.E.; Kim, K.E.; Kwon, I.C.; Ahn, H.J.; Lee, S.H.; Cho, H.; Kim, H.J.; Seong, S.C. & Lee, M.C. (2004a). Effects of the controlled-released TGF-beta 1 from chitosan microspheres on chondrocytes cultured in a collagen/chitosan/glycosaminoglycan scaffold. *Biomaterials,* 25, 4163–4173, pISSN 0142-9612

Lee, J.S.; Cha, D.S. & Park, H.J. (2004b). Survival of Freeze-Dried Lactobacillus bulgaricus KFRI 673 in Chitosan-Coated Calcium Alginate Microparticles. *J. Agric. Food Chem*., 52, 7300-7305, pISSN 0021-8561

Li, X.; Tsushima, Y.; Morimoto, M.; Saimoto, H.; Okamoto, Y.; Minami, S. & Shigemasa, Y. (2000). Biological activity of chitosan–sugar hybrids: specific interaction with lectin. *Polym. Adv. Techno*l., 11, 176–179, pISSN1042-7147

Li, Y.; Liu L. & Fang, F. (2003). Plasma-induced grafting of hydroxyethyl methacrylate (HEMA) onto chitosan membranes by a swelling method. *Polym. Int.,* 52, 285–290, pISSN 0959-8103

Lin, C.W. & Lin, J.C. (2003). Characterization and blood coagulation evaluation of the water-soluble chitooligosaccharides prepared by a facile fractionation method. *Biomacromolecules*, 4, 1691–1697, pISSN 1525-7797

Lin, S.-B.; Lin, Y.-C. & Chen, H.-H. (2009). Low molecular weight chitosan prepared with the aid of cellulase, lysozyme and chitinase: Characterisation and antibacterial activity. *Food Chem.,* 116, 47-53, ISSN 0308-8146

Liu, H.; Du, Y.; Yang, J. & Zhu, H. (2004). Structural characterization and antimicrobial activity of chitosan/betain derivative complex. *Carbohydr. Polym.,* 55, 291–297, ISSN 0144-8617

Liu, W.G.; Yao, K.& D. Liu, Q.G. (2001a). Formation of a DNA/*N*-deadecylated chitosan complex and salt-induced gene delivery. *J. Appl. Polym. Sci*., 82, 3391–3395, ISSN 1097-4628

Liu, X.F.; Guan, Y.L.; Yang, D.Z.; Li Z. & Yao, K.D. (2001b). Antimicrobial action of chitosan and carboxymethylated chitosan. *J. Appl. Polym. Sci.,* 79, 1324–1335, ISSN 1097-4628

Lorenzo-Lamosa, M.L.; Remunan-Lopez, C.; Vila-Jato, J.L. & Alonso, M.J. (1998). Design of microencapsulated chitosan microspheres for colonic drug delivery. *J. Control. Release,* 52, 109–118, pISSN 0168-3659

Lueben, H.L.; Leeuw, B.J.D.; Langemeyer, B.W.; Boer, A.G.D.; Verhoef, J.C. & Junginger, H.E. (1996). Mucoadhesive polymers in peroral peptide drug delivery. VI. Carbomer and chitosan improve the intestinal absorption of the peptide drug buserelin in vivo. *Pharm. Res.,* 13, 1668–1672, ISSN 0724-8741

Ma, L.; Gao, C.; Mao, Z.; Zhou, J.; Shen J.; Hu, X. & Han, C. (2003). Collagen/chitosan porous scaffolds with improved biostability for skin tissue engineering. *Biomaterials,* 24, 4833–4841, pISSN 0142-9612

Madihally, S.V. &, Howard, W.T. (1999). Porous chitosan scaffolds for tissue engineering. *Biomaterials*, 20, 1133-1142, pISSN 0142-9612.

Maeda, Y. & Kimura, Y. (2004) Antitumor Effects of Various Low-Molecular-Weight Chitosans Are Due to Increased Natural Killer Activity of Intestinal Intraepithelial Lymphocytes in Sarcoma 180–Bearing Mice. *J. Nutr.*, 134, 945-50, pISSN 0022-3166

Manni, L.; Ghorbel-Bellaaj, O.; Jellouli, K.; Younes, I. & Nasri, M. (2010). Extraction and Characterization of Chitin, Chitosan, and Protein Hydrolysates Prepared from Shrimp Waste by Treatment with Crude Protease from Bacillus cereus SV1. *Appl. Biochem. Biotechnol*., 162, 345–357, pISSN 0273-2289

Mao, H.Q.; Roy, K.; Troung-Le, V.L.; Janes, K.A.; Lin, K.Y.; Wang, Y.; August T. & Leong, K.W. (2001). Chitosan-DNA nanoparticles as gene carriers: synthesis, characterization and transfection efficiency. *J. Control. Release,* 70, 399–421, pISSN 0168-3659

Mao, J.S.; Cui, Y.L.; Wang, X.H.; Sun, Y.; Yin, Y.J.; Zhao, H.M. & Yao, K.D. (2004). A preliminary study on chitosan and gelatin polyelectrolyte complex cytocompatibility by cell cycle and apoptosis analysis, *Biomaterials,* 25, 3973-3981, pISSN 0142-9612

Martinou, A.; Bouriotis, V.; Stokke, B.T. & Vårum, K.M. (1998). Mode of action of chitin deacetylase from *Mucor rouxii* on partially *N*-acetylated chitosans. *Carbohydr. Res.*, 311, 71-78, pISSN 0008-6215

Min, B.M.; Lee, S.W.; Lim, J.N.; You, Y.; Lee, T.S.; Kang, P.H. & Park, W.H. (2004). Chitin and chitosan nanofibers: electrospinning of chitin and deacetylation of chitin nanofibers. *Polymer*, 45, 7137–7142, pISSN 0032-3861

Minagawa, T.; Okamura, Y.; Shigemasa, Y.; Minami, S. & Okamoto, Y. (2007). Effects of molecular weight and deacetylation degree of chitin/chitosan on wound healing. *Carbohydr. Polym*., 67, 640-644, ISSN 0144-8617

Miwa, A.; Ishibe, A.; Nakano, M.; Yamahira, T.; Itai, S.; Jinno, S. & Kawahara, H. (1998). Development of novel chitosan derivatives as micellar carriers of taxol. *Pharm Res.*, 15, 1844–1850, ISSN 0724-8741

Miya, M.; Iwamato, R. & Yoshikawa, S. (1980). I.r. spectroscopic determination of CONH content in highly deacylated chitosan. *Int. J. Biol. Macromol.*, 2, 323–324, pISSN 0141-8130

Mumper, R.; Wang, J.; Claspell, J. & Rolland, A.P. (1995). Novel polymeric condensing carriers for gene delivery. *Proc. Int. Symp. Controll. Release Bioact. Mater.,* 22, 178-179

Murugan, R. & Ramakrishna, S. (2004) Bioresorbable composite bone paste using polysaccharide based nanohydroxyapatite. *Biomaterials*, 25, 17, 3829-3835, pISSN 0142-9612

Muzzarelli, R. (1985). Removal of uranium from solutions and brines by a derivative of chitosan and ascorbic acid. *Carbohydr. Polym.*, 5, 85–89, ISSN 0144-8617

Muzzarelli, R.A.A. & Muzzarelli, C. (2005). Chitosan chemistry: Relevance to the biomedical sciences, *Adv. Polym. Sci.*, 186, 151–209, ISSN 0065-3195

Muzzarelli, R.A.A. (1997). Human enzymatic activities related to the therapeutic administration of chitin derivatives. *Cell Mol. Life Sci.,* 53, 131–140, pISSN 1420-682X

Muzzarelli, R.A.A., (Ed) (1973). *Natural Chelating Polymers*, Pergamon Press, New York, NY, USA,. pp. 83

Muzzarelli, R.A.A.; Jeuniaux, C. & Gooday, G.W. (1986). Chitin in nature and technology, Plenum Publishing Corporation, New York

Nah, J.W. & Jang, M.K. (2002). Spectroscopic characterization and preparation of low molecular, water-soluble chitosan with free-amine group by novel method. *J. Polym. Sci. A Polym. Chem.,* 40, 3796–3803, pISSN 0887-624X

Nair, R.; Reddy, B.H; Kumar, C.K.A. & Kumar, K.J. (2009) Application of Chitosan microspheres as drug carriers : A Review. *J. Pharm. Sci. & Res.*, 1, 1-12, ISSN 0975-1459

Nanjo, F.; Katsumi, R. & Sakai, K. (1991). Enzymatic method for determination of the degree of deacetylation of chiosan. *Anal. Biochem.*, 193, 164–167, pISSN 0003-2697

Neugebauer, W.; Neugebauer, E. & Brezinski, R. (1989). Determination of the degree of *N*-acetylation of chitin-chitosan with picric acid. *Carbohydr. Res.,* 189, 363–367, pISSN 0008-6215

Niola, F.; Basora, N.; Chornet, E. & Vidal, P. (1993). A rapid method for the determination of the degree of *N*-acetylation of chitin-chitosan samples by acid hydrolysis and HPLC. *Carbohydr. Res.*, 23, 1–9, pISSN 0008-6215

Nishimura, S.; Kai, H.; Shinada, K.; Yoshida, T.; Tokura, S. & Kurita, K. (1998). Regioselective syntheses of sulfated polysaccharides: specifc anti-HIV-1 activity of novel chitin sulfates. *Carbohydr. Res.,* 306, 427–433, pISSN 0008-6215

Nwe, N.; Furuike, T. & Tamura, H. (2009) The Mechanical and Biological Properties of Chitosan Scaffolds for Tissue Regeneration Templates Are Significantly Enhanced by Chitosan from Gongronella butleri. *Materials*, 2, 374-398, ISSN 1996-1944

Oh, H.; Kim, Y.; Chang, E. & Kim. J. (2001). Antimicrobial Characteristics of Chitosans against Food Spoilage Microorganisms in Liquid Media and Mayonnaise. *Biosci. Biotechnol. Biochem*., 65, 2378-83, pISSN 0916-8451

Osman, M.; Fayed, S.A.; Ghada, I.M. & Romeilah, R.M. (2010). Protective Effects of Chitosan, Ascorbic Acid and *Gymnema Sylvestre* Against Hypercholesterolemia in Male Rats. *Aust. J. Basic Appl. Sci*., 4, 89-98, ISSN 1991-8178

Ottøy, M.; Vårum, K. & Smidsrød, O. (1995). Compositional heterogeneity of heterogeneously deacetylated chitosans. *Carbohydr. Polym.*, 29, 17–24, ISSN 0144-8617

Ottøy, M.; Vårum, K.; Christensen, B.; Anthonsen, M. & Smidsrød, O. (1996). Preparative and analytical size-exclusion chromatography of chitosans. *Carbohydr. Polym.*, 31, 253–261, ISSN 0144-8617

Pa, J.H. & Yu, T. (2001). Light scattering study of chitosan in acetic acid aqueous solutions. *Macromol. Chem. Phys.*, 202, 985–991, ISSN1022-1352

Pangburn, S.H.; Trescony, P.V. & Heller, J. (1982). Lysozyme degradation of partially deacetylated chitin, its films and hydrogels. *Biomaterials*, 3, 105-108, pISSN 0142-9612

Paolicelli, P.; de la Fuente, M.; Sanchez, A.; Seijo, B. & Alonso, M.J. (2009). Chitosan Nanoparticles for Drug Delivery to the Eye. *Expert Opin. Drug Deliv.*, 6, 239–253, pISSN 1742-5247

Papineau, A.M.; Hoover, D.G.; Knorr, D. & Farkas, D.F. (1991). Antimicrobial effect of water-soluble chitosans with high hydrostatic pressure. *Food Biotechnol.*, 5, 45-47, pISSN 0890-5436

Park, I.K.; Yang, J.; Jeong, H.J.; Bom, H.S.; Harada, I.; Akaike, T.; Kima, S.I. & Cho, C.H. (2003). Galactosylated chitosan as a synthetic extracellular matrix for hepatocytes attachment. *Biomaterials,* 24, 2331–2337, pISSN 0142-9612

Park, J.-K.; Chae, S.J.; Choi, C. & Nah, J.-W. (2006). Modulation of molecular weight, charge ratio, and pH effect properties of high purity chitosan oligosaccharide for Efficient Gene Carrier. *Appl. Chem.,* 10, 53-56

Park, P.J.; Je, J.Y.; Byun, H.G.; Moon, S.H. & Kim, S.K. (2004a). Antimicrobial Activity of Hetero-Chitosans and Their Oligosaccharides with Different Molecular Weights. *J. Microbiol Biotechnol*., 14, 317-23, pISSN 1017-7825

Park, P.J.; Je, J.Y. & Kim, S.K. (2004b). Free radical scavenging activities of differently deacetylated chitosans using an ESR spectrometer. *Carbohydr. Polym*., 55, 17-22, pISSN 0144-8617

Patel, S.S. (2006). Pharmaceutical Significance of Chitosan: A Review, *Pharm. Rev.,* 4, 6, ISSN 1918-5561

Percot, A.; Viton, C. & Domard, A. (2003). Optimization of chitin extraction from shrimp shells. *Biomacromolecules*, 4, 12–18, ISSN 1525-7797

Perioli, L.; Ambrogi, V.; Pagano, C.; Scuota, S. & Rossi, C. (2009). Chitosan as a New Polymer for Metronidazole Mucoadhesive Tablets for Vaginal Administration. *Int. J. Pharm*., 377, 120–127, pISSN 0378-5173.

Pillai, C.K.S.; Paul, W. & Sharma, C.P. (2009). Chitin and chitosan polymers: Chemistry, solubility and fiber formation. *Prog. Polym. Scie*., 34, 641–678, ISSN 0079-6700

Prabaharan, M.; Rodriguez-Perez, M.A.; de Saja, J.A. & Mano, J.F. (2006). Preparation and Characterization of Poly(L-lactic acid)-Chitosan Hybrid Scaffolds With Drug Release Capability. *J. Biomed. Mater. Res.* Part B. *Appl. Biomaterials*, 81, 427-434, pISSN 0142-9612

Prochazkova, S.; Vårum, K. & Østgaard, K. (1999). Quantitative determination of chitosans by ninhydrin. *Carbohydr. Polym*., 8, 115–122, ISSN 0144-8617

Qin, C.Q.; Du, Y.M.; Xiao, L.; Gao, X.H.; Zhou, J.L. & Liu, H.L. (2002b). Effect of Molecular Weight and Structure on Antitumor Activity of Oxidized Chitosan. *Wuhan Univ. J. Nat. Sci*., 7, 231-236, ISSN 1007-1202

Qin, C.Q.; Du, Y.M.; Xiao, L.; Li, Z. & Gao, X.H. (2002a). Enzymic preparation of water-soluble chitosan and their antitumor activity. *Int. J. Biol. Macromol*., 31, 111-117, ISSN 0141-8130

Qin, C.Q.; Zhou, B.; Zeng, L.; Zhang, Z.; Liu, Y.; Du, Y.M. & Xiao, L. (2004). The physicochemical properties and antitumor activity of cellulose-treated chitosan. *Food Chem*., 84, 107-115, ISSN 0308-8146

Rabea, E.I.; Badawy, M.E.-T.; Stevens, C.V.; Smagghe, G. & Steurbaut, W. (2003). Chitosan as Antimicrobial Agent: Applications and Mode of Action. *Biomacromolecules*, 4, 1457-1465, ISSN 1525-7797

Rabea, E.I.; El Badawy, M.T.; Rogge, T.M.; Stevens, C.V.; Höfte, M.; Steurbaut, W. & Smagghe, G. (2005). Insecticidal and fungicidal activity of new synthesized chitosan derivatives. *Pest Manag. Sci.,* 61, 951–960, pISSN 1526-498X

Ravi Kumar, M.N.V. (2000). A review of chitin and chitosan applications. *React. Funct. Polym*., 46, 1–27, ISSN 1381-5148

Ravi Kumar, M.N.V.; Muzzarelli, R.A.A.; Muzzarelli, C.; Sashiwa, H A. & Domb, J. (2004). Chitosan Chemistry and Pharmaceutical Perspectives, *Chem. Rev*., 104, 6017-6084, pISSN 0009-2665

Raymond, L.; Morin, F. & Marchessault, R. (1993). Degree of deacetylation of chitosan using conductometric titration and solid-state NMR. *Carbohydr. Res*., 246, 331–336, pISSN 0008-6215

Richardson, S.C.W.; Kolbe, H.V.J. & Duncan, R. (1999). Potential of low molecular mass chitosan as a DNA delivery system: biocompatibility, body distribution and ability to complex and protect DNA. *Int. J. Pharm*., 178, 231-243, ISSN 0378-5173

Rinaudo, M. (2006). Chitin and chitosan: Properties and application. *Prog. Polym. Sci*., 31, 603–632, ISSN 0079-6700

Ringsdorf, H. (1975). Structure and properties of pharmacologically active polymers. *J. Polym. Sci. Polym. Symp*., 51, 135–153

Roberts, G.A.F. (1998). *Chitin Chemistry*, 2nd ed. MacMillan, London

Roberts, G.A.F. (1992). *Chitin Chemistry*, 1st ed. MacMillan, London

Roberts, G.A.F. (2007). The Road is long.... *Adv. Chitin Sci*., 10, 3–10, ISBN 978-975-491-250-0

Roller, S. & Covill, N. (1999). The antifungal properties of chitosan in laboratory media and apple juice. *Int. J. Food Microbiol*., 47, 67-77, pISSN 0168-1605

Saito, H.; Tabeta, R. & Ogawa, K. (1987). High-Resolution solid state ^{13}C-NMR-study of chitosan and its salts with acids. *Macromolecules*, 20, 2424–2430, pISSN 0024-9297

Sajomsang, W.; Ruktanonchai, U.; Gonil, P. Mayen, V. & Opanasopit, P. (2009a). Methylated *N*-aryl chitosan derivative/DNA complex nanoparticles for gene delivery: Synthesis and structure–activity relationships. *Carbohydr. Polym*., 78, 743–752, pISSN 0144-8617

Sajomsang, W; Tantayanon, S; Tangpasuthadol, V. & Daly, W.H. (2009b). Quaternization of N-aryl chitosan derivatives: synthesis, characterization, and antibacterial activity. *Carbohydr. Res*., 344, 2502-2511, pISSN 0008-6215

Sandford, P. (1989). *Chitosan: Commercial uses and potential applications*. In: Skjak-Braek E.; Anthonsen, T.; Standorf, P., Ed. *Chitin and chitosan: Sources chemistry, Biochemistry, Physical properties and Applications*. London, Elsevier Applied Science, pp. 51-69

Santos, N. & Castanho, M. (1996). Teaching light scattering spectroscopy: The dimensions and shape of tobaccomosaicvirus. *Biophys. J*., 71, 1641–1650, pISSN 0006-3495

Sarasam, A. & Madihally, S.V. (2005). Characterization of chitosan–polycaprolactone blends for tissue engineering applications. *Biomaterials,* 26, 5500–5508, pISSN 0142-9612

Sashiwa, H.; Saimoto, H.; Shigemasa, Y.; Ogawa, R. & Tokura, S. (1990). Lysozyme susceptibility of partially deacetylated chitin. *Int. J. Biol. Macromol.,* 12, 295–296, pISSN 0141-8130

Schatz, C.; Viton, C.; Delair, T.; Pichot, C. & Domard, A. (2003). Typical Physicochemical Behaviors of Chitosan in Aqueous Solution. *Biomacromolecules*, 4, 641–648, pISSN 1525-7797

Schipper, N.G.M.; Vårum, K. & Artursson, P. (1996). Chitosans as absorption enhancers for poorly absorbable drugs. 1: influence of molecular weight and degree of acetylation on drug transport across human intestinal epithelial (Caco-2) cells. *Pharm Res*., 13, 1686-1692, ISSN 0724-8741

Shelma, R; Paul, W. & Sharma, C.P. (2008). Chitin Nanofibre Reinforced Thin Chitosan Films for Wound Healing Application. *Trends Biomater. Artif. Organs*, 22, 111–115, pISSN 0391-3988

Shigemasa, Y.; Saito, K.; Sashiwa, H. &, Saimoto, H. (1994). Enzymatic degradation of chitins and partially deacetylated chitins. *Int. J. Biol. Macromol*., 16, 43-9, pISSN 0141-8130

Singh, D.K. & Ray, A.R. (2000) Biomedical Applications of Chitin, Chitosan, and Their Derivatives. *J.M.S.-Rev. Macromol. Chem. Phys*., 40, 69-83, pISSN 1558

Son, Y.J.; Jang, J.S.; Cho, Y.W.; Chung, H.; Park, R.W.; Kwon, I.C.; Kim, I.S.; Park, J.Y.; Seo, S.B.; Park, C.R. & Jeong, S.Y. (2003). Biodistribution and anti-tumor efficacy of

doxorubicin loaded glycol-chitosan nanoaggregates by EPR effect. *J. Control Release,* 91, 135-145, pISSN 0168-3659

Sorlier, P. (2002). Ph.D. thesis, Lyon, France

Sorlier, P.; Denuziere, A.; Viton, C. & Domard, A. (2001). Relation between the Degree of Acetylation and the Electrostatic Properties of Chitin and Chitosan *Biomacromolecules*, 2, 765-772, pISSN 1525-7797

Sorlier, P.; Viton, C. & Domard, A. (2002). Relation between Solution Properties and Degree of Acetylation of Chitosan: Role of Aging. *Biomacromolecules*, 3, 1336-1342, pISSN 1525-7797

Sosa, M.; Fazely, F.; Koch, J.; Vercellotti, S. & Ruprecht, R. (1991). *N*-Carboxymethylchitosan-*N,O*-sulfate as an anti-HIV-1 agent. *Biochem. Biophys. Res. Commun.,* 174, 489–496, pISSN 0006-291X

Strand, S.P.; Lelu, S.; Reitan, N.K.; de Lange Davies, C.; Artursson, P. & Vårum, K.M. (2010). Molecular design of chitosan gene delivery systems with an optimized balance between polyplex stability and polyplex unpacking. *Biomaterials*, 31, 975-987, pISSN 0142-9612

Struszczyk, M.H. & Struszczyk, K.J. (2007). *Medical Application of Chitin and Its Derivatives*; Polish Chitin Society, Monograph XII, 139–147

Sun, Y.; Cui, F.; Shi, K.; Wang, J.; Niu, M. & Ma, R. (2009). The Effect of Chitosan Molecular Weight on the Characteristics of Spray-Dried Methotrexate-Loaded Chitosan Microspheres for Nasal Administration. *Drug Dev. Ind. Pharm*., 35, 379-386, ISSN 0363-9045

Synowiecki, J. & Al-Khateeb, N.A. (2003). Production, Properties, and Some New Applications of Chitin and Its Derivatives. *Crit. Rev. Food Sci. Nutr.*, 43, 145–171, pISSN 1040-8398

Tan, M.L.; Choon, P.F.M. & Dass, C.R. (2009). Cancer, Chitosan Nanoparticles and Catalytic Nucleic Acids. *J. Pharm. Pharmacol*., 61, 3–12, pISSN 0022-3573

Tangsadthakun, C.; Kanokpanont, S.; Sanchavanakit, N.; Pichyangkura, R.; Banaprasert, T.; Tabata, Y. & Damrongsakkul, S. (2007). The influence of molecular weight of chitosan on the physical and biological properties of collagen/chitosan scaffolds. *J. Biomater. Sci. Polym. Ed*., 18, 147-163, pISSN 0920-5063

Tapola, N.S.; Lyyra, M.L.; Kolehmainen, R.M.; Sarkkinen, E.S. & Schauss, A.G. (2008). Safety Aspects and Cholesterol-Lowering Efficacy of Chitosan Tablets. *J. Am. Coll. Nutr*., 27, 22–30, pISSN 0731-5724

Techaarpornkul, S.; Wongkupasert, S.; Opanasopit, P.; Apirakaramwong, A.; Nunthanid, J. & Ruktanonchai, U. (2010). Chitosan-Mediated siRNA Delivery In Vitro: Effect of Polymer Molecular Weight, Concentration and Salt Forms. *AAPS Pharm. Sci.Tech*., 11, DOI: 10.1208/s12249-009-9355-6, 64-72, ISSN 1530-9932

Terbojevich, M.; Cosani, A.; Conio, G.; Marsano, E. & Bianchi, E. (1991). Chitosan: chain rigidity and mesophase formation. *Carbohydr. Res.*, 209, 251–260, pISSN 0008-6215

Thanou, M.; Nihot, T.; Jansen, M.; Verhoef, J.C. & Junginger, H.E. (2001). Mono-*N*-carboxymethylated chitosan (MCC), a polyampholytic chitosan derivative, enhances the intestinal absorption properties of low molecular weight heparin in rats. *J. Pharm. Sci.,* 90, 38–46, pISSN 0022-3549

Tiğli, R.; Karakeçili, A. & Gümüsderelioğlu, M. (2007). In vitro characterization of chitosan scaffolds: influence of composition and deacetylation degree. *J. Mater. Sci. Mater. Med.*, 18, 1665-1674, pISSN 0957-4530

Tikhonov, V.E.; Stepnova, E.A.; Babak, V.G.; Yamskov, I.A.; Palma-Guerrero, J.; Jansson, H.-B.; Lopez-Llorca, L.V.; Salinas, J.; Gerasimenko, D.V.; Avdienko, I.D. & Varlamov, V.P. (2006). Bactericidal and antifungal activities of a low molecular weight chitosans and its *N*-/2(3)-(dodec-2-enyl)succinol/-derivatives. *Carbohydr. Polym.*, 64, 66-72, pISSN 0144-8617

Tipparat, H. & Riyaphan, O. (2008). Effect of deacetylation conditions on antimicrobial activity of chitosans prepared from carapace of black tiger shrimp (*Penaeus monodon). Songklanakarin J. Sci. Technol*., 30, Suppl. 1, 1-9

Tolaimate, A.; Desbrieres, J. ; Rhazi, M. & Alagui, A. (2003). Contribution to the preparation of chitins and chitosans with controlled physico-chemical properties, *Polymer,* 44, 7939–7952, pISSN 0032-3861

Tømmeraas, K.; Köping-Höggård, M.; Vårum, K.; Christensen, B.; Artursson, P. & Smidsrød, O. (2002). Preparation and characterization of chitosans with oligosaccharide branches. *Carbohydr. Res.*, 337, 2455–2462, pISSN 0008-6215

Tsai, G.J.; Su, W.H.; Chen, H. C. & Pan, C. L. (2002). Antimicrobial activity of shrimp chitin and chitosan from different treatments and applications of fish preservation. *Fish Sci.*, 68, 170-177, pISSN 0919-9268

Tsaih, M. & Chen, R. (1997). Effect of molecular weight and urea on the conformation of chitosan molecules in dilute solutions. *Int. J. Biol. Macromol.*, 20, 233–240, pISSN 0141-8130

Ueno, H.; Mori, T. & Fujinaga, T. (2001). Topical formulations and wound healing applications of chitosan. *Adv. Drug Deliv. Rev*., 52, 105-115, pISSN 0169-409X

van der Lubben, I.M.; Verhoef, J.C.; Borchard, G. & Junginger, H.E. (2001). Review. Chitosan and its derivatives in mucosal drug and vaccine delivery. *Eur. J. Pharm. Sci.,* 14, 201–207, pISSN 0928-0987

Vårum, K.; Anthonsen, M.; Grasdalen, H. & Smidsrød, O. (1991a). Determination of the degree of *N*-acetylation and the distribution of *N*-acetyl groups in partially *N*-deacetylated chitins (chitosans) by high-field NMR spectroscopy. *Carbohydr. Res.*, 211, 17–23, pISSN 0008-6215

Vårum, K.; Anthonsen, M.; Grasdalen, H. & Smidsrød, O. (1991b). ^{13}C-NMR studies of the acetylation sequences in partially *N*-deacetylated chitins (chitosans). *Carbohydr. Res.*, 217, 19–27, pISSN 0008-6215

Vårum, K.M.; Myhr, M.M.; Hjerde, R.J.N. & Smidsrød, O. (1997). In vitro degradation rates of partially *N*-acetylated chitosans in human serum. *Carbohydr. Res*., 299, 99-101, pISSN 0008-6215

Vinsova, J. & Vavrikova, E. (2008). Recent Advances in Drugs and Prodrugs Design of Chitosan. *Curr. Pharm. Des.,* 14, 1311-1326, ISSN 1381-6128

Vishu Kumar, A.B.; Varadaraj, M.C.; Gowda, L.R. & Tharanathan, R.N. (2005). Characterization of chito-oligosaccharides prepared by chitosanolysis with the aid of papain and Pronase, and their bactericidal action against *Bacillus cereus* and *Escherichia coli*. *Biochem. J*., 391, 167-175, pISSN 0264-6021

Vruggink, H. (1970). The effect of chitin amendment on actinomycetes in soil and on the infection of potato tubers by *Streptomyces scabies*. *Neth. J. Plant Pathol., 76*., 293–295, ISSN 0929-1873

Wang, M.J.; Xie, Y.L.; Zheng, Q.D. & Yao, S.J. (2009). A Novel Potential Microflora-activated Carrier for a Colon-Specific Drug Delivery System and Its Characteristics. *Ind. Eng. Chem. Res.,* 48, 5276–5284, pISSN 0888-5885

Wang, S.-L.; Lin, T.-Y.; Yen, Y.-H.; Liao, H.-F. & Chen, Y.-J. (2006). Bioconversion of shellfish chitin wastes for the production of *Bacillus subtilis* W-118 chitinase. *Carbohydr. Res.*, 341, 2507–2515, pISSN 0008-6215

Wang, C.; Fu, X. & Yang, L. (2007). Water-soluble chitosan nanoparticles as a novel carrier system for protein delivery. *Chin. Sci. Bull.*, 52, 883-889, ISSN 1001-6538

Wang, W.; Bo, S.; Li, S. & Qin, W. (1991). Determination of the Mark-Houwink equation for chitosans with different degrees of deacetylation. *Int. J. Biol. Macromol.*, 13, 281–285, pISSN 0141-8130

Wang, X.; Yan, Y.; Lin, F.; Xiong, Z.; Wu, R.; Zhang, R. & Lu, Q. (2005). Preparation and characterization of a collagen/chitosan/heparin matrix for an implantable bioartificial liver. *J. Biomater. Sci. Polym. Ed.*, 16, 1063–1080, ISSN 0920-5063

Weinhold, M.X.; Sauvageau, J.C.M.; Keddig, N.; Matzke, M.; Tartsch, B.; Grunwald, I.; Kübel, C.; Jastorff, B. & Thöming, J. (2009). Strategy to improve the characterization of chitosan for sustainable biomedical applications: SAR guided multi-dimensional analysis. *Green Chem.*, 11, 498–509, ISSN 1463-9262

Whistler, R.J. & Kosik, M. (1971). Anticoagulant activity of oxidized and *N*- and *O*-sulfated chitosan. *Arch. Biochem. Biophys.*, 142, 106–110, pISSN 0003-9861

Wyatt, P. (1993). Light scattering and the absolute characterization of macromolecules. *Anal. Chim. Acta*, 272, 1–40, ISSN 0003-2670

Xia, W.; Liu, P.; Zhang, J. & Chen, J. (2010). Biological activities of chitosan and chitooligosaccharides. *Food Hydrocolloids*, doi:10.1016/j.foodhyd.2010.03.003, ISSN 0268-005X

Xie, W.; Xu, P. & Liu, Q. (2001). Antioxidant activity of water-soluble chitosan derivatives *Bioorg. Med. Chem. Lett.*, 11, 1699-1701, pISSN 0960-894X

Xie, W.; Xu, P.; Wang, W. & Liu, Q. (2002). Preparation and antibacterial activity of a water-soluble chitosan derivative. *Carbohydr. Polym.*, 50, 35-40, ISSN 0144-8617

Xie, Y.; Liu, X. & Chen, Q. (2007). Synthesis and characterization of water-soluble chitosan derivate and its antibacterial activity, *Carbohydr. Polym.*, 69, 142–147, ISSN 0144-8617

Xu, G.; Huang, X.; Qiu, L.; Wu, J. & Hu, Y. (2007). Mechanism study of chitosan on lipid metabolism in hyperlipidemic rats. *Asia Pac. J. Clin. Nutr.*, 16, 313-317, pISSN 0964-7058

Yadav, A.V. & Bhise, B.B. (2004). Chitosan a potential biomaterial effective against typhoid. *Curr. Sci.*, 187, 1176-1178, pISSN 0011-3891

Yan, X.L.; Khor, E. & Lim, L.Y. (2000). PEC films prepared from chitosan alginate coacervates. *Chem. Pharm. Bull.*, 48, 941–946, ISSN 0009-2363

Yang, R.; Yang, S.G.; Shim, W.S.; Cui, F.; Cheng, G.; Kim, I.W.; Kim, D.D.; Chung, S.J. & Shim, C.K. (2009b). Lung-specific delivery of paclitaxel by chitosan-modified PLGA nanoparticles via transient formation of microaggregates. *J. Pharm. Sci.*, 98, 970–984, pISSN 0022-3549

Yang, F.; Cui, X. & Yang, X. (2002). Interaction of low-molecular-weight chitosan with mimic membrane studied by electrochemical methods and surface plasmon resonance. *Biophys. Chem.*, 99, 99-106, pISSN 0301-4622

Yang, K.W.; Li, X.R.; Yang, Z.L.; Li, P.Z.; Wang, F. & Liu, Y. (2009a). Novel polyion complex micelles for liver-targeted delivery of diammonium glycyrrhizinate: in vitro and in vivo characterization. *J. Biomed. Mater. Res. A.*, 88, 140–148, pISSN 1549-3296

Yang, T.C.; Chou, C.C. & Li, C.F. (2005). Antibacterial activity of *N*-alkylated disaccharide chitosan derivatives. *Int. J. Food Microbiol.*, 97, 237-245, pISSN 0168-1605

Zhang, C.; Ping, Q.; Zhang, H. & Shen, J. (2003). Preparation of *N*-alkyl-*O*-sulfate chitosan derivatives and micellar solubilization of taxol. *Carbohydr. Polym.*, 54, 137–141, ISSN 0144-8617

Zhang, H. & Neau, S.H. (2001). In vitro degradation of chitosan by a commercial enzyme preparation: effect of molecular weight and degree of deacetylation, *Biomaterials,* 22, 1653-1658, pISSN 0142-9612

Zhang, H.-L.; Wu, S.-H.; Tao, Y.; Zang, L.-Q. & Su, Z.-Q. (2010a). Preparation and Characterization of Water-Soluble Chitosan Nanoparticles as Protein Delivery System. *J. Nanomater.,* Article ID 898910, 5 pages, doi:10.1155/2010/898910, pISSN 1687-4110

Zhang, J.; Xia, W.; Liu, P.; Cheng, Q.; Tahirou, T.; Gu W. & Li, B. (2010b). Chitosan Modification and Pharmaceutical/Biomedical Applications *Mar. Drugs*, 8, 1962-1987, ISSN 1660-3397

Zhang, L.F.; Wang, M.Y.; Kang, X.D.; Boontheung, P.; Li, N.; Nel, A.E. & Loo, J.A. (2009). Oxidative Stress and Asthma: Proteome Analysis of Chitinase-like Proteins and FIZZ1 in Lung Tissue and Bronchoalveolar Lavage Fluid. *J. Proteome Res.,* 8, 1631–1638, pISSN 1535-3893

Zhang, Y. & Zhang, M. (2002). Calcium phosphate/chitosan composite scaffolds for controlled in vitro antibiotic drug release. *J. Biomed. Mater. Res.,* 62, 378–786, pISSN 0021-9304

Zhang, Y.; Chen, J.; Zhang, Y.; Pan, Y.; Zhao J.; Ren L.; Liao, M.: Hu, Z.; Kong, L & Wang, J. (2007). A novel PEGylation of chitosan nanoparticles for gene delivery. *Biotechnol. Appl. Biochem.,* 46, 197–204, pISSN 0885-4513

Zhang, Y.; Xue, C.; Xue, Y.; Gao, R. & Zhang, X. (2005). Determination of the degree of deacetylation of chitin and chitosan by x-ray powder diffraction. *Carbohydr. Res.*, 340, 1914–1917, pISSN 0008-6215

Zhong, Z. ; Chen, R.; Xing, R.; Chen, X.; Liu, S.; Guo, Z.; Ji, X.; Wang, L. & Li, P. (2007). Synthesis and antifungal properties of sulfanilamide derivatives of Chitosan, *Carbohydr. Res.*, 342, 2390–2395, ISSN 0008-6215

Zhong, Z.; Li, P.; Xing, R. & Liu, S. (2009). Antimicrobial activity of hydroxylbenzenesulfonailides derivatives of chitosan, chitosan sulfates and carboxymethyl chitosan. *Int. J. Biol. Macromol.,* 45, 163–168, pISSN 0141-8130

3

Digital Fabrication of Multi-Material Objects for Biomedical Applications

SH Choi and HH Cheung
Department of Industrial and Manufacturing Systems Engineering
The University of Hong Kong
Hong Kong SAR, China

1. Introduction

Recent developments in medical and dental fields have warranted biomedical objects or implants with desirable properties for biomedical applications. For example, artificial hip joints, tissue scaffolds, and bone and jaw structures are now commonly used in hospitals to assist complex surgical operations, and as specimens for experiments in pharmaceutical manufacturing enterprises. But most biomedical objects are not economical to fabricate by the traditional manufacturing processes because of their complex shapes and internal structures with delicate material variations.

Layered manufacturing (LM) has been widely recognized as a potential technology for fabrication of such biomedical objects. Wang et al. (2004) developed a precision extruding deposition (PED) system to fabricate interconnected 3D scaffolds. Zeng et al. (2008) used fused deposition modelling (FDM) technology to build an artificial human bone based on computed tomography (CT) images. However, most commercial LM systems can only fabricate single-material objects, which cannot meet the needs for biomedical applications. A typical example of dental implantation requires a dental implant with functionally graded multi-material (FGM) structures to be composed of titanium (Ti) and hydroxyapatite (HAP) in order to satisfy both mechanical and biocompatible property requirements (Watari et al., 1997). Therefore, it is desirable to develop multi-material layered manufacturing (MMLM) technology for fabrication of biomedical objects.

Multi-material (or heterogeneous) objects may be classified into two major types, namely (i) discrete multi-material (DMM) objects with a collection of distinct materials, and (ii) functionally graded multi-material (FGM) objects with materials that change gradually from one type to another. In comparison with single-material objects, a DMM object can differentiate clearly one part from others, or tissues from blood vessels of a human organ, while an FGM object can perform better in rigorous environments. In particular, suitably graded composition transitions across multi-material interfaces can create an object of very different properties to suit various applications (Kumar, 1999; Shin & Dutta, 2001).

Multi-material layered manufacturing (MMLM) refers to a process of fabricating an object or an assembly of objects consisting of more than one material layer by layer from a CAD model with sufficient material information. Some researchers have explored different techniques to fabricate multi-material objects. A few experimental MMLM machines, such as a discrete multiple material selective laser sintering (M^2SLS) machine (Jepson et al., 1997;

Lappo et al., 2003), a shape deposition manufacturing machine (Merz et al., 1994; Fessler et al., 1997), a fused deposition of multiple ceramics (FDMC) machine (Jafari & Han, 2000), and a 3D inkjet-printing machine (Jackson et al., 1999; Cho et al., 2003; Wang & Shaw, 2006) have been developed. Although these systems seemed suitable for relatively simple objects of a limited variety of materials, they provided a good foundation for further hardware development. It can be said that development of MMLM is mainly concerned with three major research issues, namely (1) fabrication materials, (2) hardware mechanism for deposition of materials, and (3) software system for object modelling and subsequent process control of multiple tools for object fabrication. These three issues are generally studied by researchers of specialised expertise. Nevertheless, the development of an integrated software system for modelling and fabrication of complex multi-material objects is particularly important as it has a huge impact on the overall efficiency and the fabrication quality, especially of large and complex objects.

In order to model and subsequently fabricate a multi-material object, both material and geometric information must be made available. Although STL is now a de-facto industrial standard file format for LM, it only contains geometric information. Therefore, some researchers have recently proposed CAD representation methods for multi-material objects to facilitate general CADCAM applications, including MRPII (Kumar et al., 1998; Morvan & Fadel, 1999).

A mathematical model, called r_m-object, was proposed by enhancing the theory of r-sets to represent heterogeneous objects. While this model suited DMM objects, it was not quite suitable for FGM objects (Kumar, 1999; Kumar et al., 1998). Chiu and Tan (2000) developed a modified STL file format in which a material tree structure was used to represent a DMM object. The modified STL file, however, became large and was slow to process. Hsieh and Langrana (2001) proposed a multi-CAD system for modelling DMM objects. Firstly, this multi-CAD system organized all component STL models generated from the traditional CAD modellers; secondly, it indicated materials to the STL models; and finally, it assembled them into a DMM model. They pointed that this approach could be very cumbersome for parts comprising a lot of materials at different locations because each material in the part required a separate solid.

Indeed, the work above has laid a solid base for extending the LM technology for fabrication of simple DMM objects. However, the representation methods for DMM objects cannot represent FGM objects; this hinders extending the LM technology for fabricating FGM objects. To overcome this, some researchers have attempted to develop different methods to represent FGM objects. The following section reviews some methods for modelling FGM objects.

Jackson (2000) presented a finite element-based approach to modelling FGM parts. This approach could represent an object with complex material composition distribution, but the process was computationally intensive and required much memory because it was necessary to generate a large amount of meshes to represent the object (Shin, 2002; Kou & Tan, 2007).

Samanta and Kou (2005) proposed a feature-based method to represent FGM objects, using free-form B-spline functions to model both geometry and material features. Cheng and Lin (2001) proposed a material feature-based approach for modelling of simple FGM biomedical objects. Kou and Tan (2005) suggested a heterogeneous feature tree (HFT) for constructive heterogeneous objects, based on which a recursive material evaluation algorithm was

developed to evaluate the material compositions at specific location. However, the algorithm was computationally intensive and required large memory for handling complex objects.
Shin and Dutta (2001) proposed a constructive representation scheme for FGM objects. Constructive representations of the FGM objects were ordered binary trees whose nodes were heterogeneous primitive sets (hp-sets); an hp-set was the smallest component of an FGM object. Similar to CSG in solid modelling systems, a set of heterogeneous boolean operators, including material union, intersection, difference, and partition, was developed to construct a more complex FGM object from two or more simpler hp-sets. However, this scheme was not yet enough to model arbitrary material distributions as represented by CT or magnetic resonance imaging (MRI) images (Shin, 2002). Similarly, Kou et al. (2006) proposed a non-manifold cellular representation scheme for modelling complex FGM objects. This scheme needed huge computation efforts since the cellular model required more complicated data structures and algorithms for establishing and maintaining the spatial partitions. Kou (2005) proposed an adaptive sub-faceting method to generate mesh-based 2D slices with material composition variation information of an FGM object for visualization. It required huge memory to process complex FGM objects.
When fully developed and widely adopted, the proposed representation schemes above would be useful for MMLM. However, there are still some major problems to solve. These schemes tended to be computationally slow and needed large memory; they were not particularly suitable for complex multi-material objects for biomedical applications.
Most complex biomedical models, such as human organs and bone structures, are not designed using CAD systems. Instead, they are captured by laser digitizers, or CT/MRI scanners. Sun et al. (2005) reviewed the uses of CT/MRI techniques to model tissue scaffolds as CAD models that can be used for biomimetic design, analysis, simulation, and freeform fabrication of the tissue scaffolds. In general, the digitized images are normally processed to form a model in STL format with no material or topological information needed to extract the slice contours. Indeed, slice contours are random in nature without any explicit topological hierarchy relationship, and to process them for multi-toolpath planning remains a challenging obstacle that has yet to be surmounted. Most of the above representation schemes were incapable of modelling objects generated from CT/MRI scanners, and subsequent processing for fabrication of multi-material objects was ignored. Hence, it is worthwhile to develop an integrated computer system to represent and process multi-material biomedical objects for subsequent generation of toolpaths for fabrication control.
This chapter therefore describes a multi-material virtual prototyping (MMVP) system for modelling, visualization, and digital fabrication of discrete and functionally graded multi-material objects for biomedical applications. The MMVP system offers flexibility in representing objects designed by CAD systems or extracted from CT/MRI scan images. It also provides a virtual reality (VR) environment for digital fabrication, visualization, and quality analysis of multi-material biomedical objects. As such, the need for physical prototyping can be minimized, and the cost and time of biomedical product development reduced accordingly.

2. The Multi-Material Virtual Prototyping (MMVP) system

The MMVP system is an integrated software system for modelling, visualization, and fabrication of multi-material objects for biomedical applications. It consists mainly of (i) a

discrete multi-material virtual prototyping (DMMVP) module for modelling, visualization, and process planning of DMM objects; (ii) a functionally graded multi-material virtual prototyping (FGMVP) module for modelling, and process planning for layered manufacturing of discrete and functionally graded multi-material objects; and (iii) a virtual reality (VR) simulation module for visualization and optimization of MMLM processes for digital fabrication and quality analysis of discrete and functionally graded multi-material biomedical objects. The following sections describe these modules in detail, with case studies given to demonstrate the design and digital fabrication of multi-material biomedical objects for possible applications like surgical planning, patient's education, and implantations.

2.1 The DMMVP module

The DMMVP mainly consists of a suite of software packages for design and visualization of multi-material objects and simulation of MMLM process. The software packages includes a colour modeller for colouring monochrome STL models, a slicer for slicing colour STL models, a topological hierarchy-sorting algorithm for grouping random slice contours of DMM objects, a topological hierarchy-based toolpath planning algorithm for generation of sequential and concurrent multi-toolpaths, and a virtual prototyping package for digital fabrication of DMM objects.

Figure 1 shows the flow of the DMMVP system. Firstly, a biomedical model created by CAD or a CT/MRI scanner is converted into STL format, which is the industry de-facto standard. As STL is monochrome or single-material, an in-house package is used to paint the STL model, with each colour representing a specific material.

Secondly, a few steps are taken to prepare for subsequent simulation of the MMLM process and visualization of the resulting digital prototypes: (a) slice the colour STL model into a number of layers of a predefined thickness. The resulting layer contours and material information are stored in a modified Common Layer Interface (CLI) file; (b) sort the slice contours with a contour sorting algorithm to establish explicit topological hierarchy; (c) based on the hierarchy information, multi-toolpath planning algorithms are used to plan and generate multi-toolpaths by hatching the slice contours with a predefined hatch space. The hatch vectors are stored in the modified CLI file for fabrication of digital prototypes and build-time estimation.

Thirdly, a virtual prototyping package is used for digital fabrication of multi-material objects and allows users to stereoscopically visualize and analyze the resulting digital prototypes, with which biomedical object designs can be reviewed and improved efficiently. The following section will use a human skull to demonstrate how the DMMVP module can model and fabricate multi-material objects for biomedical applications.

Figure 2 shows a monochrome STL model of a human skull constructed from CT or MRI images. Obviously, using such a monochrome STL model, it would not be easy for users to differentiate various parts or structures of the skull. To alleviate this, the colour STL modeller is used to paint the jaw, the teeth, and a part of spine in red, white, and blue, respectively, as shown in Figure 3. As such, surgeons can visualize and differentiate the various parts of the skull more vividly to explain and plan complex surgical operations. Moreover, each colour represents a specific type of material, and hence a colour STL model can provide both geometric and material information for planning the MMLM process. To fabricate this skull prototype with discrete multi-materials, a set of nozzles (N_i, i=1, 2, …n) would deposit specific materials on appropriate slice contours. It is necessary to identify and

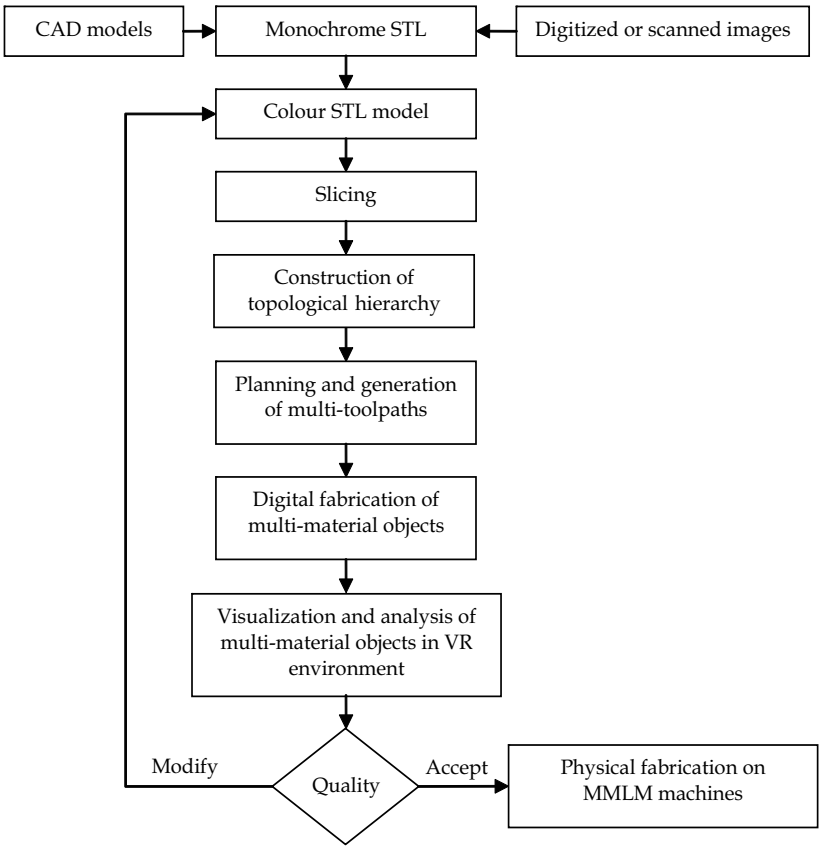

Fig. 1. The flow of the DMMVP module

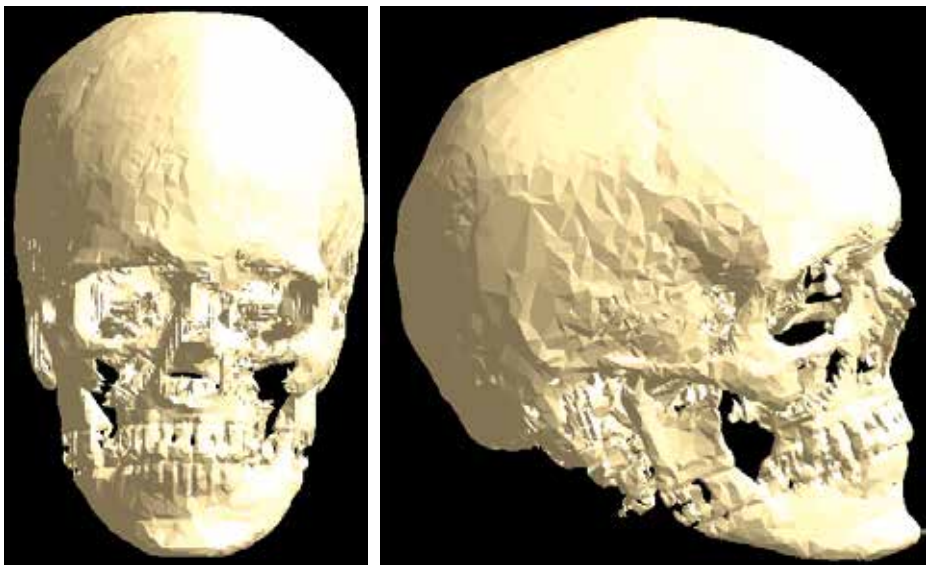

Fig. 2. A monochrome STL model of a human skull

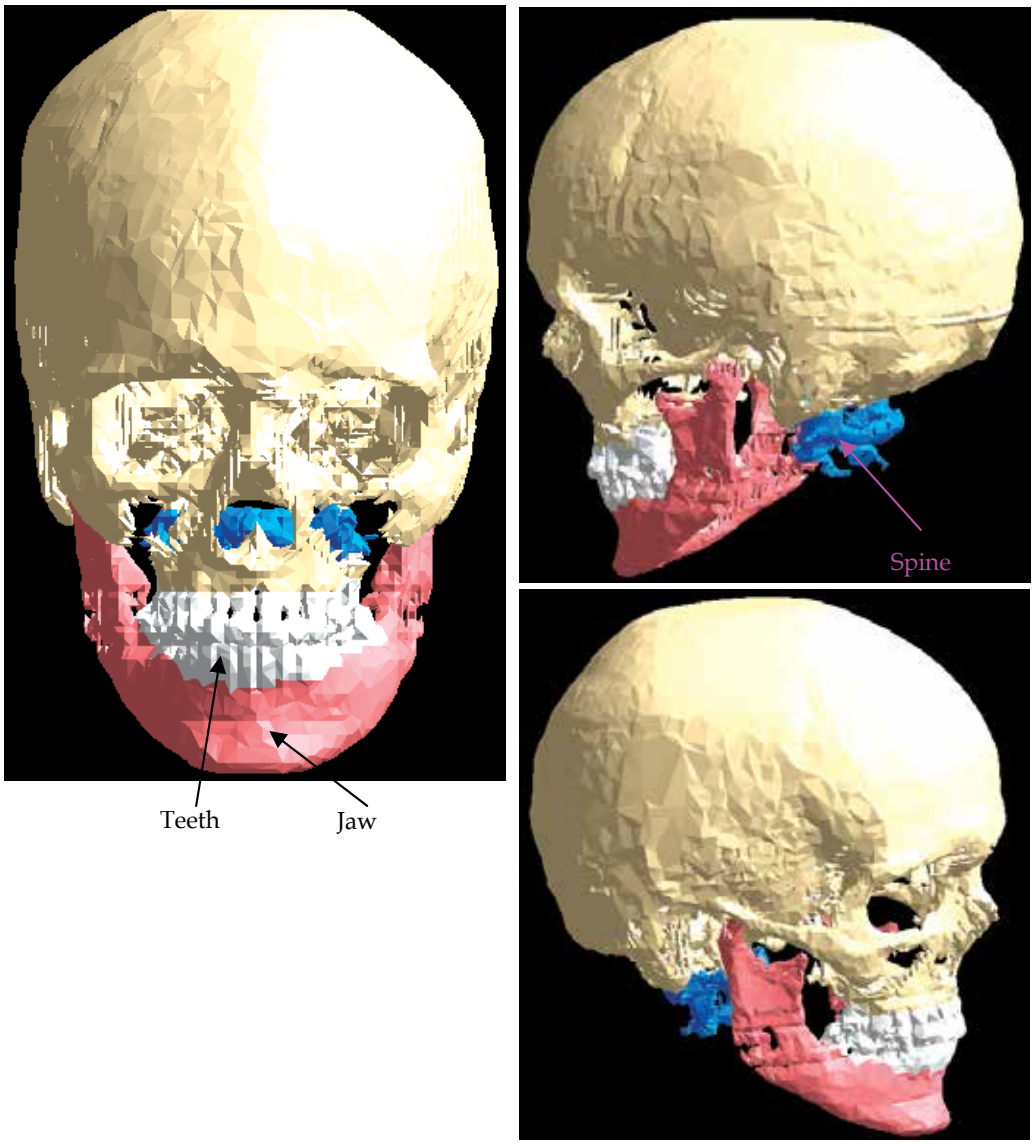

Fig. 3. A colour STL model of a human skull from different perspectives

relate specific contours of a slice to a particular tool and subsequently arrange the toolpaths to fabricate the prototype efficiently. This requires a multi-toolpath planning algorithm to generate efficient toolpaths without possible tool collisions. However, most multi-material objects tend to be complex and the slice contours do not possess any explicit topological hierarchy relationship. As a result, it is very difficult to associate specific contours with a particular tool. To tackle this problem, a topological hierarchy-based approach to toolpath planning for MMLM was proposed by the authors (Choi & Cheung, 2005; 2006a). This approach adopts a topological hierarchy-sorting algorithm to construct the topological hierarchy in terms of a parent-and-child list that defines the containment relationship of the contours of a slice. Thus, with the hierarchy relationship, it is no longer necessary to identify

and relate contours to a particular nozzle one by one for multi-toolpath planning. Indeed, only grouping of the outermost contours is required. Besides, parametric polygons are used to construct tool envelopes for contour families with the same material property to simplify detection of tool collisions during concurrent movements of nozzles. As a result, concurrent toolpaths without collisions and redundant movements can be easily generated for controlling MMLM machines to fabricate physical multi-material prototypes.

The colour STL skull model is sliced into 180 layers of multi-material contours with a layer thickness of 0.619 mm stored in the common layer interface (CLI) file format. Figure 4 shows a layer containing 27 contours to be made of three materials, namely m_1, m_2, and m_3, respectively. The topological hierarchy relationship of the contours is listed in Figure 5. The contours are grouped into 24 contour families and 24 toolpaths (P_{C1}, P_{C2}, P_{C3}, P_{C4}, P_{C6}, P_{C7}, P_{C8}, P_{C9}, P_{C10}, P_{C11}, P_{C12}, P_{C13}, P_{C14}, P_{C15}, P_{C16}, P_{C17}, P_{C21}, P_{C22}, P_{C23}, P_{C24}, P_{C25}, P_{C26}, P_{C27}, and $P_{C5,18,19,20}$) are generated for these contours accordingly with a hatch space of 0.500 mm.

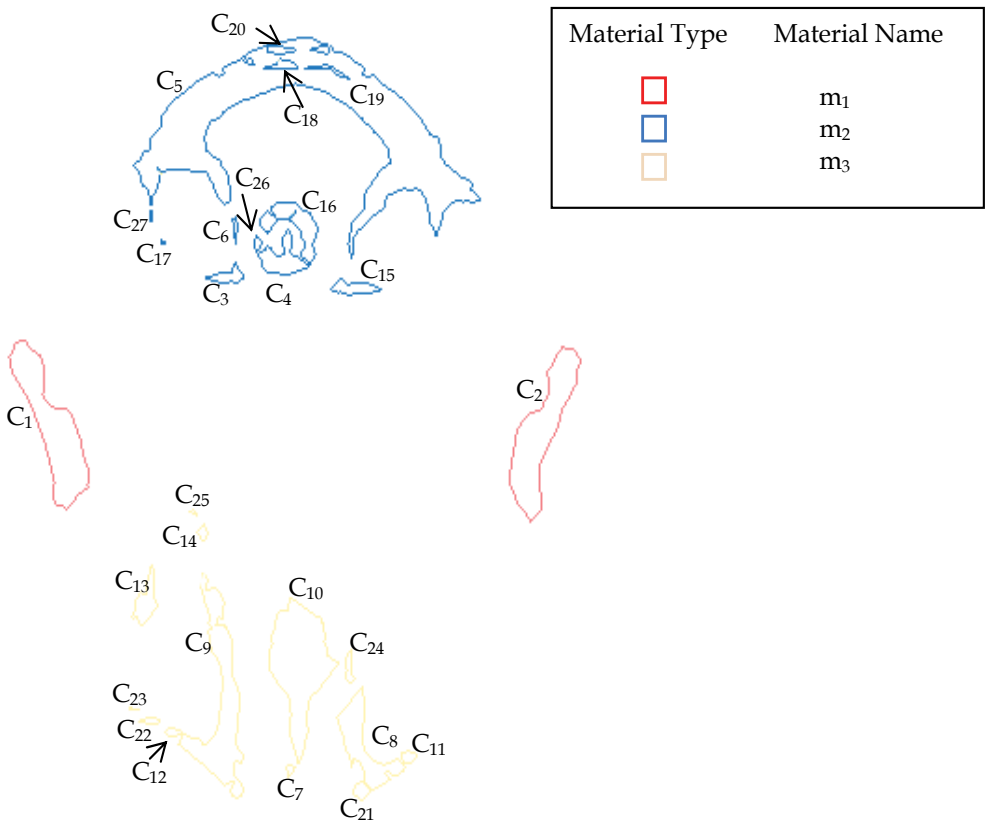

Fig. 4. A slice layer containing 27 contours to be made of 3 materials

According to the material information, the toolpaths with the same material are grouped into three toolpath-sets, namely S_1 to S_3, which are associated with three nozzles from N_1 to N_3, respectively. Subsequently, three work envelopes from E_1 to E_3 for each of these nozzles are constructed to facilitate planning of concurrent multi-toolpaths. Thus, with the hierarchy

information and association relationship between the toolpath-sets and the nozzles, concurrent toolpaths without redundant tool movements and collisions can be easily generated and planned for fabrication control.

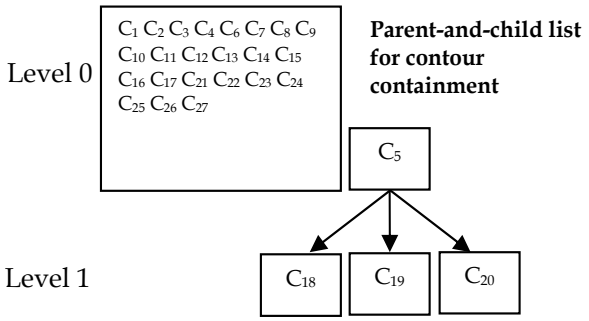

Contour Families	Toolpaths	Material
1. C_1	P_{C1}	m_1
2. C_2	P_{C2}	m_1
3. C_3	P_{C3}	m_2
4. C_4	P_{C4}	m_2
5. C_6	P_{C6}	m_2
6. C_7	P_{C7}	m_3
7. C_8	P_{C8}	m_3
8. C_9	P_{C9}	m_3
9. C_{10}	P_{C10}	m_3
10. C_{11}	P_{C11}	m_3
11. C_{12}	P_{C12}	m_3
12. C_{13}	P_{C13}	m_3

Contour Families	Toolpaths	Material
13. C_{14}	P_{C14}	m_3
14. C_{15}	P_{C15}	m_2
15. C_{16}	P_{C16}	m_2
16. C_{17}	P_{C17}	m_2
17. C_{21}	P_{C21}	m_3
18. C_{22}	P_{C22}	m_3
19. C_{23}	P_{C23}	m_3
20. C_{24}	P_{C24}	m_3
21. C_{25}	P_{C25}	m_3
22. C_{26}	P_{C26}	m_2
23. C_{27}	P_{C27}	m_2
24. $C_5 \rightarrow (C_{18}, C_{19}, C_{20})$	$P_{C5,18,19,20}$	m_2

Fig. 5. Topological hierarchy relationship of the contours in Fig. 4

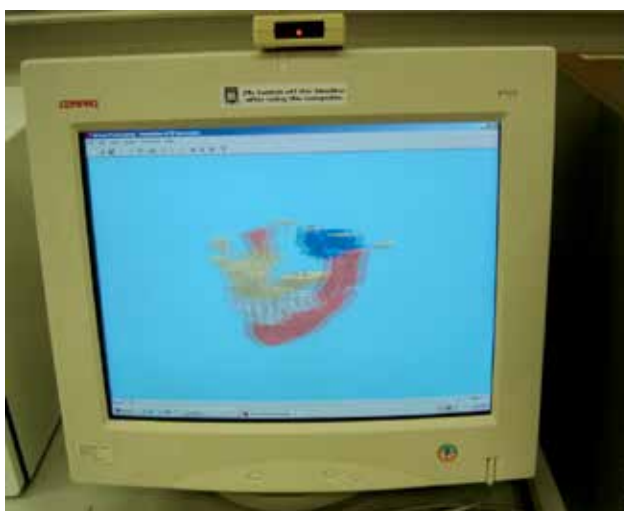

Fig. 6. Digital fabrication of a human skull prototype in a desktop VR system

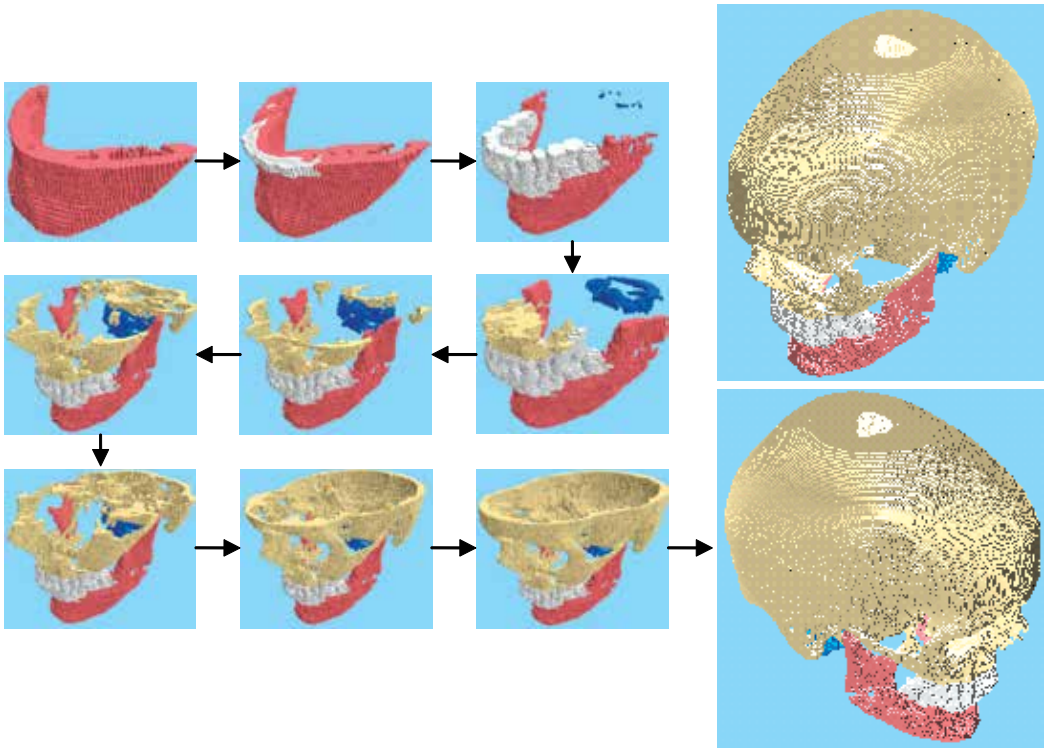

Fig. 7. Digital fabrication process of a human skull prototype

With the results of toolpath planning, a virtual prototyping system (Choi & Cheung, 2006b; 2008) is adopted to digitally fabricate the skull prototype for quality analysis through visualization in a VR environment, as shown in Figure 6. Figure 7 shows the digital fabrication process of a few layers of the skull. After fabrication, the resulting discrete multi-material skull prototype can be studied in a VR environment using the utilities provided to visualize the quality of the prototype that the MMLM machine will subsequently deliver. Besides, any dimensional deviations of the prototype beyond a tolerance limit can be identified by superimposing the colour STL skull model on its digital prototype. Therefore, using the DMMVP system, biomedical engineers can conveniently perform design iterations and quality analysis of the resulting prototype. Thus, an optimal combination of process parameters, such as layer thickness, build direction, and hatch space can be obtained for cost-effective fabrication of physical biomedical prototypes.

To repair or replace failing organs or tissues due to trauma or aging, biomedical prototypes may have to be made of functionally graded materials to mimic biological and mechanical characteristics of the organs or tissues. To achieve this, the proposed DMMVP system is enhanced to represent and fabricate FGM objects. The following section presents the FGMVP module for modelling and fabrication of FGM objects in detail.

2.2 The FGMVP module

The FGMVP module is used for modelling and fabrication of FGM objects. It is characterized by a contour-based FGM modeller, in which an FGM object is represented by material control functions and discretisation of layer contours with topological hierarchy.

Material control functions are specified across contour families of some representative layers in the X-Y plane and across layers along the Z-axis. The material composition at any location is calculated from control functions, and the slice contours are discredited into sub-regions of constant material composition. The discretisation resolution can be varied to suit display and fabrication requirements. Figure 8 shows the flow of the approach.

Firstly, it slices a monochrome STL model obtained from a traditional CAD design or digitized images, and sorts the resulting contours to build explicit topological hierarchy information.

Secondly, the contours are loaded into the FGMVP module for FGM object representation, with the following steps: (1) select a number of feature contour families in a representative layer; (2) specify control functions for material variations across layers along the Z-axis in the build direction; (3) specify control functions for material variations in the X-Y plane; and (4) discretise the slice contours into sub-regions of constant material composition.

Thirdly, the resulting contour-based FGM model containing both geometric and material composition variation information is processed for visualization, analysis, and fabrication of FGM objects.

In comparison with voxel-based representation schemes, this approach is computationally efficient and it requires little memory for processing relatively complex objects. More importantly, it facilitates physical fabrication on MMLM machines. The detail of the contour-based FGM modeller was presented in (Cheung, 2007; Choi & Cheung, 2009). In the

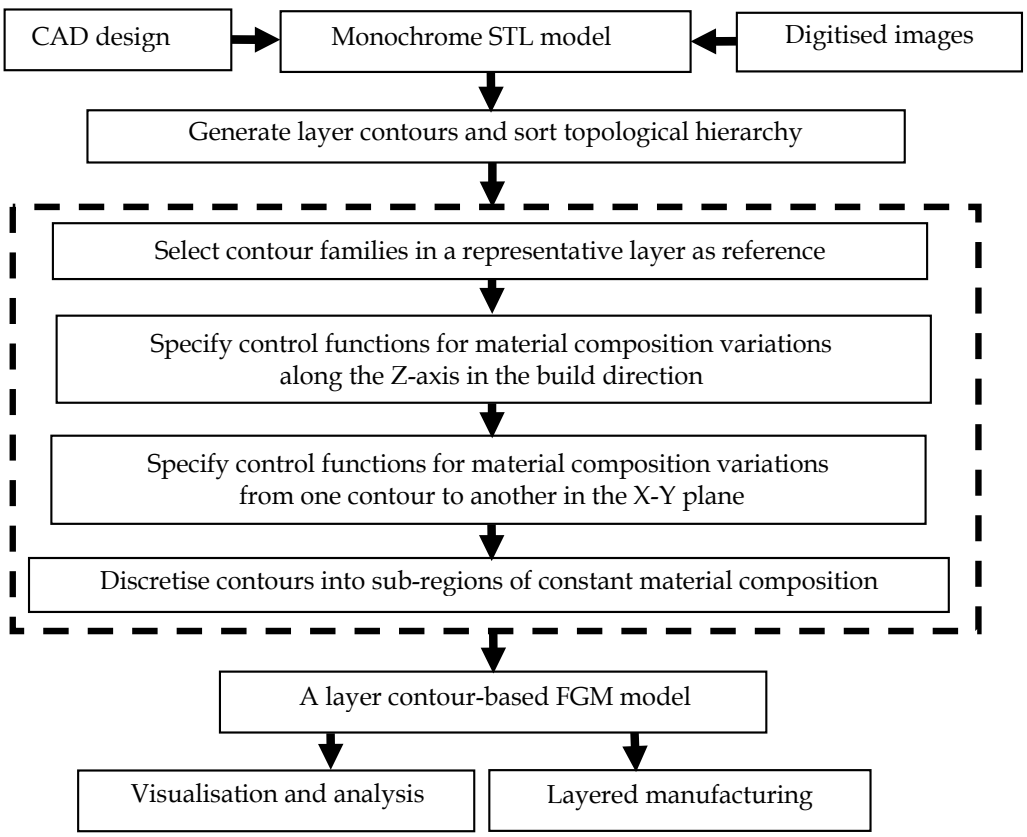

Fig. 8. The flow of processing FGM objects

following sections, a hip joint is processed to illustrate the use of the FGMVP module as a tool for design and fabrication of FGM biomedical objects.

Figure 9 shows an assembly of a prosthetic hip joint (Anné et al., 2005), which consists of three main components, including an acetabular cup, a femoral ball head, and a stem. Figure 10 shows a CAD model of the prosthesis assembly. While the fermoral ball head can be made of a single, mechanically tough material, such as titanium (Ti), the acetabular cup and the stem are preferably made of functionally graded materials to achieve desirable properties (Heida et al., 2005; España et al. 2010). The acetabular cup should have a biocompatible material at the outer surface and a mechanically tough material at the internal surface; the stem should have a biocompatible material at the lower region and a mechanically tough material at the upper region along the Z-axis. The following section

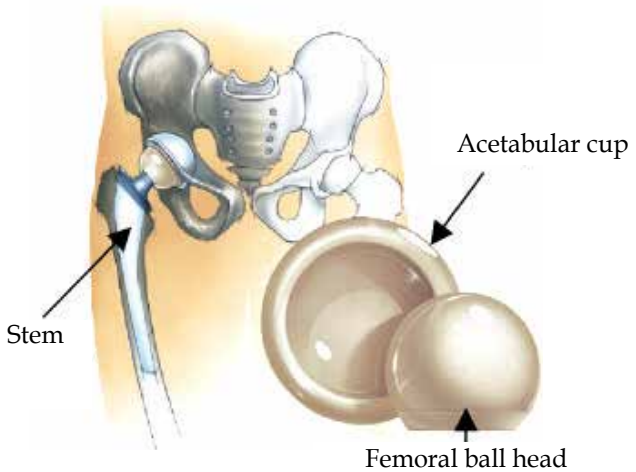

Fig. 9. An artificial joint for hip prosthesis (Anné et al., 2005)

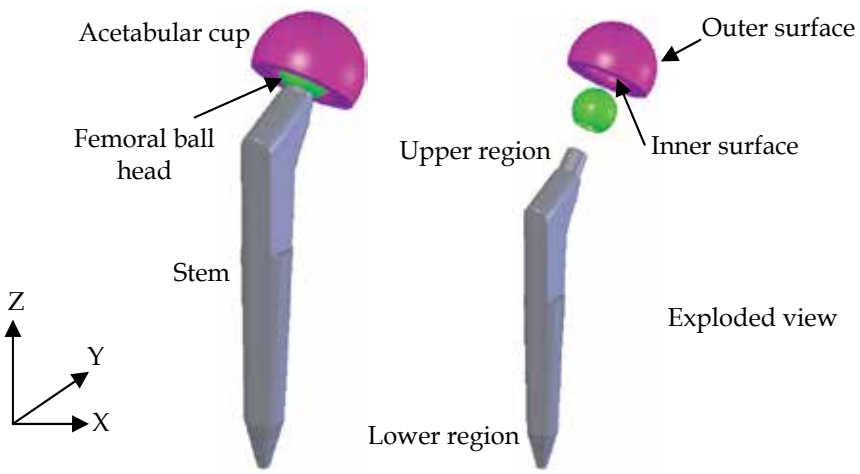

Fig. 10. Prosthesis assembly of an acetabular cup, a femoral ball head, and a stem for hip joint replacement

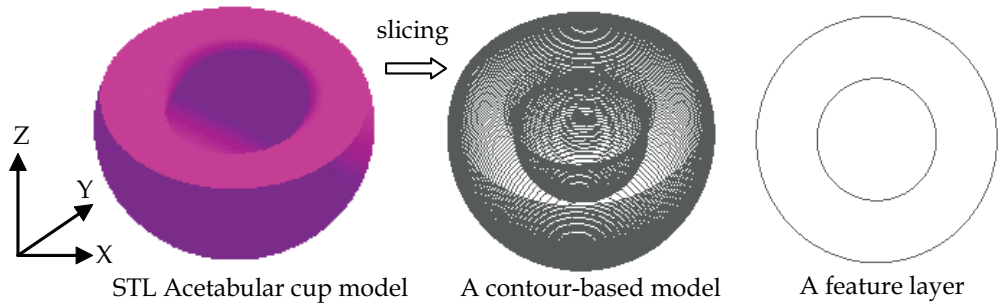

Fig. 11. Slicing an acetabular cup into a contour-based model; a feature layer is selected for assigning primary materials and material control functions

briefly demonstrates how the models of the acetabular cup and the stem are processed to represent material variations.

Using the FGMVP module, an STL model of the acetabular cup is firstly sliced into a contour-based model consisting of a number of layers, as shown in Figure 11; secondly, the topological hierarchy information of each layer is established, and a feature layer is selected for assigning primary materials and material control functions for calculation of property values of material composition; thirdly, each layer is discretised into sub-regions of constant material composition. Subsequently, the resulting geometric contours and material information are used for visualization and digital fabrication of the FGM acetabular cup prototype. Figure 12 shows a layer of the FGM acetabular cup prototype in wireframe and rendered displays, respectively. This layer has a purple/green graded variation in the X-Y plane to represent a gradual change of material composition from hydroxyapatite (HAP) at the outer surface to Ti at the inner surface, giving the desirable biocompatible properties at the surface and the desirable mechanical properties at the core of the acetabular cup. Moreover, the discretisation resolution can be easily changed accordingly to control the smoothness of material composition variations. Figure 13 shows a finer material composition variation compared with the one in Figure 12, and Figure 14 shows a contour-based FGM model of the acetabular cup from two perspectives. The digital fabrication process of an FGM acetabular cup prototype is shown in Figure 15. Therefore, the proposed FGMVP module is a practical tool for design of FGM objects and simulation of MMLM process for biomedical applications.

Similarly for the stem, its material composition changes gradually along the Z-axis from HAP at the bottom to Ti at the top, as shown in Figure 16. This variation can be represented by repeating the steps above.

2.3 The virtual reality simulation module

The DMMVP module and the FGMVP module above are integrated with a VR simulation module to form an MMVP system for modelling and digital fabrication of discrete and functionally graded multi-material objects for biomedical applications. The MMVP system provides a platform for stereoscopic visualization and analysis of digital fabrication process of multi-material objects in a VR environment (Choi & Cheung, 2005, 2006a; 2008). Through simulations, design validation and modification of a biomedical product can be iterated without incurring any manufacturing and material costs of physical prototyping. Therefore, the cost and time of product development can be reduced considerably.

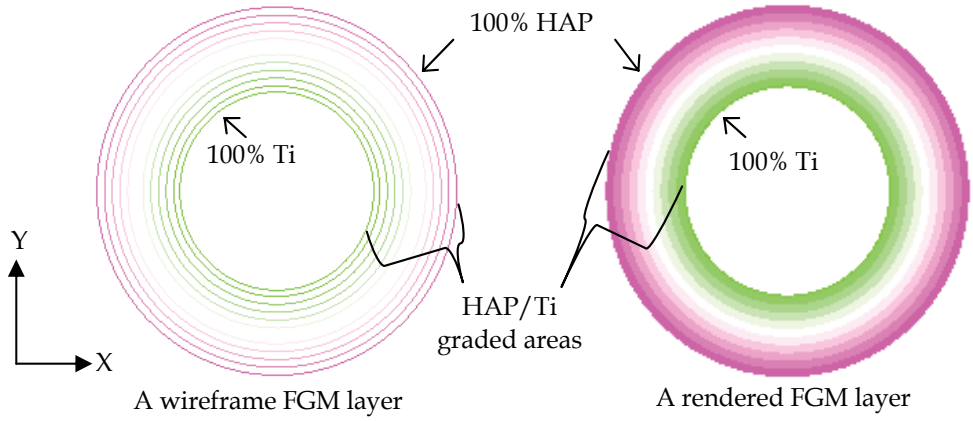

Fig. 12. The resulting FGM layer of the acetabular cup in Fig. 11

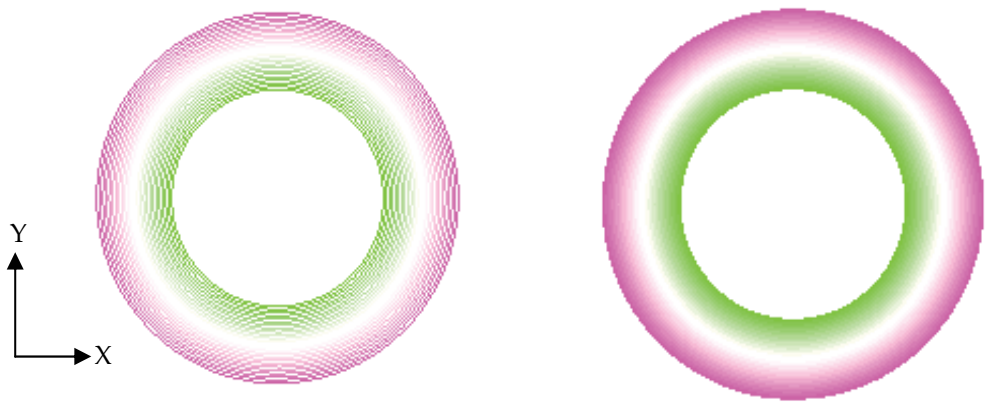

Fig. 13. A layer with a finer material composition variation

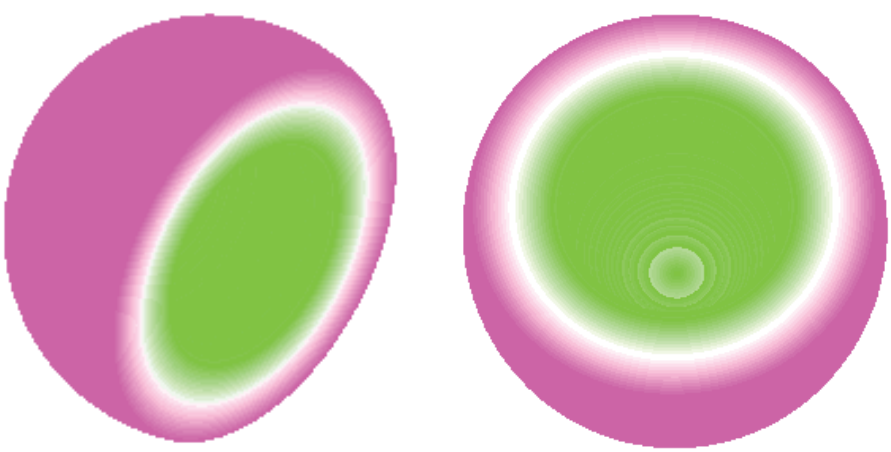

Fig. 14. A contour-based FGM model of the acetabular cup from two perspectives

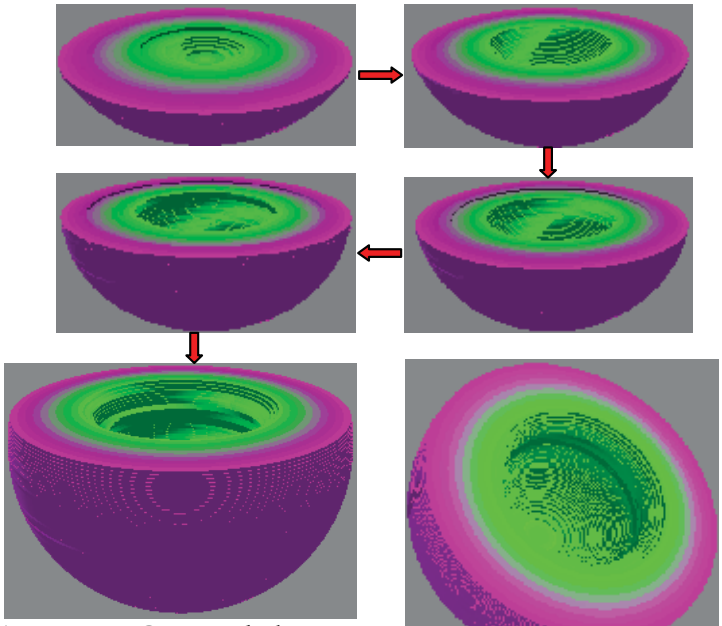

Fig. 15. Digital fabrication of an FGM acetabular cup prototype

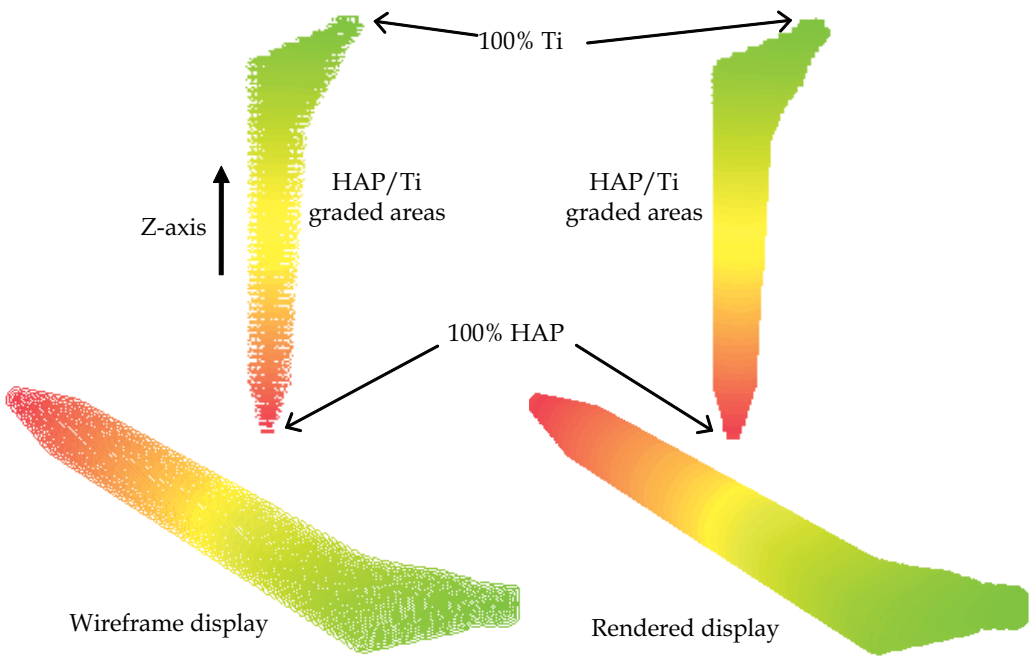

Fig. 16. A contour-based FGM model of the stem in wireframe and rendered displays

3. A case study

A functionally graded assembly for dental implant

In clinical surgery, it would be desirable to have dental implants made of functionally graded materials, such as Ti and HAP, to satisfy both mechanical and biocompatible properties. The MMVP system would be a practical tool for modelling and digital fabrication of functionally graded dental implants for such purposes.

Figure 17 shows a dental implant assembly consisting of a Ti abutment and a dental implant. To satisfy the desirable mechanical and biocompatible properties, the material composition of the dental implant is to change gradually from 100% HAP at z = 0 mm to 100% Ti at z = 15 mm along the Z-axis. The volume fraction for HAP, V_{HAP}, is expressed as

$$V_{HAP} = (\frac{L-z}{L})^{\alpha}, \qquad 0 \le z \le L \tag{1}$$

where L and z are the length of the dental implant and the height along the Z-axis, respectively; α is the volume fraction index.

The volume fraction for Ti, V_{Ti}, is thus denoted as

$$V_{Ti} = 1 - V_{HAP}. \tag{2}$$

With the FGMVP module, an STL model of a dental implant assembly, as shown in Figure 18, is sliced to obtain a contour-based model of 80 layers, for which the explicit topological hierarchy information is built accordingly. The first 56 layers comprise the dental implant, while the remaining layers belong to the abutment of a discrete material, Ti. The material composition of the dental implant changes from 100% HAP at the first layer to 100% Ti at the 56th layer along the Z-axis, controlled by Equations (1) and (2).

Hence, the lst layer contours and the 56th layer contours are selected as the two feature layers for assigning these primary materials and volume fraction equations to control the material composition of the dental implant. Figure 19 shows the resulting FGM dental implant assembly, with material variation represented by blending of red (100% HAP) and green (100% Ti) colours. Indeed, this approach can represent assemblies of both FGM and discrete materials conveniently.

The dental implant model now contains geometric and material information which can be conveniently processed for visualization, and inspection of internal material variation of each layer, multi-toolpath planning, and simulation of MMLM process. Figure 20 shows the process of digital fabrication of an FGM prototype of the dental implant assembly. The MMVP system can adjust the resolution of material composition to suit practical visualization and fabrication requirements, simply by changing the discretisation of layer contours, which is the number of layers in this case. It is therefore a practical tool for modelling and digital fabrication of biomedical objects with FGM and discrete materials.

To further demonstrate the capability of the proposed FGMVP module, it is used to design and process an artificial tooth as shown in Figure 21a, which is assumed to have material variations along the Z-axis and in the X-Y plane to mimic the desired properties of a human tooth.

A natural human tooth has material variations along various directions in order to achieve the desired properties. The enamel of a tooth can be regarded as a functionally graded natural biocomposite (He & Swain, 2009). The inner enamel has lower elastic modulus and

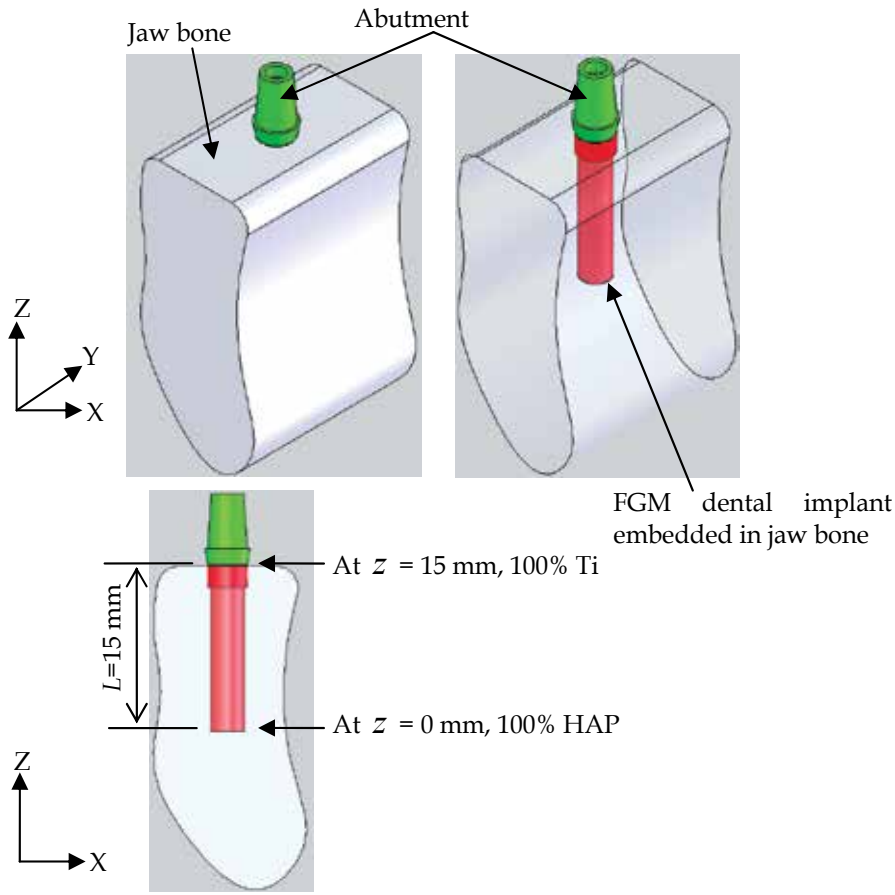

Fig. 17. A dental implant in a jaw bone

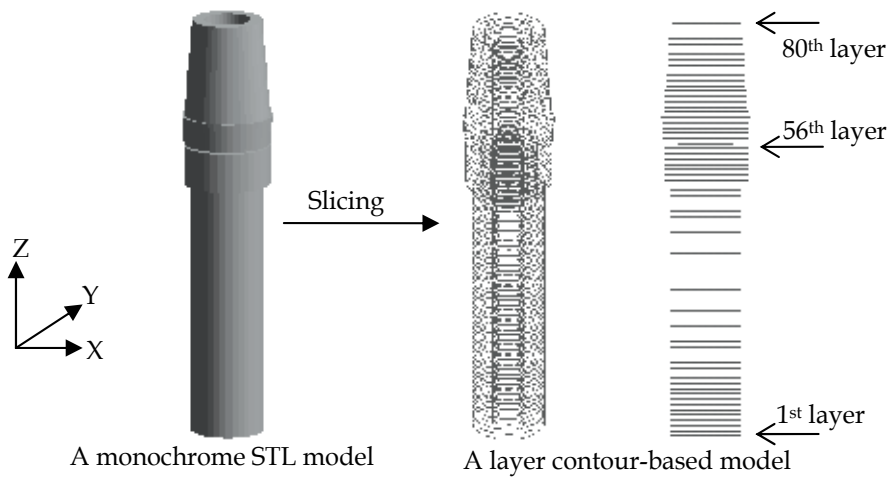

Fig. 18. Slicing an STL model of a dental implant assembly into a contour-based model for FGM modelling

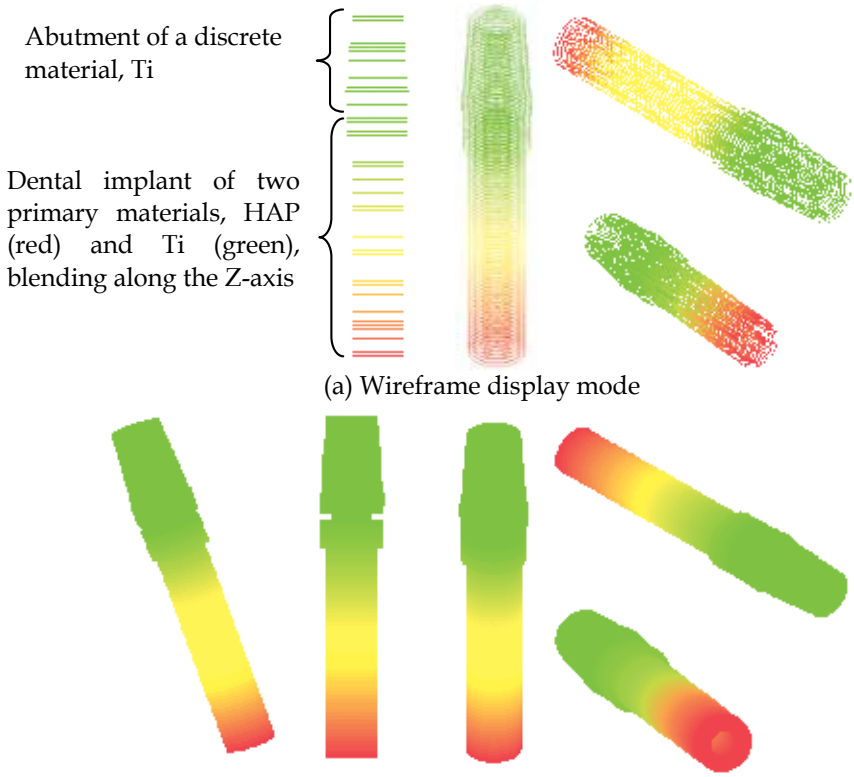

(a) Wireframe display mode

(b) Rendered display mode from various perspectives

Fig. 19. Layer contour-based representation of an FGM dental implant assembly

hardness but higher creep and stress redistribution abilities than the outer counterpart, which is related to the gradual compositional change through the enamel.
The STL tooth model is firstly sliced as a layer-contour based model of 120 layers, as shown in Figure 21. Subsequently, material functions are associated with feature layers to control material variations. The resulting FGM tooth prototype with gradual material changes along Z-axis and in the X-Y plane is shown in Figure 22. Figure 23 shows the digital fabrication of an artificial FGM tooth.

4. Conclusion

This chapter presents a multi-material virtual prototyping (MMVP) system for modelling, process planning, and subsequent digital fabrication of discrete and functionally graded material objects. The MMVP system is characterised by its topological hierarchy-based toolpath planning algorithm and contour-based approach to representation of FGM objects. Case studies showed that the system can conveniently process CAD models and CT/MRI images to represent complex multi-material objects for biomedical and dental applications. It is computationally efficient and requires relatively little memory for processing complex objects. More importantly, it facilitates visualization of the resulting multi-material objects in a VR environment. The system may be adapted to control MMLM machines with appropriate hardware for physical fabrication of biomedical objects.

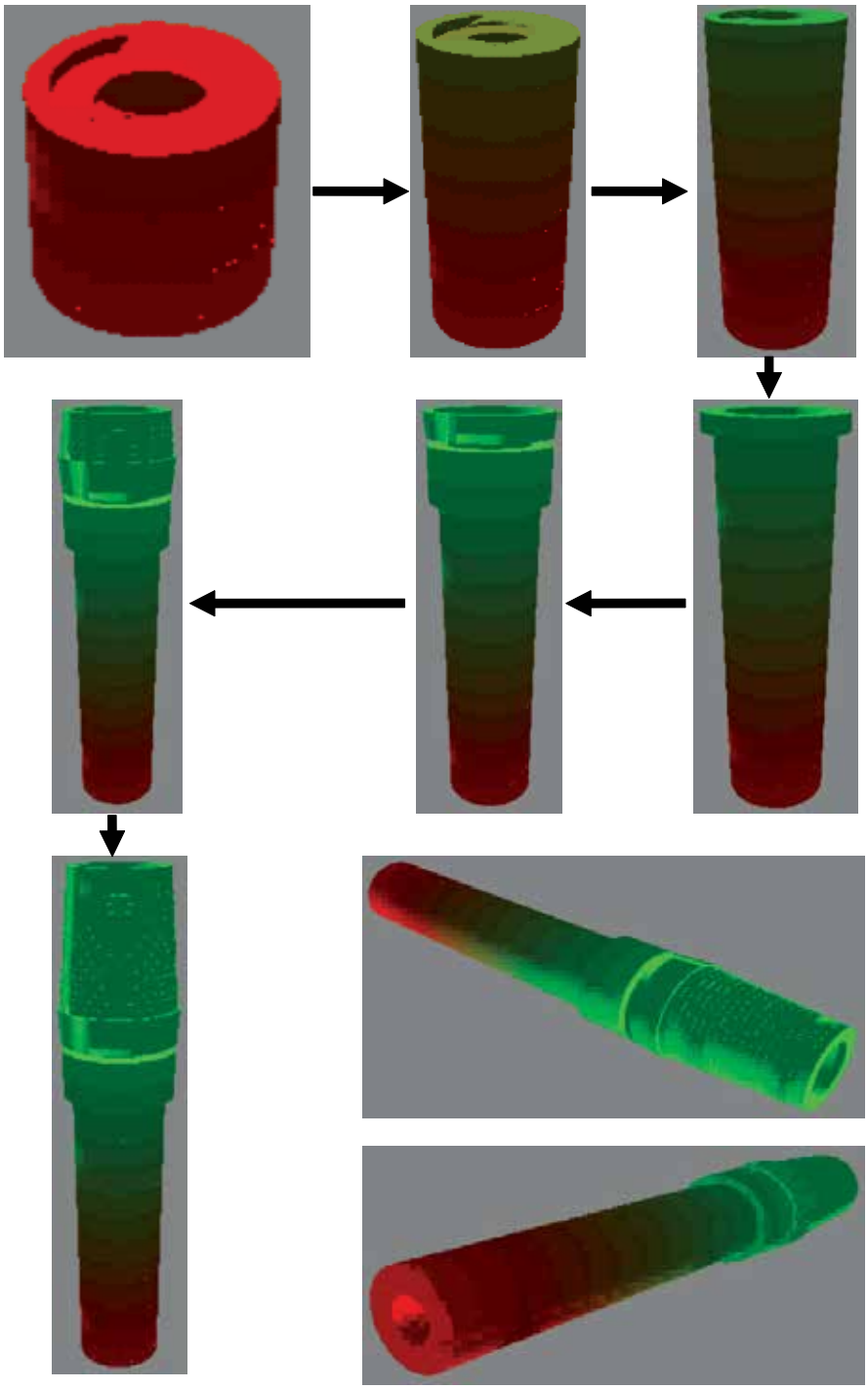

Fig. 20. Digital fabrication of a multi-material prototype of a dental implant assembly

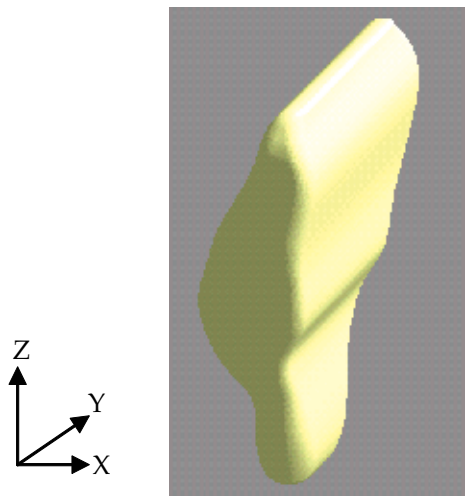

(a) A monochrome STL tooth model

(b) A homogeneous layer contour-based tooth model

Fig. 21. Slicing an STL model of a human tooth into a homogeneous contour-based model for FGM representation

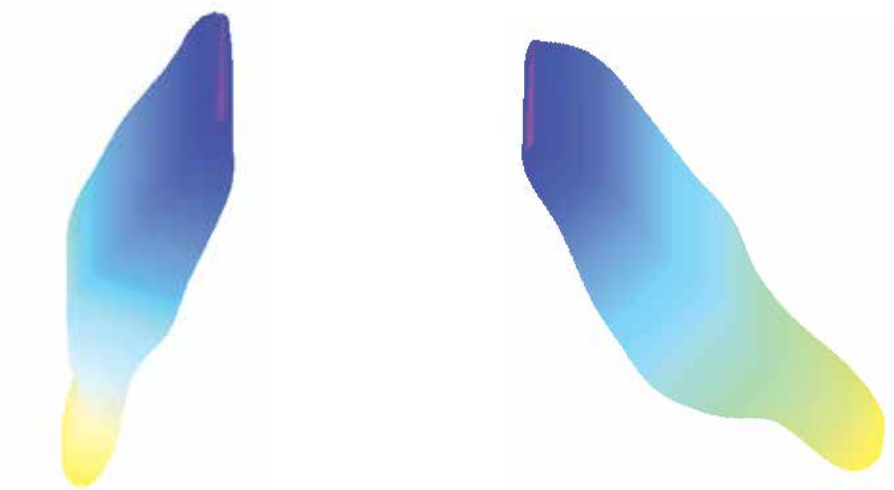

Fig. 22. An FGM tooth prototype from two perspectives

5. Acknowledgements

The authors would like to acknowledge the Research Grant Council of the Hong Kong SAR Government and the CRCG of the University of Hong Kong for their financial support for this project.

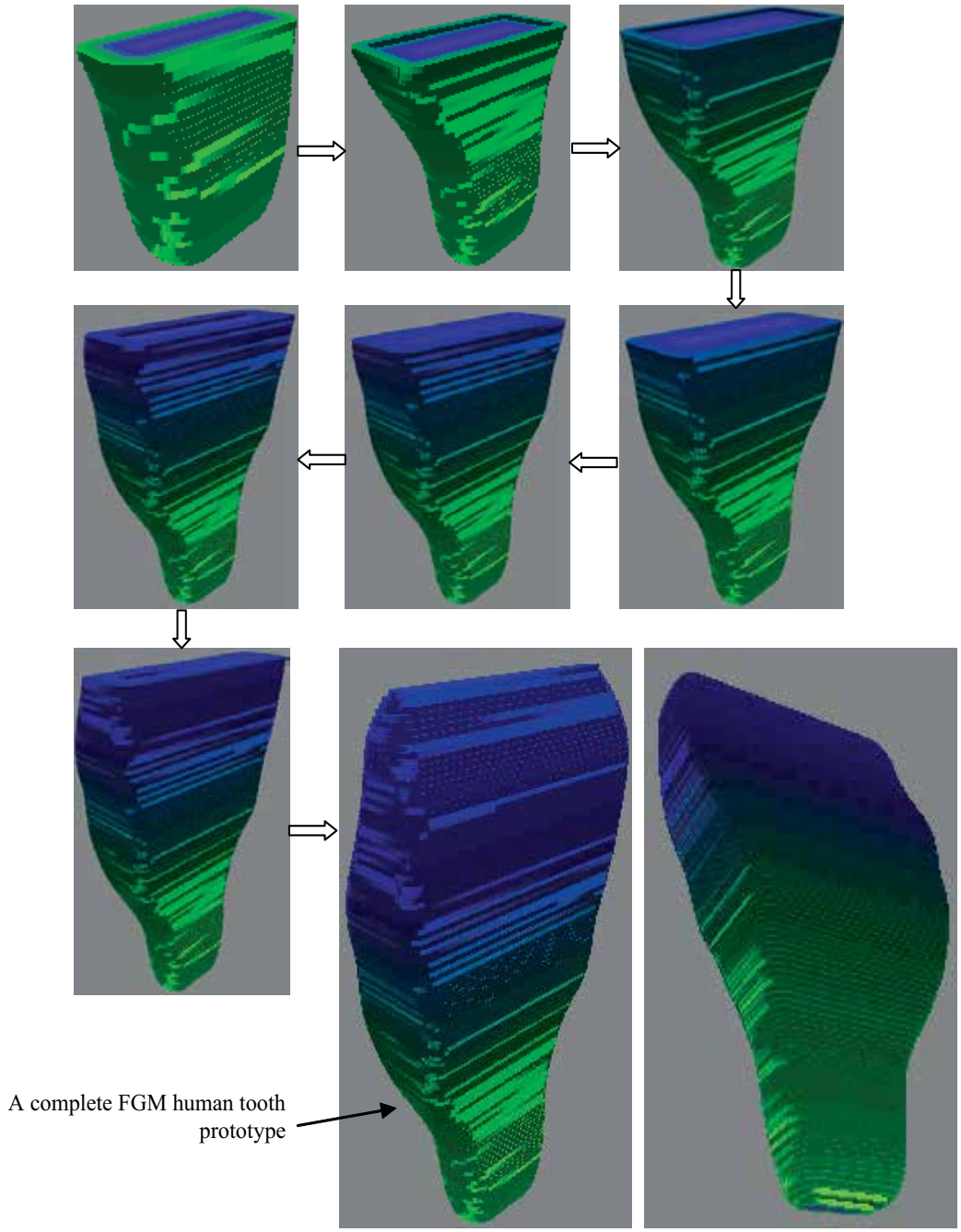

Fig. 23. Digital fabrication of an FGM human tooth

6. References

Anné, G.; Vanmeensel, K., Vleugels, J. & Biest, O.V.D. (2005). Electrophoretic deposition as a novel near net shaping technique for functionally graded biomaterials, In: *Biest, O.V. D., et al. (Eds.), The 8th International Symposium on Multifunctional and Functionally graded Materials (FGM 2004)*, pp. 213-218. Leuven, Belgium, July 11-14, 2004.

Cheng, T.H. & Langrana, N.A. (2001). A system approach in extrusion-based multi-material CAD, In: *Bourell, D.L., et al., (Eds.), Solid Freeform Fabrication Symposium*, pp. 313-321. Austin, Texas, The University of Texas.

Cheung, H.H. (2007). A versatile multi-material virtual prototyping system. *Ph.D. Thesis*. The University of Hong Kong, Hong Kong.

Chiu, W.K. & Tan, S.T. (2000). Multiple material objects: from CAD representation to data format for rapid prototyping. *Computer-Aided Design*, Vol.32, No.12, 707-717.

Cho, W.J., Sachs, E.M., Patrikalakis, E.M. & Troxel, D.E. (2003). A dithering algorithm for local composition control with three-dimensional printing. *Computer-Aided Design*, Vol.35, No.9, 851-867.

Choi, S.H. & Cheung, H.H. (2005). A multi-material virtual prototyping system. *Computer-Aided Design*, Vol.37, No.1, 123-136.

Choi, S.H. & Cheung, H.H. (2006a). A topological hierarchy-based approach to toolpath planning for multi-material layered manufacturing. *Computer-Aided Design*, Vol.38, No.2, 143-156.

Choi, S.H. & Cheung, H.H. (2006b). A CAVE-based multi-material virtual prototyping system. *Computer-Aided Design and Applications*, Vol.3, No.5, 557-566.

Choi, S.H. & Cheung H.H. (2008). A versatile virtual prototyping system for rapid product development. *Computers in Industry*, Vol.59, No.5, 477-488.

Choi, S.H. & Cheung, H.H. (2009). A topological hierarchy-based approach to layered manufacturing of functionally graded multi-material objects. *Computers in Industry*, Vol.60, No.5, 349-363.

España, F.A., Balla, V.K., Bose, S. & Bandyopadhyay, A. (2010). Design and fabrication of CoCrMo alloy based novel structures for load bearing implants using laser engineered net shaping. *Materials Science and Engineering C*, Vol.30, No.1, 50-57.

Fessler, J.R., Nickel, A.H., Link, G.R., Prinz, F.B. & Fussell, P. (1997) Functional gradient metallic prototypes through shape deposition manufacturing, In: *Bourell, D.L., et al. (Eds.), Solid Freeform Fabrication Symposium*, pp. 521-528. Austin, Texas, The University of Texas.

He, L.H. & Swain M.V. (2009). Enamel – a functionally graded natural coating. *Journal of Dentistry*, Vol.37, No.8, 596-603.

Hedia, H.S., EI-Midany, T.T., Shabara, M.A.N. & Fouda, N. (2005). Development of cementless metal-backed acetabular cup prosthesis using functionally graded material. *International Journal of Mechanics and Materials in Design*, Vol.2, No.3-4, 259-267.

Hsieh, C.T. & Langrana, N.A. (2001). A system approach in extrusion-based multi-material CAD, In: *Bourell, D.L., el al., (Eds.), Solid Freeform Fabrication Symposium*, pp. 313-321. Austin, Texas, The University of Texas.

Jackson, T.R., Liu, H., Patrikalakis, N.M., Sachs, E.m. & Cima, M.J. (1999). Modelling and designing functionally graded material components for fabrication with local composition control. *Materials & Design*, Vol.20, No.2-3, 63-75.

Jackson, T.R. (2000). Analysis of functionally graded material object representation methods. *Ph.D. Thesis*. Massachusetts Institute of Technology, USA.

Jafari, M.A. & Han, W. (2000). Mohammadi, F., Safari, A., Danforth, S.C., Langrana, N.: A novel system for fused deposition of advanced multiple ceramics. *Rapid Prototyping Journal*, Vol.6, No.3, 161-175.

Jepson, J., Beaman, J.J., Bourell, D.L. & Wood, K.L. (1997). SLS processing of functionally gradient materials, In: *Bourell, D.L., et al. (Eds.), Solid Freeform Fabrication Symposium*, pp. 1-8. Austin, Texas. The University of Texas.

Kou, X.Y. (2005). Computer-Aided design of heterogeneous objects. *Ph.D. Thesis*. The University of Hong Kong, Hong Kong.

Kou, X.Y. & Tan, S.T. (2005). A hierarchical representation for heterogeneous object modelling. *Computer-Aided Design*, Vol.37, No.3, 307-319.

Kou, X.Y., Tan, S.T. & Sze, W.S. (2006). Modelling complex heterogeneous objects with non-manifold heterogeneous cells. *Computer-Aided Design*, Vol.38, No.5, 457-474.

Kou, X.Y. & Tan, S.T. (2007). Heterogeneous object modelling: a review. *Computer-Aided Design*, Vol.39, No.4, 284-301.

Kumar, V., Rajagopalan, S., Cutkosky, M. & Dutta, D. (1998). Representation and processing heterogeneous objects for solid freeform fabrication. *The 6th IFIP WG 5.2 International Workshop on Geometric Modelling: Fundamentals and Applications*. Tokyo, Japan. The University of Tokyo, 1998.

Kumar, V. (1999). Solid modelling and algorithms for heterogeneous objects. *Ph.D. Thesis*. The University of Michigan, USA.

Lappo, K., Jackson, B., Wood, K., Bourell, D.L. & Beaman, J.J. (2003). Discrete multiple material selective laser sintering (M²SLS): experimental study of part processing, In: *Bourell, D.L., et al. (Eds.), Solid Freeform Fabrication Symposium*, pp. 109-119. Austin, Texas, The University of Texas.

Merz, R., Prinz, F.B., Ramaswami, K., Terk, M. & Weiss, L.E. (1994). Shape deposition manufacturing, In: *Bourell, D.L., et al. (Eds.), Solid Freeform Fabrication Symposium*, pp. 1-8. Austin, Texas, The University of Texas.

Morvan, S.M. & Fadel, G.M. (1999). Heterogeneous solids: possible representation schemes. In: *Bourell, D.L., et al., (Eds.), Solid Freeform Fabrication Symposium*, pp. 187-198. Austin, Texas, The University of Texa.

Samanta, K. & Koc, B. (2005). Feature-based design and material blending for free-form heterogeneous object modelling. *Computer-Aided Design*, Vol.37, No.3, 287-305.

Shin, K.H. & Dutta, D. (2001). Constructive representation of heterogeneous objects. *Journal of Computing and Information Science in Engineering*, Vol.1, No.3, 205-217.

Shin, K.H. (2002). Representation and process planning for layered manufacturing of heterogeneous objects. *Ph.D. Thesis*. The University of Michigan, USA (2002).

Sun, W., Starly, B., Nam, J. & Darling, A. (2005). Bio-CAD modelling and its applications in Computer-aided tissue engineering. *Computer-Aided Design*, Vol.37, No.11, 1097-111.

Wang, F., Shor, L., Darling, A., Khalil, S., Sun, W., Gűçeri, S. & Lau, A. (2004). Precision extruding deposition and characterization of cellular poly-ε-caprolactone tissue scaffolds. *Rapid Prototyping Journal*, Vol.10, No.1, 420-429.

Wang, J.W. & Shaw, L.L. (2006). Fabrication of functionally graded materials via inkjet colour printing. *Journal of the American Ceramic Society*, Vol.89, No.10, 3285-3289.

Watari, F., Yokoyama, A., Saso, F., Uo, M. & Kawasaki, T. (1997). Fabrication and properties of functionally graded dental implant. *Composites Part B*, Vol.28B, 5-11.

Zeng, W., Ruan, F. & Zhou, T. (2008). Fused deposition modelling of an auricle framework for microtia reconstruction based on CT images. *Rapid Prototyping Journal*, Vol.14, No.5, 280-284.

4

Developed of a Ceramic-Controlled Piezoelectric of Single Disk for Biomedical Applications

E. Suaste Gómez, J. J. A. Flores Cuautle and C. O. González Morán
Centro de Investigación y de Estudios Avanzados del Instituto Politécnico Nacional
México

1. Introduction

One of the main topical problems that biomedical discipline has the develop of medical equipment, prosthesis, diagnostically and therapy equipment, and the others. In the last field in which the work has been stimulated by the successful develop of methods for monitoring biological signal. Moreover, the aging of the humanity is the key that motivates more research in new instruments for diagnostic and therapy and the investment about new ways to have more information about the state of human health.

The development of new instruments entails the research focuses on new sensors or the improvement of the already existing ones; in this background the called smart materials are the option of choice to develop sensors and instruments based on these materials due to its thermal, mechanical, optical and electrical responses that permits to detect a variety of physics constants and at the same time are characterized for strong structure, a wide range of work frequencies, wide range of temperature operation among others features.

Several studies have been carry out in order to get the optimal material combinations such as the influence of compositionally modified ceramic bodies, or the addition of a variety of elements obtaining a doped ceramics, on the other hand multilayer capacitors, based on smart materials, are base of a variety of studies and are widespread use in the electronic market, having these concepts in mind, a metallic wire was inserted into a ferroelectric ceramic bulk, the wire has more than one propose in the ceramic: using this wire implanted, a free ceramic face is obtained and at the same time the implant provides a free charges that modify ceramic behavior, this face is used in order to measure optic and mechanic events, the wire in total immersion into the ceramic also serve as control electrode and it is named Ceramic controlled piezoelectric (CCP), (Gonzalez & Suaste, 2009).

2. Fabrication

The oxide-mixing route is the most used method for commercial purposes although it has several limitations, like difficulties in achieve microscopic compositional uniformity, is one of the cheaper methods to get ferroelectric ceramics, the method involve the general steps: mixing and grinding, calcinations, grinding, shaping, densification, and finishing, which will be next briefly described (Jaffe, 1971; Moulson, 2003).

Mixing: the raw powders are weighted in an appropriated portion with an allowance for the impurity and moisture content, the grain size is uniformed by grinding usually this part is wet by means of include some liquid to agglutinated the powder.
Calcination: the calcinations purpose is to begin the reaction by the firing the powders at temperatures around 800 – 1100° C depending of the material kind, this step not always is necessary, it depends on the material kind.
Shaping: in this stage the required dimensions and shape are forming by molding the powders and applying pressures that are around 75 - 300 MPa, is in this step that a Pt - wire is put into the middle of the ceramic in transversal way in order to obtain the third electrode.
Densification: also know as firing, it is made in a refractory recipient and at temperatures of 80 to 90 % of material melting temperature in which the constituent ions have the mobility for the solid state sintering process take place.
Finishing: the finishing involves the polishing, machining (if it is necessary), and metalizing.
A ferroelectric PLZT was chosen; this is a $Pb_{1-x}La_x(Zr_{1-y}Ti_y)_{1-x/4}O_3$ ceramic with x = 0.09 and y = 0.35 (PLZT), generally denoted as (9/65/35). This ceramic was produced by the oxide-mixing technique: the raw materials were mixed by ball-milling with an electronic mill (Pulverisette 2, Fritsch) for 20 min; polyvinyl alcohol drops were added with a rate of 1.5 drops per gram of mixture. Powders then were pressed into discs of 10 mm diameter and 2 mm of thickness; the pressure applied was 3,500 Kg/cm^2.
During this process, a Pt-wire of 0.3 mm diameter was implanted in the middle of the ceramic in a transversal way; thus a metallic electrode totally immersed in the ceramic was created. This ceramic was sintered in air with a heater ramp rate of 5 °C/min from room temperature to 600 °C and a second heater ramp rate of 10 °C/min from 600 °C to 1,200 °C; the latter process lasted for one hour in a platinum crucible.
After sinterization, silver electrodes were deposited on the lower face and the Pt-wire of the CCP. Finally the discs were electrically poled, at 1.5 kV/mm for one hour at 60 °C in a silicone oil bath, in order to be used in pulse measurements. The dielectric constant was determined by the capacitance measure. Samples were heated at a rate of 5 °C/min, until 450 °C while the capacitance was measured at 1 kHz with a Beckman LM22A RLC bridge. The dielectric constant was determined by expression (1):

$$\varepsilon = Cl/\varepsilon_0 A \tag{1}$$

where C is the capacitance in F, l is the thickness of the sample in m, A the sample area in m^2 and the vacuum permittivity $\varepsilon_0 = 8.85 \times 10{-}12\ F/m$. The dielectric constant in the CCP was determined with and without the Pt-wire taking the parallel sides as electrodes and is show in Figure 1.
Usually electrodes are taking at parallel sides and Pt-wire is the third electrode however for our applications described in this chapter only will be use one parallel side and Pt-wire as electrodes. The schematic symbol used for describing the CCP can be seen in Figure 2.
The implant as was mentioned earlier provides free charges to the ceramic and at the same time provokes a great ferroelectric domains concentration around it, this domain concentrations results in superior sensibility in the area near to the implant. Figure 3 shows a scheme in which it is possible to see the implant and the domains concentration around it, it also shows the ceramic polarization in areas far from the implant.

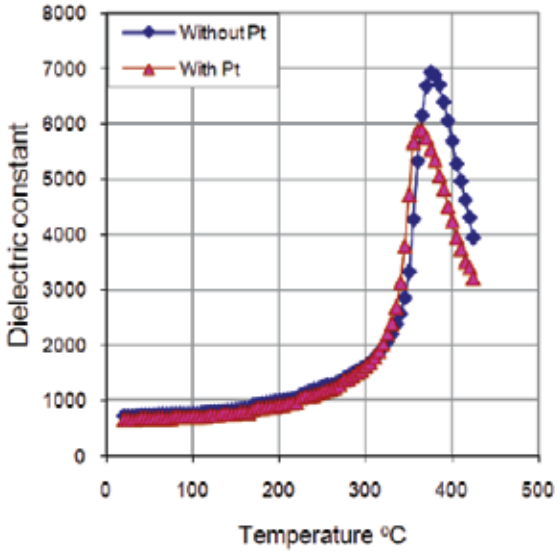

Fig. 1. Dielectric constant piezoelectric ceramic PLZT

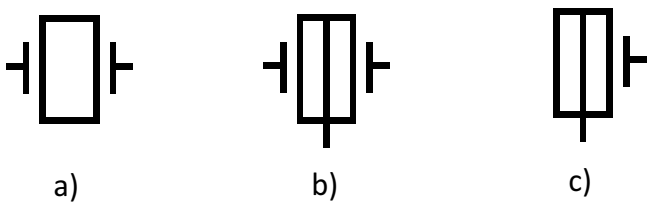

Fig. 2. Graphical symbols that represent reference piezoceramic of PLZT and CCP a) reference piezoceramic with two electrodes, b) CCP, with implant of Pt-wire and two electrodes, c) CCP without an electrode which side face is used like sensor

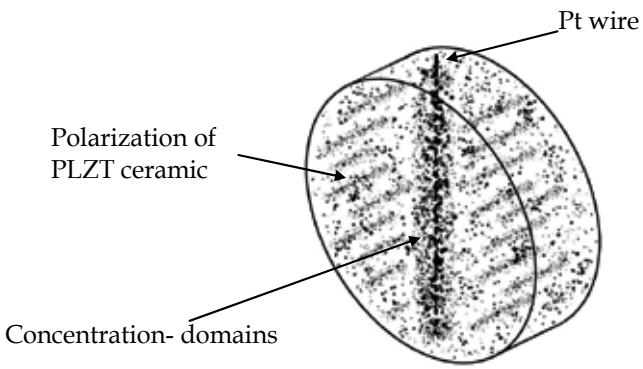

Fig. 3. Scheme from CCP and its domains distributed around Pt-wire.

When the CCP is poled, it originates a great concentration of domains on the Pt-wire because the dipoles are oriented over all its external part. These concentrations achieve free flux charges around the Pt-wire when CCP is excited by stress or light on its side face.
Considering that ferroelectric and piezoelectric materials can be used as sensors and actuators, piezoelectric pressure and acceleration sensors, as well as a variety of piezo-vibrators, are now commercially available. Among piezoelectric ceramics, CCP offers a great variety of applications in medical physics such as the human pulse detection sensor known as PZPG.
In medical physics, micro-circulation of skin blood is a subject of considerable interest due to its role in human metabolism, blood transport from and to the tissue and its role as a liquid coolant of the body in the thermoregulation process.
The measurement of the blood flow is related to the measurement of changes in volume which occur in any part of the body as result from the pulsations of blood with each heartbeat. The instruments that measure volume changes or provide outputs that can be related to them are called plethysmographs. Plethysmographs respond to changes in volume, but there are several devices that in fact measure some other variables related to volume rather than volume itself. One type of these "pseudo-plethysmographs" measures changes in diameter at a certain cross section of a finger, toe, arm, leg or other segment of the body, for example, the non-invasive reflection photoelectric plethysmograph method uses back-scattered optical signals for temporal analysis of skin blood volume pulsations.
Several applications in biomedical area has been developed having as principal component this ceramic with implant such as wireless transmission signals, in which a biological signal is applied to an oscillator by the CCP getting a frequency modulator, in other field CCP is used to obtain cardiac pulse by taking advantage of piezoelectric properties, finally an opacity sensor is an enforce in which is exploited the photoelectric effect that CCP offers, through this chapter these applications will be explained in detail.

Signal modulator

One of the main characteristics that ferroelectrics has is the high dielectric constant, this is due to domains alignment and the susceptibility of material to be polarized when an electric field is applied to the material, a metallic insert into the ceramic provides electric charges and at the same time is a way to modified its behavior (Gutierrez & Suaste, 2009).
Taking advantage of the ceramic high permittivity this ferroelectric sensor (FS) is the base of a frequency modulator, the function is as follows: the traditional electrodes are connected as part of resonance circuit of oscillator and the third electrode is connected to a signal which voltage was increased while the oscillator output was monitoring, a direct relation between control voltage and oscillator frequency was found as Figure 4 shows.
Electrocardiograph signal was also applied to the CCP in the control electrode in order to have a biological signal modulator, the biological signal provokes a difference in the CCP permittivity, as a consequence of this the oscillator output varies proportionally to the signal connected at the control electrode and a modulator frequency was obtained.
The importance of this application is in the wireless field, once the ECG signal is obtained it is only necessary to have an oscillator to modulate the signal, once upon signal was modulated it is necessary a power stage and an antenna in order to have a complete wireless transmitter.
One of the advantages that CCP has is its high ceramic impedance which guarantees the patient electrical isolation; the experimental setup used for this application is show in Figure 5.

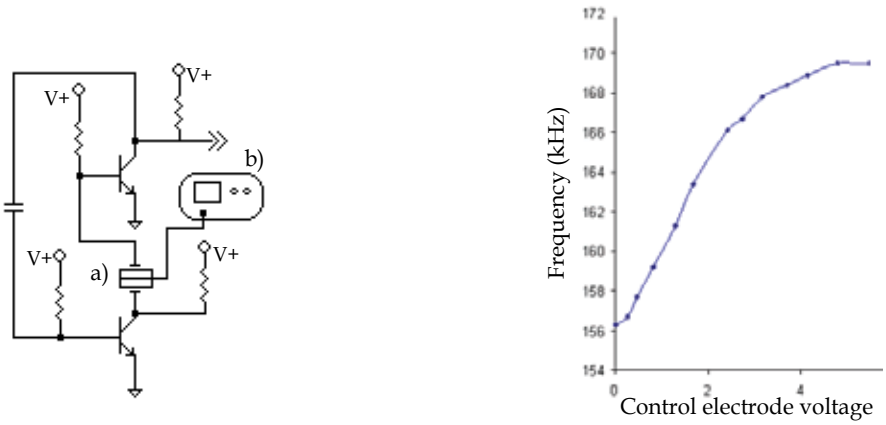

Fig. 4. Left: oscillator with FS in the resonance circuit a) FS b) variable voltage source, right: frequency as function of voltage control electrode

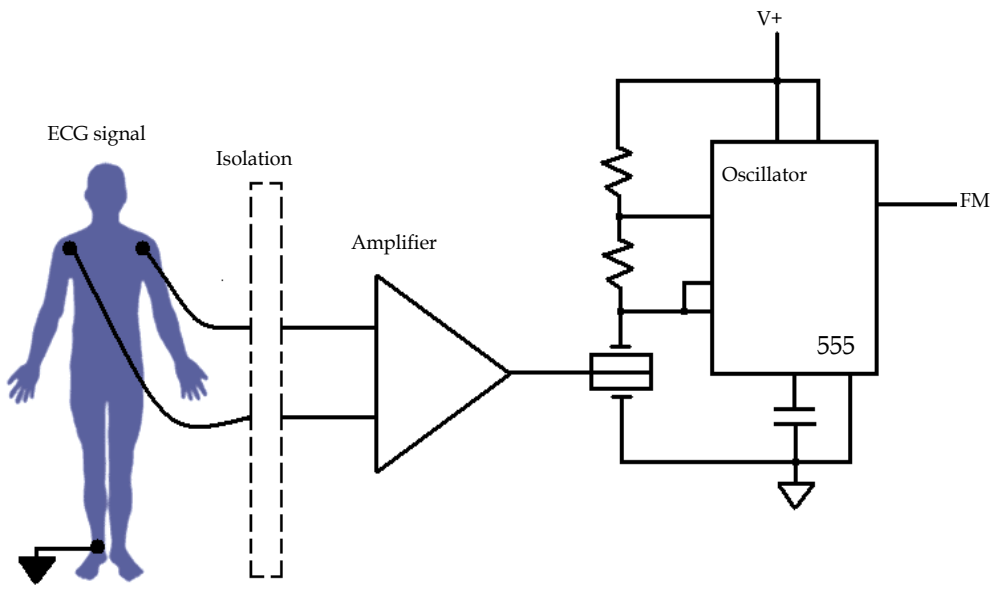

Fig. 5. CCP used as frequency modulator

By the frequency to voltage converter is possible to recover the original signal applied to the ceramic as the same way that in a FM receiver, in Figure 6 can be shown an electrocardiographic signal applied to CCP and a recovered signal after a FM demodulator.

In the Figure 6 is possible to see obtained signal after a frequency demodulator, noise that appearance in the signal is due to the low filter response since the propose of the filter was only to show that is possible to get the original signal, the principals signal characteristics of the original are in the recovered signal.

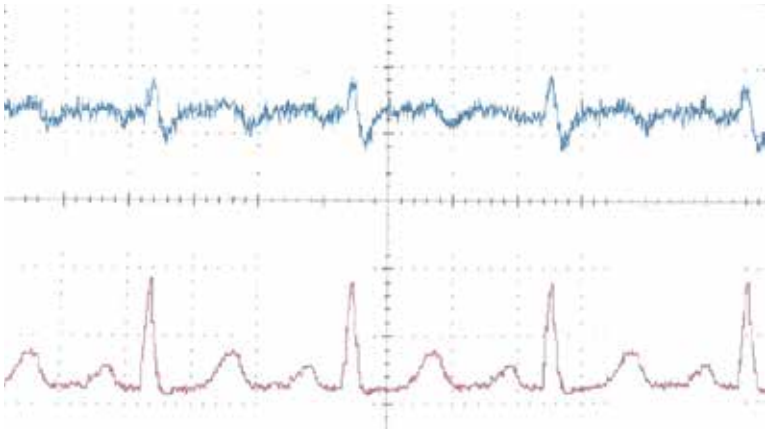

Fig. 6. Above electrocardiographic signal recovered through the frequency to voltage converter after passed to the frequency modulator, down signal applied to the control electrode

Piezo-Plethysmograph

In medical physics, micro-circulation of skin blood is a subject of considerable interest due to its role in human metabolism, blood transport from and to the tissue; it works as a liquid cooler of the body in thermoregulation process. There are several techniques which are used to follow the blood flow in living tissues (Ganong, 2005).

Piezoelectric methods seem to be the most promising for skin microcirculation studies; one advantage of piezoelectric sensors is that they can be used for true dynamic measurements due their wide range of frequency operation. Therefore, the analysis of the skin mechanic pulse piezoelectric detection provides valuable selective information on blood flow on upper skin layers, cutting off the influence of the deeper arteries and veins (Caro, 1978).

The objective of this application is to detect the heartbeat pulses from human beings. The cardiac pulse detection was recorded on an experimental setup. This development also demonstrated the enormous relevance of measuring cardiac pulses at a cross section of the index finger.

Taking advantage of the piezoelectric characteristics of the ceramic a piezo plethysmograph (PZPG) was develop with the CCP, first at all the CCP was submitted to a polarization process by means of apply an electric field of 3 kV by an hour between parallel faces. Control electrode and one face was used to obtain the signal, a free face was used as sense part.

The CCP was mounted onto a finger splint for cardiac signal detection and its signal was amplified. At the same time electro-cardiogram was obtained by means of the use bio amplifier as shown in Figure 7. The measurement of the blood flow is related to the measurement of changes in volume which occur in any part of the body as result from the pulsations of blood with each heartbeat (Suaste et al, 2010).

The CCP showed satisfactory results due to the signal response, in the cardiac monitor graphics ECG and CCP detection that provides additional diagnostic information on the vascular blood flow resistance; the height of the diastolic component of the CCP relates to the amount of the pressure wave reflection, which relates mainly to the tone of small arteries. The timing of the diastolic component relative to the systolic component depends on the pulse wave velocity of the pressure waves in the aorta and the large arteries. This, in

turn, depends on the large artery stiffness. The human vascular system is elastic and multi-branched, and each branching partially reflects back the pressure wave (Janis, 2005).
It was shown that the CCP used as piezoplethismograph has several advantages. It can be adjusted to the fingertip measurements; however, it can also easily be extended by means of spare bands, therefore it is possible to take PZPG measurements from different locations of the body, e.g., forehead, forearm, knee, neck. It is non invasive due to its mechanical detection and there are no chemical reactions with the body or possible current discharges because it is completely isolated and it does not require external electrical supply. The implant is put into the ceramic during the sintering stage, meaning that no additional steps are required, whereas coating the ceramic with a polymer or any other material involves one or more fabrication and characterization steps, which in an industrial process is more expensive. Moreover, this setup eliminates considerable electrical noise.

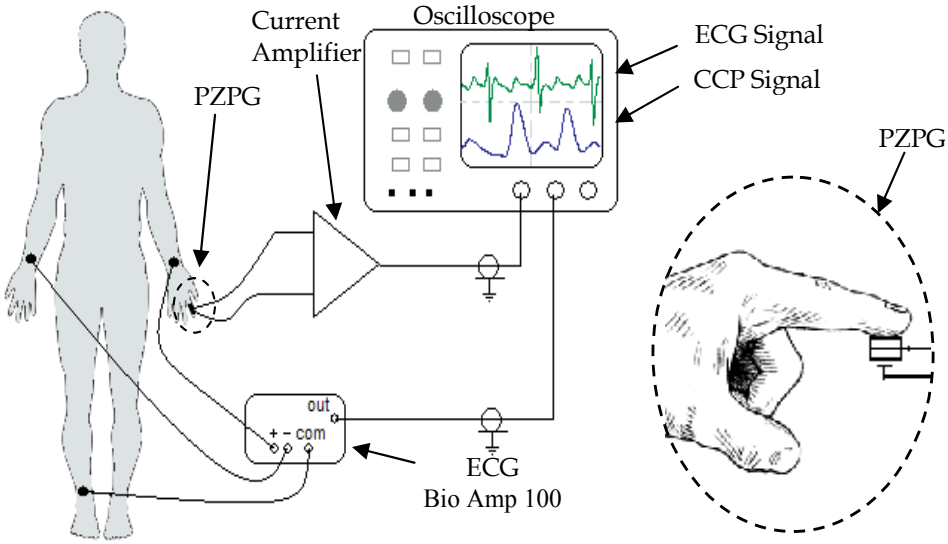

Fig. 7. Experimental setup of Piezopletysmograph in order to obtain fingertip pulses

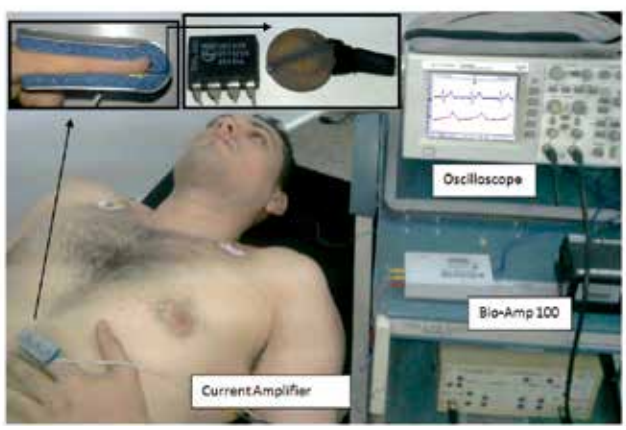

Fig. 8. Real setup used for get fingetip pulses

By the use of a system of data acquisition the cardiac pulses signal can be recorded, analyzed and compared with electrical registry of the heart (Gonzalez et al, 2010). The system of acquisition of pulse shows in a computer screen a friendly atmosphere to us that can be adapted to diverse situations of measurement, as Figure 9 shows.

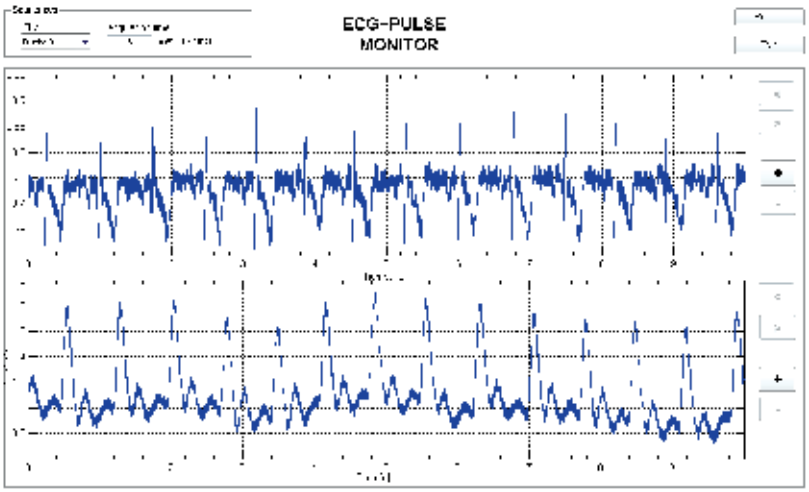

Fig. 9. Screen of acquire system captured from a computer, above ECG register, down cardiac pulse acquire with CCP

In figure 10 it is possible to see an amplified ECG and PZPG curves

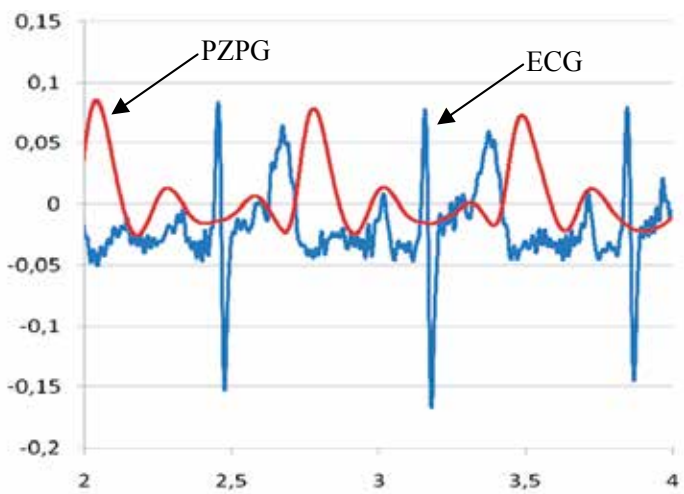

Fig. 10. PZPG and ECG curves response

The timing of the diastolic component and the reflections, according to the place of measure, can be determined with the PZPG.

With this experimental setup is possible to get a fast way to analyze cardiac frequency variability since the frequency spectrum getting by the data acquisition system is the same for both signal ECG register and PZPG signal.

Results demonstrated that the PLZT bulk with Pt-wire has the following advantages: the increase in surface analysis is superior due to the Pt-wire, which works as a third electrode; the proposed CCP can be used at much higher temperatures than the conventional Si based sensors; the CCP is easy to make and the size of this bulk material can be modified; finally, the CCP offers good versatility as a mechanical sensor due to its ferroelectricity.

Opacity sensor

There are several kinds of ferroelectric materials that exhibit photovoltaic effects under near-ultraviolet light even temperature changes. When the material is illuminated after poling, voltage and current can be generated due to the separation of photo induced electron and holes caused by its internal electric field. This is considered an optical property of the material itself which has potential applications for supplying energy transfer in microelectromechanical systems and optoelectronic devices (Sturman & Fridkin, 1992; Ichiki et al, 2004).

The steady current in the absence of applied voltage, called photocurrent, is considered the result of photo carriers and the asymmetric electromotive force induced by near-ultraviolet radiation (Tonooka et al, 1998). Therefore, photocurrent is a very important parameter for optical detection (Qin et al, 2007). In this field photovoltaic current permits to get a signal related with the light that pass thought the translucent sample getting with this opacity detector.

In this use a translucent sample is put on the free ceramic face named opacity sensor (OPS) whilea frequency modulated light beam is applied, the obtained signal is analyzed and photovoltaic current related with the sample opacity is obtained the signal getting without sample is considered as 100% and the signal with sample which diminish by the sample opacity and thickness is related as a percentage, Figure 11 shows the experimental setup used for this application. (Ichiki et al, 2005; Ichiki et al, 2006; Suaste et al, 2009).

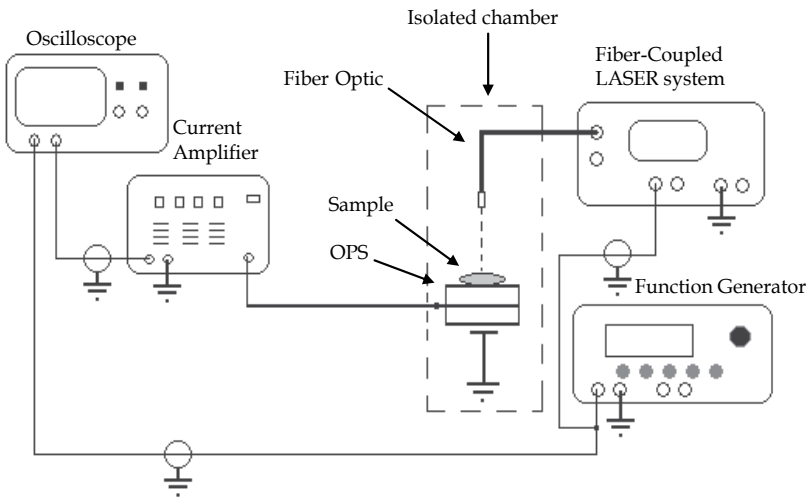

Fig. 11. Experimental setup for opacity measure

Since the CCP has not plane response curve it is necessary to get its characteristic curve in order to have a reference curve that help us to normalize the response, Figure 12 shows the CCP response without sample.

Some samples such as fruit tissues, vegetal oils and other thin materials were tested by this sensor Table 1 shows the materials and its thickness, the resultant curves are shown in Figure 13, the OPS curve is the result from stimulate sensor without sample.

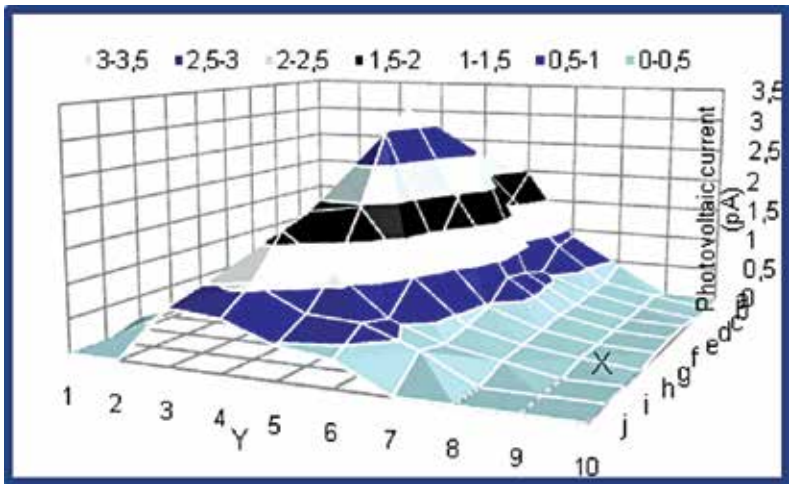

Fig. 12. CCP curve response without sample when is stimulated 160 mW/cm² of LASER illumination

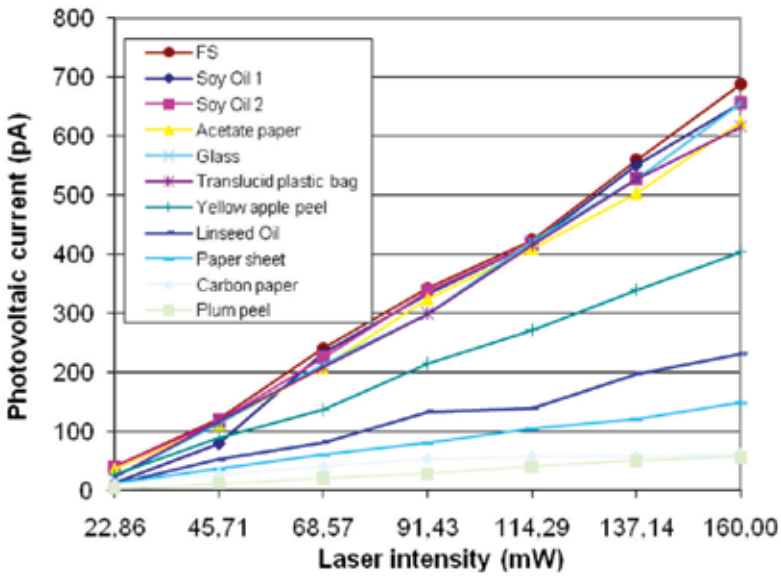

Fig. 13. CCP detected curves from different liquids and thin solids

By the use of an x-y, the ferroelectric sensor implanted allows to perform 2D scanning and generate 3D graphics or images of opacity depending on the percentage of opacity of the sample in the bi-dimensional setup coordinate system that could have novel applications such as before transplant 2-D cornea scan in order to verify its opacity, 2-D scan opacity of insects (Entomology), etc (Matusik et al, 2002; Chamberlain, 2008; Dekking, 1948), the experimental setup is showed in Figure 14.

By the use of X-Y positioning platform images about different opacity regions can be obtained. In Figure 15 it is possible to see a 3D graphic taken at a plant leaf (Myrtus communis).

Liquids and thin materials samples measured on OPS	Thickness (μm)	% of Opacity
Plum peel	76.2	91.7
Carbon paper	36.56	84.33
Paper sheet	101.6	76.61
Linseed Oil	100	60.82
Yellow apple peel	88.9	36.84
Transparent Plastic Bag	63.5	12.28
Glass	152.4	12.28
Acetate paper	109.22	5.26
Soy Oil 2	100	1.17
Soy Oil 1	100	2.92

Table 1. Opacity percentage of different liquids and thin materials at 91.43 mW/cm^2 of illumination using one-dimensional setup

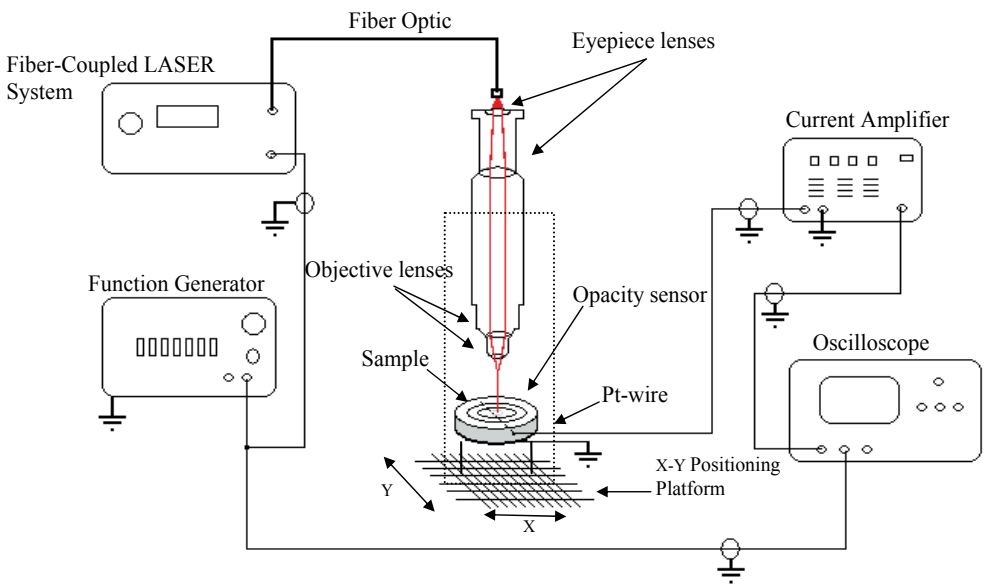

Fig. 14. Experimental setup used as 2D opacity scan

Quantitative sensitivity comparison with other types of opacity/transmission would be relative due to the chemical compositions of each sensor and because finally whatever the type of sensor, they only give a percentage measure parameter. The most significant differences among ferroelectric sensors and Si based sensors are: 1) Si based sensors require electrical external supply and do not have domains; in contrast ferroelectric sensors do not require an external electrical supply; 2) the Si based sensors have greater sensitivity than ferroelectric sensors but these last offer a good response at extreme temperatures, up to 570ºC according to its chemical composition (ferroelectric phase transition) (Jona & Shirane, 1993).

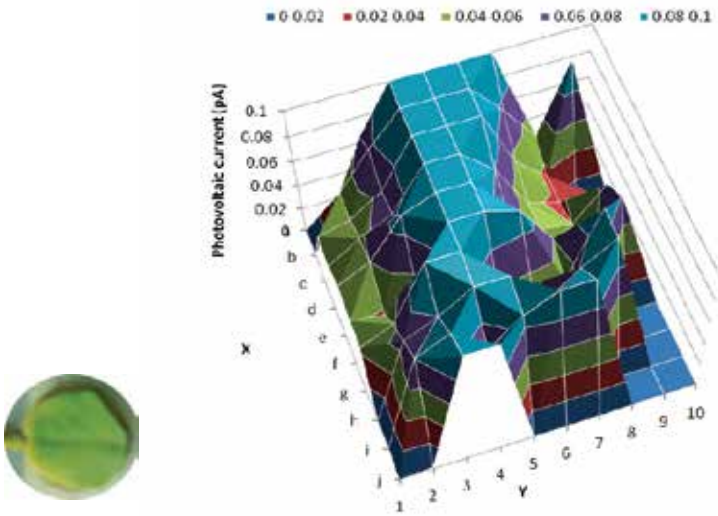

Fig. 15. CCP response with a plant leaf

3. Conclusions

The CCP device demonstrated a good performance in optic and mechanic probes as an opacity sensor and cardiac pulse measurement device, respectively. A study with several people in order to determine the study basis such as blood pressure detection, cardiac pulse in different zones of the body, continuous cardiac pulse, and the associated cardiac variability with electrocardiogram data are in current stage.

The CCP has an interesting configuration because by the one hand it provides a great ceramic insulator that does not affect human beings and on the other hand it is very significant that this sensor was developed not only for this mechanical field of study, but also has multiple applications in different areas, for example: optics, acoustics, electrical and chemical sensing. Finally is important to mention that an advantage of an implanted ceramic over a conventional ceramic (with two parallel conductive layers) is the increase of a mechanical and optical signal measured due the physical reduction (cutting the piece) making minisensors for multiple uses such as neonatal applications

Finally, the CCP recently developed such as is described in this chapter, offers a window of opportunity to the development, the circumstances are right for working not only in biomedical engineering but also in diverse fields of applied research as the examples showed.

4. References

Caro C. (1978). *The mechanics of the circulation*, Oxford University Press, 0192633236, NY-Toronto

Chamberlain, D. (2008). The transmission opacity tester. Paper Technology, Vol. 49, pp. 42-4, 0 306-252X

Dekking, H. M. (1948). Opacity meter for cornea and lens. *Ophthalmologica*, Vol. 115(4), 4, 219-226

Ganong, W. F., (2005). *Review of Medical Physiology*, McGraw-Hill Medical, New York

González-Morán C. O., Suaste-Gómez E. (2009). Developed and experimental evidence of a ceramic-controlled piezoelectric bulk implanted with Pt wire based on PLZT, *Ferroelectrics,* Vol. 392, 98-106, 0015-0193

González-Morán C. O., Flores-Cuautle J. J. A. and Suaste-Gómez E. (2010). A Piezoelectric Plethysmograph Sensor Based on a Pt Wire Implanted Lead Lanthanum Zirconate Titanate Bulk Ceramic, Sensors 2010, Vol. 10, 7146-7156

Gutierrez-Begovich, D.A.; Suaste-Gomez, E., Frequency modulation via a biological signal using a controlled piezoelectric ceramic, *Proceedings of Pan American Health Care Exchanges 2009,* pp.7-7, 978-1-4244-3668-2, México City, March 2009

Ichiki M. et al. (2006). Photovoltaic Effect of Crystalline-Oriented Lead Lanthanum Zirconate Titanate in Layered Film Structure, Vol. 45, No. 12, 9115-9118,

Ichiki M., Maeda R., Morikawa Y., Mabune Y. and Nakada T., (2004). Photovoltaic effect of lead lanthanum zirconate titanate in a layered film structure design, *Appl. Phys. Lett*., Vol. 84, pp. 395-397, 0003-6951

Ichiki M., Maeda R., Morikawa Y., Mabune Y., Nakada T. and Nonaka K. (2005). Preparation and Photovoltaic Properties of Lead Lanthanum Zirconate Titanate in Design of Multilayers, *Japanese Journal Appl. Phys.*, Vol. 44, 6927-6933, 0021-4922

Jaffe B., Cook W. R. (1971). *Piezoelectric Ceramics*, Academic Press, 0-12-379550-8, London and New York

Janis, S. Optical Non-Invasive Monitoring of skin Blood Pulsations. Appl. Opt. 2005, 44, 8

Jona F., Shirane G. (1993). Ferroelectric crystals, Oxford, 0-486-67386-3, New York

Matusik, W; Pfister, H; Ngan, A, et al. (2002). Image-based 3D photography using opacity hulls, ACM Transactions on graphics, Vol. 21 Issue 3, 427-437, 0730-0301

Moulson A. J., Herbert J. M. (2003). Electroceramics, John Wiley & Sons, 0471 49748 7, England

Qin M., Yao K., Liang Y. C., Shannigrahi S. (2007). Thickness effects on photoinduced current in ferroelectric $(Pb_{0.97}La_{0.03})(Zr_{0.52}Ti_{0.48})O_3$ thin films, *Journal of Applied Physics*, Vol. 101, 014104-1 014104-4, 0021-8979

Sturman B. I. and Fridkin V. M. (1992). *The Photovoltaic and Photorefractive Effects in Noncentrossymetric Materials Vol. 8*, Gordon and Breach Science Publishers, 288124498X, New Jersey

Suaste-Gómez E., González-Morán C. O. (2009). Photovoltaic Effect of Lead-Free Piezoelectric Ceramics, (Bi0.5Na0.5)0.935Ba0.065TiO3 and Pb0.88(Ln)0.08Ti0.98Mn0.02O3 (Ln = La, Eu), Ferroelectrics, Vol. 386, 70-76, 0015-0193

Suaste-Gómez E., González-Morán C. O. and Flores-Cuautle J. J. A. (2009). Developed and applications of a novel ceramic-controlled piezoelectric due to an implant of Pt-wire into the body of sigle disk of $BaTiO_3$ ceramic, *Proceedings of WC2009, IFMBE 25/XII,* pp. 89-92,", O. Dössel and W. C. Schlegel, 978-3-642-03892-1, Munich, Germany

Suaste-Gómez E., Flores-Cuautle J. J. A., Gónzalez-Morán C. O. (2010). Opacity Sensor Based on Photovoltaic Effect of Ferroelectric PLZT Ceramic With Pt Wire Implant, *Sensors Journal, IEEE* , vol.10, no.6, 1056-1060, 1530-437X

Tonooka K., Poosanaas P. and Uchino K. (1998). Mechanism of the bulk photovoltaic effect of ferroelectrics, *Proceedings of SPIE Volume: 3324,* 9780819427687

5

Cold Plasma Techniques for Pharmaceutical and Biomedical Engineering

Yasushi Sasai[1], Shin-ichi Kondo[1],
Yukinori Yamauchi[2] and Masayuki Kuzuya[2]
[1]*Gifu Pharmaceutical University*
[2]*Matsuyama University*
Japan

1. Introduction

Plasmas can be defined as the state of ionized gas consisting of positively and negatively charged ions, free electrons and activated neutral species (excited and radical), and are generally classified into two types, thermal (or equilibrium) plasma and cold (or non-equilibrium) plasma, based on the difference in characteristics.

The thermal plasma is the state of fully ionized gas characterized by a high gas temperature and an approximate equality between the gas and electron temperature ($Tg \approx Te$) and can be generated under atmospheric pressure. The energetic of this plasma is very high enough to break any chemical bond, so that this type of plasma can be excluded from most of organic chemistry, let alone from the field of pahramceutical science.

In contrast, the cold plasma is most characterized by a low gas temperature and a high electron temperature ($Tg << Te$), and easily generated by electric discharges under reduced pressure. The field of plasma chemistry deals with occurrence of chemical reactions in the cold plasma including atmosphere pressure glow discharge plasma.

One of the characteristics of surface treatment by cold plasma irradiation is the fact that it is surface limited (ca. 500-1000 Å) so that only the surface properties can be changed without affecting the bulk properties.

In recent years, biomedical applications of cold plasma are rapidly growing due to the fact that the use of cold plasmas is very useful to treat heat-sensitive objects such as polymeric materials and biological samples. The demonstrations of plasma technology in the biomedical field have created a new field at the intersection of plasma science and technology with biology and medicine, called "Plasma Medicine". (Fridman et al., 2008)

When the cold plasma is irradiated onto polymeric materials, the plasma of inert gas emits intense UV and/or VUV ray to cause an effective energy transfer to solid surface and gives rise to a large amount of stable free radicals on the polymer surface. In view of the fact that surface reactions of plasma treatment are initiated by such plasma-induced radicals, study of the resulting radicals is of utmost importance for understanding of the nature of plasma treatment. Thus, we have undertaken plasma-irradiation of a wide variety of polymers, synthetic and natural, and the surface radicals formed were studied in detail by electron spin resonance (ESR) coupled with the aid of systematic computer simulations. On the basis

of the findings from a series of such studies, we were able to open up novel plasma-assisted application works. (Kuzuya et al., 2001a, 2005, 2009)
This contribution focuses on our plasma techniques for pharmaceutical and biomedical engineering on the basis of findings from a series of studies on plasma-induced surface reactions in variety of polymers. For the pharmaceutical engineering field, the controlled drug release technology by using plasma-induced cross-linking and/or degradation of polymer was developed for the preparation of rate- and time-controlled drug release tablet. Furthermore, this technique was used to develop the advanced DDS such as gastric floating drug delivery system (FDDS) possessing gastric retention capabilities and patient-tailored DDS for large intestine-specific drug delivery. For the biomedical engineering fields, the durable surface hydrophilicity and lubricity on hydrophobic biomedical polymers were fabricated by plasma-assisted immobilization of carboxyl group-containing polymer onto the surface. The surfaces thus prepared were further used for the covalent immobilization of biomolecules for developing biomedical devices such as cell culture substrate, biosensing system and blood-compatible material.

2. Nature of plasma-induced polymer radicals

Plasma induced radicals on polymer surface permit reactions for surface modification in several different ways such as CASING (cross-linking by activated species of inert gas), surface graft and/or block copolymerization, and incorporation of functional groups. All these techniques are referred to as plasma techniques. However, research has essentially been phenomenological, and detailed studies of such plasma-induced surface radicals of polymer have not been reported.
Over the years, we have been working on the structural identifications of plasma-induced surface radicals of various kinds of organic polymers as studied by electron spin resonance (ESR) spectra coupled with the systematic computer simulations. (Kuzuya et al., 1991a-c, 1992a-c, 1993ab, 1994, 1995, 1996a, 1997a, 1998ab, 1999ab) One of the advantages of plasma irradiation over other types of radiations for the study of the polymer radicals is that the radical formation can be achieved with a brief plasma-duration by a simple experimental apparatus such as those we have devised. The experimental setup for the plasma-irradiation and ESR spectral measurement is schematically shown in Fig. 1. This method makes it possible not only to study the polymer radicals without a significant change of polymer morphology but also to follow readily the ESR kinetics for the radical formation, so that we can carry out systematic computer simulations with a higher credibility.

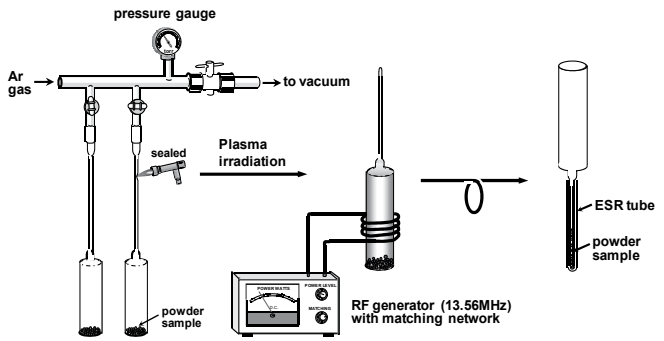

Fig. 1. Schematic representation for plasma irradiation and ESR spectral measurement

Figure 2 shows the observed ESR spectra of plasma-induced surface radicals formed on several selected polymers relevant to the present study, together with the corresponding simulated spectra shown as dotted lines. Based on the systematic computer simulations, all the observed spectra in addition to those shown here were deconvoluted and the component radical structures have been identified.

From a series of this work, we were able to establish the general relationship between the structure of radicals formed and the polymer structural features. Crosslinkable polymers give the mid-chain alkyl radical as a major component radical, while degradable polymers give the end-chain alkyl radical as a major component radical, and if polymers are of branched structure or contain the aromatic ring, the cross-link reactions occur preferentially on these moieties. And, one of the common features is that dangling-bond sites (DBS) is more or less formed in all plasma-irradiated polymers resulted from occurrence of CASING.

All kinds of plasma-irradiated polymers are eventually exposed to air for their practical use, so the studies of the auto-oxidation process are also important for plasma-irradiated polymer. Figure 3 shows a reaction scheme for the formation of peroxy radical and its ensuing process (hydroperoxide, alkoxyl radicals formation) demonstrating how auto-oxidation ends up with introduction of oxygen-containing functional groups such as hydroxyl groups, carboxyl groups and so on, and dissipation of the surface radical formed. Therefore, we have studied the nature of peroxy radical formation as an initial process of auto-oxidation.

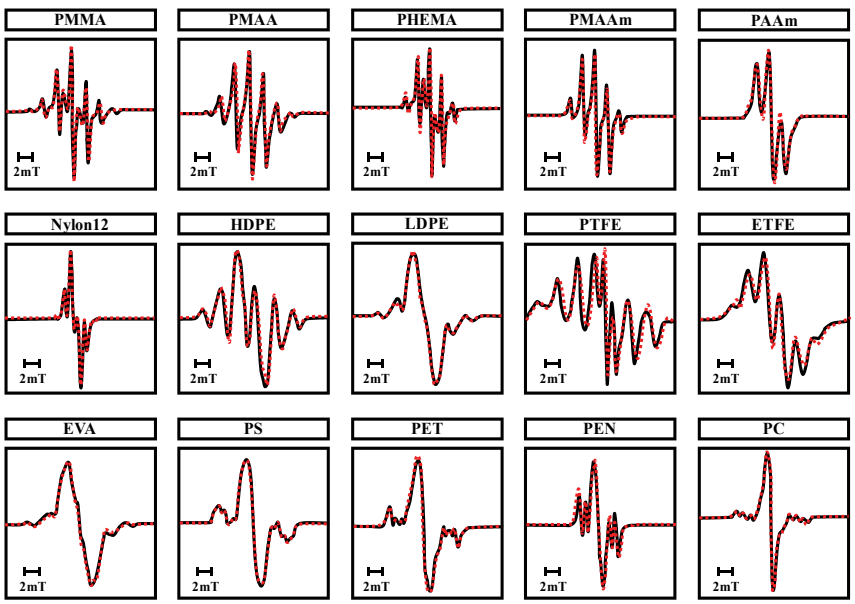

Fig. 2. Room temperature ESR spectra of plasma-induced radicals in organic polymers, together with the simulated spectra shown as dotted lines. Plasma conditions: 40W, Ar 0.5 Torr, 3 min. PMMA: polymethylmethacrylate, PMAA: polymethacrylic acid, PHEMA: poly-(2-hydroxyethyl) methacrylate, PMAAm: polymethacrylamide, PAAm: polyacrylamide, HDPE: high density polyethylene, LDPE: low density polyethylene, PTFE: polytetrafluoroethylene, ETFE: (ethylene-tetrafluoroethylene) copolymer, EVA: (ethylene-vinylacetate) copolymer, PS: polystyrene, PET: polyethyleneterephtalate, PEN: polyethylenenaphthalate, PC: polycarbonate

Figure 4 shows several examples of ESR spectra of peroxy radicals formed immediately after exposure of the plasma-irradiated polymers to air, which correspond to those shown in the previous Fig. 2, as well as the simulated spectra as shown in dotted lines. It can be seen that in some polymers, the spectral pattern remained unchanged with only lowering the intensity, and in other polymers, the spectra have been completely converted to the one exhibiting a typical spectral pattern of peroxy radical.

Note that, in most polymers, such an intensity of peroxy radicals usually decreases to less than 30-40% of the original carbon-centered radicals even immediately after exposure to air, except for polytetrafluoroethylene (PTFE), which can be best discussed on its comparison with that of high density polyethylene (HDPE) to understand the nature of auto-oxidation in more detail.

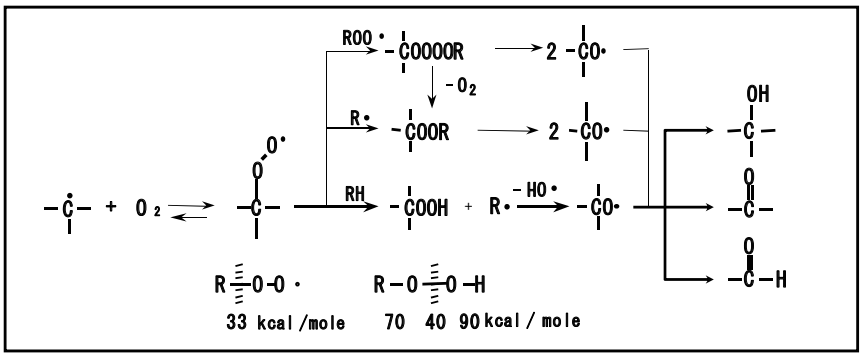

Fig. 3. Peroxy radical formation from carbon-centered radical with molecular oxygen and its reaction, resulted in introduction of oxygen functional groups on polymer surface

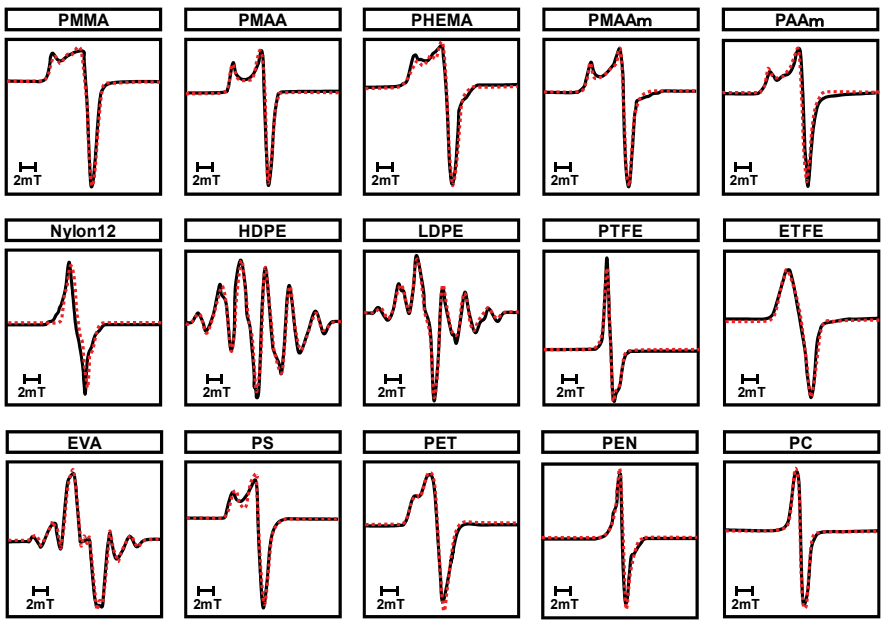

Fig. 4. Room temperature ESR spectra of various plasma-irradiated polymers after exposure to air

As shown in Fig. 5, exposure of plasma-irradiated HDPE to air at room temperature did not give the ESR spectra of peroxy radicals, but the ESR spectra did show only the decrease in the spectral intensity. On the other hand, the peroxy radicals of PTFE are extremely stable for a long period of time at room temperature. The spectral intensity, therefore, is nearly the same as that of the original radicals. The extraordinary instability of HDPE peroxy radical can be ascribed to the rapid chain termination reaction through the hydroperoxide consuming several moles of molecular oxygen, due to the presence of abundant hydrogen atoms bonded to sp^3 carbons in HDPE. Because of occurrence of this type of oxygenation reaction, plasma treatment by inert gas plasmolysis has a tendency to result in the introduction of surface wettability in many polymers. The exceptional stability of PTFE peroxy radicals can be attributed to the absence of any abstractable hydrogen in PTFE to undergo the chain termination reactions.

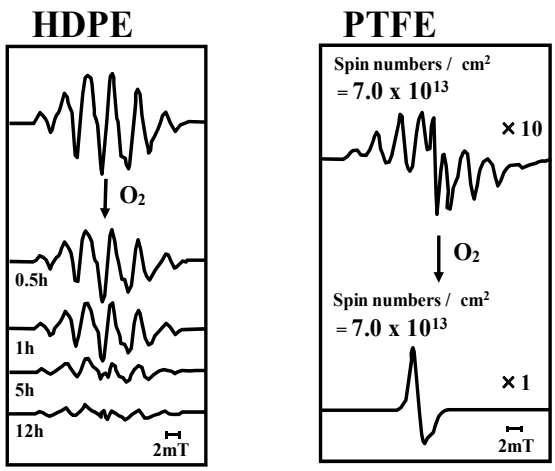

Fig. 5. Difference in free radical reactivity with oxygen between HDPE and PTFE

3. DDS preparation by plasma techniques

A drug delivery system (DDS) is a formulation or device that safely brings a therapeutic agent to a specific body site at a certain rate to achieve concentration at the site of drug action. Development of more "patient-friendly" DDS improves drug efficiency and patient compliance. A wide variety of approaches of controlled-release DDS have been thus far investigated for oral application. Oral drug delivery is the most desirable and preferred method of administrating therapeutic agents for their systematic effects such as convenience in administration, cost-effective manufacturing, and high patient compliance compared with several other routes.

As an application of plasma techniques to DDS technologies, the encapsulation of drug particle by plasma-polymerized thin film was reported. (Susut & Timmons, 2005). In this case, however, the drug molecule is exposed by plasma to cause the undesirable degradation of drug molecules. On the other hand, we have developed plasma-assisted preparation of multi-layered tablets (Fig.6). In this method, plasma is irradiated on the outermost layer of double-compressed (DC) tablets so that the direct exposure of plasma to

drug molecules in the core table can be avoided. Figures 7 and 8 illustrate the schematic representation for preparation of DC tablet and the experimental setup for plasma-irradiation on the tablets, respectively.

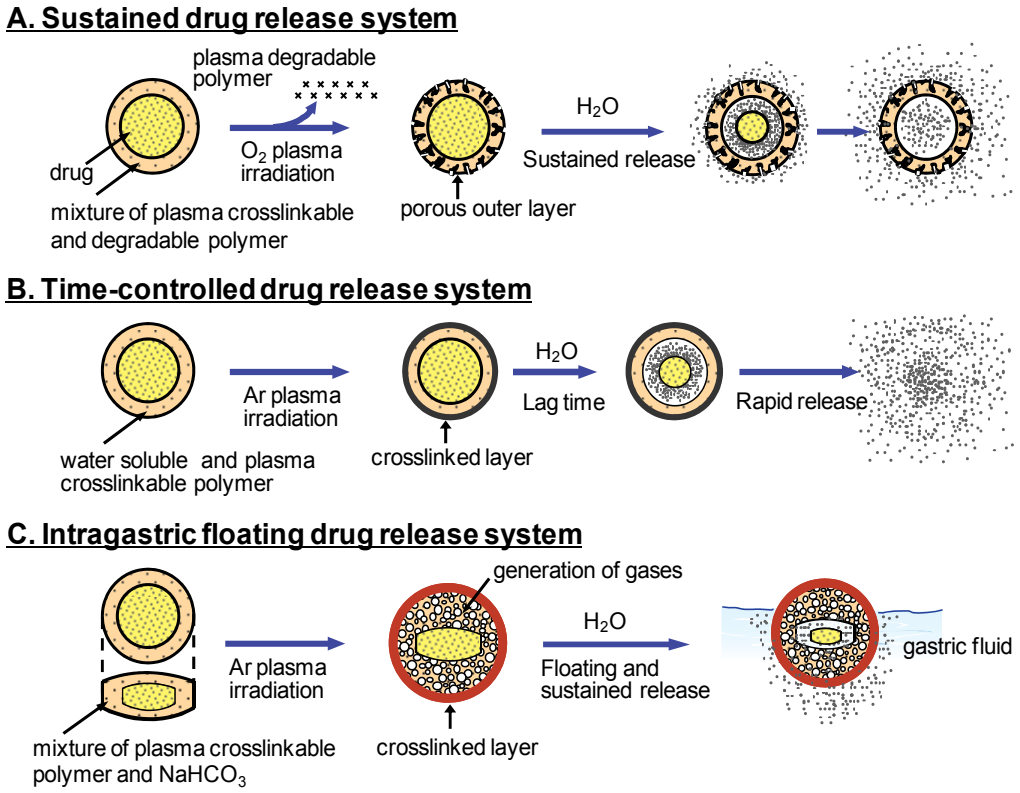

Fig. 6. Conceptual illustration for preparation of DDS for controlled drug release by plasma techniques

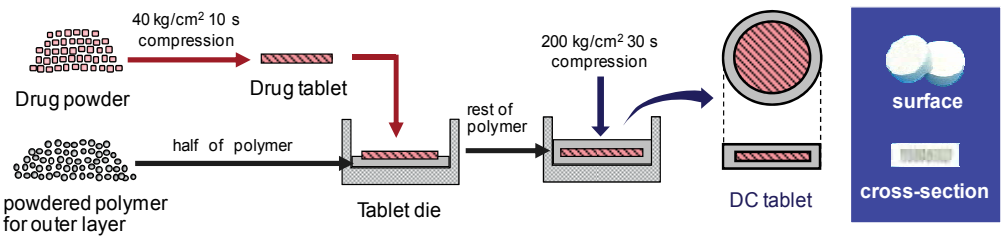

Fig. 7. Schematics for preparation of double-compressed tablets

3.1 Preparation of sustained drug release system by plasma techniques

The development of new active pharmaceutical ingredient (API) is often hampered or even blocked due to side effects of these new APIs. Some of the severe side effects may be caused by the early and high peak blood plasma concentration of APIs just after oral-administration.

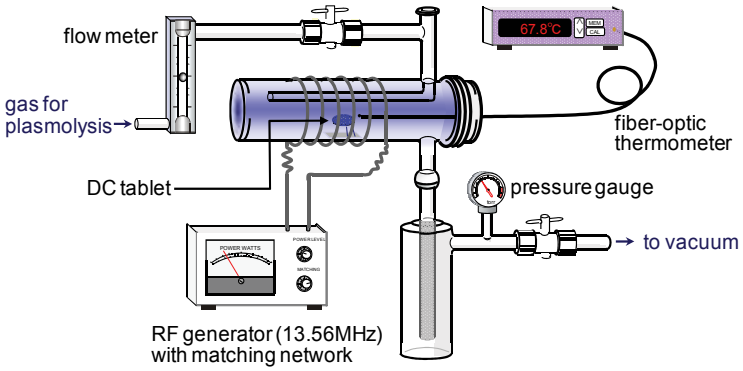

Fig. 8. Experimental setup for plasma-irradiation on DC tablet

This problem can be overcome by altering the blood plasma concentration profile so that a more gradual absorption rate is obtained. In that case, sustained-release DDS that drug is slowly released over a prolonged period of time is an ideal therapeutic system.

When oxygen plasma was irradiated to the outermost layer of the DC tablet, which consists of a drug as a core material and a mixture of plasma-crosslinkable and plasma-degradable polymer powders as a wall materials, plasma degradable polymers could be selectively eliminated and simultaneously the crosslinkable polymer undergoes the rapid cross-link reaction to result in the formation of the porous outer layer of the tablet. As a result, the drugs could be released from the tablet through the resulting micropore. (Fig. 6A) (Kuzuya et al, 1991de, 1996b; Ishikawa et al., 1993, 1995, 1996; Yamakawa et al., 1993)

Figure 9 shows the effect of oxygen plasma duration on theophylline release from the DC tablet as the representative example of the release test. As shown in Fig. 9, when a mixed powder of plasma crosslinkable polymer, polystyrene (PS), and plasma degradable polymer, polyoxymethylene (POM), for the outer layer is used, it is seen that the release rate of theophylline increases as plasma duration increases, while the blank tablet did not exhibit any appreciable release of theophylline even with longer dissolution time. (Kuzuya et al. 1991d) Thus, the release profile of theophylline from DC tablet can readily be controlled by the selection of plasma operational tunings. Based on the fact that the value of weight loss shown in parentheses increases as the plasma duration increases, it is apparent that plasma degradable polymer, POM, could be selectively eliminated by oxygen plasma-irradiation, while plasma-crosslinkable PS undergoes the cross-link reaction, to result in the formation of the porous outer layer of the tablet (Fig. 10). Then, theophylline could be released from the tablet through the resulting micropore evidenced by the scanning electron micrographs (SEM) pictures.

Similar work has included the preparation of the inplantable controlled release tablet by using bioerodible polylactic acid (PLA) in place of PS. DC tablet containing an insulin-PLA matrix tablet as a core material was prepared and the changes in blood glucose levels after the subcutaneous implantation of the DC tablet in diabetic rats was examined (Fig. 11).

(Yamakawa et al., 1993) The normal blood glucose levels were maintained for 10 days in the plasma-irradiated DC tablet and the release rate of insulin in the steady state from the plasma-irradiated DC tablet was 5 IU/h which was calculated from the data from 4 to 34 h. These results indicated that DC tablet consisting of PLA and POM as the outer layer can be applied to a long-acting implantable dosage form in the subcutaneous tissue.

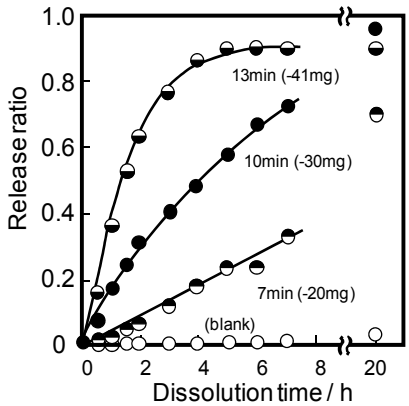

Fig. 9. Effect of oxygen plasma-irradiation on theophylline release from DC tablet (A). The values shown in parentheses denote the weight loss of the tablets after plasma-irradiation. Core tablet: 100mg (Theophylline). Outer layer : 80mg (PS: POM=1:1). Plasma conditions : Power: 50W, Pressure: 0.5 Torr, O_2 50ml/min

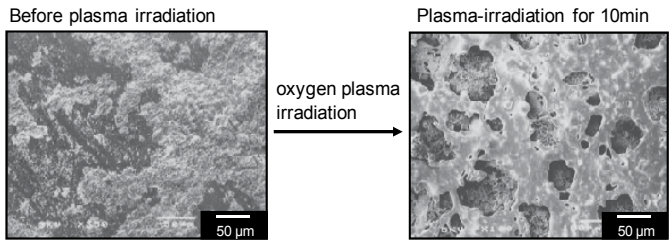

Fig. 10. Scanning electron micrograph (SEM) of DC tablet using PS/POM (1:1) as outer layer before and after oxygen plasma irradiation

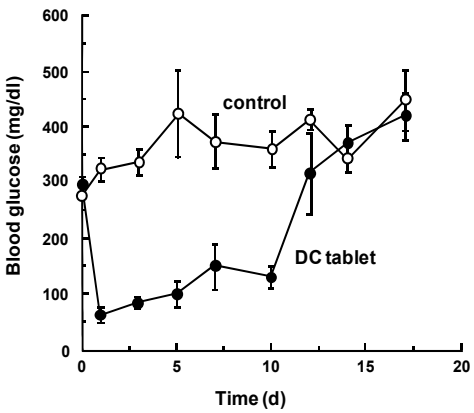

Fig. 11. Change in blood glucose levels with time after the subcutaneous implantation of the DC tablet in rats. Outer layer: a mixed powder of PLA and POM (3/1), Core tablet: a mixed powder of PLA and insulin (1/1).

Plasma conditions: 6 W, O_2 0.5 Torr, 50 mL/min, 3h

3.2 Preparation of time-controlled drug release system by plasma techniques

Today, the therapy based on the factor of biorhythmic time is becoming more and more important in the progress toward an aging society in many countries, in addition to customary controlled-release systems. Time-controlled release system has a function of timer, so that main technical point for the development of this system is how to control a lag time and a drug release after lag time. Thus, the time-controlled drug release system has been noted as orally applicable DDS that is useful for the drug delivery to the specific site of gastrointesrinal tract.

It is well known that methacrylic-acrylic acid copolymers including their derivatives with various combinations and composition ratios of the monomers have been used as pharmaceutical aids for enteric coating agents commercially known as a series of Eudragits. These Eudragit polymers turn to be water-soluble in a certain specific pH solution, and they show a different dissolution rate. The structures and the dissoluble pH values of several Eudragit polymers are shown in Fig. 12.

Since plasma-crosslinkable acrylic monomers are one of the component polymers in Eudragits L100-55, argon plasma-irradiation would lead to the suppression of Eudragit L100-55 solubility even in a dissoluble pH-value solution (pH>5.5) due to the occurrence of the surface cross-link reactions. Thus, when Eudragit L100-55 is used as a wall material of the DC tablet, the initial drug release could be completely sustained for a certain period of time.

With this expectation in mind, we have undertaken argon plasma-irradiation to examine the possibility of a rapid-release DC tablet of Eudragit L100-55, being converted into a delayed-release tablet, i.e. the time-controlled DDS. (Kuzuya et al., 2001b) (Fig. 6B)

Figures 13 and 14 show the effect of argon plasma irradiation on theophylline release profiles in pH 6.5 buffer solution and the SEM pictures of the surface of Eudragit L100-55 tablet before and after argon plasma-irradiation, respectively. It is seen that the Eudragit L100-55 tablets plasma-irradiated for 3 min and 5 min have shown to produce prolongation of lag-time for theophylline release.

The SEM pictures demonstrated that the tablet surface with 5 min-irradiation has converted into the rather smooth surface with clogging the crack presenting at particle-particle interfaces by softening of Eudragit L100-55, and into the porous outer layer with 10 min irradiation. It is considered that the porous layer was formed not only by the effect of plasma irradiation but also by physical actions such as evolved gas scattering accompanied by softening of the Eudragit L100-55 due to the plasma heat fusion.

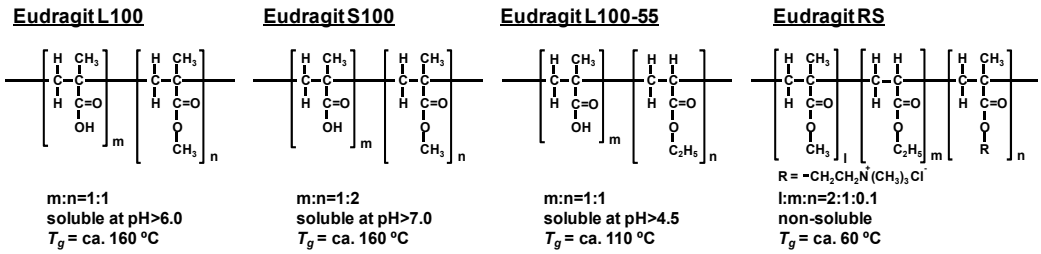

Fig. 12. Structures and dissoluble pH values of several commercial Eudragit polymers used for enteric coating agents

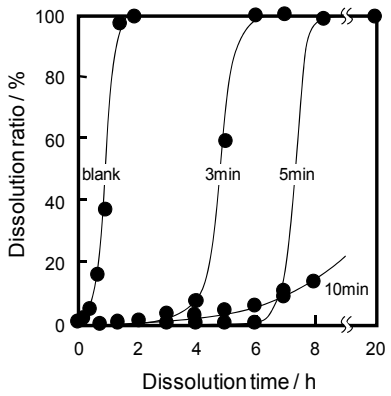

Fig. 13. Effect of plasma duration on Theophylline release from plasma-irradiated DC tablets of Eudragit L100-55 in pH 6.5 buffer solution

Plasma conditions: 50W, Ar 0.5Torr, 50mL/min.

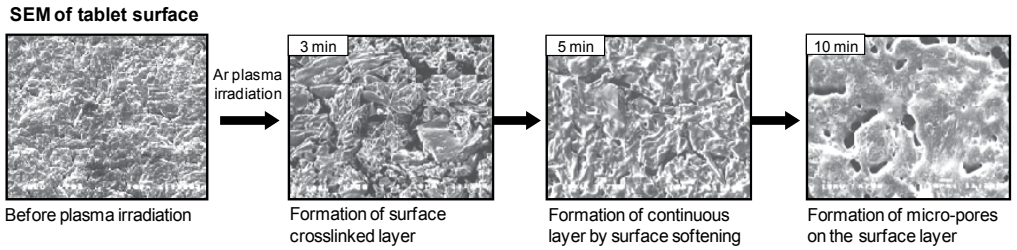

Fig. 14. SEM pictures of Eudragit L100-55 tablet before and after plasma irradiation

Plasma conditions: 50 W, Ar 0.5 Torr, 50 mL/min.

3.3 Preparation of intragastric FDDS by plasma techniques

Intragastric FDDS has been noted as orally applicable systems for the prolongation of the gastric emptying time (GET). (Singh & Kim, 2000; Streubel et al., 2006). The bulk density of FDDS is lower than that of gastric fluids and thus it remains buoyant on stomach contents for a long time in the drug releasing process. Prolonged gastric retention improves bioavailability, reduces drug waste, and improves solubility for drugs that are less soluble in a high pH environment like intestinal environment. It has applications also for local drug delivery to the stomach and proximal small intestines.

In the course of our study on plasma-assisted DDS preparation, we found that carbon dioxide was trapped in the tablet when argon plasma was irradiated onto the surface of DC tablet composed of plasma-crosslinkable polymers possessing carboxyl group as an outer layer. Based on such findings, we have obtained the intragastric FDDS by plasma-irradiation when the DC tablet was prepared using the outer layer so as to trap evolved carbon dioxide. (Fig. 6C) (Kuzuya et al., 2002a; Kondo et al., 2004; Nakagawa et al., 2006) Figures 15-17 show the floating property of the DC tablet on the simulated gastric fluid and the release property of 5-fluorouracil (5-FU) from argon pulsed plasma-irradiated DC tablet using a mixture composed of a 68/17/15 weight ratio of Povidone, Eudragit L100-55 and $NaHCO_3$ as an outer layer. As shown in Fig. 16, the plasma heat flux caused the thermal decomposition of

$NaHCO_3$ to generate carbon dioxide and resultant gases were trapped in bulk phase of outer layer, so that the tablets turned to have a lower density than the gastric contents and remained buoyant in simulated gastric fluid for a prolonged period of time. In addition, the release of 5-FU from the tablet is sustained by occurrence of plasma-induced crosslink reaction on the outer layer of tablet and the release rate of 5-FU can be well controlled by plasma operational conditions (Fig. 17). (Nakagawa et al., 2006)

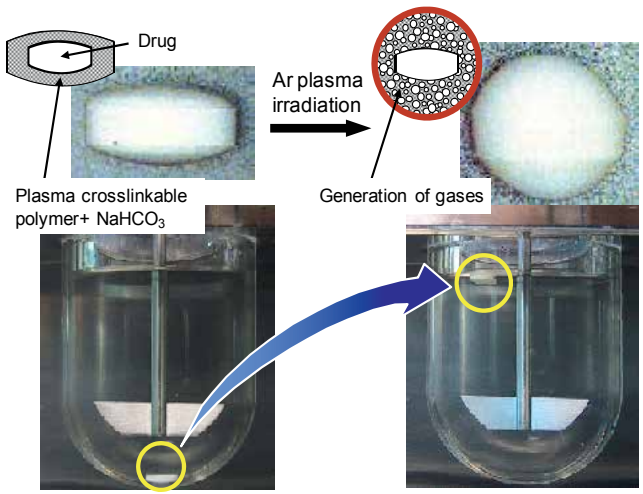

Fig. 15. Photos of DC tablet for FDDS before and after plasma irradiation

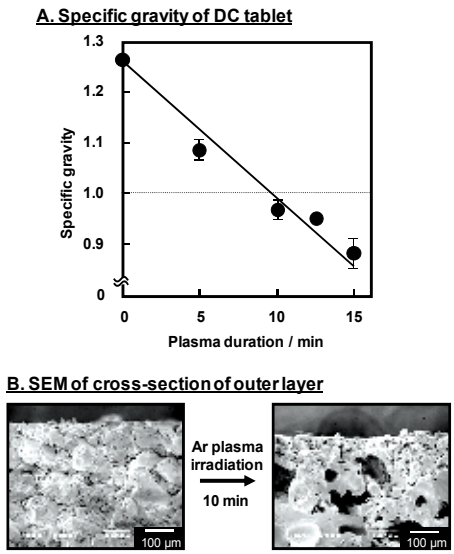

Fig. 16. Effect of plasma irradiation on the specific gravity of DC tablet (A) and SEM pictures of cross-section of DC tablet before and after plasma-irradiation. Outer layer: a mixed powder of Povidone, Eudragit L100-55 and $NaHCO_3$ (68/17/15), Core tablet: 5-fluorouracil

Plasma conditions: 20Hz pulse frequency (on/off cycle = 35ms/15ms), 100 W, Ar 0.5 Torr, 50ml/min.

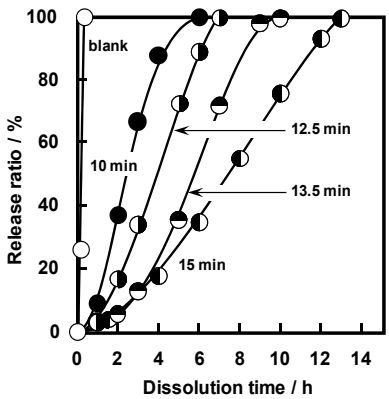

Fig. 17. Effect of pulsed plasma duration on drug release from plasma-irradiated DC tablet. Outer layer: a mixed powder of Povidone, Eudragit L100-55 and $NaHCO_3$ (68/17/15), Core tablet: 5-fluorouracil

Plasma condition : 20Hz pulse frequency (on/off cycle = 35ms/15ms), 100 W, Ar 0.5 Torr, 50ml/min.

3.4 Patient-tailored DDS for large intestine targeting

With most of today's oral DDS devices, it is difficult for all patients to obtain the expected therapeutic effects of drugs administered, because of the individual difference in the environment such as pH value and the transit time in gastrointestinal (GI) tract, which causes the slippage of time-related and positional timing of drug release. From a viewpoint of the real optimization of drug therapy, in order to fulfill the specific requirements on drug release at the appropriate sites in GI tract, the "Patient-Tailored DDS" (Tailor-Made DDS) should be administered based on the diagnosis of each patient's GI environment.

We have fabricated an experimental setup for the simulated GI tract for large intestine targeting, the dissolution test solution being changed in pH value corresponding to stomach (pH 1.2), small intestine (pH 7.4) and large intestine (pH 6.8), and examined the drug release test of plasma-irradiated double compressed tablet in the simulated GI tract.

Figure 18 has shown the preliminary result of theophylline dissolution test in pH 6.8 test solution on the DC tablets using a mixture of Eudragits L100-55/RSPO (7: 3) as outer layer. (Sasai et al., 2004) It is seen that the lag-time has increased with the extension of plasma irradiation time. The lag-time has not been largely affected by treatment in pH 1.2 and pH 7.4 test solutions, which indicated the possibility for the development of the "Patient-Tailored DDS" targeting the large intestine such as colon. We are now elaborating these initial studies aiming at more rapid drug release right after the drug preparations reached the prescribed pH value of the large intestine due to contents of semi-solid nature in large intestine.

3.5 Preparation of functionalized composite powders applicable to matrix-type DDS

The recombination of solid-state radicals is significantly suppressed due to the restriction of their mobilities, unlike radicals in the liquid or gas phase. Interactions between radicals at solid-solid interfaces do not occur under a normal condition.

We have reported the occurrence of mechanically induced surface radical recombination of plasma-irradiated polymers. (Kuzuya et al., 1996a) As shown in Fig. 19, plasma-irradiated

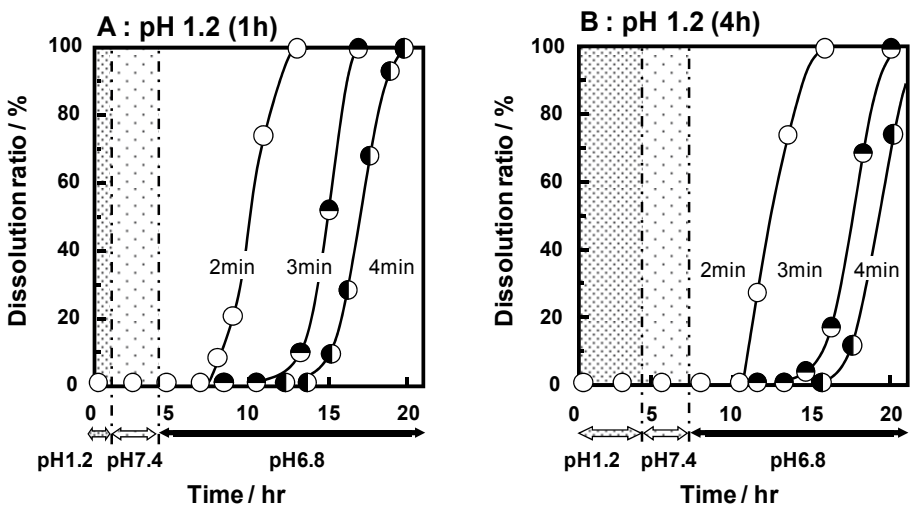

Fig. 18. Release property of theophylline from helium plasma-irradiated DC tablet in the GI tract-simulated dissolution test. (A) for 1h in pH 1.2; (B) for 4h in pH 1.2. Outer layer: a mixed powder of Eudragit L100-55 and Eudragit RS (7/3), Core tablet: theophylline

Plasma conditions: 30W, He 0.5 Torr, 50mL/min.

polyethylene (PE) powder, low-density polyethylene (LDPE) and high-density polyethylene (HDPE), was applied to mechanical vibration in a Teflon twin-shell blender for the prescribed period of time at room temperature under strictly anaerobic conditions, and submitted to ESR measurement.

As shown in Fig. 20, the spectral intensity gradually decreased, with change of the spectral pattern for the case of LDPE, as the duration of mechanical vibration increased. This clearly indicated that plasma-induced surface radicals of PE underwent effectively the solid-state radical recombination in intra- and inter-particle fashion on its mechanical vibration, since the spectral intensity did not appreciably decrease on standing at room temperature, so long as it is kept under anaerobic conditions.

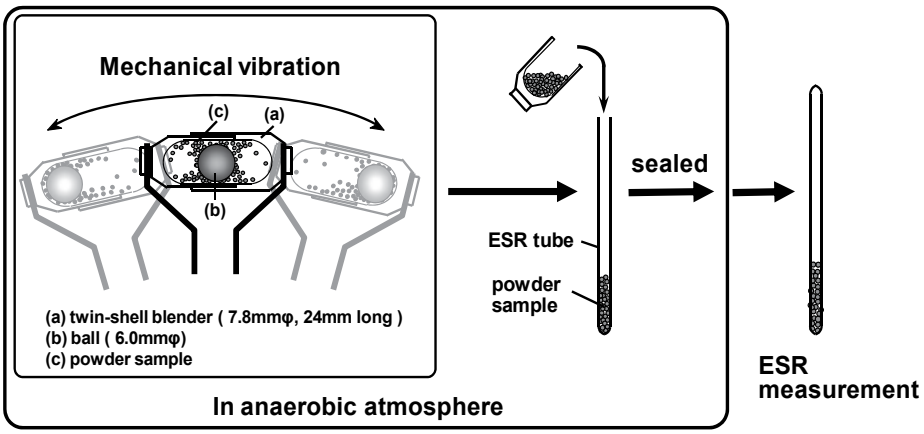

Fig. 19. Schematic representation for mechanical vibration and ESR measurement

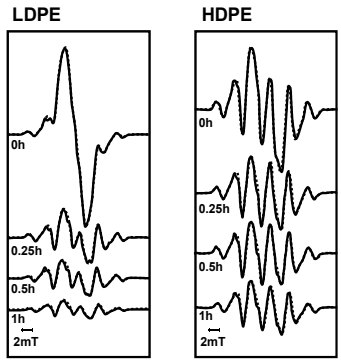

Fig. 20. Progressive changes in observed ESR spectra of 10 min plasma-irradiated LDPE and HDPE powders on mechanical vibration (60 Hz) in Teflon twin-shell blender, together with the simulated spectra shown as dotted lines

Plasma conditions : 40W, Ar 0.5 Torr, 10 min.

For the matrix-type DDS preparation, the mechanical vibration of plasma-irradiated PE powder was carried out in the presence of theophylline powder so as to immobilize the theophylline powder into PE matrix formed by inter-particle linkage of PE powder. Figure 21 shows the conceptual illustration for matrix-type DDS preparation using plasma irradiated polymer powder. Examples of the theophylline release from the resulting composite powders of LDPE and HDPE are shown in Fig. 22. It is seen that the theophylline

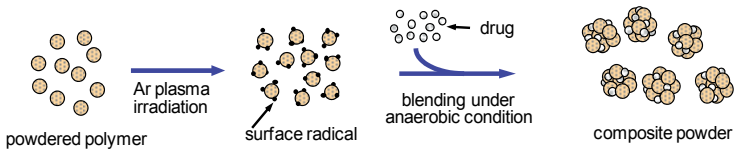

Fig. 21. Conceptual illustration for matrix-DDS for sustained drug release

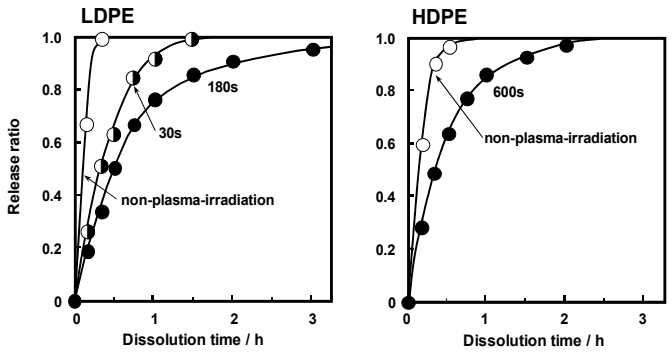

Fig. 22. Theophylline release profiles from the composite powder composed of Theophylline and Ar plasma- irradiated PE, LDPE and HDPE

LDPE plasma-irradiated for 60s: 0.5 x 10^{18} spin/g, for 180 s: 1.0 x10^{18} spin/g.
HDPE plasma-irradiated for 60s: 1.0 x 10^{18} spin/g.
Plasma conditions : 40W, Ar 0.5 Torr, 1 min.

release is apparently suppressed from each of plasma-irradiated PE powders, being proportional to the spin number of the surface radicals, due to trapping theophylline powder into the PE matrix. (Kuzuya et al., 2002b) It should be noted here that the theophylline release is further retarded from the tablet prepared by compressing the above composite PE powders.

4. Biomedical engineering by plasma techniques

Various polymers are extensively used in biomedical applications. However, most of polymers commonly used in industrial field do not always possess surface properties required/desired for biomaterials. Cold plasma irradiation has been widely used for surface treatment of biomaterials.

The wettability of polymer surface is an important characteristics relating to the biocompatibility of biomaterials. Plasma surface treatment is an effective method for hydrophilization of polymer surface. It is known, however, that the wettability introduced by plasma treatment decays with time after treatment. The mechanism has been ascribed to several reasons such as the overturn of hydrophilic groups into the bulk phase for crosslinkable polymers, and detachment of the hydrophilic lower-molecular weight species from the surface for degradable polymers.

We have reported a novel method to introduce a durable surface wettability and minimize its decay with time on several hydrophobic polymers (polyethylene-naphthalate (PEN), low-density polyethylene (LDPE), Nylon-12 and polystyrene (PS)). (Kuzuya et al., 1997b, 2001c, 2003; Sasai et al., 2008) The method involves a sorption of vinylmethylether-maleic anhydride copolymer (VEMA) into the surface layer and its immobilization by plasma-induced cross-link reaction, followed by hydrolysis of maleic anhydride linkage in VEMA to generate durable hydrophilic carboxyl groups on the surface (Fig. 23). The surfaces thus prepared have been further applied to the substrate for covalent immobilization of biomolecules, fabrication of blood-compatible material and cell culture substrate.

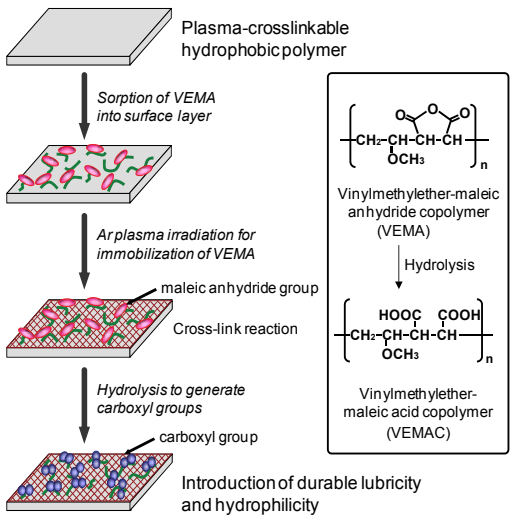

Fig. 23. Conceptual illustration for introduction of durable hydrophilicity onto the polymer surface by plasma techniques

4.1 Preparation of clinical catheter with durable surface lubricity

One of the most important requirements of clinical catheters is the durability of the surface lubricity to diminish the patient pain in use. Figure 24 shows the representative data of measurement of surface slipperiness as a function of the number form repeated rubbing of the treated catheter against silicon rubber. (Kuzuya et al., 1997b)

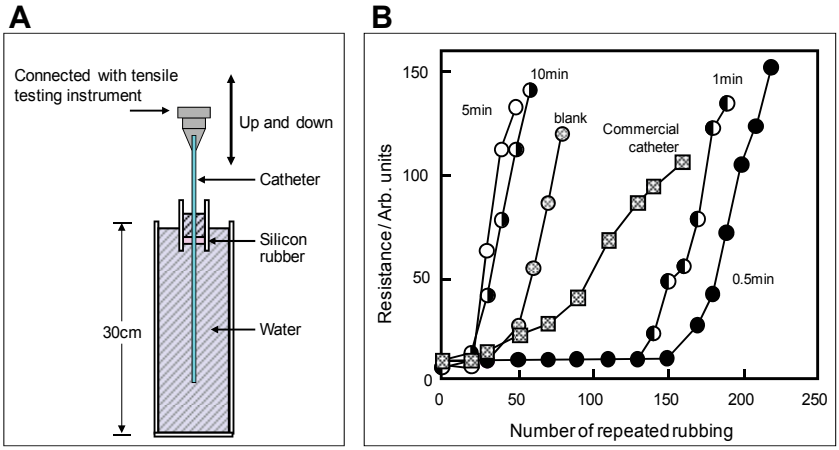

Fig. 24. Experimental setup for measurement of surface lubricity of plasma-irradiated polyurethane-made catheter (A) and durability of the surface lubricity of plasma-assisted VEMAC immobilized catheter in comparison with that of commercial catheter (B)

In can be seen that the resistance of the catheter containing VEMA without Ar plasma-irradiation and of the commercial catheter starts to gradually increase after moving the catheter back and forth around 20-30 number of times in both cases, while that of catheter containing VEMA Ar plasma irradiated for 30 s and 60 s remained low up to around 130-150 number of times. Prolonged plasma irradiation such as for 300 s and 600 s duration, however, did show very poor durability of slipperiness, probably due to the formation of too highly crosslinked surface. Thus, the result shows clearly much higher functionality in terms of durability of surface lubricity.

4.2 Cell culture application of VEMAC-immobilized substrate

In most types of cell, the adhesion to some substrates is a key primary process for the developments such as proliferation, survival, migration and differentiation. Polystyrene (PS) has been commonly used in a substrate for the in vitro cell culture due to excellent durability, low production cost, optical transparency in visible range and non-toxicity. However, PS must be subjected to a surface treatment for biomedical use because it is a very hydrophobic polymer.

In order to improve the cell adhesion properties of PS dish, VEMAC was immobilized on the surface using essentially the same method shown in Fig. 23. (Sasai et al., 2008) In addition, we also used VEMAC-immobilized PS (PS/VEMAC) as a substrate for immobilizing cell-adhesive peptide, Arginine-Glycine-Aspartic acid (RGD), to prepare the more cell-adhesive substrate. RGD containing peptide was immobilized on PS/VEMAC using EDC-NHS chemistry (1-Ethyl-3-(3-dimethylaminopropyl carbodiimide HCl and N-hydroxylsulfosuccinimide) through the surface carboxyl groups of PS/VEMAC. (Sasai et.

al., 2009) Figure 25 shows the microscopic images of mouse embryonic fibroblast, NIH3T3, adhered on each substrate after 2h in culture. As shown in Fig. 25, a distinct difference in cell attachment and spreading of NIH3T3 between on PS/VEMAC and on non-treated PS dish was observed. The PS/VEMAC surface showed much better adhesion and spreading properties, while the adhered cells were not observed on non-treated PS surface. This result indicates that the PS/VEMAC surfaces prepared by the present method have preferential culturing properties of NIH3T3. Furthermore, cell adhesion and proliferation were significantly promoted by immobilizing RGD peptide on PS/VEMAC. The immobilized RGD peptide was specifically recognized by cell surface receptor proteins, integrins, so that the RGD-immobilized surface showed the cell adhesion properties even under the non-serum culture condition. (Sasai et al., 2010) These results indicate that PS/VEMAC is useful for not only a good cell culture substrate but also a substrate for immobilization of bioactive peptide for controlling cell behavior.

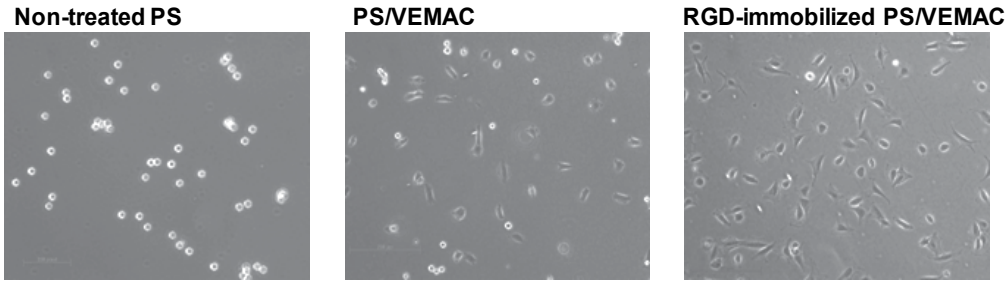

Fig. 25. Phase contrast light microscopic images of NIH3T3 on non-treated PS, PS/VEMAC and RGD peptide-immobilized PS/VEMAC after 2h in culture

The number of seeded cells: 1.0×10^5/dish
Culture medium: Dulbecco's modified Eagle medium supplemented with 10 % calf serum, 100 units/mL penicillin and 100 μg/mL streptomycin

4.3 Plasma-assisted immobilization of biomolecules onto polymer substrate

Considerable interest has focused on the immobilization of several important classes of biomolecules such as DNA, enzyme and protein, onto the water-insoluble supports. The development of DNA chips on which many kinds of *oligo*-DNA are immobilized, for example, has revolutionized the fields of genomics and bio-informatics. However, all the current biochips are disposable and lack of reusability, in part because the devices are not physically robust.

The method shown in Fig. 23 has further been extended to application for the covalent immobilization of single-stranded *oligo*-DNA onto VEMAC-immobilized LDPE (LDPE/VEMAC) sheet by the reaction of 5'-aminolinker *oligo*-DNA with a condensation reagent. (Kondo et al., 2003, 2007) The 5'-aminolinker *oligo*-DNA, which possesses an aminohexyl group as a 5'-terminal group of DNA is considered to be able to react with the carboxyl group on the surface of LDPE/VEMAC sheet. In fact, the resulting DNA-immobilized LDPE/VEMAC sheet was able to detect several complementary *oligo*-DNAs by effective hybridization.

To examine the reusability of DNA-immobilized LDPE/VEMAC sheet, we have repeatedly conducted the hybridization and de-hybridization of fluorescence-labeled complementary

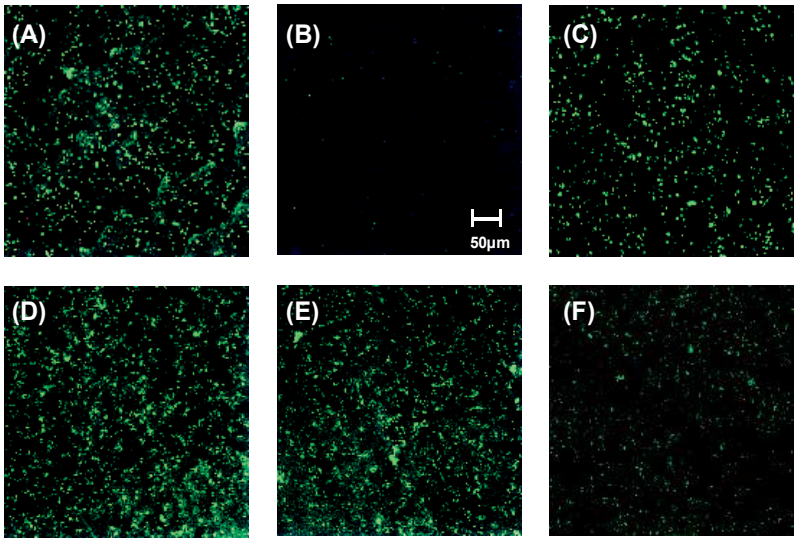

Fig. 26. Scan image of the fluorescence intensity of LDPE-VEMAC-DNA sheet for reusability test . (A); Hybridization of complementary oligo-DNA, (B); After hot water rinse of sheet (A) for 5min. Rehybridization of complementary oligo-DNA on the same sheet (C); 2 times, (D); 5 times, (E); 7 times, (F); 8 times

oligo-DNA on the same DNA-immobilized LDPE/VEMAC sheet, according to the general procedure to remove bounded target DNA from the chip (washing with hot water (90 ^{o}C) for 5min). Figure 26 shows the result of reusability test based on the confocal laser microscope images of DNA-immobilized LDPE/VEMAC sheet. It can be seen that the fluorescence is observed nearly at the same level of intensity even after the several times repetition of the hybridization and dehybridization. The result indicated that the DNA-immobilized LDPE/VEMAC sheet obtained by the present method would be reusable.

Furthermore, we used the LDPE/VEMAC surface for immobilization of enzyme. (Sasai et al., 2006, 2007) When the enzyme was immobilized covalently on solid surface, as is well known, the decrease in the enzyme activity has been commonly observed due to modifications in the tertiary structure of the catalytic sites. In fact, when an enzyme was directly immobilized on LDPE/VEMAC, the enzyme activity was really low. For the successful immobilization of enzymes on polymer substrate with retaining the activity, in this study, we prepared polyglycidylmethacrylate (pGMA) brushes on the LDPE/VEMAC sheet by atom transfer radical polymerization (ATRP) of GMA via carboxyl groups on the sheet. In the ATRP process, the polymerization degree of a monomer can be well-controlled and the resultant polymer has a narrow molecular weight distribution. (Patten et al., 1996) Figure 27 shows the reaction scheme for the functionalization of LDPE/VEMAC surface. The epoxy group of pGMA can react readily and irreversibly with nucleophilic groups like –NH_2 under mild conditions. In fact, we succeeded in the covalent immobilization of fibrinolytic enzyme, urokinase, as a model enzyme through the direct coupling with epoxy groups of GMA on the surface thus prepared. Table 1 shows the relative surface concentration of immobilized urokinase and its activity. As can be seen in Table 1, the relative surface concentration of immobilized urokinase increased with the polymerization time for the fabrication of pGMA brushes. On the other hand, the activity of immobilized urokinase also increased in the pGMA-grafted LDPE sheet prepared by ATRP up to 2 h but

it then leveled off under the present experimental conditions. Therefore, the ratio of active urokinase on pGMA-grafted LDPE sheet decreased with the increase in polymerization time. These results indicate that the LDPE surface with high enzymatic activity can be obtained by controlling the structure of interfaces between the enzyme and the substrate using the present method.

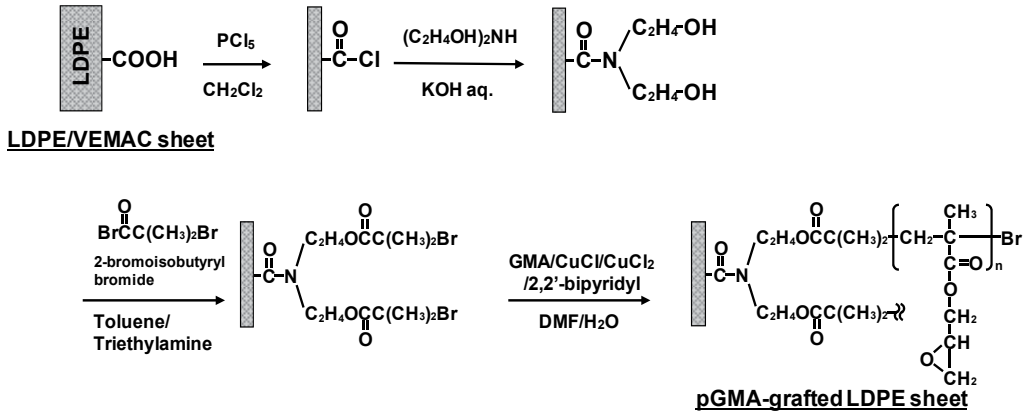

Fig. 27. Reaction scheme for fabrication of pGMA brushes on LDPE sheet by ATRP

pGMA grafted LDPE sheet	Immobilized UK (μg/cm²)(a)	Activity (IU/cm²)(b)	Ratio of active UK (%)
ATRP for 2h	0.44 ± 0.88	35.66 ± 2.77	101.3
ATRP for 4h	2.05 ± 0.88	31.34 ± 1.86	19.1
ATRP for 6h	4.53 ± 0.15	32.96 ± 4.63	9.1

(a) The amount of immobilized urokinase on the pGMA-g-LDPE sheet was determined by Bradford dye binding assay using bovine gamma globulin as the standard. (b) Activity of immobilized urokinase (IU/cm²) was assayed using Glu–Gly–L-Arg–MCA as the substrate.

Table 1. The amount of immobilized urokinase and its activity on LDPE sheet

5. Conclusion

On the basis of findings from a series of studies on the nature of plasma-induced radical formation on variety of organic polymers by ESR with the aid of systematic computer simulations, we were able to open up several pharmaceutical and biomedical applications by plasma techniques.

Plasma-assisted DDS preparations by our method contain several advantages; 1) solvent-free techniques, 2) polymer surface modification without affecting the bulk properties, 3) avoidance of direct plasma-exposure to drugs and 4) versatile control of drug release rates. It is hope that more precise insight into the scope and limitation will be gained in the course of study now in progress to establish the relationship between a drug releasing properties and plasma operational conditions.

For biomedical applications, we developed a novel method to introduce a durable surface wettability and minimize its decay with time on hydrophobic polymer substrate by plasma-assisted immobilization of carboxyl group-containing polymer, vinylmethylether maleic

acid copolymer (VEMAC). The surfaces thus prepared were potentially useful for not only the improvement of surface biocompatibility in biomaterials but also substrate for biomolecule immobilization due to the abundant surface carboxyl group.

6. References

Fridman, G.; Friedman, G.; Gutsol, A.; Shekhter, A. B.: Vasilets, V. N. & Fridman, A., (2008). Applied plasma medicine. *Plasma Processes and Polymers*, 5(6), 503-533

Ishikawa, M.; Matsuno, Y.; Noguchi, A. & Kuzuya, M., (1993). A new drug delivery system (DDS) development using plasma-irradiated pharmaceutical aids. IV. Controlled release of theophylline from plasma-irradiated double-compressed tablet composed of polycarbonate as a single wall material. *Chem. Pharm. Bull.*, 41(9), 1626-1631

Ishikawa, M.; Noguchi, T.; Niwa, J. & Kuzuya, M., (1995). A new drug delivery system using plasma-irradiated pharmaceutical aids. V. Controlled release of theophylline from plasma-irradiated double-compressed tablet composed of a wall material containing polybenzylmethacrylate. *Chem. Pharm. Bull.*, 43(12), 2215-2220

Ishikawa, M.; Hattori, K.; Kondo, S. & Kuzuya, M., (1996). A new drug delivery system using plasma-irradiated pharmaceutical aids. VII. Controlled release of theophylline from plasma-irradiated polymer-coated granules. *Chem. Pharm. Bull.*, 44(6), 1232-1237

Kondo, S.; Sawa, T. & Kuzuya. M., (2003). Plasma-assisted immobilization of bio-molecules on LDPE surface *J. Photopolym. Sci. Technol.*, 16(1), 71-74

Kondo, S.; Nakagawa, T.; Sasai,Y. & Kuzuya, M., (2004). Preparation of floating drug delivery system by pulsed-plasma techniques. *J. Photopolym. Sci. Technol.*, 17(2), 149-152

Kondo, S.; Sasai, Y. & Kuzuya, M., (2007). Development of biomaterial using durable surface wettability fabricated by plasma-assisted immobilization of hydrophilic polymer. *Thin Solid Films*, 515(9), 4136-4140

Kuzuya, M.; Noguchi, A.; Ishikawa, M.; Koide, A.; Sawada, K.; Ito, A. & Noda, N., (1991a). Electron spin resonance study of free-radical formation and its decay of Plasma-irradiated poly(methacrylic acid) and its esters. *J. Phys. Chem.*, 95 (6), 2398-2403

Kuzuya, M.; Ito, H.; Kondo, S.; Noda, N. & Noguchi, A., (1991b). Electron spin resonance study of the special features of plasma-induced radicals and their corresponding peroxy radicals in polytetrafluoroethylene. *Macromolecules*, 24(25), 6612-6617

Kuzuya, M.; Noguchi, A.; Ito, H.; Kondo, S. & Noda, N., (1991c). Electron-spin resonance studies of plasma-induced polystyrene radicals. *J. Polym. Sci., Part A: Polym. Chem.*, 29(1), 1-7

Kuzuya, M.; Noguchi, A.; Ito, H. & Ishikawa, M., (1991d). A new development of DDS (drug delivery system) using plasma-irradiated pharmaceutical aids. *Drug Delivery Syst.*, 6(2), 119-125

Kuzuya, M.; Ito, H.; Noda, N.; Yamakawa, I. & Watanabe, S., (1991e). Control released of theophylline from plasma irradiated double-compressed tablet composed of poly(lactic acid) as a wall material. *Drug Delivery Syst.*, 6(6), 437-441

Kuzuya, M.; Noda, N.; Kondo, S.; Washino, K. & Noguchi, A., (1992a). Plasma-induced free radicals of polycrystalline myo-inositol studied by electron spin resonance. Orbital rehybridization-induced effect of hydroxylalkyl radicals on their reactivities in crystalline state. *J. Am. Chem. Soc.*, 114(16) 6505-6512

Kuzuya, M.; Ishikawa, M.; Noguchi, A.; Sawada, K. & Kondo, S., (1992b). Nature of plasma-induced radicals on crosslinked methacrylic polymers studied by electron spin resonance. *J. Polym. Sci., Part A: Polym. Chem.* 30(3), 379-387

Kuzuya, M.; Kondo, S.; Ito, H. & Noguchi, A., (1992c). ESR study on the nature of oxygen plasma-induced surface radicals of Teflon and corresponding peroxy radical reactivity. *Appl. Surf. Sci.*, 60-61, 416-420

Kuzuya, M.; Kamiya, K.; Yanagihara, Y. & Matsuno, Y., (1993a). Nature of plasma-induced free-radical formation of several fibrous polypeptides. *Plasma Sources Sci. Technol.*, 2(1), 51-57

Kuzuya, M.; Niwa, J. & Ito, H., (1993b). Nature of plasma-induced surface radicals of powdered polyethylene studied by electron spin resonance. *Macromolecules*, 26(8), 1990-1995

Kuzuya, M.; Morisaki, K.; Niwa, J.; Yamauchi, Y. & Xu, K.,(1994). Spectrochemistry of Polycarbohydrate Free Radicals Generated by Argon Plasmolysis: Effect of Tertiary Structure on Free Radical Formation. *J. Phys. Chem.*, 98(44), 11301-11307

Kuzuya, M.; Yamauchi, Y.; Niwa, J.; Kondo, S. & Sakai, Y., (1995). Spectrochemistry of plasma-induced free radicals in cellulose derivatives. *Chem. Pharm. Bull.*, 43(12), 2037-2041

Kuzuya, M.; Niwa, J. & Kondo, S., (1996a). A novel collision-induced solid state radical recombination. *Mol. Cryst. Liq. Cryst. Sci. Technol., Sect. A*, 277, 703-709

Kuzuya, M.; Ishikawa, M.; Noguchi, T.; Niwa, J. & Kondo, S., (1996b). A new drug delivery system using plasma-irradiated pharmaceutical aids. VI. Controlled release of theophylline from plasma-irradiated double-compressed tablet composed of water-soluble polymers as a wall material. *Chem. Pharm. Bull.*, 44(1), 192-195

Kuzuya, M.; Matsuno, Y.; Yamashiro, T. & Tsuiki, M., (1997a). Electron spin resonance study on plasma-induced surface radicals of poly(ethylene naphthalate). *Plasmas Polym.*, 2(2), 79-89

Kuzuya, M.; Yamashiro, T.; Kondo, S. & Tsuiki M., (1997b). A novel method to introduce durable hydrophilicity onto hydrophobic polymer surface by plasma treatment. *Plasmas Polym.*, 2(2), 133-142

Kuzuya, M.; Yamashiro, T.; Kondo, S.; Sugito, M. & Mouri, M., (1998a). Plasma-induced surface radicals of low-density polyethylene studied by electron spin resonance *Macromolecules*, 31(10), 3225-3229

Kuzuya, M.; Kondo, S.; Sugito, M. & Yamashiro, T., (1998b). Peroxy radical formation from plasma-induced surface radicals of polyethylene as studied by electron spin resonance. *Macromolecules*, 31(10), 3230-3234

Kuzuya, M.; Sasai, Y. & Kondo, S., (1999a). Specificities in structures of surface radicals on substituted celluloses produced by plasma-irradiation. *J. Photopolym. Sci. Technol.*, 12(1), 75-78

Kuzuya, M.; Yamauchi, Y. & Kondo, S., (1999b). Mechanolysis of glucose-based polysaccharides as Studied by electron spin resonance. *J. Phys. Chem. B*, 103(38), 8051-8059

Kuzuya, M.; Kondo, S. & Sasai, Y., (2001a). Plasma techniques for preparation of controlled drug release system. *Plasmas & Polymers*, 6(3), 145-162

Kuzuya, M.; Ito, K.; Kondo, S. & Makita, Y., (2001b). A new drug delivery system using plasma-irradiated pharmaceutical aids. VIII. Delayed-release of theophylline from double-compressed tablet composed of Eudragit as wall material. *Chem. Pharm. Bull.*, 49(12), 1586-1592

Kuzuya, M.; Sawa, T.; Yamashiro,T.; Kondo, S. & Takai, O., (2001c). Introduction of durable hydrophilicity on nylon-12 by plasma treatment. *J. Photopolym. Sci. Technol.*, 14(1), 87-90

Kuzuya, M.; Nakagawa, T.; Kondo. S.; Sasai,Y. & Makita, Y., (2002a). Preparation of floating drug delivery system by plasma techniques. *J. Photopolym. Sci. Technol.,* 15(2), 331-334

Kuzuya, M.; Sasai, Y.; Mouri, M. & Kondo, S., (2002b). Mechanically-amplified plasma processing for drug engineering. *Thin Solid Films*, 407(1-2), 144-150

Kuzuya, M.; Sawa, T.; Mouri, M.; Kondo, S. & Takai, O., (2003). Plasma technique for the fabrication of a durable functional surface on organic polymers. *Surf. Coat. Technol.*, 169-170, 587-591

Kuzuya, M.; Kondo, S. & Sasai, Y., (2005). Recent advances in plasma techniques for biomedical and drug engineering. *Pure and Applied Chemistry*, 77(4), 667-682

Kuzuya, M.; Sasai, Y.; Kondo, S. & Yamauchi, Y., (2009). Novel application of plasma treatment for pharmaceutical and biomedical engineering. *Curr. Drug. Discov. Tech.*, 6(2), 135-150

Nakagawa, T.; Kondo, S.; Sasai,Y. & Kuzuya, M., (2006). Preparation of floating drug delivery system by plasma technique. *Chem. Pharm. Bull.*, 54(4), 514-518

Patten, T. E.; Xia, J.; Abernathy, T. & Matyjaszewski, K., (1996). Polymers with very low polydispersities from atom transfer radical polymerization. *Science*, 272(5263), 866-868

Sasai, Y.; Sakai, Y.; Nakagawa, T.; Kondo, S. & Kuzuya, M. (2004). Development of patient-tailored drug delivery system by plasma techniques *J. Photopolym. Sci. Technol.,* 17(2), 185-188

Sasai, Y.; Kondo, S.; Yamauchi, Y. & Kuzuya, M., (2006). Immobilization of antithrombotic biomolecules on LDPE surface functionalized by plasma techniques. *J. Photopolym. Sci. Technol.,* 19(2), 265-268

Sasai, Y.; Oikawa, M.; Kondo, S. & Kuzuya, M., (2007). Surface engineering of polymer sheet by plasma techniques and atom transfer radical polymerization for covalent immobilization of biomolecules. *J. Photopolym. Sci. Technol.,* 20(2), 197-200

Sasai,Y.; Matsuzaki, N.; Kondo, S. & Kuzuya, M., (2008). Introduction of carboxyl group onto polystyrene surface using plasma techniques. *Surf. Coat. Technol.*, 202(22-23), 5724-5727

Sasai, Y.; Kondo, S.; Yamauchi, Y. & Kuzuya. M., (2009), Immobilization of bioactive molecule onto polymer surface functionalized by plasma techniques and its application to cell culture. *J. Photopolym. Sci. Technol.,* 22(4), 503-506

Sasai, Y.; Kondo, S.; Yamauchi, Y. & Kuzuya. M., (2010), Plasma surface modification of polymer substrate for cell adhesion control. *J. Photopolym. Sci. Technol.,* 23(4), 595-598

Singh, B. N. & Kim, K. H., (2000). Floating drug delivery systems: an approach to oral controlled drug delivery via gastric retention, *J. Controlled Release*, 63(3), 235-259

Streubel, A.; Siepmann, J. & Bodmeier, R., (2006), Drug delivery to the upper small intestine window using gastroretentive technologies. *Curr. Opin. Pharmacol.*, 6(5), 501-508

Susut, C. & Timmons, R. B., (2005). Plasma enhanced chemical vopor deositions to encapsulate crystals in thin polymeric films: a new approach to controlling drug release rates. *Int. J. Pharm.*, 288, 253-261

Yamakawa, I.; Watanabe, S.; Matsuno, Y. & Kuzuya, M., (1993). Controlled release of insulin from plasma-irradiated sandwich device using poly(DL-lactic acid). *Biol. Pharm. Bull.*, 16(2), 182-187

6

Basics and Biomedical Applications of Dielectric Barrier Discharge (DBD)

Nikita Bibinov[1], Priyadarshini Rajasekaran[1], Philipp Mertmann[1]
Dirk Wandke[2], Wolfgang Viöl[3,4] and Peter Awakowicz[1]
[1]*Institute for Electrical Engineering and Plasma Technology, Ruhr-Universität Bochum*
[2]*Cinogy GmbH, Duderstadt*
[3]*University of Applied Sciences and Arts, Göttingen*
[4]*Laser Laboratory Göttingen*
Germany

1. Introduction

Plasmas are partially ionized gases and are described as the "fourth state" of matter. Irving Langmuir coined the word 'plasma', in 1928, for the ionized gas in which electrons, ions, and excited particles are suspended similar to the cells suspended in the blood plasma. Naturally-existing plasma includes the sun and the stars, lightening, polar lights, etc. Artificially-produced plasmas are fluorescent lamps, neon signs, plasma displays and monitors, etc. Much more applications of plasma have been made possible in the recent decades.

There are several methods for plasma generation. One among them is by applying sufficient electric field in different gas mixtures confined in a low-pressure chamber. Such low-pressure plasmas are suitable for tailoring the surface properties of different materials, for film deposition, for sterilization of non-living matter, etc. However, treatment of pressure-sensitive objects and materials is not possible using a low-pressure system. Treatment of living tissues, as in the case of medical treatment, is possible only with plasma devices which operate at atmospheric pressure.

Because of high pressure, discharge ignition at atmospheric conditions requires high voltage and can arouse high current density. The gas temperature in active plasma volume increases up to several thousand degrees. By such treatment, the living object is over heated (hyperthermia) and partially evaporated. Such plasma sources are used in surgery as plasma scalpel and blood coagulator (Stoffels, 2007).

For gentle treatment of living object at atmospheric pressure conditions, limitation of current flowing through the treated object is necessary. This can be achieved by placing the object slightly away from the active plasma volume as in the case of "indirect" plasma treatment. The other ways are short voltage pulsing (Ayan, 2008 & Walsh, 2008) and using a dielectric barrier (otherwise called 'insulator') that drastically reduces electric current through the treated object. Devices using the latter are so-called "dielectric barrier discharges (DBD)" which are useful for "direct" treatment of living object which comes in immediate contact with the plasma.

DBDs comprise of a pair of electrodes, separated by a small gap filled with a gas. When the electrodes are energized by a high voltage – high enough that the gas starts conducting, the 'breakdown' condition has been achieved. After breakdown, the gas permits current flow across the electrodes and completes the electric circuit. Usually DBD operates by AC voltage with amplitude of about 10-20 kV and frequency of 10-100 kHz. The averaged current amounts from few up to several tens of milliamps. DBDs have broad field of applications like in ozonators, air and water purification, etc. (Kogelschatz, 2003). The gas is ionized resulting in the formation of free electrons and positive ions. Free electrons are accelerated by the electric field in the gas gap and ionise neutral gas molecules by impact resulting in an electron avalanche. Neutral atoms can also be excited by electron impact. Part of these excited gas atoms and molecules relax to their ground levels through the emission of photons at a certain wavelength. This attributes to plasmas of different colours. The chemically-active radicals and long living (so-called "metastable") excited atomic and molecular species can also be produced during relaxation. This makes plasma chemically active by interaction with surrounding gas and solid body surfaces.

DBD can operate in both filamentary and homogeneous modes depending on the plasma conditions. The former consists of thin plasma channels stochastically distributed (i.e. spatially and temporally) in the gap between the working electrodes. The latter, so-called atmospheric pressure glow discharge (APGD), fills the entire gap with practically homogeneous (or uniform) plasma during short discharge pulse. DBD is a "cold" plasma where electron temperature (T_e) is about 23000 K (kT_e ~ 2 eV, where "k" is Boltzmann constant) which is higher than the gas temperature (400-500 K) in the short-living plasma channel as well as the surrounding gas temperature (about 300 K).

For gentle treatment of living tissues, both "indirect" and "direct" plasma treatments can be applied. In the former case, the living object is treated "indirectly" by flux of chemically-active atoms and radicals - which are produced in active plasma volume of the plasma source, and are transported to the treated object as an effluent by the gas flow. During transport to the treated object, the chemical composition of the effluent is changed because of chemical reactions of atoms and radicals among themselves as well as with the surrounding gas. Quantity of short-living radicals reaching the treated surface is low in indirect plasma treatment. By "direct" plasma treatment, the living object itself serves as one of the electrode as for the DBD, and the active species are produced directly near the treated surface and the short-living radicals can reach the object instantly. During "direct" plasma treatment the living object is heated, is bombarded by neutral and ionized species, and conducts electric current. The role played by the object itself during treatment is more complicated and less is known but obviously offers a big potential for applications like healing of different skin diseases. This has raised interest among different working groups to develop plasma devices that can be used for medical treatment of human body.

The first and foremost will be the study of response and influence of living objects on plasma treatment, and then the optimisation of the treatment process which requires the determination of fluxes of photons, electrons, atomic and molecular species on the treated surface. For this purpose, we apply a combination of experimental and theoretical methods for plasma characterisation which are otherwise not ideal individually and hence, when used together give reliable and valid information useful for optimization of plasma treatment.

The object of our study is to optimize a DBD for "direct" treatment of surface of human body facilitating therapeutic use of the DBD in dermatology and other medical applications (Fridman, 2008).

2. Dielectric Barrier Discharge (DBD)

Generally, DBDs comprise of two parallel or concentric electrodes connected to a high voltage power supply. The gap between electrodes amounts usually about 1-2 mm. Pulsed or AC high voltage with frequency from 50 Hz up to several 100 kHz can be applied. DBDs can be operated with different gases namely, nitrogen, oxygen, rare gases, etc. To limit the electric current between the electrodes and to avoid the formation of current arcs, atleast one of the electrodes is covered with a dielectric material namely quartz, ceramic, etc.
DBDs for medical use comprise of only one electrode which is covered with a dielectric. When supplied with a high voltage, these devices are able to generate plasma at close vicinity to the human body. In this case, the human body itself acts as the counter electrode and the plasma is generated in air in the gap between the dielectric-covered electrode and the body. This means that the applied voltage should be selected in such a way to generate plasma in air at atmospheric-pressure and more importantly, in the small gap between the working electrode and the body.

2.1 DBD in air

DBD operated in air is characterized, usually, by the formation of filament-like structures called "microdischarges". Microdischarges occur stochastically-distributed in the gap between the electrodes. These microdischarges are several tens of microns in diameter and last for several tens of nanoseconds. The electron density in microdischarges is very high and, therefore, excitation and dissociation of nitrogen and oxygen molecules during electron impact take place abundantly.
Plasma-aided chemical reactions in air contribute to complex air-plasma chemistry. Nitrogen and oxygen molecules in air are effectively excited and dissociated by the energetic electrons, resulting in the synthesis of nitric oxide (NO), ozone (O_3) and several other reactive species. Photons are emitted, in the ultra-violet (UV) range, during the relaxation of excited N_2 and NO molecules in the plasma. These chemically-active species and radiation are useful for several biomedical applications. NO, ozone and UV radiation are useful for promoting healing of chronic wounds and skin ulcers (Fridman, 2008). The anti-microbial effect of ozone and UV is used in purification of potable water (Kogelschatz, 2003 & Legrini, 1993). The same effect can also be exploited for disinfection/sterilization of skin surface through plasma treatment. Hence, air-plasma treatment can be used to disinfect wounds as well as the surrounding tissues (Boudam, 2006).

2.2 Optimization of plasma treatment of human body

Optimizing the DBD device for bio-medical application requires progressive investigation through plasma characterizations and appropriate biological studies. Plasma characterization allows for understanding the plasma parameters (namely electron distribution function and electron density) and gas temperature while biological tests are helpful to ascertain the 'safe doses' of chemically-active particles and photons. In addition, equipments which will be subjected to use on human body requires clinical trials involving people. Prior to such clinical trials, the device has to well- investigated to gain insight of the characteristics of the plasma produced by the device. Prior to using the device on human body and characterizing the plasma, small animals and simple electrodes of different materials like metals (Kuchenbecker, 2009), glass and liquid medium (Rajasekaran, 2010) are subjected to plasma treatment to gain insight into the respective plasma conditions and

thereby deduce the response of the treated object which can be helpful for optimization of the plasma device for medical applications.

3. Plasma characterization

To optimize the treatment conditions, the fluxes of chemically-active species to the surface of the treated object must be studied for which the chemical kinetics in plasma volume must be simulated. Information and values of gas temperature, electron distribution function and electron density are necessary for simulation. Concentration of gas molecules (or atoms, otherwise) and rate constants of chemical reactions are dependent on the gas temperature. The chemically-active species are produced by electron impact and therefore electron distribution function and electron density are necessary for determination of electron-impact excitation and dissociation rate of molecules.

We refer the term 'plasma characterization' to the method of determination of gas temperature (T_g) and plasma parameters namely, electron density (n_e) and electron velocity distribution function (EVDF).

3.1 Gas temperature (T_g)

Gas temperature in microdischarges of DBD differs strongly from that of surrounding gas and chemical reactions occur at different gas temperature. Therefore, for reliable simulation of chemical kinetics, the gas temperature in active plasma volume and in afterglow phase*, must be determined.

With reference to the filamentary and homogeneous modes of the DBD, when discharge is ignited in air gap between electrodes for short time (several ns), the gas temperature can reach values of 400-500 K in the filamentary discharge mode (Rajasekaran, 2009) and close to 300 K in the homogenous discharge mode (Rajasekaran, 2010). In the afterglow phase, gas temperature in the filament and in the surrounding volume decreases rapidly because of thermo-conductivity.

3.2 Electron density (n_e)

Electron density in DBD in air differs strongly in both discharge modes. In homogeneous DBD, electron density amounts to about 10^{17} m^{-3} (Rajasekaran, 2010). But in the microdischarge of the filamentary mode, electron density reaches 10^{20} – 10^{21} m^{-3} (Rajasekaran, 2009). Plasma is quasi-neutral and density of positive ions is approximately equal to the electron density. During collisions of neutral species with ions-accelerated in electric field, gas in the filament is heated up to 500 K and sometimes even more (Kuchenbecker, 2009). Electric field in the DBD channel in air is sufficient for supporting the discharge for only several nanoseconds. After that, because of charge of dielectric surface, electric field in the air gap decreases and discharge is interrupted.

3.3 Electron Velocity Distribution Function (EVDF)

Electrons are produced in the air gap during secondary emission (bombardment of cathode by positive ions) and during gas ionisation in the plasma volume by electron impact. The electrons are accelerated by the electric field in discharge gap and lose kinetic energy during

* Afterglow phase refers to the state after the microdischarge has extinguished.

inelastic collisions with atoms and molecules. To describe conditions and properties of electron gas, the electron distribution function (f) is employed. The electron distribution function can be simulated by solving Boltzmann equation (1):

$$\frac{\partial f}{\partial t} + \nabla_r f - \nabla_v \left(\frac{e}{m_e}\vec{E} f\right) = S_{coll}, \quad (1)$$

where, e - elementary charge;
m_e - electron mass;
∇ - *nabla*-differential operator denotes gradient in phase space;
$\vec{E}$ - electric field; and
S_{coll} - collision term which comprises of all kinds of binary electron-heavy particle collisions.

The Boltzmann equation is a continuity equation for distribution function in the phase space. It describes the temporal evolution of f in the co-ordinate space (second term in equation (1)) and in velocity space (third term in equation (1)). The flux in coordinate space is caused by density gradients. A flux in velocity space results from the action of electrostatic force.

The electron distribution functions in plasma can be presented in two different ways: Electron Energy Distribution Function (EEDF or $f_E(E)$) and Electron Velocity Distribution Function (EVDF or $f_v(E)$) (Bibinov, 2005). Both have different units and are differently normalised. In plasma characterisation, we determine EVDF (in $eV^{-3/2}$) applying Optical Emission Spectroscopy (OES).

4. Diagnostics methods

For plasma characterization at low pressure conditions, a Langmuir probe can be applied. Using voltage-current characteristics of the electric probe, plasma potential, electron distribution function and electron density can be determined (Lieberman, 1994). For various reasons, electron distribution function can be determined usually in electron kinetic energy region up to about 10 eV (Godyak, 1992 & Bibinov, 2008). For calculation of dissociation and excitation rates under electron impact, distribution function in broader kinetic energy region is essential. Furthermore, electric probe cannot be applied for characterisation of atmospheric pressure DBD in air because of very small plasma volume and short plasma pulse duration.

Optical emission spectroscopy (OES) is the second method, which can give information concerning EVDF in plasma. In OES, the emission due to relaxation of excited molecules and ions in the plasma is measured using a spectrometer which is then used to determine EVDF by fitting procedure. Electronic excited states of atoms and molecules are excited during impact of electrons with kinetic energy higher than 10 eV. Therefore, OES diagnostics can be used for determination of EVDF in electron kinetic energy range higher than 10 eV. Combination of probe and OES diagnostics provides EVDF in broad electron kinetic energy range and can be used for characterisation of low pressure plasmas also (Bibinov, 1998 & Bibinov, 2008).

4.1 OES diagnostics of DBD in air

Photoemission of atoms and molecules can be used for the purpose of OES diagnostics of DBD in air. For this, intensities of molecular emissions bands and atomic lines must be

measured in absolute units and mechanism of their excitation must be explicitly known. Emission spectrum (see fig. 1) of discharge in air consists mainly the emission bands of nitrogen and nitric oxide.

The two nitrogen molecular bands ("second positive" system N_2(C-B) and "first negative" system N_2^+(B-X)) which are excited by electron impact of the ground state of nitrogen molecule are observed in the emission spectrum of air plasmas at atmospheric pressure and can be used for plasma characterisation. The NO(A-X) bands detected in the UV-C region (λ < 280 nm) are excited from the ground state of nitric oxide, density of which is not known *a priori* and cannot be used for plasma characterisation.

The gas temperature in the active plasma volume is determined by comparison of measured and simulated spectra of nitrogen molecule N_2(C-B,0-0). Because of high efficiency of rotational relaxation at atmospheric pressure conditions, the temperature of rotational and translational degrees of freedom of excited neutral nitrogen molecules are equal. We simulate N_2(C-B,0-0) molecular band with variated rotational temperature and compare these spectra with measured ones (fig.2). The rotational temperature (that is equal to the gas temperature) in active plasma volume are determined in fitting procedure.

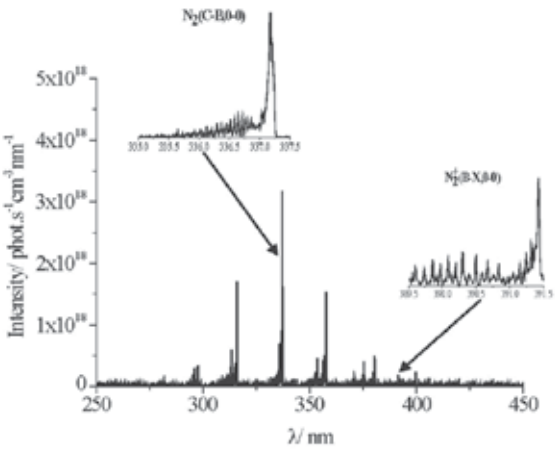

Fig. 1. Emission spectrum of DBD in air with Al-spike as opposite electrode. Inter-electrode distance amounts to 1.5 mm.

To determine real absolute intensity of photoemission in DBD, the measured emission spectrum (in counts·s^{-1} per pixel of spectrometer's CCD) is corrected to the efficiency ε (in counts·nm·photons^{-1} per pixel) of the spectrometer (Bibinov, 2007). Geometrical factor of optical diagnostics and discharge duration must also be taken into account. To determine geometrical factor for OES, two factors have to be considered namely, a) plasma volume observed by the spectrometer, and b) the fraction of photons emitted by molecules in plasma volume which reach the entrance hole of the optical fibre of the spectrometer.

To determine plasma volume which is observed by the spectrometer, acceptance angle of the optic fibre is measured. This solid angle has a cosine profile. Also, the photons emitted by excited molecules placed within this solid angle can be accepted by the optical fibre and measured by the spectrometer. For this reason, we refer to the solid angle as acceptance angle. To increase the spatial resolution of OES diagnostics, the acceptance angle of optical

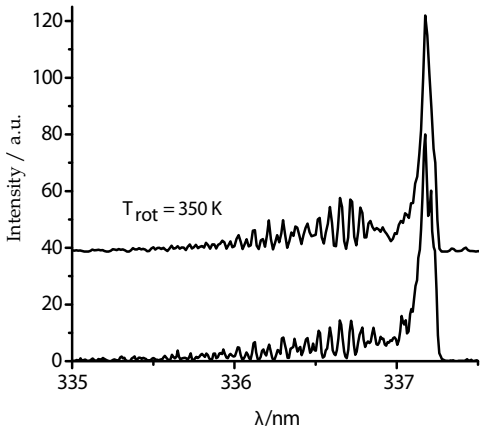

Fig. 2. Measured (bottom) and simulated (top) spectra of nitrogen emission N_2(C-B,0-0) at 1.5 mm inter-electrode distance for Al-spike. The simulated spectrum is shifted for clarity.

fibre is reduced by fitting it with a diaphragm. For OES diagnostics of DBD, an optical diaphragm with acceptance angle of ± 3° is fitted to the optical fibre. The fraction of photons emitted in acceptance angle and reaching the entrance hole of the optical fibre is calculated as the ratio between the area of entrance hole and the area of the sphere - with radius equal to the distance between the emitted molecule and entrance hole.

Generally, only Maxwell distribution function for electrons can be determined applying OES with two nitrogen bands. Maxwell distribution function is solution of Boltzmann equation (1) in assumption of ideal gas conditions, namely without taking inelastic collisions of electrons with molecules into consideration. At atmospheric-pressure conditions in DBD, inelastic collisions of electrons with nitrogen and oxygen molecules are very frequent and therefore electron distribution function differs strongly from Maxwell distribution. To solve this problem, we determine EVDF in air-DBD applying a combination of two diagnostic methods namely, numerical simulation and OES. The Boltzmann equation (1) is solved numerically in nitrogen/oxygen mixture (0.78/0.21) at atmospheric pressure, applying a program developed by the group of Prof. A P Napartovich (Stefanovich, 2001). EVDF is simulated using this program in "local" approximation by variable electric field because this parameter is not known in DBD *a priori*. "Local approximation" means that at every position EVDF can be determined from Boltzmann equation for homogeneous non-bounded plasma using local electric field strength. Therefore, EVDF in DBD is simulated applying equation (2) by neglecting the inhomogeneity term in equation (1):

$$\frac{\partial f}{\partial t} - \nabla_v \left(\frac{e}{m_e}\vec{E} f\right) = S_{coll} \tag{2}$$

Electric field strength in DBD is not known forehand. Hence, we simulate EVDF for different values of reduced electric field. Using simulated EVDF, we calculate intensities of nitrogen molecular emissions and compare them with measured ones to determine the EVDF and also the electric field strength in active plasma volume.

Intensity of molecular nitrogen emission $I_{N_2^*}$ (in photons·s^{-1}) is the integral of spectral density I_λ (in photons·nm^{-1}·s^{-1}) of measured emission spectrum and is expressed as equation (3):

$$I_{N_2^*} = \int_{\lambda} I_{\lambda} d\lambda = \int_{\lambda} \frac{I_p d\lambda}{\varepsilon(\lambda) \cdot G \cdot V \cdot F \cdot \tau} = Q_{N_2^*} \cdot [N_2] \cdot n_e \cdot k_{exc}^{N_2^*}, \quad (3)$$

where, I_p - measured emission spectrum (counts per pixel);
$\varepsilon(\lambda)$ - efficiency of spectrometer (counts·nm/photons per pixel);
G - geometrical factor
V - plasma volume observed by spectrometer (m^{-3});
F - frequency of discharge pulses (Hz); and
τ - averaged duration of discharge pulses (s).

$k_{exc}^{N_2^*} = 4\pi \cdot \sqrt{2} \int_E f_v(E) \cdot \sqrt{\frac{2 \cdot e}{m_e}} \cdot E \cdot \sigma_{exc}^{N_2^*}(E) dE$ - rate constant of excitation of nitrogen photoemission ($m^3 \cdot s^{-1}$) by electron impact.

$\sigma_{exc}^{N_2^*}(E)$ - cross section (m^2) of electron impact excitation of nitrogen photoemission (Itikawa, 2006) and

E - kinetic energy of electrons (eV).

The term $Q_{N_2^*} = \frac{A_{N_2^*}}{A_{N_2^*} + k_{N_2^*}^{N_2}[N_2] + k_{N_2^*}^{O_2}[O_2]}$ in equation (3) is the quenching factor for nitrogen emission where, $A_{N_2^*}$ - Einstein coefficient for spontaneous emission (Pancheshnyi, 2000, Kozlov, 2001);

$k_{N_2^*}^{N_2}$, $k_{N_2^*}^{O_2}$ - rate constants of quenching ($m^3 \cdot s^{-1}$) of nitrogen excited states by collisions with nitrogen and oxygen molecules, respectively (Pancheshnyi, 2000, Kozlov, 2001); and

$[N_2]$, $[O_2]$ - nitrogen and oxygen concentration (m^{-3});

Electron velocity distribution function $f_v(E)$ is normalized to fulfil equation (4):

$$4\pi \cdot \sqrt{2} \int_E f_v(E) \cdot \sqrt{E} dE = 1 \quad (4)$$

To determine discharge duration, the current through the object is measured using a current monitor. The measured current consists of the displacement current and the short discharge current pulses. Discharge duration (τ in seconds) is the full width at half maximum (FWHM) of measured discharge current pulse. To obtain the dimensions of the microdischarges, which are important for the determination of active plasma volume, microphotography using a high-speed camera with spatial resolution of 5 μm is applied.

Ratio of intensities of neutral nitrogen molecular emission N_2(C-B) to molecular ion emission N_2^+(B-X), as shown in expression (5), is used for the purpose of electric field determination.

$$\frac{I_{N_2(C-B)}}{I_{N_2^+(B-X)}} = \frac{Q_{N_2(C-B)}}{Q_{N_2^+(B-X)}} \cdot \frac{k_{exc}^{N_2(C-B)}}{k_{exc}^{N_2^+(B-X)}} \quad (5)$$

Because of difference in threshold values of electron's kinetic energy required for electron impact excitation of nitrogen emissions, and due to dependence of excitation cross section

on kinetic energy, the ratio (5) is very sensitive to variation of electric field in plasma. We solve the Boltzmann equation (2) for nitrogen/oxygen mixture at atmospheric conditions at variable electric field and determine the electron velocity distribution function for each electric field value (see fig.3). Applying these calculated electron distribution functions, we calculate excitation rate constants for nitrogen photo emissions and subsequently calculate the values of ratio (5). Calculated ratio is compared with ratio of same emissions measured using OES diagnostics. EVDF and averaged reduced electric field in observed plasma volume is determined from the best fit.

The averaged electron density is determined using measured absolute intensity of neutral nitrogen photoemission $I_{N_2(C-B)}$ in equation (6):

$$n_e = \frac{I_{N_2(C-B)}}{[N_2] \cdot Q_{N_2(C-B)} \cdot G \cdot V \cdot F \cdot \tau \cdot k_{exc}^{N_2(C-B)}} \tag{6}$$

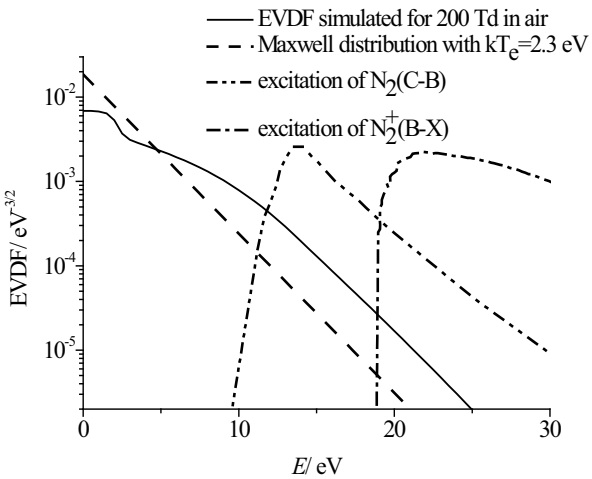

Fig. 3. Electron velocity distribution functions with the same ratio of nitrogen emissions in expression (5) simulated using numerical solution of Boltzmann equation in local approximation using equation (2) with E/N = 200 Td and Maxwell distribution function with electron temperature kT_e = 2.3 eV. Normalized integrands $f_v(E) \cdot E \cdot \sigma_{exc}^{N_2^*}(E)$ used for calculation of N_2(C-B) and N_2^+(B-X) photoemissions intensities.

5. Simulation of chemical kinetics

During discharge, chemically-active species like nitrogen and oxygen atoms and their metastables are produced by electron-impact dissociation and excitation of neutral gas molecules. Nitric oxide and ozone are produced in subsequent chemical reactions (Rajasekaran, 2009) in the discharge as well as in the afterglow phase. Chemical kinetic model of atmospheric pressure DBD in air consists of great number of reactions (Stefanovic, 2001). In the simulation presented here, we include chemical reactions (see Table 1) concerning the production and destruction of nitric oxide and ozone. Other reactions which are not included in this model have small rate constant or one (or both) of the reactants have

too small concentration in our plasma conditions. For example, in spite of the fact that O(^{1}D) metastable atoms are produced by electron impact dissociation of oxygen molecules, reactions of this metastable atom are not included in the model because of its very short life time (1.4 ns) in air at atmospheric pressure conditions, and therefore its very low concentration.

No.	Reaction	Rate constant
(7)	$O_2 + e \rightarrow O + O + e$	Calculated from EVDF, n_e
(8)	$N_2 + e \rightarrow N + N + e$	Calculated from EVDF, n_e
(9)	$N_2 + e \rightarrow N_2(A) + e$	Calculated from EVDF, n_e
(10)	$O + O + M \rightarrow O_2 + M$	$3.8 \cdot 10^{-42}\, T^{-1} \exp(-170/T)$ m^6 s^{-1}
(11)	$O + O_2 + O_2 \rightarrow O_3 + O_2$	$8.6 \cdot 10^{-43}\, T^{-1.25}$ m^6 s^{-1}
(12)	$N + N + M \rightarrow N_2 + M$	$8.3 \cdot 10^{-46} \exp(500/T)$ m^6 s^{-1}
(13)	$O + O_2 + N_2 \rightarrow O_3 + N_2$	$5.6 \cdot 10^{-41}\, T^{-2}$ m^6 s^{-1}
(14)	$O + O_3 \rightarrow O_2 + O_2$	$1.9 \cdot 10^{-17} \exp(-2300/T)$ m^3 s^{-1}
(15)	$O + NO + M \rightarrow NO_2 + M$	$9.1 \cdot 10^{-40}\, T^{-1.6}$ m^6 s^{-1}
(16)	$NO + N \rightarrow N_2 + O$	$1.8 \cdot 10^{-18}\, T^{0.5}$ m^3 s^{-1}
(17)	$N + O_2 \rightarrow NO + O$	$1.1 \cdot 10^{-20}\, T \exp(-3150/T)$ m^3 s^{-1}
(18)	$N + O_3 \rightarrow NO + O_2$	$5 \cdot 10^{-18} \exp(-650/T)$ m^3 s^{-1}
(19)	$N + O + M \rightarrow NO + M$	$1.8 \cdot 10^{-43}\, T^{-0.5}$ m^6 s^{-1}
(20)	$O_3 + NO \rightarrow NO_2 + O_2$	$9 \cdot 10^{-19} \exp(-1200/T)$ m^3 s^{-1}
(21)	$N_2(A) + O_2 \rightarrow N_2 + O + O$	$1.63 \cdot 10^{-18} (T/300)^{0.55}$ m^3 s^{-1}
(22)	$N_2(A) + O_2 \rightarrow N_2 + O_2$	$8.75 \cdot 10^{-19} (T/300)^{0.55}$ m^3 s^{-1}
(23)	$N_2(A) + N \rightarrow N_2 + N$	$2.6 \cdot 10^{-18}\, T^{0.5}$ m^3 s^{-1}
(24)	$N_2(A) + NO \rightarrow N_2 + NO(A)$	$3.5 \cdot 10^{-18}\, T^{0.5}$ m^3 s^{-1}
(25)	$N_2(A) + N_2(A) \rightarrow N_2(C) + N_2$	$8.7 \cdot 10^{-18}\, T^{0.5}$ m^3 s^{-1}
(26)	$O + O_3 \rightarrow O_2(a^1\Delta) + O_2$	$6.3 \cdot 10^{-18} \exp(-2300/T)$ m^3 s^{-1}
(27)	$O + O_3 \rightarrow O_2(b^1\Sigma) + O_2$	$3.2 \cdot 10^{-18} \exp(-2300/T)$ m^3 s^{-1}

Table 1. Plasma-chemical reactions and their rate constants (Stefanovich, 2001) included in the simulation.

The temporal behavior of chemically-active species produced in the discharge, and the fluxes of nitric oxide and ozone to the surface of the treated electrode both in the homogeneous and stochastically-distributed discharges are simulated. The equations, the boundary conditions and the assumptions made for this simulation are discussed briefly in the following sections.

5.1 Equation

The temporal behavior of the chemically-active species produced in the discharge is described by the equation of continuity (28). Gain and loss of the active species by different reactions in the discharge channel and their diffusion (according to Fick's law) are considered.

$$\frac{\partial[M]}{\partial t} = \nabla \cdot (D(T)\nabla[M]) + \sum k_{MN}(T)[M][N], \tag{28}$$

where $[M]$ and $[N]$ (in m^{-3}) are the densities of species involved in the chemical reaction, $D(T)$ (in $m^2 \cdot s^{-1}$) is the diffusion coefficient, and k_{MN} (in $m^3 \cdot s^{-1}$) is the rate constant of the corresponding chemical reaction. It describes the temporal evolution of species' density due to diffusion (first term on the right hand side of equation (28)) and different chemical reactions (second term). Cylindrical symmetry of the discharge is assumed and dependencies along the azimuth co-ordinate are neglected. Since plasma heats up the gas and the rate constants of the chemical reactions are temperature dependent, the equation of thermo-conductivity (29) is solved in the afterglow phase.

$$\frac{\partial T}{\partial t} = \nabla \cdot (\Lambda(T_g)\nabla T_g), \tag{29}$$

where T_g (in K) is the gas temperature and $\Lambda(T_g)$ (in $m^2 \cdot s^{-1}$) is the thermal diffusivity. $\Lambda(T_g)$ and $D(T_g)$ are interpolated, respectively, in equations (30) and (31) (Kohlrausch, 1996 & Marrero, 1972).

$$\Lambda(T_g) = 1.19 \cdot 10^{-6} T_g^{\,2} + 7.76 \cdot 10^{-4} T_g - 0.1 \tag{30}$$

$$D(T_g) = D_0 (T_g/273)^{\beta}, \tag{31}$$

where D_0 is the diffusion constant with a value of $0.28 \cdot 10^{-4}$ $m^2 \cdot s^{-1}$ for oxygen atoms, $0.29 \cdot 10^{-4}$ $m^2 \cdot s^{-1}$ for nitrogen atoms, $0.182 \cdot 10^{-4}$ $m^2 \cdot s^{-1}$ for nitrogen metastables and nitric oxide, and $0.170 \cdot 10^{-4}$ $m^2 \cdot s^{-1}$ for ozone (Eliasson, 1987). The parameter β in equation (31) is 1.774 for diffusion of oxygen and nitrogen atoms, 1.724 for nitrogen molecules and nitric oxide, and 1.750 for ozone.

5.2 Assumptions for homogeneous discharge mode

In the homogeneous discharge mode, the plasma appearing between the electrodes is approximately in cylindrical volume, since the upper electrode is circular in shape and is separated by a small gap from the opposite electrode. In such a discharge, the chemically-active species produced in the plasma can diffuse out of this cylindrical volume. The simulation is halted when a periodical behavior for all calculated values reaches saturation.

The flux of active species $\Gamma_{z,hom.}(r)$ (in $m^{-2}\cdot s^{-1}$) to the surface of treated electrode is then calculated in the final step by averaging the flux $\Gamma_z(r,t)$ (in $m^{-2}\cdot s^{-1}$) in equation (32) over time as shown in (33):

$$\Gamma_z(r,t) = -D\frac{\partial[M](r,t)}{\partial z} \tag{32}$$

$$\Gamma_{z,hom.}(r) = \frac{1}{t_{pulse}}\int_0^{t_{pulse}} \Gamma_z(r,t)\,dt, \tag{33}$$

where t_{pulse} is the reciprocal frequency of applied high voltage.

5.3 Assumptions for filamentary discharge

Filamentary discharge is ignited in cylindrical channel with length equal to the inter-electrode distance. Gas temperature and plasma parameters are assumed constant in the whole plasma volume during all discharge pulse. Surrounding gas temperature amounts to 293 K.

6. Results

6.1 DBD plasma source

The DBD plasma source for biomedical applications consists of a ring-shaped upper (copper) electrode (diameter = 8 mm) which is covered with a thin layer of ceramic (Al_2O_3) for a thickness of 1 mm. In principle, the human body, which has high capacitance, can be used as the opposite electrode (fig.4). Discharge is ignited when the distance to the finger surface is lower than about 2 mm. Dependence of ignition conditions on treated substrate (skin or nail) and on surface conditions (wet or dry surface) is not yet clear. The voltage amplitude and pulse frequency of power supply are selected in such a way that there is no pain caused during DBD treatment of human body.

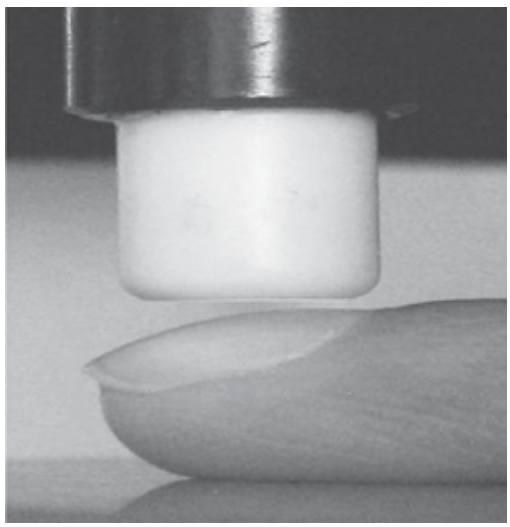

Fig. 4. Snapshot of DBD plasma source for treatment of biological objects

6.2 Microphotography

Dielectric barrier discharge is ignited in air between the upper electrode and the opposite electrode which is grounded or with a high-capacitance material like human body. According to our observations, the DBD source operated directly on human body (on the inner side of the fore finger) ignites a "twin discharge" which shows both homogeneous and filamentary regimes (Fig.5A). DBD ignited on the mouse skin surface consists also of homogeneous and filamentary discharges (see fig. 5B). The latter ignite on the some raised points (obviously hairs) for each trigger pulse. We call such a discharge as 'single-filamentary discharge' to distinguish it from normal filamentary discharge in DBD ignited on conductive electrode and which consists of number of stochastically distributed discharge channels.

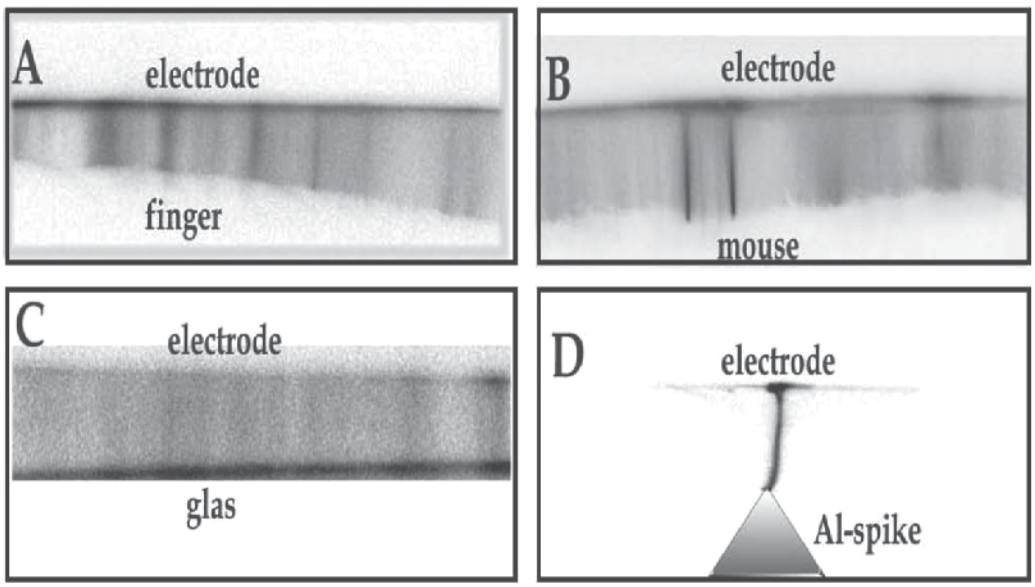

Fig. 5. Microphotography (negative image) of simultaneous homogeneous and filamentary discharges on inner side of finger (A), mouse skin (B), homogeneous discharge on glass (C) and single-filamentary discharge on Al-spike (D). Exposure time of microphotography is lower than the period of high voltage pulses.

To study and optimize the DBD source for biomedical application, especially for therapeutic use, characterization and study of factors influencing the formation of this "twin discharge" are required. Characterization of the discharge on the body of different individuals will yield results with large degrees of freedom. The varied results could be due to the different skin properties between individuals and within the same individual also. Optimization of the DBD source based on such studies are necessary at the later stages. Before that, the different discharge modes in air and the causes for such modes require detailed investigation. For this purpose, we characterize DBD operated individually in homogeneous and filamentary modes using electrodes of different materials and profiles. We observed a homogeneous discharge (figure 5C) when glass is used as the opposite electrode, and a single-filamentary discharge is ignited with aluminium spike (figure 5D). We characterize these modes individually to learn the differences in plasma conditions between the modes

and to understand the influence of the opposite electrode (its material and profile) on discharge formation. The diameter of the single-filamentary microdischarges on mouse skin and on Al-spike is comparable and amounts to about 50 μm.

6.3 Voltage-current characteristics

The voltage at the upper electrode is measured using a capacitive voltage divider (dividing factor of 1: 2000) and plasma current is measured using a current monitor (Pearson - 2877 with 1V:1A output). Voltage and current traces are recorded using an oscilloscope. A high voltage pulsed power supply of 300 Hz frequency and amplitude up to 14 kV is used (figure 6a). Each high voltage pulse has a sequential profile with damped oscillations and frequency of about 100 kHz (figure 6b). Micro discharges are ignited if the breakdown conditions in the gas gap are fulfilled. These breakdowns occur in the first quarter of the power supply period (figure 7a). The next discharge ignites at lower applied voltage because of the charged dielectric surface and, therefore, high electric field in the gas gap after first discharge. Second (and following) ignition can occur even at 0 V.

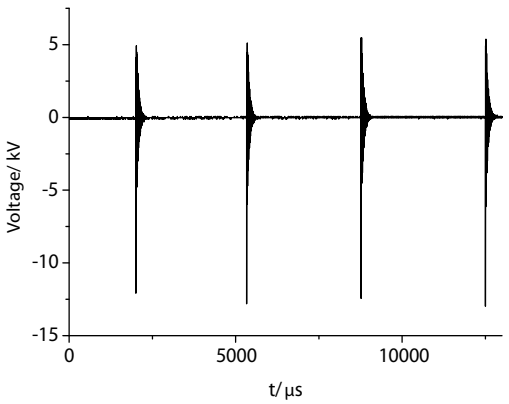

Fig. 6a. Profile of high voltage pulses

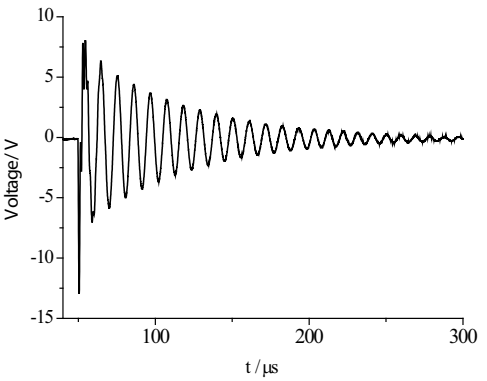

Fig. 6b. Sequence of high voltage pulses initialized by one trigger pulse

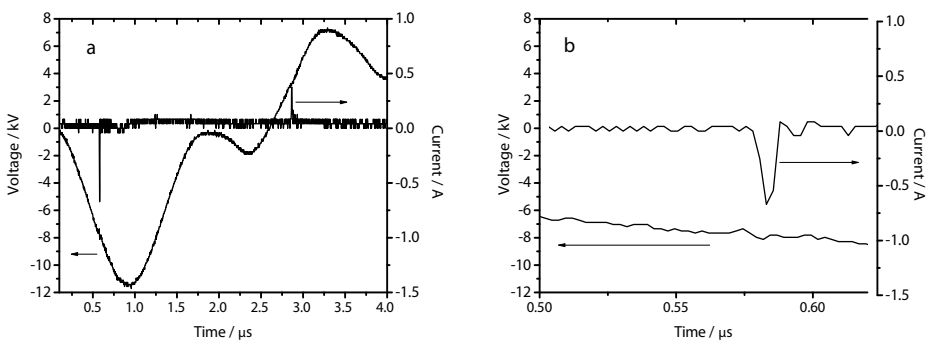

Fig. 7. Current-voltage characteristics for glass opposite electrode at 1 mm inter-electrode distance with different time resolution

To determine discharge duration (τ (in ns)), we measure the full width at half-maximum (FWHM) from the profile of the current pulses (figure 7b). These values for different DBD conditions and number of ignitions for each trigger pulse are presented in Table 2.

Opposite electrode / Parameters	Mouse (d = 1 mm)	Mouse (d = 0.5 mm)	Glass (d = 1 mm)	Al-spike (d = 1.5 mm)
τ (ns)	25 ± 5	25 ± 5	6.0 ± 1.5	23 ± 1
No. of ignitions	3	5	2	1

Table 2. Pulse duration (at FWHM) and number of discharge pulses per trigger pulse in DBD with different opposite electrodes

6.4 Gas temperature

The gas temperature in the active plasma volume, determined for DBD treatment of mouse skin, is 320 ± 20 K for both 1 mm and 0.5 mm gaps (table 3). It is worth mentioning here that the same temperature is obtained for the homogeneous discharge with glass as the opposite electrode. The gas temperature in discharge with Al-spike (T_g = 350 K) is higher than the surrounding gas temperature (T_g = 293 K) but decays back to surrounding gas temperature in afterglow phase. Solving thermo-conductivity equation (27), we calculate the spatial temperature profiles at different delay times in afterglow of micro discharges. In this calculation, we use 50 μm for diameter of discharge channel, a surrounding gas temperature of 293 K, and 350 K gas temperature in discharge channel. In afterglow phase, the gas temperature decreases rapidly (figure 8).

Opposite electrode	Mouse (d = 1 mm)	Mouse (d = 0.5 mm)	Glass (d = 1 mm)	Al-spike (d = 1.5 mm)
T_g (K)	320 ± 20	320 ± 20	320 ± 20	350 ± 20

Table 3. Gas temperature determined in DBD with different opposite electrodes

For simulation of chemical kinetics in active and afterglow phases of DBD on mouse skin, we assume that gas temperature as 310 K because the normal body temperature of the mouse is about 315 K and the ceramic that covers the electrode has a temperature of about 300 K during experiment. During active phase of the discharge, the gas temperature increases up to about 320 K, but in short time it decays to the steady state value of about 310 K.

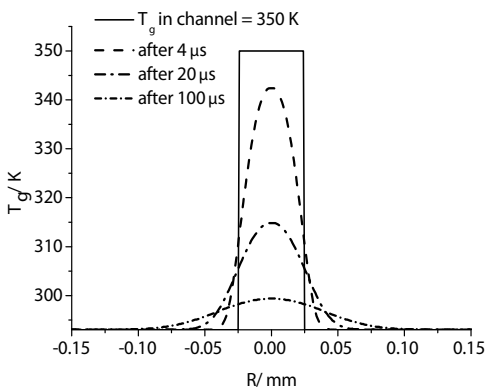

Fig. 8. Spatial distribution of the gas temperature (radially along the electrode) in the afterglow phase in the gap between electrodes for Al-spike as the opposite electrode.

6.5 Plasma parameters

Microphotography of discharge on the mouse skin shows homogeneous and single-filamentary discharges ignited simultaneously. Because of low emission intensity of single-filamentary discharge (accounting for only about 6 % of the total observed emission) in relation to the homogeneous discharge, plasma parameters are determined for the homogeneous discharge. However, the influence of single-filamentary discharge on total fluxes of chemically-active species by DBD treatment of biological object is qualitatively discussed in section 6.7.

The plasma parameters (reduced electric field and electron density) determined in DBD at different plasma conditions and dissociation cross sections of nitrogen and oxygen molecules calculated applying these plasma parameters and equation (34) are presented in table 4.

$$k_{diss} = 4\pi \cdot \sqrt{2} \int_E f_v(E) \cdot \sqrt{\frac{2 \cdot e}{m_e}} \cdot E \cdot \sigma_{diss}(E) dE, \tag{34}$$

where $\sigma_{diss}(E)$ - dissociation rate constants of nitrogen (Itikawa, 2006) and oxygen molecules (Itikawa, 1989). Reduced electric field E/N is expressed in Townsend (Td) where N is the gas density (1 Td = 10^{-21} V·m^2). E/N for different electrodes are listed in table 4.

E/N in homogenous discharge on mouse skin increases with decrease of the inter-electrode distance but is lower than that in single-filamentary mode and in homogeneous discharge on glass.

Opposite electrode	d mm	E/N Td	n_e m^{-3}	k_{diss} N_2 10^{-15} m^3·s^{-1}	k_{diss} O_2 10^{-15} m^3·s^{-1}
Mouse skin	0.5	290	$7.3 \cdot 10^{16}$	2.5	0.77
	1	280	$7.1 \cdot 10^{16}$	2.4	0.74
Al-spike	0.5	430	$4.2 \cdot 10^{21}$	4.4	1.16
	1	406	$2.4 \cdot 10^{21}$	3.9	1.11
Glass	0.5	360	$4.3 \cdot 10^{17}$	4.1	1.13
	1	320	$3.7 \cdot 10^{17}$	3.2	1.03

Table 4. Reduced electric field (E/N), electron density (n_e) for DBD on mouse skin, Al-spike and glass at different inter-electrode distances (d), and the rate constants for electron-impact dissociation of nitrogen (k_{diss} N_2) and of oxygen (k_{diss} O_2) molecules calculated using equation (34).

Electron densities in active plasma volume measured applying neutral nitrogen molecular emission by variable plasma conditions are presented in table 4. The electron density in homogeneous mode of DBD is lower than that in filamentary mode.

Using determined electric field, the electron velocity distribution functions in DBD are simulated (fig.9).

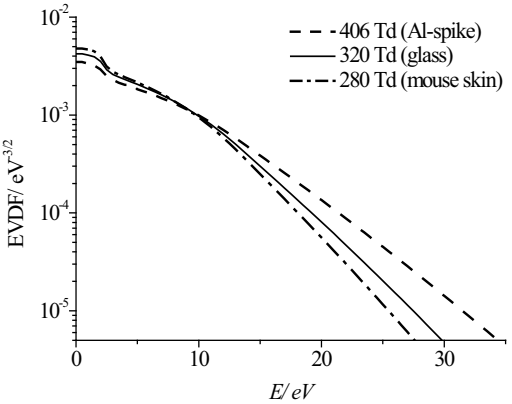

Fig. 9. Electron velocity distribution functions determined using OES and numerical simulation in DBD in air at atmospheric pressure with 1 mm inter-electrode distance and different opposite electrodes.

6.6 Validation test of 'plasma characterization with low spatial resolution OES diagnostics'

The plasma parameters (electron density and reduced electric field) are determined in this work using simulation and two spectral bands namely, the excitation emission of N_2(C-B) and of N_2^+ (B-X). These plasma parameters are averaged values in the volume observed by the spectrometer. From microphotography, it is clear that in this experiment two discharge conditions exist: i) a homogeneous discharge in the gap between the electrodes, and ii) the occurrence of microdischarge filaments along with this homogeneous discharge. Electric field and electron density differ strongly in these two DBD modes (see table 4). Furthermore, plasma parameters in homogeneous and in filamentary discharges have fine structures with higher variations of electric field and electron density with distance from the electrodes (Braun, 1992; ; Massines 1998 & Kozlov, 2001).

We study the influence of low spatial resolution of OES diagnostics on determined plasma parameters through simulation of plasma conditions with variable spatial resolution. We assume that our spectrometer observes two plasma volumes with very different electric field, one with 100 Td and the other with 1000 Td. n_e for 100 Td is assumed as $7 \cdot 10^{16}$ m^{-3} (same as that determined for 1 mm in discharge on mouse skin). Using these assumptions, we perform the validation for two cases:

i. ***First case -*** it is assumed that the two plasma volumes produce equal intensities of neutral nitrogen emission ($I_{N_2(C-B)}$). n_e at 1000 Td is calculated to be $1.4 \cdot 10^{15}$ m^{-3}. Also, the total N_2(C-B) emission intensity is the sum of $I_{N2(C-B)}$ from the two plasma volumes. 'Averaged' *E/N* is estimated from the ratio of total N_2(C-B) emission intensity to the total N_2^+ (B-X) emission intensity. Accordingly, 'averaged' *E/N* = 610 Td and corresponding n_e is calculated as $1.7 \cdot 10^{15}$ m^{-3}.

ii. ***Second case -*** it is assumed that the two plasma volumes produce equal intensities of nitrogen-ion emission ($I_{N_2^+(B-X)}$). n_e at 1000 Td in this case is $1.5 \cdot 10^{12}$ m^{-3}. The total emission intensity of N_2^+ (B-X) is calculated as the sum of $I_{N_2^+(B-X)}$ from the two plasma volumes. 'Averaged' *E/N* = 110 Td estimated in the same way as in the *first case*. n_e for 110 Td is $2.8 \cdot 10^{16}$ m^{-3}.

It can be seen that the 'averaged' plasma parameters differ strongly from space-resolved plasma parameters. But the main aim of plasma characterization is the determination of dissociation rates of nitrogen and oxygen molecules (processes (7) and (8) in table 1). These values are subsequently used in the simulation of chemical kinetics in active plasma volume and in afterglow. We calculate the dissociation rates of diatomic molecules using space-resolved parameters and compare them with the corresponding dissociation rates calculated using 'averaged' plasma parameters.

The dissociation rate constant of nitrogen molecules ($k_{diss}^{N_2}$) and of oxygen molecules ($k_{diss}^{O_2}$) using 'averaged' parameters and using the space-resolved parameters are calculated. The ratio of $k_{diss}^{O_2}$ at 'averaged' condition to that at the space-resolved condition is determined as 1.03 for the *first case* and 1.2 for the *second* case. Similarly, the ratio of $k_{diss}^{O_2}$ in the 'averaged' conditions to that in the space-resolved condition corresponds to 0.47 for the *first case* and 1.2 for the *second* case. All the values are presented in table 5.

Plasma conditions assumed for validation of averaged plasma parameters	$\frac{k_{diss}^{N_2}\text{averaged conditions}}{k_{diss}^{N_2}\text{spatial-resolved conditions}}$	$\frac{k_{diss}^{O_2}\text{ averaged conditions}}{k_{diss}^{O_2}\text{spatial-resolved conditions}}$
First case $I_{N_2(C\text{-}B)}$ at 100 Td = $I_{N_2(C\text{-}B)}$ 1000 Td at 100 Td, $n_e = 7 \cdot 10^{16}$ m^{-3} at 1000 Td, $n_e = 1.4 \cdot 10^{15}$ m^{-3} 'averaged' E/N = 610 Td; $n_e = 1.7 \cdot 10^{15}$ m^{-3}	1.03	0.47
Second case $I_{N_2^+(B\text{-}X)}$ at 100 Td = $I_{N_2^+(B\text{-}X)}$ 1000 Td at 100 Td, $n_e = 7 \cdot 10^{16}$ m^{-3} at 1000 Td, $n_e = 1.5 \cdot 10^{12}$ m^{-3} 'averaged' E/N = 110 Td; $n_e = 2.8 \cdot 10^{16}$ m^{-3}	1.2	1.2

Table 5. Plasma conditions assumed for validation of averaged plasma parameters and the corresponding dissociation rate constants for nitrogen ($k_{diss}^{N_2}$) and oxygen ($k_{diss}^{O_2}$).

When the neutral nitrogen emission in the region of high electric field is *weaker* than that in the region of low electric field (due to small number of electrons resulting from either low electron density or small plasma volume), then the averaged E/N calculated (110 Td) is closer to the E/N value of the low electric field (i.e. 100 Td) as seen in the *second case* of this estimation. In such a condition, the dissociation rates of oxygen and nitrogen molecules calculated using 'averaged' plasma parameters differ only slightly from the values determined with space-resolved plasma parameters.

Conversely, if neutral nitrogen emission in the region of high electric field is *equal* or *comparable* to that in the low electric field region, then the 'averaged' E/N calculated (610 Td) is closer to the E/N value of the high electric field (i.e. 1000 Td) as seen in the *first case* of this estimation. In this case, as can be seen in the table 5, the dissociation rate of oxygen

calculated using 'averaged' plasma parameters is under-estimated by a factor of about 2. At the same time the dissociation rate of nitrogen calculated using 'averaged' parameters did not show large deviations from the corresponding value calculated at space-resolved condition. The reason for this effect is the difference between threshold values of dissociation cross-section of nitrogen and oxygen molecules, and the difference of the 'averaged' electron distribution function from the space-resolved one. To determine dissociation rates with better accuracy at such plasma conditions space and time resolved optical emission diagnostic is needed.

When the same validation procedure was performed for two plasma volumes with 200 Td and 1000 Td, the dissociation rate of oxygen and nitrogen molecules calculated using 'averaged' parameters varied only slightly (less than 20 %) from that calculated using space-resolved parameters in the *first case* as well as in the *second case*. Hence, it can be concluded that our estimation method holds good for calculation of 'averaged' *E/N* when the plasma volumes are assigned with *E/N*=200 Td or higher. The previous condition where 100 Td and 1000 Td were assumed for estimation proves to be a severe case for this estimation procedure.

Because of relatively low averaged electric field (*E/N* ~ 300 - 400 Td) determined in DBD at plasma conditions considered here, we can establish that the influence of regions with high electric field is not so strong (as seen in the *first* case considered above). The difference in the calculated dissociation rates of nitrogen and oxygen is lower than a factor of 2 according to this estimation but actual values in the experiment will be determined in forthcoming work through space-resolved diagnostic methods.

Nevertheless, the rate of dissociation of diatomic molecules in active plasma volume is reliable (with possible deviation lower than factor 2) despite the difference between the averaged plasma parameters (determined for DBD in air at atmospheric pressure using OES) and the actual plasma parameters existing in the studied DBD conditions.

6.7 Fluxes of ozone and nitric oxide (NO)

The fluxes of ozone and NO reaching the treated surface in our plasma conditions are shown in figures 10(a) and 10(b), respectively. As it can be seen from these figures, the flux of ozone and NO determined for the homogeneous discharge on the mouse skin is similar to that for the homogeneous discharge with glass. Despite lower electric field and electron density, the fluxes of ozone and nitric oxide on the mouse skin are similar to the fluxes on glass surface which is due to the longer pulse duration and increased number of current pulses in the former.

Though the discharge ignited on mouse is assumed to be homogeneous, the influence of the simultaneously-occurring filamentary discharges (figure 5B) on the chemical kinetics cannot be ignored and is only qualitatively discussed here. From the fluxes of NO and ozone simulated for a single-filamentary discharge, it is observed that these fluxes are the highest when compared to the other modes (Rajasekaran, 2009 & Rajasekaran, 2010). However, it should be noted that the NO and ozone fluxes for a single-filamentary discharge is comparable to the respective flux in the other discharges for a small region close to the vertical axis along the length of the filament as seen in figures 10(a) and 10(b).

To compare the applications of our DBD with other plasma sources for e.g. with 'indirect' plasma sources where the relative proportion of ozone and nitric oxide in its effluent is known, we estimate the flux $\frac{[M]\cdot v_{mean}}{4\cdot 10^6}$ of chemically-active species in the DBD source

with the assumption that steady state concentration of chemically-active species in air is 1 ppm (one part per million) (figure 10). For this estimation, the mean velocity (v_{mean} in m·s^{-1}) and density of nitrogen and oxygen molecules ([M] in m^{-3}) are about 460 m·s^{-1} and 2.5·10^{25} m^{-3} correspondingly at 293 K.

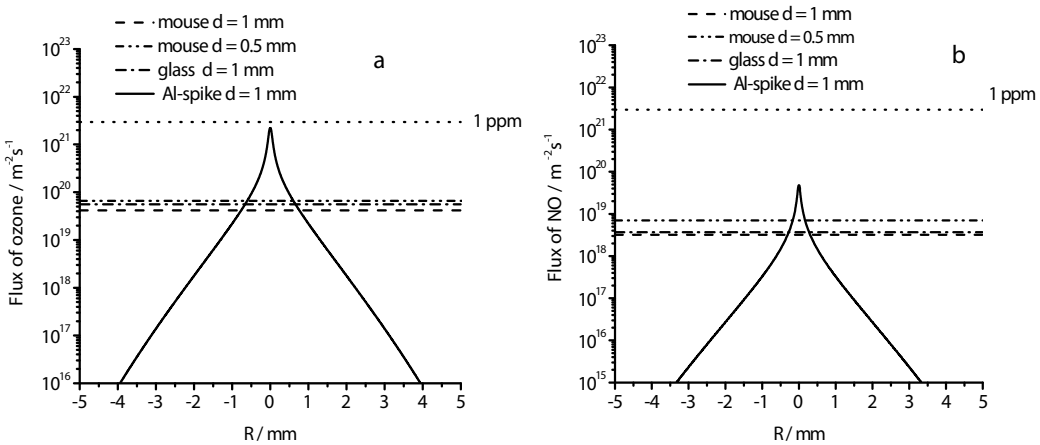

Fig. 10. Flux of ozone (a) and nitric oxide (b) reaching the treated surface across the radius of the driving electrode (R) for DBD on different substrates. The fluxes at species' concentration of 1 ppm are calculated using mean velocity and concentration of nitrogen and oxygen molecules at plasma conditions.

6.8 UV-irradiation

The UV-irradiation of mouse skin is 210 mW·m^{-2} for 0.5 mm gap, and 252 mW·m^{-2} for 1 mm gap. By decrease of inter-electrode distance, plasma volume decreases but at the same time electric field and electron density and, therefore, excitation rate constants for nitrogen UV-emission increase (see figure 11). Intensity of NO-emission in UV-C region (λ < 280 nm) is detected only for single-filamentary discharge with Al-spike and irradiation reaches a maximum of about 10 mW·m^{-2} near the discharge channel. UV-C emission for homogenous discharges on the mouse skin and glass is not detectable. We can only estimate that UV-C irradiation in this DBD mode is lower than 2 mW·m^{-2}. The irradiation of UV-A and UV-B in the UV-A - UV-B therapy used for treating atopic dermatitis (Jekler,1990) is presented in figure 11.

7. Discussion

Concentrations and fluxes of nitric oxide and ozone during DBD treatment are complicated functions consisting of parameters pertaining to different plasma conditions. The nitrogen and oxygen atoms are generated during electron impact dissociation and are lost in gas phase recombination process for the production of nitrogen and oxygen molecules. At atmospheric pressure conditions, nitric oxide and ozone molecules are also produced in the recombination process in gas phase. The loss of nitric oxide and ozone molecules occurs mainly during reactions with nitrogen atoms. These molecules produced both in the discharge and in the afterglow phase reach the surface of opposite electrode by diffusion.

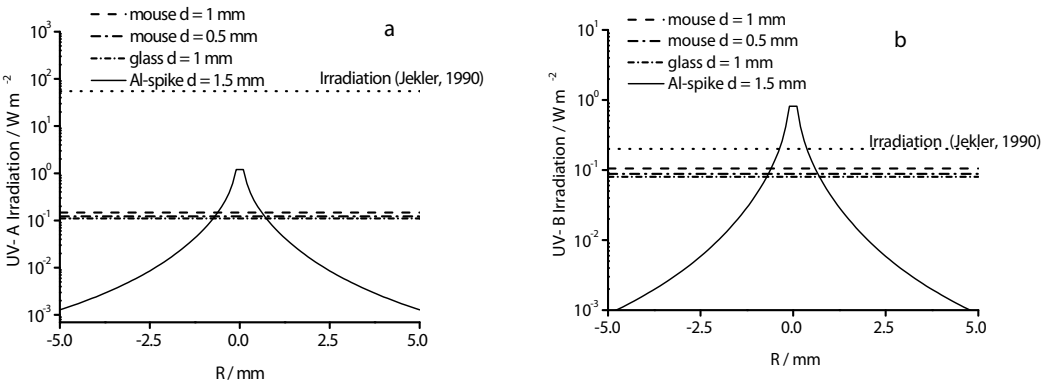

Fig. 11. Simulated UV-A (a) and UV-B (b) irradiation of treated surface for different electrode and irradiation accordingly to (Jekler, 1990).

According to our simulation, the fluxes of ozone (figure 10a) and nitric oxide (figure 10b) to the treated surface by applying our DBD in homogeneous mode is about an order of magnitude higher than that in stochastic filamentary DBD ignited on conductive Al-plate and PBS (phosphate buffered saline) solution (Rajasekaran, 2010). In both cases, the area of treated surface is approximately equal to the surface of the driving electrode. Moreover, the fluxes of nitric oxide and ozone obtained when the DBD is operated in the single-filamentary mode is higher (also about an order of magnitude) in the small area near the position of the filament. Therefore, it can be concluded that, when using the DBD plasma source for medical applications, homogeneous mode is more effective for treatment of large substrate area and single-filamentary mode is suitable for local treatment.

Both filamentary and homogeneous modes of DBD are useful for bio-medical applications like NO-therapy and ozone-therapy of skin diseases. Nitric oxide is also synthesized by skin cells during the wound healing process. This molecule plays important biological functions in the human skin as a "signaling" molecule and mediates cellular activities not only during the proliferative phase but also throughout the wound healing process (Bruch-Gerhurz, 1998, Cals-Grierson, 2004 & Childress, 2002). The low nitric oxide flux could be useful for assisting the skin cells during the different phases of wound-healing.

Ozone is a recognized 'remover' of bacteria, fungi and viruses and is used as an additional medical treatment in dermatology, stomatology, etc. Over-exposure to ozone can harm the lungs and cause irritation in the respiratory system. Therefore, the production and use of ozone are regulated by strict exposure limits, and therapeutic doses are usually higher than this permissible limit. This complexity can be overcome using DBDs generating ozone close to the treated surface. In this way, DBDs are advantageous when compared with other plasma sources which produce ozone in some active plasma volume that has to be then transported to the surface for treatment. By applying DBD in single-filamentary mode, concentration of ozone can reach 1 ppm and even more at some treatment point (Figure 10). However, ozone concentration at the distance of even 1 mm away from this point amounts to lower orders of magnitude and hence can be used for therapies which also complies with the safety norms.

7.1 Filamentary and homogeneous modes of DBD

DBD in air can be operated in both modes namely filamentary and homogeneous. Irradiation of the treated surface by photons and chemically-active species is about an order

of magnitude higher in the homogeneous DBD (Rajasekaran, 2010) when compared to the filamentary DBD. Therefore, conditions for transformation of DBD modes are very important for treatment optimization.

Previously, several investigators have used glass as dielectric for study of DBD in air at atmospheric pressure and have presented different results. Kozlov *et al* (Kozlov, 2001) reported the development of microdischarge (MD) channels in the "two-sided" barrier discharge (BD) using a pair of glass-covered electrodes powered by 6 kHz AC power supply, whereas homogeneous DBD discharges operated at nanosecond-pulsed power supply have also been reported (Walsh, 2008 & Ayan, 2009). Frequency of high-voltage pulses in sequence applied to our DBD source is about 100 kHz, yet we obtain a homogeneous discharge with glass which acts as a dielectric barrier when placed on the grounded aluminium base. This regime of homogeneous discharge could be the intermittent discharge which falls in between the above mentioned discharges (Kozlov, 2001 & Ayan, 2009).

In all cases, the primary element of each breakdown is an individual avalanche that propagates to the anode. When the avalanche moves forward, the total number of electrons increases exponentially ($e^{(\alpha-a)x}$, where α is Townsend's first coefficient, and a is attachment coefficient). The space charge generated in the avalanche generates its own electric field that distorts it. The space charge field also increases the electric field in front of the avalanche's head. This additional field is proportional to the electron number in the head of the avalanche and increases along the traversed path. When electric field in front of the avalanche head reaches a critical value, the avalanche transforms in to a streamer. In this case, the space charge grows additionally due to secondary avalanches propagating in the high electric field region and the anode-directed streamer is produced. If the distance between the electrodes is smaller than 50 mm, primary avalanches in air at atmospheric pressure cannot transform into anode-directed streamer (Raizer, 1997).

In our plasma conditions, breakdown occurs according to Townsend mechanism and the primary avalanches reach the surface of the anode. This model is confirmed in our microphotography of DBD with glass as opposite electrode. The intensity of photo emission is proportional to the electron density and hence has maximum emission near the surface of the glass, i.e. near the anode (figure 5C). After primary avalanches reach the anode, two different discharges can be ignited, either a filamentary discharge or homogeneous discharge. In the filamentary discharge, cathode-directed streamer starts in the tail of primary avalanche. Because of low mobility of heavy ions, the tail of avalanche has abundant positive charges. If the head of avalanche touches the conductive anode (e.g. aluminium plate), then the electrons are lost from the air gap, and the positively-charged avalanche trace rapidly increases electric field that can reach critical value for streamer initiation. If the anode is non-conductive (e.g. glass), electrons are *not* lost from the air gap and negative charge on the surface of the glass compensate, particularly, the positive charge of the avalanche trace. Therefore, conductivity of the anode can influence the transformation of Townsend discharge in to filamentary or homogeneous discharge.

During propagation of the avalanches, a number of metastable molecules are excited in the air gap. Energy-pooling ionization reactions like (35, 36)

$$N_2(a'^1\Sigma_g^-) + N_2(A^3\Sigma_u^+) \rightarrow N_2^+ + N_2(X) + e \quad (35)$$

$$N_2(a'^1\Sigma_g^-) + N_2(a'^1\Sigma_g^-) \rightarrow N_2^+ + N_2(X) + e, \quad (36)$$

can give rise to "seed electrons" and these electrons can initiate new avalanches. Because of relatively lower density of metastables excited in primary avalanches, energy-pooling ionization in the tail of the avalanches is delayed. These electrons are not lost from the air gap immediately after the avalanche contacts with the anode surface; instead they compensate the positive charges, particularly those in the avalanche trace. As a result, there are difficulties arising for the production of the cathode-directed streamer. The electric field in this region, for the initiation of secondary avalanches by the seed electrons, is reduced by the electric field of polarized charges of the avalanche. This causes a drop in electron number produced in the secondary avalanches. In addition, the drop in electron number is also because of the sensitivity of ionization coefficient α to the electric field variation. Hence, increase of external electric field can increase metastable excitation and thereby increase the number of seed electrons, thus preventing streamer production due to charge compensation as discussed above. The shorter rise time of the external voltage in our experiment (since the high-voltage pulses has 100 kHz frequency) could be the reason of homogeneous discharge ignition with glass as opposite electrode whereas at similar conditions but at lower frequency (6 kHz), a filamentary discharge is ignited (Kozlov, 2001). The profile of the high voltage pulse and the current-voltage characteristics for glass at an inter-electrode distance of 1 mm are shown, respectively, in figure 6 and figure 7.

7.2 Comparison of irradiation of treated surface with other treatment methods

The studied DBD source produces fluxes of photons on the treated object's surface. This flux can be compared with that of known light sources used for bio-medical applications. Phototherapy using ultraviolet radiation is available for treatment of numerous skin disorders.

The irradiation of the treated surface by UV-A and UV-B in different discharge modes are shown in figure 11a and 11b respectively. Ultraviolet A (UV-A, 320 – 400 nm) and ultraviolet B (UV-B, 280 – 320 nm) are selectively used for treatment of skin diseases like psoriasis (Coven, 1997), atopic dermatitis (Krutmann, 1992), localized scleroderma (Stege, 1997) and vitiligo (Kumar, 2009). UVA-UVB therapy is more efficient than UV-B therapy for treating skin diseases like atopic dermatitis (Hannuksela, 1985 & Jekler, 1990). Accordingly, emission from this DBD source in the wavelength range of 310 – 340 nm with a peak at 320 – 330 nm can be used for treatment of atopic dermatitis. The irradiation of UV-A and UV-B in the UVA-UVB therapy (Jekler, 1990) is comparable with that of our DBD source operated in single-filamentary mode in a region of about 1 mm diameter of the upper electrode (figure 11). Furthermore, single-filamentary DBD emits photons in the UV-C range. This irradiation can be compared with UV-C irradiation in the range of 200 – 280 nm produced in an inductively coupled plasma (ICP) reactor and applied to deactivate spores of *Bacillus atrophaeus* (Halfmann, 2007). These bacteria are commonly used as "challenging organisms" for sterilization-validation studies. UV-C irradiation near the plasma channel in single-filamentary mode of our DBD source, for a treatment time of about 10 minutes, is comparable with the ICP reactor which causes sterilization in 60 seconds with a logarithmic reduction of about 5.

Irradiation by homogeneous discharge is higher compared to that of stochastic filamentary discharges (Rajasekaran, 2010). By increasing the treatment time by two to three orders of magnitude, irradiation similar to that reported by (Jekler, 1990) can be achieved with our DBD plasma source. As in the case of UV-B for skin treatment, the irradiation values for the DBD plasma source operated in different discharge modes also appears to be comparable to

that used in the treatment of atopic dermatitis (Jekler, 1990). Through such comparisons, it is possible to optimize the plasma source in terms of treatment duration, the proximity of the source with respect to the treated surface, etc., and for treatment of different skin diseases at different dosage levels. Optimization of the source can also be achieved by varying the electrical parameters like applied voltage and frequency.

7.3 Comparison of NO and ozone fluxes with other treatment methods

Flux of NO can be effectively used for healing of wounds. In NO therapy using the 'indirect' air-plasma source 'Plazon', gas mixture in effluent of the plasma source with NO concentration of 500 ppm improved healing of skin wounds (Shekter, 2005). Our DBD plasma source generates comparatively lower NO flux which is too small for similar skin healing treatments. But mechanism of NO therapy is complicated, multifaceted and is far from known yet. The dose of NO-irradiation necessary for therapeutic effect of different diseases is not yet determined. Using simulated species' fluxes, we can determine the time necessary for full coverage of the treated surface by nitric oxide and ozone. Except small regions near the single-filamentary discharges, the treated surface is irradiated by NO and O_3 homogeneously by applying our DBD. The cross section of one molecule amounts $(3\text{-}4)\cdot10^{-20}$ m^2 and therefore, the surface under driving electrode is treated by nitric oxide in about 5 s and by ozone in fraction of a second. In general, for increasing NO production, the averaged current produced in the discharge can be increased. For this, input voltage of higher amplitude or high pulse frequency must be used. A discharge ignited with higher voltages or with higher pulse frequencies can lead to painful medical treatments and so such modifications to the source should be overlooked.

However, the production of NO by the source can be improved by using it at close vicinity to the surface of the human body, thereby reducing the gap distance. Reduced electric field and electron density increase with decrease in the inter-electrode distance. Hence, using the source close to the body can increase the dissociation of nitrogen and oxygen molecules and thus result in effective production of NO. The discharge on the surface of dielectric ignites after the discharge channel bridges the electrodes by operation in single-filamentary mode (Kuchenbecker, 2009). This surface discharge is characterized by relatively high electric field and electron density. The discharge channel on the surface of dielectric is lengthier than that ignited in the air-gap between the electrodes. Therefore, production of NO molecules in the surface discharge is more effective on the dielectric surface than in the air-gap. Also, the flux of NO molecules produced in the surface discharge increases with decreased inter-electrode distance. So, using the source close to the body surface allows the NO molecules produced in the surface discharge to reach the treated surface effectively.

Some chemical active species produced in air plasma e.g. ozone and nitric oxides can be harmful for human body when inhaled but serve useful for medical treatments like treatment of dermatological disorders and healing of wounds. At that, required concentration of these species must be supported near the treated object. An advantage of 'direct' plasma treatment is the production of chemically-active species directly on treated site of human skin. Despite the fact that these species diffuse from the active plasma volume and can reach respiratory tract, their concentration decreases drastically during diffusion and reaches the safety level at small distance away from the active plasma volume.

8. Conclusion and outlook

A DBD is investigated towards medical applications especially for skin treatment. DBD operated on human and animal skin consists of both homogeneous and single-filamentary modes, which are ignited simultaneously. Characterization of this complex discharge appears to be a complicated task. Hence, these two discharge modes namely the single-filamentary and homogeneous modes are studied separately. Single-filamentary discharge is produced with Al-spike as opposite electrode. A homogeneous discharge is obtained with glass as opposite electrode which is typically a Townsend discharge but does not attain a glow mode in our experimental conditions. Using optical emission spectroscopy, microphotography and numerical simulation, the plasma parameters and gas temperature in DBD on mouse are determined, chemical kinetics in active plasma volume and in afterglow is simulated and irradiation of the treated object by ozone, nitric oxide and UV-photons are calculated. These fluxes are compared with other sources used in dermatology. By applying the DBD in single-filamentary mode, irradiation of treated surface reaches a maximum of about 1 $W \cdot m^{-2}$ for both UV-A and UV-B spectral range, and in the homogeneous mode it is about 0.2 $W \cdot m^{-2}$. Irradiation of the treated surface by photons and chemically active particles can be increased simply by increasing the trigger pulse frequency; but electric current will also increase and could evoke pain during treatment. When the DBD is operated in the single-filamentary mode, the flux of nitric oxide and ozone to the treated surface attain a maximum of $4.8 \cdot 10^{19}$ $m^{-2} \cdot s^{-1}$ and $2.2 \cdot 10^{21}$ $m^{-2} \cdot s^{-1}$, respectively. NO flux is about $7 \cdot 10^{18}$ $m^{-2} \cdot s^{-1}$ and ozone flux about $6.6 \cdot 10^{19}$ $m^{-2} \cdot s^{-1}$, when operated in the homogeneous mode.

The presented simulation of chemical kinetics is based on the time and spatial-averaged plasma parameters and can have indefinite systematical error up to factor about 2. To improve accuracy and reliability of the simulation, optical emission diagnostics with time and spatial resolution will be applied in further studies.

To increase surface irradiation of the treated object by active species and UV photons, modified electrode arrangements where the discharge in the gas gap will be supplemented with effective surface discharge on the dielectric will be employed and studied.

9. Acknowledgment

The authors gratefully acknowledge Dr. Ch. Opländer and Prof. Dr. Ch. V. Suschek from Department of Plastic and Reconstructive surgery, Hand surgery and Burn Center (Medical Faculty, RWTH Aachen, Germany) for their valuable help in carrying out the experiment with living mouse. Financial support by German Research Foundation of the project C2 of Research Group FOR 1123 "Physics of Microplasma" is also gratefully acknowledged.

10. References

Ayan, H.; Fridman, G.; Gutsol, A.F.; Vasilets, V.N.; Fridman, A. & Fridman, G. (2008). Nansecond-pulsed uniform dielectric-barrier discharge. *IEEE Trans.Plasma Sci.*, Vol. 36, pp. 504-508

Ayan, H.; Staack, D.; Fridman, G.; Gutsol, A.F.; Mukhin, Y.; Starikovskii, A; Fridman, A. & Fridman, G. (2009). Application of nanosecond-pulsed dielectric barrier discharge

for biomedical treatment of topographically non-uniform surface. *J.Phys.D:Appl.Phys.*, Vol., 42, p. 125202 (5pp)

Bibinov, N.K.; Kokh, D.B.; Kolokolov, N.B.; Kostenko, V.A.; Meyer, D.; Vinogradov, I.P. & Wiesemann, K. (1998). A comparative study of the electron distribution function in the positive columns in N_2 and N_2/He dc glow discharges by optical spectroscopy and probes. *Plasma Sources Sci.Technol.*, Vol. 7, pp. 109-128

Bibinov, N.K.; Bratsev, V.F.; Kokh, D.B.; Ochkur, V.I. & Wiesemann, K. (2005). Spectroscoic determination of the cold electron population in very low pressure ECR discharges in N_2/He mixture. *Plasma Sources Sci.Technol.*, Vol. 14, pp. 298-309

Bibinov, N.; Halfmann, H.; Awakowicz, P. & Wiesemann, K. (2007). Relative and absolute intensity calibrations of a modern broadband echelle spectrometer. *Meas.Sci.Technol.*, Vol. 18, pp. 1327-1337

Bibinov, N.; Halfmann, H. & Awakowicz, P. (2008). Determination of the electro energy distribution function via optical emission spectroscopy and a Langmuir probe in an ICP. *Plasma Sources Sci.Technol.*, Vol. 17, p. 035004(7pp)

Boudam, M.K; Moisan, M,; Saoudi, B.; Popovici, C.; Gherardi, N. & Massines, F. (2006). Bacterial spore inactivation by atmospheric-pressure plasmas in the presence or absence of UV photons as obtained with the same gas mixture. *J.Phys.D:Appl.Phys.*, Vol., 39, pp.3494-3507

Bruch-Gerhurz, D.; Ruzicka, T. & Kolb-Bachofen, V. (1998). Nitric oxide in human skin: Curret status and future prospects. *J. Invest. Dermatol.*, Vol., 110, pp.1-7

Cals-Grierson, M.M. & Ormerod, A. D. (2004). Nitric oxide function in the skin. *Nitric Oxide*. Vo., 10, pp.179-193

Childress, B. B. & Stechmiller, J. K. (2002). Role of nitric oxide in wound healing. *Biological Research for Nursing*, Vol., 4, pp.5-15

Coven, T.R.; Burack, L.H.; Gilleaudeau, P.; Keogh, M.; Ozawa, M. & Kruege, J.G. (1997). Narrowband UV-B produces superior clinical and histological resolution of moderate-to-severe psoriasis in patients compared with broad-band UV-B_2. *Arch.Dermatol.*, Vol., 133, pp.1514-1522

Fridman, G.; Brooks, A.D.; Balasubramanian, M.; Fridman, A.; Gutsol, A.; Vasilets, V.N.; Ayan, H. & Friedman, G. (2007). Comparison of direct and indirect effects of non-thermal atmospheric-pressure plasma on bacteria. *Plasma Proc.Polymer.*, Vol., 4, pp. 370-375

Fridman, G.; Friedman, G.; Gutsol, A.; Shekhter, A.B.; Vasilets, V.N. & Fridman, A. (2008). Applied plasma medicine. *Plasma Proc.Polymer.*, Vol., 5, pp. 503-533

Gibalov, V.I. & Pietsch, G.J. (2000). The development of dielectric barrier discharges in gas gaps and on surfaces, . *J.Phys.D: Appl.Phys.*, Vol., 33, pp. 2618-2636

Godyak, V.A.; Piejak, R.B. & Alexandrovich, B.M. (1992). Measurements of electron energy distribution in low-pressure RF discharges. *Plasma Sources Sci.Technol.*, Vol. 1, pp. 36-58

Halfmann, H.; Denis, B.; Bibinov, N.; Wunderlich, J. & Awakowicz, P. (2007). Identification of the most efficient VUV/UV radiation fo plasma based inactvation of *Bacillus atrophaeus* spores. *J.Phys.D: Appl.Phys.*, Vol., 40, pp. 5907-5911

Hannuksela, M.; Karvonen, J.; Husa, M.; Jokela, R.; Katajamäki, L. & Leppisaari, M. (1985). Ultraviolet light therapy in atopic dermatitis. *Acta.Dermotol.Venerol.Suppl.(Stockh)*, Vol., 114, pp. 137-139

Itikawa, Y.; Ichimura, A.; Onda, K.; Sakimoto, K.; Takayanagi, K.; Hatano, Y.; Hayashi, M.; Nishimura, H. & Tsurubuchi, S. (1989). Cross section for collisions of electron and photons with oxygen molecules. *J.Phys.Chem.Ref.Data* , Vol., 18, pp. 23-42

Itikawa, Y. (2006). Cross section for electron collisions with nitrogen molecules. *J.Phys.Chem.Ref.Data* , Vol., 35, pp. 31-53

Jekler, J. & Larko, O. (1990). Combined UVA-UVB versus UVB phototherapy for atopic dermatitis: A paired-comparison study. *Journal of the American Academy of Dermatology*, Vol., 22, pp. 49- 53

Kishan Kumar, Y.H.; Rao, G.R.R.; Gopal, K.V.T.; Shanthi, G. & Rao K.V. (2009). Evaluation of narrow-band UVB phototherapy in 150 patients with vitiligo. *Indian J.Dermatol.Venerol.Leprol.*, Vol., 75, pp. 162-166

Kogelschatz, U. (2003). Dielectric-barrier discharges. Their history, discharge physics, and industrial applications. *Plasma Chem.Plasma Proc.,* Vol.,23, pp.1-46

Kozlov, K.V.; Wagner, H.-E.; Brandenburg, R & Michel, P. (2001). Spatio-temporally resolved spectroscopic diagnostics of the barrier discharge in air at atmospheric pressure. *J.Phys.D: Appl.Phys.*, Vol., 34, pp. 3164-3176

Krutmann, J.; Chech, W.; Diepgen, T.; Niedner, R.; Kapp, A. & Schoepf, E. (1992). High-dose UVA_1 theraphy in the treatment of patients with atopic dermatitis. *J.Am.Acad.Dermatol*, Vol., 26, pp.225-230

Kuchenbecker, M; Bibinov, N; Kaemlimg, A; Wandke, D.; Awakowicz, P. & Viöl, W. (2009). Characterization of DBD plasma source for biomedical applications. *J.Phys.D:Appl.Phys.*, Vol. 42, p.045212(10pp)

Legrini, O.; Olivers, O. & Braun, A.M. (1993). Photochemical process of water treatment. *Chem.Rev.*, Vol., 93, pp. 671-698

Libermann, M.A. & Lichtenberg, A.J. (1994). *Principles of plasma discharges and materials processing*. John Wiley & Sons Inc.

Massines, F.; Rabehi, A.; Decomps, P; Gadri, R.B.; Segur, P & Mayoux, C. (1998). Experimental and theoretical study of a glow discharge at atmospheric pressure controlled by dielectric barrier. *J.Appl.Phys.*, Vol., 83, pp.2950-2957

Pancheshnyi, S.V.; Starikovskaia, S.M. & Starikovskii A.Yu. (2000). Collisional deactivation of $N_2(C^3\Pi_u, v= 0,1,2,3)$ states by N_2, O_2, H_2 and H_2O molecules. *Chem.Phys.*, Vol., 262, pp. 349-357

Raizer, Y.P. (1997). *Gas discharge physics*, Springer-Verlag, Berlin, Heidelberg, New York

Rajasekaran, P; Mertmann, P; Bibinov, N; Wandke, D.; Viöl, W. & Awakowicz, P. (2009). DBD plasma source operated in single-filamnetary mode for therapeutic use in dermatology. *J.Phys.D:Appl.Phys.*, Vol. 42, p.225201(10pp)

Rajasekaran, P; Mertmann, P; Bibinov, N; Wandke, D.; Viöl, W. & Awakowicz, P. (2010). Filamentary and homogeneous modes of dielectric barrier discharge (DBD) in air: Investigation through plasma characterization and simulation of surface irradation. *Plasma Proc.Polymer.*, Vol. 7, pp. 665-675

Shekter, A.B.; Serezhenkov, V.A.; Rudenko, T.G.; Pekshev, A.V. & Vanin, A.F. (2005). Benefecial effect of gaseous nitric oxide on the healing of skin wounds. *Nitric oxide: Biolo.Chem.*, Vol., 12, pp. 210-219

Stege, H.; Berneburg, M.; Humke, S.; Klammer, M.; Grewe, M.; Grether-Beck, S.; Boedeker, R.; Diepgen, T.; Dierks, K.; Goerz, G. & Rizicka, T. (1997). High-dose UVA_1

radiation therapy for localized scleroderma *J.Am.Acad.Dermatol*, Vol., 36, pp. 938-944

Stoffels, E. (2007). Tissue processing with atmospheric plasmas. *Contrib.Plasma Phys.*, Vol.,47, pp. 40-48

Stefanovic, I.; Bibinov, N. K.; Deryugin, A.A.; Vinogradov, I. P.; Napartovich, A. P. & Wiesemann, K. (2001). Kinetics of ozone and nitric oxides in dielectric barrier discharges in O_2/NO_x and $N_2/O_2/NO_x$ mixtures. *Plasma Sources Sci.Technol.*, Vol., 10, pp. 406-416

Walsh, J.L; Zhi Cao & Kong, M.G. (2008). Atmospheric dielectric-barrier discharges scalable from 1 mm to 1 m. *IEEE Trans.Plasma Sci.*, Vol., 36, pp. 1314-1315

Part 2

Metallic Biomaterials

7

An Overview of Metallic Biomaterials for Bone Support and Replacement

Anupam Srivastav
College of Engineering & Technology, IFTM, Moradabad, India

1. Introduction

The National Institutes of Health Consensus Development Conference, USA defines a *Biomaterial* as – any substance (other than drugs) or combination of substances, synthetic or natural in origin, which can be used for any period of time, as a whole or as a part of a system which treats, augments or replaces any tissue, organ, or function of the body (Dee et al., 2002). Biomaterials are distinct from other classes of materials because of special requirement of meeting biocompatibility criteria.
Biocompatibility is the ability of a material to perform with an appropriate host response in a specific application. The body tissues respond differently depending upon the type of foreign material. The type of foreign material and its corresponding tissue response is given in Table 1 below.

S. No	Type of Foreign Material	Tissue Response
1	Toxic	Surrounding tissue dies
2	Nontoxic/Biologically Inactive	Fibrous tissue of variable thickness develops
3	Nontoxic / Biologically Active	Interfacial bond forms
4	Nontoxic / Resorbable	Surrounding tissue replaces material

Table 1. Types of Tissue Response to Different Foreign Materials (Hench, L.L and Best, S., 2004).

In case of implant materials, closer it is in biochemical qualities to host's tissue, more difficult it will be for the host in discriminating this implant material as a foreign object in the body. As a result of this, the accepter tissue is likely to respond through the rejection phenomenon of immunoresponce which endangers the host's body. On the other hand, material farther away in biochemical characteristics from the accepter tissue is more likely to be a better biomaterial. The material closer to the host tissue in qualities would perform poorly as they are decomposed faster, digested and absorbed, whereas materials dissimilar in qualities are identified as foreign objects and are isolated from the host tissue by means of a new fibrous membrane (Chiroff et al., 1975). Any bone implant material when used either for joint replacement such as knee and wrist joint or total hip replacement (THR), it comes in contact with sinovial fluids. The sinovial fluid which is an aqueous colloid containing chlorides and phosphates of Na, K and Ca, albumins, globulins, amino-acids, sugars and bacterias, acts as a lubricant in natural joints and reduces friction. So, the implant material for bone must have no or very insignificant reactivity with body fluids (Holmes, 1979).

Modern biomaterials are getting benefited by the developments in the fields of traditional and non-traditional materials. However, there are still two major difficulties associated with biomaterials. The first is an incomplete understanding of the physical, chemical and mechanical functioning of many biomaterials and of the human response to these materials. The second difficulty is that many biomaterials do not perform as desirably as we would like. In view of this, special attention is now being focused on development of materials which are specially suited for specific biomaterial applications, such as for orthopaedic implant applications (Osborn and Newesely, 1980; Kitsugi et al., 1981; LeGeros, R. Z., 1988; Lavernia C. and Schoenung, J. M., 1999), i.e. the materials which show little or no inflammatory response and have sufficient mechanical strength when used as implant material. Therefore Orthopaedic implant material should exhibit: a) complete body stability, b) complete biocompatibility, c) high wear strength d) high mechanical strength, e) low friction (Krause Jr. et al., 1990).

1.1 Structure and properties of human bone

The bones of the body come in a variety of sizes and shapes. The four principal types of bones are long, short, flat and irregular. Bones that are longer than they are wide are called long bones. They consist of a long shaft with two bulky ends or extremities. They are primarily compact bone but may have a large amount of spongy bone at the ends or extremities. Long bones, as shown in Figure 1, include bones of the thigh, leg, arm, and forearm.

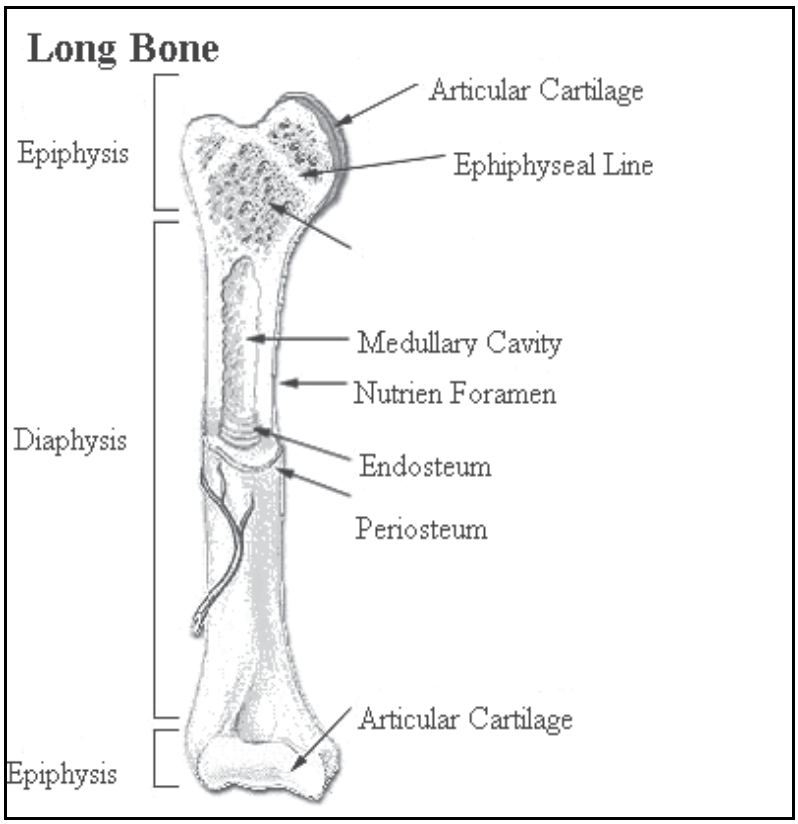

Fig. 1. Parts of a long bone (http://training.seer.cancer.gov)

There are two types of bone tissues: compact and spongy. The names imply that the two types differ in density, or how tightly the tissue is packed together. There are three types of cells that contribute to bone homeostasis. Osteoblasts are bone-forming cell, osteoclasts resorb or break down bone, and osteocytes are mature bone cells. An equilibrium between osteoblasts and osteoclasts maintains bone tissue.

1.2.1 Compact bone

Compact bone, as shown in Figure 2, consists of closely packed osteons or haversian systems. The osteon consists of a central canal called the osteonic (haversian) canal, which is surrounded by concentric rings (lamellae) of matrix. Between the rings of matrix, the bone cells (osteocytes) are located in spaces called lacunae. Small channels (canaliculi) radiate from the lacunae to the osteonic (haversian) canal to provide passageways through the hard matrix. In compact bone, the haversian systems are packed tightly together to form what appears to be a solid mass. The osteonic canals contain blood vessels that are parallel to the long axis of the bone. These blood vessels interconnect, by way of perforating canals, with vessels on the surface of the bone. Human bone thus has a complex hierarchical microstructure that can be considered at many dimensional scales (Nalla et al., 2003). At the shortest length-scale, it is composed of type-I collagen fibres (up to 15 μm in length, 50–70nm in diameter) bound and impregnated with carbonated apatite nanocrystals (tens of nanometres in length and width, 2–3 nm in thickness). These mineralized collagen fibres are further organized at a microstructural length-scale into a lamellar structure, with roughly orthogonal orientations of adjacent lamellae (3–7 μm thick) Permeating this lamellar structure are the secondary osteons (up to 200–300 μm diameter): large vascular channels (up to 50–90 μm diameter) oriented roughly in the growth direction of the bone and surrounded by circumferential lamellar rings.

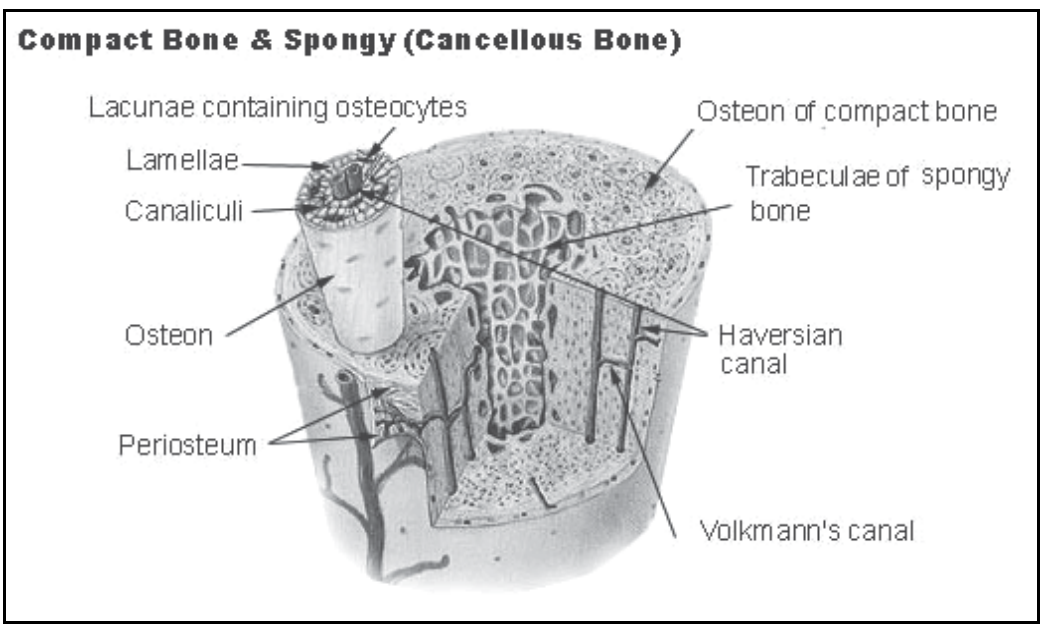

Fig. 2. Internal Structure of Bone (http://training.seer.cancer.gov)

1.2.2 Spongy (cancellous) bone

Spongy (cancellous) bone is lighter and less dense than compact bone. Spongy bone consists of plates (trabeculae) and bars of bone adjacent to small, irregular cavities that contain red bone marrow. The canaliculi connect to the adjacent cavities, instead of a central haversian canal, to receive their blood supply. It may appear that the trabeculae are arranged in a haphazard manner, but they are organized to provide maximum strength similar to braces that are used to support a building. The trabeculae of spongy bone follow the lines of stress and can realign if the direction of stress changes.

1.2.3 Mechanical properties of bone

Bone consists of a collagenous framework upon which calcium salts are deposited mainly as hydroxyapatite. The mature bone is lamellar, its collagenous fibres building regular patterns. In the cancellous bone the collagen bundles lie parallel to the long axis of the trabecula and in the compact (cortical) bone the fibres are disposed in concentric rings around the vascular spaces. Bone can also be considered as consisting of cells and extracellular matrix, with 35% of the matrix being composed of organic and 65% of inorganic ones (Martin, 1998). The inorganic part comprises of calcium salts whereas that of the organic components is collagen and noncollagenous proteins. The noncollagenous proteins form 10% of the organic material. They modulate matrix organization, bind calcium and similar to bone growth factors, regulate bone formation and resorption (Sandberg, 1991).

The mature bone can be divided into cancellous (trabecular) or compact bone, depending of the degree of bone porosity. Compact bone has a porosity of 5-30% and cancellous bone is approximately 30-90% porous, which is the proportion of the volume occupied by non-mineralized tissue (Carter and Heyes, 1977). The diaphyses of long (tubular) bones are composed mainly of compact bone whereas the epiphyses and methaphyses consist of cancellous bone that is continuous with the inner surface of the cortical shell and exists as a three-dimensional, sponge-like lattice composed of plates and columns of bone. The trabeculae divide the interior volume of bone into interconnecting pores of different dimensions. The composition and true densities of compact and trabecular bone are thought to be similar (Galante et al., 1970) as are their microscopic material properties (McEiheney et al., 1970).

A key requirement in bone is compressive strength, and the most important factor in compressive strength is the degree of mineralization. Decreased mineralization results in increased risk of fracture (Wright and Hayes, 1977). A collagen and hydoxyapatite composite is advantageous from a mechanical standpoint. Mineralized tissue can be considered as a porous, two-phase composite consisting of hydroxyapatite crystals embedded in collagen matrix (Lees and Devidson, 1977). On the other hand, increasing collagen intermolecular cross-linking is associated with increased mineralization. The resulting composite structure is much stronger and stiffer due not only to the higher mineral content but also due to the stiffening of the collagen matrix caused by the greater cross-linked density (Memmone and Hudson, 1993; Carter and Springler, 1978). It has been suggested that the longitudinal strength and stiffness of mineralized bone tissue are approximately equal to the strain rate raised to the 0.06 power.

Structurally, bone can be considered as a composite having both solid and a liquid phase. The solid phase consists of mineralized bone tissue and the fluid phase comprises of blood vessels, blood and marrow, nerve tissue, miscellaneous cells and interstitial fluid (McEiheney et al., 1970).

The compressive strength of cortical bone in humans is around 200 MPa and for the femur it is around 17 GPa (Reilly et al., 1974; Reilly and Burstein, 1975). Cancellous bone is much weaker and the results obtained have varied, depending on the location of the bone (Goldstein, 1987). Compressive strengths of 0.15-27 MPa and elastic modulus from 50 to 350 MPa have been reported for cancellous bone (Carter and Heyes, 1977; Scoenfeld, 1974).

Composition	Enamel	Dentin	Bone	Hydroxyapatite (HAp)
Calcium [wt%]	36.5	35.1	34.8	39.6
Phosphorus [wt%]	17.7	16.9	15.2	18.5
Ca/P (molar ratio)	1.63	1.61	1.71	1.67
Sodium [wt%]	0.5	0.6	0.9	--
Magnesium [wt%]	0.44	1.23	0.72	--
Potassium [wt%]	0.08	0.05	0.03	--
Total Inorganic [wt%]	97	70	65	100
Total Organic [wt%]	1.5	20	25	--
Water [wt%]	1.5	10	10	--
Elastic Modulus [GPa]	80	15	0.34-13.8	10
Compressive Strength	10	100	150	100

Table 2. Comparative composition and structural parameters of inorganic phases of adult-human calcified tissues (Dorozhkin and Epple, 2002).

2. Metallic biomaterials

Metals are used as biomaterials due to their excellent electrical and thermal conductivity and mechanical properties. The metals and alloys are used as passive substitutes for hard tissue replacement such as total hip replacement and knee joints; for fracture healing aids as bone plates and screws, spinal fixation devices; and dental implants; because of their excellent mechanical properties and corrosion resistance. Some metallic alloys are used for more active roles in devices such as vascular stents, catheter guide wires, orthodontic archwires and cochea implants.

The orthopaedic surgeons, in dealing with the vast and complex problems of reconstructive surgery and some of the more complicated fracture problems, rely on the use of metallic biomaterials for fixation and replacement of portions of bone. Common use of metals for internal fixation is as old as early 1900s. Metal implants in the form of wire, bands, screws, bolts, staples, nails and plates are applied in the temporary fixation of fractures.

Metals are also used to fabricate implants which are designed to permanently replace the load-bearing function of a bone. Some of these metals and alloys are materials such as Al, In, Sn, Ti, Zr, Cr, Mo, Ta, Fe-Ni-Cr, Co-Ni-Cr, Co-Cr-Mo, Al-V-Ti and Ti-Mo-Pd, 316 L stainless steel and Cobalt based MP 35N alloy. Total hip replacement and joint replacement are some of the areas where these materials are required to remain in the body permanently.

The problems which are associated with these implant materials are not that severe with temporary fixation devices as they are with permanent implants. Some of the common problems associated with these implant materials are biocompatibility (involving local reaction in the tissues near the implant or a general reaction or an allergic reaction distant

from implant site) (Groot, 1980), wear and friction of load bearing implants in the presence of body fluids and effect of wear debris on the surrounding tissues, corrosion and fatigue in the presence of body fluids and lack of skeletal attachments (Rieu et al., 1990; Jarcho, 1981; Damien and Parsons 1990; Klein 1990; White and Shors 1986).
In its role of temporary fixation, the orthopaedic implant is used to bone fragments and keep them from being displaced during the healing process. Once healing is completed, the bone regains its original function and the implant is removed. Due to this reason, any of the aforementioned problems except for biocompatibilities are short-lived. However, any allergic reactions due to implant itself or wear debris or corrosion products cannot be neglected. Also, in future it is likely that orthopedic surgery including total joint replacement will be used in younger patients, who will not only be more active but will require their prostheses for a longer period (Barralet et al., 2002).
The main metals in clinical use are: Titanium and its alloys, Vitallium, Aluminium, Cobalt-Chromium alloys and various Stainless Steels, all of them being inert and biocompatible to acceptable levels (Mofid et al., 1997).

2.1 Stainless steel

The first metal alloy developed specifically for human use was the "Vanadium steel" which was used to manufacture bone fracture plates and screws. Vanadium steel is no longer used in implant fabrication, as its corrosion resistance in vivo is inadequate. Later, another type of stainless steel (18.8 type 302) was used for the purpose due to its more strength and superior corrosion resistance than the vanadium steel. Subsequently, small amount of Mo was added to this type of steel to enhance its corrosion resistance and it became known as 316 stainless steel. After 1950, the percentage of Carbon in it was also reduced from 0.08 wt% to 0.03 wt% to further improve its corrosion resistance and thus it became 316 L stainless steel (Park, and Bronzino, 2000).
The 316 and 316L stainless steels are the most widely used for implant fabrication but ASTM recommends the use of 316 L stainless steel. The composition and important mechanical properties of general 316 L stainless steel are given in Tables 3 and 4 below:

S. No	Chemical Element	Composition (%)
1	Carbon	0.03 max
2	Manganese	2.00 max
3	Phosphorous	0.03 max
4	Sulfur	0.03 max
5	Silicon	0.75 max
6	Chromium	20.00 max
7	Nickel	14.00 max
8.	Molybdenum	4.00 max

Table 3. Composition of 316 L stainless steel (ASTM, F139-86, 1992)

Condition	Ultimate Tensile Strength (MPa)	Yield Strength (0.2% offset) (MPa)	% Elongation	Rockwell Hardness
Annealed	485	172	40	95 HRB
Cold-Worked	860	690	12	--

Table 4. Mechanical properties of 316 L stainless steel implant material (ASTM, F139-86, 1992)

The high Young's modulus (approximately 10 times that of bone) of 316 L stainless steel (as can be seen in Table 8) leads to stress shielding of surrounding bone and hence causes bone resorption.

2.2 Titanium and its alloys

The use of Titanium as implant material dates as late as 1930s. It is primarily due to its lightness (Table 5) and good mechano-chemical properties. There are four grades of unalloyed pure titanium, differentiated on the basis of amount of impurities such as Oxygen, Nitrogen and Iron present in them, which are used for surgical implant applications. The amount of Oxygen in particular affects the ductility and the strength of these grades.

Alloys	Density (g/cm^3)
Ti and its alloys	4.5
316 L stainless steel	7.9
Co-Cr-Mo alloy	8.3

Table 5. Density of some alloys used as implant materials

Among the Titanium alloys, Ti6Al4V whose chemical composition is given in Table 6 is most widely used for implant applications. The main alloying elements in this material are Aluminium and Vanadium. The other alloys of Ti used are Ti13Nb13Zr whose main alloying elements are Niobium and Zirconium and Ti3V11Cr3Al, having Aluminium, Chromium and Vanadium as the alloying elements.

Element	Grade 1	Grade 2	Grade 3	Grade 4	Ti6Al4V
Nitrogen	0.03	0.03	0.05	0.05	0.05
Carbon	0.10	0.10	0.10	0.10	0.08
Hydrogen	0.015	0.015	0.015	0.015	0.0125
Iron	0.20	0.30	0.30	0.30	0.25
Oxygen	0.18	0.25	0.35	0.40	0.13
Aluminium	---	---	---	---	5.50-6.50
Vanadium	---	---	---	---	3.50-4.50
Titanium	Balance	Balance	Balance	Balance	Balance

Table 6. Chemical composition of different grades of Ti and its alloy (ASTM, F67-89, 1992; ASTM, F136-84, 1992).

It can be seen in Table 7, that Ti13Nb13Zr alloy is more ductile and has higher elastic modulus than the Ti6Al4V alloy, as well as pure grades of Ti.

Property	Grade 1	Grade 2	Grade 3	Grade 4	Ti6Al4V	Ti13Nb13Zr
Tensile Strength (MPa)	240	345	450	550	860	1030
Yield Strength (2% offset) (MPa)	170	275	380	485	793	900
% Elongation	24	20	18	15	10	15
% Reduction in area	30	30	30	25	25	45

Table 7. Mechanical properties of different grades of Ti and its alloys (ASTM, F67-89, 1992; ASTM, F136-84, 1992).

The success of Ti as implant material is related to its ability to osseointegrate into the surrounding bone which means it exhibits bioactive properties in the presence of tissue, allowing the growth of bone directly up to its surface. The reason for the success of Ti implants are (i) that it being highly reactive metal, forms a dense, coherent passive oxide film which not only prevents the ingress of corrosion products into the surrounding tissues in the initial stages of implantation (Sutherland et al., 1993) but also steadily grows in-vivo (Moor and Grobe, 1990) which is stoichiometrically similar to TiO_2 which is biocompatible (Kasemo, 1983; Lausmaa and Kasemo, 1990) and (ii) reformation of this surface coating to TiOOH matrix which traps the super oxide (O_2^-) produced during the inflammatory response thus preventing the release of hydroxyl radical (OH*) (Tengvall and Lundstrom, 1989). Ti and its alloys are however more expensive than stainless steels.
These materials have poorer wear characteristics than other metals and alloys used as implant materials and therefore they are now not considered suitable for load bearing surfaces.
Titanium and its alloys have excellent resistance to corrosion. Their Elastic moduli are approximately half that of stainless steels (Table 8) and therefore create less risk of stress protection of bone.

Material	E (GPa)	Yield Strength (GPa)	Tensile Strength (MPa)	Fatigue Limit (MPa)
Stainless steel	190	221-1213	586-1351	241-820
Co-Cr alloy	210-253	448-1606	655-1896	207-950
Titanium	110	485	760	300
Ti6Al4V	116	896-1034	965-1103	620
Cortical Bone	15-30	30-70	70-150	---

Table 8. Comparison of mechanical properties of metallic biomaterial with bone (Brunski, 1996).

2.3 Co-cr alloys

There are basically two types of Co-Cr alloys which are used as implant materials, (i) Co-Cr-Mo alloy which is castable and (ii) Co-Ni-Cr-Mo alloy which is forged. The Co-Cr-Mo alloy is in use in medicine particularly in dentistry since many decades and has found use in artificial joint applications also. The Co-Ni-Cr-Mo alloy is a recent development and has found application as an implant material for heavily loaded joints such as artificial hip and knee. As per American Society for Testing and Materials, the four types of Co-Cr alloys which are recommended for use as surgical implant materials are (i) cast Co-Cr-Mo alloy, (ii) wrought Co-Cr-W-Ni alloy, (iii) wrought Co-Ni-Cr-Mo alloy and (iv) wrought Co-Ni-Cr-Mo-W-Fe alloy. The chemical composition of these alloys is given in Table 9.
Amongst all the above discussed alloys, the Co-Ni-Cr-Mo is most corrosion resistant, whereas the abrasive wear properties are similar to Co-Cr-Mo alloy. However, it is not preferred for bearing surfaces of implants due to its poor frictional properties. The superior mechanical properties (particularly fatigue strength) make it useful for implants which require long service life.

3. Corrosion of metallic implants

The physiological environment is typically modelled as a 37 ^oC aqueous solution, at pH 7.2 (Healy, and Ducheyn, 1992), with dissolved gases (such as oxygen), electrolytes, cells and

Element	Co-Cr-Mo		Co-Cr-W-Ni		Co-Ni-Cr-Mo		Co-Ni-Cr-Mo-W-Fe	
	Min	Max	Min	Max	Min	Max	Min	Max
Cr	27.0	30.0	19.0	21.0	19.0	21.0	18.0	22.0
Mo	5.0	7.0	---	---	9.0	10.5	3.00	4.00
Ni	---	2.3	9.0	11.0	33.0	37.0	15.00	25.00
Fe	---	0.75	---	3.0	---	1.0	4.00	6.00
C	---	0.35	0.05	0.15	---	0.025	---	0.05
Si	---	1.00	---	1.00	---	0.15	---	0.50
Mn	---	1.00	---	2.00	---	0.15	---	1.00
W	---	---	14.0	16.0	---	---	3.00	4.00
P	---	---	---	---	---	0.015	---	---
S	---	---	---	---	---	0.010	---	0.010
Ti	---	---	---	---	---	1.0	0.50	3.50
Co	Balance	Balance	Balance	Balance	Balance	Balance	Balance	Balance

Table 9. Chemical composition of different Co-Cr alloys (ASTM, F75-87, 1992; ASTM, F90-87, 1992; ASTM, F362-84, 1992).

proteins. Immersion of metals in this environment can lead to corrosion, which is deterioration and removal of metals by chemical reaction. During this electrochemical process of corrosion, metallic biomaterials release ions, which reduce the biocompatibility and jeopardize the life of an implant. Most metals such as iron (Fe), Chromium (Cr), Cobalt (Co), Nickel (Ni), Titanium (Ti), Tantalum (Ta), Niobium (Nb), Molybdenum (Mo) and Tungsten (W) that are used to make above discussed alloys to manufacture implants can only be tolerated by the body in minute amounts [51-53]. Sometimes, these metallic elements in naturally occurring forms, are essential in red blood functions (Fe) or synthesis of Vitamin B12 (Co), but cannot be tolerated in large amounts in the body. The biocompatibility of the metallic implants is therefore of considerable concern because these implants can corrode in an in vivo environment. The consequences of corrosion are the disintegration of implant material, which weakens the implant and the harmful effect of corrosion products on the surrounding tissues and organs.

Metallic implants used for load bearing purposes such as joint prostheses, screws and plates undergo different types of corrosion over time such as galvanic corrosion produced by two different types of metal, crevice corrosion and pitting (Gosain, and Persing, 1999;. Cohen, 1962; Traisnel et al. 1990). Further, fretting corrosion may also occur when the oxide film on the metal is damaged such as in case of a screw in a plate hole.

3.1 Corrosion of 316L stainless steel

316 L stainless steel, similar to Ti-6A1-4V and Co-Cr-Mo alloys, etc are known to be prone to corrosion and wear with sign of local macrophage reaction. Metallurgical and histological examination of implants made of biomaterials such as 316 L stainless steel, Co-Cr-Mo alloys and Ti-6AI-4V alloys, etc. show severe corrosion of the surface and even implant failure due to corrosion. In these cases, considerable amount of wear particles are released from metal-on-metal prostheses, which cause long term problems (Groot, 1980). Also, during examination of tissues adjacent to these failed implants, whole gamut of histopathological reactions from acute inflammation, through granulation of tissue to fibrosis, hyaline and a cellular collagens, and necrosis are observed (Jiang and Shi, 1998).

The characteristics tissue reaction to stainless steel implant is cylosiderosis. Stainless steel implants are also known to be associated with pain in its locality (when corroded).
In one of the detailed studies carried out on a retrieved bone plate and screw which was clinically used in-vivo to heal fracture in human patient, investigation was made to study the effect of actual body environment on the implants and to establish the reason for degradation or failure, if any (Srivastav et al., 1992).
For the study a retrieved commercially available standard 316L stainless steel bone plate and screw was selected which was implanted for a period of 2.5 months in a male human patient of about 30 years of age. These plate and screws were explanted as per routine after the healing of the fracture. The chemical composition of the implant material is given in Table 10.

Elements Present	Weight Present
Cr	17
Ni	12
Mo	03
Mn	02
Si	0.75
C	0.03
P	0.03
S	0.03
Fe	Balance

Table 10. Chemical composition of 316L stainless steel used in the study

3.2 Metallurgical investigation of corroded 316 L stainless steel implant

The 316L stainless steel plate and screw were examined by naked eye after cleaning in detergent solution. The areas warranting further examination i.e. those where corrosion was found by naked eye were prepared for observation under scanning electron microscope.
Examination of retrieved implants (bone plate and screws) with naked eyes has shown that the overall surface of the bone plate and the screws had neither any cracks nor fracture or any sign of corrosion, except clearly visible corrosion spots in and around the screw holes of the bone plate as shown in Figures 3 and 4 (Srivastav et al., 1992). It can thus be deduced that during the complete 3 months period of implantation, which can be termed as short in vivo period, 316 L stainless steel serves the purpose of bone support and helps in healing the fracture of the bone without any mechanical failure. Also, there is no significant effect of biological fluids on the material, except some localized effects around a few screw holes.
On closer investigation, it was however found that the screw hole at the top was most corroded and the bottom most hole was not at all corroded. This clearly means that the corrosion which is only localized in the screw hole, starts with the top most screw hole. In addition to this, the corrosion was found to be more pronounced inside and near the screw hole than away from the hole. The reason for this significant observation could be the fact that during this short period of implantation, the body fluids did not have as much effect on the corrosion of the plate as the physiological stresses. The load and the stresses were transmitted from the bone to the plate initially at the top. The stresses were more concentrated near the hole. This resulted in stress induced corrosion of the screw holes.

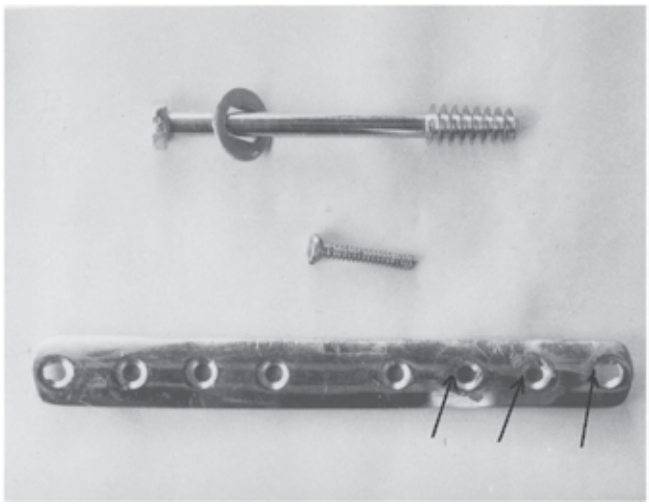

Fig. 3. Retrieved bone plate and screws showing corroded screw holes of the plate (arrow)

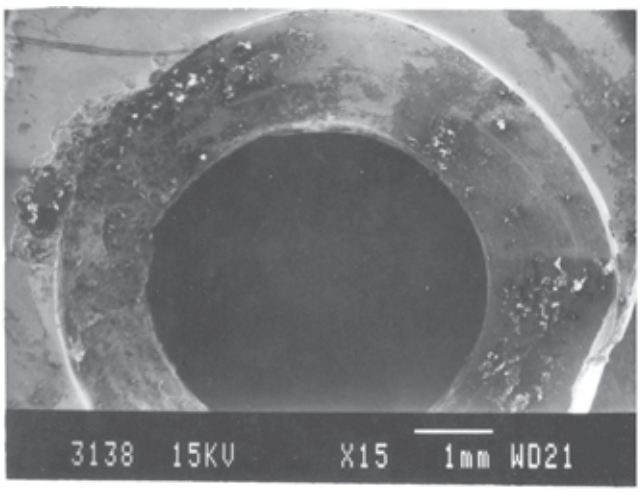

Fig. 4. Corrosion at the counter sunk of screw hole as seen at higher magnification

These corrosion spots are the potential source of metal ions and compounds which are known to have toxic effects on the tissues. The tissues adjacent to the failed or corroded implants have been reported to experience a whole gamut of histopathological reactions from acute inflammation, through granulation of the tissues to fibrosis, hyaline and a cellular collagens, and necrosis (Eggli, 1983).

Further, the improper positioning and mating of screw had resulted in crevice corrosion of the counter sunk of screw hole as has also been confirmed in other studies (Traisnel, 1990). A careful look at the corrosion area at higher magnification under SEM [Figure-5] revealed the presence of corrosion pitting and fretting, which is due to micro movements between the screw and the hole under load and which induces the crevice corrosion.

The reason for the corrosion in and around screw hole is clearly because the plate and screw surface acts as a bearing surface, where under the physiological loads, micromovements of the joint occurs, leading to formation of wear debris. The solubility of this small amount of

metal debris probably increases in presence of body fluids due to the large ratio of bearing surface area to the mass of the debris under higher stresses.

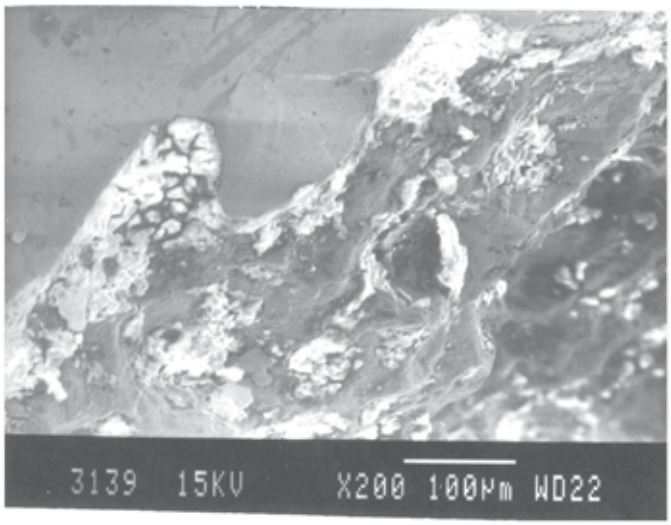

Fig. 5. Corrosion surface at higher magnification showing crevice and pitting corrosion at the countersunk (Srivastav et al., 1992)

Further, Figure-6 clearly indicates that the corrosion was spreading outwardly. This shows that eventually the whole area would have got corroded if implant was allowed to remain in the body for longer period, such as, in case of a permanent implant. This would have weakened the bone plate as found in other studies (Kwon, 2002) and if the use is continued for longer duration (six months to a year), then the bone plate would undoubtedly have fractured and failed under load as has been observed in other studies also. After the implant fails mechanically or functionally, it would require immediate removal as it has been found to induce severe pain and allergic reactions such as cytosiderosis, fibrosis in the adjacent tissues. Also, the release of Iron and its compounds, which are toxic and insoluble, may ultimately lead to cirrhosis of liver and damage to spleen (Jian and Shi, 1998).
It is most unlikely that 316 L stainless steel will behave like a safe metallic biomaterial and hence needs some kind of surface improvement or protection such as protective coatings to minimize the chances of corrosion. These materials also have their limitations and hence search for more biocompatible and reliable is needed.

3.3 An alternative to metallic biomaterials:

The integration of metallic implants to the host bone is promoted by coating them with biocompatible materials such as ceramics. These coatings are deposited by techniques such as PVD, ion plating, sputtering, etc. Using a variety of above mentioned techniques, a wide range of ceramic materials have successfully been deposited and it has been reported in many studies that these coatings significantly improve the wear characteristics of the materials on which they are deposited (Jamison, 1980; Hinterman, 1981; Asanabe, 1987). Similar bioceramic coatings can be effectively used for implants or prosthetic devices. These biocompatible coatings not only provide the implant the necessary tribological properties and the desired corrosion resistance, but also provide them with much desired superior biocompatibility.

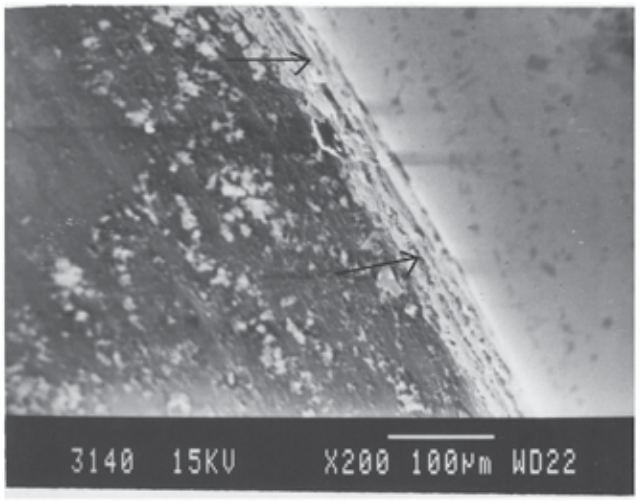

Fig. 6. Spreading of corrosion area from the screw hole to outer surface

Investigations carried out on Al_2O_3 coatings have revealed that the coated implants obtain the necessary damping capability. The damping capability of Al_2O_3 coating, which is an order of magnitude higher than that of the metallic materials used in joint prostheses, absorbs a significant energy before failure (Calderale and Vullo, 1977). The improvement of wear resistance by ion implantation on metallic joint prosthesis has also been studied in detail. Ion implantation is reported to bring improvement in other properties too such as fatigue, corrosion and fretting resistance of these metals and alloys (Rieu 1990). Similarly, the corrosion resistance of these alloys has been strongly enhanced by hard ceramic coatings when deposited by radio-frequency sputtering (Sella, 1990). In recent past, coating of plasma-sprayed apatite has been applied which leads to the formation of a strong bond between bone and metal implant (Geesink et al., 1998; Hamn et al., 199). This is particularly desired in cases such as hip arthroplasty, where implants have a tendency to detach with time. The presence of amorphous phase of HAp in these coatings is an inherent problem in manufacturing high quality implants (Zyman, 1993).

However, the life of a coated implant depends upon the life of these coatings. It is therefore desirable that the implant be coated with materials which are adherent to the implant surface as much as possible, so that it has a very slow and delayed delamination and flaking off. As a result of delamination and flaking off of these, ceramic coatings, hard ceramic particles come in between the rubbing surfaces and cause sudden and extensive damage to the interface. Once negligible or slow wear, thus becomes catastrophic. Hence, these ceramic coated surfaces are useful until the coating is intact (Komvopolouslos et al., 1987). The formation and accumulation of wear debris not only affects the life of the implant but also causes severe tissue reactions and pain, thus necessitating immediate removal. Even in case of implants which are used for non bearing surfaces, the degradation and or delamination of these coatings have been reported (Whitehead et al., 1993; Yie et al., 1995). To minimize this problem of delamination, solution such as use of composite coatings has been suggested (Srivastav and Prakash, 1992) which also has not been studied in detail and no permanent solution has been obtained except for using bulk bioceramics in place of metallic implants.

4. References

American Society for Testing and Materials (ASTM), (1992). F67-89, p.39.
American Society for Testing and Materials (ASTM), (1992). F75-87, p.42.
American Society for Testing and Materials (ASTM) (1992), F90-87, p.47.
American Society for Testing and Materials (ASTM), (1992). F136-84, p.55.
American Society for Testing and Materials (ASTM), (1992). F139-86, p. 61.
American Society for Testing and Materials (ASTM), (1992), F562-84, p.150.
Asanabe, S. (1987). Application of ceramics for tribological components, *Tribology International*, Vol.20, pp. 355-364.
Barralet , J.E., Gaunt , T., Wright, A. J., Gibson I. R. and Knowles, J. C. (2002). Effect of porosity reduction by compaction on compressive strength and microstructure of calcium phosphate cement, *J Biomed Mater Res*., Vol. 63 (1), pp. 1-9.
Brunski, J. B. (1996). Metals In- *Biomaterials Science: An introduction to materials in medicine*, (eds.) Ratner, B.D., Hoffman, A.S., Shoen, F.J. and Lemons, J. E., pp. 37-50, Academic Press, San Diego.
Calderale P. M. and Vullo, V. (1977). Damping capacity of alumina coatings for implants, Proc. *1st European Conf. on Biomaterials*, Strasbourg, pp. 233-237.
Carter D. R. and Heyes, W. C. (1977). The compressive behaviour of bone as a two phase porous structure, *J. Bone Joint Serg*, Vol. 59 A (7), pp. 954-962.
Carter, D. R. and Springler, D. M. (1978). Mechanical properties and composition of cortical bone, *Clinical Orthopaedics,* Vol. 135, pp. 192-217.
Chiroff, R. T, White, E. W., Weber, K. N. and.Roy, (D. M., (1975). Tissue ingrowth of replamineform implant, *J Biomed Mater Res*, Vol. 9(4), pp. 29-45.
Cohen, J. (1962). Corrosion testing of orthopaedic implants, *J. Bone Jt. Surg*., Vol. 44A, pp. 307-316.
Damien C. J. and Parsons, J. R. (1990). Bone Graft and Bone Graft Substitutes: A Review of Current Technology and Applications, *J. Appl. Biomaterials*, Vol. 2, pp. 187-208.
Dee, K. C., Puleo D. A. and Buzios, R. (2002). *An introduction to tissue-biomaterial interactions,* pp. 3, John Willey & Sons Inc., NJ.
Dorozhkin, S. V. and Epple, M. (2002). Biological and Medical Significance of Calcium Phosphates, *Angew. Chem. Int.,* Vol. 41, pp. 3130 -3146
Eggli, P. S., Muller W. and Schenk, R. K., (1983). Porous hydroxyapatite and tricalcium phosphate cylinders with two different pore size ranges implanted in the cancellous bone of rabbits, *Clin. Orthop*., Vol. 232, pp. 127-138.
Galante, J., Rostoker W. and Ray, R. D. (1970). Physical properties of trabecular bone, *Calcified Tisuue Research*, Vol. 5(3), pp. 236-246.
Geesink, R. G., Groot, de K. and Klein, C. P. (1998). Bonding of bone to apetite-coated implants, *J. Bone Joint Surg*., Vol. 70B (1), pp. 17-22.
Goldstein, S. A. (1987). The mechanical properties trabecular bone: dependence on anatomic location and function, *J. Biomech*., Vol. 20(11-12), pp. 1055-1061.
Gosain, A. K. and Persing, J. A. (1999). Biomaterials in the face: Benefits and risks, *J. Craniofac. Surg*, Vol.10(5), pp. 404-414.
Groot, K. de (1980). Bioceramics Consisting of Calcium Phosphate Salts, "*Biomaterials*, Vol. 1, pp 47-50.
Haman, J.D., Chittur, K.K., Crawmer D.E. and Lucas, L.C. (1999). Analytical and mechanical testing of high velocity oxy-fuel thermal sprayed and plasma sprayed calcium phosphate coatings, *J Biomed Mater Res.,* Vol. 48(6), pp. 856-60.

Healy, K. E. and Ducheyn, P. (1992). The mechanisms of passive dissolution of titanium in a model physiological environment, *J. Biomat. Res.,* Vol. 26(3), pp. 319- 338.

Hench, L.L and Best, S.(2004). In-Ratner B.D., et.al., *Biomaterials Science-An Introduction to Materials in Medicine*, p-154, Elsevier Academic Press, U.K.

Hinterman, H.E. (1981). Tribological and protective coatings by chemical vapour deposition, *Thin Solid Films,* Vol. 84, pp.215-243.

http://training.seer.cancer.gov/anatomy/skeletal/tissue.html, (2004).

Holmes, R. E. (1979). Bone regeneration within a coralline hydroxyapatite implant, *Plast Reconstr Surg*, Vol. 63(5), pp. 626-33.

Jamison, W.E. (1980). Friction and wear reduction with tribological coatings, *Thin Solid Films,* Vol. 73, pp. 227-233.

Jarcho, M. (1981). Calcium Phosphate Ceramics as Hard Tissue Prosthetics, *Clin. Orthop. Rel. Res*., Vol.157, 259.

Jiang, G. and Shi, D. (1998). Coating of hydroxyapatite on highly porous Al_2O_3 substrate for bone substitutes, *J. Biomed. Mater. Res. (Appl. Biomater.),* Vol. 43, pp. 77- 81.

Kasemo B. (1983). Biocompatibility of titanium implants: surface science aspects, *J. Proseth. Dent.*, Vol. 6, pp. 832-837, 1983.

Klein, C., Groot, K de, Weiqun, C., Yubao L. and Xingdong, Z. (1994). Osseous substance formation induces in porous calcium phosphate ceramics in soft tissues, *Biomaterials*, Vol. 15(1), pp. 31-34.

Kitsugi, T., Yamamuro, T., Kokubo T.and Ono, M. (1981). Mechanical properties of sintered hydroxyapetite for prosthetic applications", *J. Mater. Sci*., Vol 16, pp. 809-812.

Komvopolouslos, K., Saka, N. and Suh N.P., (1987). The role of hard layers in lubricated and dry sliding, *J. Tribol*, Vol.109, pp. 223-231.

Krause, R. F. Jr., Fuller, E.R. Jr. and Rhodes, J. F. (1990). Fracture resistance behaviour of silicon carbide whisker-reinforced alumina composites with different porosities, *J. Am. Cer. Soc*., Vol. 73 (3), pp. 559-566.

Kwon, S. H., Jun, Y. K., Hong, S. H., Lee, I. S., Kim H. E. and Won, Y. Y. (2002). Calcium phosphate bioceramics with various porosities and dissolution rates, *J. Am. Cer. Soc*., Vol. 85(12).

Lausmaa, G.J. and Kasemo, B. (1990). Surface spectroscopic characterisation of titanium implant materials, *Appl. Surf. Sci*, Vol. 44, pp. 133-146.

Lavernia C. and Schoenung, J. M. (1999). Calcium Phosphate Ceramics as Bone Substitutes, *Ceramic Bulletin*, Vol. 70 (1), pp. 95-100.

Lees S. and Devidson, C. L. (1977). The role of collagen in elastic properties of calcified tissues, *J. Biomech*., Vol. 10(8), pp. 473-486.

LeGeros, R. Z. (1988). Calcium Phosphate Materials in Restorative Dentistry: A Review, *Adv. Dent. Res*., Vol. 2 (1), pp. 164-180.

Martin, T.J. (1998). Cell biology in bone. In- *Baillieres Clinical Endocrinology and Metabolism*, Ed.- Martin, T.J., Ng K. W. and Nicholson, G. C. PLC Press, NY, pp. 1-29.

McEiheney, J. H., Fogle, J. L., Melvin, J. W., Haynes, R. R., Roberts V. L. and Alem, N. M. (1970). Mechanical properties of cranial bone, *J. Biomech*., Vol. 3(5), pp. 495-511.

Memmone, J. F. and Hudson, S. M. (1993). Micromechanics of bone strength and fracture, *J. Biomech*, Vol. 26(4-5), pp. 439-446

Mofid, M. M., Thompson, R. C., Pardo, C. A., Manson, P. N. and Vander Kolk, C. A. (1997). Biocompatibility of the fixation material in the brain, *Plast Reconstr Surg,* Vol.100(1), pp. 14-20.

Moor R. and Grobe, G. (1990), Auger analysis of biomaterials, *PHI Interface*, Vol. 13, pp. 6-9.

Nalla R. K., Kinney J. H. and Ritchie, R. O. (2003). Mechanistic fracture criteria for the failure of human cortical bone, *Nature (Materials)*, Vol. 2, March, pp. 164-168.

Osborn J. F. and Newesely, H. (1980). The material science of calcium phosphate ceramics, *Biomaterials*, Vol. 1 (2) , April, pp. 108-111.

Park, J. B. and Bronzino, J. D. (2000). *Biomaterials: Principles and applications*, p. 2, CRC Press LLC, USA.

Reilly, D. T., Burstein, A. H. and Frankel, V. H. (1974). The elastic modulus of bone", *J. Biomech.*, Vol. 7(3), pp. 271-275.

Reilly D. T. and Burstein, A. H. (1975). The elastic and ultimate properties of bone tissue", J. Biomech., Vol.8(6), pp. 393-405.

Rieu, J., Pichat, A., Rabbe, L.M., Chabrol C. and Robelet, M. (1990). Deterioration mechanism of joint prosthesis materials: several solutions by ion implantation surface treatments, *Biomaterials*, Vol. 11, pp.51-54.

Sandberg, M.M. (1991). Matrix in cartilage and bone development: Current views on the function and regulation of major organic components. *Annual Medicine*, Vol. 23 (3), pp. 207-211.

Scoenfeld, C. M., Lautenschlager E. P. and Mayer P. R. Jr. (1974). Mechanical properties of human cancellous bone in the femoral head, *Med. Bio. Eng.*, Vol. 12(3), pp. 313-317.

Sella, C., Martin, S.C., Lecoeur, J., Bellier, S.P., Harmand, M.F., Naji, A.,. Davidas, J.P. and Chanu, Le A. (1990). Corrosion protection of metal implants by radio-frequency sputtering, *Clinical Materials*, Vol. 5, pp. 297-307.

Srivastav A. and Prakash, R. (1992). Ceramic coated conventional implant materials as biomaterials, *TIB & AO*, Vol. 7(10), pp. 12-17.

Srivastav, A., Prakash, R., Kapoor, A. and Kumar, S. (1992). Metallurgical observations on orthopedical surgical implants which were implanted in-vivo, *TIB & AO,* Vol. 7(1), pp. 18-20.

Sutherland, D.S., Forshaw, P.D., Allen, G.C., Brown I.T. and Williams, K.R. (1993), Surface analysis of titanium implants, *Biomaterials*, Vol. 14(12), pp. 893-905.

Tengvall, P. and Lundstrom, I., (1989). Physico-chemical considerations of titanium as biomaterial, *Clin. Mater.*, Vol. 9, pp. 115-134.

Traisnel, M,. Maguer, le D. and Hilderbrand, H. F. (1990), Corrosion of surgical implants, *Clinical Mater.*, Vol. 5, pp. 309-318.

White, E. and Shors, E. C. (1986). Biomaterial aspects of Interpore-200 porous hydroxyapatite, *Dent. Clin. North Am.*, Vol. 30(1). pp. 49-67.

Whitehead, R. Y., Lacefield W. R. and Lucas, L. C. (1993). Structure and integrity of a plasma sprayed hydroxyapetite coating on titanium, *J. Biomed. Mater. Res.*, Vol. 27, pp. 1501-1507.

Wright T. M. and Hayes, W. C. (1977). Fracture mechanics parameters for compact bone – effect of density and specimen thickness, *J. Biomech.*, Vol. 10(7), pp. 419-430.

Yie, H., Hero, H., Solheim, T., Rorvik A. M. and Haanaes, H. R. (1995). Bonding capacity in bone of HIP-processed HA-coated titanium: Mechanical and histological investigations, *J. Biomed. Mater. Res.*, Vol. 29, pp. 1443-1449.

Zyman, Z., Weng, J., Liu, X., Zhang X. and Ma, Z. (1993). Amorphous phase and morphological structure of hydroxyapetite plasma coatings, *Biomaterials*, Vol. 14(3), pp. 225-228.

8

Characterization and Evaluation of Surface Modified Titanium Alloy by Long Pulse Nd:YAG Laser for Orthopaedic Applications: An *Invivo* Study

M. E. Khosroshahi
Laser and Nanobiophotonics Lab., Biomaterial Group, Faculty of Biomedical Eng., Amirkabir University of Technology, Tehran, Iran

1. Introduction

The overall reaction of the living system body to a foreign material implant is governed by a number of factors that determine whether the implant is accepted or rejected. Biocompatibility and biosafety are considered to imply that the clinical application of a biomaterial should neither cause any adverse reaction nor endanger the life of a patient. Generally, parameters determining the biocompatibility are: i- tissue as a host and ii- implant as a guest. Animal testing is an inherent component of biocompatibility testing. The use of in vitro methods can reduce the extend of animal testing and significantly reduce time and cost of testing. Knowledge of basic mechanisms of cell–material interaction and better understanding of ongoing processes at the cellular level during interaction of anchorage dependent cells can aid in the development of new biomaterials.

Factors affecting the tissue–implant interface from biocompatibility point of view include: general health, immunity factors, roughness, surface porosity, chemical reactions, corrosion and cytotoxicity. Thus, the surface characterization of biomaterials is particularly important if the biocompatibility of implants is to be understood. Possible mechanisms through which a biomaterial can interact with a metallic implant is illustrated in Fig. 1.

A variety of surface properties are believed to be responsible for the favorable performance of titanium implants, in particular the presence of a chemically very stable oxide film protecting the underlying metal from corrosion, the moderate charge of he surface under biological conditions, the very low concentration of charged species within the dissolution products and a dielectric constant ε for titanium oxide close to that of water (ε =78). The result is that the titanium surface does not lead to excessively strong interaction (and denaturation) with proteins in the extra cellular matrix; rather the surface is in some way water like, interacting gently with the hydrophilic outer surface of the protein molecules. Nature of interaction between osteoblast cells and their substrate can influence the ability of these cells to produce an osteoid matrix around an implant which in turn will determine the fate of the implant. Attachment of anchorage dependent cells is the first step in the process of cell surface interactions which in turn can affect subsequent cellular and tissue responses.

Cells attach to substrates through contact sites which are classified as focal contacts. It is important to understand the nature of contact of cells interacting with biomaterials. Changes in cell morphology can be studied using different microscopic techniques like phase contrast and electron microscopy. In case of implants intended for orthopaedic application where close apposition with bone cells is required for better osteointegration, cell attachment and adhesivity play an important role.

2.1 Kinetics of cell - bioimplants interaction

Protein adsorption

Titanium implants were first introduced by Branemark in the early 1970s [Branemark et al., 1977] and have been widely used in the medical and dental fields with excellent clinical results. In addition, bone appears to bond with the titanium oxide layer following implantation, a phenomenon termed osseointergation. However, little is known about the specificity of this process and still less is known about the proteins that adsorb on the titania surfaces. In terms of the host tissue- biomaterial interaction the role of adsorbed proteins is likely to be an important one because subsequent events may depend on the composition and conformation of this protein layer and its tendency to change over time. The final protein film may trigger the activation of complementary are coagulation cascades and other inflammatory response [Kazatchkine & Carreno, 1988; Ziats et al., 1988].

Macromolecules adsorption is a complicated process but for simplicity it can be summarized as follow:

1. The encounter of soluble molecules with surface which is determined by diffusion constants of concentration of different species.
2. A reversible binding of molecules to surface which means that bound molecules may be detached in a very short time.
3. Constant modification of the composition of adsorbed layers ie. some species may be replaced by more adhesive ones. This is the basis of Vroman effect.
4. Progressive conformation changes of adsorbed proteins hence strengthening adhesion.
5. Possibility of continues adsorption with formation of multiple protein layers.

As it is seen in Fig. 1 there are various forces such as Vander walls, bipolar, hydrogen, ionic and covalent that can play an important role in adsorption of protein molecules.

The kinetics of adsorption of proteins to solid surfaces generally consist of a very rapid initial phase that is diffusion limited, followed by a slower phase upon approach to the steady-state value. In the initial phase, the proteins typically adsorb a quickly as they arrive at the relatively empty surface. In the later, slower phase, it is presumably more difficult for the arriving proteins to find and fit into an empty spot on the surface. In as short a time as can be measured after implantation in a living system (<l sec), proteins are already observed on biomaterial surfaces. In seconds to minutes, a monolayer of protein adsorbs to most surfaces. The protein adsorption event occurs well before cells arrive at the surface. Therefore, cells see primarily a protein layer, rather than the actual surface of the biomaterial.

It is thought that the particular properties of surfaces, as well as the specific properties of individual proteins, together determine the organization of the adsorbed protein layer, and that the nature of this layer in turn determines the cellular response to the adsorbed surfaces. The soluble proteins differ from the insoluble proteins is many ways, including the

fact that they are less regular in their amino acid composition and three dimensional structure. The soluble proteins are therefore difficult to describe, this diversity originates in the linear sequence of amino acid that uniquely characterizes each protein.

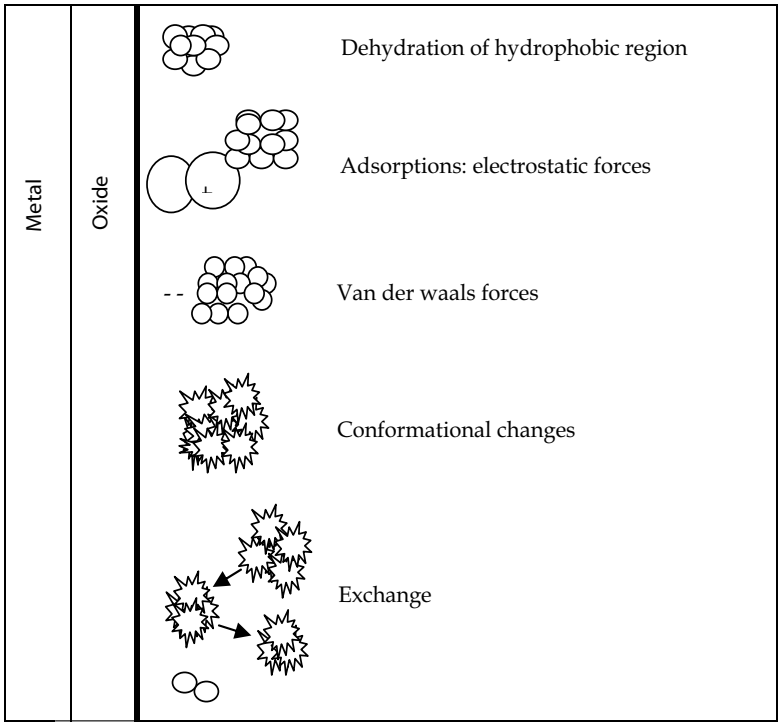

Fig. 1. Routes of protein adsorption to implant surface

It is important to note the particular structure assumed by a protein which in fact is a unique arrangement of the amino acid sequence in three – dimensional space exists for each protein. Furthermore, the spatial arrangement results in the hydrophobic residues preferentially located "inside" the protein where they are shielded from water, while the ionized and polar residues are usually on the outside of the proteins and in contact with the aqueous phase.

This spatial arrangement of the amino acids in proteins has a direct bearing on the interaction of proteins with surfaces because it means that the many residues "buried" inside the proteins may not be able to participate in bond formation with the surface. The folded proteins structures have densities of about 1.4 g/cm^3 in comparison with water's density of 1.0, or the density of most synthetic polymers of about 1.1, this basic fact about proteins reflects their tightly folded structure. Therefore, depending on the two major driving forces for adsorption, namely, the relative bulk concentration of each protein and its intrinsic surface activity, the outcome of the competitive process of adsorption is an adsorbed layer that is richer in some proteins than others; the surface composition differ from the bulk composition.

The thermodynamics of protein adsorption are not easily characterized because the process appears to be essentially irreversible. Because adsorption is irreversible, the calculation of an

equilibrium binding constant from a plot of adsorption versus bulk concentration, and its conversion to a free energy value in the usual way, is not a valid method to obtain thermodynamic information. The enthalpy of the adsorption process has been observed to vary a great deal. The observation of positive enthalpies upon spontaneous adsorption to certain surface must mean that the process is entropically driven in these cases. The net negative free energy characteristic of a spontaneous process means that TΔS is greater than the positive ΔH term in the formula $\Delta G=\Delta H-T\Delta S$. More generally, all protein adsorption processes are thought to be strongly driven by entropic changes. The important of entropic factors in this process can easily be envisaged to arise from changes in water binding to the surface and the protein as well as limited unfolding of the protein on the surface.

The orientation of proteins in the adsorbed phase must also be considered because the proteins are not uniform in properties or structure across their surface. As far as is known, proteins are not very free to rotate once adsorbed, owing to multiple bonding is exposed to the bulk phase. The reactions of proteins in the adsorbed phase may be broadly classed into noncovalent reactions represented by structural transitions, and covalent reactions, such as those that occur with proteins complements.

Cell – adhesion

There is no need to emphasize the potential interest of controlling or even predicting the outcome of encounters between cells and artificial surfaces. Indeed, such knowledge would greatly facilitate the production and use of biomaterial. Three sequential steps of cell surface interaction are considered as:1-protein adsorption , 2-formation of adhesive ligand–receptor bonds, 3-triggering specific cell function such as apoptosis, proliferation, migration (locomotion), differentiation or activation. Cell adhesion is a well – studied mechanism of cell communication. Adhesion is a form of mechanical linkage, of cells to cells and cells to the ECM, and is critically involved in cellular signaling events that control proliferation, survival, apoptosis, shape, polarity, motility, and differentiation. Adhesion is mediated by transmembrane proteins, which connect the interior of the cell to its extra cellular environment (Fig. 2). One major feature biological adhesion that is different from non-biological adhesion such as with household and industrial adhesives is that the former is mediated by chemical signals that often positively or negatively feedback to adhesion and subsequent cell behaviour. In other words, cell adhesion is more than a simple glue to hold cells and tissues together; it is also a critical signaling platform. Integrins and cadherins are two principal classes of molecules mediating primarily cell-ECM and cell-cell adhesion respectively.

Integrins are the best–understood class of adhesion receptors [Hynes, 2002]. They mediate both cell -ECM and cell-cell adhesion, differing based on the cell type and the type of receptor used in the interaction. Integrins, composed of α-β subunit heterodimer, assemble into 24 distinct integrins and bind to proteins in the ECM such as fibronectin, collagen and laminin [Hynes, 2002]. The binding of integrins initiates clustering of integrins to form structures and the recruitment of a host of signaling and adaptor proteins as well as the actin cytoskeleton [Geiger & Bershadsky, 2001]. These focal adhesions are involved in the signaling events that lead to proliferation, motility, cytoskeletal organization, and cell survival [Geiger & Bershadsky, 2001].

Cadherins mediate adhesive contact between cells in structures called adherens junctions, and play a vital role in morphogenec events during development. The best studied of these

are the classical cadherins, which mediate adhesion between adjacent cells by forming homotypic junctions at sites called adherens junctions, and are linked intracellularly to the actin cytoskeleton through beta-catenin and alpha-actinin. Similar to integrins, cadherins too have a mechanical and signaling role. Along with the mechanical that adhesion plays in tissue cohesion, cadherins, like integrins, transmit specific signals to the cell interior through proteins at the adhesion site [Shay-Salit et al., 2002; Yap & Kovacs, 2003]. Both integrin and cadherin adhesions are biochemically regulated and are both dynamic and reversible. Normal cell processes such as the rounding of spread cells during mitosis, cell sorting and migration during embryogenesis, or disease processes such as cancer cell metastasis involve active changes in adhesion strength between cell-ECM and cell-cell contacts. Also, adhesive signals regulate many of the same cell function that soluble growth factors do. Adhesion and growth factor pathways are cooperative: for example, anchorage dependent cells do not grow in the absence of adhesion when they are placed in suspension even in the presence of saturating amounts of growth factors, neither do they grow in the absence of growth factors even when adherent. It is only when both adhesive and growth factor signals are present that growth pathways are optimally activated in cells [Zhu & Assoian, 1995].

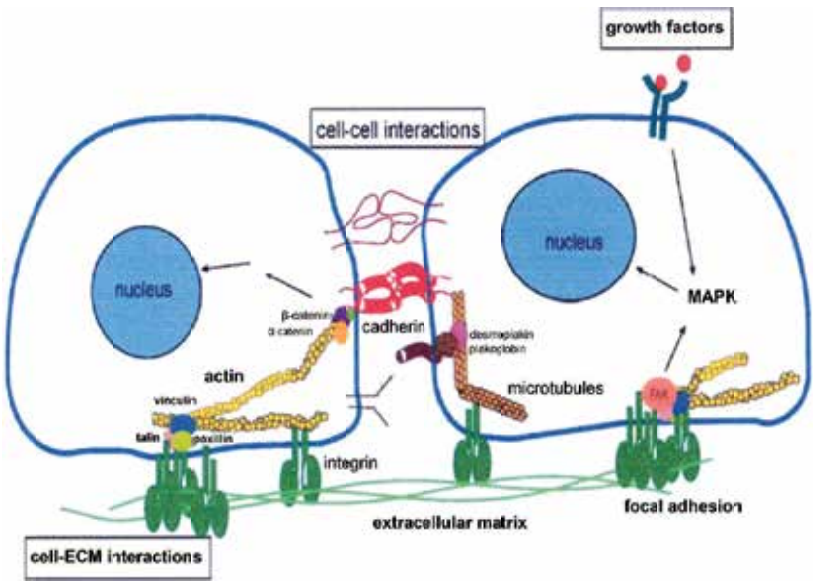

Fig. 2. Representation of the cell–biomaterial surface interaction

However, the effects observed for a given protein have been found to vary substantially depending on the nature of the underlying substrate and the method of immobilization [Neff et al., 1999; Juliano, et al., 1993]. Because cells interact with ECM proteins through receptors that bind to localized regions within their proteins ligands, the biological activity of proteins on the surface will depend upon whether specific active peptide sequence in specific proteins are accessible to the arriving cells [Yamada, 1991]. Many of the ECM proteins, like fibronectin, laminin vitronectin, von Willebrand factor, carry a sequence of amino acid, arginine-glycin- aspartic acid (RGD) to which cells can bind using specific surface receptors called integrins [Pierschbacher & Ruoslahi, 1984; Ruoslahi &

Pierschbacher, 1987]. Integrin-mediated binding of cells is the foundation for cell growth and differentiation and is the dominant mechanism by which cells communicated with noncellular surroundings [Ruoslahi, 1991].

In brief, cell adhesion is involved in various natural phenomena such as embryogenesis, maintenance of tissue structure, wound healing, immune response, metastasis as well as tissue integration of biomaterial. Surface characteristics of materials, whether their topography, chemistry of surface energy, play an essential part in osteoblast adhesion on biomaterials. Thus attachment, adhesion and spreading belong to the first phase of cell/material interactions and the quality of this first phase will influence the cells' capacity to proliferate and to differentiate itself on contact with the implant.

Cell spreading is a combined process of continuing adhesion and cytoplasm contractile meshwork activity. Cell adhesion and spreading are influenced by the physicochemical characteristics of the underlaying solid surface. Other important parameters involved in cell-adhesion are: 1- surface charge, 2- topography, 3- porosity, 4- grooves, 5- mechanicl forces, 6- texture and 7- cellular locomotion. The high ionic strength of the physiological environment and the rapid establishment of ionic equilibrium indicate that surface electrical properties do not significantly influence the formation of initially adsorbing protein layers or adhering cells. The surface topograghy of a biomaterial can be classified according to roughness, texture, and porosity. Porosity is used on a large scale to promote anchorage of biomaterials to surrounding tissue. Grooved substrata were found to induce a certain amount of cellular orientation and locomotion in the direction of the grooves. Applying grooved substrata will therefore induce cell contact guidance. Mechanical forces around an implant, especially in combination with a rough surface, induce abundant formation of fibrous tissue, owing to the constant irritation of the cells. The texture of an implant surface and its morphology can be adapted to the clinical purpose of the biomaterial by such approaches as changing the fabrication process (e.g., woven, knitted, fibrous, grooved, veloured, smooth). Cellular locomotion can be directed by various gradients in the cell environment. For example, after implantation of a biomaterial, granulocytes are attracted by a negative oxygen gradient. Fibroblasts are attracted by agents produced by macrophages.

Orthopaedic implants

Titanium and titanium alloys are largely used as implant materials because of their high in vitro and in vivo biocompatibility and load bearing. It is well established that oseteointegration is an important property of titanium implant surfaces and that the current success rate is satisfactory [Feng et al., 2003; Puleo et al., 1989; Albrektsson et al., 1981]. Osseointegration is a term introduced by Beraceras et al., 1977 to describe a loaded, stable implant in direct contact with bone. Osseointegrated implants differ from ingrown ones that are dependent upon bone growth into surface macroscopic features or irregularities. By contrast, osseointegration is dependent on tissue ingrowth into minute surface features, such as the fundamental asperities of a smooth surface or as postulated for surfaces of various crystalline calcium phosphates (such as calcium hydroxyapatite) or amorphous, bioactive glasses, on direct chemical bonding between tissue and implant. Nevertheless, some concern remains as to the effects of vanadium and aluminum which are known to be cytotoxic [Khosroshahi[(a)] et al., 2007; Deppe et al., 2005]. The chronology of the metal alloys is shown in table 1.

Alloy	Year	Application	Performance issues
Vanadium steel	1912	Bone plates	Corrosion problems
Cast Co-Cr-Mo	1937	Dental devices	Well accepted
Cast Co-Cr-Mo	1938	Orthopaedic implants	Well tolerated, adequate strength
302 stainless steel	1938	Bone plates /screws	corrosions resistance
316 stainless steel	1946	Trauma implants	Better corrosions resistance and strength
Titanium	1965	Hip implants (England)	Corrosion resistance, tissue acceptance
316LVM stainless steel	1968	Trauma implants	Further improvements in corrosion
MP35N	1972	European hip prostheses	High strength
Ti-6Al-4V	1974	Trauma implants	High strength, biocompatibility
Ti-6Al-4V	1976	Hip prostheses	High strength, low modulus
Forged Co-Cr-Mo	1978	Hip prostheses	Highest fatigue strength
22-13-5 stainless steel	1981	Hip implants, trauma	High strength, forgeability
Ti-6A1-7Nb	1982	Hip implants	High strength, biocompatibility
Cold-forged 316LVM	1983	Compression hip screw	High strength
Zirconium 2.5 Nb (zirconia cated)	1994	Joint prostheses	Improved wear resistance, Biocompatibility

Table 1. Chronology of metal alloys in orthopaedic applications

Bone – cell adhesion

The attachment phase occurs rapidly and involves short-tem events like physicochemical linkages between cells and materials involving ionic forces Van der Waal forces, etc and the adhesion phase occurs in the longer term and involving various biological molecules: extra cellular matrix proteins, cell membrane proteins, and cytoskeleton proteins which interact together to induce signal transduction, promoting the action of transcription factors and consequently regulating gene expression. Proteins involved in osteoblast cells adhesion are: 1-Extra cellular matrix proteins, 2- Cytoskeleton proteins, 3- Adhesion molecules.

1.2 Surface modification of Ti-6Al-4V alloy by long Nd:YAG laser for orthopaedic applications

It is possible to change localized areas of metals in order to obtain both compositions and microstructures with improved properties. Titanium and titanium alloys are the most frequently used material for load-bearing orthopaedic implants, due to their specific properties such as high corrosion resistance, surface oxidation layer, high strength and high-temperature resistance [Feng et al., 2003; Ducheyne & El-Ghannam, 1994; Kelly et al., 2003; Wang et al., 2003; Hsu et al., 2004; Tian et al., 2005]. Titanium and its alloys' application like

any other biomaterials involve the creation of at least one interface between the material and biological tissues. Biocompatibility and bioactivity of biomaterials rely on the interactions that take place between the interface of the biomaterials and the biological system [Wang & Zheng, 2009]. It is generally believed that proteins adsorbed on implant surface can play an important role in cell-surface response. Different proteins such as collagen, fibronectin and vitronectin which are acting as ligands are particularly important in osteoblast interaction with surface. Ligands are the junctions which facilitate adhesion of bone cells to implant surface. In another word, more ligand formation implies a better cell-surface interaction [Tirrell et al., 2002; Anselme et al., 2000]. *In vitro* studies can be used to study the influence of surface properties on processes such as cell attachment, cell proliferation and cell differentiation. However, *in vivo* studies must be performed to achieve a complete understanding of the healing process around implants. Previous studies have shown that surface characteristics named above have a significant influence on adhesion, morphology and maturation of cultured osteoblasts [Davies, 1996; Thomas et al., 1997; Cooper et al., 1998; Masuda et al., 1998]. Also, it has been demonstrated that for primary bovine osteoblasts, the wettability is one of the key factors [Meyer, 1993]. In our studies [Khosroshahi[(a)] et al., 2007; Khosroshahi[(b)], 2007; Khosroshahi[(a)] et al., 2008; Khosroshahi[(b)] et al., 2008; Khosroshahi et al., 2009] it is shown that the wettability of the surface can provide a better spreading condition for osteoblast cells due to reduced contact angle. Bearing in mind that the adhesion of bone cells to implant surface consists of two stages. In primary stage the cells must get close enough to surface in an appropriate distance known as focal distance over which the cells can easily be spread over it. In this respect, the wettability can be effective in providing a preferred accessability to surface and thus reaching the focal distance. The secondary stage includes cell-cell attachment which obeys the regular biological facts.

Interface reactions between metallic implants and the surrounding tissues play a crucial role in the success of osseointegration. The titanium and its alloys like some other medical grade metals are the materials of choice for long-term implants. The effect of implant surface characteristics on bone reactions has thus attracted much attention and is still considered to be an important issue [Albrektsson & Johansson, 2001; Buchter et al., 2005; Buchter et al., 2006]. So far as the surface characteristics of the implants are concerned, two main features that can influence the establishment of the osseointegration are the physico-chemical properties and the surface morphology. Cell adhesion is involved in various phenomena such as embryogenesis, wound healing, immune response and metastasis as well as tissue integration of biomaterial. Thus, attachment, adhesion and spreading will depend on the cell-material interaction and the cell's capacity to proliferate and to differentiate itself on contact with the implant [Chung et al., 2003; Bigerelle & Anselme, 2005].

Cell behaviour, such as adhesion, morphologic change and functional alteration are greatly influenced by surface properties including texture, roughness, hydrophilicity and morphology. In extensive investigations of tissue response to implant surfaces, it has been shown that surface treatment of implant materials significantly influences the attachment of cells [Cheroudi et al., 1995; Curtis & Wilkinson, 1998; Brunette & Cheroudi, 1999 ; Lavose-Valereto et al., 2001; Curtis & Clark, 2001 ; Sowden & Schmitz, 2002; Heinrich et al., 2008]. Additionally, these modified surfaces must resist both the mechanical wear and the corrosion [Sighvi & Wang, 1998]. It is therefore important to evaluate systematically the role of different surface properties and to assess the biological performance of different implant materials.

Titanium as a biomaterial implant has an excellent biocompatibility due to the fact that it is highly inert and is not soluble in body fluids and forms a protective oxide layer on the surface [Burser & Schenk, 1991; Breme & Helsen, 1998]. However, pure titanium could leave metal debris in the tissue due to the higher tendency to produce wear in fretting conditions. Therefore numerous titanium alloys like Ti6Al4V with improved physical and mechanical properties have been developed.

The surface morphology, as well as manipulation with the physical state and chemical composition of implant surface may be significant for bone-implant integration. Surfaces are treated to facilitate an intimate contact between bone and implant. So, the tissue response to an implant involves physical factors, depending on implant design, surface topography, surface charge density, surface free energy and chemical factors associated with the composition of the materials. These substrate characteristics may directly influence cell adhesion, spreading and signaling, events that regulate a wide variety of biological functions [Sikavitsas et al., 2001; Sun et al., 2001; Ronold & Ellingsen(a), 2002; Ronold & Ellingsen(b), 2002; Ronold et al., 2003]. Numerous surface treatments including Ion implantation [Beraceras et al., 2002, Tan et al., 2003; Assmann et al., 2007], coating [Vercaigne et al., 1998; Ong et al., 1997; Toth et al., 2002; Morra et al., 2003; Tian et al., 2004; Eisenbarth et al., 2007], shot blast [Darvell et al., 1995; Kawaura et al., 2002; Aparicio et al., 2003], machining [Sahin & Sur, 2004], plasma spray [Khor et al., 1999; Yang & Change, 2001], plasma nitrid [Galvanetto et al., 2002], nitrogen diffusion hardening [Venugopalan et al., 2000] are some of the relatively older techniques in the field of material processing which can be used to change implant's surface topography. But perhaps the laser-assisted method has recently received more attention and has been successful in meeting the new objectives in this field which is mainly because of its wavelength selectivity, coherency, very low thermal or mechanical damage, high accuracy, control and less pollution during laser treatment process.

In fact, optical and kinetics of laser parameters like fluence and pulse number as well as surface physical parameters will affect this process [Gaggl et al., 2000; Wang et al., 2000; Fancsaly et al., 2002; Hollander et al., 2005; Hao(a) et al., 2005]. For example, surface modification of metals by CO_2 [Tritca et al., 2001; Ghoo et al., 2001], HF [Deka et al., 1980; Khosroshahi, 2004], Nd:YAG [Peyer et al., 2000; Yang et al., 2004; Trtica et al., 2009], and diode lasers [Slocombe et al., 2000; Majumdar et al., 2005], titanium alloy by Nd:glass [Joob-Fancsaly et al., 2002], KrF [Deppe et al., 2005], XeCl [Tritca et al., 2005], diode lasers [Hao(b) et al., 2005] and However the recent studies on this subject using short Nd:YAG laser pulses have been performed as *In vitro* with some limited but informative results [Arisu et al., 2006; Turner et al., 2007; Mirhosseini et al., 2007]. Also recently a femtosecond laser was used for surface treatment of titanium in order to determine the potentiall of this technology for surface structuring of titanium implants [Vorobyev & Guo, 2007]. Thus, the success of uncemented orthopaedic implants depends largely upon the body›s ability to synthesize new bone directly onto the surface of the device. This gap allows micromotion of the implant, which loosense the device and ultimately leads to implant failure. Some researchers have attempted to circumvent capsule formation by coating metal implants with the synthetic bone analogue, hydroxyapatite (HA). The synthesis and deposition of new bone onto an implant requires the attachment of osteoblast precursor cells to the implant surface, as well as the subsequent differentiation of these cells. Both of these processes are likely mediated by the integrin family of cell adhesion receptors. Thus, the main intension of this work is to extend the earlier research by carrying out some detailed *In vitro* and *In vivo*

experiments using a long pulse (200μs) Nd:YAG laser radiation on surface physico-chemical changes, surface wettability, corrosion resistance, microhardness and direct osteoblast cells adhesivity of Ti6Al4V with respect to possible orthopaedic applications. Finally, to assess and compare the effects of physico- chemical modifications made on laser treated surface (LTS).

2. Materials and methods

Sample preparation

Rectangular–shaped specimens with 20×10 mm dimensions and the thickness of 2 mm, were made from a medical grade Ti6Al4V (ASTM F136, Friadent, Mannheim- Germany- GmbH) with chemical formulation Ti(91.63%) Al(5.12%) V(3.25%). The samples were divided into three groups of untreated (7 samples), laser treated (14 samples). Prior to treatment, all samples were cleaned with 97% ethanol and subsequently been washed twice by distilled water in an ultrasonic bath (Mattachanna, Barcelona-Spain). A final rinse was done by de-ionized water at a neutral pH to ensure a clean surface is obtained. Finally, an optical microscope with magnification of *x*20 was used to ensure that no particles were left on the sample surface.

Experimental setup

Surface treatment was performed by Nd: YAG laser with 1.06μm wavelength, 200μs pulse duration and pulse energy of 50 J. The output beam was suitably imaged on to the target surface in a 500 μm spot diameter where it scanned the surface at a constant velocity using a motorized XYZ translator. All the experiments were carried out in air at pulse repetition frequency of 1Hz. In order to achieve the optimum surface treatment conditions, the melting, evaporation thresholds and variation of etch depth with fluence were evaluated. Etch depth per pulse variation as a function of laser fluence can be calculated from equation (1).

$$X = a^{-1} \ln\left(F/F_t\right) \tag{1}$$

Where, X is the etch depth, α is absorption coefficient and F_t is the threshold fluence. The samples were then sterilized by de-ionized water.

Surface roughness

The surface micro roughness (R_a) measurements were carried out using a non-contact laser profilemeter (NCLP) (Messtechnik, Germany) equipped with a micro focus sensor based on an auto focusing system. R_a is the arithmetical mean of the absolute values of the profile deviations from the mean line. Five two-dimensional NCLP profiles were obtained for each surface over a distance of 3.094 mm with a lateral resolution of 1μm using a Gaussian filter and an attenuation factor of 60% at a cut-off wavelength of 0.59 mm . The roughness parameters were calculated with the NCLP software similar to that described by Wieland et al. [Wieland et al., 2001].

Surface hardness

Surface microhardness test was carried out with 50 gram load in 10 seconds by a diamond squared pyramid tip (Celemx CMT, Automatic). Each related test was considered at 5 points and reported as an average. The Vickers diamond pyramid hardness number is the applied load divided by the surface area of the indentation (mm^2) which could be calculated from below equation:

$$VHN = \left\{2FSin(136^{\circ}/2)\right\}/d^2 \tag{2}$$

This equation could be re-written approximately as:

$$VHN = 1.854\left(F/d^2\right) \tag{3}$$

Where F is load in Newton, d (mm) is the arithmetic mean of the two diagonals, d_1 and d_2 in mm and VHN is Vickers hardness. The Vickers diamond pyramid indenter is grounded in the form of a squared pyramid with an angle of 136° between faces. The depth of indentation is about 1/7 of the diagonal length. When calculating the Vickers hardness number, both diagonals of the indentation are measured and the mean of these values is used in the above formula with the load used to determine the value of VHN.

Corrosion tests

The standard Tafel photodynamic polarization tests (EG&G, PARC 273) were carried out to study the corrosion behaviour of specimens in Hank's salt balanced physiological solution at 37°C. The procedure for preparing the Hanks solution is schematically shown in The metal corrosion behaviour was studied by measuring the current and plotting the E-logI (Voltage – Current) diagram. The corrosion rate (milli per year (mpy)) was determined using equation:

$$C.R. = 0.129\left(M/n\right)\left(I_{corr}/\rho\right) \tag{4}$$

Where M is the molecular weight, n is the charge, I_{corr} is the corrosion current and ρ is the density.

Surface tension

The surface energy of the samples were determined by measuring the contact angle (θ) of test liquids (diiodo-Methane and water; Busscher) on the titanium plates using Kruss-G40-instrument (Germany).The geometric mean equation divides the surface energy in to two components of dispersive and polar and when combined with Young-s equation it yields:

$$\gamma_{1v}\left(1+\cos\theta\right) = 2\left(\gamma_1^d \cdot \gamma_s^d\right)^{0.5} + 2\left(\gamma_1^p \cdot \gamma_s^p\right)^{0.5} \tag{5}$$

Equation (5) can be rearranged as by Ownes-Wendt-Kaeble's equation:

$$\gamma_{1v}\left(1+\cos\theta\right)\Big/\left(\gamma_1^d\right)^{0.5} = \left(\gamma_s^p\right)^{0.5}\left[\left(\gamma_1^p\right)^{0.5}\Big/\left(\gamma_1^d\right)^{0.5}\right] + \left(\gamma_s^d\right)^{0.5} \tag{6}$$

Where s and l represent solid and liquid surfaces respectively, γ^d stands for the dispersion component of the total surface energy (γ) and γ^p is the polar component.

2.1 In vivo test

Anesthetization

Before depilation of the operation site, the animal was completely anesthetized with midazolam (Dormicum®, Roche, Switzerland) 2.5 mg/Kg intravenously (IV). With any sign of recovery during operation, diluted fluanisone/fentanyl (Hypnorm®, India) was injected slowly until adequate effect was achieved, usually 0.2 ml at a time.

Animal implantation

One untreated sample and two LTS were implanted on femur bone of an eight months male goat weighing 30 Kg. Specimens were steam sterilized before implantation in an autoclave (Mattachnna, Barcelona-Spain). The steam sterilization was conducted under 132 °C, 2 bar and in 45 minutes. All the specimens were labeled by separate codes for further studies. The operation site was shaved and depilated with soft soap and ethanol before surgery; the site was also disinfected with 70% ethanol and was covered with a sterile blanket. In order to proceed with implantation, cortex bone was scraped by osteotom (Mattachnna, Barcelona-Spain) after cutting the limb from one-third end in lateral side and elevating it by a self – retaining retractor. Copious physiological saline solution irrigation was used during the implantation to prevent from overheating. To ensure a stable passive fixation of implants during the healing period, they were stabilized by size 4 and 8 titanium wires (Atila ortoped®, Tehran-Iran) without any external compression forces (Fig. 3).

Fig. 3. Placement of implants in the femur bone of the goat

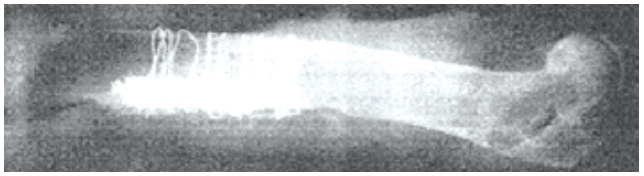

Fig. 4. The X-ray of implants wired to the bone

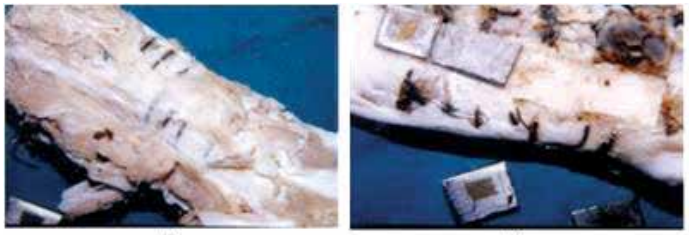

(a) (b)

Fig. 5. Implant removal from the femur bone of the goat: (a) before detachment of the wires, (b) the foot-print of the implants on the bone

After the operation the animal was protected from infection by proper prescribed uptake of Penicillin for first four days and Gentamicine for second four days. During the eight days of

recovery, the goat was administrated with multi-vitamins to help to regain its strength. During this period, the goat was kept in an isolated space under room temperature, ordinary humidity, lightening and air condition, and before it returns to its natural life environment, X-ray radiographs (Fig. 4) were taken in order to ensure that the implant has not been displaced during the maintenance period. It was observed that calus bone had grown in the vicinity of the implant. After five months the animal was sacrificed and the specimens were removed (Fig. 5).

The experiments had been approved by the Yazd School of Veterinary Science (Iran) and its animal research authority and conducted in accordance with the Animal Welfare Act of December 20th 1974 and the Regulation on Animal Experimentation of January 15th 1996. The explantation procedure was performed by first cutting the upper and lower section of femur bone using an electric saw and then the implant together with its surrounding tissues was placed in 4% formalin solution for pathological assessment and SEM.

Cell analysis

Osteoblast cells spreading (ie.lateral growth) on the six implants (three samples for imaging and three samples for coulter counter) was analyzed after removal by SEM(stero scan 360-cambridge) and their spreading condition in a specific area was studied using Image J Program software in three separate regions of each specimen at frequency of 10 cells per each region. The number of attached cells in 1 cm^2 area of each specimen was calculated by a coulter counter (Eppendorf, Germany) using enzyme detachment method and Trypsin-EDTA (0.025 V/V) in PBS media at pH = 7.5. The final amount of attached cell can be studied by plotting cell detachment rate versus time.

Histopathology

Surrounding tissues of specimens were retrieved and prepared for histological evaluation. They were fixed in 4% formalin solution (pH = 7.3), dehydrated in a graded series of ethanol (10%, 30%, 50%, 70% and 90%) and embedded in paraffin after decalcification. Then, 10 μm thick slices were prepared per specimen using sawing microtome technique. A qualitative evaluation of macrophage, osteoblast, osteoclast, PMN, giant cells, fibroblast, lymphocyte was carried out by Hematoxylin and Eosin stain and light microscopy (Zeiss, Gottingen-Germany). The light microscopy assessment consisted of a complete morphological description of the tissue response to the implants with different surface topography. Osteoblasts can be in two states; (a) active, forming bone matrix; (b) resting or bone-maintaining. Those make collagen, glycoproteins and proteoglycans of bone the matrix and control the deposition of mineral crystals on the fibrils. Osteoblast becomes an osteocyte by forming a matrix around itself and is buried. Lacunae empty of osteocytes indicate dead bone. Osteoclast, a large and multinucleated cell, with a pale acidophilic cytoplasm lies on the surface of bone, often an eaten-out hollow-Howship,s lacuna. Macrophages, are irregularly shaped cells that participate in phagocytosis.

SEM of adhered cells

After implants removal, all three group implants were rinsed twice with phosphate buffer saline (PBS) and then fixed with 2.5% glutaraldehyde for 60 minutes. After a final rinse with PBS, a contrast treatment in 1% osmium tetroxide (merck) was performed for 1 hour, followed by an extensive rinsing in PBS and dehydration through a graded series of ethanol from 30% to 90% as described in histology section. After free air drying, surfaces were thinly sputter coated with gold (CSD 050, with 40 mA about 7 min). Cell growth on implanted specimens and their spreading condition in a specific area was analyzed using Image J Program software in three separate regions of each specimen for 10 cells per each region.

Statistical analysis

All calculated data were analyzed by using a software program SPSS (SPSS Inc., version 9.0). The results of variance analysis were used to identify the differences between the cells spread area of the treated and cleaned un-treated samples ($p \leq 0.05$).

3. Results

3.1 Characterization of surface topography

Optical and Mechanical Effects

Fig. 6 indicates the variation of etch depth per pulse with the laser fluence where the metal absorption coefficient (α) can be determined from the slope of the curve using the well known beer logarithmic equation (Eq.1). From Equation 66 the values of α and F_t were found $5\times10^3 cm^{-1}$ and 73 Jcm^{-2}, respectively. It is interesting to notice that, in our case, the interaction of laser radiation with metal surface can be divided into four different regions:

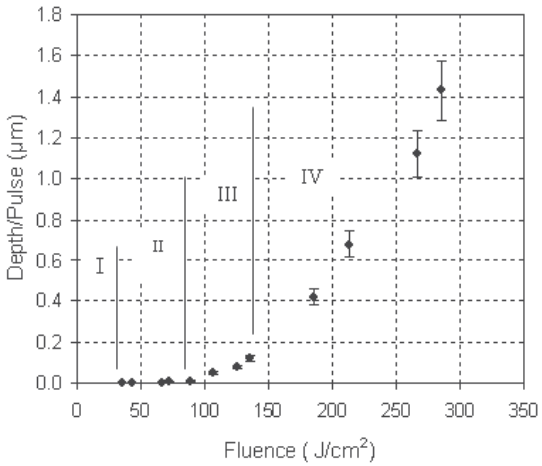

Fig. 6. Variation of etch depth as a function of fluence

In zone I (0-30 Jcm^{-2}) no morphological changes was observed but beyond that where zone II (30-70 Jcm^{-2}) commences, some minor topological alterations such as surface deformations were seen until it reached zone III (70-145 Jcm^{-2}) where the signs of melting were clearly observed and it gradually became stronger. This is consistent with the fact that the power density required for melting (I_m) most metals is in the order of 10^5 Wcm^{-2} which in this case the corresponding range would be between 365-725 $kWcm^{-2}$. It is however, important to notice from metallurgical point of view that melting initially begins due to temperature rise of different elements at the surface. Hence, gradually these island-type molten centers are joined together producing a larger molten pool. Finally, zone IV (145 Jcm^{-2}-above) represents the onset of gradual thermal ablation (vis.vapourization) of Ti6Al4V at ≥145 Jcm^{-2} with corresponding temperature of about 3280(°c). Normally this process is accompanied by the presence of plume which basically is defined as ejection of material from the metal surface as gaseous and solid phase particles. Again this behaviour is expected to become dominant with vaporization intensity threshold of about 10^6 Wcm^{-2}.It is deduced from Fig. 7 that "Incubation" effect or period can be observed at lower fluences where more laser pulses may be needed in order to reach the ablation threshold. It may be worth while to notice that this

effect had also been observed and reported for polymers by other investigators [Srinivassan et al., 1990; Dyer & Karnakis, 1994]. Also to avoid possible errors in assessment and evaluation of interaction process a distinction must be made between the actual physical ablation and surface non-linear roughness (ie. ripples) even occasionally with relatively high amplitudes which in our case this began at about 30 Jcm^{-2}. The etch depth saturation became particularly noticeable at higher fluences, which is mainly thought to be due to an intense interaction between the laser pulse and laser-induced vapor plume, hence causing some effective beam attenuation.

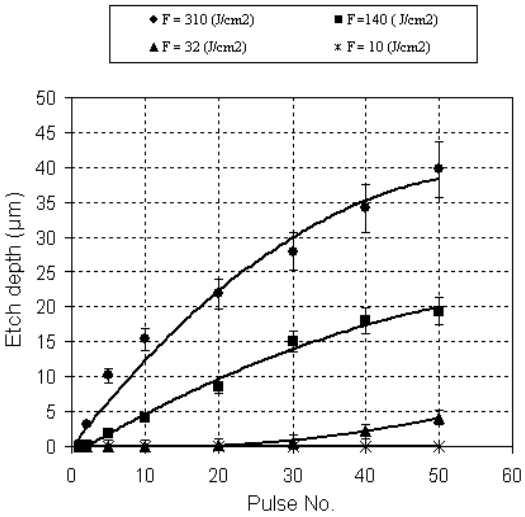

Fig. 7. Variation of etch depth as a function of laser pulse number at constant laser fluences

Since in our experiment the pulse duration is much greater than the thermal relaxation time (i.e. $\tau \approx 200\ \mu s \gg \tau_r \approx \alpha^{-2}/4k \approx 140$ ns) and that the optical absorption depth, α^{-1}, is much smaller than thermal diffusion depth, z_t, (i.e. $\alpha^{-1} \approx 2\mu m \ll z_t \approx 2(k\tau_p)^{1/2} \approx 7.5$ mm) thus, the temperature rise at the end of laser pulse on the surface is given by equation 7:

$$T_f - T_i = \frac{(1-R)F}{\rho c\left(4k\tau_p\right)^{\frac{1}{2}}} \tag{7}$$

With [Ifflander, 2001]:

- T_f, T_i = final and initial surface temperature (°c).
- R = surface reflection (0.6)
- C = specific heat capacity ($0.52 Jg^{-1}°c^{-1}$)
- ρ = density ($4.51 gcm^{-3}$)
- k = diffusivity coefficient ($0.07 cm^2s^{-1}$)
- τ_p = pulse width (200μs)

Fig. 8 indicates the variation of Ti6Al4V surface temperature as a function of laser fluence. Now by assuming the melting and vaporization points of Ti6Al4V about 1668°C and 3280°C respectively and the melting region between (73-145) Jcm^{-2}, using Fig. 6, then it would be sensible to choose zone III as the treatment area (ie. below ablation).

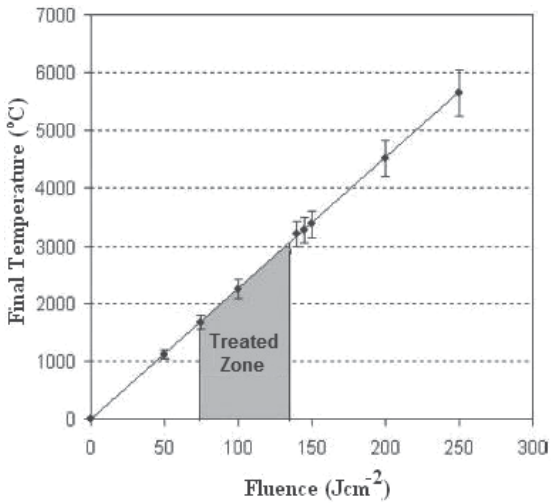

Fig. 8. Plot of Ti6Al4V surface temperature versus laser fluence

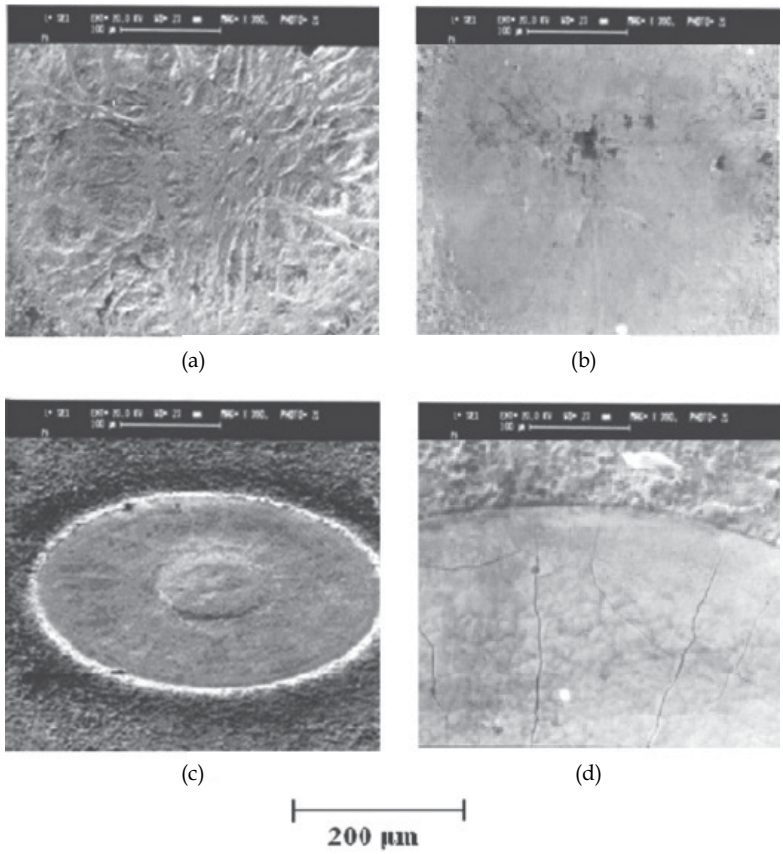

Fig. 9. Surface morphology of Ti6Al4V treated at a) 100 Jcm^{-2} b) 140 Jcm^{-2} c) 210 Jcm^{-2} d) Crack formation at Ti6Al4V surface after 10 pulses treated at 270 Jcm^{-2}

The comparison between morphologically different textures produced by laser at different energy density is shown in Fig. 9. Fig. 9a indicates the interaction effect and the pattern of dentritic melted zone at 100Jcm^{-2}. It is known that as the growth rate of solid phase increases with time during solidification process, the morphology of liquid / solid interface changes from planar to dentritic structure.These random fluctuating dentritic features are in turn defined by dentritc tip radius and their spacing between them [Dreyfus, 1992]. When the laser fluence was increased to 140Jcm^{-2}, the thermal ablation became the dominant mechanism where the irregularities and scratches due to machining and polishing process became smooth after direct laser surface thermal processing, Fig. 9b. Fig. 9c indicates the difference between the untreated and treated surface at 210Jcm^{-2} with formation of some grainy structure and cracks in cellular form in the central zone. Finally when the fluence was increased to 270Jcm^{-2} (Fig. 9d) these cracks became dominant and developed throughout the surface caused by residual mechanical stress originated from steep temperature gradients at the surface during the resolidification process.
Fig. 10 shows an example of the ablation site at fluence of ≥ 250 Jcm^{-2} (i.e. I >1mWcm^{-2}) with 10 pulses which has caused the metal eruption, cracks as well as surface melting. The spectra of colors, mainly blue, are probably because of high temperature plasma roughly defined by $T_e = C.(P\lambda\sqrt{\tau_p})^{1/2}$ where C is a material depending constant, T_e is electrons temperature, P and λ are the laser power and wavelength respectively [Majumdar & Manna, 2003]. Also, other factors like surface composition, solubility degree of alloys and base metal, thermal diffusion and rate of heating-cooling cycle may all have specific roles in crack formation which need a separate attention and analysis.

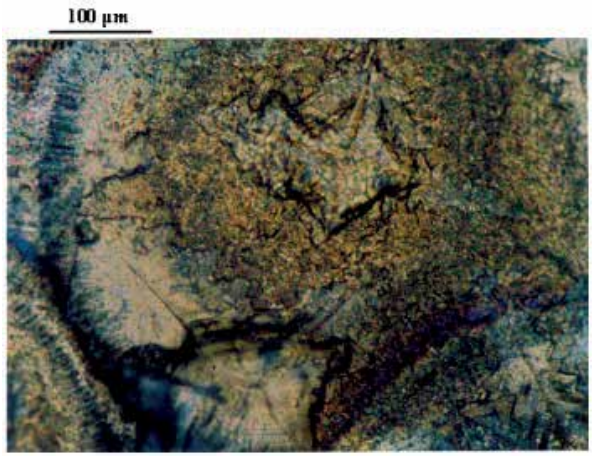

Fig. 10. Plasma –induced damage of titanium at 250 Jcm^{-2} with 10 pulses

Two morphologically different areas i.e. laser treated and untreated (Fig. 11) indicate that the inclusions are disappeared and the scratches due to machining and polishing are sealed due to direct laser surface heating. Ti6Al4V alloy is a (α+β) two-phase alloy with around 6wt% aluminum stabilizing the phase and about 4wt% vanadium stabilizing the β phase. At room temperature, the microstructure at equilibrium consists mainly of primary a phase (hcp) with some retained β phase (bcc). It is also well known that in laser surface melting, steep temperature gradient and thermal cycle leads to some micro structural changes in the heat affected zone within very short time. In particular, the α + β phase transformation

during rapid heating and decomposition of the β phase during rapid cooling. The physical and mechanical properties of Ti6Al4V alloy are known to be sensitive to its microstructure. The Ti-β phase has a diffusivity of two orders of magnitude higher than Ti-α phase and flow stress is strongly influenced by the ratio of these phases [Fan et al., 2005].

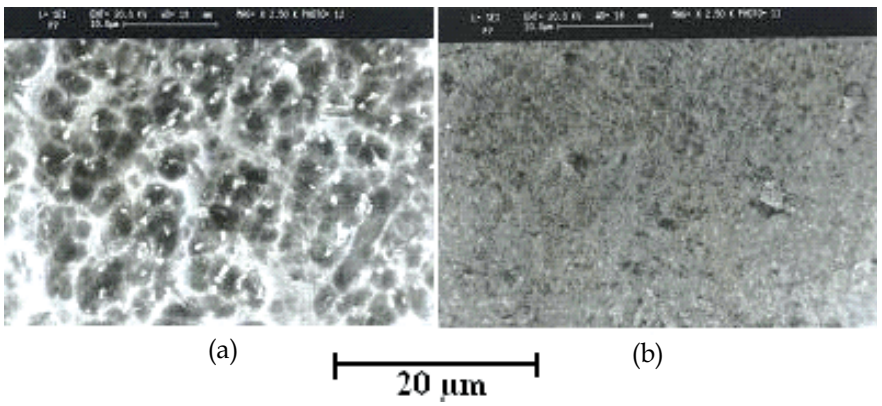

Fig. 11. Scanning electron micrographs of Ti6Al4V surface morphology for: (a) untreated, (b) laser treated at 140 Jcm^{-2} indicating the disappearing of surface scratches by laser surface melting

Surface Roughness

In order to obtain a quantitative comparison between the original and treated surface, the arithmetic average of the absolute values of all points of profile (R_a) was calculated for all samples. A value of 7±0.02 was obtained for laser treated surface at 140 Jcm^{-2}. Also the R_a values for untreated and laser treated at 100 Jcm^{-2} were 12.3±0.03 and 14.2±0.29 respectively. All the calculations were performed for n=5 and reported as a mean value of standard deviation (SD).

Surface Hardness

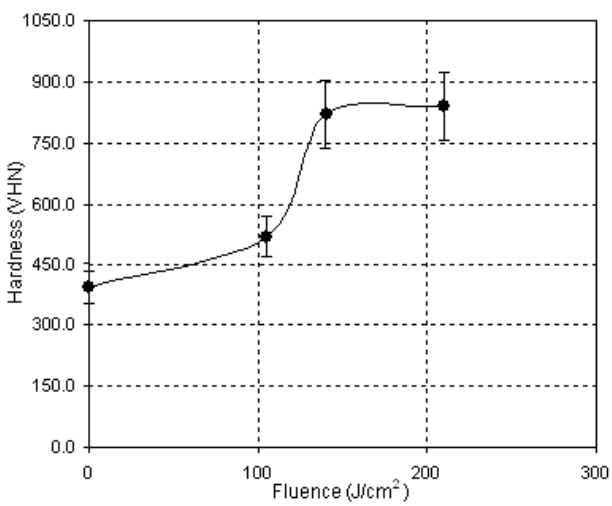

Fig. 12. Variation of surface hardness with fluence

The surface hardness measurements presented in Fig. 12 clearly indicate that micro hardness of the metal increases with laser fluence. Again a non-linear behaviour was observed where initially the values of VHN were increased gradually up to about 100 Jcm^{-2}. Afterwards a sharp increase occurred until the point of plateau was reached at 140 Jcm^{-2} which corresponds to roughly 50% improvement of surface hardness. The surface hardness was found to vary from 377 VHN for MTS to 850 VHN for LTS.
The surface hardness results for all the specimens are illustrated in table 2.

Sample	Microhardness (HVN)
Untreated	394
140 Jcm^{-2}	850

Table 2. Surface hardness tests before and after treatment

EDX analysis
The experimental results of EDX spectroscopy of the untreated and treated samples in the ambient condition is given in Fig. 13. The analysis exhibited K-α lines for aluminium and titanium for both samples, though it was expected carbon to be detected too. It is seen from Fig. 14 that as the laser fluence was increased, the vanadium percent showed a decreasing trend until it reached to its maximum reduced value at about 145Jcm^{-2} where there onwards it was increased again. Perhaps from biomedical applications point of view a better and safer cell attachment and growth can be expected in above condition since surface toxicity has reduced even further. Table 3 indicates the differences in surface elements after treating by laser irradiation.

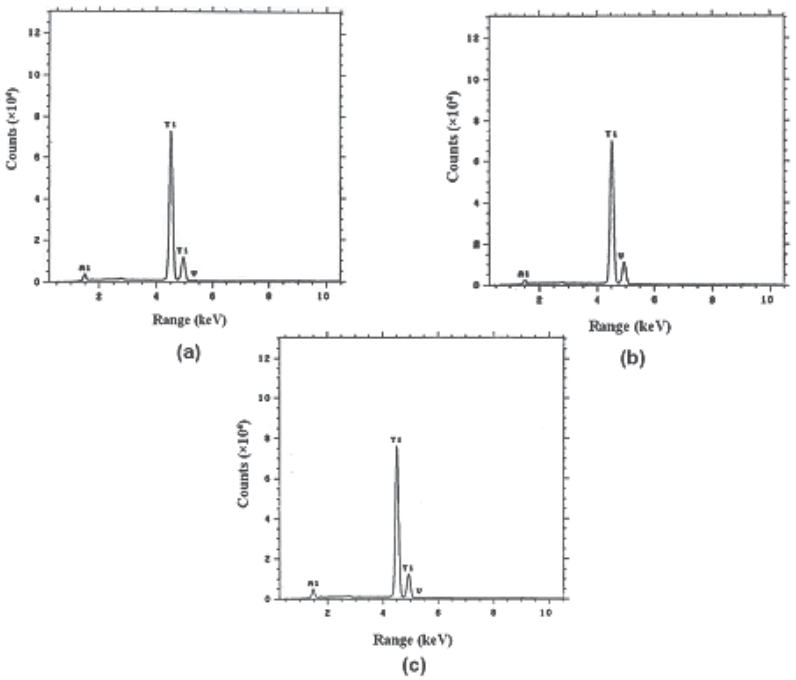

Fig. 13. EDXA analysis of the implant surface, a) untreated b) treated at 100 Jcm^{-2} c)treated at 140 Jcm^{-2}

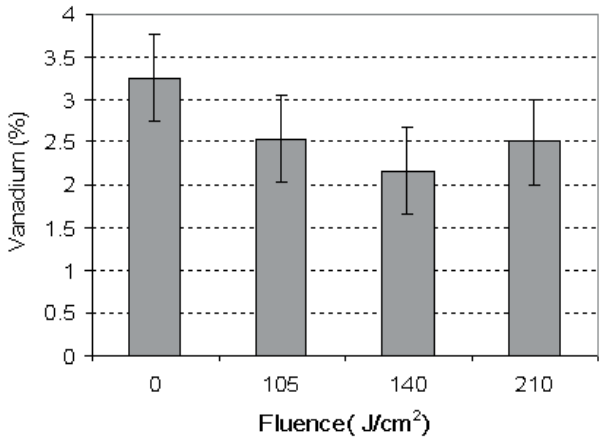

Fig. 14. Changes of Vanadium at the alloy surface as a function of fluence

Element sample	%Al	%V	%Ti
Untreated	5.15	3.25	91.6
140 Jcm^{-2}	3.96	2.54	93.5

Table 3. Surface elements composition before and after treatment

Corrosion test

The comparison of these curves indicates a few important points:1-a value of 1.77×10^{-3} mpy for untreated sample (Fig. 15a), 2- the corrosion rate for laser treated specimen reduced to 0.46×10^{-3} mpy at 140 Jcm^{-2} (Fig. 15b), 3- E_{corr} varied from -0.51 V to -0.21 V after the treatment at 140 Jcm^{-2}. This means that the laser treated specimen is placed at a higher position in the cathodic section of the curve hence releasing hydrogen easier and acts as an electron donor to electrolyte. Therefore, by smoothly reaching the passivation region, a more noble metal is expected to be achieved. The corrosion current (I_{corr}) was decreased from 2.54 µAcm^{-2} to 0.66 µAcm^{-2} after surface laser treatment which can imply a better corrosion resistance.

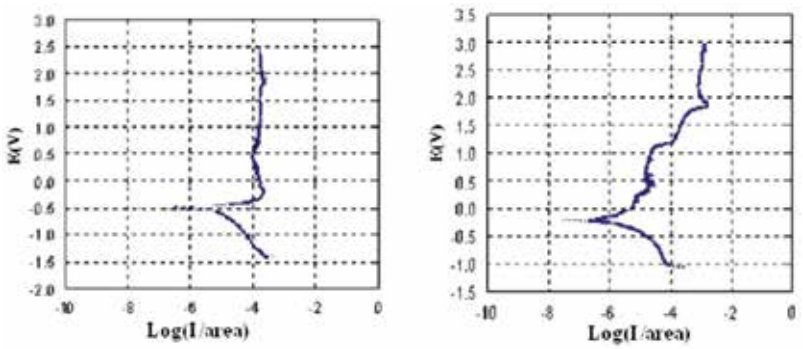

(a) (b)

Fig. 15. Tafel potentiodynamic polarization curves of Ti6Al4V for: (a) untreated, (b) at 140 Jcm^{-2}

Surface tension

The change in surface wettability was studied by contact angle measurement for all specimens treated at 100 Jcm^{-2}, 140 Jcm^{-2} (Fig. 16a). A smoother surface was achieved by laser radiation at 140 Jcm^{-2} which means a reduction in contact angle. This effectively implies an increase in degree of wettability of the metal surface. It is, however, important to note that a smoother surface and enhanced oxygen content, which depends on oxide layer thickness, can both help to reduce the contact angle. This is so because the surfaces with higher concentration of oxygen atoms and more incorporation of oxygen-base polar functionalities of surface exhibit higher wettability (ie. lower contact angle) hence an improvement of biocompatibility, though some believe that, hydrophilicity alone is an inadequate promoter of cell adhesion and retention [Baier et al., 1984]. As a result, it is emphasized that a better cell adhesion can be obtained for the specimens with apparently higher surface energy, rather than higher surface roughness.

According to primary melting centers topology, the surface roughness was increased slightly at 100 Jcm^{-2} (R_a =14.2 ± 0.29). Thus an increase of contact angle occurs from 70° to 80° indicating a lower degree of wettability. Following the laser treatment at 140 Jcm^{-2} the contact angle reduced to 37 ° showing still a more acceptable hydrophilic behaviour. Also, variation of surface tension for all specimens was calculated by measured contact angle. It is known that as contact angle decreases, the related surface tension will be increased. Therefore, a value of 58mN/m was obtained for γ at 140 Jcm^{-2} which is considerably higher than 39mN/m of the untreated sample. The corresponding values of γ for 100 Jcm^{-2} were found as 31mN/m (Fig. 16b).

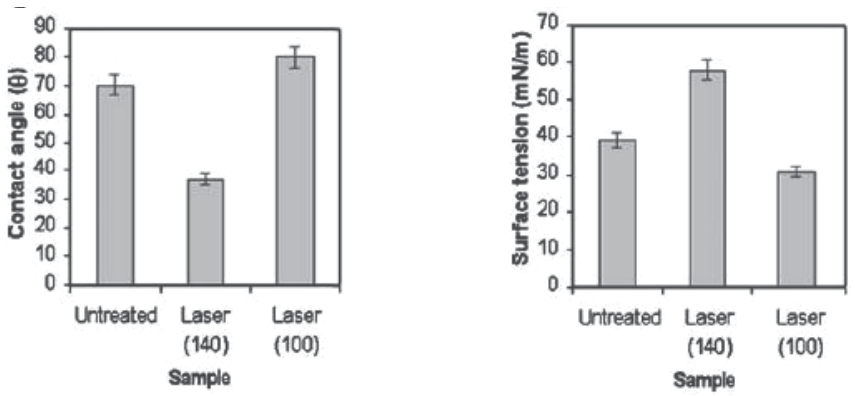

(a) (b)

Fig. 16. Variation of contact angle: (a) and surface tension, (b) with sample surface texture

In vivo

Cell spreading analysis

The experimental results of bone cell growth are given in table 4. As it can be seen, cells spreading over the specimen surface is related to laser fluence and surface texture which was measured by Image J program software (IJP). The highest spreading area (488 μm^2) belongs to the LTS at 140 Jcm^{-2}.

The SEM analysis of attached cells morphology (Fig. 17) indicates that the density of cell network is directly dependent on the laser beam fluence and surface topography. The smooth surface produced at 140 Jcm^{-2} not only caused a dense cell network but also resulted

in a wider area covered by a single cell spreading. Density of network is originated from monolayer attachment (cell-surface) change to multilayer (cell-surface & cell-cell). As it is seen no specific directional spread of attached cells was achieved in laser treated specimens.

Row	Specimens	Spread cell area (μm²)
1	untreated	352 ± 6
2	100 (Jcm^{-2})	316± 10
3	140 (Jcm^{-2})	488 ± 8

Table 4. Bone cells spread over the surface of the implanted specimens (average of ten measurements in three separate regions)

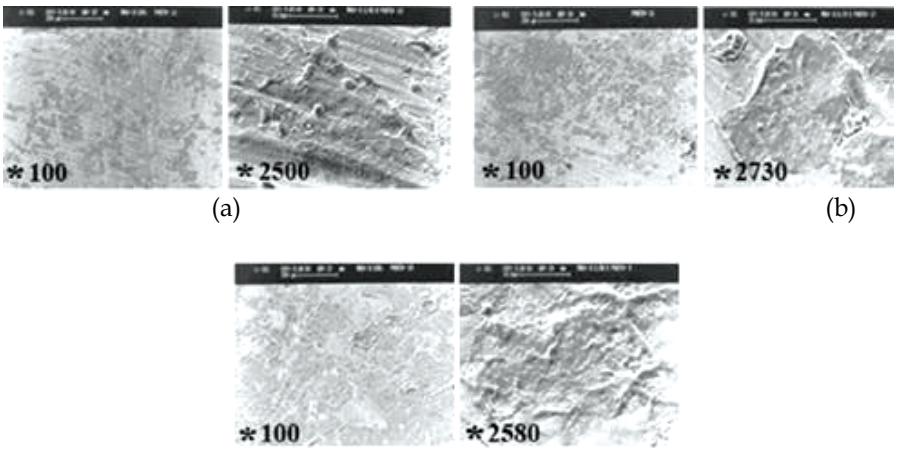

Fig. 17. Scanning electron micrographs of attached cells on the surface for: (a) untreated, (b) at 100 Jcm^{-2}, (c) at 140 Jcm^{-2}

Histopathology

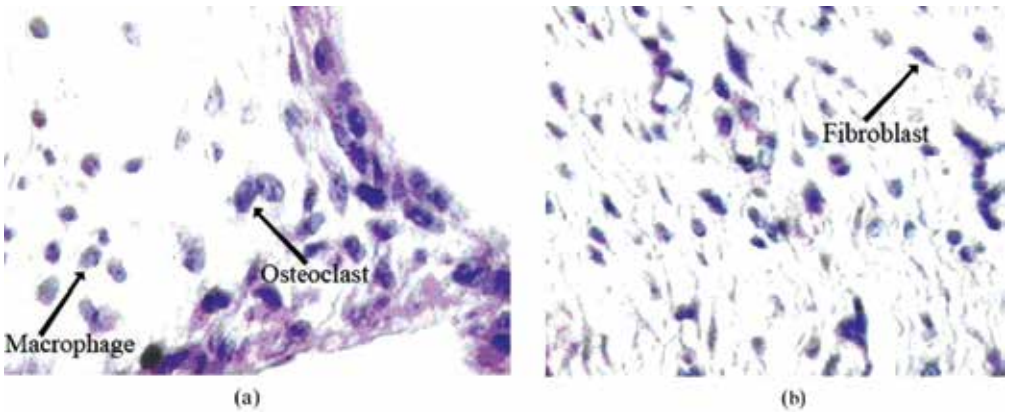

Fig. 18. Light microscopy evaluation of bone tissue for: (a) untreated, (b) samples laser treated at 140 Jcm^{-2}

When the implants were retrieved, no inflammatory reaction was observed inside or around the implants. Mineralized matrix deposition and bone cells were observed on the surface of implants which are formed during the five months implantation. This deposition was found all around of LTS (Fig. 18b) and bone formation was characterized by the occurrence of osteocyte embedded in the matrix. Also the above samples were surrounded by fibroblast and osteoblast cells and the untreated sample (Fig. 18a) showed not only less number of fibroblast cells, also contained osteoclast and polymorpho nuclear leukocytes (PMN).
As it is seen from Fig. 19 the bone tissue nutrition is carried out through the channel in LTS where as it was not observed in the case of untreated sample. No PMN, giant cells and osteoclast were seen in laser treated samples at 140 Jcm^{-2}. Also tissue healing was better conducted near mentioned implant rather than all the other evaluated specimens. Fibroblast and osteoblast cells were also numerous at 140Jcm^{-2}.

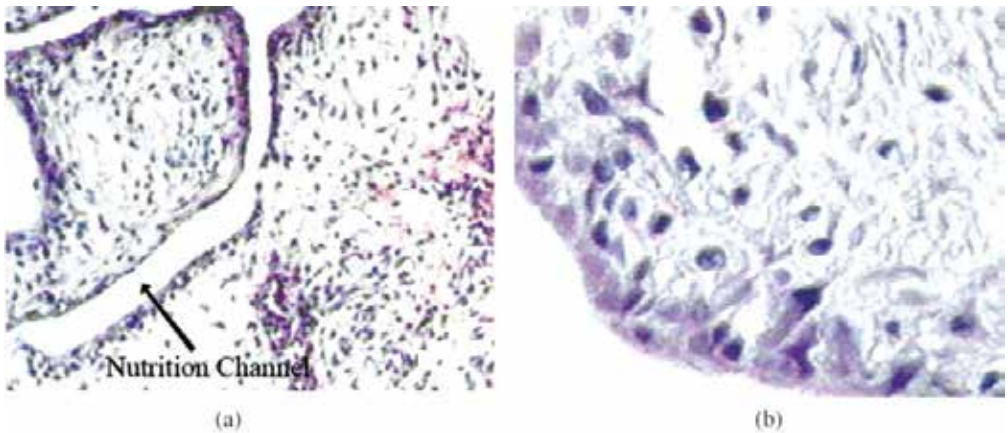

Fig. 19. (a) Light microscopy evaluation of bone tissue for: (a) laser treated sample at 140 Jcm^{-2}, with a nutrition channel shown, and (b) untreated without the channel

In table 5, The symbols indicate the presence of 2-3 cells (+), 3-5 cells (++), more than 5 cells (+++) and lack of cells (-) respectively. No PMN, giant cells and osteoclast were seen in laser treated sample at 140 Jcm^{-2}. Also tissue healing was better conducted near mentioned implant rather than all other evaluated specimens. Fibroblast and osteoblast cells were also numerous in qualitative scales for 140Jcm^{-2} case.

Sample Cell	untreated	100 Jcm^{-2}	140 Jcm^{-2}
Fibroblast	++	+++	+++
Osteoblast	+	++	+++
Giant cell	-	-	-
Osteoclast	+	-	-
PMN	+	+	-
Lymphocyte	++	+++	++
Macrophage	++	+++	++
Healing	+	+	++

Table 5. Qualitative evaluation of histology results of bone tissue around the implants

4. Discussion

The successful incorporation of bone implants strongly depends on a firm longstanding adhesion of the tissue surrounding the implants. The cellular reaction is influenced by the properties of the bulk materials as well as the specifications of the surface, that is, the chemical composition and the topography [Birte et al., 2003; Sikavitsas et al., 2003; Fischer et al., 2004; Peto et al., 2002; Gyorgy et al., 2002]. When one is considering materials for application of orthopaedic implants, it is important to consider a number of factors, such as biocompatibility and surface wettability. The stable oxide layer formed on the implant sample is known to be responsible for the biocompatibility of metal implants. Hence, for a successful laser surface processing of materials some optical and physical parameters must be carefully optimized in order to achieve a desirable surface morphology. It is known that the modification efficiency and the quality is not only the laser fluence dependent but also depend on the spatial and temporal profile of laser beam. Generally the energy absorbed from the laser is assumed to be converted to thermal energy which causes melting, vaporization of the molten material, dissociation or ionization of vaporized material and shock waves in the vapour and the solid. The interaction process was shown to be dependent on the laser fluence, as well as physico-chemical and optical properties of material. Usually, the deposited energy of laser irradiation is converted in to heat on time scale shorter than the pulse duration or laser interaction time. The resulting temperature profile depends on the deposited energy profile and thermal diffusion rate during laser irradiation. Thermal conductivity, K is related to k,ρ and c as follows:

$$K = k\rho c \tag{8}$$

This gives a value of $16WC^{-1}m^{-1}$ which is much larger than the optical absorption depth (≈2μm). Therefore, the heat source is essentially a surface source. As it was defined earlier the vertical distance (z_t) over which heat diffuses during the τ_p is about 7.5 mm wher z_t determines the temperature profile. The condition $\alpha^{-1} << z_t$ is typically applicable for laser irradiation of metals. In the present study, a non-adiabatic thermal evaporation was considered as the dominant mechanism during the laser-material interaction process.
A numerical simulation is performed based on date given in before section in order to evaluate the variation of the surface temperature of Ti6Al4V during the heating and cooling cycles. The fundamental Fourier heat transform describing the surface temperature T(x,t) is:

$$\rho c \frac{\partial T(x,t)}{\partial t} - k\nabla^2 T - Q(x,t) = 0 \qquad 0 < x < \infty \tag{9}$$

where ∇ is laplace transform and Q is the heat source.
During heating ($t<\tau_p$), the solution is

$$T(x,t) = T_h(x,t) = \frac{I_0 \alpha}{K}\left[\left(\frac{4kt}{\pi}\right)^{\frac{1}{2}} \exp\left(\frac{x^2}{4kt}\right) - xerfc\frac{x}{(4kt)^{\frac{1}{2}}}\right] + T_0 \tag{10}$$

During cooling the temperature drops for all $t>\tau_p$ and

$$T(x,t) = T_c(x,t) = \frac{I_0 \alpha}{K}(4k)^{\frac{1}{2}} \left[\sqrt{t} \times ierfc \frac{x}{(4kt)^{\frac{1}{2}}} - \sqrt{t-\tau_p} \times ierfc \frac{x}{\sqrt{4k(t-\tau_p)}} \right] + T_0 \qquad (11)$$

where *i* erf(x) is the integral of the complementary error function defined as

$$ierfc(x) = \int_x^{\infty} erfc(y)dy = \frac{1}{\sqrt{\pi}} e^{-x^2} - xerfc(x) \qquad (12)$$

Equations (10) and (11) have been solven numerically using MATHCAD computer program. Fig. 20 shows the calculated surface temperature variation with the time for the Ti6Al4V irradiated by the pulsed Nd:YAG laser. The followings results can be calculated from the numerical simultion: (i) increasing the laser fluence, increasing the surface temperature, (ii) the numerical results indicate that the maximum temperature achieved at the end of the laser pulse in higher than experimental values of melting (≈1668°C) and vaporization (3280°C) temperatures, (iii) almost all the pulse energy at 70 Jcm^{-2} is expended to raise the surface temperature to melting point at the end of its duration (i.e., 200 μs). (iv) consequently, at high fluences, a less time is required to reach the melting point and hence the rest of available time is spent for vaporization and some thermal damage. (v) at higher fluences the temperature gradient become steeper and hence the probability of an unstable front leading to dentritics or crack increases during the cooling cycle.

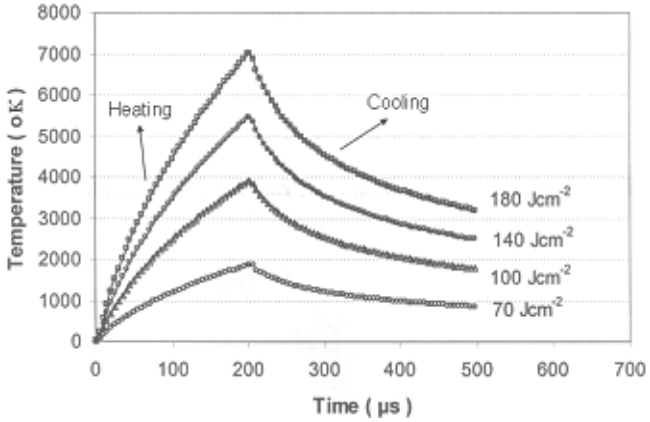

Fig. 20. The surface temperature variation of Ti6Al4V with time

Therefore, selecting a correct energy density for surface treatment has direct influence on the physical properties such as surface microhardness, corrosion resistance, wettability and surface tension of Ti6Al4V. For example, it seems uniformly accepted that any contamination has unfavorable biological effects which may catalyze oxidation, hence it may enhance the dissolution of Ti ions from implant surface. With this view, it is suggested [Joob-Fancsaly, 2002] that the surface contamination decreases the surface energy of material which is responsible for the surface adsorption of proteins at molecular level.

The contact angle decreased by about 50 percent between 100 Jcm^{-2} and 140 Jcm^{-2} when the surface became smoother It is, however important to notice that the NCLP method cannot measure the topographic features smaller than 1μm which are often found on the roughened

implant surface due to its resolving power limitation. Also, a superior microhardness value was exhibited by the sample which can be attributed to grain refinement associated with laser melting and rapid solidification.

Generally a change in the corrosion potential (E_{corr}) indicates a microstructural modification in the metal. For this purpose the Tafel potentiodynamic polarization experiments were performed on Ti6Al4V in Hank's salt balanced physiological solution for untreated, laser treated, see Fig. 15. Also, an increase of corrosion resistance by about 74% which is mainly thought to be due to removal of surface inclusions and surface micro-smoothing during the laser treatment possibly caused by the lateral flow of molten material due to surface tension. Practiclly this means that the laser treated specimen is placed at a higher position in the cathodic section of the curve hence releasing hydrogen easier and acts as an electron donor to electrolyte. Therefore, by smoothly reaching the passivation region, a more noble metal is expected to be achieved which should be more impermeable and resistant to corrosion. This effect was observed within zone III (Fig. 6), where the surface melting was set at about 70 Jcm^{-2}. Among the possible involved mechanisms controlling the hydrodynamics of the melt region is its displacement resulting from the local pressure applied to the liquid surface as a result of the evaporation process. In this range, surface porosities and irregularities of untreated sample became almost completely sealed, Fig. 9b, and the roughness was reduced. Treatment at fluence of 140 Jcm^{-2} with 10 pulses produced optimum effects on the surface. However, at higher fluences in zone IV, even though melting and vaporization are both at work, the surface roughness mainly defined by grainy structure, meandering , cell boundaries, and the cracks were increased, Fig. 9d. This effect may be resulted from reduced thermal accumulation on the metal surface by blasting off the sealed layer hence, causing the increase of local roughness. The grains, surface cooling rate after laser treatment, heat transfer from lower or lateral metal layer and short time duration between heating and cooling cycle may all cause some changes in remaining β phase shape. In addition to surface morphology, the properties of implant materials affect cellular behaviour such as wettability. The wettability of the surface plays an important role with respect to protein adsorption, cell attachment and spreading. It is known that surfaces with high surface free energy are to be more adhesive than those with a low surface free energy. In this study the values for surface free energy showed significant differences between laser treated, untreated sample.

It is also worth to notice that all the samples were treated in an ambient condition and were steam sterilized which would have a great influence on surface composition of Ti especially in TiO_2 formation. It is proved that the samples irradiated by laser beam during the treatment can cause oxygen diffusion through the molten materials and thus to oxidize the titanium [Perez del Pino et al., 2002]. Also the variation of surface oxidation layer thickness depends on steam sterilization process and the time of exposure to air [Sitting et al., 2000]. As the oxygen content of surface increases, the measured contact angle decreases. This is explained by the fact that surfaces with higher concentration of oxygen atoms and more incorporation of oxygen-base polar functionalities of surface exhibit higher wettability (lower contact angle). The local presence of the alloying elements Al and V within the passive oxide film is likely to influence the adsorption of proteins and their conformation on the surface which in turn is expected to modify cell-surface interaction. If cells are affected by the presence of hydroxides on the surface, then developing an understanding of the mechanisms that control this interaction could lead to the optimization of this parameter in

current and future metallic biomaterials [Bern et al., 2004]. Also, other factors like surface composition, solubility degree of alloys and base metal, thermal diffusion and heating/cooling rate may have a specific role in crack formation which needs a separate attention and analysis.

The interaction of living cells with foreign materials is complicated matter, but fundamental for biology medicine and is a key for understanding the biocompatibility. The initial cellular events which take place at the biomaterials interface mimic to a certain extent the natural adhesive interaction of cells with the extra cellular matrix (ECM). The osteoblasts, which play a principal role in bone formation, readily attach to the material surfaces via adsorbed protein layer consisting or RGD containing ligands like fibronectin, vitronectin or fibrinogen. Family of cell surface receptors that provide trans- membrane links between the ECM and the cytoskeleton. The focal point in laser treated surface at 140 Jcm^{-2} should be approximately 10 nm which is convenient for bone cells to get close enough to be activated and attach to the surface in order to form an extra cellular matrix. In this state, bone cells will spread over the smooth surface much more easily and fluently.

Our study showed that surface micro grooves can affect the orientation guidance of bone cells i.e. the deeper grooves were more effective in guiding the cells as it was evaluated by SEM. However, we did not conduct or evaluate systematically the exact effects of grooves depth and size on cell orientation, but our preliminary results were similar to those reported by Xiong & Yang, 2003. It seems, however, that laser treated surface did not regulate the cells shape exactly similar to other investigations. The finding of most research works that the osteoblast cells grow slightly better on the rougher surface indicate the fact the surface topography indeed affects the osteoblast cell proliferation. However, our results showed that laser treated samples at 140 Jcm^{-2} produced a smoother and higher wettability characteristics than the mechanically roughend surface. This finding agrees with Hao[(a)] et al., 2005 and Mirhosseini et al., 2007 works where they found similar results with Ti6Al4V using diode laser. It is, believed that oxygen content of material surface can contribute to the improvement of the wettability characteristics in laser surface modification. It is also equally important from our point of view to carefully distinguish and discuss the difference between the mechanism of cell attachment on a rough surface and cell adhesivity on a smooth surface and their impacts on biomedical engineering [Hao[(a)] et al., 2005, Hao[(b)] et al., 2005].

5. Conclusion

This study was focused on the topographic effects of Ti6Al4V produced by laser radiation on goat bone cell adhesion. The results showed a common feature reported in the previous studies on a variety of cell types and substrates ie, topographic features strongly affects the cell guidance. We found a significant difference when comparing the cells behaviour on unevenly micro grooves and smooth surfaces. This study shows that a smooth surface can exhibit more cell adhesivity compared with micro grooved surface due to its increase of surface tension and reduction of contact angle and probably the presence of oxygen content at the surface. The test confirmed that the highest number of cells are attached to the LTS at 140 Jcm^{-2}. It is also concluded from the SEM, contact angle measurements and preliminary i*n vitro* and *in vivo* tests that Nd:YAG laser can induce a desirable surface modification on Ti6Al4V alloy for cell adhesivity and that a noble and biocompatible Ti alloy with better

physico–chemical properties can be obtained under suitably defined optical condition. Finally it is suggested that more detailed experiments are required and would be useful to distinguish and clarify the difference between attachment on the rough surface via physical anchoring and adhesion on smooth surface by chemical binding. Also, the relation between the grooves size and their orientation must be studied more carefully with respect to cell attachment and their reliability as well as endurance.

6. References

Albrektsson, T.; Branemark, P.I.; Hansson, B.O. & Lindstrom, J. (1981). Osseointegrated titanium implants. *Acta Orthop. Scand*, 52, 155-170

Albrektsson, T. & Johansson, C. (2001). Osteoinduction, osteoconduction and osseointegration. *Eur. Spine. J.*, 10, 96-101

Anselme, K.; Linez, P.; Bigeralle, M.; Maguer, D.L.; Maguer, A.L.; Hardouin, P.; Hildebrand,H.F.; Iost, A. & Leroy, J. M. (2000). The relative influence of the topography and chemistry of Ti-6A1-4V surfaces on osteoblastic cell behaviour. *Biomaterials*, 21, 1567-1577

Aparicio, C.; Javier, F.; Fonceca, C.; Barbosa, M. & planell, J. A. (2003). Corrosion behaviorof commercially pure titanium shot blasted with different material and sizes of shot particles for dental implant applications. *Biomaterials*, 24, 263-273

Arisu, H.D.; Turkoz, E. & Bala, O. (2006). Effects of Nd:YAG laser irradiation on osteoblast cell cultures. *Laser in Medical Sci.*, 21, 175-180

Assmann, W.; Schubert, M.; Held, A.; Pichler, A.; Chill, A.; Kiermaier, S.; Schlösser, K.; Busch, H.; Schenk, K. & Streufert, D. (2007). Biodegradable radioactive implants for glaucoma filtering surgery produced by ion implantation. *Nucl. Inst. and Methods. In phys. Res. Sec.B*, 257,108-113

Baier, R.E ; Meyer, A.E. ; Natiella, J.R. ; Natiella R.R. & Carter, J.M. (1984). Surface properties determine bioadhesive out comes: methods and results. *J. Biomed. Mater. Res.*, 18, 337-355

Beraceras, I.; Alava, I.; Onate, J.I. & Maezto, M.A. (2002). Improved osseointegration in ion implantation-treated dental implants. *Surf. & Coat. Tech.*, 158-159, 28-36.

Birte, G.S.; Neubert, A.; Hopp, M.; Griepentrog, M. & Lange, K.P. (2003). Fibroblast growth on surface modified dental implants: An in vitro study. *J. Biomed. Mater. Res.* 64A,591-599

Bigerelle, M. & Anselme, K. (2005). Bootstrap analysis of the relation between initial adhesive events and long-term cellular functions of human osteoblasts cultured onbiocompatible metallic substrates. *Acta biomaterialia*,1, 499-510

Branemark, P.I.; Hansson, B.O.; Adell, R. & et al. (1977). Osseointegrated implants in the treatment of the edentulous jaw. *Scand. J. Plastic recounst. Surg. Suppl.*, 16, 1-116

Breme, H. J. & Helsen, J.A. (1998). Metals as Biomaterials, West Sussex:wiley, 30-70

Brunette, D.M. & Cheroudi, B. (1999). The effect of topography of micromachined titaniumsubstrate on cell behaviour in vitro and invivo. *J. Biomech. Eng.*, 121, 49-57

Buchter, A.; Kleinheinz, J.; Wiesman, H.P.; Kersken, J.; Nienkemper, M.; Weyhrother, H.; Joos, U. & Meyer, U. (2005). Biological and biomechanical evaluation of bone remodeling and implant stability after using an ostetome technique. *Clin. Oral Implants Res.*, 1, 1-8

Buchter, A.; Joos, U.; Wiessman, H.P.; Seper, L. & Meyer, U. (2006). Biological andbiomechanical evaluation of interface reaction at conical screw-type implant. *Head and Face Med.*, 2, 5-18

Burser, D. & Schenk, R.K. (1991). Influence of surface characteristics on bone integration of titanium implants. A histomorphometric study in miniature pigs. *J. Biomed. Mat. Res.*, 25, 889-902

Bern, L.; English, L.; Fogarty, J.; Policoro, R.; Zsidi, A.; Vance, J.; Drelich, J.; White, C.; Dunahu, S. & Rohly, K. (2004). Effect of surface characteristics of metallic biomaterials on interaction with osteoblast cells.7th World Biomat. Cong., 1121-1122

Cheroudi, B.; Soorany, E.; Black, N. & Weston, L. (1995). Computer-assisted 3D reconstruction of epithelial cells attached to percutaneous implant. *J. Biomed. Mater. Res.*, 29, 371-379

Chung, T.; Liu, D. & Wang, S. (2003). Enhancement of the growth of human endothelial cells by surface roughness at nanometer scale. *Biomaterials*, 24, 4655-4661

Cooper, L. F.; Masuda, T.; Yliheikkila, P.K. & Felton, D. A. (1998). Generolization regardingthe process and phenomena of osseointegration, part II. *Int. J. Oral Maxillofac. Implants*, 13, 163 -174

Curtis, A.S. & Wilkinson, C.D. (1998). Reaction of cells to topography. *J. Biomat. Sci. Polymer Ed.*, 9, 1311-1324

Curtis, A.S. & Clark, P. (2001). The effect of topographic and mechanical properties of materials on cell behaviour. *Crit. Rev. Biocompat.*, 9, 1313-1329

Darvell, B.W.; Samman, N & Luk, W.K. (1995). Contamination of titanium casting by aluminium oxid blasting. *J. Detistry*, 23, 319-322

Davies, J.E. (1996). In vitro modeling of the bone implant interface. *Anatomical Recorded*, 245, 426- 445

Deka, B.; Dyer, P.E. & Sayers, J. (1980). Investigation of laser supported detonation waves and thermal coupling 2.8 μm laser irradiated metal targets. *J. De Physique*, 41, C9-75

Deppe, H.; Warmuth, S.; Heinrich, A. & Korner, T. (2005). Laser- assisted three dimensional surface modifications of titanium implants: preliminary data. *Laser in Med. Sci.*, 19, 229-233

Dreyfus, R.W. (1992). Comparison of the ablation of dielectrics and metals at high and low laser Powers. In: Fogarassy, E and Lazare, S(eds). *Laser Ablation of elrctronic materials. NewYork Elsevier science*, 61-68

Ducheyne, P. & El-Ghannam, A. (1994). Effect of bioactive glass templates on osteoblast proliferation and in vitro synthesis of bone-like tissue. *J. Cell Biochem.*, 56, 162-167

Dyer, P.E. & Karnakis, D. (1994). Analysis of UV radiation transport in polymers exhibiting one-photon incubated absorption. *Appl. Phys. A*, 59, 275-279

Eisenbarth, E.; Velten, D. & Breme, J.(2007). Biomimetic implant coatings. *Biomolecul. Eng.*, 24, 27-32

Fan, Y.; Chen, P.; Yao, Y.L.; Yang, Z & Egland, K. (2005). Effect of phase transformations on laser forming of Ti-6Al-4V alloy. *J. Appl. Phys.*, 98, 1-10

Fancsaly, A. J.; Divinyi, T.; Fazekas, A.; Daroczi, C.S. & karacs, A. (2002). Pulsed laser–induced micro and nanosized morphology and composition of titanium dental implants. *Smart Mater. Struct.*, 11, 819-824

Feng, B.; Weng, J.; Yang, B.C.; Qu, S.X. & Zhang, X.D. (2003). Characterization of surface oxide films on titanium and adhesion of osteoblast. *Biomaterials*, 24, 4663-4670.

Fischer, P.; Leber, H.; Romano, V.; Webber, H.P. & Glardon, R. (2004). Microstructure of near-infrared pulsed laser dintered titanium samples. *Appl. Phys. A*, A78, 1219-1227

Gaggl, A.; Schultes, G.; Muller, W.D. & Karcher, H. (2000). Scaning electron mircroscopical analysis of laser–treated titanium implant surfaces–acomparative study. *Biomaterials*, 21, 1067-1073

Galvanetto, E.; Galliano, F.P.; Fassati, A. & Borgioli, F. (2002). Corrosion resistance properties of plasma nitrided Ti-6AL-4V alloy in hydrochloric acid solutions. *Corrosion science*, 44, 1593-1606

Geiger, B. & Bershadsky, A. (2001). Assembly and mechanosensory function of focal contacts. *Curr. Opin. Cell Biol.*, 13, 584-592

Ghoo, B.Y.; Keum, Y.T. & Kim, Y.S. (2001). Evaluation of the mechanical properties of welded metal in tailored steel sheet welded by CO_2 laser. *J. Mater. Proce. Tech.*, 113, 692-698

Gyorgy, E.; Mihailesco, I.N.; Serra, P. & Morenza, J.L. (2002). Single pulse Nd:YAG laser irradiation of titanium: influence of laser intensity on surface morphology. *Surf. & Coating Tech.* 154, 63-67

Hao(a), L.; Lawerence, J. & Li, L. (2005). The wettability modification of bio-grade stainlesssteel in contact with simulated physiological liquids by the means of laser irradiation. *Appl. Sur. Sci.*, 247, 453-457

Hao(b), L.; Lawerence, J. & Li, L. (2005). Manipulation of the osteoblast response to a Ti-6Al-4V titanium alloy using a high power diode laser. *Appl. Sur. Sci.*, 247, 602-606

Heinrich, A.; Dengler, K.; Koerner, T.; Haczek, C.; Deppe, H. & Stritzker, B. (2008). Laser-modified titanium implants for improved cell adhesion. *Laser in Medical science*, 23, 5-58

Hollander, D.; Walter, M.; Wirtz, T.; Paar, O. & Eril, H. (2005). Structural mechanical and invitro characterization of individually structured Ti-6Al-4V produced by direct laser forming. *Biomaterials*, 27, 955-963

Hsu, R.; Yang, C.; Huang, C. & Chen, Y. (2004). Electrochemical corrosion properties of Ti-6Al-4V implant alloy in the biological environment. Mat. Sci. Eng. A, 380, 100-109.

Hynes, R.O. (2002). Integrins: bidirectional, allosteric signaling machines. *Cell*, 110, 673- 687

Ifflander, R. (2001). Solid State lasers for Materials Processing. Berlin, Springer series in optical sciences

Joob-Fancsaly, A.; Divinyi, T.; Fazekas, A.; Daroczi, C.S.; Karacs, A. & Peto, G. (2002). Pulsed laser-induced micro- and nanosized morphology and composition of titanium dental implants. *Smart. Mater. Struct.*, 11, 819-824

Juliano, D.J.; Saaedra, S. S. & Truskey, G.A. (1993). Effect of the conformation orientation of adsorbed fibronectin on endothelial cell spreading and the strength of adhesion. *J. Biomed Mater. Res.*, 27, 1103-1113

Kawaura, H.; Kawahara, H.O.; Nishino, K. & Saito, T. (2002). New surface treatment using shot blast for improving oxidation resistance of Ti-6Al-4V base alloys. *Mate. Sci. & Eng. A*, 329-331, 589-595

Kazatchkine, M.D. & Carreno, M.P. (1988). Activation of the complement system at the interface between blood and artificial surfaces. *Biomaterials, (Ibid),* 9, 30-35

Kelly, R.G.; Schully, J.R. & Shoesmith, D.W. (2003). Electrochemical Techniques in Corrosion Science and Engineering. *New York:Marcel Dekker Inc.*, 81,240

Khor, K.A.; Vreeling, A.; Dong, Z.L. & Cheang, P. (1999). Laser treatment of plasma sprayed HA coatings. *Mater. Sci. Eng. A*, 266, 1-8

Khosroshahi, M.E.; Valanejad, A. & Tavakoli, J. (2004). Evaluation of mid-IR laser radiation effect on 316L stainless steel corrosion resistance in physiological solution. *Amirkabir J. of Sci. & Tech.*,15, 107-115

Khosroshahi(a), M.E.; Mahmoodi, M. & Tavakoli, J. (2007). Characterization of Ti-6Al-4V implant surface treated by Nd:YAG laser and emery paper for orthopaedic applications. *Appl. Surf. Sci.*, 253, 8772-8781

Khosroshahi(b), M.E.; Tavakoli, J. & Mahmoodi, M. (2007). Analysis of bioadhesivity of osteoblast on titanium by Nd:YAG laser. *J. of Adhesion*, 83, 151-172

Khosroshahi(a), M.E.; Mahmoodi, M.; Saedinasab, H. & Tahriri, M. (2008). Evaluation of mechanical and electrochemical properties of laser surface modified Ti-6AL-4V for biomedical application: in vitro study. *Surf. Eng*., 24, 209-218

Khosroshahi(b), M.E.; Mahmoodi, M. and Tavakoli, J. & Tahriri, M. (2008). Effect of Nd:YAG laser radiation on Ti6AL4V alloy properties for biomedical application. *J. of Laser Applications*, 20, 209-217

Khosroshahi, M.E.; Mahmoodi, M. & Saedinasab, H. (2009). In vitro and in vivo studies of osteoblast cell response to a Ti6A14V surface modified by Nd:YAG laser and silicon carbide paper. *Laser Med. Sci*., 24, 925-939

Lavose-Valereto, I.C.; Wolynec, S.; Deboni, M.C. & Konig, B.J.R. (2001). In vitro and in vivo biocompatibility testing of Ti-6Al-7Nb alloy with and without plasma- sprayed hydroxyapatite coating. *J. Biomed. Mater. Res*., 58, 727-733

Majumdar, J.D. & Manna, I. (2003). Laser processing of materials. *Sadhana J*., 28, 495-562.

Majumdar, J.D.; Pinkerton, A.; Liu, Z. & Manna, I. (2005). Microstructure characterisation and process optimization of laser assisted rapid fabrication of 316L stainless steel. *Appl. Surf. Sci*., 247, 320- 373

Masuda, T.; Yliheikkila, P.K.; Felton, D.A. & Cooper, L.F.(1998). Generolization regarding the process and phenomena of osseointegration: in vivo studies, *part I. Int. J. Oral Maxillofac. Implants*, 13, 17- 29

Meyer, U.; Szulezewsli, D.H.; Moller, K.; Heide, K. & Jones, D.B. (1993). Attachment kinetics and differentiation of osteoblasts on different biomaterial surfaces. *Cells Mater*., 3, 129-140

Mirhosseini, N.; Crouse, P.L.; Schmidth, M.J.J. & Garrod, D. (2007). Laser surface micro-texturing of Ti-6Al4V substrates for improved cell integration. *Appl. Sur. Sci*., 253, 7738-7743

Morra, M.; Cassinelli, C.; Cascardo, G.; Cahalan, P.; Cahalan, L.; Fini, M. & Giardion, R. (2003). Surface engineering of titanium by collagen immobilization. Surface characterization and in vitro and in vivo studies. *Biomaterials*, 24, 4639- 4654

Neff, J.A.; Tresco, P.A. & Caldwell, K.D. (1999). Surface modification for controlled studies of cell-ligand interactions. *Biomaterials*, 20, 2377-2393

Ong, J.L.; Raikar, G.N. & Smoot, T.M. (1997). Properties of calcium phosphate coating before and after exposure to simulated biological fluid. *Biomaterials*, 18, 1271-1275

Perez del Pino, A.; Serra, P. & Morenzo, J.L. (2002). Oxidation of titanium through Nd:YAG laser irradiation. *Appl. Sur. Sci*., 8129, 1-4

Peto, G.; Karacs, A.; Paszti, Z.; Guczi, L.; Diviny, T. & Joob, A. (2002). Surface treatment of screw shaped titanium dental implants by high intensity laser pulses. *Appl. Sur. Sci.*, 186, 7-13

Peyer, P.; Scherpereel, X.; Berthe, L.; Carboni, C.; Fabbro, R. & Lemaitre, C. (2000). Surface modification induced in 316L steel by laser peening and shot- peening: Influence of pitting corrosion. *Mat. Sci. Eng.*, 280, 294-302

Pierschbacher, M.D. & Ruoslahi, E. (1984). Cell attachment activity of fibronectin can be duplicated by small synthetic fragments of the molecule. *Nature*, 309, 30-33

Puleo, D.A.; Holleran, L.A.; Doremus, R.H. & Bizios, R. (1989). Osteoblast responses to orthopaedic implant materials in vivo. *J. Biomed. Mater. Res.*, 25, 11- 23

Ruoslahi, E. & Pierschbacher, M.D. (1987). New perspectives in cell adhesion: RGD and integrins. Science, 238, 491-497

Ruoslahi, E. (1991). Integrins. *J. Clin Invest*, 87, 1-5

Ronold[(a)], H.J. & Ellingsen, J.E. (2002). Effect of micro-roughness produced by TiO_2 blasting-tensile testing of bone attachment by using coin shaped. *Biomaterials*, 23, 4211-219

Ronold[(b)], H.J. & Ellingsen, J.E. (2002). The use of a coin shaped implant for direct insitu measurment of attachment strenght for osseointegrating biomaterials surface. *Biomaterials*, 23, 2201- 2209

Ronold, H.J.; Lyngstadaas, S.P. & Ellingsen, J.E. (2003). A study on the effect of dual blasting with TiO_2 on titanium implant surfaces on functional attachment in bone. *J. Biomed. Mater. Res.*, 67A, 524-530

Shay-Salit, A.; Shushy, M.; Wolfovitz, E.; Yahav, H.; Breviatrio, F.; Dejana, E. & Resnick, N. (2002). VEGF receptor 2 and the adherencs junction as a mechanical transducer in vascular endothelial cells. *Proc, Natl, Acad, Sci U.S.A.*, 99, 9462-9467

Sowden, D. & Schmitz, J.P. (2002). Self-drilling and self-tapping screws in rat bone: an ultra structural study of the implant interface. *J. Oral Maxillofac Surg.*, 60, 294-299

Sighvi, R. & Wang, D.I. (1998). Review: Effects of substratum morphology on cell physiology. *Biotech. Bioeng.*, 43, 764-771

Sikavitsas, V.I.; Temenoff, J.S. & Mikos, A.G. (2001). Biomaterials and bone mechano transduction. *Biomaterials*, 22, 2581-2593

Sun, R.L.; Mao, J.F. & Yang, D.Z. (2001). Microstructural characterization of NiCr, BSiC, laser clad layer on titanium alloy substrate. *Surf. & Coat. Technol.*,150, 199-204

Sahin, Y. & Sur, G. (2004). The effect of Al_2O_3 ,TiN and Ti (C,N) based CVD coating on tool wear in maching metal. *Surface & Coating*, 179, 349-355

Slocombe, A.; Taufik, A. & Li, L. (2000). Diod laser ablation machining of 316L stainless steel powder/polymer composite material: effect of powder geometery. *Appl. Surf. Sci.*, 168, 17-20

Srinivassan, R.; Braran, B. & Casey, K. (1990). Nature of "incubation pulse" in the ultraviolet laser ablation of polymethyl methacrylate. *J. Appl. Phys.*, 68, 1842-1847

Sikavitsas, V.I.; Dolder, J.; Bancroft, G. & Jansen, J. (2003). Influence of the in vitro culture period on the in vivo performance of cell/titanium bone tissue- engineered constructs using a rat cranial size defect model. *J. Biomed. Mater. Res.*, 67A, 944-951

Sitting, C.; Textor, M.; Spencer, N.D.; Wieland, M. & Vallotton, H. (2000). Surface characterization of implant materials c.pTi, Ti-6Al-4V band Ti-6Al-4V with different pretreatments. *J. Mater. Sci.*, 10, 35-46

Tan, L.; Dodd, R. & Crane, W. (2003). Corrosion and wear- corrosion behaviour of NiTi modified by plasma source ion implatation. *Biomaterials*, 24, 3931- 3939

Tian, Y.S; Chen, C.Z.; Lee, S.T. & Huo, Q.H. (2005). Research progress on laser surface modification of titanium alloys. *Appl. Surf. Sci.*, 242, 177-184

Tirrell, M.; Kokkoli, E. & Biesalski, M. (2002). The role of surface science in bioengineered materials. *Surf. Sci.*, 500, 61-63

Thomas, C.H.; McFarland, C.D.; Jenkins, M.L. & Rezania, A. (1997). The role of vitronectin in the attachment and spatial distribution of bone-drived cells on materials with patterned surface chemistry. *J. Bomed. Mater. Res.*, 37, 81- 93

Toth, C.; Szobo, G.; Kovacs, L.; Vargha, K.; Barabas, J. & Nemeth, Z. (2002). Titanium implants with oxidized surfaces: the background and long–term results. *Smart Mater. Stru.*, 11, 813-818

Tian, Y.S.; Chen, C.Z.; Yue, T.M. & Wang, Z.L. (2004). Study on microstructures and mechanical properties of in-situ formed multiphase coating by laser cladding of titanium alloy with silicon and graphite powder. Chin. *J. Laser*, 31, 1-12

Tritca, S.; Gakovic, M.; Nenadovic, M. & Mitrovic, M. (2001) Surface modification of stainless steel by TEA CO_2 laser. *Appl. Surf. Sci.*, 177, 48-57

Tritca, M.S.; Tarasenko, V.; Gakovic, B. & Fedenev, A. (2005). Surface modification of TiN coating by pulsed TEA CO_2 and XeCl lasers. *Appl. Sur. Sci.*, 252, 474-482

Trtica, M.S.; Radak, B.B.; Gakovic, B. M.; Milovanovic, D.S.; Batani, D. & Desai, T. (2009). Surface modifications of Ti6A14V by a picosecond Nd:YAG Laser. *Laser and particle Beams*, 27, 85-90

Turner, M.W.; Crouse, P.L. & Li, L. (2007). Comparative interaction mechanisms for different laser systems with selected materials on titanium alloys. *Appl. Surf. Sci.*, 253, 7992-7997

Venugopalan, R.; Weimer, J.J.; George, M.A. & Lucas, L. C. (2000). The effect of nitrogen diffusion hardening on the surface chemistry and scratch resistance of Ti-6AL-4V alloy. *Biomaterials*, 21, 1669-1677

Vercaigne, S.; Wolk, J. & Jansen, J. (1998). The effect of titanium plasma-sprayed implants on trabecular bone healing in the goat. *Biomaterials*, 19, 1093-1099

Vorobyev, A. Y. & Guo, Ch (2007). Femtosecond laser structuring of titanium implants, *Appl. Surf. Sci.*, 253 (17), 7272-7280

Wang, X.X.; Yan, W.; Hayakawa, S.; Tsuru, K. & Osaka, A. (2003). Apatite deposition on thermally and anodically oxidized titanium surfaces in a simulated body fluid. *Biomaterials*, 24, 4631-4631

Wang, Y.B. & Zheng, Y.F. (2009). Corrosion behaviour and biocompatibility evalution of low modulus Ti-16Nb shape memory alloy as potential biomaterial. *Material Letters*, 63, 1293-1295

Wang, J. T.; Weng, C. & Chang, J.G. (2000). The influence of temperature and surface conditions on surface absorptivity in laser surface treatment. *J. Appl physics*, 87, 3245-3253

Wieland, M.; Textor, M.; Spencer, N.D. & Brunette, D.M. (2001). Wavelength-roughness: a quantitative approach to characterizing the topography of rough titanium surfaces. *Int J Oral Maxilloface Impl*, 16(2), 163-181

Xiong, L. & Yang, L. (2003). Quantitative analysis of osteoblast behaviour on microgroovedhydroxyapatite and titanium substrata. *J. Biomed. Mater. Res.*, 66A, 677-687

Yap, A.S. & Kovacs, E.M. (2003). Direct cadherin – activated cell signaling: a view from the plasma membrane. *J. Cell Biol.*, 160, 11-16

Yamada, K. (1991). Adhesive recognition sequences. *J. Biol. Chem.*, 266, 12809-12812

Yang, Y.C. & Change, E. (2001). Influence of residual stress on bonding strength and fracture of plasma–sprayed hydroxyapatite coatings on Ti-6AL-4V substrate. *Biomaterials*, 22, 1827-1836

Yang, J.; Lian, J.; Dong, Q. & Guo, Z. (2004). Nano structured films formed on the AlSi 329 stainless steel by Nd:YAG pulsed laser irradiation. *Appl. Surf. Sci.*, 229, 2-8

Ziats, N.P.; Miller, K.M. & Anderson, J.M. (1988). In vitro and in vivo interactions of cells with biomaterials. *Biomaterials, (Ibid)*, 9, 5-13

Zhu, X. & Assoian, R. K. (1995). Integrin-dependent activation of MAP kinase: a link to shape-dependent cell proliferation. *Mol. Biol. Cell*, 6, 273-282

9

Novel Titanium Manganese Alloys and Their Macroporous Foams for Biomedical Applications Prepared by Field Assisted Sintering

Faming Zhang and Eberhard Burkel
Physics of New Materials, University of Rostock
August Bebel Str.55, 18055 Rostock
Germany

1. Introduction

In this chapter, a novel titanium (Ti) alloy and foam suitable for biomedical applications will be introduced. As we know, Ti and its alloys are widely used as biomaterials especially for orthopedic implants in load bearing sites as dental and orthopedic implants and heart valves, due to their high mechanical properties, corrosion resistance and biocompatibility (Geetha et al., 2009). Pure Ti was once used as biomaterial, but its disadvantage as implant materials is low strength and insufficient hardness. Therefore, the Ti6Al4V alloy is preferentially in clinical use because of its favourable mechanical properties. However, some studies showed that the vanadium (V) and aluminium (Al) release in Ti6Al4V alloy could induce Alzheimer's disease, allergic reaction and neurological disorders (Mark & Waqar, 2007). Therefore, the exploration of high strength new Ti alloys without Al and V for medical implants has gained great attention in the past years and it is still ongoing. Al and V free alloys containing non-toxic elements such as iron (Fe), niobium (Nb), zirconium (Zr), tantalum (Ta), molybdenum (Mo), nickel (Ni), gold (Au), or silicon (Si), etc. were investigated (Zhang, Weidmann et al, 2010). As long-term load-bearing implants in clinic, the incorporation of porous structures into the Ti and its alloys could lead to a reliable anchoring of host tissue into the porous structure, and allow mechanical interlocking between bone and implant (Li et al, 2005). The porous structure is preferable for Ti and its alloys used as bone implants. Many techniques have been applied to produce Ti foams in recent years. Nevertheless, there are still problems to be solved in the field of Ti foams for biomedical applications (Zhang, Otterstein et al., 2010): the difficulty to create controlled porosity and pore sizes, the insufficient knowledge of porous structure-property relationships, the requirements of new sintering techniques with rapid energy transfer and less energy consumption and so on.

The Ti alloys and foams are difficult to be produced from the liquid state due to high melting point, high reactive activity at high temperature above 1000 ^{o}C and contamination susceptibility. The production of Ti alloys and foams via a powder metallurgy (PM) route is attractive due to the ability to produce net-shaped components. Because of their stable

surface oxide film (TiO_2), the Ti alloys are difficult to be sintered by traditional PM sintering techniques. Thus, the spark plasma sintering (SPS), a pulsed electric current field assisted sintering technique has been introduced to prepare the Ti alloys. Spark plasma sintering, commonly also defined as field assisted sintering (FAST) or pulsed electric current sintering (PECS) is a novel pressure assisted pulsed electric current sintering process utilizing ON-OFF DC pulse energizing. Due to the repeated application of an ON-OFF DC pulse voltage and current between powder materials, the spark discharge point and the Joule heating point (local high temperature-state) are transferred and dispersed to the overall specimen (Munir & Anselmi-Tamburini, 2006). The SPS process is based on the electrical spark discharge phenomenon: a high energetic, low voltage spark pulse current momentarily generates spark plasma at high localized temperatures, from several to ten thousand degrees between the particles resulting in optimum thermal and electrolytic diffusion. During SPS treatment, powders contained in a die can be processed for diverse novel bulk material applications, for example nanostructured materials (Gao et al., 1999), functional gradated materials (Lou et al., 2003), hard alloys (Zhang et al., 2004), biomaterials (Gu et al., 2004), porous ceramics (Jayaseelan et al., 2002) and diamonds (Zhang et al., 2005) etc. The research group of the author (E.B) has applied the SPS technique also for the synthesis of new materials such as nanostructured magnets, quasicrystals, nanoceramics and Ti alloys (Nicula, Cojocaru et al., 2007; Nicula, Turquier, et al., 2007; Nicula, Lüthen et al., 2007).

The preparation of dense Ti alloys by using the SPS was reported extensively, but still fewer studies were on porous Ti foams (Zhang, Otterstein et al, 2010). The SPS studies on porous Ti alloys were mainly using low temperature and low pressure to decrease the relative density of samples. The samples exhibited pore sizes of some tens of micrometers and a porosity in the range of 20-45%. As bone foams, high porosity (>50%) and macropore size (>200 μm) are essential requirements for the bone growth and the osteoconduction.

We aim at

1. the exploration of new elements within Ti alloys for biomedical applications,
2. the development of new methods to prepare Ti foams for biomedical applications,
3. the deep understanding of the relationships between the microstructure and properties of the new Ti alloy and foams.

Manganese (Mn) is one of the essential trace elements in human body. In recent decades research has discovered the special role manganese plays as a co-factor in the formation of bone cartilage and bone collagen, as well as in bone mineralization (Brown, 2006). The Mn is also beneficial to the normal skeletal growth and development. It is important for enzymes in the body like the superoxide dismutase and, therefore, involved in the elimination of radicals (Zhang, Weidmann et al., 2010). Titanium-manganese (TiMn) alloys have been extensively used in aerospace and hydrogen storage, but not yet in biomedicine. The results in our group showed that the Mn incorporation into the Ti-Al-V alloy could enhance the cell adhesion properties (Nicula, Lüthen et al., 2007). In this chapter, the Mn element was incorporated into the Ti system and TiMn alloys with different Mn amounts were prepared by SPS technique. The preparation process, microstructures, mechanical properties, cytotoxicity and cell proliferation properties of the TiMn alloys were investigated for exploration of their biomedical applications. Macroporous Ti foams with controlled architectures were also prepared using the SPS technique and subsequently modified with TiO_2 nanostructures. The relationship between the properties and the porous architectures was analyzed and discussed.

2. Major raw materials and methods

- The precursor Ti and Mn powders with purities above 99.0% were obtained from Alfa Aesar, Germany. The space holder materials for preparation of Ti foams with 99.0% purity were also obtained form Alfa Aesar and sieved in the range of 100 to 1000 μm.
- The mechanical alloying of the alloy powders is completed using a high energy planetary ball milling machine (Retsch PM400, Germany). The SPS experiments were performed using a Model HPD-25/1 FCT spark plasma sintering system (FCT systeme GmbH, Rauenstein, Germany).
- The analysis of the phase transformation of the alloys was conducted with a differential scanning calorimetry (DSC, DSC 404 C Pegasus®, Germany). The microstructure analysis was performed using X-ray diffraction (XRD, Bruker D8, Germany) and Scanning electron microscopy (SEM, Zeiss Supra 25, Germany). The Ti foam architecture was examined by using X-ray microcomputed tomography (Micro-CT, GE, USA).
- The hardness and the elastic modulus of the dense alloys were measured by Universal CETR Nano+Micro tester with a model UNMT-1 multi-specimen test system. The mechanical behaviour of the Ti foams was investigated by uniaxial compression experiments at room temperature. The plateau stress and further elastic modulus measurements were carried out on a universal testing machine Zwick Roell Z050.
- The human osteoblastic cells MG-63 (osteosarcoma cell line, ATCC, LGC Promochem) were used to investigate the in vitro biocompatibility of the TiMn alloys. The cytotoxicity of the alloys were measured by the methyltetrazolium salt (3-(4,5-dimethylthiazol-2-yl)-5 -(3-carboxy -methoxyphenyl)) (MTS) method. The flow cytometry for determining the cells proliferation property on the alloys was also performed.
- The surface modification of the Ti foams was conducted by soaking in a strong alkali solution and heat treatment. The in vitro bioactivity of the modified foams was tested using a simulated body fluid solution in a shaking bath kept at 37.0 °C.

3. Titanium Manganese alloys

3.1 Phase diagram of the TiMn alloys

The binary phase diagram of TiMn alloys is shown in Fig. 1. It shows the conditions at which thermodynamically distinct phases can occur in equilibrium. The TiMn alloy powders were designed by varying the amount of Mn in the Ti with 2, 5, 8 and 12 (wt.%) compositions on the base of phase diagram. In Fig. 1, the locations of the phases of the Ti-2, 5, 8, 12 wt.% Mn alloys discussed in this work are indicated as straight lines in the phase diagram. The phase compositions of the TiMn alloys with Mn below 12 wt.% are all Ti2Mn2 phase.

3.2 Preparation of the TiMn alloys

The TiMn alloy powders with 2, 5, 8 and 12 wt.% Mn compositions were mixed and mechanical alloyed for various hours in a high energy ball milling machine. Fig. 2 shows the XRD patterns of the pure Ti and Mn powders and of the TiMn alloy powders after 60 hours mechanical alloying. The pure Ti and Mn peaks completely disappeared and TiMn phases

were formed after 60 hours of mechanical alloying. The pure Ti powders show the α-Ti phase (PDF# 65-3362) with hexagonal structure and the pure Mn powders the α-Mn phase (PDF# 32-0637) with cubic structure. The synthesized TiMn powders contain the α-TiMn phase (PDF# 07-0132) with tetragonal structure. There are no obvious changes in the phase compositions with increasing Mn amount up to 12 wt% in Ti, which corresponds to the binary phase diagram of the TiMn alloy (Fig. 1). The powders are analyzed by SEM revealing agglomerates with mean particle sizes of 4-5 μm in diameter with a narrow size distribution. The EDX spectra indicate that the Ti, Mn peaks belong to the TiMn powder. The C and O peaks are resulting from adsorption of air, and the small Fe peak is due to the contamination from the steel balls and vials during the mechanical alloying.

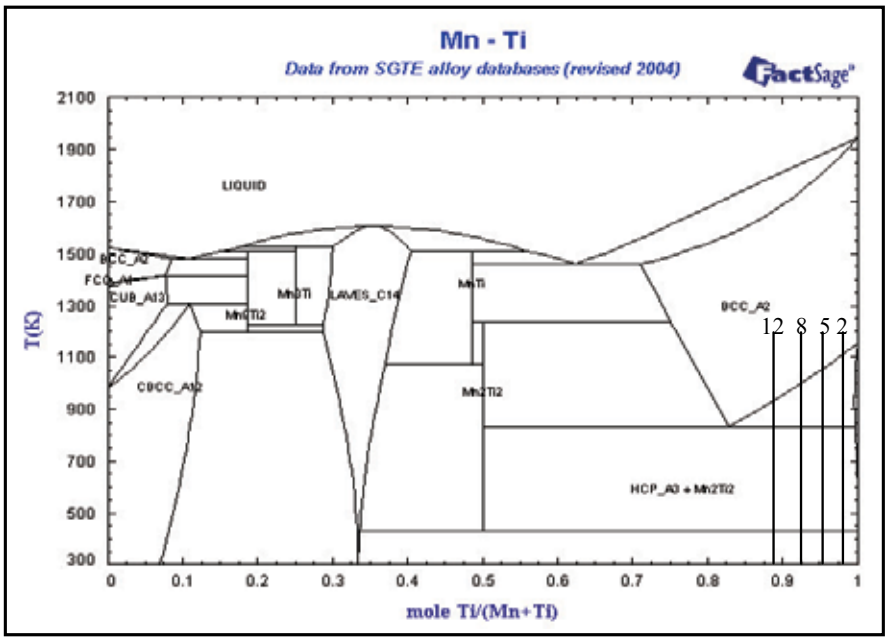

Fig. 1. Binary phase diagram of TiMn alloy showing the phases of the Ti-2, 5, 8, 12 wt.% Mn alloys.

The phase transformation behaviors of the TiMn alloy powders were analyzed by using differential scanning calorimetry. Fig. 3 shows the transformation temperatures of the TiMn alloys in comparison with the pure Ti. In the case of pure Ti, the transformation temperature from α to β phase occurs at about 840 ºC. The transformation temperature in Ti2Mn is at about 735 ºC while that of the Ti5Mn alloys is at about 700 ºC. The transformation temperatures are at about 665 ºC and at about 660 ºC in Ti8Mn and Ti12Mn alloys, respectively. With increasing amount of Mn, the transformation temperature decreased to a lower temperature value. The addition of Mn in Ti has depressed the transformation temperature from the α to the β phase. The elements V, Mo, Nb, Fe, Cr, etc are all β stabilizers and an addition of these elements depresses the β transition temperature. The results in Fig. 3 show that the Mn has decreased the transformation temperature from the α to the β phase. The influence of manganese on the α to β transition temperature is significant. It is confirmed that the Mn is a β stablizing addition element for Ti metals.

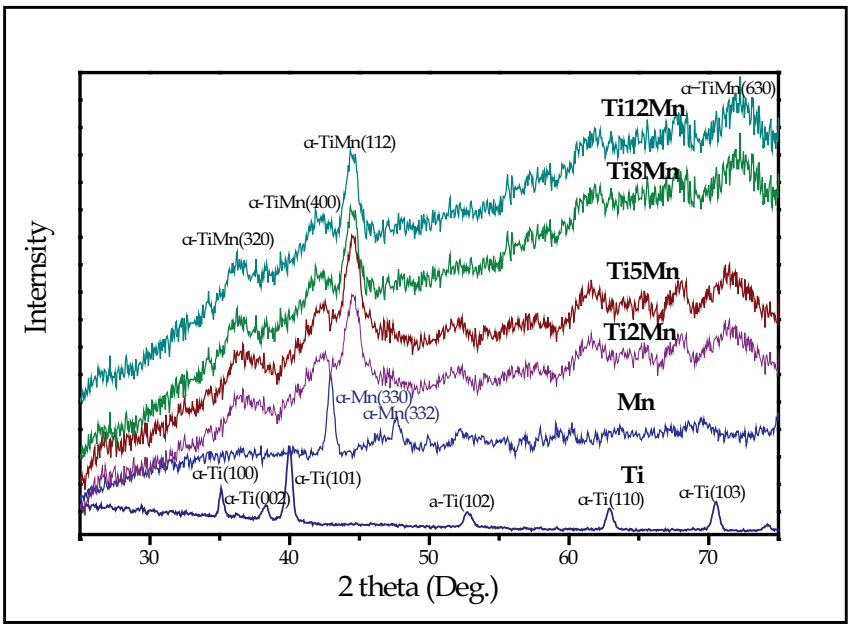

Fig. 2. XRD patterns of the Ti, Mn powders, and TiMn alloy powders prepared by mechanical alloying showing the formation of α-TiMn phases.

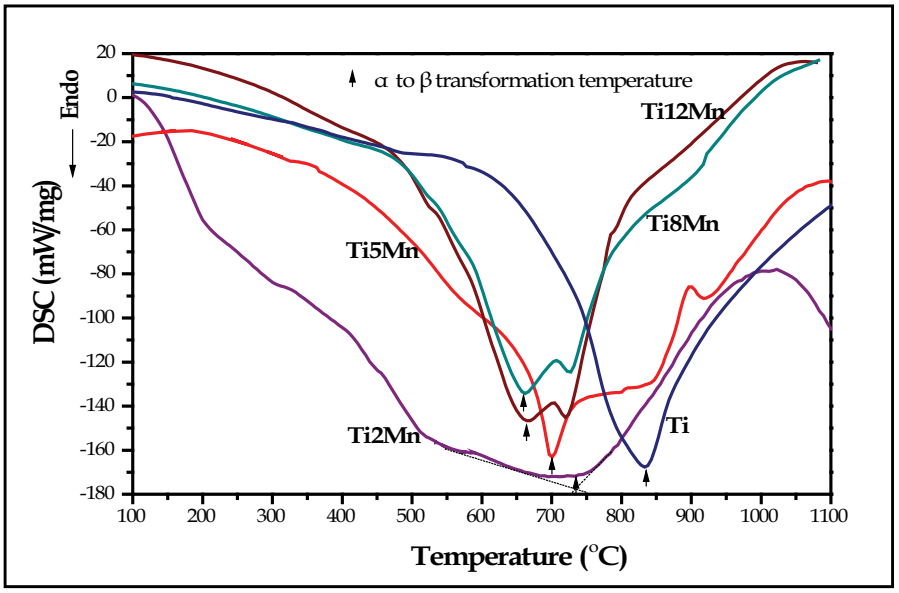

Fig. 3. Phase transformation behaviours of the TiMn alloys measured by DSC showing the decrease of the α to β transformation temperatures with increasing Mn amount.

After characterization, the alloy powders were subjected to the SPS furnace. The relative densities of the spark plasma sintered pure Ti at different temperatures and the TiMn alloys with various Mn amounts were also investigated. With a temperature increase from 550°C

to 800ºC, the relative density of the Ti metal increased from 68% to 99%. The relative density of the TiMn alloys increased with higher Mn amount. The Ti8Mn alloys showed 99% relative density after sintering at 700ºC for 5 min. The SPS method reduces the sintering temperature of Ti and TiMn alloys. The Mn addition increased the relative density of Ti metal during the SPS treatment. Finally, high density Ti metal was prepared by using the SPS application at 750ºC for 5 min and high density TiMn alloys were sintered at 700ºC with a holding time of 5 min. By using the traditional sintering techniques, high temperatures of 1100-1300ºC would be required to get pure or alloyed high density Ti. The SPS has decreased the sintering temperature of Ti and TiMn alloys. The Mn has increased the relative density of Ti alloy, which is due to the lower β transformation temperatures in the TiMn alloys. The low sintering temperature is ascribed to the ionization of particles by local sparks during SPS. Pulsed current generated plasmas are expected to lead surface activation of the powder particles, melting the titanium oxide films and forming neck junctions among powder particles at a lower temperature (Zhang, Weidmann, 2009).

3.3 Microstructures of the TiMn alloys

Fig. 4 (a) shows X-ray diffraction (XRD) patterns of the spark plasma sintered Ti, Mn and TiMn samples. The pure Ti and Mn still retain the α-Ti and the α-Mn phases because of the lower sintering temperature of 700ºC during the SPS treatment. However, most of the TiMn alloys show the β-TiMn phase (PDF# 11-0514) with cubic structure. There is still a small amount of the α-TiMn phase in the alloy; therefore, the TiMn sample is an α+β phase alloy. The synthesized alloy has α+β microstructures which are similar to those of an Ti6Al4V alloy.

The SEM micrograph of the fracture surface of the spark plasma sintered Ti8Mn sample is shown in Fig.4 (b). There are very few micropores in the fracture surface of the TiMn alloys. The grain size of the Ti8Mn alloys is about 500 nm indicating an ultrafine microstructure and the fracture mode of the alloy is primary intergranular cracking. During the SPS, a simultaneous pressure impact causes a plastic flow of the powders, which enables the creation of the dense Ti alloys with ultrafine microstructures at high heating rates, lower temperature and short holding time.

3.4 Properties of the TiMn alloys

The mechanical properties of the TiMn alloys are shown in Fig. 5. The microindentation hardness results show that the hardness value tended to rise with increasing Mn contents (Fig. 5a). The hardness values of all TiMn alloys are significantly higher than that of pure Ti. The pure Ti shows a hardness of 1.60 GPa ± 0.20 GPa; Ti2Mn 2.40 GPa ± 0.25 GPa; Ti5Mn 3.65 GPa ± 0.29 GPa; Ti8Mn 4.98 GPa ± 0.32 GPa and Ti12Mn 5.28 GPa ± 0.37 GPa. The detected hardness value (5.28 GPa ± 0.37 GPa) of the Ti12Mn alloy is comparable to that of the pure Mn (5.44 GPa ± 0,34 GPa). From statistical analysis, the hardness values of the TiMn alloys are significantly higher than that of pure Ti. The elastic modulus results are shown in Fig. 5(b). The pure Ti is 105.3 GPa ± 6.0 GPa, Ti2Mn 83.3 GPa ± 3.0 GPa, Ti5Mn 95.0 GPa ± 5.0 GPa, Ti8Mn 106 GPa ± 4.1 GPa, and Ti12Mn 122 GPa ± 6.2 GPa, Mn 68.72 GPa ± 4.3 GPa. The ductility results of the TiMn alloys are shown in Fig. 5 (c). The pure Ti exhibits 25.0% ± 2.0% ductility, Ti2Mn 21.3% ± 2.4%, Ti5Mn 18.2% ± 2.2%, Ti8Mn 15.0% ± 1.3% and Ti12Mn 11.7% ± 1.9%. The ductility decreased with increasing Mn amounts in the TiMn alloy. For comparison, the mechanical properties of the Ti6Al4V

alloy were also measured with the same methods. This shows a hardness of 4.3 GPa ± 0.3 GPa, an elastic modulus of 122 GPa ± 4.0 GPa, and a ductility of 14.0 GPa ± 1.5 GPa which are almost identical with reported literature values (Barbieri et al., 2007). The Ti2Mn, Ti5Mn and Ti8Mn alloys possess lower elastic modulus and higher ductility than the Ti6Al4V alloy.

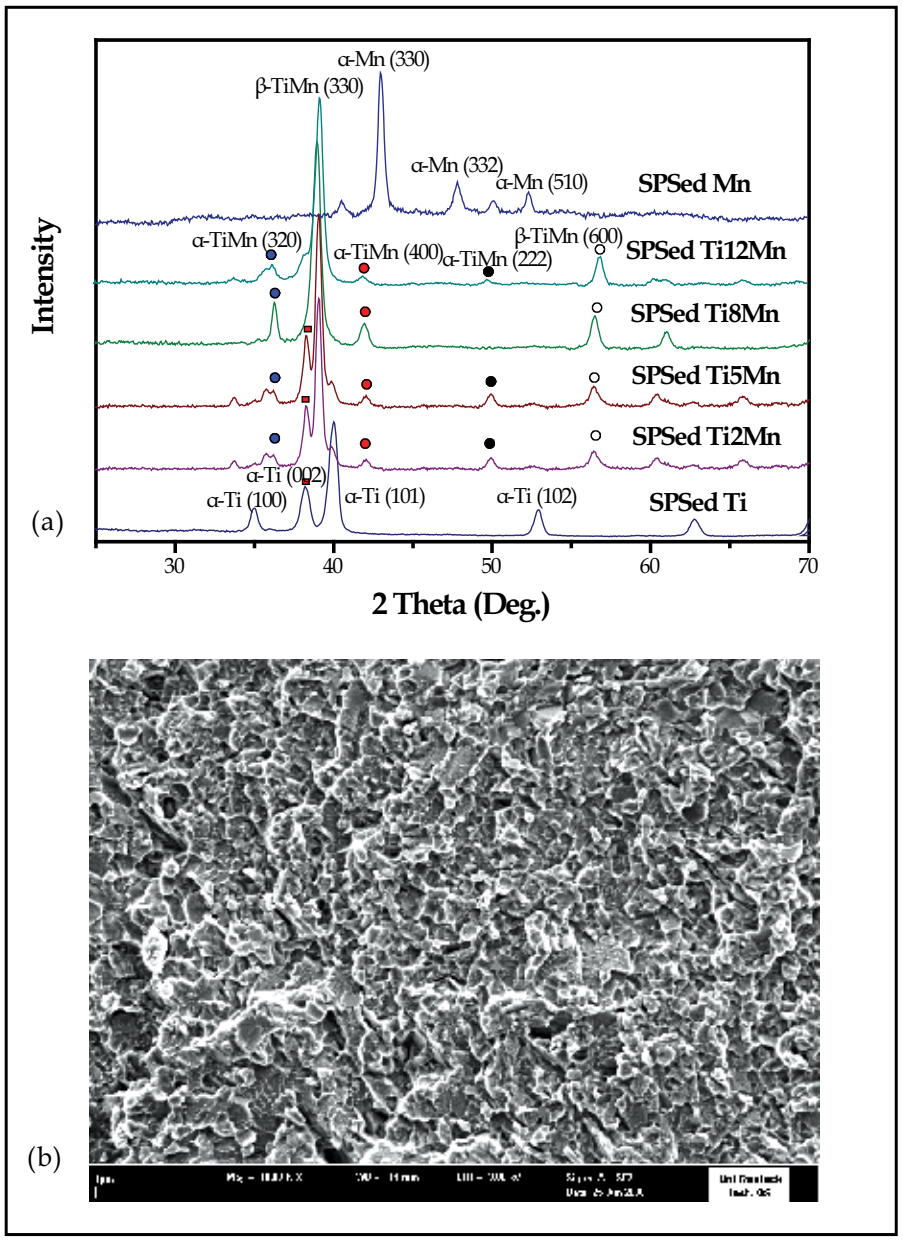

Fig. 4. XRD patterns of the spark plasma sintered Ti, Mn and TiMn alloys showing the TiMn alloys are α+β phase alloy (a) and SEM micrograph of the fracture surface of a Ti8Mn alloy.

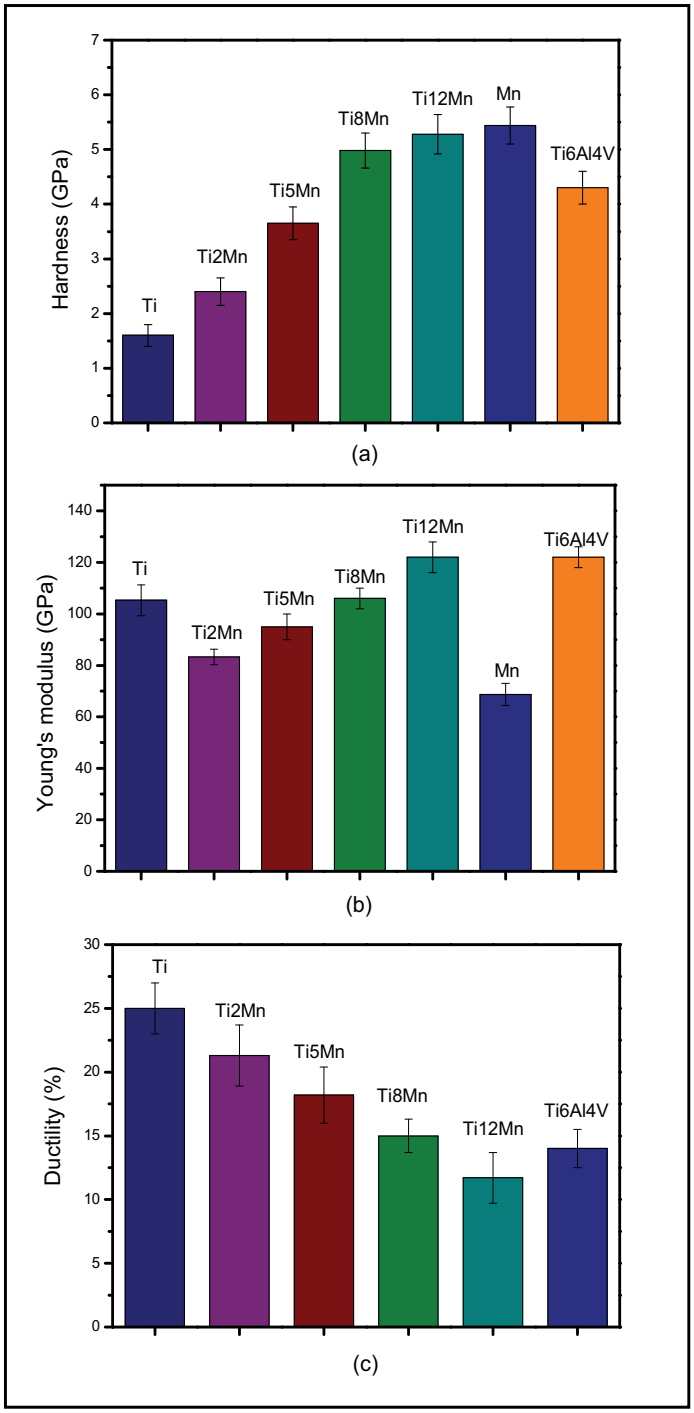

Fig. 5. Hardness (a) and Elastic modulus (b) of the Ti, Mn, TiMn and Ti6Al4V alloys obtained by microindentation tests, as well as ductility values at room temperature (c) of the TiMn alloys

The TiMn alloys provide higher hardness and elastic modulus than those of the pure Ti. The Ti5Mn and Ti8Mn alloys show comparable hardness but lower elastic modulus compared to the Ti6Al4V alloy. The increment of the hardness and elastic modulus of the TiMn alloys is ascribed to the formation α+β TiMn phases which are intermetallic phases with excellent mechanical properties. The Ti6Al4V alloy was chosen for orthopedic implant for several reasons. Excellent ductility is one of the most important reasons for its wide use in biomedical industry. The ductility of Ti6Al4V alloy is measured to be 14% at room temperature. The ductility of the TiMn alloy decreased from 21.3% (Ti2Mn) to 11.7% (Ti12Mn) with increase of Mn amount. However, the Ti2Mn, Ti5Mn, Ti8Mn alloys have higher ductility than that of the Ti6Al4V. Compared with the Ti6Al4V, the Ti2Mn alloy presents lower hardness (2.4 GPa) with better elastic modulus (83.3 GPa) and ductility (21.3%). The Ti5Mn alloy exhibits comparable hardness (3.65 GPa) and better elastic modulus (95.0 GPa) and ductility (18.2%) and the Ti8Mn alloy shows better hardness (4.98 GPa) and elastic modulus (106 GPa) with a comparable ductility (15.0%). In the light of their mechanical properties, the Ti2Mn, Ti5Mn and Ti8Mn alloys are suitable as biomedical implants.

Fig. 6 represents the cytotoxicity and cell proliferation results of the TiMn alloys. The tissue culture polystyrene (TCPS) was used as a control material. The MG-63 osteoblast cell viability (%) of the pure Ti and TiMn alloys by MTS assay is shown in Fig. 6(a). The cytotoxicity increases with increasing amount of the Mn contents in the Ti alloy. Cell's viability on pure Mn and Ti12Mn was about 50 % and 72 %, respectively ($p<0.05$). However, cells on the Ti5Mn and Ti8Mn alloys were also influenced concerning viability without statistical difference ($p>0.05$), but it reached comparative high values (89 %, 86 %, respectively) comparable with that of pure Ti (93 %). The proliferation of MG-63 osteoblasts on the TiMn alloys using flow cytometric cell proliferation analysis is demonstrated in Fig. 6 (b). The percentage of cells on the pure Ti and TiMn alloys decreases in contrast to the TCPS control (53.67 %). The number of proliferating cells on TiMn alloys (Ti2Mn 41.17%, Ti5Mn 40.50 %, Ti8Mn 41.57% and Ti12Mn 39.99 %) is reduced compared with that of pure Ti (48.93 %), however, with $p>0.05$ not significantly and all acceptable for biomedical applications. However, the percentage of proliferating cells grown on pure Mn is significantly reduced to 35.87 % ($p<0.05$). The student t-test, an established statistical method, shows that the proliferation of MG-63 osteoblast cells on TiMn alloys is not remarkably inhibited. Only Mn is significantly decreased ($p<0.05$). The decrease in pure Mn is about 27% from the Ti value. It is indicated that only a very high amount of Mn inhibits cell proliferation. Combining the cytotoxicity and cell proliferation results, leads to the assumption that the amount of Mn below 8 wt.% has a negligible effect on the cytotoxicity and cell proliferation of all tested Ti alloys.

Some commercial Ti alloys also contain Mn as an alloying component. The Mn has been doped in magnesium alloy with 1.2 wt. % and it was found that the Mn has no toxicity and can improve the corrosion resistance and mechanical properties of Mg (Xu et al., 2007). The Mn was doped to tri-calcium phosphate bioceramics and showed good cell compatibility (Sima et al., 2007). Recently, a Fe-35Mn alloy was prepared and showed higher strength and ductility, degradable properties. These observations make it suitable for biodegradable stent applications (Hermawan et al., 2007). The values concerning cytotoxicity and cell proliferation of the TiMn alloys demonstrate a dependency on the Mn concentration. A lower Mn content (<8 wt.%) in Ti has a low effect on the cytotoxicity and cell proliferation properties ($p>0.05$). In general, the Ti2Mn, Ti5Mn and Ti8Mn were comparable in viability

and cell proliferation properties with pure Ti. The Ti6Al4V alloy was firstly used in aerospace industry, and then applied in biomedical field as bone and dental implants. Until now, the Ti8Mn alloy as one of the typical α+β Ti alloys has been extensively used in aerospace industry because of its excellent mechanical properties. Our research here suggests that the application of the Ti8Mn alloy could be extended to biomedical field. As well as the Ti2Mn and Ti5Mn alloys, they exhibit higher ductility and lower elastic modulus than those of Ti6Al4V. The lower values of the elastic modulus of metals for joint prosthesis could decrease the stress-shielding effect in bone-implant coupling. The Ti2Mn, Ti5Mn and Ti8Mn alloys all exhibit acceptable cytotoxicity and cell proliferation of the human osteoblasts. Consequently, all the Ti2Mn, Ti5Mn and Ti8Mn alloys have a potential for the use in the biomedical field as new bone substitutes and dental implants.

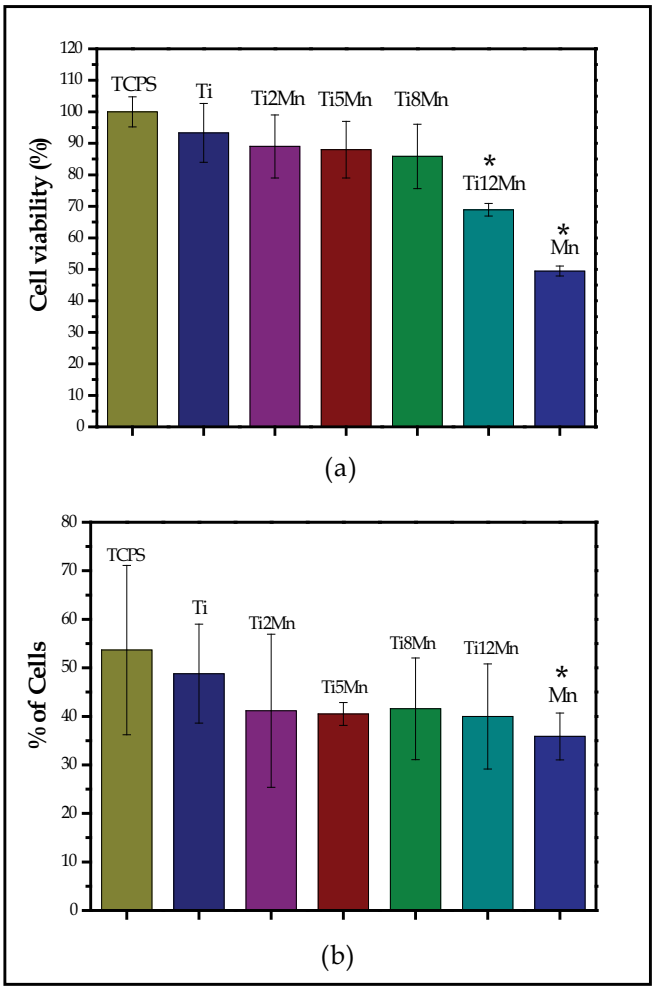

Fig. 6. Cytotoxicity (a) and cell proliferation (b) of MG-63 osteoblasts on the Ti and TiMn alloys showing the comparable cell viability of Ti2Mn, Ti5Mn and Ti8Mn alloys with that of pure Ti, and the proliferation of osteoblasts was not inhibited on TiMn alloys but only significantly on pure Mn. Mean ±SD, n=5, Student t-test * $p<0.05$.

4. Macroporous Titanium foams

4.1 Preparation and microstructures of the Titanium foams

High density pure Ti, and TiMn alloys were prepared by using the SPS in the above section. In this section, the preparation of Ti and TiMn foams by using the SPS will be introduced. Firstly, the pure Ti foams were prepared by the free pressureless SPS method developed by Zhang et al. (Zhang et al., 2008). The Ti powders were mixed with 15 wt. % of NH_4HCO_3 and 2 wt. % of TiH_2 powder as pore forming agents. Then the powder mixture was sintered at 1000°C by the SPS under a pressureless condition. Using 3D reconstruction by topographical methods is the most realistic way to get information on the internal structure of the foams in a non-destructive way. Fig. 7 shows the 3D reconstructions of the obtained Ti foams. The 3D cropped isometric view of cross sections in this Ti foam shows the non-uniform pore distribution and poor interconnectivity (Fig. 7a). The Micro-CT 2D top view and side views show that the macropore shapes are in irregular cross sections and randomly distributed (Fig. 7b-d). The 3D cropped internal surface exhibits pore size of 410 ± 90 μm. The XRD results indicate that these Ti foams by free pressureless SPS method are in β-Ti phase (Ibrahim, Zhang et al, 2011).

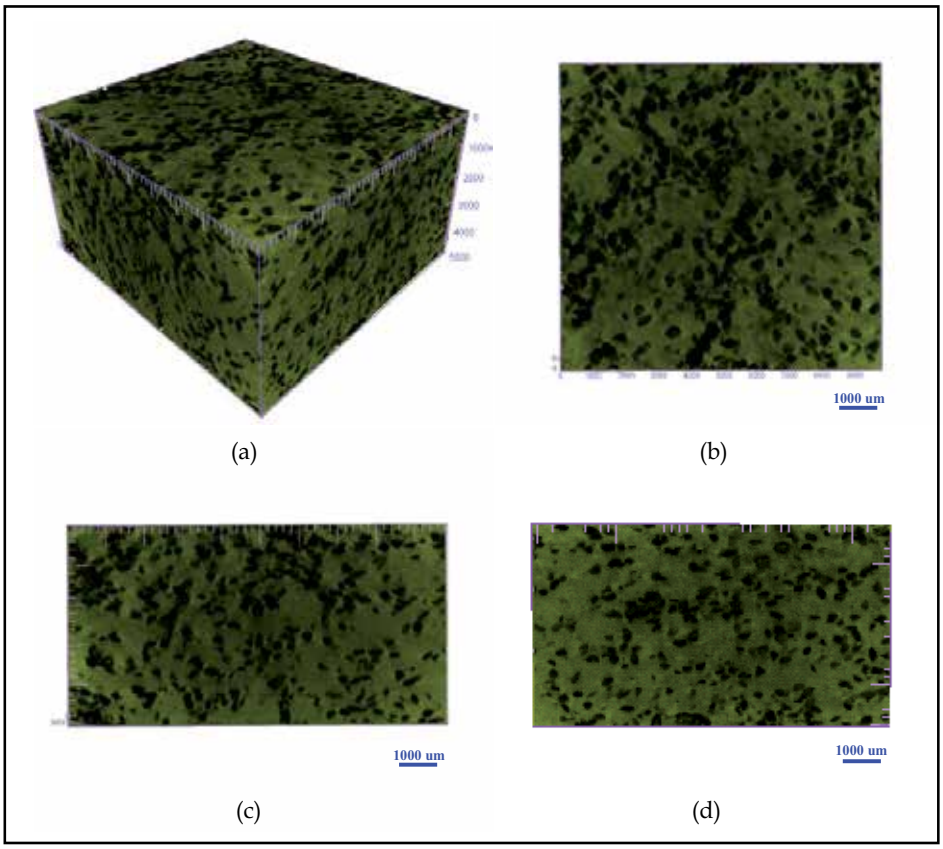

Fig. 7. Micro-CT 3D reconstructions of the Ti foam with NH_4HCO_3 and TiH_2 as pore forming agents produced at 1000°C by free pressureless SPS method with an isometric view (a), 2D top view (b), left side view (c), and right side view (d). Scale spacing, 1000 μm.

Alternatively, Ti foams with NaCl as spacer material were prepared at 700 ºC by SPS under 50 MPa. Fig. 8 shows the 3D μ-CT reconstructions of the obtained Ti foams. This spark plasma sintered titanium foams shows 55% porosity and 250 μm pore size. The 3D cropped isometric view of cross sections in the Ti foam shows the uniform pore distribution and interconnected 3D porous structures with a high porosity (Fig. 8 a). The Micro-CT 2D top view and side views show that the macropore shapes are in square cross sections, uniform distribution of pore sizes with high interconnectivity (Fig. 8b-d). The 3D surface, the cell wall thickness and the connectivity were examined by the Micro-CT in a non-destructive way. The 3D cropped internal surfaces exhibit highly porous structures and interconnectivity with pore sizes of 243±50 μm and a cell wall average thickness of 20.4 μm. The XRD results indicate that these Ti foams are in α-Ti phase.

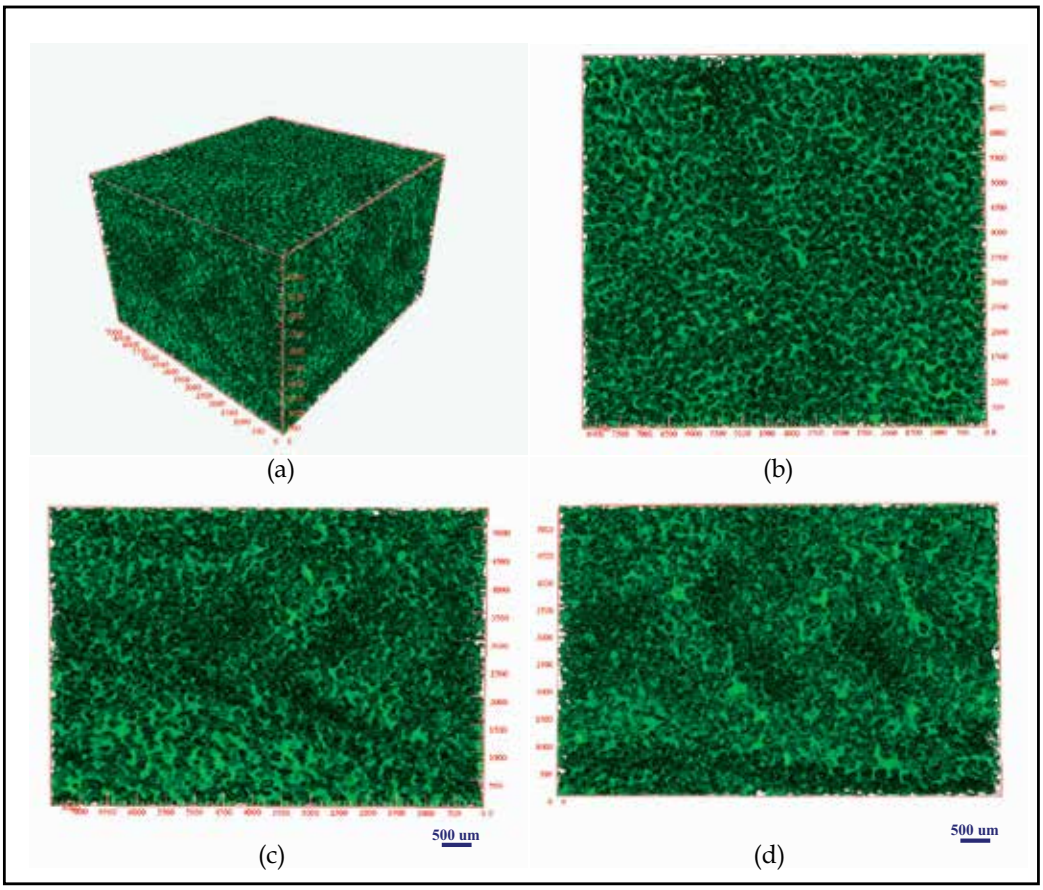

Fig. 8. Micro-CT 3D reconstructions of the Ti foam with NaCl as spacer material prepared by SPS at 700 ºC under 50 MPa with an isometric view (a), 2D top view (b), left side view (c), and right side view (d). Scale spacing, 500 μm.

The results in Fig.7 and Fig. 8 indicate that the Ti foams have been prepared successfully by using the SPS technique. The foams prepared by the SPS and NaCl dissolution method show better interconnectivities than those prepared by the free pressureless SPS method. High

interconnectivity of the foams will support the osteconduction of bone tissue. Therefore, Ti foams with different pore sizes and porosities were prepared by the SPS and NaCl dissolution method. The influence of the weight ratio and particle size of NaCl on the porosity and pore size of Ti foams with corresponding SPS parameters is shown in Table 1. The pore sizes of the sintered foams were measured from the SEM images. This shows a mean pore size of about 125 μm in the foams with the NaCl spacing material being in the range of 88-149 μm, a mean pore size of 250 μm with NaCl of the sizes 224-297 μm, a pore size of 400 μm with NaCl of 388-500 μm sizes and a pore size of 800 μm with NaCl of 784-1000 μm sizes. After the porosity characterization by the Archimedes method, it was noticed that more NaCl particles were needed to obtain the same porosity in the large pore sized foams. To achieve a porosity of 55% in the 125 μm foams, the weight ratio of Ti:NaCl is about 1:1.28. However, the weight ratio of Ti:NaCl is about 1:1.75 in the 800 μm foams for the same porosity. This might be due to the decreased specific surface area in the large sized NaCl particles as spacer materials.

Ti powder	NaCl powder	Weight ratio (Ti: NaCl)	Porosity	Pore size	SPS parameters (Temperature, dwell time)
10-30 μm	88-149 μm (170-100 mesh)	1:1.28	~55%	~125 μm	700 °C, 8 min
10-30 μm	149-297 μm (100-50 mesh)	1:0.72	~30%	~250 μm	700 °C, 8 min
		1:0.93	~45%	~250 μm	700 °C, 8 min
		1:1.32	~55%	~250 μm	550 °C, 8 min
					600 °C, 8 min
					650 °C, 8 min
					700 °C, 8 min
					730 °C, 8 min
					750 °C, 5 min
					800 °C, 3 min
		1:1.64	~70%	~250 μm	700 °C, 8 min
10-30 μm	354-500 μm (45-35 mesh)	1:1.46	~55%	~400 μm	700 °C, 8 min
10-30 μm	707-1000 μm (25-18 mesh)	1:1.75	~55%	~800 μm	700 °C, 8 min

Table 1. The influence of the weight ratio and particle size of NaCl on the porosity and pore size of the Ti foams with corresponding SPS parameters.

The SEM micrographs of the Ti foams with the same porosity of 55% but different pore sizes of 125 μm, 250 μm, 400 μm, and 800 μm are shown Fig. 9. All the foams from 125 to 800 μm exhibit highly interconnected porous structures and uniform pore distributions. It is found

that the pores have irregular quadratic cross sections. They are similar to those of the initial NaCl particles of cuboid shapes.

Fig. 10 shows the SEM micrographs of the porous Ti foams with the same pore size of 250 μm with different porosities of 30 %, 45%, 55% and 70%. The thickness of the pore walls in the 30% porosity foams is about 100 μm, decreasing to 50 μm in 45% porosity foams, and to 20 μm in 55%, finally ending at 10 μm in 70% porosity foams. The interconnectivity was also enhanced with the increase in porosity. The 30% and 45% porosity foams show poor interconnectivity because of the lower porosity. But the 55% and 70% higher porosity samples show good interconnectivity. The macropores are in square cross sections in all the Ti foams with different porosities.

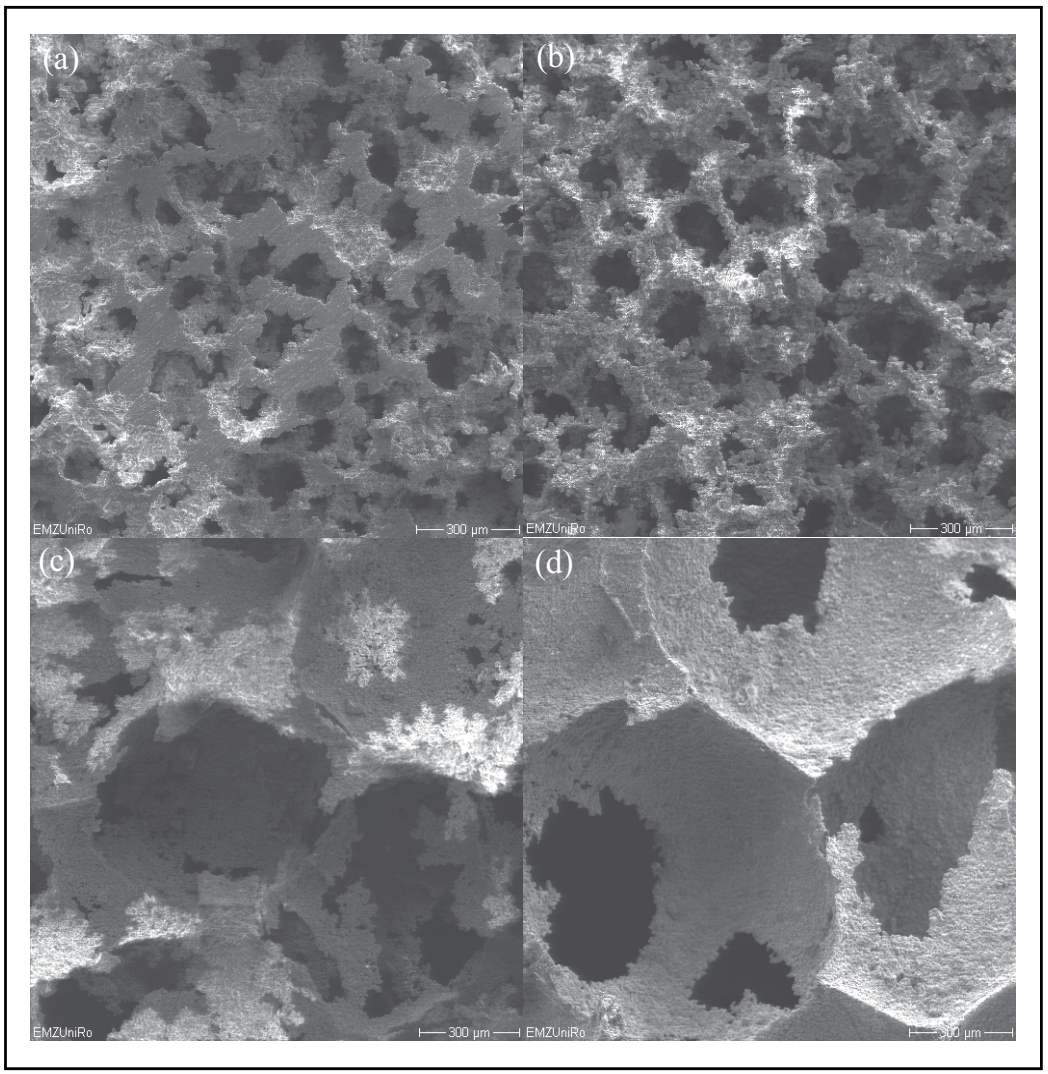

Fig. 9. SEM micrographs of the Ti foams with the same porosity of 55% but different pore sizes of 125 (a), 250 (b), 400 (c) and 800 μm (d). Scale bars, 300 μm.

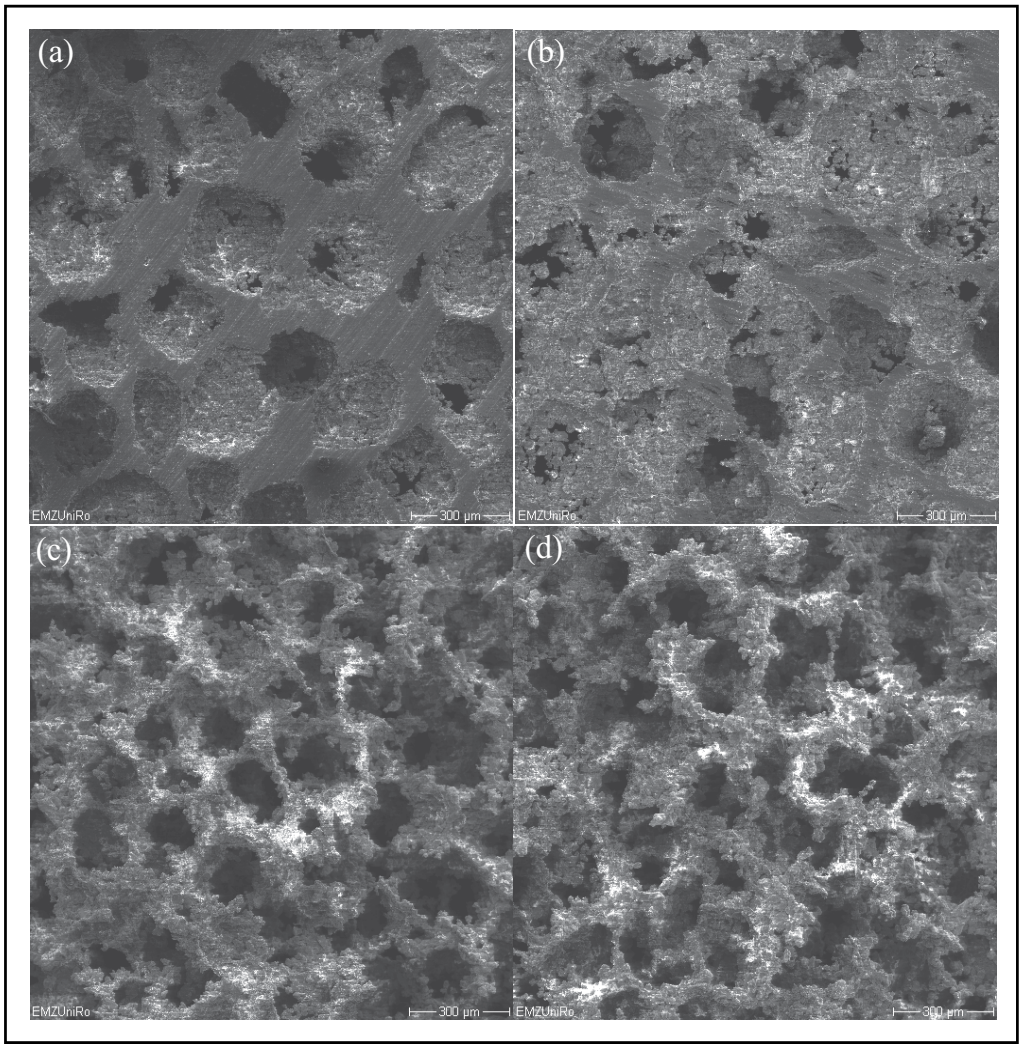

Fig. 10. SEM micrographs of the Ti foams with the same pore size of 250 µm but different porosities of 30 % (a), 45% (b), 55% (c) and 70% (d). Scale bars, 300 µm.

4.3 Mechanical properties of the Ti foams

Fig. 11 shows the effect of pore size and porosity on the plateau stress and Young's modulus of the porous Ti foams. The measured plateau stress and Young's modulus of the Ti foams were compared with values calculated following Gibson-Ashby model. According to the Gibson-Ashby model, the relationship between the relative plateau stress and relative density is given by (Wen et al., 2002):

$$\sigma/\sigma_0 = C\left(\rho/\rho_0\right)^{3/2} \tag{1}$$

where σ is the plateau stress of the foams, σ_0 is the yield stress of the dense material; C is a constant 0.3 from the data of cellular metals and polymers (Gibson & Ashby, 1997), ρ is the

density of the foams, ρ_0 is the density of the dense material. The density of the pure Ti is 4.5 g/ cm³ with yield stress of 692 MPa (Long & Rack, 1998). The density of the Ti foam with 55% porosity and 250 μm pore size is 1.69 g/cm³. Substituting these values in Equation 1, the theoretical value was calculated to be 47.78 MPa, which is comparable to the measured plateau stress 45.1±3.0 MPa.

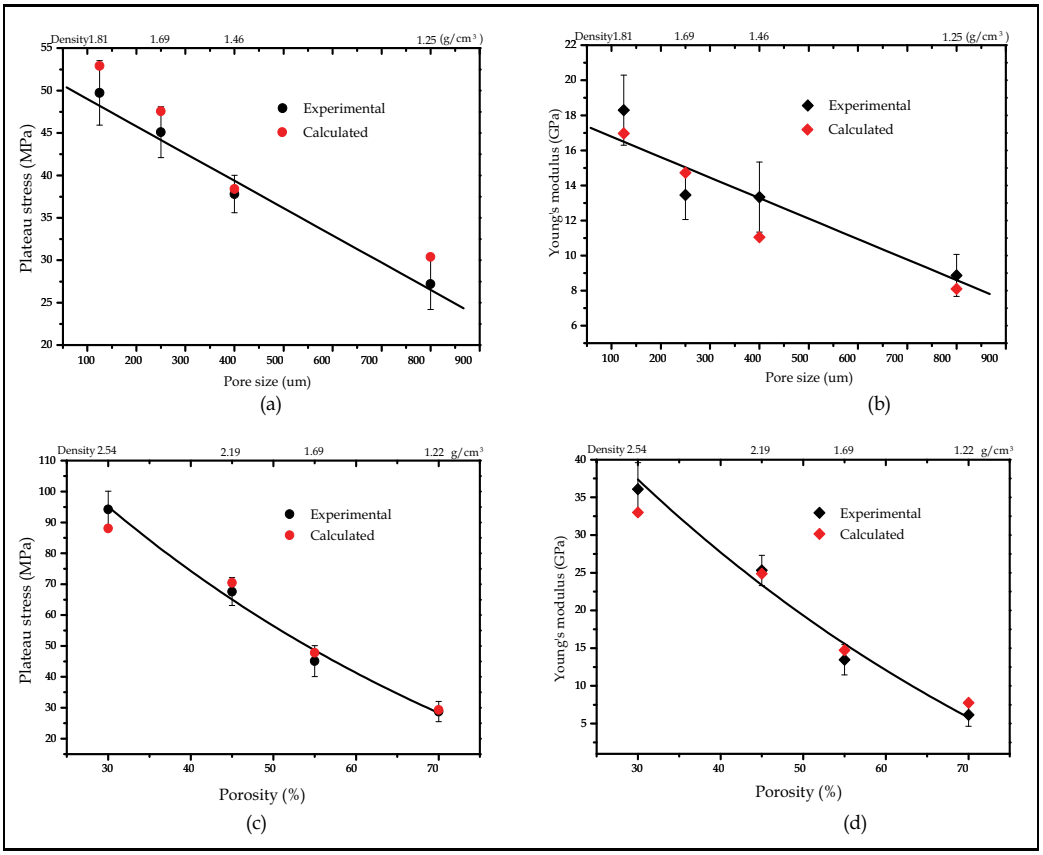

Fig. 11. The effects of pore sizes (a, b) and porosities (c, d) on the plateau stress and Young's modulus of the Ti foams.

According to the Gibson-Ashby model, the relationship between the relative Young's modules and relative density is given by (Wen et al., 2002):

$$E/E_0 = A\left(\rho/\rho_0\right)^2 \tag{2}$$

where E is the Young's modulus of the foams, E_0 is the Young's modulus of the dense materials, A is a constant of 1 including data of metals, rigid polymers, elastomers and glasses. The Young's modulus of the pure Ti is 105 GPa according to the Equation 2 (Long & Rack, 1998). The measured Young's modulus of the above Ti foams with 55% porosity is 13.46 GPa ± 1.4 GPa. Substituting the values into Equation 2, gives the theoretical value of 14.81 GPa which is also comparable to the measured one. All the Ti foams prepared by the SPS were measured and calculated.

As seen from the Fig. 11, it can be deduced that all the experimental data agree with the Gibson-Ashby model (1) and (2) in the present study. The relationship between the pore sizes and the mechanical properties of the Ti foams is shown in Fig. 11 (a, b). The plateau stress decreased from 49.7 MPa ±3.8 MPa to 27.2 MPa ± 3.0 MPa with the pore size increase (Fig. 11a). The Young's modulus reduced from 18.3 GPa ±2.0 GPa to 8.9 GPa ±1.5 GPa with the pore size increase (Fig. 11b). It coarsely obeys a linear decay with the pore size increase. The effect of the porosity on the mechanical properties of the Ti foams is shown in Fig. 11 (c, d). The plateau stress decreased from 94.2 MPa ± 5.9 MPa to 28.8MPa ± 3.3 MPa, and the Young's modulus decreased from 36.1 GPa ± 3.5 GPa to 6.2 GPa ± 1.8 GPa with porosity increase. It generally obeys the rule of exponential decline with the porosity increase.
The plateau stress and Young's modulus coarsely obey linear declines with the pore size increase and exponential decay with the porosity increase. Liu found that the plateau stress of the porous hydroxylapatite ceramics decreases linearly with increasing macropore size for a given total porosity (Liu, 1997). In this study, we found the plateau stress and Young's modulus coarsely obey linear declines with the pore size increase (Fig. 11 a, b). Rice RW has proposed a function for the relationship of the porosity and the strength of porous solids (Rice, 1993),

$$\sigma = \sigma_0 \exp(-cp) \tag{3}$$

where σ_0 is zero-porosity strength, σ is the strength at pore volume fraction p, and the constant c is related directly to the pore characteristics such as pore shape and size. In this study, we used the same Ti powder and NaCl spacer material; therefore, σ_0 and c can be considered as constant. According to the above function, the strength (σ) should decrease exponentially as the pore volume fraction (p) increases. Our results in Fig. 11 (c, d) are well in accordance with the above function.

4.4 Surface modification

Using the SPS and NaCl dissolution method, Ti8Mn foams were also prepared at SPS temperature of 700 °C under 50 MPa. Fig.12 (a) shows the SEM micrograph of the Ti8Mn foams. It shows pore sizes of about 300 μm with interconnected pore distributions. The porosity of the Ti8Mn foam is 65% determined by the Archimedes principal method. These Ti8Mn foams process a compressive plateau stress of 68.5 MPa ± 13 MPa and an elastic modulus of 32.3 GPa ± 1.8 GPa. Additionally, the obtained TiMn foams were surface modified by immersing in a NaOH solution at 60 °C for several hours. The foams were washed and heat treated at 600 °C (Takemoto, 2006). The SEM micrographs of a Ti8Mn foam sample with a surface modified by TiO_2 nanostructures are shown in Fig. 12 (b-d). The micrographs at different magnifications show that oriented nanowire structures cover all the surfaces of the pore walls in the TiMn foams. The X-ray diffraction results confirmed the surface TiO_2 nanostructures as anatase/rutile phases.
Finally, the in vitro bioactivity of surface modified Ti8Mn foams was tested by suspending in polystyrene bottles containing simulated body fluid solution at 37.0°C in a shaking bath. At certain times, the samples were taken out, rinsed with deionized water, and dried in an oven. The results show that these anatase/rutile phases of the TiO_2 nanostructures on the Ti8Mn foams have very high *in vitro* bioactivity. They formed apatite (hydroxyapatite) on the pore walls of the Ti8Mn foams after only 3 days soaking in the simulated body fluid (Fig.13). The EDX analysis indicates the precipitation of bone-like biomimetic apatite. The

deposition of the apatite on the pore walls is a biomineralization process where the TiO_2 nanostructures provide proper nucleation sites. This high *in vitro* bioactivity of the TiO_2 modified Ti8Mn foams indicates a high bone-bonding ability of these foams *in vivo*.

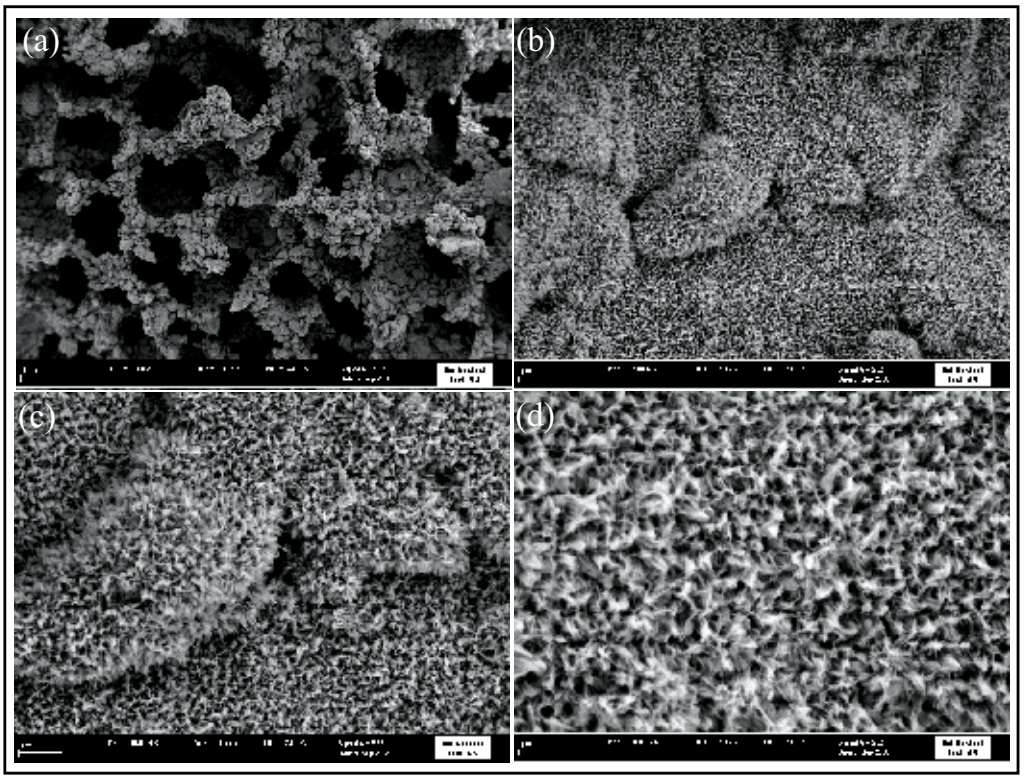

Fig. 12. SEM micrograph of the Ti8Mn foams prepared by the SPS and NaCl dissolution method (a), and morphologies of the surface modified TiO_2 nanostructures on the porous wall of the foams at different magnifications (b-d).

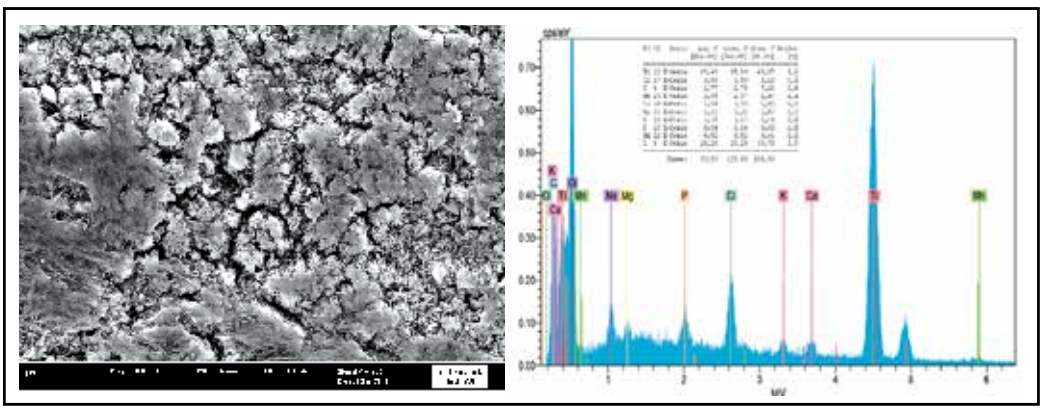

Fig. 13. SEM micrograph (a) and EDX (b) of the TiO_2 modified Ti8Mn foam immersed in simulated body fluid for 3 days showing the apatite formation.

Implants sometimes were used to substitute bone defects in tumour or spine surgery. Porous Ti and its alloy foam with their osteoconductive properties are an ideal alternative bone graft. The porous structure with pore sizes of 200-500 μm of the Ti foams may be able to permit bone cell penetration and tissue integration. The plateau stress of the human vertebral bone (load-bearing site) ranges from 24 to 43 MPa, and femoral cancellous bone (load-bearing site) is in the range of 48-80 MPa (Zhang et al, 2007). The average Young's modulus of compact bone of human ranges 7-30 GPa (Zhang et al, 2007). The plateau stress of the presented Ti and Ti8Mn foams in the range of 27-94 MPa is comparable to that of the cancellous bone which is sufficient for biomedical applications. For biomedical applications, the main problem of Ti and Ti alloys in clinical view is their high Young's modulus. Stress shielding is known to lead to bone resumption and eventual loosening of the implant. The dense Ti generally showed much higher Young's modulus (70-120 GPa) than that of human bone. Thus, the porous structures were incorporated in the Ti and Ti alloys. In this study, the porous Ti and Ti8Mn foams show lower Young's modulus values (6.2-36.1 GPa) than that of dense ones which are comparable to those of natural compact bone (7-30 GPa). The macroporous Ti and Ti8Mn foams with plateau stress 27.2-94.2 MPa and Young's modulus 6.2-36.1 GPa have a potential to be used as bone implants. The low Young's modulus of titanium foams is desirable to reduce the amount of stress shielding of the bone into which the foam is implanted. Thus, the good biocompatibility, the interconnected porous structure achieved by the SPS and the NaCl dissolution method and the observed mechanical properties comparable to those of human bones make pure Ti and Ti8Mn foams to ideal bone implant materials.

5. Conclusions and outlook

The α+β type TiMn alloys with high relative density and ultrafine microstructures were prepared by using mechanical alloying for 60 hours and spark plasma sintering at 700 °C for 5 min. The Mn reduced the α to β transformation temperature of Ti and was confirmed as a β stabilizer element. The hardness increased significantly ranging from 2.4 GPa (Ti2Mn) to 5.28 GPa (Ti12Mn), the elastic modulus ranging from 83.3 GPa (Ti2Mn) to 122 GPa (Ti12Mn) and the ductility decreased ranging from 21.3% (Ti2Mn) to 11.7% (Ti12Mn) with increasing manganese content in the Ti. Concentrations of Mn below 8 wt.% in titanium reveal negligible effects on the metabolic activity and the cell proliferation of human osteoblasts. Therefore, the Mn could be used in lower concentrations as an alloying element for biomedical titanium. The Ti2Mn, Ti5Mn and Ti8Mn alloys all have a potential for use as new bone substitutes and dental implants.

Macroporous Ti foams were successfully fabricated by the free pressureless SPS technique. Micro-CT results showed the non-uniform pore distribution and poor interconnectivity in these foams. Alternatively, macroporous pure Ti foams with porosities of 30-70% and pore sizes of 125-800 μm were prepared by using SPS and NaCl dissolution method. The Ti foams prepared by SPS at 700 °C for 8 min under 50 MPa showed pure α-Ti phase structure. The Ti foams consist of interconnected macropores with square cross sections. The plateau stress and Young's modulus agree with the Gibson-Ashby models, and coarsely obey linear declines with the pore size increase and exponential decays with the increase of porosity. Ti8Mn foams were also prepared in α+β phases with a porosity of 65% and pore sizes of 300 μm by using the SPS and NaCl dissolution method. TiO_2 nanostructures in anatase/rutile phases were modified on the pore walls of the Ti8Mn foam uniformly by NaOH solution

soaking and heat treatment. This surface modified TiMn foam exhibited high *in vitro* bioactivity with a fast apatite-forming ability in the simulated body fluid. The Ti and Ti8Mn foams processed by SPS and NaCl dissolution method showed mechanical properties within those of human bone range making these materials to be ideal bone implant foams.

As load bearing and long term hard tissue repair materials, Ti and its alloys are the most outstanding metallic materials nowadays. The modification (processing and/or surface) of the clinic used Ti alloys, and the exploration of new Ti alloy systems for biomedical applications are still the tasks for the future. For the Ti foams, the development of processing techniques to create controlled porosity, pore sizes and interconnectivity is still required. The relationship between the relative density and mechanical properties of the Ti foams can be predicted well with the Gibson-Ashby model. However, the relationships between the porosity-functional properties (thermal, flow, transport, absorption and so on) are not well modelled yet. The effects of pore architecture, pore size, pore interconnectivity, inter-connective pore size on the mechanical and functional properties of Ti foams are still not clear, and need more investigations. Energy saving is one of the hot issues in 21st century. There are high requirements of new sintering techniques with rapid energy transfer and less energy consumption to produce dense Ti alloys and foams. The SPS is considered as a novel field sintering technique for fast preparation of diverse bulk materials with a near net shape. The future highlights will be the preparation of nanostructured Ti alloys and the processing of Ti foams with complex shapes by using the SPS technique. The application of the SPS in preparation of the biomedical Ti alloys and foams has perspective future.

6. Acknowledgements

Funding for this research was supported by the DFG-Deutschen Forschungsgemeinschaft (German Research Foundation) with grant No. GRK1505/1 (Welisa). The authors acknowledge the group of PD Dr. Barbara Nebe in Department of Cell Biology of Rostock University for the help in the cell experiments, and the group of PD Dr. Ulrich Beck in Department of Electrical Engineering and Informatics of Rostock University for the help in the SEM experiments.

7. References

Barbieri, F.C.; Otani, C.; Lepienski, C.M.; Urruchi, W.I.; Maciel, H.S.; Petraconia, G. (2007). Nanoindentation study of Ti6Al4V alloy nitrided by low intensity plasma jet process. *Vacuum,* 67: 457–461.

Brown, S.E. (2006). Bone Nutrition, In: *Scientific Evidence for Musculoskeletal, Bariatric, and Sports Nutrition*, Editor: Ingrid Kohlstadt, CRC Press, ISBN: 978-0849337246, US.

Gao, L.; Wang, H.Z.; Hong, J.S.; Miyamoto, H.; Miyamoto, K.; Nishikawa, Y.; Torre, S.D.D.L.(1999). Mechanical properties and microstructure of nano-SiC-Al2O3 composites densified by spark plasma sintering. *Journal of the European Ceramic Society*.19(5): 609-613.

Geetha, M.; Singh, A.K.; Asokamani, R.; and Gogia, A.K. (2009). Ti based biomaterials, the ultimate choice for orthopaedic implants – A review. *Progress in Materials Science*, 54: 397-425.

Gibson L. J. & Ashby M.F. (1997). *Cellular solids: structure and properties.* Cambridge University Press, ISBN: 0-521-49560-1.UK.

Gu, Y.W.; Khor, K.A.; Cheang, P. (2004). Bone-like apatite layer formation on hydroxyapatite prepared by spark plasma sintering (SPS). *Biomaterials*. (25)18: 4127-34.

Hermawan, H.; Dube, D.; Mantovani, D. (2007). Development of degradable Fe-35Mn alloy for biomedical applications. *Advanced Materials Research*.15-17: 107-122.

Ibrahim, A; Zhang, F; Otterstein, E.; and Burkel, E. (2011). Processing of porous Ti and Ti5Mn foams by spark plasma sintering. *Materials & Design*. 32(1):146-153.

Jayaseelan, D. D.; Kondo, N.; Brito, M.E.; Ohji, T. (2002). High-strength porous alumina ceramics by the pulse electric current sintering technique. *Journal of the American Ceramic Society*. 85(1): 267-269.

Li, J.P.; Li, S.H.; Van Blitterswijk, C.A.; de Groot, K. (2005). A novel porous Ti6Al4V: characterization and cell attachment. *J Biomed Mater Res A,* 73: 223-233.

Liu, D.M. (1997). Influence of porosity and pore size on the compressive strength of porous hydroxyapatite ceramic. *Cera. Inter.* 23: 135-139.

Long, M.; Rack, H. J. (1998). Titanium alloys in total joint replacement—a materials science perspective. *Biomaterials*. 19, 1621-1639.

Lou, Y.; Pan, W.; Li, S.; Wang, R.; Li, J. (2003). A novel functionally graded materials in the Ti-Si-C system. *Materials Science and Engineering A.* 345(1-2):99-105.

Mark, J.J.; & Waqar, A. (2007). *Surface Engineered Surgical Tools and Medical Devices*, Springer, ISBN: 978-0-387-27028-9, US.

Munir, Z. A.; Anselmi-Tamburini, U. (2006). The effect of electric field and pressure on the synthesis and consolidation of materials: A review of the spark plasma sintering method. J Materials Science. 41:763–777.

Nicula, R.; Cojocaru, V.D.; Stir, M.; Hennicke, J.; Burkel, E.. (2007). High-energy ball-milling synthesis and densification of Fe–Co alloy nanopowders by field-activated sintering (FAST). Journal of Alloys and Compounds, 434-435: 362-366.

Nicula, R.; Lüthen, R.; Stir, M.; Nebe, J.B.; Burkel, E. (2007). Spark plasma sintering synthesis of porous nanocrystalline titanium alloys for biomedical applications. *Biomolecular Engineering*. 24: 564-567.

Nicula, R.; Turquier, F.; Stir, M.; Kodash, V.Y.; Groza, J.R.; Burkel E. (2007). Quasicrystal phase formation in Al–Cu–Fe nanopowders during field-activated sintering (FAST). *Journal of Alloys and Compounds*. 434-435: 319-323.

Rice, R.W. (1993). Comparison of physical property-porosity behaviour with minimum solid area models. *J. Mater. Sci.* 8: 2187-2190.

Sima, F.; Socol, G.; Axente, E.; Mihailescu, I.N.; Zdrentu, L.; Petrescu, S.M.; Mayer, I. (2007). Biocompatible and bioactive coatings of Mn2+-doped β-tricalcium phosphate synthesized by pulsed laser deposition. *Applied Surface Science.* 254: 1155-1159.

Takemoto, M.; Fujibayashi, S.; Neo, M.; Suzuki, J.; Matsushita, T.; Kokubo, T.; Nakamura, T. (2006). Osteoinductive porous titanium implants: effect of sodium removal by dilute HCl treatment. *Biomaterials*. 27:2682-2691.

Wen, C. E.; Yamada, Y.; Shimojima, K.; Chino, Y.; Asahina, T.; Mabuchi, M. (2002). Processing and mechanical properties of autogenous titanium implant materials. *J. Mater. Sci.: Mater. Med.* 2002,13, 397-401.

Xu, L. P.; Yu, G.; Zhang, E.; Pan, F.; Yang, K. (2007). In vivo corrosion behavior of Mg-Mn-Zn alloy for bone implant application. *J Biomed Mater Res A*. 83: 703–711.

Zhang, F.; Shen, J.; Sun, J. (2004). The Effect of Phosphorus additions on Densification, Grain growth and Properties of nanocrystalline WC/Co composites. *Journal of Alloys and Compounds*. 385(1-2): 96-103.

Zhang, F.; Shen, J.;Sun,J.; Zhu, Y.Q.;Wang, G.; and McCartney, G. (2005) Conversion of Carbon Nanotubes to Diamond by a spark plasma sintering. *Carbon*. 43 (6): 1254-1258.

Zhang, F.; Chang, J.; Lu, J.; Lin, K.; and Ning, C. (2007). Bioinspired structure of bioceramics for bone regeneration in load-bearing sites. *Acta Biomaterialia,* 3(6): 896-904.

Zhang, F.; Lin, K.; Chang, J.; Lu, J.; and Ning, C. (2008). Spark plasma sintering of macroporous calcium phosphate scaffolds from nanocrystalline powders. *Journal of the European Ceramic Society*. 28 (3): 539-545.

Zhang, F.; Weidmann, A.; Nebe, B. J. ; Burkel, E. (2009) . Preparation of TiMn alloy by mechanical alloying and spark plasma sintering for biomedical applications. *Journal of Physics: Con. Series*. 144: 012007.

Zhang, F.; Weidmann, A.; Nebe, J.B.; Beck, U.; Burkel., E. (2010). Preparation, microstructures, mechanical properties, and cytocompatibility of TiMn alloys for biomedical applications. *J Biomed Mater Res Part B,Appl Biomater,* 94: 406–413.

Zhang, F.; Otterstein E.; Burkel E. (2010). Spark plasma sintering, microstructures and mechanical properties of macroporous titanium foams. *Advanced Engineering Materials.* 12(9): 863-872.

10

Development and Application of Low-Modulus Biomedical Titanium Alloy Ti2448

Rui Yang, Yulin Hao and Shujun Li
Shenyang National Laboratory for Materials Science,
Institute of Metal Research, Chinese Academy of Sciences
P. R. China

1. Introduction

Economic development leads to improved living standard, but is also attended by the following consequences: increased number of senile people who, due to degenerative diseases such as arthritis, may need medical assistance in maintaining their convenience of mobility, increased volume of transportation in terms of the number of cars and associated traffic accidents, and increased amount of leisure time channeled to sports that have a higher than average risk of injuries. All these require orthopaedic surgeries and cause increased consumption of biomedical materials.

Load bearing orthopedic implants must satisfy the following requirements (Wang, 1996; Long & Rack, 1999): First of all they are ideally without cytotoxicity, and this places stringent restriction to the choice of alloying elements. Secondly, their long service life coupled with the variety of human activity demands excellence in mechanical properties, primarily high strength and high fatigue resistance, but low elastic modulus. This is a big challenge because for crystalline materials their strength and elastic modulus tend to increase or decrease simultaneously. Thirdly, wear resistance is important because wear causes not only implant loosening but also harmful reactions if the wear debris is deposited in the tissue. Finally, biochemical compatibility requires the implanted materials to possess superior corrosion resistance in body environment and be bioactive. The first two aspects clearly fall into the domain of alloy design; the last two, though closely related to alloy type and composition, are normally the subjects of surface modification.

Judging from the above requirements titanium alloys stand out as the best class of implant materials due to a combination of acceptable biocompatibility and good properties such as high strength, low density, relatively low elastic modulus and excellent corrosion resistance. While Ti–6Al–4V is used earliest in biomedical engineering and is still a benchmark among biomedical alloys (Froimson et al., 2007), it was not purpose-designed. In terms of cytotoxicity, vanadium is toxic both in the elemental state and in the form of oxide (Wapner, 1991; Eisenbarth et al., 2004), and there exits some correlation between V and Al ions released from the alloy and long-term health problems such as Alzheimer disease, neuropathy and ostemomalacia (Nag et al., 2005). These facts highlight the importance of careful choice of alloying additions when designing new alloys specifically for biomedical use.

The main mechanical effect of an implant on the bone relates to stress shielding, i.e., reduction in bone stress *in vivo* following the introduction of the implant. The stress needed by cells around the implant is thus shielded and the cells do not survive. The change in stress

Factor	P-value
Bending stiffness ratio	0.0002
Torsional stiffness ratio	0.0001
Stem bending stiffness	0.0150
Stem tortional stiffness	0.0140
Stem design type	0.2100
Age	0.8500
Sex	0.4700

Table 1. Statistical significance of correlation between severe stress shielding and various influencing factors (Wan et al., 1999).

distribution in the affected bone causes bone loss and originates from the mismatch of stiffness. There is a clinical study (Wan et al., 1999) showing statistical correlation between stress shielding related bone loss in hip arthroplasty and stem to bone stiffness ratio (Table 1). While stiffness of the implant can be adjusted by different design, its shape and function are normally predetermined and do not allow much variation. The main route to improve the match of stiffness between the implant and the bone then is to reduce the elastic modulus of the implant material which is normally 3 or 4 times that of the bone ($4 \sim 30$ GPa (Black & Hastings, 1998))). Recent efforts have brought the Young's modulus down to 55 GPa in the alloy Ti–29Nb–13Ta–7.1Zr but this is still almost twice that of bone (Table 2).

The titanium alloy we developed over the past few years, Ti–24Nb–4Zr–8Sn, code named Ti2448, has a record low incipient Young's modulus of 42 GPa, while maintaining a high strength of over 850 MPa (Hao et al., 2005)). The alloy has undergone a full cycle of development, biosafety examination, implant part design and manufacturing, *in vivo* tests and clinical trials. In the following, we first outline key design considerations of this low-modulus, high-strength biomedical alloy, followed by some details of alloy development and optimization. Biomechanical properties of Ti2448 will then be described, with particular attention paid to the peculiar mechanisms of elasticity. A number of surface modification strategies have been tried on this new alloy and the outcome will be briefly reviewed. We conclude this chapter after a mention of the *in vivo* and clinical test results.

Alloy	E (GPa)	Alloy	E (GPa)
CoCr (Cast)	240	Ti–13Nb–13Zr	77
AISI 316L	210	Ti–29Nb–13Ta–4Mo	74
Commercial Pure Ta	200	Ti–29Nb–13Ta–6Sn	74
Ti–6Al–4V	112	Ti–29Nb–13Ta–4.6Sn	66
Ti–6Al–7Nb	110	Ti–29Nb–13Ta–4.5Zr	65
Ti–5Al–1.5B	110	Ti–29Nb–13Ta–2Sn	62
Commercial Pure Ti	100	Ti–29Nb–13Ta–7.1Zr	55
Ti–16Nb–13Ta–4Mo	91	NiTi	48
Ti–12Mo–6Zr–2Fe	85		
Ti–15Mo–5Zr–3Al (ST) aged	80	Ti2448 (Ti–24Nb–4Zr–8Sn)	42
Ti–29Nb–13Ta–4.6Zr (aged)	80	Bone	30

Table 2. Young's modulus E of biomedical alloys compiled in a recent review (Geetha et al., 2009), in comparison with that of Ti2448 and of bone.

2. Primary design considerations

For most binary titanium alloys formed with transition metal (TM) elements the variations of their Young's moduli with solute concentration are as shown in Fig. 1. Ti–Fe is typical of the so-called β-eutectoid alloys formed with elements such as Cr, Mn, Fe, Co and Ni, while Ti–Mo is representative of the β-isomorphous alloys such as Ti–V, Ti–Mo and Ti–Nb. Roughly, the distinction between these two families of alloys is that right of the peak on the modulus curve, with increasing solute concentration, E continues to decrease (before final increase) for Ti–Fe, but increases right away for Ti–Mo. On the schematic drawing of Fig. 1c, at low e/a with decreasing solute concentration the β phase becomes less stable and the formation of the α phase or α' martensite causes the Young's modulus to increase. At high e/a the β phase is stabilized and the Young's modulus increases with solute content. The peak in the middle is essentially caused by the formation of metastable ω phase which has a higher modulus than the β. The effect of the α'' martensite is superimposed on the curve and its formation helps to shape the valley left of the peak.

In designing a new generation of biomedical titanium alloys the first principle is to exclude elements that are toxic or are allergic in human body. We use the following alloying strategy to reduce the elastic modulus: First, the alloying additions must remove the ω phase as it is not only responsible for the peak in elastic modulus but also regarded as highly undesirable due to its embrittling effects. Secondly, the alloying should ideally depress the martensite start point to below ambient temperature so that the transformation can be stress induced. This transformation can then be employed to improve superelasticity, a characteristic useful in many biomedical applications. Thirdly, it can be seen from Fig. 1 that even after the peak is removed the elastic modulus represented by the minimum on the dotted curve is still far higher than that of bone. So the alloying scheme must be able to further reduce the intrinsic elastic modulus of the β phase. Finally, of course, strength should not be compromised as a result of alloying.

A first principles method to estimate the bulk moduli of body-centred cubic metals was proposed by computing the binding energy per atom of an atomic cluster and then taking the second order derivative of the binding energy vs. unit cell volume plots at the equilibrium point (Song, Yang, Li, Wu & Guo, 1999). By constructing a cluster containing a solute the bulk modulus of β-type titanium alloys can be estimated and the results for a series of Ti–TM

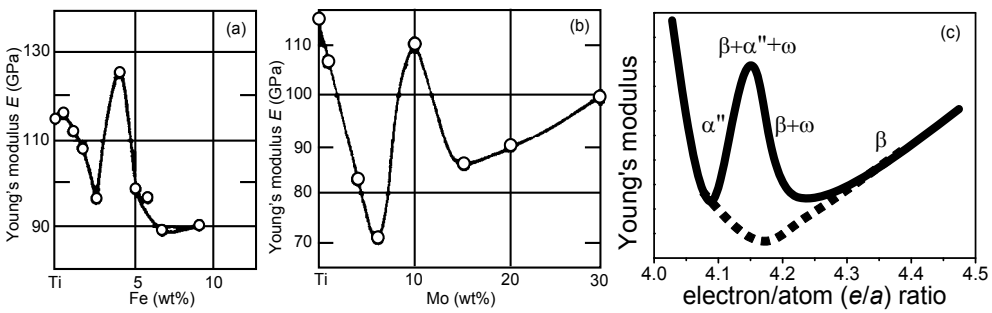

Fig. 1. Young's moduli, E, of Ti-Fe (a) and Ti-Mo (b) alloys as functions of composition (Fedotov, 1973). A schematic of the E vs. e/a plot for Ti-TM alloys is shown in (c) with the dotted curve indicating the intrinsic minimum in E of the β phase (Hao, Li, Sun, Zheng & Yang, 2007).

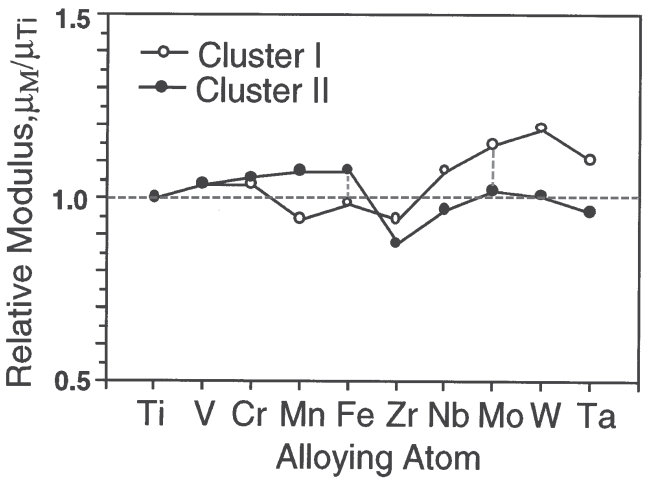

Fig. 2. Relative modulus of Ti–TM alloys to the β-Ti control. The open and solid symbols are estimates from clusters containing 15 and 27 atoms, respectively (Song, Xu, Yang, Li, Wu & Guo, 1999). Dotted lines are for guiding the eye.

alloys were reported (Song, Xu, Yang, Li, Wu & Guo, 1999). Figure 2 shows plots of the relative modulus (compared to pure β-Ti) of both β-eutectoid and β-isomorphous type alloys. Because calculations with a larger cluster take into account more atomic interactions the results are considered more reliable. It can be seen from the plot for Cluster II that Zr, followed by Nb and Ta, reduces the intrinsic modulus of β-Ti.

The change of the relative modulus for a given alloying addition for the two atomic clusters in Fig. 2 is worth noting. Because a solute atom in a smaller β-Ti cluster qualitatively corresponds to a higher solute concentration than that in a larger cluster, the computed results appear to agree with the two types of modulus curve represented by Fig. 1a and b. In Fig. 2, for the β-eutectoid alloys (e.g., Fe addition) the modulus for cluster I is smaller than for cluster II, while for the β-isomorphous alloys (e.g., Mo addition) the reverse is true (although for V, modulus values for the two clusters are similar, suggesting a slow increase in elastic modulus with increasing V addition).

In deciding the primary binary alloy system as a basis for further alloy development, we consider Ti–Zr not suitable because Zr is in the same group as Ti on the periodic table. To modify the properties that are sensitive to the c/a, such as the β phase stability, alloying with Zr is inefficient. A recent, more sophisticated first principles calculation (Hu et al., 2008) confirmed the above empirical rule. The theoretical results also show that although Zr stabilizes the β phase energetically (thermodynamically) this phase remains elastically (mechanically) unstable. Ta on the other hand is heavy and has a high melting point. As a result alloys containing Ta are prone to segregation and are more difficult and costly to melt. The high cost of elemental Ta and its high density compared to other TM metals certainly do not favour its use in biomedical alloys. The above considerations left Ti–Nb as our choice of the primary alloy system for further property improvement and composition optimization.

3. Development and optimization

Zr and Sn are very effective in suppressing the α'' martensitic transformation of alloys based on Ti–Nb, and the addition of 1 wt% of Zr and Sn reduces the martensitic start temperature

by 41.2 K and 40.9 K, respectively, as compared to 17.6 K by 1 wt% of Nb (Hao et al., 2006). First principles computations (Hu et al., 2008) suggest that the addition of Nb to Ti increases both the elastic and phase stability of the β. Our theoretical Nb concentration above which the β phase is stable is about 24 at.%, in perfect agreement with experimental values of 21 – 23 at.% (Collings, 1984; Dobromyslov & Elkin, 2001). However, a stable β phase of binary Ti–Nb (with at least 24 at.% Nb) possesses undesirbable high elastic moduli. Replacing some of the Nb with Zr suppresses the elastic moduli to a relatively low level, but Zr does not effectively improve the stability of the β phase. Adding Sn improves efficiently the phase stablity of the β while avoiding to harden most of the elastic moduli. Excessive amount of Sn, however, has the undesirable consequence of increasing $E_{\langle 111\rangle}$ and $G_{\{001\}\langle 010\rangle}$. Systematic composition optimization has to be carried out to achieve the best biomechanical properties.

Atomic interactions become more complex in multicomponent alloys and two results of the first principles computation (Hu et al., 2008) are particularly worth noting. The first is that the stabilizing effects of Sn and Zr on the β phase become weaker in the ternary alloys (containing 15 at.% Nb) than in the binary alloys. Thus the alloying effects on the phase stability of β-type titanium alloys cannot be simply superimposed. The second is the stronger β-stabilizing effect of Sn than Nb which is unexpected because Sn is commonly believed to be a weak α stabilizer while Nb certainly is a β stabilizer in most $\alpha + \beta$ two-phase alloys. This effect of Sn must be due to the new patterns of constituent phases of the β-type alloys, where the α phase has been suppressed and the rivals become metastable phases such as the ω and the α''.

Table 3 presents the constituent phases of Ti–Nb–Zr–Sn alloys with compositions in the interested range, as identified by x-ray diffraction analysis. It can be seen that for most compositions a metastable phase, either the ω or the α'', accompanies the β, but there does exist a composition range in which the β phase is sufficiently stabilized to be alone. This composition range corresponds to the dotted curve of Fig. 1c, i.e., the peak of the Young's modulus has been successfully removed. Because Ti–Nb is a β-isomorphous system we need to keep Nb content to a minimum in order to minimize the elastic modulus. Thus alloys around the composition of Ti–24Nb–4Zr–7.5Sn are of interest and potentially possess the lowest Young's modulus.

The cyclic tensile stress-strain curves of the $\beta + \omega$ and β type microstructures are compared in Fig. 3. In the former the tensile curves are normal and the alloy exhibits linear elastic deformation before plastic yield at about 1% strain. The β type microstructure, however, shows stress-strain behaviour that sharply contrasts the two-phase microstructure. The "double yield" feature characteristic of stress induced martensitic transformation is quite evident, and the shoulder on the curve corresponds to the formation of the α'' martensite during tensile straining. Recoverable strain increases to about 2% enclosing a fairly significant hysterisis loop.

	20Nb	22Nb	24Nb	26Nb
2Zr–7.5Sn			$\beta + \alpha''$	
4Zr–7.5Sn	$\beta + \alpha''$	$\beta + \alpha''$	β	β
8Zr–7.5Sn			$\beta + \omega$	
4Zr–3.5Sn	$\alpha'' + \omega$	$\alpha'' + \omega$	$\beta + \alpha''$	$\beta + \alpha''$
4Zr–11.5Sn	$\beta + \omega$		$\beta + \omega$	$\beta + \omega$

Table 3. Nominal chemical composition (wt%) and corresponding phase constitution of as-quenched Ti–Nb–Zr–Sn alloys determined by x-ray diffraction analysis (Hao et al., 2006).

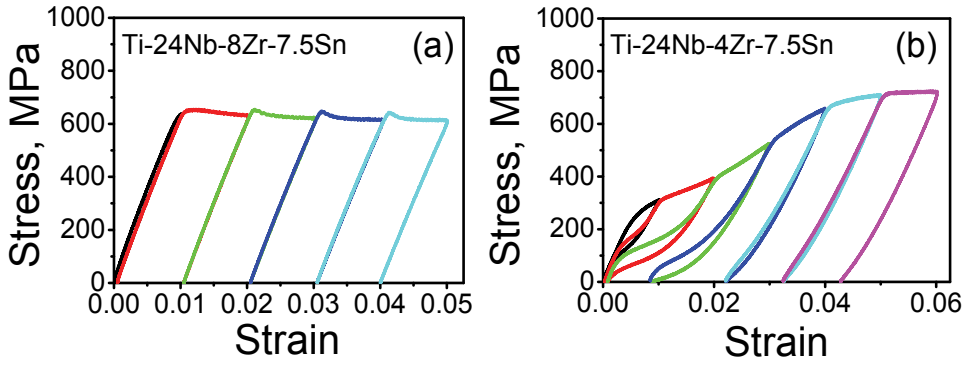

Fig. 3. Stress-strain curves at 294 K of water quenched Ti–24Nb–8Zr–7.5Sn with $\beta + \omega$ (a), and Ti–24Nb–4Zr–7.5Sn with β (b) starting microstructure.

Detailed experimental studies show that the recoverable strain and the shape of the cyclic stress-strain curve are sensitive to oxygen and Sn content. The double yield feature is most pronounced in the lower-solute alloys. At intermediate solute content of Ti–24Nb–4Zr–7.9Sn–(0.11∼0.12)O (Hao et al., 2005; Hao, Li, Sun, Sui & Yang, 2007), total recoverable strain is large and strongly nonlinear, but the characteristic form of a superelastic flow curve is smoothed such as to obscure any signs of a plateau characteristic of double yield phenomena. These alloys represent the optimized compositions and we code name them Ti2448 to reflect the nominal composition of Ti–24Nb–4Zr–8Sn.

It is worth noting that Zr is a very potent strengthener in Ti2448 whose tensile strength after hot work ranges between 690–920 MPa depending on interstitial content. This compares to a mere 460 MPa of Ti–24.3Nb–8.3Sn (Nitta et al., 2004), nearly equal to the Ti2448 composition less Zr. Removal of the stress plateau on the stress-strain curve of Ti2448 makes it particularly suitable for biomedical applications which require high strength and high fatigue endurance.

4. Biomechanical properties

As mentioned in the previous sections, key to implant applications are low elastic modulus and preferably good elasticity, as well as high strength and fatigue resistance. These biomechanical properties with reference to Ti2448 will be reviewed in this section.

First of all the definition of Young's modulus should be noted. For linear elastic behaviour the tensile Young's modulus is defined as the slope of the linear elastic range before the onset of plastic deformation. For materials exhibiting nonlinear elastic behaviour, such as β-type titanium alloys, however, linearity does not extend to the whole elastic range, and Young's modulus becomes a function of elastic strain. In such cases, *incipient* Young's modulus, which refers to the slope of tangent at zero strain on the stress-strain curve, should be differentiated from *average* Young's modulus which is defined as that of an intersection line from zero to the upper limit of fully recovered strain during unloading. Figure 4 illustrates the point with hot-rolled Ti2448 tensile strained to slightly above the fully recovered strain. Since the initial 0.5% tensile strain of Ti2448 is almost linear, incipient Young's modulus is conveniently defined as the slope of the linear elastic range up to 0.5%. This method gives better accuracy than employing the tangent at the zero strain point of the stress-strain curve. The average Young's modulus is a good measure of stiffness at large strains and is in general smaller than the incipient Young's modulus. The implant for hard tissue replacement however is not

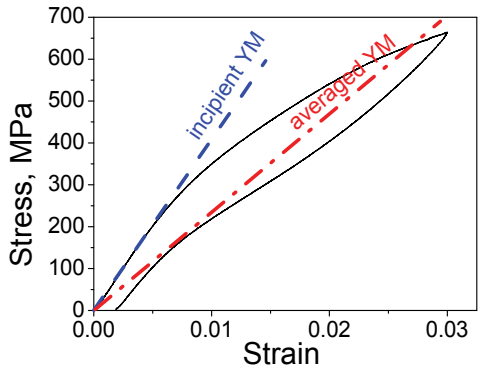

Fig. 4. Stress-strain curves of loading-unloading deformation of as hot-rolled Ti2448, illustrating definition of the Young's modulus (YM)(Hao, Li, Sun, Zheng & Yang, 2007).

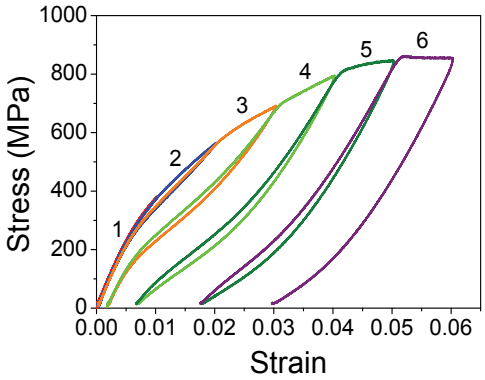

Fig. 5. Cyclic loading-unloading stress-strain curves of hot-rolled Ti2448 to a total strain of 0.06 at a strain step of 0.01 (Hao et al., 2005).

expected to undergo large deformation and the incipient Young's modulus is a more suitable quantity to describe the elastic compatibility with human bone. In this chapter, all Young's modulus, except otherwise stated, refers to the incipient Young's modulus.

The typical cyclic loading stress-strain curves of Ti2448 is shown in Fig. 5. As mentioned in the previous section, the plateau on the loci of stress-strain curves typical of double yield has completely disappeared, making it difficult to judge if stress induced martensitic transformation took place during loading. Compared to the two kinds of shapes of stress-strain curves in Fig. 3, Fig. 5 represents a new kind. Apparent from the stress-strain curves, Ti2448 does not exhibit work hardening, and the ultimate tensile strength of this particular sample (influenced by oxygen content) is 850 MPa. The cyclic straining experiment allows us to gain the following information: The recoverable strain, at about 2.8% for the virgin sample, slightly increases with prestrain to a maximum of about 3.3% in the fourth cycle. The incipient Young's modulus measured from the stress-strain curve for the first loading cycle is 42 GPa, and maintains approximately this value for the second and third cycle. For subsequent cycles with unrecoverable strains, however, the incipient Young's modulus progressively decreases, to a value of 18 GPa in the sixth loading cycle. We term this uncommon behaviour elastic softening due to prestrain.

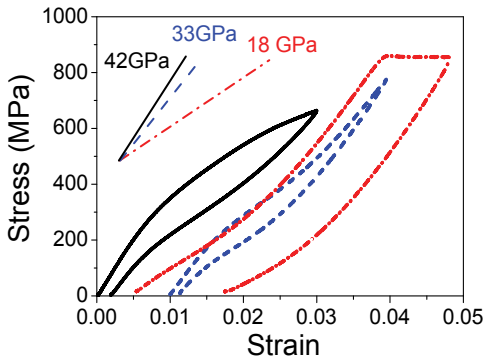

Fig. 6. Elastic softening during prestrain and recovery durign ambient temperature ageing of the as hot-rolled Ti2448. Solid, dash-dot, and dash curves are respectively single step loading-unloading (Fig. 4), the sixth cycle stress-strain curve in Fig. 5, and stress-strain curve of the same tensile sample tested 6 days after the cyclic deformation experiment, demonstrating partial recovery of incipient Young's modulus (Hao, Li, Sun, Zheng & Yang, 2007).

Even more striking is the recovery of the softened elastic modulus during ageing at room temperature, which is unusual for titanium alloys (Fig. 6). The cyclic tensile tested sample was subjected to straining experiment again after 6 days (to a strain of 0.03, see Fig. 6)) and it was observed that the incipient Young's modulus increased from 18 GPa to 33 GPa. The same experiment after 6 month on the same sample showed that the incipient Young's modulus is stabilized at about 33 GPa and does not recover in a significant way any further.

The above elastic softening due to prestrain and recovery behaviour appear to mimic the biological characteristics of human bone. With sport or movement induced strain, the incipient Young's modulus of the implant would progressively decrease to fall to the modulus range of human bone to allow complete elastic matching. During rest the implant would gradually recover its modulus to a value slightly above that of human hard tissue. Understanding of the elastic softening and recovery of Ti2448 is incomplete, but some clues to this extraordinary behaviour will be discussed in the next section.

The effects of different heat treatment on the mechanical properties of Ti2448 have been systematically investigated (Hao, Li, Sun, Zheng & Yang, 2007). Solution treatment at high temperature has weak effect on superelasticity but causes the decrease of strength and slight increase of the incipient Young's modulus (by about 8 GPa). Slower cooling (such as air cooling) causes a slight increase of tensile strength and incipient Young's modulus (3–5 GPa) and reduces the recoverable strain compared to water quenching after solution treatment. This is interpreted as a consequence of the precipitation of the α phase during slow cool. The β stabilizers such as Nb are enriched in the β phase as a result of the precipitation to make the β phase more resistant against elastic deformation and phase transformation. The formation of the α phase and increased content of Nb in the β phase both increase the elastic modulus of the alloy, as is clear from Fig. 1c. It should be noted that the ω phase that normally appears under such conditions in most β-type titanium alloys does not appear in this alloy, although it may form in alloys with different contents of alloying additions of the Ti–Nb–Zr–Sn system. For ageing treatment up to 30 min at both 723 K and 773 K, nonlinear elastic deformation is still present. Short time ageing of 10 min at both temperatures causes slight increase in both strength and incipient Young's modulus; the recoverable strain, however, seems not

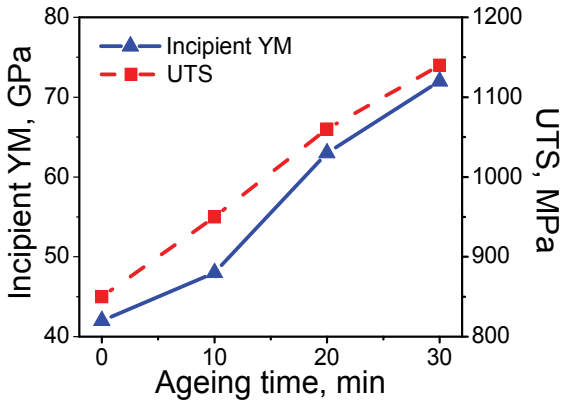

Fig. 7. Variation of the incipient Young's modulus and ultimate tensile strength with ageing time at 773 K (Hao, Li, Sun, Zheng & Yang, 2007).

affected as compared to the as hot-rolled samples. Further increase in ageing time causes the recoverable strain to decrease gradually and the elastic deformation tends to the normal linear behaviour.

Although the incipient Young's modulus increases with the increase of strength as a result of the low temperature ageing treatment, a balance of the two properties better than previously reported alloys has been achieved (Fig. 7). For the present composition, 10 min ageing at 773 K raises the incipient Young's modulus to ∼48 GPa and increases the ultimate tensile strength to 950 MPa; at a strength of ∼1150 MPa, the incipient Young's modulus is only ∼72 GPa. Under the condition of identical strength, comparison shows that Ti2448 has lower elastic modulus than previously reported β-type titanium alloys (Long & Rack, 1999; Niinomi, 2002; Matsumoto et al., 2005).

Since structural biomedical materials are used under cyclic loading conditions fatigue properties of an implant is key to its application. For materials exhibiting the double yield phenomenon during tensile testing, the first yield corresponds to the critical stress to trigger the α'' martensitic transformation from the β phase. This exceptionally low strength of the first yield raises concern over the endurance life of implants of such materials in human body. Because of the significant effect of Sn in depressing the martensitic start temperature, a reduction of Sn content over Ti2448 would produce the double yield as can be seen from Fig. 3b. Interstitial oxygen in the β is known to increase its phase stability against martensitic transformation. We have studied the fatigue properties of an alloy with the composition of Ti–24Nb–4Zr–7.6Sn–0.07O (instead of the normal ∼0.11 O) ((Li, Cui, Hao & Yang, 2008)). The obtained data should represent the lower bound of the fatigue properties of Ti2448.

The fatigue endurance limit of the hot-forged 7.6Sn alloy is comparable to that of commercial pure titanium but lower than that of Ti–6Al–4V ELI. In 0.9% NaCl the 7.6Sn alloy performs slightly better than in air in the low cycle regime. Ageing treatment at 673 K for 4 h, allowing the α phase to precipitate, increased the fatigue limit of the 7.6Sn alloy to higher than 425 MPa, which is comparable to the fatigue limit of Ti–6Al–4V ELI. This increase in fatigue strength is largely due to increased resistance to the fatigue crack initiation and to small fatigue crack propagation (Niinomi, 2003). The fatigue resistance of the cold-rolled sheets is ∼50% higher than the hot-forged bars and the data are compared to Ti–6Al–4V ELI in Fig. 8. Cold-processing techniques such as rolling and swaging are reasonable options to improve fatigue properties of this material (∼375 MPa in the case of cold rolling). Increasing

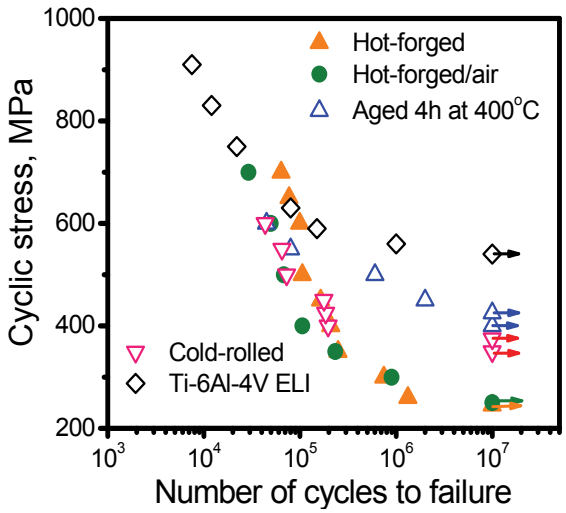

Fig. 8. *S-N* curves of Ti–24Nb–4Zr–7.6Sn tested in 0.9% NaCl except that noted in air. Data of the hot-forged Ti–6Al–4V ELI are also shown for comparison (Li, Cui, Hao & Yang, 2008).

the contents of both Sn and oxygen are effective measures to increase the fatigue strength of this class of alloys. The combination of composition optimization and heat treatment leads to a much better balance of strength, modulus and fatigue endurance in Ti2448 than Ti–6Al–4V ELI. In applications where fatigue endurance property is critical, for example, Ti2448 can be heat treated to a strength range of 1000 to 1150 MPa (with corresponding incipient Young's modulus of 60 to 72 GPa, see Fig. 7), ensuring higher high-cycle fatigue life than Ti–6Al–4V ELI while gaining the benefit of a 35% to 45% reduction in the incipient Young's modulus.

Strain-controlled low cycle fatigue properties of the hot-forged 7.6Sn alloy and Ti–6Al–4V ELI were investigated at a strain ratio 0.1 and a frequency of 0.5 Hz in air at room temperature. Figure 9 compares the maximum cyclic strains plotted against the number of cycles to failure, and it can be seen that a linear relation is obtained for both alloys. The 7.6Sn alloy shows a much higher fatigue resistance than Ti–6Al–4V ELI in the strain-controlled fatigue test. For cyclic strains between 0.25% and 2.5%, in particular, the 7.6Sn alloy reaches $\sim 4\times10^4$ cycles to failure but Ti–6Al–4V ELI withstands only $\sim 6\times10^2$ cycles.

The cyclic stress-cycle curves of the 7.6Sn alloy is compared to Ti–6Al–4V ELI in Fig. 10. For the 7.6Sn alloy, at low strains ($<\sim$3.5%), an obvious cyclic hardening after the initial cyclic softening can be observed, while the softening trend continues at high strains ($>\sim$4.0%). Ti–6Al–4V ELI, on the other hand, exhibits no hardening for all strains in the studied range larger than $\sim$2.5% (well beyond its elastic limit of $\sim$0.6%). The cyclic hardening of the 7.6Sn alloy is not fully understood yet, and is believed to be related to the stress induced α'' martensitic transformation as well as the heterogeneous formation of a tiny amount of the ω phase at high cycles (Li, Cui, Hao & Yang, 2008).

Figure 11 compares the hysteresis loops of the 7.6Sn alloy and Ti–6Al–4V ELI with a maximum strain of $\sim$2.5%. The hysteresis loop per cycle of the 7.6Sn alloy is not symmetrical and the plastic strain per cycle is much smaller than that of Ti–6Al–4V ELI. The cycle numbers to failure (N_f) and the plastic strain per cycle ($\Delta\varepsilon_p$) of both alloys can be fitted to the Coffin-Manson equation (Puska & Golovin, 1985): $N_f^{\gamma}\Delta\varepsilon_p = C$, in which γ and C are constants related to the elongation to fracture of material in static loading. The obtained values of these

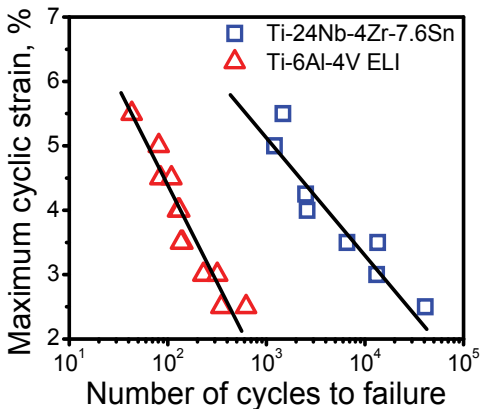

Fig. 9. Low cycle fatigue curves of as-forged Ti–24Nb–4Zr–7.6Sn and Ti–6Al–4V ELI tested in air (Li, Cui, Hao & Yang, 2008).

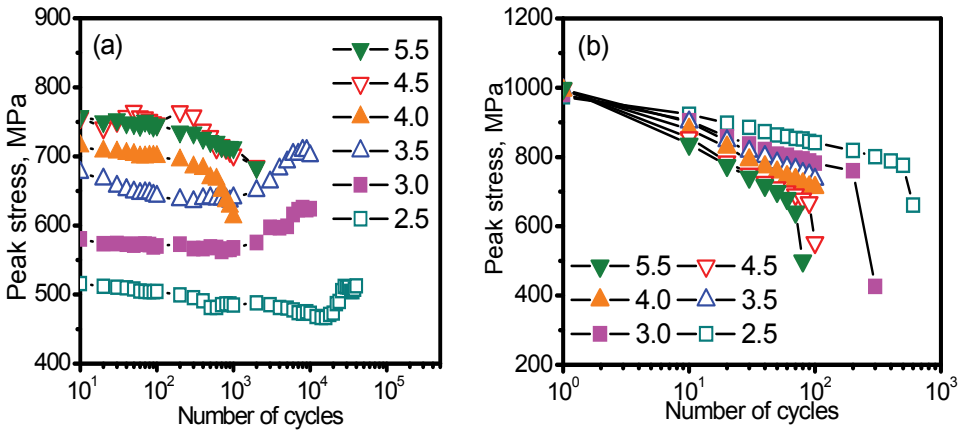

Fig. 10. Cyclic stress response curves of as-forged Ti–24Nb–4Zr–7.6Sn (a) and Ti–6Al–4V ELI (b) at different maximum strains (in percent) (Li, Cui, Hao & Yang, 2008).

two parameters for the 7.6Sn alloy are 0.46 and 0.22, respectively, both much lower than those for Ti–6Al–4V ELI (0.72 and 1.21, respectively). The low values of the $\Delta\varepsilon_p$ and γ are in accord with materials exhibiting superelastic deformation behaviour.

The beneficial effects of low incipient Young's modulus on implant robustness have been demonstrated by a study of biomechanical properties of lumbar interbody fusion cages made of the 7.6Sn alloy and Ti–6Al–4V, with incipient Young's modulus of 50 GPa and 110 GPa, respectively (Zhu et al., 2009). Both types of cages were found to be able to withstand identical compression load of ∼9.8 kN (much larger than the physiological load of human body) and endure fatigue cycles beyond 5×10^6 without functional or mechanical failure under 2.0 kN axial compression. The anti-subsidence capability of both group cages was examined by axial compression of thoracic spine specimens dissected freshly from the calf with average age of 6 months. The stiffness of the vertebral bodies (K_v), which reflects resistance of the cage against subsidence, determined from this study for the 7.6Sn alloy and Ti–6Al–4V is 724 ± 8 N/mm and 527 ± 14 N/mm, respectively. These results demonstrate a clear advantage of the

low modulus alloy over conventional Ti–6Al–4V in biomechanical performance for interbody fusion cage applications.

5. Elastic and plastic deformation

The record low incipient Young's modulus of Ti2448 is a result of its peculiar elastic constants. These elastic properties also lead to new mechanisms of elastic deformation as well as unusual plastic behaviour, as will be reviewed in the following.

5.1 Elastic deformation

As mentioned in the previous sections, the widely accepted mechanism of elastic deformation in β-type titanium alloys is stress induced α'' martensitic transformation. While the double yield feature is apparent in the 7.5Sn (Fig. 3b) and 7.6Sn alloys, it is not observable for Ti2448 (Fig. 5), although after plastic deformation the α'' phase could be detected by x-ray diffraction (Hao et al., 2005). These results suggest that the stress induced phase transformation in Ti2448 possesses new characteristics compared with commonly observed α'' martensite.

It should be noted that both the β and the α can be regarded as special cases of the orthorhombic structure of the α'' phase, and can be achieved by changing the principal strains of the orthorhombic unit cell and atomic shuffle of the basal plane of $(110)_\beta \parallel (010)_{\alpha''}$ (Bendersky et al., 1994). The principal strains of the invarant plane strain transformation β-α'' can be reduced through alloying ((Hao et al., 2006)), to such a degree that the α'' phase cannot be detected by lab-scale x-ray diffraction during *in situ* straining experiment. This is true for both Ti–30Nb–10Ta–5Zr (Obbard et al. (2010)) and Ti2448 (Hao, Li, Sun, Sui & Yang (2007); Obbard (2010)). Only with synchrotron x-ray diffraction could such a stress induced transformation be detected.

Detailed analysis of synchrotron x-ray diffraction of *in situ* tensile experiment with Ti2448 sheds light on the stress induced phase transformation process. The thoroughness of shuffle of the $(110)_\beta$ atomic planes is much less in Ti2448 than in binary Ti–Nb alloys: the fraction of those achieving complete shuffle is only $0.26 \sim 0.43$ for Ti2448, but $0.60 \sim 0.83$ for binary Ti–Nb (Obbard et al. (2011)). Interstitial oxygen reduces both the degree of $(110)_\beta$ shuffle and the principal strains of the β-α'' transformation, to the effect that the critical stress for the α'' formation is increased, and stress plateau on the stress-strain curves is shortened. On the

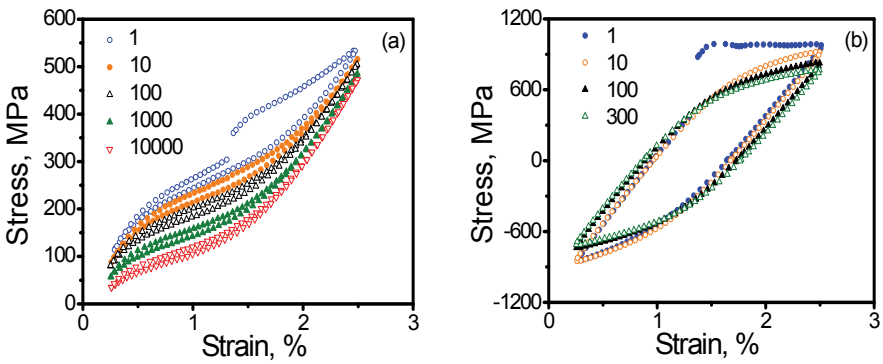

Fig. 11. Hysteresis loop of as-forged Ti–24Nb–4Zr–7.6Sn (a) and Ti–6Al–4V ELI (b) recorded at different cycles of maximum strain 2.5% during the low cycle fatigue test (Li, Cui, Hao & Yang, 2008).

other hand, the habit plane of the α'' transformation in Ti2448, $\{755\}_\beta$, is of relatively high symmetry, making the stress plateau even steeper than other alloys. These two factors lead to the disappearance of the double yield feature on the stress-strain curves of Ti2448.

Figure 12 compares the experimental stress-strain curves of both the 7.6Sn alloy and Ti2448 with theoretical ones obtained by sophisticated modelling based on synchrotron x-ray diffraction data and a model of α'' phase transformation (Obbard et al. (2011)). With increasing stress the mechanisms of recoverable strain of thermoelastic martensitic materials include martensitic shape change, detwinning of martensitic variants (Gao et al. (2000)), and martensite reorientation (Heinen et al. (2009)). The above model accounts for only the first mechanism. The detwining mechanism could reasonably be discounted here because of the small probability of twinned variants in Ti2448 due to the small transformation strains. The theoretical curves in Fig. 12 can be seen to depict the main features of the experimental curves and the agreement is better for the 7.6Sn alloy. The difference is larger for Ti2448, with the experimental strain higher than the theoretical one, and can be partly attributed to the omitting of the martensite reorientation mechanism. Other mechanisms to be discussed below also contribute to the difference. The theoretical model assumes a critical stress for the start of the transformation below which the stress-strain relation is linear. This is seen clearly from Fig. 12 to be in disaccord with experiment.

Figure 13 shows the change in peak width of $\{110\}_\beta$ and $(021)_{\alpha''}$ during 3 load cycles for both the 7.6Sn alloy and Ti2448. The difference between the two alloys is that the $(021)_{\alpha''}$ peak for the 7.6Sn alloy is sharp and its width decreases during loading; that for Ti2448 however is wide and the width tends to increase during loading below the nominal yield stress (Fig. 13d,e) while the peak width decreases during loading above the nominal yield stress (Fig. 13f). These results indicate that the α'' transformation in the 7.6Sn alloy is relatively easy to judge but it is much more difficult in the case of Ti2448. Other forms of deformation, such as precursor transformation and decomposition of the parent phase, cannot be ruled out.

The departure from linear elasticity at low applied stress before the onset of the α'' transformation may also be due to lattice distortion of the β phase. Figure 14 compares the bulk and shear moduli of Ti2448 with typical solid materials (Hao, Li, Sun, Sui & Yang (2007)). The bulk modulus of Ti2448, at 23.9 GPa, clearly reaches a record low value; and it is almost identical to the shear modulus. Low bulk modulus and Young's modulus correspond to low ideal strength and it was estimated that the β phase of Ti2448 has an ideal strength of $\sim$ 1.6 GPa. The difference between such an ideal strength and a tensile strength of 800$\sim$900 MPa is

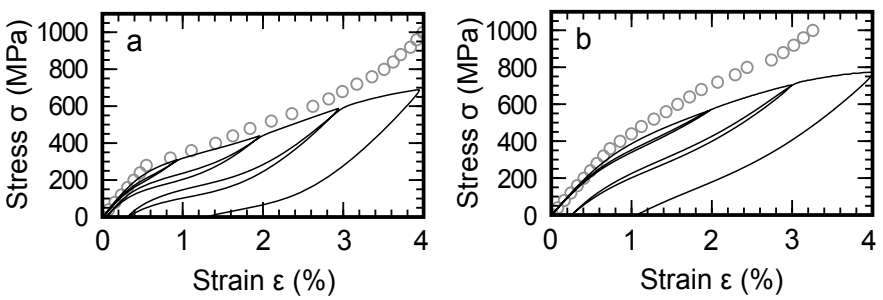

Fig. 12. Cyclic stress-strain plots (solid lines) and strain (circles) calculated using a phase transformation model applying texture and crystallography observed through synchrotron x-ray diffraction: (a) Ti–24Nb–4Zr–7.6Sn–0.08O; (b) Ti–24Nb–4Zr–8Sn–0.15O (Obbard et al., 2011).

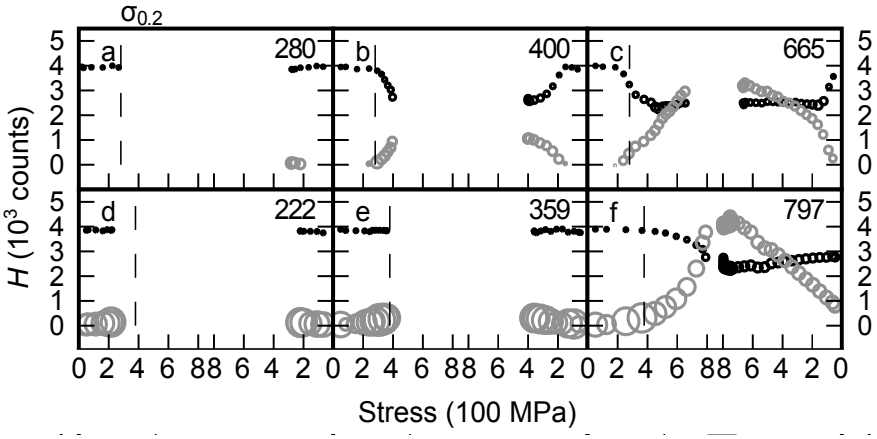

Fig. 13. Height and width of diffraction peaks over three consecutive load cycles for Ti–24Nb–4Zr–7.6Sn–0.08O (top) and Ti–24Nb–4Zr–8Sn–0.15O (bottom). Dark and light symbols show normalised H of $\{110\}_\beta$ and the absolute H of $(021)_{\alpha''}$. Radius of symbols is proportional to peak half-width-half-maximum; vertical lines mark nominal yield stress measured from stress-strain curves; inset stress is maximum (in MPa) for given cycle (Obbard et al., 2011).

therefore very small, leading to postulation that the β phase is approaching its limit of elastic stability in Ti2448 under applied stress. Because bulk modulus is a measure of resistance against bond length change a low value suggests more significant elastic softening under hydraulic tensile stress. Such softening would contribute to the nonlinear elastic deformation of Ti2448 below the critical stress for α'' phase transformation.

The peculiar elastic properties of Ti2448 are expected to modify its plastic deformation behaviour as will be discussed in the next subsection. A condition for dislocation based plasticity is bulk modulus being larger than shear modulus which is true for most structural metals. To investigate dislocation behaviour we choose the 7.6Sn alloy which has a higher bulk modulus (43 GPa) than Ti2448 and a shear modulus of 21 GPa. During *in situ* tensile test under high-resolution transmission electron microscopy, dislocation loops were found to nucleate homogeneously from the β phase and these loops may expand under applied

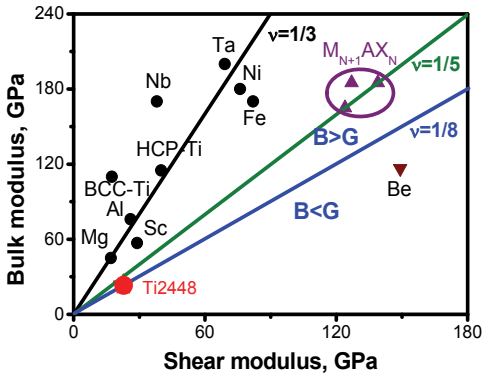

Fig. 14. A collection of shear and bulk moduli of some metals and metal-like ceramics $M_{N+1}AX_N$ in comparison with Ti2448 (Hao, Li, Sun, Sui & Yang, 2007).

stress, and shrink when the sample was held (stress relaxation) to complete disappearance (Fig. 15) (Cui et al., 2009). Dislocations normally nucleate heterogeneously at crysal defects that supply the enery needed to overcome the nucleation barrier. Homogeneous nucleation of dislocations is quite unusual and the energy needed in this case is probably supplied by the significant lattice distortion prior to the nucleation event. The reversible process of the formation and annihilation of the dislocation loops means that this plastic event has become an elastic mechanism. This novel mechanism contributes to the nonlinear elastic deformation prior to the stress induced α'' martensitic transformation.

Because the structural difference between the β and the α'' phase in Ti2448 is much reduced compared to Ti–Nb binary alloy, it is very difficult to judge experimentally when the martensitic transformation starts during loading. For the 7.6Sn alloy with slightly larger transformation strains (compared to Ti2448), differential scanning calorimetry managed to detect a peak due to the transformation. For Ti2448 which exhibits a more sluggish transformation to the α'', no peak of the new phase could be detected using this technique. It should be pointed out that the different mechanisms of elasticity may have originated from the same characteristics of the parent phase. A low energy phonon mode ($T_1\frac{1}{2}[110]$) can be noted on the phonon dispersion curves of pure titanium at 1293 K (Petry et al., 1991). This phonon mode may be softened further to a local minimum as a result of alloying and it is likely the common origin of the different modes of elastic deformation. In fact, the homogeneously nucleated dislocation loops observed in the 7.6Sn alloy are of the $k[1\bar{1}0](110)$ type, and a structure based on a stack of these loops is rather similar to the early stage of the α'' phase. These mechanisms of elasticity are therefore closely related to each other but clarifications of the specific links and delicacies require further investigation.

5.2 Plastic deformation

Plastic deformation of Ti2448 exhibits peculiar features that have not been observed in other metals. At a compression ratio of only 50% at a strain rate of $\sim 1\ s^{-1}$, highly localized plastic zones were observed in the deformed samples, leading to significant rotation of local volume and rapid grain refinement (Fig. 16). In Fig. 16a, for example, sandwiched between two nanostructure bands, local volumes rotate by almost 29 degrees (from ~[111] to ~[113]) in a spatial span of 1 μm. In Fig. 16b, the top and bottom regions of the view field (belonging to the same original grain) become amorphous and nanocrystalline, respectively.

The extraordinary behaviour of plastic deformation of Ti2448 has its origin in the elastic properties. Because bulk modulus and shear modulus respectively represent resistance

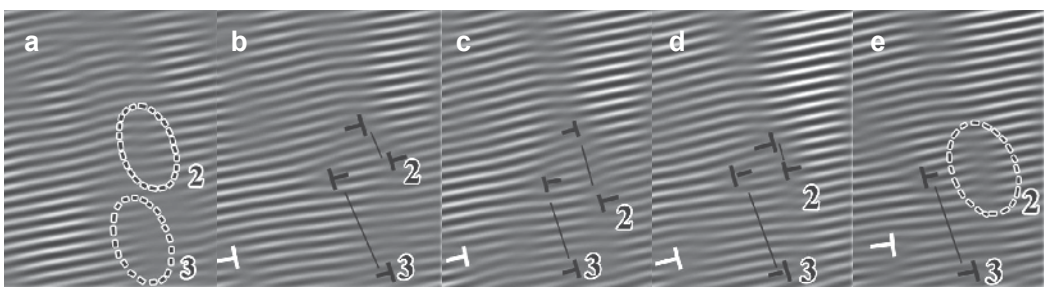

Fig. 15. Frames from a recorded digital video of a high-resolution transmission electron microscope observation of *in situ* tensile test of Ti2448, showing nucleation, expansion and shrinking of a dislocation loop (marked 2). The relative time from (a) to (e) is 0 s, 0.12 s, 0.2 s, 0.24 s, and 0.32 s (Cui et al., 2009).

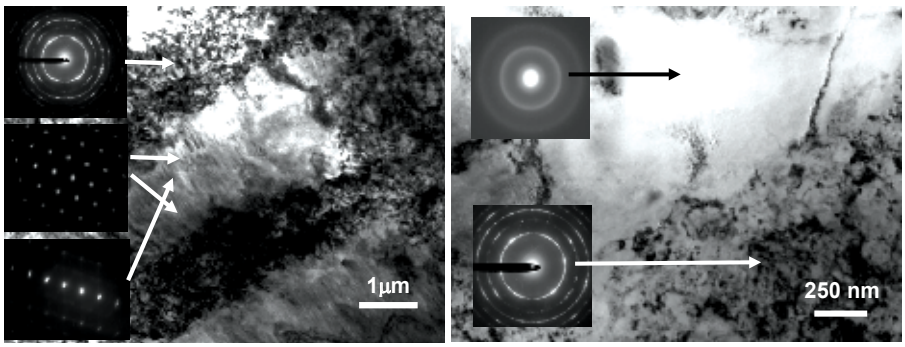

(a) (b)

Fig. 16. Bright-field transmission electron micrographs of hot-rolled Ti2448 after 50% compression. (a) Nanostructure band (indicated by diffraction pattern of top inset) and heavily rotated region (indicated by diffraction patterns of middle and bottome insets, close to zone axis [111] and [113], respectively) (Hao et al., 2005); (b) amorphous (top) and nanostructured (bottom) regions (Hao, Li, Sun, Zheng & Yang, 2007).

against changes in atomic bond length and bond angle, approximately equal values of the two elastic moduli imply that under an applied tensile stress atomic bonds in a local volume exhibit simultaneous tendencies to dilate and to rotate, rather than the domination of uniform rotation that leads to domination by shear deformation in the plastic stage in crystals whose bulk modulus is significantly greater than shear modulus (Fig. 17). In other words, atoms in a local volume undergo rather confusing and chaotic movement under an applied stress, and if the strain rate exceeds the rate for atomic relaxation, amorphous state may result, as was observed experimentally.

A mechanism of severe local lattice rotation is envisaged in Fig. 18a, with a stack of aligned dislocation loops, forming effectively a disclination type defect. At low density these loops act as a mechanism of elastic deformation as described in the previous subsection, at high density or after the loops are expanded to a sufficient size, these loops are no longer able to shrink and

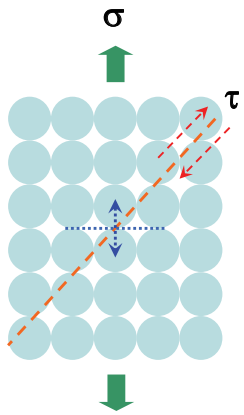

Fig. 17. Schematic illustrating atomic bond breaking across the dot line or atomic shear along the dash line, depending on the relative values of bulk modulus *B* and shear modulus *G*.

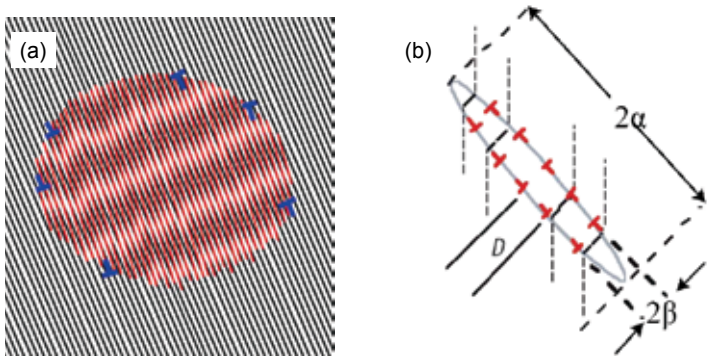

Fig. 18. (a) Schematic illustrating (a) rotation of a local volume through stacked dislocation loops (Cui et al., 2009), and (b) the incipient kink band mechanism (Barsoum et al., 2003).

they undertake plastic deformations. This mechanism can be compared to the incipient kink band that is proposed to interpret the deformation behaviour of hexagonal metals or ceramics which effectively have one easily operative slip system, loaded parallel to the basal plane. Our recent study of Ti2448 single crystals (Zhang, 2010) shows that the $C' = (C_{11} - C_{12})/2$ of the β phase is only 10.55 GPa, a record low among β-type titanium alloys. This, together with a high elastic anisotropy factor ($2C_{44}/(C_{11} - C_{12})$), makes the (110) atomic plane of the β phase the easist to shear or shuffle.

Figure 19a shows an image of nanosized grains of Ti2448 after cold rolling. Interestingly the activation energy for grain growth is different on both sides of the $\beta/(\alpha + \beta)$ transus of 923 K, being much lower on the low temperature, two-phase side (Fig. 19b). This was interpreted as a result of the nonequilibrium nature of the grain boundaries in the cold-rolled state, which is to a large extent retained during annealing in the two-phase field, but is destroyed by high temperature annealing in the β field. The very low elastic stability of the β phase in Ti2448 appears to produce a rich spectrum of metastable states. The energy barriers between these different states, either metastable phase or deformation induced defect structure, are small, making it relatively easy for transformation between these states to occur. This is the basis of the partial recovery of incipient Young's modulus at room temperature after prestrain (Fig. 6).

6. Biochemical properties and surface modification

In general surface modification methods that improve biocompatibility of titanium alloys can be used without problem on Ti2448. For example, Fig. 20 compares the cell attachment and growth behaviour of commercial pure Ti with the 7.6Sn alloy with and without hydroxyapatite coating. In this case the coating was prepared by immersion in a KOH solution followed by a heat treatment. The cell culture experiment clearly shows that the apatite layer favours adhesion and proliferation of rat osteoblast as compared to the naked samples. The uncoated 7.6Sn alloy behaves similarly to commercial pure Ti.

A two-step procedure involving thermal treatment and hydrothermal treatment for Ti2448 was also developed. Figure 21a compares the surface energy of differently treated samples. The difference in efficiency of the single-step and two-step procedure is apparent from Fig. 21c and d with the naked surface (Fig. 21b) as a reference. The surface layer resulting from the two-step procedure is both hard and bioactive.

A technique featuring the roles of the specific alloying additions of Ti2448 is micro-arc oxidation plus heat treatment. A calcium acetate electrolyte was used and the surface oxide

consists of two layers: a thin, compact and uniform inner layer and a porous outer layer. Ca ions are incorporated into the oxide layer in the form of CaO while Ti, Nb and Sn participate in the oxidation to form TiO_2, Nb_2O_5 and SnO_2, respectively. Subsequent heat treatment improves the apatite forming ability, and *in vitro* cell test on rabbit osteoblast shows that these surfaces are improved considerably in cell proliferation (Fig. 22).

A long-standing controversy concerns the relation between the grain size of metallic implant materials and biocompatibility (Hao et al., 2008). It has been speculated that refined grain size in the nanometer range improves biocompatibility but systematic investigation providing convincing proof has not been carried out, probably due to difficulty in obtaining nanostructured materials of useful dimension. Ti2448 which is easily processed into nanometer range grain size was employed to clarify this issue, and the biocompatibility of samples with 100 μm (CT) and 100 nm (NT) grain size was comparatively studied ((Zheng, 2009). Figure 23 compares the atomic force images of the two types of samples, an analysis of which yields surface roughness values of 1.45 nm and 1.94 nm for the CT and NT, respectively. Similarly, the surface energy of the CT and NT is 39 $J{\cdot}m^{-2}$ and 45 $J{\cdot}m^{-2}$, respectively (Fig. 24a), while the contents of hydroxy group on the surface of the NT sample are 69% higher

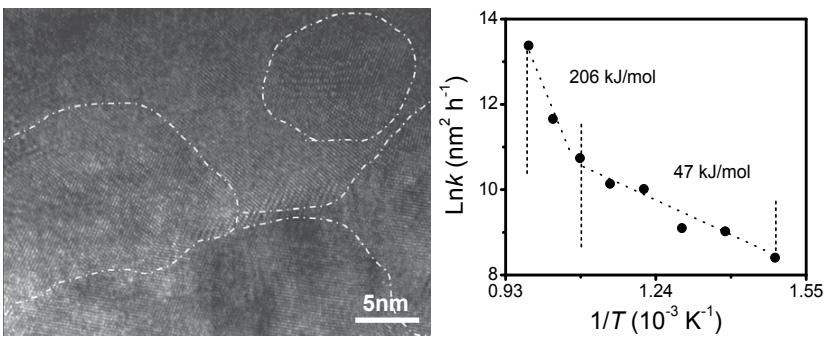

(a) (b)

Fig. 19. (a) High-resolution transmission electron micrograph showing nano-size grains of as cold-rolled Ti2448, with grain boundaries delineated by white curves; (b) Arrhenius plot of the rate constant k for grain growth against reciprocal of annealing temperature (Li, Zhang, Sun, Hao & Yang, 2008).

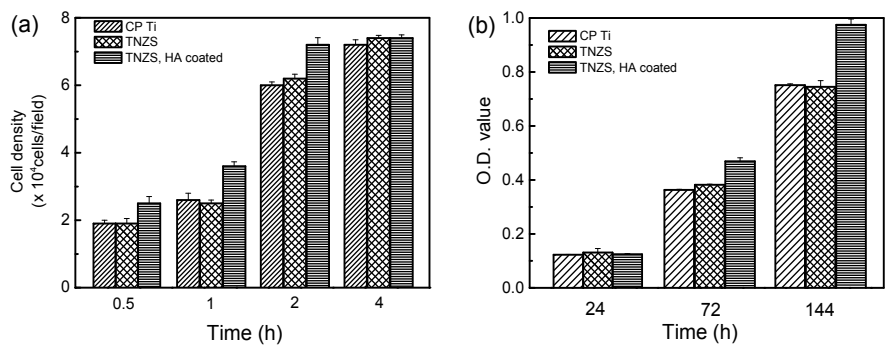

Fig. 20. Cell attachment (a) and cell growth rate (b) of Ti–24Nb–4Zr–7.6Sn (TNZS), HA-coated TNZS compared to CP Ti (Zheng et al., 2007).

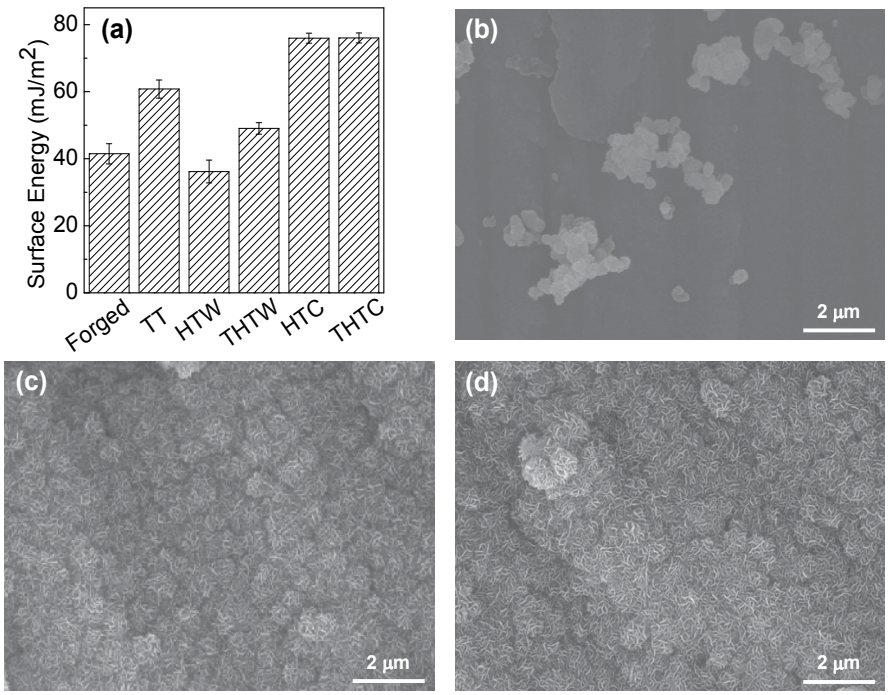

Fig. 21. (a) Surface energies of differently treated Ti2448 samples (TT: thermal treated; HT: hydrothermal treated; THT: thermal plus hydrothermal treated; W and C indicate the media of distilled water and supersaturated $Ca(OH)_2$ solution, respectively). The apatite morphologies of samples soaked in simulated body fluid are shown in the micrographs: (b) as-forged condition for 30 days; (c) HTC for 15 days; (d) THTC for 3 days (Zheng et al., 2009).

than that of the CT sample (Fig. 24b). This investigation also found that, under identical condition, the time required to form a whole layer of hydroxyapatite on the surface is 28 days for the CT sample, but only 21 days for the NT sample, and thus provided definitive evidence of the beneficial effect of surface nanostructure on the integration of titanium alloys and human tissues.

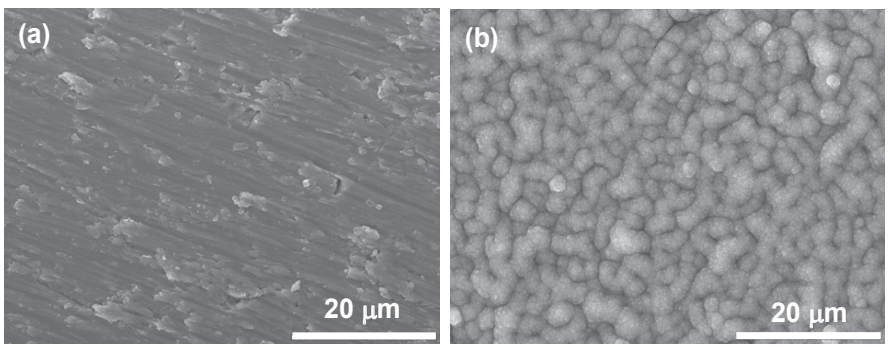

Fig. 22. Scanning electron micrographs showing apatite morphologies after soaking in simulated body fluid at 310 K for 1 week: (a) untreated surface; (b) micro-arc plus heat treated surface (Tao et al., 2009).

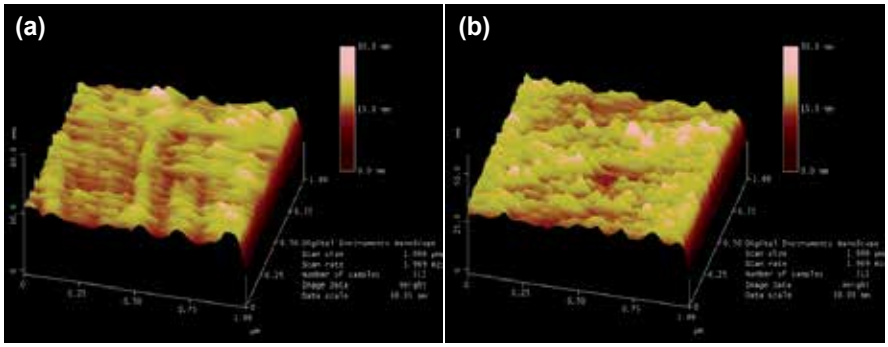

Fig. 23. Atomic force microscope images of surfaces with (a) 100 μm grain size and (b) 100 nm grain size of Ti2448 (Zheng, 2009).

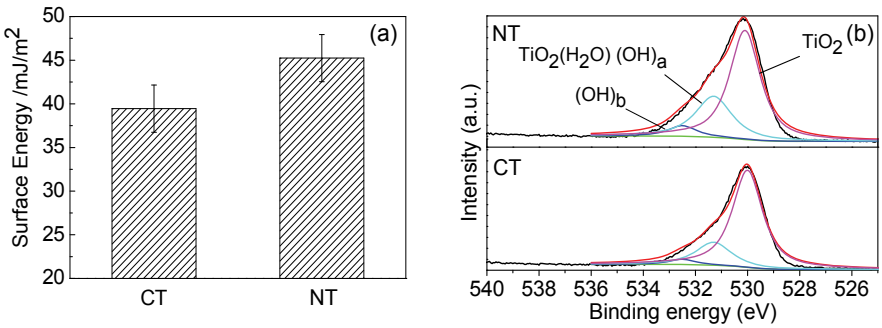

Fig. 24. (a) Comparison of surface energy of CT and NT samples; (b) x-ray photoelectronic spectrum O 1*s* peaks obtained from CT and NT samples (Zheng, 2009).

7. *In vivo* Tests and clinical trials

Extensive *in vivo* tests of Ti2448 have been conducted in the past few years in order to investigate the correlation of elastic matching between bone and implant to the healing of fractured bone. In a recent report ((Guo et al., 2009)), for example, intramedullary nails made of Ti2448 were implanted in New Zealand white rabbits in order to study the bone healing and stability of implants. It was found that the low modulus of Ti2448 leads to significant improvement in new bone formation in fractured rabbit tibiae as compared with the control group made of Ti–6Al–4V ELI (Fig. 25). These results suggest that, in the early days of fixation, nails made of low modulus Ti2448 improved new bone formation in the marrow cavity.
Clinical trials of a number of implant parts made of Ti2448, such as bone plates, nails, and spinal fixtures, have been completed. Two examples featuring repair of ankle bones and spine are shown in Figs. 26 and 27. A license application was submitted to the State Food and Drug Administration of China for large-scale production of these parts.

8. Concluding remarks

Employing a methodology that combines first principles computations of alloying effects and physical metallurgy principles, we developed a biomedical titanium alloy, Ti2448, that possesses an incipient Young's modulus of 42 GPa and a high tensile strength of over 850 MPa. The progressive softening of the incipient Young's modulus with prestrain and the ability to

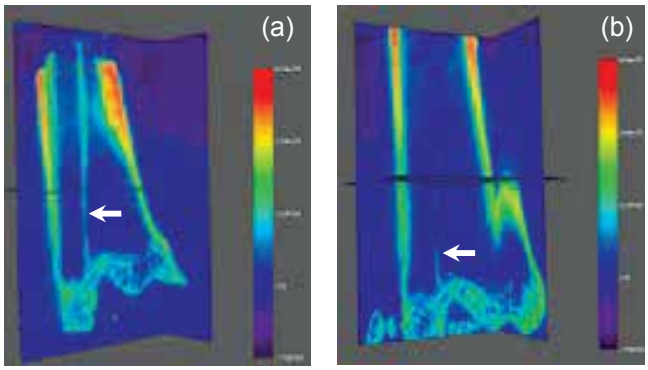

Fig. 25. Micro-CT view of (a) Ti2448 and (b) Ti–6Al–4V nails 4 weeks after implantation in rabbit tibiae. Newly formed bones are indicated by arrows (Guo et al., 2009).

recover during ambient temperature relaxation mimic the biological functions of human bone. A number of implant parts made of Ti2448 have completed clinical trials.
Ti2448 possesses superelasticity that involves new mechanisms of significant lattice distortion and homogeneous nucleation of dislocation loops in addition to stress induced martensitic

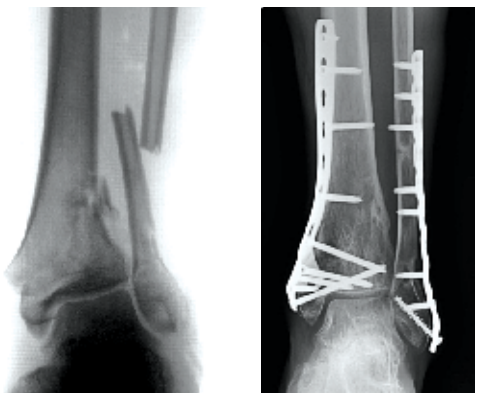

Fig. 26. Clinical application of Ti2448 bone plates and nails in repairing broken ankle bones.

Fig. 27. Clinical application of Ti2448 implants used to repair a broken spine.

transformation. To what extent these mechanisms operate remains to be understood. We found clues to the peculiar plastic deformation that leads to rapid grain refinement of Ti2448 but the details need to be clarified. How these deformation characteristics influence biomechanical performance of implants, such as fatigue, needs systematic investigation.

9. Acknowledgement

The work was supported in part by the National Science Foundation of China grants 59925103 and 50631030, and the Ministry of Science and Technology of China grants TG2000067100 and 2006CB605104. We were drawn to the subject of titanium alloys as biomedical materials more than 10 years ago through interesting interactions with Professor Z.-X. Guo, now at University College London, and Professor Mitsuo Niinomi, now at the Institute for Materials Research, Tohoku University. We would like to thank our collaborators, Professor Zheng Guo of the Fourth Military Medical University, Professor Yue Zhu of China Medical University, and our industrial partner, Weigao Group, for their efforts in making the application of Ti2448 implants a reality. Particular thanks also go to our colleague Professor Qingmiao Hu and our former colleagues, Professors Yan Song (now at Harbin Institute of Technology at Weihai) and Manling Sui (now at Beijing University of Technology), whose valuable input has enriched our understanding of the extraordinary behaviour of β-type titanium alloys.

10. References

Barsoum, M., Zhen, T., Kalidindi, S., Radovic, M. & Murugaiah, A. (2003). Fully reversible, dislocation-based compressive deformation of Ti_3SiC_2 to 1 GPa, *Nature Mater.* 2: 107–111.

Bendersky, L., Roytburd, A. & Boettinger, W. (1994). Phase transformations in the $(Ti,Al)_3Nb$ section of the Ti–Al–Nb system — I. microstructural predictions based on a subgroup relation between phases, *Acta Metall. Mater.* 42: 2323–2335.

Black, J. & Hastings, G. (1998). *Handbook of biomaterials properties*, Chapman and Hall, London.

Collings, E. (1984). *The Physical Metallurgy of Titanium Alloy*, ASM, Metals Park, OH.

Cui, J. P., Hao, Y. L., Li, S. J., Sui, M. L., Li, D. X. & Yang, R. (2009). Reversible movement of homogenously nucleated dislocations in a β-titanium alloy, *Phys. Rev. Lett.* 102: 045503.

Dobromyslov, A. V. & Elkin, V. A. (2001). Martensitic transformation and metastable β-phase in binary titanium alloys with d-metals of 4–6 periods, *Scripta Mater.* 44: 905–910.

Eisenbarth, E., Velten, D., Muller, M., Thull, R. & Breme, J. (2004). Implications of metallic corrosion in total knee arthroplasty, *Biomaterials* 25: 5705–5713.

Fedotov, S. (1973). Peculiarities of changes in elastic properties of titanium martensite, *in* R. Jaffee & H. Burte (eds), *Titanium Science and Technology (Proc. 2nd Int. Conf. on Titanium)*, Plenum Press, New York, pp. 871–881.

Froimson, M. I., Garino, J., Machenaud, A. & Vidalain, J. P. (2007). Minimum 10-year results of a tapered, titanium, hydroxyapatite-coated hip stem, *J. Arthroplasty* 22: 1–7.

Gao, X., Huang, M. & Brinson, L. (2000). A multivariant micromechanical model for SMAs: part 1. crystallographic issues for single crystal model, *Int. J. Plast.* 16: 1345–1369.

Geetha, M., Singh, A., Asokamani, R. & Gogia, A. (2009). Ti based biomaterials, the ultimate choice for orthopaedic implants – a review, *Prog. Mater. Sci.* 54: 397–425.

Guo, Z., Fu, J., Zhang, Y., Hu, Y., Wu, Z., Shi, L., Sha, M., Li, S., Hao, Y. & Yang, R. (2009). Early effect of Ti–24Nb–4Zr–7.9Sn intramedullary nails on fractured bone, *Mater. Sci. Eng.*

C 29: 963–968.

Hao, Y., Li, S., Sun, B., Sui, M. & Yang, R. (2007). Ductile titanium alloy with low Poisson's ratio, *Phys. Rev. Lett.* 98: 216405.

Hao, Y., Li, S., Sun, S. & Yang, R. (2006). Effect of Zr and Sn on Young's modulus and superelasticity of Ti–Nb-based alloys, *Mater. Sci. Eng. A* 441: 112–118.

Hao, Y., Li, S., Sun, S., Zheng, C., Hu, Q. & Yang, R. (2005). Super-elastic titanium alloy with unstable plastic deformation, *Appl. Phys. Lett.* 87: 091906.

Hao, Y., Li, S., Sun, S., Zheng, C. & Yang, R. (2007). Elastic deformation behaviour of Ti–24Nb–4Zr–7.9Sn for biomedical applications, *Acta Biomater.* 3: 277–286.

Hao, Y., Li, S. & Yang, R. (2008). Nanostructured titanium alloys for implant applications, *in* D. Reisner (ed.), *Bionanotechnology: Global Prospects*, Chapter 5, CRC Press, New York, pp. 61–70.

Heinen, R., Hackl, K., Windl, W. & Wagner, M. (2009). Microstructural evolution during multiaxial deformation of pseudoelastic NiTi studied by first-principles-based micromemicromechanical modeling, *Acta Mater.* 57: 3856–3867.

Hu, Q., Li, S., Hao, Y. & Yang, R. (2008). Phase stability and elastic modulus of Ti alloys cotaining Nb, Zr, and/or Sn from first principles calculations, *Appl. Phys. Lett.* 93: 121902.

Li, S., Cui, T., Hao, Y. & Yang, R. (2008). Fatigue properties of a metastable β-type titanium alloy with reversible phase transformation, *Acta Biomater.* 4: 305–317.

Li, S., Zhang, Y., Sun, B., Hao, Y. & Yang, R. (2008). Thermal stability and mechanical properties of nanostructured Ti–24Nb–4Zr–7.9Sn alloy, *Mater. Sci. Eng. A* 480: 101–108.

Long, M. & Rack, H. (1999). Titanium alloys in total joint replacement – a materials science perspective, *Biomaterials* 19: 1621–1639.

Matsumoto, H., Watanabe, S. & Hanada, S. (2005). Beta TiNbSn alloys with low youngs modulus and high strength, *Mater. Trans.* 46: 1070–1078.

Nag, S., Banerjee, R. & Fraser, H. L. (2005). Microstructural evolution and strengthening mechanisms in Ti–Nb–Zr–Ta, Ti–Mo–Zr–Fe and Ti–15Mo biocompatible alloys, *Mater. Sci. Eng. C* 25: 357–362.

Niinomi, M. (2002). Recent metallic materials for biomedical applications, *Metall. Mater. Trans. A* 33: 477–486.

Niinomi, M. (2003). Fatigue performance and cyto-toxicity of low rigidity titanium alloy, *Biomaterials* 24: 2673–2683.

Nitta, K., Watanabe, S., Masahashi, N., Hosoda, H. & Hanada, S. (2004). Ni-free Ti–Nb–Sn shape memory alloys, *in* M. Niinomi (ed.), *Structural Biomaterials for the 21st Century*, TMS, Warrendale, PA, pp. 25–34.

Obbard, E. (2010). *Superelasticity in biomedical β titanium alloys*, Ph.D. Thesis, Institute of Metal Research, Chinese Academy of Sciences, Shenyang.

Obbard, E., Hao, Y., Akahori, T., Talling, R., Niinomi, M., Dye, D. & Yang, R. (2010). Mechanics of superelasticity in Ti–30Nb–(8–10)Ta–5Zr alloy, *Acta Mater.* 58: 3557–3567.

Obbard, E., Hao, Y., Talling, R., Li, S., Zhang, Y., Dye, D. & Yang, R. (2011). The effect of oxygen on α'' martensite and superelasticity in Ti–24Nb–4Zr–8Sn, *Acta Mater.* 59: 112–125.

Petry, W., Heiming, A., Trampenau, J., Alba, M., Herzig, C. & Vogl, H. R. S. G. (1991). Phonon dispersion of the bcc phase of group IV metals: I. bcc titanium, *Phys. Rev. B* 43: 10933.

Puska, A. & Golovin, S. (1985). *Fatigue in materials: cumulative damage processes*, Elsevier, Amsterdam.

Song, Y., Xu, D., Yang, R., Li, D., Wu, W. & Guo, Z. (1999). Theoretical study of the effects of alloying elements on the strength and modulus of β-type bio-titanium alloys, *Mater. Sci. Eng. A* 260: 269–274.

Song, Y., Yang, R., Li, D., Wu, W. & Guo, Z. (1999). Calculation of theoretical strengths and bulk moduli of bcc metals, *Phys. Rev. B* 59: 14220.

Tao, X., Li, S., Zheng, C., Fu, J., Guo, Z., Hao, Y., Yang, R. & Guo, Z. (2009). Synthesis of a porous oxide layer on a multifunctional biomedical titanium by micro-arc oxidation, *Mater. Sci. Eng. C* 29: 1923–1934.

Wan, Z., Dorr, L. D., Woodsome, T., Ranawat, A. & Song, M. (1999). Effect of stem stiffness and bone stiffness on bone remodeling in cemented total hip replacement, *J. Arthroplasty* 14: 149–158.

Wang, K. (1996). The use of titanium for medical applications in the USA, *Mater. Sci. Eng. A* 213: 134–137.

Wapner, K. (1991). Implications of metallic corrosion in total knee arthroplasty, *Clin. Orthop. Relat. Res.* 271: 12–20.

Zhang, Y. (2010). *Elastic and plastic deformation of Ti2448 single crystals*, Ph.D. Thesis, Institute of Metal Research, Chinese Academy of Sciences, Shenyang.

Zheng, C. (2009). *An investigation on the biocompatibility of* T*i–24*N*b–4*Z*r–8*S*n alloy*, Ph.D. Thesis, Institute of Metal Research, Chinese Academy of Sciences, Shenyang.

Zheng, C., Li, S., Tao, X., Hao, Y. & Yang, R. (2009). Surface modification of Ti–Nb–Zr–Sn alloy by thermal and hydrothermal treatments, *Mater. Sci. Eng. C* 29: 1245–1251.

Zheng, C., Li, S., Tao, X., Hao, Y., Yang, R. & Zhang, L. (2007). Calcium phosphate coating of Ti–Nb–Zr–Sn titanium alloy, *Mater. Sci. Eng. C* 27: 824–831.

Zhu, Y., Li, F., Li, S., Hao, Y. & Yang, R. (2009). Effect of elastic modulus on biomechanical properties of lumbar interbody fusion cage, *J. Mater. Sci. Technol.* 25: 325–328.

11

Ti-based Bulk Metallic Glasses for Biomedical Applications

Fengxiang Qin, Zhenhua Dan, Xinmin Wang,
Guoqiang Xie and Akihisa Inoue
Institute for Materials Research, Tohoku University, Japan

1. Introduction

Biomedical materials can improve the life quality of a number of people each year. The range of applications includes such as joint and limb replacements, artificial arteries and skin, contact lenses, and dentures. So far the accepted biomaterials include metals, ceramics and polymers. The metallic biomaterials mainly contain stainless steel, Co-Cr alloys, Titanium and Ti-6Al-4V. Recently, bulk metallic glasses as novel materials have been rapidly developed for the past two decades in Mg-, Ln-, Zr-, Fe-, Ti-, Pd-, Cu-, Ni-based alloy systems because of their unique physical, chemical, magnetic and mechanical properties compared with conventional crystalline alloys. Metallic glass formation is achieved by avoiding nucleation and growth of crystalline phases when cooling the alloy from the molten liquid. Therefore, the different atomic configurations induced significantly different characteristic features such as high strength, good corrosion resistance and excellent electromagnetic properties, which are from their crystalline counterparts. Among different bulk metallic glasses, Ti-based bulk metallic glasses are expected to be applied as biomedical materials due to high strength, high elastic limit, low Young's modulus, excellent corrosion resistance and good bioactivity of Ti element. Many Ti-based metallic glasses have been developed in Ti-Cu-Ni, Ti-Cu-Ni-Co, Ti-Cu-Ni-Zr, Ti-Cu-Ni-Zr-Sn, Ti-Cu-Ni-Sn-B-Si, Ti-Cu-Ni-Sn-Be, Ti-Cu-Ni-Zr-Be, Ti-Cu-Ni-Zr-Hf-Si and Ti-Cu-Ni-Zr-Nb (Ta) alloys, based on the Inoue's three empirical rules (Inoue, 1995) i.e., 1) multi-component consisting of more than three elements, 2) significant atomic size mismatches above 12% among the main three elements, and 3) negative heats of mixing among the main elements.

2. Problem description

Bulk metallic glasses have been extensively explored owing to their fundamental scientific importance and engineering applications. Bulk metallic glasses exhibit unique properties, e.g. high strength about 2-3 times of its crystalline counterparts, large elastic limit about 2% which is very near to some polymer materials, high corrosion resistance, high wear resistance, etc. These properties, which can be rarely found in crystalline materials, are attractive for the practical application as a new class of structural and functional materials. Although many Ti-based bulk metallic glasses have been developed during the past two decades, all the Ti-based bulk metallic glassy alloys with good glass-forming ability contain

some toxic elements of Ni and/or Be, which can cause an allergy, cancer or other diseases, limiting the application of Ti-based bulk metallic glasses in medical fields. Recently the Ti-based bulk metallic glasses without Ni were in Ti-Zr-Cu-Pd-Sn and Ti-Zr-Cu-Pd alloy systems in our group. Investigations on corrosion properties of the Ti-Zr-Cu-Pd-Sn bulk metallic glasses revealed that these glassy alloys are promising biomaterials due to their spontaneously passivated ability in simulated body fluid. And Ti-Zr-Cu-Pd alloy system shows a larger glass-forming ability with a critical diameter of 6 mm. Furthermore, higher strength and lower Young's modulus of 2000 MPa and 90 GPa have been obtained in Ti-Zr-Cu-Pd, which is much higher and lower than that of Ti-6Al-4V alloy. The development of new Ni-free Ti-Zr-Cu-Pd-Sn and Ti-Zr-Cu-Pd bulk metallic glasses exhibiting large glass-forming ability, high strength and distinct plastic strain fabricated make it possible that Ti-based bulk metallic glasses are applied as biomaterials. In this chapter, we will descript the relationship between corrosion properties, mechanical properties and microstructure as well as bioactivity of the Ni-free Ti-based bulk metallic glasses. Those properties are very important for metallic implants for application as artificial dental root materials or other biomedical materials. We succeeded in resolving the following problems which limit the application of Ti-based bulk metallic glasses in biomedical fields. First is that we developed the novel Ni-free Ti-based bulk metallic glasses since most of the Ti-based bulk metallic glasses with large glass-forming ability contain some toxic elements of Ni and/or Be, which will cause an allergy, cancer or other diseases in human body. The second one is that large plastic deformation was obtained in the Ti-based nano-crystalline/glassy composite alloys. The third one is that good bioactivity has been achieved in the new developed Ti-based bulk metallic glasses after some pre-treatments.

3. Experimental results

3.1 Mechanical property and microstructure

Bulk metallic glasses usually exhibit low plasticity due to the absence of dislocation activities and strain hardening. Therefore, for real applications, it seems important to improve the ductility of bulk metallic glasses without a significant sacrifice in the strength. To improve the plasticity of bulk metallic glasses, extensive research has been done over the past two decades. The low plasticity is caused by inhomogeneous plastic deformation, i.e., the severe shear localization. The general method is to introduce second phases in the metallic glassy matrix to inhibit the rapid propagation of shear bands. Furthermore, these second phases can interact with shear bands and effectively induce multiplication, branching, and restriction of shear bands to increase the plasticity of bulk metallic glasses. The second phases include nano-crystals (quasi-crystals), crystalline particles, fibers, ceramics and pores. To fabrication bulk metallic glassy composite, one common method is to change the composition or heat the as-cast bulk metallic glasses forming an in-situ second phases.

3.1.1 Thermal stability and microstructure

In order to improve the ductility of $Ti_{40}Zr_{10}Cu_{36}Pd_{14}$ bulk metallic glass, we take two approaches of heat treatment and changing the composition. Firstly we heat treated the as-cast $Ti_{40}Zr_{10}Cu_{36}Pd_{14}$ bulk metallic glass at different temperatures. The as-cast $Ti_{40}Zr_{10}Cu_{36}Pd_{14}$ bulk metallic glass shows a distinct glass transition temperature, T_g, of 669 K, an onset temperature of crystallization, T_x, of 720 K, followed by two-stage

crystallization processes (Fig. 1). When the as-cast glassy alloy is isothermally annealed at 693 K (between T_g and T_x) for 10 min, partial crystallization occurs, corresponding to a crystallization fraction of about 20%. The fraction was evaluated by comparing the crystallization enthalpy of the exothermic peaks of the as-cast alloy with that of the annealed alloys. With increasing its annealing temperature to 723 K, the first crystallization peak disappears and its crystallization fraction reaches about 40 %. After annealing at 823 K for 10 min, the residual glassy phase is completely crystallized.

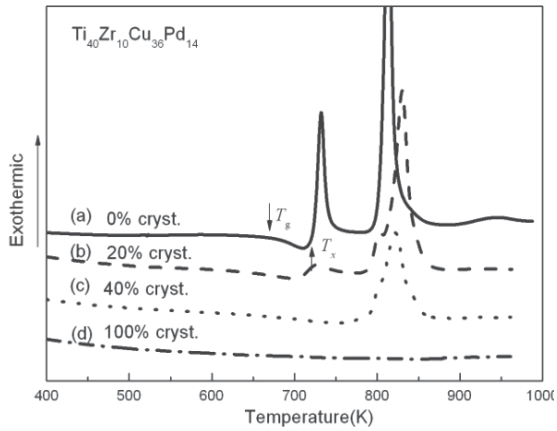

Fig. 1. DSC curves of the $Ti_{40}Zr_{10}Cu_{36}Pd_{14}$ bulk metallic glass and its annealed alloys: as-cast (a), annealed at 693 K (b), 723 K (c) and 823 K (d) for 10 min.

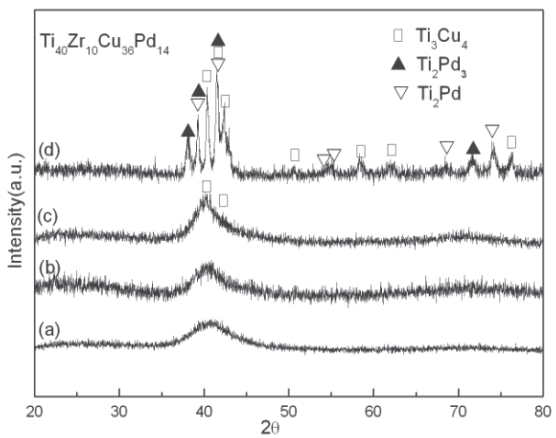

Fig. 2. XRD patterns of the $Ti_{40}Zr_{10}Cu_{36}Pd_{14}$ bulk metallic glass and its annealed alloys: as-cast (a), annealed at 693 K (b), 723 K (c) and 823 K (d) for 10 min.

Only a halo peak appears in the XRD pattern of the as-cast $Ti_{40}Zr_{10}Cu_{36}Pd_{14}$ bulk metallic glass, indicating that a glassy phase is formed in the cast alloy (Fig. 2). Although no obvious crystalline peaks appear in the XRD pattern after annealing at 693 K, the main halo peak becomes sharper as compared with the as-cast alloy, and some weak diffraction peaks identified as Ti_3Cu_4 appear in the pattern of the alloy annealed at 723 K. The low intensity peaks of the precipitates indicate the possibility of forming a nano-crystalline structure in

the glass matrix for the samples after annealing at 693 and 723 K, which can not be identified by XRD. Recently it was reported that (Jiang, 2003), in Cu–Zr–Ti bulk metallic glasses, significant volume fractions of nano-crystals embedding in the glassy matrix were observed in their HRTEM images, even if only one broad peak was found by XRD. On the other hand, the bulk metallic glass crystallized completely by annealing at 823 K. Many crystalline phase peaks appear and can be identified as tetragonal Ti_3Cu_4, orthorhombic Ti_2Pd_3 and tetragonal Ti_2Pd.

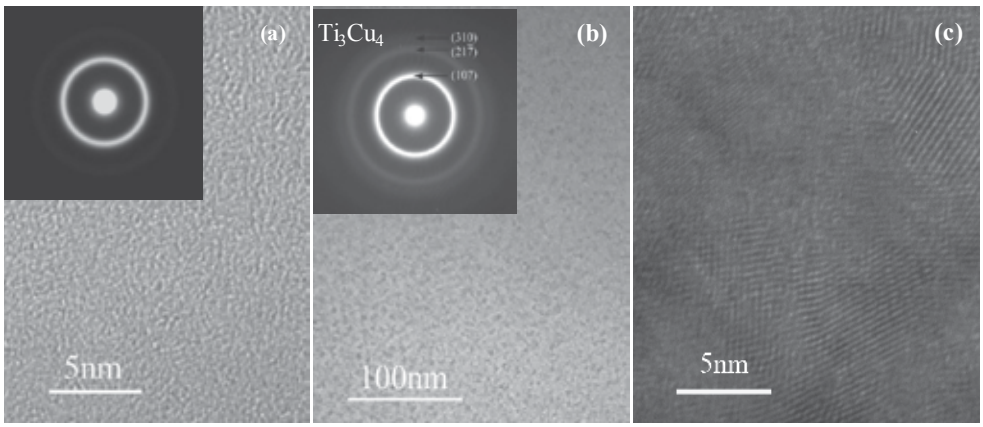

Fig. 3. HREM images, TEM images and corresponding selected area diffractions of the $Ti_{40}Zr_{10}Cu_{36}Pd_{14}$ as-cast bulk metallic glass (a) and alloy annealed at 693 K (b) and (c).

In microstructure, the as-cast bulk metallic glass has a typical glassy structure. Neither ordered structure nor crystalline phase is observed. Furthermore, only one halo ring appears in the corresponding SAED pattern. Figure 3 (b) and (c) show bright field TEM and HREM images of the alloy annealed at 693 K for 10 min. A mixed structure consisting of nano-particles homogeneously embedded in the glassy matrix is observed. The SADP consists of several ring patterns superimposed on a diffuse halo patterns, also indicating a mixture of nano-crystalline and residual glassy phase. The nano-particles are identified as a tetragonal

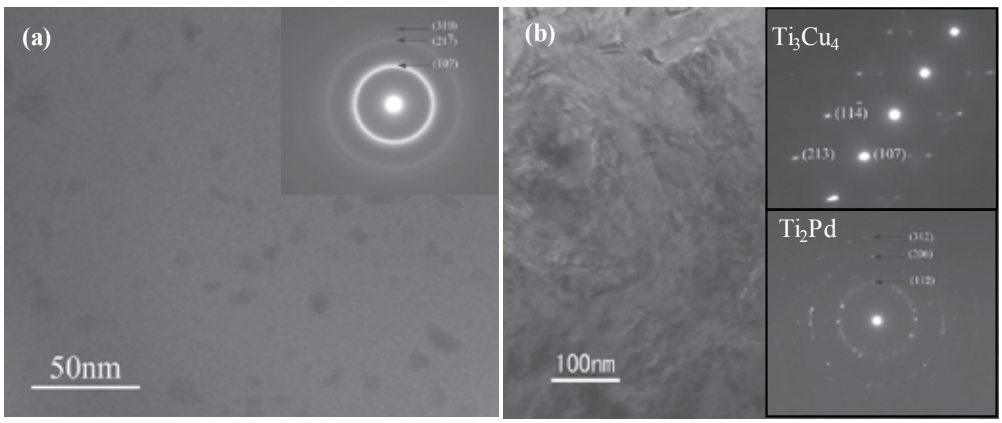

Fig. 4. Bright field TEM images and corresponding selected area diffractions of the $Ti_{40}Zr_{10}Cu_{36}Pd_{14}$ alloys annealed at 723 K (a) and 823 K (b).

Ti_3Cu_4. The HREM image of the same specimen in Fig. 3 (c), shows that the size of nano-Ti_3Cu_4 is less than 5 nm. The results are consistent with that of XRD in Fig. 2. By annealing at 723 K, Ti_3Cu_4 nano-particles grow up accompanying with the increase in the diffraction intensity of (107), $(21\bar{7})$ and (310) crystal planes (Fig. 4 (a)). With annealing temperature to 823 K, a Ti_2Pd was also identified in addition to Ti_3Cu_4 phase (Fig. 4 (b)).

3.1.2 Mechanical properties and fracture morphology.

The deformation of the as-cast bulk metallic glasses occurs mainly by elastic deformation (Fig. 5). The fracture surface shows a typical vein pattern originating from the deformation of narrow shear band. The partly nano-crystallized alloy annealed at 693 K exhibits high strength of 2165 MPa (Fig. 5 (b)), which is higher than those of the as-cast alloy and other annealed alloys. Furthermore, distinct plastic deformation of about 0.8 % for the partly nano-crystallized alloy after annealing at 693 K is also observed presumably because the nano-particles can suppress the deformation of shear bands and a high density of free volumes can be introduced by the annealing treatment in the supercooled liquid region. In addition, the fracture surface of the alloy annealed at 693 K is still in the vein-like pattern

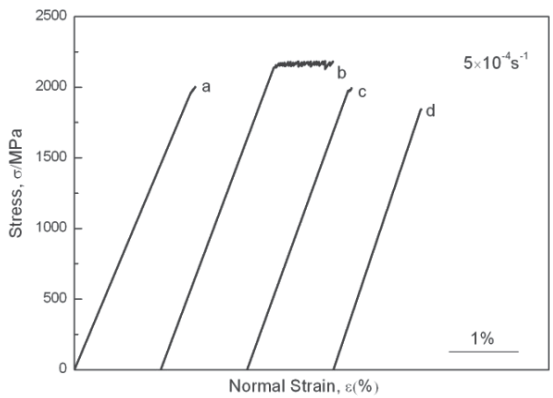

Fig. 5. Compressive strain-stress curves of the $Ti_{40}Zr_{10}Cu_{36}Pd_{14}$ bulk metallic glass and its annealed alloys: as-cast (a), annealed at 693 K (b), 723 K (c) and 823 K (d) for 10 min

type (Fig. 6 (b)). With further increasing annealing temperature to 723 K, the fracture mode changes to a brittle type, shown in Fig. 6 (c) and (d). Xing et al. (Xing et al., 1998) found that the crystalline fraction of 40%-45% leads to the change in the fracture surface from ductile to brittle type and porosity plays an important role in multiple cracking of annealed alloys. Meanwhile, for the alloy annealed at 823 K, the fracture surface is a totally brittle fracture type as shown in Fig. 6 (e). At the same time, compressive strength decreased for the alloys annealed at 723 K and 823 K.

As above-mentioned, nano-crystalline structure is formed in the Ti-Zr-Cu-Pd bulk metallic glass subjected to an optimum annealing treatments. The crystallized structure changes seriously the mechanical properties and fracture morphology. That is, the deformation behavior is associated with the nature of crystallites precipitated in the glassy matrix. Annealing of the bulk metallic glass at 693 K for 10 min, i.e., between glass transition temperature and onset temperature of crystallization, results in the formation of nano-particles of Ti_3Cu_4 with sizes smaller that 5 nm in the glassy matrix.

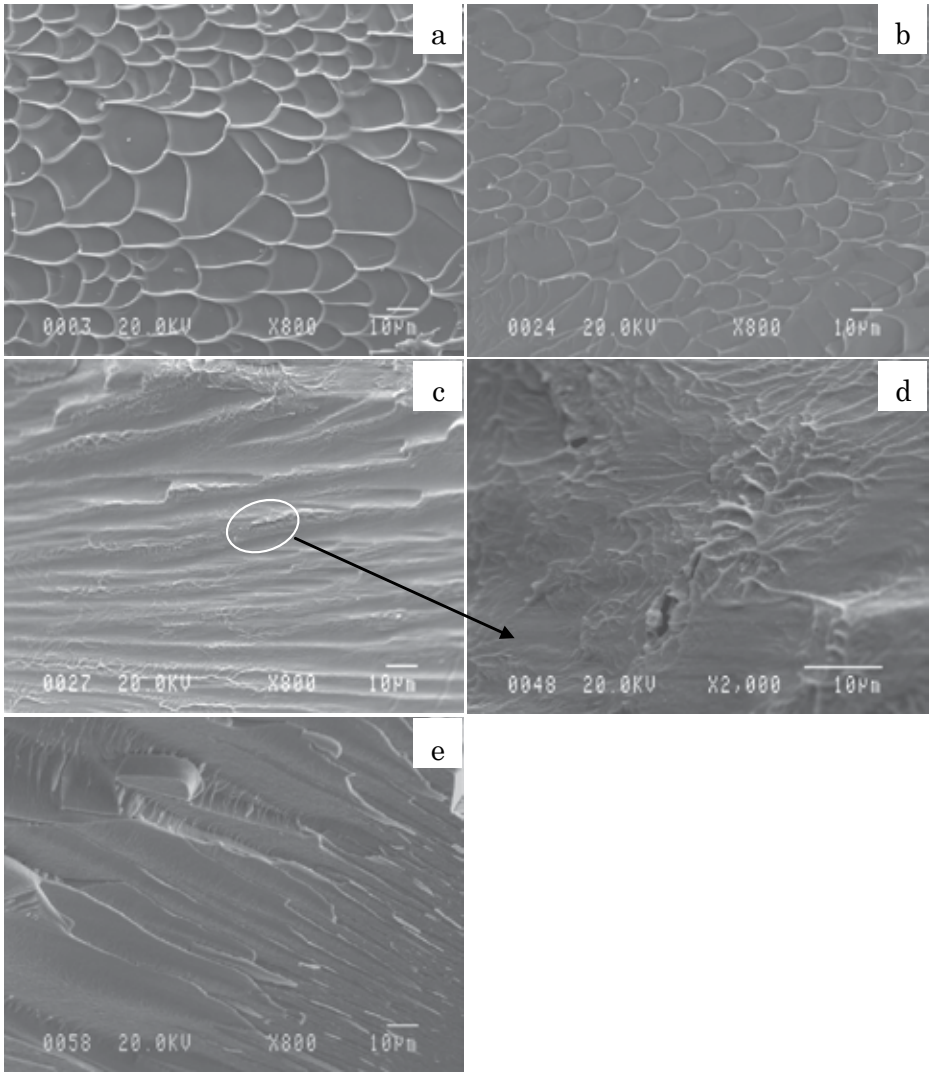

Fig. 6. Fracture morphologies of the $Ti_{40}Zr_{10}Cu_{36}Pd_{14}$ bulk metallic glass and its annealed alloys: as-cast (a), annealed at 693K (b), 723 K (c) (d), and 823 K (e) for 10 min.

In general, the formation of the nano-composite in metallic glass requires both the ease of homogeneous nucleation of crystalline phase and difficulty of the subsequent crystal growth. When the nano-particles are much smaller than the shear bands and the nano-particles are separated by glassy matrix (Xing et al., 1998), the deformation of the shear band is dominated by the glassy matrix, and the nano-particles will inhibit the deformation of the shear bands. Inoue et al. (Inoue, et al., 2000) classified the mechanism for high strength and good ductility of the bulk nano-crystalline alloys into two types by the nano-particles and remaining glassy matrix. The nano-particles with perfect crystal structure may act as inhibitor against shear deformation of the glassy matrix. In addition, the nano-particle/glassy matrix interface has a highly dense packed atomic configuration due to low interface energy. Furthermore, the localized deformation mode of the glassy matrix

enhances the deformability owing to the softening caused by the increase of temperature in the localized region. Then higher strength and good plastic deformation were obtained for the alloy annealed at 693 K. On the other hand, both the as-cast bulk metallic glass and the alloy annealed at 693 K show vein like patterns. There are several hypotheses those expatiate the vein pattern in fracture surface of the metallic glasses. One is proposed that the behavior of the shear band was similar to a thin viscous layer between two parallel plates under tension. During the process of deformation, shallow cavities originate and the bridges between them break, resulting in the veins. The other hypotheses mentioned the decrease of viscosity due to the intensive increase of the free volume in the shear band owing to a high hydrostatic tension. It is also found that local melting occurs within the shear band and melting droplets on the fracture surfaces of hydrostatic deformed glass result in vein like patterns. In this study, further annealing at 723 K for 10 min, i.e., the first crystallization peak, results in the growth of Ti_3Cu_4 phase and the increase of crystallization fraction. The deformation is not dominated by the glassy matrix when the nano-particles occupy a high volume fraction of 40 %. Consequently the brittle morphology was found in the alloy annealed at 723 K shown in Fig. 6 (c) and (d). Figure 6 (d) is the enlarged area of the circle area in Fig. 6 (c). Some pores are observed in the surface of the alloy annealed at 723 K, which act as crack initiators, and the alloy fails in a brittle manner (Dasa et al., 2005). It should be pointed out that the highest strength of 2100 MPa obtained in the $Ti_{40}Zr_{10}Cu_{36}Pd_{14}$ bulk nano-composite is much higher than that of Ti-6Al-4V alloy (Lűtjering et al., 1999).
High strength and distinct plastic strain have been also observed in the stress-strain curves for the Nb-added alloys (Fig. 7). Especially, yield strength exceeding 2050 MPa, low Young's modulus of about 80 GPa and distinct plastic strain of 6.5 % and 8.5 % corresponding to serrated flow sections are attributed to the propagation of narrow shear bands.

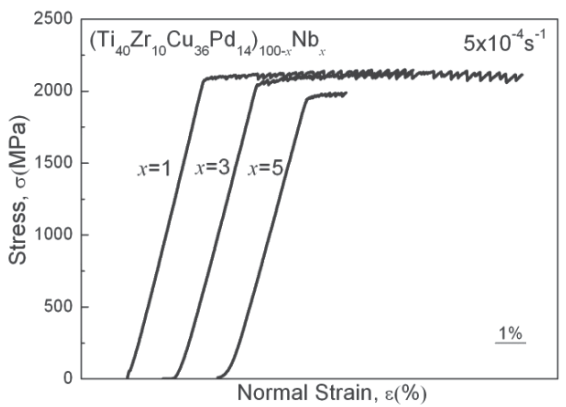

Fig. 7. Compressive strain-stress curves of the $(Ti_{40}Zr_{10}Cu_{36}Pd_{14})_{100-x}Nb_x$ as-cast rods with a diameter of 2 mm.

The fracture surface shows a vein pattern originating from the deformation of narrow shear band. With further increasing the content of Nb to 5 %, the plastic strain decreases to 1.0 %, not as large as the former ones. On the side surface, a number of shear bands are observed near the fracture edge of the 1 % and 3 % Nb-added alloys, and some of shear bands are jagged and interdicted, as shown in Fig. 8 (a) and (b).

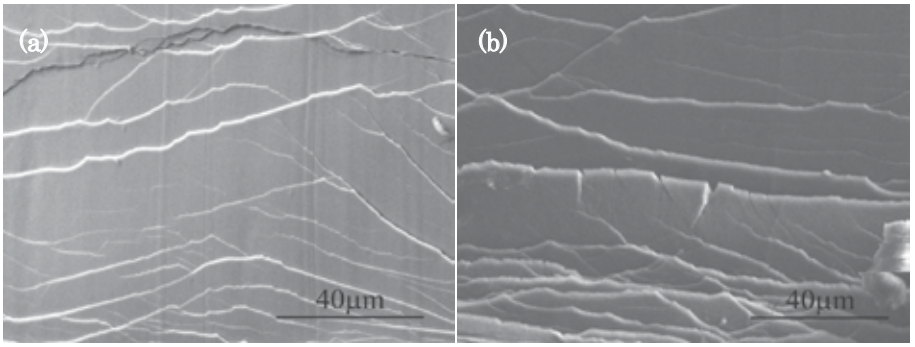

Fig. 8. Lateral surface of the $(Ti_{40}Zr_{10}Cu_{36}Pd_{14})_{100-x}Nb_x$ as-cast rods after fracture (a) x=1, (b) x=3.

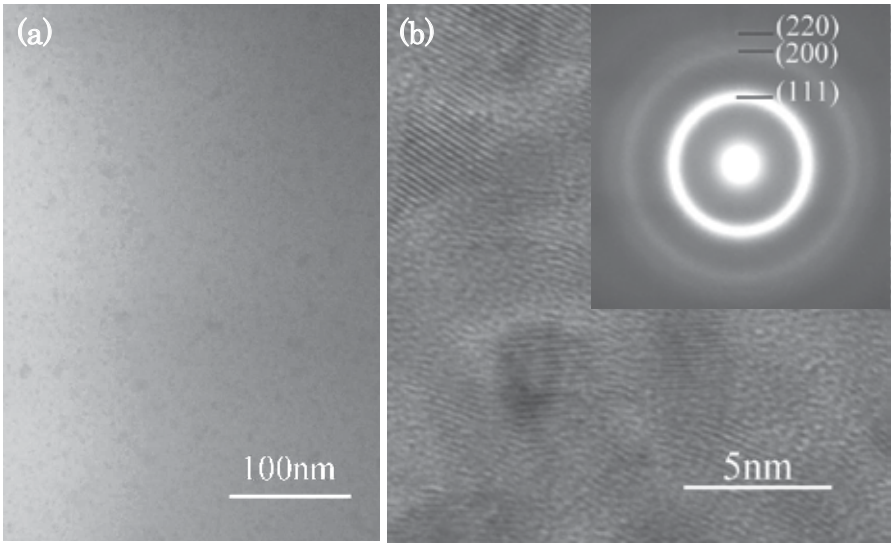

Fig. 9. Bright-field TEM (a) and HREM (b) images as well as corresponding SAD pattern of the $(Ti_{40}Zr_{10}Cu_{36}Pd_{14})_{100-x}Nb_x$ as-cast rods, x=1.

Some nano-particles with volume fraction of 8 % are uniformly dispersed the glassy matrix for 1 % Nb-added rod (Fig. 9 (a) and (b)). The HREM image of the 1 % Nb-added rod shows that the size of nano-particles is smaller than 5 nm in Fig. 9 (b). Several ring patterns superimposing on the diffuse halo ring in corresponding SAD pattern also indicates a mixture of nano-crystalline and residual glassy matrix. The nano-particles are identified as a Pd_3Ti phase with crystal planes of (111), (200) and (220). With 3 % Nb addition, the ring patterns superimposed on the diffuse halo ring in SAD pattern are sharper because of the increase in the volume fraction of Pd_3Ti nano-particle to 13 % (Fig. 10). With further increasing Nb content to 5 %, the volume fraction of nano-particles increases to 20 % associated with the increase of their size as shown in Fig. 11. The NBD pattern taken from the nano-particle along its [111] zone axis confirms the cubic structure as the Pd_3Ti with the lattice parameter a=0.3167nm. The particle size of Pd_3Ti phase increases accompanying with the increase in the diffraction intensity of (111), (200), (220) and (311) crystal planes. The TEM results showing obvious nano-particles with several nano-meters are not contradicted with the amorphous-like peak in XRD patterns.

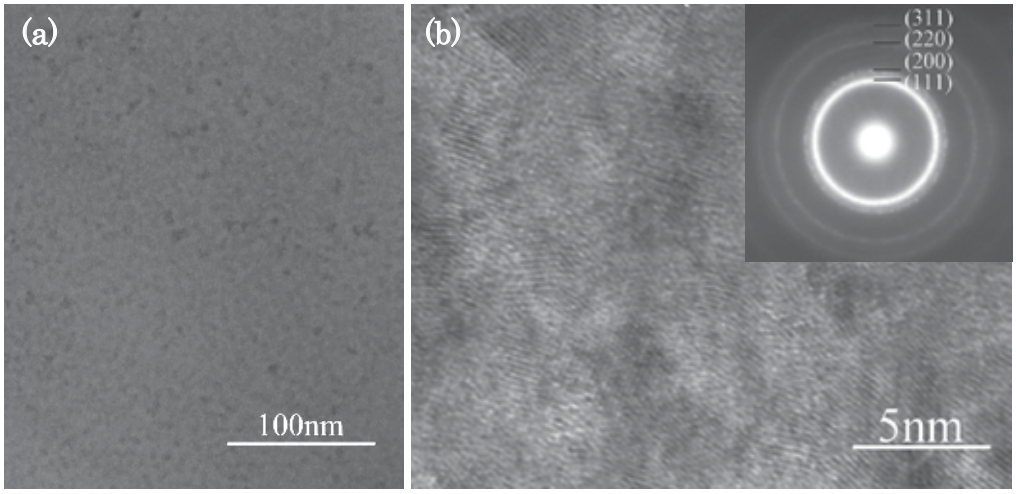

Fig. 10. Bright-field TEM(a) and HREM(b) images as well as corresponding SAD pattern of the $(Ti_{40}Zr_{10}Cu_{36}Pd_{14})_{100-x}Nb_x$ as-cast rod, x=3.

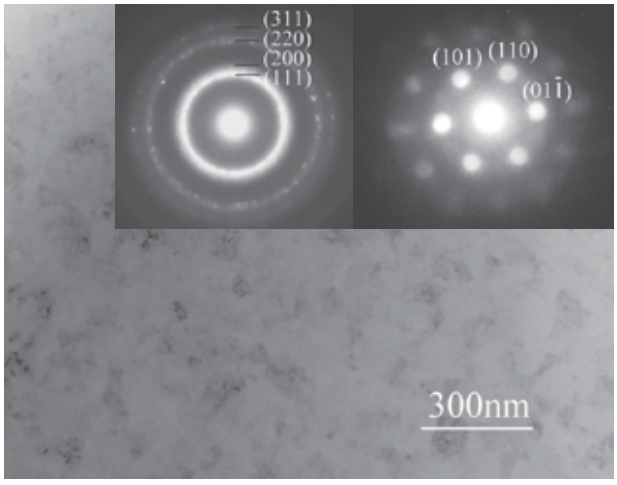

Fig. 11. Bright-filed image and corresponding SAD pattern as well as NBD pattern of the $(Ti_{40}Zr_{10}Cu_{36}Pd_{14})_{100-x}Nb_x$ as-cast rod, x=5.

Good mechanical properties of Ti-Zr-Cu-Pd-Nb bulk metallic glass are also attributed to the mixed state of nano-particles and glassy matrix. The size and volume fraction of Pd_3Ti nano-particles in the Ti-Zr-Cu-Pd-Nb bulk metallic glass can be distinctly changed with different Nb additions. Consequently, it is conduced that the microstructure consisting of nano-particles and glassy phase improves significantly the mechanical property of Ti-Zr-Cu-Pd-Nb alloys.

3.2 Corrosion behaviour

The potentiodynamic polarization curves of the Ti-based bulk metallic glass and its crystalline alloys in Hanks' solution at 310 K are shown in Fig. 12. For the sake of comparison the data of a commercial Ti-6Al-4V alloy were also included in the figure. In

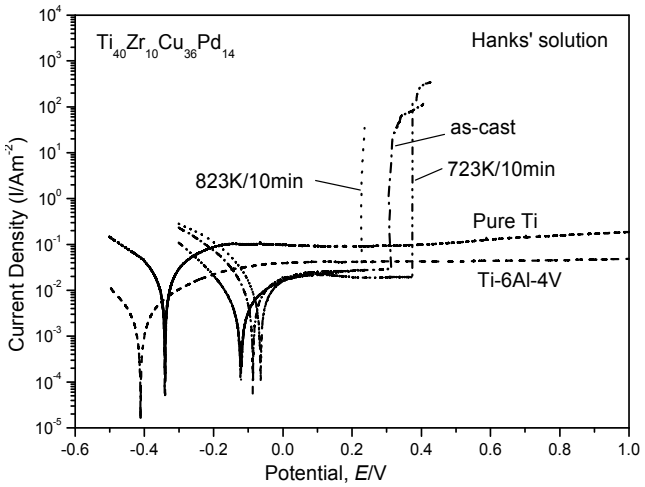

Fig. 12. Anodic and cathodic polarization curves of the $Ti_{40}Zr_{10}Cu_{36}Pd_{14}$ bulk metallic glass and its crystalline alloys at 310 K in Hanks' solution.

Hanks' solution, both the as-cast bulk metallic glass and its crystalline counterparts are spontaneously passivated. With further increase anodic potential, the passivity breakdown occurs. It is seen that the passive current densities and pitting potentials in Hanks' solution are dependent on the annealing temperatures. The as-cast bulk metallic glass and the alloy after annealing below 723 K have lower passive current densities located about 10^{-2} A/m^2, lower than that of commercial Ti-6Al-4V alloy, meaning that more protective and denser passive film formed on the surface of the alloys in the anodic process. Furthermore, noble pitting potential has been observed for the partly crystalline alloy annealed at 723 K. The pitting potentials for the as-cast glass and the alloys annealed below 723 K are about several hundreds of microvolts higher than their open-circuit potentials, meaning that spontaneous pitting corrosion may not occur in human body environment. However, the fully crystalline alloy annealed at 823 K exhibits a much higher passive current density and a lower pitting potential.

In AES depth profiles of the as-cast $Ti_{40}Zr_{10}Cu_{36}Pd_{14}$ bulk metallic glass and its crystalline alloys after immersion in Hanks' solution at 310 K for 168 h (Fig. 13). The thickness of the oxide layer was estimated from the thickness where the oxygen concentration became 50%. The concentration of each metal element comes from both oxidic state and metallic state because difference in chemical states could not be distinguished by AES. It is obvious that the oxide films formed on all the alloys are smaller than 5 nm, suggesting high corrosion resistance of the alloy system. The surface films formed on the as-cast and crystalline alloys in Hanks' solution mainly contain titanium, especially in their outermost region. In addition, the concentration of Zr is also higher that of nominal concentration in the bulk. The comparison of the thickness of the oxide film reveals that the layers formed in Hanks' solution for the as-cast metallic glass and the nano-crystalline alloy annealed at 723 K are thinner than that of the completely crystalline alloy annealed at 823 K. The thicker film formed on the completely crystalline sample in Hanks' solution is due to a higher oxidation rate of the fully crystalline alloy. Recently it has been reported that partial nano-crystallization of the glassy alloys exhibited higher corrosion resistance in Cr-based,

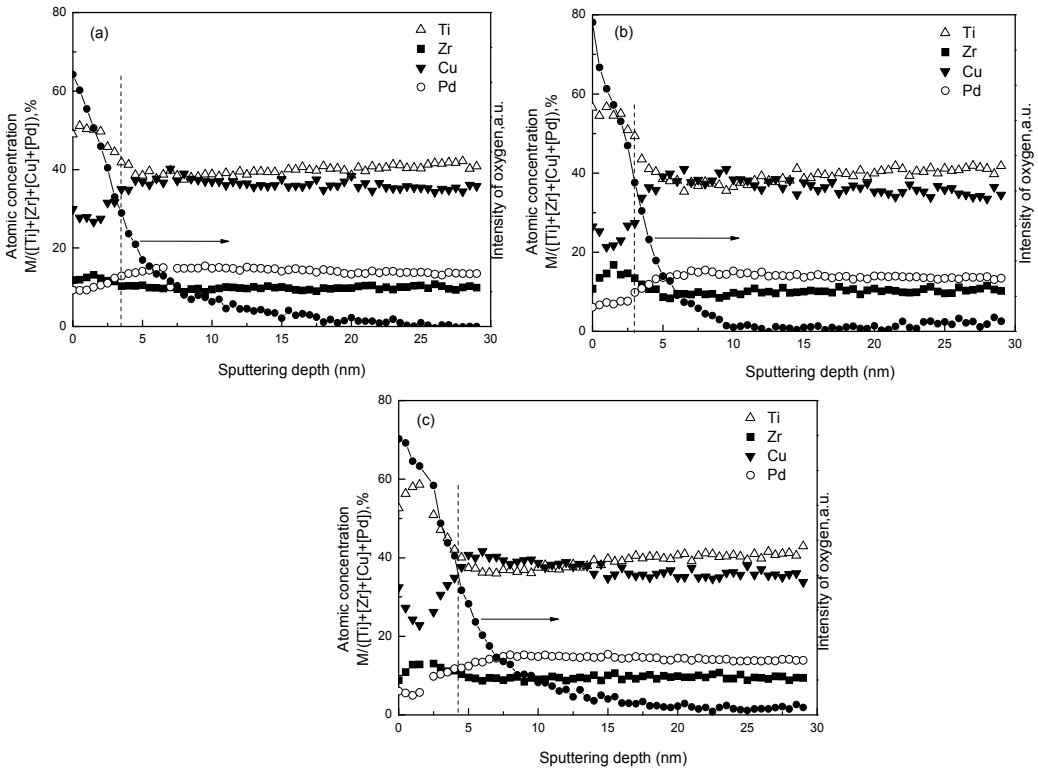

Fig. 13. AES depth profiles of the $Ti_{40}Zr_{10}Cu_{36}Pd_{14}$ bulk metallic glass and its crystalline alloys after immersion at 310 K in Hanks' solution for 168 h as-cast (a) and annealed at 723 k (b) 823 K (c).

Ni-based, Zr-based and Fe-based glassy alloys. Some authors (Mondal et al., 2005) attributed higher corrosion resistance to the structure relaxation and stress relief caused by annealing. That is because structural relaxation decreases the free energy of the alloy, consequently decreases the elemental reactivity and increases the alloy's chemical stability. Some authors (Mehmood et al., 1998, Alvarez et al., 1998) considered that the formation of nano-particles induced more protective films formed in the underlying surface. The Zr-rich nano-crystalline phases formed after heat treatment in Cr-Zr alloys ennobled the pitting potential in aggressive HCl solution due to the fact that the formation of the hcp zirconium phase leads to an increase in the Cr content of the matrix phase which is able to form thin protective Cr-rich passive films covering the entire homogeneous alloy surface. But the pitting potential of the Cr-Zr alloys after heat treatment was also dependent on the heating temperature, i.e. the size of nano-crystalline phase played an important role. When the size of nano-crystalline phases exceeds a critical size of 20 nm, the protective passive films can't completely cover the precipitates and the pitting corrosion reduced. In this study, enhancement of pitting potential of partly nano-crystalline alloy annealed at 723 K as shown in Fig. 5, can be explained by the formation of Ti_3Cu_4 phase, resulting in the enrichment of Pd in the glassy matrix, which is helpful to form protective passive film. At the same time, the phases are in the nano-scale, thus a large number of interface defects are expected in the nano-crystalline alloys. The breakdown of passive film is more uniform because of more

defects in the passive film, leading to uniform corrosion. More uniform distribution of the passive current density over the preferred corrosion attack sites allows the nano-crystalline alloys to maintain passivity over large potential range on the noble side and resist localized Cl ion attack (Mehmood et al., 1998). Whereas $Ti_{40}Zr_{10}Cu_{36}Pd_{14}$ bulk metallic glass is completely crystallized, not only Ti_3Cu_4 phase but also Ti_2Pd and Ti_2Pd_3 nucleate and grow-up to larger size, it may cause micro-galvanic corrosion between Cu-rich phase and Pd-rich phases. Thus higher passive current density is observed, indicating that both the size and composition of crystalline phase play an important role in controlling the corrosion behavior of Ti-based alloys.

3.3 Bioactive property

A simple chemical and thermal two-step treatment method has been widely used because the bone-like apatite can be formed on conventional alloys in biomimetic solutions. However this method seems to be ineffective on Ti-based bulk metallic glasses. In this study, a new two-step method consisting of hydrothermal-electrochemical treatment followed by pre-calcification treatment is developed. The nucleation and growth of bone-like apatite on the $Ti_{40}Zr_{10}Cu_{36}Pd_{14}$ metallic glass are investigated.

A microporous and network structure is formed on the surface of $Ti_{40}Zr_{10}Cu_{36}Pd_{14}$ metallic glass after treatment in 1 M NaOH solution at 90 °C for 2 h under a direct current density of 2 mA/cm², as shown in Fig. 14(a). A grown composite layer with the whole thickness of about 500 nm is observed in the cross section of the treated $Ti_{40}Zr_{10}Cu_{36}Pd_{14}$ metallic glass. The outer layer is the porous and network layer formed by the reaction of the alloy components with the alkali solution under the above mentioned experimental condition. The inner layer is the intermediated layer lying between the metallic glass substrate and the outer porous layer, which is formed by elemental diffusion to the outer layer. In addition, Cu and Pd elements are detected by EDS on the surface of the counter electrode Pt. These elements are dissolved from the metallic glass anodic electrode and deposit on the counter electrode Pt.

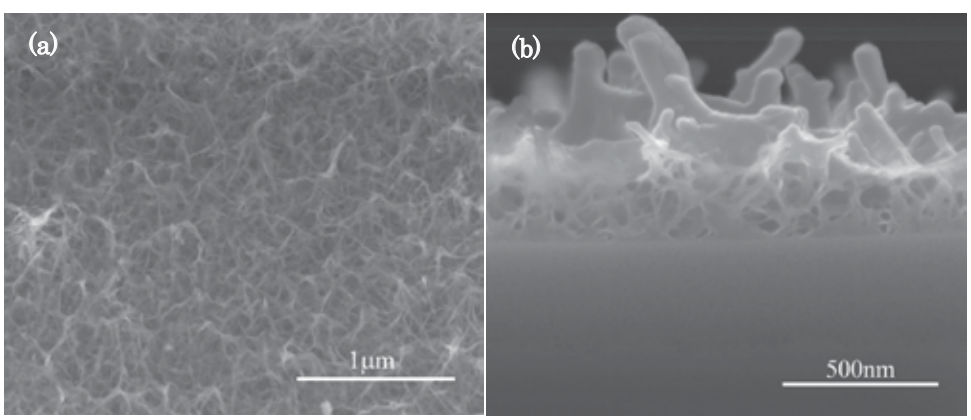

Fig. 14. SEM surface morphology (a) and cross section morphology (b) of $Ti_{40}Zr_{10}Cu_{36}Pd_{14}$ metallic glass after electrochemical-hydrothermal treatment in 1 M NaOH solution.

Some white nuclei distributed on the surface of the electrochemical-hydrothermal treated $Ti_{40}Zr_{10}Cu_{36}Pd_{14}$ metallic glass subjected to pre-calcification treatment (Fig. 15). The sizes of

nuclei are about 1 μm in length and enriched with Ca and P elements analyzed by EDS (Fig. 15 (b)). Under high magnification, some smaller white granules can also be observed. Both HPO_4^{2-} and Ca^{2+} ions could be adsorbed into the micro-porous titanium oxide surface to stimulate the nucleation and growth of dicalcium phosphate during immersion in Hanks' solution.

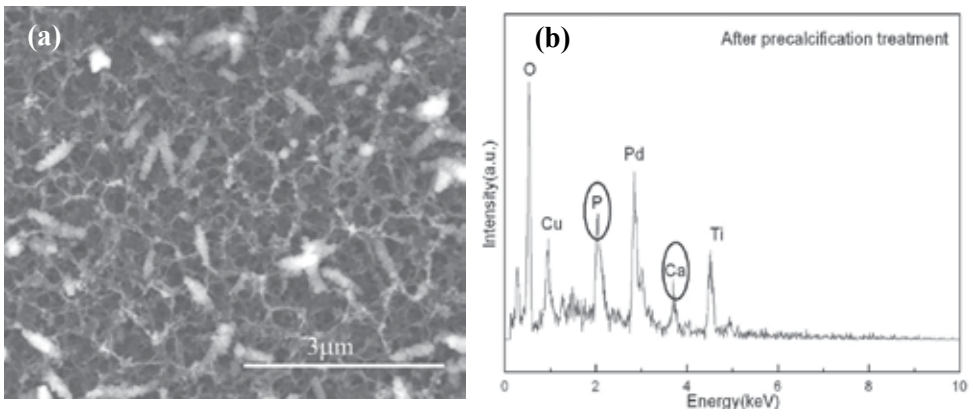

Fig. 15. SEM image (a) and EDS spectrum (b) of electrochemical-hydrothermal treated $Ti_{40}Zr_{10}Cu_{36}Pd_{14}$ metallic glass after pre-calcification treatment.

After soaking in Hanks' solution for one day, a thin and homogeneous layer appears in the network surface (Fig. 16 (a)), which is composed of Ca, O and P. The Ca/P ratio is identified to be 1.3 by EDS. Then the layer grows and the Ca content increases with an increase of immersion time. With further increasing time to six days, the Ca/P ratio reaches about 1.6, which is similar to the ratio of apatite. From the cross section SEM image of the two-step treated $Ti_{40}Zr_{10}Cu_{36}Pd_{14}$ metallic glass after immersion in Hanks' solution for six days shown in Fig. 17, it is obvious that the porous apatite is strongly bonded with the porous surface of the metallic glass in the absence of a visible interface after the electrochemical-hydrothermal treatment. The thickness of the resulting apatite probable is about several hundreds nanometers. However, if the samples were only performed by hydrothermal treatment with pre-calcification or by hydrothermal-electrochemical treatment without pre-calcification, no calcium phosphate precipitation was observed on the surface of $Ti_{40}Zr_{10}Cu_{36}Pd_{14}$ metallic glass even after immersion in Hanks' solution for 30 days.

In the XRD pattern of the surface of the $Ti_{40}Zr_{10}Cu_{36}Pd_{14}$ metallic glass after immersion in Hanks' solution for 4 days, as shown in Fig. 18. The peaks arising from apatite as well as a broad peak at about 46.5° from the metallic glass substrate are identified. It indicates that the substrate remains a glassy state after the treatment. The hydrothermal-electrochemical pretreatment temperature of 90 °C is much lower than the glass transition temperature (396 °C) of $Ti_{40}Zr_{10}Cu_{36}Pd_{14}$ bulk metallic glasses. Therefore, after such a serious treatment, the substrate remains a glassy state as evident from XRD pattern, which is very important for retaining excellent properties of bulk metallic glasses in real application.

Figure 19 shows the AES spectra before and after sputtering to a depth of 1 μm as well as elemental depth profile of the hydrothermal-electrochemical treated $Ti_{40}Zr_{10}Cu_{36}Pd_{14}$ metallic glass. Strong Ti and O signals are detected on the surface together with small signal of Cu and C before sputtering. The depth profile shows that titanium oxide exists as a main phase on the

surface of the Ti-based metallic glass after subjected to hydrothermal- electrochemical method in alkali solution. After sputtering, all of Ti, Cu, Pd and Zr in the alloy can be detected.

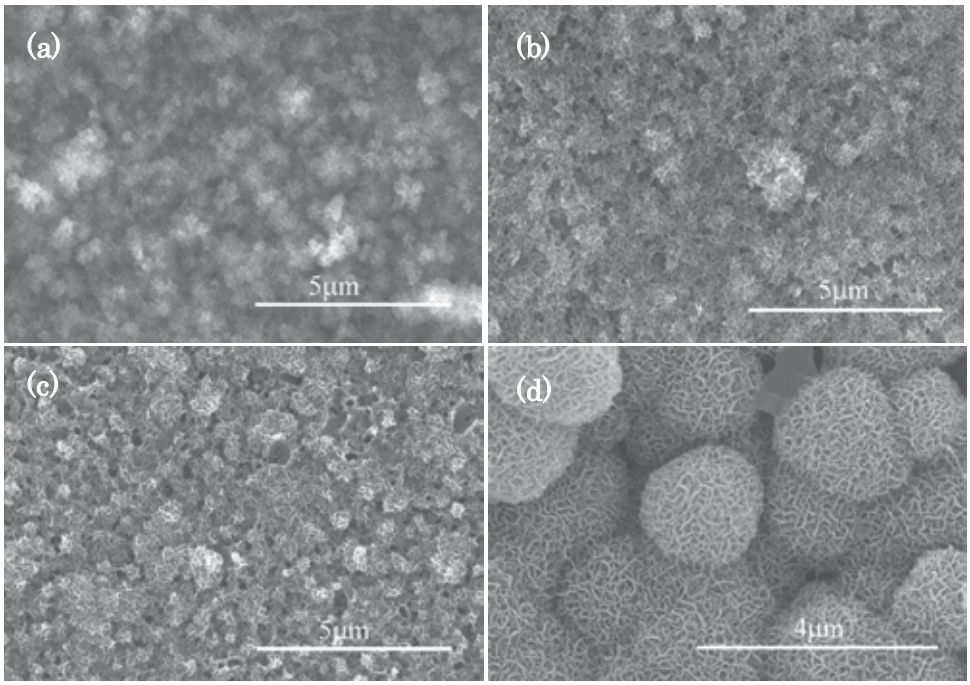

Fig. 16. SEM images of two-step pretreated $Ti_{40}Zr_{10}Cu_{36}Pd_{14}$ metallic glass after immersion in Hanks' solution for (a) one (b) two (c) three and (d) six days.

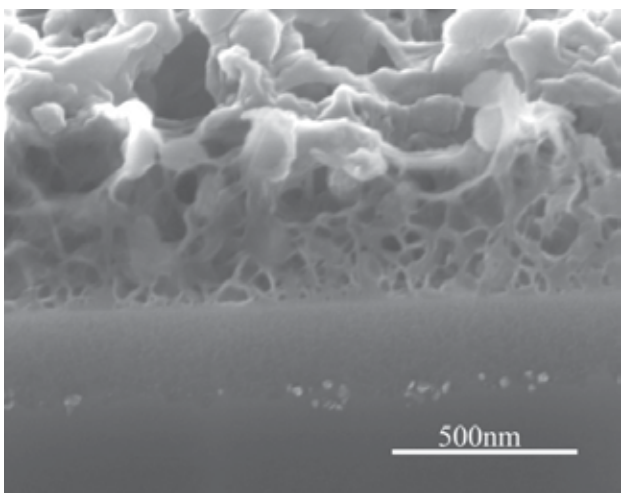

Fig. 17. Cross sectional SEM image of two-step treated $Ti_{40}Zr_{10}Cu_{36}Pd_{14}$ metallic glass after immersion in Hanks' solution for six days.

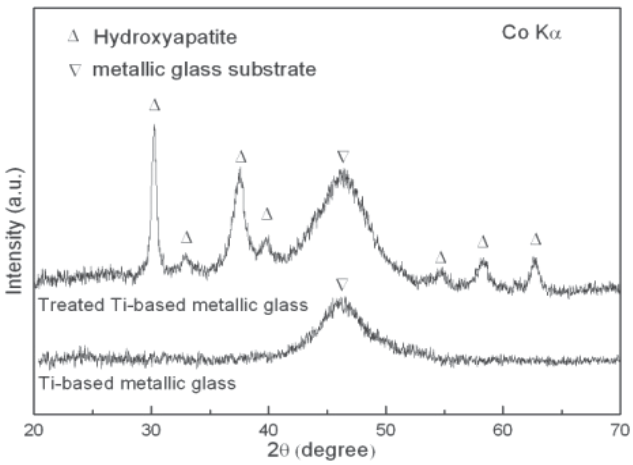

Fig. 18. XRD patterns of two-step treated the $Ti_{40}Zr_{10}Cu_{36}Pd_{14}$ metallic glass and monolithic $Ti_{40}Zr_{10}Cu_{36}Pd_{14}$ metallic glass after immersion in Hanks' solution for six days.

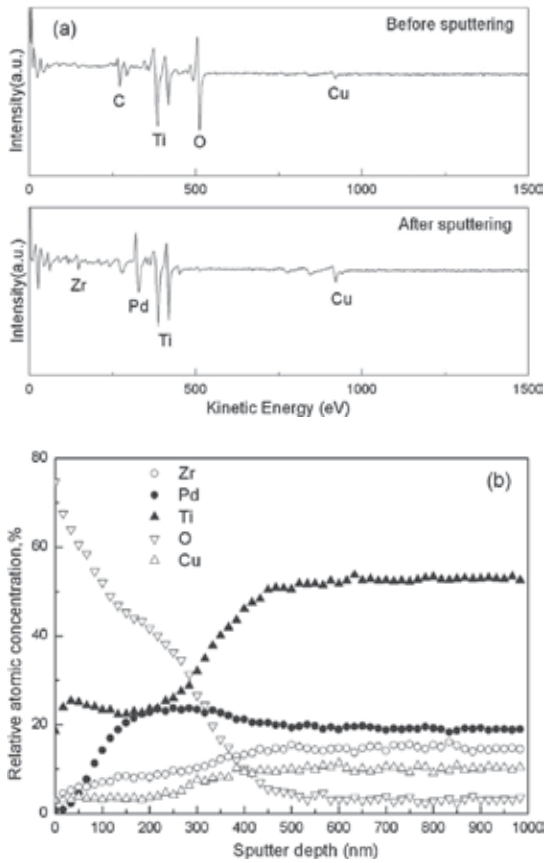

Fig. 19. AES spectra and elemental depth profiles of the electrochemical hydrothermal treated $Ti_{40}Zr_{10}Cu_{36}Pd_{14}$ metallic glass in 1 M NaOH solution.

The surface consists mainly of Ca, P and O before sputtering after immersion in Hanks' solution for six days (Fig. 20). It was also demonstrated that the Ca concentration increases with increasing immersion time in Hanks' solution. The above mentioned results indicate that only the combination of hydrothermal-electrochemical treatment and pre-calcification treatment causes the nucleation and improve growth rate of apatite on the $Ti_{40}Zr_{10}Cu_{36}Pd_{14}$ metallic glass. The bioactivity of metallic implants can be evaluated by the formation of apatite in body fluid and the growth rate of the apatite layer. Usually the possible mechanism of nucleation and growth of apatite on alkali pretreated alloy immersion in SBF has been proposed as follows (Shukla et al., 2006): 1) A sodium titanate gel layer is formed on the surface after alkali treatment; 2) Na^+ ion releases into the surrounding SBF via an ion exchanging with H_3O^+ to form Ti-OH group; 3) The Ti-OH groups interact with Ca to form a calcium titanate; 4) The calcium titanate reacts with phosphate ion to form apatite nuclei; 5) Once the nuclei are formed, the apatite nuclei automatically grow up by consuming the Ca and P ion in surrounding fluid. According to the above idea, sodium titanate hydrogel film formed after alkali treatment can initiate apatite nucleation itself.

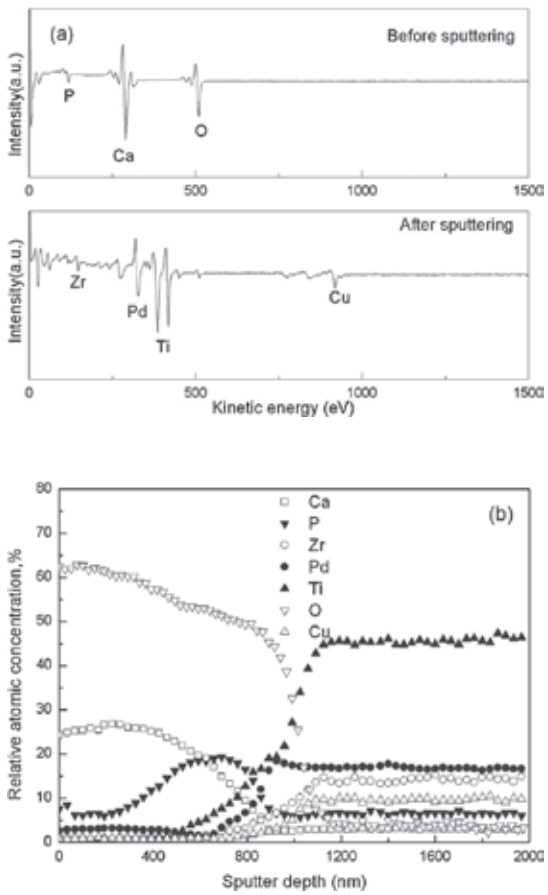

Fig. 20. AES spectra and elemental depth profiles of the two-step treated $Ti_{40}Zr_{10}Cu_{36}Pd_{14}$ metallic glass after immersion in Hanks' solution for six days.

Our previous work revealed that simple alkali soaking at 60 °C even for one day, can't induce the formation of apatite on the surface of Ti-based bulk metallic glasses due to high concentration other metals such as Cu, Pd and Zr. The effect of the hydrothermal-electrochemical treatment can increase the surface roughness as well as the Ti concentration on the outer layer of metallic glass. In addition to the hydrothermal-electrochemical treatment in 1 M NaOH solution, a much thicker TiO_2 layer, instead of native thin TiO_2 layer, is formed, which is beneficial to the nucleation of apatite. Thus, the hydrothermal-electrochemical treatment is effective of high surface roughness and negative-charged TiO_2 layer of metallic glass.

After hydrothermal-electrochemical and hydrothermal treatments in NaOH, an amorphous sodium titanate gel layer is formed as shown in formula (1). Sodium ions are released from the surface via NaOH dissolving in water when the samples are completely washed by distilled water as formula (2).

$$TiO_2 + NaOH \rightarrow NaHTiO_3 \tag{1}$$

$$NaHTiO_3 + H_2O \rightarrow TiO_2 \cdot OH^- + H^+ + NaOH \tag{2}$$

Therefore, no sodium can be observed by EDS or AES after hydrothermal treatment. Our results indicate that the exchanging process between Na^+ ion and H_3O^+ which initiates the apatite nucleation don't have to occur in SBF. It is suggested that the micro-porous surface leads to the adsorption of Ca and P ions. The spatially submicron-scaled micro-architecture of the treated samples was one of the most probable factors. It is well known that the surface modification of Ti alloys is necessary in order to improve implant-tissue osseo-integration. In particular, TiO_2 layer on the surface of Ti alloys plays an important role in determining biocompatibility and corrosion behavior of Ti implant alloys. Furthermore, the hydrothermal-electrochemical treatment at low temperature is suitable for a metallic glassy alloy which will be crystallized by annealing at high temperature around glass transition temperature.

On the other hand, only the hydrothermal-electrochemical treatment, failed to form an active surface on the Ti-based metallic glass. The pre-calcification procedure accelerated the calcium phosphate precipitation on the surface of electrochemical-hydrothermal treated $Ti_{40}Zr_{10}Cu_{36}Pd_{14}$ metallic glass. As mentioned in the results, calcium phosphate can't precipitate on the surface of the hydrothermal-electrochemical treated metallic glass without pre-calcification treatment soaking in Hanks' solution even for 30 days. The pre-calcification treatment is necessary to acquire the nuclei of Ca-P inducing the growth of bone-like apatite. Ca-P coating can also be inducted on titanium surface with treatment of H_3PO_4 pretreatment (Feng et al., 2002), $Ca(OH)_2$ pretreatment (Yang et al, 2006) or combination treatment of Na_2HPO_4 and $Ca(OH)_2$ treatments. All the above pretreatment can accelerate the nucleation of calcium phosphate on Ti. In addition, this calcium phosphate nucleates homogeneously and grows up to layer upon layer. Before the samples were immersed in Hanks' solution, HPO_4^{2-} and Ca^{2+} ions were adsorbed homogeneously onto the micro-porous and network surface on $Ti_{40}Zr_{10}Cu_{36}Pd_{14}$ metallic glass. The hydrothermal-electrochemical treatment makes a much larger surface area on the Ti metallic glass than that without current two-step treatments. The micro-porous surface leads to much more adsorption of HPO_4^{2-} or/and Ca^{2+} ions stimulating the nucleation of calcium phosphate layer on Ti-based metallic glass

followed by immersion in Hanks' solution (Healy, 1992). From the AES in Fig. 20, the consuming process of Ca ion can be found. Then a homogeneous calcification phosphate layer formed on the surface, rather than an island nucleate.

As mentioned in a previous work, the $Ti_{40}Zr_{10}Cu_{36}Pd_{14}$ bulk metallic glass can be fabricated in the diameter range up to 6 mm. In this research, $Ti_{40}Zr_{10}Cu_{36}Pd_{14}$ ribbon samples were used for convenience. There must be no problem to achieve the same results in the bulk samples with the same alloy composition. The present hydrothermal-electrochemical and pre-calcification treatments seem to be more suitable for the application of the Ti-based bulk metallic glasses, owning to a relative low concentration of Ti. This study demonstrates that the combination of hydrothermal-electrochemical treatment and pre-calcification treatment can dramatically accelerate the nucleation and growth of calcium phosphate on the surface of Ti-based metallic glass. For conventional Ti-6Al-4V, Ti-Zr-Nb or other alloys, it may be also a promising method. We may propose the formation mechanism of apatite on Ti-based metallic glass as follows. Step one of hydrothermal-electrochemical treatment might have three effects on the as-prepared metallic glass surface. The first is an increasing concentration of Ti on the outer surface by forming a porous layer. The second is the formation of micro-porous network structure in the aggressive boiling alkali solution. The third is the formation of thicker titanium oxide layer in the outer surface than that of native titanium oxide layer. Ti-OH groups are also presented on the porous TiO_2 surface. Negative-charged and micro-porous surfaces are the main reason for the good bioactivity (Heuer et al., 1992). Step two of pre-calcification treatment stimulates the adsorption of HPO_4^{2-} and Ca^{2+}, which are necessary for the nucleation of apatite. Once formed, bone-like apatite grows up by consuming calcium and phosphate ions in surrounding simulated body fluid. The apatite is strongly bonded with the similar porous structure on the surface of the electrochemical-hydrothermal treated $Ti_{40}Zr_{10}Cu_{36}Pd_{14}$ metallic glass without a visible interface.

4. Conclusion

In this chapter, we research on mechanical property, corrosion behavior, microstructure and bioactivity of Ni-free Ti-Zr-Cu-Pd (-Nb) bulk metallic glasses or its crystallized counterpart alloys. The results were concluded as follows,

The strength and plastic deformation can be improved by compositing bulk metallic glasses with nano-crystals produced by heat treatment or in-situ casting by changing of composition. Nano-composites are formed in the alloys annealed at 693 and 723 K. High strength of over 2100 MPa and distinct plastic deformation of 0. 8% are obtained in the alloy annealed at 693 K. The minor addition of Nb to Ti-Zr-Cu-Pd bulk metallic glasses induced the formation of Pd_3Ti nano-particles by copper mold casting. High yield strength of over 2050 MPa, low Young's modulus of about 80 GPa and distinct plastic strain of over 6.5 % were achieved in 1 % and 3 % Nb-added alloys, due to the nano-particles dispersed in the glassy matrix blocks the propagation of shear bands. With further increasing Nb content to 5 %, the plastic strain decreased to 1.0 %. The most optimum Nb addition was 3 %.

The $Ti_{40}Zr_{10}Cu_{36}Pd_{14}$ bulk metallic glass and its crystalline counterparts examined are spontaneously passivated by anodic polarization with the passive current density of about 10^{-2} A/m^2 in simulated body fluid. The higher corrosion resistance for the Ti-base bulk

metallic glass and its partial nano-crystalline alloys is attributed to stable and protective passive films.

The combination application of hydrothermal-electrochemical and pre-calcification treatments on the $Ti_{40}Zr_{10}Cu_{36}Pd_{14}$ metallic glass dramatically accelerates the nucleation and growth rates of apatite in Hanks' solution. The hydrothermal-electrochemical treatment makes a much larger surface area, increases the thickness of titanium oxide and titanium concentration on the surface of the $Ti_{40}Zr_{10}Cu_{36}Pd_{14}$ metallic glass. The micro-porous and network surface leads to much more adsorption of HPO_4^{2-} or/and Ca^{2+} ions stimulating the nucleation of calcium phosphate layer on the $Ti_{40}Zr_{10}Cu_{36}Pd_{14}$ metallic glass followed by immersion in Hanks' solution. Apatite layer can be formed quickly for only several days through two-step treatment.

Owing to the simultaneous achievement of low Young's modulus, high strength and large plastic strain, as well as good bioactivity, the Ni-free Ti-Zr-Cu-Pd-(Nb) bulk metallic glass composites are potential candidates for biomaterials. It makes it possible to apply Ti-based bulk metallic glasses with excellent properties as novel biomedical metallic implants.

5. Acknowledgement

This work is financially supported by Advanced Materials Development and Integration of Novel Structured Metallic and Inorganic Materials, Institute for Materials Research, Tohoku University.

6. References

Alvarez, M.G.; Vazquez, S.M.; Audebert, F. & Sirkin. H. (1998). Corrosion behaviour of Ni-B-Sn amorphous alloys. *Scrip. Mater.* 39, pp. 661-664

Dasa, K.; Bandyopadhyay, A. & Gupta, Y. M. (2005). Effect of crystallization on the mechanical properties of $Zr_{56.7}Cu_{15.3}Ni_{12.5}Nb_{5.0}Al_{10.0}Y_{0.5}$ bulk amorphous alloy. *Mater. Sci. Eng. A,* 394, pp. 302-311

Feng, B.; Chen, J.Y.; Qi, S.K.; He, L.; Zhao, J.Z. & Zhang, X.D. (2002). Carbonate apatite coating on titanium induced rapidly by precalcification. *Biomaterials,* 23, pp. 173-179

Healy, K.E. & Ducheyne, P. (1992). Hydration and preferential molecular adsorption on titanium *in vitro*. *Biomaterials,* 13, pp. 553-561

Heuer, A.H.; Fink, D.J.; Laraia, V.J.; Arias. J.L.; Calvert, P.D.; Kendall, K.; Messing, G.L.; Blackwell, J.; Rieke, P.C.; Thompson, D.H.; Wheeler, A.P.; Veis, A. & Calpan, A.I.; (1992). Innovative materials processing strategies: a biomimetic approach. *Science,* 255, pp. 1098-1105

Inoue, A. (1995). High strength bulk amorphous alloys with low critical cooling rates, *Mater. Trans. JIM,* 36, pp. 866-875

Inoue, A. (2000). Stabilization of metallic supercooled liquid and bulk amorphous alloys. Acta Materialia, 48, pp. 279-306

Jiang, J. Z.; Saida, J.; Kato, H. & Inoue, A. (2003). Is $Cu_{60}Ti_{10}Zr_{30}$ a bulk glass-forming alloy. *Appl. Phys. Lett.,* 82, pp. 4041-4042

Lűtjering, G. (1999). Property optimization through microstructural control in titanium and aluminum alloys. *Mater. Sci. Eng. A,* 263, pp. 117-126

Mehmood, M.; Zhang, B.P.; Akiyama E.; Habazaki, H.; Kawashina, A.; Asami, K. & Hashimoto, K. (1998). Experimental evidence for the critical size of heterogeneity areas for pitting corrosion of Cr-Zr alloys in 6 M HCl. *Corro. Sci*. 40, pp.1-17

Mondal, K.; Murty, B.S. & Chatterjee, U.K. (2005). Electrochemical behaviour of amorphous and nanoquasicrystalline Zr–Pd and Zr–Pt alloys in different environments. *Corro. Sci*. 47, pp. 2619-2635

Shukla, A.K. & Balasubramaniam, R. (2006). Effect of surface treatment on electrochemical behavior of CP Ti, Ti–6Al–4V and Ti–13Nb–13Zr alloys in simulated human body fluid. *Corro. Sci*. 48, pp. 1696-1720

Xing, L.Q.; Bertrand, C.; Dallas, J.P. & Cornet, M. (1998). Nanocrystal evolution in bulk amorphous $Zr_{57}Cu_{20}Al_{10}Ni_8Ti_5$ alloy and its mechanical properties. *Mater. Sci. Eng. A*, 241, pp. 216-225

Yang, X.J.; Hu, R.X.; Zhu. S.L.; Li, C.Y.; Chen, M.F.; Zhang, L.Y. & Cui, Z.D. (2006). Accelerating the formation of a calcium phosphate layer on NiTi alloy by chemical treatments. *Scrip. Mater*. 54, pp. 1457-1480

12

Surface Treatments of Nearly Equiatomic NiTi Alloy (Nitinol) for Surgical Implants

Dixon T. K. Kwok[1], Martin Schulz[2], Tao Hu[1],
Chenglin Chu[3] and Paul K. Chu[1]
[1]*Plasma laboratory, Department of Physics and Materials Science, City University of Hong Kong,*
[2]*Institute of Lightweight Engineering and Polymer Technology, Faculty of Mechanical Engineering, Dresden University of Technology,*
[3]*School of Materials Science and Engineering, Southeast University,*
[1,3]*China*
[2]*Germany*

1. Introduction

Since the discovery of the shape memory effect in equiatomic NiTi alloy by Buechler in 1962 in the Naval Ordnance Laboratory [1], nitinol (Nickel-Titanium Naval Ordnance Laboratory) has attracted a great deal of commercial interest especially in medical applications [2, 3]. T. Duerig, A. Pelton, and D. Stockel wrote an excellence overview on nitinol medical applications in 1999 [3]. They pointed out that there were three reasons for the sudden explosive growth of Nitinol in the 1990's. The most important was that the medical industry had been trying to pare costs and simplify medical procedures. Conventional materials like 316L stainless steel could not fulfill this new demand by medical devices. Furthermore, the availability of microtubing and ability to laser cut tubings with high precision favored new materials like Nitinol. Last but not least, sharing of technology developed by materials scientists and companies among product designers and doctors should not be underestimated. They specifically pointed out 11 specific reasons for the application of Nitinol to the medical industry [3, 4]:

a. elastic deployment allowing an efficient deployment of a medical device;
b. thermal deployment and by using the shape memory effect, the nitinol device can recover to its 'pre-programmed' shape by body temperature after the deployment;
c. kink resistance which allow the medical device to pass through tortuous paths without stain localization and changing its shape;
d. good biocompatibility which means that the foreign implants are well accepted by the body. Nitinol has been reported to have extremely good biocompatibility due to the formation of a passive titanium-oxide layer (TiO_2) [3]. However, Ni is allergenic and toxic to humans and reports have shown that the Ni release from commercial ready-to-use nitinol orthodinitc wires vary in a wide range from 0.2 to 7 μg cm^{-2} [5]. Therefore, Ni release from nitinol remains a serious health concern and surface modification of nitinol devices will be discussed later in this chapter;
e. constant stress allowing the design of a medical device that applies a constant stress over a wide range of shapes;

f. biomechanical compatibility meaning that a medical implant that is mechanically similar to the adjacent biological materials promotes bone in-growth and proper healing by sharing loads with the surrounding tissue;
g. dynamic interference implying that the long-range nature of nitinol causes less damage to the surrounding tissue;
h. hysteresis which is a desirable feature for stents that provide a very low dynamic outward force (COF) and a very high radial resistive force (RRF);
i. magnetic resonance image (MRI) compatibility because nitinol is non-ferromagnetic that allows a clearer and crisper magnetic resonance image than stainless steel;
j. exceptional fatigue resistance under high strain making nitinol drills perfect in dental root canal procedures;
k. uniform plastic deformation having advantages in ballon expansion nitinol stents.

2. Shape memory effect and super-elasticity

Nitinol shape memory alloys (SMA's) have been used in biomedical implants for more than three decades because they can recover from large strain through the application of heat [6, 7]. Nitinol shape memory alloys undergo thermoelastic martensitic transformation giving rise to the shape memory effect (SME) and superelasticity (SE) also named as pseudoelasticity (PE) properties. Since the body temperature is a very stable, the phase transition temperature can be precisely control in order to maximize the SME and SE behavior at 37°C. The SME and SE properties are related to the thermo-elastic martensitic transformation and reverse phase transformation. Some phase transformation is irreversible and this irreversible process repeats during thermal cycles. Heat treatment of nitinol focuses on the austenitic phase transition (reverse martensitic transformation). SE depends on the temperature difference ΔT between the working temperature T and austenite finish temperature A_f. The forward and reverse phase transition temperatures of nitinol between the martensitic phase (B19′) and austenitic phase (B2) must be carefully determined during the heat treatment process. The important heat treatment parameters include the cooling rate, heat treatment temperature, and processing time. The heat treatment temperature can be divided into three ranges, solid solution between 800 and 900 °C, aging between 400 and 550°C, and another aging treatment between 200 and 400 °C. Cooling can be preformed in different ways, for example, furnace cooling, air cooling, water quenching, etc. To achieve a phase transition temperature at 37°C, the nitinol devices can be, for example, heat-treated at 500°C for 1 hr in a furnace followed by water quenching [8] or heat-treated at 580°C for 30 mins in air followed by quenching in air to room temperature [9]. It is worth mentioning that any surface modification method should not vary the phase transition temperature and shall be performed at a relatively low temperature. Previous studies have shown that a treatment temperature of 210°C for 4 hours can destroy the super-elastic and shape memory effects at body temperature and must be avoid [8]. We will discuss the importance of maintaining a low treatment temperature for surface modification of nitinol in the following sections.

3. Ntinol medical implants and devices

Stainless steel has been replaced by nitinol in many traditional medical implants. Because of the super-elasticity and shape memory effect, nitinol has been used to make many novel

devices and several successful and representative nitinol implants and devices are described below.

1. Stents

Although the word "stents" was originally used in dentistry, it is nowadays reserved for devices used to scaffold the inside circumference of tubular passages or lumens, i.e., the biliary duct, esophagus, and blood vessels including coronary, carotid, iliac, aorta, and femoral arteries [3, 4]. Stenting is a typical procedure following balloon angioplasty. The application of a stent immediately after angioplasty shows a significant decrease of propensity for restenosis. Nitinol is preferred in stents because of its outstanding super-elasticity. It is 10 to 20 times more flexible than stainless steel, and it can spring back with strain as high as 11%. Figure 1 depicts a crush recoverable nitinol stent [4]. Vessels such as the carotid and femoral arteries are always subjected to outside pressure which may crush stainless steel stents leading to serious consequences. Nitinol urethral stents also exhibit excellent biocompatibility with no evidence of foreign body reactions or corrosion when tested in dogs [10].

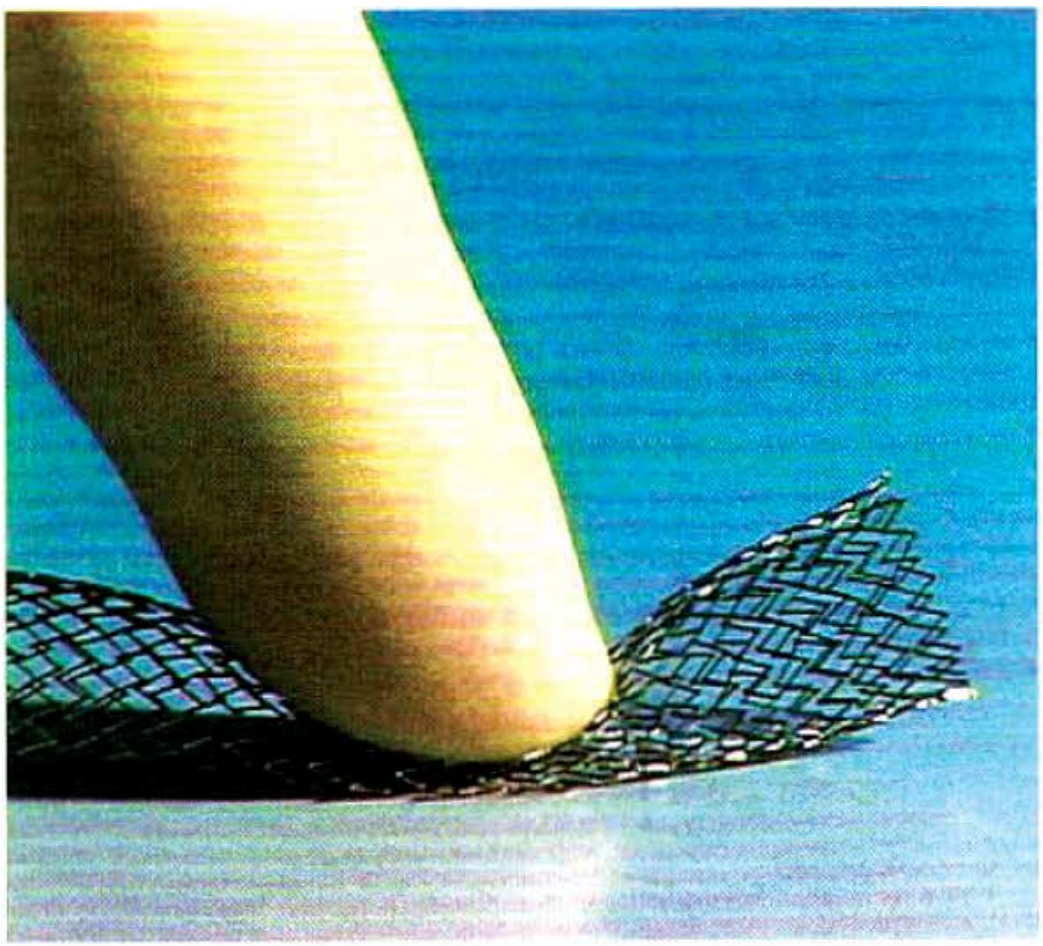

Fig. 1. Crush recoverable nitinol stent (Reproduced from ref [4]).

2. Clamps for small bone surgery

A good example of medical applications of nitinol is clamps used in small bone surgery [11]. The provision of stable fixation of bone fragments is essential to small bone surgery because passive and active motion can start soon thereafter [11]. Moreover, early rehabilitation can prevent rigidity of the broken joints and expedite healing [11]. The key advantage of using shape memory alloy is that the fixative can contract by applying heat stimulus after the surgery. This contraction does not only reduce or eliminate the gap between the bone fragments to be joined, but also applies the appropriate compression, consequently resulting in stable fixation and promoting healing. Figure 2 depicts a successful talocalcaneal arthrodesis by using three TiNi clamps [11]. However, sterilization must be done at a temperature below 45°C at which phase transformation occurs. Gamma irradiation is used for sterilization of nitinol clamps.

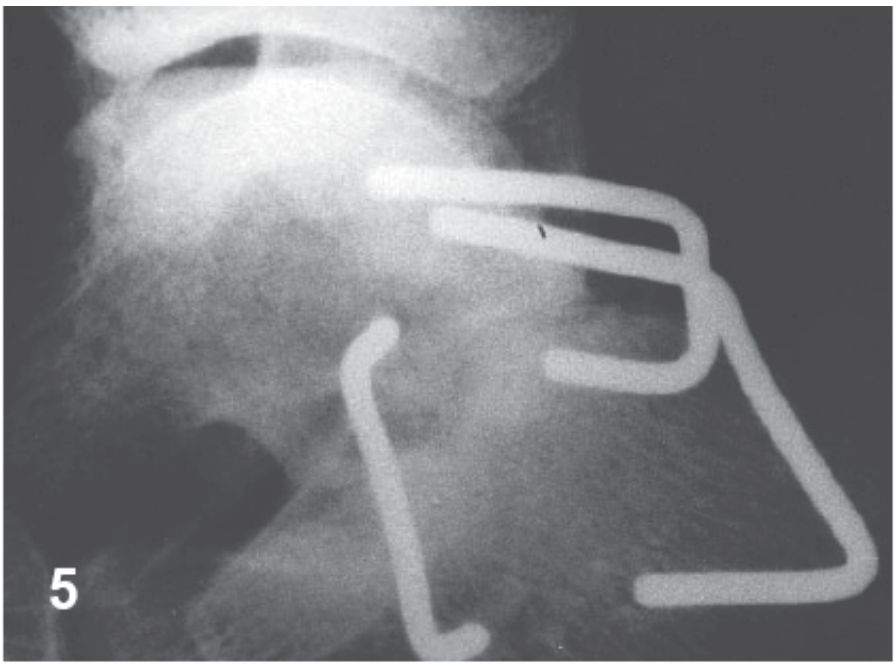

Fig. 2. Talocalcaneal arthrodesis by using three nitinol clamps (Reproduced from ref [11]).

3. S-shape bar for surgical correction of scoliosis

The shape memory effect of nitinol, that is, being flexible at low temperature but retaining its original shape when heated, has attracted a lot of interest for scoliosis correction [12, 13]. In cases of severe spinal deformity, surgeries have to be performed to straighten the patient's spine. The success of correction depends on how well the fixative, i.e., the S-shape rod, is fixed to the spine. Moreover, a force that is too large can cause bone fracture and tissue damage. On the other hand, a force being too small will lead to under-correction. Owing to the super-elastic and shape memory properties, nitinol is the ideal materials choice for the S-shape fixing rod. Figure 3 demonstrates the constant recovery force of the rod after implantation into a goat verifying the feasibility of the surgical procedures [13]. Before the operation, the rod is colled down to below the phase transition temperature, for example 15°C which is lower than the body temperature. At this temperature, the rod is soft

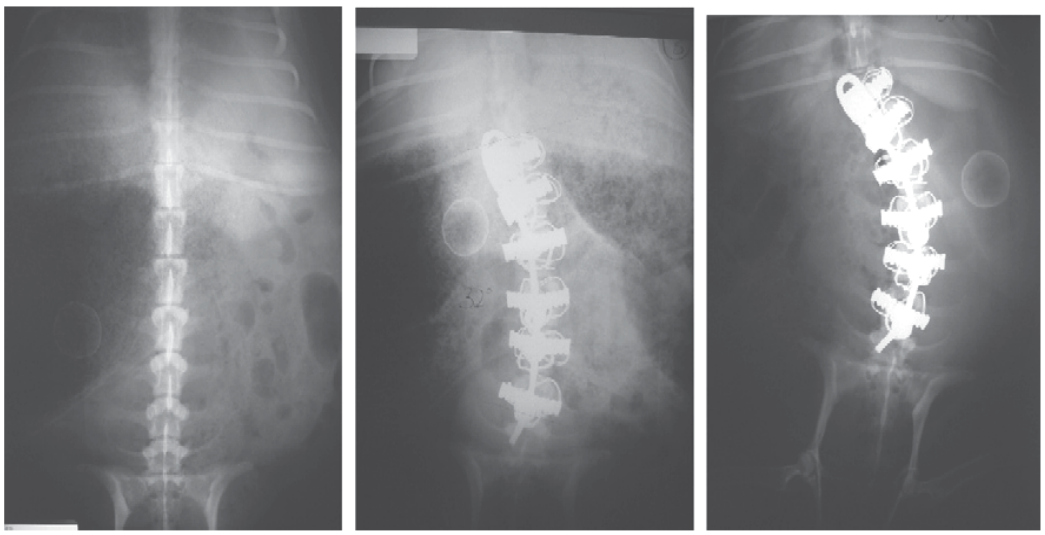

Fig. 3. X-ray photos of the spine of the operated goat: (Left) before surgery; (Middle) one day after implantation of a nitinol rod; (Right) one week after surgery. The spine of the goat that was straight before surgery became progressively bent by the constant recovery force of the rod thereby verifying the feasibility of the surgical procedures (Reproduced from [13]).

and can be bent to fit the deformed spinal. After the operation, the nitinol rod is heated to the body temperature of 37°C to revert back to its original shape. Therefore, gradual correction can take place under a constant force obviating the need for multiple corrective surgeries.

4. Patellar concentrator

The nitinol patellar concentrator (NT-PC) is designed for initial and continuous compression of patellar fractures [14]. NT-PC consists of two basis patellae claws, three apex patella claws, and a conjunctive waist [14]. The NT-PC is constructed by nitinol plates of different sizes that have undergone different heat treatments. The final product exhibits the one-way shape memory effect at a phase transformation temperature of 30 ± 2 °C and reversible deformation of 8%. During implantation, the NT-PC is cooled down to below 30 °C and unfolded in aqua astricta. The patellar concentrator can easily be put on to the fractured patellar. Figure 4 displays a nitinol patellar concentrator downloaded from Yangzhou Yahua Biological Technics Project Co. Ltd. After the operation, the concentrator is warmed and recovers to its original shape with a compressive force. This compressive force will fix the concentrator tightly onto the patellar until the fracture heals. The key element of treating patellar fractures is to reduce facies articularis and it is known that the memorial compressive stress generated by the nitinol patellar concentrator can promote the healing of cartilage.

4. Problematic leaching of Ni

Although unique properties such as the shape memory effect and super-elasticity can enhance the performance of medical implants, the biocompatibility of the materials remains a concern [15]. There are two main factors determining the biocompatibility of materials, namely the host reaction induced by the materials and degradation of the materials in the body environment. Nitinol consists of 50% of Ni and dissolution of Ni ions can induce

Fig. 4. Nitinol patellar concentrator downloaded from Yangzhou Yahua Biological Technics Project Co. Ltd.

allergic [16], toxic [17], and carcinogenic [18] effects. The corrosion performance of nitinol *in vivo* determines the release of Ni ions. Studies have shown that the corrosion performance can range from excellent to poor indicating the lack of complete understanding of the chemistry of the nitinol surface [15]. For small diameter devices such as fine wires and caliber vascular stents, a small surface defect may be sufficient to increase the leaching of Ni. Implants in the body are usually under stress / stain because of loading / unloading conditions and such actions can aggravate Ni release. In addition, sterilization procedures may modify the materials surface and accelerate Ni release and a multitude of factors must be considered simultaneously.

In vivo studies of nitinol clamps show that after proper passivation, a 3-4 nm thick TiO_2 layer forms. Afterwards, only traces of metallic Ni are detected and no major change is observed during a period between 4 and 12 months after implantation [19]. In the investigation, the proper passivation procedure calls for the samples (clamps with desired structure and memory parameters) to be etched in a solution of HF, HNO_3 and H_2O (1:2:3 vol% for 30mins), pre-deformed, ultrasonically cleaned in ethanol, and sterilized by X-ray at room temperature [19]. However, after improper surface passivation by sputter cleaning and re-oxidation in pure oxygen (5 Torr, room temperature, 10 mins), trace amounts of ~1 at% of Ni are detected [19]. Although oxidation can promote the growth of a passive native film, it is usually not complete at room temperature [15]. At high temperature, a heterogeneous surface with a mixture of various types of oxide tends to form and a mixture of various phases rather than a single oxide renders nitinol more vulnerable to corrosion.

Shabalovskaya et al. reviewed critically the nitinol surfaces and surface modification for medical applications [5]. Electrolytic etching can induce highly porous NiTi surfaces that

may increase Ni release, but this porous structure can also promote cell attachment [20]. After chemical etching and electropolishing, the surface oxide films are a few nanometers thick. Oxidation is promoted by boiling in water thereafter. The gentle treatment of boiling in water assists atomic diffusion and Ni release into the water and the oxide thickness increases to 10 to 20 nm. This oxide layer which is more stoichiometric depletes surface Ni and mitigates subsequent Ni release. It has been reported that anodization of nitinol does not reduce the Ni surface content and a severely cracked surface is obtained using the optimized anodizing parameters. However, it is not surprising that good corrosion resistance is observed after anodization and chemical etching following by boiling in water. No surface cracking upon 6% strain is observed after immersion in a corrosive solution.

Prevention of Ni release can be done by surface oxidation via heat treatment in air, argon and partially reduced atmosphere [5]. After oxidation in air at between 300 and 500°C for 30 mins, TiO, pure Ni, and NiTi B2 are detected. When the annealing temperature goes up to 600 °C, different phases of TiO_2, Ni, and Ni_3Ti are observed. However, the simultaneously presence of austenitic B_2 and martensitic NiTi phases implies alteration in the shape recovery temperature. Annealing at 600°C can produce a Ti oxide film at least 5 times thicker but accumulate Ni below the surface. The accumulated Ni can be eliminated by chemical etching. Since the shape memory and super-elasticity of nitinol is optimized in the temperature ranges of 450 to 550°C, the oxidation temperature should be below 300°C.

Laser surface melting (LSM) can be carried out in either argon or air (dry) [21]. New phases of Ti_2Ni and $TiNi_3$ are observed and part of the surface changes to martensite B19′ in argon. When LSM is conducted on nitinol in dry air, TiO_2 and Ti_4Ni_4O phases are observed from the near surface. Ni release is significantly reduced only on the first day of exposure to Hanks′ solution. However, the presence of the B19′ martensite phase after LSM is an indication that the surface has been overheated.

Diamond-like carbon (DLC) is well known for its good mechanical properties such as high hardness, low friction coefficient, chemical inertness, high corrosion resistance, and excellent biocompatibility [5, 22]. DLC can be deposited on NiTi devices to prevent Ni release and improve the biocompatibility. Different gases (acetylene C_2H_2 and benzene C_6H_6) and processes such as no-bias deposition and plasma immersion ion implantation have been adopted to synthesize DLC on NiTi. In plasma immersion ion implantation (PIII), the sample is immersed in a gas plasma and then pulse-biased to a high negative voltage of tens of kV [13]. A plasma sheath forms around the sample when the voltage pulse is applied. Positive ions are accelerated by the electric field and simultaneously bombard all exposed surfaces on the sample. Therefore, PIII is a non-line-of-sight process especially suitable for medical implants with a complex geometry [13]. However, direct coating results in delamination of the deposited layers and SiC is used as an interlayer to improve adhesion. A 50 nm thick DLC coating with enhanced hardness and Young's modulus can be obtained by annealing at 600°C for 5 hrs after PIII but it should be noted that annealing at 600°C for 5 h may alter the shape memory properties and super-elasticity.

5. TiN layer to blocking Ni release from Nitinol

Titanium nitride belongs to the refractory transition metal family [23] and consists of both covalent and metallic bonds [23, 24]. TiN has found many applications in microelectronic fabrication because of its good conductivity and excellent adhesion. It is used as a diffusion barrier between the silicon substrate and aluminum metallization. TiN is also commonly

used in coating cutting tools because of its high hardness and good resistance to wear and corrosion. TiN is useful in biomedical applications because of its intrinsic biocompatibility and can be found on orthopedic implants such as hip. The materials are also widely used as hard coatings on dental implants and dental surgical tools. Direct implantation of nitrogen can produce titanium nitride is possible because TiN forms preferentially over NiN.

The powder immersion reaction assisted coating (PIRAC) nitriding method has been developed to produce TiN on NiTi [24]. NiTi samples with a phase transform temperature at A_f = 15°C are annealing at 900°C for 1.5 h and then 1000°C for 1 hr in sealed containers. Nitrogen atoms diffuse into the samples and atmospheric oxygen is stopped by a steel foil with a large percentage of Cr. The modified surface consists of a thin outer layer of TiN and a thicker Ti_2Ni layer underneath. The PIRAC samples exhibit significantly improved corrosion resistance. No pitting is observed on the surface and the surface hardness is also increased remarkably. Hence, leaching of harmful Ni *in vivo* can be reduced. However, a fully crystallized TiN layer may not sustain deformation without cracking and annealing at 900 ^oC for 1.5 hrs will no doubt alter the phase transformation temperature.

Laser gas nitriding (LGN) has been demonstrated to improve the surface performance of Ti and Ti alloys [25]. LGN is conducted on NiTi with a laser beam emitted from a 2 kW Nd-YAG laser at a wavelength of 1.06 μm [25]. At a scanning rate of 5 mm/sec with a beam diameter of 2 mm, defect free single tracks are observed on the NiTi shape memory alloy plates. By overlapping the single track at the 50% melt width interval, a large nitrided surface is achieved [25]. The defect/crack free TiN layer protects the NiTi surface from wear and corrosion and therefore reduces leaching of harmful Ni. However, LGN is a line-of-sight process and may not handle NiTi biomedical devices with a complex shape. Moreover, the strong laser may affect the phase transformation temperature especially for very thin NiTi samples such as RITA tissue ablation devices with sharp and curved tubular needles [3].

Plasma immersion ion implantation (PIII) is well known for the production of dense, crack free surface layers [26]. It is a non-line-of-sight process and can implant the whole surface of a sample with an odd shape. It also boast a high throughput [13, 26, 27]. Nitrogen PIII has been conducted on NiTi alloy to produce TiN on the surface [8, 28, 29]. After nitrogen PIII, the Ni concentration in the implanted surface is much lower than that in the unimplanted surfaces [29]. A high degree of cell proliferation after 8 days of culturing is observed on the N-PIII samples as well [29]. The depression of near-surface Ni and good biocompatibility can be attributed to the formation of the TiN barrier layer [26, 29]. However, the phase transformation temperature and hence the shape memory effect and super-elasticity properties of the the NiTi alloy strongly depend on the ion energy and treatment temperature [8, 28]. The sample temperature during the PIII treatment has been observed to be over 210°C [8] and at this temperature, the preset shape memory effect and super-elasticity, i.e., the phase transformation temperature, can be modified and even lost [8]. Therefore, the treatment parameters such as pulsing frequency, total treatment time, and other factors must be carefully optimized [8, 28].

6. Advantages of formation TiN layer on Nitinol implants by Quasi-DC PIII

As described in previous sections, a titanium nitride barrier is a good choice to mitigate Ni release and TiN also increases the hardness, wear resistance, and biocompatibility. However, almost all the available methods used to produce titanium nitride involve the use

of direct or indirect high temperature annealing which can shift the phase transformation temperature and destroy the preset shape memory function at the body temperature. One can suggest that surface modification can be performed before the phase temperature setting procedure, but it is not very practical. To fine tune the phase transformation temperature requires precise thermal cycling and the surface modification process may not fit well. The most important reason is that the manufacturers seldom vary their production line to accommodate other process and any additional processes are regarded to increase production steps and cost.

The quality of the titanium nitride film formed on NiTi implants may differ from those on conventional products such as cutting tools. The TiN coatings on these products tend to be quite thick (on the order of μm or more) and hard (harder than stainless steel) because good wear resistance is required. Therefore, a fully crystalline TiN layer is preferred. However, the requirements for biomedical implants are quite different. In the human body, the NiTi devices are surrounded by mainly soft tissues and so an extremely hard surface is not necessary since it may damage the surrounding tissues. It has been shown that a uniform amorphous titanium oxide layer can withstand corrosion much better than a non-uniform titanium oxide layer composed of various phases and many cracks. Unlike cutting tools which are hard, NiTi implants are super-elastic that can withstand many cycles of stress and stain loadings. A thick and fully crystallized TiN layer has a better chance to crack during the stress and strain cycles. Therefore, a uniform amorphous titanium nitride layer of several tens of nm thick is sufficient to block harmful Ni release from NiTi implants.

Our recently developed quasi direct-current (DC) plasma immersion ion implantation that can process three dimensional (3D) objects has large potential in the surface modification of NiTi biomedical devices [30]. In conventional PIII, a negative high voltage between 20 and 40 kV or higher and with a frequency between 50Hz and 200 Hz is applied to the sample. The pulse duration is typially between 30 and 100 μsec. Even for a short pulse width of 30 μsec, the ion sheath can propagate far away from the sample at a negative voltage of -35kV. The implantation process becomes nonuniform spatially especially on 3D objects since the ion sheath is not conformal to the objects. To improve the uniformity of the PIII treatment, we can reduce the pulse duration and increase the ion (plasma) density. However, increasing the ion density will increase the conductivity in space and may cause arcing problems especially when the objects have sharp edges and corners. Using a smaller voltage may alleviate the arcing problems but the surface modified layer will be thinner. To compensate for the reduced efficiency when adopting a short pulse duration, the pulsing frequency and treatment time need to be increases. A high pulsing frequency will increase the workload of the power supply and pulse modulator. The displacement current generated (displacement current is a quantity that is defined in terms of the rate of change of electric displacement field) during the pulse rise time will increase with high pulsing frequency. Therefore, the sample temperature during PIII treatment is inevitably increased and the mechanical properties of the NiTi sample can be compromised.

In the quasi DC-PIII setup, the reliability and stability of the implantation process is improved by using a grounded Al housing and stainless steel mesh surrounding the specimen [30]. Numerical simulation reveals that the implantation fluence distribution along the major curvature of an S-shape bar used in surgical correction of scoliosis is more uniform and less than that obtained by conventional PIII [31]. X-ray photoelectron spectroscopy (XPS) depth profiling reveals that the retained dose uniformity along the length of the S-shape bar is greatly improved and differential scanning calorimetry (DSC)

curves also illustrate that the sample temperature during implantation is well controlled and does not affect the shape memory effect and other mechanical properties of the NiTi alloy [32].

The quasi DC PIII setup for 3D objects is based on an extension of the direct-current PIII idea developed in the Plasma Laboratory of City University of Hong Kong in 2000 originally used for large planar samples such as silicon wafers [33]. To reduce the unnecessary ion currents impacting the sample stage, the stage is enshrouded by a grounded metal cylindrical cage [30]. To further minimize the non-uniformity ion fluence caused by the non-conformal expanding ion sheath, the S-shape bar is surrounded by a cylindrical stainless mesh cage. To completely shield off the negative high voltage, a flat solid steel dish is placed on top of the mesh cage. The schematic of the 3D setup is displayed Figure 5 [30]. Numerical simulation discloses that the expanding ion sheath is blocked by the grounded mesh cage. Although the ion sheath covers up more ions through expansion, ions can diffuse inside the mesh cage since a weak RF sheath is established between the bulk plasma and grounded mesh cage [34]. Compared to conventional PIII, the total ion flux implanted into the S-shape bar is reduced. By using a grounded mesh cage, the plasma density can be lower and therefore, arcing problems can be alleviated in spite of the use of a high negative voltage. A longer pulse duration can also be employed and the displacement currents generated during the pulse rise-time can be reduced as well. In addition, the sample temperature can be more precisely controlled and the implanted dose uniformity can be improved by rotating the samples [32]. We have recently applied nitrogen quasi DC PIII to patellar concentrator and other bones concentrator. A uniform gold color is observed from the samples shown in Fig. 6 suggesting that a relatively uniform titanium nitride layer is formed on the entire surface of the sample. This method has many applications and more work is being done in our laboratory in order to realize its full potential.

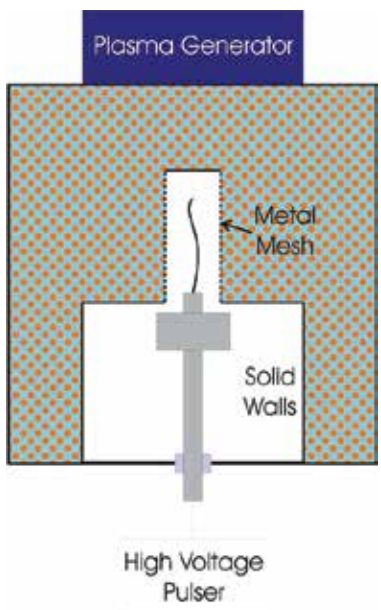

Fig. 5. Quasi-DC PIII setup with grounded stainless steel cage encompassing the sample and grounded Al (Reproduced from [30]).

Fig. 6. Patellar concentrators and other bone concentrators with the left one showing two raw concentrators and the right one showing the three concentrators after the quasi DC-PIII treatment.

7. Conclusion

This chapter briefly reviews the mechanical properties of NiTi shape memory alloys and applications in biomedical engineering. Because of leaching of harmful Ni from the materials to biological issues, various methods have been adopted. Some of the important surface methods are described and particular emphasis is put on the novel direct-current plasma immersion ion implantation technique which has high potential.

8. References

[1] W. J. Buehler, J. V. Gilfrich, and R. C. Wiley, "Effect of low temperature phase changes on the mechanical properties of alloy near composition Ni-Ti," *Journal of Appled Physics*, vol. 34, pp. 1475-1477, 1963.

[2] S. A. Shabalovskaya, "Physicochemical and biological aspects of Nitinol as a biomaterial," *International Materials Review*, vol. 46, pp. 1 - 18, 2001.

[3] T. Duerig, A. Pelton, and D. Stockel, "An overview of nitinol medical applications," *Materials Science and Engineering*, vol. A273-275, pp. 149 - 160, 1999.

[4] Stoeckel, "Nitinol Medical Devices and Implants," *Min Invas Ther \& Allied Technol*, vol. 9(2), pp. 81 - 88, 2000.

[5] S. Shabalovskaya, J. Anderegg, and J. V. Humbeeck, "Critical overview of Nitinol surfaces and their modifications for medical applications," *Acta Biomaterialia*, vol. 4, pp. 447 - 467, 2008.

[6] K. W. K. Yeung, K. M. C. Cheung, W. W. Lu, and C. Y. Chung, "Optimization of thermal treatment parameters to alter austenitic phase transition temperature of NiTi alloy for medical implant," *Materials Science and Engineering A*, vol. 383, pp. 213-218, 2004.

[7] M. Pattabi, K. Ramakrishna, and K. K. Mahesh, "Effect of thermal cycling on the shape memory transformation behavior of NiTi alloy: Powder X-ray diffraction study," *Materials Science and Engineering A*, vol. 448, pp. 33 - 38, 2007.

[8] R. W. Y. Poon, P. K. Chu, K. W. K. Yeung, J. C. Y. Chung, S. C. Tjong, C. L. Chu, W. W. Lu, K. M. C. Cheung, and K. K. D. Luk, "Effects of pulsing frequency on shape recovery and investigation of nickel out-diffusion after mechanical bending of nitrogen plasma implanted NiTi shape memory alloys," *Surface \& Coatings Technology*, vol. 201, pp. 8286 - 8290, 2007.

[9] K. Wada and Y. Liu, "Thermomechanical training and the shape recovery characteristics of NiTi alloys," *Materials Science and Engineering A*, vol. 481 - 482, pp. 166 - 169, 2008.

[10] D. Latal, J. Mraz, P. Zerhau, M. Susani, and M. Marberger, "Nitinol urethral stents: long-term results in dogs," *Urological Research*, vol. 22, pp. 295-300, 1994.

[11] J. Musialek, P. Filip, and J. Nieslanik, "Titanium-nickel shape memory clamps in small bone surgery," *Archives of Orthopaedic and Trauma Surgery*, vol. 117, pp. 341-344, 1998.

[12] J. O. Sanders, A. E. Sanders, R. More, and R. B. Ashman, "A Preliminary Investigation of Shape Memory Alloys in the Surgical Correction of Scoliosis," *Spine*, vol. 18, pp. 1640-1646, 1993.

[13] P. K. Chu, "Plasma surface treatment of artificial orthopedic and cardiovascular biomaterials," *Surface and Coatings Technology*, vol. 201, pp. 5601-5606, 2007.

[14] S. Xu, C. Zhang, S. Li, J. Su, and J. Wang, "Three-Dimensional Finite Element Analysis of Nitinol Patellar Concentrator and Its Clinical Significance," *Materials Science Forum*, vol. 394-395, pp. 45-48, 2002.

[15] S. A. Shabalovskaya, "Surface, corrosion and biocompatibility aspects of Nitinol as an implant material," *Bio-Medical Materials and Engineering*, vol. 12, pp. 69 - 109, 2002.

[16] S. A. Lacy, K. Merritt, S. A. Brown, and A. Puryear, "Distribution of nickel and cobalt following dermal and systemic administration with in vitro and in vivo studies," *Journal of Biomedical Materials Research*, vol. 32, pp. 279-283, 1996.

[17] R. Goyer, *Toxic effect of metals, in: Cassarett and Doull's Toxicology*. New York: Macmillan, 1986.

[18] R. B. Hayes, "The carcinogenicity of metals in humans," *Cancer Causes and Control*, vol. 8, pp. 371 - 385, 1997.

[19] P. Filip, J. Lausmaa, J. Musialek, and K. Mazanec, "Structure and surface of TiNi human implants," *Biomaterials*, vol. 22, pp. 2131 - 2138, 2001.

[20] A. Bansiddhi, T. D. Sargeant, S. I. Stupp, and D. C. Dunand, "Porous NiTi for bone implants: A review," *Acta Biomaterialia*, vol. 4, pp. 773 - 782, 2008.

[21] Z. D. Cuia, H. C. Mana, and X. J. Yang, "The corrosion and nickel release behavior of laser surface-melted NiTi shape memory alloy in Hanks, solution," *Surface \& Coatings Technology*, vol. 192, pp. 347 - 357, 2005.

[22] S. Kobayashia, Y. Ohgoea, K. Ozekib, K. Satoa, T. Sumiyac, K. K. Hirakuria, and H. Aokib, "Diamond-like carbon coatings on orthodontic archwires," *Diamond \& Related Materials*, vol. 14, pp. 1094 - 1097, 2005.

[23] X. Liu, P. K. Chu, and C. Ding, "Surface modification of titanium, titanium alloys, and related materials for biomedical applications," *Materials Science and Engineering: R: Reports*, vol. 47, pp. 49-121, 2004.

[24] D. Starosvetsky and I. Gotman, "Corrosion behavior of titanium nitride coated Ni-Ti shape memory surgical alloy," *Biomaterials*, vol. 22, pp. 1853-1859, 2001.

[25] Z. D. Cui, H. C. Man, and X. J. Yang, "Characterization of the laser gas nitrided surface of NiTi shape memory alloy," *Applied Surface Science*, vol. 208-209, pp. 388-393, 2003.

[26] S. MÃ¤ndla and B. Rauschenbach, "Improving the biocompatibility of medical implants with plasma immersion ion implantation," *Surface and Coatings Technology*, vol. 156, pp. 276 - 283, 2002.

[27] P. K. Chu, J. Y. Chen, L. P. Wang, and N. Huang, "Plasma-surface modification of biomaterials," *Materials Science and Engineering R*, vol. 36, pp. 143 - 206, 2002.

[28] S. MÃ¤ndl, "PIII treatment of Ti alloys and NiTi for medical applications," *Surface \& Coatings Technology*, vol. 201, pp. 6833 - 6838, 2007.

[29] K. W. K. Yeung, R. W. Y. Poon, X. Y. Liu, J. P. Y. Ho, C. Y. Chung, P. K. Chu, W. W. Lu, D. Chan, and K. M. C. Cheung, "Investigation of nickel suppression and cytocompatibility of surface-treated nickel-titanium shape memory alloys by using plasma immersion ion implantation," *Inc. J Biomed Mater Res*, vol. 72A, pp. 238 - 245, 2005.

[30] M. Schulz, D. T. K. Kwok, H. Tao, and P. K. Chu, "Three-Dimensional Quasi-Direct-Current Plasma Immersion Ion Implantation Into Biomedical Nickel-Titanium Shape Memory Alloy Rod," *Plasma Science, IEEE Transactions on*, vol. 37, pp. 2245-2249, 2009.

[31] D. T. K. Kwok, J. Li, X. Ma, and P. K. Chu, "Hybrid particle-in-cell (PIC) ions and Boltzmann electron distribution simulation of direct-current plasma immersion ion implantation into three-dimensional objects," *Journal of Physics D: Applied Physics*, vol. 43, pp. 095203, 2010.

[32] Q. Y. Lu, T. Hu, D. T. K. Kwok, and P. K. Chu, "Enhanced retained dose uniformity in NiTi spinal correction rod treated by three-dimensional mesh-assisted nitrogen plasma immersion ion implantation," *Journal of Vacuum Science & Technology A: Vacuum, Surfaces, and Films*, vol. 28, pp. 407-410, 2010.

[33] D. T. K. Kwok, X. Zeng, C. Chan, and P. K. Chu, "Direct current plasma implantation using a grounded conducting grid," *Journal of Applied Physics*, vol. 87, pp. 4094-4097, 2000.

[34] M. A. Lieberman and A. J. Lichtenberg, *Principles of plasma discharges and materials processing*, 2nd ed. Newark, NJ: Wiley, 2005.

13

Electrochemical Aspects in Biomedical Alloy Characterization: Electrochemical Impedance Spectroscopy

Carlos Valero Vidal and Anna Igual Muñoz
Universidad Politécnica de Valencia
Spain

1. Introduction

Metals and alloys are widely used as biomedical materials and are essential for orthopaedic implants, bone fixations, artificial joints, external fixations... since they can substitute for the function of hard tissues in orthopaedic. In particular, toughness, elasticity, rigidity, and electrical conductivity are important properties for metallic materials used in medical devices. Because the most important property of biomaterials is safety and biocompatibility, corrosion-resistant materials such as stainless steel, cobalt-chromium-molybdenum alloys and titanium alloys are commonly employed. However, there is still a significant concern associated with biomedical alloys related to the production of metal particles and ions (Fleury et al., 2006; Okazaki & Gotoh, 2005) which can lead to cellular toxicity (Germain et al., 2003; Catelas et al., 2001; Horowitz et al., 1998), metal hypersensitivity (Granchi et al., 2005; Hallab et al., 2000), and chromosomal changes (Massè et al., 2003).
Corrosion of orthopedic biomaterials is a complex multifactorial phenomenon that depends on geometric, metallurgical, mechanical and physico-chemical parameters, thus a firm understanding of these factors and their interactions is required in order to comprehend how and why implant materials fail (corrode, degrade). Electrochemical measurements are powerful in situ methods that allow analyzing the interface properties and corrosion behaviour between metal biomaterials (passive oxide film) and the involved body fluids. Within this group of techniques, the Electrochemical Impedance Spectroscopy (EIS) is a useful tool which provides information about the interface, its structure, passive film properties and the reactions taking place on the interface electrolyte/oxide passive film. The impedance spectroscopy is a technique that permits the measurement of uniform corrosion and passive dissolution rates, the elucidation of reaction mechanisms, the characterization of surface films and it is also used for testing coatings or surface modifications.
The aim of the present chapter is to describe the EIS technique and its potentiality in the fundamental understanding of the processes occurring at the metal/human body interface in bio-systems. The chapter will be mainly focused on its application in characterizing CoCrMo biomedical alloys.

2. Corrosion: an electrochemical reaction

The corrosion process is an irreversible chemical or electrochemical reaction occurring at the interface of the material representing the spontaneous dissolution of the metal (M) by its reaction with the environment resulting in the loss of the material or in the dissolving of one of the constituents of the environment into the material (Landolt, 2007). The oxidation of the metal, equation (1), is coupled to the reduction of the oxidizing agent (environment) which takes the electrons from the oxidation reaction. The equations (2) and (3) show the reduction reactions favoured in acidic media, while the equations (4) and (5) take place in neutral or basic media.

$$M \rightarrow M^{+n} + ne^{-} \tag{1}$$

$$2H^{+} + 2e^{-} \rightarrow H_2 \tag{2}$$

$$O_2 + 4H^{+} + 4e^{-} \rightarrow 2H_2O \tag{3}$$

$$O_2 + 2H_2O + 4e^{-} \rightarrow 4OH^{-} \tag{4}$$

$$2H_2O + 2e^{-} \rightarrow H_2 + 2OH^{-} \tag{5}$$

Fig. 1 shows a scheme of the reaction steps (anodic and cathodic) occurring at the biomaterial surface during the corrosion process in liquid environments.

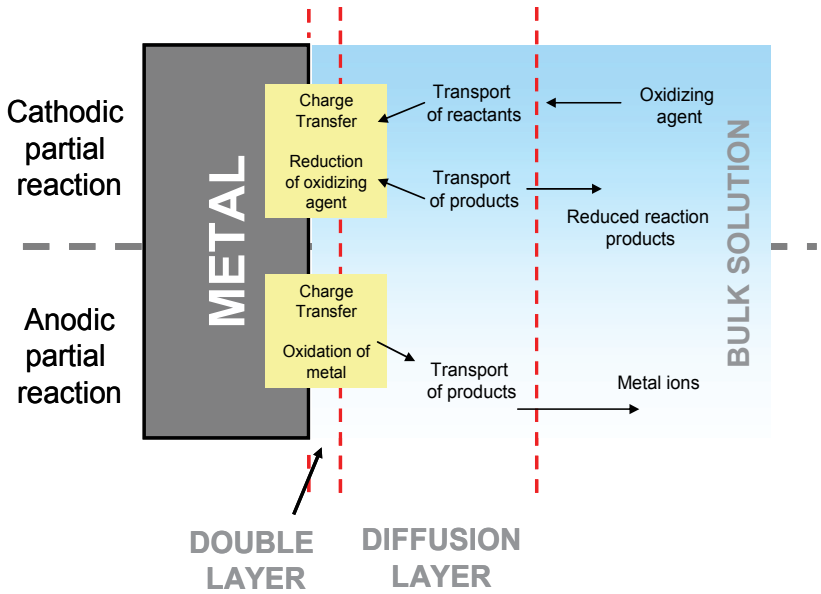

Fig. 1. Reaction steps during the corrosion of a metal in liquid environments (Landolt, 2007).

In a bio-system involving metallic biomaterials several corrosion phenomena can take place: active dissolution, passivation, passive dissolution, transpassive dissolution, localized corrosion and adsorption.

The **passivity** of metals consists in the formation of a thin oxide layer on their surface which protects the metal from its environment. Thus, the biomaterials are self-protected by the spontaneous formation of this thin oxide film being the kinetic factor that controls the corrosion rate in biological aqueous solutions. Therefore, the biocompatibility of these biomaterials is closely related to the stability of this oxide layer. The passive film plays two roles in limiting both the anodic and cathodic reactions, serving as a physical barrier for cations (ions positive charged) and anions (ions negative charged) transported to the metal surface as well as an electronic barrier for electrons.
On the other hand, the metals free of oxide film are in their **active state**. The dissolution of these metallic materials is denominated **active dissolution** and involves a charge transfer at the metal-electrolyte interface. The ions generated are dissolved into the solution in form of hydrated or complexed species according to equation (1). However, **passive dissolution** takes place when passive metals are dissolved. In this case, the cations are also generated in the interface metal-oxide film by a charge transfer reaction and the ions migrate across the passive film-electrolyte interface. Equation (6) shows the formation of the oxide film as a consequence of the cation (M^{+n}) migration towards the outer surface and the anion (O^{-2}) migration in the opposite direction while the equation (7) represents the passive dissolution where the cations are dissolved from the passive film into the solutions. The overall reaction (equations (6) and (7)) is equivalent to equation (1).

$$M + \frac{n}{2} H_2O \rightarrow MO_{n/2} + nH^+ + ne^- \tag{6}$$

$$MO_{n/2} + nH^+ \rightarrow M^{+n} + \frac{n}{2} H_2O \tag{7}$$

Transpassive dissolution: occurs when the protecting passive film is oxidized to species with higher solubility (i.e. Cr^{+6}, Co^{+6}) (Marcus & Oudar, 1995). It can occur below the potential for oxygen formation (uniform transpassive dissolution by film oxidation) or when oxygen evolution is observed (high-rate transpassive dissolution). Dissolution at transpassive potentials is relevant to corrosion in strongly oxidizing media.
An important type of corrosion is the **localized corrosion** in which an intensive attack takes place in small local sites at a much higher rate than the rest of the surface (which is corroding at a much lower rate). The localized corrosion is associated with other mechanical process (such as stress, fatigue and erosion) and others forms of chemical attack. The main form of localized corrosion in passive alloys (i.e. stainless steel) is the **pitting corrosion**; the metal is removed preferentially from vulnerable areas on the surface. The pitting corrosion is a local dissolution leading to the formation of cavities in passive metals or alloys that are exposed to environments with aggressive ions (i.e. chlorides) (Szklarska-Smialowska, 1986; Bi et al., 2009).
Other common phenomenon in biological systems is **adsorption** of certain species presents in the body fluid (i.e. proteins) onto the surface of metallic materials. The adsorption is established between the adsorbed species and the surface due to weak forces or the Van der Waals and it can modify the passive dissolution rate of the biomaterials among others.

3. Fundamentals of the electrochemical impedance spectroscopy

The Electrochemical Impedance Spectroscopy (EIS) is a relatively modern technique widely extended in several scientific fields. The EIS consists on a non-destructive technique when

working under equilibrium conditions (free corrosion potential or open circuit potential), particularly sensible to small changes in the system that allows to characterize material properties and electrochemical systems even in low conductive media.
The impedance method consists in measuring the response of an electrode to a sinusoidal potential modulation of small amplitude (typically 5-10 mV) at different frequencies. The alternative current (ac) modulation is superimposed either onto an applied anodic potential or cathodic potential or onto the corrosion potential (Scully et al., 2003).

3.1 Electrode response to a sinusoidal perturbation of the potential

An excitation sinusoidal signal *E(t)* is superimposed onto the steady-state potential of an electrode, expressed as a function of time (*t*):

$$E(t) = E_0 \cdot \cos(\omega f) \tag{8}$$

where E_0 is the amplitude (in volts), ω is the radial frequency (in radians per second) defined also as $\omega=2\pi f$ and f is the frequency expressed in Hertz (Hz). In order to maintain a linear response of the electrode the modulation amplitude must not exceed 10mV.
The sinusoidal introduction of the perturbation of potential on the system induces a sinusoidal current *I(t)*. The response signal *I(t)* is shifted in phase and has different amplitude.

$$I(t) = I_0 \cdot \cos(\omega f - \varphi) \tag{9}$$

where I_0 is the amplitude (in amperes) and φ is the phase (in degrees).
The **Electrochemical Impedance** (*Z*) is defined as the relation between the applied potential and the resulting intensity. The impedance expresion is function of the magnitude (Z_0) and the phase shift (φ). The ratio of the amplitudes of the applied signal and the response signal on the one hand and the phase shift between both signals on the other determines the impedance.

$$Z = \frac{E(t)}{I(t)} = \frac{E_0 \cdot \cos(\omega f)}{I_0 \cdot \cos(\omega f - \varphi)} = Z_0 \frac{\cos(\omega t)}{\cos(\omega t - \varphi)} \tag{10}$$

Using Euler's relationship (equation (11)) it is possible to represent these functions in the complex plane.

$$\exp(i\theta) = \cos\theta + isen\theta \tag{11}$$

where i^2=-1 is the imaginary number and θ is the angle.
The sinusoidal perturbation of the potential and the current response are represented therefore by two vectors in the complex plane. Thus, the impedance *Z* is represented by a vector sum of the real and the imaginary part (equation (13)) characterized by the modulus Z_0 and the phase shift φ.

$$Z = \frac{E_0 \exp(j\varpi t)}{I_0 \exp(j\varpi t - j\varphi)} = Z_0 \exp(j\varphi) = Z_0(\cos\varphi + jsen\varphi) \tag{12}$$

$$Z = Z_{\mathrm{Re}} + j\, Z_{\mathrm{Im}} \tag{13}$$

The modulus (equation (14)) and the phase shift (equation (15)) can be calculated using Pythagoras' theorem and the adequate trigonometric relations:

$$|Z| = \sqrt{Z_{\mathrm{Re}}^2 + Z_{\mathrm{Im}}^2} \tag{14}$$

$$\theta = \arctan\left(\frac{Z_{\mathrm{Im}}}{Z_{\mathrm{Re}}}\right) \tag{15}$$

Two graphical representations of the impedance spectrum are possible. If the impedance Z is represented in the complex plane, where the real part is plotted on the x-axis and the imaginary part on the y-axis of a chart for different frequencies, the graphic is called **Nyquist diagram** (Fig. 2(a)).
The impedance can also be represented displaying the modulus $|Z|$ (in logarithmic scale) and the phase shift φ (both on the y-axis) as a function of the logarithmic of the frequency f. This presentation method is the **Bode plot** (Fig. 2(b)).

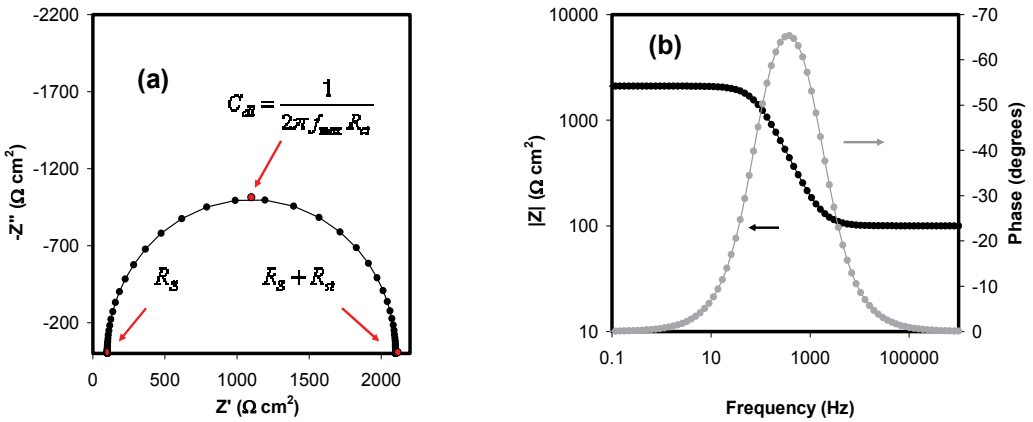

Fig. 2. (a) Nyquist diagram and (b) Bode plot of impedance data for a simple equivalent circuit (Randless circuit with solution resistance (R_s) of 100Ωcm², double layer capacitance (C_{dl}) of 1·10⁻⁶Fcm⁻² and charge transfer resistance (R_{ct}) of 2000Ωcm²).

3.2 Interpretation of the impedance results

The interpretation of the impedance spectra requires the selection of an electric model that suitably fits the experimental data to a combination of electrical elements, Table 1. Thus, according to the selected model and its properties it is possible to obtain information about the electrochemical mechanisms and properties of the system. Common electrical elements and their corresponding meaning are described as follows:

- Resistance (*R*): describes some charge transfer across certain interface (i.e. metal/electrolyte).
- Capacitance (*C*): is characteristic to charge structures (double layers) considering these layers as parallel plate condenser.
- Inductance (*L*): is associated with adsorption-desorption process occurring in the formation of layers (passive film).

- Warburg (W): it represents linear diffusion under semi-infinite conditions. This also assumes the diffusion layer to possess an infinite thickness. The Warburg impedance is defined through an admittance Y_0, and a diffusion parameter B.

Table 1 summarizes the real and imaginary part of the impedance expression of the commonly used electrical elements.

The simplest equivalent circuit used for fitting the experimental results is represented in the Fig. 3. In this case, the theoretical transference function is represented by means of parallel combination of the resistance R_{ct} (charge transfer resistance) and the capacitance C_{dl} (double layer capacitance related to the interactions in the electrode/electrolyte interface) both in series with the resistance R_s (electrolyte resistance).

Element	Impedance
Resistance	R
Capacitance	$-\frac{i}{\omega C}$
Inductor	$i\omega L$
Warburg (infinite)	$-\frac{1}{Y_0\sqrt{i\omega}}$
Warburg (finite)	$\frac{\tanh\left(B\sqrt{i\omega}\right)}{\left(Y_0\sqrt{i\omega}\right)}$

Table 1. Impedance expression of the electrical elements.

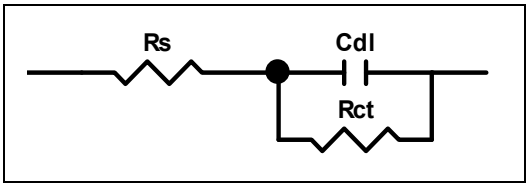

Fig. 3. Equivalent Electric Circuit (Randless) of the electrode-electrolyte interface.

The impedance value of the system represented in Fig. 3 is shown in equation (16):

$$Z(\omega) = R_S + \left(\frac{1}{\frac{1}{R_{ct}} + i\,\omega C_{dl}} \right) \tag{16}$$

The impedance spectrum obtained for the Randless Circuit is represented in Fig. 2. This spectrum shows, in the higher frequency region, that $log|Z|$ tends to a constant value with a phase shift close to 0^o when the frequency increases. This is a resistive behaviour and the values of the impedance correspond to R_S.

In the medium-lower frequencies range a linear relationship between $log|Z|$ and $log\ f$ is observed. For an ideal capacitive behaviour the slop is approximately -1. Generally, the non-

ideal systems present certain modification from an ideal capacitance behavior (lower value of the slope and lower phase angles). A constant phase angle element (CPE) is introduced to replace the capacitance and to describe the non-ideal behaviour which can be due to different physical phenomenon such as surface heterogeneity resulting from surface roughness, impurities, dislocations or grain boundaries. CPE is defined as:

$$Z(\omega) = Z_0(i\omega)^{-n} \tag{17}$$

where Z_0 is the CPE constant and n is the CPE exponent. Depending on n, CPE can represent resistance (n=0, Z_0=R), a capacitance (n=1, Z_0=C) or a Warburg impedance (n=0.5, Z_0=W). For $0.5<n<1$ the CPE describes a distribution of dielectric relaxation times in the frequency space.

The value of the capacitance is a useful parameter since it could be related to the film thickness according to the following expression (Helsen & Breme, 1998):

$$C = \varepsilon \cdot \varepsilon_0 \cdot \frac{A}{d} \tag{18}$$

where ε denotes the relative dielectric constant of the layer, ε_0 is the permittivity of the vacuum (8.85×10^{-14} Fcm^{-1}), A the active area (in cm^2) and d the film thickness (in cm).

In general, the usual guidelines for the selection of the best-fit EEC are (i) a minimum number of circuit elements employed to describe the electrochemical system, (ii) the Chi-squared value (X^2) should be suitable low ($X^2 \leq 10^{-4}$) and (iii) the errors associated with each element must be up to 5% (Metikos, 2006).

3.3 Instrumentation

A conventional three-electrode cell configuration is commonly employed for carrying out the EIS experiments. A potential (V) is applied between the working electrode (WE, i.e. biomaterial) and the reference electrode (RE, i.e. Ag/AgCl electrode) and the current density (I) flowing through the working electrode and the counter electrode (CE, i.e. platinum) is measured.

The basic electronic instrumentation that allows to obtain the impedance spectra in electrochemical systems consists on a generator-analyzer of functions denominated Frequency Response Analyzer (FRA) or "lock-in amplifier". The FRA can analyze and apply sinusoidal signals in a widespread frequencies range to the potentiostat with fast response and sensibility.

A potentiostat applies a sinusoidal signal (equation (8)) to the working electrode in the electrochemical cell. The latter is often built into a two-channel transfer function analyzer, thus permitting simultaneously measurement of the potential and the current. The system responds with a signal (equation (9)) that differs from the equation (8) by its phase and amplitude. The response of the electrode, measured by the analyzer, determines the impedance Z response of the electrochemical system and the phase shift corresponding to each frequency.

3.4 Experimental considerations for biomaterials

Biological systems are specific corrosion media which requires several experimental considerations in order to obtain significant data from EIS measurements:

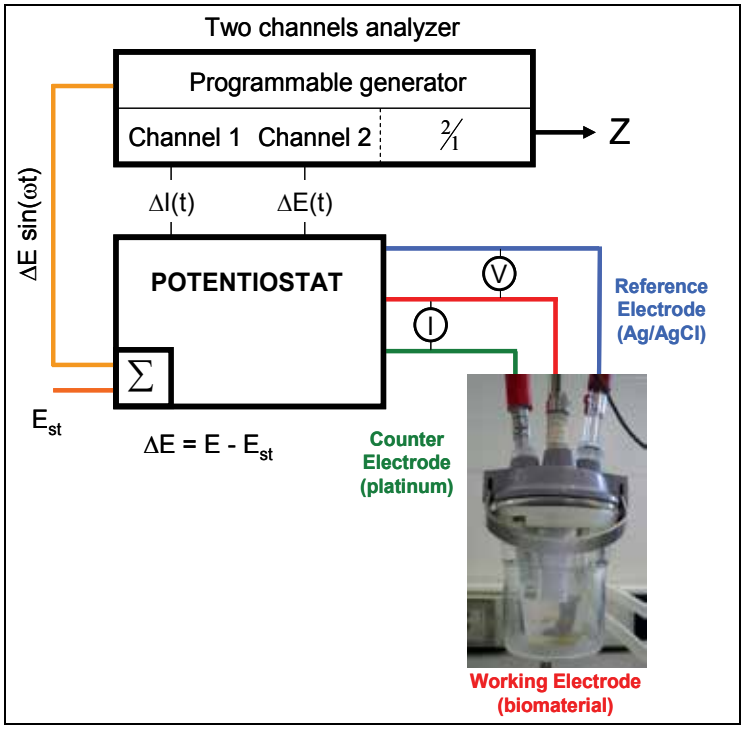

Fig. 4. Experimental set up for impedance measurements using a transfer function analyser under potentiostatic control (a sinusoidal of weak amplitude $\Delta E=E-E_{st}$ is superimposed onto the steady state potential E_{st} of an electrode).

1. The properties of the biomaterials and the biological environments may strongly change depending on the electrochemical conditions. Selection of very low frequencies in the impedance sweep requires longer experimental times and might conduct changes in the electrode surface, altering the steady-state conditions needed for the adequate impedance measurements. Thus, it is important to adapt the final frequency of the sweep to the system since it can introduce error in the impedance measurements obtained at the lowest frequencies (Hodgson et al., 2004).
2. The adsorption of organic compounds on the electrode surfaces may affect the impedance response; i.e. the adsorption of proteins in the reference electrode may cause errors in the potential measurements.
3. The biological solutions are highly susceptible to be contaminated by external agents (such as acids and metallic ions). For this reason, it is important the cleaning of the instrumentation to carry out the experimental tests. Furthermore, the use of sterilized materials is advisable when accurate results are desirables.

4. CoCrMo biomedical alloys

Biomaterials for medical devices and prostheses are implanted into the human body to replace, repair or restore the function of the tissues or bones. Metals are more suitable for load-bearing applications compared with ceramic or polymeric materials because they combine high mechanical strength, high fracture toughness and good processability.

However, the failure of the implants and their revision at relative short times is commonly required. For example, it has been documented higher rate of failure ranking from 30% to 56% in patients under 40 years of age after 10-12 years when conventional hip arthroplasty was performed (Ebied & Journeaux et al., 2002). In particular, about 10% of the metal-on-metal (MoM) total hip replacements (THR) implanted since 1988 had to be replaced in the last years (Wolner et al, 2006). Nevertheless, the MoM replacements are required over other type of materials (i.e. UHMWPE implants) since they improve the osteolisis problems among others (Tipper et al., 2005). Therefore, there is a need to use metallic materials as implant devices (due their good benefits) but it is necessary to reduce the failure and revision times.

Within the group of metallic biomaterials for implants, cobalt-chromium-molybdenum alloys (CoCrMo) are widely used in the last years. These alloys are characterized for their highly biocompatibility and corrosion resistance and they are a good alternative for orthopaedics and dental prosthesis. There are basically two types of Co-Cr alloys in clinical practice; CoCrMo alloy (F75-87) used in as-cast pieces and CoNiCrMo alloy (F562-84) adapted for forged pieces at high temperatures. The latter is mainly used in those cases where mechanical loads are required. On the other hand, there are some other Co-Cr alloys with iron and tungsten addition but they are not so commonly used in implant devices: CoCrWNi (F90-87) and CoNiCrMoWFe (F563-88).

4.1 General electrochemical behaviour of the CoCrMo biomedical alloy

The high biocompatibility of the CoCrMo is related to the spontaneous formation of an oxide film that protects the metal from the surrounding environment (body fluid). It is well known that the properties of this oxide film control the chemical and mechanical properties of the biomaterial and therefore, its durability into the human body. The physico-chemical properties of the passive film also control the corrosion behaviour of the materials, the interaction with tissues and the electrolyte and thus the degree of the material biocompatibility. The properties of the film may change depending on the external conditions (i.e. temperature, potential…) but usually present similar composition due to the stability of that passive film.

The composition of the passive film of CoCrMo alloys presents high content in Cr (mainly Cr(III) and smaller amount of $Cr(OH)_3$) with a minor contribution of Co and Mo oxides (Milosev & Strehblow, 2003; Hodgson et al., 2004; Igual & Mischler, 2007; Valero et al., 2010). A direct relation between the thickness of the passive film and the applied potential (increasing around 1nm/V in the passive domain) was observed by Milosev and Strehblow (2003). Hanawa et al. (2001) studied by X-ray photoelectron spectroscopy (XPS) the surface oxide film formed on CoCrMo in quasi-biological environments and determined that Cr and Mo were distributed at the inner layer of the film while the Co was dissolved from the film, reaching a thickness of 2.5-2.9 nm.

The exact chemistry of the passive layer is highly dependent on the chemical composition of the electrolyte (Igual & Mischler, 2007; Valero & Igual, 2008). Therefore, special care has to be taken when formulating the simulated body fluids in order to obtain electrochemical results for clinical application.

From this point of view, the main components present in the body fluids are salts (NaCl, KCl, $CaCl_2$), organic molecules (proteins) and inorganic species (phosphates). The general composition of the human biological fluids (plasma or serum and synovial fluid) is shown

in Table 2. Fluid properties and composition can readily change as a result of disease, aging and drug ingestion (Black & Hastings, 1998).
At this moment, there is not a general consensus in the scientific community about the best "simulated body fluid" to be used for characterizing metallic biomedical alloys. Further research the influence of the solution chemistry on the corrosion mechanisms is required to solve this problem (to avoid this uncertainty).

Compound	Plasma (serum)	Synovial fluid
Bicarbonate	25-30 mM	-
Calcium	2.12-2.72 mM	1.2-2.4 mM
Cloride	100-108 mM	87-138 mM
Phosphorous (total)	2.87-4.81 mM	-
Potassium	3.5-4.7 mM	3.5-4.5 mM
Sodium	134-143 mM	133-139 mM
Amino acids	20-51 mg/mL	-
Glucosa	650-966 mg/mL	-
Uric acid	30.5-70.7 mg/mL	39 mg/mL
Water	930-955 mg/mL	960-988 mg/mL
Albumin	37.6-54.9 mg/mL	6-10 mg/mL
IgG	6.4-13.5 mg/mL	1.47-4.62 mg/mL
Fibrinogen	2-4 mg/mL	-

Table 2. General chemical composition of the human biological (Black & Hastings, 1998).

4.1.1 Passive dissolution of CoCrMo alloys

The main corrosion mechanism of CoCrMo alloys in the body fluids is passive dissolution. In vitro (Germain et al., 2003; Okazaki & Gotoh, 2005) and in vivo (Massè et al., 2003; Dumbleton & Manley, 2005) tests confirm the metal release from the CoCrMo alloys through that corrosion mechanism. Different variety of phenomena as a consequence of metal ion release takes place into the human body such as transportation, metabolism, accumulation in organs, allergy and carcinoma (Hanawa, 2004). These effects can be generally harmful for human health, mainly in the case of the CoCrMo where the alloying elements Cr and Co generate high risk of carcinogenicity. Although the definitive effects of these metal ions have not been determined, toxicity and metall alergy are the most significant concerns. For example, it has been demostrated that Cr^{3+} and Co^{+2} have a toxicity effect on osteoblasy and induced cell mortality (Fleury et al., 2006).
Therefore, there is still a need of fundamental understanding of the electrochemical behaviour of CoCrMo alloys in order to improve their corrosion resistance and minimize the metal ion releases in the human body.

4.2 Evaluation of the electrochemical behaviour of CoCrMo alloys by EIS

EIS has demonstrated to be a useful tool to analyze the corrosion behaviour of the CoCrMo biomedical alloys as well as to study the modifications of the properties of the passive film depending on several external conditions (i.e. temperature, chemical composition of the electrolyte, potential). It is possible to obtain information about the passive film dissolution (kinetics) and passive film properties (film thickness, passive film dielectric constants, diffusion coefficient of the diffusing species) by EIS.

The CoCrMo alloy spontaneously passivates resulting in the formation of an oxide film in contact with the biological environment (biofilm) according to the scheme represented in Fig. 5. EIS results under passive conditions (Fig. 6(a)) show high values of impedance (around 100KΩcm^2) which can be due to two superposed semicircles (time constants). Those impedance results are good fitted with the EEC proposed in Fig. 6(a), consisting on two R-C groups disposed in series. The physical meaning of the selected EEC is attributed to the resistance oxide (R_{in})/capacitance (C_{in}) in parallel combination across the oxide and to the charge transfer resistance (R_{out})/double layer capacitance (C_{out}) parallel combination. In this case, R_p (polarization resistance of the system) can be calculated as the sum of R_{out} and R_{in} after fitting the experimental results to the EEC.

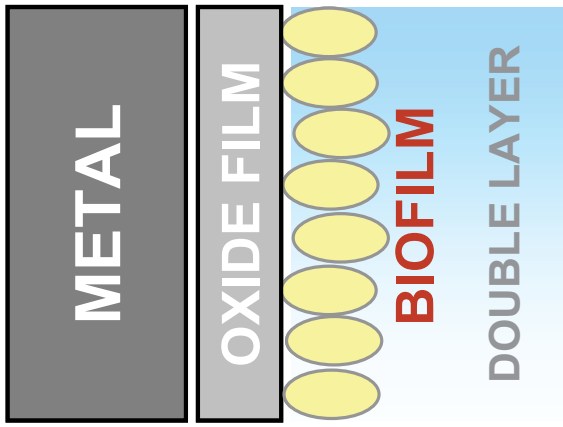

Fig. 5. Scheme of the interface of a metallic surface in contact with biological environments where the metal is covered by an oxide layer, and by an adsorbed organic film ("biofilm").

Because the corrosion mechanisms are highly dependent on the prevailing electrochemical conditions (i.e. applied potential), Fig. 6 shows the EIS spectra obtained at different applied potentials; (a) passive, (b) cathodic and (c) transpassive. Under cathodic conditions (Fig.6(b)) the impedance values at high frequencies are much lower than in the passive domain, because the cathodic reaction is favoured thus reducing passivation. At low frequencies the slope of 45^o in the Nyquist diagram is observed and this feature is characteristic of Warburg-like behaviour. The impedance data are fitted to the Equivalent Circuit presented in Fig. 6(b). The elements of the EEC proposed are R_s (solution resistance), CPE_{out} (constant phase element of the double layer), R_{out} (charge transfer resistance of the outer layer) and W-R (Warburg element) related to the mass transport limitation by diffusion. The high frequencies loop can be attributed to the charge transfer which takes place at the interface. The low frequencies loop represents to the diffusion of dissolved oxygen from the electrolyte to the interface.

The presence of oxidizing agents in the electrolyte may favour the anodic reaction of the passive film and modifies the interface solution-alloy. The impedance spectrum under transpassive conditions (Fig. 6(c)) is characterized by a high frequency capacitance loop related to the charge transfer due to the dissolution of the metal as a result of the anodic applied potential, an inductive loop at medium frequency and a semi-arc obtained at the lowest frequencies which indicates the presence of an inner surface film. The EEC proposed to describe the system is shown in Fig. 6(c). The circuit consists of the following elements:

CPE_{out} represents the capacity of the metal/film/electrolyte interface, R_{out} is the outer layer resistance, RL element (resistance and inductance) is attributed to the relaxation of the corrosion product on the electrode surface, CPE_{in} is the capacitance of the inner oxide layer and the R_{in} the inner oxide layer resistance.

Therefore, EIS technique has been demonstrated to be a useful tool to analyze the corrosion behaviour of CoCrMo alloys as well as to study the modification of the passive film properties depending on the applied potential under potentiostatic conditions.

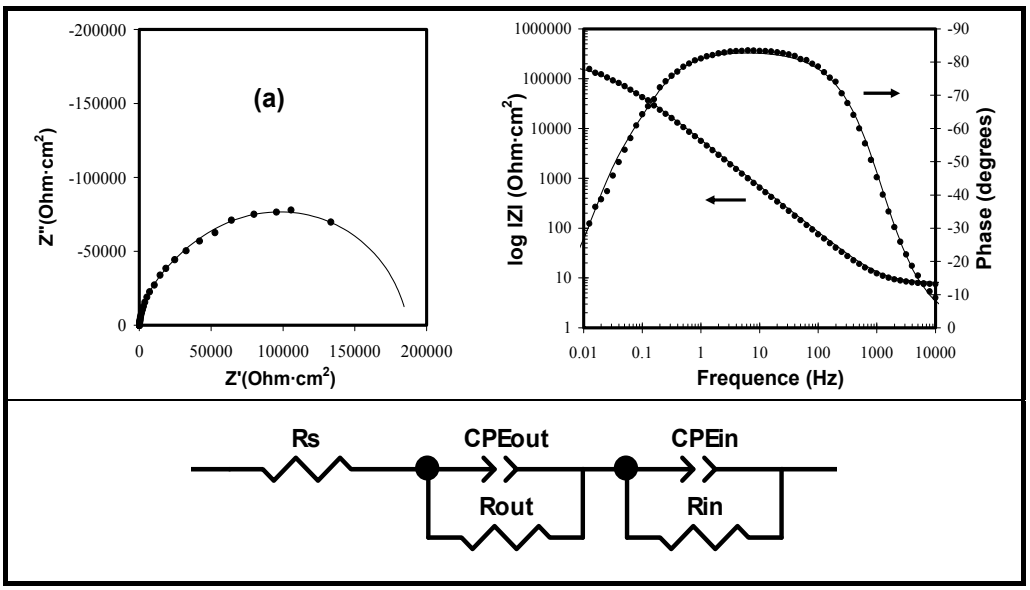

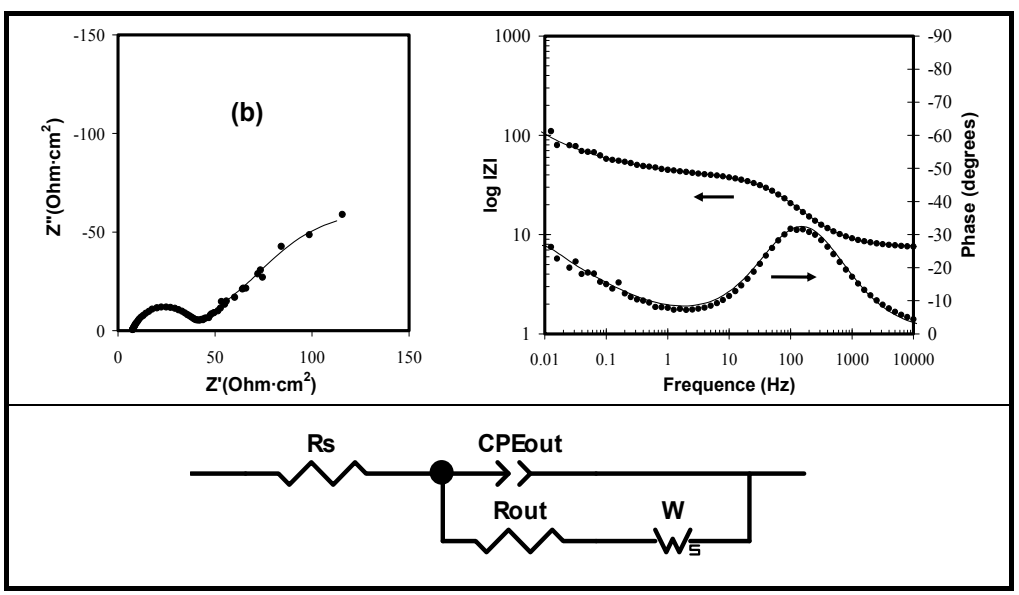

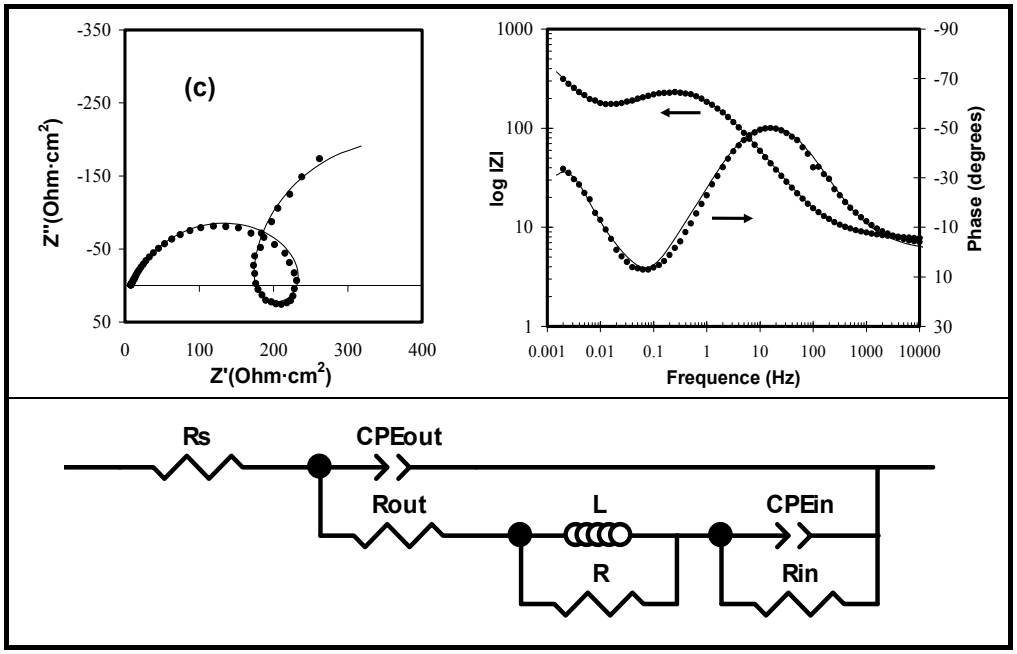

Fig. 6. Nyquist diagrams (left), Bode plots (right) and Equivalent Electrical Circuits (bottom) of a CoCrMo alloy at (a) passive (b) cathodic and (c) transpassive potential in bovine serum solution at 37ºC and pH 7.4.

4.2.1 Influence of temperature

Temperature is an important parameter that can change electrochemical reaction rates. In biological systems, temperature favours the release of metallic ions into the body and it can even change the corrosion mechanisms from that occurring at room temperature (Virtanen et al., 2008). It is necessary to control the temperature when carrying out electrochemical in-vitro tests since certain chemical compounds (i.e. proteins) can modify their behaviour depending on this parameter. For example, some proteins modify their conformational structure with temperature. The Bovine Serum Albumin (BSA), the most common protein in the fluids of human body, is characterized by its globular structure with high tendency to aggregate in macromolecular assemblies, where its three-dimensional structure is composed of three domains, each one formed by six helices and its secondary structure in α-helix. This structure is perfectly defined and stabilized at room temperature however, when the temperature increases, some molecular regions become accessible to new intermolecular interactions, producing soluble aggregates through disulphide and non-covalent bonds (Militello et al., 2003). Temperature can also modify the behaviour of inorganic species, i.e. the precipitation of Ca-phosphates is favoured at higher temperatures and it is hardly observed at room temperature. The precipitation of inorganic species can form a layer covering the biomaterial surface, blocking the mass transport of oxygen and/or of reaction products and/or from the alloy surface reducing the corrosion rate and the ion release. Thus changes in temperature contributes to changes in the corrosion mechanisms.

Impedance spectra of a CoCrMo alloy in form of Nyquist diagrams and Bode plots at different temperatures are shown in Fig. 7(a) and Fig. 7(b) respectively. The main effect of

temperature on the corrosion behaviour of the CoCrMo alloy is the decrease of the R_{ct} values, which is due to the higher passive dissolution rate of the alloy. Temperature also displaces the maximum value of the phase diagrams in the Bode plots towards higher frequencies which is related to a modification of the double layer capacitance.

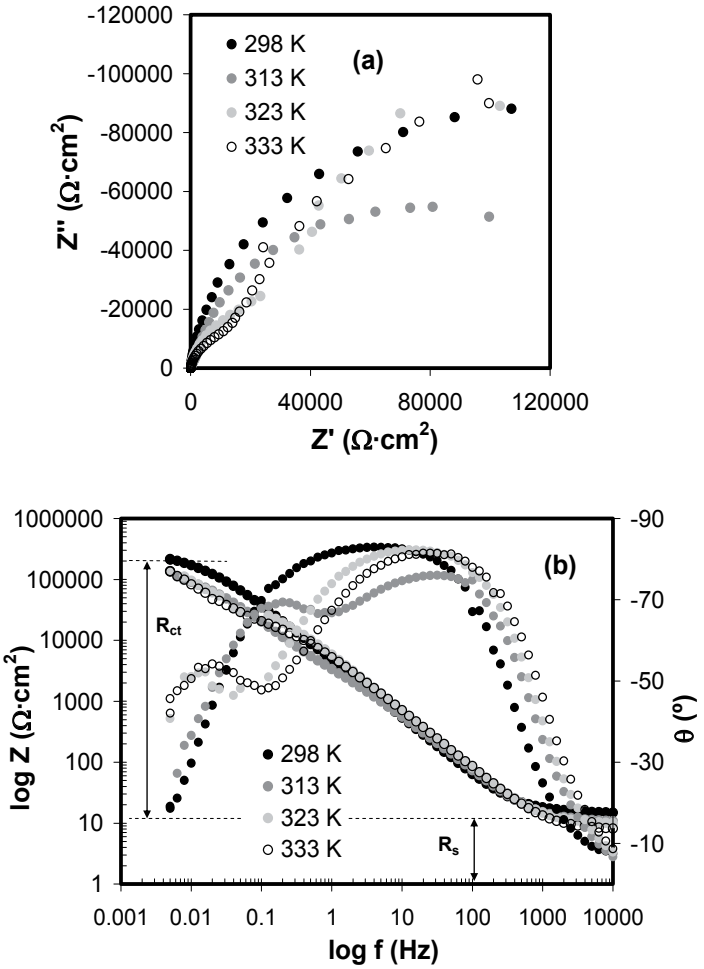

Fig. 7. (a) Nyquist diagrams and (b) Bode plots of a CoCrMo alloy at OCP in NaCl+50 mg/L BSA at different temperatures and pH 7.4 (Valero & Igual, 2010).

The Bode plots (Fig. 7(b)) clearly shows two phase maxima which correspond to two time constants in the electrochemical system. According to the EEC proposed in Fig. 6(a) the experimental impedance data has been fitted to the two RC groups disposed in series and the calculated electrical parameters show that CPE_{in} increases with temperature indicating the diminution of the thickness of the passive film (equation (18)). The decrease of the R_{out} with temperature is related to the denaturation process of the protein.

An important chemical parameter that allows one to correlate the temperature with the rate of the corrosion process taking place in the biomaterial interface is the **activation energy** (*Ea*, $Jmol^{-1}$). This parameter is generally defined as the minimum energy required to start a

chemical reaction or the energy that must be overcome for a chemical reaction to occur. The EIS technique permits to obtain the activation energy of an electrochemical process in a temperature range for a fixed electrolyte composition. The procedure for determining the activation energy from EIS measurements is described as follows:
The Arrhenius equation is represented as:

$$i_{corr} = A \cdot e^{-E_a/RT} \tag{19}$$

where i_{corr} (Acm^{-2}) is the corrosion current density (current flowing under steady-state conditions), T (K) is the temperature, R ($Jmol^{-1}K^{-1}$) is the gas constant and A is a pre-exponential factor.
Corrosion current density (i_{corr}) is related to the R_{ct} through the Stern-Geary equation:

$$i_{corr} = \frac{b_a b_b}{2.303(b_a + b_b)} \cdot \frac{1}{R_{ct}} \tag{20}$$

where b_a and b_c (V $decade^{-1}$) are the anodic and cathodic Tafel slopes (obtained from polarization measurements) respectively, and are defined as $b_{a,c}=2.303RT/\alpha_{a,c}F$ (where α is the charger transfer coefficient and F is the Faraday's constant with the value of 96500 C/eq). Applying logarithms to equation (19) and substituting i_{corr} by equation (20) the following expression is obtained:

$$\ln \frac{R_{ct}}{T} = \frac{E_a}{R} \cdot \frac{1}{T} + \text{constant} \tag{21}$$

From the plot of $\ln(R_{ct}/T)$ against $1/T$ it is possible to obtain a straight line which slope gives one the *Ea* of the corrosion process.
Fig. 8 shows an example of the influence of BSA on the Ea of a CoCrMo alloy. R_{ct} values were extracted from EIS tests carried out at different temperature and BSA concentrations (Valero et al., 2010)

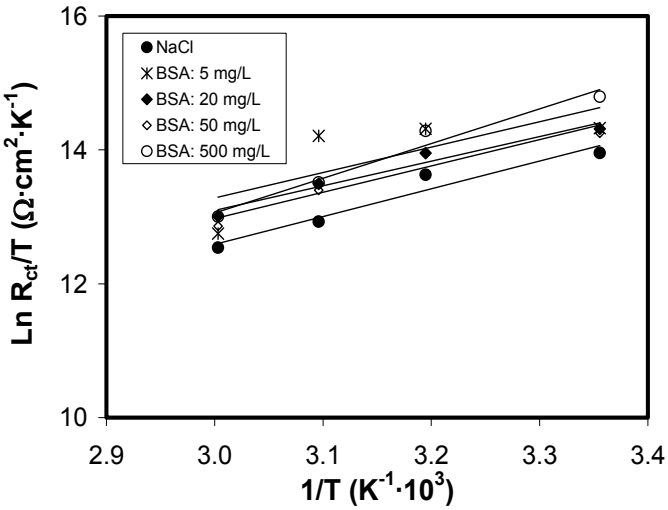

Fig. 8. Effect of temperature on the charge transfer resistance of CoCrMo alloy in 0.14M NaCl and different BSA additions, Arrhenius plot (Valero et al., 2010).

The increase of BSA concentration caused a decrease in the corrosion activation energy which means that the adsorption of BSA molecules onto the CoCrMo surface occurred by charge transfer mechanism, favouring the corrosion reaction occurring on metal surface.

4.2.2 Influence of the chemical composition of the simulated body fluid

The body fluids are considered high corrosive solutions due the presence of several aggressive compounds such a chloride ions and complex species (proteins) at relative high temperature (37°C).

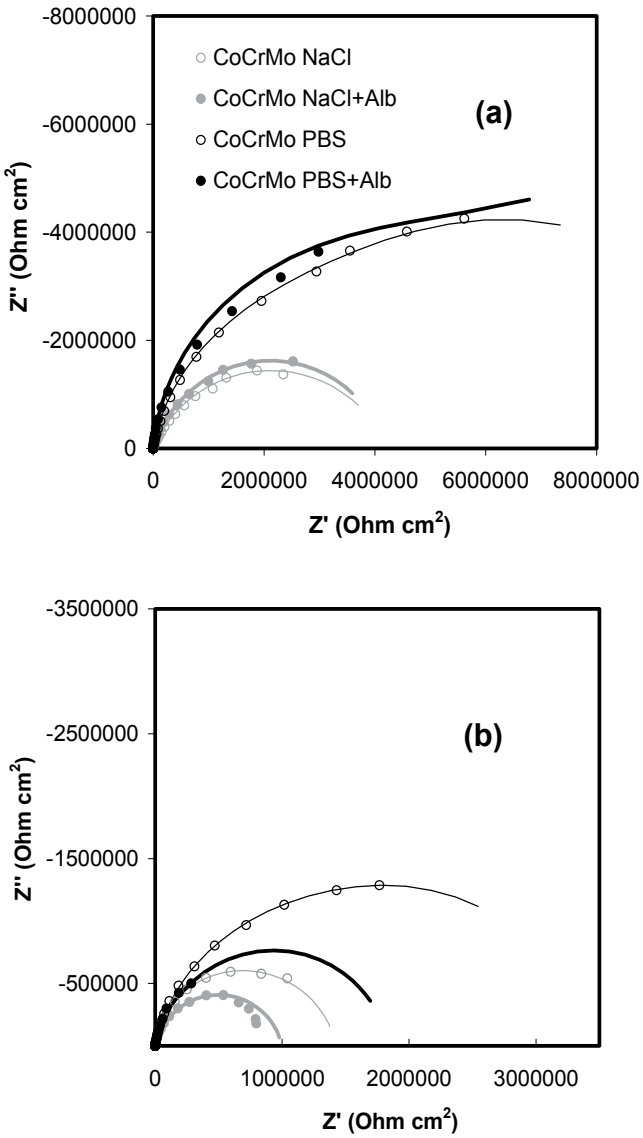

Fig. 9. Nyquist diagram of CoCrMo in different solutions at (a) passive potential and (b) OCP, pH 7.4 and 37°C (Igual & Mischler, 2007).

EIS can be employed to investigate changes in the interface passive film/electrolyte on CoCrMo depending on the chemical composition of the electrolyte. Fig. 9 shows the Nyquist Diagrams obtained at an applied passive potential (Fig. 9(a)) and at OCP (Fig. 9(b)) in different simulated body fluids. Under potentiostatic conditions a well-defined electrochemistry can be achieved and therefore the effect of solution chemistry on CoCrMo corrosion behaviour can be studied.
The Nyquist diagrams are different depending on the solution chemistry. Phosphates (PBS) increased the corrosion resistance of the alloy under both electrochemical conditions (higher diameter of the Nyquist semicircle) while the effect of the BSA varies depending on the applied potential. This behaviour can be explained by the competitive adsoption of phosphates ions and BSA molecules on the CoCrMo alloy. The adsorption of phosphates produces a blocking effect on the passive film and reduces the corrosion rate of the alloy. The adsorption of the BSA can act in different ways: it limits the adsorption of phosphates (accelerating the corrosion) but can modify the passive film properties and, by acting as cathodic inhibitor, can reduce the corrosion rate. The EIS is a good tool for determine the different actuation of these components.
The EIS results can be fitted to the EEC shown in Fig. 6(a) and it is observed that the solution chemistry does not significantly affect the thickness of the passive film. This conclusion is obtained from the analysis of the values of the resistance R_{in} and capacitance CPE_{in}; all those values slightly change in presence of BSA and PBS. On the contrary, different solution compositions lead to larger effects on the electrical properties of the outer layer (R_{out} and CPE_{out}). These results are in good agreement and well-supported with Surface Analysis (X-Ray Photoelectron Spectroscopy (XPS) and Auger Electron Spectroscopy (AES)) (Igual & Mischler, 2007).
When comparing the impedance results at the different applied potentials, passive potential (Fig.9(a)) and OCP (Fig.9(b)) it is possible to observe that the higher resistance is related to the highest applied potential (applied potential). The effect of both, PBS and BSA depends on the prevailing electrochemical conditions (surface chemistry).

4.2.3 Adsorption of proteins

The study of the adsorption of proteins onto metallic surfaces can be carried out by EIS (Igual & Mischler, 2007; Valero & Igual, 2008; Valero et al.; 2010). There is an increasing interest in the interfacial behaviour of proteins in the metallic components implanted in the human body as a result of problems associated to bacterial growth (Khan et al., 1996; Kanagaraja et al., 1996) and metal dissolution (Hallab et al., 2001; Virtanen et al., 2008). In the field of biomaterials and medical implants, it is widely accepted that one event that significantly influence the biocompatibility and stability of the biomaterial is the nearly instantaneous adsorption of proteins from biological fluids.
Analyzing the theoretical isotherm which better fits the protein behaviour allows one to characterize the protein adsorption mechanisms by means of chemical parameters.
Specially, the adsorption of the BSA onto the CoCrMo surface is described by the Langmuir isotherm:

$$\Gamma = \frac{B_{ADS}\Gamma_{\max}c}{1 + B_{ADS}c} \tag{22}$$

where c (mol cm^{-3}) is the equilibrium concentration of the adsorbate (BSA) in the bulk solution, Γ (mol cm^{-2}) is the amount of protein adsorbed, i.e. surface concentration, Γ_{max} (mol cm^{-2}) is the maximum values of Γ, and the parameter B_{ADS} (cm^3 mol^{-1}) reflects the affinity of the protein molecules towards adsorption sites.
The parameters Γ_{max} and B_{ADS} can be determined by rearranging the equation (22):

$$\frac{c}{\Gamma} = \frac{1}{B_{ADS}\Gamma_{\max}} + \frac{c}{\Gamma_{\max}} \tag{23}$$

A plot of c/Γ versus concentration should yield a straight line with parameters Γ_{max} and B_{ADS} derived from the slope and intercept, respectively. The surface concentration (Γ) of BSA can be correlated with the charge transfer resistance due the protein addition ($R_{ct,c}$), i.e. $1/R_{ct,c} \propto \Gamma$ (proportional). The resistance values can be obtained from the corrected values for the resistance obtained in the protein-free solution ($R_{ct,0}$) in each incremental addition of protein ($R_{ct,i}$) by the expression:

$$R_{ct,c} = R_{ct,i} - R_{ct,0} \tag{24}$$

In the equation (23) the surface concentration (Γ) can be substituted by the resistance values. Thus, the dependence of $c \cdot R_{ct,c}$ versus BSA concentration in the solution it is also linear over the investigated temperature range. This procedure allows obtaining B_{ADS} and Γ_{max} parameters from EIS data (Valero et al., 2010).
The parameter B_{ADS}, which reflects the affinity of the adsorbate molecules toward adsorption sites at a constant temperature, can be presented as:

$$B_{ADS} = \frac{1}{c_{solvent}} \exp\left(\frac{-\Delta G_{ADS}}{RT}\right) \tag{25}$$

where ΔG_{ADS} (J mol^{-1}) is the Gibbs free energy of adsorption, and $c_{solvent}$ is the molar concentration of a solvent, which in this case is the water (c_{H2O} = 55.5 mol dm^{-3}).
Finally, it is possible to determine the enthalpy and the entropy related to the adsorption process from Gibbs free energy:

$$\Delta G_{ADS} = \Delta H_{ADS} - T \cdot \Delta S_{ADS} \tag{26}$$

Fig. 10 shows the ΔG_{ADS} results of the study carried out on the adsorption mechanisms of BSA on a CoCrMo alloy using EIS (Valero et al., 2010) according to the previous procedure. The positive value of ΔH_{ADS} shows that the process is endothermic. The gain in entropy represents the driving force for the adsorption of the protein onto the metallic surface (the term $T\Delta S_{ADS}$ is considerably higher than the enthalpy value). These results reflects that the structure and hence dimensions of the molecule changes when the protein adsorbs onto the metallic surface. The induced structural changes can lead to a considerably entropy gain, which appears to be the driving force for the adsorption of the BSA.

4.2.4 Effect of the microstructure

In order to improve the corrosion and wear resistance of CoCrMo alloys, they are commonly subjected to different thermal treatments (i.e. solution annealing, hot isostatic pressure). Fig. 11 shows examples of the microstructures of an as-cast commercial CoCrMo alloy subjected to three thermal treatments:

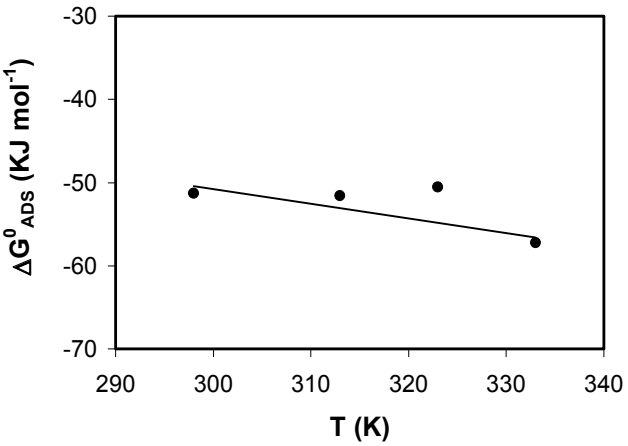

Fig. 10. Dependence of the Gibbs energy of adsorption on the temperature for BSA onto CoCrMo surface in NaCl solution (pH 7.4) by EIS (Valero et al., 2010).

- **Treatment 1**: solution annealing (cyclic thermal treatment) applied after as-cast process. A typical temperature cycle of one solution annealing in CoCrMo biomedical alloy consist of maintaining the alloy at 1119ºC during 240 minutes (in inert atmosphere) and cooling before at 24ºC/min until reaching the temperature of 760ºC. The combination of temperature and time is variable depending on the material and the desirable conditions.
- **Treatment 2**: a solution annealing + hot isostatic pressing (HIP) + solution annealing. The HIP is a thermal process in which high temperatures at the the isostatic pressure of one gas is applied to the material.
- **Treatment 3**: solution annealing + porous coating + HIP + solution annealing. The porous coating procedure is a thermal treatment employed in the manufacturing of surface prostheses. In this, spherical beads are bonded to each other and the solid substrate by sintering at high temperatures (1300ºC) to achieve a strong particle-particle substrate bond (Jacobbs et al, 1990).

The microstructure **1** reveals high amount of carbides in the matrix and in the grain boundaries after the solution annealing. The microstructure of the thermal treatment **2** presents greater homogeneity of the carbide precipitation than thermal treatment **1** (decrease in the number of carbides). This fact is due to the dissolution of carbides within the cobalt matrix as a consequence of more complex process in the thermal treatments. Finally, the microstructure **3** is characterized by an enhanced growth of the grain size and a diminution of the amount of carbides due to the porous coating process.

The Nyquist diagram represented in Fig. 11 was obtained at an applied passive potential. According to these diagrams the EEC used to model the experimental data is shown in Fig. 6(a). The impedance spectrum of the alloy strongly changes depending on the thermal treatment; R_{in} increases and CPE_{in} diminishes with the carbide solubilisation. In this case, the treatment **3** (which presents the highest grain size and the lowest amount of carbides) provides to the CoCrMo alloy the most protective layer under passive conditions (highest values of R_{in}) and the thickest passive film (lowest value of the CPE_{in}).

Thus impedance technique allows comparing the resistance of the passive dissolution of a CoCrMo alloy subjected to different thermal treatments and concluding that changing grain

size and carbide content in the alloy it is possible to improve the biocompatibility of the biomaterial.

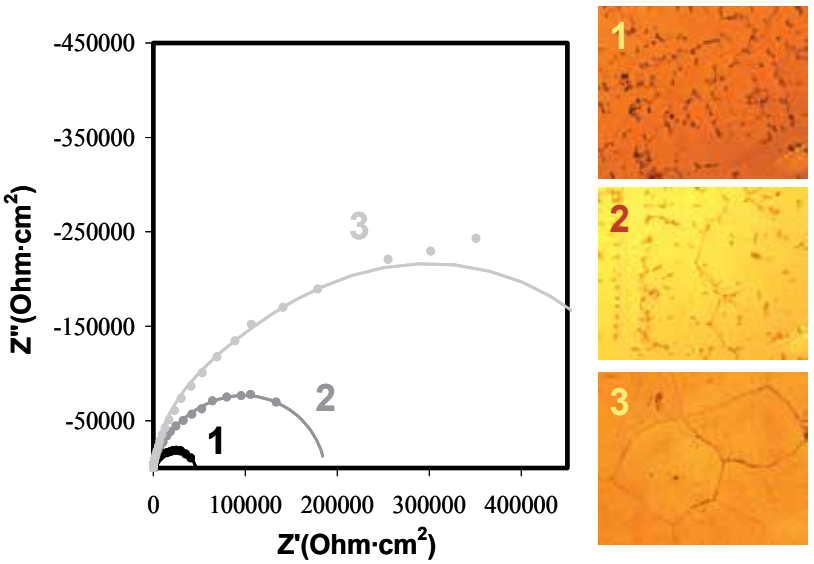

Fig. 11. Optical images of the microstructures of three different thermal treatments applied on an as-cast CoCrMo alloy and the Nyquist diagram of each sample at an applied passive potential in Bovine Serum solution (Valero & Igual, 2009).

5. Conclusions

Electrochemical Impedance Spectroscopy (EIS) has been demonstrated to be a sensitive and powerful tool for characterizing the interface and quantifying the metal release (biocompatibility) of biomedical alloys in simulated body fluids. In this chapter, the influence of material properties (chemical composition, grain size, and carbide content) and environmental factors (temperature, chemical composition of the simulated body fluids and adsorption of proteins) on the electrochemical behaviour of CoCrMo biomedical alloys has been studied by EIS.

The analysis of the impedance results allows the characterization and the quantification of different electrochemical and chemical process occurring on the biomaterial surface. It is possible to quantify the amount of adsorbed protein onto the surface and to calculate thermodynamic and kinetic parameters of the process (i.e. Gibbs free energy of adsorption, activation energy) by using the values of the charge transfer resistance with impedance measurements.

Corrosion mechanisms have been elucidated by EIS under well-established electrochemical conditions (potentiostatically controlled in order to work with specific surface chemistry): in the passive state the corrosion mechanisms of CoCrMo is governed by passive dissolution, while under cathodic conditions the mass transport limitation by diffusion takes place. At an applied transpassive potential the corrosion process is accompanied by an adsorption process (due to presence of proteins) attributed to the relaxation of the corrosion products on the electrode surface.

The most common procedure to interpret impedance data is to propose an Equivalent Electrical Circuit (EEC) which quantitatively provides information about the interface characteristics, its structure, passive film properties, corrosion mechanisms and reactions taking place on the interface electrolyte/oxide passive film. But the possibility to use different EEC to represent the same electrochemical system makes difficult to establish a real model of the system. This uncertainty can be solved by a previous knowledge of the system (physical and electrochemical properties) and the use of Surface Analysis techniques as complementary tools to the electrochemical measurements. X-Photoelectron Spectroscopy (XPS) and Auger Electron Spectroscopy (AES) are examples of complementary techniques used to complete the information obtained by EIS measurements (composition of the passive film and oxidation state of the constituent elements). The accurate knowledge of the surface chemistry is an essential aspect for the fundamental understanding of the electrochemical processes occurring on the interface biomaterial/body fluid.
On the other hand, several experimental aspects must be considered for the analysis of the EIS results. The technique is limited by the steady-state conditions needed for the impedance measurements which is difficult to assure when working with biological systems (dynamic systems). Metallic implants are commonly subjected to mechanical loads and relative movements (non-steady conditions). Thus, further development of EIS technique should be done in order to characterize the metal behaviour under mechanical-electrochemical phenomena such as those found in tribocorrosion situations.

6. References

Bi, Q.; Liu, W.; Ma, J.; Yang, J. ; Pu, Y. & Xue, Q. (2009). Tribocorrosion bevavior of Ni-17.5Si-29.3Cr alloy in sulfuric acid solution. *Tribology International, 42*, 7, (July 2009) (1080-1087), ISSN 0301-679X.

Black, J. & Hastings G. (1998). *Handbook of biomaterial properties (Blood and related fluids)*, Chapman & Hall, ISBN 0-412-60330-6, London, United Kingdom.

Catelas, I.; Petit, A.; Zukor, D.J. & Huk, O.L. (2001). Cytotoxic and apoptotic effects of cobalt and chromium ions on J774 macrophages- Implication of caspase-3 in the apoptotic pathway. *Journal of Materials Science: Materials in Medicine, 12*, 10-12, (December 2001) (949-953), ISSN 0957-4530.

Dumbleton, J.M. & Manley J.M. (2005). Metal-on-metal total hip replacement: What does the literature say?. The Journal of Arthroplasty, 20, 2, (February 2005) (174-188), ISSN 0883-5403.

Ebied, A. & Journeaux, S. (2002). Mini-symposium: hip replacement. (iv) Metal-on-metal hip resurfacing. *Current Orthopaedics, 16*, 6, (December 2002) (420-425), ISSN 0268-0890.

Fleury C.; Petit A.; Mwale F.; Antoniuou J.; Zukor D.J.; Tabrizian M. & Huk O.L. (2006). Effect of cobalt and chromium ions on human MG-63 osteoblasts in vitro: Morphology, cytotoxicity, and oxidative stress. *Biomaterials, 27*, 18, (June 2006) (3351-3360), ISSN 0142-9612.

Germain, M.A.; Hatton A.; Williams S.; Matthews J.B.; Stone M.H.; Fisher J. & Ingham E. (2003). Comparison of the cytotoxicity os clinically relevant cobalt-chromium and alumina ceramic wear particles in vitro. *Biomaterials, 24*, 3, (February 2003) (469-479), ISSN 0142-9612.

Granchi, D.; Cenni, E.; Trisolino, G.; Giunti, A. & Baldini N. (2006). Sensitivity to implant materials in patients undergoing total hip replacement. *Journal of Biomedical*

Materials Research. Part B: Applied Biomaterials, 77, 2, (May 2006) (257-264), ISSN 1552-4973.

Hallab, N.J.; Mikecz, K. & Jacobs J.J. (2000). A triple assay technique for the evaluation of metal-induced, delayed-type hypersensitivity responses in patients with or receiving total joint arthroplasty. *Journal of Biomedical Materials Research, 53*, 5, (September 2000) (480-489), ISSN 0021-9304.

Hallab, N.J.; Mikecz, K.; Vermes, C.; Skipor, A. & Jacobs, J.J. (2001) Orthopaedic implant related metal toxicity in terms of human lymphocyte reactivity to metal-protein complexes produced from cobalt-base and titanium-base implant alloy degradation. *Molecular and Cellular Biochemistry, 222*, 1-2, (June 2001) (127-136) ISSN 0300-8177.

Hanawa (2001). Characterization of the surface oxide film of a Co–Cr–Mo alloy after being located in quasi-biological environments using XPS. Applied Surface Science, 183, 1-2, (November 2001) (68-75), ISSN 0169-4332.

Hanawa, T. (2004). Metal ion release from metal implants. *Materials Science and Engineering C, 24*, 6-8, (December 2004) (745-752), ISSN 0928-4931.

Helsen J.A. & Breme H.J. (1998). *Metals as biomaterials,* John Wiley & Sons Ltd, ISBN 0-471-96935-4, United Kingdom.

Hodgson, A.W.E; Kurz, S.; Virtanen, S.; Fervel, V.; Olsson, C.-O.A. & Mischler, S. (2004). Passive and tranpassive behaviour of CoCrMo in simulated biological solutions. *Electrochimica Acta, 49*, 13, (May 2004) (2167-2178), ISSN 0013-4686.

Horowitz, S.M; Luchetti, W.T.; Gonzales, J.B. & Ritchie, C.K. (1998). The effect of cobalt chromium upon macrophages. *Journal of Biomedical Materials Research, 41*, 3, (September 1998) (468-473), ISSN 0021-9304.

Igual Muñoz, A. & Mischler, S. (2007). Interactive effects of albumin and phosphates ions on the corrosion of CoCrMo implant alloy. *Journal of the Electrochemical Society, 154*, 10, (August 2007) (C562-C570), ISSN 0013-4651.

Igual Muñoz, A. & Casabán Julián, L. (2010). Influence of electrochemical potential on the tribocorrosion behaviour of high carbon CoCrMo biomedical alloy in simulated body fluids by electrochemical impedance spectroscopy. *Electrochimica Acta, 55*, 19, (30 July 2010) (5428-5439), ISSN 0013-4686.

Jacobs, J.J.; Latanision, R.M.; Rose R.M. & Veeck, S.J. (1990). The effect of porous coating processing on the corrosion behavior of cast Co-Cr-Mo surgical implant alloys. *Journal of Orthopaedic Research, 8*, 6, (November 1990) (874-882), ISSN 0736-0266.

Kanagaraja, S.; Lundström, I.; Nygren, H.; Tengvall, P. Platelet binding and protein adsorption to titanium and gold after short time exposure to heparinized plasma and whole blood. *Biomaterials, 17*, 23, (1996) (2225-2232), ISSN 0142-9612.

Khan, M.A.; Williams, R.L. & Williams D.F. (1996). In-vitro corrosion and wear of titanium alloys in the biological environment. *Biomaterials, 17*, 22, (November 1996) (2117-2126), ISSN 0142-9612

Kocijan, A.; Milosev, I.; Merl, D.K. & Pihlar B. (2004). Electrochemical study of Co-based alloys in simulated physiological solution. *Journal of Applied Electrochemistry, 34*, 5, (May 2004) (517-524), ISSN 0021-891X.

Landolt, D. (2007). *Corrosion and surface chemistry of metals,* EPFL Press, ISBN 978-2-940222-11-7, Lausanne, Switzerland.

Marcus, P. & Oudar, J. (1995). *Corrosion mechanisms in theory and practice,* Marcel Dekker, ISBN 0-8247-9592-X, New York, Unites States of America.

Massè A.; Bosetti, M.; Buratti, C.; Visentin, O.; Bergadano, D. & Cannas M. (2003). Ion release and chromosomal damage from total hip prostheses with metal-on-metal articulation. *Journal of Biomedical Materials Research. Part B: Applied Biomaterials, 67*, 2, (November 2003) (750-757), ISSN 1552-4973.

Metikos-Hukovic, M.; Pilic, Z.; Babic, R. & Omanovic, D. (2006). Influence of alloying elements on the corrosion stability of CoCrMo implant alloy in Hank's solution. *Acta Biomaterialia, 2*, 6, (November 2006) (693-700), ISSN 1742-7061.

Metikos-Hukovic, M. & Babic, R. (2007). Passivation and corrosion behaviours of cobalt and cobalt-chromium-molybdenum alloy. *Corrosion Science, 49*, 9, (September 2007) (3570-3579), ISSN 0010-938X.

Militello, V.; Vetri V. & Leone, M. (2003). Conformational changes involved in thermal aggregation processes of bovine serum albumin. *Biophysical Chemistry, 105*, 1, (August 2003) (133-141), ISSN 0301-4622.

Milosev, I. & Strehblow, H.-H. (2003). The composition of the surface passive film formed on CoCrMo alloy in simulated physiological solution. *Electrochimica Acta, 48*, 19, (August 2003) (2767-2774), ISSN 0013-4686.

Okazaki Y. & Gotoh E. (2005). Comparison of metal release from various metallic biomaterials in vitro. *Biomaterials, 26*, 1, (January 2005) (11-21), ISSN 0142-9612.

Ouerd, A.; Alemany-Dumont, C.; Normand, B. & Szunerits, S. (2008). Reactivity of CoCrMo alloy in physiological medium: Electrochemical characterization of the metal/protein interface. *Electrochimica Acta, 53*, 13, (May 2008) (4461-4469), ISSN 0013-4686.

Scully J.R.; Silverman D.C. & Kending M.W. (1993). *Electrochemical impedance. Analysis and interpretation,* American Society for testing and materials (ASTM), ISBN 0-8031-1861-9, Philadelphia, United States of America.

Szklarska-Smialowska, Z. (1986). *Pitting corrosion of metals*, National Association of Corrosion Engineers (NACE) publications, ISBN 0-915567-19-9, Houston, Texas, United States of America.

Tipper, J.L; Ingham, E.; Jin, Z.M. & Fisher, J. (2005). Mini-symposium: hip replacement. (iv) The science of metal-on-metal articulation. *Current Orthopaedics, 19*, 4, (August 2005) (280-287), ISSN 0268-0890.

Valero Vidal, C. & Igual Muñoz, A. (2008). Electrochemical characterisation of biomedical alloys for surgical implants in simulated body fluids. *Corrosion Science, 50*, 7, (July 2008) (1954-1961), ISSN 0010-938X.

Valero Vidal, C. & Igual Muñoz, A. (2009). Effect of termal treatment and applied potencial on the electrochemical behaviour of CoCrMo biomedical alloy. *Electrochimica Acta, 54*, 6, (February 2009) (1789-1809), ISSN 0013-4686.

Valero Vidal, C.; Olmo Juan, A. & Igual Muñoz, A. (2010). Adsorption of bovine serum albumin on CoCrMo surface: effect of temperature and protein concentration. *Colloids and Surfaces B: Biointerfaces, 80*, 1, (October 2010) (1-10), ISSN 0927-7765.

Valero Vidal, C.; Mischler S.; Olsson, C.-O.A. & Igual Muñoz A. (2010). Passive behaviour of a CoCrMo biomedical alloy studied by EQCM and XPS, *Proceedings of 51st Corrosion Science Symposium*, Abstract 27, September 2010, Southampton.

Virtanen S.; Milosev, I.; Gomez-Barrena, E.; Trebse, R.; Salo, J. & Konttinen Y.T. (2008). Special modes of corrosion under physiological and simulated physiological conditions. *Acta Biomaterialia, 4*, 3, (May 2008) (468-476), ISSN 1742-7061.

Wolner, C.; Nauer, G.E.; Trummer, J.; Putz, V. & Tschegg, S. (2006). Possible reasons for the unexpected bad biocompatibility of metal-on-metal hip implants. *Materials Science and Engineering C, 26*, 1, (January 2006) (34-40), ISSN 0928-4931.

14

Recent Advances in the Modeling of PEG Hydrogel Membranes for Biomedical Applications

T. Ipek Ergenç and Seda Kızılel
Koc University
Department of Chemical and Biological Engineering Istanbul, Turkey

1. Introduction

PEG hydrogels have been studied intensively as tissue engineering scaffolds because they can provide a highly swollen three dimensional (3-D) environment similar to soft tissues and allow diffusion of nutrients and cellular waste through the elastic networks. (Lee and Mooney 2001; Hoffman 2002) PEG has played a significant role as hydrophilic polymer for biomedical applications which include surface modification, bioconjugation, drug delivery and tissue engineering due to the critical properties such as resistance to protein adsorption, biocompatibility, non-immunogenecity. (Lee, Lee and Andrade 1995; Alcantar, Aydil and Israelachvili 2000) PEG has a basic structure, known as PEG diol with two hydroxyl end groups which can be utilized to be converted into other functional groups for conjugation of biomolecules. (Peppas, Keys, Torres-Lugo and Lowman 1999) These functional groups consists of methyloxyl, carboxyl, amine, thiol, azide, vinyl sulfone, azide, acetylene, and acrylate. PEG also has either linear or branched (multiarm or star) structures (Scheme 1).
Several approaches have been used to synthesize crosslinked PEG hydrogels, such as free radical photopolymerization of PEG acrylates,(Elisseeff, Anseth, Sims, McIntosh, Randolph and Langer 1999; Buxton, J Zhu, Marchant, West, Yoo and Johnstone 2007; Hahn, McHale, Wang, Schmedlen and West 2007; Beamish, Zhu, Kottke-Marchant and Marchant 2010; Hubbell 1998; Kizilel, Perez-Luna and Teymour 2004; Kizilel, Sawardecker, Teymour and Perez-Luna 2006) and chemical reactions that include condensation, (Hubbell 1998) Michael type addition,(Metters and Hubbell 2005; Park, Lutolf, Hubbell, Hunziker and M 2004) click chemistry,(Polizzotti, Fairbanks and Anseth 2008; Malkoch et al. 2006) native chemical ligation,(Hu, Su and Messersmith 2009) and enzymatic reaction. (Sanborn, Messersmith and Barron 2002; Ehrbar et al. 2007; Ehrbar, Rizzi, Schoenmakers, BS, JA, Weber and Lutolf 2007) Among these approaches, the synthesis of PEG hydrogels through photopolymerization is the most common approach which uses light to convert PEG prepolymer solutions into crosslinked insoluble hydrogels. This technique not only allows the synthesis of hydrogel scaffolds with spatial and temporal control, it is also utilized for encapsulation of cells and biological molecules at physiological temperature and pH. (Truong and West 2002; Fisher, Dean, Engel and Mikos 2001) The major type of macromers used for photopolymerization includes PEG diacrylates (PEGDA), multiarm PEG acrylate

(n-PEG-acr), and PEG dimethacrylate (PEGDMA). PEG hydrogels can be modified to be degradable through incorporation of degradable segments, such as polyester, (Sawhney, Pathak and Hubbell 1993; Clapper, Skeie, Mullins and Guymon 2007; Jiang, Hao, You, Liu, Wang and Deng 2008) polypropylene fumarate (PPF),(Kretlow, Klouda and Mikos 2007; S'Engel and Mikos 2000) acetal,(Ksihara, Matsumura and Fisher 2008) and disulfide. (Zhang, Skardal and Prestwich 2008) Poly (lactic acid) (PLA), poly (glycolic acid) (PGA), and poly caprolactone (PCL) are common hydrolytically degradable blocks, which have been used to synthesize triblock (ABA) polymers by ring opening polymerization. These triblock polymers have been further terminated with acrylates to form PLA-PEG-PLA diacrylate and PGA-PEG-PGA diacrylate. (Sawhney, Pathak and Hubbell 1993; Burdick, Mason, Hinman, Thorne and Anseth 2002; Ifkovits and Burdick 2007) In order to enhance the degradation of the ester bonds linked to PEG chains in the hydrogel structure, thiol-acrylate reaction has also been used. (Jo, Gantz, Hubbell and MP 2009; Hudalla, Eng and Murphy 2008; Rydholm, Anseth and Bowman 2007; Rydholm, Bowman and Anseth 2005; Nuttelman, Tripodi and Anseth 2005; Nuttelman, Rice, Rydholm, Salinas, Shah and Anseth 2008).

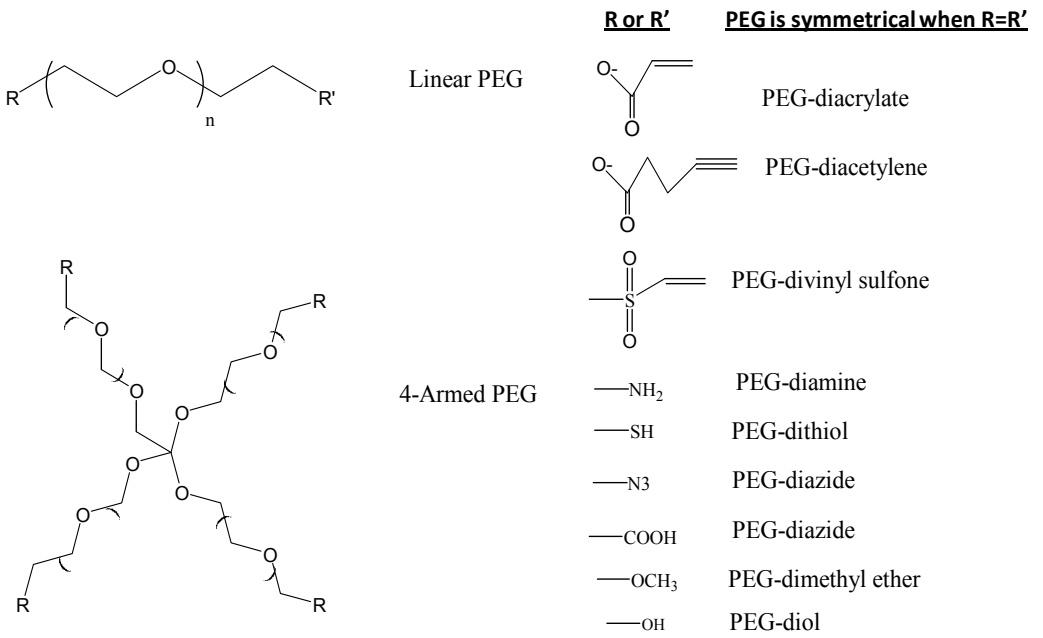

Scheme 1. Linear PEG and 4-armed PEG structures with various possible functional end groups.

PEG hydrogels are attractive as scaffolds, because they provide 3D environment for tissue regeneration. The limitation of PEG hydrogels on the other hand, is that they exhibit no biological activity, because PEG chains are not adhesive by their nature. (Lee, Lee and Andrade 1995) In order to mimic the natural extracellular matrix (ECM), researchers developed various types of biofunctional PEG hydrogels. (Lutolf 2009; Cushing and KS 2007; Lutolf and Hubbell 2005; Tibbitt and Anseth 2009) The components in the natural ECM is crucial in mediating cell functions, and possess critical role such as cell adhesion,

proteolytic degradation, and growth factor binding. (Badylak 2002; Badylak 2007) Various strategies have been used to tether ECM-derived biological molecules to PEG hydrogel structure, which provided fundamental knowledge to understand ligand incorporation within PEG hydrogels as well as cell/scaffold interactions. (Lutolf and Hubbell 2005; Cushing and KS 2007) Various cell lines including fibroblasts, chondrocytes, vascular smooth muscle cells (SMCs) and endothelial cells (ECs), osteoblasts, neural cells, and stem cells have been studied to observe their immobilization on biofunctional PEG hydrogels. (Lutolf and Hubbell 2005; Tibbitt and Anseth 2009) In order to regulate specific cellular responses for tissue formation, control of biomolecule concentration, spatial incorporation, and distribution within PEG hydrogels have been investigated. (Ma 2008; Ksihara, Matsumura and Fisher 2008; Ifkovits and Burdick 2007; Shin, Jo and Mikos 2003; Liao, Chan and Ramakrishna 2008; Sands and Mooney 2007)

This chapter addresses the recent progresss in the modeling of biofunctional PEG hydrogel scaffolds which can be utilized for the development of biofunctional PEG hydrogels as tissue engineering scaffolds. The chapter begins with a discussion of the structure and function of the natural ECM model, and then highlights the ECM derived ligands that have been used to synthesize biofunctional PEG hydrogels, followed by current approaches for the development of mathematical models for PEG hydrogels, which can be used to control specific cues, such as cell adhesion and function, and growth factor binding.

2. ECM as a natural model:

Natural ECM has been used as a model for designing biomimetic scaffolds as a result of rapid increase in the development and understanding of matrix biology. In the human body, tissues contain significant extracellular space and ECM molecules are secreted by the cells into this space and form a complex network. The function of ECM is to provide mechanical support for tissues, to organize cells into tissues, and to control cell behaviour (Scheme 2).

Proteins and glycans are the two classes of biomacromolecules that make up the natural ECM. (Rhodes and Simons 2007; Gailit and Clark 1994) The tensile strength to the ECM is provided by collagen and elasticity by elastin, both of which are structural fibrous proteins. (Gailit and Clark 1994; Ottani, Raspanti and Ruggeri 2001; Rhodes and Simons 2007) Type I and Type II that possess a fibrillar structure are two of the many types of collagen (Celse, Poschl and Aigner 2003). Type I collagen is found in skin, bone and tendons, while Type II collagen is what gives cartilage its tensile strength. (Brodsky and Ramshaw 1997; Kuhn 1985) Found specifically in basal lamina, Type IV collagen forms networks. (Kuhn 1994) Laminin (LN) and fibronectin (FN) are adhesive proteins that bind cells to the ECM. LN, with its cross-shaped trimer structure, provides binding sites for membrane receptors, Type IV collagen, heparan sulfate proteoglycan (HSPG) and entacin as the major adhesive protein in basal lamina (Aumaille and Smyth 1998; Beck, Hunter and Engel 1990; Gole and Pohl 2002; Kumagai, Okano and Kitagawa 2000). The many binding domains of FN, a V-shaped dimer, facilitate the connection between the ECM and cell membrane (Potts and Campbell 1994), in addition to binding proteins and cell-surface receptors. (Johansson, Svineng, Wennerberg, Armulik and Lohikangas 1997; Potts and Campbell 1994) Glycosaminoglycans (GAGs) and proteoglycans (PGs) are the glycans that make up the highly negatively charged, gelatinous ground substances rich in polysaccharide and in which the ECM proteins are embedded. (Horkay, 2008; Papagiannopoulos 2008; Rhodes 2007; Scott 1995) Sulfated GAGs, such as chondroitin, dermatan, heparan and keratin sulfates, that can

assemble on proteins rich in serine to form PGs and non-sulfated ones like hyaluronic acid (HA) are the two types of GAGs which are linear polymers of repeated disaccharide derivative. (Dudhia 2005; Luo, Guo, Zheng, Chen, Wang and Vertel 2000; Vertel 1995) Molecular signaling and nutrient diffusion are facilitated by glycans. When tissues are under pressure, GAGs and PGs prevent tissue collapse to some extent by absorbing compressive stresses because they swell in the aqueous environment between protein fibrils.

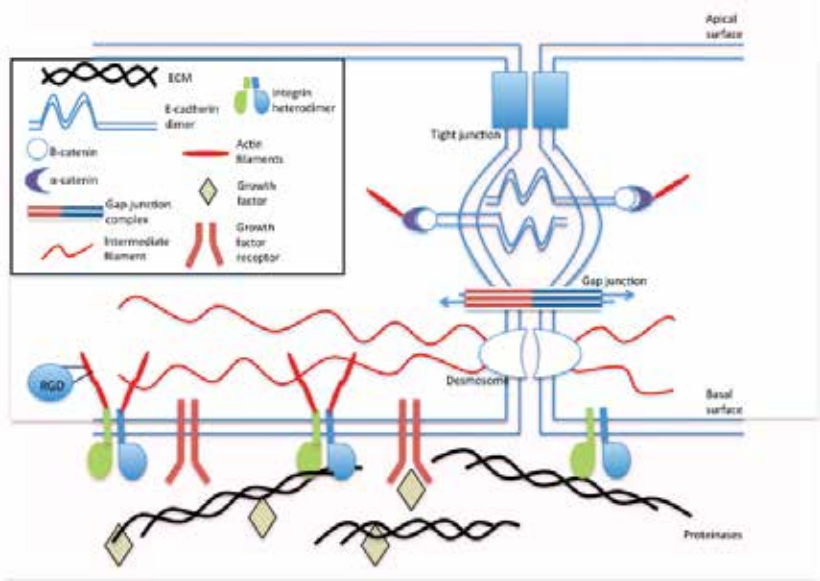

Scheme 2. Model of cell-extra cellular matrix (ECM) interactions.

Cell adhesion, proteolytic degradation and growth factor (GF)-binding are the three basic biofunctions of the ECM. Forming complex 3D networks by self-assembly or cell-directed assembly, (Traub 1978; Obrink, Laurent and Carlsson 1975; Guidetti, Bartolini, Bernardi, Tira, Berndt, Balduini and al. 2004; Zhu, Latridis, Hlibczuk, Ratcliffe and Mow 1996) the ECM components provide an environment for cell receptors to bind. Following this binding, the role of a cell in a tissue is determined by gene and protein expression which is affected by a series of intracellular enzymatic reactions initiated by these receptor-ligand interactions. (Cukierman, Pankov and Yamada 2002) Meanwhile, the microenvironment of the cells is formed and degenerated by the signals from these cells. Hence, the ECM has the role of providing a bioactive and dynamic environment for cellular functionality, in addition to filling up the extracellular space as a mechanical scaffold. (Rhodes and Simons 2007)

Most functions of the cell such as cell proliferation and cell migration can occur only after the cell's attachment to the ECM. (Jensen and Host 1997; Huttenlocher, Sandborg and Horwitz 1995; Humphries and Newham 1998) Many cell-surface receptors, such as integrins, selectins, CD44 and syndecan,(Cohen, Joester, Geiger and Addadi 2004; Henricks and Nijkamp 1998; Woods, Oh and Couchman 1998; Woods and Couchman 1998) are served cell-adhesive domains by the ECM. Integrins are responsible for cell anchorage and signal trigger through attachment to the ECM that lead to cell functioning, cell-cycle progression and different phenotype expression; (Woods, Oh and Couchman 1998; Ruoslahti and Pierschbacher 1987; Haas and Plow 1994; Katz, Zamir, Bershadsky, Kam,

Yamada and Geiger 2000; Webb, Parsons and Horwitz 2002) therefore they play an important role in tissue development, organization and maintenance by binding to the functional cell binding domains in the ECM such as FN, LN and collagen. (Chen, Chang, Gilson 2006; Woods, Couchman 2000)

A number of biological processes, such as cell migration, tissue repair and remodeling are actuated by the proteolytic degradation of the natural ECM. (Ellis and Murphy 2001; Murphy and Gavrilovic 1999; Murphy, Knauper, Atkinson, Gavriliovic and Edwards 2000) There are specific clevage sites on collagen, fibrin, FN, LN and other ECM proteins for degradation by enzymes such as matrix metalloproteinasas (MMPs), plasmin and elastase. (Seiki 2002; Chang and Werb 2001; Giannelli, Falk-Marzillier, Schiraldi, Stetler-Stevenson and Quaranta 1997; Ogura, Matsunaga, Nishiyama and Amano 2008; Mydel, Shipley, Adair-Kirk, Kelley, Broekelmann and Mecham 2008) Collagenases gelatinases, stromelysins, matrilysins, and membrane-type MMPs, which are made up of several domains including propeptide, catalytic, and hemopexin (except for matrilysin) domains, and are responsible for the degradation of collagens, proteoglycans, and various glycoproteins, (Turk, Huang, Piro and Cantley 2001; Nagase and Fields 1996) the five families of cell-secreted MMPs, which are endo-peptidases dependent on zinc and involved in the remodeling of the ECM, have effect on morphogenesis, angiogenesis, arthritis, skin ulcer, tumor invasion and metastasis. (Amano, Akutsu, Matsunaga, Kadoya, Nishiyama, Champliaud and al. 2001) MMPs, inactive zymogens as secreted, need to be activated in order to function. Tissue inhibitors of metalloproteinase's (TIMPs) regulate the activity of MMPs in the post-transcriptional stage; therefore regulated degradation to delineate the cellular environment is performed by MMPs and TIMPs. (Amano, Akutsu, Matsunaga, Kadoya, Nishiyama, Champliaud and al. 2001; Nagase and Fields 1996; Turk, Huang, Piro and Cantley 2001)

Binding to the ECM controls the stability, activity, release and spatial localization of growth factors (GFs), proteins that regulate gene expression and cell functions like differentiation, migration and proliferation depending on the conditions of the cell environment, (Silva, Richard, Bessodes, Scherman and Merten 2009; Babensee, McIntire and Mikos 2000) during the natural tissue development. (Zisch, Lutolf and Hubbell 2003) When they are in contact, ECM proteoglycans are associated with GFs, including fibroblast growth factor (FGF), transforming growth factor (TGF), epidermal growth factor (EGF), vascular endothelial growth factor (VEGF) and platelet-derived growth factor (PDGF), in order to provide integrations and eliminate immediate dispatch.

3. Bioactive modification of ECM-mimic

The scaffolds in tissue engineering should be able to perform cell-specific adhesion and promote the motion of signaling biomolecules, in addition to being biocompatible, biodegradable, highly porous and not prone to causing immunogenic reactions. Although PEG hydrogels are preferred in designs that require flexibility and porosity similar to cartilage, they are not optimum in supplying the cells with the environment they need due to PEG's inability to adhere to cells and not being biodegradable. The addition of bioactive materials such as cell adhesive peptides (CAPs), enzyme-sensitive peptides (ESPs) and growth factors is necessary to obtain the similar biofunction of ECM such as specific cell adhesion, enzyme-sensitive degradation and GF-binding, respectively; because addition of segments like PLA and PGA, which are hydrolytically open to change, is not enough to increase biodegradability.

Biofunctions of the ECM like cell binding, proteolytic degradation and GF-binding are often chemically accomplished by short peptide sequences present in collagen, elastin, FN, LN and PGs. (Mel, Jell, Stevens and Sefalian 2008; Heino 2007; Mineur, Guignandon, Lambert, Lapiere and Nusgens 2005; Luzak, Golanski, Rozalski, Boncler and Watala 2003; Pocza, Suli-Vargham, Darvas and Falus 2008; Girotti, Reguera and Rodriguez-Cabello 2004; Nomizu, Weeks, Weston, Kim, Kleinman and Yamada 1995; Fosang, Last, Knauper, Murphy and Neame 1996; Ruoslahti 2003; Leahy, Aukhil and Erickson 1996; Lin, Takahashi, Liu and Zamora 2006) PEG hydrogels are modified with these ECM-derived short peptides,(Shin, Jo and Mikos 2003) proteins(Hynd, Frampton, Dowell-Mesfin, Turner and Shain 2007; Halstenberg, Panitch, Rizzi, Hall and Hubbell 2002; Nie, Akins and Kiick 2009; Moon, Lee and West 2007) or proteoglycans. (Bryant, Arthur and Anseth 2005; Li, Williams, Sun, Wang, Leong and Elisseeff 2004; Masters, Shah, Walker, Leinwand and Anseth 2004; Khetan, Katz and Burdick 2009) Short peptide sequences are more stable, easier to synthesize and harder to denature or degrade than the entire protein structure. (Massia and Hubbell 1992) Reactive groups such as acrylate, amine, thiol, azide, maleimide and bitin/streptavidin have been used in order to bind ECM-derived biomolecules covalently into PEG hydrogel networks.

4. Bioactive molecules for biofunctional PEG hydrogel

The following sections summarize different types of biofunctional PEG hydrogels which have been synthesized through incorporation of biomolecules.

Cell adhesion bearing sites in PEG Hydrogels

Inability of PEG hydrogels to perform cell specific adhesion is a major limitation in tissue engineering. A variety of cell adhesive peptides (CAPs), mainly derived from four ECM proteins, FN (e. g. , RGD, KQAGDV, REDV and PHSRN), LN (e.g., YIGSR, LGTIPG, IKVAV, PDGSR, LRE, LRGDN and IKLLI), collagen (e.g., DGEA and GFOGER) and elastin (e.g., VAPG) have been used for modifying PEG hydrogels. RGD peptides, whose cell binding domains are derived from FN, LN and collagen, are most commonly used modifications. (Hersel, Dahmen and Kessler 2003; Ruoslahti 2003) While linear RGD peptides inrease the affinity for cell binding, (Leahy, Aukhil and Erickson 1996) cyclic RGD (cRGD) peptides increase biological activity up to 240 times compared to linear ones. (Haubner, Schmitt, Holzemann, Goodman, Jonczyk and Kessler 1996; Haubner, Gratias, Diefenbach, Goodman, Jonczyk and Kessler 1996; Locardi, Mullen, Mattern and Goodman 1999; Kaufmann, Fiedler, Junger, Auernheimer, Kessler and Weberskirch 2008) A better mimic of RGD loop structure and enhanced cell specific adhesion in PEG hydrogels have been achived by the incorporation of cRGD peptides. (Zhu, Tang, Kottke-Marchant and Marchant 2009)

Enzymatically-responsive PEG Hydrogels

It is important that the degradation rate of scaffolds matches the new tissue regeneration at the defect site. More rapid degradation than tissue regeneration will cause the scaffolds to lose their carrier function for cell growth, whereas slower degradation than tissue regeneration will decrease the efficiency of tissue regeneration. Although PEG hydrogels have ester bonds that can be hydrolized, this degradation is not fast enough both in vitro and in vivo. Incorporation of polyester segments such as PLA and PGA promotes hydrolytic degradation of PEG hydrogels; however, the process stays non-responsive to cellular signals or cell-secreted enzymes. Incorporation of enzyme-sensitive peptide (ESP) sequences for proteolytic degradation is the best way to accomplish biodegradability. Cell adhesion to PEG hydrogels have also been modulated by such enzyme-sensitive designs.

Growth-factor Binding PEG Hydrogels

Growth factors (GFs), which are polypeptides that transmit signals to operate cellular activities, have short half-lives in free forms or in the circulation and need to bind to matrix molecules for activity and stabilization. Binding to the receptors on the surface of target cells is what initiates their action. Cell functions and tissue formation are guided by binding of GFs to proteoglycans. (Zisch, Lutolf and Hubbell 2003) GFs are best incorporated in PEG hydrogels during the formation of the gel; however, rapid burst release during the initial swelling phase can be observed with this direct loading method. (Burdick, Mason, Hinman, Thorne and Anseth 2002) It is hard to control this mechanism since the rate of protein release is diffusion-controlled within a hydrogel. Two major strategies, covalent attachment and specific interaction, have been developed to mimic the GF-binding function of the ECM in PEG hydrogels. GFs have been modified with several functional groups for covalent attachment. Besides this modification, GF-binding hydrogels is another approach in delivering GFs. This method prevents potential damage to GFs during covalent modification and therefore biological activity of GFs can be maintained during release period. Chemical modification of heparin, chondroitin sulfate (CS) and hyaluronic acid (HA) with various reactive groups, such as acrylate, thiol, or maleimide, followed by reacting with the functionalized derivatives of PEG or multiarm PEG to form GAG-bearing PEG hydrogels by carboxyl/amine conjugation, copolymerization, Michael addition, and specific interaction between heparin and GFs or heparin binding peptides (HBPs) have been the central efforts to develop this mechanism. (Cai, Liu, Zheng and Prestwich 2005; Yamaguchi, Zhang, Chae, Palla, Furst and Kiick 2007; Zhang, Furst and Kiick 2006) Thiol-acrylate photopolymerization to incorporate thiol-containing biotin into PEG hydrogels for specific interaction with strepavidin-modified GFs like bFGF is another method to make GF-binding PEG hydrogels. (Lin and Anseth 2009; Zhu 2010)

Immunoisolation with PEG Hydrogels

Additional challenges come up in controlling the function and survival of cells encapsulated in PEG hydrogels during the transition between *in vitro* to *in vivo* studies. Although PEG hydrogels can act as a barrier between the encapsulated cells and the immune or inflamatory cells, small cytotoxic molecules like reactive oxygen species (ROS) and pro-inflammatory cytokines, such as tumor necrosis factor-a (TNFa, 17. 4 kDa) and interleukin-1b (IL-1b, 17 kDa) can still diffuse through the gel. Apoptosis or impaired cell function can result from the penetration of these molecules into the hydrogel. A polymerizable superoxide dismutase (SOD)-mimetic macromer, tetraacrylate of Mn(III)tetrakis(1-methyl-4-pyridyl) porphyrin pentachloride (MnTMPyP), have been synthesized and copolymerized with PEGDA to form hydrogel networks that provide SOD-mimetic activity to protect encapsulated cells from ROS-mediated damage. (Cheung, McCartney and KS 2008) Immobilizing cytokine-antagonizing antibodies like anti-Fas MAb (binding to the Fas antigen of Jurkat T cells) in PEG hydrogels has been another attempt; however, the large size for conjugation, poor stability and immunogenicity have been the concerns for this method. (Cheung and KS 2006)

Drug Delivery from PEG Hydrogels

Critical properties of PEG hydrogels like good biocompatibility, non-immunogenity and resistance to protein adsorption makes them an important type of hydrophilic polymers that can be used for drug delivery. (Lee, Lee and Andrade 1995; Alcantar, Aydil and Israelachvili 2000) An example of this is pressure-sensitive adhesive hydrogel matrix based on a poly-complex between poly(N-vinylpyrrolydone) (PVP) and oligomeric PEG which has been

designed to enhance transdermal drug delivery (Feldstein et al. 1997; Feldstein, Plate, Sohn, Voicu and protection 1999; Feldstein, Tohmakhchi, Malkhazov, Vasiliev and Plate 1996).

5. Free radical copolymerization for bioactive modification of PEG hydrogels

PEG hydrogels from PEGDA macromers have been made with the method of free radical polymerization (FRP), especially photopolymerization where photoinitiators are present. In order to make biofunctional PEG hydrogels, copolymerization of acrylated biomolecules have been performed to incorporate bioactive molecules into PEG hydrogel networks. Copolymerization with peptide monoacrylates or diacrylates and thiol-acrylate photopolymerization are the common methods used for this strategy.

In order to make bulk cell-adhesive hydrogels, PEGDA can be copolymerized with monoacrylates of CAPs. By functionalizing the N-terminal amines of RGD peptides with N-hydroxyl succinimide (NHS) ester of acrylic acid (AA-NHS) and acryloyl-PEG-NHS (Acr-PEG-NHS, Mw 3400) to produce mono-acrylamidoyl RGD (RGD-MA) and RGD-PEG monoacrylate (RGD- PEGMA), monoarcylated RGD with or without PEG spacers can be synthesized, respectively. (Hern and Hubbell 1998) As a result, cell-adhesive hydrogels can be made by the copolymerization of RGD-MA or RGD-PEGMA monomers with PEGDA upon photopolymerization. Having a PEG spacer, PEGDA hydrogels with RGD-MA can spread the cells specifically. Several cell lines, such as fibroblasts, chondrocytes, vascular endothelial cells (ECs), osteoblasts, neural cells, and stem cells, have been observed to immobilize on bioactive PEG hydrogels. (Lutolf 2009; Nuttelman, Rice, Rydholm, Salinas, Shah and Anseth 2008)

Using peptide monoacrylates in this method results in random distribution of RGD peptides in hydrogels. In addition, hydrogel formation and its mechanical properties are limited due to the limitations in peptide incorporation in the hydrogel when monoacrylates are used. Creating a peptide-containing PEGDA macromer like RGD-PEGDA with RGD attached to two PEG monoacrylates, which has a similar structure to PEGDA with two C-C double bonds for polymerization is a method to control cell behavior. (Zhu, Beamish, Tang, Kottke-Marchant and RE 2006) This way, the spatial organization of peptide ligands in hydrogels can be controlled and the effort of peptide incorporation can be eliminated. Enzyme-sensitive peptide (ESP)-containing PEGDA (ESP-PEGDA), another important type of peptide-modified PEG diacrylates, has a different structure than that of CAP-PEGDA. With its two reactive groups on both ends for conjugation with Acr-PEG-NHS, ESP is inserted between two PEG monoacrylate (PEGMA) chains, whereas a CAP with two amines on one end for attachment as a pendant on the PEGDA chain synthesizes CAP-PEGDA. Proteolytic degradation of the natural ECM by specific enzymes, such as plasimin, elastase and MMPs, is mimicked by ESP-PEGDA for photopolymerization to form hydrogels. Also, bioactive PEG hydrogels with dual biofunctions like enzyme-sensitive degradation and specific cell adhesion can be made by the copolymerization of ESP-PEGDA with cell-adhesive PEG macromers like RGD-PEGMA. (Patel, Gobin, West and Patrick 2005; Lee, Moon, Miller and West 2007; Gobin and West 2003)

The molecular weight of polymers created by free radical polymerization (FRP) is controlled by thiol-containing compounds used as chain transfer reagents. Cysteine-containing peptides are expected to play a similar role as chain transfer reagents in the FRP of PEGDA, which leads to the incorporation of cysteine-containing peptides into the PEG hydrogel network. (Reddy, Cramer and Bowman 2006; Cramer, Reddy, O'Brien and CN 2003; Cramer

and Bowman 2001; Houllier and Bunel 2001) Thiol-acrylate photopolymerization can be utilized to bioactively modify PEG hydrogels as an alternative approach. (Polizzotti, Fairbanks and Anseth 2008; DeForest, Polizzotti and KS 2009; Salinas and KS 2008; Salinas and Anseth 2008) Stoichiometric ratios, polymerization time and pH are not limitations for this method and it results in a robust, cost-efficient and cytocompatible reaction scheme for the incorporation of peptide sequences into PEG hydrogels for 3D cell culture and directing cellular function. (Salinas and Anseth 2008)

6. Mathematical models for the prediction of PEG hydrogel membrane properties for biological applications

Recent studies have provided evidence that it is important to control the swelling ratio, diffusion rate, and mechanical properties of a crosslinked polymer in the design of PEG hydrogels for biomedical applications. (Elliott, Anseth and Bowman 2001) It has also been shown that, polymer synthetic peptide epitopes might be useful, specifically in the design of an ECM mimic to promote tissue survival and function. (Weber, Hayda and Anseth 2008; Weber and Anseth 2008; Weber, Hayda, Haskins and Anseth 2007) Thickness and permeability of the membrane, as well as the level of peptide incorporation within the membrane, are all critical factors that determine the success of immunoprotective devices and tissue function. These are crucial because a thick membrane can present a large diffusion barrier to oxygen, nutrient, metabolites, and/or the therapeutic agent released by the cell, yet a very thin barrier is more likely to have defects that may expose the transplanted cells to the immune system of the host. (Ji, Childs and Mehta 2001) Development of a biofunctional PEG hydrogel requires the control of ligand concentration which is important to direct the desired signaling pathways. (West 2005) For example, microencapsulation via surface initiated photopolymerization of PEG hydrogel is one method to make microcapsules around cells or islets. (Pathak, Sawhney and Hubbell 1992) Release of the insulin through the membrane capsule and the viability of the encapsulated islets after transplantation depend on the structure and the thickness of the capsule. Experimentally, a variety of parameters such as the chemical composition of the photopolymerization system, the duration of photopolymerization and the intensity of the excitation light source have been found to affect the gel thickness(Cruise, Hegre, Scharp and Hubbell 1998) and permeability characteristics of the capsule wall. (Cruise, Scharp and Hubbell 1998) In previous studies, Kızılel *et al.* developed experimental and mathematical models to describe the details of the complex process of PEG hydrogel and biofunctional PEG hydrogel formation which were based on an understanding of the individual fundamental steps of the photopolymerization process. (Kizilel, Sawardecker, Teymour and Perez-Luna 2006; Kizilel, Perez-Luna and Teymour 2009; Kizilel, Perez-Luna and Teymour 2006; Kizilel, Perez-Luna and Teymour 2004; Kizilel 2010; MacDonald, El-kholy, Riedel, Salapatek, Light and MB 2002) Those models greatly improved our understanding of such a complex polymerization system and provided important information on the effect of parameter variation (e. g. monomers or initiator concentration, light intensity, duration of photopolymerization) on properties of the membrane such as thickness, crosslink density, gelation, and the distribution of biological ligands within the hydrogel as these variables are changed. These models not only lead to better optimization strategies based upon numerical simulations of parameter variation such as monomer, light intensity, duration of photopolymerization, but also give further insights into the hydrogel properties at the

microscopic level that cannot be obtained through experimental observations such as the presence of gradients in peptide incorporation, crosslink density, the evolution of these gradients with time and the early stages of hydrogel formation.

Model Description

The process of hydrogel membrane formation by free radical copolymerization of PEG-DA VP, and acrl-PEG-GLP-1 involves excitation of surface bound eosin to its triplet state as a result of irradiation with green light (514 nm). (Valdes-aguilera, Pathak, Shi, Watson and Neckers 1992) Electron transfer and proton loss from the triethanolamine to the excited eosin results in the formation of the neutral α-amino radical (TEA•), which initiates polymerization in this system. (Neckers, Hassoon and Klimtchuk 1996; Kumar and Neckers 1991) It must be noted that, in this polymerization process, the TEA• free radicals are generated at the cell-prepolymer interface and TEA• radicals will diffuse away from the surface, and initiate polymerization in a region that is in close proximity with the surface. The process of biofunctional PEG hydrogel membrane formation is a nonlinear polymerization process where a branched polymer chain is formed through propagation of a radical through the pendant double bonds present in PEG-DA chains. Excessive crosslinking occurs through pendant double bond (PDB) propagation followed by termination by combination. Since crosslinking leads to the formation of a very large molecule of infinite molecular weight, complicated solution techniques are required to mathematically describe gel formation.

In previous studies, Kızılel et al. described the branching characteristics and crosslinking mechanism in PEG-DA/VP copolymerization that lead to gel formation, and the method of moments(Bamford and Tompa 1954) along with the pseudo-kinetic rate constant approach(Hamielec and MacGregor 1983) has been applied to develop a mathematical model for the process of islet encapsulation within biofunctional PEG hydrogel through interfacial photopolymerization. (Kizilel, Perez-Luna and Teymour 2006; Kizilel 2010) In those models, new features are also included; concentration dependent propagation of VP monomer, and the reaction diffusion termination for all monomers. In order to derive the kinetic model, several assumptions such as monoradical assumption, and the diffusion of vinyl pyrrolidone through the newly formed hydrogel were made about the copolymerization system. As the polymerization proceeds, capsule starts to form on the surface. Since the thickness varies with time, this becomes a moving boundary problem. The growth of the membrane occurs as a result of reaction of monomers at the membrane surface.

The polymerization system consists of initiation, propagation, chain transfer to TEA, radical termination by combination and reaction through pendant double bond steps. It is also assumed that the terminal model of copolymerization is applicable and termination by disproportionation step is not included. The process involves the copolymerization of *A (VP), B (PEG-DA)* and C (acrl-PEG-GLP-1) whose elementary reactions are shown below. The symbols *A*, B*,* and *C** are used to indicate the type of monomer unit at the chain end identity of the propagating radical. These denote VP, PEG-DA and acrl-PEG-GLP-1 respectively.

Initiation:

In this step the initiator radical (R_{in}), which was also called α-amino radical in this system, forms as a result of its reaction with eosin Y and reacts with the monomers to form live radicals of length one.

$$Y_{ac} \underset{k_{-1}}{\overset{\nu k_1}{\Leftrightarrow}} Y^* \nu K \tag{1}$$

$$Y^* + TEA \rightarrow Y_{in} + R_{in} \bullet \mathrm{k_f} \tag{2}$$

$$R_{in} \bullet + A \rightarrow A_1 \bullet \mathrm{k_{i1}} \tag{3}$$

$$R_{in} \bullet + B \rightarrow B_1 \bullet \mathrm{k_{i2}} \tag{4}$$

$$R_{in} \bullet + C \rightarrow C_1 \bullet \mathrm{k_{i3}} \tag{5}$$

where $\nu K = \nu \frac{k_1}{k_{-1}}$, K is the equilibrium constant for excitation and, νK represents the amount of excitation radiation absorbed by eosin Y molecules. Thus, ν would take into account the intensity of the light source because an increase of excitation intensity would result in a larger number eosin molecules excited to the triplet state.

Propagation:

Propagation of the three monomers, *A (VP), B (PEG-DA),* and *C (acrl-PEG-peptide)* leads to three types of propagating species, one with *A* at the propagating end, one with *B* at the propagating end, and the other with C at the propagating end. These are represented by *A*, B*,* and *C**. This classification is made because the reactivity of the propagating species is dependent on the monomer unit at the end of the chain. (Odian 2004; Dotson, Galvan, Laurence and Tirrell 1996) Radical chains of length j react by adding monomer units to the polymer chain to form longer radical chains of length j+1 according to the following mechanism:

$$A_j \bullet + A \rightarrow A_{j+1} \bullet \mathrm{k_{p11}} \tag{6}$$

$$A_j \bullet + B \rightarrow B_{j+1} \bullet \mathrm{k_{p12}} \tag{7}$$

$$A_j \bullet + C \rightarrow C_{j+1} \bullet \mathrm{k_{p13}} \tag{8}$$

$$B_j \bullet + A \rightarrow A_{j+1} \bullet \mathrm{k_{p21}} \tag{9}$$

$$B_j \bullet + B \rightarrow B_{j+1} \bullet \mathrm{k_{p22}} \tag{10}$$

$$B_j \bullet + C \rightarrow C_{j+1} \bullet \mathrm{k_{p23}} \tag{11}$$

$$C_j \bullet + A \rightarrow A_{j+1} \bullet \mathrm{k_{p31}} \tag{12}$$

$$C_j \bullet + B \rightarrow B_{j+1} \bullet \mathrm{k_{p32}} \tag{13}$$

$$C_j \bullet + C \rightarrow C_{j+1} \bullet \mathrm{k_{p33}} \tag{14}$$

Termination:
Termination by combination reaction leads to the formation of longer dead polymer chains. Termination by combination reaction must be taken into account because it also leads to branching and gelation.

$$A_j \bullet + A_p \rightarrow P_{j+p}\, \mathrm{k_{tc11}} \tag{15}$$

$$A_j \bullet + B_p \rightarrow P_{j+p}\, \mathrm{k_{tc12}} \tag{16}$$

$$A_j \bullet + C_p \rightarrow P_{j+p}\, \mathrm{k_{tc13}} \tag{17}$$

$$B_j \bullet + B_p \rightarrow P_{j+p}\, \mathrm{k_{tc22}} \tag{18}$$

$$B_j \bullet + C_p \rightarrow P_{j+p}\, \mathrm{k_{tc23}} \tag{19}$$

$$C_j \bullet + C_p \rightarrow P_{j+p}\, \mathrm{k_{tc33}} \tag{20}$$

Chain Transfer to TEA:
The radicals can also react with the chain transfer agent, TEA. In this case the growing radical is transferred to TEA, which hinders the growth of a polymer chain while at the same time generating a free radical capable of starting the growth of another polymer chain as follows:

$$A_j \bullet + TEA \rightarrow P_j + R_{in} \bullet \mathrm{k_{tr1}} \tag{21}$$

$$B_j \bullet + TEA \rightarrow P_j + R_{in} \bullet \mathrm{k_{tr2}} \tag{22}$$

$$C_j \bullet + TEA \rightarrow P_j + R_{in} \bullet \mathrm{k_{tr3}} \tag{23}$$

Reaction through a Pendant Double Bond:
When a newly formed radical reacts through a pendant double bond, a quaternary branch point is created.

$$A_j \bullet + P_p \rightarrow B_{j+p} \bullet \mathrm{k^*_{p12}} \tag{24}$$

$$B_j \bullet + P_p \rightarrow B_{j+p} \bullet \mathrm{k^*_{p22}} \tag{25}$$

$$C_j \bullet + P_p \rightarrow B_{j+p} \bullet \mathrm{k^*_{p32}} \tag{26}$$

Membrane thickness:
The equation describing the increasing size of the polymer membrane can be formulated as:

$$\varphi_p \rho_{polymer} \frac{dv}{dt} = v \left[-\frac{d[A]}{dt}\bigg|_{r_m} MW_{VP} - \frac{d[B]}{dt}\bigg|_{r_m} MW_{PEG} - \frac{d[C]}{dt}\bigg|_{r_m} MW_{PEG-pep} \right] \tag{27}$$

where $\rho_{polymer}$ is polymer density (g. L^{-1}), MW_{PEG}, MW_{VP}, and $MW_{PEG\text{-}pep}$ are the molecular weights of PEG-DA, VP, and acrl-PEG-GLP-1 respectively, dv/dt represents volume growth rate of the hydrogel membrane, $dv = Sdr$, and S is the surface area of the capsule. The equation can be written in general form as:

$$\frac{dr}{dt} = \frac{r}{a\varphi_p \rho_{polymer}} \left[-\frac{d[A]}{dt}\bigg|_{r_m} MW_{VP} - \frac{d[B]}{dt}\bigg|_{r_m} MW_{PEG} - \frac{d[C]}{dt}\bigg|_{r_m} MW_{PEG-pep} \right] \quad (28)$$

and a is equal to 3 for the case of spherical model (islet is assumed to be perfectly spherical), and it is equal to 1, for the case of rectangular coordinates. Mass growth rate of the polymer capsule is related to the consumption of monomers *A, B*, and *C*, and $\boldsymbol{\varphi}_p$ represents the volume fraction of the polymer chains in the water swollen hydrogel. Molecular weights of *PEG-DA*, *VP*, and *acrl-PEG-peptide* are 3400, 111. 43, and 6754. 67 g. mol^{-1} respectively.

Boundary Conditions:

As stated earlier, it was assumed that the VP monomer and the initiator radicals could diffuse through the newly formed hydrogel. This imposes the following boundary conditions in this model:

$$\frac{\partial[A]}{\partial r}\bigg|_{cell\ surface} = 0 \quad (29)$$

i. e. , VP cannot diffuse into the cell or through the solid surface.

The rate of formation of initiator free radicals at the surface is given by its rate of formation by electron transfer from TEA to excited eosin Y, plus its consumption with the monomers of type *A, B*, and *C* to form live radicals of length one, plus its formation through the reaction of live radicals with TEA, plus its outward diffusion.

$$\frac{\partial[R_{in}]}{\partial t}\bigg|_{cell\,surface} = \left[\begin{array}{l} k_{in}\left([Y_{tot}] - [Y_{in}]\right)TEA - \bar{k}_i[M][R_{in}] \\ \qquad + \bar{k}_{tr}[TEA][Y_0] + D_{R_{in}} \dfrac{a}{r} \dfrac{\partial[R_{in}]}{\partial r} \end{array} \right]_{r=r_0} \quad (30)$$

where r_o is the radius at the cell surface, a is equal to 3 for spherical coordinates and it is equal to 1 for rectangular coordinates. The predictions of membrane thickness for different concentrations have been done for rectangular coordinate system, when the comparisons were made with experimental observations. It has been observed that the predicted differences of thicknesses between rectangular and spherical coordinate system were not statistically significant, therefore spherical coordinate system have been used for the remaining thickness predictions.

Effects of VP and PEG-DA Concentrations on Membrane Thickness. The effects of PEG-DA and VP concentrations on the thickness of the hydrogel membrane and crosslink density demonstrated that VP and PEG-DA has a positive effect on the membrane thickness, and that higher PEG-DA and VP concentration results in thicker membranes. The positive effect of VP on thickness was explained by the effect of VP propagation (k_{p11}) and termination rate constants (k_{tc11}), which have been incorporated into the present model as a function of VP concentration as was suggested in previous recent studies. (Stach, Lacik, Chorvat, Buback,

Hesse, Hutchinson and Tang 2008; White, Liechty and Guymon 2007) Recently, Stach et al measured the propagation rate coefficient (k_{p11}) of N-vinyl pyrrolidone (NVP) in aqueous solution at a concentration range from 1. 8% to 100 wt % NVP via pulsed-laser polymerization-size exclusion chromatography method (PLP-SEC). (Stach, Lacik, Chorvat, Buback, Hesse, Hutchinson and Tang 2008) The authors observed that k_p increases toward lower NVP concentrations in water, and that k_{p11} is enhanced during polymerization to higher monomer conversion of a given aqueous solution of NVP. The pronounced increase of VP propagation rate constant, k_{p11}, toward lower VP concentrations in water was assigned to a genuine entropic effect. According to transition state theory (TS), the preexponential factor in the Arrhenius equation is determined by the geometry of the rotating groups in the reactants, and by the rotational potentials of the relevant internal motions in the TS. (White, Liechty and Guymon 2007; Heuts, Gilbert and Radom 1995) Large hindrance of rotational freedom is associated with significant entropy penalty, and this results in smaller Arrhenius constant (A), and propagation constant, k_p. When water molecules replace monomer molecules, the environment of the TS structure for the addition of a monomer molecule to a macroradical changes, which results in higher degree of rotational freedom at the chain end. As a result, k_p increases toward lower VP concentrations, and k_p is enhanced during polymerization to higher monomer conversion of a given aqueous solution of VP. (Stach, Lacik, Chorvat, Buback, Hesse, Hutchinson and Tang 2008)
Following formula correlates the relationship between k_p and concentration of NVP (C_{NVP}):

$$k_p = M_1 \upsilon_{rep} / (M_0 C_{NVP}) \tag{31}$$

where M_1 and ν_{rep} are the parameters measured in PLP experiments, M_0 and C_{NVP} represent molecular weight (MW_{VP}=111. 43 g. mol^{-1}) and concentration of NVP respectively. The relationship between propagation and termination rate constants of NVP has also been described recently in a separate study by White et al. ,(White, Liechty and Guymon 2007) where the authors investigated the importance of reaction-diffusion controlled termination in crosslinked acrylate/NVP copolymerization, and suggested that reaction diffusion termination, R, is expressed by:

$$R = \frac{k_t}{k_p M} \tag{32}$$

where M and R are the monomer double bond concentration, and reaction diffusion parameter respectively. In the recent biofunctional PEG hydrogel modeling study by Kızılel, the value of R has been taken as 25 L/mol, which was the value measured in NVP/diacrylate polymerization systems for conversions greater that 0. 2. (White, Liechty and Guymon 2007; Kizilel 2010) It was also considered that termination rate constants for PEG-DA and acrylate-PEG-GLP-1, k_{t22} and k_{t33}, are proportional with k_{p22} and k_{p33} respectively, with a proportionality constant of 30, as was measured previously. (Anseth, Wang and Bowman 1994; Anseth, Wang and Bowman 1994) The dependence of termination and propagation rate constants of VP on its concentration have also been incorporated into the model. VP is a common reactive diluent to photopolymerizable formulations, and is known to reduce the inhibition of free radical photopolymerization by atmospheric oxygen. It has been observed that for up to 45 double bond % NVP concentrations, NVP/diacrylate polymerizations are faster than that of bulk polymerizations of diacrylate. As a result of

positive contribution of VP on polymerization rates, thicker membranes were obtained as VP concentration in the prepolymer solution is increased.

The comparison of thicknesses for 25 % (w/v) PEG-DA condition ([acrl-PEG-GLP-1] = 14. 8 μM, [TEA]=225 mM) is illustrated in Figure 1 as thickness versus VP concentration for a total polymerization time of 150 seconds, where squares represent experimental measurements and line represents model simulation. As shown in Figure 1, a thickness of about 60 μm was reached at around 150 seconds of photopolymerization for a VP concentration of 37 mM. The thickness of the hydrogel membrane measured for the 25% (w/v) PEG-DA condition increases with VP concentration duration and reaches a limiting value of about 110 μm at around 592 mM VP concentration and becomes stationary at 110 μm at 592 mM VP for 150 seconds of polymerization time (Figure 1).

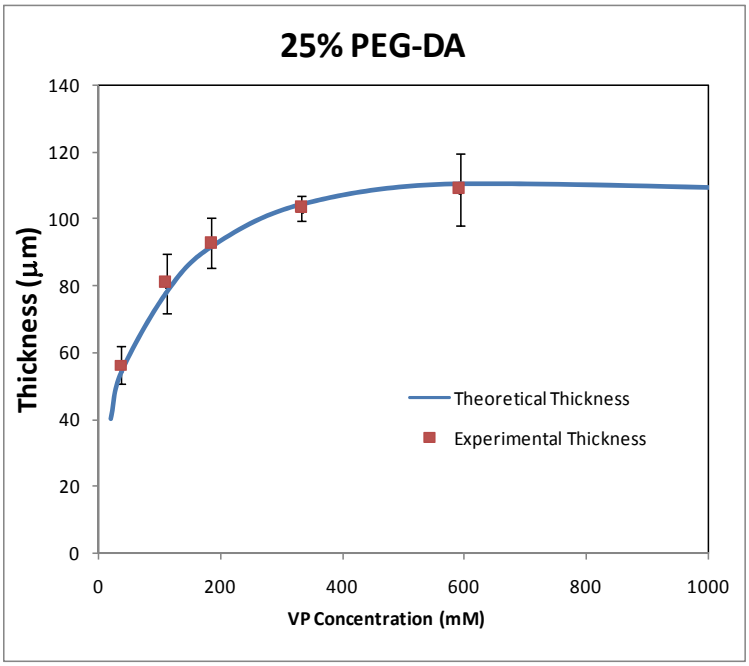

Fig. 1. The thickness of GLP-1 functionalized PEG hydrogel membrane versus VP concentration ([TEA]=225 mM, [acrl-PEG-GLP-1=14. 8 μM, photopolymerization time=150 seconds), and 25% PEG-DA in prepolmer solution. Squares denote experimental measurements and line represents model simulation.

The growth profile of the hydrogel membrane for various PEG-DA concentrations also demonstrated that increasing the concentration of PEG-DA in the prepolymer solution resulted in the formation of thicker membranes (Figure 2). The fact that the thickness of the resulting hydrogel was increased as the amount of PEG-DA in the precursor solution increased was consistent with previous observations. (Cruise, Hegre, Scharp and Hubbell 1998; Kizilel, Perez-Luna and Teymour 2006) The effect of PEG-DA concentration on thickness shows that, increasing PEG-DA concentration from 15% to 40 % (w/v) increases the membrane thickness by 40 μm for a total laser exposure time of 150 seconds ([acrl-PEG-GLP-1] =14. 8 μM, [TEA]=225 mM, [VP]=37 mM) (Figure 2).

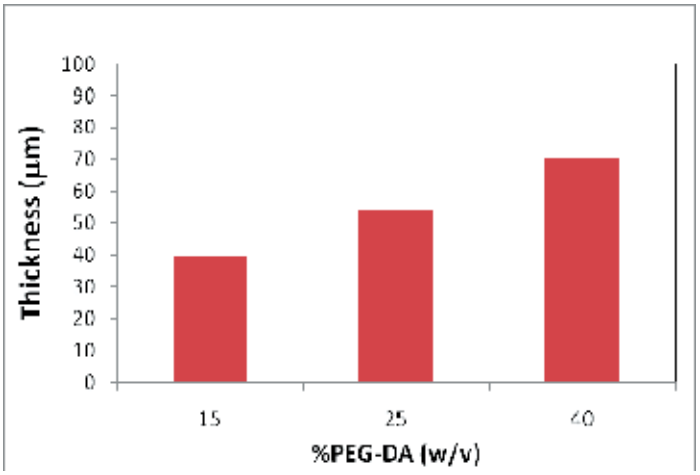

Fig. 2. Effect of % (w/v) PEG-DA in prepolymer on the thickness of GLP-1 functionalized PEG hydrogel membrane ([TEA]=225 mM, [acrl-PEG-GLP-1=14. 8 µM)

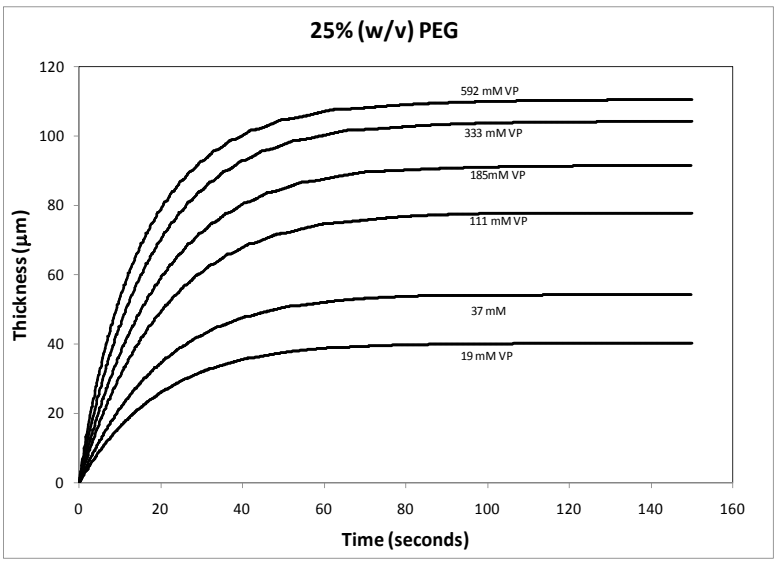

Fig. 3. Effect of concentration changes of VP on the thickness of GLP-1 functionalized PEG hydrogel membrane ([TEA]=225 mM, [acrl-PEG-GLP-1=14. 8 µM), and 25% (w/v) PEG-DA in prepolmer solution.

For all the conditions studied, the thickness of the hydrogel membrane increases rapidly with time during the early stages of photopolymerization, and then saturates to the maximum value (Figure 3). Therefore, once the saturation thickness is obtained, longer photopolymerization times would not result in higher membrane wall thickness. This was explained by the limited diffusion of photoinitiator through the newly formed hydrogel membrane. Higher thicknesses achieved for higher photoinitiator concentrations condition is caused by the formation and diffusion of more radical fragment (R_{in}) through the hydrogel membrane, which increases total amount of polymer (hydrogel) in the medium.

In addition to the comparison of thicknesses of the model and experiments, swelling experiments were used to confirm the capability of the model to capture dynamic features of experiments. Swelling ratios for 25% (w/v) PEG-DA concentration ([acrl-PEG-GLP-1] = 14. 8 μM, [TEA]=225 mM) and VP concentrations within the range of 19-592 mM is compared with the dimensionless crosslink density of the model (Figure 4). Crosslink density is a physical property related to the permeability of hydrogel. Therefore, high crosslink densities indicate that the permeability and swelling ratio of the hydrogel is low, whereas hydrogels with higher permeabilities and swelling ratios have lower crosslink densities. As shown in Figure 4, inverse of the swelling ratio has similar trend with the dimensionless crosslink density versus VP concentration. Both crosslink density and inverse of the swelling ratio increase up to a VP concentration of 185 mM, and VP concentrations beyond 185 mM does not increase the crosslink density and swelling ratio further. The comparisons of the results obtained for both thickness and swelling ratio proves that the model is valid to predict the thickness and permeability trends of this biofunctional PEG hydrogel polymerization process.

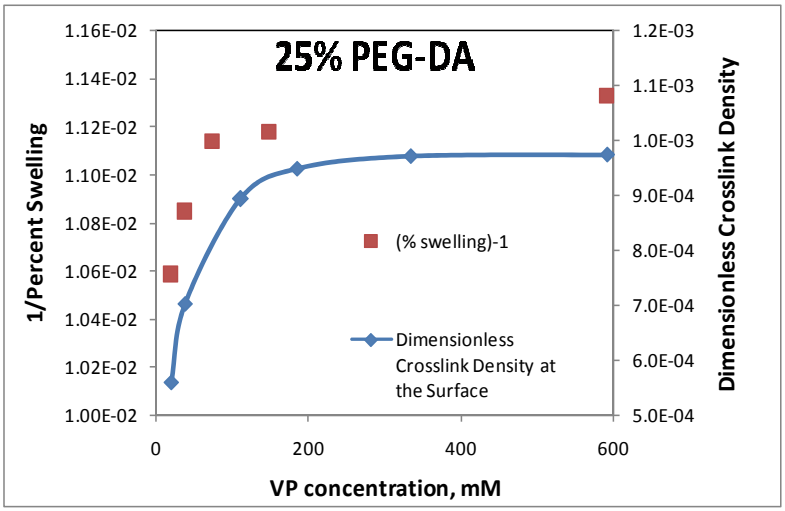

Fig. 4. Comparison of the dimensionless crosslink density of GLP-1 functionalized PEG hydrogel membrane and inverse of experimental swelling ratio versus VP concentration for 25% PEG-DA in prepolmer solution. ([TEA]=225 mM, [acrl-PEG-GLP-1=14. 8 μM, photopolymerization time=150 seconds) Squares denote experimental measurements and line represents model simulation.

Effects of VP and PEG-DA Concentrations on Crosslink Density. Crosslink density is an important property of PEG hydrogels, and is related to the permeability of the membrane. Membranes with higher the values of crosslink densities will be less permeable. The overall crosslink density (i. e. that for the membrane as a whole) was described earlier, and is defined as the ratio of QBP balance (F_1) to the first moment of dead polymer chains (Q_1), expressed as:(Kizilel, Perez-Luna and Teymour 2006)

$$\rho = \frac{[F_1]}{[Q_1]} \tag{33}$$

Highly crosslinked membranes (membranes with lower permeability and high mechanical strength) were obtained, as the concentration of VP in the precursor solution was increased. In our recent study for the modeling of biofunctional PEG hydrogel, propagation rate coefficient (k_{p11}) and termination rate coefficient (k_{tc11}), which were inversely proportional with the concentration of VP, were expressed as a function of VP concentration. The swelling measurements in that study also confirmed the positive effect of VP on crosslink density (Figure 4). The observed and predicted increases in crosslink density as a function of VP concentration was a direct result of increased acrylate conversion, as was observed by White et al. (White, Liechty and Guymon 2007). The increase of VP concentration influences crosslink density as a result of increase in the rate of polymerization. It has been shown in previous studies that significant differences in the polymerization rates would be observed with incorporation of VP, and that in VP/diacrylate polymerization systems adding VP increases polymerization rate. (White, Liechty and Guymon 2007) Furthermore, copolymerization of VP with acrylates can significantly increase the overall conversion of a crosslinked acrylate polymer, which can influence the crosslink density and thermomechanical properties. The results obtained in the recent study by Kızılel also emphasize that using optimal amounts of VP in the prepolymer solution allow significant increase in the crosslink density, and improvement in properties. Above a critical VP concentration (~185 mM), the influence of mono-vinyl monomer, VP, on hydrogel crosslink density was not observed; probably due to the maximum acrylate conversion achieved around 185 mM VP (Figure 5). The observed increases in crosslink densities were a direct result of increases in acrylate conversion, and above a critical concentration, the effect of VP, mono-vinyl monomer, on conversion was not sufficient to increase crosslink density further. The effect of VP concentration on crosslink density is illustrated in figure 5. As shown, the capsule crosslink density decreases with location for all the cases studied. This also shows that the capsule crosslink density decreases with membrane location moving from cell surface to membrane surface. The presence of gradient in crosslink density is a unique feature of this mathematical model and would be very difficult to obtain experimentally. Thus, this model could help design better transport properties and/or surface properties (polymer brush at the hydrogel-liquid interface) for these interfacially photopolymerized hydrogels. It was also observed that the crosslink densities will be higher for membranes obtained for higher PEG-DA concentration in the prepolymer. The lower crosslink densities obtained for the lower PEG-DA concentration (15 % (w/v)) was consistent with previous predictions of Kızılel et al. ,(Kizilel, Perez-Luna and Teymour 2006) and other studies, (Cruise, Hegre, Scharp and Hubbell 1998) and was explained by the presence of lower number of bi-functional monomers compared to the higher (25 and 40 % (w/v)) PEG-DA conditions. The fact that increasing PEG-DA concentrations decreased permeabilities of proteins implies that higher concentrations of PEG-DA in the prepolymer increases crosslink density, and that this result is consistent with the simulation results of this study. Lower concentration of bifunctional monomer results in a less branched and hence, less crosslinked structure. This result also emphasizes that, by increasing PEG-DA concentrations in the prepolymer solution, one would obtain membranes with higher crosslink densities and higher mechanical strength, which would mean lower membrane permeability.

Effects of VP and PEG-DA Concentrations on GLP-1 Incorporation. Incorporation of peptides to develop bioactive PEG hydrogels is an archetypal engineering problem, which requires the control of physical and chemical properties. In order to develop a functional extracellular matrix mimic, hydrogel crosslink density or mechanical properties,

incorporation of peptides, thickness of the membrane, and transport kinetics must be tuned effectively. (Griffith and Naughton 2002; Saha, Pollock, Schaffer and Healy 2007)

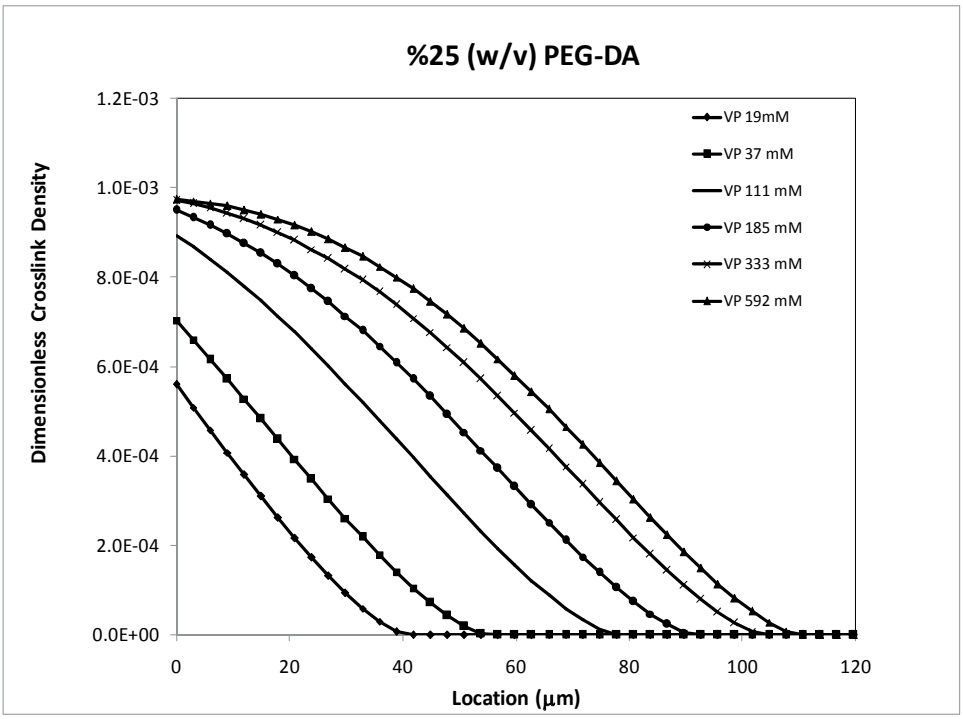

Fig. 5. Effect of concentration changes of VP on the dimensionless crosslink density versus location of GLP-1 functionalized PEG hydrogel membrane ([TEA]=225 mM, [acrl-PEG-GLP-1=14. 8 μM), 25% (w/v) PEG-DA in prepolmer solution.

GLP-1, a potent incretin hormone produced in the L cells of the distal ileum, stimulates insulin gene transcription, islet growth, and neogenesis. (MacDonald, El-kholy, Riedel, Salapatek, Light and MB 2002) Therefore, when GLP-1 is immobilized within the PEG hydrogel capsule around the islet, insulin secretion in response to high glucose levels was expected to increase, thereby reducing the number of islets required to normalize blood glucose of a diabetic patient, and improving the insulin secretion capability of microencapsulated islets. Recently, it was shown that, GLP-1 coated islets exhibited a higher response to glucose challenge, in terms of insulin secretion, compared to the untreated islets *in vitro*. (Kizilel, Scavone, Liu, Nothias, Ostrega, Witkowski and Millis 2010) This suggested that similar effect could be observed when GLP-1 is immobilized within the PEG hydrogel capsule around the islet. Therefore, it was important to design PEG hydrogel coatings with high GLP-1 concentrations at points closer to the surface in the case of islet microencapsulation within PEG hydrogel. This should allow interaction of GLP-1 with its receptor on insulin secreting β-cells, which will subsequently stimulate insulin secretion in response to high glucose. Therefore, the mathematical model developed, included acrl-PEG-GLP-1 as the third monomer of the polymerization process, due to the presence of acrylate group in the acrl-PEG-GLP-1 conjugate structure. As a result, the concentration of GLP-1 within the PEG hydrogels as a function of photopolymerization time or membrane location

for different PEG-DA or VP concentrations could be predicted. Figure 6 illustrates the variation of GLP-1 concentration with location at the photopolymerization time of 150 seconds for various VP and PEG-DA concentrations. As shown, GLP-1 concentration decreases with location for all the conditions studied, as a result of gradient in monomer conversion. For 25 % PEG-DA in the prepolymer, the profile extends to further points at higher VP concentrations due to the fact that higher thicknesses obtained at higher VP concentrations (Figure 6). The presence of gradient of GLP-1 is a unique feature of this mathematical model, and surface initiated polymerization, and would be very difficult to characterize experimentally. Incorporation of GLP-1 within a biofunctional PEG hydrogel could be done via radiolabeling experiments for the case of bulk polymerization, however for the case of surface initiated polymerization, characterization of GLP-1 concentration versus hydrogel location would be an experimental challenge. Therefore, theoretical prediction of peptide concentrations (GLP-1 in this case) within a biofunctional PEG hydrogel formed via surface initiated polymerization is clearly an advantage in this field. The presence of GLP-1 gradient would also allow efficient localization of the peptide to the islet surface, and hence may result in increased possibility of the peptide's interaction with its receptor to enhance insulin secretion.

7. Modeling of PEG hydrogel membrane based on numerical fractionation technique:

The mathematical models for PEG hydrogel membranes mentioned in the previous section was developed based on the method of moments along with the pseudo-kinetic rate constant approach. (Hamielec and MacGregor 1983; Kizilel, Perez-Luna and Teymour 2009) As presented, the method of moments reduced the number of equations to be solved, and zeroth and first moments of dead polymer chains were calculated in order to determine the crosslink density of the overall hydrogel. However, in nonlinear polymerizations systems where the polymer chain branching and/or crosslinking lead to the formation of a gel phase, the second and higher molecular weight moments diverge at the gel point. Thus a numerical solution past the gel point cannot be carried out into the post gel regime. In this study, in order to obtain a numerical solution past the gel point, we used the Numerical Fractionation (Teymour and Campbell 1994; Kizilel, Perez-Luna and Teymour 2009) (NF) technique, which refers to the numerical isolation of various polymer generations based on the degree of complexity of their microstructure. NF utilizes the kinetic approach but is based on a "variation" of the classical method of moments and is a powerful method to describe and model polymerization systems that result in gel formation. The technique has been used by various researchers to model different nonlinear polymerization systems. (Kizilel, Papavasiliou, Gossage and Teymour 2007; Arzamendi and Asua 1995; Kizilel 2004) The NF technique segregates the polymer into two distinct phases, a soluble (sol) phase and a gel phase. Modeling the sol phase and isolating the gel phase allows for the determination of the polymer properties such as, the gel point, and the reconstruction of the polymer molecular weight distribution (MWD). Isolation of the sol from the gel makes it possible to predict polymer properties in the post-gel region. Furthermore, the sol fraction is subdivided into generations that are composed of linear and branched polymer chains. The basic assumption of the NF technique is that gel is formed via a geometric growth mode present in the reacting system. Linear polymerization will not lead to gel formation. In order for gel formation to occur, a re-initiation reaction has to be coupled to a reaction in

which two radical chains join, such as termination by combination or having a radical react through a pendant double bond. The geometric growth mode applies specifically to the generations. Rules that govern the transfer from one generation to the next are as follows: Transfer to first generation occurs through a branching (e. g. chain transfer to polymer) or crosslinking reaction (reaction through a pendant double bond). The resulting polymer can keep adding linear polymer chains, but still belong to the first generation. Transfer to second generation will occur if two first generation molecules combine, e. g. through termination by the combination of two radicals or having a radical react through a pendant double bond. A polymer molecule belonging to the second generation can keep adding more linear or first generation branched polymer, but will only transfer to third generation when it combines with another second generation molecule. Combination of molecules belonging to different generations will result in the combined molecule belonging to the higher generation (Scheme 3).

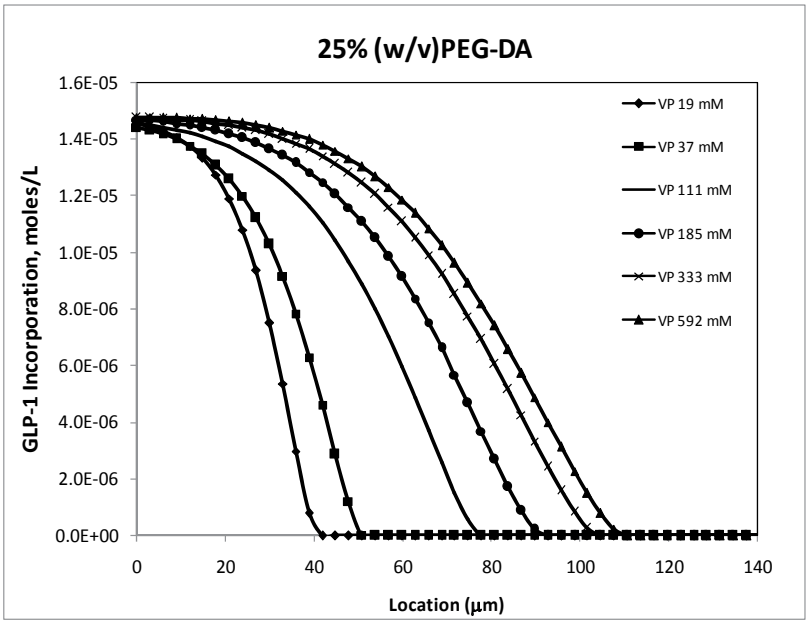

Figure 6. Effect of concentration changes of VP on the GLP-1 incorporation within the hydrogel versus location of GLP-1 functionalized PEG hydrogel membrane ([TEA]=225 mM, [acrl-PEG-GLP-1=14. 8 μM) 25% (w/v) PEG-DA in prepolmer solution.

The application of the NF technique for the process of PEG-DA hydrogel formation on substrate surfaces through interfacial photopolymerization was the first instance of the previous applications which involved homogeneously mixed systems with no spatial distribution. The application of this technique to dynamic membrane growth allowed the prediction of spatial profiles for the gel fraction, molecular weight properties, composition and crosslink density. Insight obtained from the model was also used to propose methodologies for the design of membranes with predetermined property profiles, such as progression through gelation, gelation time, crosslink density of the gel and soluble phases, degree of gel and sol fraction that might lead to advanced applications in biosensors and tissue engineering.

The authors used similar kinetic mechanism in the NF model, where they considered the polymerization system consisting of initiation, propagation, chain transfer to TEA, radical termination by combination and reaction through pendant double bond. (Kizilel, Perez-Luna and Teymour 2009) Chain transfer to PEG-DA (and hence to polymer) would provide an additional branching mechanism, which was not considered in the model development. It was also assumed that the terminal model of copolymerization was applicable and termination by disproportionation was not included. The copolymerization of *A (VP)* and *B (PEG-DA)* was considered, and the symbols A_{ijkl} or B_{ijkl} were used to indicate the type of monomer unit at the chain end identity of the propagating radical, where the four subscripts represented respectively the generation, the total chain length of each radical (live) and dead polymer, the number of unreacted pendant double bonds (PDB), and the number of quaternary branch points (QBP).

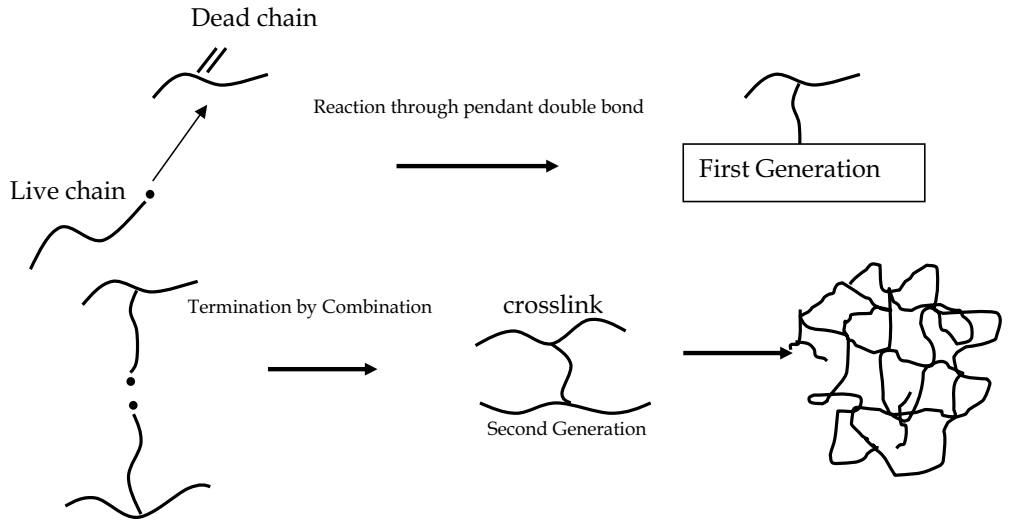

Scheme 3. Reactions leading to gel formation.

Initiation:
In this step the initiator radical (R_{in}), which is also called α-amino radical in this system, forms as a result of its reaction with eosin Y and reacts with the monomers to form live radicals of length one.

$$Y_{ac} \Leftrightarrow Y^* \qquad \nu K \tag{34}$$

$$Y^* + C_{TEA} \rightarrow Y_{in} + R_{in}\bullet \qquad k_f \tag{35}$$

$$R_{in}\bullet + A \rightarrow A_{0100}\bullet \qquad k_{i1} \tag{36}$$

$$R_{in}\bullet + B \rightarrow B_{0110}\bullet \qquad k_{i2} \tag{37}$$

where $\nu K = \nu \frac{k_1}{k_{-1}}$, K is the equilibrium constant for excitation and, νK represents the amount of excitation radiation absorbed by eosin Y molecules. Thus, ν would take into account the

intensity of the light source because an increase of excitation intensity would result in a larger number eosin molecules excited to the triplet state.

Propagation

Propagation of the two monomers, *A (VP)* and *B (PEG-DA)* leads to two types of propagating species, one with *A* at the propagating end and the other with *B*. These are represented by A• and *B*•. This classification is made because the reactivity of the propagating species is dependent on the monomer unit at the end of the chain. (Dotson, Galvan, Laurence and Tirrell 1996; Scott and Peppas 1999) Radical chains of length j react by adding monomer units to the polymer chain to form longer radical chains of length j+1 according to the following mechanism:

$$A_{ijkl}\bullet + A \rightarrow A_{i,j+1,k,l}\bullet \; k_{p11} \tag{38}$$

$$A_{ijkl}\bullet + B \rightarrow B_{i,j+1,k+1,l}\bullet \; k_{p12} \tag{39}$$

$$B_{ijkl}\bullet + A \rightarrow A_{i,j+1,k,l}\bullet \; k_{p21} \tag{40}$$

$$B_{ijkl}\bullet + B \rightarrow B_{i,j+1,k+1,l}\bullet \; k_{p22} \tag{41}$$

Termination:

Termination by combination reaction leads to the formation of longer dead polymer chains. Termination by combination reaction must be taken into account because it also leads to branching and gelation.

$$A_{ijkl}\bullet + A_{opqr}\bullet \rightarrow P_{i',j+p,k+q,l+r}\bullet \; k_{tc11} \tag{42}$$

$$A_{ijkl}\bullet + B_{opqr}\bullet \rightarrow P_{i',j+p,k+q,l+r}\bullet \; k_{tc12} \tag{43}$$

$$B_{ijkl}\bullet + B_{opqr}\bullet \rightarrow P_{i',j+p,k+q,l+r}\bullet \; k_{tc22} \tag{44}$$

Chain Transfer to TEA

The radicals can also react with the chain transfer agent, TEA. In this case the growing radical is transferred to TEA, which hinders the growth of a polymer chain while at the same time generating a free radical capable of starting the growth of another polymer chain as follows:

$$A_{ijkl}\bullet + TEA \rightarrow P_{ijkl} + R_{in}\bullet \; k_{tr1} \tag{45}$$

$$B_{ijkl}\bullet + TEA \rightarrow P_{ijkl} + R_{in}\bullet \; k_{tr2} \tag{46}$$

Reaction through a Pendant Double Bond:

When a newly formed radical reacts through a pendant double bond, a quaternary branch point is created.

$$A_{ijkl}\bullet + P_{opqr} \rightarrow B_{i',j+p,k+q,l+r-1}\bullet \; k^*_{p12} \tag{47}$$

$$B_{ijkl}\bullet + P_{opqr} \rightarrow B_{i',j+p,k+q,l+r-1}\bullet \; k^*_{p22} \tag{48}$$

The mathematical model was developed by formulating population balances on each species in the system, which included: the live and dead polymer chains for the overall polymer, linear polymer chains and subsequent polymer generations. A set of moments was then applied to the above mentioned species. The quasi-steady state approximation was applied to all radical species. The pseudo-kinetic rate constant equations, moment equations, boundary conditions, and membrane thickness equations were similar to the model developed for biofunctional PEG hydrogel membrane, which was mentioned in the previous section. The moments were derived from the population balances using the NF technique. (Kizilel, Perez-Luna and Teymour 2009)

Crosslink Density and Crosslink Density Distribution

NF offers the unique capability of following the evolution of moment equations for each generation in both the pre-gel and post-gel regimes. The crosslink density of a polymer chain is defined as the fraction of units on that chain that contains quaternary branch points. In the systems that gel, the gel has a higher crosslink density than the sol. In the NF model, five types of crosslink densities were considered: the overall crosslink density (i. e., that for the polymer as whole), the crosslink density of each generation, the crosslink density of the sol, the crosslink density of the branched sol, and the crosslink density of the gel.

Figure 7 displays crosslink density versus time for each generation 1-10 (linear polymer has a crosslink density of zero and belongs to the zeroth generation), at the islet surface, for the surface initiated photopolymerization of PEG-DA. The geometric growth mechanism by which the generations were defined by the NF technique, explains the reason behind the collapse of the crosslink density curves for the higher generations onto a single curve. The collapse also demonstrates that in a polymerizing system, the intensive properties of the higher molecular weight molecules tend towards the same value.

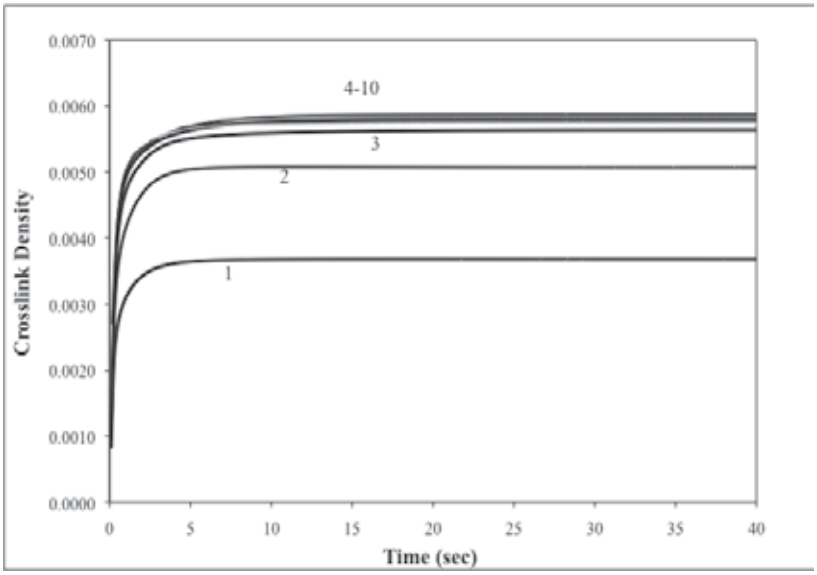

Fig. 7. Average crosslink density for each generation versus time at the cell surface (x=0 μm)

In addition to the crosslink density definitions given for each generation and for the overall polymer, NF technique was used to calculate crosslink densities for the sol (r_S), the branched sol (r_B), and the gel (r_G) which are defined by the following equations:

Crosslink density of the sol:

$$\rho_S = \frac{\sum_{i=1}^{n_C} F_{i,1}}{\sum_{i=1}^{n_C} Q_{i,1}} \tag{49}$$

Crosslink density of the branched sol:

$$\rho_B = \frac{\sum_{i=1}^{n_C} F_{i,1}}{\sum_{i=1}^{n_C} Q_{i,1}} \tag{50}$$

Crosslink density of the gel:

$$\rho_G = \frac{F_1 - \sum_{i=1}^{n_C} F_{i,1}}{Q_1 - \sum_{i=0}^{n_C} Q_{i,1}} \tag{51}$$

where, n_c is the highest generation modeled as sol. Figure 8 displays the crosslink densities of the sol, the branched sol, the gel, and overall polymer versus time for the process of hydrogel formation through surface initiated photopolymerization of PEG-DA at various membrane locations. As it is shown in the figure, crosslink densities of the sol (r_S) and the overall polymer (r) coincide up to the gel point. After the gel point, r continues to increase while r_S decreases due to the preferential loss of the larger sol molecules to the gel. The reason for the saturation behavior of the gel phase and stationary profile for the branched sol phase is due to the consumption of PEG-DA monomer. Initially PEG-DA concentration is equal to its bulk value at all points, however, once the membrane starts to grow away from the surface, PEG-DA (monomer B) cannot diffuse through the membrane, only VP can. So, the total number of unreacted pendant double bonds continually decreases and at this point only growth mechanism available is propagation with VP (monomer A). This explains the saturation of overall and gel crosslink density.

8. Other mathematical models developed for PEG hydrogel membranes

In the design of hydrogels for biomedical applications controlling the swelling ratio, diffusion rate, and mechanical properties of a crosslinked polymer is important, where each of these factors depends strongly on the degree of crosslinking. Primary cyclization occurs when a propagating radical reacts intramolecularly with a pendant double bond on the same chain, and decreases the crosslinking density which results in an increase in the molecular weight between crosslinks. The extent of primary cyclization is strongly affected by solvent concentration. Elliott *et al.* investigated the effect of solvent concentration and comonomer composition on primary cyclization using a novel kinetic model and experimental measurement of mechanical properties for crosslinked PEG hydrogels. (Elliott,

Anseth and Bowman 2001) The authors investigated two divinyl crosslinking agents, diethyleneglycol dimethacrylate (DEGDMA) and polyethyleneglycol 600 dimethacrylate (PEG(600)DMA), and each was copolymerized with hydroxyethyl methacrylate (HEMA) and octyl methacrylate (OcMA). The model was further used to predict the gel point conversion and swelling ratio of PAA hydrogels polymerized in the presence of varying amounts of water. Model results showed that increasing the solvent concentration during the polymerization increases the molecular weight between crosslinks by nearly a factor of three, and doubles the swelling ratio. Furthermore, experimental results provided quantitative agreement with model predictions. The model was developed and solved the differential kinetic equations accounting for the difference in reactivity of the pendant double bonds spatially and during the polymerization. In order to capture the local dynamics and reactivity of the pendant double bonds, monomeric and pendant double bonds were tracked separately. Based on the kinetic expression for a bimolecular collision, (the kinetic parameter k_p times the concentrations of monomeric double bonds and radical species in bulk solution [R_b]) the rate of consumption of monomeric double bonds was calculated. The bulk radicals [R_b] concentration was calculated using the pseudo-steady-state assumption. When a multifunctional monomer is consumed, a pendant double bond is created, which can react either by crosslinking or cyclization (Scheme 4).

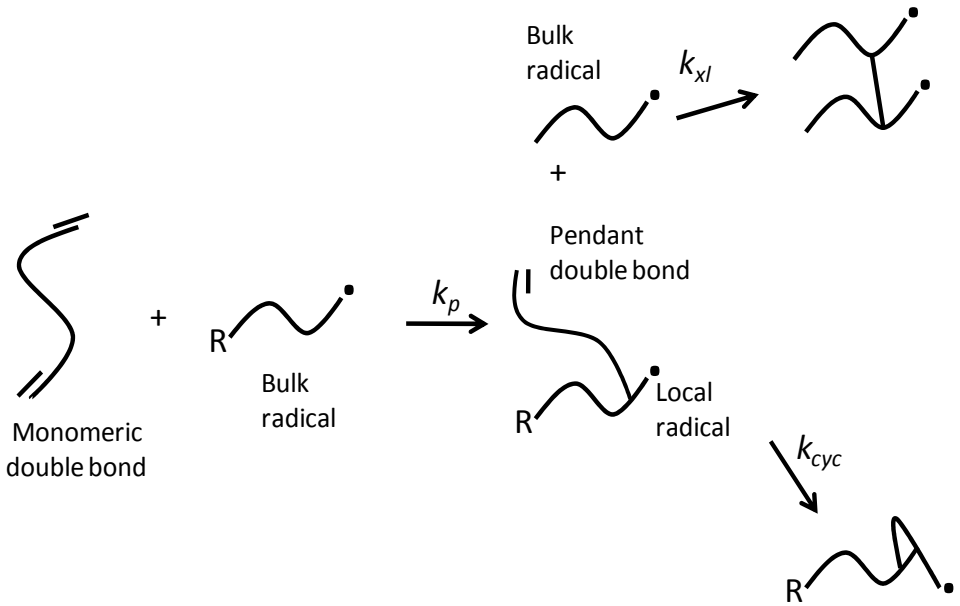

Scheme 4. Monomeric and pendant double bond reaction mechanism.

Both of these two mechanisms of propagation of pendant double bonds (R_{pen}) were considered in the model: the reaction of pendant double bonds with the radical on the same propagating chain (local radicals) to form cycles and the reaction of pendant double bonds with bulk radicals to form crosslinks. Secondary cycles were considered as equivalent to crosslinks. The difference in reactivity of the two competing mechanisms was also incorporated into the apparent radical concentrations relevant to the crosslinking and cyclization reactions.

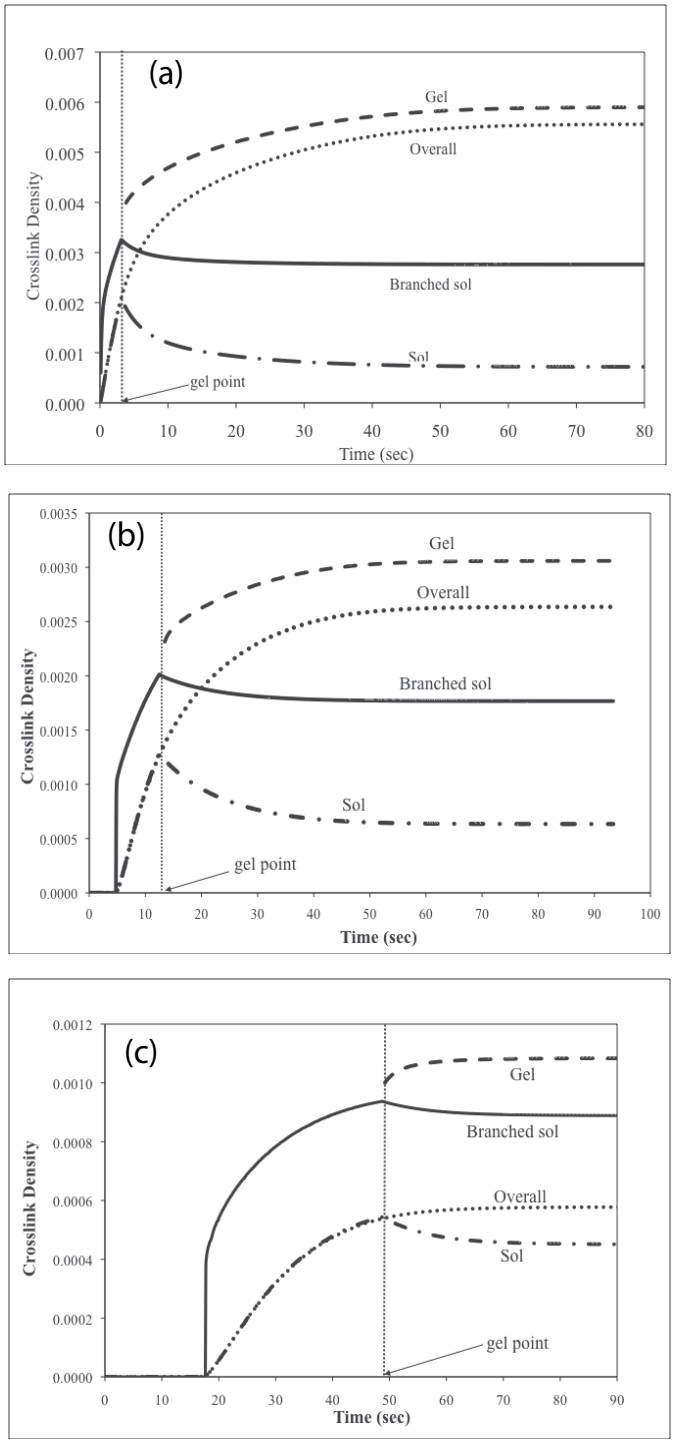

Fig. 8. Crosslink density for the sol, gel, branched sol, overall hydrogel versus time (a) at the cell surface (x=0 μm), (b) at x=56 μm, (c) at x=126 μm.

It is important to form degradable hydrogels having controlled network structure for applications related to both drug delivery and tissue engineering. Even though significant advances have occurred, these applications still cannot reach full potential without the availability of materials with tunable degradation behavior. To this end, Anseth and Bowman group developed thiol–acrylate degradable networks, which provided a simple method for forming degradable networks having specific degradation profiles. (Reddy, Anseth and Bowman 2005) These degradable thiol–acrylate networks were formed from copolymerizing a thiol monomer with PLA-b-PEG-b-PLA based diacrylate macromers (Scheme 5). The authors also developed a theoretical model to describe the kinetic chain length distribution, the bulk degradation behavior, and the reverse gelation point of these thiol–acrylate hydrogels.

Thiol–acrylate polymerizations are radical reactions that proceed through a unique mixed step-chain growth mechanism. In the first step, the thiyl radical propagates through the vinyl functional group to form a carbon based radical. In the second step of the reaction, this carbon-based radical either chain transfers to a thiol to regenerate a thiyl radical, or homopolymerizes in the third step with vinyl moieties. The basic reaction mechanism for the case of vinyl moieties that do not readily homopolymerize, as in pure thiol-ene reactions, is sequential propagation-chain transfer mechanism that leads to step growth polymerization. For most thiol-ene systems, the step growth mechanism dominates over the chain growth homopolymerization of the ene monomers. (Cramer and Bowman 2001) In thiol–acrylate systems on the other hand, where the acrylic vinyl monomer undergoes significant homopolymerization, a competition exists between step growth and chain growth mechanisms. Thus, in polymerization of thiol–acrylate systems, the reaction is a combination of both chain growth and step growth polymerization mechanisms. Therefore, the network structure and the degradation behavior is controlled by the balance of these two mechanisms.

$$\left.\begin{array}{r} RS\bullet + R'CH=CH_2 \xrightarrow{k_{pS-C}} R'C\bullet H-CH_2-SR \\ R'C\bullet H-CH_2-SR+RSH \xrightarrow{k_{CT}} R'CH_2-CH_2-SR+RS\bullet \end{array}\right\}\text{Step Growth} \qquad \begin{array}{r}(52)\\(53)\end{array}$$

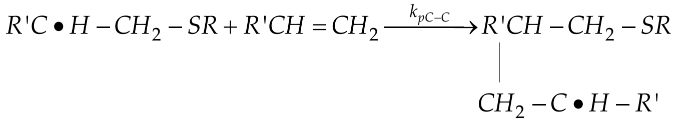

$$R'C\bullet H-CH_2-SR+R'CH=CH_2 \xrightarrow{k_{pC-C}} \begin{array}{l} R'CH-CH_2-SR \\ \;| \\ CH_2-C\bullet H-R' \end{array} \qquad \text{Chain Growth} \qquad (54)$$

In this recent study by Reddy et al, thiol functionality, as well as the relative stoichiometries of the thiol and acrylate functional groups were varied in order to control the kinetic chain length distribution and the concomitant degradation behavior of these systems. (Reddy, Anseth and Bowman 2005) The authors described theoretical bulk degradation profiles of degradable thiol–acrylate systems using modeling approaches where all the parameters were related to physically relevant aspects of the system. Since the degradation behavior was impacted by the number of crosslinks per kinetic chain,(Metters, Bowman and Anseth 2000) the kinetic chain length (KCL) distribution in these systems were first estimated. Then, the bulk degradation model based on probability and mean field kinetics were utilized to predict the degradation phenomena of the model thiol–acrylate degradable networks. It was shown that the KCL, and hence number of crosslinks per chain, were shown to decrease with increasing thiol concentration or decreasing thiol functionality, which could allow a

control on the network evolution and degradation behaviour. This approach is also applicable to other crosslinked, bulk degradable hydrogel networks that are formed through mixed step-chain polymerizations.

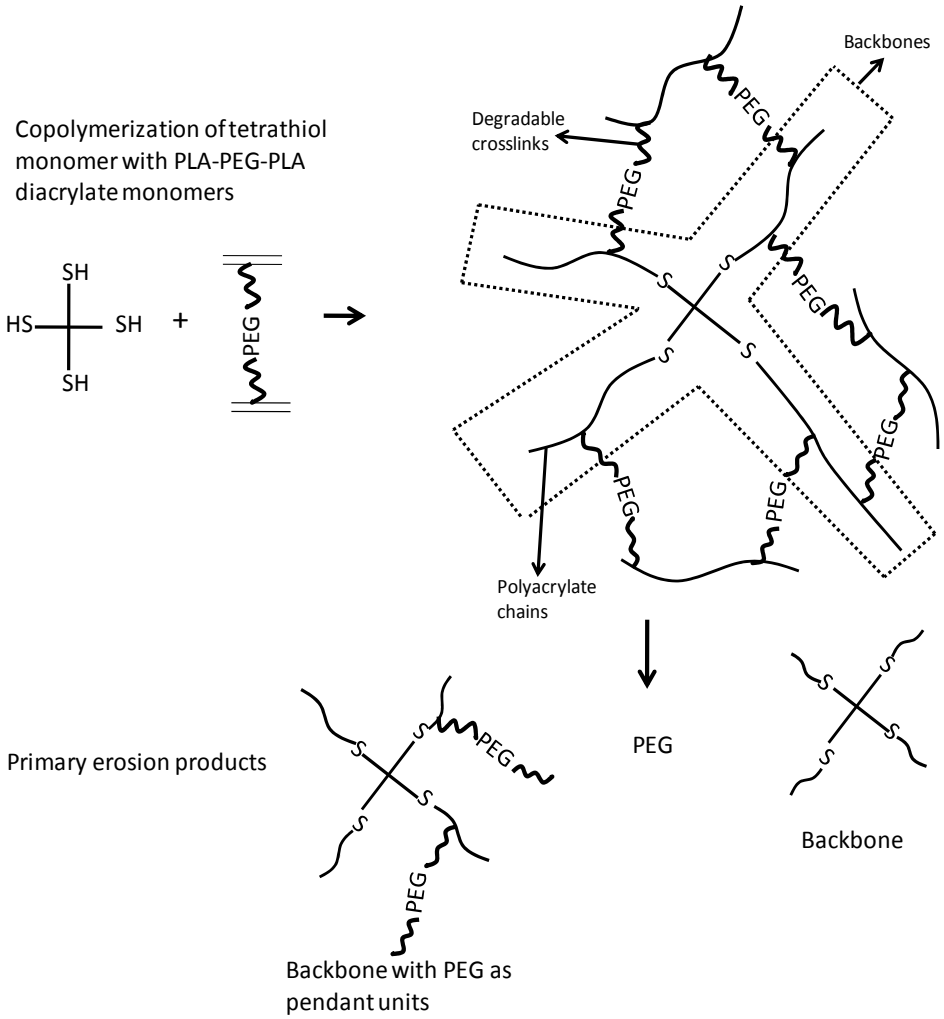

Scheme 5. Network formation of thiol–acrylate hydrogels and their subsequent degradation. The degradable polylactide units are represented as ~~~.

Despite the possibilities that exist for tuning the degradation of hydrolytically degradable gels, it is still impossible to predict exact degradation rate required for a specific cell source. Even though the degradation profile can be adjusted by addition of small amounts of macromonomers with longer or shorter PLA repeat units, the control that this allows over hydrogel degradation does not necessarily solve any problems associated with different rates of ECM production by different cell sources. One possible solution could be to replace PLA blocks with a block whose degradation depends on the concentration of a particular catalyst, then it might be possible to degrad the gel at a certain rate or not at all. This degradation could be tuned by the delivery of an enzyme released by the cells encapsulated

in the gel, which may correspond to the temporal development of ECM. In the study of Rice et al. hydrogels were synthesized by photopolymerization of a dimethacrylated tri-block copolymer, polycaprolactone-*b*-poly(ethylene glycol)-*b*-polycaprolactone (PEG-CAP-DM) macromonomers, where the crosslinks were degradable by a lipase enzyme. (Rice, Sanchez-Adams and Anseth 2006) The authors monitored the mass loss of these gels in the presence or absence of lipase, and compared this loss to the model predictions using a Michaelis-Menten derived kinetic model of reaction rate, coupled with a statistical aspect gleaned from structural information. It was observed that the rate of degradation, which was characterized by mass loss and mechanical testing, depended on both the number of repeat units in the cap blocks and also on the concentration of the active lipase enzyme. The model was developed to describe the mass loss in these materials, starting from reactions associated with classical enzyme kinetics and a simplified statistical adaptation of degradation in the gel network.

Besides, predicting the thickness and crosslink density of properties of PEG hydrogels for the purpose of immunoisolation barriers, the rational design of the hydrogel membranes require an understanding of protein diffusion and how alterations to the network structure affect protein diffusion. In order to address this need, Weber *et al.* studied the the diffusion of six model proteins with molecular weights ranging from 5700 to 67,000 g/mol through hydrogels of varying crosslinking densities, which were formed via the chain polymerization of dimethacrylated PEG macromers of varying molecular weight. (Weber, Lopez and Anseth 2009) Next, the diffusion coefficients for each protein/gel system that exhibited Fickian diffusion were estimated, using the release profiles of these proteins through these hydrogel membranes. Authors used the diffusion coefficients calculated using the Stokes-Einstein equation as a rough approximation for comparison with experimentally derived diffusion coefficients for proteins in hydrogels of varying crosslinking density. Insulin diffusivity was reduced by approximately 40% in the PEG gels with the lowest crosslinkable bond concentration and up to 60% in PEG gels with the highest concentration, when compared to the approximate diffusion coefficient in solution predicted by the Stokes–Einstein equation:

$$D_0 = \frac{kT}{6\pi\eta R_s} \tag{55}$$

The diffusion coefficients of larger proteins, such as trypsin inhibitor and carbonic anhydrase, on the other hand were decreased to approximately 10% of that in aqueous solution. The equation that correlates the diffusion coefficient of a given solute through a gel network (D_g) relative to that of the solute in solution (D_o) demonstrates that the diffusion is dependent on the solute radius (r_s) relative to a crosslinked network characteristic length (ξ) and the equilibrium water content of the hydrogel network, which is described as the polymer volume fraction in the gel (v_2):

$$\frac{D_g}{D_o} = \left(1 - \frac{r_s}{\xi}\right)\exp\left(-Y\left(\frac{v_2}{1-v_2}\right)\right) \tag{56}$$

where Y is the ratio of the critical volume required for a successful translational movement of the solute to the average free volume per liquid molecule and it is usually taken as 1, and v_2 is the inverse of the equilibrium swelling ratio (Q). The authors observed that the

diffusion coefficients were on the order of 10^{-6}–10^{-7} cm^2/s, such that protein diffusion time scales ($t_d=L^2/D$) from 0. 5-mm thick gels varied from 5 min to 24 h.

In this chapter, we introduced various approaches for modeling of PEG hydrogels for biomedical applications. The mathematical models developed for ECM-mimic of PEG hydrogels could be considered in the design of future PEG hydrogel or biofunctional PEG hydrogel systems where drugs, proteins or cells are microencapsulated within these membranes to predict the growth, crosslink density profiles, and the level of ligand incorporation. These models could also be utilized for the modulation of concentration of biological cues in highly permissive and biofunctional PEG hydrogels for optimizing engineered tissue formation.

9. References

Alcantar, N., E. Aydil & J. Israelachvili (2000) Polyethylene glycol-coated biocompatible surfaces. *J Biomed Mater Res,* 51, 343-351.

Amano, S. , N. Akutsu, Y. Matsunaga, K. Kadoya, T. Nishiyama, M. Champliaud & e. al. (2001) Importance of balance between extracellular matrix synthesis and degradation in basement membrane formation. *Exp Cell Res,* 271, 249-262.

Anseth, K. S. , C. M. Wang & C. N. Bowman (1994) Kinetic Evidence of Reaction-Diffusion during the Polymerization of Multi(Meth)Acrylate Monomers. *Macromolecules,* 27, 650-655.

Anseth, K. S. , C. M. Wang & C. N. Bowman (1994) Reaction Behavior and Kinetic Constants for Photopolymerizations of Multi(Meth)Acrylate Monomers. *Polymer,* 35, 3243-3250.

Arzamendi, G. & J. Asua (1995) Modeling Gelation and Sol Molecular Weight Distribution in Emulsion Polymerization. *Macromolecules,* 28, 7479-7490.

Aumaille, M. & N. Smyth (1998) The role of laminins in basement membrane function. *Anat*, 1-21.

Babensee, J. , L. McIntire & A. Mikos (2000) Growth factor delivery for tissue engineering. *Pharm Res,* 17, 497-504.

Badylak, S. (2002) The extracellular matrix as a scaffold for tissue reconstruction. *Semin Cell Dev Biol,* 13, 377-383.

Badylak, S. (2007) The extracellular matrix as a biological scaffold material. *Biomaterials,* 28, 3587-3593.

Bamford, C. & H. Tompa (1954) The Calculation of Molecular Weight Distributions From Kinetic Schemes. . *Trans. Faraday SOC,* 50, 1097.

Beamish, J. , J. Zhu, K. Kottke-Marchant & R. Marchant (2010) The effects of monoacrylate poly(ethylene glycol) on the properties of poly(ethylene glycol) diacrylate hydrogels used for tissue engineering. . *J Biomed Mater Res A,* 92, 441-450.

Beck, K. , I. Hunter & J. Engel (1990) Structure and function of laminin: anatomy of a multidomain glycoprotein. *FASEB*, 148-60.

Brodsky, B. & J. Ramshaw (1997) The collagen triple-helix structure. *Matrix Biol*, 545-54.

Bryant, S. , J. Arthur & K. Anseth (2005) Incorporation of tissue-specific molecules alters chondrocyte metabolism and gene expression in photocrosslinked hydrogels. *Acta Biomater* 1, 243-252.

Burdick, J. , M. Mason, A. Hinman, K. Thorne & K. Anseth (2002) Delivery of osteoinductive growth factors from degradable PEG hydrogels influences osteoblast differentiation and mineralization. . *J Control Release,* 83, 53-63.

Buxton, A. , J Zhu, R. Marchant, J. West, J. Yoo & B. Johnstone (2007) Design and characterization of poly(ethylene glycol) photopolymerizable semiinterpenetrating networks for chondrogenesis of human mesenchymal stem cells. *Tissue Eng,* 13, 2549-2560.

Cai, S. , Y. Liu, X. Zheng & G. Prestwich (2005) Injectable glycosaminoglyosaminoglycan hydrogels for controlled release of human basic fibroblast growth factor. *Biomaterials,* 26, 6054-6067.

Celse, K. , E. Poschl & T. Aigner (2003) Collagens-structure, function, and biosynthesis. *Adv Drug Deliv Rev*, 1513-46.

Chang, C. & Z. Werb (2001) The many faces of metalloproteases: cell growth, invasion, angiogenesis and metastasis. *Trends Cell Biol* 11, S37-S43.

Chen, W. , C. Chang & M. Gilson (2006) Concepts in receptor optimization: targeting the RGD peptide. *J Am Chem Soc* 128, 4675-4684.

Cheung, C. & K. A. KS (2006) Synthesis of immunoisolation barriers that provide localized immunosuppression for encapsulated pancreatic islets. *Bioconjug Chem,* 17, 1036-1042.

Cheung, C. , S. McCartney & K. A. KS (2008) Synthesis of polymerizable superoxide dismutase mimetics to reduce reactive oxygen species damage in transplanted biomedical devices. *Adv Funct Mater,* 18, 3119-3126.

Clapper, J. , J. Skeie, R. Mullins & C. Guymon (2007) Development and characterization of photopolymerizable biodegradable materials from PEG-PLA-PEG block macromonomers. . *Polymer* 48, 6554.

Cohen, M. , D. Joester, B. Geiger & L. Addadi (2004) Spatial and temporal sequence of events in cell adhesion: from molecular recognition to focal adhesion assembly. *ChemBioChem,* 5, 1393-1399.

Cramer, N. & C. Bowman (2001) Kinetics of thiol–ene and thiol–acrylate photopolymerizations with real-time fourier transform infrared. *Journal of Polymer Science Part A: Polymer Chemistry,* 39, 3311-3319.

Cramer, N. , S. Reddy, A. O'Brien & C. B. CN (2003) Thiol-ene photopolymerization mechanism and rate limiting step changes for various vinyl functional group chemistries. *Macromolecules,* 36, 7964-7969.

Cruise, G. M. , O. D. Hegre, D. S. Scharp & J. A. Hubbell (1998) A sensitivity study of the key parameters in the interfacial photopolymerization of poly(ethylene glycol) diacrylate upon porcine islets. *Biotechnology and Bioengineering,* 57, 655-665.

Cruise, G. M. , D. S. Scharp & J. A. Hubbell (1998) Characterization of permeability and network structure of interfacially photopolymerized poly(ethylene glycol) diacrylate hydrogels. *Biomaterials,* 19, 1287-1294.

Cukierman, E. , R. Pankov & K. Yamada (2002) Cell interactions with threedimensional matrices. *Curr Opin Cell Biol* 14, 633-639.

Cushing, M. & K. A. KS (2007) Hydrogel cell culture. *Science* 316, 1133-1134.

DeForest, C. , B. Polizzotti & K. A. KS (2009) Sequential click reactions for synthesizing and patterning three-dimensional cell microenvironments. *Nature Materials,* 8, 659-664.

Dotson, N. , R. Galvan, R. Laurence & M. Tirrell. 1996. *Polymerization Process Modeling*. New York: VCH Publishers.

Dudhia, J. (2005) Aggrecan, aging and assembly in articular cartilage. *Cell Mol Life Sci*, 2241-56.

Ehrbar, M. , S. Rizzi, R. Hlushchuk, V. Dionov, A. Zisch, J. Hubbell, F. Weber & M. Lutolf (2007) Enzymatic formation of modular cell-instructive fibrin analogs for tissue engineering. *Biomaterials,* 28, 3856-3866.

Ehrbar, M. , S. Rizzi, R. Schoenmakers, B. M. BS, J. H. JA, F. Weber & M. Lutolf (2007) Biomolecular hydrogels formed and degraded via site-specific enzymatic reactions. *Biomacromolecules,* 8, 3000-3007.

Elisseeff, J. , K. Anseth, D. Sims, W. McIntosh, M. Randolph & R. Langer (1999) Transdermal photopolymerization for minimally invasive implantation. *Proc Natl Acad Sci U S A,* 96, 3104-3107.

Elliott, J. , K. Anseth & C. Bowman (2001) Kinetic modeling of the effect of solvent concentration on primary cyclization during polymerization of multifunctional monomers *Chem Eng Sci,* 56, 3173-3184.

Ellis, V. & G. Murphy (2001) Cellular strategies for proteolytic targeting during migration and invasion. *FEBS Lett,* 506, 1-5.

Feldstein, M. , V. Igonin, T. Grokhovskaya, T. Lebedeva, S. Kotomin, V. Kulichikhin, N. Plate, K. Brain, V. James & K. Walters (1997) Performance of hydrophilic transdermals as an explicit function of the molecular structure of polymer matrix. *Perspectives of Percutaneous Penetration,* 5b, 228-232.

Feldstein, M. , N. Plate, T. Sohn, V. Voicu & N. R. C. c. a. f. p. f. protection (1999) A structure-property relationship and quantitative approach to the development of universal transdermal drug delivery system. *NBC Risks - Current capabilities and future perspectives for protection*, 441-58.

Feldstein, M. , V. Tohmakhchi, L. Malkhazov, A. Vasiliev & N. Plate (1996) Hydrophilic polymeric matrices for enhanced transdermal drug delivery. *Int J Pharm,* 2, 229-42.

Fisher, J. , D. Dean, P. Engel & A. Mikos (2001) Photoinitiated polymerization of biomaterials. *Annu Rev Mater Res,* 31, 171-181.

Fosang, A. , K. Last, V. Knauper, G. Murphy & P. Neame (1996) Degradation of cartilage aggrecan by collagenase-3 (MMP-13). *FEBS Lett,* 380, 17-20.

Gailit, J. & R. Clark (1994) Wound repair in the context of extracellular matrix. *Curr Opin Cell Biol* 717-25.

Giannelli, G. , J. Falk-Marzillier, O. Schiraldi, W. Stetler-Stevenson & V. Quaranta (1997) Induction of cell migration by matrix metalloprotease-2 cleavage of laminin-
5. *Science* 277, 225-228.

Girotti, A. , J. Reguera & J. Rodriguez-Cabello (2004) Design and bioproduction of recombinant multi(bio)functional elastin-like protein polymer containing cell adhesion sequences for tissue engineering purposes. *J Mater Sci Mater Med* 15, 479-484.

Gobin, A. & J. West (2003) Effects of epidermal growth factor on fibroblast migration through biomimetic hydrogels. *Biotechnol Prog* 19, 1781-1785.

Gole, T. & U. Pohl (2002) Laminin binding conveys mechanosensing in endothelial cells. *News Physiol Sci*, 166-9.

Griffith, L. G. & G. Naughton (2002) Tissue engineering - Current challenges and expanding opportunities. *Science,* 295, 1009-+.

Guidetti, G. , B. Bartolini, B. Bernardi, M. Tira, M. Berndt, C. Balduini & e. al. (2004) Binding of von Willebrand factor to the small proteoglycan decorin. *FEBS Lett,* 574, 95-100.

Haas, T. & E. Plow (1994) Integrin-ligand interactions: a year in review. *Curr Opin Cell Biol,* 6, 656-662.

Hahn, M. , M. McHale, E. Wang, R. Schmedlen & J. West (2007) Physiologic pulsatile flow bioreactor conditioning of poly(ethylene glycol)-based tissue engineered vascular grafts. . *Ann Biomed Eng,* 35, 190-200.

Halstenberg, S. , A. Panitch, S. Rizzi, H. Hall & J. Hubbell (2002) Biologically engineering protein-graft-poly(ethylene glycol) hydrogels: a cell adhesive and plasmindegradable biosynthetic material for tissue repair. *Biomacromolecules,* 3, 710-723.

Hamielec, A. & J. MacGregor. 1983. *Polymer Reaction Engineering*. New York: Hanser Publisher.

Haubner, R. , R. Gratias, B. Diefenbach, S. Goodman, A. Jonczyk & H. Kessler (1996) Structural and functional aspects of RGD-containing cyclic pentapeptides as highly potent and selective integrin avb3 antagonists. *J Am Chem Soc,* 118, 7461-7472.

Haubner, R. , W. Schmitt, G. Holzemann, S. Goodman, A. Jonczyk & H. Kessler (1996) Cyclic RGD peptides containing b-turn mimetics. *J Am Chem Soc,* 118, 7881-7891.

Heino, J. (2007) The collagen family members as cell adhesion proteins. *BioEssays,* 29, 1001-1010.

Henricks, P. & F. Nijkamp (1998) Pharmacological modulation of cell adhesion molecules. *Eur J Pharmacol* 344.

Hern, D. & J. Hubbell (1998) Incorporation of adhesion peptides into nonadhesive hydrogels useful for tissue resurfacing. *J Biomed Mater Res* 39, 266-276.

Hersel, U. , C. Dahmen & H. Kessler (2003) RGD modified polymers: biomaterials for stimulated cell adhesion and beyond. *Biomaterials,* 24, 4385-4415.

Heuts, J. P. A. , R. G. Gilbert & L. Radom (1995) A priori prediction of propagation rate coefficients in free-radical polymerizations: Propagation of ethylene. *Macromolecules,* 28, 8771-8781.

Hoffman, A. (2002) Hydrogels for biomedical applications. *Adv Drug Delivery Rev,* 43, 3-12.

Horkay, F. , P. Basser, A. Hecht, E. Geissler & 2008; 128:135103. (2008) Gel-like behavior in aggrecan assemblies. *Chem Phys*, 135103.

Houllier, L. & B. Bunel (2001) Photoinitiated cross-linking of a thiol-methacrylate system. *Polymer,* 42, 2727-2736.

Hu, B. , J. Su & P. Messersmith (2009) Hydrogels cross-linked by native chemical ligation. *Biomacromolecules,* 10, 2194-2200.

Hubbell, J. (1998) Synthetic biodegradable polymers for tissue engineering and drug delivery. *Curr Opin Solid ST M,* 3, 246-251.

Hudalla, G. , T. Eng & W. Murphy (2008) An approach to modulate degradation and mesenchymal stem cell behavior in poly(ethylene glycol) networks. *Biomacromolecules,* 9, 842-849.

Humphries, M. & P. Newham (1998) The structure of cell-adhesion molecules. *Trends Cell Biol* 8, 78-83.

Huttenlocher, A. , R. Sandborg & A. Horwitz (1995) Adhesion in cell migration. *Curr Opin Cell Biol* 7, 697-706.

Hynd, M. , J. Frampton, N. Dowell-Mesfin, J. Turner & W. Shain (2007) Directed cell growth on protein-functionalized hydrogel surfaces. *J Neurosci Methods,* 162, 255-263.

Ifkovits, J. & J. Burdick (2007) Review: photopolymerizable and degradable biomaterials for tissue engineering applications. *Tissue Eng,* 13, 2369-2385.

Jensen, L. & N. Host (1997) Collagen: scaffold for repair or execution. *Cardiovasc Res,* 33, 535-539.

Ji, J. , R. F. Childs & M. Mehta (2001) Mathematical model for encapsulation by interfacial polymerization. *Journal of Membrane Science,* 192, 55-70.

Jiang, Z. , J. Hao, Y. You, Y. Liu, Z. Wang & X. Deng (2008) Biodegradable and thermosensitive hydrogels of poly(ethylene glycol)-poly(e-caprolactone-co-glycolide)-poly(ethylene glycol) aqueous solutions. . *J Biomed Mater Res A,* 87, 45-51.

Jo, Y. , J. Gantz, J. Hubbell & M. L. MP (2009) Tailoring hydrogel degradation and drug release via neighboring amino acid controlled ester hydrolysis. *Soft Matter,* 5, 440-446.

Johansson, S. , G. Svineng, K. Wennerberg, A. Armulik & L. Lohikangas (1997) Fibronectine-integrin interactions. *Front Biosci*, 126-146.

Katz, B. , E. Zamir, A. Bershadsky, Z. Kam, K. Yamada & B. Geiger (2000) Physical state of the extracellular matrix regulates the structure and molecular composition of cell-matrix adhesions. *Mol Biol Cell,* 11, 1047-1060.

Kaufmann, D. , A. Fiedler, A. Junger, J. Auernheimer, H. Kessler & R. Weberskirch (2008) Chemical conjugation of liner and cyclic RGD moieties to a recombinant elastin-mimetic polypeptide e a versatile approach towards bioactive protein hydrogels. *Macromol Biosci,* 8, 577-588.

Khetan, S. , J. Katz & J. Burdick (2009) Sequential crosslinking to control cellular spreading in 3-dimensional hydrogels. *Soft Mater,* 5, 1601-1606.

Kizilel, S. 2004. Theoretical and Experimental Investigation for Interfacial Photopolymerization of Poly(ethylene glycol) Diacrylate. In *Biomedical Engineering*. Chicago: Illinois Institute of Technology.

Kizilel, S. (2010) Mathematical Model for Microencapsulation of Pancreatic Islets within Biofunctional PEG Hydrogel. *Macromolecular Theory and Simulations,* DOI: ((mats. 201000033)).

Kizilel, S. , G. Papavasiliou, J. Gossage & F. Teymour (2007) Mathematical model for vinyl-divinyl polymerization. *Macromolecular Reaction Engineering,* 1, 587-603.

Kizilel, S. , V. H. Perez-Luna & F. Teymour (2004) Photopolymerization of poly(ethylene glycol) diacrylate on eosin-functionalized surfaces. *Langmuir,* 20, 8652-8658.

Kizilel, S. , V. H. Perez-Luna & F. Teymour (2006) Mathematical model for surface-initiated photopolymerization of poly(ethylene glycol) diacrylate. *Macromolecular Theory and Simulations,* 15, 686-700.

Kizilel, S. , V. H. Perez-Luna & F. Teymour (2009) Modeling of PEG Hydrogel Membranes for Biomedical Applications. *Macromolecular Reaction Engineering,* 3, 271-287.

Kizilel, S. , E. Sawardecker, F. Teymour & V. H. Perez-Luna (2006) Sequential formation of covalently bonded hydrogel multilayers through surface initiated photopolymerization. *Biomaterials,* 27, 1209-1215.

Kizilel, S. , A. Scavone, X. A. Liu, J. M. Nothias, D. Ostrega, P. Witkowski & M. Millis (2010) Encapsulation of Pancreatic Islets Within Nano-Thin Functional Polyethylene Glycol Coatings for Enhanced Insulin Secretion. *Tissue Engineering Part A,* 16, 2217-2228.

Kretlow, J. , L. Klouda & A. Mikos (2007) Injectable matrices and scaffolds for drug delivery in tissue engineering. *Adv Drug Deliv Rev* 59, 263-273.

Ksihara, S. , S. Matsumura & J. Fisher (2008) Synthesis and characterization of cyclic acetal based degradable hydrogels. *Eur J Pharm Biopharm,* 68, 67-73.

Kuhn, K. (1985) Structure and biochemistry of collagen. Aesthetic Plast Surg. 141-4.

Kuhn, K. (1994) Basement membrane (type IV) collagen. *Matrix Biol*, 439-45.

Kumagai, C. , M. Okano & Y. Kitagawa (2000) Three heterotrimeric laminins produced by human keratinocytes. *Cytotechnology*, 167-74.

Kumar, G. S. & D. C. Neckers (1991) Laser-Induced 3-Dimensional Photopolymerization Using Visible Initiators and Uv Cross-Linking by Photosensitive Comonomers. *Macromolecules,* 24, 4322-4327.

Leahy, D. , I. Aukhil & H. Erickson (1996) 2. 0Å crystal structure of a four-domain segment of human fibronectin encompassing the RGD loop and synergy region. *Cell Transplantation,* 84, 155-164.

Lee, J. , H. Lee & J. Andrade (1995) Blood compatibility of polyethylene oxide surfaces. *Prog Polym Sci* 20, 1043-1079.

Lee, K. & D. Mooney (2001) Hydrogels for tissue engineering. *Chem Rev,* 101, 1869-1879.

Lee, S. , J. Moon, J. Miller & J. West (2007) Poly(ethylene glycol) hydrogels conjugated with a collagenase-sensitive fluorogenic substrate to visualized collagenase activity during three-dimensional cell migration. *Biomaterials,* 28, 3163-3170.

Li, Q. , C. Williams, D. Sun, J. Wang, K. Leong & J. Elisseeff (2004) Photocrosslinkable polysaccharides based on chondroitin sulfate. *J Biomed Mater Res A,* 68, 28-33.

Liao, S. , C. Chan & S. Ramakrishna (2008) Stem cells and biomimetic materials strategies for tissue engineering. *Mater Sci Eng C,* 28, 1189-1202.

Lin, C. & K. Anseth (2009) Controlling affinity binding with peptide-functionalized poly(ethylene glycol) hydrogels. *Adv Funct Mater,* 19, 2325-2331.

Lin, X. , K. Takahashi, Y. Liu & P. Zamora (2006) Enhancement of cell attachment and tissue integration by a IKVAV containing multi-domain peptide. *BBA-Gen Subjects,* 1760, 1403-1410.

Locardi, E. , D. Mullen, R. Mattern & M. Goodman (1999) Conformations and pharmacophores of cyclic RGD containing peptides which selectively bind integrin avb3. *J Pept Sci,* 5, 491-506.

Luo, W. , C. Guo, J. Zheng, T. Chen, P. Wang & B. Vertel (2000) Aggrecan from start to finish. *Bone Miner Metab*, 51-6.

Lutolf, M. (2009) Spotlight on hydrogels. *Nat Mater* 8, 451-453.

Lutolf, M. & J. Hubbell (2005) Synthetic biomaterials as instructive extracellular microenvironments for morphogenesis in tissue engineering. *Nat Biotechnol,* 23, 47-55.

Luzak, B. , J. Golanski, M. Rozalski, M. Boncler & C. Watala (2003) Inhibition of collageninduced platelet reactivity by DGEA peptide. *Acta Biochim Pol,* 50, 1119-1128.

Ma, P. (2008) Biomimetic materials for tissue engineering. *Adv Drug Deliv Rev,* 60, 184-198.

MacDonald, P. , W. El-kholy, M. Riedel, A. Salapatek, P. Light & W. MB (2002) The multiple actions of GLP-1 on the process of glucose-stimulated insulin secretion. . *Diabetes* 51, S434-S442.

Malkoch, M. , R. Vestberg, N. Gupta, L. Mespouille, P. Dubois, A. Mason, J. Hedrick, Q. Liao, C. Frank, K. Kingsbury & C. Hawker (2006) Synthesis of well-defined hydrogel networks using Click chemistry. *Chem Commun*, 2774-2776.

Massia, S. & J. Hubbell (1992) Tissue engineering in the vascular graft. *Cytotechnology,* 10, 189-204.

Masters, K. , D. Shah, G. Walker, L. Leinwand & K. Anseth (2004) Designing scaffolds for valvular interstitial cells: cell adhesion and function on naturally derived materials. *J Biomed Mater Res A,* 71, 172-180.

Mel, A. d. , G. Jell, M. Stevens & A. Sefalian (2008) Biofunctionalization of biomaterials for accelerated in situ endothelialization: a review. *Biomacromolecules,* 9, 2969-2979.

Metters, A. , C. Bowman & K. Anseth (2000) A Statistical Kinetic Model for the Bulk Degradation of PLA-b-PEG-b-PLA Hydrogel Networks. *The Journal of Physical Chemistry B,* 104, 7043-7049.

Metters, A. & J. Hubbell (2005) Network formation and degradation behavior of hydrogels formed by Michael-type addition reactions. . *Biomacromolecules,* 6, 290-301.

Mineur, P. , A. Guignandon, C. Lambert, C. Lapiere & B. Nusgens (2005) RGDS and DGEA-induced [Ca2þ]i signaling in human dermal fibroblast. *BBA-Mol Cell Res,* 1746, 28-37.

Moon, J. , S. Lee & J. West (2007) Synthetic biomimetic hydrogels incorporated with Ephrin-A1 for therapeutic angiogenesis. *Biomacromolecules,* 8, 42-49.

Murphy, G. & J. Gavrilovic (1999) Proteolysis and cell migration: creating a path? *J. Curr Opin Cell Biol* 11, 614-621.

Murphy, G. , V. Knauper, S. Atkinson, J. Gavriliovic & D. Edwards (2000) Cellular mechanisms for focal proteolysis and the regulation of the microenvironment. *Fibrinol Proteol,* 14, 165-174.

Mydel, P. , J. Shipley, T. Adair-Kirk, D. Kelley, T. Broekelmann & R. Mecham (2008) Neutrophil elastase cleaves laminin-332 (lamini-5) generating peptides that are chemotactic for neutrophils. *J Biol Chem,* 15, 9513-9522.

Nagase, H. & G. Fields (1996) Human matrix metalloproteinase specificity studies using collagen sequence-based synthetic peptides. *Biopolymers,* 40, 399-416.

Neckers, D. C. , S. Hassoon & E. Klimtchuk (1996) Photochemistry and photophysics of hydroxyfluorones and xanthenes. *Journal of Photochemistry and Photobiology a-Chemistry,* 95, 33-39.

Nie, T. , R. Akins & K. Kiick (2009) Production of heparin-containing hydrogels for modulating cell responses. *Acta Biomater,* 5, 865-875.

Nomizu, M. , B. Weeks, C. Weston, W. Kim, H. Kleinman & Y. Yamada (1995) Structure-activity study of a laminin a1 chain active peptide segment IleeLyseValeAlaeVal (IKVAV). *FEBS Lett,* 365, 227-231.

Nuttelman, C. , M. Rice, A. Rydholm, C. Salinas, D. Shah & K. Anseth (2008) Macromolecular monomers for the synthesis of hydrogel niches and their application in cell encapsulation and tissue engineering. *Prog Polym Sci,* 33, 167-170.

Nuttelman, C. , M. Tripodi & K. Anseth (2005) Synthetic hydrogel niches that promote hMSC viability. . *Matrix Biol* 24, 208-218.

Obrink, B. , T. Laurent & B. Carlsson (1975) The binding of chondroitin sulphate to collagen. *FEBS Lett* 56, 166-169.

Odian, G. 2004. *Principles of Polymerization*. New Jersey: John Wiley and Sons, Inc.

Ogura, Y. , Y. Matsunaga, T. Nishiyama & S. Amano (2008) Plasmin induces degradation and dysfunction of laminin 332 (laminin 5) and impaired assembly of basement membrane at the dermal-epidermal junction. *Br J Dermatol,* 159, 49-60.

Ottani, V. , M. Raspanti & A. Ruggeri (2001) Collagen structure and functional implications. *Microscopy*, 251-60.

Papagiannopoulos, A. , T. Waign & T. Hardingham (2008) The viscoelasticity of self-assembled proteoglycan combs. *Faraday Discuss*, 337-57.

Park, Y. , M. Lutolf, J. Hubbell, E. Hunziker & M. W. M (2004) Bovine primary chondrocyte culture in synthetic matrix metalloproteinase-sensitive poly(ethylene glycol)-based hydrogels as a scaffold for cartilage repair. . *Tissue Eng,* 10, 515-522.

Patel, P. , A. Gobin, J. West & C. Patrick (2005) Poly(ethylene glycol) hydrogels system supports preadipocyte viability, adhesion, and proliferation. *Tissue Eng,* 11, 1498-1505.

Pathak, C. P. , A. S. Sawhney & J. A. Hubbell (1992) Rapid Photopolymerization of Immunoprotective Gels in Contact with Cells and Tissue. *Journal of the American Chemical Society,* 114, 8311-8312.

Peppas, N. , K. Keys, M. Torres-Lugo & A. Lowman (1999) Poly(ethylene glycol)-containing hydrogels in drug delivery. . *J Control Release,* 62, 81-87.

Pocza, P. , H. Suli-Vargham, Z. Darvas & A. Falus (2008) Locally generated VGVAPG and VAPG elastin-derived peptides amplify melanoma invasion via the galectin-3 receptor. *Int J Cancer,* 122, 1972-1980.

Polizzotti, B. , B. Fairbanks & K. Anseth (2008) Three-dimensional biochemical patterning of Click-based composite hydrogels via thiol-ene photopolymerization. *Biomacromolecules,* 9, 1084-1087.

Potts, J. & I. Campbell (1994) Fibronectin structure and assembly. *Curr Opin Cell Biol*, 648-55.

Reddy, S. , K. Anseth & C. Bowman (2005) Modeling of network degradation in mixed step-chain growth polymerizations. *Polymer,* 46, 4212-4222.

Reddy, S. , N. Cramer & C. Bowman (2006) Thiol-vinyl mechanisms. 1. Termination and propagation kinetics in thiol-ene photopolymerizations. *Macromolecules,* 39, 3673-3680.

Rhodes, J. & M. Simons (2007) The extracellular matrix and blood vessel formation; not just a scaffold. *J Cell Mol Med,* 11, 176-205.

Rhodes, J. & M. Simons (2007) The extracellular matrix and blood vessel formation; not just a scaffold. *Cell Mol Med*, 176-205.

Rice, M. , J. Sanchez-Adams & K. Anseth (2006) Exogenously Triggered, Enzymatic Degradation of Photopolymerized Hydrogels with Polycaprolactone Subunits: Experimental Observation and Modeling of Mass Loss Behavior. *Biomacromolecules* 7, 1968-1975.

Ruoslahti, E. (2003) The RGD story: a personal account. *Matrix Biol,* 22, 459-465.

Ruoslahti, E. & M. Pierschbacher (1987) New perspectives in cell adhesion: RGD and integrins. *Science,* 238, 491-497.

Rydholm, A. , K. Anseth & C. Bowman (2007) Effects of neighboring sulfides and pH on ester hydrolysis in thiol-acrylate photopolymers. *Acta Biomater,* 3, 449-455.

Rydholm, A., C. Bowman & K. Anseth (2005) Degradable thiol-acrylate photopolymers:polymerization and degradation behavior of an in situ forming biomaterial. . *Biomaterials,* 26, 4495-4506.

S'Engel, P. J. & A. Mikos (2000) Synthesis of poly(ethylene glycol)-tethered poly (propylene fumarate) and its modification with GRGD peptide. . *Polymer,* 41, 7595-7604.

Saha, K. , J. F. Pollock, D. V. Schaffer & K. E. Healy (2007) Designing synthetic materials to control stem cell phenotype. *Current Opinion in Chemical Biology,* 11, 381-387.

Salinas, C. & K. Anseth (2008) Mixed mode thiol-acrylate photopolymerizations for the synthesis of PEG-peptide hydrogels. *Macromolecules,* 41, 6019-6026.

Salinas, C. & K. A. KS (2008) The enhancement of chondrogenic differentiation of human mesenchymal stem cells by enzymatically regulated RGD functionalities. *Biomaterials,* 29, 2370-2377.

Sanborn, T. , P. Messersmith & A. Barron (2002) In situ crosslinking of a biomimetic peptide-PEG hydrogel via thermally triggered activation of factor XIII. *Biomaterials,* 23, 2703-2710.

Sands, R. & D. Mooney (2007) Polymers to direct cell fate by controlling the microenvironment. *Curr Opin Biotechnol* 18, 448-453.

Sawhney, A., C. Pathak & J. Hubbell (1993) Bioerodible hydrogels based on photopolymerized poly(ethylene glycol)-co-poly(a-hydroxy acid) diacrylate macromers. *Macromolecules* 26, 581-587.

Scott, J. (1995) Extracellular matrix, supramolecular organization and shape. *Anat*, 259-69.

Scott, R. & N. Peppas (1999) Kinetics of Copolymerization of PEG-Containing Multiacrylates with Acrylic Acid. *Macromolecules,* 32, 6149-6158.

Seiki, M. (2002) The cell surface: the stage for matrix metalloproteinase regulation of migration. *Curr Opin Cell Biol* 14:, 624-632.

Shin, H. , S. Jo & A. Mikos (2003) Biomimetic materials for tissue engineering. *Biomaterials,* 24, 4353-4364.

Silva, A. , C. Richard, M. Bessodes, D. Scherman & O. Merten (2009) Growth factor delivery approaches in hydrogels. *Biomacromolecules,* 10, 9-18.

Stach, M. , I. Lacik, D. Chorvat, M. Buback, P. Hesse, R. A. Hutchinson & L. Tang (2008) Propagation rate coefficient for radical polymerization of N-vinyl pyrrolidone in aqueous solution obtained by PLP-SEC. *Macromolecules,* 41, 5174-5185.

Teymour, F. & J. D. Campbell (1994) Analysis of the Dynamics of Gelation in Polymerization Reactors Using the Numerical Fractionation Technique. *Macromolecules,* 27, 2460-2469.

Tibbitt, M. & K. Anseth (2009) Hydrogels as extracellular matrix mimics for 3D cell culture. *Biotechnol Bioeng,* 103, 655-663.

Traub, W. (1978) Molecular assembly in collagen. *FEBS Lett,* 92, 114-120.

Truong, K. & J. West (2002) Photopolymerizable hydrogels for tissue engineering applications. *Biomaterials,* 23, 4307-4314.

Turk, B. , L. Huang, E. Piro & L. Cantley (2001) Determination of protease cleavage site motifs using mixture-based oriented peptide libraries. *Nat Biotechnol,* 19, 661-667.

Valdes-aguilera, O., C. P. Pathak, J. Shi, D. Watson & D. C. Neckers (1992) Photopolymerization Studies Using Visible-Light Photoinitiators. *Macromolecules,* 25, 541-547.

Vertel, B. (1995) The ins and outs of aggrecan. *Trends Cell Biol*, 458-64.

Webb, D. , J. Parsons & A. Horwitz (2002) Adhesion assembly, disassembly and turnover in migrating cells e over and over and over again. *Nat Cell Biol,* 4, E97-E99.

Weber, L. M. & K. S. Anseth (2008) Hydrogel encapsulation environments functionalized with extracellular matrix interactions increase islet insulin secretion. *Matrix Biology,* 27, 667-673.

Weber, L. M. , K. N. Hayda & K. S. Anseth (2008) Cell-Matrix Interactions Improve beta-Cell Survival and Insulin Secretion in Three-Dimensional Culture. *Tissue Engineering Part A,* 14, 1959-1968.

Weber, L. M. , K. N. Hayda, K. Haskins & K. S. Anseth (2007) The effects of cell-matrix interactions on encapsulated beta-cell function within hydrogels functionalized with matrix-derived adhesive peptides. *Biomaterials,* 28, 3004-3011.

Weber, L. M. , C. G. Lopez & K. S. Anseth (2009) Effects of PEG hydrogel crosslinking density on protein diffusion and encapsulated islet survival and function. *Journal of Biomedical Materials Research Part A,* 90A, 720-729.

West, J. 2005. Bioactive hydrogels: Mimicking the extracellular matrix with synthetic materials. In *Scaffolding in Tissue Engineering* ed. J. Elisseeff, 275-281. Boca Raton, FL: CRC Press.

White, T. J. , W. B. Liechty & A. Guymon (2007) The influence of N-vinyl pyrrolidone on polymerization kinetics and thermo-mechanical properties of crosslinked acrylate polymers. *Journal of Polymer Science Part a-Polymer Chemistry,* 45, 4062-4073.

Woods, A. & J. Couchman (1998) Syndecans: synergistic activators of cell adhesion. *Trends Cell Biol,* 8, 189-191.

Woods, A. & J. Couchman (2000) Integrin modulation by lateral association. *J Biol Chem,* 275, 24233-24236.

Woods, A. , E. Oh & J. Couchman (1998) Syndecan proteoglycans and cell adhesion. *Matrix Biol,* 17, 477-483.

Yamaguchi, N. , L. Zhang, B. Chae, C. Palla, E. Furst & K. Kiick (2007) Growth factor mediated assembly of cell receptor-responsive hydrogels. *J Am Chem Soc,* 129, 3040-3041.

Zhang, J. , A. Skardal & G. Prestwich (2008) Engineered extracellular matrices with cleavable crosslinkers for cell expansion and easy cell recovery. *Biomaterials,* 29, 4521-4531.

Zhang, L. , E. Furst & K. Kiick (2006) Manipulation of hydrogel assembly and growth factor delivery via the use of peptide-polysaccharide interactions. *J Control Release* 114, 130-142.

Zhu, J. (2010) Bioactive modification of poly(ethylene glycol) hydrogels for tissue engineering. *Biomaterials,* 31, 4639-56.

Zhu, J. , J. Beamish, C. Tang, K. Kottke-Marchant & R. M. RE (2006) Extracellular matrix-like cell-adhesive hydrogels form RGD-containing poly(ethylene glycol) diacrylate. *Macromolecules* 39, 1305-1307.

Zhu, J. , C. Tang, K. Kottke-Marchant & R. Marchant (2009) Design and synthesis of biomimetic hydrogel scaffolds with controlled organization of cyclic RGD peptides. *Bioconjug Chem,* 20, 333-339.

Zhu, W., J. Latridis, V. Hlibczuk, A. Ratcliffe & V. Mow (1996) Determination of collageneproteoglycan interactions in vitro. *J Biomech* 29, 773-783.

Zisch, A. , M. Lutolf & J. Hubbell (2003) Biopolymeric delivery matrices for angiogenic growth factors. *Cardiovasc Pathol,* 12, 295-310.

Part 3

Nanomaterials

15

Synthesis, Characterization, Toxicity of Nanomaterials for Biomedical Applications

A. K. Pradhan, K. Zhang, M. Bahoura, J. Pradhan,
P. Ravichandran, R. Gopikrishnan and G. T. Ramesh
Norfolk State University,
United State of America

1. Introduction

Nanomaterials are widely used for biomedical applications as their sizes are comparable with most of the biological entities. Many diagnostic and therapeutic techniques based on nanoscience and nanotechnologies are already in the clinical trial stages, and encouraging results have been reported. The progress in nanoscience and nanotechnology has led to the formation and development of a new field, nanomedicine, which is generally defined as the biomedical applications of nanoscience and nanotechnology. Nanomedicine stands at the boundaries between physical, chemical, biological and medical sciences, and the advances in nanomedicine have made it possible to analyze and treat biological systems at the cell and sub-cell levels, providing revolutionary approaches for the diagnosis, prevention and treatment of some fatal diseases, such as cancer. Nanomagnetism is at the forefront of nanoscience and nanotechnology, and in the field of nanomedicine, magnetic nanomaterials are among the most promising for clinical diagnostic and therapeutic applications. Similarly, luminescent materials are equally important for tagging and imaging applications.

The nanomaterials used for biomedical purposes generally include zero-dimensional nanoparticles, one-dimensional nanowires and nanotubes, and two-dimensional thin films. For example, magnetic nanoparticles and nanotubes are widely used for labeling and manipulating biomolecules, targeting drugs and genes, magnetic resonance imaging (MRI), as well as hyperthermia treatment. Magnetic thin films are often used in the development of nanosensors and nanosystems for analyzing biomolecules and diagnosing diseases. As the synthesis and characterization of these nanostructures are completely interdisciplinary, there is a need of coordinated efforts for the successful implementation of these nanomaterials. The synthesis of nanoparticles with required shape, size, and core-shell configuration (surface coating) along with proper characterization are still in the early stage of research. On the other hand, due to the similar size to biological systems, nanoparticles pose potential threats to health and they could consequently have a large impact on industry and society. Hence, apart from successful synthesis and characterization of various nanomaterials, an effort to understand the toxicological impacts of nanomaterials much research has to be done to establish standards and protocols for the safe use of nanomaterials in industry as well as in the public arena, including academia and research laboratories.

Nanoparticles have sparked intense interest in anticipation that this unexplored range of material dimensions will yield size-dependent properties. The physical and chemical

properties vary drastically with size and use of ultra fine particles clearly represents a fertile field for materials research. The modern biology and biomedical science have stepped into the molecular level. Effectively probing biological entities and monitoring their biological processes are still a challenge for both basic science investigation and practical diagnostic/therapeutic purposes. Since nanomaterials possessing analogous dimensions to those of functional aggregates organized from biomolecules they are believed to be a promising candidate interface owing to their enhanced interaction with biological entities at the nano scale (Whitesides, 2003). For this reason, nanocrystals with advanced magnetic or optical properties have been actively pursued for potential biomedical applications, including integrated imaging, diagnosis, drug delivery and therapy (Lewin et al., 2000; Hirsch et. al., 2003; Alivisatos, 2004; Kim et. al., 2004; Liao and Hafner, 2005). The development of novel biomedical technologies involving *in vivo* use of nanoparticles present multidisciplinary attempts to overcome the major chemotherapeutic drawback related to its spatial nonspecificity. For example, in most biomedical and magnetofluidic applications, magnetic nanoparticles of fairly uniform size and Curie temperature above room temperature are required. On the other hand, as the major advantage of nanotubes, the inner surface and outer surface of nanotubes can be modified differently due to their multi-functionalization. While the inner surface was tailored for better encapsulation of proper drugs, the outer surface can be adjusted for targeted accessing. On the other hand, the strong magnetic behavior made maghemite nanotubes easier controlled by a magnetic field, especially compared with hematite nanotubes. Mainly due to their tubular structure and magnetism, magnetic nanotubes are among the most promising candidates of multifunctional nanomaterials for clinical diagnostic and therapeutic applications. The tubular structure of magnetic nanotubes provides an obvious advantage as their distinctive inner and outer surfaces can be differently functionalized, and the magnetic properties of magnetic nanotubes can be used to facilitate and enhance the bio-interactions between the magnetic nanotubes and their biological targets (Son et. al., 2009; Liu et. al., 2009). One application paradigm of magnetic nanotubes is drug and gene delivery (Plank et. al., 2003). One of the major applications of magnetic nanomaterials is targeted drug delivery. In chemotherapies, to improve the treatment efficiency and decrease or eliminate the adverse effects on the healthy tissues in the vicinity of a tumor, it is practically desirable to reduce or eliminate undesirable drug release before reaching the target site, and it is really critical that the drugs are released truly after reaching the target site, in a controllable manner via external stimuli (Satarkar & Hilt, 2008; Chertok et. al., 2008; Hu et. al., 2008; Liu et. al., 2009). This remains one of the important fields of research for the development of smart drug carriers, whose drug release profiles can be controlled by external magnetic fields, for example the drug to be released is enclosed in a magnetic-sensitive composite shell.

With rapid development of nanotechnology and handling of nanoparticles in various industrial and research and medical laboratories, it is expected that the number of people handling nanoparticles could double in few years from now putting more urge towards its safe use (Tsuji et. al. 2005). However, knowing the potential use and burden of exposure, there is little evidence to suggest that the exposure of workers from the production of nanoparticles has been adequately assessed (Shvedova et. al., 2003; Tsuji et. al. 2005). Despite these impressive, futuristic, possibilities, one must be attentive to unanticipated environmental and health hazards. In view of the above, the exposure to nanoparticles and nanotubes could trigger serious effects including death, if proper safety measures are not taken. Few findings from published articles certainly justify a moratorium on research

involving nanoparticles, if not all nanoparticles, until proper safeguards can be put in place, moreover safety tests need to be carried out keeping in view the type of nanomaterials present. Currently, the literature surveys on suggested nanotoxicity are few to draw any conclusion on the exposure dose of nanoparticles required for toxicity.

2. Eu^{3+} doped Gd_2O_3 luminescent nanostructures

The nanoscale structures, which include nanoparticles, nanorods, nanowires, nanotubes and nanobelts (He et. al., 2003; Chang et. al., 2005; Li et. al., 2007; Mao, et. al., 2008; Zhang et al., 2009), have been considerably investigated due to their unique optical, electronic properties and prospective application in diverse fields, such as high quality luminescent devices, catalysts, sensors, biological labeling and other new functional optoelectronic devices. The precise architectural manipulation of nanomaterials with well-defined morphologies and accurately tunable sizes remains a research focus and a challenging issue due to the fact that the properties of the materials closely interrelate with geometrical factors such as shape, dimensionality, and size. The properties and performances of nanostructures strongly depend on their dimensions, size, and morphologies (Liu et. al., 2007). Therefore, synthesis, growth, and control of morphology in the crystallization process of nanostructures are of critical importance for the development of novel technologies.

Rare earth doped oxides are promising new class of luminescent material due to their electronic and optical properties that arises from their 4f electrons. Therefore, much attention has been paid to their luminescent characteristics such as their large stokes shift, sharp emission visible spectra, long fluorescence lifetime (1-2 ms), and lack of photo-bleaching compared with dyes (Wang et. al., 2005; Nichkova et. al., 2006). These materials, especially in the nanostructure, have been widely used in the lighting industry and biotechnology, including plasma display panel, magnetic resonance imaging enhancement, and microarray immunoassays for fluorescence labels (Seo et. al., 2002; Nichkova et. al., 2005; Bridot et. al., 2007; Petoral et. al., 2009). Since the morphology and dimensionality of nanostructures are of vital factors, which particularly have an effect on the physical, chemical, optical, and electronic properties of materials, it is expected that rare earth doped oxides synthesized in the form of nanoscale may take on novel spectroscopic properties of both dimension controlled and modified ion-phonon confinement effect compared to their bulk counterparts. Gd_2O_3, as a rare earth oxide, is a useful paramagnetic material and good luminescent rare earth doped host. Eu^{3+} ions can be doped into Gd_2O_3 easily since they are all trivalent ions and have the same crystal structure. Furthermore, $^5D_0$ -$^7F_2$ of Eu^{3+} transitions exhibit red characteristic luminescence at a wavelength of 611 nm. Therefore, lanthanide oxide doped nanostructures can be used as electrical, magnetic or optical multifunction materials.

Recently, considerable efforts have been made to synthesize low dimensional nanostructures (Chang et. al., 2005; Li et. al., 2007; Liu et. al., 2008). However, these processes have to be involved in hydrothermal routine, template, and catalysts. The nanostructure formed depends somehow on the pressure, template, and catalysts. This results in experimental complexity, impurities, defects and high cost. In addition, these methods especially could not meet large scale produce in industry. Therefore, it is necessary to find new methods to synthesize shape, size, and dimensionality controlled lanthanide doped oxides. On the other hand, because of the distinct low effective density, high specific

surface area, and encapsulation ability in hollow nanotubes these nanostructures are exceptionally promising in various fields such as confined catalysis, biotechnology, photonic devices, and electrochemical cells (Xu & Asher, 2004; Lou et. al., 2006; Wei et. al., 2008). Although lanthanide oxides are excellent host lattices for the luminescence of various optically active lanthanide ions (Mao et. al., 2009), Gd_2O_3 is a promising host matrix for down- and up conversion luminescence because of its good chemical durability, thermal stability, and low phonon energy (Yang et. al., 2007; Jia et. al., 2009).

3. Synthesis of Gd_2O_3: Eu^{+3} nanostructures

Gd_2O_3 doped with Eu^{3+} nanostructures were synthesized by either sol-gel or co-precipitation wet chemical solution methods. Nanoparticles were synthesized by a sol-gel method from their acetate hydrate precursors, which were dissolved in water. This solution was mixed with citric acid solution in 1:1 volume ratio ultrasonically for about 30 min. The mixture was heated in a water bath at 80 °C until all water is evaporated, yielding a yellowish transparent gel. The gel was further heated in an oven at 100 °C which formed a foamy precursor. This precursor decomposed to give brown-colored flakes of extremely fine particle size on further heating at 400 °C for 4 h. The flakes were ground and sintered at 800 °C for duration of 2 h. Further heating in O_2 ambient removed the carbon content.

The nanoparticles of Eu:Gd_2O_3 were coated by adopting a base-catalyzed sol-gel process. 100 mg of Eu:Gd_2O_3 were dispersed in 20 ml of 2-propanol solution and sonicated for 30 min. 75 µl of tetraethoxysilane (TEOS) and 25 µL of 25% NH_3H_2O solution were injected into the above mixture and sonicated for 30 min at 60 ^oC. By means of centrifugation the suspended silica capsulated Eu:Gd_2O_3 were obtained. The coated particles were washed several times by using acetone and methanol in order to remove any excess unreacted chemicals. The purified powder was naturally dried. This procedure produces a very uniform SiO_2 coating, as determined using a transmission electron microscope (TEM). By changing the formulation of the coating solution, we can control the coating thickness.

In the co-precipitation method, 0.5 M aqueous solution was prepared by dissolving $Gd(NO_3)_3$ and $Eu(NO_3)_3$ in deionized H_2O. The nitrate solutions with cationic molar ratio of Gd to Eu is 0.95: 0.05 were mixed together and stirred for 30 minutes. The aqueous solution of 0.2 M NH_4HCO_3 was prepared and mixed with the nitrate solution drop wise while stirring to form the precipitate. It is noted that in this experiment extra 10 mol% NH_4HCO_3 was added in order to ensure all the rare earth ions reacted completely to obtain rare earth carbonates. The white precipitate slurry obtained was aged for 24 hours at room temperature with continuous stirring. Then the precipitates were centrifugated and washed with deionized water for 5 times in order to completely remove NO^{3-}, NH^{4+} and HCO^{3-} followed by drying at about 75 ^oC in the stove. After drying, the white precursor was ground several times. It is noted that the dried precursor powders were very loosely agglomerated and can be pulverized very easily. To get Gd_2O_3 doped with Eu^{3+} nanostructures, the as-synthesized samples were further calcined at 600, 800, and 1000 ^oC in air for 2 hours in the furnace, respectively.

Eu^{3+} doped Gd_2O_3 nanotubes were synthesized according to a modified wet chemical method (He et. al., 2003). A mixture of 30 ml of 0.08 M $Gd(NO_3)_3$ and $Eu(NO_3)_3$ with a nominal molar ratio of Eu/Gd 5 atom %, in a form of clear solution, were added into flasks through ultrasound for 10 min. 30 ml of 25 wt % of ammonia solution was added quickly

into the solution under vigorous stirring for 20 min. Meanwhile, the pH value of the mixture was measured which came to a value of about 10. The mixture was heated under vigorous stirring in a 70 °C silicon oil bath for 16 hours. After this procedure, a white precipitate precursor was obtained. The final as-prepared precipitates were separated by centrifugation, washed with deionized water and ethanol for 4 times, respectively, and dried for 12 hours at 65 °C in air to get as-grown sample. To get Gd_2O_3 product, the as-synthesized samples were further annealed in air for 2 hours at 600 °C in the furnace.

Figure 1 (a-c) shows the representative TEM morphologies of Eu:Gd_2O_3 nanoparticles. The size distribution is rather narrow, and the nanocrytallite size is in the range of 20-30 nm for as-prepared nanoparticles by citric-gel technique. However, the nanoparticles are slightly agglomerated. The particle sizes increase to 30-40 nm if the nanoparticles are calcined up to 800 °C. Figure 1 (c) represents the TEM image of Eu:Gd_2O_3 nanoparticle coated by SiO_2 indicating distinctly well dispersed nanoparticles. It is noted that the size of the SiO_2 shell can be controlled by controlling TEOS and NH_3H_2O solution.

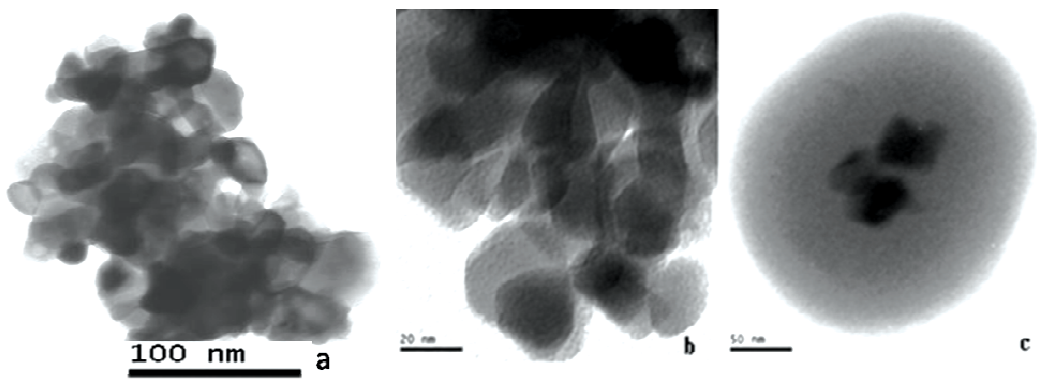

Fig. 1. Transmission electron microscopy (TEM) image of Eu:Gd2O3 nanopowders of (a) as prepared, (b) calcined at 800 °C and (c) SiO2 coated.

Figure 2 shows the emission spectra of citric-gel technique synthesized Eu doped Gd_2O_3 nanoparticles. The photoluminescence spectrum illustrates the Eu^{3+} ions are in cubic symmetry and indicate the characteristics of red luminescent Eu:Gd_2O_3, in which the $^5D_0 \rightarrow {}^7F_2$ transition at about 611 nm is prominent, and the relatively weak emissions at the shorter wavelengths are due to the $^5D_0 \rightarrow {}^7F_1$ transitions. The cubic structure provides two sites, C_2 and S_6, from two different crystalline sites, in which the $^5D_0 \rightarrow {}^7F_2$ transition originates from the C_2 site of the electric dipole moment of Eu^{3+} ions that scarcely arises for the S_6 site because of the strict inversion symmetry. This suggests that the emission emerges mainly from the C_2 site in the cubic structure. The emission spectra show similar characteristics after SiO_2 coating on the surface of Eu:Gd_2O_3 nanoparticles. This clearly suggests that the emission properties of Eu ions remain intact even after SiO_2 coating, and can be utilized for biomedical tagging.

Figure 3 shows the magnetic moment of Eu:Gd_2O_3 and SiO_2 coated Eu:Gd_2O_3 nanoparticles at 300 K. Both nanoparticles demonstrate paramagnetic behavior at room temperature. On the other hand, the coated nanoparticles showed reduced magnetization compared to Eu:Gd_2O_3 due to reduction in the volume fraction caused by SiO_2 coating.

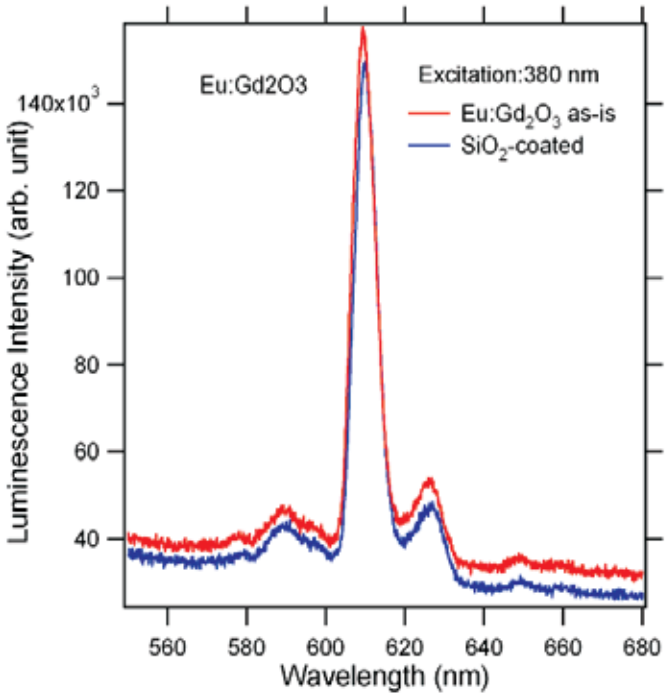

Fig. 2. Photoluminescence of $Eu:Gd_2O_3$ nanoparticles calcined at 800 ^{0}C.

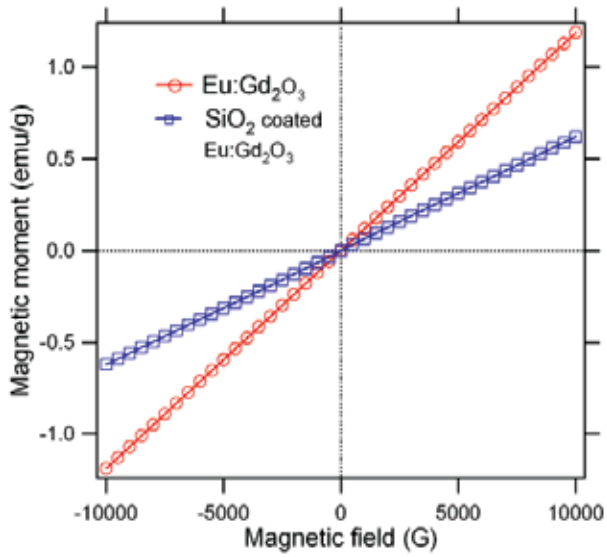

Fig. 3. Magnetic moment of $Eu:Gd_2O_3$ and SiO_2 coated $Eu:Gd_2O_3$ nanoparticles.

The morphology of Eu^{3+} doped Gd_2O_3 nanorods obtained after calcination at 600 ^{o}C for 2 hours strongly depends on the heat treatment temperature. The formation of nanorods with low aspect ratio is preferred at 600 ^{o}C. It can be seen from the micrograph that all the nanorods display uniform morphology having size of 10 nm in diameter and more than 300

nm in length (Figure 4(a)). In contrast, the nanorods grow bigger in diameter (about 25 nm) and shorter in length (about 100 nm) after the heat treatment at 800 °C as shown in Figure 4(c). However, it is evident that Eu^{3+} doped Gd_2O_3 nanorods maintain the anisotropic shape during heat treatment from 600 °C to 800 °C. It can also be observed that the formation of nanorods is related to the fact that the growth direction are preferred along the [211] crystallographic orientation. This is because the spacing between fringes along nanorod axes is about 0.40 nm which is close to the interplanar distance of the cubic (211) plane as shown in Figure 4 (b) and (d). Figure 4(e) presents the TEM images of Eu^{3+} doped Gd_2O_3 nanoparticles with size of 60 nm in diameter obtained by heat treatment at 1000 °C. The morphology of Eu^{3+} doped Gd_2O_3 nanostructure dependent on the heat treatment temperature is possibly attributed to meta-stable states which are able to recrystallize at 1000 °C. A favorable growth pattern parallel to the (222) plain corresponding to interplanar spacing of 0.3 nm dominates the recrystallization of nanorods and transFigures to form nanoparticles as shown in Figure 4(f).

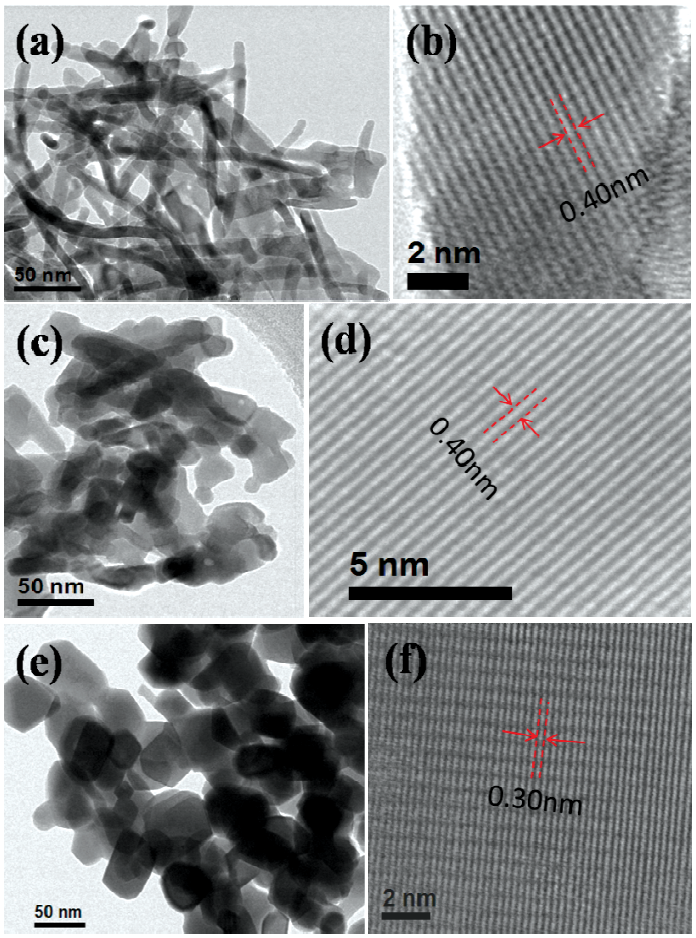

Fig. 4. Eu^{3+} doped Gd_2O_3 nanostructures TEM photographs of low and high magnification after annealing at (a) and (b) 600 °C, (c) and (d) 800 °C, and (e) and (f) 1000 °C, respectively.(b), (d) and (f) represent the HR-TEM images of respective nanostructures.

The optical properties and characteristics of nanostructures used in the photonic application are typically determined by their dimensions, size, and morphologies. The intensity of photoluminescence of Eu^{3+} doped Gd_2O_3 nanorods strongly depends on the annealing temperature at which the morphology of nanostructures gets modified. Figure 5 shows the emission spectra of Eu^{3+} doped Gd_2O_3 nanorods excited by 263 nm ultraviolet light.

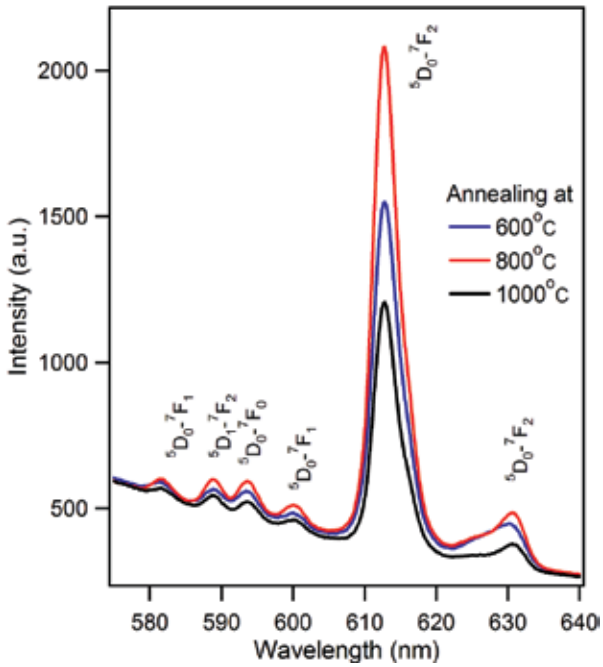

Fig. 5. Photoluminescence spectra of Eu^{3+} doped Gd_2O_3 nanostructures annealing at 600 °C, 800 °C, and 1000 °C, respectively.

The emission spectra exhibit a strong red emission characteristic of the $^5D_0$-$^7F_2$ (around 613 nm) transition which is an electric-dipole-allowed transition. The weaker band around 581 nm, 589 nm, 593 nm, 600 nm and 630 nm are ascribed to $^5D_0$-$^7F_1$, $^5D_1$-$^7F_2$, $^5D_0$-$^7F_0$, $^5D_0$-$^7F_1$, and $^5D_0$-$^7F_2$, respectively (Liu et. al., 2008). The emission spectra indicates that the Eu^{3+} doped Gd_2O_3 nanostructures represent strong, narrow, and sharp emission peaks. As shown in Figure 5, the intensity of emission at 613 nm of nanorods increases when the annealing temperature increases from 600 °C to 800 °C modifying the morphology of the nanorods as described earlier. However, when the annealing temperature reaches 1000 °C, the emission intensity is reduced significantly, even less than the one annealed at 600 °C. The performance change of photoluminescence in these nanostructures can be attributed to the morphological transformation of the nanostructures as described below. At low annealing temperature, the Eu^{3+} doped Gd_2O_3 exhibits nanorod morphology with more surface area containing a larger number of luminescent centers. However, when the temperature was increased to 1000 °C, the nanorods transformed to nanoparticles which have more surface area altogether. This increase in surface area resulted in more defects, especially surface defects and strains, located on the surface of the nanoparticles. Although high annealing temperature can increase crystal perfection, the defects on the surface of these nanoparticles can overwhelm, causing reduced photoluminescence.

In order to systematically investigate the correlation of morphology and optical characteristics of Eu^{3+} doped Gd_2O_3 samples, the 5 at.% Eu^{3+} doped Gd_2O_3 nanorods fabricated at 600 ^oC were used. Representative TEM and SEM images of Eu^{3+} doped Gd_2O_3 nanotubes are shown in Figure 6. It can be observed these nanostructures demonstrate tubular shape with a length in the range about 0.7-1 μm and the wall thickness of 20 nm. It also reveals that these one dimension nanostructures have open ends, smooth surface and straight morphology as shown in Figure 6 (a) and (b). Figure 6(c) demonstrates the Field Emission-Scanning Microscope (FE-SEM) image large number of uniform nanotubes. The open end and the associated fine feature, such as uniform size and shape, of these nanotubes are shown in the inset of Figure 6.

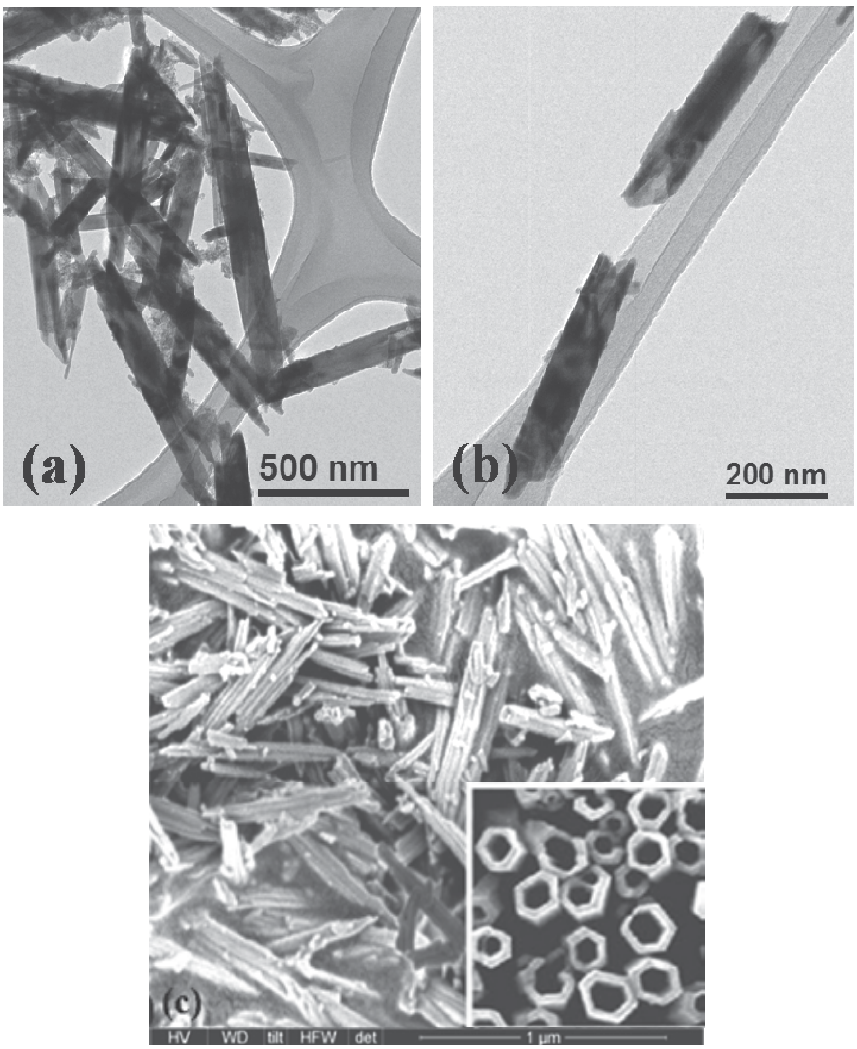

Fig. 6. (a) and (b) Low magnification TEM photographs and (c) FE-SEM images of Eu^{3+} doped Gd_2O_3 nanotubes after annealing at 600 ^oC. The inset in (c) demonstrates the nanotube feature of Eu^{3+} doped Gd_2O_3.

It is obviously revealed that the emission intensity of nanotubes is larger than the nanorods of Eu^{3+} doped Gd_2O_3 samples as shown in Figure 7. Nanotubes have more surface area than the nanorods. It is worth mentioning that the emission measurements were performed with a very similar conditions and volume fractions of nanomaterials used in this study. Although, the number of defects increases with the increase of area in nanotubes, the layer surface area overwhelms the luminescent intensity.

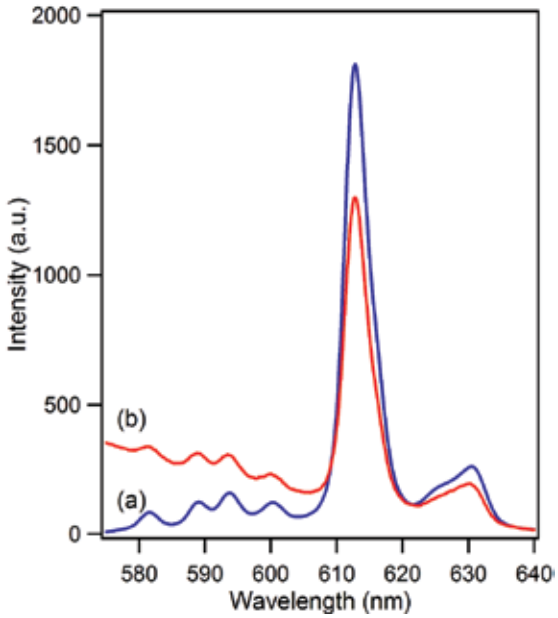

Fig. 7. Photoluminescence spectra comparison of Eu^{3+} doped Gd_2O_3 nanotubes (a) and nanorods (b) annealed at 600 ^oC, respectively.

4. ZnO nanostructures

Zinc oxide (ZnO) is a semiconductor material with various configurations, much richer than of any other known nanomaterial (Pradhan et. al., 2006; Ma et. al., 2007). At nanoscale, it posses unique electronic and optoelectronic properties and finds application as biosensors, sunscreens, as well as in medical applications like dental filling materials and wound healing (Ghoshal et. al., 2006). Because of the indiscriminate use of ZnO nanoparticles, it is important to look at their biocompatibility with biological system. A recent study on ZnO reports that it induces much greater cytotoxicity than non-metal nanoparticles on primary mouse embryo fibroblast cells (Yang et. al., 2009), and induces apoptosis in neural stem cell (Deng et. al., 2009). Published reports have shown that ZnO inhibits the seed germination and root growth (Lin & Xing, 2007); exhibit antibacterial properties towards *Bacillus subtilis* and to a lesser extent to *Escherichia coli* (Adams et. al., 2006). Inhalation of ZnO compromises pulmonary function in pigs and causes pulmonary impairment and metal fume fever in humans (Fine et. al., 1997; Beckett et. al., 2005). Literature evidences showed that ZnO nanoparticles are the most toxic nanoparticle with the lowest LD50 value among the engineered metal oxide nanoparticles (Hu et. al., 2009). On the other hand, it was also reported that zinc oxide was not found to be cytotoxic to cultured human dermal fibroblasts

(Zaveri et. al., 2009). In recent years, there has been an escalation in the development of techniques for synthesis of nanorods and subsequent surface functionalization. ZnO nanorods exhibit characteristic electronic, optical, and catalytic properties significantly different from other nano metals. Keeping in view of the unique properties and the extensive use of ZnO in many fields and also contradictory results on ZnO toxicity from both in-vitro and in-vivo studies, we report here to synthesize and characterize the ZnO nanorods on hela cells for its biocompatibility/toxicity.

5. Synthesis: ZnO nanotubes

The typical method employed is as follows. Equal volume of 0.1 M aqueous Zinc acetate anhydrous and Hexamethylenetetramine were mixed in a beaker using ultrasonication for 30 min. After the mixture was mixed well, it was heated at 80 °C in water bath for 75 min, during which white precipitates were deposited at the bottom. Then it was incubated for 30 min in ice cold water to terminate the reaction. The product was washed several times (till the pH of solution becomes neutral) using the centrifuge with deionized water and alcohol, alternatively to remove any by-product and excess of hexamethyleneteteamine. After washing, the solution was centrifuged at 10,000 rpm (12,000×*g*) for 20 min and the settled ZnO was dried at 80 ◦C for 2 h.

Fig. 8 (a, b) shows the SEM micrograph collected on synthesized ZnO nanorods surface morphology. The nanorod was grown perpendicular to the long-axis of the matrix rod and grew along the [001] direction, which is the nature of ZnO growth. The morphology of ZnO nanorod was further confirmed by the TEM image as shown in Fig. 8 (c, d). Though the rod cores were monodisperse, the length of the nanorod was estimated to be around 21 nm in diameter and the length around 50 nm.

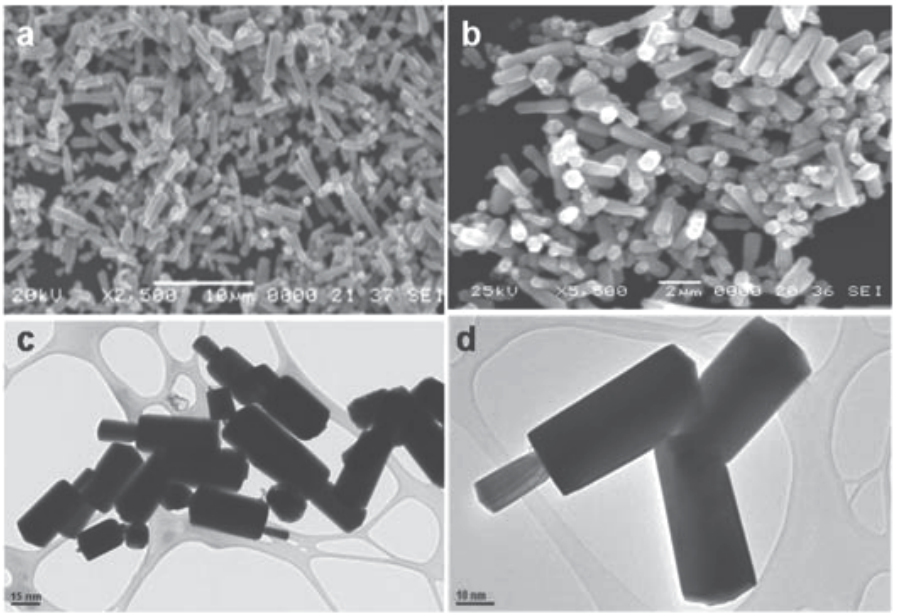

Fig. 8. (a and b) Scanning electron micrograph of ZnO nanorods. (c and d) Transmission electron micrograph of ZnO nanorods.

6. Toxicity studies: Eu:Gd_2O_3 nanoparticles

For cell culture and treatments, rat lung epithelial cell line (LE, RL 65, ATCC; CRL- 10354) from ATTC was grown at 37 °C in an atmosphere of 5% CO_2 and in complete growth medium supplemented with 1% penicillin/streptomycin and 10% fetal bovine serum (FBS). Eu:Gd_2O_3 were suspended in Dimethyl formamide (DMF) and sonicated for 5 minutes and henceforth in all control experiments the cells were treated with equivalent volume of DMF. The cells were incubated with or without nanoparticles in 96 well plates for time intervals as indicated in the respective Figure legends.

The measurements of intracellular reactive oxygen species (ROS) were performed in the following way. Oxygen radicals collectively called as reactive oxygen species play a key role in cytotoxicity. Increased ROS levels in cells by chemical compounds reflect toxicity and cell death. To study the induction of oxidative stress in LE cells, $1x10^4$ cells/well were seeded in 96 well plate and grown overnight under standard culture conditions. The cells were then treated with 10 µM of dichlorofluorescein [5-(and-6)-carboxy-2,7`-dichloro-dihydroxyfluorescein diacetate, H_2DCFDA, (C-400, Molecular Probes, Eugene, OR) for 3 h in Hank's balanced salt solution (HBSS) in incubator. Following 3 h of incubation, cells were washed with phosphate buffered saline (PBS) and treated with different concentrations of Eu:Gd_2O_3 nanoparticles. Following incubation the intensity of fluorescence is measured at different time intervals at excitation and emission of wavelength at 485/527 nm, respectively and expressed as fluorescence units.

LE cells were seeded at $5x10^3$ cells/well in a 96 well plate and allowed to grow overnight. After 18 h in serum-free medium, cells were treated with different concentrations of nanoparticles and grown for 72 h. At the end of the incubation, cells were additionally treated with 3-[4, 5-dimethylthiazol- 2-yl]-2,5-diphenyltetrazolium bromide] MTT for 3 h. The cells were then washed with chilled PBS and formazon formed was solubilized in 100 µL of acidic propanol and the absorbance was read at 570 nm.

The results of the toxicity test are presented in Fig. 9. The cytotoxicity assay was essentially performed as described elsewhere (Zveri et. al., 2009). Figure 9 indicates the effect of coated and uncoated Eu:Gd_2O_3 on rat LE cells suggesting that they induce ROS in a dose dependent manner. Uncoated Eu:Gd_2O_3 increased ROS by 0.5 folds as compared to control at a concentration as low as 2.5 µg were as coated Eu:Gd_2O_3 showed 1 fold increase in ROS. Coated and uncoated Eu:Gd_2O_3 induces very less ROS. To study the extent of damage caused by coated and uncoated Eu:Gd_2O_3 on cell viability, MTT assay was carried in LE cells treated with various concentrations and the results suggest that the cell viability decreases with increase in concentration of nanoparticles by 72 hrs compared to control. It was found that 60% of cells found to be viable at 2.5µg/ml of uncoated Eu:Gd_2O_3 where as 50% found to be viable with cells treated with coated Eu:Gd_2O_3. In all, measurement of intracellular reactive oxygen species and MTT assay results show that Eu:Gd_2O_3 nanoparticles are relatively nontoxic and the toxicity is further decreased on SiO_2 coating (Zhang et. al., 2009).

7. Toxicity studies of ZnO nanorods

Hela cells, which are immortalized cervical cancer cells, are used for the testing of ZnO nanorods. Hela cells were treated with different concentration (0.5, 1.0, 2.0, 2.5, 5.0,10

µg/ml) of ZnO nanorods for 3 h. They showed no significant induction of ROS **(**Fig. 10 a**).** Earlier studies on different nanoparticles such as single and multi walled carbon nanotubes showed significantly increased levels of ROS at 5-10µg/ml (Manna et. al., 2005; Sarkar et. al., 2007; Ravichandran et. al., 2009), whereas no increase in ROS level even in 20µg/ml was detected in ZnO nanorods. The time kinetics was also performed to check the formation of ROS (Fig. 10 b). It is seen that there is no significant ROS level formed as early as 30 min with 10µg/ml of ZnO nanorods and remained same till 150 min is passed. However, at later time intervals the increase in ROS was observed in 10µg/ml but very less as compared to the control. This may be due to osmotic pressure created by excess of nanorods. Next, the level of lipid peroxidation in ZnO nanorods exposed hela cells was investigated. This is another possible player for oxidative stress induction. It was observed that very minimal (as low as 0.1 fold) increase in lipid peroxidation level with 10µg/ml of ZnO nanorods as compared to the control.

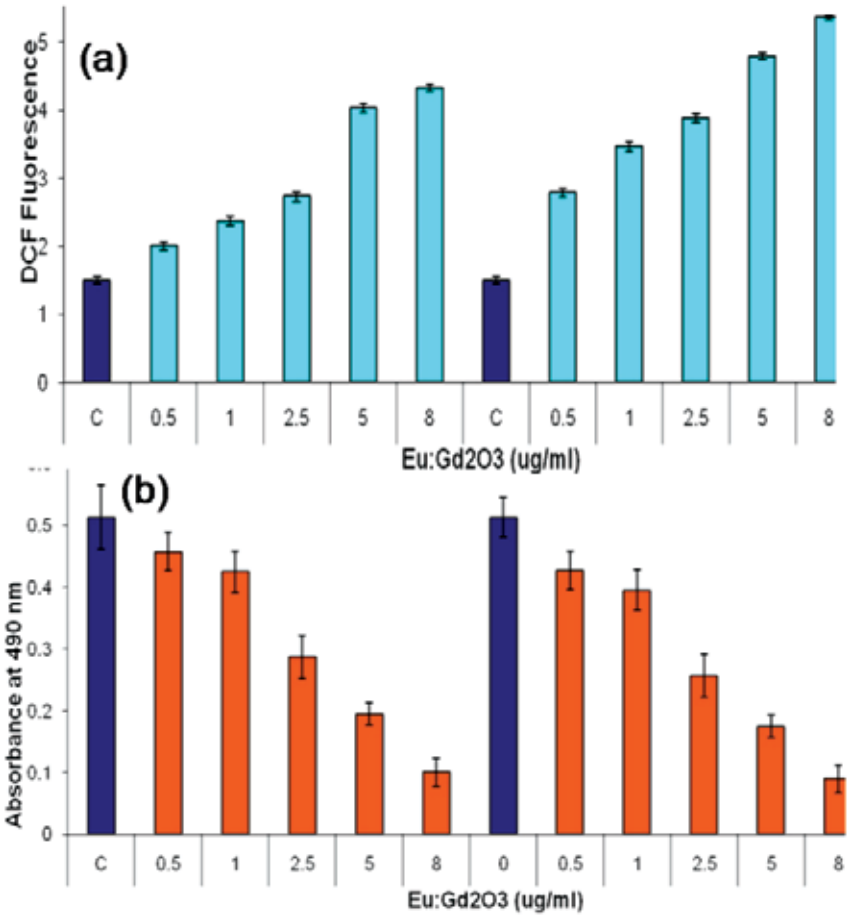

Fig. 9. (a) Uncoated (left) and coated (right) Eu:Gd_2O_3 induces ROS in rat LE cells, and (b) MTT assay effect of uncoated (left) and coated (right) Eu:Gd_2O_3 on cell viability.

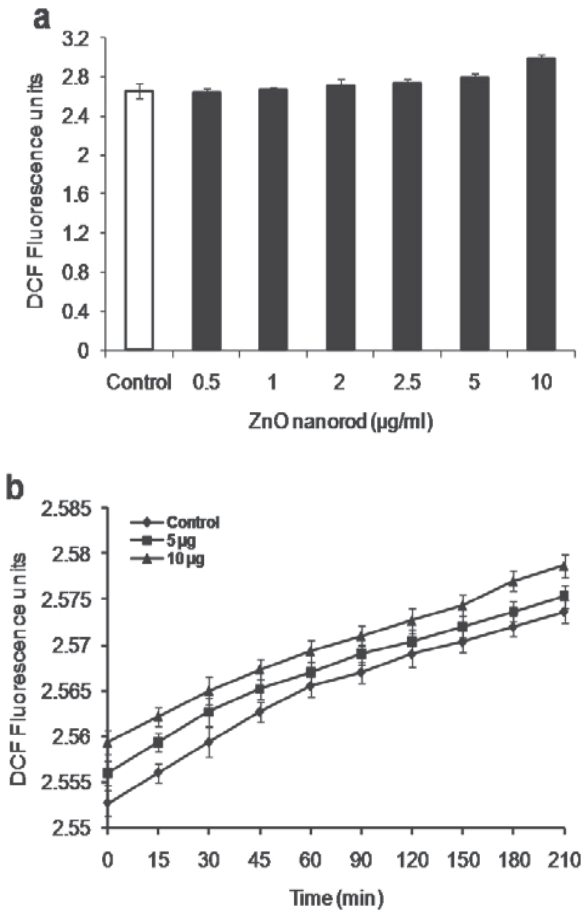

Fig. 10. Effect of ZnO nanorods on oxidative stress. Equal numbers of 1×105 hela cells/well were grown for 18 h. (a) The grown cells were incubated with 10 µM of DCF for 3 h, treated with different concentration of ZnO nanorods. Fluorescence was measured at excitation and emission wavelengths of 485 and 527 nm, respectively, at the end of 3 h. (b) Time kinetics of ROS formation by ZnO nanorods. Overnight grown hela cells were treated with 1, 5, and 10 µg/ml of ZnO nanorods. Fluorescence was measured at excitation and emission wavelengths of 485 and 527 nm, respectively, at different time points. The values are expressed as DCF fluorescence units, mean ± SD of eight wells and the Figure is a representative of three experiments performed independently

In order to check whether ZnO nanorod has any role on toxicity without altering oxidative stress, analysis of cell damage using MTT assay after exposing to various concentration of ZnO nanorods (0.5, 1.0, 2, 2.5, 5.0, 10 µg/ml) (Fig. 11a) was performed. The MTT assay showed no significant decrease in cell viability suggesting that ZnO nanorods did not have any effect on cell toxicity. More than 98% of cells were viable at concentration of 10 µg/ml ZnO nanorods which is also confirmed by live dead cell assay (Fig. 11b). 50% of cell death was observed in mouse neuroblastoma cells using 100 µg/ml of ZnO (Prasad et. al., 2006), whereas other reports have also shown 100% cytotoxicity at 15 µg/ml of ZnO on mesothelioma MSTO-211H or rodent 3T3 fibroblast cells (Brunner et. al., 2006), and 90% cell

death with 20mgL−1 of ZnO nanoparticles on HELF cells (Yuan et. al., 2010). Also, 5 mM of ZnO nanoparticle are shown to be less toxic to human T cells (Reddy et. al., 2007). Previous studies from our laboratory on hela cells and other cells such as lung epithelial, H1299, A549 and HaCaT cells showed the decrease in cell viability at 5 µg/ml when they were exposed to SWCNT and MWCNT (Manna et. al., 2005; Sarkar et. al., 2007; Ravichandran et. al., 2009). Toxicological studies on hela cells and conclude that ZnO nanorods could be the safe nanomaterials (Gopikrishnan el. al., 2010) for biological applications.

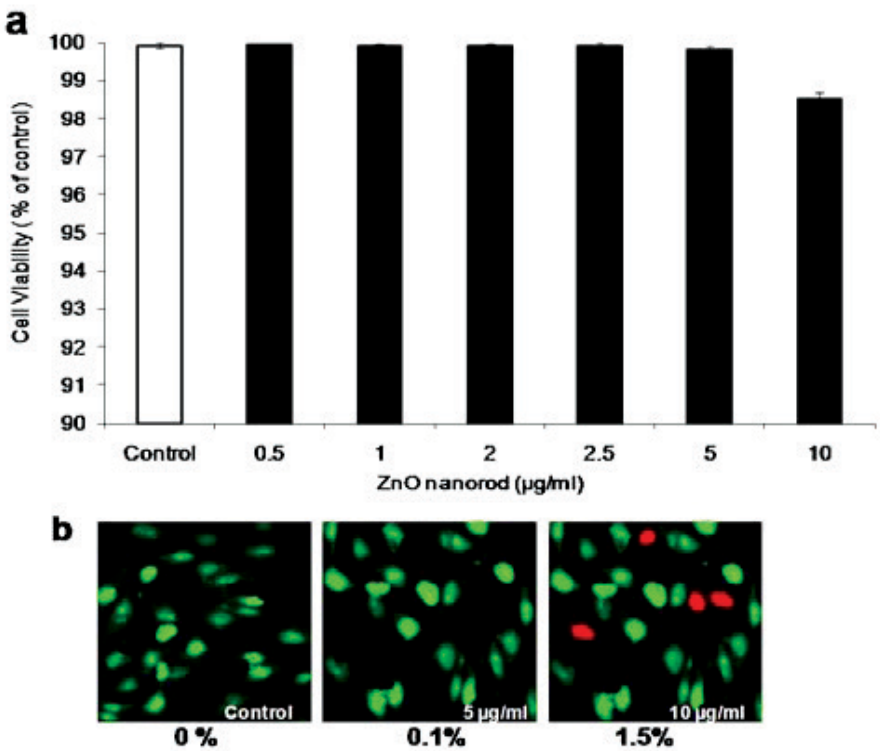

Fig. 11. Effect of ZnO nanorods on cell viability. HeLa cells (2000/well in a 96-well plate) were incubated for 12 h and treated with different concentration of ZnO nanorods for 72h. (a) Cell viability was assayed by MTT dye uptake. The mean absorbance at 570 nm is represented as cell viability percentage of the control and is mean ± SD of eight wells. (b) HeLa cells were treated with 5 µg/ ml and10 µg/ml of ZnO nanorods for 72 h and the dead cell (red color) numbers were counted. The percentage of dead cells is indicated below each photograph.

8. Magnetic nanoparticles

8.1 Synthesis: LaSrMnO nanoparticles

$La_{0.7}Sr_{0.3}MnO_3$ nanoparticles were synthesized by a sol-gel method from their acetate hydrate precursors, which were dissolved in water (Pradhan el. al., 2008; Zhang el. al., 2010). This solution was mixed with citric acid solution in 1:1 volume ratio ultrasonically for about 30 min. The mixture was heated in a water bath at 80 °C until all water is evaporated,

yielding a yellowish transparent gel. The gel was further heated in an oven at 100 °C which formed a foamy precursor. This precursor was decomposed to give black-colored flakes of extremely fine particle size on further heating at 400 °C for 4 h. The flakes were ground and sintered at 800 °C for duration of 2 h. Further heating in O_2 ambient removed the carbon content. The ball milling was used with methanol to reduce the size of nanoparticles of LSMO (Fig. 12). The solution containing suspended LSMO nanoparticles was separated using ultra-high centrifuge using methanol for several times.

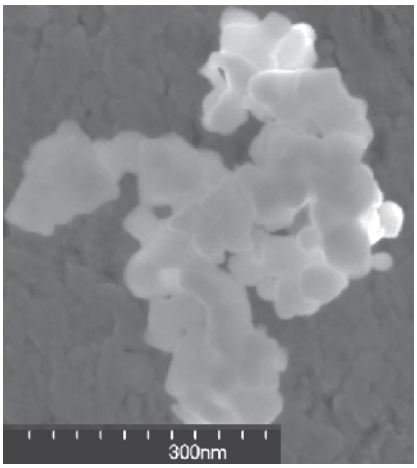

Fig. 12. FE-EM image of LSMO nanoparticles annealed at 800 ^{o}C, showing the individual nanoparticles.

The nanoparticles of ball milled LSMO were coated by adopting a base-catalyzed sol-gel process. 100 mg of LSMO were dispersed in 20 ml of 2-propanol solution and sonicated for 30 min and the nanoparticles were shown in Fig. 13 (a). 75 µl of TEOS and 25 µL of 25% NH_3H_2O solution were injected into the above mixture and sonicated for 30 min at 60 ^{o}C. The suspended silica capsulated LSMO nanoparticles were obtained by means of centrifugation. The coated nanoparticles were washed several times by using acetone and methanol in order to remove any excess unreacted chemicals. The purified powder was naturally dried. This procedure produces a very uniform SiO_2 coating, as determined using a transmission electron microscope. By changing the formulation of the coating solution, the coating thickness can be controlled.

8.2 FeCo nanoparticles

FeCo nanoparticles were synthesized by a coprecipitation method under Ar atmosphere from their chloride hydrate precursors. The FeCo nanopowders were dried in Ar gas, and were dispersed in 2- propanol solvent with 10^{-2} M and sonicated for 1 hour followed by addition of TEOS and 25% ammonia solution of volume ration 3:1. The mixture was sonicated for 1 h to coat the SiO_2 onto the surface of FeCo nanoparticles. The solution containing suspended FeCo-SiO_2 nanoparticles was decanted and purified using methanol several times in order to remove unreacted Fe and organic materials from the surface. The coated nanopowders were naturally dried in air. Figure 14 (a) shows XRD pattern of the as-synthesized samples, indicating typical amorphous phase. The amorphous phase in FeCo nanoparticles is generated because the coprecipitation reaction takes place below the glass

transition temperature and boron atoms are presented in the nanoparticles. The solution containing suspended FeCo-SiO_2 nanoparticles was decanted and purified using methanol several times in order to remove unreacted Fe and organic materials from the surface. The coated nanopowders were naturally dried in air.

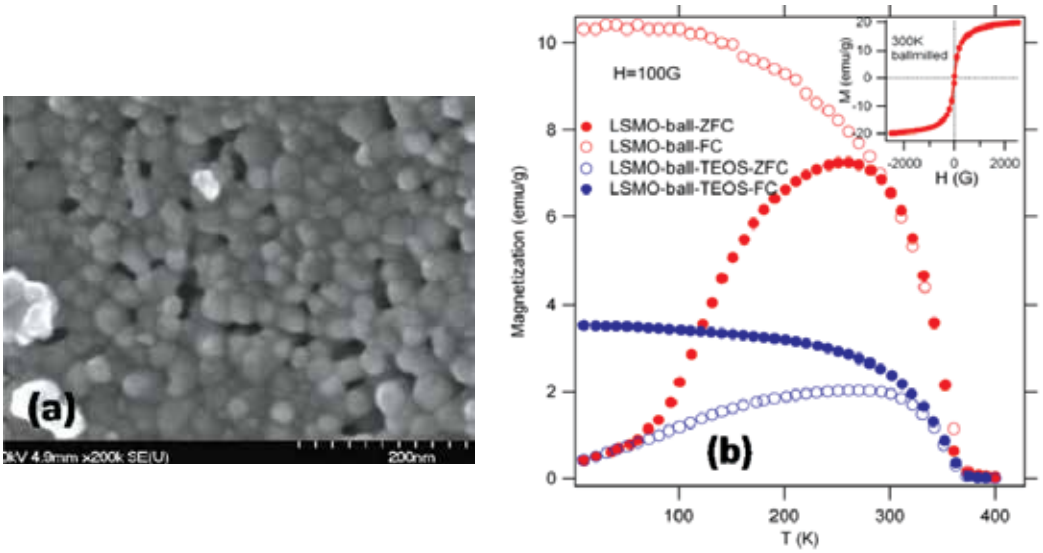

Fig. 13. (a) FE-SEM image of ball-milled LSMO nanopowder. (b) Temperature dependence of FC and ZFC magnetization of ballmilled and TEOS-coated nanoparticles. The inset shows the MH curve for ball-milled sample at 300 K.

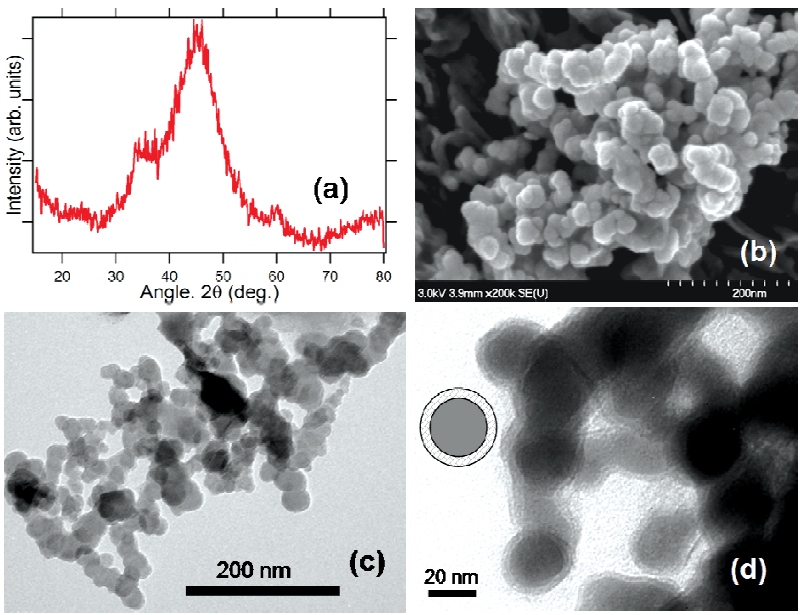

Fig. 14. (a) XRD patterns of FeCo nanoparticles prepared for 4 h, (b) FE-SEM and (c) TEM images of as synthesized FeCo nanoparticles, and (d) FeCo nanoparticles coated with silica.

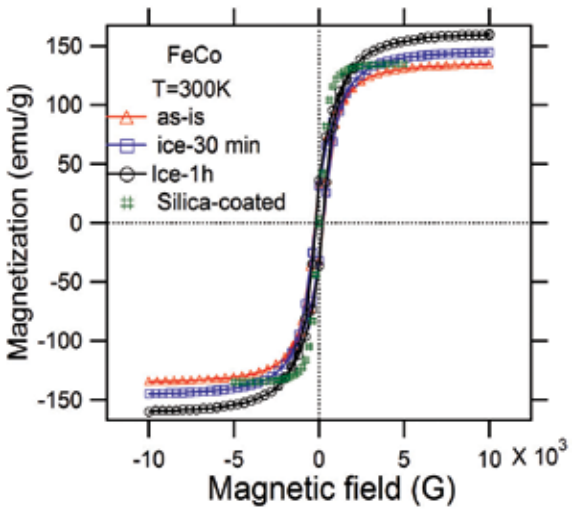

Fig. 15. Magnetization hysteresis loops of FeCo nanoparticles synthesized at various conditions and FeCo nanoparticles coated with silica.

Figure 14 (b) and (c) show the FE-SEM and TEM image of the uncoated FeCo nanoparticles, respectively. The FeCo nanoparticles are spherical in shape with about 20 nm in size and well-dispersed. The size distribution is very uniform, indicating the high-quality of the nanoparticles. Figure 14 (d) shows the TEM image of the silica coated FeCo nanoparticles, exhibiting well-formed FeCo cores with SiO_2 shell of couple of nm. It was realized that the shell diameter can be increased with increasing coating time, concentration and temperature. Figure 15 shows the magnetic hysteresis of FeCo nanoparticles. It is noted that the magnetization saturation moment increases when FeCo nanoparticles are synthesized at lower temperature (such as at ice temperature) due to controlled nucleation compared to as-grown nanoparticles. The magnetization of silica coated FeCo decreases, mainly due to the reduction in the demagnetization factor among nanoparticles through coupling, which is generally induced through direct exchange coupling and dipolar interaction. The magnetization reduction in coated FeCo is not significant, illustrating a strong dipolar exchange coupling.

9. Toxicity of magnetic nanoparticles

9.1 LSMO nanoparticles

The effect of LSMO and silica-coated LSMO NPs on reactive oxygen species were measured by a real time assay. To study the induction of oxidative stress in lung epithelial (LE) cells, $1x10^4$ cells/well were seeded in 96 well plate and grown overnight under standard culture conditions. The cells were then treated with 10 μM of dichlorofluorescein [5-(and-6)-carboxy-2, 7-dichloro-dihydroxyXuorescein diacetate, H_2DCFDA, (C-400, Molecular Probes, Eugene, OR)] for 3 h in Hank's balanced salt solution (HBSS) in incubator. Following 3 h of incubation, cells were washed with phosphate buffered saline (PBS) and 5 μg, 10 μg and 60 μg of LSMO and Si coated-LSMO NPs was added respectively and incubated at 37 °C. Cells were incubated in an incubator for 3 h as detailed in the Figure caption of Fig. 16, and fluorescence was measured at excitation wavelength of 485 nm and emission was recorded at 527 nm (Thermo Lab Systems, Franklin, MA). It is very clear from Fig. 16 that silica-coated LSMO NPs generate less oxidative stress in LE cells compared to uncoated NPs.

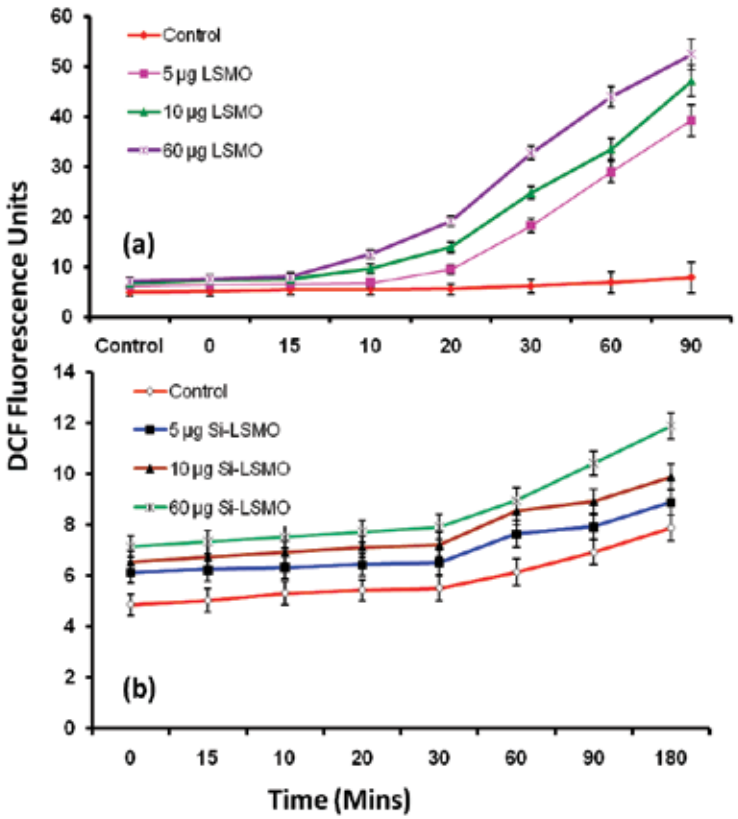

Fig. 16. Effects of magnetic nanoparticles on time kinetics of ROS in LE cells. (a) LSMO generates oxidative stress in LE cells. $1x10^5$ cells/well were seeded in a 96 well plate and grown at standard conditions for 24 h. Following overnight incubation, cells were starved in serum free medium for 24 h. Then cells were washed with phosphate buffered saline and incubated with 10 µM DCF for 3 h in HBSS. The cells were then treated with 5, 10 and 60 µg of LSMO. The change in DCF fluorescence was measured at 485 and 527 nm respectively after each time interval as shown. Values are mean ± SD of eight wells and are a representative from three experiments performed independently. (b) Silicon coated LSMO generates less oxidative stress in LE cells using the experiment described in (a).

The cytotoxicity assay was essentially performed as described earlier. The LE cells were seeded at $5x10^3$ cells/well in a 96 well plate and grown overnight. After 18 h in serum-free medium, cells were treated with different concentrations of LSMO and Si coated-LSMO and grown for 72 h. At the end of the incubation, cells were additionally treated with 3-[4, 5-dimethylthiazol- 2-yl]-2,5-diphenyltetrazolium bromide] MTT for 3 h. The cells were then washed with chilled PBS and formazon formed was extracted in 150 µL of acidic methanol and the absorbance was read at 570 nM. Fig. 17 demonstrates that the silica-coated LSMO NPs have better cell viability compared to uncoated NPs.

The above cytotoxicity tests (ROS and cell viability) demonstrate that LSMO nanoparticles can be potential candidate for various biomedical applications. Further perfection can be made achieved by coating the nanoparticles with silica in a controlled way. Apart from *in*

vivo biomedical applications, LSMO nanoparticles can also be utilized in protein purification due to their size-dependent magnetic properties, where large size (> 50 nm) NPs show strong ferromagnetic properties at room temperature. The LSMO nanoparticles may be complementary to paramagnetic nanoparticles composed of Ni and NiO (Rodríguez-Llamazares et. al, 2008; Wong et. al., 2008). The *in situ* modification of the surface during the precipitation (Wong et. al., 2008) used for LSMO nanoparticles becomes very effective in reducing the cytotoxicity.

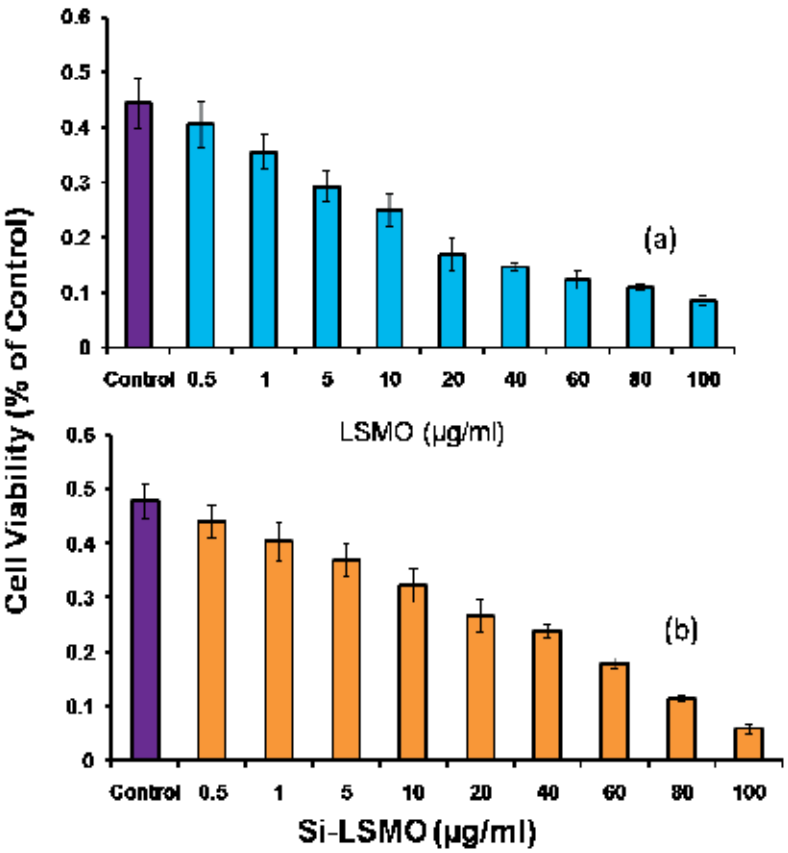

Fig. 17. Effect of magnetic nanoparticles on cell viability. (a) LSMO decreases cell viability in LE cells. 2000 cells/well were seeded in a 96 well and grown under standard condition for 24 h. Following overnight incubation, cells were starved in serum free medium for 24 h. Cells were then treated with 0.5, 1, 5, 10, 20, 40, 60, 80 and 100 µg of LSMO and allowed to grow for 72 h. The MTT assay was then performed. The mean absorbance at 570 nm is represented as percent of control and is mean ± SD of eight wells. The values are a representative from three experiments performed independently. (b) Effect of silica-coated LSMO cell viability using the procedure described in (a).

9.2 FeCo nanoparticles

The result of the toxicity test is presented in Fig. 18. The effect of FeCo and silica-coated FeCo nanoparticles on rat LE cells suggests that they induce ROS in a dose dependent

manner. Uncoated FeCo nanoparticles increased ROS by 3.2 folds as compared to control at a concentration as low as 2.5 µg. The coated FeCo nanoparticles showed 3.6 fold increase in ROS (Fig. 18 (b)). To study the extent of damage caused by coated and uncoated FeCo on cell viability, MTT assay was carried in LE cells treated with various concentrations and the results suggest that the cell viability decrease with increase in concentration of FeCo nanoparticles by 72 hrs compared to control. Only 40% of cells found to be viable at 2.5 µg/ml of uncoated FeCo, where as 35% found to be silica-coated FeCo nanoparticles. This suggests that the silica shell thickness should be increased in order to reduce the toxicity of FeCo nanoparticles for any biomedical applications.

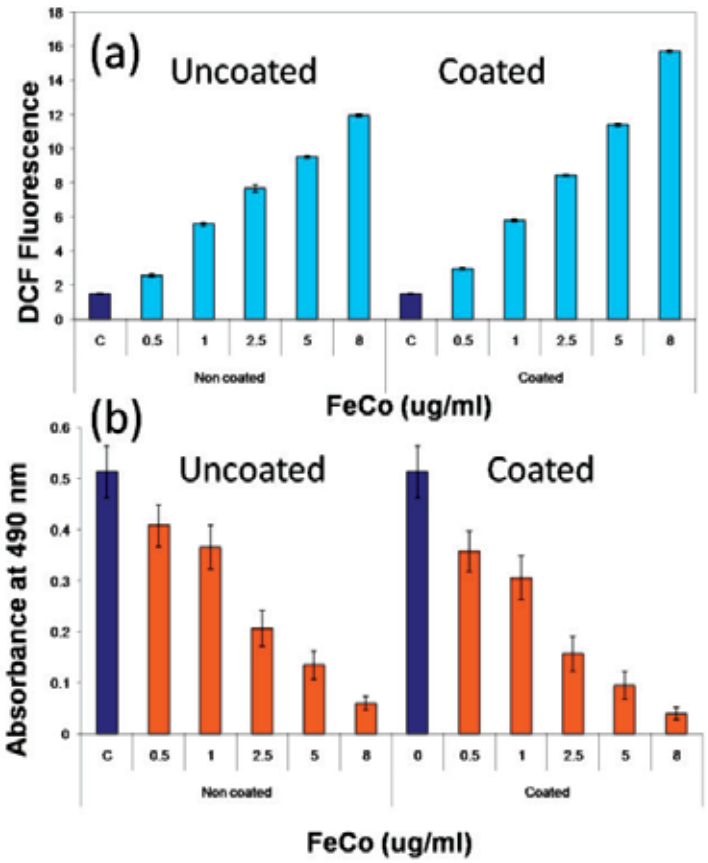

Fig. 18. MTT assay effect of (a) uncoated and (b) coated FeCo nanoparticles on cell viability.

10. Conclusion

Nanomaterials are widely used for biomedical applications because their sizes are comparable with most of the biological entities. The development of novel biomedical technologies involving *in vivo* use of nanoparticles presents multidisciplinary attempts to overcome the major chemotherapeutic drawbacks. Nanomaterials stand at the boundaries between physical, chemical, biological and medical sciences, and the advances in this field impact analyzing and treating biological systems at the cell and sub-cell levels, providing

revolutionary approaches for the diagnosis, prevention and treatment of some fatal diseases, such as cancer. However, the synthesis, characterization and use of these nanomaterials need thorough studies. The synthesis and characterization of several kinds of nanomaterials, such as luminescent, semiconducting and magnetic, are discussed. The toxicity associated with these nanomaterials is also discussed.

Luminescent nanostructures. Eu^{3+} doped Gd_2O_3 nanomaterials are very promising luminescent as well as magnetic material. Some typical growth process for varieties of nanostructures, such as nanoparticles, nanorods, nanotubes and encapsulated nanoparticles, are described with some insight into their microstructures and their optical and magnetic properties. The toxicity studies of some of these nanostructures demonstrate that Eu:Gd_2O_3 nanoparticles are relatively nontoxic and the toxicity is further decreased on silica coating.

Semiconductor nanostructures. A typical chemical route was explored to synthesize large scale ZnO nanorods with about 21 nm in diameter and 50 nm in length. Toxicological studies on hela cells show that ZnO nanorods could be the safe nanomaterials for biological applications.

Magnetic nanostructures. Manganites and FeCo nanoparticles were synthesized by the chemical technique and the nanostructures were coated with TEOS and other macromolecules. The manganites display essential magnetic properties applicable for hyperthermia applications. On the other hand, FeCo nanoparticles display strong magnetism appropriate for protein purification.

The cytotoxicity tests (ROS and cell viability) demonstrate that both manganites and FeCo nanoparticles can be potential candidate for various biomedical applications. Further perfection can be made achieved by coating the nanoparticles with silica in a controlled way. The silica shell thickness should be increased in order to reduce the toxicity of FeCo nanoparticles for any biomedical applications.

11. Acknowledgments

This work is supported by the NSF for Research Infrastructure in Science and Education (RISE) grant No. HRD-0734846 and RISE-HRD-0931373. The authors are thankful to T. Holloway for experimental help.

12. References

Adams, L. K.; Lyon, D. Y. & Alvarez, P. J. (2006). Comparative eco-toxicity of nanoscale TiO_2, SiO_2, and ZnO water suspensions**.** *Water Research*, 40, 19, pp. 3527-3532 (November 2006), ISSN 0043-1354

Alivisatos, P. (2004). The use of nanocrystals in biological detection. *Nature Biotechnology*, 22,1, (January 2004) pp. 47–52, ISSN 1087-0156

Beckett, W. S.; Chalupa, D. F.; Pauly-Brown, A.; Speers, D. M.; Stewart, D. J.; Frampton, M. W.; Utell, D. J.; Huang, L. S.; Cox, C.; Zareba, W. & Oberdorster, G. (2005). Comparing Inhaled Ultrafine vs Fine Zinc Oxide Particles in Healthy Adults:A Human Inhalation Study. *American Journal of Respiratory and Critical Care Medicine*, 171, 10, (May 2005) pp. 1129-1135, ISSN 1073-449X

Bridot, J.-L.; Faure, A.-C.; Laurent, S.; Rivière, C.; Billotey, C.; Hiba, B.; Janier, M.; Josserand, V.; Coll, J.-L.; Vander Elst, L.; Muller, R.; Roux, S.; Perriat, P. & Tillement, O. (2007). Hybrid gadolinium oxide nanoparticles: multimodal contrast agent for in vivo

imaging. *Journal of the American Chemical Society*, 129, 16, (March 2007) pp. 5076-5084, ISSN 0002-7863

Brunner, T. J.; Wick, P.; Manser, P.; Spohn, P.; Grass, P. N.; Limbach, L.; Bruinink, A. & Stark, W. J. (2006). In Vitro Cytotoxicity of Oxide Nanoparticles: Comparison to Asbestos, Silica, and the Effect of Particle Solubility. *Environmental Science & Technology*, 40, 14, (March 2006) pp. 4374-4381, ISSN 0013-936X

Chang, C.; Kimura, F.; Kimura, T. & Wada, H. (2005). Preparation and characterization of rod-like Eu:Gd_2O_3 phosphor through a hydrothermal routine. *Materials Letters,* 59, 8-9, (April 2005) 1037-1041, ISSN 0167-577X

Chertok, B; Moffat, B. A.; David, A.E.; Yu F. Q.; Bergemann, C.; Ross, B. D. & Yang, V. C. (2008). Iron oxide nanoparticles as a drug delivery vehicle for MRI monitored magnetic targeting of brain tumors. *Biomaterials*, 29, 4, (February 2008) pp. 487-496, ISSN 0142-9612

Deng, X. Y.; Luan, Q. X.; Chen, W. T.; Wang, Y. L.; Wu, M. H.; Zhang, H. J. & Jiao, Z. (2009). Nanosized zinc oxide particles induce neural stem cell apoptosis. *Nanotechnology*, 20, 11, (February 2009) 115101, ISSN 0957-4484

Dosev, D.; Nichkova, M.; Liu, M.; Guo, B.; Liu, G.; Hammock, B. B. & Kennedy, L. M. (2005). Application of luminescent Eu:Gd_2O_3 nanoparticles to the visualization of protein micropatterns. *Journal of Biomedical Optics*, 10,6, (November 2005) 064006, ISSN 1083-3668

Fine, J. M.; Gordon, T.; Chen, L. C.; Kinney, P.; Falcone, G. & Beckett, W. S. (1997). Metal Fume Fever: Characterization of Clinical and Plasma IL-6 Responses in Controlled Human Exposures to Zinc Oxide Fume at and Below the Threshold Limit Value. Journal of Occupational & Environmental Medicine, 39, 8, (August 1997) pp. 722-726, ISSN 1076-2752

Ghoshal, T.; Kar, S. & Chaudhuri, S. (2006). Synthesis and optical properties of nanometer to micrometer wide hexagonal cones and columns of ZnO. *Journal of Crystal Growth*, 293, 2, (August 2006) pp. 438-446, ISSN: 0022-0248

Gopikrishnan, R.; Zhang, K.; Ravichandran, P.; S. Baluchamy, Ramesh, V.; Biradar, S.; Ramesh, P.; Pradhan, J.; Hall, J. C.; Pradhan, A. K. & Ramesh, G. T. (2010). Synthesis, Characterization and Biocompatibility Studies of Zinc oxide (ZnO) Nanorods for Biomedical Application. *Nano-Micro Letters*, 2, 1, (2010) pp. 27-30, ISSN: 2150-5551

He, Y.; Tian, Y. & Zhu, Y. (2003). Large-scale-synthesis of luminescent Y_2O_3: Eu nanobelts. *Chemistry Letters*, 32, 9, (August 2003) pp. 862-863, ISSN 0366-7022

Hirsch, L. R.; Stafford, R. J.; Bankson, J. A.; Sershen, S. R.; Rivera, B.; Price, R. E.; Hazle, J. D.; Halas, N. J. & West, J. L. (2003). Nanoshell-mediated near-infrared thermal therapy of tumors under magnetic resonance guidance. *Proceedings of the National Academy of Sciences of the United States of America*, 100, 23, (November 2003) pp. 13549–13554, ISSN 1091-6490

Hu, S. H.; Chen, S. Y.; Liu, D. M. & Hsiao, C. S. (2008). Core/single-crystal-shell nanospheres for controlled drug release via a magnetically triggered rupturing mechanism. *Advanced Materials,* 20, 14, (July, 2008) pp. 2690-2695, ISSN 1521-4095

Hu, X.; Cook, S.; Wang, P. & Hwang, H. (2009). In vitro evaluation of cytotoxicity of engineered metal oxide nanoparticles. *Science of The Total Environment*, 407, 8, (April 2009) pp. 3070-3072, ISSN 0048-9697

Jia, G.; Liu, K.; Zheng, Y.; Song, Y.; Yang, M. & You, H. P. (2009). Highly uniform $Gd(OH)_3$ and Gd_2O_3:Eu^{3+} nanotubes: facile synthesis and luminescence properties. *Journal of Physical Chemistry C*, 113,15, (March 2009) pp. 6050-6055, ISSN 1932-7447

Kim, S.; Lim, Y. T.; Soltesz, E. G.; De Grand, A. M.; Lee, J.; Nakayama, A.; Parker, J. A.; Mihaljevic, T.; Laurence, R. G.; Dor, D. M.; Cohn, L. H.; Bawendi, M. G.; & Frangioni, J. V. (2003). Near-infrared fluorescent type II quantum dots for sentinel lymph node mapping. Nature Biotechnology, 22, 1, (December 2003) pp. 93–97, ISSN 1087-0156

Lewin, M.; Carlesso, N.; Tung, C.-H.; Tang, X.-W.; Cory, D.; Scadden, D. T.; & Weissleder, R. (2000). Tat peptide-derivatized magnetic nanoparticles allow in vivo tracking and recovery of progenitor cells. *Nature Biotechnology*, 18, 4, (April 2000) pp. 410–414, ISSN 1087-0156

Li, S.; Song, H.; Yu, H.; Lu, S.; Bai, X.; Pan, G.; Lei, Y.; Fan, L. & Wang, T. (2007). Influence of annealing temperature on photoluminescence characteristics of Gd_2O_3:Eu/AAO nanowires. *Journal of Luminescence*, 122-123, 1, (January-April 2007) pp. 876-878, ISSN 0022-2313

Liao, H. W. & Hafner, J. H. (2005). Gold nanorod bioconjugates. *Chemistry of Materials*, 17, 18, (August 2005) pp. 4636–4641, ISSN 0897-4756

Lin, D. H. & Xing, B. S. (2007). Phytotoxicity of nanoparticles: Inhibition of seed germination and root growth. Environmental Pollution, 150, 2, (November 2007) pp. 243-250, ISSN 0269-7491

Liu, G. X.; Hong, G.Y.; Dong, X.T. & Wang, J.X. (2008). Preparation and characterization of Gd_2O_3:Eu^{3+} luminescence nanotubes. *Journal of Alloys and Compounds*, 466, 1-2, (December 2007) pp. 512–516, ISSN 0925-8388

Liu, L.; Ma, E.; Li, R.; Liu, G. & Chen, X. (2007) Effects of phonon confinement on the luminescence dynamics of Eu^{3+} in Gd_2O_3 nanotubes. *Nanotechnology*, 18, 1, (January 2007) pp. 015403-015407, ISSN 0957-4484

Liu, T. Y.; Hu S. H.; Liu, D. M., Chen, S. Y. & Chen, I. W. (2009). Biomedical nanoparticle carriers with combined thermal and magnetic responses. *Nano Today*, 4, 1, (February 2009) pp. 52-65, ISSN 1748-0132

Lou, X. W.; Wang, Y.; Yuan, C.; Lee, J. Y. & Archer, L. A. (2006). Template-free synthesis of SnO_2 hollow nanostructures with high lithium storage capacity. *Advanced Materials*, 18, 17, (September 2006) pp. 2325-2329, ISSN 1521-4095

Ma, T.; Guo, M.; Zhang, M.; Zhang, Y. & Wang, X. (2007). Density-controlled hydrothermal growth of well-aligned ZnO nanorod arrays. *Nanotechnology*, 18, 3, (January 2007) 035605, ISSN 0957-4484

Manna, S. K.; Sarkar, S.; Barr, J.; Wise, K.; Barrera, E. V.; Jejelowo, O.; Rice-Ficht, A. C. & Ramesh, G. T. (2005). Single-Walled Carbon Nanotube Induces Oxidative Stress and Activates Nuclear Transcription Factor-κB in Human Keratinocytes. *Nano Letters*, 5, 9, (August 2005) pp. 1676-1684, ISSN: 1530-6984

Mao, Y. B.; Tran, T.; Guo, X.; Huang, J. Y.; Shih, C. K.; Wang, K. L. & Chang, J. P. (2009). Luminescence of nanocrystalline erbium-doped yttria. *Advanced Functional Materials*, 19, 5, (March 2009) pp. 748-754, ISSN 1616-3028

Mao, Y.; Huang, J. Y.; Ostroumov, R.; Wang, K. L. & Chang, J. P. (2008). Synthesis and luminescence properties of Erbium-doped Y_2O_3 nanotubes. *Journal of Physical Chemistry C*, 112, 7, (January 2008) pp. 2278-2285, ISSN 1932-7455

Nichkova, M.; Dosev, D.; Gee, S. J.; Hammock, B. D. & Kennedy, I. M. (2005). Microarray immunoassay for phenoxybenzoic acid using polymer encapsulated Eu:Gd_2O_3 nanoparticles as fluorescent labels. *Analytical Chemistry*, 77, 21, (September 2005) pp. 6864-6873, ISSN 0003-2700

Nichkova, M.; Dosev, D.; Perron, R.; Gee, S. J.; Hammock, B. D. & Kennedy, I. M. (2006). Eu^{3+}-doped Gd_2O_3 nanoparticles as reporters for optical detection and visualization

of antibodies patterned by microcontact printing. *Analytical and Bioanalytical Chemistry*, 384, 3, (February 2006) pp. 631-637, ISSN 1618-2642

Petoral Jr., R. M.; Söderlind, F.; Klasson, A.; Suska, A.; Fortin, M. A.; Abrikossova, N.; Selegård, L.; Käll, P.; Engström, M. & Uvdal, K. (2009). Synthesis and characterization of Tb^{3+}-doped Gd_2O_3 nanocrystals: a bifunctional material with combined fluorescent labeling and MRI contrast agent properties. *Journal of Physical, Chemistry C*, 113, 17, (April 2009) pp. 6913-6920, ISSN 1932-7447

Plank, C.; Schillinger, U.; Scherer, F.; Bergemann, C.; Rémy, J. S.; Krötz, F.; Anton, M.; Lausier, J. & Rosenecker, J. (2003). The magnetofection method: using magnetic force to enhance gene delivery. Biological Chemistry, 384, 5, (May 2003) pp. 737-747, ISSN 1431-6730

Pradhan, A.K.; Bah, R.; Konda, R. B.; Mundle, R.; Mustafa, H.; Bamiduro, O.; Rakhimov, R. R.; Wei, Xiaohui; & Sellmyer, D. J. (2008). Synthesis and magnetic characterizations of manganite-based composite nanoparticles for biomedical applications. *Journal of Applied Physics*, 103, 7, (2008) 07F704, ISSN 0021-8979

Pradhan, A.K.; Williams, T.M.; Zhang, K.; Hunter, D.; Dadson, J.B.; Lord, K.; Roy, U.N.; Cui, Y. & Burger, A. (2006). Growth of aligned ZnO Nanorods. *Journal of Nanoscience and Nanotechnology*, 6, 7, (July 2006) pp. 1985-1989, ISSN 1550-7033

Prasad, V.; Souza, C. D.; Yadav, D.; Shaikh, A. J.; & Vigneshwaran, N. (2006). Spectroscopic characterization of zinc oxide nanorods synthesized by solid-state reaction. *Spectrochimica Acta Part A*, 65, 1, (September 2006) pp. 173-178, ISSN 1386-1425

Ravichandran, P.; Periyakaruppan, A.; Sadanandan, B.; Ramesh, V.; Hall, J. C.; Jejelowo, O. and Ramesh, G. T. (2009). Induction of apoptosis in rat lung epithelial cells by multiwalled carbon nanotubes. *Journal of Biochemical and Molecular Toxicology*, 23, 5, (October 2009) pp. 333-344, ISSN 1099-0461

Reddy, K. M.; Feris, K.; Bell, J.; Wingett, D. J.; Hanley, C. & Punnoose, A. (2007). Selective toxicity of zinc oxide nanoparticles to prokaryotic and eukaryotic systems. *Applied Physics Letters*, 90, 21, (May 2007) 213902, ISSN 0003-6951

Rodríguez-Llamazares, S.; Merchán, J.; Olmedo, I.; Marambio, H. P.; Muñoz, J. P.; Jara, P.; Sturm, J. C.; Chornik, B.; Peña, O.; Yutronic, N.; & Kogan, M. J. (2008). Ni/Ni Oxides Nanoparticles with Potential Biomedical Applications Obtained by Displacement of a Nickel-Organometallic Complex. *Journal of Nanoscience and Nanotechnology,* 8, 8, (August 2008) pp. 3820-3827, ISSN 1550-7033

Sarkar, S.; Sharma, C.; Yog, R.; Periakaruppan, A.; Jejelowo, O.; Thomas, R.; Barrer, E. V.; Rice-Ficht, A. C.; Wilson, B. L. & Ramesh, G. T. (2007). Analysis of Stress Responsive Genes Induced by Single-Walled Carbon Nanotubes in BJ Foreskin Cells. Journal of Nanoscience and Nanotechnology, 7, 2, (February 2007) pp. 584-592, ISSN 1550-7033

Satarkar, N. S. & Hilt, J. Z. (2008). Magnetic hydrogel nanocomposites for remote controlled pulsatile drug release. *Journal of Controlled Release*, 130, 3, (September 2008) pp. 246-251, ISSN 0168-3659

Seo, S. Y.; Sohn, K. S.; Park, H. D. & Lee, S. (2002). Optimization of Gd_2O_3-based red phosphors using combinatorial chemistry method. *Journal of the Electrochemical Society*, 149, 1, (December 2002) pp. H12-H18, ISSN 0013-4651

Sharma, C. S.; Sarkar, S.; Periyakaruppan, A.; Barr, J.; Wise, K.; Thomas, R.; Wilson, B. L. & Ramesh, G. T. (2007). *Journal of Nanoscience and Nanotechnology*, 7, 7, (July 2007) pp. 2466-2472, ISSN 1550-7033

Shvedova A. A.; Castranova V.; Kisin E. R.; Schwegler-Berry D.; Murray A. R.; Gandelsman V. Z.; Maynard A. & Baron P. (2003). Exposure to carbon nanotube material: assessment

of nanotube cytotoxicity using human keratinocyte cells. Journal of Toxicology and Environmental Health, Part A, 66, 20, (June 2003) pp. 1909-1926, ISSN 1528-7394

Son, S. J.; Reichel, J.; He, B.; Schuchman, M. & Lee, S. B. (2005). Magnetic nanotubes for magnetic-field-assisted bioseparation, biointeraction, and drug delivery. *Journal of the American Chemical Society*, 127, 20, (April 2005) pp. 7316-7317, ISSN 0002-7863

Tsuji, J. S.; Maynard, A. D.; Howard, P. C.; James, J. T.; Lam, C. W.; Warheit, D. B. & Santamaria, A. B. (2005). Research Strategies for Safety Evaluation of Nanomaterials, Part IV: Risk Assessment of Nanoparticles. *Toxicological Sciences*, 89, 1, (September 2005) pp. 42-50, ISSN 1096-0929

Wang, H.; Uehara, M.; Nakamura, H.; Miyazaki, M. & Maeda, H. (2005). Synthesis of well-dispersed Y2O3:Eu nanocrystlas and self-assembled nanodisks using a simple non-hydrolytic route. Advanced Materials, 17, 20, (October 2005) pp. 2506-2509, ISSN 1521-4095

Wei, W.; Ma, G. H.; Hu, G.; Yu, D.; Mcleish, T.; Su, Z. G. & Shen, Z. Y. (2008). Preparation of hierarchical hollow $CaCO_3$ particles and the application as anticancer drug carrier. *Journal of the American Chemical Society*, 130, 47, (November 2008) pp. 15808-15810, ISSN 0002-7863

Whitesides, G. M. (2003). The 'right' size in nanobiotechnology. *Nature Biotechnology*, 21, 10, (September 2003) pp. 1161-1165, ISSN 1087-0156

Wong, J. E.; Gaharwar, A. K.; Müller-Schulte, D.; Bahadur, D. & Richtering, W. (2008). Magnetic Nanoparticle-Polyelectrolyte Interaction: A Layered Approach for Biomedical Applications. *Journal of Nanoscience and Nanotechnology*, 8, 8, (August 2008) pp. 4033-4040, ISSN 1533-4880

Xu, X. L. & Asher, S. A. (2004). Synthesis and utilization of monodisperse hollow polymeric particles in photonic crystals. *Journal of the American Chemical Society*, 126, 25, (June 2004) pp. l7940-7945, ISSN 0002-7863

Yang, H.; Liu, C.; Hui, Yang, D.; Zhang, H. & Xi, Z. (2009). Comparative study of cytotoxicity, oxidative stress and genotoxicity induced by four typical nanomaterials: the role of particle size, shape and composition. *Journal of Applied Toxicology*, 29, 1, (August 2009) pp. 69-78, ISSN 1099-1263

Yang, J.; Li, C. X.; Cheng, Z. Y.; Zhang, X. M.; Quan, Z. W.; Zhang, C. M. & Lin, J. (2007). *Size-tailored synthesis and luminescent properties of one-dimensional* Gd_2O_3*: Eu nanorods and microrods*. *Journal of Physical Chemistry C*, 111, 49, (November 2007) pp. 18148-18154, ISSN 1932-7447

Yuan, J. H.; Chen, Y.; Zha, H. X.; Song, L. J.; Li, C. Y.; Li, J. Q. & Xia, X. H. (2010). Determination, characterization and cytotoxicity on HELF cells of ZnO nanoparticles. Colloids and Surfaces B: Biointerfaces, 76, 1, (March 2010) pp. 145-150, ISSN 0927-7765

Zaveri, T.; Dolgova, N.; Chu, B. H.; Lee, J.; Lele, T.; Ren, F. & Keselowsky, B. G. (2009). *Proceedings of IFMBE*, pp. 119-120, ISSN 1680-0737, Miami, Florida, USA, May 2009, Springer, Berlin, Heidelberg

Zhang, K.; Holloway, T.; Pradhan, J.; Bahoura, M.; Bah, R.; Rakhimov, R. R.; Pradhan, A. K.; Prabakaran, R. & Ramesh, G. T. (2010). Synthesis and Magnetic Characterizations of $La_{1-x}Sr_xMnO_3$ Nanoparticles for Biomedical Applications. *Journal of Nanoscience and Nanotechnology*, 10, 9, (September 2010) pp. 5520-5526, ISSN 1550-7033

Zhang, K.; Holloway, T.; Bahoura, M.; Pradhan, A. K.; Prabakaran, R.; Pradhan, J.; Smith, S.; Hall, J. C.; Ramesh, G. T.; Sahu, D. R.; Huang, J.-L. (2009) Europium doped Gd_2O_3 and FeCo nanoparticles for biomedical application. *Proceedings of SPIE*, 7291, (March 2009) 729104-10, ISSN 0277-786X

16

Nanopatterned Surfaces for Biomedical Applications

Rebecca McMurray, Matthew J Dalby and Nikolaj Gadegaard
University of Glasgow,
UK

1. Introduction

1.1 Nanotopography and stem cells

Topography was first identified to influence cell behaviour as early as 1911 when R.G. Harrison observed the guidance of cells along the fibres of a spider's web (Harrison 1911). Since this discovery, investigations into the topographical effect on cell behaviour identified that topography can have not only a strong affect on cell morphology, but it can also influence cell adhesion, proliferation and gene expression.

The development of biomaterials has lead to the generation of tissue engineering, whereby a combinatorial approach is utilized, merging elements of biology and engineering with the overall aim to develop functional tissues. The first generation of biomaterials were developed to be bioinert and provide mechanical support, the next generation were designed to be bioactive (elicit a desired cell response) and third generation biomaterials will need to provide reproducible influence of cells at the molecular level (Hench and Polak 2002). The inclusion of factors such as topography may allow this reproducible level of molecular influence to be incorporated into materials that are e.g. biodegradable and/or load-bearing without sacrificing their engineering role.

It is interesting that nanotopography appears to have as strong an influence on cells as microtopography (Dalby, Riehle et al. 2002; Teixeira, Abrams et al. 2003; Curtis, Gadegaard et al. 2004) as it is on the same size scale as the cell receptors rather than the whole cell. It is this rather bottom-up organisational approach with cells being e.g. aligned by nanogrooves one adhesion (containing integrin recptors) at a time rather than the top-down alignment of microgrooves where the whole cell has to conform to the feature and the adhesions will then follow. Importantly, current research has gone on to show that nanotopography has the ability to elicit specific cues and promote the controlled differentiation of stem cells *in vitro*. The use of stem cells to potentially generate patient-specific tissues using biomaterials provides huge scope for their use in regenerative medicine. A pioneering and historic perspective has been published by Curtis (Curtis 2004).

The ability to produce such topographical substrates has largely come from fabrication techniques that are routinely used within the electronics industry. These techniques include photolithography and electron beam lithography, to produce precise, reproducible nanoscale topographies. As technology has advanced within this field, it has allowed the production of increasingly smaller feature sizes; currently electron beam lithography enables the production of feature sizes down to approximately 5 nm (Vieu 2000). Injection

moulding further provides a viable platform for the fast, relatively inexpensive polymer replication of many identical topographical substrates produced by such techniques. Other techniques for producing nanotopographical substrates include, polymer phase separation and electro-spinning; these, however, produce more random topographies.
These nanoscale topographies have gained more prominence in terms of biomimetic comparison as *in vivo* nanotopographical patterns of tissues and their biological implications has become more widely acknowledged. It is the potential to replicate these features and thereby their biological properties *in vitro* that holds great potential. Typically within a tissue there is a hierarchy of features, for instance in bone, the bone tissue itself is in the macro scale, with fibrillar structures at the micro scale and then nanometer scale interactions such as protein: protein. This interaction of proteins and cells is hugely important; binding of integrin receptors to the extracellular matrix (ECM) form what are known as focal complexes, points of attachment between a cell and the extracellular matrix. The disruption or alteration of these focal complexes may have a two-fold effect altering cell signalling, gene expression and ultimately differentiation. This can be either indirectly influenced via intracellular signalling of focal adhesion kinase and activation of downstream molecules in a signal cascade (McBeath, Pirone et al. 2004; Kilian, Bugarija et al. 2010), or directly influenced via changes in the cytoskeleton and nucleoskeleton leading to alterations in gene expression via changes in chromosomal packing and positioning (Dalby, Biggs et al. 2007).

2. Micro- and nanofabrication technology

A major leap in investigating cell response to topographic features was made possible by the continuous development of semiconductor technologies such as lithography and etching techniques. With these new techniques in hand it was now possible to design and manufacture various patterns with very specific dimensions. It quickly became clear that cells responded to features in the micron range and thus sparked the question of how small dimensions cells can detect. At that time, the technology required to fabricate patterns in the sub-micron range was immature and it was not till the 1990s that electron beam lithography (EBL) successfully was deployed to make such patterns. The strength of EBL is its maskless properties where any micron and sub-micron shape can be realised, in contrast to all other lithography techniques. The results from the EBL patterns clearly showed that cells can respond to features as small as 15-30 nm which is comparable to the size of individual proteins or cell receptor ligands. In the early days of cell engineering, most of the results were realised by optical and electron microscopy. This provided important information on a single cell level. In turn this meant that the requirements for samples could be limited to $1mm^2$-$1cm^2$, thus each sample could be directly produced from the lithography and etching processes. Typical materials at the time were quartz for its optical properties and silicon because the fabrication flow was "borrowed" from the semiconductor industry. With the aim to gain a deeper understanding of the molecular mechanisms controlling the cell behaviour, biochemical and genetic methods were later being applied. Such techniques required larger patterns or more samples to gather sufficient material for the assays. Replication techniques such as hot embossing and later injection moulding have enabled the fabrication side to supply the biological demand. Modern lithographic and replication techniques will be presented and discussed in the next sections.
Today, most of the topographies investigated have been fabricated to produce more or less specific patterns for the cells to be exposed to. There are several good text books describing

the lithographic process in more detail (Franssila 2004; Madou 2011) as well as advanced fabrication technologies are available (Wang 2010). In most cases the fabrication flow requires three distinct steps to make the samples for the biological experiments:

1. Pattern definition
2. Pattern transfer
3. Pattern replication

2.1 Clean rooms

With a continuously decreasing size of features fabricated it is necessary to operate in dust-free conditions, since the features fabricated are comparable or smaller than dust particles. Such clean conditions are obtained in a clean room where the air is constantly filtered and when entering the room its temperature and humidity is also very carefully controlled. The most common measure for the quality of a clean room is it operational class, where a class 1000 clean room has less than 1000 particles (0.5 μm or smaller) in a cubic foot. Most academic labs operate between class 1000-10000, whereas semiconductor industry is 1-10.
Other important factors inside a clean room are stable temperature and humidity. The stability of the temperature is important as the chemical processes carried out are sensitive to variations in the temperature and an increase in temperature will lead to an increase in the rate of a chemical reaction. Some of the polymers (resists) being used in the clean room are sensitive to moisture and will change their properties depending of the humidity, hence the important to keep that stable too. Finally, because the resists are sensitive to light, the lighting in a clean room is yellow which prevent inadvertent exposure of the resists.

Fig. 1. Preparing for entering the clean room involves dressing in a clean room suit. The yellow light of the clean room area is visible in the background. Image courtesy of the James Watt Nanofabrication Centre @ Glasgow

2.2 Patterning techniques

The first step in producing substrates with a given surface topography, a lithographic process is carried out. There are several ways to generate surface topographies depending on the length scale and degree of control one is aiming at, Fig. 2. One of the first techniques to generate precise and well-defined topographies at a length scale comparable to a single cell (5-100 micrometer), was photolithography (Brunette 1986; Clark, Connolly et al. 1987; Clark, Connolly et al. 1990; Oakley and Brunette 1993; Curtis and Wilkinson 1997; Walboomers, Monaghan et al. 1999) and is still a frequently used technology. However, with an increasing interest in smaller length scales, alternative methods have been developed to

meet these demands. As this is primarily driven by the biomaterials community access to clean room facilities is often limited. A relatively simple method to generate micro- and nanotopographies with a certain degree of control is by phase separation of polymers. This can either be polymer blends (Affrossman, Henn et al. 1996; Affrossman, Jerome et al. 2000) or block copolymers (Olayo-Valles, Lund et al. 2004; Krishnamoorthy, Pugin et al. 2006). Here the polymers are dissolved in a common solvent and spin coated on relevant substrates (often glass). During the evaporation of the solvent the incompatibility of the polymers drives the phase separation leading to a topographical landscape with features of varying lateral dimensions but with identical height. By carefully controlling the topographical parameters, it is possible to tune the cellular response to the generated topography (Dalby, Giannaras et al. 2004). It is noteworthy that the samples can be used directly and does not require further processing unlike most other techniques.
A step up in controlling the degree of topographical order, is the use of colloids. Here colloidal particles ranging from 30 nm to several microns (Denis, Hanarp et al. 2002; Hanarp, Sutherland et al. 2003) are suspended in an ionic solution and cast on the substrate. Depending on the strength of the ionic solution, the distance between the colloids can be controlled (Hanarp, Sutherland et al. 2003). The deposited colloids then acts as a mask in further processing steps to obtain a master substrate. The resulting substrate has features of identical lateral and vertical dimensions but their geometric arrangement is poorly controlled.

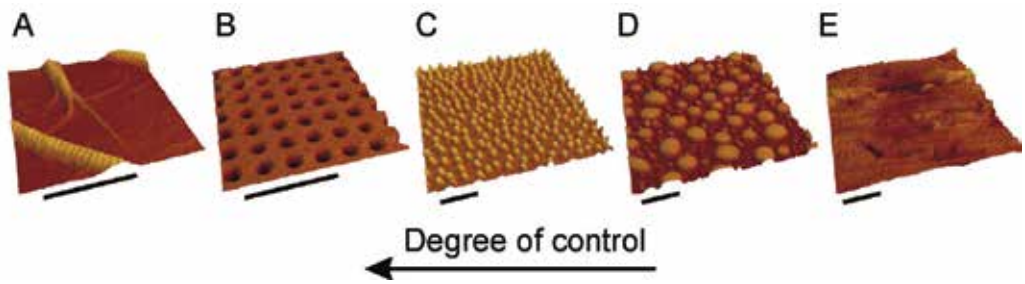

Fig. 2. AFM micrographs of various nano topographies used to control cell behavior. The topographies are arranged by the degree of control. A) Collagen is a naturally occurring protein which forms fibrils with a characteristic 67 nm cross-banding topography. B) Electron beam lithography pattern of highly ordered nanopits. C) Colloidal lithography. D) Polymer phase separation. E) Titanium surface. Scale bar is equal to 1 μm (Gadegaard, Dalby et al. 2006).

Besides the lithographic techniques described above, some attempts have been made to replicate the structure of the natural environment the cells are surrounded by. Flemming et al prepared PMMA replicas of decelluralised blood vessels containing the 3-dimensional structure of the extra cellular matrix (Flemming, Murphy et al. 1999). Gadegaard et al demonstrated the ability to replicate the nanometric structure of collagen fibrils and fibres (Gadegaard, Mosler et al. 2003).
Although, there is a range of alternative technologies available for patterning surfaces for biological applications, the majority of the research is still applying semiconductor techniques such as photolithography and electron beam lithography. We will discuss theses techniques in more details in the next sections.

2.3 Photolithography

Although the main aim of this chapter is to describe the impact of nanotopography for cell and tissue engineering applications, microlithography started this field in the early 1980's and the processing step involved are similar to the ones used in for modern nanolithography. Moreover, there is still a large activity on micropatterned materials in stem cell research (Kilian, Bugarija et al. 2010). Photolithography was the first semiconductor technology applied to make artificial patterns for cell engineering research (Curtis and Wilkinson 1997). An excellent historical overview covering both optical and electron beam lithography has been given by Wilkinson (Wilkinson 2004). At the time photolithography was the only technology capable to preparing precise patterns with dimensions comparable to the size of a single cell.

The first step in the lithographic process is to choose a relevant substrate material for the fabrication process. The choice is typically between quarts (or glass) and silicon. Both substrate materials are available with very low surface roughness, typically below 1 nm, which is crucial for the fabrication process. The most notable differences between the two materials is that quarts is optically transparent and non-conduction whereas the opposite is the case for silicon. The next step in the process is to apply a light sensitive polymer coating to the substrate called resist. This is applied by spin coating where the substrate quickly is rotated (2000-6000 rpm) leaving a very reproducible and uniform coating of the resist. To remove remaining solvent from the resist, a soft bake step is carried out before exposure. The resist is then patterned through a mask which is a quartz substrate with a chrome pattern preventing light to pass through. This step is typically carried out using a mask aligner which enables precise illumination time and the possibility to register the mask to the sample if required. The exposure time for a complete wafer 4-8 inches in diameter is typically 1-30 seconds depending on the pattern and resist.

Fig. 3. The photolithographic patterning is done on a mask aligner where acurate exposure can be controlled. Image courtesy of the James Watt Nanofabrication Centre @ Glasgow

There are two types of resists to chose from, coined positive and negative tone. Positive tone resists are the most commonly used in the fabrication process and exposed areas are dissolved during the development process, whereas negative tone resist become insoluble in the exposed areas. A notable negative resist commonly used in microfabrication for biological devices is SU-8 (Campo and Greiner 2007). Two main factors play a role in the

popularity of SU8-8 in this field. One is that the polymer is biocompatible and cells interact positively with the polymer which means that it can be a part of the final device. The other factor is that it is possible to make thick layers (20-100 micron, or more) which is ideally suited for microfluidic systems (Delamarche, Bernard et al. 1997).
These steps complete the lithographic process.

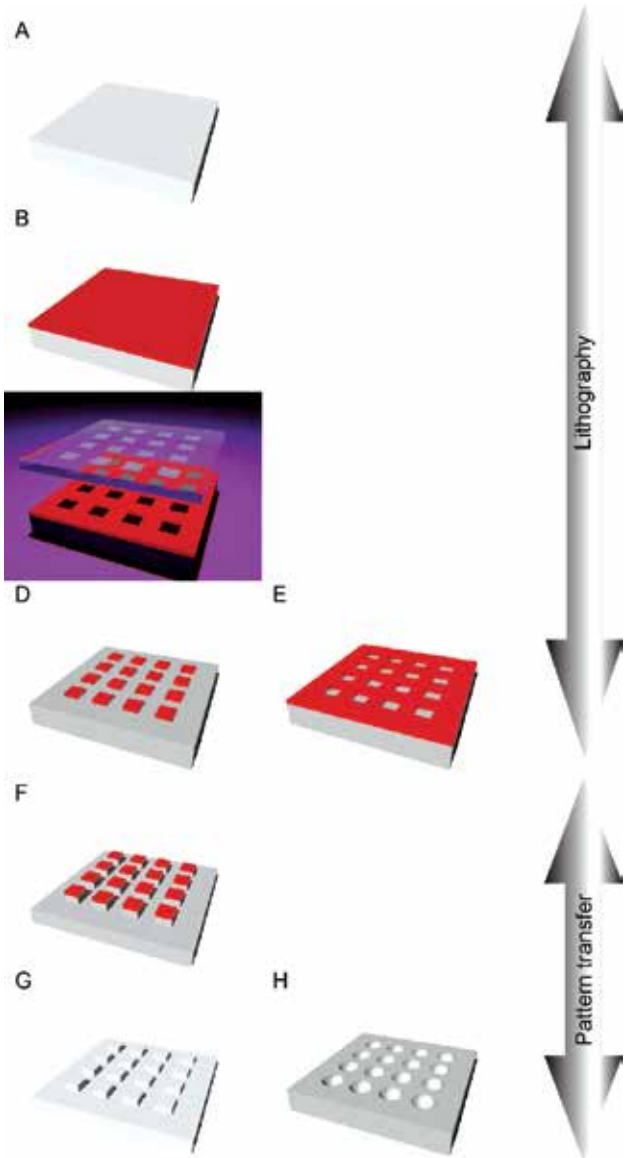

Fig. 4. Lithographic fabricaiton flow. (A) a substrate is cleaned and prepared for use. (B)A light sensitive polymer is coated on the substrate. (C) the sample is exposed through a quartz mask with the desired pattern. After development, the final pattern is realised in (D) positive or (E) negative resist. (F) The patterned is then transferred into the substrate through an etching process. (G-H) Finally the resist is removed completing the process.

The achievable resolution by photolithography can be estimated by the Rayleigh criterion where the wavelength used (λ) can be related to the smallest feature obtainable, *R*.

$$R = \frac{0.61\lambda}{NA} \tag{1}$$

In most academic research facilities i-line (365 nm) mask aligners are used which results in 250 nm (λ=365nm, NA=0.9). However, in reality the best obtainable resolution is typically about 1 μm. So with the exception of the complicated "tricks" played by the semiconductor industry on highly specialized equipment where features below 30 nm are obtainable, the only possibility is to reduce the wavelength.

2.4 Electron beam lithography

Electron beam lithography (EBL) is *the* technology of choice for full control of pattern arrangement and lateral dimensions in the sub-micron range. Dimensions as small as 3-5 nm are possible (Vieu, Carcenac et al. 2000). It is based on the principle of a scanning (transmission) electron microscope where electrons are accelerated from an electron source. The beam of electron are focused to a narrow spot, typically about 2-5 nm, through a set of electrostatic lenses, Fig. 5.

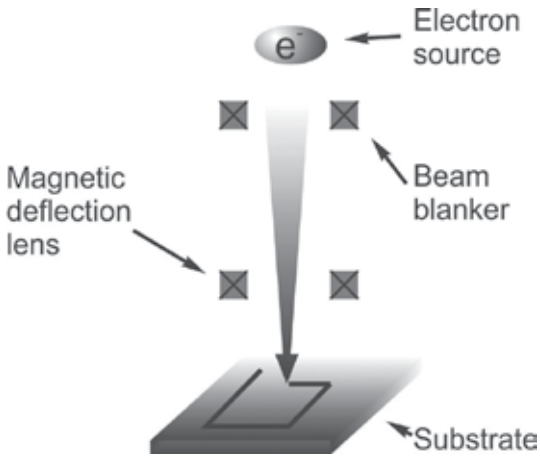

Fig. 5. Cartoon of an electron beam lithography set-up

Deflection coils are then used to control the position of the electron beam on the sample surface, much in the same way as a TV screen, and so make is possible to raster scan the surface. One of the main reasons that electron beam lithography is able to make patterns down to just 5 nm is the fact that the wavelength of the electrons is much shorter than for photolithography. The wavelength of an electron accelerated in an electrical field can be calculated from the equation below

$$\lambda = \frac{h}{\sqrt{2m_0 eU}} \tag{2}$$

where h is Planck's constant, m_0 is the rest mass of the electron, e is the charge of an electron and U is the acceleration potential. Most electron beam lithography systems operate at 100

kV which gives a wavelength of λ = 0.003 nm. This is also known as the de Broglie wavelength.

Where photolithography is a parallel process (a whole wafer can be exposed at the same time), electron beam lithography is a serial technology. For example with a pixel size of 10x10 nm^2 and a patterning rate of 5 million pixels per second (typical values for general patterns) it will take nearly 6 hours to pattern a 1x1 cm^2 area with 10% pattern density. This time exclude the stage movement, calibration and settle time during the exposure which easily can double the actual lithography time. To overcome this time constraint we have developed a method that dramatically reduces the exposure time (Gadegaard 2003). This will be described in more detail in the following section.

The fabrication procedure is similar to photolithography, where a substrate is coated with a resist sensitive to radiation. In contrast to photolithography which uses light, EBL uses an electron sensitive polymer which either breaks down during exposure (positive tone) or cross-links (negative tone). After exposure the sample is developed to reveal the exposed pattern. One major difference between the two lithographic techniques is that EBL requires a conducting sample or the surface will build charge as a result of the electron bombardment. Here either a conducting substrate is used (typically silicon) or a metallic film can be deposited on non-conducting substrates.

2.5 A fast and flexible EBL nanopatterning model system

To gain the ultimate degree of pattern control at the nanometre length scale Gadegaard has for a decade used electron beam lithography (EBL). EBL is found at the heart of semiconductor production in the generation of the photolithographic masks for exactly this ultimate performance. Its nature of serial patterning means that it is generally regarded a slow technique. However, over the years we have developed technologies to overcome this limitation. A first endeavour has been to develop a highly flexible model system able to prepare areas of at least 1x1 cm^2.

When designing patterns for EBL suitable CAD software is used to generate the relevant data files for the tool. When exposing the patterns the features are made up from several smaller exposures, Fig. 6A. This is very similar to the operation of a printer, however, this is a lengthy process. Thus we have increased the size of the exposure to match the feature size desired and only using a single exposure, Fig. 6B. This accelerates the process by nearly two orders of magnitude.

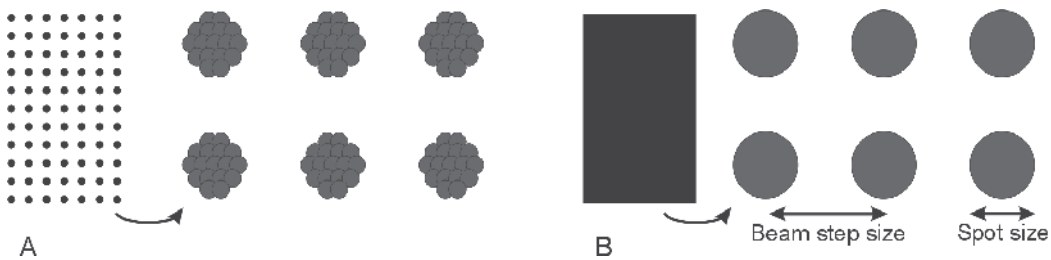

Fig. 6. (A) In a traditional design and exposure process, the features are designed in a CAD software and exposed on the EBL tool using multiple exposure for each features. (B) In our fast EBL patterning, a rectangle is drawn covering the areas for exposure. The diameter of the feature is controlled by the spot size (larger than traditionally) and the pitch by the beam step size.

With the fast EBL technique it is also possible to exactly control (see Fig. 7.):

- Feature size (Gadegaard 2003; Gadegaard, Dalby et al. 2008)
- Surface coverage (pitch) (Gadegaard 2003; Gadegaard, Dalby et al. 2008)
- Geometric arrangement of the features (Curtis, Gadegaard et al. 2004; Dalby, Gadegaard et al. 2007; Gadegaard, Dalby et al. 2008)
- Polarity (holes or pillars) (Gadegaard, Thoms et al. 2003; Martines, Seunarine et al. 2005; Martines, Seunarine et al. 2005)
- Height/depth (Martines, Seunarine et al. 2005; Martines, Seunarine et al. 2006)

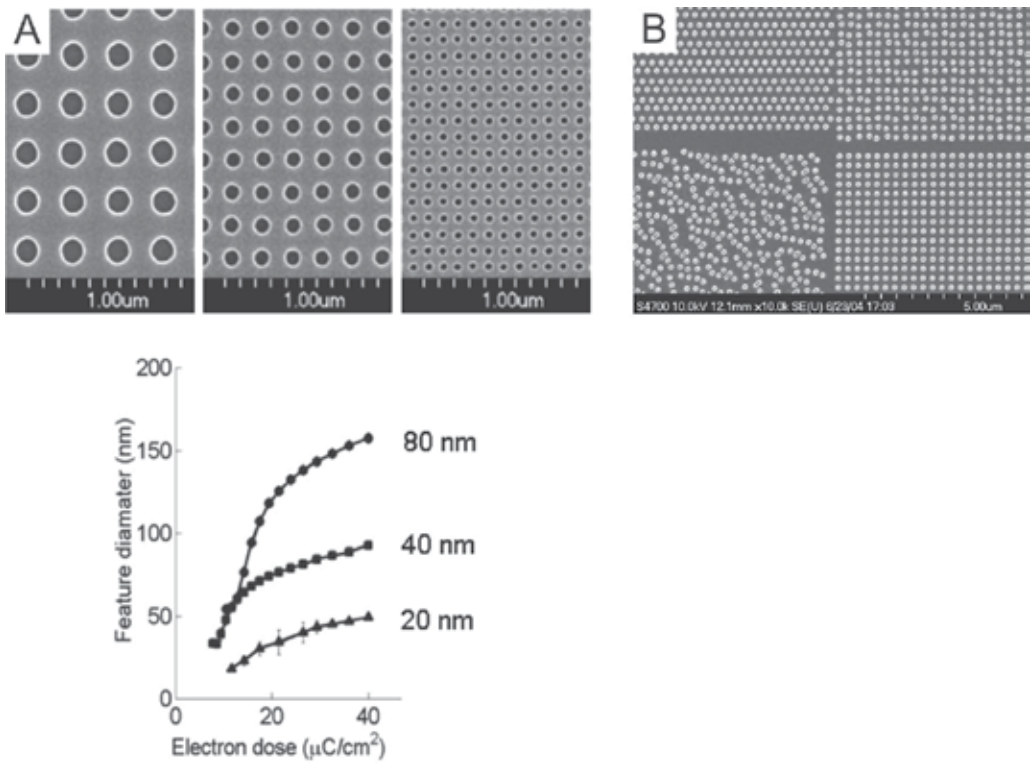

Fig. 7. (A) The dot diameter is controlled by a combination of spot size and the electron dose. (B) SEM image of 100 nm diameters dots arranged in different geometries illustrating the flexibility of the fast EBL patterning platform.

2.6 Pattern transfer

Once the pattern has been lithographically established it is in most cases necessary to transfer the patterns into the supporting substrate. This step is typically carried out using an etch process which can be more or less selective to the substrate. The patterned resist will act as a mask during the etching process. Depending on the substrate material and the type of etch, two etch geometries are possible, Fig. 8. During anisotropic etching the etch rate is different in different directions of the samples. Most typically such anisotropic etching is obtained in a reactive ion etching equipment where the reactive gas is directed towards the sample. For isotropic etching, the etch rate is the same in all direction of the sample resulting in half-pipe or hemispherical shapes in the substrate. Such etching is typical for wet etching.

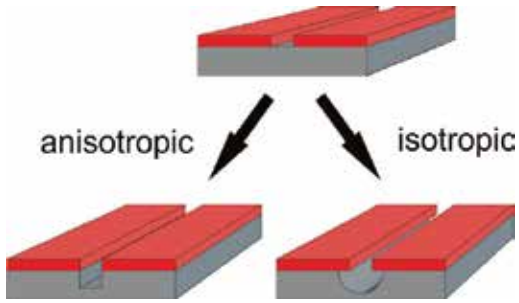

Fig. 8. The patterned resist will act as a mask during etching. There are different types of etching depending on the substrate and type of etch yielding ether anisotropic or isotropic profile.

2.7 Replication

As the fabrication process often is lengthy and expensive it is rarely feasible to use the fabricated samples directly for biological experiments. Hence, the lithographically prepared master sample can be replicated either by hot embossing or injection moulding, Fig. 9.

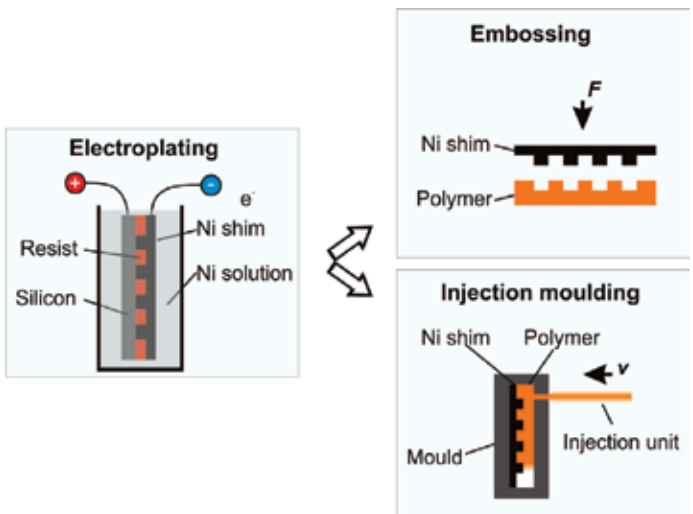

Fig. 9. Replication techniques. From the lithographically prepared master it is possible to make nickel shims used for either hot embossing or injection moulding.

The most commonly used materials used for *in vitro* cell experiments are polymeric materials for a number of different reasons. An important feature is that many polymers do not pose toxic properties to the cells and can support cell adhesion. Another important feature is that the original topographical pattern fabricated by lithography and pattern transfer can easily be replicated in a polymer in a very simple and fast manner by heating and cooling the polymer.

For injection moulding, a nickel shim is prepared through a galvanic process originally developed by the CD and DVD industry. The lithographically defined master is first sputter coated with a thin metal layer which acts as an electrode during the galvanic plating. The sample is inserted into a tank with nickel ions and when drawing a current a layer of nickel

can be deposited in the master substrate. This shim will then be fixed in the cavity of the injection moulding tool (Gadegaard, Mosler et al. 2003).

2.8 Hot embossing

On an academic scale, hot embossing is the most common technique by which samples can be prepared (Gadegaard, Thoms et al. 2003; Mills, Martinez et al. 2005). Here a thermoplastic polymer is heated above its glass transition temperature where the polymer becomes soft enough to deform if a pressure is applied. Once melted a master substrate is pressed into the polymer and then left to cool down before the polymer replica is released from the master. A particularly simple setup can be as simple as a hot plate, Fig. 10. Typically it takes 5-20 min to make a single replica.

Fig. 10. A simple setup for hot embossing using a hotplate.

2.9 Injection moulding

On an industrial scale, injection moulding is the preferred technology platform for producing thousands of polymeric replicas. Currently, the most demanding injection moulding process for replicating surface topographies is that of optical storage media such as CDs, DVDs and Blu-ray discs.

The injection unit consists of a hopper which feeds the polymer granulates to the screw, Fig. 11. The screw has a number of functions. It transports the polymer from the hopper to the melting zone, where it is plasticized, homogenised, and degassed. The plasticization is a

combination of heating from the heating bands and mechanical friction. The mechanical friction can to some extent be controlled by the backpressure. The backpressure prevents the screw from moving back during rotation thus forcing the polymer melt to flow over the thread leading to friction and as a result extra heat is supplied to the melt. Controlling the backpressure may be critical because the temperature at the core of the polymer melt may be higher than what is read out at the thermocouples near the heating bands. The effect is amplified due to the low thermal conductivity of polymers.
The extra heating as a result of an applied backpressure results in a more homogenous temperature of the melt. However, by applying too high a backpressue the polymer could be degraded caused by an excess in temperature. Finally the screw acts as a piston during the reciprocating motion. The cavity in front of the screw is normally filled with slightly more (<10%) polymer material than is needed to fill the object cavity. This is to prevent degradation of the polymer during extended time in the screw chamber.

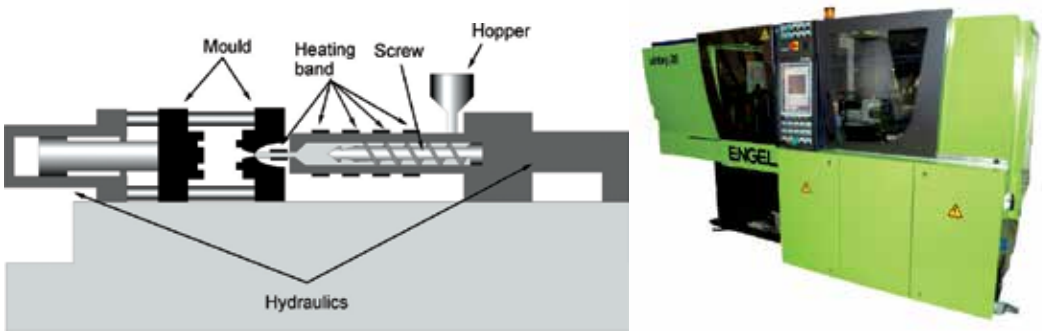

Fig. 11. Left, cartoon of an injection moulding machine illustrating key components. Right, photo of an industrial injection moulding machine.

The melt is injected into the mould cavity that is kept at a temperature below the glass transition temperature, T_g. The means that once the polymer is introduced into the mould it very quickly cools and the injection moulded part can be removed from the cavity without loosing its shape at the end of the injection moulding cycle. This means that the polymer will solidify at the walls during injection. This thin *skin layer* will build up behind the polymer melt front. There is no evidence that under normal moulding behaviour that the melt slides along the walls of the cavity (Rosato and Rosato). The polymer melt is injected at a specified pressure which, after the cavity has been filled, is changed to the packing pressure. The packing pressure minimises the shrinkage of the part during cooling. A high packing pressure results in good part dimensions but may also lead to difficulties in separating the part from the mould. A low packing pressure gives less residual stress in the part.
The filling speed is important to control properly. A high filling speed minimises the thickness of the frozen skin layer before packing pressure is applied. This is of paramount importance in this work where nanostructures are attempted to be replicated to the surface of the polymer part. However, a high injection velocity also leads to heating of the polymer melt near the mould walls caused by shear. In worst case this could lead to degradation of the polymers leaving it unusable for surface replication. Finally, high filling speed also results in an increased residual stress which could be important in certain application, e.g. optical applications (Pranov, Rasmussen et al. 2006).

3. Stem cells

Stem cells can be categorized into two groups; pluripotent (embryonic) and multipotent (adult or tissue specific), and they share two properties which separate them from other somatic cells; firstly, the ability to self-renew, and secondly, to undergo differentiation into a specific cell type given sufficient cues. Pluripotent stem cells however have a multi-lineage potential, and have been identified as having the ability to differentiate into all cell types of the body. Multipotent, on the other hand, are lineage–restricted in their differentiating potential, and this is usually determined by their tissue of origin, e.g. bone marrow-derived mesenchymal stem cells have the ability to differentiate into bone, fat, cartilage etc. Controversially these stem cells are also thought to have the ability to trans-differentiate into neuronal cells, a phenomena which may point towards the potential for these stem cells having a more pluripotent phenotype. Following recent advances in stem cell development, there are now two main types of pluripotent stem cells, the first of which, embryonic stem cells, are derived from the blastocyst of an embryo and the second, are known as induced-pluripotent stem (iPS) cells. These were first developed by reprogramming an adult somatic cell, typically a fibroblast, using viral transfection of four key genes including oct3/4, sox2, kfl4 and c-Myc. Recent studies however have also shown that somatic cells can be reprogrammed without the need for viral vectors, a necessary requirement if iPS cells were ever to be feasibly used for stem cell therapy in humans.

Embryonic stem cells therefore have a distinct advantage over adult stem cells in their differentiation potential, but this can become overshadowed by difficult cell culture requirements (ES cells require complicated cell culture techniques involving mouse embryonic fibroblasts (MEFs)), and the many ethical issues surrounding their use. With the development of iPS cells at least some of these issues have the potential to be overcome. Adult stem cells, although only being multipotent have their own advantages. They require lower-level ethical consent for use and are relatively easy to culture. However, one drawback raises under long-term culture conditions when adult stem cells are prone to undergo spontaneous differentiation (asymmetric cell division as opposed to symmetrical) resulting in a loss of the stem cell population.

With regards to stem cells, there are two requirements for which biomaterials may serve a purpose. Firstly, there is a need to maintain an undifferentiated, proliferating cell population; the ability to promote symmetrical cell division in adult stem cells and in the case of ES cells, feeder-free maintenance is desirable. Secondly, the ability to direct differentiation down a specific cell lineage in a non-invasive manner without the need for chemical supplements, which may either be toxic or contain animal products, and therefore unable to be used, or with only restricted use, within the body. In response to these requirements, researchers have been working to develop material strategies to overcome these problems.

3.1 Embryonic stem cells

Currently, the in vitro maintenance of embryonic stem cells (ESCs) requires the use of feeder layers. This requirement makes investigations into the effect of nanotopography on pluripotent stem cells often difficult to undertake due to possible masking of the nanotopography by the feeder layer. As a result there is a lack of scientific papers exploring the effect of nanotopography on embryonic stem cell self-renewal. In one key study however, Nur-E-Kamal et al were able to investigate the effect of a three-dimensional

polyamide nanofibre substrate, designed to mimic the in vivo extracellular matrix/basement membrane, on the self-renewal of mouse embryonic stem cells (mES) (Nur, Ahmed et al. 2006). This study was conducted largely in the absence of mouse embryonic fibroblast (any MEFs used were carried over from passaging (~5%)). By culturing mES cells on 3D nanofibrillar substrates an increase in colony size of undifferentiated stem cells was noted when compared to culture on a glass coverslip. Interestingly, when cultured on flat polyamide alone cells were unable to attached indicating that it is in fact the 3D nanotopography that was influencing cell proliferation.

Not only is it necessary to identify biomaterials with properties favourable to controlling stem cell self-renewal and differentiation, but it is also important to decipher the mechanisms behind their effect in an attempt to gain further insight into stem cell biology. In light of this, the authors went on to further elucidate the mechanism behind the response of mES cells to the 3D nanofibrillar structure. By identifying the levels of Rac, a protein of the Rho family of GTPases involved in cell growth, proliferation and cellular signalling, in mES cells culture on flat and 3D nanofibrillar substrates it was shown that increased Rac activity occurs in cells on the 3D nanofibrillar substrates, and plays an essential part in the increased levels of proliferation seen only in cells cultured on the 3D nanofibrillar substrates. The authors then went on to identify upregulation of Nanog, an essential protein required for maintaining the stem cell pluripotency, in response to the 3D nanofibrillar substrates via the PI3K pathway; a pathway linked to Rac.

By showing that pluripotent stem cells can be induced to undergo self renewal and proliferation in response to a 3D system culture system, where the only distinction between a flat control is the topographical mimicry of an in vivo ECM/basement membrane identifies the extent that geometry alone can influence stem cell fate, and further provides an exciting platform for feeder-free culture.

In contrast to maintenance of self-renewal and proliferation, the main goal of tissue engineering is to produce functional tissues. In the case of embryonic stem cells, their use is of critical importance when it comes to replacement of diseased or injured tissues, where an affected site is too large for an autologous graft or the patients' own stem cells are defective. This is of particular necessity when a disease is hereditary or in the case of neural degeneration from diseases such as Alzheimer's and Parkinson's disease. It is therefore no surprise that the main areas of research were nanoscale topography have been applied are in the development of neurogenic (Xie, Willerth et al. 2009; Lee, Kwon et al. 2010) and bone tissue(Smith, Liu et al. 2009; Smith, Liu et al. 2009; Smith, Liu et al. 2010). Several material strategies have been employed including nanofibres (Smith, Liu et al. 2009; Smith, Liu et al. 2009; Xie, Willerth et al. 2009; Smith, Liu et al. 2010), grooves (Lee, Kwon et al. 2010) and carbon nanotubes (Chao, Xiang et al. 2009).

By developing 2D and 3D nanofibre substrates that are designed to mimic the topographical pattern of in vivo type I collagen the authors were able to show that both mES and hES cells undergo osteogenic differentiation. Conversely, Xie et al showed that in the presence of neurogenic media mES cells when cultured on nanofibres particularly in an aligned geometry, the nanotopography acts to enhance the differentiation of mES cells into mature neural cells. Human ES cells were also shown by Lee et al to undergo neural differentiation, in the absence of any differentiation supplements, this time using nanogrooved substrates. A similar result was also seen when hES cells were cultured on the carbon nanotubes coated with poly (acrylic acid).

3.2 Skeletal stem cells

Skeletal stem cells (SSCs) as mention previously, have been found to undergo differentiation into various cell lineages including bone, fat, cartilage (Owen and Friedenstein 1988; Pittenger, Mackay et al. 1999) and neurons (Song and Tuan 2004; Shih, Fu et al. 2008) using chemically defined media. It is now becoming clear however that topography alone or in conjunction with standard differentiation protocols may provide a more efficient means for directing stem cell differentiation. The use of nanotopography to direct skeletal stem cell differentiation has two areas of application, i) implant surface patterning to promote bone encapsulation of an implant; currently implant failure occurs due to soft tissue formation, and ii) in vitro growth/differentiation of autologous stem cells for implantation back into the patient.

Results from several key studies have generated compelling evidence on the effect that substrates topography, especially at the nanoscale, can have on skeletal stem cells. It has been found that by changing only a few parameters, this can have a dramatic effect on stem cell differentiation. In a study by Dalby et al, it was shown that osteogenic differentiation of SSCs can be initiated by alterations in the geometry and degree of disorder of nanopits embossed into the polymer polymethylmethacrylate (PMMA), Fig. 12. By creating a nanopitted topographical pattern having a fundamentally square geometry, but with a controlled level of disorder has the ability to promote the differentiation of SSCs down an osteoblastic lineage (Dalby, McCloy et al. 2006; Dalby, Gadegaard et al. 2007).

In a similar study undertaken by Oh et al. SSCs were shown to differentiate down an osteoblast lineage, this time in response to carbon nanotubes with a diameter of 100 nm (Oh, Brammer et al. 2009). In this case, the diameter of the nanotubes was identified as a crucial factor in promoting differentiation, with SSCs cultured on nanotubes of less than 50 nm producing negligible amounts of osteogenic markers.

Other studies have included investigation the effect of nanotopography on metal surfaces, as a pre-emptive step towards orthopaedic clinical applications (Popat, Chatvanichkul et al. 2007; Sjostrom, Dalby et al. 2009).

In addition, the transdifferentiation of SSCs down a lineage of endodermal origins into neuronal-like cells has been shown to occur in response to nanogratings (Yim, Pang et al. 2007). Yim et al identified the upregulation of mature neuronal markers when SSCs were cultured on nanogratings in the absence of differentiation media. Interestingly, the authors went on to report higher levels of neuronal marker expression in response to the nanograting topography without differentiation media than chemical induction alone.

It is therefore evident that nanotopography can have a huge effect on skeletal stem cell differentiation but the mechanisms which underlie this topographical regulation, such as those described above are only recently beginning to be deciphered. It is hypothesized that the distinct topographical profile of a substrate primarily affects focal adhesion formation via altered protein adsorption to the surface as indicated by Oh et al who hypothesized that protein adsorption decreased with increasing nanotube diameter altering the sites for initial cell attachment(Yamamoto, Tanaka et al. 2006; Oh, Brammer et al. 2009; Scopelliti, Borgonovo et al. 2010) or the disruption of the cells ability to form focal complexes. In 2007, Dalby et al demonstrated that nanotopography could lead to changes in gene expression and later identified differences in gene expression patterns between topographically and chemically differentiated SSCs (Dalby, Gadegaard et al. 2007; Dalby, Andar et al. 2008) which indicates that topography may work via a distinct mechanism. Biggs et al went on to

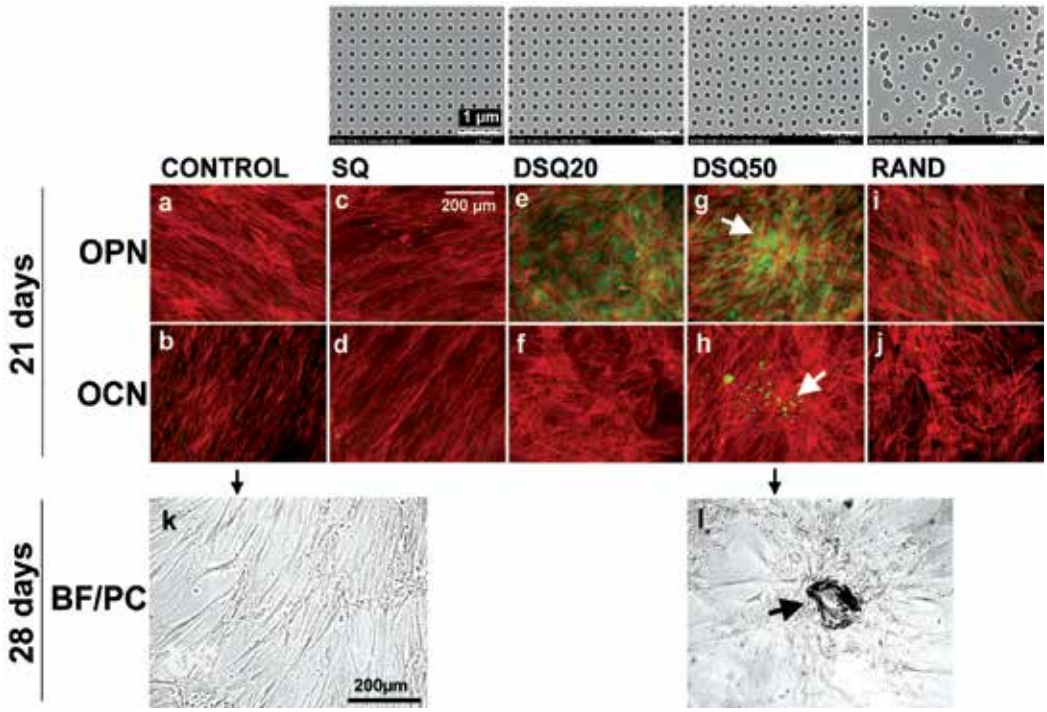

Fig. 12. OPN and OCN staining of MSC cells after 21 days and phase-contrast/bright-field images of alizarin-red-stained cells after 28 days. The top row shows images of nanotopographies fabricated by EBL. All have 120-nm-diameter pits (100nm deep, absolute or average 300nm centre–centre spacing) with square, displaced square 20 (±20nm from true centre), displaced square 50 (±50nm from true centre) and random placements. a–j, MSCs on the control (a,f), note the fibroblastic appearance and no OPN/OCN positive cells; on SQ (b,g), note the fibroblastic appearance and no OPN/OCN positive cells; on DSQ20 (c,h), note OPN positive cells; on DSQ50 (d,i), note OPN and OCN positive cells and nodule formation (arrows); on RAND (e,j), note the osteoblast morphology, but no OPN/OCN positive cells. k,l, Phase-contrast/bright-field images showing that MSCs on the control (k) had a fibroblastic morphology after 28 days, whereas on DSQ50 (l), mature bone nodules containing mineral were noted, (Dalby, Gadegaard et al. 2007)

further correlate these changes in gene expression with differences in focal adhesion formation on various nanotopgraphical substrates (Biggs, Richards et al. 2009; Biggs, Richards et al. 2009). In a later study Yim et al identified that the disruption of focal adhesion formation results in changes in the mechanical properties of cells, and also identified changes in gene expression (Yim, Darling et al. 2010).

3.3 Neural stem cells

The identification of neural stem cells (NSCs) in the adult mammalian brain has lead to renewed hope for cures for debilitating diseases such as multiple sclerosis and other degenerative diseases of the nervous system, as well as replacement of tissues caused by injury e.g. spinal cord damage. Currently nerve repair is limited due to scar tissue formation, and in many cases once destroyed nerve cells are usually not replaced leading to

permanent loss. It is therefore of critical importance to develop substrates which induce the differentiation of neural stem cells for replacement of tissues or that guide nerve repair with minimal scar formation.

Nanotopographical effects on NSCs have largely been investigated in response to nanofibers, a topography that mimics natural collagen. Studies conducted have investigated NSC response with respect to fiber diameter, orientation as well as 2D and 3D matrices. It has been found that fiber diameter plays an important part in both proliferation and differentiation of NSCs, with a smaller fiber diameter increasing both proliferation (Christopherson, Song et al. 2009) and differentiation (Yang, Murugan et al. 2005). In a comprehensive study, Lim et al identified a correlation between fiber diameter and orientation on the morphology and subsequent differentiation of NSCs (Lim, Liu et al. 2010). In this instance the alignment of fibers was found to promote elongation of the cells leading to changes in the cell cytoskeleton and subsequent intracellular signalling, specifically the Wnt/β-catenin pathway. The authors proposed β-catenins dual role as a cytoskeletal/cellular signalling component in linking changes in morphology caused by the aligned nanofibers with increased Wnt/β-catenin activity, a pathway involved in neurogenesis.

It has been demonstrated that even the slightest alteration in geometry, width, depth, orientation or pattern can affect the differentiation of stem cells. The use of nanotopographical substrates therefore provides a highly tuneable non-invasive platform for the control of stem cell differentiation; a highly valuable tool with many application for use in regenerative medicine.

4. Outlook

A real step change is needed from the current curiosity driven research to meet the future demands from clinical applications. Nanotechnological solutions for clinical applications are very promising, however, there are still many hurdles to overcome before this becomes precedence rather that exception. One of the grand challenges is the use of a broader range of clinical relevant materials than is currently deployed at the research level. This would include metals/alloys, composites and (biodegradable) polymers. Although many examples of nanopatterning of such materials with the associated differential biological response have been demonstrated, they are more often special cases of a specific treatment of a given material rather than engineered solutions. Most studies have focused on a specific cell response, and in the case of adult stem cells specific lineage differentiation. Such a single lineage differentiation is limiting for the broader use of such materials in regenerative medicine. In reality it is much more likely that clinical applications will demand the use of mix and match patterning to elicit several different lineage specific differentiations in specific positions.

Area specific patterning can be met through various lithographic processes, however, as has been demonstrated high precision will be needed. This means, as it has been the case so many times in the past, we should be looking at the future of semiconductor manufacturing. As always, there is a continuous increase in the complexity of the designs accompanied by a constant decrease in feature dimensions. The latter may although prove not to be so important for the regenerative medicine in the future, whereas precise pattern control and placement seems critical. Such requirements are readily met by for example electron beam lithography (EBL), which offers the high resolution and pattern flexibility as described above. Another important aspect to by met, is the demand of scalability from the current

research level of relatively small areas of 0.2x0.2 – 1x1 cm^2 to what is needed in a clinical device which easily could extend to tens of cm^2. Here, EBL may fall short to deliver due to the serial manner the patterns are produced. As already is in place, this can be overcome through a replication process. Finally, the majority of the materials produced so far are two dimensional as a result of the fabrication technologies. This is particularly true for semiconductor lithographic processes, whereas a biomedical implant inherently will require 3D patterning. This pattering may range from non-planar surfaces to truly 3D interconnected materials. This is a complexity level not yet tackled by the semiconductor industry and new innovations from other fields can be expected. The dual requirement of scalability and 3D may be met by technologies such as injection moulding or imprint technologies, e.g. nanoimprint lithography and flash imprinting (Seunarine, Gadegaard et al. 2006).

As the first products may start to hit the market the next trends to be expected will be a more predictive system from which multiple tissues can be targeted. This is currently dealt with through a comprehensive library of patterns and materials reported in the literature but produced in many different ways. The interplay between material design and biological response directly aimed at regenerative medicine will need a commitment from engineering, biological and computing disciplines.

5. Acknowledgements

The authors would like to acknowledge the University of Glasgow for a Lord Kelvin-Adam Smith studentship for RM. NG has also received support from EC project NaPANIL (Contract no. FP7-CP-IP 214249-2).

6. References

Affrossman, S.; Henn, G., et al. (1996). Surface Topography and Composition of Deuterated Polystyrene−Poly (bromostyrene) Blends. *Macromolecules* 29, 14, (5010-5016).

Affrossman, S.; Jerome, R., et al. (2000). Surface structure of thin film blends of polystyrene and poly(n-butyl methacrylate). *Colloid and Polymer Science* 278, 10, (993-999).

Biggs, M. J. P.; Richards, R. G., et al. (2009). Interactions with nanoscale topography: Adhesion quantification and signal transduction in cells of osteogenic and multipotent lineage. *Journal of Biomedical Materials Research Part A* 91A, 1, (195-208).

Biggs, M. J. P.; Richards, R. G., et al. (2009). The use of nanoscale topography to modulate the dynamics of adhesion formation in primary osteoblasts and ERK/MAPK signalling in STRO-1+enriched skeletal stem cells. *Biomaterials* 30, 28, (5094-5103).

Brunette, D. M. (1986). Spreading and Orientation of Epithelial Cells on Grooved Substrata. *Experimental Cell Research* 167, (203-217).

Campo, A. & Greiner, C. (2007). SU-8 : a photoresist for high-aspect-ratio and 3D submicron lithography. 81.

Chao, T. I.; Xiang, S. H., et al. (2009). Carbon nanotubes promote neuron differentiation from human embryonic stem cells. *Biochemical and Biophysical Research Communications* 384, 4, (426-430).

Christopherson, G. T.; Song, H., et al. (2009). The influence of fiber diameter of electrospun substrates on neural stem cell differentiation and proliferation. *Biomaterials* 30, 4, (556-564).

Clark, P.; Connolly, P., et al. (1987). Topographical control of cell behaviour. I. Simple step cues. *Development (Cambridge, England)* 99, 3, (439-448).

Clark, P.; Connolly, P., et al. (1990). Topographical control of cell behaviour: II. Multiple grooved substrata. *Development (Cambridge, England)* 108, 4, (635-644).

Curtis, A. & Wilkinson, C. (1997). Topographical control of cells. *Biomaterials* 18, 24, (1573-1583).

Curtis, a. S. G. (2004). Small is beautiful but smaller is the aim: review of a life of research. *European cells & materials* 8, (27-36).

Curtis, A. S. G.; Gadegaard, N., et al. (2004). Cells react to nanoscale order and symmetry in their surroundings. *Ieee Transactions on Nanobioscience* 3, 1, (61-65).

Curtis, a. S. G.; Gadegaard, N., et al. (2004). Cells react to nanoscale order and symmetry in their surroundings. *IEEE transactions on nanobioscience* 3, 1, (61-65).

Dalby, M. J.; Andar, A., et al. (2008). Genomic expression of mesenchymal stem cells to altered nanoscale topographies. *J R Soc Interface* 5, 26, (1055-1065).

Dalby, M. J.; Biggs, M. J. P., et al. (2007). Nanotopographical stimulation of mechanotransduction and changes in interphase centromere positioning. *Journal of cellular biochemistry* 100, 2, (326-338).

Dalby, M. J.; Gadegaard, N., et al. (2007). The control of human mesenchymal cell differentiation using nanoscale symmetry and disorder. *Nature materials* 6, 12, (997-1003).

Dalby, M. J.; Giannaras, D., et al. (2004). Rapid fibroblast adhesion to 27 nm high polymer demixed nano-topography. *Biomaterials* 25, 1, (77-83).

Dalby, M. J.; McCloy, D., et al. (2006). Osteoprogenitor response to semi-ordered and random nanotopographies. *Biomaterials* 27, 15, (2980-2987).

Dalby, M. J.; Riehle, M. O., et al. (2002). In vitro reaction of endothelial cells to polymer demixed nanotopography. *Biomaterials* 23, 14, (2945-2954).

Delamarche, E.; Bernard, a., et al. (1997). Patterned delivery of immunoglobulins to surfaces using microfluidic networks. *Science (New York, N.Y.)* 276, 5313, (779-781).

Denis, F. a.; Hanarp, P., et al. (2002). Fabrication of Nanostructured Polymer Surfaces Using Colloidal Lithography and Spin-Coating. *Nano Letters* 2, 12, (1419-1425).

Flemming, R. G.; Murphy, C. J., et al. (1999). Effects of synthetic micro- and nano-structured surfaces on cell behavior. *Biomaterials* 20, 6, (573-588).

Franssila, S. (2004). *Introduction to Microfabrication*. Wiley-Blackwell, 0470851066.

Gadegaard, N. (2003). Arrays of nano-dots for cellular engineering. *Microelectronic Engineering* 67-68, (162-168).

Gadegaard, N.; Dalby, M. J., et al. (2006). Nano Patterned Surfaces for Biomaterial Applications. *Advances in Science and Technology* 53, (107-115).

Gadegaard, N.; Dalby, M. J., et al. (2008). Optimizing substrate disorder for bone tissue engineering of mesenchymal stem cells. *Journal of Vacuum Science & Technology B: Microelectronics and Nanometer Structures* 26, 6, (2554-2554).

Gadegaard, N.; Mosler, S., et al. (2003). Biomimetic Polymer Nanostructures by Injection Molding. *Macromolecular Materials and Engineering* 288, 1, (76-83).

Gadegaard, N.; Thoms, S., et al. (2003). Arrays of nano-dots for cellular engineering. *Microelectronic Engineering* 67-68, (162-168).

Gadegaard, N.; Thoms, S., et al. (2003). Arrays of nano-dots for cellular engineering. *Microelectronic Engineering* 67-8, (162-168).

Hanarp, P.; Sutherland, D. S., et al. (2003). Control of nanoparticle film structure for colloidal lithography. *Colloids and Surfaces A-Physicochemical and Engineering Aspects* 214, 1-3, (23-36).

Harrison, R. G. (1911). On the stereotropism of embryonic cells. *Science* 34, 1, (279-281).

Hench, L. L. & Polak, J. M. (2002). Third-generation biomedical materials. *Science* 295, 5557, (1014-1017).

Kilian, K. A.; Bugarija, B., et al. (2010). Geometric cues for directing the differentiation of mesenchymal stem cells. *Proceedings of the National Academy of Sciences of the United States of America* 107, 11, (4872-4877).

Krishnamoorthy, S.; Pugin, R., et al. (2006). Tuning the dimensions and periodicities of nanostructures starting from the same polystyrene-block-poly(2-vinylpyridine) diblock copolymer. *Advanced Functional Materials* 16, 11, (1469-1475).

Lee, M. R.; Kwon, K. W., et al. (2010). Direct differentiation of human embryonic stem cells into selective neurons on nanoscale ridge/groove pattern arrays. *Biomaterials* 31, 15, (4360-4366).

Lim, S. H.; Liu, X. Y., et al. (2010). The effect of nanofiber-guided cell alignment on the preferential differentiation of neural stem cells. *Biomaterials*.

Madou, M. J. (2011). *Fundamentals of Microfabrication and Nanotechnology*. (3) CRC Press, 0849331803.

Martines, E.; Seunarine, K., et al. (2005). Superhydrophobicity and superhydrophilicity of regular nanopatterns. *Nano letters* 5, 10, (2097-2103).

Martines, E.; Seunarine, K., et al. (2005). Superhydrophobicity and superhydrophilicity of regular nanopatterns. *Nano Letters* 5, 10, (2097-2103).

Martines, E.; Seunarine, K., et al. (2006). Air-trapping on biocompatible nanopatterns. *Langmuir : the ACS journal of surfaces and colloids* 22, 26, (11230-11233).

McBeath, R.; Pirone, D. M., et al. (2004). Cell Shape , Cytoskeletal Tension , and RhoA Regulate Stem Cell Lineage Commitment. *Cell* 6, (483-495).

Mills, C. A.; Martinez, E., et al. (2005). Production of structures for microfluidics using polymer imprint techniques. *Microelectronic Engineering* 78-79, (695-700).

Nur, E. K. A.; Ahmed, I., et al. (2006). Three-dimensional nanofibrillar surfaces promote self-renewal in mouse embryonic stem cells. *Stem Cells* 24, 2, (426-433).

Oakley, C. & Brunette, D. M. (1993). The sequence of alignment of microtubules, focal contacts and actin filaments in fibroblasts spreading on smooth and grooved titanium substrata. *Journal of cell science* 106 (Pt 1, (343-354).

Oh, S.; Brammer, K. S., et al. (2009). Stem cell fate dictated solely by altered nanotube dimension. *Proc Natl Acad Sci U S A* 106, 7, (2130-2135).

Olayo-Valles, R.; Lund, M. S., et al. (2004). Large area nanolithographic templates by selective etching of chemically stained block copolymer thin films. *Journal of Materials Chemistry* 14, 18, (2729-2731).

Owen, M. & Friedenstein, A. J. (1988). Stromal stem cells: marrow-derived osteogenic precursors. *Ciba Found Symp* 136, (42-60).

Pittenger, M. F.; Mackay, A. M., et al. (1999). Multilineage potential of adult human mesenchymal stem cells. *Science* 284, 5411, (143-147).

Popat, K. C.; Chatvanichkul, K. I., et al. (2007). Osteogenic differentiation of marrow stromal cells cultured on nanoporous alumina surfaces. *Journal of Biomedical Materials Research Part A* 80, 4, (955-964).

Pranov, H.; Rasmussen, H. K., et al. (2006). On the Injection Molding of Nanostructured Polymer Surfaces. *Engineering*.

Rosato, D. V. & Rosato, D. V. (1995). *Injection Molding Handbook*. Chapman & Hall, 0-412-99381-3.

Scopelliti, P. E.; Borgonovo, A., et al. (2010). The effect of surface nanometre-scale morphology on protein adsorption. *PLoS One* 5, 7, (e11862).

Seunarine, K.; Gadegaard, N., et al. (2006). 3D polymer scaffolds for tissue engineering. *Nanomedicine* 1, 3, (281-296).

Shih, C. C.; Fu, L., et al. (2008). Derivation of neural stem cells from mesenchymal stem cells: evidence for a bipotential stem cell population. *Stem Cells Dev*.

Sjostrom, T.; Dalby, M. J., et al. (2009). Fabrication of pillar-like titania nanostructures on titanium and their interactions with human skeletal stem cells. *Acta Biomater* 5, 5, (1433-1441).

Smith, L. A.; Liu, X., et al. (2009). The influence of three-dimensional nanofibrous scaffolds on the osteogenic differentiation of embryonic stem cells. *Biomaterials* 30, 13, (2516-2522).

Smith, L. A.; Liu, X., et al. (2010). The enhancement of human embryonic stem cell osteogenic differentiation with nano-fibrous scaffolding. *Biomaterials* 31, 21, (5526-5535).

Smith, L. A.; Liu, X., et al. (2009). Enhancing osteogenic differentiation of mouse embryonic stem cells by nanofibers. *Tissue Eng Part A* 15, 7, (1855-1864).

Song, L. & Tuan, R. S. (2004). Transdifferentiation potential of human mesenchymal stem cells derived from bone marrow. *Faseb J* 18, 9, (980-982).

Teixeira, A. I.; Abrams, G. A., et al. (2003). Cell behavior on lithographically defined nanostructured substrates. *Cell*(683-687).

Vieu, C. (2000). Electron beam lithography: resolution limits and applications. *Applied Surface Science* 164, 1-4, (111-117).

Vieu, C.; Carcenac, F., et al. (2000). Electron beam lithography: resolution limits and applications. *Applied Surface Science* 164, (111-117).

Walboomers, X. F.; Monaghan, W., et al. (1999). Attachment of fibroblasts on smooth and microgrooved polystyrene. *Journal Of Biomedical Materials Research* 46, 2, (212-220).

Wang, M., Ed. (2010). Lithography, INTECH.

Wilkinson, C. D. W. (2004). Making Structures for Cell Engineering. *European Cells & Materials* 8, (21-26).

Xie, J.; Willerth, S. M., et al. (2009). The differentiation of embryonic stem cells seeded on electrospun nanofibers into neural lineages. *Biomaterials* 30, 3, (354-362).

Yamamoto, S.; Tanaka, M., et al. (2006). Relationship between adsorbed fibronectin and cell adhesion on a honeycomb-patterned film. *Surface Science* 600, 18, (3785-3791).

Yang, F.; Murugan, R., et al. (2005). Electrospinning of nano/micro scale poly (L-lactic acid) aligned fibers and their potential in neural tissue engineering. *Biomaterials* 26, 15, (2603-2610).

Yim, E. K.; Darling, E. M., et al. (2010). Nanotopography-induced changes in focal adhesions, cytoskeletal organization, and mechanical properties of human mesenchymal stem cells. *Biomaterials* 31, 6, (1299-1306).

Yim, E. K.; Pang, S. W., et al. (2007). Synthetic nanostructures inducing differentiation of human mesenchymal stem cells into neuronal lineage. *Exp Cell Res* 313, 9, (1820-1829).

17

Magnetic and Multifunctional Magnetic Nanoparticles in Nanomedicine: Challenges and Trends in Synthesis and Surface Engineering for Diagnostic and Therapy Applications

Laudemir Carlos Varanda[1],
Miguel Jafelicci Júnior[2] and Watson BeckJúnior[1]
[1]*Institute of Chemistry of São Carlos – University of São Paulo, Colloidal Materials Group,*
[2]*Institute of Chemistry of Araraquara – São Paulo State University,*
Labor. of Magnetic Materials and Colloids,
Brazil

1. Introduction

Today, the nanotechnology has achieved a development level reaching a stage where it is possible to produce and specially tailor the functional properties of nanoparticles (NPs) for biomedical and biotechnological applications (Gupta et al., 2007; Gupta & Gupta, 2005; Pankhurst et al., 2009). Among different types of NPs, magnetic (MNPs) and more recently, multifunctional magnetic nanoparticles (MFMNPs) have attracted a great deal of attention in nanomedicine over the past decade. These functionalized nanomagnets can be directly injected onto the body vessels and properly manipulated by an external magnetic force. The action at a distance and the non invasive technique provide tremendous advantages for these NPs uses, making these nanomaterial ideal for either *in vitro* or *in vivo* biomedical applications (de Dios & Díaz-Garcia, 2010; Lu et al., 2007; Salgueirino-Maceira & Correa-Duarte, 2007). In the biomedicine area, their applications including magnetic resonance contrast agent in Magnetic Resonance Imaging (MRI), magnetohyperthermia for cancer treatment, magnetic force-assisted drug delivery, tissue repair, cell and tissue targeting and transfection, and protein isolation (Lu et al., 2007; Sanvicens & Marco, 2008; Varanda et al., 2008). In this context, the combination of nanotechnology and molecular biology has developed into an emerging new class of nanomagnetics for biomedicine, which combine the MNP properties and the most modern surface engineering techniques resulting in biocompatible and bioselectable MFMNPs (de Dios & Díaz-Garcia, 2010; Majewski & Thierry, 2007; Salgueirino-Maceira & Correa-Duarte, 2007; Selvan et al., 2010).

Down to the nanoscale, on the order of around two dozen or less, the magnetic particles change from paramagnetic to superparamagnetic (SPM) behavior, where magnetic moment of the particle as a whole is free to fluctuate in response to thermal energy, while the individual atomic moments maintain their ordered state relative to each other. Thus, the superparamagnetic NPs can only be magnetized in the presence of an external magnetic field and do not retain any magnetism after removal of the magnetic field, which makes

them capable of forming stable colloids in a physio-biological medium (Lu et al., 2007; Majewski & Thierry, 2007; Santos et al., 2008; Sorensen, 2001; Varanda et al., 2002a; Varanda et al., 2001; Varanda et al., 2007; Varanda et al., 2008; Varanda & Jafelicci, 2006). Combining the SPM behavior with appropriate surface functionalizations, besides other intrinsic NPs properties such as low cytotoxicity, bioactivity and ability to conjugate with optically active molecules or compounds, makes their multifunctionalized nanomaterials strong biomedical tools for using in sensing, diagnostic or therapy fields. It appears reasonable to accurately consider that the aim of surface modification is not only to stabilize the NP suspension *in vitro* and govern their *in vivo* fates, but also to minimize the remnant magnetization. It is now recognized that internalization of particle also depends strongly on the size of the magnetic particle (Gupta et al., 2007). In addition, successive surface modifications realized to obtain functional or multifunctional NPs generally require additions of the non-magnetic materials on MNPs surface. Thus, at the final of the functionalization process, the magnetic core emanation has been dramatically decreased and the efficient NP application was strongly compromised (Selvan et al., 2010; Sun et al., 2008; Varanda et al., 2008). Besides the morphological strict control required for the MNPs, which have been effectively achieved due to advances in synthetic routes, their use in biomedicine is guided by two key challenges: (i) the surface engineering to promote the chemical/biological functionalizations that lead to required biocompatibility and bioselectivity and (ii) improving the magnetic properties of the core in order to stand different functionalizations keeping the magnetic emanation at high enough levels for their effective applications. According to exposed, this Chapter focuses on the synthesis, protection, functionalization, and applications of the MNPs to the biomedical areas, as well as emphasizing the features of magnetic properties of nanostructured systems. In addition, also describe some potentially useful design and applications of MFMNPs for biomedicine, which have been attracting increased research efforts because of their easily accessible multimodality.

2. Features and required properties of the magnetic nanoparticles

According to several studies reported in the literature relating MNPs for biomedical applications and properly summarized in a bright review published by *Gupta et al.* (Gupta & Gupta, 2005), the effectiveness of these NPs depends upon:

a. SPM behavior and high magnetic susceptibility for effective magnetic response even after multifuncionalization with non-magnetic compounds;
b. narrow particle size distributions with size ranging from 6 to 20 nm. Particles below a critical size (~20 nm) would consist of a single magnetic domain (state of uniform magnetization at any field with superparamagnetism and high saturation magnetization values). In addition, the particles in this size range are rapidly removed through extravasations and renal clearance besides avoiding the capillary embolism.
c. tailored/targeting surface chemistry for specific functionalization.

Fundamental changes in the magnetic structure of ferro, ferri, and even antiferromagnetic materials when sizes are dramatically reduced for the nanoscale can be observed in the two most important effects, i.e., finite-size and highest-surface. In macroscopic scale or in large magnetic particles, there are magnetic domains regions (spins pointing in the same directions and acting cooperatively) with uniform magnetization separated by domain walls. The domain walls formation is driven by the balance between magnetostatic energy (ΔE_M), directly proportional to the material volume, and the domain-wall energy (E_{DW}),

which increases proportionally to the interfacial area between domains. As the particle size decreases toward some critical particle diameter (D_C), the formation of domain walls becomes energetically unfavorable leading to the single-domain state. The multidomain to single-domain state limit is reached when $\Delta E_M = E_{DW}$ and the D_C values can be easily calculated for many materials according to the magnetic particle properties such as magnetization, anisotropy constant, particle shape, etc (Batlle & Labarta, 2002). Changes in magnetization can no longer occur through domain-wall motion and instead require the coherent rotation of spins resulting in large coercivities. A single-domain particle, on the other hand, is uniformly magnetized with all the spins aligned in the same direction. The magnetization will be reversed by spin rotation since there are no domain walls to move. This is the reason for the very high coercivity observed in the small NPs (Lu et al., 2007).

Continuos decreasing in the particle size below the single-domain value increasingly affect the spins by thermal fluctuations and the system becomes SPM (Salgueirino-Maceira & Correa-Duarte, 2007; Sorensen, 2001). Under SPM behavior, the mechanism of magnetization reversal can only occur via the rotation of the magnetization vector from magnetic easy axis to another via a magnetically hard direction (Stoner & Wohlfarth, 1948). However, the superparamagnetismo can be understood considering the magnetic anisotropy energy per particle, which is responsible for holding the magnetic moments along a certain direction. This energy barrier to moment reversal has several origins including both intrinsic and extrinsic effects, such as the magnetocrystalline and shape anisotropies, respectively, but used as a simplest form expressing the uniaxial effect or an effective anisotropy constant, K_{eff}. This energy barrier is given by:

$$E = K_{eff} V \sin^2 \theta \,, \tag{1}$$

where V is the particle volume and θ is the angle between the magnetization and the easy axis. With decreasing particle size, the thermal energy $k_B T$ exceed the energy barrier $K_{eff} V$, in which k_B and T is the Boltzmann's constant and the temperature, respectively. This direct proportionality between E and V is the reason that superparamagnetism (the thermally activated flipping of the net direction of the magnetic moment) is very important for small particles, because for them E is comparable to thermal energy at room temperature. For $k_B T > K_{eff} V$ the system behaves like a paramagnetic, instead of atomic magnetic moments, there is now a giant (super) moment inside each particle. The underlying physics of superparamagnetism is founded on activation for the relaxation time τ of particle net magnetization given by Néel-Brown (Eq. 2) (Lu et al., 2007; Sorensen, 2001) where $\tau_0 \approx 10^{-9}$ s.

$$\tau = \tau_0 exp\left(K_{eff} V / k_B T \right) \tag{2}$$

Thus, it is important to recognized that observations of superparamagnetism are implicitly dependent not only the temperature, but also on the measurement time, τ_m, of the used experimental technique (Salgueirino-Maceira & Correa-Duarte, 2007). If the particle magnetic moment reverses at times shorter than the experimental time scale, the system is in a SPM state, if not, it is in the so-called blocked state. The temperature, which separates these two regimes, the so-called blocking temperature, T_B, can be calculated by considering the time window of the measurement. The blocking temperature depends on the effective anisotropy constant, the size of the particles, the applied magnetic field, and the experimental measuring time. For example, if the blocking temperature is determined using

a technique with a shorter time window, such as ferromagnetic resonance which has a $\tau \approx 10^{-9}$ *s*, a larger value of T_B is obtained than the value obtained from *dc* magnetization measurements. Moreover, a factor of two in particle diameter can change the reversal time from 100 years to 100 nanoseconds. While in the first case the magnetism of the particles is stable, in the latter case the assembly of the particles has no remanence and is SPM.
The second observed effect as the particle size decreases is related to the large percentage of all atoms in the NPs is surface atoms. This characteristic implies that surface and/or interface phenomena become more significant and important for the nanosized system properties, such as reactivity, and colloidal/chemical stabilities. According to the NP size and structure, it is usual to find about 60-70% of the total number of spins as surface spins. Immediate consequence of the large surface atoms/bulk atoms ratio is the local breaking of the structure symmetry might lead to changes in the band structure, lattice constant, and/or atoms coordination, which make an important contribution, besides other materials properties, to the NP magnetization. Under these conditions, surface/interface effects such as surface anisotropy occur and, in addition, according to the phases present on the NP surface and bulk, core-surface exchange anisotropy or interactions take place changing the resulting magnetic properties (Benitez et al., 2008; Hyeon et al., 2001; Hyeon, 2003b; Lu et al., 2007; Varanda et al., 2008).

3. Synthesis of magnetic nanoparticles

It has long been of scientific and technological challenge to synthesize the MNPs of customized size and shape (Gupta & Gupta, 2005). In a general way, physical methods such as gas phase deposition and electron beam lithography are elaborate procedures that suffer from the inability to control the size of particles in the nanometer size range (Pratsinis & Vemury, 1996; Rishton et al., 1997). The wet chemical routes to MNPs are simpler, more tractable and more efficient with appreciable control over size, chemical composition and sometimes even the shape of the NPs (Hyeon, 2003b; Malheiro et al., 2007; Santos et al., 2008; Sun et al., 2000; Sun & Zeng, 2002; Varanda & Jafelicci, 2006). Considering the high number of potential applications for high quality MNPs, especially for iron oxide case focused in the biomedical applications, it is not surprising that numerous synthetic routes have been described with different level of control on the size, polydispersity, shape, and crystallinity. Concerning only the wet chemical routes, the MNPs have been synthesized with a number of different compositions and phases, including iron oxides, such as Fe_3O_4 and γ-Fe_2O_3 (Hyeon et al., 2001; Mornet et al., 2006; Sun & Zeng, 2002), pure metals, such as Fe, Ni and Co (Puntes et al., 2001), spinel-type structure as ferrite of Mg, Mn, and Co (Park et al., 2004), as well as alloys, such as CoPt and FePt (Varanda & Jafelicci, 2006). Especially during the last few years, many publications have described efficient synthetic routes to shape-controlled, highly stable, and monodisperse MNPs. Several popular methods including co-precipitation, thermal decomposition/reduction, micelle synthesis, hydrothermal synthesis, and laser pyrolysis techniques can all be directed at the synthesis of high-quality MNPs. The most widely general accepted mechanism of the particles preparation in the solution under optimum synthetic conditions takes place by the rapid and homogenous formation of nuclei in a supersaturated medium, followed by controlled crystal growth, according to the well-known LaMer's diagram (LaMer & Dinegar, 1950). The latter process is controlled by mass transport and by the surface equilibrium of addition and removal of individual monomers, i.e., atoms, ions, or molecules. Hereby, the driving force for monomer removal increases

with decreasing particle size. Thus, within an ensemble of particles with slightly different sizes, the large particles will grow at the cost of the small ones. This mechanism is called Ostwald ripening and is generally believed to be the main path of crystal growth. Magnetite particles obtained under different synthetic conditions, for example, may display large differences regarding their magnetic properties. These differences are attributed to changes in structural disorder, creation of antiphase boundaries, or the existence of a magnetically dead layer at the particle surface (Gupta & Gupta, 2005). The saturation magnetization (*Ms*) values found in nanostructured materials are usually smaller than the corresponding bulk phases, provided that no change in ionic configurations occurs. Accordingly, experimental values for *Ms* in magnetite NPs have been reported to span the 30–50 emu/g range, lower than the bulk magnetite value of 90 emu/g. Many studies have been reported on the origin of the observed reduction in magnetization in fine magnetic particles generally concerning the high-surface effects. The first studies on the decrease in magnetization performed in γ-Fe_2O_3 showed that this reduction is due to the existence of noncollinear spins at the surface. Also, in magnetite fine particles, *Varanda et al.* have reported a linear correlation between saturation magnetization and particle size, suggesting that defects at the particle surface can influence the magnetic properties. The surface curvature of the NP was much larger for smaller particle size, which encouraged disordered crystal orientation on the surface and thus resulted in significantly decreased *Ms* in smaller NPs (Varanda et al., 2002b). In this context, advancement in the use of magnetic particles for biomedical applications depends on the new synthetic methods with better control of the size distribution, magnetic properties and the particle surface characteristics. Typical and representative discussion of each main synthetic pathway in a general form is presented and the main features of the different routes are summarized in the Table 1. Today, the most used MNPs as potential magnetic materials for biomedical applications are based on the magnetic iron oxide NPs, generally described as SPION (SPM iron oxide nanoparticles) (Roca et al., 2009). Nevertheless, most of the NPs available to date have been prepared using variations of the aqueous **co-precipitation method**. In these processes, a nucleation phase is followed by a growth phase with good control over de particle size and polydispersity. Iron oxides, either Fe_3O_4 (magnetite) or γ-Fe_2O_3 (maghemite), can be synthesized from aqueous mixture of Fe^{2+} and Fe^{3+} salt solutions by the addition of a base under inert atmosphere at controlled temperature. The size, shape, and chemical composition of the MNPs are strongly dependents on the salts (e.g. chlorides, sulfates, nitrates, etc.), the Fe^{2+}/Fe^{3+} ratio, the reaction temperature, the pH value and ionic strength of the medium. According to the thermodynamics of this reaction, a complete precipitation of Fe_3O_4 should be expected between pH 9 and 14, while maintaining a molar ratio of Fe^{3+}:Fe^{2+} is 2:1 under a non-oxidizing oxygen free environment (Cornell & Schwertmann, 2003).

Magnetite NPs are not also very stable under ambient conditions, and are easily oxidized to maghemite or dissolved in an acidic medium. Since maghemite is a ferrimagnet, oxidation is the minor problem. Therefore, magnetite particles can be subjected to deliberate oxidation to convert them into maghemite. This transformation is achieved by dispersing them in acidic medium, then addition of iron(III) nitrate. The maghemite particles obtained are then chemically stable in alkaline and acidic medium. However, even if the magnetite particles are converted into maghemite after their initial formation, the experimental challenge in the synthesis of MNPs by co-precipitation lies in control of the particle size and thus achieving a narrow particle size distribution.

Synthetic method	Nanoparticle characteristics							
	Size		Shape control	Synthesis	Reaction			Surface-capping agents
	Range	Distribution			Temperature	Time	Yield	
Aerosol/vapor (pyrolisys)	5-60 nm	Broad	Good	Complicated, vacuum/ controlled atmosphere	High/ very high	Minutes /hours	Medium	Needed, after reaction
Gas deposition	5-50 nm	Narrow	Good	Complicated, vacuum/ controlled atmosphere	Very high	Minutes	High/ scalable	Needed, after reaction
Sol-gel	3-150 nm	Narrow/ broad	Good	Simple	20-90 °C	Hours/ days	Medium	Needed, during reaction
Co-precipitation	10-50 nm	Broad/ narrow	Poor	Very simple	20-90 °C	Minutes	High/ scalable	Needed, during reaction
Thermal decomposition	2-20 nm	Very narrow	Very good	Complicated, inert atmosphere	100-330 °C	Hours	High/ scalable	Needed, during reaction
Microemulsion	4-15 nm	Narrow	Good	Complicated	20-70 °C	Hours/ days	Low	Needed, during reaction
Hydrothermal	10-150 nm	Narrow	Very good	Simple, high pressure	100 °C -high	Hours/ days	Medium	Needed, during reaction

Table 1. Comparison of different synthetic methods to produce MNPs.

Particles prepared by co-precipitation unfortunately tend to be rather polydisperse as indicated in the Fig. 1a. It is well known that a short burst of nucleation and subsequent slowly controlled growth is crucial to produce monodisperse particles. Controlling these processes is therefore the key in the production of monodisperse iron oxide MNPs. In order to prevent them from possible oxidation in air as well as from NPs agglomeration, co-precipitated NPs are usually coated with organic or inorganic molecules during the precipitation process. Recently, significant advances in preparing monodisperse magnetite NPs, of different sizes, have been made by the use of organic additives as stabilizing and/or reducing agents. The NP preparation can be achieved in presence of stabilizing agents such as dextran, polyvinyl alcohol, citrate, polyethyleneimine, block copolymers, and using various silane-based chemistry (Majewski & Thierry, 2007). Recent studies also showed that oleic acid is the best candidate for the stabilization of Fe_3O_4 (Cushing et al., 2004; Willis et al., 2005). The effect of organic ions on the formation of metal oxides or oxyhydroxides can be rationalized by two competing mechanisms. Chelation of the metal ions can prevent nucleation and lead to the formation of larger particles because the number of nuclei formed is small and the system is dominated by particle growth. However, the adsorption of additives on the nuclei and the growing crystals may inhibit the growth of the particles, which favors the formation of small units.

On the other hand, better control over size, monodispersity and shape can be achieved using **emulsions, microemulsion (μe) or nanoemulsion (ne) systems** (water-in-oil or oil-in-water) that provide a confined environment during nucleation and growth of the iron oxide NPs (Gupta & Wells, 2004). In practice, however, little control can actually be driven over the size

and size distribution of the nanostructures and, moreover, only small quantities of iron oxide can be obtained, owing to the constraints of low reagent amount required by this synthetic procedure. A *με* is defined as a thermodynamically stable isotropic dispersion of two immiscible liquids, since the microdomain of either or both liquids has been stabilized by an interfacial film of surface-active agents. In water-in-oil *με*, the aqueous phase is dispersed as microdroplets (typically 1–50 nm in size) surrounded by a monolayer of surfactant molecules in the continuous hydrocarbon phase. The size of the reverse micelle is determined by the molar ratio of water to surfactant. When a soluble metal salt is incorporated in the aqueous phase of the *με*, it will remain in the aqueous microdroplets surrounded by oil. By mixing two identical water-in-oil *με* containing the desired reactants, these microdroplets will continuously collide, coalesce, and break again (Malheiro et al., 2007). By the addition of solvent, such as acetone or ethanol to the *με*, the precipitate can be extracted by filtering or centrifuging the mixture. In this sense, a *με* can be used as a nanoreactor for the formation of NPs. Using the *με* technique, metallic NPs and alloys (Co, Fe, FeCo, FePt, CoPt, etc.) or magnetic oxide such as iron oxide or spinel ferrites, MFe_2O_4 (M: Mn, Co, Ni, Cu, Zn, Mg, or Cd, etc.) have been synthesized in reverse micelles (water in oil systems) by using many different surfactants and co-surfactants molecules (O'Connor et al., 1999). Co-surfactant molecules, generally an alcohol with small chain, have an important role in the reverse micelle structure formation increasing the molecules density onto the *με* threshold and avoiding the metallic cations percolation (Malheiro et al., 2007). For example, highly monodispersed iron oxide NPs were synthesized by using the aqueous core of aerosol-OT (AOT)/*n*-hexane reverse micelles (w/o *με*) as showed in Fig. 1b. The reverse micelles have aqueous inner core, which can dissolve hydrophilic compounds, salts, etc. A deoxygenated aqueous solution of the Fe^{3+} and Fe^{2+} salts (molar ratio 2:1) was dissolved in the aqueous core of the reverse micelles formed by AOT in *n*-hexane. Chemical precipitation was achieved by using a deoxygenated solution of sodium hydroxide. Smaller and more uniform particles were prepared by precipitation of magnetite at low temperature in the presence of nitrogen gas. As described in the conventionally *με* preparation methods, two identical *με* systems are mixed and coalesced. During coalescence stage, the microdroplet size was continuously varying while the aqueous solution mixture becomes reacting and the initial nucleation step took place. Thus, although many types of MNPs have been synthesized in a controlled manner using the *με* method, the particle size and shapes usually vary over a relative wide range. This problem have been solved by using a cation-substituted surfactant molecules in which the polar head containing the desired cation and the aqueous solution was formed by second reactant, such as the alkaline. In this way, the coalescence stage is avoided and the microdroplet size control is more effective. Moreover, the working window for the synthesis in *με* is usually quite narrow and the yield of NPs is low compared to other methods, such as thermal decomposition and co-precipitation. Large amounts of solvent are necessary to synthesize appreciable amounts of material. It is thus not a very feasible process and also rather difficult to scale-up.

Inspired by the synthesis of high-quality semiconductor nanocrystals and oxides in non-aqueous media by **thermal decomposition** (Lu et al., 2007; O'Brien et al., 2001), the most promising method for the synthesis of MNPs with control over size and shape have been developed to date. Monodisperse magnetic nanocrystals with smaller size can essentially be synthesized through the thermal decomposition of organometallic compounds in high-boiling organic solvents containing stabilizing surfactants with long chain carboxylic acids and amines (Hyeon, 2003a; Sun et al., 2000; Varanda & Jafelicci, 2006). The organometallic

precursors include metal acetylacetonates, metal cupferronates or carbonyls. The reagent proportions, reaction temperature, reaction time, as well as aging period are crucial for the precise control of size and morphology. If the metal in the precursor is zero-valent, such as in carbonyls, thermal decomposition initially leads to formation of the metal, but two-step procedures can be used to produce oxide NPs. For instance, iron pentacarbonyl can be decomposed in a mixture of octylether and oleic acid with subsequent addition of trimethylamine oxide $(CH_3)_3NO$ as a mild oxidant at elevated temperature, results in formation of monodisperse γ-Fe_2O_3 nanocrystals with a size of approximately 13 nm (Hyeon et al., 2001). Decomposition of precursors with cationic metal centers leads directly to the oxides, that is, to Fe_3O_4, if $[Fe(acac)_3]$ is decomposed in the presence of 1,2- hexadecanediol, oleylamine, and oleic acid in phenylether, as showed in Fig. 1c. The size and shape of the nanocrystals could be controlled by variation of the reactivity and concentration of the precursors. The reactivity was tuned by changing the chain length and concentration of the surfactants. Generally, the shorter the chain length, the faster the reaction rate is. Alcohols or primary amines could be used to accelerate the reaction rate and lower the reaction temperature. *Hyeon et al.* (Park et al., 2004) have also used a similar thermal decomposition approach for the preparation of monodisperse iron oxide NPs. They used nontoxic and inexpensive iron(III) chloride and sodium oleate to generate an iron oleate complex in situ which was then decomposed at high temperatures in different solvents, such as 1-hexadecene, octylether, 1-octadecene, 1-eicosene, or trioctylamine. Particle sizes are in the range of 5–22 nm, depending on the decomposition temperature and aging period. The NPs obtained are dispersible in various organic solvents including hexane and toluene. However, water soluble MNPs are more desirable for applications in biotechnology. For that purpose, a very simple synthesis of water-soluble magnetite NPs was reported recently. Using $FeCl_3 \cdot 6H_2O$ as iron source and 2-pyrrolidone as coordinating solvent, water soluble Fe_3O_4 nanocrystals were prepared under reflux (245 °C) (Li et al., 2005). The mean particles size can be controlled at 4, 12, and 60 nm, respectively, when the reflux time is 1, 10, and 24 h. With increasing reflux time, the shapes of the particles changed from spherical at early stage to cubic morphologies for longer times. More recently, the same group developed a one-pot synthesis of water-soluble magnetite NPs prepared under similar reaction conditions by the addition of a dicarboxyl-terminated poly(ethylene glycol) as a surface capping agent (Hu et al., 2006). These NPs can potentially be used as magnetic resonance imaging contrast agents for cancer diagnosis. The thermal decomposition method is also used to prepare metallic NPs (Varanda et al., 2007; Varanda & Jafelicci, 2006). The advantage of metallic NPs is their larger magnetization compared to metal oxides. Metallic iron, cobalt, nickel and alloys such as FePt (Fig. 1d), CoPt, NiPt, and CrPt or using Ru instead Pt in the alloys NPs were synthesized by thermal decomposition of different metallic precursors in a varied of solvents. Magnetic alloys have many advantages, such as high magnetic anisotropy, enhanced magnetic susceptibility, and large coercivities. Beside $CoPt_3$ and FePt, metal phosphides are currently of great scientific interest in materials science and chemistry. For example, hexagonal iron phosphide and related materials have been intensively studied for their ferromagnetism, magnetoresistance, and magnetocaloric effects (Luo et al., 2004). In addition, the thermal decomposition method can be used to synthesized antiferromagnetic NPs such as MnO (Fig. 1e) and FeO which have been waking is very interesting due to potential application in MRI as water relaxation time T_2 interfering. Due to their versatility, the thermal decomposition method has been also combining with the seed-mediated growth methodology in order to synthesis core-shell nanosctrutuctured NPs such as Fe_3O_4-coated FePt ($FePt@Fe_3O_4$, Fig. 1f) (Varanda et al., 2008).

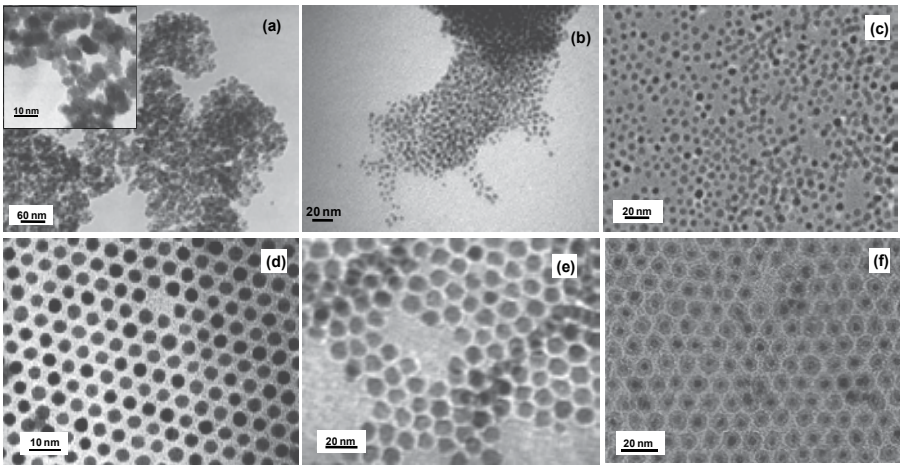

Fig. 1. TEM of MNPs prepared using different synthetic routes: above, magnetite synthesized by (a) co-precipitation, (b) microemulsion, and (c) thermal decomposition; bellow, (d) FePt, (e) MnO, and (f) FePt@Fe_3O_4 synthesized by thermal decomposition.

4. Surface engineering

The functionalization of NP surface is one method for tuning the overall properties of particles to fit targeted applications. The surface modification of NPs by functional molecules/particles/polymers has different tasks to fulfill (de Dios & Díaz-Garcia, 2010):

a. stabilize the NPs in solution to control the growth of the embryonic particles and determine their shape during the growth process;
b. provide functional groups at the surface for further derivatization;
c. enhance NP solubilization in various solvents extending their application possibilities;
d. capping layers can modify the electronic, optical, magnetic and chemical properties of the particles, providing a plethora of controllable nanotools;
e. modify the capability to assemble the particles in specific arrays or the ability to target desired chemical, physical, or biological environments;
f. improve mechanical and chemical performances of the NP surface, e.g. passivation;
g. in some instances a reduction of their toxicity is achieved.

Colloidal nanostructures dispersed in a medium collide with each other frequently and the overall colloidal stability of the dispersion, which is critical to most potential NP applications, is dictated by the fate of the individual particles after each collision (Hunter, 2001). Attractive interactions leads to irreversible aggregation of the NPs, and in the case of magnetite particles, magnetic dipole-dipole interactions can provide an additional attractive force. A critical requirement is therefore to surface-engineer the NPs with (macro) molecules that provide repulsive forces large enough to counter the attractive ones in the collision processes. Repulsive forces can be achieved in the presence of an electrical double layer on the particles (electrostatic stabilization) or in presence of polymeric chains providing steric stabilization. Attractive van der Waals and repulsive Coulombian forces are strongly influenced by the dispersion medium properties. Colloidal stability of NP dispersion must therefore be considered for a specific system, especially in the setting of bio-applications that require colloidal stability in complex biological medium such as blood or plasma. Steric

stabilization provided by adsorption or grafting of polymers on the NPs is the most efficient way to prevent aggregation in bio-systems (Majewski & Thierry, 2007).
Biomedical applications often require stringent control of the NPs bio-interfaces. Along with the need for colloidal stability in complex biological environment, a major requirement for the successful integration of MNPs in biomedical application is indeed to minimize biologically non-specific adsorption events, for example, the adsorption of plasma proteins on the NP surfaces. Such non-specific events can drastically hamper molecular recognition processes at the surface of the NPs, therefore reducing the efficiency of MNP-based bio-assays. A pre-requisite to the widespread use of NPs *in vivo* is also their ability to resist non-specific adsorption of opsonins. Opsonization of NPs by plasma proteins results into rapid elimination from the blood by the mononuclear phagocyte system (MPS) with consequent accumulation in organs of the reticuloendothelial system (RES, phagocytic cells residing in tissues forming party of the body immune system) such as spleen and liver. The nature (e.g., complement proteins and immunoglobulins) and amount of plasma proteins adsorbing on NPs is directly related to the physicochemical characteristics of the NPs surfaces. Adsorbed opsonins potentially lead to specific interactions with receptors on the surface of macrophages and hepatocytes and the subsequent elimination of the NPs (Vonarbourg et al., 2006; Yan et al., 2005). For instance, concerning NP sizes, for example, the overall particle size must be small enough to evade uptake by the RES, but large enough to avoid renal clearance. Procedures to achieve high quality bio-interfaces able to resist non-specific interaction have been implemented on macroscopic surfaces. It is commonly admitted that non-fouling surfaces should posses the following characteristic: (1) hydrophilic, (2) hydrogen bond acceptors, (3) no hydrogen bond donors, (4) neutral. In summary, colloidal electrostatic stabilization arising from repulsion of surface charges on the NPs is typically not adequate to prevent aggregation in biological solutions due to the presence of salts or other electrolytes that may neutralize this charge. Furthermore, upon intravenous injection the surfaces of MNPs are subjected to adsorption of plasma protein, or opsonization, as the first step in their clearance by the RES. Evading uptake by the RES and maintaining a long plasma half-life is a major challenge for many MNP applications in medicine (Berry & Curtis, 2003; Sun et al., 2008). In order to minimize these critical effects, besides other considerations such as toxicity, biodistribution, and blood circulation time (see Section 7), many coating process have been used to modify/functionalize the NP surfaces, that provide a biocompatible surface, and after properly derivatization with targeting ligands, a bio-selectable surface for an specific body tissue, as schematically represented in the Fig. 2.

4.1 Polymeric coatings

Polymeric coatings provide a steric barrier to prevent NP agglomeration and avoid opsonization. These coatings also provide a means to tailor the surface properties of MNPs such as surface charge and chemical functionality. Some critical aspects with regard to polymeric coatings may affect the MNP performance including nature of the polymer chemical structure (e.g. hydrophilicity/hydrophobicity, biodegradation characteristics, etc.), the length or molecular weight of the polymer, the manner in which the polymer is anchored or attached (e.g. electrostatic or covalent bonding), the conformation of the polymer, and the degree of particle surface coverage. Various monomeric species, such as bisphosphonates, dimercaptosuccinic acid, and alkoxysilanes, have been evaluated as anchors to facilitate attachment of polymer coatings on MNPs (Sun et al., 2008).

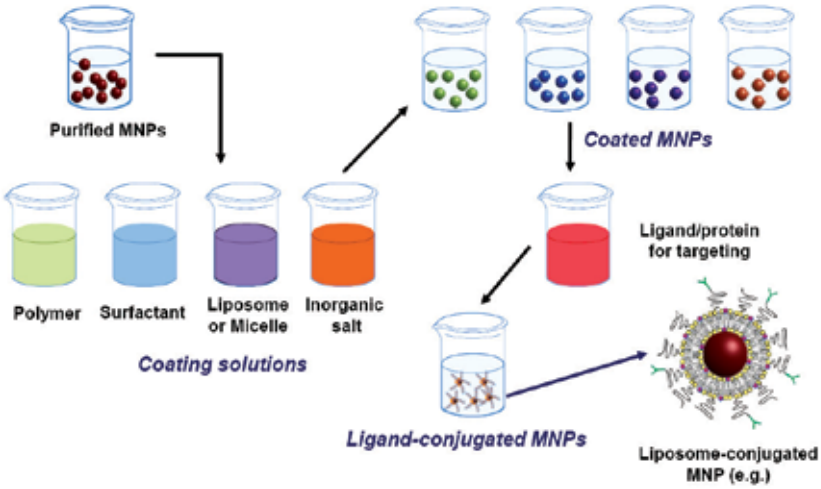

Fig. 2. Representative MNPs surface engineering coating process using polymer, surfactant, liposome, and inorganic salt (core-shell nanostructure) followed by derivatization surface with targeting ligands (biocompatible and biosselective MNPs for biomedical applications).

The molecular weight and geometric orientation of the polymer on the surface of the particles in the form of loops, trains, and tails or as end-grafted brushes or as fully encapsulated polymer shells not only affect the antifouling characteristics of the NP, but also contribute to their effective hydrodynamic size, which is another key factor in avoiding recognition by the RES. A variety of natural and synthetic polymers have been evaluated for use as coatings on MNPs. Readers are directed to several reviews on the topic for a comprehensive analysis of these materials (Gupta et al., 2007; Gupta & Gupta, 2005). In this section the most widely utilized and successful polymer coating for *in vivo* applications will be emphasized. Among several nature and synthetic polymers used as coating in MNPs for biomedical applications, many monomers due to systematic uses can be mentioned: (a) ***dextran***, biocompatible and biodegradable, may be administered by an intravenous or oral route and used to stabilizer the colloidal solution and enhancer the blood circulation time (Massia et al., 2000). Dextran coatings can be achieved directly during the preparation of magnetite NPs in the co-precipitation technique but also by conjugating reactive dextran, for example, ***carboxymethyl dextran*** and partially oxidized dextran (via formation of Schiff's bases linkages), onto functionalized NPs. The nature of the dextran derivative, the number of reactive groups and immobilization conditions (e.g., ionic strength, pH) can be used to control the final polymer conformation on the surfaces (Majewski & Thierry, 2007). As mentioned earlier, an issue when working with NPs is to avoid irreversible aggregation during coating procedures subsequent to synthesis. Optimizing experimental conjugation conditions, monodisperse carboxymethyl dextran-coated monocrystalline magnetite NPs prepared by microemulsion methodology have been prepared without detectable aggregation; (b) ***poly(ethylene glycol), PEG,*** is another widely used polymer for NP coating owing to its hydrophilicity and no-antigenic and no-immunogenic properties (Brus et al., 2004; Gupta et al., 2007). The antifouling nature of PEG has been shown to reduce NP uptake by macrophages and extend blood circulation time *in vivo*. Various methods have been utilized to attach PEG to MNPs including silane grafting to oxide surfaces, polymerization at the surface of MNPs, and modification through sol–gel approaches

(Gupta et al., 2007). To control polymer conformation and provide stable covalent linkages to the surface of iron oxide NPs, *Kohler et al.* developed bifunctional PEG silanes capable of forming self-assembled monolayers (SAMs) and increasing the packing density of the polymer chains onto the NPs surface (Kohler et al., 2004; Zhang et al., 2002). In addition, terminal amine or carboxyl groups extending out from the NP surface provide sites for conjugation of functional ligands, as demonstrated by the attachment of folic acid. The strong attachment of the PEG molecules not only improved the steric stabilization of the MNPs *in vivo* against interactions with opsonins and cells, but also imparts the prolonged circulation in blood and reduced RES uptake (Gupta & Curtis, 2004; Gupta & Wells, 2004). In addition, PEG-coated MNPs are hugely internalized by cells, presumably owing to the fluid phase endocytosis mechanism, probably their high solubility in cell membranes, since it is an amphiphilic molecule; (c) ***polyvinyl alcohol (PVA***) is used to prevent agglomeration and enhancing the colloidal stability (Xue & Sun, 2001); (d) ***polyacrylic acid (PAA)*** increase the stability and biocompatibility of the NP and also helps in bioadhesion (Burugapalli et al., 2004). Another consideration to take into account while utilizing polymer coatings is their effects on the NP magnetic properties, where the saturation magnetization generally decreases with the thickness polymer coating increases (Mikhaylova et al., 2004).

4.2 Non-polymeric stabilizers (surfactants)

Surfactants or polymers are often employed to passivate the surface of the NPs during or after the synthesis to avoid agglomeration. In general, electrostatic repulsion or steric repulsion can be used to disperse NPs and keep them in a stable colloidal state. In the case of ferrofluids, the surface properties of the magnetic particles are the main factors determining colloidal stability. The major measures used to enhance the stability of ferrofluids are the control of surface charge and the use of specific surfactants (Lu et al., 2007). For instance, magnetite NPs synthesized through the co-precipitation of Fe^{2+} and Fe^{3+} in ammonia or NaOH solution are usually negatively charged, resulting in agglomeration. In general, surfactants can be chemically anchored or physically adsorbed on MNPs to form a single or double layer which creates repulsive (mainly as steric repulsion) forces to balance the magnetic and the van der Waals attractive forces acting on the NPs. Thus, by steric repulsion, the magnetic particles are stabilized in suspension. Additionally, in order to stabilize the colloidal dispersion, *Gedanken et al.* studied the adsorption of alkanesulphonic and alkanephosphonic acids on the surfaces of amorphous Fe_2O_3 NPs and proposed two possible bonding schemes for the phosphonate ions on Fe^{3+}, i.e., one O or two O atoms of the phosphonate groups binding onto the surface (Yee et al., 1999). *Sahoo et al.* have reported the surface derivatization of magnetite by oleic acid, lauric acid, dodecylphosphonic acid, hexadecylphosphonic acid, dihexadecylphosphonic acid etc. to stabilize the NPs in organic solvents (Sahoo et al., 2001). They found that alkyl phosphonates and phosphates could be used for obtaining thermodynamically stable dispersions of MNPs. The authors suggested on the basis of the results obtained from the temperature and enthalpy desorption studies that these ligands form a quasi-bilayer structure with the primary layer strongly bonded to the surface of NPs. The ferrofluids, frequently dispersed in hexadecane as the carrier medium, may be stabilized by various long-chain surfactants, the classic example being oleic acid, which has a C18 (oleic) tail with a cis-double-bond in the middle, forming a kink. Such kinks have been postulated as necessary for effective stabilization, and indeed stearic acid, with no double-bond in its C18 (stearic) tail, cannot stabilize ferrofluid suspensions (Gupta

& Gupta, 2005). The long chain surfactants uses such as oleic acid and oleylamine, generally employed in the thermal decomposition synthesis, leads too much stabilized NPs suspension in organic media (e.g. hexane), but is desired water stabilized NPs suspension for biomedical applications. In this cases, ligand exchanges or coating with water compatible molecules/compounds can be use to stabilizer these NPs in water suspension instead organic solvents. Because use of polymers leads to thick surface layers, *Portet et al.* have (Portet et al., 2001) developed monomeric organic molecules as coating materials. The main property of these small molecules is to produce a homogeneous coating of the entire iron oxide core that is able to inhibit the protein absorption. Phosphorylcholine (PC)-derived polymers are known to protect prosthesis against protein contamination, but pure PC coatings do not allow colloidal stability at physiological pH (Denizot et al., 1999).

4.3 Liposomes and micelles

The development of liposomes as drug delivery vehicles can be considered one of the earliest forms of nanomedicine recently developed. These phospholipid bi-layered membrane vesicles, as indicated in the Fig. 2, can range from100 nm up to 5 μm in size and have been utilized for the delivery of small molecules, proteins and peptides, DNA, and MR imaging contrast agents (Sun et al., 2008; Torchilin, 2005). An advantage of liposome encapsulation or micelar nanoparticle environment (MNE) is that it *in vivo* behavior already has been well established with processes such as PEGylation resulting in long circulation times. Another favorable feature of liposomes is the ability to encapsulate a large number of MNP cores and deliver them together, avoiding dilution, to a target site. Combining a therapeutic agent in the payload further enhances the multifunctionality of these delivery vehicles. Magnetic fluid-loaded liposomes (MFLs) with hydrodynamic size of 195±33 nm were formed by film hydration coupled with sequential extrusion and were capable of encapsulating up to 1.67 mol of iron per mol of lipid. *In vivo* evaluation in mice using MR angiography demonstrated that these MFLs were still present in the blood 24 h after intravenous injection confirming their long circulating behavior. Similarly, multifunctional micelles formed with amphiphilic block copolymers have also been used to entrap MNPs for these applications (Sutton et al., 2007). Many micelar system mainly based on the phospholipid or phospholipid-derivated have been studying in order their potential application in drug delivery system and, in addition, their biocompatible properties has used as coating system in order to promote the MNP increases blood circulation, biodistribution and cell membrane internalization.

4.4 Inorganic coating (core-shell nanostructure)

In addition to organic coatings, core–shell structures utilizing biocompatible silica, gold or other noble metal, carbon, etc., to encapsulate the MNPs have become another attractive approach for developing MNPs for biomedical applications. These NPs have inner iron oxide/alloys magnetic core with an outer metallic shell of inorganic materials. These inert coatings, or shells, provide not only the stability to the NPs in solution but also protection against chemical degradation of magnetic cores, prevent the release of potentially toxic components, and helps in binging the many biological ligands at the NP surface since that functionalization chemistries are generally better established with these materials than those that comprise MNPs. Silica shells are attractive options to serve as protective coatings on MNPs due to their stability under aqueous conditions and ease of synthesis. An advantage

of having a surface enriched in silica is the presence of surface silanol groups that can easily react with alcohols and silane coupling agents to produce dispersions that are not only stable in non-aqueous solvents but also provide the ideal anchorage for covalent bounding of specific ligands. The strong binding makes desorption of these ligands a difficult task. In addition, the silica surface confers high stability to suspensions of the particles at high volume fractions, changes in pH or electrolyte concentration (Gupta & Gupta, 2005). Thus, a silica shell does not only protect the magnetic core, but can also prevent the direct contact of the core with additional agents linked to the silica surface avoiding unwanted interactions. Sol–gel processes using tetraethoxysilane (TEOS) are generally utilized throughout the literature to produce coatings of controlled thickness (Lu et al., 2002). The use of functional alkoxysilanes, such as 3-aminopropyltriethyoxysilane (APS), allows for surface reactive groups to be easily added to these core–shell structures. In addition, the ability to encapsulate functional molecules, such as alternative imaging or therapeutic agents, within this protective matrix is a unique feature to these nanostructures (Tada et al., 2007).
The Stöber method and sol–gel processes are the prevailing choices for coating MNPs with silica. The coating thickness can be tuned by varying the concentration of ammonium and the ratio of TEOS to H_2O. The functionalization could introduce additional functionality, so that the magnetic particles are potentially of use in biolabeling, drug targeting, and drug delivery. In previous studies involving the coating of hematite spindles and much smaller magnetite clusters with silica, the iron oxide cores could subsequently be reduced in the dry state to metallic iron (Varanda et al., 2002a; Varanda et al., 2001). The advantage of this method is that silica coating was performed on an oxide surface, which easily binds to silica through OH surface groups. Since the iron oxide surface has a strong affinity towards silica, no primer was required to promote the deposition and adhesion of silica. Owing to the negative charges on the silica shells, these coated MNPs are re-dispersible in water without the need of adding other surfactants. Though great progress in the field of silica-coated NPs has been made, the synthesis of uniform silica shells with controlled thickness on the nanometer scale still remains challenging. As an alternative, the microemulsion method was also tried resulting in a best silica thickness control. Although metals protected by silica can be synthesized by reduction after synthesis, silica deposition directly on pure metal particles is more complicated because of the lack of OH groups on the metal surface. An additional difficulty for coating metallic NPs, such as iron and cobalt with silica, which has to be overcome, is that iron and cobalt are readily oxidized in the presence of dissolved oxygen. Therefore, it is necessary to use a primer to make the surface "vitreophilic" (glasslike), such as coat precious metals or realize the metal surface passivation by the gentle oxidation as starting materials for such silica coating. From the mentioned examples above, it can be seen that silica coating of magnetic oxide NPs is a fairly controllable process. However, silica is unstable under basic condition, in addition, silica may contain pores through which oxygen or other species could diffuse. Coating with other oxides is much less developed and therefore alternative methods, especially those which would allow stabilization under alkaline conditions, are needed. Gold offers several advantages as a coating material for MNPs due to its low chemical reactivity and unique ability to form self-assembled monolayers (SAMs) on their surface using alkanethiols (Sun et al., 2008). Unfortunately, this chemical inertness may also lead to difficulty in forming gold shells over MNPs. Recent advances in synthesizing gold-coated iron NPs through a variety of methods ranging from reversed microemulsion, combined wet chemical, to laser irradiation, redox transmetalation, iterative hydroxylamine seeding, have been reviewed by *Lu et al.* (Lu et al., 2007). Gold

coating of MNPs is especially interesting, since the gold surface can be further functionalized with thiol groups. This treatment allows the linkage of functional ligands which may make the materials suitable for catalytic and optical applications. Although to date most studies have focused on the development of polymer or silica protective coatings, recently carbon-protected MNPs are receiving more attention, because carbon-based materials have many advantages over polymer or silica, such as much higher chemical and thermal stability as well as biocompatibility. Since then, many studies have shown that in the presence of metal NPs, graphitized carbon structures, such as carbon nanotubes and carbon onions, are formed under arc-discharge, laser ablation, and electron irradiation. The well-developed graphitic carbon layers provide an effective barrier against oxidation and acid erosion. These facts indicate that it is possible to synthesize carbon-coated MNPs, which are thermally stabile and have high stability against oxidation and acid leaching, which is crucial for some applications (Lu et al., 2007).

5. Multifunctional magnetic nanoparticles

Despite the potential benefits that MNPs have rendered to biomedicine, some applications remains challenging, for instance, *in vivo* real-time monitoring of cellular events, specific targeting to the action site or efficient drug delivery inside the target cell. In this context, the design of multifunctional NPs could significantly improve already existing NPs characteristics and help to surmount these challengers. Whereas a monofunctional NP provide a single function, i.e. a liposome can transport drugs but does not have the inherent property to distinguish between healthy and unhealthy cells or tissues, a multifunctional NPs combine different functionalities in a single stable construct. For example, a core particle could be linked to a specific targeting function that recognizes the unique surface signatures of their target cells. Simultaneously, the same particle can be modified with an imaging agent to monitor the drug transport process, a function to evaluate the therapeutic efficacy of a drug, a specific cellular penetration moiety and a therapeutic agent (Sanvicens & Marco, 2008). Thus, the fabrication of bifunctional or multifunctional NPs has received a great deal of attention in recent years. Hybrid inorganic NPs are emerging as useful probes for magnetic-based targeting, delivery, cell separation, MRI, and fluorescence-based biolabeling applications. Gold (Au) NPs have been extensively used to prepare multifunctional composites with quantum dots (QDs) and MNPs. Typical examples include Fe_3O_4-Au (Yu et al., 2005), CdSe-Au (Mokari et al., 2004), and PbSe-Au-Fe_3O_4 (Shi et al., 2006). Multifunctional NPs have been actively explored for the enhancement of imaging, targeting, and delivery. In the field of biological and biomedical imaging, QDs and MNPs have been enjoying greater roles in biolabeling and MRI respectively. A combination of optical and magnetic properties in a single material would enable simultaneous biolabeling/imaging and cell sorting/separation. Nanocomposites consisting of semiconductor and MNPs, known as magnetic quantum dots (MQDs) or luminomagnetic nanoparticles (LMNPs) (Sun et al., 2008), are of great interest as a new class of materials (Selvan et al., 2010). Despite all of these advances, the application of multifunctional NPs in *in vivo* imaging is still in its infancy. As discussed throughout this Chapter, the ability to add components to MNPs in a modular fashion allows for specific features and functional moieties to be interchanged or combined. Ligands such as targeting agents, permeation enhancers, optical dyes, and therapeutic agents can all be conjugated on the surface or incorporated within these nanostructures (Fig. 3, left).

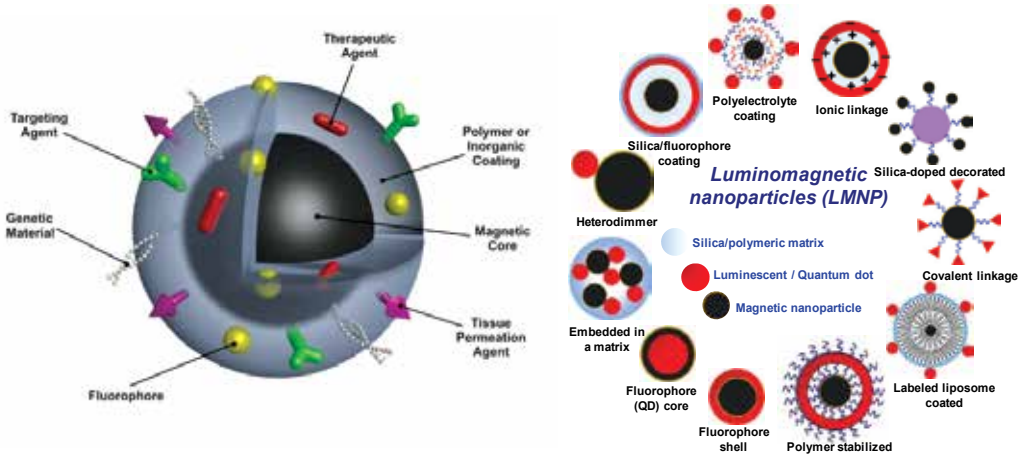

Fig. 3. (left) Targeting, therapeutic, luminescent and biocompatibility agents on the same NP surface enabling multifunctionality in a single MFMNP; (right, adapted from (Corr et al., 2008) Many different types of LMNPs according to their preparation route.

To perform such nanoscale engineering, bioconjugation chemistries and techniques utilized for protein coupling have been studied (Sun et al., 2008). Techniques such as avidin–biotin binding, use of heterobifunctional linkers to form amide, ester, or disulfide bonds, and more recently "click" chemistries (Nandivada et al., 2007), have all been shown to be useful in attaching functional ligands to MNPs. In addition to understanding the mechanisms of these reactions, those utilizing these techniques on MNPs may also find it useful to review basic concepts of colloidal science to avoid unwanted NP flocculation or aggregation (Hunter, 2001). One example of adding functionality to MNPs has been the combination of organic dyes or fluorophores as optical agents allowing detection by multiple imaging modalities.

Both magnetic and fluorescent inorganic NPs have been shown to play a significant role in nanotechnology. Just looking at the wealth of possible applications open to magnetic and fluorescent materials, it is not hard to see why the combination of these two entities opens up the opportunity to provide new nanocomposites which could act as multi-targeting, multi-functional and multi-treating tools. It is expected that the combination of magnetic and fluorescent properties in one nanocomposite would open up great prospects both in nano- and biotechnology, enabling the engineering of unique targeted, nanoscale photonic devices which could be manipulated using an external magnetic field. The combination of a magnetic and a fluorescent entity in a new bimodal ''two-in-one'' LMNP may provide a new multifunctional nanomaterial with a broad range of potential applications. First of all, multimodal magnetic-fluorescent assays would be very beneficial for *in vitro* and *in vivo* bio-imaging applications such as MRI and fluorescence microscopy. Second of all, these nanocomposites can be utilized as agents in nanomedicine. For example, one of their most promising applications is a bimodal anticancer therapy, encompassing photodynamic and hyperthermic capabilities. LMNPs can also serve as an all-in-one diagnostic and therapeutic tool, which could be used, for example, to visualize and simultaneously treat various diseases. Another exciting application of LMNPs is in cell tracking, cytometry and magnetic separation, which could be easily controlled and monitored using fluorescent microscopy. A specific difficulty in the preparation of two-in-one LMNPs is the risk of quenching of the fluorophore on the surface of the particle by the magnetic core. In addition, if there are a

number of fluorescent molecules attached to the surface of the particle, they may act to quench each other. The problem of quenching can be partially resolved by providing the MNP with a stable shell prior to the introduction of the fluorescent molecule, or by first treating the fluorophore with an appropriate spacer. Finally there are typical problems related to instability and aggregation of the nanocomposites in solutions. Therefore, a careful design and an extremely accurate synthesis methodology are required for the development of the LMNPs to avoid their aggregation and precipitation in comparison to the developed techniques used in the case of MNPs. Most of these nanocomposites are core-shell nanostructures. In general, we can identify eight main types of LMNPs (Fig. 3, right) (Corr et al., 2008). Recently, the conjugation of near-infrared fluorescent (NIRF) dyes to MNPs has received significant attention due to the deep penetration of NIRF light through tissues. The integration of NIRF detectability may allow for these NPs to be used for both presurgical planning by MRI and intraoperative resection of malignant tissues by optical imaging. Since both MRI and optical signals come from the same NPs, the MR image can serve as a roadmap to the fluorescently labeled tumor cells (Sun et al., 2008).

6. Biomedical applications of nanomagnetics

6.1 Magnetic resonance imaging - MRI

MRI is one of the most powerful imaging techniques for living organisms as it provides images with excellent anatomical details based on soft-tissue contrast and functional information in a non-invasive and real-time monitoring manner. MRI has further advanced by the development of contrast agents that enable more specific and clearer images and enlargements of detectable organs and systems, leading to a wide scope of applications of MRI not only for diagnostic radiology but also for therapeutic medicine. Current MRI contrast agents are in the form of either paramagnetic complexes or MNPs. Paramagnetic complexes, which are usually gadolinium (Gd^{3+}) or manganese (Mn^{2+}) chelates, accelerate longitudinal (T_1) relaxation of water protons and exert bright contrast in regions where the complexes localize. For instance, gadolinium diethylenetriamine pentaacetate (Gd-DTPA) has been the most widely used of such complexes and its main clinical applications are focused on detecting the breakage of the blood-brain barrier (BBB) and changes in vascularity, flow dynamics, and perfusion (Na et al., 2007; Weinmann et al., 2003). Iron oxide NPs were the first, and are the most commonly used MNP-based contrast agents for MRI. Importantly, it have been taken through regulatory approval and may be safety, and legally, used in human (Pankhurst et al., 2009). The limitations of using MNPs, however, are that millions of particle with very high saturation magnetization values are required to achieve sufficient contrast (Gupta et al., 2007). The efficacy, as MRI contrast agent, of iron oxide NPs depends to a large extent on their physicochemical properties, particularly their size and surface chemistry, the later properly bioconjugated with targeting agents. The spin-spin relaxation time (T_2) depends of the MNP size and larger particles exhibit larger T_2 effect (Bin Na et al., 2007). In addition, the intrinsic magnetization of the particles is also important and metallic or alloys NPs are preferable than iron oxides concerning the *Ms* of these latter. In this context, cobalt NPs present much higher room temperature *Ms* than those iron oxides, which could be resulting in a larger effect on proton relaxation giving improved MRI contrast and allowing smaller MNPs core use without compromising sensitivity. However, water-soluble Co NPs is very difficult to obtain and stabilizer, besides their high toxicity intrinsic to the metal NPs. As observed with Co, Fe and FePt NPs present advantage

compared with the oxide for enhanced MRI contrast, but their potential uses require further improvement in biostabilization and functionalization because their toxicity. In addition, the negative contrast effect and magnetic susceptibility artifacts of iron oxide NPs are significant drawbacks. The resulting dark signal can mislead the clinical diagnosis in T_2-weighted MRI because the signal is often confused with the signals from bleeding, calcification, or metal deposits, and the susceptibility artifacts distort the background image. For the extensive applications of MRI to diagnostic radiology and therapeutic medicine and to overcome the above-mentioned drawbacks of Gd^{3+}- and Mn^{2+}-based T_1 contrast agents and MNP-based T_2 contrast agents, there has been great demand for a new class of contrast agent that satisfies the following characteristics: 1) positive (T_1) contrast ability, 2) intracellular uptake and accumulation for imaging cellular distribution and functions, 3) nanoparticulate form for easy surface modification and efficient labeling with targeting agents for applications in molecular and cellular imaging, and 4) favorable pharmacokinetics and dynamics for easy delivery, efficient distribution to biomarkers, and safe clearance from patients with minimal side effects. Recently, the development of a long-awaited T_1 MRI contrast agent that satisfies all of these desirable characteristics was proposed by using MnO NPs (Na et al., 2007).

6.2 Drug delivery and gene delivery (magnetofection)

The surface of magnetite NPs have been functionalized with drugs, proteins, and genetic materials to achieve localized delivery of therapeutic agents. The need for localized delivery of bioactive agents stems in the systemic toxicity often associated with non-targeted administration of these agents. Potential elimination of systemic side-effects could potentially be achieved through efficient targeting of NPs carrying high payload of active agents. Although still the object of much debate the ability to magnetically target *in vivo* drug-loaded MNPs has attracted considerable attention (Dobson, 2006a). Whether an external magnetic field can be used to capture MNPs injected intravenously depends on the strength of the applied magnetic field, as well as on the magnetic properties and volume of the NPs. Alternatively, targeting moieties on the surface of the NPs functionalized with bioactive agents have been used to target or internalize specific tissue or tumor *in vivo*. Ideally, they could bear on their surface or in their bulk a pharmaceutical drug that could be driven to the target organ and released there. Physical constraints placed upon magnetic targeting, such as the rapid diminishing of field strength with target depth in the body and the difficulties of bypassing intervening vasculature and tissue structures (Dobson, 2006a; Dobson, 2006b), have hampered the clinical realization of this technology. Much of the recent work in this area has focused on the development of high-moment MNP carriers with novel, multifunctional coatings and novel techniques for enhancing the body own targeting systems (Pankhurst et al., 2009). The development of novel MNP carrier formulations continues apace. In general, advances are focusing on novel, multifunctional coatings, and the use of high-moment materials for the particle cores and the development of thermoresponsive hydrogels and particles (Ankareddi & Brazel, 2007). Although there have been numerous small animal studies reported since our last review, due to the technical barriers mentioned above, the goal of clinical applications remains largely unfulfilled.

Magnetofection (MF) is a method in which MNPs associated with vector DNA are transfected into cells by the influence of an external magnetic field. A high-field, high-gradient magnet is generally placed underneath a cell culture dish or multi-well plate. The particle–gene complex is introduced into the cell growth medium and the magnetic field

rapidly pulls the particles into contact with the cells growing on the bottom of the dish. This has been shown to promote endocytosis of the particles, resulting in rapid and efficient transfection (Pankhurst et al., 2003). By using whether viral or nonviral vectors, MF has been shown to enhance the efficiency of the vectors up to several thousand times.

6.3 Hyperthermia

The idea of hyperthermia has been recognized as a useful therapeutic modality for treating malignant tumors, the idea being that it may be possible to kill cancer, not with drugs, but with targeted nanoscale heaters that would essentially cook malignant cells to death from the inside out. Magnetic materials with Curie temperatures between 42 and 60 °C are the best candidates for effective treatment, since they act as *in vivo* temperature control switches, preventing overheating. It is known that tumor cells are more sensitive to temperature increases than healthy cells, therefore intracellular hyperthermia methods have been suggested and developed using MNPs, whereby the particles are concentrated at the tumor site and remotely heated using an applied magnetic field to required hyperthermic temperatures (42–45°C) by hysteresis loss (multidomain particles) or energy dissipation (superparamagnetic NPs) (Berry, 2009). Magnetic field is not absorbed by the living tissues and can be applied to deep region in the living body. The amount of heat generated depends on the nature of magnetic material and of magnetic field parameters. Magnetic particles embedded around a tumor site and placed within an oscillating magnetic field will heat up to a temperature dependent on the magnetic properties of the material, the strength of the magnetic field, and the frequency of oscillation and the cooling capacity of the blood flow in the tumor site. Cancer cells are destroyed at temperature higher than 43 °C, whereas the normal cells can survive at higher temperatures (Gupta & Gupta, 2005). In a general way, when MNPs are injected into an organ with a tumor, they tend to accumulate in the tumor due to the unorganized vasculature, thus effectively heating the tumor as opposed to the surrounding healthy tissue. Direct injection into solid tumors, followed by exposure to an alternating magnetic field, has been shown to be capable of inducing tumor regression. Studies have highlighted the potential of MNPs in human cancer models, such as breast cancer, whereby 10–30 nm iron oxide particles were heated effectively. Choosing high-power magnetic particles combined with appropriate external magnetic field, very small amounts of magnetic fine particles in the order of tenth of milligram may easily be used to raise the temperature of biological tissue locally up to cell necrosis. However, the major technical difficulty associated with heat-based cancer therapy is to heat only the tumor tissues without damaging the healthy ones. Considerable interest has therefore been drawn to MNP to achieve intracellular hyperthermia procedures, for instance by targeting MNPs conjugated with a monoclonal antibody such as anti-HER2. In addition, if it is the aim to generate enough of a temperature rise throughout the target tissue volume for the induced hyperthermia to be therapeutic in its own right, then the method used to get the NPs into the target becomes critical (Wust et al., 2006). MagForce have pursued the concept of interstitial heating via multiple-site direct injection of their NPs and have developed sophisticated measures to ensure that the specific absorption rate (SAR) throughout the entire target volume will be enough to result in a therapeutic thermal dose, expressed as cumulative equivalent minutes at 43 C for 90% of the tumor volume (Pankhurst et al., 2009). This is an extremely demanding requirement since it only requires a very small part of the target volume to remain cool for the entire treatment to be compromised. The two

most obvious reasons why a small section of a tumor may not be heated are either because of a locally increased level of blood flow, say because of a nearby blood vessel, or an inadequate concentration of implanted MNPs.
A study highlights the difficulty in obtaining a uniformly effective thermal dose throughout the tumor volume. Animal model was used to examine the effect on tumor growth of NP-mediated hyperthermia by comparing two methods of NP administration. In one group, small deposits of a viscous emulsion of MNPs were injected directly into the centre of the tumors (group 1), while in the second group microspheres (ca 30μm in diameter) containing the same type of MNPs were administered via the arterial blood supply to the tumors (group 2). In both cases the thermal response, as measured by discrete temperature probes located in and around the tumor, appeared to be adequate although the group 1 heated much more rapidly than the group 2. The somewhat unexpected result, however, was that the therapeutic outcomes were very different and revealed a distinct advantage of the second approach, despite an apparently inferior thermal response initially. This result could be explained by the differences in the distribution of the magnetic particles throughout the tumor that are not reflected in the measured thermal response (Moroz et al., 2002).

6.4 Tissue repair – tissue engineering (TE) and regenerative medicine (RM)

Tissue repair using MNPs is accomplished either through welding, apposing two tissue surfaces then heating the tissues sufficiently to join them, or through soldering, where protein or synthetic polymer-coated NPs are placed between two tissue surfaces to enhance joining of the tissues. Temperatures greater than 50°C are known to induce tissue union. This is believed to be induced by the denaturation of proteins and the subsequent entanglement of adjacent protein chains (Gupta & Gupta, 2005). NPs that strongly absorb light corresponding to the output of a laser are also useful for tissue-repairing procedures. Specifically, gold- or silica-coated MNPs have been designed to strongly absorb light. The NPs are coated onto the surfaces of two pieces of tissue at the site where joining was desired. This technique affords methods to minimize tissue damage by using the least harmful wavelengths of light and/or lower powered light sources. Stem cells are the body master cells and have a unique ability to renew them and give rise to other specialized cell types. These cells, therefore, have the potential to be used for transplantation purposes, for example, to replace degenerated cells or repairing of a damaged tissue, providing signals so that the stem cells can yield the appropriate cell types for the development of a tissue. An obstacle to developing such therapy is a lack of targeting strategies on both neural stem cells and on the signals that determine their behavior and fate for tissue development. The superparamagnetic NPs could be coupled to the cells and used to target these cells at the desired site in the body. In addition, various proteins, growth factors, etc., could be bound to these NPs that might be delivered at the damaged tissue, where it would play a role in tissue development (Gupta & Gupta, 2005). In this context, over the past decade another novel application of MNPs has emerged: nanomagnetic actuation for TE and RM. Magnetic actuation can also be used to influence the growth and differentiation characteristics of stem cells. For many TE/RM applications, mechanical cues provide vitally important stimuli to the cells that promote the production of functional tissue matrix, especially bone, cartilage, muscle and connective tissue. However, applying the correct stress profiles to cells growing in a 3D scaffold within a bioreactor or within a patient's body has proven difficult. To overcome this problem, nanomagnetic actuation has been developed to apply targeted, controlled stress to cells growing in bioreactors and *in vivo* (Pankhurst et al., 2009). Although

the use of MNPs for TE/RM and stem cell research and therapy is at an early stage, the potential for this technology to make a major contribution to this field is great.

6.5 Cellular labeling and cell separation

Cell labeling with MNPs is an increasingly common method for *in vivo* cell separation (Olsvik et al., 1994) as the labeled cells can also be detected by MRI. Most current labeling techniques utilize either of two approaches: (a) attaching MNPs to the cell surface or (b) internalizing biocompatible magnetic particles by fluid phase endocytosis, receptor-mediated endocytosis or phagocytosis (Gupta & Gupta, 2005). One strategy for efficient and specific cell labelling of MNPs is to modify their surface with a ligand efficient to taken up by target cells. Targeting agents (e.g. transferrin, lactoferrin, albumin, insulin, growth factors, etc.) have been shown preference for target cell surface, because the receptors for these ligands are frequently overexpressed on the mammalian cells surface (Qian et al., 2002). These receptors are not only cellular markers, but also have been shown efficiency in the internalize molecules coupled to them. Furthermore, many of these ligands are stable, and generally poorly immunogenic. In the absence of any system to inhibit endocytosis, most NPs are endocytosed by cells and eventually sequestered in digestive vacuoles in the cell. Once the particles are endocytosed, they are probably removed from contact with specific cell surface receptors and become effectively ineffective. As a result of these events, the cells are at high risk of apoptosis from overload with particles. If the particles can be prevented from leaving the cell surface, they will remain in contact with their specific receptors and would be expected to leave the cell in a state of prolonged stimulation while protecting the cells from side effects due to endocytosis (Gupta & Gupta, 2005).

7. Challengers and trends

Although significant advances were obtained, the challengers faced by using MNPs *in vivo* still remains such as: need to extend the particles blood circulation time, the difficult to targeting specific tissue, and, more recently, due to increasing the complexity of the multifunctions by derivatized-layered coating the MNP surface generally using no-magnetic materials, there is a need to improve the magnetic core emanation in order to support these multifunctional capping. The need to extend NPs blood circulation time to allow for their accumulation in target tissues has long been recognized as one of the primary challenges in the development of MNPs (Berry, 2009; Sun et al., 2008). The ability to evade uptake by the RES is critical to achieving a long blood half-life. Like other colloidal carriers, the physicochemical properties of these MNP platforms, such as size, morphology, charge, and surface chemistry, dictate their fate *in vivo*, since determine their pharmacokinetics, toxicity, and biodistribution. The overall size of MNPs must be sufficiently small to evade rapid splenic filtration but large enough to avoid renal clearance. NPs larger than 200 nm are sequestered by phagocytotic cells of the spleen, while particles smaller than 5.5 nm are rapidly removed through renal clearance (Berry, 2009). In addition, particles smaller than 40 nm present both biodistribution and half-life determined by the coating materials rather than the mean hydrated size (Briley-Saebo et al., 2004). Particles that escape filtration are then subject to opsonization resulting in recognition and clearance by Kupffer cells and other tissue macrophages. Coatings including hydrophilic polymers, such as PEG, have been utilized to create a non-fouling coating on the particle surface. In addition to the biofouling nature of MNPs, surface charge plays a critical role in blood half-lives of colloids

and polymers. Positively charged polymers and particles tend to non-specifically stick to cells. This non-specific adsorption can have a significant impact on blood half-life. Strong negative charges on the particle surface are also detrimental in that they result in increased liver uptake. Therefore, it is generally agreed that NPs with a neutral surface experience extended blood circulation times. The development of long-circulating NPs has allowed for many MNP platforms to exploit structural abnormalities in the vasculature of particular pathologies, such as tumors, inflammatory, and infectious sites. This phenomenon, known as the enhance permeability and retention (EPR) effect, is based on the mechanism that these tissues possess "leaky" vasculature which allows macromolecules and NPs to extravasate and accumulate more readily. In the case of tumors, poorly organized vascular beds also result in impaired lymphatic drainage from these tissues. This nonspecific accumulation, or passive targeting, has been demonstrated with NPs ranging from 10 to 500 nm in diameter. Passive targeting can also occur through the inherent clearance by the RES. Comprised of bone marrow progenitors, blood monocytes, and tissue macrophages, the uptake of MNPs by these phagocytic cells provides a means of delivering contrast agents and drug carriers to related organs. One promising approach toward increasing the local accumulation of MNPs in diseased tissue, known as active targeting or specific targeting, is by the conjugation of targeting molecules that possess high affinity toward unique molecular signatures found on malignant cells. Often augmented by the EPR effect, these receptor–ligand or antigen–antibody interactions provide an effective strategy to improve the residence time in malignant tissues, such as tumors. Targeting ligands, such as proteins, peptides, aptamers, and small molecules, have been investigated to increase the site specific accumulation of MNPs. In some cases, specific binding can also facilitate internalization of the NP by receptor-mediated endocytosis. Another area of extensive investigation has been the targeting of MNPs to receptors overexpressed on tumor neovasculature. The formation of new blood vessels, or angiogenesis, is an essential component of tumor growth and has been shown to be highly specific for neoplasia (Sun et al., 2008). The use of short peptides and small molecules as targeting agents also offers the advantage of increased binding affinity through multivalent attachment (Weissleder et al., 2005). This targeting phenomenon has been examined with folic acid, a vitamin whose receptor is overexpressed on the surface of many human tumor cells, including ovarian, lung, breast, endometrial, renal, and colon cancers (Ross et al., 1994). Another advantage of utilizing small molecules as targeting agents is that they are generally more robust than proteins or peptides thereby reducing possibility of loss of functionality through the synthesis of such MNPs. An essential step in the use of MNPs for drug delivery is the internalization of the MNP and/or its therapeutic payload, as well as the subsequent release of these therapeutic agents to cell cytoplasm for desired actions to take place. Several mechanisms have been proposed to describe the uptake of NPs into cells, including receptor-mediated endocytosis and internalization by caveolae structures (Berry & Curtis, 2003). NP size and surface properties play a critical role in moving across the plasma membrane. NPs smaller than 50 nm or those coated with lipophilic polymers, such as PEG, have been shown to efficiently diffuse through cell membranes (Zhang et al., 2002). Although general guidelines, such as those discussed in regard to the physicochemical properties of MNPs, may provide some insight on their behavior in the body, no universal set of criteria has been elucidated to predict this critical aspect of nanomedicine. Mechanisms of clearance can vary significantly depending on the wide range of structures that are employed in the development of MNPs. One can make the obvious distinction that the metabolism, clearance, and toxicity profiles associated with a

gold-coated FePt core–shell NP will be drastically different from that of an iron oxide filled liposome and these structures therefore necessitate their individual evaluation. Recently, increased emphasis has been placed on standardizing preclinical characterization of biomedical NPs to better elucidate structure-activity relationships (SARs) (Sun et al., 2008). Recently, a new challenger involving MNPs or MFMNPs seems to be related with the core emanation. Several coating and molecular/compounds used to change de MNP surface from naked to multifunctional biocompatible and targeting leads also to dramatically decrease in the magnetic core emanation. In this context, either, new magnetic materials or combined magnetic materials in an enhanced new composite must be used in order to preserve the magnetic signal response of the external field (Varanda et al., 2008).

8. Conclusion

Progress and uses of MNPs in biomedicine have been highlighted, in both the traditional targeting and imaging, as well as the more novel cell manipulation techniques, it is believed that the future of MNP development must be directed towards further improving on the biocompatibility, specific targeting and image resolution available, extent the blood circulation time, and improvement of the magnetic core emanation in order to support the additional coating for multifunctionality. In addition, the potential of MNPs to have a multifunctional role in diagnosis, monitoring and treatment, is an exciting prospect.

9. Acknowledgments

Authors thank the Brazilian agencies ***FAPESP*** and ***CNPq*** by the financial support.

10. References

Ankareddi, I. & Brazel, C.S.(2007). Synthesis and characterization of grafted thermosensitive hydrogels for heating activated controlled release. *Int. J. Pharm.*, Vol. 336, No 2, 241-247, ISSN: 0378-5173.

Batlle, X. & Labarta, A. (2002). Finite-size effects in fine particles: magnetic and transport properties. *J. Phys. D-Appl. Phys.*, Vol. 35, No 6, R15-R42, ISSN: 0022-3727.

Benitez, M. J.; Petracic, O.; Salabas, E. L.; Radu, F.; Tuysuz, H.; Schuth, F. & Zabel, H. (2008). Evidence for core-shell magnetic behavior in antiferromagnetic Co_3O_4 nanowires. *Phys. Rev. Lett.*, Vol. 101, No 9, ISSN: 0031-9007.

Berry, C. C. (2009). Progress in functionalization of magnetic nanoparticles for applications in biomedicine. *J. Phys. D-Appl. Phys.*, Vol. 42, No 22, ISSN: 0022-3727.

Berry, C. C. & Curtis, A. S. G. (2003). Functionalisation of magnetic nanoparticles for applications in biomedicine. *J. Phys. D-Appl. Phys.*, Vol. 36, No 13, R198-R206, ISSN: 0022-3727.

Bin Na, H.; Lee, I. S.; Seo, H.; Il Park, Y.; Lee, J. H.; Kim, S. W. & Hyeon, T. (2007). Versatile PEG-derivatized phosphine oxide ligands for water-dispersible metal oxide nanocrystals. *Chem. Commun.*, No 48, 5167-5169, ISSN: 1359-7345.

Briley-Saebo, K.; Bjornerud, A.; Grant, D.; Ahlstrom, H.; Berg, T. & Kindberg, G. M. (2004). Hepatic cellular distribution and degradation of iron oxide nanoparticles following single intravenous injection in rats: implications for magnetic resonance imaging. *Cell Tissue Res.*, Vol. 316, No 3, 315-323, ISSN: 0302-766X.

Brus, C.; Petersen, H.; Aigner, A.; Czubayko, F. & Kissel, T. (2004). Physicochemical and biological characterization of polyethylenimine-graft-poly(ethylene glycol) block copolymers as a delivery system for oligonucleotides and ribozymes. *Bioconjugate Chem.*, Vol. 15, No 4, 677-684, ISSN: 1043-1802.

Burugapalli, K.; Koul, V. & Dinda, A. K. (2004). Effect of composition of interpenetrating polymer network hydrogels based on poly(acrylic acid) and gelatin on tissue response: A quantitative in vivo study. *J. Biomed. Mater. Res. Part A*, Vol. 68A, No 2, 210-218, ISSN: 0021-9304.

Cornell, R. M. & Schwertmann, U. (2003). *The iron oxide. Structure, properties, reaction, occurrence and uses*, Wiley-VCH, ISBN: 3-527-30274-3, Weiheim, Germany.

Corr, S. A.; Rakovich, Y. P. & Gun'ko, Y. K. (2008). Multifunctional magnetic-fluorescent nanocomposites for biomedical applications. *Nanoscale Res. Lett.*, Vol. 3, No 3, 87-104, ISSN: 1931-7573.

Cushing, B. L.; Kolesnichenko, V. L. & O'Connor, C. J. (2004). Recent advances in the liquid-phase syntheses of inorganic nanoparticles. *Chem. Rev.*, Vol. 104, No 9, 3893-3946, ISSN: 0009-2665.

de Dios, A. S. & Díaz-Garcia, M. E. (2010). Multifunctional nanoparticles: Analytical prospects. *Anal. Chim. Acta*, Vol. 666, No 1-2, 1-22, ISSN: 0003-2670.

Denizot, B.; Tanguy, G.; Hindre, F.; Rump, E.; Le Jeune, J. J. & Jallet, P. (1999). Phosphorylcholine coating of iron oxide nanoparticles. *J. Colloid Interface Sci.*, Vol. 209, No 1, 66-71, ISSN: 0021-9797.

Dobson, J. (2006a). Magnetic nanoparticles for drug delivery. *Drug Dev. Res.*, Vol. 67, No 1, 55-60, ISSN: 0272-4391.

Dobson, J. (2006b). Magnetic micro- and nano-particle-based targeting for drug and gene delivery. *Nanomedicine*, Vol. 1, No 1, 31-37, ISSN: 1743-5889.

Gupta, A. K. & Curtis, A. S. G. (2004). Surface modified superparamagnetic nanoparticles for drug delivery: Interaction studies with human fibroblasts in culture. *J. Mater. Sci.-Mater. Med.*, Vol. 15, No 4, 493-496, ISSN: 0957-4530.

Gupta, A. K. & Gupta, M. (2005). Synthesis and surface engineering of iron oxide nanoparticles for biomedical applications. *Biomaterials*, Vol. 26, No 18, 3995-4021, ISSN: 0142-9612.

Gupta, A. K.; Naregalkar, R. R.; Vaidya, V. D. & Gupta, M. (2007). Recent advances on surface engineering of magnetic iron oxide nanoparticles and their biomedical applications. *Nanomedicine*, Vol. 2, No 1, 23-39, ISSN: 1743-5889.

Gupta, A. K. & Wells, S. (2004). Surface-modified superparamagnetic nanoparticles for drug delivery: Preparation, characterization, and cytotoxicity studies. *IEEE Trans. Nanobiosci.*, Vol. 3, No 1, 66-73, ISSN: 1536-1241.

Hu, F. Q.; Wei, L.; Zhou, Z.; Ran, Y. L.; Li, Z. & Gao, M. Y. (2006). Preparation of biocompatible magnetite nanocrystals for in vivo magnetic resonance detection of cancer. *Adv. Mater.*, Vol. 18, No 19, 2553-+, ISSN: 0935-9648.

Hunter, R. J. (2001). *Foundations of colloid science*, Oxford University Press, ISBN: 0198505027, Oxford, UK.

Hyeon, T. (2003a). *Synthesis of monodisperse and highly-crystalline nanoparticles of metal, alloys, metal oxides, and multi-metallic oxides without a size-selection process*. Korea, Patent N° WO 03/031323.

Hyeon, T. (2003b). Chemical synthesis of magnetic nanoparticles. *Chem. Commun*., Vol. 8, 927-934, ISSN: 1359-7345.

Hyeon, T.; Lee, S. S.; Park, J.; Chung, Y. & Na, H. B. (2001). Synthesis of highly crystalline and monodisperse maghemite nanocrystallites without a size-selection process. *J. Am. Chem. Soc.*, Vol. 123, 12798-12801, ISSN: 0002-7863.

Kohler, N.; Fryxell, G. E. & Zhang, M. Q. (2004). A bifunctional poly(ethylene glycol) silane immobilized on metallic oxide-based nanoparticles for conjugation with cell targeting agents. *J. Am. Chem. Soc.*, Vol. 126, No 23, 7206-7211, ISSN: 0002-7863.

LaMer, V. K. & Dinegar, R. H. (1950). Theory, production and mechanism of formation of monodispersed hydrosols. *J. Am. Chem. Soc.*, Vol. 72, No 11, 4847-4855, ISSN: 0002-7863.

Li, Z.; Sun, Q. & Gao, M. Y. (2005). Preparation of water-soluble magnetite nanocrystals from hydrated ferric salts in 2-pyrrolidone: Mechanism leading to Fe_3O_4. *Angew. Chem. Int. Edit.*, Vol. 44, No 1, 123-126, ISSN: 1433-7851.

Lu, A. H.; Salabas, E. L. & Schuth, F. (2007). Magnetic nanoparticles: Synthesis, protection, functionalization, and application. *Angew. Chem.-Int. Edit.*, Vol. 46, No 8, 1222-1244, ISSN: 1433-7851.

Lu, Y.; Yin, Y. D.; Mayers, B. T. & Xia, Y. N. (2002). Modifying the surface properties of superparamagnetic iron oxide nanoparticles through a sol-gel approach. *Nano Lett.*, Vol. 2, No 3, 183-186, ISSN: 1530-6984.

Luo, F.; Su, H. L.; Song, W.; Wang, Z. M.; Yan, Z. G. & Yan, C. H. (2004). Magnetic and magnetotransport properties of Fe_2P nanocrystallites via a solvothermal route. *J. Mater. Chem.*, Vol. 14, No 1, 111-115, ISSN: 0959-9428.

Majewski, P. & Thierry, B. (2007). Functionalized magnetite nanoparticles - Synthesis, properties, and bio-applications. *Crit. Rev. Solid State Mat. Sci.*, Vol. 32, No 3-4, 203-215, ISSN: 1040-8436.

Malheiro, A. R.; Varanda, L. C.; Perez, J. & Villullas, H. M. (2007). The aerosol OT plus n-butanol plus n-heptane plus water system: Phase behavior, structure characterization, and application to $Pt_{70}Fe_{30}$ nanoparticle synthesis. *Langmuir*, Vol. 23, No 22, 11015-11020, ISSN: 0743-7463.

Massia, S. P.; Stark, J. & Letbetter, D. S. (2000). Surface-immobilized dextran limits cell adhesion and spreading. *Biomaterials*, Vol. 21, No 22, 2253-2261, ISSN: 0142-9612.

Mikhaylova, M.; Kim, D. K.; Bobrysheva, N.; Osmolowsky, M.; Semenov, V.; Tsakalakos, T. & Muhammed, M. (2004). Superparamagnetism of magnetite nanoparticles: Dependence on surface modification. *Langmuir*, Vol. 20, No 6, 2472-2477, ISSN: 0743-7463.

Mokari, T.; Rothenberg, E.; Popov, I.; Costi, R. & Banin, U. (2004). Selective growth of metal tips onto semiconductor quantum rods and tetrapods. *Science*, Vol. 304, No 5678, 1787-1790, ISSN: 0036-8075.

Mornet, S.; Vasseur, S.; Grasset, F.; Veverka, P.; Goglio, G.; Demourgues, A.; Portier, J.; Pollert, E. & Duguet, E. (2006). Magnetic nanoparticle design for medical applications. *Prog. Solid State Chem.*, Vol. 34, No 2-4, 237-247, ISSN: 0079-6786.

Moroz, P.; Jones, S. K. & Gray, B. N. (2002). Tumor response to arterial embolization hyperthermia and direct injection hyperthermia in a rabbit liver tumor model. *J. Surg. Oncol.*, Vol. 80, No 3, 149-156, ISSN: 0022-4790.

Na, H. B.; Lee, J. H.; An, K. J.; Park, Y. I.; Park, M.; Lee, I. S.; Nam, D. H.; Kim, S. T.; Kim, S. H.; Kim, S. W.; Lim, K. H.; Kim, K. S.; Kim, S. O. & Hyeon, T. (2007). Development of a T-1 contrast agent for magnetic resonance imaging using MnO nanoparticles. *Angew. Chem. Int. Edit.*, Vol. 46, No 28, 5397-5401, ISSN: 1433-7851.

Nandivada, H.; Jiang, X. W. & Lahann, J. (2007). Click chemistry: Versatility and control in the hands of materials scientists. *Adv. Mater.*, Vol. 19, No 17, 2197-2208, ISSN: 0935-9648.

O'Brien, S.; Brus, L. & Murray, C. B. (2001). Synthesis of monodisperse nanoparticles of barium titanate: Toward a generalized strategy of oxide nanoparticle synthesis. *J. Am. Chem. Soc.*, Vol. 123, No 48, 12085-12086, ISSN: 0002-7863.

O'Connor, C. J.; Seip, C. T.; Carpenter, E. E.; Li, S. C. & John, V. T. (1999). Synthesis and reactivity of nanophase ferrites in reverse micellar solutions. *Nanostruct. Mater.*, Vol. 12, No 1-4, 65-70, ISSN: 0965-9773.

Olsvik, O.; Popovic, T.; Skjerve, E.; Cudjoe, K. S.; Hornes, E.; Ugelstad, J. & Uhlen, M. (1994). Magnetic Separation Techniques in Diagnostic Microbiology. *Clin. Microbiol. Rev.*, Vol. 7, No 1, 43-54, ISSN: 0893-8512.

Pankhurst, Q. A.; Connolly, J.; Jones, S. K. & Dobson, J. (2003). Applications of magnetic nanoparticles in biomedicine. *J. Phys. D-Appl. Phys.*, Vol. 36, No 13, R167-R181, ISSN: 0022-3727.

Pankhurst, Q. A.; Thanh, N. K. T.; Jones, S. K. & Dobson, J. (2009). Progress in applications of magnetic nanoparticles in biomedicine. *J. Phys. D-Appl. Phys.*, Vol. 42, No 22, ISSN: 0022-3727.

Park, J.; An, K. J.; Hwang, Y. S.; Park, J. G.; Noh, H. J.; Kim, J. Y.; Park, J. H.; Hwang, N. M. & Hyeon, T. (2004). Ultra-large-scale syntheses of monodisperse nanocrystals. *Nat. Mater.*, Vol. 3, No 12, 891-895, ISSN: 1476-1122.

Portet, D.; Denizot, B.; Rump, E.; Lejeune, J. J. & Jallet, P. (2001). Nonpolymeric coatings of iron oxide colloids for biological use as magnetic resonance imaging contrast agents. *J. Colloid Interface Sci.*, Vol. 238, No 1, 37-42, ISSN: 0021-9797.

Pratsinis, S. E. & Vemury, S. (1996). Particle formation in gases: A review. *Powder Technol.*, Vol. 88, No 3, 267-273, ISSN: 0032-5910.

Puntes, V. F.; Krishnan, K. M. & Alivisatos, A. P. (2001). Colloidal nanocrytal shape and size control: the case of cobalt. *Science*, Vol. 291, 2115-2117,

Qian, Z. M.; Li, H. Y.; Sun, H. Z. & Ho, K. (2002). Targeted drug delivery via the transferrin receptor-mediated endocytosis pathway. *Pharmacol. Rev.*, Vol. 54, No 4, 561-587, ISSN: 0031-6997.

Rishton, S. A.; Lu, Y.; Altman, R. A.; Marley, A. C.; Bian, X. P.; Jahnes, C.; Viswanathan, R.; Xiao, G.; Gallagher, W. J. & Parkin, S. S. P. (1997). Magnetic tunnel junctions fabricated at tenth-micron dimensions by electron beam lithography. *Microelectron. Eng.*, Vol. 35, No 1-4, 249-252, ISSN: 0167-9317.

Roca, A. G.; Costo, R.; Rebolledo, A. F.; Veintemillas-Verdaguer, S.; Tartaj, P.; Gonzalez-Carreno, T.; Morales, M. P. & Serna, C. J. (2009). Progress in the preparation of magnetic nanoparticles for applications in biomedicine. *J. Phys. D-Appl. Phys.*, Vol. 42, No 22, ISSN: 0022-3727.

Ross, J. F.; Chaudhuri, P. K. & Ratnam, M. (1994). Differential Regulation of Folate Receptor Isoforms in Normal and Malignant-Tissues In-Vivo and in Established Cell-Lines -

Physiological and Clinical Implications. *Cancer*, Vol. 73, No 9, 2432-2443, ISSN: 0008-543X.

Sahoo, Y.; Pizem, H.; Fried, T.; Golodnitsky, D.; Burstein, L.; Sukenik, C. N. & Markovich, G. (2001). Alkyl phosphonate/phosphate coating on magnetite nanoparticles: A comparison with fatty acids. *Langmuir*, Vol. 17, No 25, 7907-7911, ISSN: 0743-7463.

Salgueirino-Maceira, V. & Correa-Duarte, M. A. (2007). Increasing the complexity of magnetic core/shell structured nanocomposites for biological applications. *Adv. Mater.*, Vol. 19, No 23, 4131-4144, ISSN: 0935-9648.

Santos, F. J.; Varanda, L. C.; Ferracin, L. C. & Jafelicci, M. (2008). Synthesis and electrochemical behavior of single-crystal magnetite nanoparticles. *J. Phys. Chem. C*, Vol. 112, No 14, 5301-5306, ISSN: 1932-7447.

Sanvicens, N. & Marco, M. P. (2008). Multifunctional nanoparticles - properties and prospects for their use in human medicine. *Trends Biotechnol.*, Vol. 26, No 8, 425-433, ISSN: 0167-7799.

Selvan, S. T.; Tan, T. T. Y.; Yi, D. K. & Jana, N. R. (2010). Functional and Multifunctional Nanoparticles for Bioimaging and Biosensing. *Langmuir*, Vol. 26, No 14, 11631-11641, ISSN: 0743-7463.

Shi, W. L.; Sahoo, Y.; Zeng, H.; Ding, Y.; Swihart, M. T. & Prasad, P. N. (2006). Anisotropic growth of PbSe nanocrystals on Au-Fe3O4 hybrid nanoparticles. *Adv. Mater.*, Vol. 18, No 14, 1889-+, ISSN: 0935-9648.

Sorensen, C. M. (2001). Magnetism, In: *Nanoscale Materials in Chemistry*, Klabunde, K. J. (Ed.), 169-221, Wiley-Interscience Publications, ISBN: 9780471383956, New York.

Stoner, E. C. & Wohlfarth, E. P. (1948). A Mechanism of Magnetic Hysteresis in Heterogeneous Alloys. *Phil. Trans. R. Soc. A*, Vol. 240, No 826, 599-642, ISSN: 0080-4614.

Sun, C.; Lee, J. S. H. & Zhang, M. Q. (2008). Magnetic nanoparticles in MR imaging and drug delivery. *Adv. Drug Deliv. Rev.*, Vol. 60, No 11, 1252-1265, ISSN: 0169-409X.

Sun, S.; Murray, C. B.; Weller, D.; Folks, L. & Moser, A. (2000). Monodispersed FePt nanoparticles and ferromagnetic FePt nanocrystal superlattices. *Science*, Vol. 287, 1989-1992, ISSN: 0036-8075.

Sun, S. & Zeng, H. (2002). Size-controlled synthesis of magnetite nanoparticles. *J. Am. Chem. Soc.*, Vol. 124, 8204-8205, ISSN: 0002-7863.

Sutton, D.; Nasongkla, N.; Blanco, E. & Gao, J. M. (2007). Functionalized micellar systems for cancer targeted drug delivery. *Pharm. Res.*, Vol. 24, No 6, 1029-1046, ISSN: 0724-8741.

Tada, D. B.; Vono, L. L. R.; Duarte, E. L.; Itri, R.; Kiyohara, P. K.; Baptista, M. S. & Rossi, L. M. (2007). Methylene blue-containing silica-coated magnetic particles: A potential magnetic carrier for photodynamic therapy. *Langmuir*, Vol. 23, No 15, 8194-8199, ISSN: 0743-7463.

Torchilin, V. P. (2005). Recent advances with liposomes as pharmaceutical carriers. *Nat. Rev. Drug Discov.*, Vol. 4, No 2, 145-160, ISSN: 1474-1776.

Varanda, L. C.; Goya, G. F.; Morales, M. P.; Marques, R. F. C.; Godoi, R. H. M.; Jafelicci, M. & Serna, C. J. (2002a). Magnetic properties of acicular ultrafine iron particles. *IEEE Trans. Magn.*, Vol. 38, No 5, 1907-1909, ISSN: 0018-9464.

Varanda, L. C.; Imaizumi, M.; Santos, F. J. & Jafelicci, M. (2008). Iron Oxide Versus $Fe_{55}Pt_{45}/Fe_3O_4$: Improved Magnetic Properties of Core/Shell Nanoparticles for

Biomedical Applications. *IEEE Trans. Magn.*, Vol. 44, No 11, 4448-4451, ISSN: 0018-9464.

Varanda, L. C. & Jafelicci, M. (2006). Self-assembled FePt nanocrystals with large coercivity: Reduction of the fcc-to-$L1_{(0)}$ ordering temperature. *J. Am. Chem. Soc.*, Vol. 128, No 34, 11062-11066, ISSN: 0002-7863.

Varanda, L. C.; Jafelicci, M. & Goya, G. F. (2001). Magnetic properties of spindle-type iron fine particles obtained from hematite. *J. Magn. Magn. Mater.*, Vol. 226, 1933-1935, ISSN: 0304-8853.

Varanda, L. C.; Jafelicci, M. & Imaizumi, M. (2007). Temperature dependence and magnetocrystalline anisotropy studies of self-assembled $L1_{(0)}$-$Fe_{55}Pt_{45}$ ferromagnetic nanocrystals. *J. Appl. Phys.*, Vol. 101, No 12, ISSN: 0021-8979.

Varanda, L. C.; Jafelicci, M.; Tartaj, P.; O' Grady, K.; Gonzalez-Carreno, T.; Morales, M. P.; Munoz, T. & Serna, C. J. (2002b). Structural and magnetic transformation of monodispersed iron oxide particles in a reducing atmosphere. *J. Appl. Phys.*, Vol. 92, No 4, 2079-2085, ISSN: 0021-8979.

Vonarbourg, A.; Passirani, C.; Saulnier, P. & Benoit, J. P. (2006). Parameters influencing the stealthiness of colloidal drug delivery systems. *Biomaterials*, Vol. 27, No 24, 4356-4373, ISSN: 0142-9612.

Weinmann, H. J.; Ebert, W.; Misselwitz, B. & Schmitt-Willich, H. (2003). Tissue-specific MR contrast agents. *Eur. J. Radiol.*, Vol. 46, No 1, 33-44, ISSN: 0720-048X.

Weissleder, R.; Kelly, K.; Sun, E. Y.; Shtatland, T. & Josephson, L. (2005). Cell-specific targeting of nanoparticles by multivalent attachment of small molecules. *Nat. Biotechnol.*, Vol. 23, No 11, 1418-1423, ISSN: 1087-0156.

Willis, A. L.; Turro, N. J. & O'Brien, S. (2005). Spectroscopic characterization of the surface of iron oxide nanocrystals. *Chem. Mat.*, Vol. 17, No 24, 5970-5975, ISSN: 0897-4756.

Wust, P.; Gneveckow, U.; Johannsen, M.; Bohmer, D.; Henkel, T.; Kahmann, F.; Sehouli, J.; Felix, R.; Ricke, J. & Jordan, A. (2006). Magnetic nanoparticles for interstitial thermotherapy - feasibility, tolerance and achieved temperatures. *Int. J. Hyperthermia*, Vol. 22, No 8, 673-685, ISSN: 0265-6736.

Xue, B. & Sun, Y. (2001). Protein adsorption equilibria and kinetics to a poly(vinyl alcohol)-based magnetic affinity support. *J. Chromatogr. A*, Vol. 921, No 2, 109-119, ISSN: 0021-9673.

Yan, X. D.; Scherphof, G. L. & Kamps, J. A. A. M. (2005). Liposome opsonization. *J. Liposome Res.*, Vol. 15, No 1-2, 109-139, ISSN: 0898-2104.

Yee, C.; Kataby, G.; Ulman, A.; Prozorov, T.; White, H.; King, A.; Rafailovich, M.; Sokolov, J. & Gedanken, A. (1999). Self-assembled monolayers of alkanesulfonic and phosphonic acids on amorphous iron oxide nanoparticles. *Langmuir*, Vol. 15, No 21, 7111-7115, ISSN: 0743-7463.

Yu, H.; Chen, M.; Rice, P. M.; Wang, S. X.; White, R. L. & Sun, S. H. (2005). Dumbbell-like bifunctional Au-Fe_3O_4 nanoparticles. *Nano Lett.*, Vol. 5, No 2, 379-382, ISSN: 1530-6984.

Zhang, Y.; Kohler, N. & Zhang, M. Q. (2002). Surface modification of superparamagnetic magnetite nanoparticles and their intracellular uptake. *Biomaterials*, Vol. 23, No 7, 1553-1561, ISSN: 0142-9612.

18

Ferromagnets-Based Multifunctional Nanoplatform for Targeted Cancer Therapy

Valentyn Novosad[1] and Elena A. Rozhkova[2]
[1]*Materials Science Division,*
[2]*Center for Nanoscale Materials,*
Argonne National Laboratory,
USA

1. Introduction

Nanotechnology emerges from the physical, chemical, biological, and engineering sciences, where novel techniques are being developed to probe and manipulate single atoms and molecules. While significant progress has been made in materials science, it is apparent that nanoscience and nanotechnology-based approaches are poised to revolutionize many research and technology areas. In particular, novel magnetic nanoplatforms with dimensions of few nanometers to few microns have great potential for application in biomedical sciences. Main approaches of particular clinical relevance include magnetic separation technologies, magnetic resonance imaging (MRI) contrast enhancement, targeted drug delivery, and magnetically induced hyperthermia.

In this chapter we describe the fabrication process, magnetic behavior, biofunctionalization, as well as targeted destruction of cancer cells *in vitro* using multifunctional ferromagnetic microdisks. The microdisks posses unique properties such as high magnetization of saturation, zero remanence due to spin vortex formation, intrinsic spin resonance at low frequencies, and capability of delivering more than one type of bio-substance at once. Furthermore, because of the anisotropic shape, lithographically-defined magnetic particles oscillate under application of alternative magnetic field of small amplitude. This phenomenon is further advanced as a new anticancer therapy approach by the application of an unprecedentedly slow and weak magnetic fields. We show that successful interfacing of *lithographically defined ferromagnetic* materials with a spin vortex ground state with cancer cells can be achieved *in vitro*. When an alternative magnetic field is applied the magnetic vortices shift, leading to oscillatory motion of the disks causing the magneto-mechanic stimulus is to be transmitted directly to the cell membrane and then into sub-cellular compartments. Such magnetic spin vortex-induced magneto-mechanical stimulus results into (a) cancer cell membrane pertrubation, as well as into (b) cellular signal transduction and amplification, causing initiation of apoptosis, a type of a *programmed cell death*. Manifestation of apoptosis is of clinical significance because the malignant cells are known to be almost "immortal" (due to suppressed apoptosis), and, consequently, highly resistant to conventional therapies.

2. Magnetic nanoparticles for biomedical applications

2.1 Traditional approach

Small magnetic objects (nanoparticles) have been actively explored for application in biomedicine (Pankhurst et al., 2009). This technology is based on the ability of biological substances (cells or bio-molecules) to form molecular superstructures when they are mixed with magnetic particles, and especially valuable in the field of nanomedicine (Ferrari, 2005). In principle, selective adhesion is possible if the surface of the particle is covered by a special layer, such as gold (core-shell structure) functionalized with ligands capable of biological recognition. Here, the magnetic nature of the particle is used as a transduction mechanism for the target-directed delivery, detection, manipulation, and functional control of attached bio-molecules and cells. The future of this new area of research greatly depends on progress with (1) incorporating multiple functionalities properties within a single nanoplatform, including targeting, enhanced anticancer therapy, drug delivery, imaging and detection capabilities, and (2) preparing the particles with superior magnetic properties (Nel, et al., 2009).

Major efforts up to date have been directed to synthesize and explore magnetic particles prepared by solid, gas, and solution synthesis methods. Interested readers may refer to a number of excellent reviews for the details (Krishnan, 2010; Gao, et al., 2009; Goya et al., 2008; Gupta, & Gupta, 2005). The solid route involves the mechanical milling of powder materials to produce nanoparticles. Contamination introduced during the process as well as difficulties with controlling the particles size distribution are major drawbacks of this otherwise straight forward and low cost approach. In gas and chemical methods, the nanoparticles are synthesized through phase- conversion or phase build-up. In the first case scenario thermal decomposition or chemical reduction is employed. The phase-build-up process occurs in the gas phase (chemical or physical vapor deposition) or in the liquid phase (chemical precipitation). These techniques produce uniform nanoparticles of different shapes by using appropriate precursors and capping ligands during the reaction. Surfactant and various capping layers also help to prevent aggregation of the particles. The magnetic nanoparticles (~10s nm) typically are superparamagnetic. In final application they are often dispersed in, layered onto, or coated with a matrix to form beads ~1 μm in diameter. Known challenges related to the traditional approach include difficulty in controlling the growth process, broad size and shape distributions, and variable structural and magnetic properties. Because of their superparamagnetic nature and low value of the magnetization of saturation, high magnetic fields are required to detect or manipulate these particles. Conversely, if highly magnetic particles are synthesized (that is, larger particles with single domain spin arrangement), agglomeration may occur owing to magnetic fringe fields. On the other hand when a magnet is confined to two dimensions, the spin arrangement often takes on an interesting pattern known as a *spin vortex state* (Cowburn, et al., 1999; Shinjo, et al., 2000). This system can be scaled down to sub-100nm lateral dimensions with preserving closed flux spin structure and magnetic properties. Such novel magnetic particles can be fabricated using thin film growth techniques, combined with mask-transfer lithography.

2.2 Lithographically defined particles

Microfabrication methods were recently used to synthesize magnetic particles suitable for biomedical applications. By combining physical vapor deposition techniques (such as magnetron sputtering or electron beam evaporation) with optical, nano-imprint or laser interferometer lithography it is possible to produce monodisperse particles of virtually any

shape, multicomponent and multilayered, with tunable magnetic properties and size down to ~100 nm. Such magnetic materials are used in giant magnetoresistance spin valve or magnetic tunnel junction sensors capable to detect minute concentrations (down the picomolar) of DNA and proteins *in vitro* (Wang, & Li, 2008; Fu et al., 2009), as advanced MRI enhancement agents (Zabow, et al., 2008; Zabow, et al., 2009) and in magnetofection experiments (Mair, et al., 2009). In brief, the main advantages of the lithographically defined particles can be outlined as follows:

- Multifunctional & scalable, biocompatible nanoplatform;
- Zero remanence (disks will not agglomerate during delivery process ;
- High saturation magnetization can be achieved using 3d metal alloys;
- Strong magneto-mechanical coupling – new way to destroy targeted cells via initiation of the intracellular biochemical signaling leading to apoptosis;
- Vortex resonant properties: possibilities for high sensitivity ac detection;
- Excellent MRI enhancement capacity;
- Targeted drug release is possible via magneto-mechanical actuation;
- The disks show inductive heating when subjected to 100s kHz ac fields.

Here below, we describe the fabrication, magnetic properties, surface modification, and application of a single ferromagnetic layer, disk-shaped particles for targeted destruction of cancer cells *in vitro.*

3. Size-dependent magnetic properties

3.1 Energy terms

The magnetization distribution (spin arrangement) in small ferromagnetic particles depends on their size and can be non-uniform. It is well known that large particles, adopt multi-domain states, where details of the magnetization distribution depend on the interplay between the exchange, magnetostatic and crystalline anisotropy energies (Fig. 1).

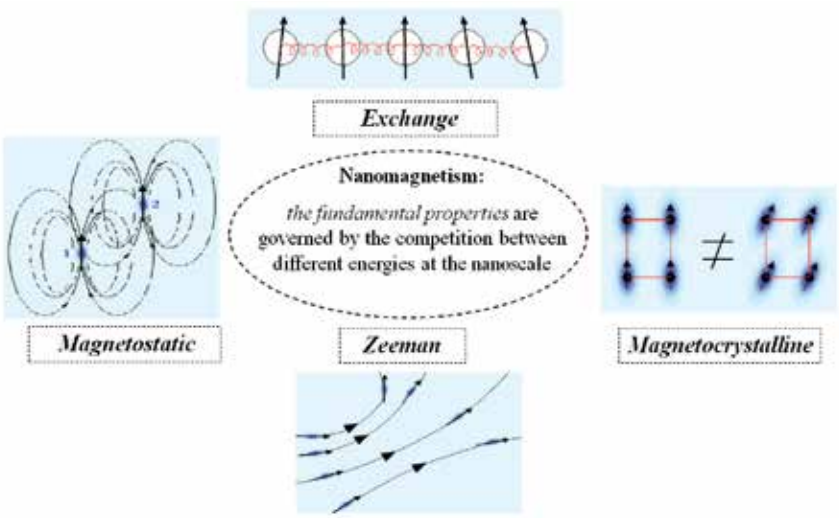

Fig. 1. Schematic representation of different energy terms governing the magnetic properties of small ferromagnetic elements.

The short-range exchange interaction is responsible for parallel alignment of the neighboring spins. Although this interaction is a purely quantum mechanical phenomenon, it can be described phenomenologicaly, by introducing the material specific exchange constant. On the other hand, the magnetostatic interaction describes how the magnetic moments interact over long range distances within the ferromagnet.

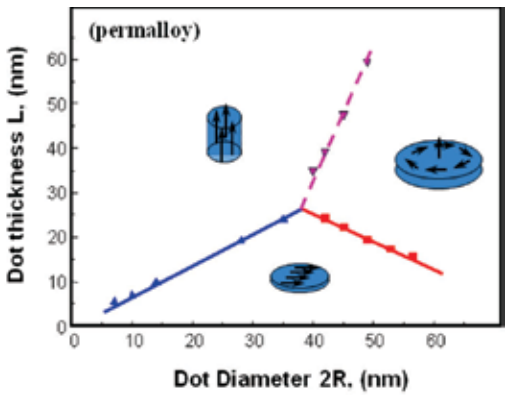

Fig. 2. Calculated magnetic phase diagram for disk-shaped Permalloy (Fe20Ni80) elements. The magnetic vortex state is a ground state down to sub-100nm lateral dimensions of the disk.

The magnetostatic interaction energy is increased when the spin arrangement leads to formation of magnetic charges on the surface or within the sample volume. Shrinking the particle size leads to an increase of role of exchange energy; the magnetization distribution gradually becomes more uniform up to almost a saturated (in- or out- of plane single-domain states (Fig. 2). For immediate particle sizes and non-ellipsoidal particle shapes the spin structure becomes non-uniform with significantly reduced or even zero macroscopic moment in remanence. A model example is the "vortex" magnetization distribution in soft magnetic materials. Thus, it is the competition between the exchange and magnetostatic energies that leads to formation of domain walls or magnetic vortices. The size at which a particle becomes single domain depends on the balance between the above energies, on the shape of the particle and on its anisotropy.

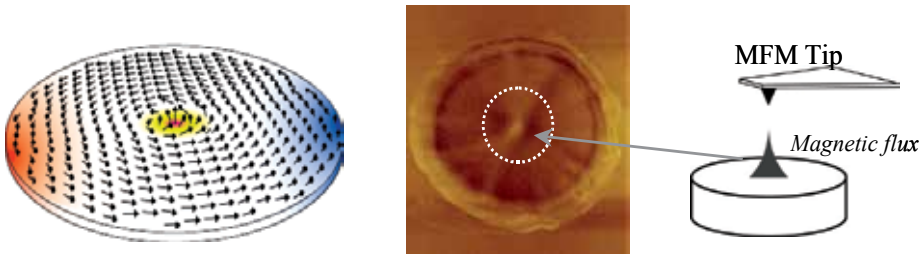

Fig. 3. Magnetization distribution in the magnetic vortex state obtained by micromagnetic modeling (left), and its magnetic force microscope image (right).

The characteristic magnetic length (so-called the magnetic exchange length) that results from the above energy competition is defined as $\xi_{ex} = (2A\mu_o/M_s)^{1/2}$, where A is the exchange constant and M_s is the saturation magnetization. A magnetically soft particle with lateral dimensions smaller than the exchange length is expected to remain in a single domain state at remanence. Here we are considering circular particles of permalloy (Py, $Fe_{19}Ni_{81}$) with

thickness and diameter larger than ξ_{ex}. It is well-established that a magnetic vortex structure is the ground state within a wide range of dot sizes from a few tens of *nm* up to few tens of microns (Scholz, et al., 2003; Chung, et al., 2010).

A magnetic vortex consists of a mainly in-plane flux-closure magnetization distribution with a central core that is magnetized perpendicular to the dot plane (Fig. 3). It was experimentally demonstrated by spin-polarized scanning tunneling microscopy that the core radius is about 10 nm, i.e. approximately the material exchange length (Wachowiak, et al., 2002). A vortex can have a particular polarization $p = \pm 1$ that describes whether the core is oriented up or down and a particular chirality, i.e., the direction of the in-plane magnetization rotation.

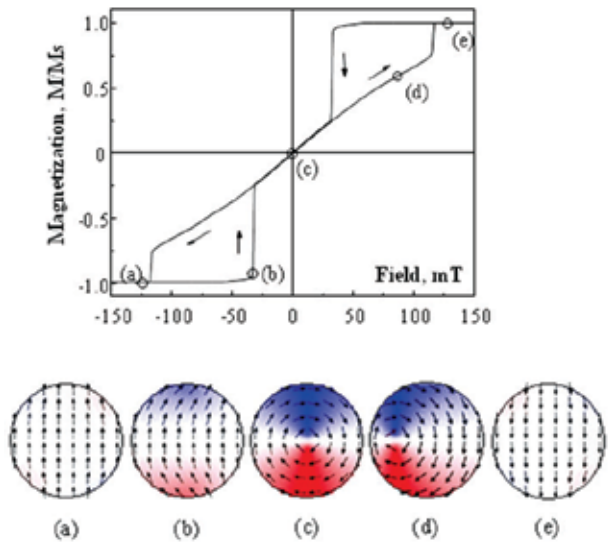

Fig. 4. The magnetization reversal in magnetically soft disk-shaped particle is accompanied by nucleation and annihilation of the magnetic vortex state.

The magnetization reversal process in individual particles can be effectively modeled using Landau-Lifshitz-Gilbert (LLG) micromagnetic calculations (Donahue, & Porter, 1999). Figure 4 shows a typical hysteresis loop and the field evolution of the spin structure, calculated for 2R=200nm diameter and L=30 nm thin circular dot. For the calculations, permalloy values for M_s (750 emu/cm^3) and A (1.05x10^{-6} erg/cm) were used and the magnetocrystalline anisotropy was neglected. The hysteresis loops were simulated by relaxing the system under sequentially applied magnetic fields to approximate a progression of equilibrium states, and simulations of the remanent state were carried out by allowing the system to relax from saturation in the absence of an applied field. The sample was modeled using three-dimensional 1 x 1 x 1 nm^3 macrospin cells For all simulations a large damping parameter (0.5) was used. When the magnetic field is decreased from saturation (Fig. 4a - 4b), a magnetic vortex nucleates at the nucleation field H_n, accompanied by an abrupt decrease in the average dot magnetization. This results in a gain in the magnetostatic energy. The center of the vortex stays at the center of the dot at remanence (Fig. 3c). The reversible part of the loop corresponds to the vortex core movement perpendicular to the applied field (Fig. 3d). When the magnetic field reaches the annihilation field H_{an}, the vortex vanishes completely. This process stabilizes the saturated, single-domain state in the dot (Fig. 3e). The values of H_n, H_{an}, and the slope of the linear part of the hysteresis loop are strongly size dependent (Guslienko, et al., 2001).

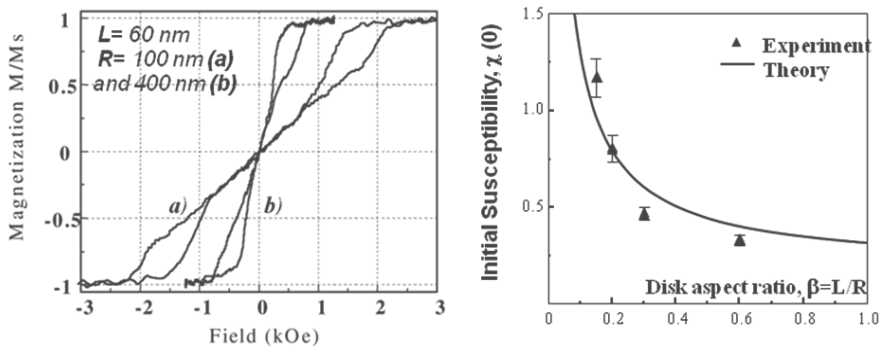

Fig. 5. Size dependent experimental hysteresis loops (left) and susceptibility (right) for sub-micron permalloy disks.

For example, Fig. 5 (left plot) compares the experimental hysteresis loops measured for two kinds of dot arrays with the same thickness and different diameters of 200 and 800 nm. Decrease in the dot aspect ratio leads to reduced vortex stability, and hence to decrease in the vortex nucleation and annihilation fields. Similarly, the magnetic susceptibility (Fig. 5, right plot) scales as a function of the dot aspect ratio for given materials. This suggests that the magnetic properties of the soft (with no crystalline anisotropic) magnetic dots are entirely predetermined by the geometry of the sample, e.g. precisely controlled lateral dimensions and thickness during the fabrication process will result in magnetically undistinguishable particles.

3.2 Spin dynamics

Besides unique reversal process, the vortex magnetization distribution leads to a considerable modification of the spin excitation spectrum in comparison to those in the uniform (single domain) state. The dynamic response of the vortex core can be considered as a harmonic oscillator trapped in parabolic potential well due to magnetostatic interaction (Fig. 6, left plot). Thus, when the sample is subjected to a time-varying (*ac* or pulse-like) magnetic field, the vortex core experiences a force (gyroforce) perpendicular to its displacement from equilibrium position that results in a relatively slow (sub-GHz) frequency, spiral-like motion of the core. This excitation is known as a translational or gyrotropic mode of the magnetic vortex. The direction of rotation depends only on the core polarization, as demonstrated in time-resolved magneto-optical Kerr (Park, et al., 2003) and X-ray magnetic circular dichroism imaging experiments (Ade, & Stoll, 2009). The other higher frequency (sub-ten GHz) excitations within some approximation can be understood as the quantized spin waves in restricted geometries (Demokritov, et al., 2001).

Surprisingly, the summarized results of the calculations for different dot thickness L and diameter $2R$ scales universally when plotted as a function of the disk aspect-ratio L/R. (Fig. 6, right plot). The eigenfrequency of the vortex translational mode in a disk-shape dot can calculated analithycally (Guslienko 2001) as:

$$\omega_0 = 2\gamma M_s \left[4\pi \int_0^\infty dt t^{-1} f(\beta t) I^2(t) - 0.5 \left(\xi_{ex} / R \right)^2 \right], \quad (1)$$

where γ is the gyromagnetyic constant , $\beta=L/R$, $f(x)=1-(1-\exp(-x))/x$ and ξ_{ex} is the magnetic exchange length. Therefore, the frequency can be predicted and adjusted if needed just by

modifying *R* or *L*. Please note, that the value of all frequencies is in ~100s MHz, accessible by using rather conventional instrumentation. The resonant properties of ferromagnetic microdisks may offer an additional and very important functionality for bio-medical applications. Namely, the disk-shaped particles subjected to *ac* magnetic field oscillating at the frequency of the vortex translational mode will demonstrate strong enhancement of the absorption losses. Therefore, it could be possible to significantly improve the magnetic particles detection using experimental set-up schematically shown in Fig. 7. The magnitude of real and imaginary part of the dynamic permeability could be used for *counting* the magnetic particles flowing through the measurements cell. A significant increase in absorption losses (and therefore, enhanced sensitivity) is expected at the frequencies when the eigenmodes of collective spin motion are excited. In principle, one should be able to achieve a single particle detection via the dynamic susceptibility measurements.

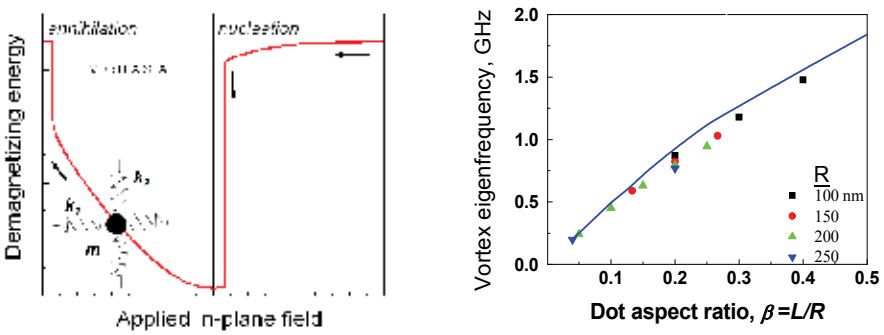

Fig. 6. The magnetic vortex core shows a harmonic oscillator response and can be viewed as a particle trapped in a potential well (left plot). The eigenfrequency of the system scales universally as a function of the disk thickness to diameter ratio (right plot) and can be fine-tuned in sub–GHz frequency range.

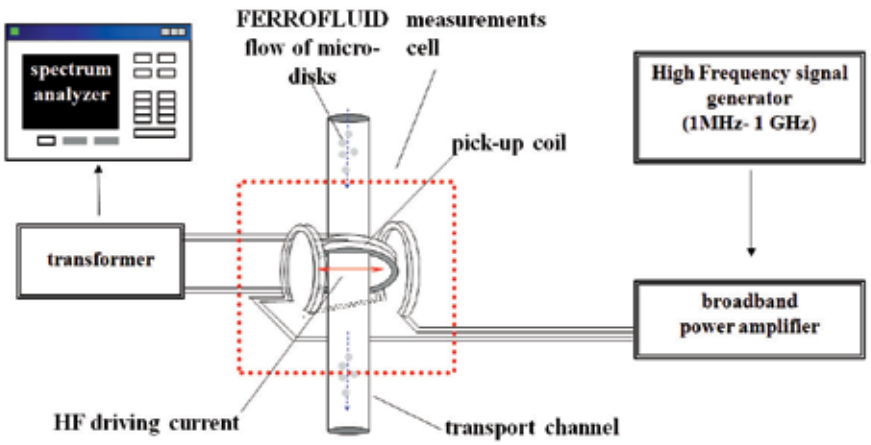

Fig. 7. Block-diagram of the experimental set-up for detection of magnetic particles (high-frequency permeability measurements). The spectrum analyzer attached to a pickup coil; a separate drive coil is connected a 1 watt, up to 1 GHz, broadband amplifier driven by a frequency generator.

3.3 Magnetostatic interaction

Since we are considering use of fluid suspension of the particles, the inter-particle interaction effects should be carefully examined.

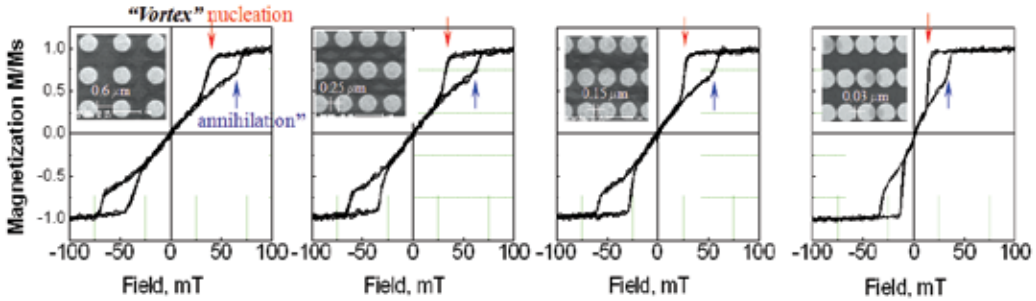

Fig. 8. The interdot magnetostatic interaction decrease the spin vortex state stability, yet, even for very small separation distances the particles show zero net magnetic moment in remanence due to vortex state formation. The later eliminates the long-range magnetostatic forces otherwise responsible for magnetic particle agglomeration.

Figure 8 compares four hysteresis loops for 40nm thin dots with a diameter of 600 nm, but variable interdot distances ranging from 600 to 30nm. The field was applied along the horizontal direction. Macroscopic measurements technique yields information on the magnetization reversal process averaged over many 1000's of dots. Nevertheless, the loops have a clear signature of the magnetization reversal with ''nucleation'' and ''annihilation'' of magnetic vortices. We find that hysteresis loop depend not only on the dot diameter and the thickness, but also on the interdot distance. As seen in Fig. 8, nucleation and annihilation fields decrease, whereas an initial susceptibility of the vortex increases with decreasing interdot distance. Although the dipole-dipole interaction decreases the vortex state stability for small inter-particle separation distances, it is possible to design the particles so that they posses vortex ground state even for smallest separation distances (Novosad, et al., 2002). This is important since magnetic flux closure reduces the long-range magnetostatic forces otherwise responsible for magnetic particle agglomeration.

4. Magnetic vortex microdisks for targeted cancer cell destruction

So far we were considering properties of the individual disks arranged in planar arrays on the wafer. By properly modifying the microfabrication process it is possible to release the disks into solution.

4.1 Microfabrication

The fabrication process includes optical lithography and magnetron sputtering (Kim, et al., 2010). Use of the master mask with 1 μm diameter disks arranged on a 3 x 3 μm^2 square lattice covering 3 x 3 cm^2 area will result in ~10^8 disks.

The process starts with negative tone photoresist spin coating on a silicon wafer. After the master mask is placed in contact with the layer of pre-baked photoresist, the sample is illuminated with UV light. An organic solvent dissolves and removes photoresist that is not exposed. Finally, magnetron sputtering is used to deposit a 5 nm underlayer gold, followed by 60nm of permalloy, and topped with another 5nm of gold layer. The disks can easily be

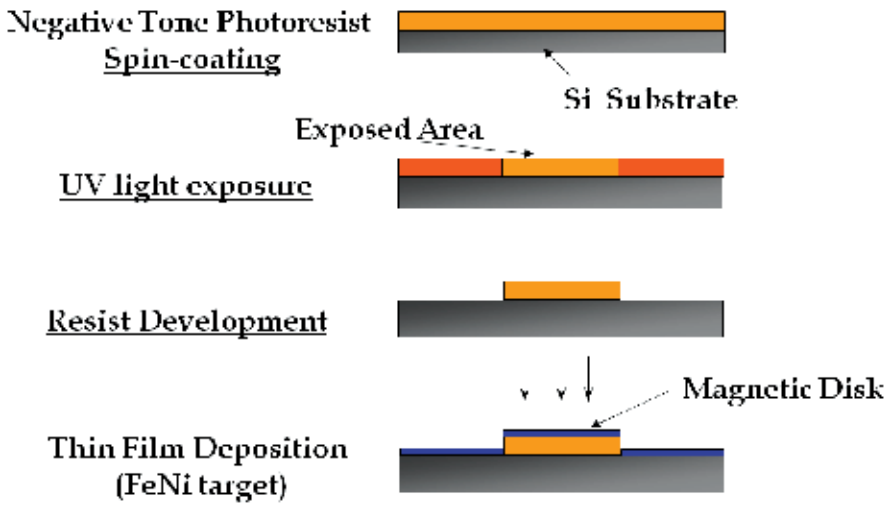

Fig. 9. Microdisks fabrication of MDs by optical lithography and magnetron sputtering.

released from the wafer by the lift-off process in acetone. The approach allows low cost production of uniformly sized particles (Fig 10). The details of the process flow schematically shown in Fig. 9 are given below.

- **Resist:** N-1410 negative tone resist supplied by Micro Resist Technology GmbH (www.microresist.de).
- **Optical lithography mask:** 1 micron diameter circular dot array arranged in 3 micron period square lattice covering a 3x3 cm^2 area was used.
- **Wafers: 2 inches prime quality** (100) silicon wafers with surface flatness < 2 μm supplied by University Wafers Inc., (www.UniversityWafer.com)
- **Resist spin coating:** Speed 3000 rpm, 60 sec; resulting resist thickness of ~1 micrometer.
- **Hot plate baking:** 90°C for 120sec.
- **Exposure:** 365nm light; 150uC/cm2 for 10sec.
- **Resist Development:** 533-S solvent, 30-40sec.
- **5 nm Au/ 60nm Fe20Ni80/ 5nm Au deposition:** DC magnetron sputtering (power 50W), base pressure 5×10^{-8} Torr; deposition rate 1A/sec @ 3 mTorr Ar pressure.
- **Lift-off process**: acetone, 30min, ultrasound assisted.
- **Centrifugation:** in 3 steps, 10 min @ 3,500 rpm, with fresh acetone wash between steps.
- **Transfer into aqueous solution:** 24h dialyze in MilliQ followed by centrifugation and dispersion in phosphate buffer solution (PBS, 0.1 M, pH 7.2) for further bio-functionalization.

Fig. 10 shows the representative optical microscope image of the dried suspension of the as fabricated microdisks.

Here we focus on testing ~1 micron diameter disks. It migh be desirable, especially from the view-point of future *in-vivo* application, to scale the system down to ~100nm dimensions. In this regard, the following shold be concidered: 1**) Scalability of the spin vortex state**. The Fig. 2. shows theoretical magnetic phase diagram of the magnetically soft disks shape particle. The magnetic vortices in deep submicron disks were experimentally imaged by many groups, see for example (Chung, et al., 2010). Thus, from the energy minimization viewpoint the magnetic vortex state remains stable ("ground") spin state for magnetically

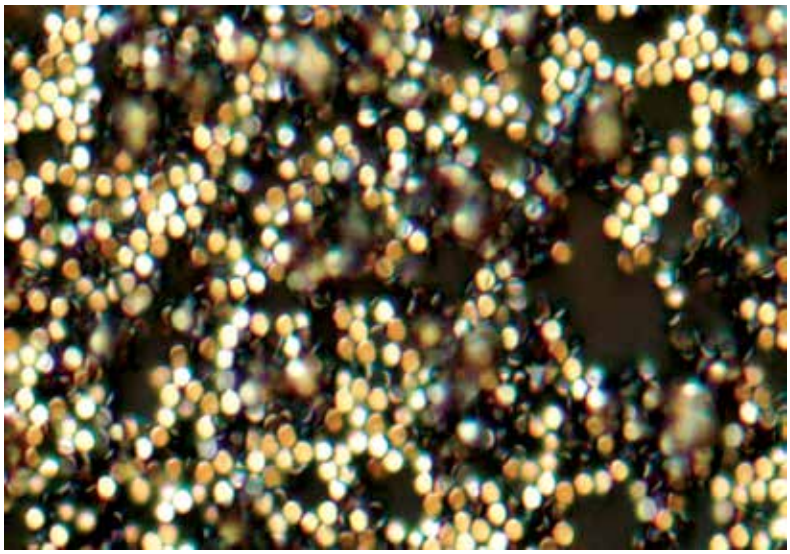

Fig. 10. A high resolution optical microscope image of the dried suspension of 60-nm-thick, 1 micron diameter permalloy disks coated with a 5-nm-thick layer of gold on each side. The discs were prepared by means of magnetron sputtering and optical lithography (Fig.9).

soft disk down to deep sub-100 nm diameters. 2) **Feasibility of nanofabrication.** Mass production of ~100s nm diameter disks can be achieved using more advanced technique, such as nanoimprint lithography. The disks detachment from substrate (after gold / magnetic / gold films deposition) can be facilitated by employing bi-layer polymer resist structure combined with ultrasonic-assisted lift-off process. Importantly, nanoimprint lithography is based on "stamp & repeat" approach, e.g. with using a master mask that can be employed many times. It is a truly a low cost and mass production method with exceptionally narrow size distribution of the final structures (Hu, et al., 2008, Wang, et al., 2008). 3) **Scaling of the magneto-mechanical coupling strength.** Decrease in the disk size will inevitable decrease the total magnetic moment **m** per disk (because of reduced particle volume). One can expect that the magnetic torque **m** x **H,** where H is applied magnetic field, will decrease accordingly. However, this torque that drives rotational motion of the nanodisk can easily be recovered by increasing the magnetic field amplitude. For instance, ten times smaller volume disks (e.g. using ~270 nm diameter, ~17 nm thin disks instead of the currently used ones), will experience the same magnetic torque if subjected to ~2.7 kOe field, instead of ~90 Oe field used in the in-vitro experiments below. A stronger magnetic fields are easy to achieve since the required frequency of magnetic field is of few ~10s Hz only. Thus, there appear no major conceptual or feasibility problems to employ the nanosize magnetic disks.

4.2 Magnetic properties

After fabrication the samples were characterized using conventional magnetometry and light scattering experiments. The hysteresis loop data (not shown) agree with the concept of the magnetization reversal due to nucleation and annihilation of the magnetic vortices. In zero field (remanent state) the vortex core is in the center of each disk, whereas under

magnetic field application the vortex shifts (reversibly) to develop the magnetization component parallel to the field (see Fig. 4 d). Owning to the flat geometry, the disks rotate under an alternating magnetic field. This can be used for testing the concept of advanced therapies, which include combined drug delivery and magneto-mechanical cell destruction when targeting tumor cells. To verify a mechanical responsiveness of the microdisks we investigated the field-dependent intensity of laser beam passing though the aqueous solution (10^7 disk / ml), Fig. 11 (left). In the absence of the magnetic field, the disks are randomly oriented causing significant light scattering. Under application of magnetic field parallel to the laser beam direction, the disks are instantly aligned to have their plane parallel to the field. The scattering cross-section is therefore reduced leading to a rapid increase in the transmitted light intensity (Fig. 11, right).

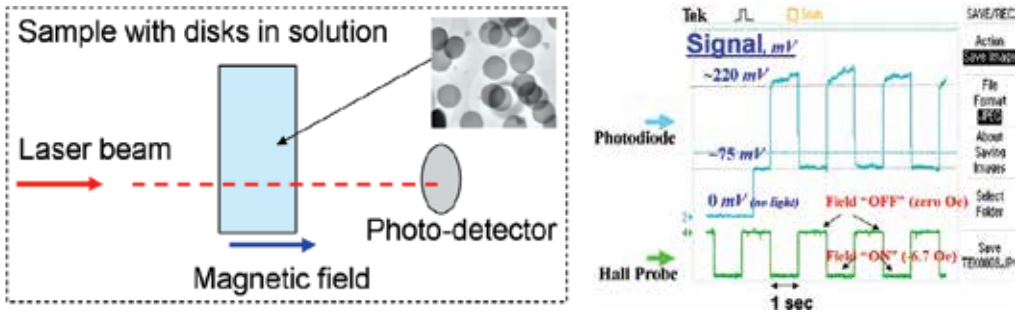

Fig. 11. Schematics of the experimental arrangement to probe the microdisk responsiveness to an external magnetic field (left) and representative data for 7 Oe / 1 Hz applied field (right). The light scattering cross-section is reduced leading to a rapid increase in the transmitted light intensity.

Consequence of the magneto-mechanical coupling is that the magnetic vortices can be used as a mediators to deliver the energy of an external source (of magnetic field) to the cell. Thus, the targeted cell destruction for cancer therapy becomes possible.

4.3 *In vitro* experiments

The feasibility of the proposed concept was tested using Glioblastoma multiforme (GBM), an aggressive form of brain cancer a model for an *in vitro* experiment (Kim et al., 2010). The specific targeting of microdisks to N10 glioma cancer cells (Da, at al., 1990) was achieved by functionalization of the inorganic material with antihuman-IL13α2R antibody (hereafter referred to as mAb), because IL13α2R is over-expressed on the surface of glioma cells (Debinski, et al., 1999; Kawakami, at al., 2001) and serves as a marker for targeting by cytotoxic elements, including nanoparticles (Rozhkova, et al., 2009). Thiolate groups that readily react with the gold surface were first randomly introduced into the mAb using N-succinimidyl-S-acetylthioacetate (SATA). After deprotection of the thioacetylated protein, the free thiolate groups of the mAb immediately reacted with the gold surface of the microdisks (Fig. 12).

To evaluate the magnetic field-induced cytotoxicity the loss of cell membrane integrity was assayed via release of cellular lactate dehydrogenase (LDH test). The *N10* GBM cells were incubated with the mAb-modified microdisks and exposed to an *ac* magnetic field of 90 Oe with frequency of 20 Hz using experimental set-up shown in Fig. 13.

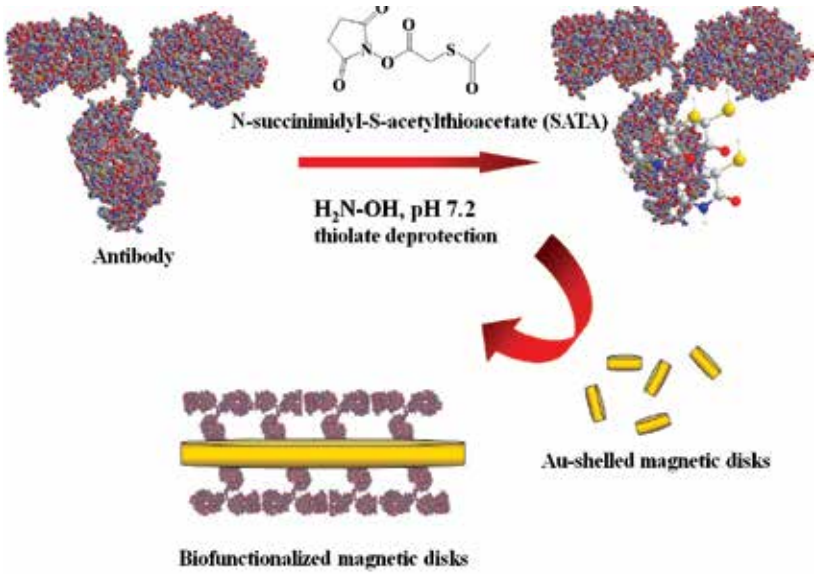

Fig. 12. The microdisk biofunctionalization with antihuman-IL13α2R antibody.

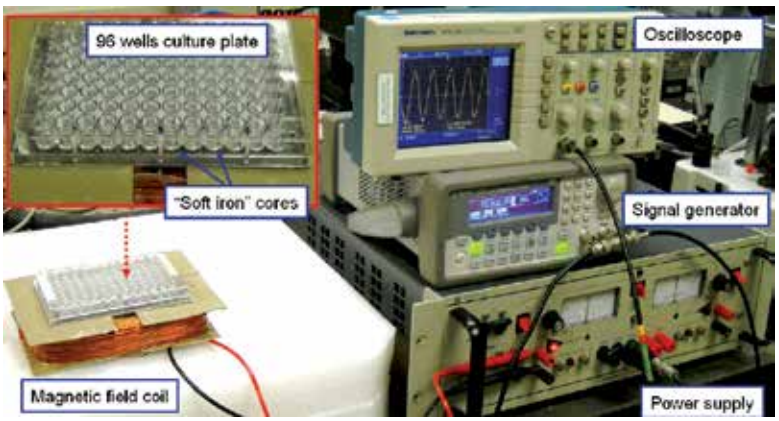

Fig. 13. The experimental set-up for magnetic field application *in-vitro.*

Field-treated MD-mAb-cell culture exhibited up to ~90% cytotoxicity effect (Kim et al., 2010). Furthermore, dramatic cell morphology changes were observed after the magnetic field application (Fig. 14). Figure 15 compares representative AFM images of the control *N10* cells pre-incubated with MD-mAb (left), and the cells after *m*agnetic field exposure (right) after 1 hr recovery culture. Since the observed morphological characteristics are typical for apoptosis, we also demonstrated other important characteristics of apoptotis, - severe nuclear DNA nicking (data not shown). Apoptosis is one of the main types of programmed cell death used by nature for elimination of damaged or unneeded cells without local inflammation (Mpoke, & Wolfe, 1997). The fundamental importance of correct execution of apoptosis is evident from the many human diseases with aberrancies in apoptosis, including cancer. During cancer development, various imbalances can arise in the apoptotic machinery (Kasibhatla, & Tseng, 2003).

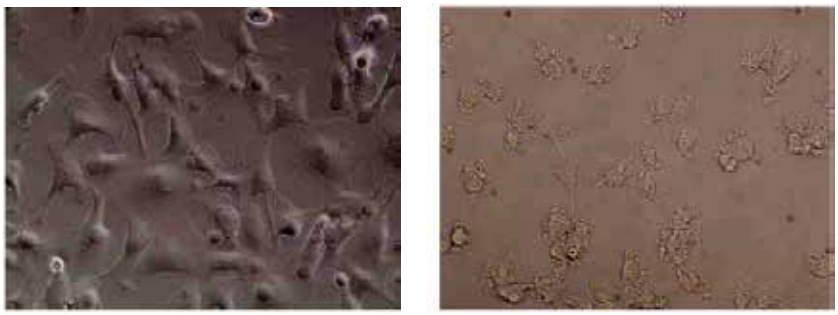

Fig. 14. Representative x50 optical microscope images of cancer cells for two distinctive cases. Left image: Binding experiments: Human glioma *N10* cells incubated with IL13-functionalized disks; no field was applied. The morphology of the cell is essentially the same as for control sample (e.g. cells without magnetic disks; not shown). Right image: an optical micrograph of the cells incubated with IL13-functionalized disks after 20 Hz / 90 Oe *ac* magnetic field was applied for 10min.

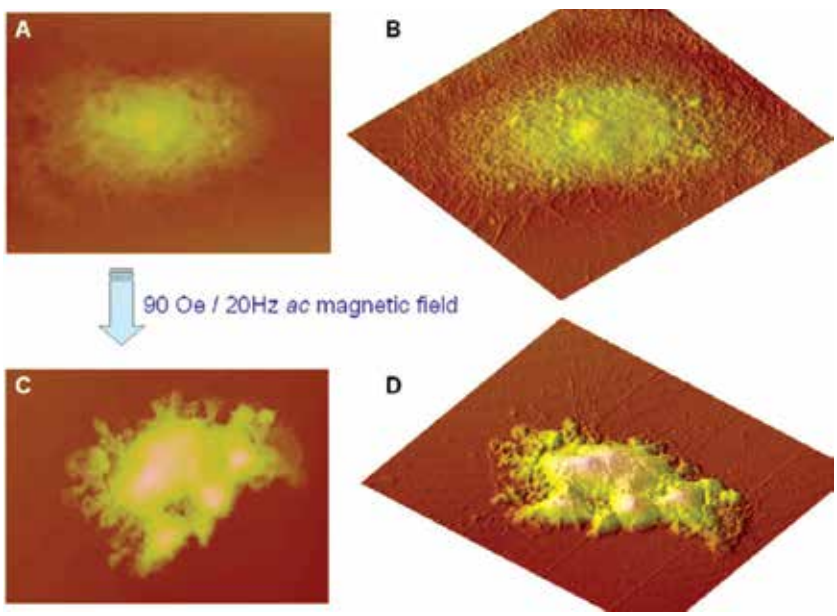

Fig. 15. 2D and 3D Atomic Force Microscope images of control (conjugated with MDs, but untreated) cell (upper images), and treated *N*10 glioma cell subjected to 90 Oe / 20 Hz magnetic field (lower images).

Consequently, sensitivity towards apoptosis is progressively reduced, which ultimately leads to inappropriate cell survival, resistance to cytotoxic drugs, and malignant progression. Induction of apoptosis plays a central role as a potential anticancer strategy (Kasibhatla, & Tseng, 2003). Although a detailed understanding of the intracellular pathways responsible for cell death induced by magneto-mechanical actuation is still lacking, the proposed approach opens wide research horisonts to explore applicability of magnetic particles for anti-cancer theraphies using low frequency magnetic fields.

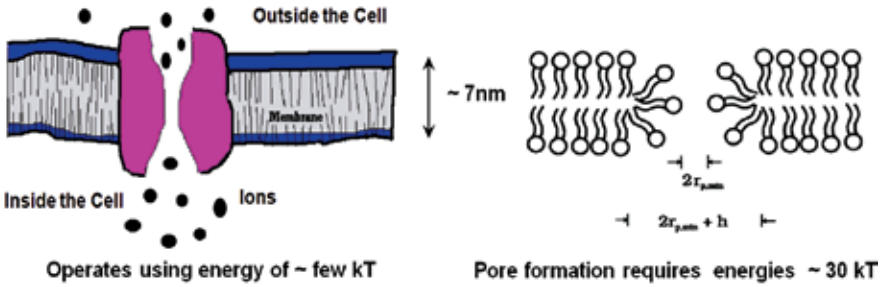

Fig. 16. The magnetic vortex forces are strong enough to mechanically actuate the existing ion channels (left), as well as to interrupt the barrier function of the cell membrane through formation of ~ 10nm pores (right). The later could lead to altered molecular transport into and out of cells, therefore altering intra cellular machinery function.

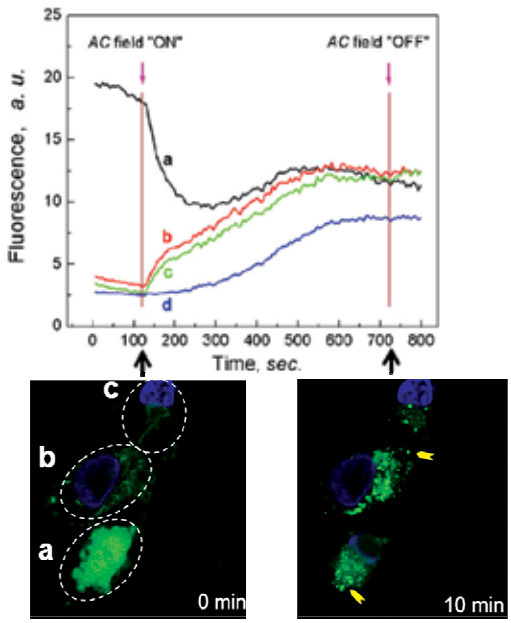

Fig. 17. Time-evolution of the calcium fluorescence signal averaged for three difference cells (a, b and c), as well as for whole field of microscope view (d), and Optical microscope image calcium ffluorescence intensity image prior (left) and after (right) application of *ac* magnetic field.

In these experiments, the magnetically actuated microdisks delivered to the cell surface mechanical force of ~50-100 pN (upper limit estimate). On the other hand, forces as small as few pN were reported to be sufficient to activate a single ion channel (Guharay, & Sachs, 1984; Martinac, 2004; Mannix, 2007). Furthermore, a theoretically calculated energy barrier (Vaughan, & Weaver, 1996) to create a pore in the cell membrane comparable in diameter to its thickness (~7nm) using rotational forces produced by a magnetic particle is of order ~30 k_BT, where k_B=1.38*10^{-23} J/K is the Boltzmann constant, T is the temperature. For comparison, the Zeeman energy of the magnetic vortex subjected to 100 Oe field is of ~1*10^{17} J, e.g. of order ~1000 k_BT. Thus, the magnetic vortex forces are strong enough to

mechanically actuate the existing ion channels, as well as to interrupt the barrier function of the cell membrane through pores formation. The later could lead to altered molecular transport into and out of cells, therefore altering intra cellular machinery function. To clarify this possibility, we have performed experiments on imaging of intercellular calcium re-localization during application of *ac* magnetic field (10Hz / 90Oe) in *N10* glioblastoma cells. The role of the calcium as a universal secondary messenger in execution of the cell-death process is well-established and is reported in connection with the studies of drug-induced cytotoxicity (Clapham, 1995; Duchen, 2000; Boehning, et al., 2003; Mattson et al., 2003; Smulson, et al., 1999; Yakovlev, et al., 1999).

To investigate whether calcium ions signaling is involved in the observed magnetic-vortex-driven cell death the *N10* cells were preloaded with Fluo-4AM, a calcium indicator dye and studied using a dual wavelength laser confocal microscopy. A magnetic coil was mounted on the microscope sample stage. Figure 17 shows semi-quantitative data on changes in intracellular concentration of calcium during *ac* field application in a nominally calcium-free Hank's buffer solution. Fluorescence intensity was detected in areas **a**, **b**, **c** corresponding to three cells with different initial fluorescence intensities due to different steps of a life cycle. Total fluorescence (including cells and background) was measured as an area **d**. Once ac field is applied noticeable changes in fluorescence were detected. Thus, for cells **b** and **c** constant steady increasing of fluorescence intensity (up to two-folds) was observed. In contrast, for the cell **a** with originally higher calcium concentration initial sharp slope was followed by smooth increase of calcium levels.

The global increase in the cytoplasmic calcium triggers the simultaneous release of cytochrome *c* from mitochondria, formation of the apoptosome and activation of specific protease caspases. Caspases together with nucleases then finalize the cell death process by cleaving protein substrates and nuclear DNA. Importantly, the number of TUNEL-stained cells was observed to fall remarkably (~50%) after the addition of 20 μM Z-VAD-FMK, an inhibitor of caspase proteases, the key role-players in apoptosis. Therefore, we can anticipate that magnetic vortex mediated mechanical stimulus may eventually be converted into a downstream chemical signal cascade able to initiate apoptosis and cell destruction.

Altogether these confocal microscopy data confirmed our proposal on magneto-mechanically-induced ionic channels actuation or/and cell membrane pores formation altering calcium homeostasis and resulting in re-programming of important intracellular biochemical pathways. Future studies, including application of specific inhibitors of stretch-activated membrane protein complexes and experiments with controlled concentrations of calcium in cell culture media may help to further clarify intriguing details of the proposed mechanism. The details of the above described *in vitro* experiments and used materials are given below.

5. Materials & methods

Materials: Monoclonal anti-human-IL13Ralpha2 (designated mAb), cat# MAB6141, clone 83807, human IL-13 Rα2 biotinylated affinity purified polyclonal detection antibody, cat # BAF614, and Mouse IgG1 Isotype Control, cat # MAB002, clone 11711, were from R&D Systems, Minneapolis, MN, USA. N-Succinimidyl S-Acetylthioaceteate (SATA), dimethylsulfoxide (DMSO), hydroxylamine·HCl, Ethylenediaminetetraacetic acid tetrasodium salt dihydrate (EDTA) were from Sigma (St. Louis, MO, USA). Poly-L-lysine (0.01% soln) was purchased from Sigma (St. Louis, USA). Other reagents of the highest

grade available were obtained from Sigma IR spectra were recorded with a FT-IR spectrophotometer (Bruker Vertex 70, Billerica, MA). For cell imaging Axio imager Z1m; camera: Axio Cam MRM; image analysis program: Axiovision were used. Atomic Force Microscope was from Nano V, Veeco (Santa Barbara, CA, USA). CytoTox-ONE Homogeneous Membrane Integrity Assay kit (Promega, Madison, WI, USA). ApopTag®.
Plus Peroxidase *In Situ* Apoptosis Kit was from Chemicon (Millipore). Z-VAD-FMK (carbobenzoxy-valyl-alanyl-aspartyl-[O-methyl]-fluoro-methylketone) caspase inhibitor was purchased from Promega Corp.

Cell culture. The human glioma tumor cell line No. 10 cells (*N10*) were purchased from the Japanese Tissue Tumor Bank (Tokyo, Japan). No. 10 cells were grown in 96-well plates in RPMI medium (Gibco, Life Technologies, USA) supplemented with 10% (v/v) FBS (CellGrow, MediaTech, Heydon, VA), 2 mM L-glutamine, and penicillin/streptomycin, and incubated in a humidified atmosphere with 5% CO_2 at 37°C.

Bio-functionalization. 27.8 µl of 55 mM SATA solution in DMSO and 2.8 µl of 60 µM IL13 solution were mixed and incubated at room temperature with continuous gentle shaking in the dark for 30 minutes. To deprotect thiolate groups the SATA-modified antibody solution was combined with 4 µl of 0.5 M hydroxylamine·HCl and 25 mM EDTA solution in 0.1 M PBS, pH 7.4 and incubated for 2 hours at room temperature. 500 µl of MDs suspension ($5x10^8$ ea/ml) were degassed by nitrogen gas bubbling for 15 minutes, and then the deacetylated antibody solution was immediately mixed with the MDs suspension with continuous gentle shaking in the dark at room temperature for ~2 hours. The final MD-mAb was spin-washed 3 times with 500 µL 0.1 M PBS, pH 7.4 to remove unbound protein, and then redispersed in 500 µl of 0.1 M PBS, pH 7.4 and stored at 4C.

Magnetic field application. A magnetic field station plate was made by inserting ¼ inch soft iron rod into the under well in 96 well-plate. The station circumference was wound by Cu wire as a coil. Power supply/amplifier (KEPCO, Flushing, NY, USA), Function generator (Agilant 33220A, USA), oscilloscope (TEKTRONIX, Beverton, OR, USA) was connected with the magnetic field station for generating *ac* magnetic field. For experiment 96 well plate with samples was positioned on to of magnetic field station plate. Magnetic field strength was calibrated with Hall probe. After the treatment, the necrosis and apoptosis of treated cells was assessed with standard lactate dehydrogenase (LDH) test, Terminal Deoxynucleotidyl Transferase dUTP nick end labeling (TUNEL) assay.

Morphological analysis of cell viability by optical and atomic force microscopy. Human glioma cells from the N10 cell line were cultivated on poly-L-lysine coated coverslips. The human glioma tumor cell line No. 10 cells (N10) were grown on the coverslips in 24 well plates for 24 hours to reach 10^4 cells per a coverslip. The cells on the coverslips were exposed to *ac* magnetic fields as it is described above in the magneto-mechanical cell destruction set-up. The treated cells were fixed in 4% paraformaldehyde and analyzed by optical microscopy or recovery cultured in standard conditions for 4 hours and then fixed for AFM. Coverslips were thoroughly rinsed with MilliQ water prior to imaging. Bright or dark field images of the cells were taken using a 10X, 20X, 50X and 100X of objective lens. AFM surface images of the cells were acquired in non-contact mode.

Laser confocal intracellular calcium imaging. For the Calcium assays the *N10* cells were grown in 35 mm Fluorodish cell culture dishes (World Precision Instruments, FL, USA) to reach ~10,000 cells per dish and then incubated with MD-mAb at standard conditions. Cells were loaded with 1 µM Fluo-4-AM containing 0.02% Pluronic® F-127 (Molecular Probes)

and 1μg/ml Hoechst 33342 (Molecular Probes) at 37°C for 20 and 5 min respectively, washed and then assayed in Hank's buffer. A magnetic coil was placed on top of a sample stage of a dual-wavelength Leica SP5 Tandem Scanner Spectral 2-Photon Confocal Microscope. After 2 min of dye-loaded cell initial fluorescence imaging, an alternating magnetic field was applied to stimulate MDs on the cell surface during 10 min.

ELISA. The human malignant glioma N10 cell line was grown in 96 well plate for 24 hours to reach 10^4 cells per well. Next day cells were blocked with PBS supplemented with 4% BSA for 1 hour at 37C followed by 3 times PBS washing. MD-mAb or free antibodies in concentrations 1-105ng/ml were added to the cells. After incubation with conjugates or free antibodies cells were washed and incubated with secondary anti-mouse HRP conjugated antibodies. In 1 hour cells were PBS washed and ELISA was developed by using TMB peroxidase substrate solution (Pierce, Rockford, IL). After 30-min incubation, plates were read at 450 nm on a plate reader.

LDH assay. Cells were grown in 96-well plates with concentration of $1x10^4$ cells per well. N10 glioma cells were treated with either mock, IgG or IL13-MDs for 1 hr followed by exposure to magnetic fields of 0 ~ 60 Hz (90 Oe) for 10 min. After magnetic field application, 50 μl of LDH substrate solution was added to each well with following incubation for 30 min at room temperature. Next, 50 μl of stop solution was added to each well in the plate and read on a micro-ELISA reader (Biotec 800, ISC Bioexpress, USA) at a wavelength of 490 nm. The percentage of cytotoxicity was calculated with control wells containing cell culture medium without any treatment. LDH leakage (%)=$[A_{test}]/[A_{control}]$ X 100, where $[A_{test}]$ is the absorbance of the test sample and $[A_{control}]$ is the absorbance of the untreated control sample.

TUNEL assay. 2 x 10^4 N10 glioma cells were seeded and grown on polylysine-coated coverslips. Then, N10 glioma cells were incubated with either mAb or negative control IgG1-modified MDs for 1 hr followed by exposure to magnetic fields of 0 ~ 130 Oe (20 Hz) for 10 min. In control experiment 20μM caspase Inhibitor Z-VAD-FMK was added. The cells were then washed with serum-free DMEM media and fixed with 1% Formalin-PBS solution (Boston Bioproduct, Boston, USA). After washing 3 times with 500 μml PBS, treated N10 cells on the coverslips were processed by a TUNEL assay kit according to the vendor recommendations. Briefly, the slides after treatment were fixed and then labeled by incubation with the reaction mixture containing TdT and digoxigenin-conjugated dUTP for 1 hr at 37°C. Labeled DNA was visualized with peroxidase-conjugated anti-digoxigenin antibody with 3, 3′-diaminobenzidene as the chromagen.

6. Conclusion & outlook

The magnetic properties, fabrication, and biofunctionalized of the lithographically defined microdisks with spin vortex state were described. It was shown that targeted magneto-mechanical cancer cell destruction can be achieved using properly biofunctionalized microdisks subjected to an unprecedentedly slow magnetic field. In these experiments an external energy power supplied to the cell cultures was ~10^5 times smaller than the typical hyperthermia use of magnetic nanoparticles (Hergt, 2006; Liu, 2007; Goya, 2008). The weak fields mean that the method has great potential for a low cost, large working volume and minimally invasive therapies. Besides the field frequencies and amplitude, the most striking difference is that in our approach allows the energy is delivered directly to the cell, e.g. potentially without damaging the surrounding normal cells or tissues. Furthermore, if was found that the microdisk-induced mechanical stimulus results into intracellular signal

transduction and amplification, causing initiation of programmed cell death. Future efforts could focussed on (1) testing different cancer cell line, including human cell line, (2) use the microdisk in *in vivo* models by combining low-frequency (magnetomechanical destruction) and high frequency (thermal ablation) fields, and (3) exploring scalability of this approach down to ~100nm dimentions.

7. Acknowledgements

We thank our collaborators Drs. S. D. Bader, R. Divan, D.-H. Kim, J. Pearson, T. Rajh, V. G. Yefremenko from Argonne, Drs. V. Bindokas, M. S. Lesniak and I. V. Ulasov from the University of Chicago for continued involvement and interest to this project. Work at Argonne and its Center for Nanoscale Materials and Electron Microscopy Center is supported by the US Department of Energy Office of Science, Basic Energy Sciences, under contract No DE-AC02-06CH11357.

8. References

Ade, H. & Stoll, H. Near-edge X-ray absorption fine-structure microscopy of organic and magnetic materials. *Nature Materials* vol. 8, pp. 281-290 (2009).

Boehning, D., Patterson, R. L., Sedaghat, L., Glebova, N. O., Kurosaki, T. & Snyder S. H. Cytochrome c binds to inositol (1,4,5) trisphosphate receptors, amplifying calcium-dependent apoptosis. *Nature Cell Biology* vol. 5, pp. 1051 - 1061 (2003).

Clapham D. E., Calcium signaling. *Cell* 80, 259-268 (1995).

Chung, S.-H.; McMichael, R.; Pierce, D & J. Unguris, Phase diagram of magnetic nanodisks measured by scanning electron microscopy with polarization analysis. *Physical Review B*, vol. 81, 024410 (2010).

Cowburn, R. P., Koltsov, D. K., Adeyeye, A. O., and Welland, M. E. Single-Domain Circular Nanomagnets, *Phys. Rev. Lett.* Vol. 83, pp. 1042-1045 (1999).

Da, K., Shiyama, K., Naka, R., Hiyama, A. & Anishi, T. GFAP-positive human glioma cell lines: no. 10, no.11. *Human Cell* vol. 3, pp. 251-256 (1990).

Debinski, W., Gibo, D., Hulet, S., Connor, J. & Gillespie, G. Receptor for interleukin 13 is a marker and therapeutic target for human high-grade gliomas. *Cancer Res.* Vol.5, pp. 985-990 (1999).

Demokritov, S.; Hillebrands B. & Slavin, N. Brillouin light scattering studies of confined spin waves: linear and non-linear confiment. *Physics Reports,* vol. 348 pp. 441-489 (2001).

Dobson, J. Remote control of cellular behaviour with magnetic nanoparticles. *Nature Nanotechnology* 3, 139-148 (2008).

Donahue, M. & Porter, D. Object Oriented Micromagnetic Framework (OOMMF) User's Guide, Version 1.0, Interagency Report NIST IR 6376, National Institute of Standards & Technology, Gaithersburg, MD, 1999.

Duchen. M. R. Mitochondria and calcium: from cell signalling to cell death. *Journal of Physiology* 529, 57-68 (2000).

Ferrari, M. Cancer nanotechnology: opportunities and challenges. *Nature Reviews Cancer* 5, 161–171 (2005).

Fu, A. ; Hu, W. ; Xu, L. ; Wilson, R. ; Yu, H., Osterfeld, S.; Gambhir, S. & Wang, S. Protein-functionalized synthetic antiferromagnetic nanoparticles for biomolecule detection and magnetic manipulation, *Angew. Chem. Int. Ed.*, vol. 48, pp. 1620. (2009).

Gao, J.; Gu, H. & XU, B. Multifunctional magnetic nanoparticles: design, synthesis, and biomedical applications. *Accounts of chemical research*, Vol. 42, No. 8, pp. 1097-1107, 2009.

Goya, G. F., Grazu, V. & Ibarra, M. R. Magnetic nanoparticles for cancer therapy. *Current Nanoscience* 4, 1-16 (2008).

Guharay, F. & Sachs, F. J. Stretch-activated single ion channel currents in tissue-cultured embryonic chick skeletal muscle. *Physiol.* (London) 352, 685-701 (1984).

Gupta, A. K. & Gupta, M. Synthesis and surface engineering of iron oxide nanoparticles for biomedical applications. *Biomaterials* 26, 3995–4021 (2005).

Guslienko, K.; Novosad, V.; Otani, Y.; Shima, H. & and Fukamichi, K. Magnetization reversal due to vortex nucleation, displacement, and annihilation in submicron ferromagnetic dot arrays. *Phys. Rev. B* vol. 65, p. 024414 (2001).

Hergt, R.; Dutz, S.; Muller, R. & Zeisberger, M. Magnetic particle hyperthermia: nanoparticle magnetism and materials development for cancer therapy. *J. Phys. Condens. Matter.* Vol. 18, pp. 2919 -2923 (2006).

Hu, W.; Wilson, R.; Koh, A.; Fu, A.; Faranesh; A. Z.; Earhart, C.; Osterfeld, S.; Han, S.-J.; Xu, L.; Guccione, S.; Sinclair, R.; & Wang, S. High-Moment Antiferromagnetic Nanoparticles with Tunable Magnetic Properties. *Advanced Materials*, vol., pp. 1479–1483 (2008).

Kasibhatla S, & Tseng, B. Why Target Apoptosis in Cancer Treatment? *Molecular Cancer Therapy, vol. 2, pp.* 573-580 (2003).

Kawakami, K., Kawakami, M., Snoy, P. J., Husain, S. R. & Puri, R. *In vivo* overexpression of IL-13 receptor α 2 chain inhibits tumorigenicity of human breast and pancreatic tumors in immunodeficient mice. *J. Exp. Med*. 194, 1743-1754 (2001).

Kim, D.-H.; Rozhkova, E.; Ulasov, I.; Bader, S.; Rajh, T., Lesniak, M. & Novosad, V. Biofunctionalized magnetic-vortex microdiscs for targeted cancer-cell destruction. *Nature Materials,* vol.9, pp. 165 - 171 (2010).

Krishnan, K. Biomedical nanomagnetics: a spin through possibilities in imaging, diagnostics, and therapy. *IEEE Transactions in Magnetics*, vol. 46, No. 7, pp. 2523- 2558, (2010).

Liu, X.; Novosad, V.; Rozhkova, E.; Chen, H.; Yeferemenko, V.; Pearson, J.; Torno, M.; Bader, S. & Rosengart, A. Surface Functionalized Biocompatible Magnetic Nanospheres for Cancer Hyperthermia, *IEEE Transactions on Magnetics*, vol. 43, issue 6, pp. 2462-2464 (2007).

Mair, L. ; Ford, K. ; Alam, M.; Kole, R.; Fisher, &M. Superfine, R. Size-uniform 200 nm particles: Fabrication and Application to Magnetofection. *J. Biomed Nanotechnol.* Vol. 5, pp. 182-191, (2009).

Mannix, R. J., Kumar, S., Cassiola, F., Montoya-Zavala, M., Feinstein, E., Prentiss, M. & Ingber D. E., Nanomagnetic actuation of receptor-mediated signal transduction. *Nature Nanotechnology* vol. 3, pp. 36-40 (2007).

Martinac, B. Mechanosensitive ion channels: molecules of mechanotransduction. *J. Cell Science* 117, 2449-2460 (2004).

Mattson, M. P. & Chan, S. L. Calcium orchestrates apoptosis. *Nature Cell Biology* 5, 1041 - 1043 (2003).

Mpoke, S. S. & Wolfe, J. Differential Staining of Apoptotic Nuclei in Living Cells: Application to macronuclear elimination in tetrahymena. *J. Histochem. Cytochem.* Vol. 45, 675-684 (1997).

Muller, D., Helenius J., Alsteens D, & Dufrêne Y. Force probing surfaces of living cells to molecular resolution. *Nature Chem. Biology,* vol. 5, 383-391 (2009).

Nel, A.; Mädler, L.; Valegol, D.;, Xia. T.; Hoek, E.; Somasundaran, P.; Klaessig, F.; Castranova, V. & Thompson, M. Understanding biophysicochemical interactions at the nano-bio interface. *Nature Materials,* vol. 8, pp. 2442-15 (2009).

Novosad, V.; Guslienko, K.; Shima, H.; Otani, Y.; Kim, S.; Fukamichi,K.; Kikuchi N.; Kitakami, O. & Shimada, Y. Effect of interdot magnetostatic interaction on magnetization reversal in circular dot arrays. *Phys. Rev. B*, vol. 65, 060402 (2002).

Pankhurst, Q.; Thanh, N.; Jones, S. & Dobson, J. Progress in applications of magnetic nanoparticles in biomedicine. *J. Phys. D: Appl. Phys.* Vol. 42, 224001 (2009).

Rozhkova, E.; Ulasov, I.; Lai, B.; Dimitrijevic, N.; Lesniak, M. & Rajh, T. A High-Performance Nanobio Photocatalyst for Targeted Brain Cancer Therapy. *NanoLetters* 9, 3337 - 3342 (2009).

Scholz,W.; Guslienko, K.; Novosad, V.; Suess,D.; Schrefl, T.; Chantrell, R. & Fidler, J. Transition from single-domain to vortex state in soft magnetic cylindrical nanodots. *Journal of Magnetism and Magnetic Materials*. Vol. 266, No. 1-2, pp. 155-163, (2003).

Shinjo, T.; Okuno, T.; Hassdorf, R.; Shigeto, K. & Ono, T. Magnetic vortex core observation in circular dots of permalloy. *Science* 289, 930-933 (2000).

Sen, S., Subramanian, S. & Discher, D. E. Indentation and adhesive probing of a cell membrane with AFM: theoretical model and experiments, *Biophysical Journal*, 89, 3203-3213 (2005).

T. Vaughan, J. Weaver, Energetic constraints on the creation of cell membrane pores by magnetic particles. *Biophysical Journal*, vol. 71, pp. 616-622 (1996).

Wachowiak, A.; Wiebe, J.; Bode, M.; Pietzsch, O.; Morgenstern, M. & Wiesendanger, R. Direct observation of internal spin structure of magnetic vortex cores. *Science* 298, 577-580 (2002).

Wang, S, & Li, G. Advances in giant magnetoresistance biosensors with magnetic manoparticle tags: review and outlook. *IEEE Trans. Mag.* Vol. 44, 1687 (2008).

Yakovlev, A.G., Wang, G., Stoica, B. A., Simbulan-Rosenthal, C. M., Yoshihara, K. & Smulson, M. E. Role of DNAS1L3 in Ca2+- and Mg2+-dependent cleavage of DNA into oligonucleosomal and high molecular mass fragments. *Nucleic Acids Research* 27, 1999-2005 (1999).

Zabow, G. ; Dodd, S. ; Moreland, J. & Koretsky, A. Micro-engineered local field control for high-sensitivity multispectral MRI. *Nature*, vol. 453, 1058 (2008).

Zabow, G. ; Dodd, S. ; Moreland, J. & Koretsky, A. The fabrication of uniform cylindrical nanoshells and their use as spectrally tunable MRI contrast agents. *Nanotechnology*, vol. 20, 385301 (2009).

Part 4

Polymers

19

Life Assessment of a Balloon-Expandable Stent for Atherosclerotic Renal Artery Stenosis

Hao-Ming Hsiao[1], Michael D. Dake, MD[2],
Santosh Prabhu[3], Mahmood K. Razavi, MD[4],
Ying-Chih Liao[5] and Alexander Nikanorov, MD[3]
[1]*National Taiwan University, Department of Mechanical Engineering, Taipei*
[2]*Stanford University, Department of Cardiothoracic Surgery, Stanford, CA 94305*
[3]*Abbott Laboratories, Abbott Vascular, Santa Clara, CA 95054*
[4]*St. Joseph Vascular Institute, Orange, CA 92868*
[5]*National Taiwan University, Department of Chemical Engineering, Taipei*
[1,5]*Taiwan*
[2,3,4]*USA*

1. Introduction

A stent is a small wire-mesh tube that can be deployed into a blood vessel and expanded using a small balloon (or self-expanded) during angioplasty to open a narrowed blood vessel. The expanded stent exerts radial force against the walls of the artery, thereby preventing reclosure of the artery. The scaffolding provided by the stent can also help prevent small pieces of plaque from breaking off and traveling downstream to cause major events such as stroke in distal organs.

Atherosclerotic Renal Artery Stenosis (RAS) is a common manifestation of generalized atherosclerosis and the most common disorder of the renal arterial circulation. Untreated renal artery stenosis can lead to progressive hypertension, renal insufficiency, kidney failure, and increased mortality. Despite the proven efficacy of traditional surgical procedures such as endarterectomy and renal artery bypass, endovascular therapy has emerged as an effective strategy for treatment. Renal angioplasty and endoluminal stenting are performed at an increasing rate, especially in patients with the most complex form of the disease (Blum et al., 1997; Zeller et al., 2003). Balloon-expandable stenting for aorta-ostial renal artery stenosis has been demonstrated to be a safe and effective therapy (Rocha-Singh et al., 2005). It offers more permanent relief to patients without lifelong prescription for medications or surgical procedure. Figure 1 shows the Computed Tomography Angiography (CTA) of the stented left renal artery with severe calcification. A longitudinal image cut through the aorta and the stented left renal artery reveals the cross section of stent struts and the extent of calcification around the renal artery wall.

During normal breathing, the kidneys move up and down due to the diaphragm motion and the renal arteries subsequently experience bending at or close to the point of fixation to the aorta. Figure 2 shows the angiograms of the kidney and the renal artery motion during respiration. Figure 3 shows their motion using a guidewire and a catheter for tracking. It is unclear what impact this kidney motion has on stents implanted in renal arteries. This kidney/arterial motion is important in the evaluation of patients receiving balloon-

expandable stents in order to understand potential risks of stent fractures or in-stent restenosis associated with renal stenting (stent fracture may trigger intimal hyperplasia leading to restenosis). This raises the question of whether the motion of the kidneys and subsequent bending of the arteries would negatively impact balloon-expandable stent fatigue life and cause stent fractures?

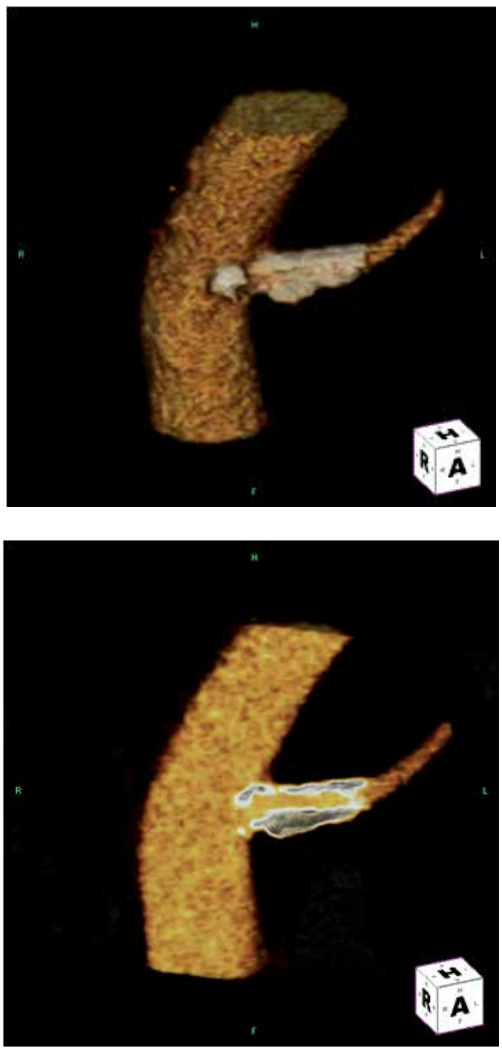

Fig. 1 (a, b) Computed Tomography Angiography of the stented left renal artery with severe calcification, (a) CTA 3D reconstructed image, (b) longitudinal cut through the aorta and the stented left renal artery

Although stent fractures in various vascular and nonvascular beds may not necessarily threaten the patients' life, it is an undesirable event that should be avoided if possible. A literature review revealed that stent fractures have been observed in renal arteries. Bessias et al. reported stent thrombosis in a 47-year-old patient with a single kidney and diseased renal artery who underwent implant of a balloon-expandable stent (Bessias et al., 2005). The

patient presented 25 days after the procedure with renal insufficiency and uncontrolled hypertension. Angiography showed a thrombosed stent which required an aortorenal bypass. The explanted renal artery revealed a fractured incompletely-expanded stent. Similarly, Sahin et al. observed a fractured stent in a 55-year-old patient with mobile kidney (Sahin et al., 2005). They observed fracture of the stent resulted from mobility of the left kidney and suspected that the intimal hyperplasia the patient had 2 months after stenting was triggered by inflammatory reaction at the stent fracture points due to destruction and irritation of the vessel wall. The former case report underscores the possibility of "missed" fractures in balloon-expandable stents that could lead to restenosis and/or thrombosis and the latter points to a possible mechanism. Stent fractures in renal arteries are difficult to identify and may be missed if they are not carefully looked for.

Earlier studies investigated the impact of respiration-induced motion of the kidneys for the purpose of radiotherapy planning to accurately treat tumors. It was reported that the kidneys moved approximately 20-40 mm in the craniocaudal dimension during normal respiration, but provided limited quantitative information on the renal artery movement. Additionally, Magnetic Resonance Imaging (MRI) revealed that displacements of the left and right kidney during normal respiration varied from 2 to 24 mm and 4 to 35 mm, respectively (Moerland et al., 1994). Forced respiration (maximal inspiration and expiration) displacement of the left and right kidney varied from 10 to 66 mm and 10 to 86 mm, respectively. The maximal vertical motion of 39 mm for the superior pole and 43 mm for the inferior pole was reported in another MRI study (Schwartz et al., 1994).

A recent study (Draney et al., 2005) evaluated not only the kidney movement but also the displacement and bending of the renal arteries during respiration using enhanced Magnetic Resonance Angiography (MRA) in healthy male volunteers. The left and right kidneys were displaced 10.1 mm and 13.2 mm, respectively. It was found that the renal ostia were relatively fixed with the displacement of 10-fold less than that of the kidneys. The differential in displacement between the renal ostia and the kidneys resulted in statistically significant changes in renal branch angle. The branches exhibited a greater branch angle at inspiration and were more perpendicular at expiration.

In the current medical device industry, most of the coronary and endovascular stents are assessed using accelerated in-vitro fatigue testing and Finite Element Analysis (FEA) to ascertain whether the device will survive a fatigue life of ten years under simulated physiological loading conditions. To design against such fatigue failures, the majority of prior research on stent fatigue was focused on determining the stress/strain-life (*S-N*) properties of wires and stents (Harrison & Lin, 2000; Pelton et al., 2003; Wagner et al., 2004).

Marrey et al. developed a new damage–tolerant analysis for quantitatively predicting the fatigue life of a balloon-expandable stent (Marrey et al., 2006). Their approach was to base the primary fatigue-life assessment on a traditional, yet conservative version of an *S-N* analysis, and to further use fracture mechanics in order to evaluate the role of pre-existing flaws. Similar work was extended to the nickel-titanium stents for endovascular applications (Robertson & Ritchie, 2007).

Hsiao et al. presented the first evaluation of the impact of the kidney motion on the renal stent fatigue performance (Hsiao et al., 2007 & 2009). It was concluded that the fatigue performance of the studied balloon-expandable stent is excellent under cardiac pulsatile fatigue alone, but compromised to certain degrees when respiration-induced renal artery bending fatigue was also considered. The change in bending angle was more significant for the overlapped stent configuration, resulting in lower fatigue performance when compared to the implant of only one single stent. The following strategy was employed during the study:

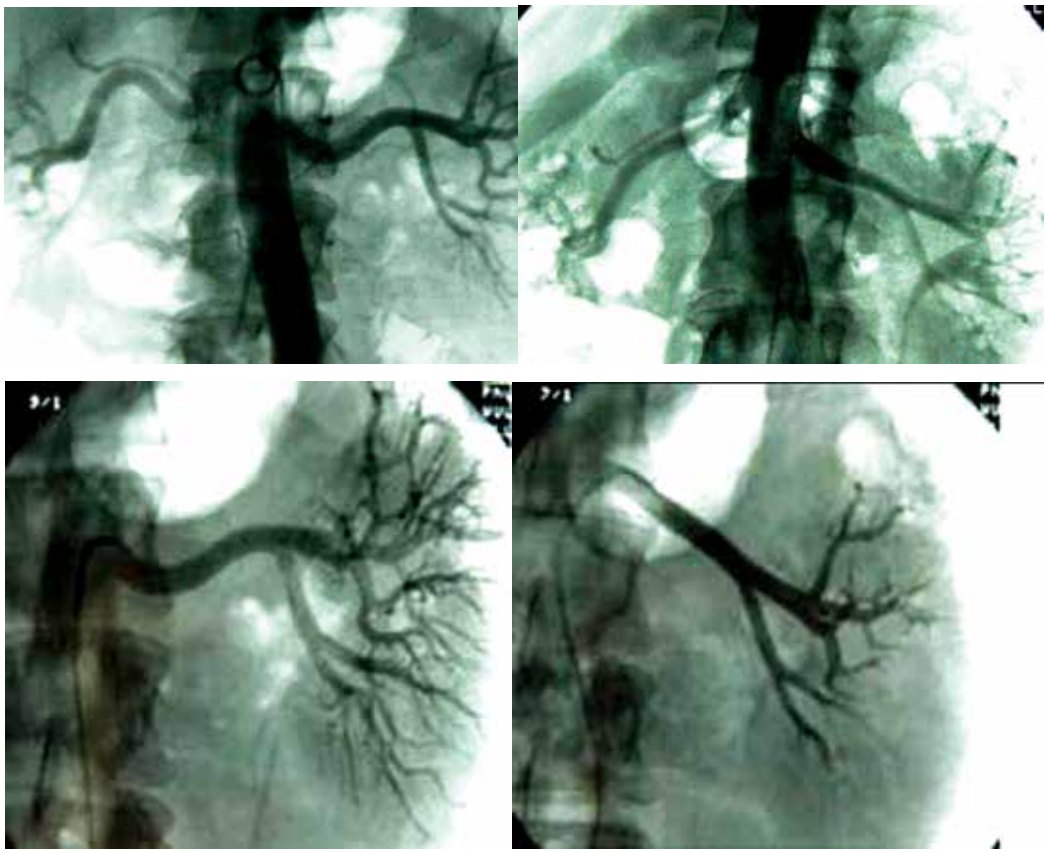

Fig. 2. (a, b) Angiograms showing the kidney and the renal artery motion during respiration, (a) expiration (kidneys moving up), (b) inspiration (kidneys moving down)

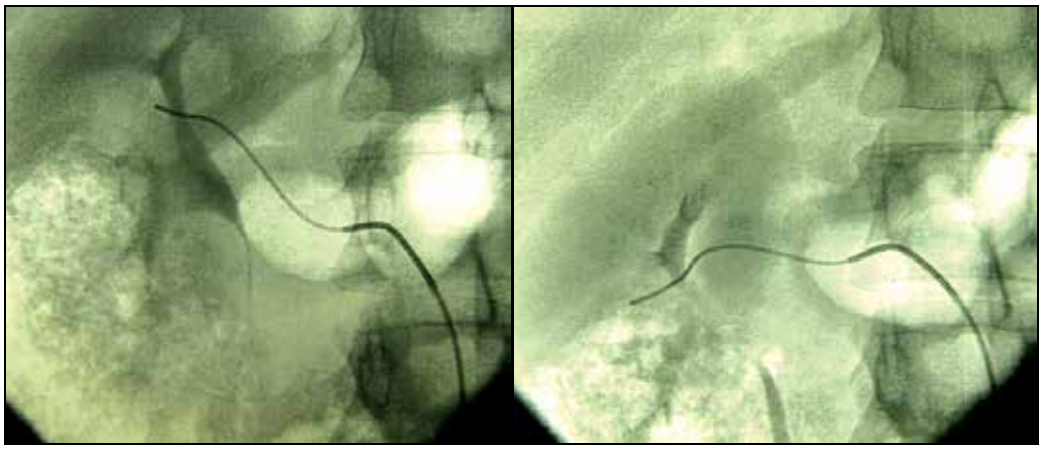

Fig. 3. (a, b) Fluorograms recorded during the right renal artery catheterization demonstrating the kidney and the renal artery motion during respiration by tracking a guidewire and a catheter placed in the renal artery, (a) expiration, (b) inspiration

1. Fluoroscopic images of the stented renal arteries were taken from cadavers at simulated inspiration/expiration positions. Respiratory motion was simulated by manual manipulation of the kidneys to reflect their craniocaudal movement observed clinically.
2. Stent bending during simulated respiration was measured from fluoroscopic images and used as input parameters for the subsequent finite element model.
3. Finite element analysis was performed to assess the balloon-expandable stent bending fatigue performance during respiration.

2. Cadaveric model study

A newly developed L-605 cobalt-chromium balloon-expandable stent was used in this study (Fig. 4). The use of the cobalt-chromium material enables reduction of the stent's wall thickness relative to traditional stainless steel to improve the stent's hemodynamic properties while retaining adequate visibility under fluoroscopy. Figure 5 shows the radiopacity comparison between this new cobalt-chromium stent and its stainless-steel counterpart. It appears that the cobalt-chromium stent has higher radiopacity than the stainless-steel stent. The stent was designed to form a series of nested rings interconnected with small bridging connectors. The design parameters such as crown (or apex) radius and strut dimension were tailored to optimize the stent performance. The unique stent design provides excellent flexibility and low profile to allow physicians' easy device delivery. The stent family covers the nominal stent inner diameters from 4 to 7 mm. In clinical use, the stent may be post-expanded to 1 mm greater than the nominal diameter if necessary. The stents were processed by laser cutting the intended design pattern onto the surface of the hypotube, the starting tube for the manufacture of intravascular stents and other biomedical devices. The as-cut stent surfaces were then electrochemically polished to achieve a good surface finish (Fig. 6).

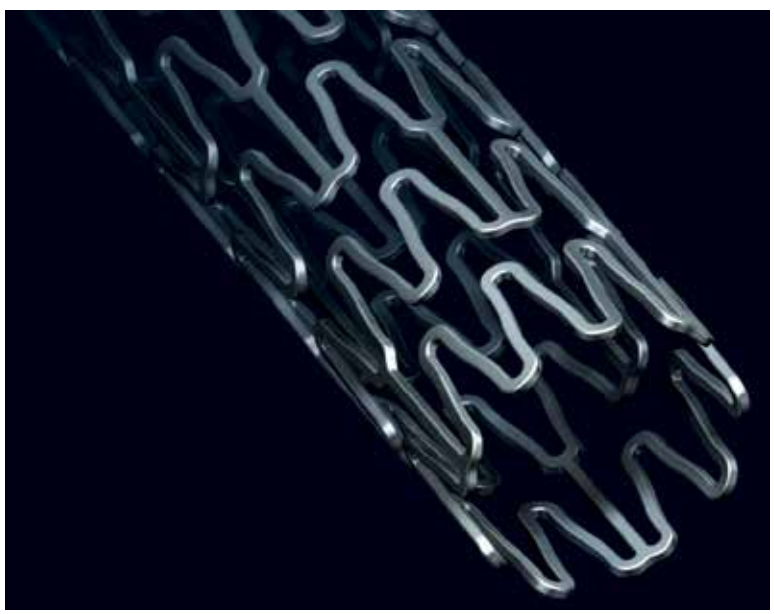

Fig. 4. Newly designed cobalt-chromium balloon-expandable stent used in this study

To test this balloon-expandable stent not yet approved for clinical use at the time of this work, a cadaveric study was performed where two cadavers (henceforth designated as Cadaver A, Cadaver B) were used. Both cadavers were middle-aged individuals, one male and one female. Their cause of death in both cases was unrelated to cardiovascular diseases. The cadavers were prepared based on the methods developed by Garrett (Garrett, 2001) to allow warm (body temperature) saline through the vasculature to simulate blood flow and maintain lumen pressure. The artery lumen was pressurized with saline during renal artery catheterization and stent deployment. Each cadaver was placed in the supine position. To implant stents, endovascular access to the renal arteries was obtained via the femoral artery. The first 7 x 18 mm stent was deployed into the renal arteries of two cadavers through a transfemoral approach such that the end of the stent completely covered the renal ostium where the lesion is usually located. The stent was expanded to 7 mm (inner diameter) and then post-expanded slightly.

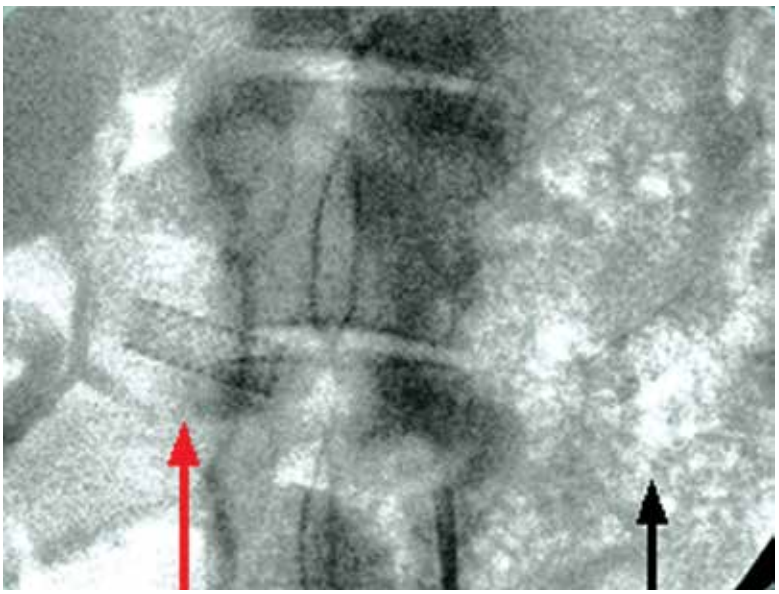

Fig. 5. Radiopacity comparison between the studied cobalt-chromium stent (left) and its stainless-steel counterpart (right)

Surgical access to the abdominal cavity and retroperitoneal space was then obtained via the midline incision through the abdominal wall. Contents of the abdominal cavity were partially removed to allow access to the renal arteries and kidneys. Mineral oil was used to lubricate the tissues of the body cavities and inside the renal arteries to ensure ease movement of tissues against each other. Sutures were sewn to the tissues surrounding the renal arteries and umbilical tape was looped around the renal arteries at the midpoint to facilitate manual manipulation and displacement of the kidneys. It should be noted that, although saline was continuously pumped into the vasculature during procedure, lumen pressure dropped due to saline leaking through the small arterial branches after surgical exposure of the kidneys and renal arteries. Respiratory movement was simulated by manual manipulation of the kidneys (Fig. 7). The displacement of the kidneys was estimated to be 40 mm based on the clinical human data. The stents were implanted when

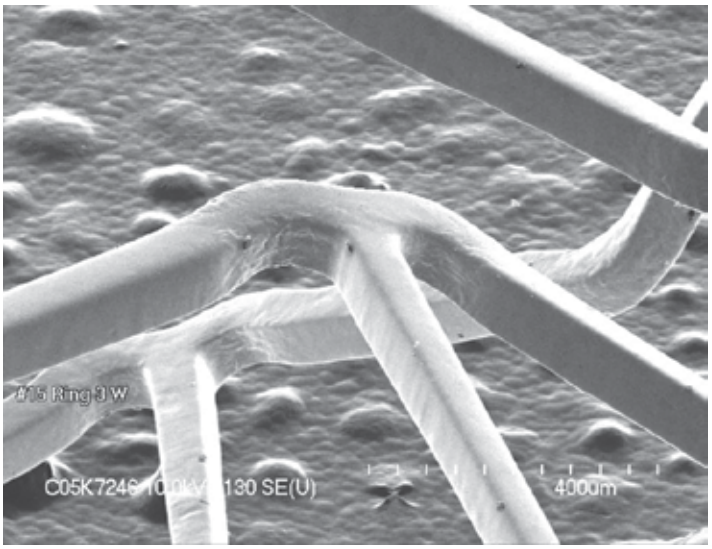

Fig. 6. Scanning Electron Microscopy (SEM) image of the studied cobalt-chromium stent showing a good surface finish after electrochemical polishing

kidneys were in the neutral position. The displacements of +20 mm cranial (towards head for expiration simulation) and -20 mm caudal (towards legs for inspiration simulation) from the kidney were measured with a ruler to establish the upper and lower bounds of the kidney movement. The manual simulation of the kidney movement was attempted in such a way that the kidney movement plane was considered close to perpendicular to the plane of view. Therefore, it is believed that the measurements were able to capture the true bending angle changes. The guide wire tip position, C-Arm (X-ray mobile diagnostic machine) floor position, and cadaver position remained unchanged throughout each cycle of one simulated inspiration and expiration movement to ensure consistency of the reference points. Fluoroscopic images were collected for later analysis.

After implanting the first stent, a second stent was deployed into the renal arteries of two cadavers such that the proximal portion of the second stent overlapped the distal portion of the first stent by approximately 3-4 mm. This was to simulate a potentially worst case clinical scenario. Respiration motion was again simulated by manual manipulation of the kidneys and fluoroscopic images were collected. Figure 8 shows the explanted and opened aortic segment with two overlapped stents implanted in the renal artery.

3. Finite element analysis

Stents placed in the vasculature are subjected to various modes of cyclic loading that may consequently compromise the structural integrity of the stents during their functional life resulting in fatigue failure. In this study, Finite Element Analysis (FEA) was performed to evaluate the stent structural integrity and fatigue performance. Simulation was performed to ensure whether the stent will survive 4×10^8 cycles under simulated physiological environment with a combination of cardiac pulsatile fatigue loading and respiratory bending fatigue loading. Ten years of fatigue life, accepted as a standard for stents today, is equivalent to 4×10^8 cardiac systolic/diastolic cycles and approximately 0.5×10^8 - 1×10^8 respiratory cycles (assuming human breath rate is 10-20 times per minute). Therefore, the

combined cardiac pulsatile and respiratory bending fatigue simulation (4 x 10^8 cycles for each) performed in this study represents a far more conservative assessment to the studied stent fatigue performance. The fatigue mean stress of 1689 MPa was obtained at Abbott Vascular using the Instron mechanical testing machine in accordance with the procedures outlined in ASTM E8-98, ASTM E83-96, and ASTM E345-93. The test procedure involved standard tensile strength testing of the L-605 cobalt-chromium tubing using extensometers for strain measurements. The fatigue alternating stress of 483 MPa was obtained from the material supplier and verified by literature publications (Bjork, 1985).

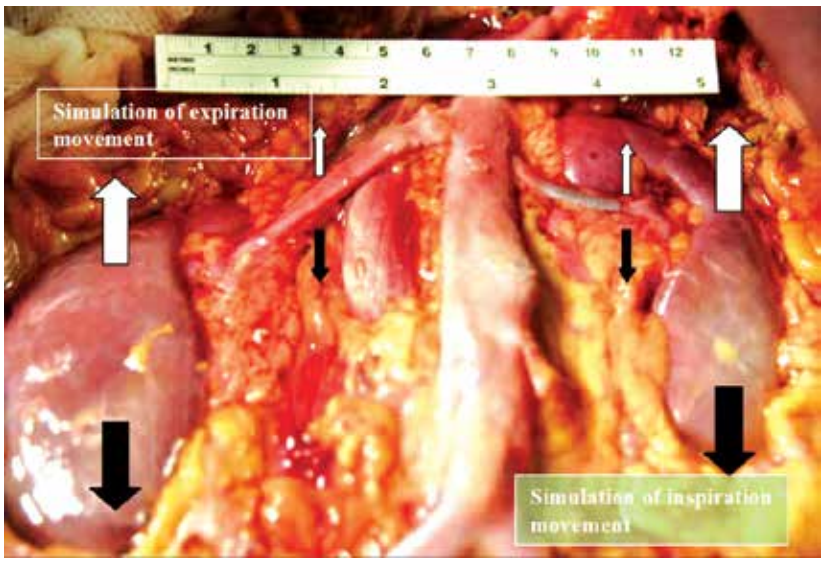

Fig. 7. Simulation of the kidney and the stented renal artery motion during the respiratory cycle

A finite element model was developed to evaluate the stent response to various loading conditions involved in preparing and deploying an intravascular stent consistent with clinical practice such as manufacturing (crimped onto a balloon catheter), *in vivo* deployment (expanded into an artery), and clinical vascular environment (systolic/diastolic pressure, respiration-induced bending). The stent fatigue analysis determined the state of stress and strain due to loading imposed by the following procedure:

Step 1. Stent crimping from 2.54 mm to 1.36 mm OD
Step 2. Stent recoil after crimping
Step 3. Stent expansion to 7.0 mm ID
Step 4. Stent recoil after expansion
Step 5. Stent bending during inspiration superimposed with systolic/diastolic pressure (180/80 mmHg)
Step 6. Stent bending during expiration superimposed with systolic/diastolic pressure

In order to evaluate the stent long-term fatigue performance under the loading conditions imposed by inspiration and expiration along with the systolic and diastolic arterial blood pressure loading, a Goodman fatigue analysis was performed using the multi-axial stress state experienced in Step 5 and 6. Since the stent is diametrically over-expanded relative to the vessel, there is a significant compressive preload imposed on the stent that results in

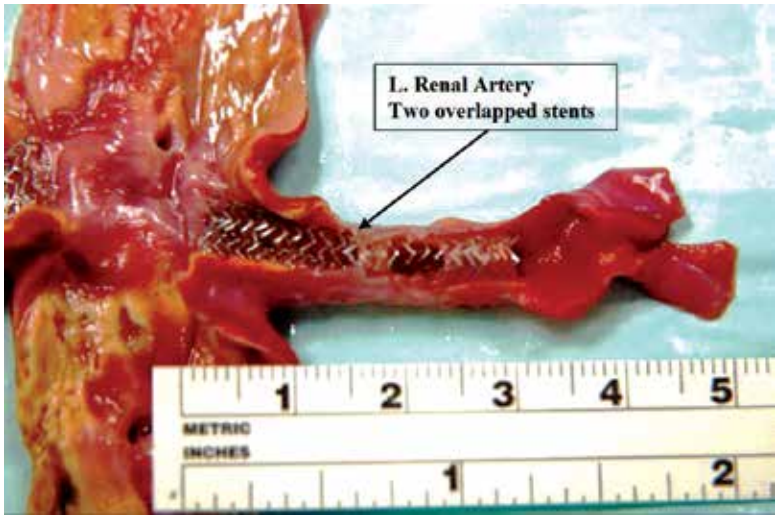

Fig. 8. Partially exposed explanted aortic segment with the left renal artery demonstrating position of the implanted overlapped stents

fatigue cycling with a mean stress not equal to zero. It should be noted that mean stress could also be a result of the plastic deformations of crimping and deployment. The Goodman relation states that fatigue failure will occur if the stress state in the component satisfies the relation:

$$\left(\frac{\sigma_a}{\sigma_e}\right)+\left(\frac{\sigma_m}{\sigma_u}\right)\geq 1 \tag{1}$$

where σ_a is the stress amplitude applied to the component, σ_e is the modified material endurance limit for non-zero mean stress, σ_m is the mean stress applied to the component, and σ_u is the material ultimate stress. The Goodman fatigue analysis was performed using the following effective mean stress and effective stress amplitude equations:

$$\sigma_m=\frac{1}{\sqrt{2}}\sqrt{(\sigma_{1m}-\sigma_{2m})^2+(\sigma_{2m}-\sigma_{3m})^2+(\sigma_{3m}-\sigma_{1m})^2} \tag{2}$$

$$\sigma_a=\frac{1}{\sqrt{2}}\sqrt{(\sigma_{1a}-\sigma_{2a})^2+(\sigma_{2a}-\sigma_{3a})^2+(\sigma_{3a}-\sigma_{1a})^2} \tag{3}$$

where σ_m is the effective mean stress, σ_a is the effective stress amplitude, σ_{1m}, σ_{2m}, σ_{3m} are the principal mean stresses, and σ_{1a}, σ_{2a}, σ_{3a} are the principal stress amplitudes experienced. The principal stresses σ_1, σ_2, σ_3 were first extracted at each integration point for the combined pulsatile and bending loading conditions. These principal stresses were used to calculate the principal mean stresses and stress amplitudes. Once the principal mean stresses and stress amplitudes were determined, the effective mean stress and stress amplitude were then calculated at each integration point using the above equations.

The Fatigue Safety Factor (FSF) is defined as the ratio of the stress amplitude against the modified endurance limit, where the stress amplitude is the stress difference and the mean stress is the average stress on the element stresses. It quantifies the proximity of the mean

stress and stress amplitude at any given numerical integration point to the limiting Goodman curve. The integration points were used instead of nodal points in this study for accuracy and consistency reasons. While the integration points do not allow for recovered surface stresses, they offer the true exact solution without any extrapolation errors associated with nodal values. Fatigue Safety Factor less than 1.0 indicates a fatigue failure.

$$FSF = \frac{\sigma_e}{\sigma_a} \tag{4}$$

The ABAQUS/Standard finite element solver was used to perform the stent fatigue analysis. In order to prevent shear locking induced by bending loads, the stent struts were modeled using C3D8I fully integrated 3D solid elements with incompatible modes. The models were three-layers deep through the thickness and contained six elements in the width dimension to ensure that stress variation was adequately captured (Fig. 9). Mesh density studies of similar problems were performed to select the appropriate mesh density for the representative stress and strain distribution throughout the stent. It was concluded from the studies that the maximum stresses with the selected 6x3 mesh were able to converge within 5% of the true values. The mid-section of the stent was free to deform during crimping and expansion. Contact surfaces were defined at the strut edges to prevent inter-penetration between the struts during the crimping process. Additional contact surfaces were imposed as needed on the outer and inner stent surfaces to provide stent interaction with the crimping and expanding rigid surfaces during the crimping and expansion processes. The analytical rigid surfaces were defined to change in radius with each increment during the simulation. Contact was removed between the stent and the rigid surface during the recoil phases to allow the stent free deformation. The recoil process resulted in the relaxation of elastic strain energy and did not incur any change in the plastic strain distribution. A pressure of 180 mmHg (systolic) and 80 mmHg (diastolic) was used during steps 5-6 to simulate the cyclic fatigue loading applied to the stent by the blood pressure. In order to account for the loading imposed by the arterial wall, the arterial pressure loading corresponding to the interaction between the stent and the artery was imposed on the stent. The bending fatigue model consisted of four stent rings, approximately 1/3 of the single stent length. When two stents are deployed in a tortuous vessel and overlapped, the overlapped section is relatively stiff compared to the other two free ends. Therefore, the overlapped section of the stent was considered to be the fixed end with the non-overlapped section of the stent hanging free. The analytical rigid surface was defined to change in bending curvature during the simulation. The applied bending curvatures to the FEA model were calculated based on the average bending angles measured from fluoroscopic images of the cadaveric study.

4. Results and discussion

4.1 Respiration-induced Stent Bending Angle Measurement

Figures 10 and 11 show the representative fluoroscopic images of the stented renal arteries at simulated inspiration and expiration positions for the single and overlapped stents, respectively. As shown, the stents were subjected to bending during respiration with significant rigid body motion (translation and rotation) involved. Rigid body motion does not contribute to the stent deformation and was therefore ignored in the analysis. It is

interesting to note that, for the single stent configuration, the stented portion of the renal arteries was relatively straight (indicating minor bending), thus pushing the vessel bending distally towards the kidney during expiration. However, for the overlapped stent configuration, the overlapped stents took the bending curvature of the renal arteries smoothly but they were apparently subjected to greater degree of bending.

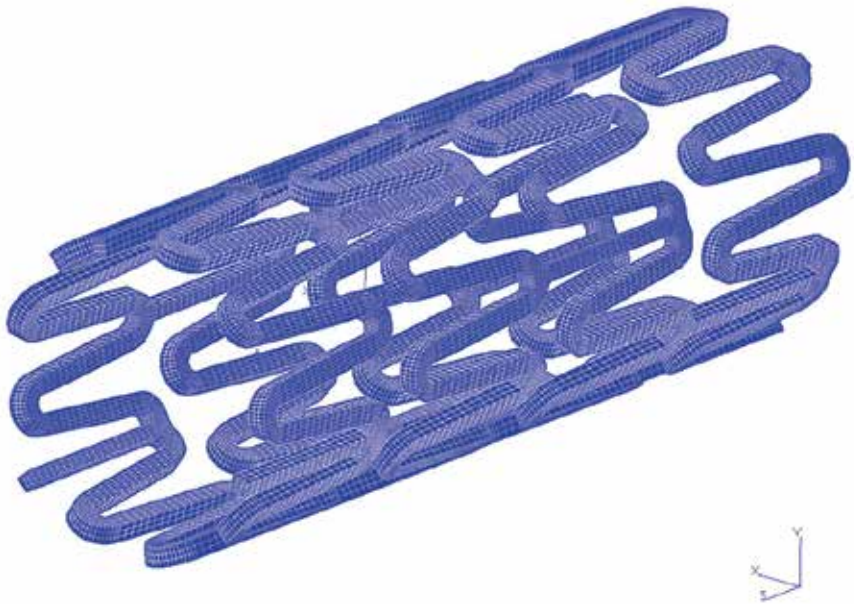

Fig. 9. A 6x3 mesh stent finite element model for combined cardiac pulsatile fatigue and respiratory bending fatigue

Kidney motion during respiration results in bending of the renal arteries, thereby deforming the longitudinal axis of the stent into a curved line. Figure 12a illustrates the deflection curve of a stent subjected to bending. A line tangent to the deflection curve at the stent end forms angle θ to the x-axis which represents the bending angle of the stent. When drawing tangent lines to the deflection curve from both ends, based on analytic geometry, the acute intersection angle of these two tangents is 2θ which is twice the defined bending angle. When the bending curvature is non-uniform along the stent length, the bending angle is defined as θ for one end and ϕ for the other end. As a result, the intersection angle of the two tangents is $\theta + \phi$ instead of 2θ. Procedures to determine the bending angle at the stent ends were:

1. Imported fluoroscopic images to AutoCAD software (AutoCAD LT 2000i).
2. Ignored rigid body motion (both translation and rotation).
3. Drew tangential lines to the deflection curve at the stent ends.
4. Measured the acute intersection angle $\theta + \phi$ of the two tangents.
5. Divided $\theta + \phi$ by 2. This is the average bending angle at the end points of the stent. The average bending angle can be related to the average curvature κ or average radius of curvature κ with the following definition:

$\kappa = 1/\rho = 2$ (average bending angle) / L = $(\theta + \phi)$ / L,
where L is the combined stent length.

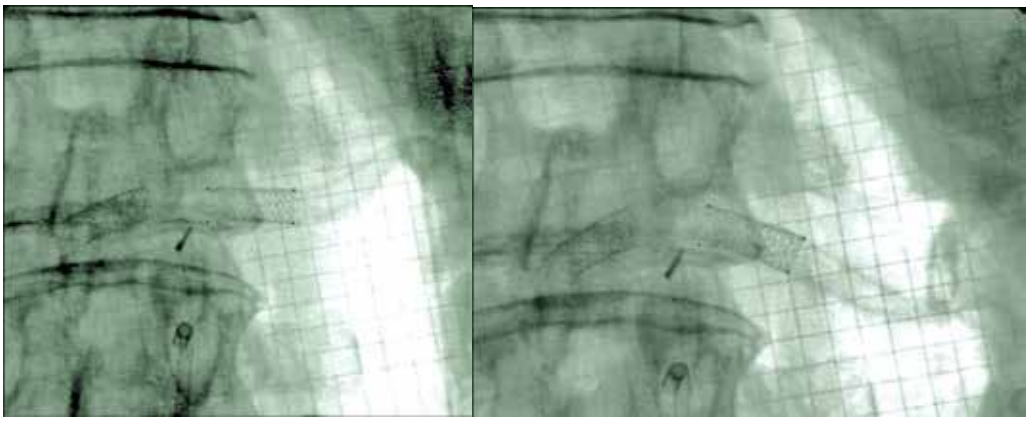

Fig. 10. (a, b) Fluoroscopic images of the stented renal arteries at simulated respiratory positions for the single stent case, (a) expiration, (b) inspiration

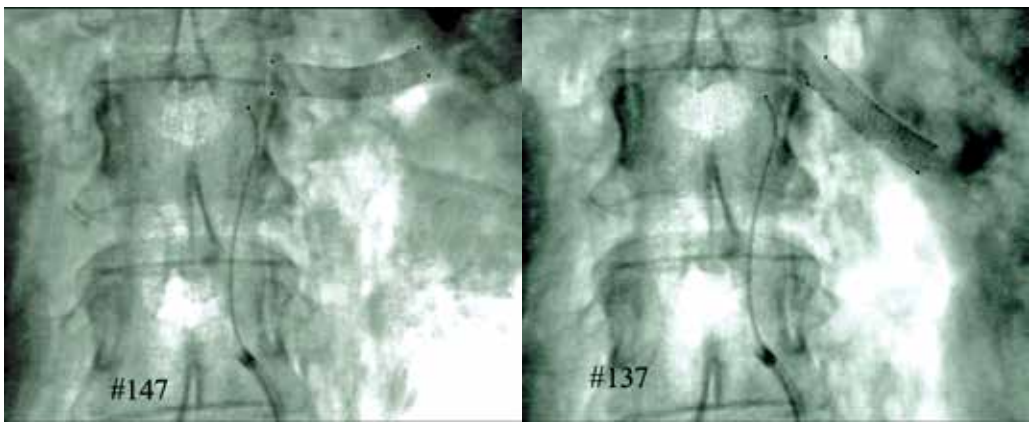

Fig. 11. (a, b) Fluoroscopic images of the stented renal arteries at simulated respiratory positions for the overlapped stent case, (a) expiration, (b) inspiration

The example shown in Figure 12b has the measured acute intersection angle of 20°. In this case, the resulting average bending angle at the stent end is half of that value, 10°, and its corresponding curvature is 0.011 mm^{-1} (radius of curvature: 92 mm). It is interesting to note that, since the intersection point of the two tangents is not at the stent mid point, this implies the stent bending deformation is not uniform.

Table 1 summarizes the average measured bending angle at the stent ends from fluoroscopic images and the calculated bending curvature for both single and overlapped stent cases. As shown, the change in bending angle between inspiration and expiration for the overlapped stent case was approximately 9°, which is considerably greater than the single stent case of 1.7°. The increased bending angle measured at the stent ends of the overlapped stents was partially due to larger bending curvature and partially due to longer overall stent length.

This information was used for the subsequent Finite Element Analysis wherein these bending angles/curvatures were superimposed upon forces associated with high hemodynamic pressure (blood pressure 180/80 mmHg) to simulate conditions achievable in the intended patient population.

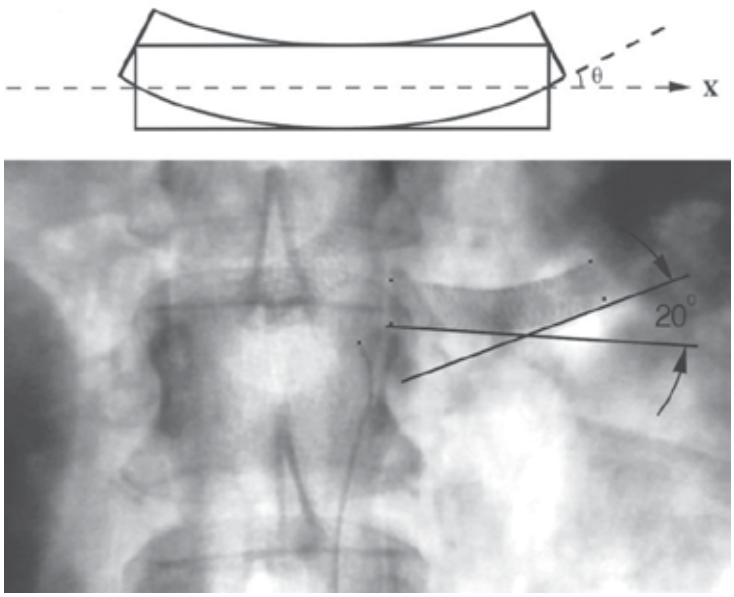

Fig. 12. (a) Deformations of a stent in bending (top), (b) Measured acute intersection angle at expiration (bottom)

	Inspiration		Expiration	
	Bending Angle	Curvature	Bending Angle	Curvature
Single Stent	3.90°	0.008 mm^{-1}	2.20°	0.004 mm^{-1}
Overlapped Stent	2.75°	0.003 mm^{-1}	11.75°	0.013 mm^{-1}

Table 1. Average bending angles and curvatures for the single and overlapped stent cases

4.2 Stent fatigue life

Stents deployed in the single and overlapped configurations were studied. The single stent configuration has been widely used in renal applications, whereas the overlapped stent configuration is to simulate a potential clinical situation where a physician has to deploy two stents overlapping at the ends. An 18 mm long stent, the standard implant size for renal stenting, was used in this study. For the overlapped stent configuration, two 18-mm long stents were overlapped at the stent ends by 3-4 mm, making the total stented renal artery length of approximately 32-33 mm. Although uncommon in renal stenting, this is a common clinical practice in other applications such as in the coronary artery stenting.

Based on the fluoroscopic images of the stented arteries during simulated motion, the single stent and the overlapped stents implanted in the renal arteries behave in a different way during the kidney motion. For the single stent configuration, the stented portion of the renal arteries was relatively short and straight, pushing most of the vessel tortuosity distally towards the kidney (Fig. 10). As a result, the stent was only subjected to minor bending and affected less by kidney motion. However, for the overlapped stent configuration, the longer overlapped stents were forced to conform to the bending curvature of the renal arteries and apparently subjected to a greater degree of bending than the single stent (Fig. 11).

Figures 13-15 show the contour plots of von Mises stress developed during the different steps of the loading process (crimping, expansion, and respiration-induced bending coupled with cardiac pulsatile pressure loading) for the studied balloon-expandable stent. The maximum von Mises stresses and maximum equivalent plastic strains at each loading step occurred on the inner surface of the curved crown "U", "Y", and "W" struts of the model. Figure 14 shows the comparison between FEA simulation and *in-vitro* expansion of the studied stent inside a tube. Results show that the developed FEA model is able to predict the stent expansion geometry very well. Figure 16, an enlargement of struts "U" and "W" at bending, illustrates that the inner surface of the curved crowns experienced high plastic deformation, while the straight links and the curved crown legs were under elastic deformation.

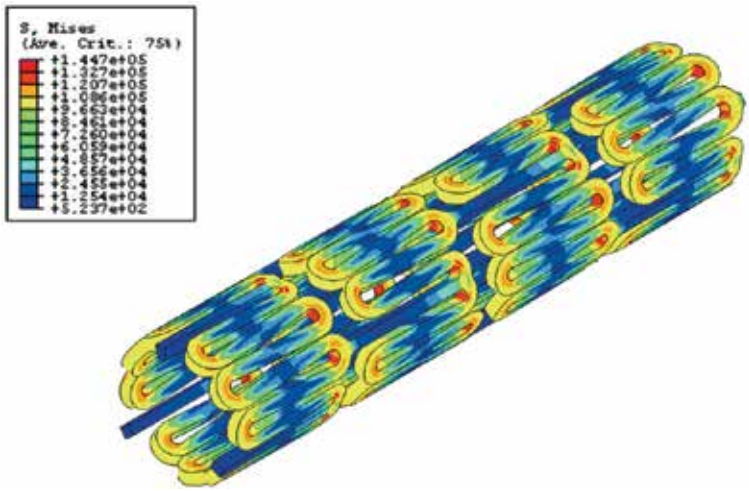

Fig. 13. Contour plots of von Mises stress for the studied balloon-expandable stent at crimping

A Goodman diagram of bending fatigue coupled with pulsatile fatigue is shown in Fig. 17 for the overlapped stent configuration. Calculated data were below the Goodman diagram failure line, indicating the studied balloon-expandable stents in the overlapped configuration are able to pass the fatigue life of 4×10^8 cycles under combined pulsatile and bending fatigue. Comparing Fig. 17b to Fig. 17a where the very same stent was assessed for pulsatile fatigue alone, it is shown that the calculated data of the overlapped stents under combined pulsatile and bending fatigue migrated towards the Goodman diagram failure line, indicating a drop in Fatigue Safety Factor and thus lower fatigue resistance during respiration. This finding also implies that, should longer stents be used clinically in renal applications, more pronounced respiration-induced bending may occur on stents. The degree of bending is likely to increase as the overall stent length becomes longer. The stented portion of the renal artery would become long enough such that it is forced to conform to the curvature the renal artery forms during respiration. Therefore, it is likely that a longer stent or multiple overlapped stents would have a shorter fatigue life than a shorter stent in renal applications. Since most of the renal artery stenosis occurs at the renal ostial region (renal artery and aorta junction), this short region should become the primary focus of the treatment instead of stenting a long section of the renal artery which requires a long stent or multiple overlapped stents.

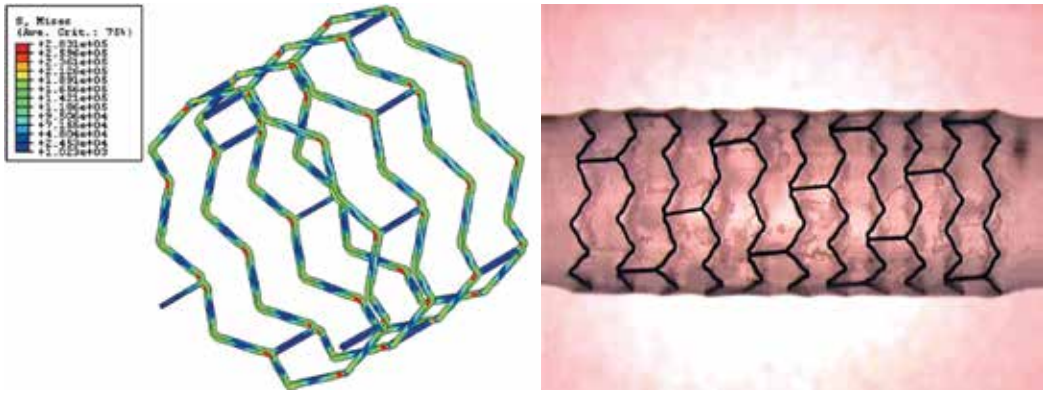

Fig. 14. (a, b) (a) Contour plots of von Mises stress for the studied balloon-expandable stent at expansion, (b) *in-vitro* stent expansion inside a tube

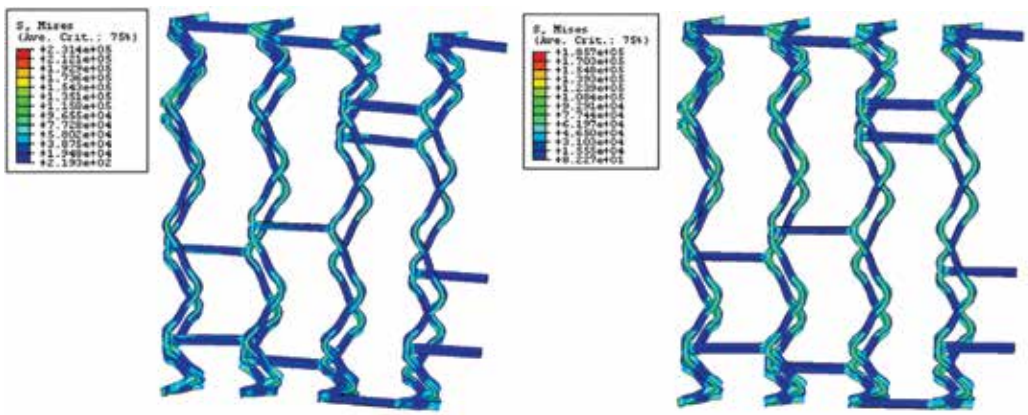

Fig. 15. (a, b) Contour plots of von Mises stress for the studied balloon-expandable stent under respiration-induced bending coupled with cardiac pulsatile pressure loading for the overlapped stent case, (a) expiration, (b) inspiration

It should be noted that the simulated distance between inspiration and expiration (about 40 mm) used in this study represents greater degrees of bending than the actual bending normally seen in the clinical overlapped stent case. The reason for this is that when two stents are overlapped, the entire renal artery becomes stiff enough such that, under similar respiratory forces, the kidney movement may be constrained and thus the movement is not as pronounced as 40 mm observed in other studies during normal breathing with no stents implanted. Therefore, it is hypothesized that the overlapped stent results presented in this paper were considered as the worst case scenario that may be more conservative than the actual.

The stent design also plays a critical role in the stent bending fatigue life. The stent design parameters such as strut width and thickness, crown radius, ring height, and connector number and geometry all have significant impact on the overall stent behavior. When the stent design is less flexible (in contrast to the studied balloon-expandable stent which is very flexible), it tends to straighten out the vessels considerably and pushes the vessel tortuosity distally. This could create kink points at the stent/vessel junctions, which could disturb the

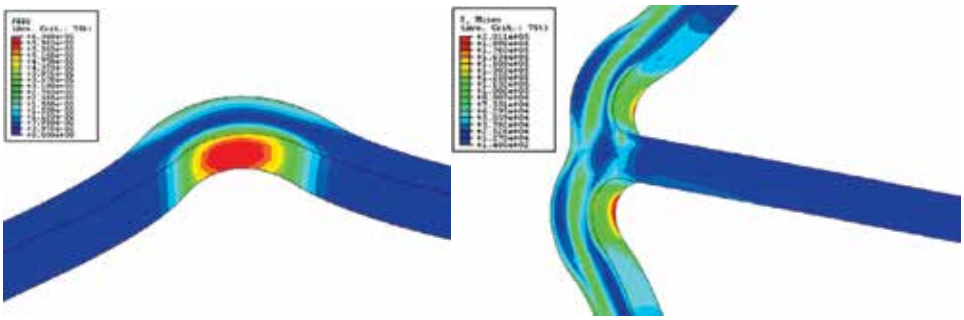

Fig. 16. (a, b) Zoom-in contour plots of the figure 15, (a) maximum strain contour plot at strut U, (b) maximum strain contour plot at strut W

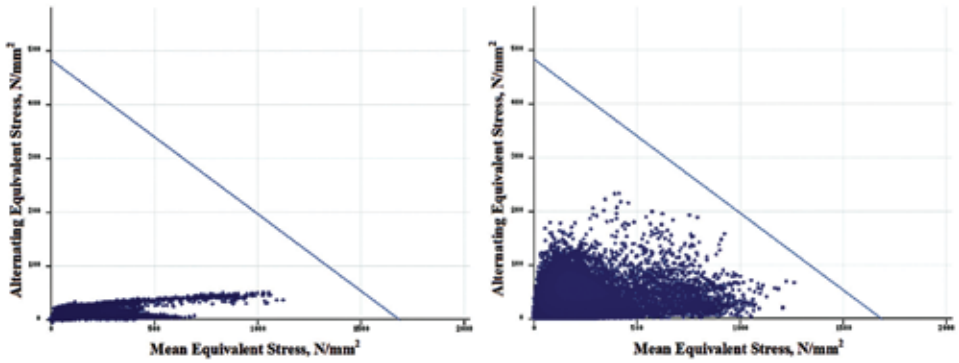

Fig. 17. (a, b) Goodman diagram of the studied balloon-expandable stent for the overlapped stent case, (a) pulsatile fatigue, (b) combined pulsatile and bending fatigue

blood flow and trigger adverse events such as vessel spasm and thrombosis. Such stiffer stent is also likely to have a shorter fatigue life due to the higher stresses created by the stent design itself and its interaction with the surrounding vessel movement. Therefore, it is very important to select the appropriate stent designs for specific applications. For applications subjected to greater degrees of bending such as the renal artery and the superficial femoral artery, a flexible stent design is preferred and should be used. However, for other applications such as carotid stenting where the primary concern is the potential stroke risk of emboli dislodgement from plaque, a stent with greater scaffolding should be considered as the main candidate to help pave the artery better.

5. Conclusion

The purpose of this study was to determine whether the motion of the kidneys during respiration, and subsequent bending of the renal artery, would negatively impact the stent fatigue life. To address this issue, stents were deployed into the renal arteries of two cadavers and respiratory motion was simulated by manual manipulation of the kidneys. Stent bending angles were measured from fluoroscopic images and Finite Element Analysis was performed.

For the single stent configuration, the stented portion of the renal arteries was relatively straight, thus pushing the vessel bending distally towards the kidney. However, for the

overlapped stent configuration, the overlapped stents took the bending curvature of the renal arteries smoothly but they were apparently subjected to greater degree of bending. Measured bending angles and curvatures applied to Finite Element Analysis indicated the stent fatigue resistance became lower and thus the stent life became shorter when the degree of stent bending increased.

This study concluded that the fatigue performance of the studied balloon-expandable stent is excellent under cardiac pulsatile fatigue alone, but compromised to certain degrees when respiration-induced renal artery bending fatigue was also considered. The change in bending angle was more significant for the overlapped stent configuration, resulting in lower fatigue life when compared to the implant of one single stent. Results showed that the studied ballon-expandable stent is not at risk for bending fatigue failure during respiratory motion for both single and overlapped stent configurations. It is strongly recommended that, in addition to the standard cardiac pulsatile fatigue analysis, similar bending fatigue life analysis should be performed on other vascular bed applications such as coronary arteries, carotid arteries, peripheral arteries, etc., in order to ensure the safety and efficacy of the new designed stents.

6. Acknowledgement

This work is supported by National Science Council of Taiwan (NSC 98-2218-E-002-043 and NSC 99-2218-E-002-018) and Abbott Laboratories (Abbott Vascular division). The authors gratefully acknowledge their continued support of the program.

7. References

Bessias, N.; Sfyroeras, G. & Moulakakis, K.G. (2005). Renal Artery Thrombosis Caused by Stent Fracture in a Single Kidney Patient. *Journal of Endovascular Therapy*, Vol. 12, No. 4, pp. 516-520.

Bjork, V.O.; Lindblom, D. & Henze, A. (1985). The Monostrut Strength. *Scand J Thor Cardiovasc Surg*, Vol. 19, pp. 13-19.

Blum, U.; Krumme, B.; Flugel, P.; Gabelmann, A.; Lehnert, T.; Buitrago-Tellez, C.; Schollmeyer, P. & Langer, M. (1997). Treatment of Ostial Renal-Artery Stenoses with Vascular Endoprostheses after Unsuccessful Balloon Angioplasty. *New England Journal of Medicine*, Vol. 336, pp. 459-465.

Draney, M.; Zarins, C.K. & Taylor, C.A. (2005). Three-Dimensional Analysis of Renal Artery Bending Motion During Respiration. *Journal of Endovascular Therapy*, Vol. 12, pp. 380-386.

Garrett, H.E. Jr. (2001). A Human Cadaveric Circulation Model. *J Vasc Surg*, Vol. 33, pp. 1128-1130.

Harrison, W.J. & Lin, Z.C. (2000). The Study of Nitinol Bending Fatigue, *Proceedings of the International Conference on Shape Memory and Superelastic Technologies*, Pacific Grove, CA, April 2000, pp. 391-396.

Hsiao, H.M.; Prabhu, S.; Nikanorov, A. & Razavi, M. (2007). Renal Artery Stent Bending Fatigue Analysis. *ASME J Medical Devices*, Vol. 1, No. 2, pp. 113-118.

Hsiao, H.M.; Nikanorov, A.; Prabhu, S. & Razavi, M. (2009). Respiration-induced Kidney Motion on Cobalt-Chromium Stent Fatigue Resistance. *J Biomed Mater Res Part B: Appl Biomater*, Vol. 91B, No. 2, pp. 508-516.

Marrey, R.V.; Burgermeister, R.; Grishaber R.B. & Ritchie R.O. (2000). Fatigue and Life Prediction for Cobalt-chromium Stents: A Fracture Mechanics Analysis. *Biomaterials*, Vol. 27, pp. 1988-2000.

Moerland, M.A.; van den Bergh, A.C.; Bhagwandien, R.; Janssen, W.M.; Bakker, C.J.; Lagendijk, J.J. & Battermann, J.J. (1994). The Influence of Respiration Induced Motion of the Kidneys on the Accuracy of Radiotherapy Treatment Planning, a Magnetic Resonance Imaging Study. *Radiotherapy and Oncology*, Vol. 30, No. 2, pp. 150-154.

Pelton, A.R.; Gong, X.Y. & Duerig, T.W. (2003). Fatigue Testing of Diamond-shaped Specimens, *Proceedings of the International Conference on Shape Memory and Superelastic Technologies*, Menlo Park, CA, pp. 293-302.

Robertson, S.W. & Ritchie, R.O. (2007). In Vitro Fatigue-crack Growth and Fracture Toughness Behavior of Thin-walled Superelastic Nitinol Tube for Endovascular Stents: A Basis for Defining the Effect of Crack-like Defects. *Biomaterials*, Vol. 28, pp. 700-709.

Rocha-Singh, K.; Jaff, M.R. & Rosenfield, K. (2005). Evaluation of the Safety and Effectiveness of Renal Artery Stenting after Unsuccessful Balloon Angioplasty. *Journal of the American College of Cardiology*, Vol. 46, No. 5, pp. 776-783.

Sahin, S.; Memis, A.; Parildar, M. & Oran, I. (2005). Fracture of a Renal Artery Stent due to Mobile Kidney. *Cardiovascular Interventional Radiology*, Vol. 28, pp. 683-685.

Schwartz, L.H.; Richaud, J.; Buffat, L.; Touboul, E & Schlienger, M. (1994). Kidney Mobility During Respiration. *Radiotherapy and Oncology*, Vol. 32, No. 1, pp. 84-86.

Wagner, M.; Sawaguchi, T.; Kaustrater, G.; Hoffken, D. & Eggler, G. (2004). Structural Fatigue of Pseudoelastic NiTi Shape Memory Wires. *Mater Sci Eng A*, Vol. 378, pp. 105-109.

Zeller, T.; Frank, U.; Muller, C.; Burgelin, K.; Sinn, L.; Bestehorn, H.; Cook-Bruns, N. & Neumann, F. (2003). Predictors of Improved Renal Function after Percutaneous Stent-supported Angioplasty of Severe Atherosclerotic Ostial Renal Artery Stenosis. *Circulation*, Vol. 108, pp. 2244-2249.

20

Synthesis and Characterisation of Styrene Butadiene Styrene Based Grafted Copolymers for Use in Potential Biomedical Applications

James E. Kennedy and Clement L. Higginbotham
Department of Polymer Engineering,
Athlone Institute of Technology, Dublin Rd, Athlone, Co. Westmeath,
Ireland

1. Introduction

In the annals of history the evolution of the synthetic rubber industry can be traced to the early 1930s where the first emulsion polymerised styrene butadiene rubber known as Buna S was prepared by I. G. Farbenindustrie in Germany. But it was not until the US Government in 1940 established the Rubber Reserve Company, a stockpile of natural rubber and the development of a synthetic rubber program came into full fruition. However, when the United States entered World War II, the synthetic rubber plants owned by the US Government were either closed or sold to private industry between the years 1946 and 1955, and from this the development of this formidable technology began. In the early 1960's one primary objective prevailed and that was the economical polymerisation of polyisoprene with a high cis–1,4 structure, which is the synthetic version of natural rubber(Holden & Hansen, 2004). Around this time, workers at Shell investigated lithium metal initiators for isoprene polymerisation and found that alkyllithiums yielded some interesting results. In particular, there was no chain termination or chain transfer steps present. Thus, when all of the original monomer was consumed, the polymer chain still remained active and could initiate further polymerisation if more monomer, either of the same or different species, were added (Holden & Hansen, 2004). Parallel with these developments, tri-block copolymers using difunctional initiators were also reported in the literature (Szwarc et al., 1956; Szwarc, 1956). These block copolymers were produced under conditions that gave polydiene segments a relatively low 1,4 content(Holden & Hansen, 2002). However, poor elastomeric properties were acknowledged whereby the rheological properties of both polybutadiene (PB)(Gruver, 1964) and isoprene(Holden, 1965) resulted in the materials exhibiting Newtonian behaviour and the viscosities of the pure polymers approach constant values as the shear rate approaches zero. This behaviour resulted in bales of these elastomers appearing to be solid but in fact behaved as viscous liquids which hindered both their storage and commercial attractiveness. In light of this, Shell chemical research polymerised polydiene elastomers with various molecular weights to combat this problem (Holden & Hansen, 2004). Later studies included work on block copolymers resulting in the formation of a material which contained short blocks of polystyrene on either end of the elastomeric chain to form a styrene butadiene styrene (SBS), as illustrated in Figure 1. In contrast to the diene homopolymer, these block copolymers demonstrated, non-Newtonian

behaviour, high tensile strength, high elongation and rapid and almost complete recovery after elongation (Holden & Hansen, 2004; Holden, 1962)

Fig. 1. Structure of a styrene-butadiene-styrene block copolymer.

Depending on the overall butadiene content, SBS block copolymers can either be used as thermoplastic elastomers (Holden & Kricheldorf, 2004) or as blend components enhancing the mechanical performance of transparent polystyrene (PS)-based plastics (Knoll & Niessner, 1998) and (Wagner, 2004). A very similar behaviour is also found for styrene–isoprene (SI) block copolymers. Due to their compatibility with PS and the wide range of possible mechanical properties, these two materials dominate the market for block copolymers in plastics even over 40 years after their discovery (Nestle et al.,2007).

2. Phase separation of SBR and SBS copolymers

One of the most important properties of a SBS structure is the phase separated system, where the two phases (polystyrene and polybutadiene) retain many of the properties of their respective homopolymers. For example, tri-block copolymers have two glass transition temperatures (T_g) which are characteristic of the respective homopolymer (Polystyrene ~100°C and Polybutadiene ~-90°C) whereas styrene butadiene rubber copolymers have a single intermediate T_g. Regarding the aforementioned material, experimentally a single glass transition can be found at about -65°C which is in accordance with a material with a styrene content of 23% (Van der Vegt, 2005). A graphic illustrating the glass rubbery transition of the two aforementioned copolymers is presented in Figure 2. Thus, at room temperature the polystyrene phase is strong and rigid where as the polybutadiene phase is soft and elastomeric.

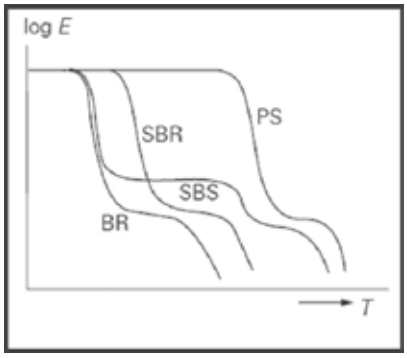

Fig. 2. The glass–rubber transitions for styrene and butadiene copolymer systems (Van der Vegt, 2005).

If the polystyrene phase is only a minor part of the total volume, it is then reasonable to postulate a phase structure as illustrated in Figure 3. From this structure, the polystyrene phase consists of separate spherical regions known as domains. Since both ends of each polybutadiene chain are terminated by polystyrene segments, these rigid domains act as

multifunctional junction points to give a crosslinked elastomer network similar in many respects to that of a conventional vulcanised rubber (Brydson, 1978). Thus, when SBS is heated, the domains soften and the network loses its strength resulting in the ability of the block copolymer to flow which is one of the main characteristics associated with these types of thermoplastic elastomers. When the heated block copolymer is cooled, the domains become hard and the original properties are regained.

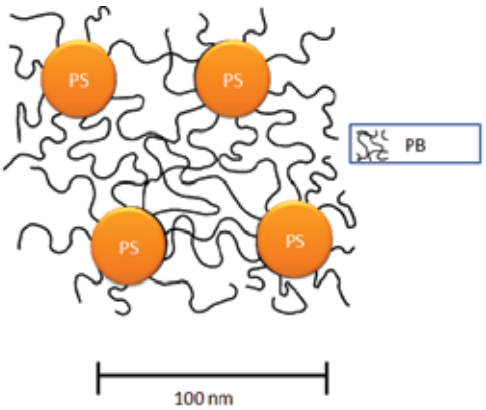

Fig. 3. Phase structure of SBS.

Therefore, when one or more blocks are capable of crystallising, additional transitions (corresponding to the T_ms of the blocks) will be observed whilst both the morphology and solution properties will be more complicated (Brydson, 1978).

3. Morphology evaluation of SBS

Three types of microphase segregation can occur within SBS systems in which one or another of the components are either in spheres, rods (cylinders) or lamellae where the morphology depends on the concentrations of styrene or butadiene used. In an ideal situation the greatest interest is in a system by which the polystyrene segments are concentrated into spherical domains. If, however, a system was produced in which one of the components exists in cylindrical or rod like domains uniformly oriented in a single direction, or the two components were arranged in lamellae, then it should be possible to obtain rubbers which demonstrate anisotropic mechanical properties (Brydson, 1978). According to Adhikari et al.,(2003), when investigating the deformation behaviour of styrene butadiene star block copolymer/hPS blends, the microphase separated blends with PS particles in lamellar matrix exhibited debonding at the particle-matrix interface. Therefore, the morphology formation in block copolymers is influenced by a number of factors: these include monomer types, chemical composition and even the processing history. Burford et al., (2003) found that interpenetrating networks (IPNs) made by the polymerisation/crosslinking of styrene in the dispersed styrene rich phase of a block copolymer within a crosslinked elastomeric matrix formed networks which combined stiffness and toughness. This formation of IPNs can allow the production of materials with controlled morphologies and the greater probability of synergistic property enhancement. But the morphologies of these IPNs are generally complex because they show varying degree of phase separation, with phases varying in size, shape and definition at interfaces. Adhikari and co-workers (2004) have researched into the deformation behaviour of

styrene/butadiene block copolymers with a polystyrene content of ~ 70%. They noted that the phase separation behaviour of the copolymers was found to be strongly affected by asymmetric molecular architecture. It has been demonstrated that the phase behaviour of a binary block copolymer/homopolymer mixture is primarily governed by the length of the homopolymer chains relative to the corresponding block of the block copolymer (i.e. the ratio $N_{homo\text{-}A}/N_{block\text{-}A}$, where $N_{homo\text{-}A}$ and $N_{block\text{-}A}$ represent the degree of polymerisation of added homopolymer A and corresponding block A in the block copolymer AB respectively). Thus, there is competition between microphase and macrophase separation in a binary block copolymer/homopolymer blend composition. In such blends, according to Adhikari et al.,(2004) low molecular weight homopolymer is solubilised within the corresponding block of the copolymer at low concentration. As the molecular weight of homopolymer approaches that of the corresponding molecular weight of PS or PB in the copolymer, it tends to segregate to the middle of the microdomains. However, if the molecular weight of the homopolymer is larger than that of the corresponding block of the block copolymer, macrophase separation tends to predominate.

4. Microphase separation of SBS copolymer

Microstructures occur when SBS copolymers undergo microphase separation due to the thermodynamic incompatibility of PS and PB blocks. This separation is a result of the miscibility gap of polybutadiene and polystyrene in the solid-state and is crucial for the properties of the material. Since both the chain architecture of the block copolymer and the microphase separation affect the mobility of the butadiene-rich phase (Nestle et al., 2007). These elements, rich in one block, take the form of either spherical, cylindrical or lamellar domains (as previously discussed) dispersed in a continuous matrix of the other component. The phase-separated structure for SBS contains two homogeneous, nearly pure phases and a third diffuse interphase (Spaans et al., 1999). A schematic of these phases is illustrated in Figure 4.

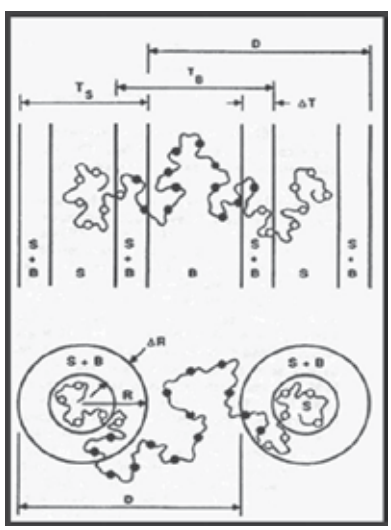

Fig. 4. Schematic representation of SBS molecule embedded in a phase separated microstructure consisting of matrix B, core S and a broad interphase of mixed S and B. S represents styrene and B represents butadiene (Spaans et al., 1999).

Spaans et al., (1999) has correlated this information with a typical DSC thermograph of SBS to represent the locations of these microphase domains. A graphical representation illustrating Spaans concept is shown in Figure 5.

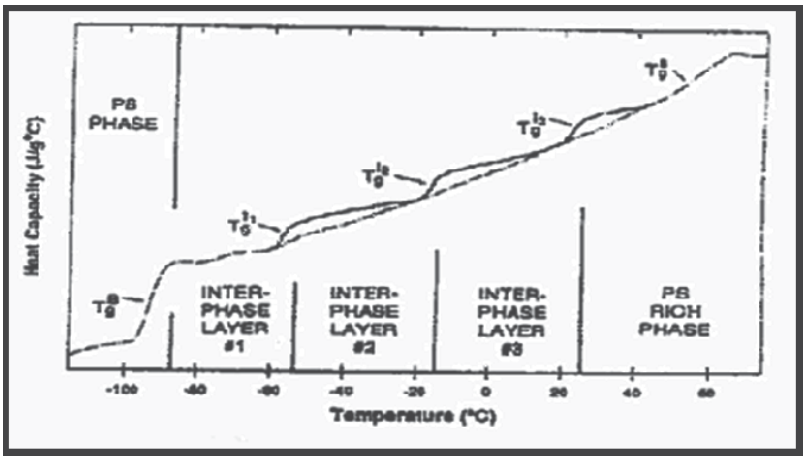

Fig. 5. A graphical representation of a DSC thermograph illustrating the Tg changes in the local heat capacity at a sequence of positions through the interfacial region, as the sample experiences a broad temperature range (Spaans et al., 1999).

5. Thermal properties of a SBS copolymer

Based on experimental data carried out by the authors, a linear tri-block SBS with 69% butadiene content under the trade name Kraton D1101 (see Table 1) was investigated. As presented in Figure 6, a T_g value at -92°C was located in the butadiene rich microphase domain which coincides with the T_g (-90°C) of pure PB and this result is in agreement with the findings of Spaans et al.,(1999) and Kennedy et al., (2009). The glass transition of the PS domain in SBS copolymer can be detected at around 67°C which corresponds with the findings of Spaans et al.,(1999) , Kennedy et al., (2009) and Mohammady et al.,(2005). This value was significantly lower than the T_g at 100°C for a PS homopolymer of comparable molecular weight.

Butadiene/styrene ratio (wt%)	69/31
Total molecular weight	102,000g/mol
Microstructure of PB	
1,4-trans (%)	42
1,4-cis (%)	49
1,2 (%)	9

Table 1. Physical properties of Kraton D1101

The glass transition for the PS phase in thermoplastic elastomer block copolymer tends to be lower than that of pure homopolymer of the same chemical structure which is due to the

entrapment of some centre block rubbery segments, a kinetic effect which is not thermodynamically favoured (Spaans &Williams, 1995; Escobar et al., 2003). This lowering effect is a consequence of premature molecular motions in the PS domain induced by PB segmental mobility. Munteanu and Vasile (2005) have stated that copolymers with microphase separated morphology can be considered as finite confined systems. This confinement applied by the PB matrix to the PS discrete phase may decrease the T_g of PS in SBS. According to Muhammady *et al*., (2001) the interfacial interaction and miscible fraction at the domain boundaries also lowers the value of the glass transition. Between T_g values of PB and PS a broad continuous curvature is evident on the DSC thermograph shown in Figure 6. This curvature should be found in all block copolymers which have homogeneous microphases present, as stated by Spaans *et al*., (1999). At 241°C a thermal transition occurs for SBS block copolymer which is believed to be a first order phase transition and corresponds to findings in literature (Spaans et al., 1999; Kennedy et al., 2009). At this transition the polymer merges into segmental homogeneity resulting in a disorganised/homogeneous state. It has been well established that when block copolymers such as SBS are heated above the upper glass transition temperature, the microstructure of the polymer will be eventually destroyed and the block copolymer will form a homogenous phase. The critical temperature at which this occurs is called an order-disorder transition (ODT) temperature (Spaans et al., 1999; Kennedy et al., 2009; Spaans & Williams, 1995).

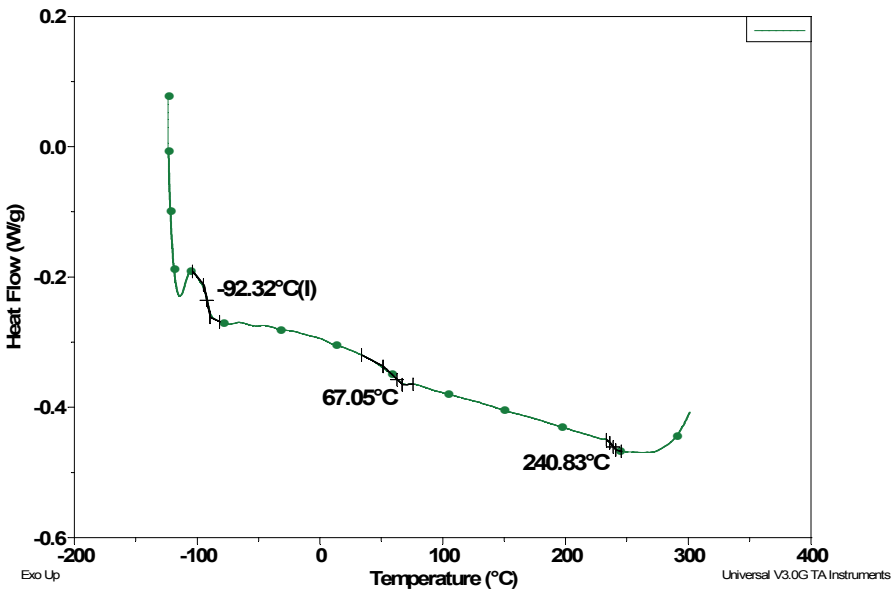

Fig. 6. A DSC thermograph of a SBS copolymer (Kraton D1101), where the T_g values for PB and PS are -92°C and 67°C respectively. The separation temperature, T_s is 241°C.

6. A review of Styrenic graft copolymerisation

Huang and Sundberg (1995a, 1995b, 1995c, 1995d), have published a number of studies on the graft copolymerisation of styrene, benzyl acrylate and benzyl methacrylate onto a cis-

polybutadiene. In their kinetic study, they have shown by the use of different initiators two possible mechanisms occurred where initiators such as benzoyl peroxide (BPO) can abstract allylic hydrogen atoms from polybutadiene while azobisisobutyronitrile (AIBN) cannot extract the allylic hydrogen atom. According to Jiang and Wilkie (1998) neither initiator appears to have significant reactivity towards addition of primary radicals to the double bond of the polybutadiene and the allylic radicals which are generated by hydrogen abstraction can initiate polymerisation of reactive monomers such as styrene and methacrylates leading to the formation of graft copolymers. Graft copolymerisation will still occur for monomers which are initiated by the allylic backbone radicals. This process occurs by addition of the growing polymeric radical to the polybutadiene double bond, producing a saturated alkyl radical which is capable of further initiation of low reactivity monomers. De Sarkar et al.,(1999) found that 1,2 -vinyl double bonds of butadiene occur in a pendant position along the polymer chain making bonds more accessible for grafting. They also postulated that the order of reactivity for vinyl groups are, (*i*) saturation of 1,2-vinyl bonds is easier than 1,4–trans and (*ii*) PB is directly proportional to the amount of 1,2-vinyl bonds (De Sarkar et al., 1999). The various structural sequences associated with butadiene are illustrated in Figure 7.

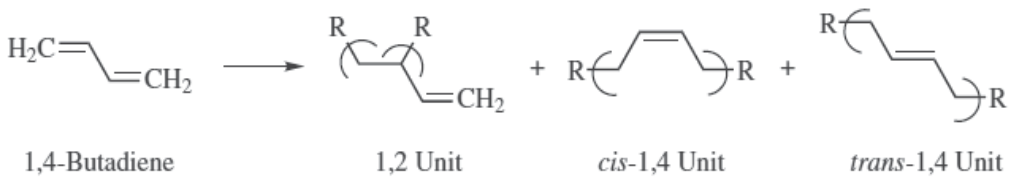

Fig. 7. Various structural formations associated with butadiene.

In the research performed by Madhusudhan and Raghunath (1999), maleic anhydride (MAH) was grafted onto ABS by the addition to the double bond initiated by BPO. Sheng and co-workers (1990) found that BPO initiated the removal of an allylic hydrogen atom while AIBN acted upon the addition of the double bond of SBR which is in agreement with the findings of Huang and Sundberg(1995a, 1995b, 1995c, 1995d). Mrrov and Velichksva (1993) described how MAH was grafted onto SIS only by the removal of an allylic hydrogen atom, whereas Zhang and Li (2003) have investigated the grafting mechanism of SBS with MAH using BPO and AIBN. They found that the variation of C=C content in SBS-g-MAH was used to verify the different graft mechanisms of BPO and AIBN. They concluded that the grafting reaction occurs by the addition onto C=C bond when AIBN was used, while the removal of an allylic hydrogen atom was evident when BPO was used to initiate the reaction.

7. Grafted copolymers with potential medical application

The latest wave of biomedical materials can strengthen the capabilities of many of today's medical products. Some polymeric materials demonstrate properties such as lubricity, biocompatibility and antimicrobial action on device surfaces while others may crack, tear, slip and flake off medical devices due to inherent design flaws. There has been considerable

interest and activity in the application of synthetic polymers in medicine, particularly for surgical and dental implants. The most critical property of a polymeric material is that it has acceptable tissue compatibility. If this criterion is not met, local tissue irritation may result.
In general, the chemical structure, electric charge, hydrophilicity and hydrophobilicity, surface roughness, micro-heterogeneity, and flexibility of the materials affect the performance of cells and tissues on the materials (Minoura,1993; Yang & Tsai, 2010). Biocompatibility can be characterised by a whole series of negatives, for example that the material was non-toxic, non-irritant, non-thrombogenic, non-carcinogenic and so on. Such a state of compatibility was most likely to be achieved by a material being inert and unrecognisable by the tissue. A desirable property of a synthetic polymeric material used in biomedical applications is that it has acceptable tissue compatibility. If this criterion is not met, local tissue irritation may result. One particular method used to obtain these desired properties is grafting hydrophilic compounds namely a hydrogel onto hydrophobic backbones. Hydrogels have physical properties similar to those of human tissue and possess excellent tissue compatibility and are used as biomedical materials. The main disadvantages of hydrogels are their poor mechanical properties after swelling. To overcome this problem, Yang & Hsiue (1996) grafted hydroxyethyl methacrylate (HEMA) onto SBS via UV radiation. The mechanical properties of SBS-g-HEMA were found to be superior to those of poly(HEMA) and were identical to those of SBS. From their measurements, the contact angle and blood clotting time, the wetting and non-thrombogenic properties of SBS-g-HEMA were better than those of SBS. Yang *et al*., (1997) have also researched into the graft copolymerisation of dimethyl amino ethyl methacrylate (DMAEMA) with SBS and it was found that the degree of grafting was related to the irradiation time, DMAEMA concentration and temperature, but the adsorption of albumin and fibrinogen decreased with an increase in the amount of grafting. They continued on their work by the substitution of amino groups on the SBS-g-DMAEMA graft copolymer membrane which was treated with heparin to prepare the heparin containing SBS-g-DMAEMA (SBS-g-DMAEMA-HEP). It was found that, with increased grafting and heparin content, the surface tension and the water content of the SBS-g-DMAEMA membrane increased whereas the contact angle decreased (Yang et al., 1998). Over the past few years, N-isopropylacrylamide (NIPAAm) has appeared in the literature with increasing frequency (Durne et al., 2005; Zhang et al., 2005; Geever et al., 2008; Geever et al., 2007; Geever et al., 2006; kennedy et al., 2009). Lee and Chen (2001) have grafted N-isopropylacrylamide (NIPAAm) onto SBS via solution polymerisation using benzoyl peroxide as the initiator. This was carried out to improve the water absorption and thermo sensitivity of SBS. Thus, a biomedical material often needs to function dependably without significantly altering the physical or mechanical properties of the substrate. Kennedy et al.,(2009, 2010) have successfully grafted SBS with acrylic acid (AA) and SBS with N- isopropylacrylamide(NIPAAm) respectively via UV polymerisation techniques for use as a potential biomedical material and in doing so; they proved that the glass transition values for each of the grafted copolymers increased in the butadiene domain, thus proving that grafting had occurred.

8. Synthesis of graft copolymers of SBS via UV polymerisation

UV polymerisation has become a well established technology which has found a large number of industrial applications due to the relative ease in which the reaction occurs. In

general, a liquid resin containing a photoinitiator (Benzophenone (BP)), is transformed into a solid polymer simply by exposure to UV light (Xiang et al., 2001; Murata et al., 2004; Rohr et al., 2003; Kim et al., 2002). In order to ascertain a possible reaction site of the base polymer, Mateo et al.,(2000) investigated the photoreactions of model compounds of SBS structures 1-heptene, 3-heptenes and cumene. They concluded that the main photoreaction induced by BP in heptene derivatives, models of the cis, trans and vinyl-double bonds of the polybutadiene sequences, is the abstraction of an allylic hydrogen atom by the BP, and that, in minor extension of other hydrogen atoms of the heptene aliphatic chain. In developing grafted systems it was considered by the authors that the allylic hydrogen associated with butadiene in SBS copolymers reacted with the hydrogel monomers using benzophenone via UV polymerisation, as illustrated in Figures 7 and 8 respectively.

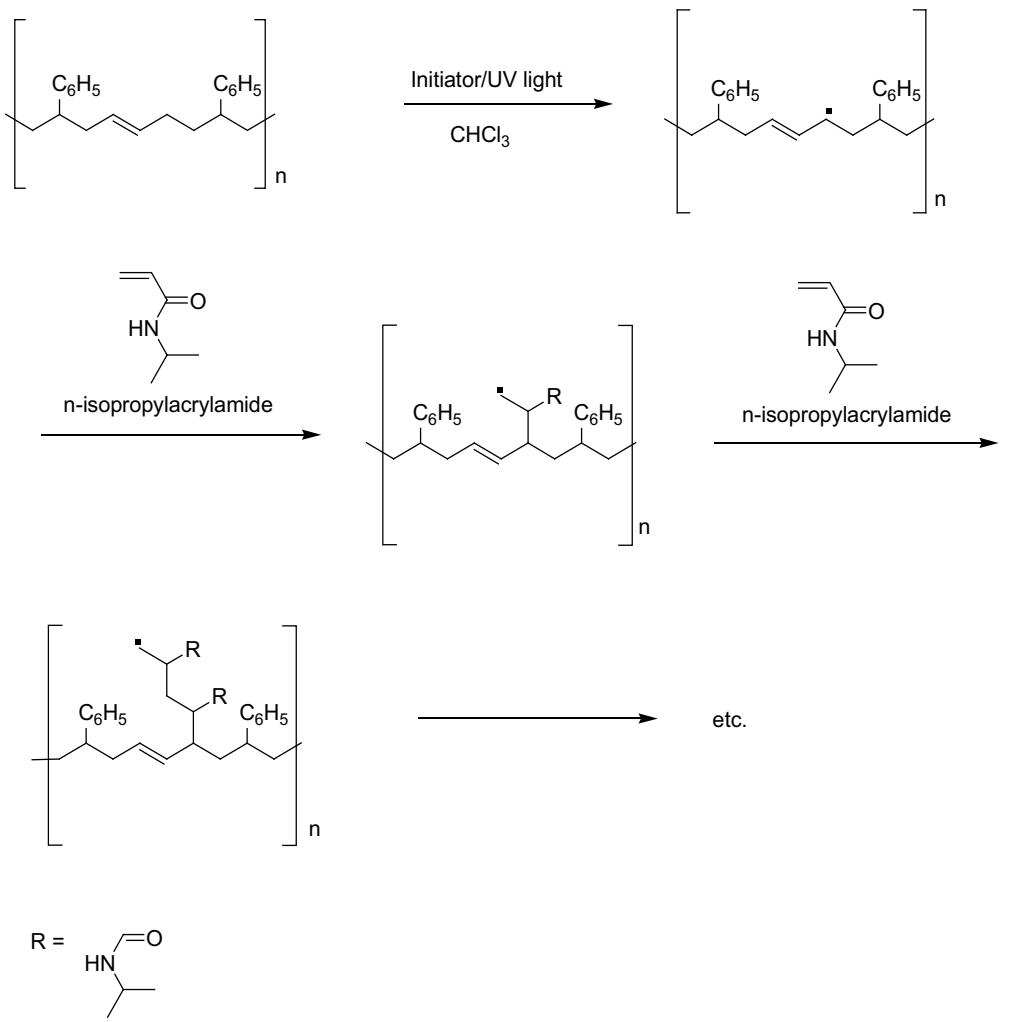

Fig. 7. A scheme showing the reaction of SBS and NIPAAm to yield SBS-g-NIPAAm copolymers (Kennedy et al.,2010).

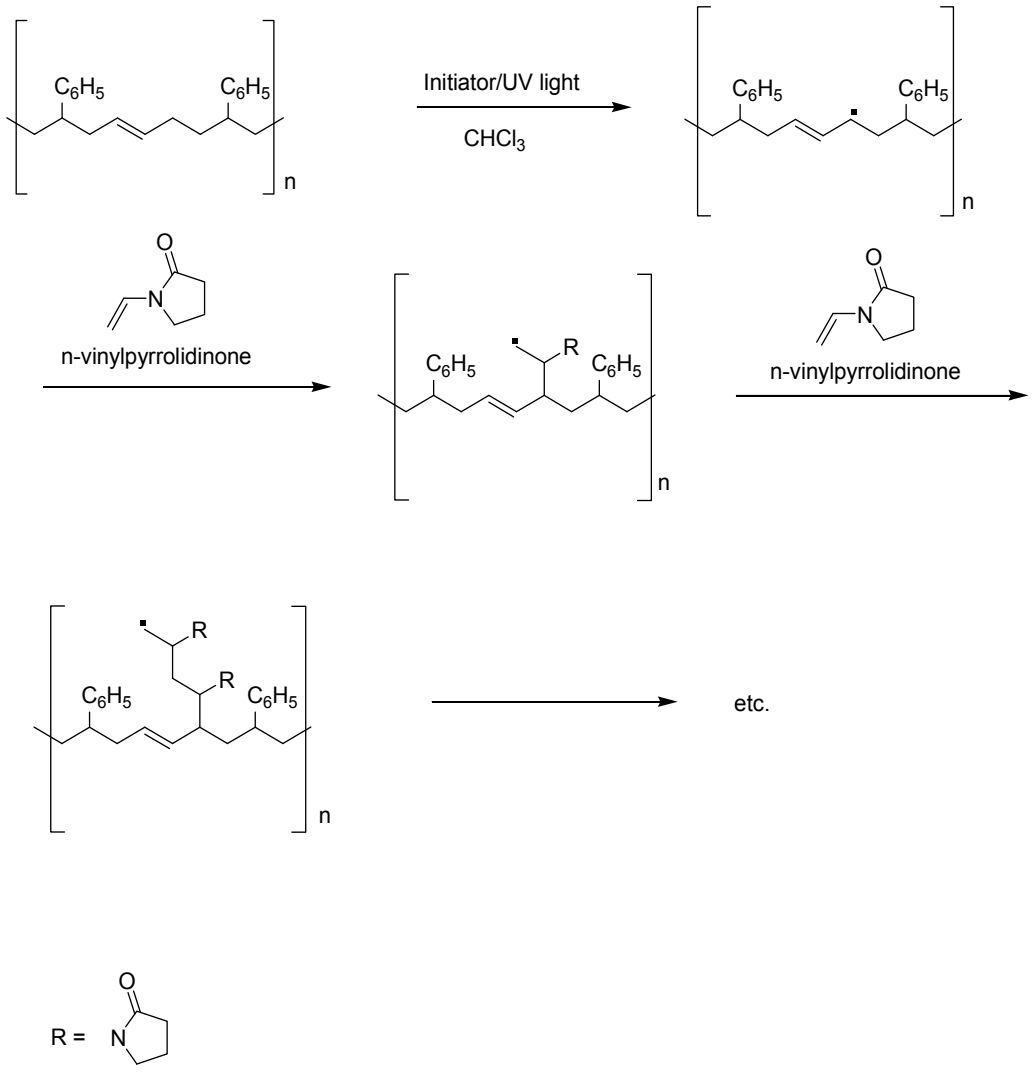

Fig. 8. A proposed scheme illustrating the reaction of SBS and NVP to yield SBS-g-NVP copolymers using Benzophenone as the initiator (Kennedy & Higginbotham, 2010)

9. Thermal-mechanical analysis of the grafted SBS copolymers

To appreciate the importance of these materials for biomedical use, one needs to understand the thermal properties associated with the grafted copolymers. From experimental data (Kennedy et al., 2010) the authors present DSC thermographs showing several concentrations of SBS-g-NIPAAm copolymers (Figure 9). As depicted by the DSC thermographs, exothermic variability existed in the temperature region between 50 and 200°C for each of the grafted copolymers. This variability was the result of both the breakdown of crosslink's which were formed within the SBS copolymer during UV polymerisation and the polymerisation of the monomers to form homopolymers. It was

found, by exposing SBS to concentrated UV light, crosslinking takes place which has an effect on the flexibility of the material. When analysing the butadiene domain, all of the grafted samples have a broad thermal transition when compared to the PB domain of SBS. According to Rohr et al.,(2003) graft copolymerisation can also occur between the homopolymers, thus creating branched or crosslinked architectures. However, within the PB domains, the grafted copolymers that contained higher concentrations (3, 3.5 and 4 mL) of monomer followed the same thermal profile as that of SBS. This behaviour suggests that the pure monomer reacted more readily with itself forming a homopolymer, thus reducing the amount of grafting taking place, thus, increasing the variability within the system. The grafted copolymers which contain monomer concentrations below 2.5mL have broader DSC thermographs within the butadiene rich domain resulting in T_g values of the grafted samples being shifted up wards in the sub ambient domain, suggesting that grafting had occurred within this region, which coincides with the reaction sequences as presented in Figure 7. Similar observations were also found when SBS was grafted onto NVP via DSC analysis.

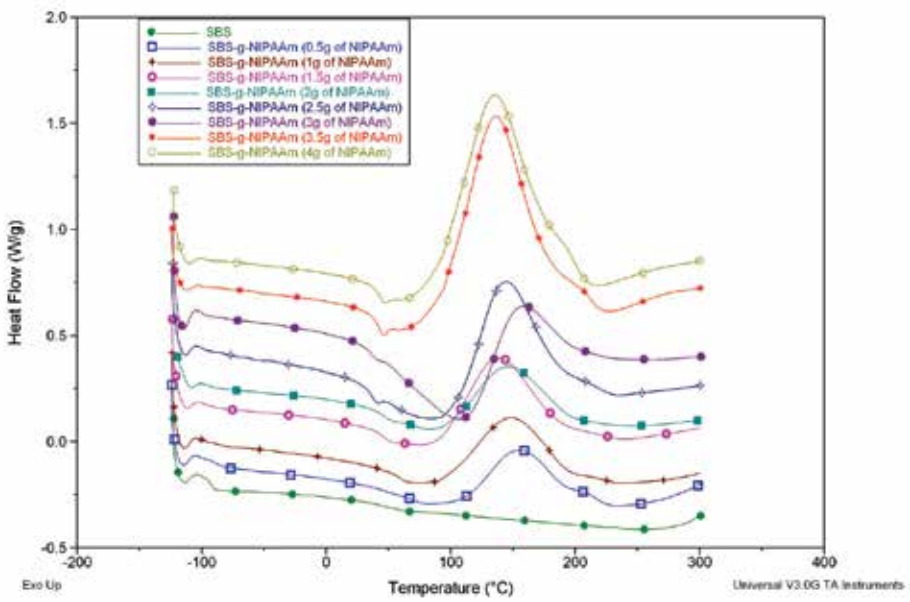

Fig. 9. DSC thermographs of SBS-g-NIPAAm resulting from the reaction of SBS and various concentrations (0.5, 1.0, 1.5, 2.0, 2.5, 3.0, 3.5 and 4.0 g) of NIPAAm.

From DSC analysis it can be speculated that grafting took place for each of the samples tested. However, to further verify the presence of grafting, Dynamic Mechanical Thermal Analysis (DMTA) studies can be utilised (Kennedy et al., 2010). In each of the loss tangent thermograms, illustrated in Figure 10, the peak height of the tan δ value corresponds to the glass transition (T_g) of the samples being tested. From thermogram shown in Figure 10, a tan δ value for SBS can be detected at -92°C which is associated with the polybutadiene segment. However, there was an increase in tan δ from -92°C to -79°C for non-washed SBS-g-NIPAAm copolymer, indicated that grafting had occurred. This reduction in the tan δ is an indication that the backbone of the SBS copolymer has lost some of its flexibility, due to

the grafting of a hydrogel to its backbone. To back up this claim, the samples were washed in chloroform under soxhlet extraction for eight days and the tan δ value shifted to -74°C. Therefore, it is evident that the tan δ values for each of the samples tested increased, establishing that grafting had occurred onto various butadiene segments along the SBS backbone. Thus, suggesting that grafting will increase the T_g of the PB phase by increasing the thermal energy required to free polymer molecules from additional constraints.

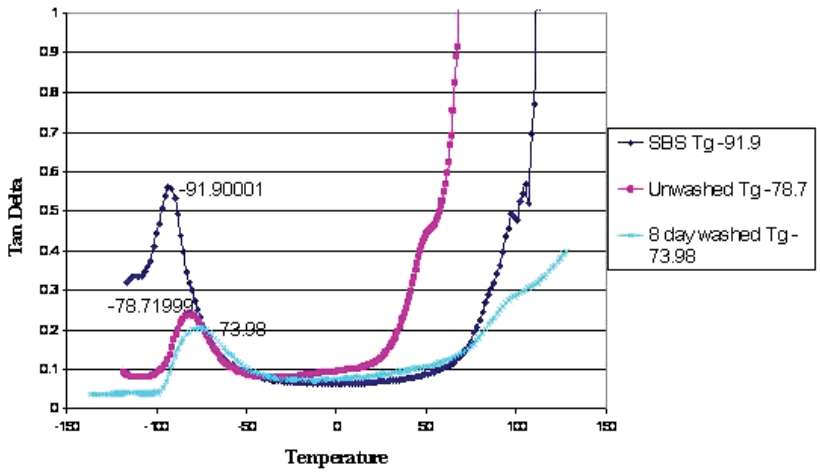

Fig. 10. DMTA spectra representing SBS, non-washed SBS-g-NIPAAm and washed SBS-g-NIPAAm samples after 8 days.

10. Spectral analysis of the grafted SBS copolymers

Infrared spectroscopy has been a valuable technique for materials analysis in the laboratory for over seventy years. An infrared spectrum represents a fingerprint of a sample with absorption peaks which correspond to the frequencies of vibrations between the bonds of the atoms making up the material. Because each material is a unique combination of atoms, no two compounds produce the exact same infrared spectrum. Therefore, infrared spectroscopy can result in a positive identification (qualitative analysis) of every different kind of material. In addition, the size of the peaks in the spectrum is a direct indication of the amount of material present. With modern software algorithms, infrared is an excellent tool for quantitative analysis. The technique of Attenuated Total Reflectance (ATR) has in recent years revolutionised solid and liquid sample analyses because it combats the most challenging aspects of infrared analyses, namely sample preparation and spectral reproducibility. Within the context of this work Fourier transform infrared spectroscopy was carried out using the Attenuated Total Reflectance (ATR-FTIR) technique as this generated the best results for the study. ATR-FTIR spectroscopy was carried out on SBS, NIPAAm and SBS-g-NIPAAm copolymers as shown in Figure 11. The main bands for characterising the butadiene segment within SBS (Figure 11 (a)) are CH_2 scissoring at 1449 cm^{-1}, trans-1,4 C=C out of phase deformation at 964 cm^{-1}, =CH stretching at 3005 cm^{-1} and C-H stretching at 2916 and 2844 cm^{-1}. Regarding the PS segments, styrene absorption occurs at 697 cm^{-1}, C-H out of plane deformation occurs at 3060 cm^{-1} and at 1601 cm^{-1} aromatic C-C stretching occurs (Munteanu & Vasile, 2005; Romero-Sanchez et al., 2005a; Romero-Sanchez

et al., 2005b). The ATR-FTIR spectrum for NIPAAm shown in Figure 11(b) illustrates bands corresponding to C=O stretching and NH bending for secondary amides at 1655cm^{-1} and 1544cm^{-1}. These bands are present as small shoulders in SBS-g-NIPAAm copolymer shown in Figure 11 (c). The peak at 1545 cm^{-1} for NIPAAm and SBS-g-NIPAAm copolymer was assigned as a symmetric deformation of NH_3^+. These results correspond to the finding of Erbil et al., (2004) and Ju et al.,(2002). However, the peaks present at 1617 cm^{-1} (C=C) and 1407 cm^{-1} (CH2=) in the NIPAAm spectrum disappeared for SBS-g-NIPAAm copolymer as illustrated in Figure 11(b). This suggests that NIPAAm had grafted to SBS resulting in the loss of the double bond associated with the monomer.

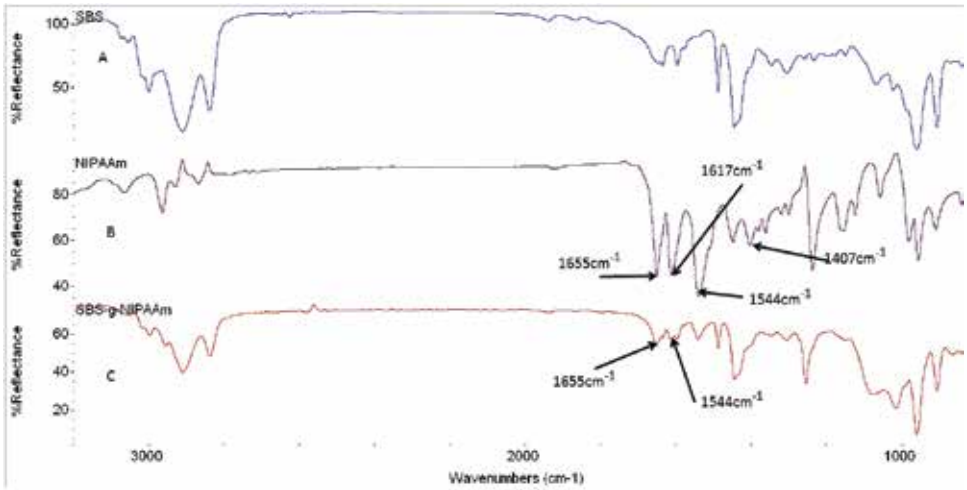

Fig. 11. Comparisons between the different ATR-FTIR spectrums where (a) is SBS (b) is NIPAAm and (c) is SBS-g-NIPAAm.

ATR-FTIR spectral analysis was used in conjunction with the DSC thermographs to analyse SBS-g-NVP copolymers. For illustrative purposes spectra containing non grafted NVP which polymerised to poly *N*-vinyl-2-pyrrolidinone (PVP), SBS-g-NVP using 2.5 g of NVP and SBS are shown in Figure 12. In the case of the PVP spectrum, Figure 12 (a), a broad C=O stretching band was found at 1650 cm^{-1} which corresponds to results obtained by Devine & Higginbotham (2003). Certain authors have found an absorption band for PVP at 1660cm^{-1} and this is called amide I. This band is a combined mode with contributions of C=O and C-N stretching (Muta et al., 2002; Cheryl & Youngli, 2002). ATR-FTIR spectrum for the grafted sample depicted in Figure 12 (c) exhibited a peak at approximately 1664 cm^{-1}, corresponding to the carbonyl group of PVP, which indicates monomeric growth of the grafted side chain. Szaraz et al.,(2000) has found that for pure liquid NVP two very strong bands occur in the IR spectrum. The band at 1629 cm^{-1}, is a carbon-carbon double bond, corresponding to olefinic C=C stretching which is usually found in the region of 1680-1630 cm^{-1}. The band at 1706 cm^{-1} is due to carbonyl stretching between 1750 -1700 cm^{-1}. However, as shown in the ATR-FTIR spectrum for grafted SBS-g-NVP copolymer, a small shoulder formed at 1714 cm^{-1} indicating that carbonyl stretching had occurred. This band is associated with un-reacted NVP as outlined by Szaraz et al., (2000) suggesting that NVP is still present within the grafted matrix, and so there is need to wash the samples after they have been fully synthesised.

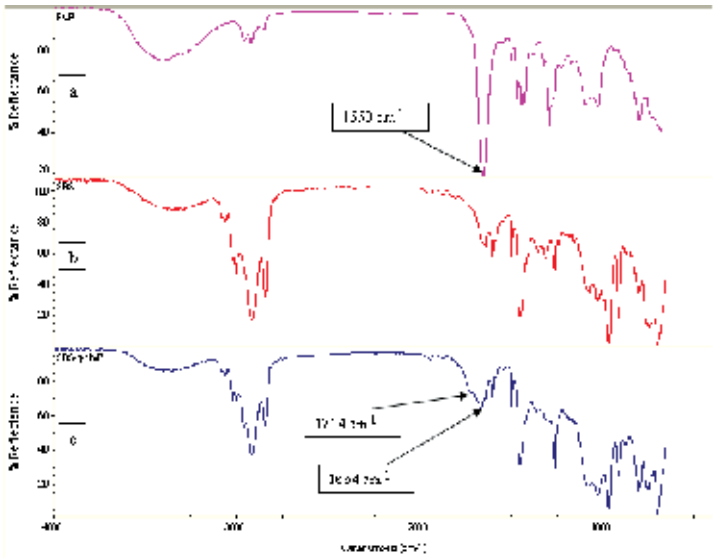

Fig. 12. Comparisons between the different ATR-FTIR spectra where (a) is PVP, (b) is SBS and (c) is SBS-g-NVP. (Kennedy & Higginbotham, 2010)

11. Topography of SBS and the grafted SBS coatings

Improved compatibility is a desired feature for biomedical product such as a coating which comes in contact with blood during clinical use. The response of blood to a foreign material can be aggressive, resulting in surface-induced thrombus (clot) formation, which can impair or disable the function of the coating and most importantly threaten a patient's health. In light of the biomedical potential of SBS based copolymers it is important to have a firm understanding of the materials surface properties. In order to minimise interfacial problems between the host tissues and the fluids, a biomedical material must exhibit a specific surface chemical behaviour (Yang & Tsai, 2010; Adamson, 1990; Andrade, 1985). All synthetic materials used in blood-contacting medical coatings promote surface-induced thrombotic phenomena to various extents. These events are initiated by non-specific protein adsorption followed by platelet adhesion, activation and aggregation on the biomaterial surface. The resulting thrombus can impair the function of the implanted devices, while thromboembolic events can occlude blood vessels leading to serious cardiovascular complications. Hence, non-thrombogenicity is a highly desired surface property for blood-contacting biomaterials. Thus, surface roughness is of significant interest in biomedical coatings because it is an important property which influences friction as well as wettability when in contact with a biological environment.

11.1 White light profilometry

One method of determining surface values of a material is to employ a technique known as White light profilometry which scans a surface using white light, thus providing surface structural analysis without using physical contact. The surfaces are characterised using amplitude parameters such as average surface roughness (Ra) or root mean square (RMS) roughness which can be summarised by a single "average roughness" value which is a close approximation of the arithmetic average roughness-height, calculated from the profile chart

of the surface. The Ra value is the average deviation of all points, calculated using equation 1, from a plane fit of the test surface. A graphic representation showing how Ra is conceived is illustrated in Figure 13.

$$R_a = \frac{1}{L}\int_0^L z(x)\,dx \tag{1}$$

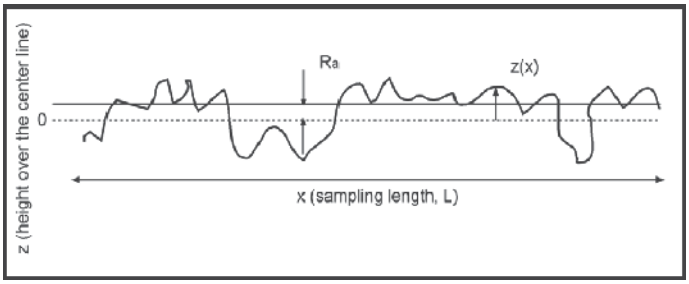

Fig. 13. Illustration of the average roughness, Ra, where z(x) is the surface height in point x relative to a mean line and L is the overall length of the profile under examination.

The standard deviation of the profile heights, RMS, is a parameter calculated by the average of the square roots of all of the Ra values. This parameter is the most widely used and its numerical value is about 11% higher than the Ra value. This parameter is calculated using equation 2.

$$RMS = \sqrt{\frac{1}{L}\int_0^L z(x)^2\,dx} \tag{2}$$

The height of a selected material can be evaluated using Peak to Valley (PV) value which is the distance between the highest and lowest points within the sample. A graphical representation of how a PV value is determined is illustrated in Figure 14.

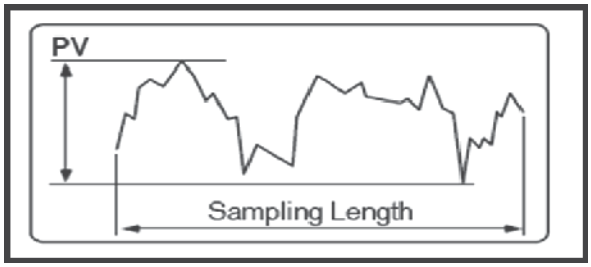

Fig. 14. Illustration of the peak to valley height (PV).

Kennedy et al.,(2010) used this technique to evaluate the roughness and height of SBS-g-NIPAAm grafted copolymers. As illustrated in Figure 15, the root mean square (RMS), as well as Peak to Valley (PV) values were 0.128μm and 1.651μm respectively for the SBS copolymer. However, when these values were compared to a SBS-g-NIPAAm and SBS-g NVP copolymers as shown in Figures 16 and 17 respectively, the RMS parameter (1.125μm for SBS-g-NIPAAm and 0.859μm for SBS-g-NVP) and the PV value (13.878μm for SBS-g-

NIPAAm and 6.896μm for SBS-g-NVP) were greater than that of SBS. It was found that the PV of each of the grafted copolymers tested was influenced by monomeric concentrations and the amount of chloroform (used to dissolve SBS) still present in the sample after UV polymerisation. This is an important property characteristic which directly affects the non-thrombogenic properties of the material within a specific biological environment i.e. the smoother the surface, the less likely that thrombosis will occur. However, this roughness may aid in the muco-adhesion properties of the material which is advantageous in biological environments such as arteries.

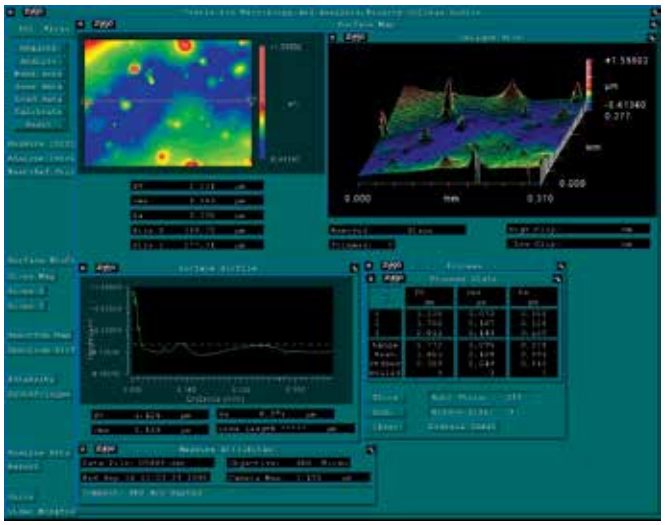

Fig. 15. A white light profilometry scan for a SBS copolymer illustrating 2D and 3D surface profiles as well as the PV value, 1.651μm and the RMS parameter, 0.128μm.

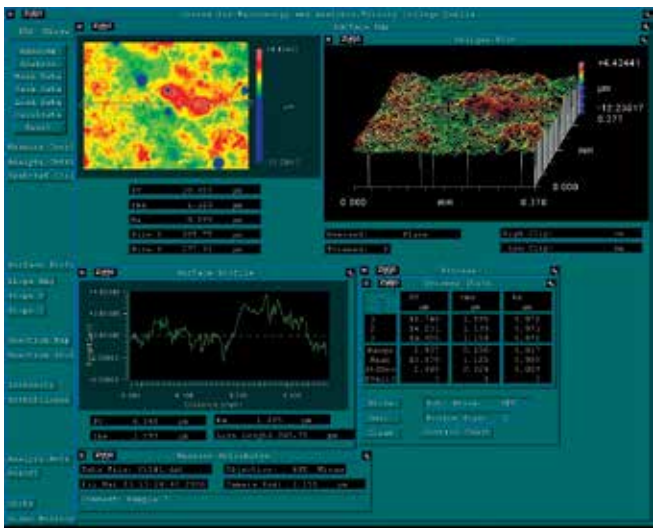

Fig. 16. A white light profilometry scan for a SBS-g-NIPAAm copolymer illustrating 2D and 3D surface profiles as well as the PV value, 13.878μm and the RMS parameter, 1.125μm.

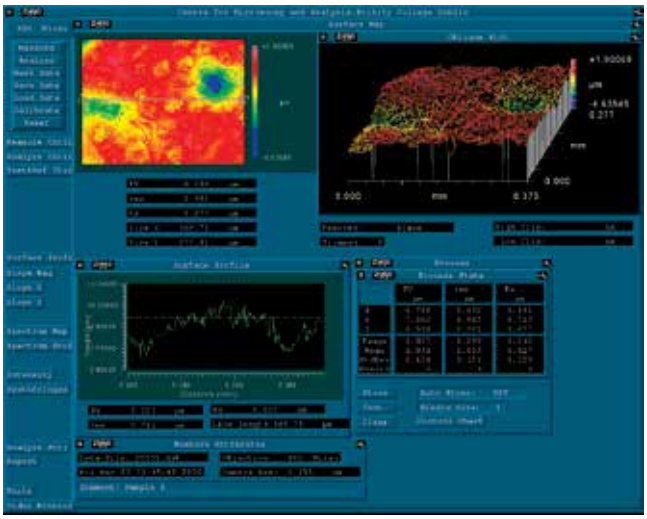

Fig. 17. A white light profilometry scan for a SBS-g-NVP coating illustrating 2D and 3D surface profiles as well as the PV value, 6.896µm and the RMS parameter, 0.859µm.

11.2 Scanning electron microscopy

SEM micrographs of SBS, selected grafted polymers are illustrated in Figures 18 to 20.

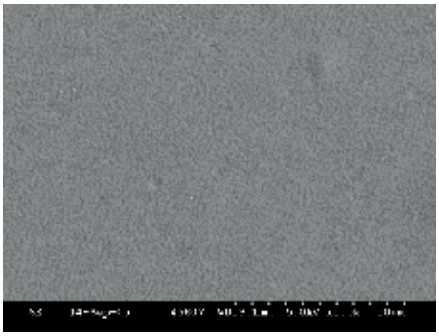

(a)

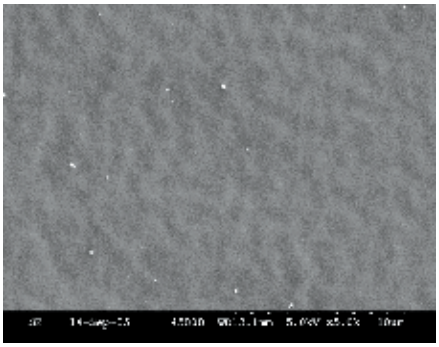

(b)

Fig. 18. SEM images of SBS at resolutions of 50µm (a) and 10 µm (b).

Mohammady et al., (2002) has confirmed that SBS, kraton D1101, exhibits a mixture of PS cylinders and lamellae embedded in the PB matrix when analysed by SEM. These findings correspond with observations made by the Authors, as shown in Figure 18, where SBS exhibits a uniform and dense structure with no pores present whereas the remaining grafted samples illustrated in Figures 19 and 20 revealed porous sponge like membranes due to the migration of chloroform during the UV polymerisation process.

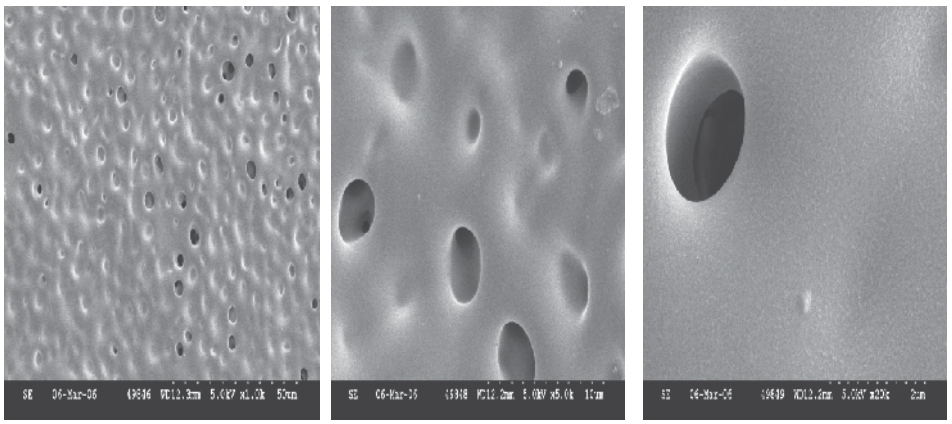

(a) (b) (c)

Fig. 19. SEM images of SBS-g-NIPAAm at resolutions of 50µm (a), 10µm (b) and 2µm (b).

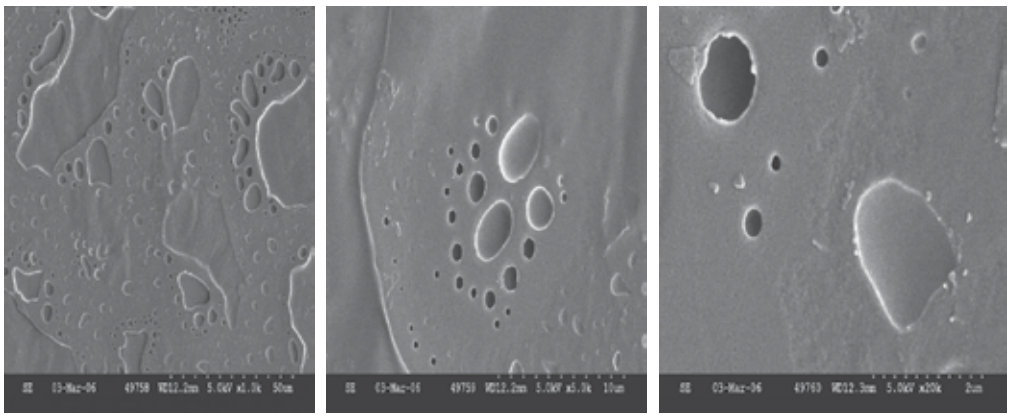

(a) (b) (c)

Fig. 20. SEM images of SBS-g-NVP at resolutions of 50µm (a), 10µm (b) and 2 µm (c).

11.3 Contact angle analysis of SBS and grafted SBS copolymers

For the fabrication of biomedical coatings coming into contact with blood and tissue, it is usually desirable to create or utilise materials which exhibit high degrees of wettability. One technique used to predict wetting properties of biomedical polymers is the use of contact angles. When a droplet impacts onto a solid surface, a liquid film is formed which spreads out with a retarding velocity, due to the influence of both the surface tension and surface forces, resulting in the liquid film attaining a maximum spread when it comes to a stop. Young's law provides a relation between those forces outlined in equation 3.

$$\sigma_{lv}.\cos\theta + \sigma_{ls} = \sigma_{sv} \quad (3)$$

where θ is the angle of contact the liquid makes on the solid, σ_{lv}, σ_{ls}, and σ_{sv} represent the interfacial tensions at the boundaries between liquid (l), solid (s) and vapour (v).The contact angle, θ, is usually referred as the wettability of a surface. The liquid is non-wetting when 90° < θ < 180° and wetting when 0°< θ < 90° (Moite & Moreira, 2003). Wettability can be assessed directly using goniometry by measuring the angle formed between a solid surface and the tangent to the drop surface. A graphic illustrating the concept of wettability is shown in Figure 21.

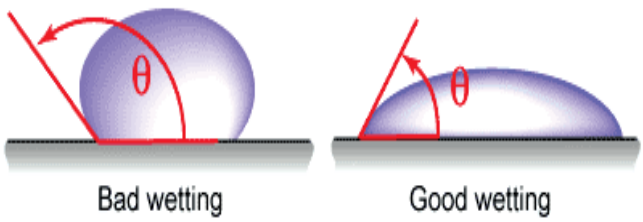

Fig. 21. A graphical representation of wettability.

Therefore, wettability is often referred to as hydrophilicity and is considered to be a surface property of a material as opposed to true hydrophilicity, which is considered to be a bulk property. A caveat to this design criterion is the fact that polymers are generally hydrophobic in nature due to their generally low surface tensions, resulting in polymers exhibiting poor wettability. For visual purposes, to illustrate principles of wettability, a digital goniometer was used and the results are illustrated in Figure 22, these images best demonstrate the affect of wettability on SBS as well as grafted SBS copolymers.

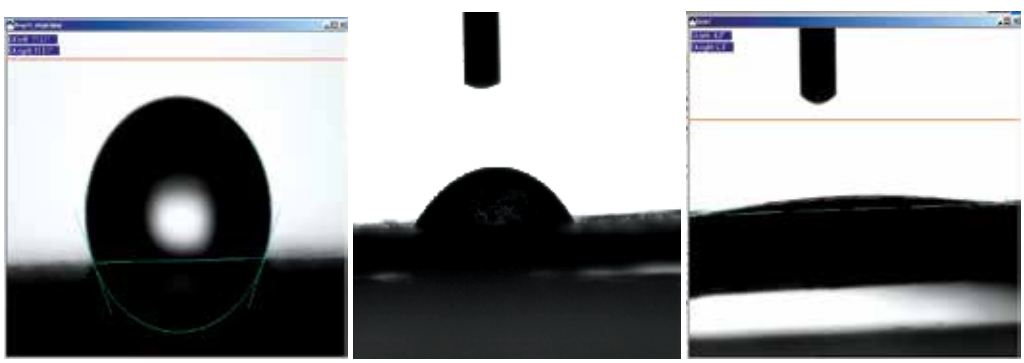

(a) 113° (b) 52° (c) 6°

Fig. 22. Contact angles representing the copolymers, where (a) SBS, (b) SBS-g-NIPAAm and (c) SBS-g-NVP.

From the images obtained the modification in the surface chemistry and wettability is reflected by the dramatic reduction in the contact angles as shown in Figures 22. Lassalle *et al*.,(2004) has found a contact angle of 95° when 1% of N-carbamyl maleamic acid was grafted onto SBS. Whereas, Yang *et al*.,(Yang 7Hsiue, 1996; Yang et al., 1997; Yang et al., 1998) reported similar trends when vinyl pyridine was grafted onto SBS and when dimethyl amino ethyl methacrylate was grafted onto SBS, contact angles of 77° and 76° were obtained.

Therefore, by grafting a hydrophilic monomer/polymer onto a hydrophobic backbone the wettability of the material is increase. It is important to note, that the samples tested where not washed and the low contact angle for the SBS-g-NVP copolymer was in part due to the migration on polymerised poly *N*- vinyl-2-pyrrolidone which is an excellent hydrophilic hydrogel, but the principle still applies whereby a hydrophobic material such as SBS can be made into a hydrophilic compound via grafting technologies.

12. Conclusion

Polymer science is by nature an interdisciplinary field, where it has found refuge in the traditional domains of engineering, chemistry and physics. However, the importance of this branch of science has now expanded and by the further integration of other disciplines such as biology, medicine and computing, new innovations have emerged resulting in opportunities which very much find itself in the fields of biomaterials. This chapter looked at such possibilities, where the tradition SBS copolymer (a thermoplastic elastomer) was modified into a grafted copolymer utilising hydrogel technology to create a potential medical application in the area of biomedical coatings.

To truly appreciate the breath and depth of the opportunities one must have a detailed understanding of the fundamental principles which occur within the materials such as phase separation, the domain theory, topography and reaction kinetics to name but a few. Only then can new materials be commercialised which capture the needs society has place on them.

13. References

Adamson, A.W. (1990).*Physical Chemistry of Surfaces*, Wiley, ISBN-13: 978-0471610199, New York,

Adhikari, R; Michler, GH; Godehardt,R; Ivan'kova EM.(2003). Deformation behaviour of styrene butadiene star block copolymer/hPS blend: influence of morphology. *Polymer*, Vol., 44, No., 26 (December 2003) pp 8041-8051, ISSN 0032-3861

Adhikari, R; Michler, GH; Knott, RB.(2004). Morphology and micromechanical behaviour of binary blends comprising block copolymers having different architectures. *Polymer*, Vol., 45, No., 1(January 2004) pp 241-246, ISSN 0032-3861

Andrade, J.D.(1985). *Surface and Interfacial Aspects of Biomedical Polymers: Surface Chemistry and Physics Vol. 1*, Plenum Publications, ISBN-13: 978-0306417412, New York.

Brydson, J.A.(1978) *Rubber Chemistry*, Applied Science Publishers, ISBN-13: 978-0853344360, London.

Burford, RP; Markotsis, MG; Knott, RB.(2003) Small angle neutron scattering and transmission electron microscopy studies of interpenetrating polymer networks from thermoplastic elastomers. *Nuclear Instruments and Methods in Physics Research Section B: Beam Interactions with Materials and Atoms*, Vol.208, pp 58-65, ISSN 0168-583X

Cheryl, L; Youngli, M.(2002). A study of blending and complexation of poly(acrylic acid)/poly(vinyl pyrrolidone). Polymer, Vol. 43.., No. 3, (February 2002) pp 823-829, ISSN : 0032-3861

De Sarkar, M; De, PP; Bhowmick, AK.(1999). Influence of hydrogenation and styrene content on the unaged and aged properties of styrene-butadiene copolymers. *J. Material Science*, Vol. 34, No.8(April 1999), pp 1741-1747, ISSN 0022-2461

Devine D.M; Higginbotham C.L.(2003). The synthesis of a physically crosslinked NVP based hydrogel. *Polymer*, Vol. 44, No.26 (December 2003), pp7851-7860, ISSN 0032-3861.

Durne, KV; Mele, B; Loos, W; Du Prez, F.(2005). Introduction of silica into thermo-responsive poly(N-isopropylacrylamide) hydrogels. A novel approach to improve response rates. *Polymer*, Vol. 46, No.23 (November 2005), pp 9851-9862, ISSN 0032-3861

Erbil, C; Kazancioglu, E; Uyanik, N.(2004). Synthesis, characterisation and thermoreversible behaviours of poly (dimethylsiloxane)/ poly(N-isopropylacylamide) semi - interpenetrating network, *European Polymer Journal*, Vol. 40, No.6 (June 2004), pp 1145-1154, ISSN 00143057.

Escobar-Barrios,VA; Najera,RH; Petit,A ; Pla, F.(2003). Selective hydrogenation of butadiene styrene copolymers using a Ziegler-Natta type catalyst 2. Thermal properties European Polymer Journal, Vol. 39,No.6 (June 2003), pp 1151-1167, ISSN 0014-3057

Geever, L.M.; Cooney, C.C; Lyons, J.G; Kennedy, J.E; Nugent, M. J.D; Devery,S; Higginbotham, C.L.(2008). Characterisation and controlled drug release from novel drug-loaded hydrogels, *European Journal of Pharmaceutics and Biopharmaceutics*, Vol. 69, No.3 (August 2008), pp 1147-1159, ISSN 0939-6411.

Geever, L.M; Devine, D.M; Nugent, M. J.D; Kennedy, J.E; Lyons, J.G; Hanley, A; Higginbotham, C.L.(2006). Lower critical solution temperature control and swelling behaviour of physically crosslinked thermosensitive copolymers based on N-isopropylacrylamide, *European Polymer Journal,* Vol. 42, No.10 (October 2006), pp 2540-2548, ISSN 0014-3057.

Geever, L.M; Mínguez, C, M; Devine, D.M; Nugent, M. J.D; Kennedy, J.E; Lyons, J.G; Hanley, A; Devery, S; Tomkins, P.T; Higginbotham, C.L.(2007). The synthesis, swelling behaviour and rheological properties of chemically crosslinked thermosensitive copolymers based on N-isopropylacrylamide, *Journal of Materials Science,* 2007 Vol. 42, No.12 (March 2007), pp 4136-4148, ISSN : 0022-2461.

Gruver, J.T; Kraus, G.(1964). J.Appl.Polym.Sci. Pt A 2, pp 797, cited in Holden, G; Kricheldorf H.R; Quirk R.P Editors(2004). *Thermoplastic Elastomers,* Hanser, ISBN 9783446223752, Munich.

Hirata, I.(2004). Simple method for preparation of ultra-thin poly(N-isopropylacrylamide) hydrogel layers and characterization of their thermo-responsive properties, *Polymer,* Vol. 45, No.16 (July 2004), pp 5569-5578, ISSN 0032-3861.

Holden G. J. (1965) Appl. Polym. Sci. Vol 9, pp 2911, cited in Holden, G; Kricheldorf H.R; Quirk R.P Editors(2004). *Thermoplastic Elastomers,* Hanser, ISBN 9783446223752, Munich.

Holden, G; Kricheldorf H.R; Quirk R.P Editors(2004). *Thermoplastic Elastomers,* Hanser, ISBN 9783446223752, Munich.

Holden, G; Hansen, D.R. (2004). *Styrenic Thermoplastic Elastomers*. pp 45-65. In: Holden, G; Kricheldorf H.R; Quirk R.P Editors(2004). *Thermoplastic Elastomers,* Hanser, ISBN 9783446223752, Munich.

Holden, G; Milkovich,R.(1962) (to shell oil co), U.S. Patent 3,265,765, filed January 1962.

Huang, NJ; Sundberg, DC. (1995 a). Fundamental Studies of Grafting Reactions in Free Radical Copolymerisation. 1. A Detailed kinetic Model for Solution Polymerisation. Journal of Polymer Science Part A, *Polymer Chemistry*, Vol. 33, No.15 (November 1995), pp 2533-2550, ISSN 0887-624X .

Huang, NJ; Sundberg, DC. Fundamental Studies of Grafting Reactions in Free Radical Copolymerisation.2.(1995b). Grafting of Styrene, Acrylate, and Methacrylate Monomers onto cis-Polybutadiene Using AIBN Initiator in Solution

Polymerisation. Journal of Polymer Science Part A: *Polymer Chemistry*, Vol. 33, No.15 (November 1995), pp 2551-2570, ISSN 0887-624X.

Huang, NJ; Sundberg, DC.(1995 c). Fundamental Studies of Grafting Reactions in Free Radical Copolymerisation.3. Grafting of Styrene, Acrylate, and Methacrylate Monomers onto cis-Polybutadiene Using Benzoyl Peroxide Initiator in Solution Polymerisation. Journal of Polymer Science Part A, *Polymer Chemistry*, Vol. 33,No.15 (November 1995), pp 2571-2586, , ISSN 0887-624X.

Huang, NJ; Sundberg, DC.(1995 d). Fundamental Studies of Grafting Reactions in Free Radical Copolymerisation.4. Grafting of Styrene, Acrylate, and Methacrylate Monomers onto vinyl-polybutadiene using benzoyl peroxide and AIBN Initiators in Solution Polymerisation. Journal of Polymer Science Part A, *Polymer Chemistry*, Vol. 33,No.15 (November 1995), pp 2587-2603 , ISSN 0887-624X.

Jiang, DD; Wilkie, CA.(1998). Graft copolymerisation of Methacrylic acid, Acrylic acid and Methyl acrylate onto Styrene- butadiene Block copolymers. *Eur. Polym. Journal,* Vol. 34, No.7 (July 1998), pp997-1006, ISSN 0014-3057.

Ju, H.K; Kim, S.Y; Kim, S.J; Lee ,Y.M.(2002). pH/Temperature responsive semi-IPN hydrogels composed of alginate and poly(N-isopropylacrylamide), *J Appl Polym Sci.* Vol. 83, No. 5(January 2002), pp 1128-1139, ISSN 0021-8995 .

Kennedy, J.E; Devine, D.M; Lyons J.G; Geever, L.M; Higginbotham, C. L.(2009). The synthesis and characterisation of grafted random styrene butadiene for biomedical applications. *Journal of Materials Science*, Vol. 44., No. 3(February 2009) pp 889-896, ISSN 1573-4803.

Kennedy, JE; Higginbotham, CL.(2010). Synthesis and characterisation of styrene butadiene styrene-g-N-isopropylacrylamide via UV polymerisation for potential use in biomedical applications, *Journal of Materials Science*, Vol. 45, No. 3 (February 2010), pp 599-606, ISSN 0022-2461.

Kennedy, JE; Higginbotham, CL.(2010) Synthesis and characterisation of styrene butadiene styrene-g-N vinyl -2-pyrrolidinone for use in biomedical applications, *Materials Science and Engineering C*, doi:10.1016/j.msec.2010.09.004

Kennedy, JE; Lyons, JG; Geever, LM; Higginbotham, CL.(2009) Synthesis and characterisation of styrene butadiene styrene-g-acrylic acid for potential use in biomedical applications, *Materials Science and Engineering C*, Vol. 29, No.5 (June 2009), pp 1655–1661, ISSN 0928-4931

Kim, J. K; Kim, W. H; Lee, D. H.(2002). Adhesion properties of UV crosslinked polystyrene-block-polybutadiene-polystyrene copolymer and tackifier mixture. *Polymer*, Vol. 43, No.18 (August 2002), pp 5005-5010, ISSN 0032-3861.

Knoll, K; Niessner, N.(1998). Styrolux+ and styroflex+ : From transparent high impact polystyrene to new thermoplastic elastomers syntheses, applications and blends with other styrene based polymers. *Proceedings of Macromol. Symp,* pp 231-243, ISBN 3-527-29800-2, Paris, 7-11 July, 1997, Wiley-VCH, Switzerland

Lasalle, V.L; Failla, M.D; Valles, E.M; Martin-Martinez, JM.(2004). Chemical modification of styrene-butadiene-styrene co-polymer by grafting of N- carbamyl maleamic acid, *J Adhesion Sci. Technol,* Vol. 18, No. (15-16), pp1849-1860, ISSN 0169-4243 .

Lee, W; Chen, Y. Graft copolymerisation of N-isopropylacrylamide on styrene-butadiene-styrene block copolymer.(2001). *Journal of Applied Polymer Science*, Vol. 82, No.11 (December 2001), pp 2641-2650, ISSN 0021-8995.

Madhusudhan, RB; Raghunath, RP.(1999). Grafting of maleic anhydride onto acrylonitrile-butadiene-styrene ter-polymer: synthesis and characterization. *Polym Plast Technol* Eng, Vol. 38, No.5 (November 1999), pp 967-977, ISSN 0360-2559.

Mateo, JK; Bosch, P; Serrano, J; Calvo, M.(2000). Sorption and diffusion of organic solvents through photo crosslinked SBS block copolymers, *European Polymer Journal*, Vol. 36, No.9 (September 2000), pp 1903-1910, ISSN 0014-3057.

Minoura, F.N., Soft tissue compatible polymers.(1993) In: *Biomedical Applications of Polymeric Materials*, Tsuruta, T; Hayashi, T; Kataoka, K; Ishihara, K; Kimura, Y. Editors, p. 118. CRC Press, ISBN-13: 9780849345197, Boca Raton, FL,

Mohammady, S.Z; Mansour, A.A; Knoll, K; Stoll, B.(2002). Detection of the glass relaxation process of the PS- phase in block copolymers. *Polymer*, Vol. 43, No. 8(April 2002), pp 2467-2478, ISSN 0032-3861.

Mohammady, S.Z; Mansour, A.A; Stoll.B.(2001). Dynamic Mechanical Relaxation Behaviour of Block Copolymers at High temperatures. *Journal of Polymer Science Part B: Polymer Physics*, Vol. 39, No.18 (September 2001), pp 2198-2206, ISSN 0887-6266

Moita, A. S. H; Moreira, A. L. N.(2003). Influence of Surface Properties on the Dynamic Behaviour of Impacting Droplets. 9th International Conference on Liquid Atomization and Spray Systems

Mrrov ,Z ; Velichkova, R.(1993). Modification of styrene–isoprene block copolymer-3. Addition of maleic anhydride-mechanism. *Eur Polym Journal*, Vol.29, No. 4(April 1993), pp 597-601, ISSN 0014-3057.

Munteanu, SB; Vasile, C.(2005). Thermal and thermo-oxidative behaviour of butadiene-styrene copolymer with different architectures. *Polymer Degradation and Stability*, Vol .89, No.3, (September 2005) pp 501-512, ISSN 0141-3910.

Murata, H; Chang, B. J; Prucker, O; Dahm, M; Ruhea, J.(2004). Polymeric coatings for biomedical devices. *Surface Science,* Vol. 570, No.1-2 (October 2004), pp 111-118, ISSN 0039-6028

Muta, H; Ishida, K; Tamaki, E; Satoh, M.(2002). An IR study on ion-specific and solvent-specific swelling of poly(N-vinyl-2-pyrrolidone) gel. *Polymer*, Vol. 43, No.1 (January 2002), pp 103-110, ISSN 0032-3861

Nestle, H; Heckmann,W; Steininger,H; Knoll,K.(2007). Towards quantification of butadiene content in styrene–butadiene block copolymers and their blends with general purpose polystyrene (GPPS) and the relation between mechanical properties and NMR relaxation times. *Analytica chimica acta*, Vol. 604, No.1 (November 2007), pp 54-61, ISSN 0003-2670.

Rohr, T; Ogletree, D. F; Svec, F; Frechet, J. M .J.(2003). Surface Functionalisation of Thermoplastic Polymer for the Fabrication of Microfluidic Devices by Photoinitiated Grafting. *Adv. Funct. Material*, Vol. 13, No.4(April 2003), pp 264-270.

Romero-Sánchez, MD; Pastor-Blas, MM; Martín-Martínez, JM. (2005a). Environmental friendly surface treatments of styrene-butadiene-styrene rubber: Alternative to the solvent-based halogenation treatment. *International Journal of Adhesion and Adhesives*, Vol. 25, No.1 (February 2005), pp 19-29, ISSN 0143-7496

Romero-Sánchez, MD; Pastor-Blas, MM; Martín-Martínez, JM; Walzak, MJ. (2005b) Addition of ozone in the UV radiation treatment of a synthetic styrene-butadiene-styrene (SBS) rubber. *International Journal of Adhesion and Adhesives*, Vol. 25, No.4 (August), pp 358-370, ISSN 0143-7496

Sheng, J; Lu, XL Yao, KD. (1990). Investigation of graft polymerization of maleic anhydride onto polybutadiene rubber. *J. Macromol Sci-Chem*, Vol. 27, No.2 (February 1990), pp 167-178, ISSN 0022-233X.

Spaans, RD; Muhammad, M; Williams, MC.(1999). Probing the interfacial region of microphase separated block copolymers by differential scanning calorimetry. *Journal of Polymer Science Part B: Polymer physics,* Vol. 37, No. 4(February 1999), pp 267-274,

Spaans, RD; Williams, MC.(1995). Non linear Viscoelasticity of ABA Block copolymers Melts: Stress Relaxation and Recovery. *Ind. Eng. Chem. Res.* Vol. 34, No.10 (October 1995), pp 3496-3507, ISSN 0888-5885.

Szaraz, L; Forsling, W.(2000). A Spectroscopic study of the solvation of 1-vinyl-2-pyrrolidone and poly(1-vinyl-2-pyrrolidone) in different solvents. *Polymer*, Vol. 41, No.13 (June 2000), pp 4831-4839, ISSN 0032-3861.

Szwarc, M. Nature. (1956) Vol. 178, pp 1168-1169. cited in Holden, G; Kricheldorf H.R; Quirk R.P Editors (2004). *Thermoplastic Elastomers,* Hanser, ISBN 9783446223752, Munich.

Szwarc, M; Levy,M; Milkovich, R. J. (1956). Am. Chem. Soc. Vol.78, pp 2656- 2657. cited in Holden, G; Kricheldorf H.R; Quirk R.P Editors(2004).*Thermoplastic Elastomers,* Hanser, ISBN 9783446223752, Munich.

Van der Vegt, A.K. (2005) From polymers to plastics. Delf University press Netherlands:

Wagner D.(2004), Kunststoffe Plast Europe 6/2004,
available online from www.kunststoffe.de/peusing using DOI: PE102911

Xiang, ZC; Qinghua, L; Jie, Y. (2001). Photochemical surface modification of polyinide containing benzophenone unit by UV light source. *Chemistrymag.org.* Vol. 3, No.11 (November2001)pp54-60.Available from
http://www.mdpi.org/cji/cji/2001/03b054pe.htm

Yang, JM; Hsiue, GH. (1996). Radiation-induced graft copolymer SBS-g-VP for biomaterial usage. *Journal of Biomaterials Materials Research*, Vol 31, No.2 (June 1996) pp 281-286, ISSN 0021-9304.

Yang, JM; Jong, YJ; Hsu, KY. Hsu; Chang, CH.(1998). Preparation and characterisation of heparin-containing SBS-G-DMAEMA copolymer membrane. *J Biomed. Mater Research*, Vol. 39, No.1(January 1998) pp 86-91, ISSN 0021-9304.

Yang, JM; Jong, YJ; Hsu, KY.(1997). Preparation and properties of SBS -G-DMAEMA copolymer membrane by ultraviolet radiation. *Journal of Biomaterials Materials Research* , Vol. 35, No. 2(May 1997) pp 175-180, ISSN 0021-9304.

Yang, JM; Tsai, SC. (2010). Biocompatibility of epoxidized styrene–butadiene–styrene block copolymer membrane. *Materials Science and Engineering: C*, 2010 doi:10.1016/j.msec.2010.06.014]

Zhang, A ; Li,C. (2003). Chemical initiation mechanism of maleic anhydride grafted onto styrene–butadiene–styrene block copolymer. *European Polymer Journal* , Vol. 39, No.6 (June 2003) pp 1291-1295, ISSN 0014-3057.

Zhang, X; Lewis, P; Chu, C.(2005). Fabrication and characterization of a smart drug delivery system: microsphere in hydrogel. *Biomaterials*, Vol. 26, No.16 (June 2005) pp 3299-3309, ISSN 0142-9612

21

Synthetic Strategies for Biomedical Polyesters Specialties

Zinck Philippe
Unité de Catalyse et Chimie du Solide, UCCS, Equipe Catalyse et Chimie Moléculaire, UMR CNRS 8181, USTL-ENSCL, Université Lille – Nord de France, France

1. Introduction

Aliphatic polyesters are biocompatible and biodegradable polymers exhibiting good mechanical properties and hydrolyzability. They are among the best characterized and most studied biodegradable systems for temporary biomedical applications such as drug delivery systems, resorbable implants or tissue engineering scaffolds. Properties such as hydrophilicity and biodegradation can be tailored by the introduction of biologically relevant functional groups in the polymer. This chapter examines critically the various strategies implemented for this purpose.

Polyesters can be synthesized by polycondensation (step growth polymerization) or by ring opening polymerization (chain growth polymerization). A specific functionality can be introduced via these polymerizations using functionalized monomers or functionalized initiators. The presence of functional groups such as hydroxyls for instance can be detrimental for both polymerization methods, leading to deactivation and/or undesirable crosslinking reactions. Protection/deprotection chemistries are thus usually applied prior and after polymerization. These strategies will be presented and illustrated by relevant examples. Such multistep approaches provide interesting and sophisticated materials but require long production times and high production costs. For practical applications however, biomedical materials must also be cost-effective, introducing a balance between sophistication and ease of production. Recent advances enabling a one pot approach for each strategy are of particular interest (Zinck 2009) and are further presented and discussed in this frame.

The polyesters classically used for biomedical applications are poly(ε-caprolactone), poly(lactic acid), poly(glycolic acid) (Fig. 1) and their copolymers, and in a lesser extent, poly(3-hydroxybutyrate) and polyorthoesters. This chapter focuses essentially on the first three polyesters, with some extensions to other polyesters when the synthetic strategy or functionalization concept is judged relevant. These polyesters can be synthesized by the ring-opening polymerization of the corresponding cyclic ester (ε-caprolactone, lactide and glycolide, respectively, the two latter being dimers) and by polycondensation of the corresponding ω-hydroxyacid (6-hydroxyhexanoic, lactic and glycolic acids respectively). 6-hydroxyhexanoic acid is scarcely isolable, and the polycondensation route for the formation of poly(ε-caprolactone) is rarely used. Lactic acid has a stereocenter, and can be found as L-lactic acid, D-lactic acid or a racemic mixture of both forms. The lactide dimer exhibits thus

two diastereomeric forms. The most widely used forms of the polymer are poly(L-lactic acid) or poly(L-lactide) and poly(D,L-lactic acid) or poly(D,L-lactide).

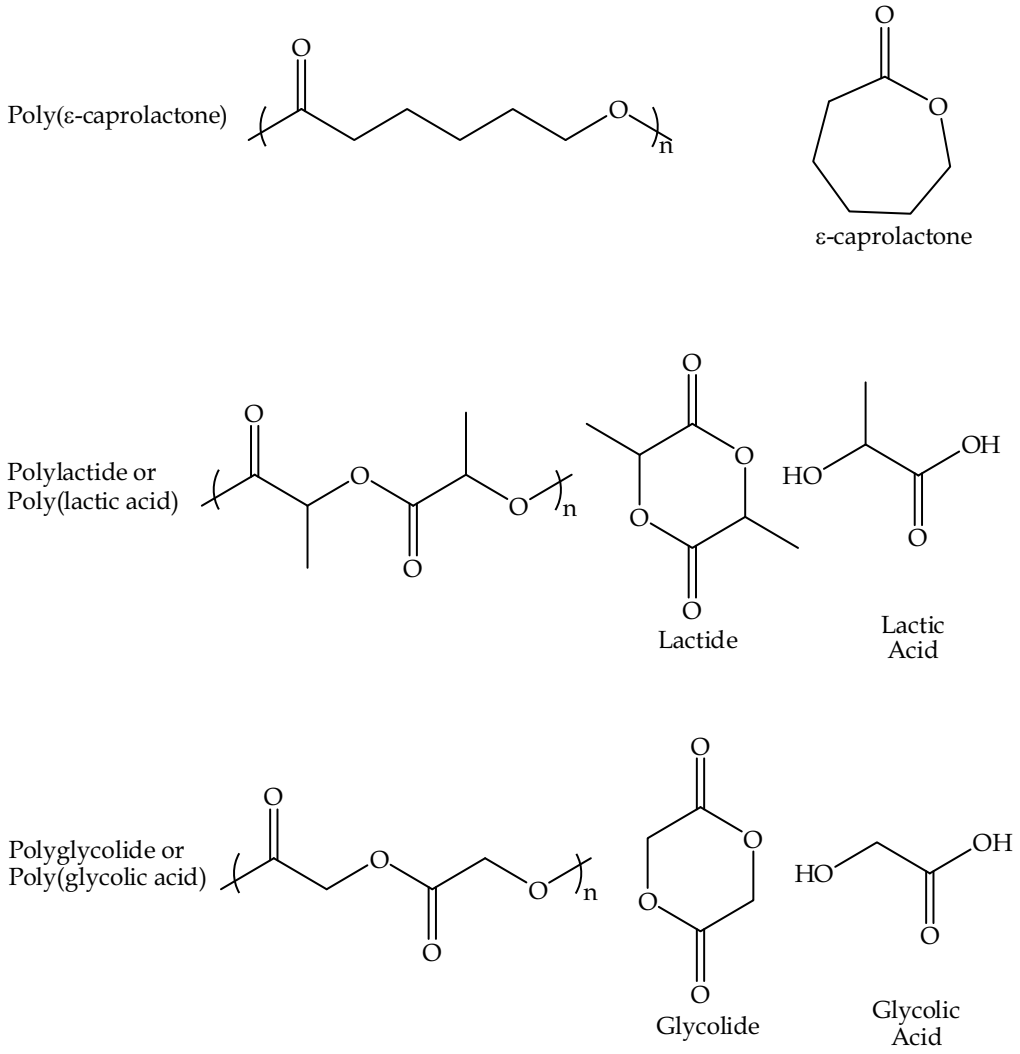

Fig. 1. Polyesters used for biomedical applications and their monomers

This chapter deals mainly with linear polymers and graft copolymers, with some extensions to star-shape polymers. Networks (*e.g* hydrogels), dendrimers and hyperbranched macromolecules have not been considered. Post-polymerization modifications of the polymers have not been dealt with in a systematic manner, but appear when judged relevant for specific strategies. Metal mediated polymerizations can lead to the presence of residual metal traces in the material, which can be detrimental for the targeted applications. This can be circumvented by the use of organic molecules or enzymes as polymerization mediators. A particular emphasis on organocatalysis and enzymatic catalysis will be made in this frame. Recent approaches based on click chemistry will also be presented. This multistep strategy has gained much interest in the last years, due to its relative simplicity

and the tolerance of the groups formed. The chapter is divided into three sections covering the main strategies in the field of ring-opening polymerization, polycondensation and transesterification illustrated by several examples.

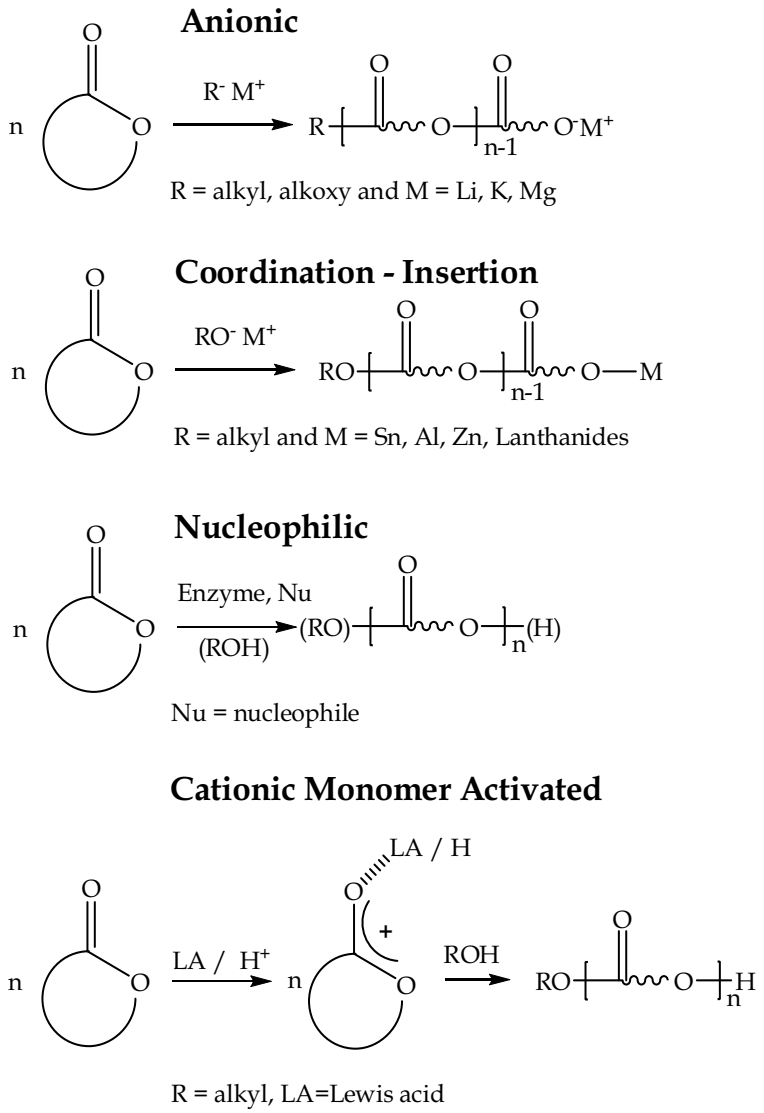

Fig. 2. Ring-opening polymerization mechanisms

2. Ring-opening polymerization

2.1 Basics and concepts

2.1.1 Ring-opening polymerization mechanisms

Ring-opening polymerization of cyclic esters can occur via different mechanisms, and readers interested in more details are invited to consult reviews on this subject (see for example Albertsson & Karma, 2003). The ring-opening polymerization pathways reported in

this chapter are anionic, coordination-insertion, nucleophilic and cationic, and are shown in Fig. 2. Organocatalytic ring-opening polymerization can be considered when using organic molecules as catalysts or initiators for the polymerization. It can be found here as nucleophilic polymerization or cationic monomer activated polymerization.

2.1.2 Statistical, sequential block copolymerizations and end functionalization

The simplest strategies used for modifying the properties of a polymer are statistical and sequential block copolymerizations (Fig. 3). Copolymerization involves the use of more than one monomer. When two monomers are polymerized simultaneously, the polymerization is called statistical. In a sequential block copolymerization, one of the monomers is polymerized in a first step, and the second monomer is polymerized after completion of the first step. The polymerization has to be living in this case, *i.e* the active species has to be stable at the end of the first step. Numerous catalytic systems developed in the recent years for the ring-opening polymerization of cyclic esters enables statistical and sequential block copolymerization of lactide, glycolide and ε-caprolactone. Copolymers between poly(lactic acid) and poly(glycolic acid) can also be synthesized by polycondensation techniques, and enables to confer more hydrophilicity to the resulting copolymer and a higher degradation rate in comparison with pure poly(lactic acid). Of interest is also the combination of polyesters with poly(ethylene glycol), a water-soluble polymer also called poly(ethylene oxide), which confers also hydrophilicity to the resulting materials (the structure of poly(ethylene glycol) can be seen in Fig. 19). Such a combination can be done by numerous ways that will be presented in this chapter. The anionic sequential block copolymerization of ethylene glycol and D,L-lactide for example results in the formation of such block copolymers (Yasugi et al., 1999).

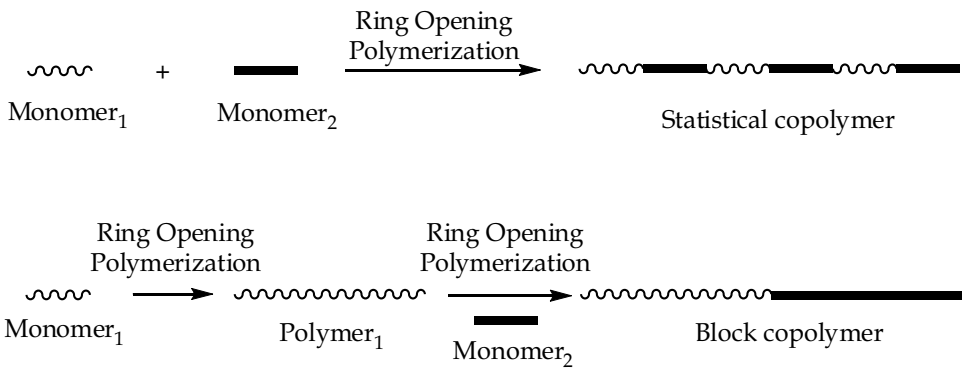

Fig. 3. Statistical and sequential block copolymerizations

The living character of certain polymerizations enables also a sequential end functionalization of the polymer. Instead of a second monomer, a functional group is introduced at the end of the first step, leading to a sequential end-functionalization of the polymer. This differs from one-pot end functionalization, where the functionalized compound is introduced at the beginning of the polymerization, as discussed in section 2.2. Coupling reactions can also be performed. For example, telechelic carboxylic chlorides end-capped poly(ethylene glycol) can react with the hydroxyl end group of poly(ε-caprolactone) to yield triblock copolymers (Morikawa et al., 2008).

2.1.3 Graft copolymerizations

Graft copolymers represent another kind of architecture that can be obtained. The synthesis of graft copolymers can be realized by three different ways (Fig. 4). In the grafting from method, the grafts are polymerized starting from the polymeric backbone, which can be considered as a macroinitiator. The graft can also be introduced on the monomer, whose polymerization leads to the graft copolymer. This is known as the grafting through process. In the grafting onto approach, a polymer end-capped with a reactive group is grafted onto the macromolecular backbone via reaction with another reactive group.

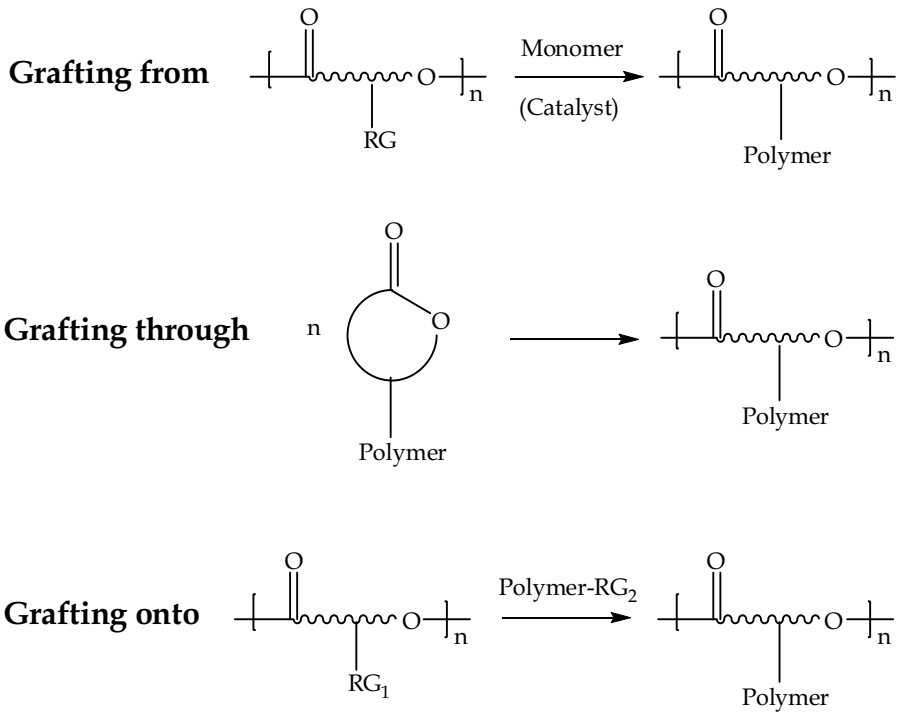

Fig. 4. Graft copolymerization strategies. RG represents a reactive group

2.2 One-pot end functionalization and grafting from methods (Fig. 5)

Ring opening polymerization can occur via anionic, coordination-insertion, nucleophilic or cationic mechanism. Alcohols and/or alkoxy groups can initiate the growth of one macromolecular chain for these polymerizations (see Fig. 2). The general functionalization strategy consists in the use of relevant hydroxyl bearing compounds:

i. to modify the initiator of anionic and coordination/insertion ring-opening polymerization

$$ROH + M\text{-}R' \rightarrow RO\text{-}M + R'H$$

ii. as a co-initiator, as presented in Fig. 2 for nucleophilic and cationic mechanisms.

The presence of high amount of hydroxyl groups is thus detrimental, and protection/deprotection chemistries are usually applied in the presence of highly hydrophilic compounds such as carbohydrate derivatives. This will be presented for anionic and coordination/insertion ring opening polymerization in section 2.2.1 and 2.2.2 respectively.

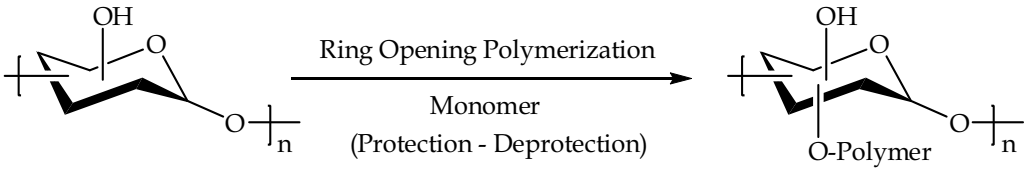

Fig. 5. End functionalization and grafting from methods, using carbohydrates as polymerization initiators

The use of regioselective catalysts such as enzymes or certain organic molecules can lead to regioselective end-functionalization and/or grafting from approaches without protection/deprotection steps. This will be presented in sections 2.2.3 and 2.2.4, respectively. Section 2.2 focuses essentially on carbohydrates derivatives for the end-functionalization of polyester, regarding the scope of the article. Note that the overall strategy can also be applied to the synthesis of block copolymers, using hydroxyl end-capped polymers such as poly(ethylene glycol) for instance as ROH initiator (via organocatalytic (Nyce et al., 2003) and coordination/insertion (Choi et al., 2006) ring opening polymerization).

2.2.1 Anionic ring-opening polymerization

The strategy consists here to use the carbohydrate compound as the counter-ion of the metal catalyst (Fig. 6, Ouchi et al., 2001). Protected D-glucose bearing an hydroxyl in the C1 position is allowed to react with the ^{t}BuOK anionic initiator to form the corresponding glucosate. This latter compound is used to polymerize L-lactide in tetrahydrofuran at room temperature. Subsequently, the removal of O-protecting benzyl groups in the terminal carbohydrate can be carried out by hydrogenolysis with Pd/C to obtain D-glucose-end-capped poly(L-lactide). Number-average molecular weights of 5700 g/mol were reported with polydispersity index of 1.35. Due to the living character of anionic polymerization, this strategy can also be used to synthesize monosaccharide end-capped poly(D,L-lactide)-*block*-polyethylene glycol copolymers (Yasugi et al., 1999).

2.2.2 Coordination – insertion

The strategy is close to that reported for anionic polymerization, *i.e* the carbohydrate compound serves as counter-ion of the catalyst metal. The main difference resides in the possibility of rapid and reversible chain transfer for coordination – insertion ring opening polymerization. The reaction can operate in the presence of excess alcohol *vs.* catalyst metal, leading to the growth of several macromolecular chains per metal atom (Fig. 7).

One may distinguish here end functionalization and grafting from strategy. The polymerization starts from a single compound such as monosaccharide for the former, while the grafting from method starts from a polymer such as a polysaccharide for the latter. Poly(ε-caprolactone) (Hamaide et al., 2001) and poly(L-lactide) (Bernard et al., 2003) were polymerized starting from protected monosaccharides, yielding monosaccharides end-capped polymers and eventually nanoparticles (Hamaide et al., 2001). The number-average molecular weight and polydispersity indexes were up to 4000 g/mol *vs.* polystyrene standards and 1.2 for poly(L-lactide) (Bernard et al., 2003) and up to 10 000 g/mol and 1.1 for poly(ε-caprolactone) (Hamaide et al., 2001). Linear protected carbohydrates end-capped poly(D,L-lactide) (Tang et al., 2008 – Fig. 8) and macrocyclic polycaprolactone were also synthesized by this way (Kricheldorf & Stricker, 2000 – Fig. 9) as well as poly(ethylene

glycol)-*block*-poly(ε-caprolactone) copolymers (Choi et al., 2006). The polymerization is initiated by a hydroxyl end-capped poly(ethylene glycol) in this latter case.

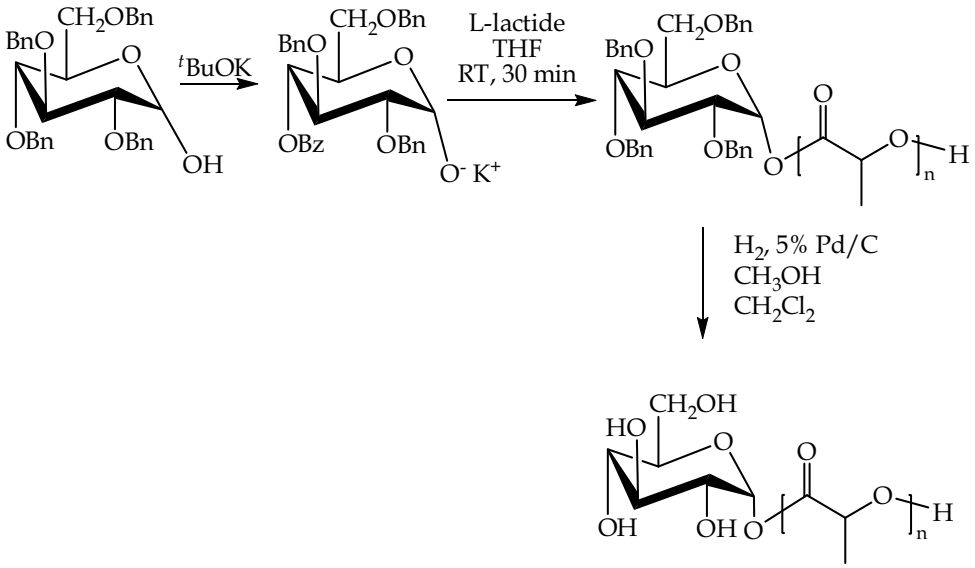

Fig. 6. Poly(L-lactide) end functionalization via anionic ring-opening polymerization (Ouchi et al., 2001) - Bn = benzyl

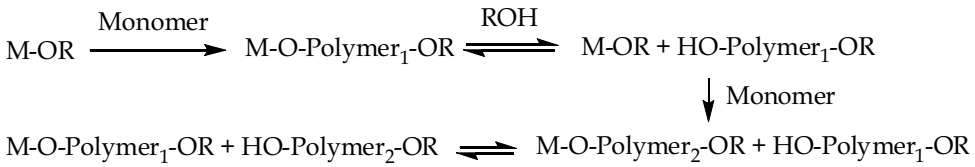

Fig. 7. Transfer reactions in coordination/insertion ring-opening polymerization conducted in the presence of excess alcohol *vs.* catalyst

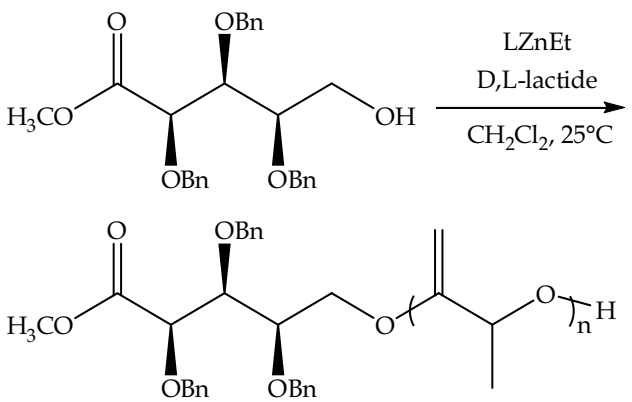

Fig. 8. Poly(D,L-lactide) end functionalization via coordination/insertion ring-opening polymerization using linear derivatives (Tang et al., 2008)

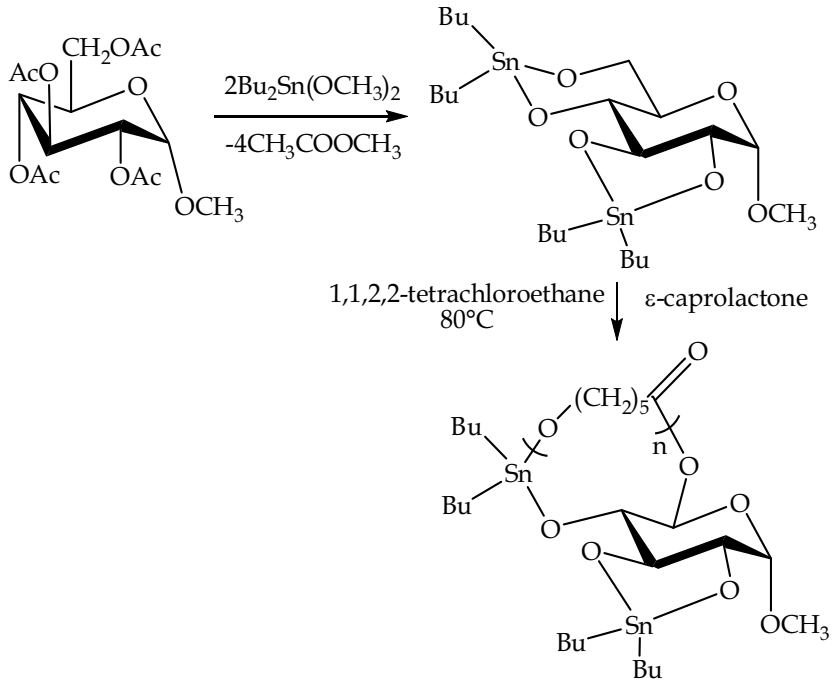

Fig. 9. Macrocyclic poly(ε-caprolactone) (Kricheldorf & Stricker, 2000) - Ac = CH_3CO-

Coordination/insertion ring-opening polymerization was also used for grafting from approaches. Dextran was used as an initiator for the grafting from approach, leading to poly(ε-caprolactone)-*graft*-dextran (Ydens et al., 2000) and poly(D,L-lactide)-*graft*-dextran copolymers (Nouvel et al., 2004). The polysaccharide was protected in a first step, and could be easily deprotected after the polymerization (Fig.10). Aluminum, tin and zinc alkyls or alkoxy are the most widely used catalysts for the strategies presented in this section.

2.2.3 Enzymatic ring opening polymerization

Poly(ε-caprolactone) was functionalized by this way using *Candida antartica* lipase B (Novozym 425, Córdova et al., 1998) and porcine pancreatic lipase (Bisht et al., 1998). The reactions were conducted at 60-70°C in bulk, using alkyl galacto- and glucopyranoside as carbohydrate initiators. The reactions conducted without protection – deprotection steps were found to be highly regioselective, the oligo(ε-caprolactone) chains formed being attached by an ester link to the primary hydroxyl moiety of the carbohydrate initiator (Fig. 11). Weight-average molecular weights around 4000 g/mol were reported with polydispersity indexes around 1.3 using *Candida antartica* lipase B (Córdova et al., 1998), while weight-average molecular weights of 2200 g/mol (*vs.* polystyrene standards) were reported for porcine pancreatic lipase (Bisht et al., 1998). The resulting carbohydrate end-capped oligo(ε-caprolactone) can be further used for the synthesis of multi-arm poly(lactide-*co*-(ε-caprolactone)) via coordination/insertion ring opening polymerization (Deng et al., 1999). The oligo(ε-caprolactone) hydroxyl end group is first protected by lipase catalyzed acetylation, and the remaining carbohydrate free hydroxyl groups can further initiate the polymerization of L-lactide mediated by tin octanoate (Fig. 11).

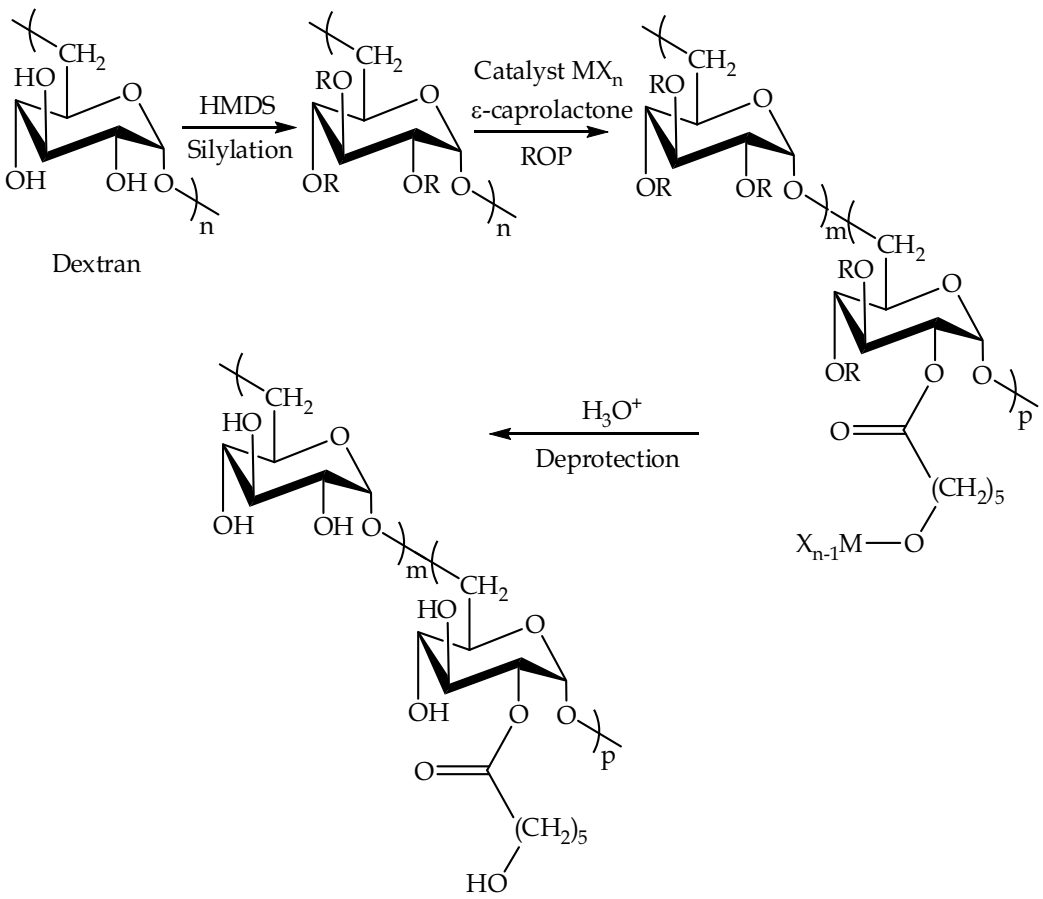

Fig. 10. Synthesis of poly(ε-caprolactone)-*graft*-dextran via coordination/insertion ring-opening polymerization (Ydens et al. 2000) - HMDS = 1,1,1,3,3,3-Hexamethyldisilazane, R = -Si(CH_3)$_3$ or H.

2.2.4 Organocatalysis

Personn et al. (2004) reported the use of lactic acid as a catalyst for the ring-opening polymerization of ε-caprolactone initiated by unprotected mono, di and tri-saccharides. The reaction was conducted at 120°C in bulk. The main products were regioselectively acylated on the primary hydroxyl groups of the carbohydrate end groups. Weight-average molecular weights of 2000 g/mol (*vs.* polystyrene standards) were reported with polydispersity indexes of 1.5. This one-step approach conducted without protection – deprotection steps lead to both carbohydrate (major product) and lactic acid end-capped poly(ε-caprolactone), as lactic acid also initiates the polymerization of ε-caprolactone under the experimental condition reported. (Fig. 12)

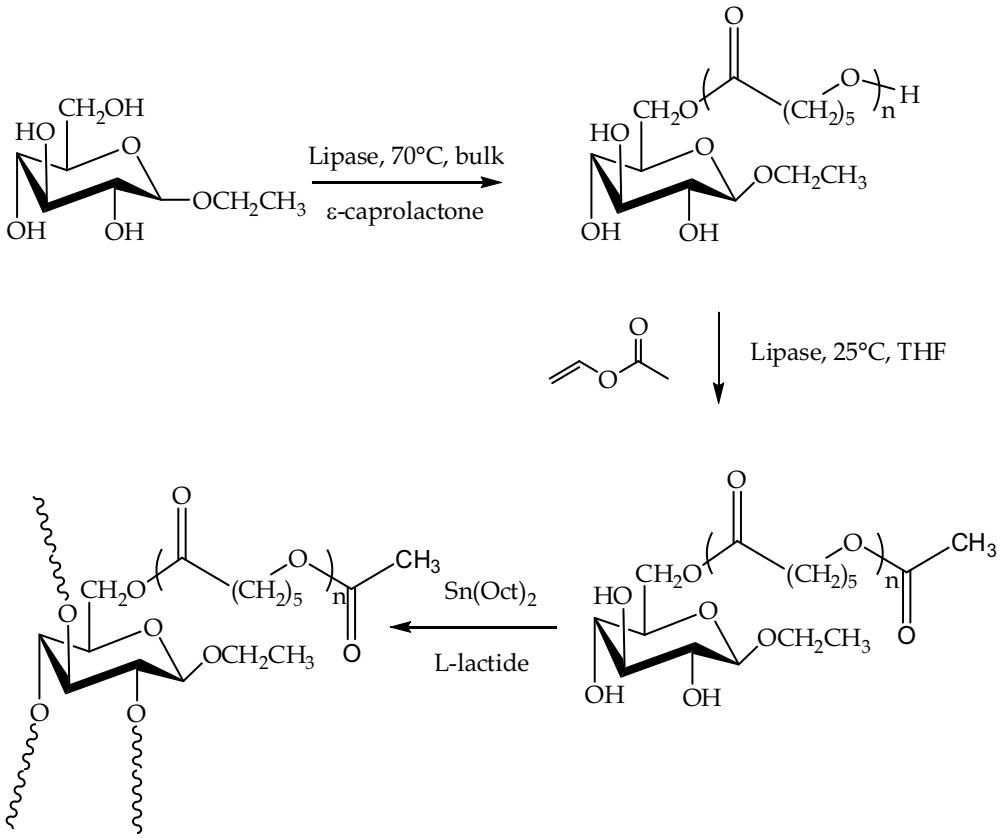

Fig. 11. Regioselective one-step poly(ε-caprolactone) end functionalization via enzymatic ring-opening polymerization (Bisht et al., 1998) and subsequent multiarm formation via coordination/insertion ring-opening polymerization of L-lactide (Deng et al., 1999) - Ethylglucopyranoside consists of a mixture of α- and β-anomers

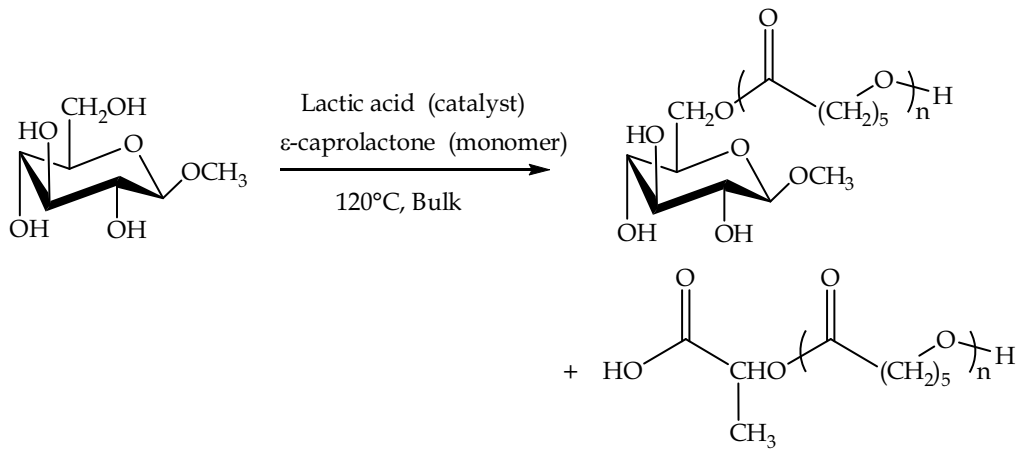

Fig. 12. One-pot poly(ε-caprolactone) end functionalization via organocatalytic ring-opening polymerization (Persson et al., 2004)

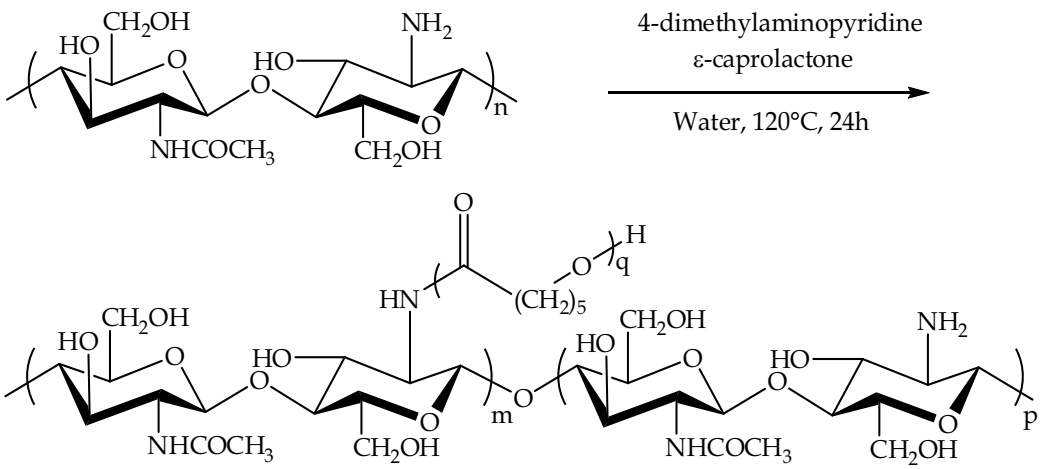

Fig. 13. Synthesis of poly(ε-caprolactone)-*graft*-chitosan via organocatalytic ring-opening polymerization (Feng et al. 2004)

The grafting from approach was also applied using organocatalysis. Feng et al. (2004) reported the synthesis of poly(ε-caprolactone)-*graft*-chitosan using 4-dimethylaminopyridine as a catalyst and water as a swelling agent starting from unprotected chitosan. The amino group of chitosan initiated the graft polymerization of ε-caprolactone through the chitosan backbone, while the hydroxyl group (HO-CH_2) of chitosan did not react (Fig. 13). Unprotected cyclodextrins were also used as initiators for the ring opening polymerization of lactones in the absence of catalysts. The yield remains modest for the polymerization of ε-caprolactone initiated by β-cyclodextrin in bulk at 100°C, but the reaction was shown to be regioselective, yielding a polymer attached to the *C*2-hydroxyl group of a single glucopyranose unit of the cyclodextrin (Takashima et al., 2004).

2.3 Use of functionalized compounds as (co-)monomers

The polymerization of functionalized cyclic esters represented in Fig. 14 is often rendered difficult by the chemical nature of the functional group. The latter must not interfere with the ring-opening polymerization, or has to be protected. Deprotection of sensitive functional groups and/or derivatization are thus applied, in addition to the synthesis of the functionalized monomer. This section presents some of the strategies developed in this field.

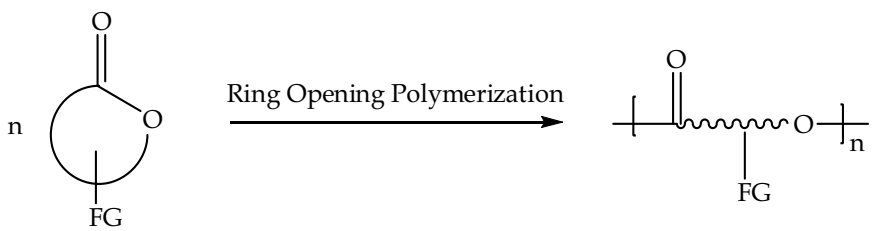

Fig. 14. Use of functionalized compounds as monomer or comonomer for the ring-opening polymerization of cyclic esters - FG represents a functional group

2.3.1 Protection strategies

A typical example of the synthesis of a cyclic ester bearing a protected hydroxyl group is presented in Fig. 15 (Trollsas et al., 2000). The ε-caprolactone derivative is generated by the Bayer-Villiger oxidation of the corresponding cyclohexanone, and is polymerized using tin octanoate, followed by the deprotection of the hydroxyl group. The authors reported also

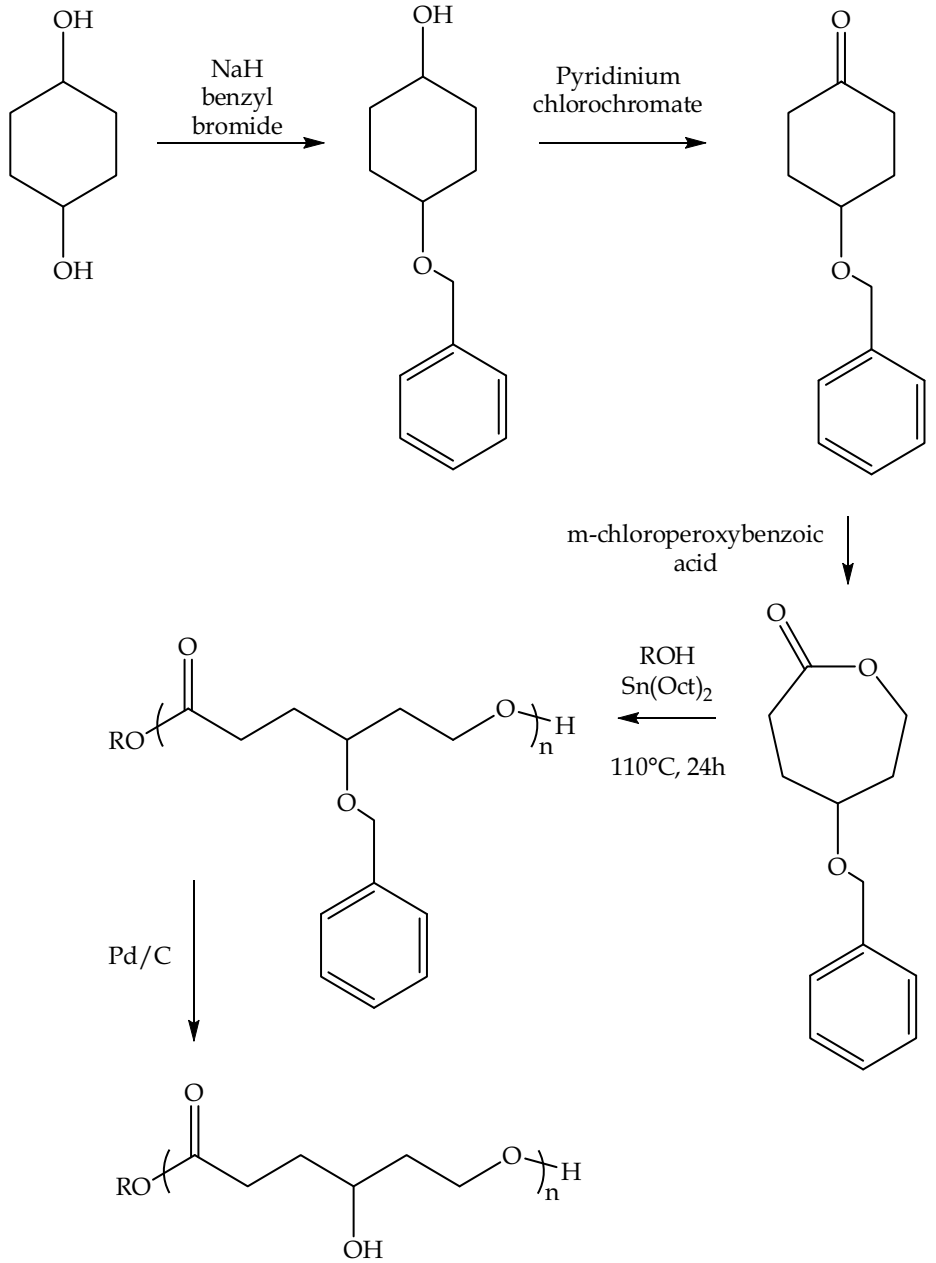

Fig. 15. Synthesis and polymerization of cyclic esters bearing a protected hydroxyl group (Trollsas et al., 2000)

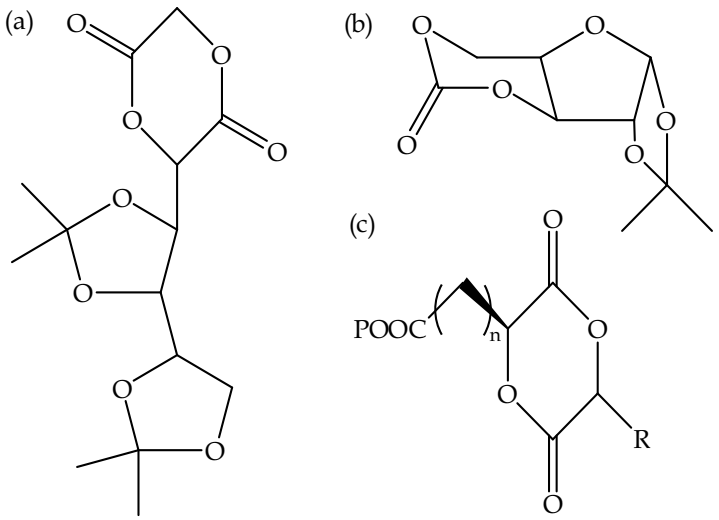

Fig. 16. Examples of carbohydrate derived monomers : 3-(1,2-3,4-tetraoxobutyldi-isopropylidene)dioxane-2,5-dione ((a), Benabdillah et al., 1999), 1,2-o-isopropylidene-[D]-xylofuranose-3,5-cyclic carbonate ((b), Chen & Gross, 1999) and 1,4-dioxane-2,5-diones featuring pendant carboxyl groups (P = protecting group, x=1, R=CH_2COOP; x=1, R=H; x=2, R=CH_3, Thillaye du Boulay et al., 2008)

the synthesis of bishydroxyl, amino, and carboxyl functionalized poly(ε-caprolactone) using similar strategies. New carbohydrate derived cyclic esters or carbonate monomers where the functional groups are protected have also been synthesized (Fig. 16). They can be further polymerized or co-polymerized with classical polyester precursors.

2.3.2 Non-sensitive functional groups and derivatization

The synthesis of ε-caprolactone bearing allyl or cyclopentene pendent groups that are not sensitive to ring opening polymerization was reported (Mecerreyes et al., 2000 and Parish & Emrick 2004). The resulting monomer can be copolymerized with ε-caprolactone and lactide, and derivatization can be further performed, such as bromination, epoxidation, and hydrosylilation of the allyl group. The obtention of graft copolymers with poly(ethylene glycol) is also possible by conversion of the cyclopentene groups to 1,2-diols, and coupling of the hydroxyl groups to poly(ethylene glycol)-carboxylic acid derivatives. This latter approach, known as grafting onto, is presented in the next section using click chemistry.

2.3.3 Grafting onto methods and click chemistry

Grafting onto methods knows a recent regain of interest due to the development of click chemistry. Click chemistry considers reactions that can be carried out under mild conditions, in the presence of various functional groups, leading to high yields and to the generation of few or none harmless by-products. Among the reactions used in click chemistry, the most popular is the copper(I)-catalyzed alkyne-azide cycloaddition represented in Fig. 17. The application of this reaction for *in vitro* and *in vivo* studies suggests that the resulting 1,2,3-triazole group is biocompatible.

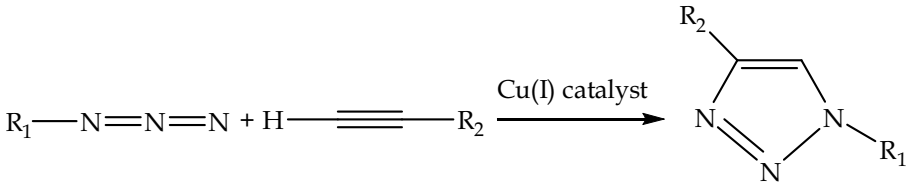

Fig. 17. Copper(I)-catalyzed alkyne-azide cycloaddition

The use of click chemistry for the functionalization of polyesters has also been reported for block copolymerization and for the synthesis of star-shaped polymers (Lecomte et al. 2008), but the most interesting strategies remain the grafting onto and grafting through approaches. The latter will be briefly described in the next paragraph. For the grafting onto strategy, cyclic esters bearing an azide or alkyne functional group are synthesized in the first step, followed by ring-opening polymerization and the grafting of an azide or alkyne end-capped polymer onto the functionalized polyester backbone.

Parrish et al. (2005) pioneered this approach synthesizing a α-propargyl-δ-valerolactone that was further copolymerized with ε-caprolactone (Fig. 18). The resulting alkyne grafted aliphatic polyester served as backbone for clicking oligopeptide moities and poly(ethylene glycol) onto the backbone. The synthesis of other monomers of interest such as α-azide-ε-caprolactone (Riva et al., 2005) and 3,6-dipropargyl-1,4-dioxane-2,5-dione (Jiang et al., 2008) and subsequent polymerization and grafting have also been reported in the literature, leading notably to poly(ethylene glycol)-*graft*-poly(ε-caprolactone) and –polylactides, respectively. Note that the reactive groups used for the grafting onto method can also be introduced by post-polymerization modification of a chloro-functionalized polyester backbone (Riva et al., 2005).

2.3.4 Grafting through methods

In this approach, a cyclic ester bearing a pendant macromolecular chain is synthesized and polymerized. Poly(ethylene glycol) chains end-capped by an ε-caprolactone unit have been synthesized by living anionic ring-opening polymerization of ethylene oxide initiated by the potassium alkoxide of 1,4-dioxaspiro[4,5]decan-8-ol, followed by derivatization of the acetal into a ketone and the Baeyer-Villiger oxidation of the ketone into a lactone (Rieger et al., 2004). The polymerization of this monomer lead to poly(ethylene glycol)-*graft*-poly(ε-caprolactone). This is represented in Fig. 19. Click chemistry can also be used for the synthesis of poly(ethylene glycol) macromonomers based on ε-caprolactone and lactide (Riva et al., 2005 and Jiang et al., 2008, respectively).

3. Polycondensation (Fig. 20)

The synthesis of polyesters can take place by polycondensation of diols with diacids (AA – BB) or by the polycondensation of hydroxyacids (AB), leading to the formation of water as by-product. The reaction often takes place under vacuum to remove the water formed. High molecular weights are generally difficult to achieve. The section begins with the description of melt/solid polycondensation, a strategy developed to obtain high molecular weight poly(lactid acid) and poly(glycolic acid). The introduction of functional groups into polyesters by polycondensation is rendered difficult by the sensitivity of the functional groups, often secondary alcohols, to the polymerization. The brief description of protection

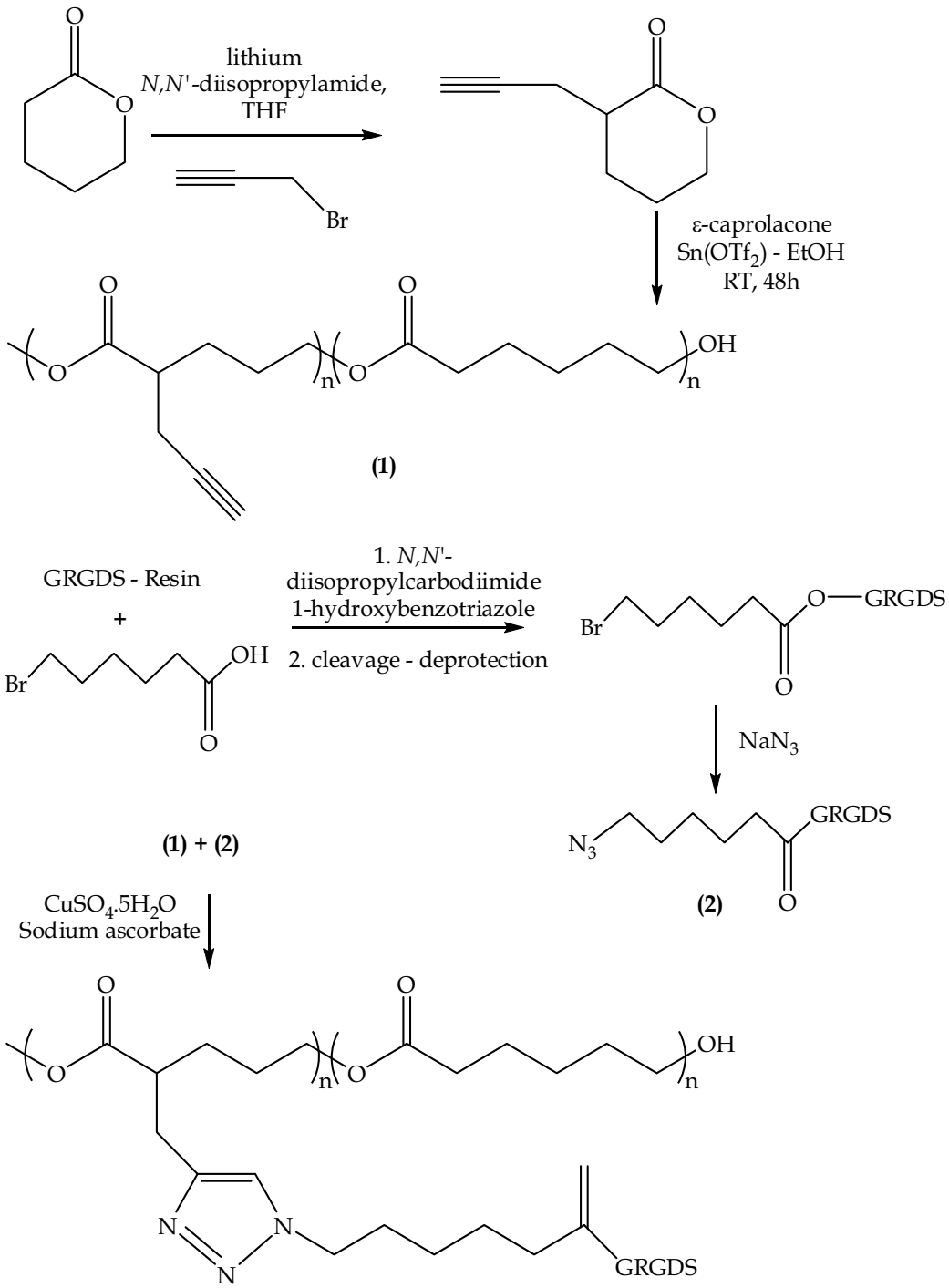

Fig. 18. Synthesis of oligopeptide-*graft*-aliphatic polyester via click chemistry and grafting onto approach (Parrish et al., 2005) - GRDS is an oligopeptide sequence.

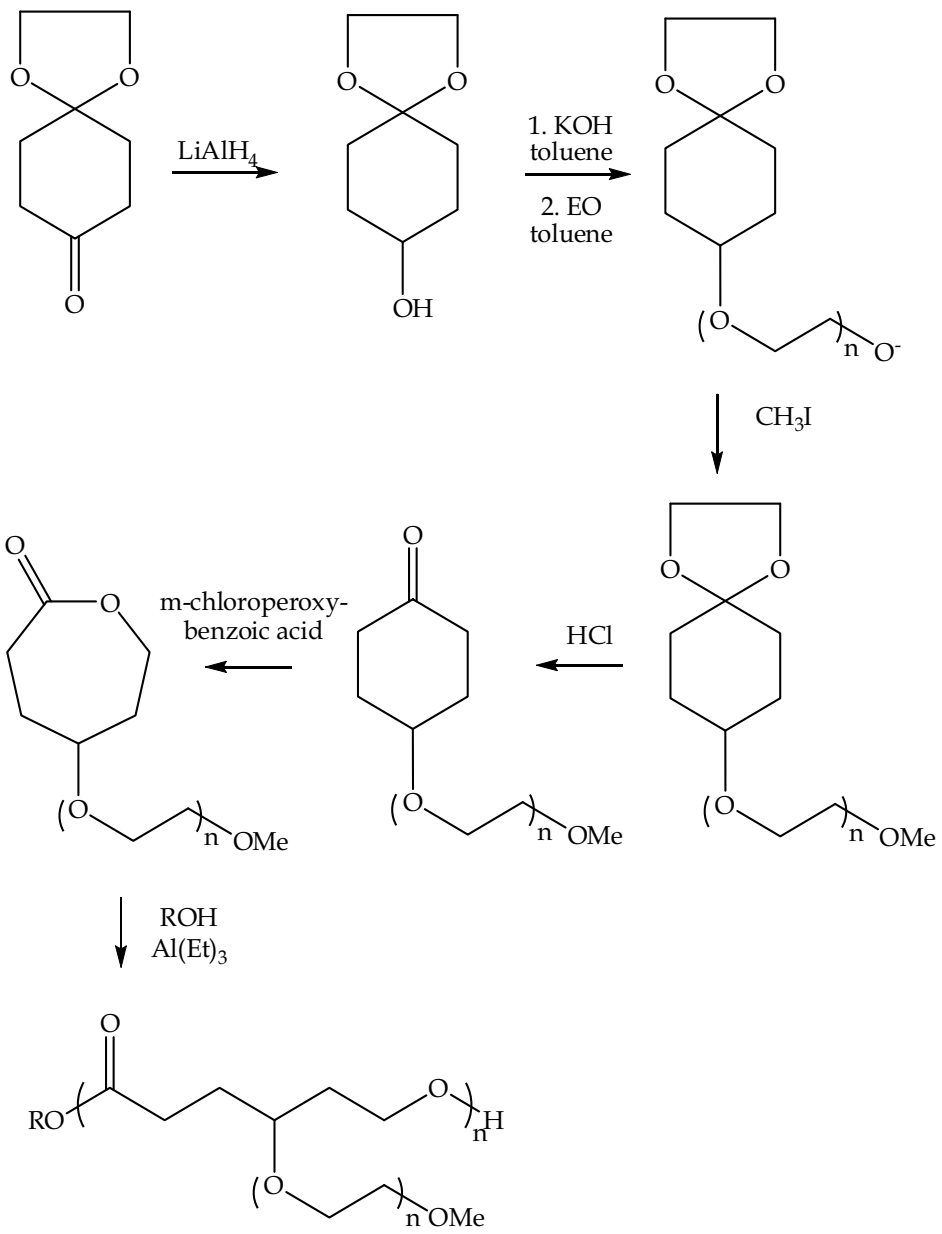

Fig. 19. Synthesis of poly(ethylene glycol)-*graft*-poly(ε-caprolactone) copolymers via the grafting through method (Rieger et al., 2004). EO = ethylene oxide.

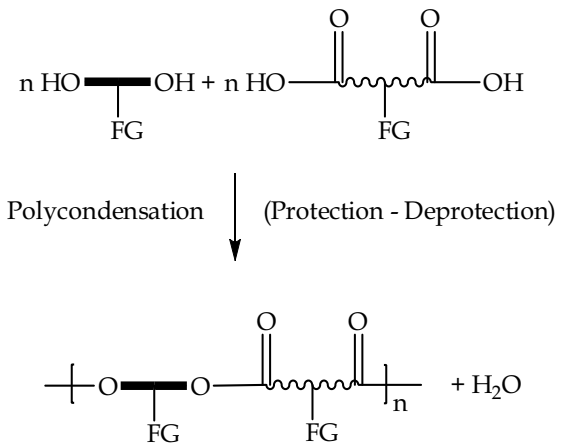

Fig. 20. Polycondensation. FG represents a functional group.

strategies used for this purpose is followed by recent advances in one-step strategies enabling the functionalization of polyesters by polycondensation without the need to protect the functional group, *i.e* enzymatic and Lewis acid catalysis. Note that these one-pot strategies lead to polyesters bearing multiple functional groups along the polymeric backbone.

3.1 Melt and solid polycondensation

The acid form of ε-caprolactone, 6-hydroxyhexanoic acid, is scarcely isolable, and thus, poly(ε-caprolactone) is rarely synthesized by polycondensation techniques. Lactic and glycolic acids are in turn naturally occurring products, and their polymers and copolymers can also be made via polycondensation. A major drawback is the removal of the water formed during the polymerization, leading often to modest number-average molecular weight. This drawback can be overcome via melt and solid polycondensation techniques.

Melt polycondensation is conducted under reduced pressure at high temperature, starting from oligomers of the targeted polymer. One may distinguish melt polycondensation from solid polycondensation; in the former case, the polymerization is conducted at a temperature above the melting temperature of the polymer. For example, the melt polycondensation of oligo(L-lactic acid) was conducted using $SnCl_2$ combined to protonic acids such as *p*-toluenesulfonic acid monohydrate or *m*-phosphoric acid (Moon et al., 2000). Weight average molecular weights up to 100 000 g/mol were obtained. The crystallization of the so-obtained poly(L-lactic acid) and subsequent solid polycondensation at temperature below the melting temperature lead to weight average molecular weights up to 500 000 g/mol using similar catalytic systems (Moon et al., 2001). Melt/solid polycondensation can also be applied to oligo(glycolic acid) (Takahashi et al., 2000).

3.2 Protected monomers

The introduction of functional groups such as secondary hydroxyls is rendered difficult by the possible reaction of these groups with the acid functionality, leading to cross-linking and gelation. The strategy consists thus usually in the protection of secondary alcohols on a functional compound, or to the synthesis of monomers where the secondary hydroxyl functions are protected. There are numerous works dealing with the synthesis of new

monomers with protected functional groups, often starting from carbohydrate derivatives. For example, protected gluconic acid in the form of 2,4,3,5-di-O-methylene-D-gluconic acid can by polymerized with benzoyl chloride (Mehltretter & Mellies 1955). The same strategy can also be applied to AA-BB polycondensation (Metzke et al., 2003, among others).

3.3 One step introduction of functional groups into polyesters

The synthesis of linear polyesters via one step polycondensation of monomers bearing secondary pendant hydroxyl groups relies on the selectivity of specific catalysts toward primary alcohols. Using such catalysts, the acid functionality reacts with primary alcohols, but not with lateral secondary alcohols, avoiding cross-linking and gelation. This can be done by enzymatic and Lewis acid catalysis.

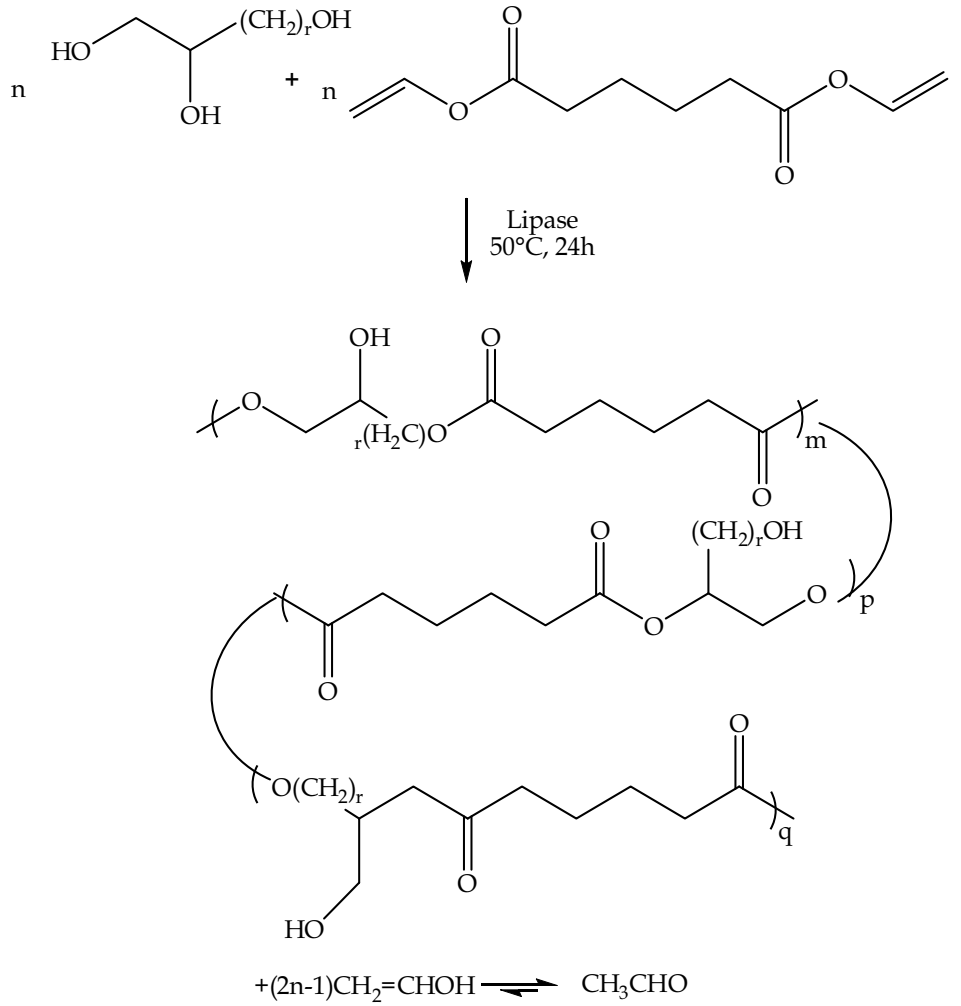

Fig. 21. Lipase catalyzed regioselective polycondensation between triols and divinyl adipate. R=1, glycerol, R=2, 1,2,4-butanetriol, and R=4, 1,2,6 trihydroxyhexane (Kline et al., 1998)

3.3.1 Enzymatic catalysis

Enzymatic catalyzed polycondensation enables a one-step synthesis of hydroxyl pendant polyesters using renewable resources as the polyol monomer. Using Novozyme-435 lipase and *Candida antartica* lipase B, glycerol, 1,2,4-butanetriol and 1,2,6 trihydroxyhexane can be copolymerized with divinyl esters to yield low to high molecular weight linear hydroxypolyesters (Kline et al. 1998, Uyama et al. 2001 – Fig. 21). The reaction is regioselective, as the pendant hydroxyl groups in the polymer are mainly secondary. Glycerol can also be copolymerized with adipic acid and 1,8-octanetriol using Novozyme-435, yielding a few intermolecular crosslinks in addition to hydroxyl pendant groups (Kumar et al. 2003). Carbohydrate polyols such as sorbitol (Fig. 22) and alditols were also successfully copolymerized with 1,8-octanediol and adipic acid using the aforementioned enzyme as catalyst (Kumar et al., 2003, Hu et al., 2006).

3.3.2 Lewis acid catalysis

Lewis acid catalyzed polyesterification is another type of chemistry enabling a one step synthesis of linear polyesters bearing pendant hydroxyl groups. Using trifluoromethane sulfonate salts (known as triflate - $M(OSO_2CF_3)_n$), sorbitol and glycerol were successfully copolymerized with diacids (Takasu et al. 2007). Lewis acid catalysis is rather versatile as diacids bearing pendant hydroxyl groups such as tartaric and malic acids could also be copolymerized selectively with diols in bulk and under reduced pressure. The resulting polyesters had low to average molecular weights. The procedures are represented in Fig. 23.

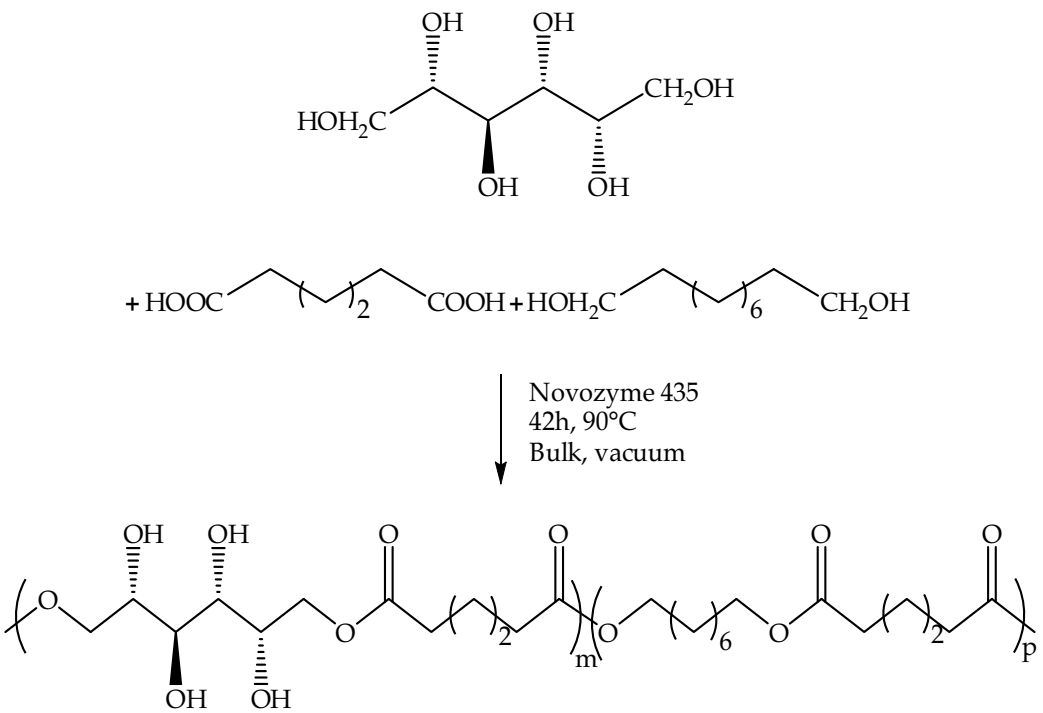

Fig. 22. Novozyme-435-catalyzed regioselective polymerization of sorbitol with adipic acid and 1,8-octanetriol (Kumar et al., 2003)

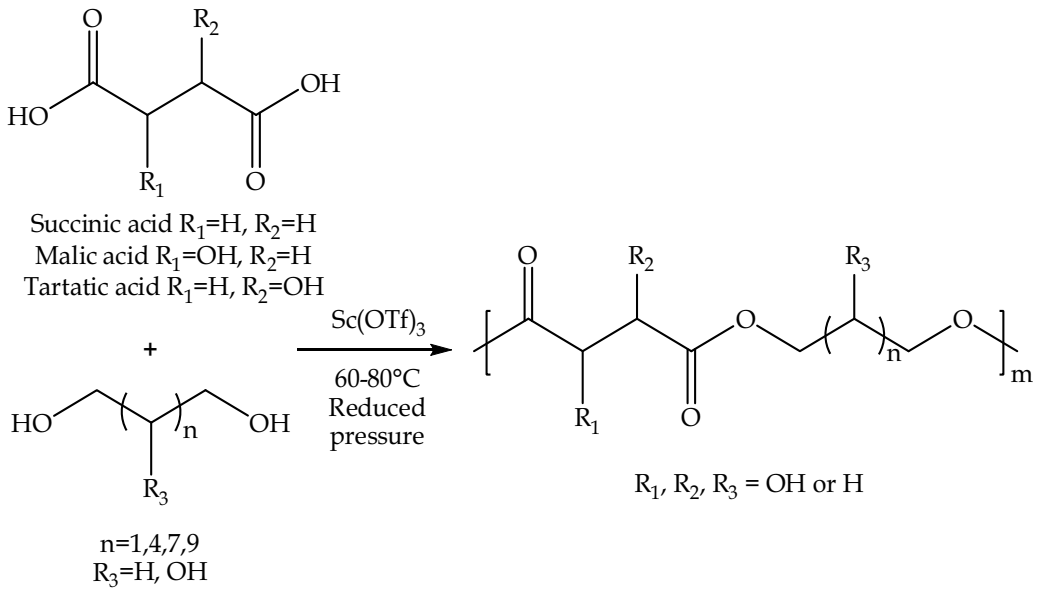

Fig. 23. Scandium triflate catalyzed regioselective polycondensation of dicarboxylic acids and diols having pendant hydroxyl groups (Takasu et al., 2007)

4. Transesterification

The principle of transesterification is presented in Fig. 24. The reaction can start from an ester and an alcohol, or from two ester groups. Transesterification commonly occurs in the molten state, producing first block copolymers and finally statistical copolymers.

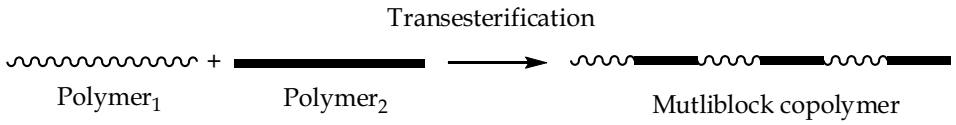

Fig. 24. Transesterification

Transesterification of poly(D,L-lactide) and polyethylene glycol was reported in acetone, without catalysts, leading to copolymers with number-average molecular weights up to 6000 g/mol (Piskin et al., 1995). The polymer precursors exhibit number average molecular weights between 2000 and 4000 g/mol. Additional purification steps are necessary in order to remove the remaining homopolymer. The resulting copolymer was shown to form micelles, poly(D,L-lactide) being the hydrophobic segment and polyethylene glycol the hydrophilic segment, and were further used as drug carriers. The composition of the copolymer can be simply changed by varying the ratio of polymer precursors. The molecular weight of the resulting copolymer can be significantly increased starting from precursors of higher molecular weight. Using succinic acid as chain extender for poylethylene glycol, poly(L-lactide) and poly(D,L-lactide) of high molecular weight and titanium isopropoxyde as transesterification catalyst, molecular weight up to 40 000 g/mol *vs.* polystyrene standards could be achieved (Mai et al. 2009).

5. Conclusion

The synthetic strategies for the functionalization of polyesters are numerous, and result in a great diversity of polyesters specialties for potential biomedical applications. Various architectures can be synthesized, including statistical and block copolymers, as well as graft and star-shape copolymers. Ring-opening polymerization leads generally to higher molecular weights than polycondensation, and has been more studied. Enzymatic and organocatalyzed ring-opening polymerization are particularly interesting, as they enable one-pot regioselective end-functionalizations of polyesters by carbohydrate derivatives notably, without protection/deprotection steps. Regioselective polymerization can also be conducted by polycondensation, considering enzymatic and Lewis acid catalysis. This leads to a higher number of functionalities along the polymeric backbone, which can only be achieved by protection / deprotection strategies or derivatization considering ring-opening polymerization. Transesterification leads on the other side to interesting microstructures, and can be conducted without catalysts in certain conditions.

6. Acknowledgments

Drs. Till Bousquet and Andreia Valente are gratefully acknowledged for careful reading.

7. References

Albertsson, A.C.; Varm I.K. (2003) Recent developments in ring opening polymerization of lactones for biomedical applications. *Biomacromolecules*. Vol. 4, 1466-1486.

Benabdillah K.M.; Coudane J.; Boustta M.; Engel M.; Vert M. (1999). Synthesis and characterization of novel degradable polyesters derived from D-gluconic and glycolic acids. *Macromolecules*. Vol. 32, 8774-8780.

Bernard K.; Degée P.; Dubois P. (2003). Regioselective end-functionalization of polylactide oligomers with D-glucose and D-galactose. *Polym. Int*. Vol. 52. 406-411.

Bisht K.S.; Deng F.; Gross R.A.; Kaplan D.L.; Swift G. (1998). Ethylglucoside as a multifunctional initiator for enzyme-catalyzed regioselective lactone ring-opening polymerization. *J. Am. Chem. Soc*. Vol. 120, 1363-1367

Choi C.; Chae S.Y.; Kim T-H.; Kweon J.K.; Cho C.S.; Jang M-K.; Nah J-W. (2006). Synthesis and Physicochemical Characterization of amphiphilic block copolymer self-aggregates formed by poly(ethylene glycol)-block-poly(ε-caprolactone). *J. App. Polym. Sci.* Vol 99, 3520-3527.

Chen X.; Gross R.A. (1999). Versatile copolymers from [L]-lactide and [D]-xylofuranose. *Macromolecules*. Vol. 32, 308-314.

Cordova A.; Iversen T. (1998). Lipase-catalyzed synthesis of methyl 6-O-poly(ε-caprolactone)glycopyranosides. *Macromolecules*. Vol. 31, 1040-1045.

Deng F.; Bisht K.S.; Gross R.A.; Kaplan D.L. (1999). Chemoenzymatic synthesis of a multiarm poly(lactide-co-ε-caprolactone). *Macromolecules*. Vol. 32, 5159-5161.

Feng H.; Dong C.M. (2004). Preparation and characterization of chitosan-graft-poly(ε-caprolactone) with an organic catalyst. *J. Polym. Sci., Polym. Chem*. Vol. 44, 5353-5361.

Hamaide T.; Pantiru M.; Fessi H.; Boullanger P. (2001). Ring-opening polymerisation of ε-caprolactone with monosaccharides as transfer agents. A novel route to functionalised nanoparticles. *Macromol. Rapid Commun*. Vol. 22, 659-663.

Hu J; Gao W; Kulshrestha A; Gross R.A. (2006). "Sweet polyesters": Lipase-catalyzed condensation-polymerizations of alditols. *Macromolecules* Vol. 39, 6789-6792.

Jiang X.; Smith M.R.; Baker G.L. (2008). Water-soluble thermoresponsive polylactides. *Macromolecules*. Vol. 41, 318-324.

Kline B.J.; Beckman E.J.; Russel A.J. (1998). One-step biocatalytic synthesis of linear polyesters with pendant hydroxyl groups. *J. Am. Chem. Soc.* Vol. 120, 9475-9480.

Kricheldorf H.R.; Stricker A. (2000). Macrocycles. 13. Stannylenated glucose glycosides as cyclic initiators of ε-caprolactone and the synthesis of biodegradable networks; *Macromolecules*. Vol. 33, 696-703.

Kumar R.; Gross R.A. (2002). Biocatalytic route to well defined macromers built around a sugar core. *J. Am. Chem. Soc.* Vol. 124, 1850-1851.

Kumar A.; Kulshresta S.; Gao W.; Gross R.A. (2003). Versatile route to polyol polyesters by lipase catalysis. *Macromolecules.* Vol. 36, 8219-8221.

Lecomte P.; Riva R.; Jérôme C.; Jérôme R. (2008). Macromolecular engineering of biodegradable polyesters by ring-opening polymerization and "click" chemistry. *Macromol. Rapid Commun*. Vol. 29, 982-997.

Mai S.; Abbot A.; Norton D.; McKean R., Ryan J.R. (2009). Synthesis and characterization of block copoloymers of polyoxyethylene and polylactide with different architectures. Macromol. Chem. Phys. Vol. 210, 840-851

Mecerreyes D.; Miller R.D.; Hedrick J.L.; Detrembleur C.; Jérôme R. (2000). Ring-opening polymerization of 6-hydroxynon-8-enoic acid lactone: novel biodegradable copolymers containing allyl pendent groups. *J. Polym. Sci., Polym. Chem.* Vol. 38, 870-875.

Mehltretter C.L.; Mellies R.L. (1955). The Polyesterification of 2,4 ;3,5-Di-O-methylene-D-gluconi acid. *J. Am. Chem. Soc.* 427-428.

Metzke M.; Bai J.Z.; Guan Z. (2003). A novel carbohydrate-derived side-chain polyether with excellent protein resistance. . *J. Am. Chem. Soc.* Vol. 125, 7760-7761.

Moon S.I.; Lee C.W.; Miyamoto M.; Kimura Y. (2000). Melt polycondensation of L-lactic acid with Sn(II) catalysts activated by various proton acids: a direct manufacturing route to high molecular weight poly(L-lactic acid)., *J. Polym. Sci., Polym. Chem.* Vol. 38, 1673-1679.

Morikawa Y.; Kinoshita H.; Asahi M.; Takasu A.; Hirabayashi T. (2008). Tailor-made amphiphilic biodegradable polymers gels. 1. Gel preparation via controlled ring-opening polymerization using glucopyranoside as initiator and subsequent coupling with α-ω-bifunctional PEG. *Polym. J.* Vol. 40, 217-222.

Moon S.I.; Lee C.W.; Taniguchi I.; Miyamoto M.; Kimura Y. (2001) Melt/solid polycondensation of L-lactic acid: an alternative route to poly(L-lactic acid) with high molecular weight. *Polymer.* Vol. 42, 5059-5062

Nouvel C.; Dubois P.; Dellacherie E.; Six J-L. (2004). Controlled synthesis of amphiphilic biodegradable poly(lactide)-graft-dextran copolymers. *J. Polym. Sci., Polym. Chem.* Vol. 42, 2577-2588

Nyce G.W.; Glauser T.; Connor E.F.; Möck A.; Waymouth R.M.; Hedrick J.L. (2003). In situ generation of carbenes: a general and versatile platform for organocatalytic living polymerization. *J. Am. Chem. Soc*., Vol. 125, 3046-3056.

Ouchi T.; Uchida T.; Ohya Y. (2001). Synthesis of poly(L-lactide) with one terminal D-glucose residue and wettability of its film surface. *Macromol. Biosci.* Vol. 1, 371-375.

Parrish B.; Emrick T. (2004). Aliphatic polyesters with pendant cyclopentene groups: controlled synthesis and conversion to polyester-graft-PEG copolymers. *Macromolecules*. Vol. 37, 5863-5865.

Parrish B.; Breitenkamp R.B.; Emrick T. (2005) PEG- and peptide-grafted aliphatic polyesters by click chemistry. *J. Am. Chem. Soc.* Vol. 127, 7404-7410.

Persson P.V.; Schröder J.; Wickholm K.; Hendenström E.; Iversen T. (2004) Selective organocatalytic ring-opening polymerization: a versatile route to carbohydrate-functionalized poly(ε-caprolactone). *Macromolecules*. Vol. 37, 5889-5893.

Piskin, E.; Kaitian, X.; Denkbas E.B.; Kücükyavuz. (1995) . Novel PDLLA/PEG copolymer micelles as drug carriers. *J. Biomater. Sci. Polymer Ed*. Vol. 7, No. 7, 359-373.

Rieger J.; Bernaerts K.V.; Du Prez F.E.; Jérôme R.; Jérôme C. (2004). Lactone end-capped poly(ethylene oxide) as a new building block for biomaterials. *Macromolecules*. Vol. 37, 9738-9745

Riva R.; Schmeits S.; Stoffelbach F.; Jérôme C.; Jérôme R.; Lecomte P. (2005). Combination of ring-opening polymerization and ''click'' chemistry towards functionalization of aliphatic polyesters. *Chem. Commun*. 5334-5336.

Takahashi K.; Taniguchi I.; Miyamoto M.; Kimura Y. (2000). Melt/solid polycondensation of glycolic acid to obtain high-molecular-weight poly(glycolic acid). *Polymer*. Vol. 41, 8725-8728.

Takashima Y.; Osaki M.; Harada A. (2004). Cyclodextrin-initiated polymerization of cyclic esters in bulk: formation of polyester-tethered cyclodextrins. *J. Am. Chem. Soc*. Vol. 126, 16588-13589

Takasu A.; Shibata Y.; Narukawa Y.; Hirabayashi T. (2007). Chemoselective dehydration polycondensations of dicarboxylic acids and diols having pendant hydroxyl groups using the room temperature polycondensation method. *Macromolecules* Vol. 40, 151-153.

Tang M.; Haider F.A.; Minelli C.; Stevens M.M.; Williams C.K. (2008). Lactide polymerization co-initiated by carbohydrate esters and pyranoses. *J. Polym. Sci., Polym. Chem*. Vol. 46, 4352-4362.

Thillaye du Boullay O.; Colin Bonduelle C.; Martin-Vaca B.; Bourissou D. (2008). Functionalized polyesters from organocatalyzed ROP of gluOCA, the O-carboxyanhydride derived from glutamic acid. *Chem. Commun*, 1786-1788.

Trollsås M.; Lee V.Y.; Mecerreyes D.; Lowenhielm P.; Möller M.; Miller R.D.; Hedrick J.L. (2000). Hydrophilic aliphatic polyesters: design, synthesis, and ring-opening polymerization of functional cyclic esters. *Macromolecules*, Vol. 33, 4619-4627.

Uyama H.; Inada K.; Kobayashi S. (2003) Regioselectivity control in lipase-catalyzed polymerization of divinyl sebacate and triols. *Macromol. Biosci.* Vol. 1, 40-44.

Yasugi K.; Nakamura T.;, Nagasaki Y.; Kato M.; Kataoka K. (1999). Sugar-installed polymer micelles: Synthesis and micellization of poly(ethylene glycol)-poly(D,L-lactide) block copolymers having sugar groups at the PEG chain end. *Macromolecules.* Vol. 32, 8024-8032.

Ydens I.; Rutot D.; Dege P.; Six J-L.; Dellacherie E.; Dubois P. (2000). Controlled synthesis of poly(ε-caprolactone)-grafted dextran copolymers as potential environmentally friendly surfactants. *Macromolecules.* Vol. 33. 6713-6721

Zinck P. (2009). One-step synthesis of polyesters specialties for biomedical applications. *Rev. Environ. Sci. Biotechnol.* Vol. 8. 231-234.

22

Prevention of Biofilm Associated Infections and Degradation of Polymeric Materials used in Biomedical Applications

Peter Kaali, Emma Strömberg and Sigbritt Karlsson
Royal Institute of Technology,
Sweden

1. Introduction

Biomedical polymers have a wide variety of applications for external and internal use. Similar criteria must be fulfilled by biomedical polymeric materials used as internal or partly internal (invasive) devices, where the polymer gets in contact with the human environment. The material needs to be biocompatible, neutral to the human body and have to express excellent stability and resistance against tissues, cells, enzymes and different body fluids. The body response to the polymer can be acceptance or rejection and depending on the location of the material, these responses are influenced by different factors. Besides the body response, the microbiological effect and biofilm formation on the internal medical devices are of great importance. If biofilm adheres to the surface it can initiate a degradation process of the material, and due to the high concentration of microorganisms, infections and health related problems can be caused. The biocompatibility of polymers does not only depend on the chemical structure, the capability of microbes and the body environment to adhere or also initiate the degradation inside the human body is highly structure dependant. Once degradation occurs, along with the migration of additives and low molecular weight compounds, the polymer loses its biocompatibility and stability, which can lead to the failure of the device or could cause health related issues. Therefore the understanding of the different degradation processes that may occur inside the human body due to blood, tissue or biofilm interaction is very important. This chapter gives an overview on the mechanism of biofilm formation and adherence to surfaces, and means to characterize and determine its presence. Furthermore, the effect and the role of body-polymer interaction, the degradation mechanisms and the factors influencing the degradation of medical polymers are discussed. The factors that should be controlled are the biofilm formation and the prevention of infections caused by the microorganisms that usually generate intensive body reactions. Means to modify the polymeric materials by incorporating antimicrobial agents into the bulk of the polymer or right onto the surface as a coating is presented.

2. Biofilm

2.1 Characteristics and formation

By definition, biofilms are aggregates of microorganisms, which are formed due to the attachment of cells to each other and/or to a host surface in an aqueous environment. (Lynch

et al., 2003) In general, biofilms can host microorganisms such as bacteria, fungi, protozoa, algae and their mixtures, and usually the constituent cells require similar conditions to initiate and progress the cell growth. The factors that influence the biofilm formation are humidity, temperature, pH of the environment or medium, atmospheric conditions and nutrition sources. Besides microorganism cells, biofilms usually contain 80-90% of water and depending on the host surface their thickness may vary between 50-100μm.

Biofilm formation starts with the deposition of microorganisms on the surface of the material, followed by growth and spreading of the colonies. Microbial colony numbers are often very high and the emerging biofilms contain several layers of microorganisms, resulting in a highly complex structure (Flemming, 1998). The microbial cells are encased in an adhesive matrix produced by the microorganisms of the biofilm, called extracellular polymer substance or exopolysaccharide (EPS), which contains proteins, nucleic acids, lipids and polysaccharides. (Mayer et al., 1999, Beech, 2004). EPS influences the adhesion to the surface and plays an important role in the protection of the biofilm from outer environment. Therefore, the biofilms have an improved resistance against toxins, detergents and antimicrobial agents. In some cases the resistance of bacterial biofilms against antibiotics can be increased up to 1000 fold compared to isolated colonies.

2.2 Microbial adhesion

Since biofilm plays a vital role in a wide variety of industrial, environmental and medical applications, the understanding of its formation mechanism and factors that influence the attachment to surfaces is essential. The environment which surrounds the surface may catalyze the biofilm formation; however, the process in most of the cases is similar.

Fowler and Mckay were the first ones to investigate and describe the dynamic mechanism of bacterial adhesion. They took into account the initial physicochemical characteristics of the two surfaces that interact (Fowler and Mckay, 1980). The adhesion of the bacterial cell is a sequence of dynamic processes which involves characteristic forces, time scales and length scales (Denyer et al., 1993, Dickinson et al., 2000). In the first sequence, the cell is transported to the surface by gravitational force (sedimentation) and hydrodynamic forces (fluid flow, cell motility) where it reaches a diffusive boundary layer (Fig. 1). At this interface diffusion is the main driving force and, due to the small size of the cell, Brownian motion plays a vital role in the diffusive transport even closer to the surface. In the interval of the diffusive boundary layer there is a certain distance where direct interaction takes place between the cell surface and the substrate through attractive and repulsive forces (that includes Van der Waals and double layer interactions). At this distance the attachment of the cell to the surface is reversible since the interactions between both surfaces are weak (Oliveira, 1992). Initially both surfaces are negatively charged and therefore the attractive forces to ensure the adhesion must overcome an electrostatic repulse ion barrier.

The interaction range between the cell and the surface is relatively small (<1 micron), however, the characteristic length of the stronger irreversible forces is around 5 to several hundreds of nanometers. The time scale of the transport process to the surface is flow dependent which is on the scale of $5x10^{-9}$ cm^2/s for a cell having 1 micron in diameter. Once the cell has attached to the surface the strength of the attachment is governed by short range interactions (<5nm) which involves the resistance to detachment of the particle (irreversible) (Dickinson et al., 2000, Oliveira, 1992). These interactions include hydrogen bonding, shorter range Van der Waals forces, electrostatic, ionic and dipole interactions (Bos et al., 1999). The

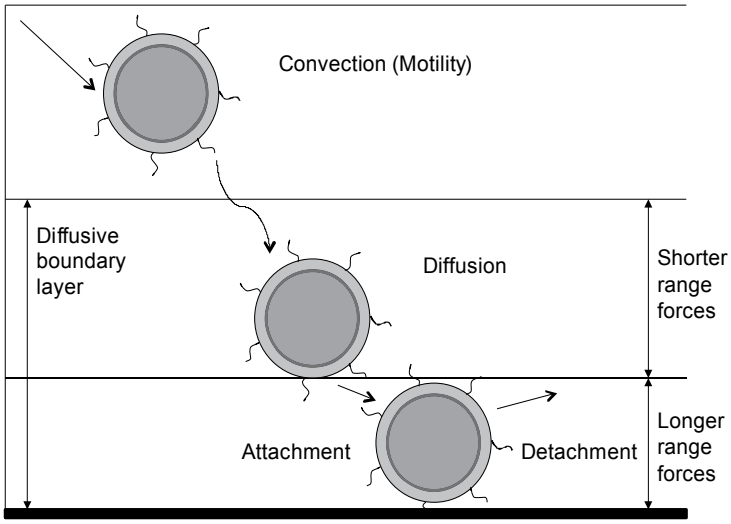

Fig. 1. Cell attachment mechanism redrawn from (Dickinson et. al., 2000)

long, short range forces and electrostatic interactions which play an important role in the bacterial attachment are described by the DLVO theory (Derjaguin and Landau, 1941, Verwey and Overbeek, 1948). The theory was developed originally to explain the coagulation behaviour of charged colloidal particles; however, it could also be applied to explain the interaction between a colloidal particle (as a bacterial cell) and a macroscopic surface (Fig.2).

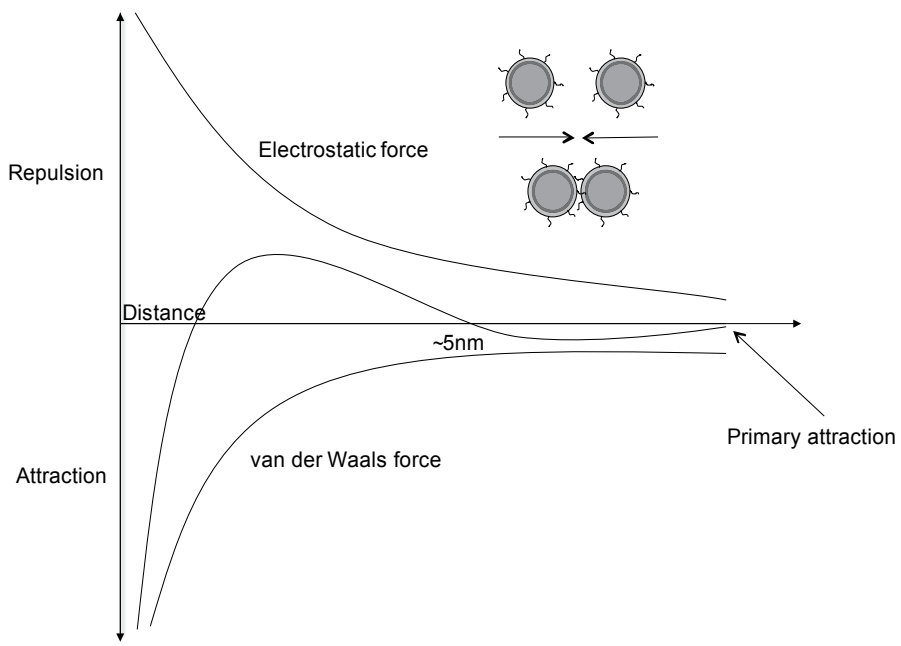

Fig. 2. The DLVO theory

Type of interaction	Interaction forces	Approximate interaction energy (kJ/mol)
Reversible Long range, weak, low specificity	Van der Waals Electrostatic	20-50
Irreversible Short rage, high specificity	Dipole-dipole Dipole-induced dipole Ion-dipole Ionic Hydrogen bonds Hydrophobic	40-400

Table 1. Reversible and irreversible interaction during bacterial attachment(Oliveira, 1992)

2.3 Biodeterioration of polymeric materials

Biofilm formation is common on most polymeric materials used in environments with high humidity. The nutrition sources necessary for successful colonisation may consist of the material itself or a variety of pollutants that end up on the surface of the material. The biofilm-polymer interactions depend on several factors which can be evaluated separately and in various combinations in authentic artificial environments that mimic the material's end-use conditions(Wallström et al., 2002, Wallström et al., 2005). The characterization of the biofilm growth is also essential and is in general conducted by microscopic (i.e. optical, scanning electron microscope) methods, however, a few studies showed that the biofilm growth can be monitored by fluorescence lidar imaging as well (Bengtsson et al., 2005, Wallström and Karlsson, 2004).

For polymers, biodegradation is usually a complex system, starting with consumption of accessible additives and propagating with the decomposition of the matrix (Figure 3)(Flemming, 1998).Although biofilm formation on some surfaces does not lead to polymer biodegradation it can result in the loss of functionality. Through biofouling, the spreading of the biofilm over the surface, the original properties of the material such as hydrophobicity may be altered. The deterioration of the medical function by clotting and disrupting the flow through for example a urinal catheter may cause pain for the patient or result in a serious infection. Medical implants are convenient surfaces for microbial growth, both the short-term devices (urinary catheters) and the long-term implants (artificial joints). The notorious biofilms consisting of various bacterial strains are protected from the attack by the immune system, antibiotics and other antimicrobial agents due to difficulties in penetrating into the biofilm.

Plastic materials usually contain additives, low molecular weight compounds, residues of the polymer synthesis as well as shorter chains resulting from the degradation of the material, which migrate out of the material and interact with the biofilm. It is known that fillers such as polyesters, adiapates, epoxidised fatty acids, oleates, stearates and carbon-based plasticisers are perfect nutrition sources for microorganisms in the biofilm (Seal and Morton, 1986, Flemming, 1998). The most disputed material in biomedical applications is poly (vinyl chloride) (PVC), widely used for tubing purposes. During service life, toxic phthalate plasticisers tend to migrate out of the material, exposing the patient and providing nutrition to a growing biofilm. This leads to a harder and more brittle material, still insusceptible to biodegradation but instead sensitive to physical degradation.

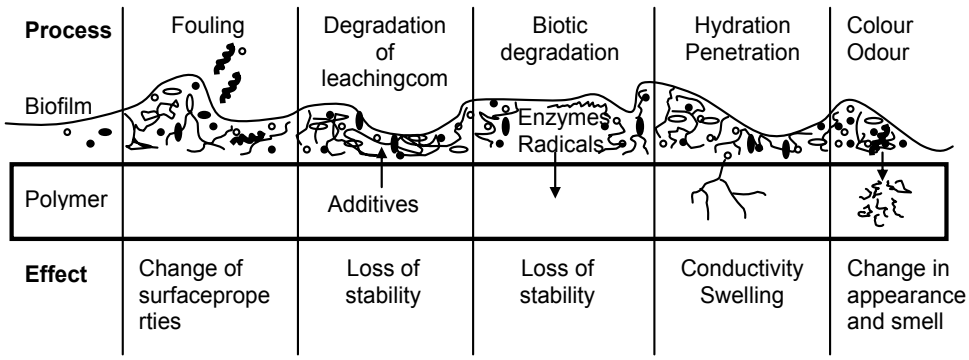

Fig. 3. Effect of biofilm formation on polymer material surface (redrawn from (Flemming, 1998)

Factors influencing the rate of biodegradation are pH, environment, oxygen, salts, redox potential and temperature. Salts could be formed by anions which can be final products of microbial metabolism and react with cations (Wallström, 2005). An increase in salt concentration or significant change in pH highly assists the breakdown of the polymer (Sand, 1997). The transformed surface conditions, including the increasing humidity, induce the decomposition rate of the material.

The excretion of enzymes from microorganisms may accelerate material degradation. Microorganisms are capable to cause enzymatic degradation of the polymer, this is the main biodegradation process for several medical polymers (e.g. polyurethane etc.) (Albertsson and Karlsson, 1994, Karlsson and Albertsson, 1998)). It has been reported that many fungi develop powerful enzyme systems to degrade highly stable polymers. These enzyme systems promote the reduction of peroxides to free radicals. Fungal hyphae can penetrate into the polymer, influencing mechanical stability and facilitate water diffusion into the material. Hyphal penetration provides mechanical degradation as a complement to chemical breakdown. (Flemming, 1998, Wallström et al., 2002, Gu, 2003, Gu et al., 1997)

The microorganisms in a biofilm may cause a discolouration of the polymer surface, through diffusion of lipophilic pigments into the material. These substances do not alter the properties of the polymer, but are impossible to remove (Flemming, 1998). The discolouration can also be induced by other environmental factors such as oxidation of filler, additives or the polymer it self (Wallström, 2005). Another concern during biodegradation is the formation of low molecular weight compounds which may cause various odours. In biomedical context the main issue is the potential harmful effect such compounds may have to the patient.

2.4 Medical problems caused by biofilm

Clinical trials on polyurethane tracheostomy tubes and silicone voice prosthesis showed that in most of the cases when a medical device is exposed to microorganisms, biofilm formation initiates and ultimately causes degradation of the material (Backman et al., 2009, Bjorling et al., 2007, Neu et al., 1993). Besides the negative effects of biofilm on polymeric medical devices, there is a high risk for emergence of infections. Recent research showed that

biofilms are involved in 65% of microbial infections in the body (Potera, 1999), such as urinary tract infections, catheter associated and middle-ear infections, formation of dental plaque, gingivitis, coating contact lenses, and less common but more lethal processes i.e. endocarditis, infections in cystic fibrosis, and infections of permanent indwelling devices such as joint prostheses and heart valves (Costerton et al., 1999, Jarett et al., 2002, Potera, 1999). The body defence against infections is the production of antibodies (lymphocytes), however, the immune system is in capable of penetrating the biofilm and destroying the cells. Antibiotic therapy is effective only against free floating bacterial cells and the released antigen produced by the biofilm (Lynch and Robertson, 2008, Vergara-Irigaray et al., 2009). The reasons for biofilm resistance to antibiotic agents are:

- antibiotics are not able to penetrate the full depth of the biofilm and the diffusion of antibiotics in EPS is relatively slow
- many antimicrobial agents are incapable of destroying slow growing or not growing cells (stationary phase), in addition, some of the cells in the biofilm have a low nutrition intake or live in starved state, which render cell survival
- there are differences in cell wall protein between bacteria in biofilm and their free floating counterparts, some bacteria in biofilm can survive without dividing which makes them resistant to antibiotics that attack dividing cells or breakdown specific cell wall types.

3. Polymeric materials in medical applications

The biocompatibility of a medical device or implant, i.e. the ability of a material to perform without causing a host response, or having toxic or injurious effects, is highly important throughout the lifetime of the biomedical application. (Williams, 1999, Dorland, 1980).A non-biocompatible implant is rapidly encapsulated by collagen tissues, resulting in failure of the desired function of the product. The amount of the tissue growth around the material depends on the polarity; non-polar polymers are surrounded by less tissue, than polar ones (Akmal and Usmani, 2000). In case of rejection, the body tries to expel the polymer through chemical reactions by phagocytic or enzymatic activity (Gebelein, 1985, Akmal and Usmani, 2000), resulting in the emergence of inflammations. The body response is highly dependent on the form (foam, fibre, film), shape, and movement of the implant, as well as the location in the body. A smooth, rounded shape gives less interaction and reduces tissue adhesion around the material more than a rough-edged shape. Powdered polymers give high tissue interactions owing to the large surface area (Akmal and Usmani, 2000). Adsorption of various body chemicals (e.g. triglycerides and steroids) by the material can alter polymer properties and also lead to degradation (Gebelein, 1985).

All polymeric materials degrade to some extent when in contact with the human body environment. Polymer implants, under normal circumstances, always undergo abrasion and stress (Hofmann et al., 2009). Poor long-term properties such as low resistance to wear and mechanical stress result in discomfort or pain for the patient, or costly replacement operations. The device or implant must be non-harmful during interactions with tissues and no toxic substances may be formed or leach out during the implementation of the application. Biomedical materials must be non-toxic, non carcinogenic, non-thrombogenic, non-inflammatory and non-immunogenic (King and Lyman, 1975, Venkatraman et al., 2008). Low molecular weight additives and degradation products produce significant tissue interactions due to their mobility and solubility in body chemicals. Therefore, polymers that

contain additives, residual monomers and polymerisation catalysts are not suitable for implant purposes.

Many extracorporeal devices have to be biocompatible with blood due to constant blood exposure. The surface treatment of the biomedical devices by anticoagulants (e.g. heparin) is essential to reduce the probability of clotting the application. Only a few polymeric materials have good blood compatibility; hydrogels, polyether urethane ureas, and materials made by affixing biologically inactivated natural tissue to the polymer surface (Akmal and Usmani, 2000).

The most commonly used materials for internal medical purposes are polyurethanes, polyolefins, silicones, fluoropolymers, vinyl- and acrylic polymers. Polyether type polyurethanes are used in a variety of applications (ligament replacements, heart valve prostheses, vascular graft prostheses, breast prosthesis, catheter, cannulae etc.) due to the materials good biocompatibility, high resistance against hydrolysis and body fluids, excellent mechanical properties (high tensile strength, highly elastomeric) and showing a low degree of degradation. The application of the polymer is versatile, from foam to film and as a bulk material.

Silicone rubber, a medical elastomer (poly(dimethylsiloxane)), is as prevalent and versatile as polyurethanes. The material can be synthesized in very pure form, is highly inert and shows excellent chemical resistance (due to the high hydrophobicity). Besides poly(dimethylsiloxane), vinyl- and aromatic (phenyl) dimethylsiloxanes are also preferably used as a medical polymer due to the superior surface properties (e.g. super hydrophobicity). This surface characteristic and the aromatic groups in the structure make the silicone rubbers surface less attractive to microorganisms, thus avoiding biofilm formation. The silicone rubbers are used in artificial skin, joint replacement, vitreous replacement, artificial heart, breast implants, different types of catheters and cannulae.

Polyolefins (polyethylene, polypropylene), fluoropolymers (teflon etc.) and acrylic polymers are mostly used as prosthetic devices. They express high degree of biocompatibility (almost totally neutral), excellent chemical resistance and superior mechanical properties. Compared to metallic implants the main advantage of polyolefins and fluoropolymers is the low friction coefficient and wear resistance due to their self-lubricating characteristic. The main medical applications are hip joints, knee implants etc. Acrlylic polymers show even better mechanical properties. They are mostly used as dental materials and bone cements to anchor artificial joints to the body. Due to the excellent optical properties methacrylates are also used in contact lenses.

Polymers such as poly(vinyl chloride) (PVC), poly(lactic acid) (PLA), polycaprolactone (PCL) and poly(vinyl alcohol) (PVA)have a variety of different medical applications. PVC is commonly used for lung bypass sets, catheters and cannulae, tubing for dialysis, endotracheal feeding etc. PVC is preferably used since the material is easy to sterilise and simple to process into products that do not crack or leak. The main drawback of PVC is the necessity of plasticizers, phthalates, for achieving the required mechanical properties, softness and flexibility, since the material itself is stiff. The low molecular weight plasticizers can be a target for microbial attack and under certain circumstances they migrate out of material and cause toxic reactions in the human body. On the other hand, the loss of these additives deteriorates the mechanical properties of the material. PLA is used as a biodegradable polymer in controlled-drug release systems, resorbable sutures and resorbable bone plates.

4. Degradation mechanisms of medical polymers

The human body contains a variety of enzymes and chemicals that may cause degradation of the polymer (Williams, 1992, Williams, 1991). Polymers containing ester or amide linkages (i.e. polyurethane) are more likely to hydrolyze or oxidize, while polyether type polymers are more stable, showing minimal degradation during long-term exposure to human body environment. Chain-scissions and/or crosslinking occur in addition to hydrolytic degradation (Kaali et al., 2010a).

As previously discussed, the biofilm attachment to the surface of the polymeric materials plays a vital role in the initiation and propagation of the degradation process. The biofilm formation is more pronounced for invasive materials, however, implants, after the implantation, are rarely exposed to such aggressive biological milieus. Biofilm can also cause immunological response (i.e. infections) that changes the surrounding body environment resulting in a negative effect on the material properties (Gumargalieva et al., 1982).

Based on the molecular, chemical and mechanical interactions with the human body environment, four types of degradation mechanisms of polymers used in medical applications can be distinguished: hydrolysis, oxidation, enzymatic- and physical degradation (Lyu and Untereker, 2009). The kinetics of the processes differ, and the key factors are the structure of the material and the surrounding environment (Göpferich, 1996). Body fluids represent the environment of the given location in the body or liquids (enzymes) produced by the body as an immunological response. In this case, the important factor in the material degradation is the change of pH of the surrounding environment, since some polymers (i.e. polyesters, polyamides) are highly pH sensitive (Göpferich, 1996, Williams, 1992). Another significant factor is the water uptake by the material (which is highly dependent on the hydrophobicity). The adsorbed water acts as a plasticizer, altering the physical properties of the material, swells the polymer, causing dimensional instability of the device or implant, and initiates the degradation of the polymer by hydrolysis.

In general, the degradation of the polymer by hydrolysisoccurs through three stages, however, depending on the molecular weight and the type, some polymers undergo only one or two stages (Lyu and Untereker, 2009). In the first stage, the polymer adsorbs water and becomes saturated in a short period of time, thereafter reactions between the water molecules and the polymer chains initiate. At this stage no auto-acceleration occurs since the water content of the polymer is constant, the molecular weight is high and the chain-ends concentration is low. This is followed by the second stage, where the molecular weight of the polymer decreases, increasing the chain-end concentration to a certain level, where auto-acceleration initiates and catalyzes the degradation process. Due to the increase in the chain-end concentration, the water adsorption of the polymer increases extending the polymer-water interactions, resulting in further decrease in the molecular weight. There is a point where the molecular weight becomes so low that it becomes soluble in the media. This corresponds to stage three. The low molecular weight compounds that form due to the reactions dissolve in the media and the molecular weight of the polymer gradually decreases until the polymer is completely dissolved. Although the water uptake of medical polymers is low (i.e. polyesters 1%), hydrolysis and bond-cleavage in the polymer chain result in a material with a decreased molecular weight and increased number of hydrophilic chain-ends. The chain-ends may adsorb an increasing amount of water which can further catalyze the reaction and lead to the complete breakdown of the material.

This is the typical degradation mechanism for polyesters, polyamides and polycarbonates, however, the hydrolytic degradation of the stable poly(dimethylsiloxane) may also occur

during *in vivo* use (Kaali et al., 2010a, Lukasiak et al., 2003). Recent long-term studies have confirmed that silicone tracheostomy tubes undergo hydrolytic degradation during use (Kaali et al., 2010a). Tubes, with an exposure time from one to six months, from several patients were collected and the analysis by Scanning Electron Microscopy (SEM), Fourier Transform Infrared Spectroscopy (FTIR) and Matrix Assisted Laser Desorption/Ionization Time of Flight Mass Spectrometry (MALDI TOF MS) showed degradation of silicone rubber after just 1 months exposure. The SEM micrographs clearly showed evidence of the surface alteration during the whole exposure period, which was also confirmed by the contact angle measurements, where the change in surface hydrophobicity was established.

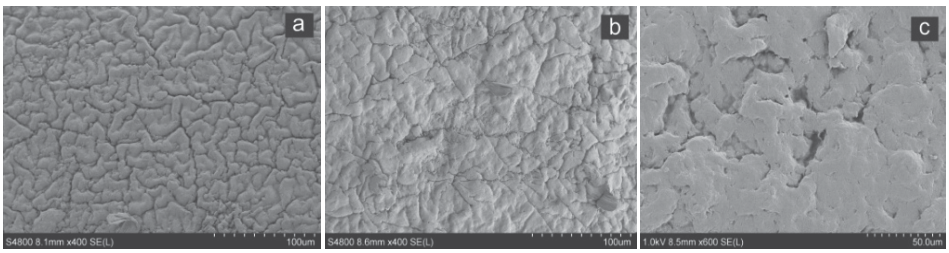

Fig. 4. SEM micrographs of unexposed silicone rubber tracheostomy tubes (a) and exposed to human environment for (b) three and (c) six months. (Kaali et al., 2010a)

The contact angle slightly decreased as a function of time, however, it must be noted that the surface of the silicone remained hydrophobic. The evidence of hydrolytic degradation was established by MALDI and FTIR. The FTIR analysis showed the formation of –OH groups, which may correspond to materials water uptake, however unlikely due to the high hydrophobicity of the silicone material. Besides, traces of protein, resulting from the attachment of the biofilm during the service life of the material, were also identified from the FTIR spectra. The hydrolytic degradation of the material was confirmed by MALDI TOF MS. The formation of low molecular weight silicone compounds with hydroxyl groups was identified. These compounds were absent in the unexposed samples. The extended results of this study showed that the degradation of polymeric materials and the rate of degradation within the human body depend on the biotic degradation, on the surrounding body environment and also the applied drug treatment. In addition to MALDI TOF MS, Gas Chromatography (GC) and High-Performance Liquid Chromatography (HPLC) are widely used for determination of low molecular weight compounds, as reported in several studies (Haider and Karlsson, 2002, Hillborg et al., 2001, Khabbaz et al., 2000, Flassbeck et al., 2001, Flassbeck et al., 2003, Gruemping and Hirner, 1999).

The oxidative degradation of medical polymers occurs inside the human body and can be monitored in simulated environments (Backman et al., 2009, Kaali et al., 2010b). The reaction is caused by the peroxides produced by the human body against "non-accepted" implant materials, the rejection mechanism (Lyu and Untereker, 2009, Santerre et al., 2005). Inflammation takes place at the implantation site, monocytes are migrating to the site and the production of macrophages initiates. If rejection is not possible, the body tries to encapsulate the material by foreign body giant cells. These cells and macrophages produce peroxides in order to try to break down the material to eliminate it from the body (Lyu and Untereker, 2009). The oxidation mechanism begins with the increasing number of free radicals due to the oxygen adsorbed from the surrounding tissues or blood. The oxygen

molecules react with the existing free radicals (Lyu and Untereker, 2009), resulting in an accelerated process where each oxygen molecule produces two radicals. The formed free radicals are transported to different parts of the polymer chain causing chain scission and formation of new chain-ends, one carrying a free radical and the other containing a double bond. The double bonded end can react further and form acids, ketones, while the free radical end continues the before mentioned process. This reaction propagates until the chains become too short for further degradation. The most susceptible medical polymers for oxidation are polyolefins, vinyl polymers, polyethers and polyamides. Several authors have reported that polyether type polyurethanes are quite stable against hydrolysis without exposure to oxidation (Frautschi et al., 1993, Santerre et al., 2005, Wiggins et al., 2001). The oxidative degradation takes place primarily at the ether linkage of the polymer, where the peroxide radical attacks the αcarbon of the soft segment. This reaction leads to the formation of an ester linkage which is susceptible to hydrolysis. The oxidative degradation of polyether urethane is therefore followed by hydrolysis. The polymeric materials that are susceptible or less susceptible to certain degradation processes are summarized in Table 2.

In the human body, materials undergo also enzymatic degradation(Christenson et al., 2006, Duguay et al., 1995, Santerre et al., 1995, Santerre et al., 1993). This is also a defensive response of the body against implant materials and can be linked to the activity of the tissues and cells. Although enzymes are produced for specific interaction, they are capable to recognize "unnatural" substrates such as polymers (Santerre et al., 2005).

In order to interact with the polymer, the enzyme must diffuse into the material either by swelling or hydrolysis (Duguay et al., 1995). This is considered to be the primary contact between the enzyme and the polymers surface. At this stage the enzyme becomes inactive, forming an "enzyme-bond" complex by attaching to an enzymatically susceptible bond (i.e. urethane, ester etc.).If this complex is relatively stable, bond scission may occur between the interface bonds and the bound enzyme, which results in the formation and release of various compounds.

	Susceptible	Less susceptible
Hydrolysis	Polyanhydride Polyorthoester Polyketal Polyester (aliphatic)	Polyolefin Polyether Polysulfone PDMS Polycarbonate Polyimide Polyurethane Polyester (aromatic) Polyamide
Oxidation	Polyolefins Vinyl polymers Polyethers Polyamines	Fluoropolymers Polyesters Methacrylates Silicone Polysulfone Polyetheretherketone

Table 2. Polymeric materials susceptible to degradation

These compounds then undergo further degradation and cleavage. Two kinds of enzymatic degradation can be distinguished, oxidation or hydrolysis of the material, which are based on the type of the enzyme produced (Albertsson and Karlsson, 1994). The enzymatic systems are highly specific and are able to catalyze degradation of the particular polymer chains summarised in Table 3.

Due to the complexity of the human body, the materials are exposed to most of the discussed degradation mechanisms simultaneously. The different degradation factors need to be evaluated separately and in various combinations in artificial environments that mimic the product's end-use conditions, in order to predict and understand the property changes that will occur in the material during its lifetime. The negative body response to a foreign material is the production of peroxides, therefore the most commonly used solvent to simulate this oxidative environment is hydrogen peroxide (Christenson et al., 2006, Lyu et al., 2008). Different artificial body fluids are used to test the biocompatibility or degradability of the material, such as phosphate buffered saline (PBS) which is used to mimic the blood plasma, and artificial lysosomal fluid (ALF) and Gamlbe´s solutions for simulating more complex systems. ALF solution simulates the enzymes that may initiate the breakdown of the polymer while Gamble´s solution represents the environment of the deep lungs (Herting et al., 2007, Midander et al., 2007). In a recent study silicone rubber and polyester type polyurethane were exposed to both ALF and Gamble´s solution at 37°C (the body temperature) for 3 months (Kaali et al., 2010b). During the exposure the formation and increasing concentration of low molecular weight compounds in silicone rubber were observed. These substances were the same hydrolyzed compounds that were detected during the *in vivo* use of silicone rubber tracheostomy tubes (Kaali et al., 2010a). In addition, polyurethane showed chemical property changes due to the exposure to artificial body fluids and based on the results it was determined that oxidative degradation took place. These results confirmed that artificial body fluids and simulated environments give similar results to *in vivo* experiments and represent good tools for testing new materials that are going to be implanted into the patents. In addition the application of *in vitro* studies reduce the costs and experiment time significantly.

Polymer	Enzyme
Polyurethanes	Cholesterol esterase, xanthine oxidase, cathepsin B, collagenase
Polyglycolic acid	Esterase, chymotrypsin, trypsin
Polyester	Esterase
Polyester urea	Urease, pepsin, chymitrypsin
Polycaprolactone	Lipase, carboxytic esterase
Polyamide Polymethylmethacrylate	Esterase, papain, trypsin, chymotrypsin

Table 3. Polymers susceptible to enzymatic degradation (Santerre et al., 1995)

Besides chemical degradation, physical degradation of the polymers also occurs in the human body. This is most relevant for implants that are exposed to different mechanical forces during their use, and therefore excellent mechanical properties are key requirements. These materials are usually knee and hip joints or other kinds of orthopaedic implants. The most common failures of these materials are wearing, breaking or cracking and erosion

(Göpferich, 1996). These failures may appear together or separately depending on the application, however, it is typical that the orthopaedic implants undergo mechanical friction which is associated with motion under pressure. Although UHMWPE is a superior material for joint purposes, some studies have reported high degree of mechanical degradation on hip and knee implants (Brach del Prever et al., 1996, Heisel et al., 2004, Kabo et al., 1993). It was also determined that the wear, friction and oxidative properties are better for cross-linked UMPWE than the conventional one (Heisel et al., 2004, Heisel et al., 2005, Markut-Kohl et al., 2009) and that during the mechanical wear, oxidative degradation of the polyethylene may occur.

4.1 Effects of sterilization on polymer degradation

During the manufacture biomedical materials are exposed to microorganisms and other substances even in a very pure production environment. Therefore they have to be sterilized and well sealed for storage in order to avoid any contamination or microbes that may cause infections or health problems right after the implantation. The sterilizationprocedures are presentedin Figure 5.

Dry heat and autoclaving involve high temperature (~120-180^{o}C) and pressure. The sterilization process by these methods could take from 3 minutes up to a couple of hours. During this exposure the materials may undergo thermal degradation caused by the temperature and hot steam that penetrates into the structure of the materials. Therefore commonly used sterilization methods for medical materials used in the human body are sterilization by either irradiation or gaseous chemicals (ethylene oxide).

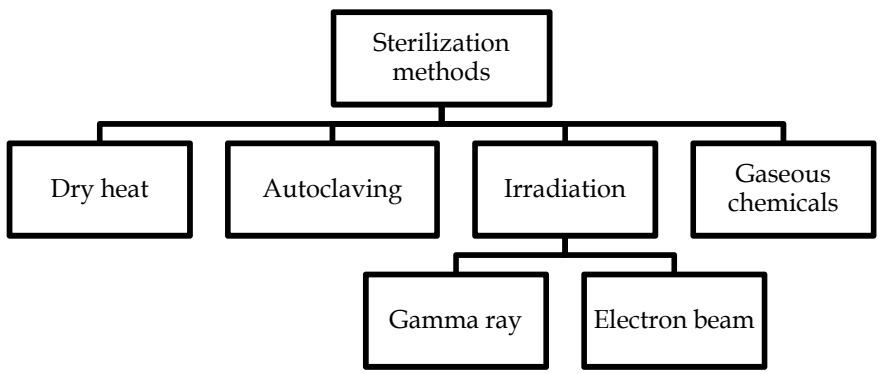

Fig. 5. Sterilization methods of medical polymers

There are two types of irradiation sterilization processes; gamma ray and electron beam. During gamma sterilization gamma rays are produced from Co_{66} source and have a high penetration capability up to 50 cm into the material. Electron beam sterilization is performed by an electron beam generator (1MeV-12MeV), which generates high-energy electrons. The penetration depth is around 5 cm, however, compared to gamma rays at the same strength, the dosage rate for the electron source is many times greater. This is due to the characteristic of the electron beam, which is unidirectional and therefore more concentrated on a smaller area, while gamma rays are less focused and cover a bigger surface. Both electron and gamma rays have such a high energy that the microorganisms that remain in the material after the production are accurately destroyed. From the material point of view these high-

energy impacts initiate changes in the structure of the material. These changes can be bonds scission, cross-linking, branching and degradation of additives. It has been reported that polyurethane catheters treated with electron beam sterilization undergo oxidative degradation, which leads to chain scissions in the hard and soft segments. This leads to the formation of smaller highly volatile soft segment fractions. In addition cross-linking occurs, that is thought to be influenced by the chain scissions of the hard segment, and forms on the urethane linkage sites. Most of the medical polymers contain additives that can be degraded by the electron beam and therefore can be easily released from the polymer. This causes a decrease in the stability of the polymer and could cause cytotoxicity (Guignot et al., 2001, Mrad et al., 2009a, Mrad et al., 2009b, Ravat et al., 2001a, Ravat et al., 2001b). Gamma irradiation has similar influence on the material. Due to the gamma sterilization, branching on polyurethanes (Haugen et al., 2007) and an extremely high rate of oxidation was observed on UHMWPE implants (Bracco et al., 2006, Goldman et al., 1998). During the irradiation, oxygen penetrates into the amorphous region of the polymer where misfit strain is developed. As a result the lamellae boundaries become tortuous which leads to further strain development and microcracking. Microcracking is a serious problem for materials designed for prosthetic purposes since it influences the mechanical properties negatively and the lifetime of the material decreases. Besides the types of irradiation, the dosage, flux and the outer environment have an effect on the degradation rate and degradation mechanisms that occur. For instance, the higher flux and the presence of oxygen increase the oxidation, since it generates anincreased formation of free radicals.

Besides irradiation, the use of gaseous chemicals is also prevalent. For this purpose usually ethylene oxide is used which is a strong alkylating agent, toxic and carcinogenic gas. The effectiveness of this gas on sterilization depends on the sterilization method which includes several factors. These are regarded as the gas concentration, temperature, relative humidity, the permeability and absorbance of the polymer. It has been reported that sterilization with ethylene oxide has no or very minimal influence on the structure of the polymer (Abraham et al., 1997, Burgos and Jiménez, 2009, Gilding et al., 1980, Lucas et al., 2003). However, the residues of the gas that remain after the process could at a certain concentration (above 400 ppm)cause toxicity (Bolt, 2000, MacNeil and Glaser, 1997). In principle the amount of remaining residue depends on the applied sterilization method and the polymers absorbance. Therefore with a proper method development that suits for the polymer and allows the complete release of ethylene oxide is necessary. Among the currently used sterilization processes the treatment with ethylene oxide has a big potential compared to irradiation techniques due to the reduced risk for degradation and subsequent health related issues.

4.2 Effects of degradation products on the human body

The degradation of the biomedical materials and formation of the degradation products have a serious influence on the human body (Lyu and Untereker, 2009). For instance, due to hydrolysis carboxylic acid and/or hydroxyl chain ends may form. Hydroxyl groups can be further oxidized and the reaction may produce different kinds of degradation products i.e. aldehydes, ketones or carboxylic acids. The degradation rate and its influence on the body depend on the size and location of the implant. However, if a biocompatible material starts to degrade it loses its stability and from the application point of view causes decreased service time. An example for body reaction is the formation of carboxylic acid, which

changes the local pH, causing inflammatory response. As an example during the production of some polyurethanes, methylene diamine is used, which is a toxic compound. In case ofthese kind of toxic precursors biodegradation is not relevant since base monomer usually don´t form due to chemical degradation. However residues of these monomers may remain in the material after the production. This is a technological question and the ability of human body to handle these kind of compounds depends on several factors i.e. can the compound be diluted or transported to organs (i.e. kidney) where it can be further degraded or flushed away.

5. Inhibition of biofilm formation and prevention of related infections

5.1 Current applications

The potential risk of biofilm formation is a big problem influencing the degradation of invasive materials and may cause health related issues. It has been reported (Kumon et al., 2001) that patients often face catheter associated infections (CAI). From the patient point of view, depending on the type of catheter (central venous, urinary etc.), the infection might be lethal. For the hospitals, these infections appear as a cost increase for patient therapy, which might be anticipated if the biofilm can be properly removed from the surface of the device or the material itself would have antimicrobial effect. Invasive materials that are permanently exposed to the human environment (especially tracheostomy tubes) require occasional checkups in order to determine the physical condition of the device and the biofilm growth on the surface. Usually biofilm formation is quite intensive right after the implantation, therefore a proper and regular cleaning is needed to remove the biofilm from the surface, reduce the biofilm related infections and the risk of the polymer degradation. If the biofilm can be completely removed, the surface will be less susceptible to microorganisms than in case where some residues or biofilm cells are remaining on the surface. In principle the cleaning procedure of medical devices is performed in two steps. The first step is the cleaning of the surface with oxidisers or detergents that weakens the physical stability of the biofilm and removes dead cells from the surface. In the second step the interaction between the surface and biofilm needs to be broken which can only be done by an intensive physical action i.e. brushing, scraping or flushing with high pressure of water (Wallström, 2005). Since some biofilm cells attach to the surface through ligands and chemical compounds, their removal is not possible without the physical surface damage of the material. Therefore in the field of biofilm inhibition, the development and improvement of cleaning techniques play only a secondary role. There are some promising methods i.e. mucus shaver and different sterilization treatments (argon plasma etc.) for the reduction or removal of biofilm after the attachment (Berra et al., 2006, Lee et al., 2009),however, the main priority is to inhibit the ability of the biofilm to attach to polymeric surfaces.

Most of the currently used medical devices that express antimicrobial effect contain either biocides or silver. It is known that silver has antimicrobial effect, however, the mechanism is not fully understood. Silver ion has the capability to be exchanged by ions that exist in the environment (Ca^+, Zn^+ etc.) and attach to bacterial cells (Schierholz et al., 1998). It forms chelate-complexes with the DNA of the bacteria. These complex molecules block the main transport processes of the cell, which leads to its decay. The sensitivity of Gram negative and Gram positive strains to silver varies due to the structural differences and is influenced by the attachment of silver to murein in the cell wall by adsorption. If it reaches a certain concentration in the cell wall it forms the chelate complex with the DNA. By increasing the

silver ion concentration the antimicrobial activity can be increased, however, a certain concentration in the human environment (10mg/L ,(Schierholz et al., 1998)) is cytotoxic and may lead to argyria.

The antimicrobial efficiency and the performance of antibiotics and silver treated catheters against CAI have been compared in several studies (Böswald et al., 1999, Lyu and Untereker, 2009, Paterson et al., 1999, Walder et al., 2002). The most commonly used antibiotics for treatment of the catheters are minocycline-rifampin, piperacillin, gentamicin, and ofloxacin. Silver indifferent forms (ion, compound, hydrogel, metallic) can be used inmedical devices. The most common ones for invasive materials are chlorohexidine-silver-sulfadiazine and impregnated silver. The studies showed that use ofmonociclyne-rifampin, ofloxacim and chlorohexidine-silver-sulfadiazine resulted in the least number of CAI compared to the other agents. Silver sulfadiazine expressed a high degree of biocompatibility and applicability in human environment (Böswald et al., 1999, Paterson et al., 1999), however, monocycline-rifampin showed better antiseptic properties. The antibacterial mechanism of silver-sulfadiazine is not completely understood. In a trial it was shown that in case of central venous catheters (CVC´s), probably the chlorine was responsible for the decreased CAI since it secedes from the surface of the polymer easier (Schierholz et al., 1998) Impregnated silver was less accurate because the mechanism is based on the migration and diffusion. Since silver-sulfadiazine is a salt it dilutes easily from the surface while impregnated silver ions must diffuse out in order to get in contact with the outer environment. Results of short and long term ion release studies of impregnated silver and silver-oxide coated catheters showed that during the first month the release of silver ions decreased significantly as a function of time while after four months it remained unaltered. During the exposure the impregnated catheter showed better antimicrobial results compared to a control sample where, the initial silver release was 2,5 ppm(Kubey et al., 1995). The use of hydrogels as antimicrobial agents in the medical industry is exceeding. Silver-hydrogels are preferably used as dressings for wound healing (Castellano et al., 2007, Ip et al., 2006), however, they show good antiseptic properties as polymer coatings on urinary catheters as well (Kwan and Fontecchio, 2002). Besides silver containing coatings, it was confirmed that nitrofurazone is also an excellent antibacterial agent that reduces the risk of urinary and blood-stream infections (Johnson et al., 2006).

The different forms of application of silver as an antimicrobial and antiseptic agent for invasive materials is promising based on the clinical trials, however, the real efficiency is sometimes questionable (Walder et al., 2002). In order to use silver in medical applications, the standardization of this material is necessary. This standardization is difficult since the effect is influenced by several factors; the destruction of different bacterial strains requires different silver concentrations and the minimum inhibitory results may give broad intervals of concentration. As an example, the minimum inhibitory concentration (MIC) for *Stapylococcusaureus* and *Pseudomonas aeruginosa* can vary 8-80mg/L (Chopra, 2007). The broad interval depends on the variation of the silver concentrations in different products and the variation of the release as a function of time depending on the nature of the material (i.e. water absorption) and the physical, chemical form of the silver and the location in the material. Moreover, there are bacterial strains that are resistant to silver and this mechanism is yet not well understood. There are species that become resistant by the modification of gene mutation or identification of the silver as a toxic material when it gets into the cell resulting in a rejection mechanism. Besides silver, certain bacterial strain has resistance

against specific antibiotics (e.g. MRSA: Methicillin-Resistant *Staphylococcus aureus*) or in extreme cases this resistance can expand to several groups of drugs.
During the improvement and development of antimicrobial and antiseptic materials that inhibit the biofilm formation and infections, these factors must be well considered.

5.2 Research strategies and trends to decrease device related infections and biofilm formation

There is a variety of developments and improvements in this field, however, the different forms and applications of silver or other antibacterial metals give the main direction of the research. Silver, copper and titanium nanoparticles are usually used and their *in vitro* antimicrobial efficiency is more or less confirmed, however silver is superior compared to other metals. The antimicrobial mechanism of the nanoparticles is not known but it can be assumed that it is similar to the ions. This is due to their small size and high specific surface area which makes them extremely reactive with the environment. If a nanoparticle interacts with a bacteria cell, ions may attach to the cell blocking the main transport phenomena and the replication of the DNA. The particles are incorporated into the material by mixing, bulk reduction (composite) or by a surface modification procedure (implantation, coating). During the production of composites aggregation of the particles takes place. This is a big problem, since the size of the particles increases due to the aggregation, which influences the diffusion and the antimicrobial properties (Jeong et al., 2005, Schmidt and Malwitz, 2003). Besides the size, the shape of the nanoparticles also influences the antimicrobial properties. It has been reported that truncated cone shaped particles express better efficiency against microbial growth than the spherical ones (Pal et al., 2007). In order to reach a homogenous dispersion of the particles by mixing, the use of a surfactant is necessary (Dirix et al., 1999). Therefore bulk reduction is a better procedure to prepare polymer matrix nanocomposites. In this process, theoretically, the polymer is responsible for the stabilization of the nanoparticles. In principle, the first step is the addition of silver in to the polymer by mixing a silver compound (i.e. $AgNO_3$) with the polymer solution. As a second step, a reduction agent is added to the system and the formation of nanoparticles initiates. This change is usually followed by a colour change. The effectiveness of this procedure has been confirmed by several studies (Akamatsu et al., 2000, Babu et al., 2006, Mahapatra and Karak, 2008, Sambhy et al., 2006). Another perspective of silver-polymer composites is the incorporation of silver ions into zeolite which is then mixed into the bulk polymer. It is known that zeolite is a natural mineral and has a high ion-exchange capability. Research papers confirm high efficiency of Ag-zeolite polymer against microorganisms (Kam et al., 2008, Kawahara et al., 2000, Pehlivan et al., 2005, Kaali et al., 2010b). The efficiency is based on the silver content which is linked to the zeolite content. The higher the zeolite content the better the antimicrobial efficiency. However, zeolite is a hydrophilic material and therefore adsorbs moisture and water easily. An *in vitro* study showed that the increasing zeolite content in polymeric materials results in a higher rate of degradation due to the increased water uptake of the material (Kaali et al., 2010b). In this case, zeolite content above 1% showed significant degradation compared to an unfilled material. Therefore the only solution that can be applied for zeolite-polymer composites is the increase of the ion content. In case of composites, for microbial interaction diffusion is the main transport of the antimicrobial agent to the surface. It is usually governed by a concentration gradient, which forms between the material and the environment. In order to reach the equilibrium the agents are concentrated on the surface and if it is possible diffuse out. This process depends

on several factors such as the material, temperature, humidity etc. The problem with composites is that due to the diffusion, the release of the agent is slow and the antimicrobial effect might be limited. Therefore the bigger part of the research focuses on surface modification (i.e. plasma immersion)(Akamatsu et al., 2000, Huang et al., 2004, Zhang and Chu, 2008, Zhang, 2000) or coating of the materials. By the immersion techniques the antimicrobial agent can be incorporated onto the surface of the materials where they physically or chemically bond to the matrix. They remain at the interface region and can interact easier with the microorganisms than the antimicrobials in composite materials. In case of metallic coatings, the main challenge is the adhesion. Since polymeric and metallic surfaces are not compatible with each other, the development of coatings is based on the improvement of the adhesion between the polymer and metallic surface by different deposition techniques. The strength of adhesion between these two interfaces depends on the structure of the polymer, hydrophobicity and surface roughness. Some papers describe that the surface must be activated before the coating procedure which is usually done by plasma or neutral nuclear beam (Dowling et al., 2003, Dowling et al., 2001, Gray et al., 2005). The activation is followed by the deposition of the substrate. Dowling used magnetron to deposit silver coating and platinum. As a result, the thickness of the coating was estimated to 7-28nm and the coating passed the tape test. In case of physically bonded coatings, depending on application, the deposited layer may easily crack if the material is softer than the substrate. Most of the polymers are exposed to mechanical stress and during the use of a coated catheter, where bending of the device is common, the coating will sooner or later peel off the material. In contrast metallic coatings that are bonded chemically to functional groups of the polymer may show better elastic properties. Electroless deposition is a useful chemical process to coat polymer surfaces with metals without electric current. Studies have confirmed (Gray et al., 2005, Li et al., 2004)that the silver coating which is deposited by this technique bond chemically to the surface through carbonyl groups by forming Ag-O-C bond. The higher the amount of the carbonyl groups on the surface the better adhesion can be reached. Studying the antibacterial effect of these metallic antimicrobial coatings show promising results (MIC of Stapylococcusaureus 0,5-10mg/L). However, the investigation of cytotoxicity is a very important issue, since these surfaces may release a high amount of ions that may cause toxic reaction for the human body. The most common ways for detection of released metallic particles from polymers are atomic absorption spectroscopy (AAS) and ionic plasma coupled mass spectrometry (ICP-MS). These two techniques allow to monitor even very low concentrations of metallic ions. Since ICP has a lower detection limit it is used to monitor the ion release of both composites and coatings, AAS is applicable for metallic coatings and pure metals (Herting et al., 2007, Midander et al., 2007).

Besides metallic coatings, research is focusingon variousnon-metallic coatings. One of the main interests in this field is based on multifunctional hydroxyapatite coatings that can be loaded with metallic particles or antibiotics (Brohede et al., 2009, Noda et al., 2009, Shimazaki et al., 2009). The application of this coating is mainly on hip joints and other metallic prostheses. Hydroxyapatite (HA) is a calcium apatite natural mineral that can be found in the body (teeth, bones) and therefore highly biocompatible. The role of hydroxyapatite as a coating is to ensure the tissue growth around the implant and decrease probability of rejection by the human body. Besides biocompatibility, if antibiotics or antimicrobial metallic particles are incorporated into the structure of HA the risk for infections and biofilm formation can be decreased. The trials showed that silver and antibiotics loaded HA coatings express superior antimicrobial properties on short term and

due to the slow release of the agent this characteristic can also be obtained on long term. Polymeric hydrogel coatings have also a great perspective. The main advantage of these materials is similar to hydroxyapatite, they are biologically inert, have good physicochemical properties and can be incorporated with either different antibiotics, or metallic nanoparticles to ensure their antimicrobial efficiency. The antimicrobial mechanism of hydrogels is the release of the agent to the environment. This release is governed by diffusion and influenced by the swelling and surface properties of the hydrogels. In principle this mechanism is the same as for antimicrobial-composites, however, the diffusion rate is much higher. Moreover, due to the chemical structure of the hydrogels, the release of antimicrobial agents is more even and pulsatile than in polymer composites. There is a wide variety of hydrogels which have different structures and release properties and therefore, for certain applications, these materials can be optimized to the antimicrobial agent. Besides the surface and release properties, hydrogels have to express good mechanical properties to be suitable for coatings. Based on a study, where the different hydrogel structures were tested, hydroxyethyl methacrylate and isopropylacrylamide based copolymers seemed to have the best properties (swelling, pulsatile release) for medical applications or drug delivery (Jones et al., 2008). Besides invasive materials, hydrogels are currently used for wound healing and clinical trials have confirmed their efficiency against infections. The antimicrobial and antiseptic properties depend also on the type of agent. So far silver nanoparticles incorporated into hydrogel coatings show the best antiseptic efficiency (Thomas et al., 2007, Dabbagh et al., 2008, Wu et al., 2009, Varaprasad et al.). However, due to the risk for silver toxicity (that may happen in case of high release rate) new antimicrobial agents are currently under development which are non-cytotoxic for human cells but has good efficiency against a variety of microorganisms (i.e. chitosan and bioactive antibodies)(Rojas et al., 2000, Yang et al., 2007)

Besides synthetic materials, biological coatings or surface modifications are also reported and this field is growing extensively to exchange the currently used synthetic materials with more “human friendly” ones. In these studies biosurfactants produces by bacteria strains and bacteriophages as a coating to inhibit the biofilm formation on the surfaces (Goldman et al., 2009, Rivardo et al., 2009, Rodrigues et al., 2006) give the main frame of the research. The efficiency of these materials against biofilm formation was confirmed; in some cases 90% of growth reduction was observed. The mechanism that is responsible for inhibition of the biofilm is based on the enzymes that are produced by the bacteriophages. These enzymes are capable to destroy the EPS of biofilms. The eradication efficiency of antibiotics against urinary infective strains was also increased by the biosurfactants. In contrast,biosurfactants are not capable of destroying planktonic cells and inhibit only the growth of certain strains. Moreover, bacteriophages are only efficient against specific strains and therefore the solution might be the combined use of different surfactants and/or bacteriophages together. The idea of biological biofilm inhibitors and antibacterial agents has a great perspective, but further development and improvement is necessary in order to be used in medical applications. Peptides can be placed into this group as well. They are known as agents of the immune system and can be found in a wide variety of living organisms (i.e. bacteria, insects, human body etc.). These peptides are usually obtained from different sources as macrophages, neutrophils, epithelial cells etc. and exhibit high activity against microorganisms. Peptides are either chemically bonded or incorporated into the surface. The main advantage of chemically bonded peptides is that they express antimicrobial activity locally and in contrast to the synthetic coatings, where antimicrobial agents are released via

mechanical or chemical processes, these peptides remain on the surface of the material. Therefore, no release takes place resulting in a higher stability, lower toxicity and longer activity against microorganisms. The other application of antimicrobial peptides is a single or multilayer coating, where each peptide layer is followed by a biodegradable polymer layer. Due to the exposure to human environment these polymer layers degrade one by one and slowly release the antimicrobial peptide. The main advantages of the application of antimicrobial peptides compared to metallic or synthetic agents are the high biocompatibility, very low toxicity and well controlled release.

6. Summary

It has been shown that biofilm formation on polymeric medical devices is an issue and its effects on both of the human body and the device are negative. The attachment and formation mechanism of biofilm on surfaces is a very complex phenomenon. In general it is based on colloid chemistry and surface-surface interactions, where the adhesion strength depends on short and long range interactions (Van der Waals forces, hydrogen bonding, electrostatic interactions etc.). After the cell attachment, the biofilm formation begins by colonization and production of extracellular polymeric substance that embeds the microorganisms, ensures the adhesion to the surface and protects the biofilm from the outer environment and impacts. The extracellular polymer substance provides stability for the biofilm and protection against antimicrobial agents, which in turn causes initiation of the material degradation and induction of serious infections. The requirements for an implant or invasive materials are biocompatibility, non-toxicity, non-carcinogenicity and extreme stability, however, degradation of the material may occur due to the body response. The acceptance or rejection response of the human body depends highly on the size, shape and location of the material in the body. The sensitivity of the material to rejection and degradation is highly dependant on the chemical structure of the polymer. There are four major mechanisms that are responsible for degradation of biomedical materials: hydrolysis, oxidative, enzymatic and mechanical degradation. Enzymatic degradation can also be caused by biofilms. The mechanical degradation is referring to the swelling and friction under motion and pressure of the polymer and not directly influenced by the human body. The sterilization procedure also is one of the factors promoting the degradation of the devises. Due to gamma and electron sterilization, oxidative degradation of the polymer can occur resulting in a decrease of the molecular weight and degradation of additives. Low molecular weight compounds can leach out of the material causing toxic reactions. The sterilization of medical polymers with ethylene oxide does not lead to any significant degradation of the polymer structure, but the residues of ethylene oxide can cause toxic reactions.

In order to prevent the negative effects of biofilms on the polymer surfaces and in the human body, the inhibition and control of biofilmformation is necessary. For this purpose antibiotics, silver- nanoparticles, salts and compounds are incorporated into the surface or the bulk of the material. Silver nanoparticles are also used as metallic coatings on the surface in physically or chemically bonded form. Clinical trials confirm that certain antibiotics and silver products are efficient as antiseptic agents and decrease the number of medical device associated infections in healthcare. The efficiency of silver is based on the silver ions released from the material, however, this is material and application dependant and not well controlled yet. A high concentration of silver released into the body can cause toxicity.

New coatings are under development for controlled and appropriately slow release of antibiotics or silver from the medical devices. Polymeric hydrogels can be one of the solutions for the controlled release due to their network structures, which allow a constant and sufficient release of the antimicrobial agents. Studies have shown that hydrogel dressings incorporated with antibiotics or nanoparticles assist the wound healing of the patients and decrease the risk for infections. Another recent development is extracellular polymeric substance that embeds the modification ofhydroxyapatite, a natural mineral that exists in the human body. Its pores can be filled with a variety of antimicrobial agents and provide a slow release mechanism. A new approach of research in inhibition of biofilm formation is the use of biological substances. Biological surfactants and bacteriophages are capable to inhibit the growth or destroy the biofilm. However, surfactants are not efficient against planktonic cells and not able to reduce the risk of infections caused by microorganisms. In addition bacteriophages can destroy only certain strains. The solution might be the combined use of different bacteriophages and surfactants to make these biological substances more universal against a variety of microorganisms. Their efficiency is confirmed, but since these solutions are newly introduced and developed, there is a big research potential in this field.

7. References

Electrostatic Charge and Bacterial Adhesion. Newcastle University, Department of Oral Biology

Abraham, G. A.; Frontini, P. & Cuadrado, T. (1997). Physical and mechanical behavior of sterilized biomedical segmented polyurethanes,*Journal of Applied Polymer Science*, Vol.65, 1193-1203

Akamatsu, K.; Takei, S.; Mizuhata, M.; Kajinami, A.; Deki, S.; Takeoka, S.; Fujii, M.; Hayashi, S. & Yamamoto, K. (2000). Preparation and characterization of polymer thin films containing silver and silver sulfide nanoparticles,*Thin Solid Films*, Vol.359, 55-60

Akmal, N. & Usmani, A. M. (2000).Medical polymers and diagnostic reagents, In:*Handbook of polymer degradation*, Hamid, S. (Ed.)2 ed, Marcel Dekkel Inc.,New York

Albertsson, A. C. & Karlsson, S. (1994). Chemistry and biochemistry of polymer biodegradation, In:*Chemistry and technology of biodegradable polymers*, Griffin, G. J. I. (Ed.), Springer,0751400033, New York

Babu, R.; Zhang, J.; Beckman, E. J.; Virji, M.; Pasculle, W. A. & Wells, A. (2006). Antimicrobial activities of silver used as a polymerization catalyst for a wound-healing matrix *Biomaterials*, Vol.27, 4304-4314

Backman, S.; Björling, G.; Johansson, U. B.; Lysdahl, M.; Markström, A.; Schedin, U.; Aune, R. E.; Frostell, C. & Karlsson, S. (2009).Material wear of polymeric tracheostomy tubes: A six-month study,*The Laryngoscope*, Vol.119, 657-664

Beech, I. B. (2004). Corrosion of technical materials in the presence of biofilms--current understanding and state-of-the art methods of study,*International Biodeterioration & Biodegradation*, Vol.53, 177-183

Bengtsson, M.; Grönlund, R.; Sjöholm, M.; Abrahamsson, C.; Dernfalk, A. D.; Wallström, S.; Larsson, A.; Weibring, P.; Karlsson, S.; Gubanski, S. M.; Kröll, S. & Svanberg, S.

(2005). Fluorescence lidar imaging of fungal growth on high-voltage outdoor composite insulators,*Optics and Lasers in Engineering*, Vol.43, 624-632

Berra, L.; Curto, F.; Li Bassi, G.; Laquerriere, P.; Baccarelli, A. & Kolobow, T. (2006).Antibacterial-coated tracheal tubes cleaned with the Mucus Shaver,*Intensive Care Medicine*, Vol.32, 888-893

Bjorling, G.; Axelsson, S.; Johansson, U.-B.; Lysdahl, M.; Markstrom, A.; Schedin, U.; Aune, R. E.; Frostell, C. & Karlsson, S. (2007). Clinical Use and Material Wear of Polymeric Tracheostomy Tubes,*Laryngoscope*, Vol.9, 1552-1559

Bolt, H. M. (2000). Carcinogenicity and Genotoxicity of Ethylene Oxide: New Aspects and Recent Advances,*Critical Reviews in Toxicology*, Vol.30, 595-608

Bos, R.; van der Mei, H. C. & Busscher, H. J. (1999).Physico-chemistry of initial microbial adhesive interactions – its mechanisms and methods for study,*FEMS Microbiology Reviews*, Vol.23, 179-230

Böswald, M.; Mende, K.; Bernschneider, W.; Bonakdar, S.; Ruder, H.; Kissler, H.; Sieber, E. & Guggenbichler, J. P. (1999).Biocompatibility testing of a new silver-impregnated catheter *in vivo*,*Infection*, Vol.27, S38-S42

Bracco, P.; Brunella, V.; Luda, M. P.; Brach del Prever, E. M.; Zanetti, M. & Costa, L. (2006).Oxidation behaviour in prosthetic UHMWPE components sterilised with high-energy radiation in the presence of oxygen,*Polymer Degradation and Stability*, Vol.91, 3057-3064

Brach del Prever, E.; Crova, M.; Costa, L.; Dallera, A.; Camino, G. & Gallinaro, P. (1996). Unacceptable biodegradation of polyethylene in vivo,*Biomaterials*, Vol.17, 873-878

Brohede, U.; Forsgren, J.; Roos, S.; Mihranyan, A.; Engqvist, H. & Strømme, M. (2009).Multifunctional implant coatings providing possibilities for fast antibiotics loading with subsequent slow release,*Journal of Materials Science: Materials in Medicine*, Vol.20, 1859-1867

Burgos, N. & Jiménez, A. (2009). Degradation of poly(vinyl chloride) plasticized with non-phthalate plasticizers under sterilization conditions,*Polymer Degradation and Stability*, Vol.94, 1473-1478

Castellano, J. J.; Shafii, S. M.; Ko, F.; Donate, G.; Wright, T. E.; Mannari, R. J.; Payne, W. G.; Smith, D. J. & Robson, M. C. (2007). Comparative evaluation of silver-containing antimicrobial dressings and drugs,*International Wound Journal*, Vol.4, 114-122

Chopra, I. (2007). The increasing use of silver-based products as antimicrobial agents: a useful development or a cause for concern?,*J. Antimicrob. Chemother.*, Vol.59, 587-590

Christenson, E. M.; Patel, S.; Anderson, J. M. & Hiltner, A. (2006). Enzymatic degradation of poly(ether urethane) and poly(carbonate urethane) by cholesterol esterase,*Biomaterials*, Vol.27, 3920-3926

Costerton, J. W.; Stewart, P. S. & Greenberg, E. P. (1999). Bacterial Biofilms: A Common Cause of Persistent Infections,*Science*, Vol.284, 1318-1322

Dabbagh, M. A.; Moghimipour, E.; Ameri, A. & Sayfoddin, N. (2008). Physicochemical Characterization and Antimicrobial Activity of Nanosilver Containing Hydrogels,*Iranian Journal of Pharmaceutical Research*, Vol.7, 21-28

Denyer, S. P.; Hanlon, G. W. & Davies, M. C. (1993).Mechanisms of Microbial Adherence, In:*Microbial Biofilms: Formation and Control*, Denyer, S. P., Gorman, S. P. & Sussman, M. (Eds.), Blackwell Scientific Publications,Cambridge

Derjaguin, B. & Landau, L. (1941). Theory of stability of strongly charged lyophobic sols and of the adhesion of strongly charged particles in solutions of electrolytes,*Acta Physicochimcal URSS*, Vol.14, 733-762

Dickinson, R. B.; Ruta, A. G. & Treusdal, S. E. (2000). Physicochemical Basis of Bacterial Adhesion to Biomaterial Surfaces, In:*Antimicrobial/Anti-Infective Materials*, Sawan, S. & Manivannan, G. (Eds.),1 ed, Technomic Publishing Company, Inc.,Lancaster

Dirix, Y.; Bastiaansen, C.; Caseri, W. & Smith, P. (1999).Preparation, structure and properties of uniaxially oriented polyethylene-silver nanocomposites,*Journal of Materials Science*, Vol.34, 3859-3866

Dorland, W. A. N. (1980).*Dorland's Medical Dictionary* W.B. Saunders Company, Philadelphia, Pennsylvania, USA, 0721631428, 9780721631424

Dowling, D. P.; Bettsa, A. J.; Popea, C.; McConnella, M. L.; Eloyb, R. & Arnaudb, M. N. (2003). Anti-bacterial silver coatings exhibiting enhanced activity through the addition of platinum *Surface and Coatings Technology*, Vol.163-164, 637-640

Dowling, D. P.; Donnellya, K.; McConnella, M. L.; Eloyb, R. & Arnaudb, M. N. (2001).Deposition of anti-bacterial silver coatings on polymeric substrates,*Thin Solid Films*, Vol., 602-606

Duguay, D. G.; Labow, R. S.; Santerre, J. P. & McLean, D. D. (1995). Development of a mathematical model describing the enzymatic degradation of biomedical polyurethanes. 1. Background, rationale and model formulation,*Polymer Degradation and Stability*, Vol.47, 229-249

Flassbeck, D.; Pfleiderer, B.; Grumping, R. & Hirner, A. V. (2001).Determination of Low Molecular Weight Silicones in Plasma and Blood of Women after Exposure to Silicone Breast Implants by GC/MS,*Anal. Chem.*, Vol.73, 606-611

Flassbeck, D.; Pfleiderer, B.; Klemens, P.; Heumann, K. G.; Eltze, E. & Hirner, A. V. (2003).Determination of siloxanes, silicon, and platinum in tissues of women with silicone gel-filled implants,*Analytical and Bioanalytical Chemistry*, Vol.375, 356-362

Flemming, H.-C. (1998). Relevance of biofilms for the biodeterioration of surfaces of polymeric materials,*Polymer Degradation and Stability*, Vol.59, 309-315

Fowler, H. W. & Mckay, A. J. (1980). The measurement of microbial adhesion, In:*Microbial Adhesion to Surfaces*, Berkeley, R. C. W., Lynch, J. M., Melling, J., Rutter, P. R. & Vincet, B. (Eds.), Ellis Horwood,Chichester

Frautschi, J. R.; Chinn, J. A.; Phillips Jr, R. E.; Zhao, Q. H.; Anderson, J. M.; Joshi, R. & Levy, R. J. (1993). Degradation of polyurethanes in vitro and in vitro: comparison of different models,*Colloids and Surfaces B: Biointerfaces*, Vol.1, 305-313

Gebelein, C. G. (1985). Medical Applications of Polymers, In:*Applied Polymer Science*,

Gilding, D. K.; Reed, A. M. & Baskett, S. A. (1980). Ethylene oxide sterilization: effect of polymer structure and sterilization conditions on residue levels,*Biomaterials*, Vol.1, 145-148

Goldman, G.; Starosvetsky, J. & Armon, R. (2009). Inhibition of biofilm formation on UF membrane by use of specific bacteriophages,*Journal of Membrane Science*, Vol.342, 145-152

Goldman, M.; Gronsky, R.; Long, G. G. & Pruitt, L. (1998). The effects of hydrogen peroxide and sterilization on the structure of ultra high molecular weight polyethylene,*Polymer Degradation and Stability*, Vol.62, 97-104

Göpferich, A. (1996). Mechanisms of polymer degradation and erosion,*Biomaterials*, Vol.17, 103-114

Gray, J. E.; Norton, P. R. & Griffiths, K. (2005). Mechanism of adhesion of electroless-deposited silver on poly(ether urethane) *Thin Solid Films*, Vol.484, 196-207

Gruemping, R. & Hirner, A. V. (1999). HPLC/ICP-OES determination of water-soluble silicone (PDMS) degradation products in leachates,*Fresenius' Journal of Analytical Chemistry*, Vol.363, 347-352

Gu, J.-D. (2003). Microbiological deterioration and degradation of synthetic polymeric materials: recent research advances,*International Biodeterioration & Biodegradation*, Vol.52, 69-91

Gu, J. D.; Lu, C.; Mitchell, R.; Thorp, K. & Crasto, A. (1997). Fungal degradation of fiber-reinforced composite materials,*Materials Performance*, Vol.36, 37-42

Guignot, C.; Betz, N.; Legendre, B.; Le Moel, A. & Yagoubi, N. (2001).Degradation of segmented poly(etherurethane) Tecoflex® induced by electron beam irradiation: Characterization and evaluation,*Nuclear Instruments and Methods in Physics Research Section B: Beam Interactions with Materials and Atoms*, Vol.185, 100-107

Gumargalieva, K. Z.; Moiseev, Y. V.; Daurova, T. T. & Voronkova, O. S. (1982).Effect of infections on the degradation of polyethylene terephthalate implants,*Biomaterials*, Vol.3, 177-180

Haider, N. & Karlsson, S. (2002). Loss and transformation products of the aromatic antioxidants in MDPE film under long-term exposure to biotic and abiotic conditions,*Journal of Applied Polymer Science*, Vol.85, 974-988

Haugen, H. J.; Brunner, M.; Pellkofer, F.; Aigner, J.; Will, J. & Wintermantel, E. (2007). Effect of different γ-irradiation doses on cytotoxicity and material properties of porous polyether-urethane polymer,*Journal of Biomedical Materials Research Part B: Applied Biomaterials*, Vol.80B, 415-423

Heisel, C.; Silva, M.; dela Rosa, M. A. & Schmalzried, T. P. (2004).Short-Term in Vivo Wear of Cross-Linked Polyethylene,*J Bone Joint Surg Am*, Vol.86, 748-751

Heisel, C.; Silva, M. & Schmalzried, T. (2005). In vivo wear of bilateral total hip replacements: conventional versus crosslinked polyethylene,*Archives of Orthopaedic and Trauma Surgery*, Vol.125, 555-557

Herting, G.; Odnevall Wallinder, I. & Leygraf, C. (2007).Metal release from various grades of stainless steel exposed to synthetic body fluids,*Corrosion Science*, Vol.49, 103-111

Hillborg, H.; Karlsson, S. & Gedde, U. W. (2001).Characterisation of low molar mass siloxanes extracted from crosslinked polydimethylsiloxanes exposed to corona discharges,*Polymer*, Vol.42, 8883-8889

Hofmann, D.; Entrialgo-Castaño, M.; Kratz, K. & Lendlein, A. (2009). Knowledge-Based Approach towards Hydrolytic Degradation of Polymer-Based Biomaterials,*Advanced Materials*, Vol.21, 3237-3245

Huang, N.; Yang, P.; Leng, Y. X.; Wang, J.; Sun, H.; Chen, J. Y. & Wan, G. J. (2004). Surface modification of biomaterials by plasma immersion ion implantation *Surface and Coatings Technology*, Vol.186, 218-226

Ip, M.; Lui, S. L.; Poon, V. K. M.; Lung, I. & Burd, A. (2006). Antimicrobial activities of silver dressings: an in vitro comparison,*J Med Microbiol*, Vol.55, 59-63

Jarett, W. A.; Ribes, J. & Manaligod, J. M. (2002).Biofilm formation on tracheostomy tubes,*Ear , Nose & Throat Journal*, Vol.81, 659-661

Jeong, S.; Yeo, S. & Yi, S. (2005). The effect of filler particle size on the antibacterial properties of compounded polymer/silver fibers,*Journal of Materials Science*, Vol.40, 5407-5411

Johnson, J. R.; Kuskowski, M. A. & Wilt, T. J. (2006).Systematic Review: Antimicrobial Urinary Catheters To Prevent Catheter-Associated Urinary Tract Infection in Hospitalized Patients,*Ann Intern Med*, Vol.144, 116-126

Jones, D. S.; Lorimer, C. P.; McCoy, C. P. & Gorman, S. P. (2008). Characterization of the physicochemical, antimicrobial, and drug release properties of thermoresponsive hydrogel copolymers designed for medical device applications,*Journal of Biomedical Materials Research Part B: Applied Biomaterials*, Vol.85B, 417-426

Kaali, P.; Momcilovic, D.; Markström, A.; Aune, R.; Czel, G. & Karlsson, S. (2010a). Degradation of biomedical polydimethylsiloxanes during exposure to in vivo biofilm environment monitored by FE-SEM, ATR-FTIR, and MALDI-TOF MS,*Journal of Applied Polymer Science*, Vol.115, 802-810

Kaali, P.; Strömberg, E.; Aune, R. E.; Czél, G.; Momcilovic, D. & Karlsson, S. (2010b). Antimicrobial properties of Ag+ loaded zeolite polyester polyurethane and silicone rubber and long-term properties after exposure to in-vitro ageing,*Polymer Degradation and Stability*, Vol.95, 1456-1465

Kabo, J. M.; Gebhard, J. S.; Loren, G. & Amstutz, H. C. (1993). In vivo wear of polyethylene acetabular components,*J Bone Joint Surg Br*, Vol.75-B, 254-258

Kam, K.; Aksoy, E. A.; Akata, B.; Hasirci, N. & Baç, N. (2008).Preparation and characterization of antibacterial zeolite-polyurethane composites,*Journal of Applied Polymer Science*, Vol.110, 2854-2861

Karlsson, S. & Albertsson, A.-c. (1998). Biodegradable polymers and environmental interaction,*Polymer Engineering & Science*, Vol.38, 1251-1253

Kawahara, K.; Tsuruda, K.; Morishita, M. & Uchida, M. (2000).Antibacterial effect of silver-zeolite on oral bacteria under anaerobic conditions,*Dental Materials*, Vol.16, 452-455

Khabbaz, F.; Karlsson, S. & Albertsson, A. C. (2000). PY-GC/MS an effective technique to characterizing of degradation mechanism of poly (L-lactide) in the different environment,*Journal of Applied Polymer Science*, Vol.78, 2369-2378

King, R. N. & Lyman, D. J. (1975). Polymers in Contact with the Body,*Environmental Health Perspectives*, Vol.11, 71-74

Kubey, W.; Luneburg, P.; Ericson, S.; Brown, J. & Holmes, C. J. (1995). A longitudinal in vitro antimicrobial evaluation of two silver polymer surface treatments for peritoneal dialysis catheters,*Advances in peritoneal dialysis. Conference on Peritoneal*

Kumon, H.; Hashimoto, H.; Nishimura, M.; Monden, K. & Ono, N. (2001). Catheter-associated urinary tract infections: impact of catheter materials on their management,*International Journal of Antimicrobial Agents*, Vol.17, 311-316

Kwan, K. L. & Fontecchio, S. A. (2002). Use of silver-hydrogel urinary catheters on the incidence of catheter-associated urinary tract infections in hospitalized patients,*American Journal of Infection Control* Vol.30, 221-225

Lee, M. H.; Park, B. J.; Chang, S.; Kim, D.; Han, I.; Kim, J.; Hyun, S. O.; Chung, K.-H. & Park, J.-C. (2009).Removal and sterilization of biofilms and planktonic bacteria by microwave-induced argon plasma at atmospheric pressure,*New Journal of Physics*, Vol.11, 115-122

Li, Y.; Lu, Q.; Qian, X.; Zhu, Z. & Yin, J. (2004).Preparation of surface bound silver nanoparticles on polyimide by surface modification method and its application on electroless metal deposition,*Applied Surface Science*, Vol.233, 299-306

Lucas, A. D.; Merritt, K.; Hitchins, V. M.; Woods, T. O.; McNamee, S. G.; Lyle, D. B. & Brown, S. A. (2003). Residual ethylene oxide in medical devices and device material,*Journal of Biomedical Materials Research Part B: Applied Biomaterials*, Vol.66B, 548-552

Lukasiak, J.; Dorosz, A.; Prokopowicz, M.; Rosciewski, P. & Falkiewicz, B. (2003). Biodegradation of Silicones,*Biopolymers*, Vol.9, 539-568

Lynch, A. S. & Robertson, G. T. (2008). Bacterial and Fungal Biofilm Infections,*Annual Review of Medicine*, Vol.59, 415-428

Lynch, J. F.; Lappin-Scott, H. M. & Costerton, J. W. (2003).*Microbial biofilms,* Cambridge University Press, Cambridge,

Lyu, S.; Schley, J.; Loy, B.; Luo, L.; Hobot, C.; Sparer, R.; Untereker, D. & Krzeszak, J. (2008). In vitro biostability evaluation of polyurethane composites in acidic, basic, oxidative, and neutral solutions,*Journal of Biomedical Materials Research Part B: Applied Biomaterials*, Vol.85B, 509-518

Lyu, S. & Untereker, D. (2009). Degradability of Polymers for Implantable Biomedical Devices,*International Journal of Molecular Sciences*, Vol.10, 4033-4065

MacNeil, J. R. & Glaser, Z. R. (1997).Comparison of health care-based sterilization technologies: safety, efficacy and economics,*J Healthcare Safety Compliance Infect Control* Vol., 91-106

Mahapatra, S. S. & Karak, N. (2008).Silver nanoparticle in hyperbranched polyamine: Synthesis, characterization and antibacterial activity,*Materials Chemistry and Physics*, Vol.112, 1114-1119

Markut-Kohl, R.; Archodoulaki, V. M.; Seidler, S. & Skrbensky, G. (2009).PE-UHMW in Hip Implants: Properties of Conventional and Crosslinked Prosthetic Components,*Advanced Engineering Materials*, Vol.11, B148-B154

Mayer, C.; Moritz, R.; Kirschner, C.; Borchard, W.; Maibaum, R.; Wingender, J. & Flemming, H.-C. (1999). The role of intermolecular interactions: studies on model systems for bacterial biofilms,*International Journal of Biological Macromolecules*, Vol.26, 3-16

Midander, K.; Wallinder, I. O. & Leygraf, C. (2007).In vitro studies of copper release from powder particles in synthetic biological media,*Environmental Pollution*, Vol.145, 51-59

Mrad, O.; Saunier, J.; Aymes Chodur, C.; Rosilio, V.; Agnely, F.; Aubert, P.; Vigneron, J.; Etcheberry, A. & Yagoubi, N. (2009a). A comparison of plasma and electron beam-sterilization of PU catheters,*Radiation Physics and Chemistry*, Vol.79, 93-103

Mrad, O.; Saunier, J.; Chodur, C. A.; Agnely, F. & Yagoubi, N. (2009b). Influence of electron beam sterilization on polymers when incubated in different media,*Journal of Applied Polymer Science*, Vol.111, 3113-3120

Neu, T. R.; Van der Mei, H. C.; Busscher, H. J.; Dijk, F. & Verkerke, G. J. (1993).Biodeterioration of medical-grade silicone rubber used for voice prostheses: a SEM study,*Biomaterials*, Vol.14, 459-464

Noda, I.; Miyaji, F.; Ando, Y.; Miyamoto, H.; Shimazaki, T.; Yonekura, Y.; Miyazaki, M.; Mawatari, M. & Hotokebuchi, T. (2009). Development of novel thermal sprayed antibacterial coating and evaluation of release properties of silver ions,*Journal of Biomedical Materials Research Part B: Applied Biomaterials*, Vol.89B, 456-465

Oliveira, D. R. (1992). Physico-chemical aspects of adhesion, In:*Biofilms: Science and Technology*, Melo, L. F., Bott, T. R., Fletcher, M. & Capdevile, B. (Eds.), Kluwer Academic Publishers,Dordrecht

Pal, S.; Tak, Y. K. & Song, J. M. (2007).Does the Antibacterial Activity of Silver Nanoparticles Depend on the Shape of the Nanoparticle? A Study of the Gram-Negative Bacterium Escherichia coli,*Appl. Environ. Microbiol.*, Vol.73, 1712-1720

Paterson, D. L.; Bach, A.; Maury, E.; Offenstadt, G.; Yasukawa, T.; Fujita, Y.; Sari, A.; Darouiche, R. O. & Raad, I. I. (1999). Antimicrobial-Impregnated Central Venous Catheters,*N Engl J Med*, Vol.340, 1761-1762

Pehlivan, H.; Balköse, D.; Ülkü, S. & Tihminlioglu, F. (2005).Characterization of pure and silver exchanged natural zeolite filled polypropylene composite films,*Composites Science Technology*, Vol.65, 2049-2058

Potera, C. (1999). MICROBIOLOGY:Forging a Link Between Biofilms and Disease,*Science*, Vol.283, 1837-1839

Ravat, B.; Grivet, M. & Chambaudet, A. (2001a). Evolution of the degradation and oxidation of polyurethane versus the electron irradiation parameters: Fluence, flux and temperature,*Nuclear Instruments and Methods in Physics Research Section B: Beam Interactions with Materials and Atoms*, Vol.179, 243-248

Ravat, B.; Grivet, M.; Grohens, Y. & Chambaudet, A. (2001b).Electron irradiation of polyesterurethane: study of chemical and structural modifications using FTIR, UV spectroscopy and GPC,*Radiation Measurements*, Vol.34, 31-36

Rivardo, F.; Turner, R.; Allegrone, G.; Ceri, H. & Martinotti, M. (2009). Anti-adhesion activity of two biosurfactants produced by <i>Bacillus</i> spp. prevents biofilm formation of human bacterial pathogens,*Applied Microbiology and Biotechnology*, Vol.83, 541-553

Rodrigues, L.; Van Der Mei, H.; Banat, I. M.; Teixeira, J. & Oliveira, R. (2006).Inhibition of microbial adhesion to silicone rubber treated with biosurfactant from Streptococcus thermophilus A,*FEMS Immunology & Medical Microbiology*, Vol.46, 107-112

Rojas, I. A.; Slunt, J. B. & Grainger, D. W. (2000).Polyurethane coatings release bioactive antibodies to reduce bacterial adhesion,*Journal of Controlled Release*, Vol.63, 175-189

Sambhy, V.; MacBride, M. M.; Peterson, B. R. & Sen, A. (2006). Silver Bromide Nanoparticle/Polymer Composites: Dual Action Tunable Antimicrobial Materials,*Journal of the American Chemical Society*, Vol.128, 9798-9808

Sand, W. (1997). Microbial Mechanisms of Deterioration of Inorganic Substrates- A General Mechanistic Overview,*International Biodeterioration & Biodegradation*, Vol.40, 183-190

Santerre, J. P.; Duguay Daniel, G.; Labow Rosalind, S. & Brash John, L. (1995). Interactions of Hydrolytic Enzymes at an Aqueous?Polyurethane Interface, In:*Proteins at Interfaces II*, American Chemical Society,

Santerre, J. P.; Labow, R. S. & Adams, G. A. (1993). Enzyme-biomaterial interactions: Effect of biosystems on degradation of polyurethanes,*Journal of Biomedical Materials Research*, Vol.27, 97-109

Santerre, J. P.; Woodhouse, K.; Laroche, G. & Labow, R. S. (2005). Understanding the biodegradation of polyurethanes: From classical implants to tissue engineering materials,*Biomaterials*, Vol.26, 7457-7470

Schierholz, J. M.; Lucas, L. J.; Rumpc, A. & Pulverer, G. (1998). Efficacy of silver-coated medical devices,*Journal of Hospital Infection*, Vol.40, 257-262

Schmidt, G. & Malwitz, M. M. (2003).Properties of polymer-nanoparticle composites,*Current Opinion in Colloid & Interface Science*, Vol.8, 103-108

Seal, K. J. & Morton, L. G. H. (1986). Chemical Materials, In:*Microbial Degradations*, Schönborn, W. (Ed.), VCH,Dusseldork

Shimazaki, T.; Miyamoto, H.; Ando, Y.; Noda, I.; Yonekura, Y.; Kawano, S.; Miyazaki, M.; Mawatari, M. & Hotokebuchi, T. (2009). In vivo antibacterial and silver-releasing properties of novel thermal sprayed silver-containing hydroxyapatite coating,*Journal of Biomedical Materials Research Part B: Applied Biomaterials*, Vol.92B, 386-389

Thomas, V.; Yallapu, M. M.; Sreedhar, B. & Bajpai, S. K. (2007). A versatile strategy to fabricate hydrogel-silver nanocomposites and investigation of their antimicrobial activity,*Journal of Colloid and Interface Science*, Vol.315, 389-395

Varaprasad, K.; Mohan, Y. M.; Ravindra, S.; Reddy, N. N.; Vimala, K.; Monika, K.; Sreedhar, B. & Raju, K. M. Hydrogel–silver nanoparticle composites: A new generation of antimicrobials,*Journal of Applied Polymer Science*, Vol.115, 1199-1207

Venkatraman, S.; Boey, F. & Lao, L. L. (2008).Implanted cardiovascular polymers: Natural, synthetic and bio-inspired,*Progress in Polymer Science*, Vol.33, 853-874

Vergara-Irigaray, M.; Valle, J.; Merino, N.; Latasa, C.; García, B.; Mozos, I. R. d. l.; Solano, C.; Toledo-Arana, A.; Penades, J. R. & Lasa, I. (2009).Relevant Role of Fibronectin-Binding Proteins in Staphylococcus aureus Biofilm-Associated Foreign-Body Infections,*Infection and Immunity*, Vol.77, 3978-3991

Verwey, E. J. W. & Overbeek, J. T. G. (1948).*Theory of the Stability of Lyophobic Colloids,* Elsevier, New York, 0-486-40929-5

Walder, B.; Pittet, D. & Tramer, M. (2002).Prevention of bloodstream infections with central venous catheters treated with anti-infective agents depends on catheter type and

insertion time: evidence from a meta-analysis.,*Infection Control and Hospital Epidemiology*, Vol.23, 748-756

Wallström, S. (2005). Biofilms on silicone rubber materials for outdoor high voltage insulation,*Department of Fibre and Polymertechnology.* Royal Institute of Technology, Stockholm

Wallström, S.; Dowling, K. & Karlsson, S. (2002). Development and comparison of test methods for evaluating formation of biofilms on silicones,*Polymer Degradation and Stability*, Vol.78, 257-262

Wallström, S. & Karlsson, S. (2004). Biofilms on silicone rubber insulators; microbial composition and diagnostics of removal by use of ESEM/EDS: Composition of biofilms infecting silicone rubber insulators,*Polymer Degradation and Stability*, Vol.85, 841-846

Wallström, S.; Strömberg, E. & Karlsson, S. (2005).Microbiological growth testing of polymeric materials: an evaluation of new methods,*Polymer Testing*, Vol.24, 557-563

Wiggins, M. J.; Wilkoff, B.; Anderson, J. M. & Hiltner, A. (2001). Biodegradation of polyether polyurethane inner insulation in bipolar pacemaker leads,*Journal of Biomedical Materials Research*, Vol.58, 302-307

Williams, D. F. (1991). Interfacial reactions in the degradation of polymers by cells and bacteria,*Biofouling: The Journal of Bioadhesion and Biofilm Research*, Vol.4, 225 - 230

Williams, D. F. (1992). Mechanisms of biodegradation of implantable polymers,*Clinical Materials*, Vol.10, 9-12

Williams, D. F. (1999).*The Williams Dictionary of Biomaterials,* Liverpool University Press, Liverpool, 0853237344

Wu, J.; Hou, S.; Ren, D. & Mather, P. T. (2009). Antimicrobial Properties of Nanostructured Hydrogel Webs Containing Silver,*Biomacromolecules*, Vol.10, 2686-2693

Yang, S. H.; Lee, Y. S. J.; Lin, F. H.; Yang, J. M. & Chen, K. s. (2007). Chitosan/poly(vinyl alcohol) blending hydrogel coating improves the surface characteristics of segmented polyurethane urethral catheters,*Journal of Biomedical Materials Research Part B: Applied Biomaterials*, Vol.83B, 304-313

Zhang, W. & Chu, P. K. (2008). Enhancement of antibacterial properties and biocompatibility of polyethylene by silver and copper plasma immersion ion implantation,*Surface and Coatings Technology*, Vol.203, 909-912

Zhang, X. (2000). Anti-Infective Coatings Reduce Device-Related Infection, In:*Antimicrobial/Anti-Infective Materials*, Sawan, S. & Manivannan, G. (Eds.),1 ed, Technomic Publishing Company, Inc.,Lancaster

23

The Challenge of the Skin-Electrode Contact in Textile-enabled Electrical Bioimpedance Measurements for Personalized Healthcare Monitoring Applications

Fernando Seoane[1,2], Juan Carlos Marquez[1,2], Javier Ferreira[1,3,4], Ruben Buendia[1,5] and Kaj Lindecrantz[6]
[1]*School of Engineering, University of Borås,*
[2]*Department of Signal & Systems, Chalmers University of Technology, Gothenburg,*
[3]*Swedish School of Textiles, University of Borås,*
[4]*Department of Telematics Architectures and Engineering at the Polytechnic University of Madrid,*
[5]*Department of Theory of the Signal and Communication., University of Alcalá, Madrid,*
[6]*School of Technology and Health, Royal Institute of Technology, Huddinge,*
[1,2,3,6]*Sweden*
[4,5]*Spain*

1. Introduction

Textile technology has gone through a remarkable development in the field of Smart Textiles and more specifically in the area of conductive fabrics and yarns. Important research efforts have been done worldwide and especially in Europe, where the EU-commission has supported several research projects in the near past *e.g. BIOTEX IST-2004-016789, CONTEXT IST- 2004-027291 and MyHeart IST-2002-507816*. As a result of such worldwide R&D efforts, textile sensors and electrodes are currently available commercially. Nowadays there are even consumer products with textile sensing technology for heart rate monitoring integrated in the apparel *e.g. Adistar Fusion T-shirt from Adidas or the Numetrex's Cardio shirt*.

Since one of the main areas of focus where R&D efforts have been concentrated is Personalized Healthcare Monitoring (PHM) and the fact that most of the efforts developing textile sensors have been focused on developing electrodes for biopotential signals recording, it is natural that the main targeted application has been the acquisition of electrical biopotentials and especially monitoring the ElectroCardioGraphic activity, but also other types of textile sensors have been investigated *e.g. textile stretching sensor* (Mattmann *et al.*, 2008). Nowadays textile-enable stretch sensors are available commercially like the one manufactured by Merlin Systems. While the application of this type of sensor aims at other applications than biopotential recordings, an important area of application of stretch sensors

still is PHM and fitness. This type of sensors can be used for respiration monitoring or plethysmography applications.

2. Electrical bioimpedance

Electrical Bioimpedance (EBI) is a well spread and established technology that has been used as a non-invasive monitoring and health assessment technique for more than 50 years. Since the key-sensing element in EBI measurement technology is an electrode, EBI technology is a strong candidate to benefit from the current progress in the development of textile electrodes and conductive yarns.

Currently EBI technology allows non-invasive monitoring of the respiration cycle by measuring impedance changes across the thorax, cardiac cycle dynamics by measuring changes in the impedance caused by circulating blood across main arteries as well as assessment of body composition and body fluid distribution by measuring EBI at several frequencies. All these current uses of EBI measurements open for several potential textile-enabled applications within PHM, like Heart Failure management home-bounded patients aimed by the EU-FP7 MyHeart Project (Habetha, 2006).

Even though EBI technology is a clear beneficiary of textile-based electrode technology and despite the fact that EBI-enabled wearable physiological measurements is not a new concept, NASA already in 1969 implemented it during the Apollo XI mission, the potential provided by textile electrodes is not fully exploited in EBI technology.

In recent years several investigations (Beckmann *et al.*, 2010; Hännikäinen *et al.*, 2007; Marquez *et al.*, 2009; Medrano *et al.*, 2007) focused on the development of EBI-enabled physiological variables measurement systems with textile electrodes have produced very encouraging results suggesting the feasibility to implement EBI textile-enable applications. The only negative issue with the obtained results is that reliable measurements of EBI have been obtained only when wetting the textile electrodes.

3. Skin-electrode interface and measurements of EBI

The contact between the skin and the electronic instrumentation in a non-invasive measurement system is achieved by electrodes. The system resulting from connecting the measurement leads, the electrodes and the skin creates an electrical interface that might influence the measurement process. A schematic of the equivalent circuit is depicted in Figure 1.

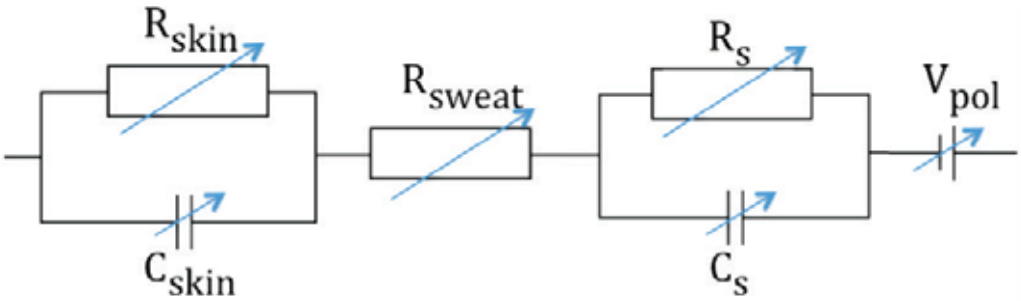

Fig. 1. Electrical Equivalent of the Skin-Electrode Interface

The model of the electrical interface contains a voltage source in series with several impedance elements. The so-called motion artifact in biopotential recordings is represented by changes in the voltage source. In most cases there are several hardware and software solutions available to compensate for it (Witte *et al.*, 1987).

An important difference between biopotential and EBI measurements systems is that the latter, in addition to a voltage measurement, need an injected electrical current through the skin into the body. The need to inject current into the body requires a good electrical contact between the measurement system, the electrode and the skin. It is desirable that the impedance of the electrical interface and the electrode polarization impedance, Zep, represented in Figure 1 are small enough to be negligible. If a 2-electrode method is used to measure the EBI, Zep will be added to the measurement and the obtained measurement will contain not only the EBI but also the interface impedance. When measuring with a 4-electrode method, it is possible to get an EBI measurement without the contribution of Zep or the interface impedance.

The existence of the impedance in series with the measurement load and the stray capacitance creates a frequency dependent current divider, see Figure 2. If the value of the impedance created by the skin-electrode interface present in the current leads is large, the electrical current will avoid flowing through the electrode and the skin, leaking away from the body. Thus the EBI measurement will not be performed at all or in the best case the obtained measurement data will be corrupted with capacitive leakage. See Figure 3. The Figure shows an impedance plot, capacitive reactance vs resistance, with the experimental data plotted with dots, the Cole model estimated from the corrupted data plotted with a fine line and the Cole model estimated from the artifact-free measurement plotted with a coarse line.

4. Textile electrode in EBI measurements

Although as in any other electrode, both the contact area and the material of the electrode are very important factors behind setting the values of the elements constituting the skin-electrode interface. In regular Ag/AgCl electrodes, the electrolytic gel acts "wetting" the interface and facilitating the charge transfer between the electrodes to the skin. The lack of an electrolytic agent in dry textile fabrics increases remarkably the resistance, Rs, depicted in Figure 1.

The value of Rs decreases by wetting the electrodes with water, conductive gel or body sweet, the latter is often available during exercise. Another alternative is to manufacture textile electrodes with a special conductive-textile yarn or the appropriate textile structure aiming to maximize the contact surface.

In any case, until a good and stable skin-electrode interface has been created, EBI measurements are unreliable. Spectroscopy applications and time-base analysis applications, where accuracy is a mandatory requirement for implementation, are absolutely compromised. The unpredictability of the impedance of the Skin-electrode interface creates an uncertainty that impedes the deployment of any EBI-based healthcare monitoring at the moment. Fitness and well-being applications might be more robust to a poor skin-contact electrode due to the sweating factor, but at the moment no EBI-textile monitoring system has been made commercially available yet.

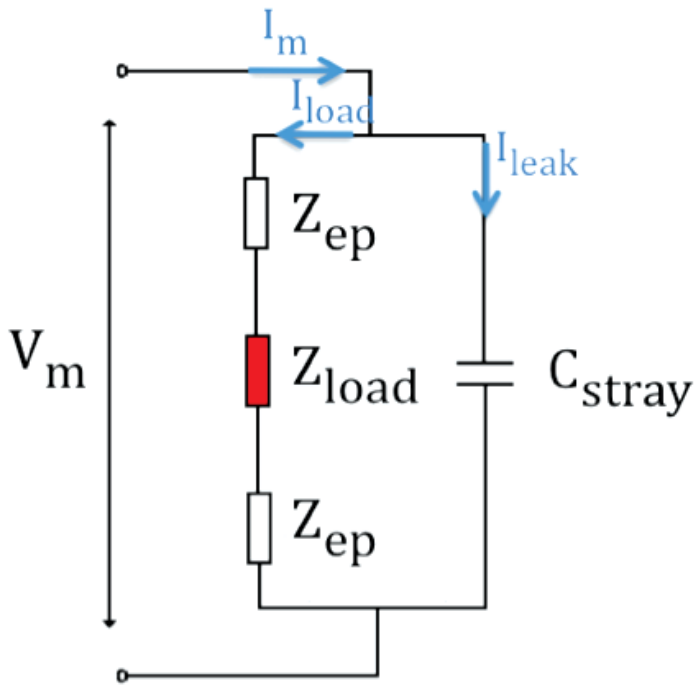

Fig. 2. Electrical equivalent of a EBI measurement setup with a parasitic capacitance in parallel with the impedance load.

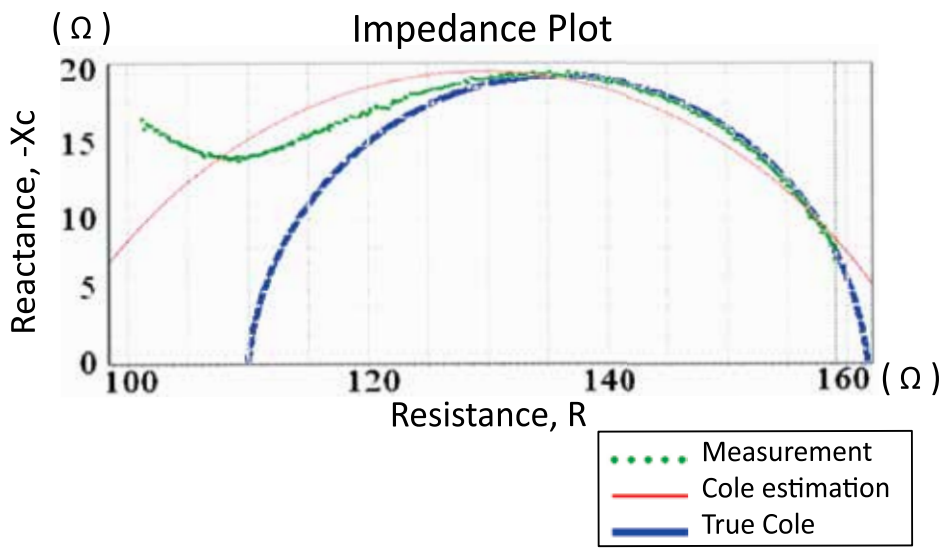

Fig. 3. Typical impedance plot of a measurement showing data deviation caused by a capacitive leakage.

5. Conclusion

The natural dryness of the textile material used nowadays as electrodes may not be an impediment for acquiring biopotentials, but it definitely influences in the skin-electrode contact. A dry interface increases the impedance in series with the current injection leads impedance thus preventing the electrical current used to perform the EBI measurement from entering the body. Such impeding electrode-skin interface contributes to generate measurement artifacts producing unreliable EBI data, which consequently delays any deployment of textile-enabled EBI applications. The availability of a *'wet'* textile electrode that could facilitate the ionic transfer of charges across the Skin-Electrode interface would definitely facilitate the proliferation of textile-based EBI applications.

Meanwhile such a material is made available the most likely alternative to produce textile electrodes that create a large contact surface with the skin decreasing the value of the skin-electrode as much as possible to facilitate the charge transfer from the measurement system to the measurement load i.e. the body through the skin.

EBI technology can be used to assess on hydration status, monitor the cardiac function, detect fluid accumulation on the limbs and lungs for early edema monitoring, detect ischemic tissue for detection of rejection in organ transplantation and also for monitoring lung function as well as respiration rate.

The successful integration of textile-based sensors in EBI measurements systems would enable the implementation of e-health application for Personal Healthcare Monitoring that would truly cause a shift on how clinical practices are delivery nowadays.

6. References

Beckmann, L., Neuhaus, C., Medrano, G., Jungbecker, N., Walter, M., Gries, T., et al. (2010). Characterization of textile electrodes and conductors using standardized measurement setups. *Physiol Meas, 31*(2), 233-247.

Habetha, J. (2006). The MyHeart project--fighting cardiovascular diseases by prevention and early diagnosis. *Conf Proc IEEE Eng Med Biol Soc, Suppl*, 6746-6749.

Hännikäinen, J., Vuorela, T., & Vanhala, J. (2007). Physiological measurements in smart clothing: a case study of total body water estimation with bioimpedance. *Transactions of the Institute of Measurement and Control*(29), 337-354.

Marquez, J. C., Seoane, F., Valimaki, E., & Lindecrantz, K. (2009). Textile electrodes in electrical bioimpedance measurements - a comparison with conventional Ag/AgCl electrodes. *Conf Proc IEEE Eng Med Biol Soc, 1*, 4816-4819.

Mattmann, C., Clemens, F., & Tröster, G. (2008). Sensor for Measuring Strain in Textile. *Sensors, 8*(6), 3719-3732.

Medrano, G., Beckmann, L., Zimmermann, N., Grundmann, T., Gries, T., & Leonhardt, S. (2007). *Bioimpedance Spectroscopy with textile Electrodes for a continuous Monitoring Application.* Paper presented at the 4th International Workshop on Wearable and Implantable Body Sensor Networks (BSN 2007).

Witte, H., Glaser, S., & Rother, M. (1987). New spectral detection and elimination test algorithms of ECG and EOG artefacts in neonatal EEG recordings. *Medical and Biological Engineering and Computing, 25*(2), 127-130.

Part 5

Biomedical Engineering Trends: High Level View

24

Project Alexander the Great: An Analytical Comprehensive Study on the Global Spread of Bioengineering/Biomedical Engineering Education

Ziad O. Abu-Faraj, Ph.D.
American University of Science and Technology
Beirut,
Lebanon

1. Introduction

Bioengineering/Biomedical Engineering is globally considered as one of the most acclaimed fields in science and technology, and has been a primer for advancements in medicine and biology. Recently, healthcare practices have been guided towards new emerging frontiers, including, among others, functional medical imaging, regenerative medicine, nanobiomedicine, and artificial sensory substitution. On the other hand, bioengineering/biomedical engineering education has been evolving and proliferating since the late 1950's, and is undergoing advancement in leading academic institutions worldwide (Harris *et al.*, 2002). The first program to be officially launched in biomedical engineering was at Drexel University, Philadelphia, PA, USA, in 1959 at the master's level. This program was soon followed by Ph.D. programs at Johns Hopkins University, Baltimore, MD, USA, and the University of Pennsylvania, Philadelphia, PA, USA, (Pilkington *et al.*, 1989). At present, a surge in the development of new curricula in bioengineering/biomedical engineering around the world is witnessed, particularly in developing and transitional countries. These programs are somewhat diverse and vary in their academic content, as well as within the different tracks constituting the various areas of bioengineering/biomedical engineering: artificial organs; assistive technology and rehabilitation engineering; bioelectromagnetism; bioethics; biomaterials; biomechanics; biomedical instrumentation; biomedical sensors; bionanotechnology; biorobotics; biotechnology; clinical engineering; medical and bioinformatics; medical and biological analysis; medical imaging; neural engineering; physiological systems modeling, simulation, and control; prosthetic and orthotic devices; and tissue engineering and regenerative medicine.

Notwithstanding these advancements in Bioengineering/Biomedical Engineering, there still exist several shortcomings related to the lack of coordinated interaction among an intricate body of key-players within this field, involving students, universities, hospitals, industries, professional societies and organizations, and governmental agencies and ministries. These shortcomings have brought forth the formation of "the right hand not knowing what the left hand is doing" syndrome among the constituting entities. Thus, in order to enhance the

spread of the said field, and strongly contribute to its solidification, these deficiencies await to be appropriately rectified. There is no doubt that there exists awareness within the bioengineering/biomedical engineering community of the aforementioned shortcomings; however, the work done on alleviating these deficiencies has been restricted per se to organized student internships in industry and consortia of universities on a limited scale, and national and international conferences held by professional societies and organizations on a larger scale.

The above mentioned syndrome could be effectively and strategically remedied by taking advantage of the world-wide-web to establish an interactive cyber-space network involving all key-players within the field and thus enhancing the communication among these entities. Consequently, this study, bearing the name 'Project Alexander the Great', was designed with an attempt to effectively augment the remedy of this syndrome.

Project Alexander the Great is an original study on the global spread of bioengineering/biomedical engineering education (Abu-Faraj, 2008a). This endeavor began in September 2007 by the Department of Biomedical Engineering at the American University of Science & Technology (AUST, Beirut, Lebanon). The objectives of this project are to identify, disseminate, and network, through the world-wide-web, all those institutions of higher learning that provide bioengineering/biomedical engineering education, with the potential of incorporating emerging programs. This endeavor will create the foundation and environment necessary for the above sought interactive communication among the various stakeholders within the field of Bioengineering/Biomedical Engineering.

The provided information is essential, up-to-date, and could be used by the following bioengineering/biomedical engineering target audience: students, faculty, research scientists, and practitioners. In addition to other closely related vocational professions, such as industry, accreditation agencies, professional societies, academic institutions of higher education, ministries of higher education, and other governmental agencies.

Before expounding, the reader's attention is drawn to the fact that this chapter refers to bioengineering and biomedical engineering interchangeably. Katona emphasized that "there is no consistent distinction between academic departments bearing one or the other designation and the two terms are often used interchangeably" (Katona, 2002).

2. Background

An early study pertaining to the academic growth of biomedical engineering as a new career was conducted by Schwartz and Long (1975). This study was based on a 1974 survey around biomedical engineering education, and was jointly conducted by the American Society for Engineering Education and the Engineering in Medicine and Biology group of the IEEE. The objective of this survey was to "identify all the engineering schools in the U.S. having Biomedical Engineering degrees, options or programs". This survey utilized a questionnaire that was administered at 222 engineering schools, and whose major findings as reported by the authors are presented in Table 1.

Potvin *et al.* (1981) conducted a quantitative study about biomedical engineering education comparable with that reported by Schwartz and Long (1975). However, this study utilized an in-depth survey questionnaire that was modified from the one used in 1974, and was distributed to 251 engineering schools in the United States.

Total U.S. engineering schools surveyed (early months of 1974)	**222**
Schools having degrees or programs in Biomedical Engineering (BME)	121
Schools with no programs or degrees in BME	76
Schools who did not respond	25
Schools awarding degrees in BME	**49**
B.S. degree	25
M.S. degree	37
Ph.D. degree	38
Schools offering options or programs in BME in which the student received some other engineering degree	88
BME student enrollment for the 1973 fall semester	**3769**
B.S. degree	1530
M.S. degree	1306
Ph.D. degree	933
BME degrees awarded between 1965 and 1973 fall semester	**2889**
B.S. degree	574
M.S. degree	1424
Ph.D. degree	891

Table 1. Summary of reported results from Schwartz and Long (1975).

The new questionnaire covered enrolment, courses, and degrees data for the academic year 1979-1980, as well as employment data from the academic year 1978-1979. Table 2 summarizes the major findings of this survey. According to this study, the number of schools offering B.S., M.S., and Ph.D. programs in biomedical engineering increased, without exception, within the five years that preceded the study.

The study was sponsored by the Education Committees of four societies: i) the Biomedical Engineering Division of the American Society of Engineering Education; ii) the IEEE Engineering in Medicine and Biology Society; iii) the Biomedical Engineering Society; and iv) the Alliance for Engineering in Medicine and Biology.

In 2002, a web-based directory of 102 universities with biomedical engineering programs within the United States was released by the IEEE Engineering in Medicine and Biology Society, Piscataway, NJ, USA (Anonymous, 2002). Four years later, the Whitaker Foundation, Arlington, VA, USA, published an on-line biomedical engineering curriculum database covering 119 programs (Anonymous, 2006).

Then, Nagel *et al.* (2007) published a comprehensive document on medical and biological engineering and science in the higher educational system in Europe. The document began with an elucidation of the Bologna Declaration, signed on June 19, 1999, and its objectives, which subsequent to their implementation have led to the Bologna Process; a European reform process aiming at establishing a European Higher Education Area (EHEA) by 2010.

The authors reported that, in compliance with the European Union (EU) list of priorities, the Bologna movement provoked the European Medical and Biological Engineering and Science (MBES) community to establish their 'Higher Education Area' by pursuing the following guidelines that they later adopted as their target objectives: i) "harmonizing the educational programs"; ii) "specifying minimum qualifications"; and iii) "establishing criteria for an efficient quality control of education, training, and lifelong learning".

Total U.S. engineering schools surveyed (academic year 1979-1980)	**251**
Schools having degree programs in BME	71
Schools having official minor or option programs in BME	35
Schools with no programs or degrees in BME	107
Schools who did not respond	38
BME Programs accredited by the Accreditation Board for Engineering Training/Engineers Council for Professional Development	**22**

Schools awarding degrees in BME	**71**
B.S. degree	37
M.S. degree	48
Ph.D. degree	41
Schools offering options or minors in BME in which the student received some other engineering degree	**35**
B.S. degree	41
M.S. degree	42
Ph.D. degree	34
BME student enrollment for the 1979-1980 academic year	**4158**
B.S. degree	2859
M.S. degree	830
Ph.D. degree	469
BME degrees awarded during the academic year 1978-1979	**820**
B.S. degree	464
M.S. degree	249
Ph.D. degree	107
Placement of the BME graduates of the academic year 1978-1979	**630**
Industry	253
Government	23
Academia	35
Hospitals or clinics	66
Medical school	100
BME graduate schools	96
Other graduate or professional schools	57

Table 2. Summary of reported results from Potvin *et al.* (1981).

Within the same context, the authors reported that more than 200 institutions of higher learning in Europe offer academic programs in MBES at the three levels of education: bachelor, master, and doctoral. Additionally, the authors emphasized the lack of international coordination with regard to "contents and required outcome qualifications". Notwithstanding this fact, they reported that the interactions in biomedical engineering education between Europe and the United States have been strong despite the differing educational environments. The authors continued by stating that starting in 1999 a Europe-wide consortium has been i) "engaged in projects aiming at creating a comprehensive survey of the status of MBES education and research in Europe"; ii) "charting the MBES

community"; iii) "developing recommendations on harmonized MBES education, training, and certification"; and iv) "establishing criteria for the accreditation of MBES programs in Europe".

Subsequently, in 2004, a Europe-wide participation project under the name 'BIOMEDEA' was conceived in order to attain the above said objectives as has been described in Biomedical Engineering Education in Europe – Status Reports (Nagel, 2005). According to these reports, BIOMEDEA, which is mainly sponsored by the International Federation for Medical and Biological Engineering, IFMBE, Zagreb, Croatia, has been progressing in a productive manner and that 80 European academic institutions had participated in the three meetings that had taken place. Moreover, agreements had been reached on i) the "Criteria and Guidelines for the Accreditation of Biomedical Engineering Programs in Europe" and ii) a "European Protocol for the Training of Clinical Engineers."

3. Materials and methods

The initial phase of Project Alexander the Great was to create a database of the academic institutions offering bioengineering/biomedical engineering education. Accordingly, a survey was conducted on all 10453 universities recognized by the International Association of Universities, UNESCO, Paris, France (Anonymous, 2007a), spread among the 193 member states of the United Nations, New York, NY, USA, within the six continents. Table 3 depicts the classifications comprising the database that was created thereof. A 0.06125% discrepancy exists in the sum total of the continent population from that of the total population, reflecting the population of small islands and Western Sahara which was not accounted for.

A world-wide-web search, using Google's search engine, Google Inc., Mountain View, CA, USA, was initiated, by continent. Once an institution was identified with a bioengineering/biomedical engineering program, the department's name, address, Uniform Resource Locator (URL), year established, and director's name and coordinates were gathered. Because of the scale and the perseverance required to gather the desired data, a methodical search procedure was deemed necessary and accordingly was set and implemented. This procedure consisted of two iterations explained herein.

The main iteration was to utilize the web. A cut-off limit of 15 minutes was set for the search of whether or not an academic institution had a bioengineering/biomedical engineering program, after which the search proceeded to the next institution. This approach was found mandatory in order to avoid any blockage that may unnecessarily hinder the process. Instances of such hindrances include, but not limited to, language barriers, weak website design, and no or poor internet accessibility. Subsequent to this iteration, the success rate was calculated as the ratio of the number of successes to that of failures. A *success* was coined with the ability to connect, confirm (existence or no existence), and acquire information; while, *failure* meant the inability to connect or no information.

A complementary iteration, aiming at contacting the pertinent embassies/consulates/ ministries of higher education, was executed at the end of the first iteration in order to assert the study's findings. This iteration served to boost the success rate.

Moreover, the possibility of having a bioengineering/biomedical engineering program erroneously marked as 'failure' is not considered problematic, because of the obtained high

CLUSTERS	PROPERTIES		
Continent	Countries	Population	Academic Institutions
Africa	53	1007430000	793
Asia	44	4244615000	4147
Europe	47	610708000	2204
N. America	23	539611000	2401
Oceania	14	33946000	75
S. America	12	388868000	833
TOTAL	**193**	**6829361000**	**10453**

Table 3. The clusters and properties of the study database. (Population Data Source: World Population Prospects - The 2008 Revision, Department of Economic and Social Affairs, United Nations, New York, NY, USA, 2009).

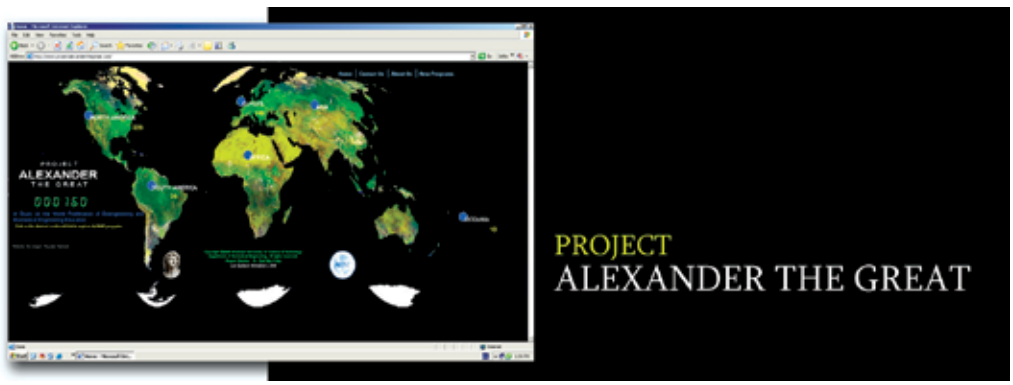

Fig. 1. The front side of an early flyer made to promote Project Alexander the Great.

rate of success, and which could be alleviated by having the concerned academic institution filling out and submitting an *e*-form, which is provided on the project's website, whose URL is www.projectalexanderthegreat.com. Figure 1 shows an early flyer used to promote the project in regional and international assemblies of bioengineering/biomedical engineering.

4. Results and discussion

Statistical results pertaining to the distribution of bioengineering/biomedical engineering education in the six continents are presented in Table 4. The *success* rates were 70.74% for Africa, 66.19% for Asia, 82.67% for Europe, 94.13% for North America, 94.67% for Oceania, and 96.76% for South America. The obtained *success* rates for South America, Oceania, North America, and Europe strongly support the methodology implemented in Project Alexander the Great. With regard to those obtained for Africa and Asia, which are considered satisfactory, there are several possible reasons behind these numbers. The difficulties encountered in this project include, language barriers – particularly in Asia because of the vast spectrum of differing languages, e.g., Russian, Farsi, Chinese, Japanese, Korean, etc.; inexistence of a website; weak/non-interactive website design; no or poor

internet accessibility; lack/inadequate published information; contaminated websites, among others. In any case, encountered *failures* are expected to diminish with time as long as the sustainability of Project Alexander the Great is maintained.

Table 4 contains 19 items with data pertaining to the six continents. For ease of navigation, the data could be compartmentalized into five categories: i) generic data about the world population, world countries, and recognized world universities; ii) basic demographic, geographic, and academic data by continent; iii) Project Alexander the Great survey data pertaining to universities and countries offering bioengineering/biomedical engineering education by continent; iv) statistical distributions pertaining to demographic, geographic, and academic data by continent; and v) Project Alexander the Great statistical distributions pertaining to universities and countries offering bioengineering/biomedical engineering education by continent.

According to the number of universities offering curricula in bioengineering/biomedical engineering, as depicted in Figure 2, there is good evidence that education in this field has globally proliferated. What is worth noting, however, is the fact that the aforementioned numbers are clustered within each continent as depicted in the percent of countries in continent offering bioengineering/biomedical engineering: 13.21% for Africa, 52.27% for Asia, 61.70% for Europe, 26.09% for North America, 14.29% for Oceania, and 50.0% for South America.

Nevertheless, an appraisal of the evolution and proliferation of bioengineering/biomedical engineering as a field of study, in a chronological order since its inception (Abu-Faraj, 2008b), as well as the current global explosion of technology that is outreaching what were once considered as remote areas, indicate that the next few decades will probably witness a wider diffusion of bioengineering/biomedical engineering education into new countries within each continent. Furthermore, if the coordinated interaction among the key players within the field of Bioengineering/Biomedical Engineering, namely students, universities, hospitals, industries, professional societies and organizations, and governmental agencies and ministries, is enriched and solidified, then such diffusion is more viable.

The mapping of bioengineering/biomedical engineering education within the six continents is illustrated in Figures 3-a through 3-f, and is concurrently followed by a basic analysis pertaining to the academic distribution of the said field within each continent.

However, in order to better understand the illustrated distribution within each continent, a metric had to be formulated by dividing the number of population in a continent by the number of bioengineering/biomedical engineering programs offered within the same continent. Then, the smallest of the six obtained numbers was selected to normalize all values to a unitary value. The following factors were obtained: 32.31 for Africa, 6.44 for Asia, 1.68 for Europe, 1.00 for North America, 1.42 for Oceania, and 5.59 for South America. It should be noted that the smaller the factor the higher is the outreach of bioengineering/biomedical engineering education per individual per continent.

Accordingly, upon examining Figure 3a for Africa, it is apparent from the extent of the white shading that this continent lags behind that of North America by a factor of 32.31:1.00. For example, if equal samples of 1000 individuals from both continents are considered, then for every 32 individuals receiving bioengineering/biomedical engineering education in North America, only one individual is offered such an education in Africa, resulting in a ratio of approximately 1000:31.

World Population						6829361000
World Countries						193
Total World Universities						10453
CONTINENT DATA	**AFRICA**	**ASIA**	**EUROPE**	**NORTH AMERICA**	**OCEANIA**	**SOUTH AMERICA**
Continent Population	1007430000	4244615000	610708000	539611000	33946000	388868000
Total Continent Countries	53	44	47	23	14	12
Continent Countries w/ Universities	48	44	46	17	7	12
Continent Population Offered Higher Education	1006566000	4244615000	610708000	539611000	33946000	388868000
Continent Population Not Offered Higher Education	864000	0	0	0	0	0
Number of Universities in Continent	793	4147	2204	2401	75	833
Number of People Per Single Continent University	1269314	1023539	277091	224744	452613	466828
Number of Universities in Continent Offering Bioengineering/Biomedical Engineering	13	275	152	225	10	29
Number of Countries in Continent Offering Bioengineering/Biomedical Engineering	7	23	29	6	2	6
% of World Population in Continent	14.75%	62.15%	8.94%	7.90%	0.50%	5.69%
% of Continent Population Not Offered Higher Education	0.09%	0.00%	0.00%	0.00%	0.00%	0.00%
% of World Countries in Continent	27.46%	22.80%	24.35%	11.92%	7.25%	6.22%
% of Total Continent Countries w/ Universities	90.57%	100.00%	97.87%	73.91%	50.00%	100.00%
% of Total World Universities in Continent	7.59%	39.67%	21.08%	22.97%	0.72%	7.97%
% of Universities in Continent Offering Bioengineering/ Biomedical Engineering	1.64%	6.63%	6.90%	9.37%	13.33%	3.48%
% of Countries in Continent Offering Bioengineering/ Biomedical Engineering	13.21%	52.27%	61.70%	26.09%	14.29%	50.00%

Table 4. The distribution of bioengineering/biomedical engineering education in the six continents. (Population Data Source: World Population Prospects - The 2008 Revision, Department of Economic and Social Affairs, United Nations, New York, NY, USA, 2009).

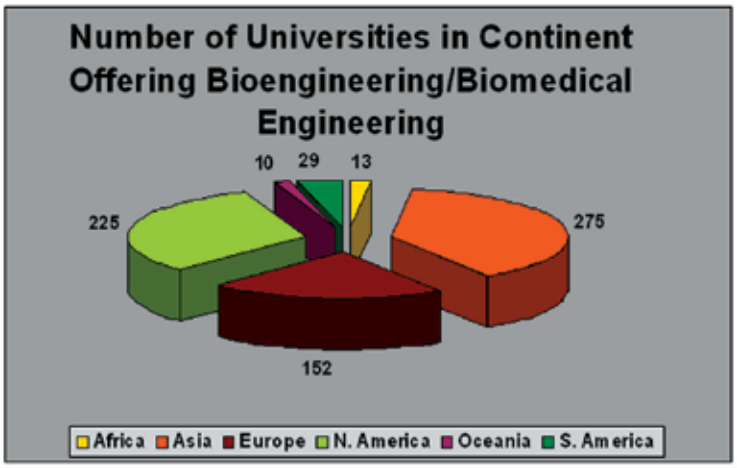

Fig. 2. A pie chart showing the number of universities in each continent offering bioengineering/biomedical engineering education.

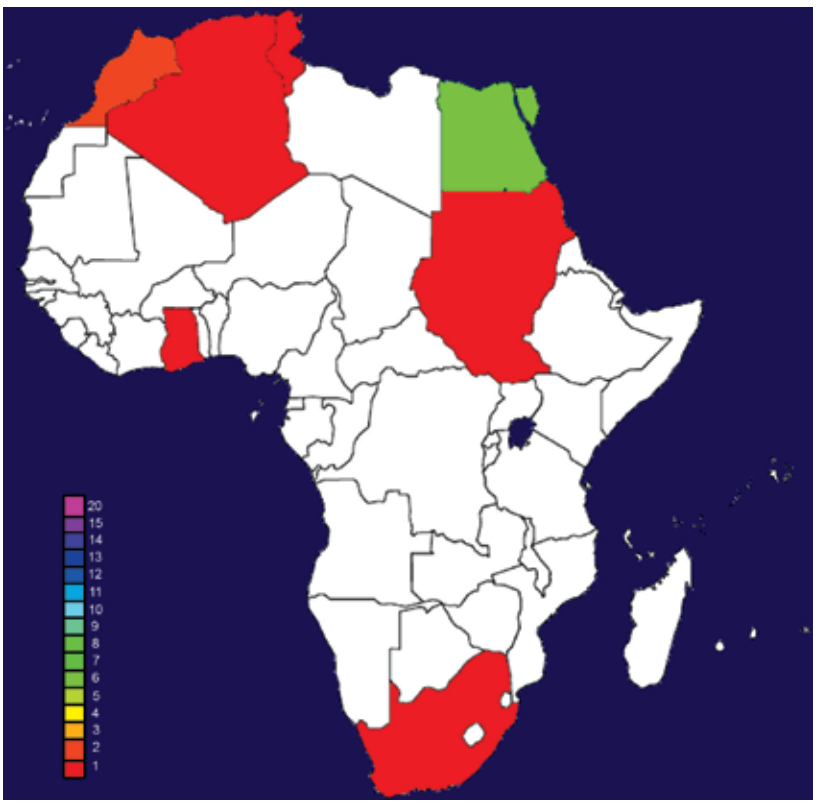

Algeria	1	Ghana	1	Sudan	1	South Africa	1
Egypt	6	Morroco	2	Tunisia	1		

Fig. 3a. The mapping of bioengineering/biomedical engineering education in Africa. Note that the white shade indicates zero programs in a country.

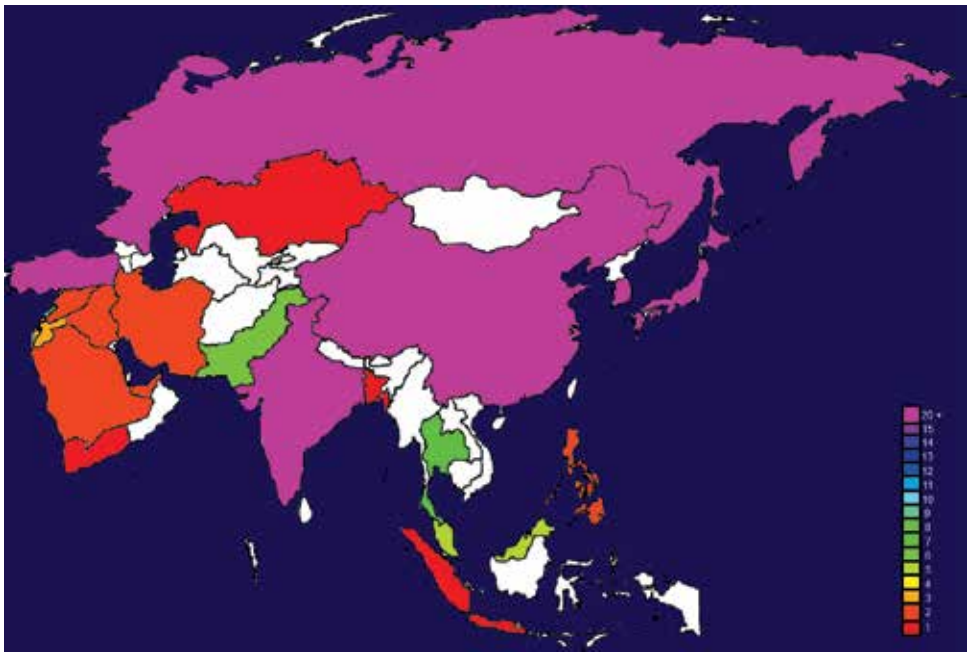

Bangladesh	1	Israel	3	Malaysia	5	Syria	2
China	90	Japan	32	Pakistan	6	Thailand	7
India	31	Jordan	3	Philippines	2	Turkey	21
Indonesia	1	Kazakhstan	1	Russian Federation	24	United Arab Emirates	2
Iran	2	Korea	27	Saudi Arabia	2	Yemen	1
Iraq	2	Lebanon	8	Singapore	2		

Fig. 3b. The mapping of bioengineering/biomedical engineering education in Asia.

With regard to Asia (Figure 3b), even though it lags behind that of North America by a factor of 6.44:1.00, yet it contains the largest number of universities offering bioengineering/biomedical engineering education; i.e., 275 vs. 225. Of particular interest within this continent are the numbers obtained for China, Japan, India, Korea, Russian Federation, and Turkey. Europe (Figure 3c) is comparable with North America with a factor of 1.68:1.00; most prominently are the numbers of programs within the United Kingdom and Germany. It is important to note that there is a discrepancy between the number found in this study for Europe, 152, and that of Nagel *et al*. (2007) who reported that there are more than 200 institutions of higher learning in Europe offering academic programs in MBES. This discrepancy requires further investigation. As for North America (Figure 3d), the U.S. presents a formidable number of 189 programs to be followed by the 23 programs found in Canada. Though small in population, Oceania (Figure 3e) is also comparable with North America with a factor of 1.42:1.00; yet, bioengineering/biomedical engineering education is restricted to Australia and New Zealand. Lastly, although South America (Figure 3f) lags behind North America with a factor of 5.59:1.00, yet it has 29 programs in the said field ensuring the coverage of 50% of the continent's countries.

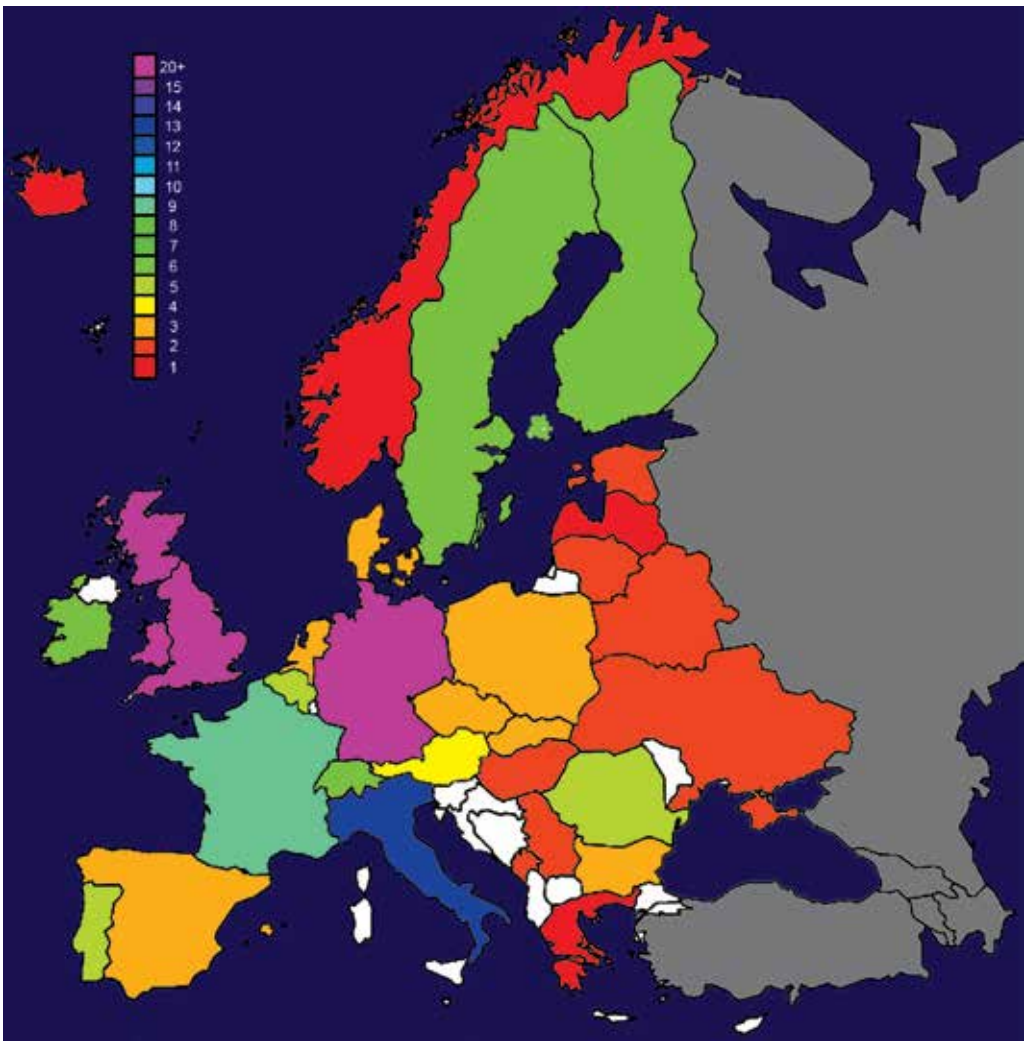

Austria	4	France	9	Lithuania	2	Spain	3
Belarus	2	Germany	23	Netherlands	3	Sweden	6
Belgium	5	Greece	2	Norway	1	Switzerland	6
Bulgaria	3	Hungary	2	Poland	3	Ukraine	2
Czech Republic	3	Iceland	1	Portugal	5	United Kingdom	26
Denmark	3	Ireland	6	Romania	5		
Estonia	2	Italy	13	Serbia	2		
Finland	6	Latvia	1	Slovak Republic	3		

Fig. 3c. The mapping of bioengineering/biomedical engineering education in Europe.

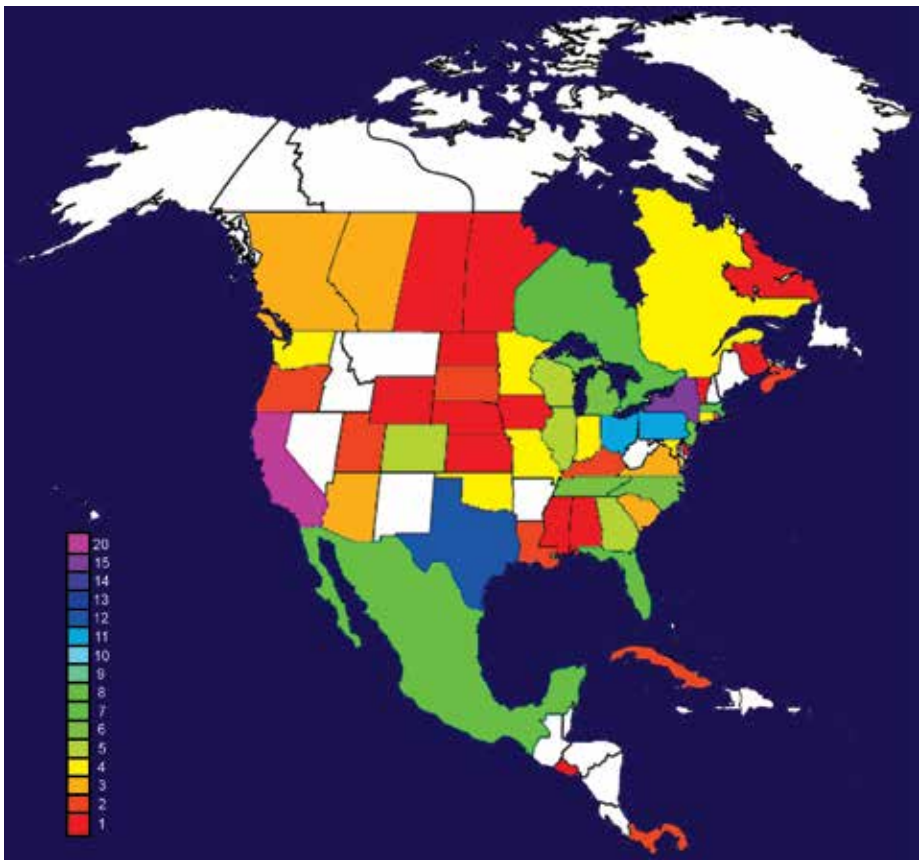

Canada-Alberta	3	USA-Delaware	1	USA-New York	15
Canada-British Columbia	3	USA-District of Columbia	2	USA-North Carolina	6
Canada-Manitoba	1	USA-Florida	8	USA-North Dakota	1
Canada-New Brunswick	1	USA-Georgia	5	USA-Ohio	11
Canada-Newfoundland & Labrador	1	USA-Illinois	5	USA-Oklahoma	4
Canada-Nova Scotia	2	USA-Indiana	4	USA-Oregon	2
Canada-Ontario	7	USA-Iowa	1	USA-Pennsylvania	11
Canada-Quebec	4	USA-Kansas	1	USA-Rhode Island	2
Canada-Saskatchewan	1	USA-Kentucky	2	USA-South Carolina	3
Cuba	2	USA-Louisiana	2	USA-South Dakota	2
El Salvador	1	USA-Maryland	4	USA-Tennessee	6
Mexico	8	USA-Massachusetts	8	USA-Texas	12
Panama	2	USA-Michigan	6	USA-Utah	2
USA-Alabama	1	USA-Minnesota	4	USA-Vermont	1
USA-Arizona	3	USA-Mississippi	1	USA-Virginia	3
USA-California	20	USA-Missouri	4	USA-Washington	4
USA-Colorado	5	USA-Nebraska	1	USA-Wisconsin	5
USA-Connecticut	4	USA-New Jersey	6	USA-Wyoming	1

Fig. 3d. The mapping of bioengineering/biomedical engineering education in North America.

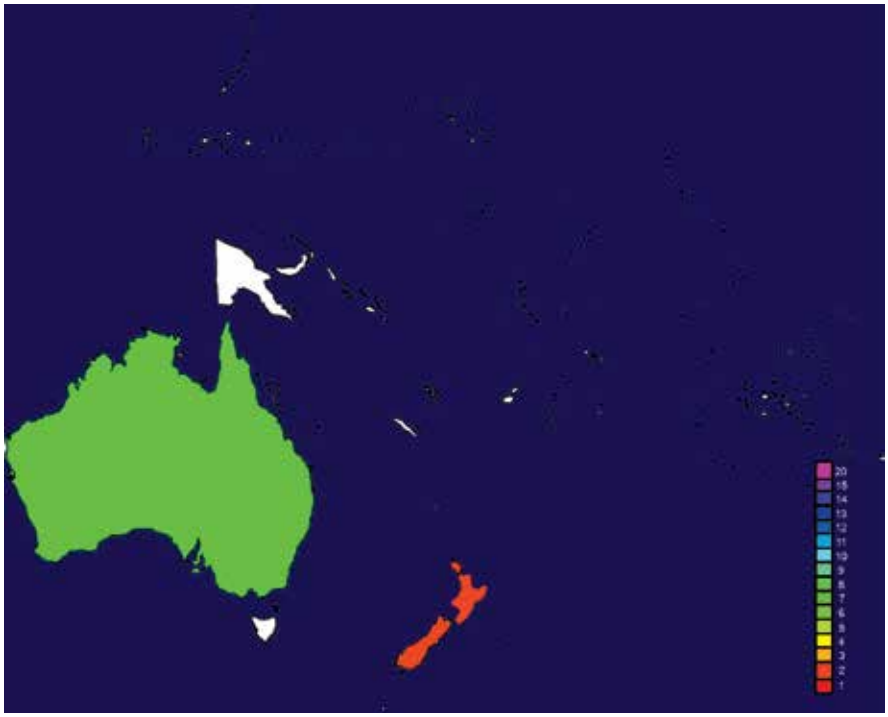

Australia 8 New Zealand 2

Fig. 3e. The mapping of Bioengineering/Biomedical Engineering education in Oceania.

5. Conclusions

Project Alexander the Great revealed that bioengineering/biomedical engineering education is globally undergoing a healthy growth. There are currently 704 programs in bioengineering/biomedical engineering worldwide, offered in 6.73% of the world universities; two numbers that are worth constant monitoring as the world is witnessing a rapid perpetual change in this field.

The U.S. Department of Labor, Washington, DC, USA, reported that "the number of biomedical engineering jobs will increase by 31.4 percent through 2010 ... double the rate for all other jobs combined." Hence, the overall job growth in this field will by then average a 15.2 percent (Anonymous, 2007b).

This forecast for bioengineering/biomedical engineering jobs is reflected in Figure 4, which highlights the student enrollment in biomedical engineering within the United States in 1975-2003. A particular feature of this figure is the rapid surge in bioengineering/biomedical engineering enrollment that started in 1999.

Despite this overwhelming anticipated growth, employment indicators show that it is unlikely that this field will saturate any time soon.

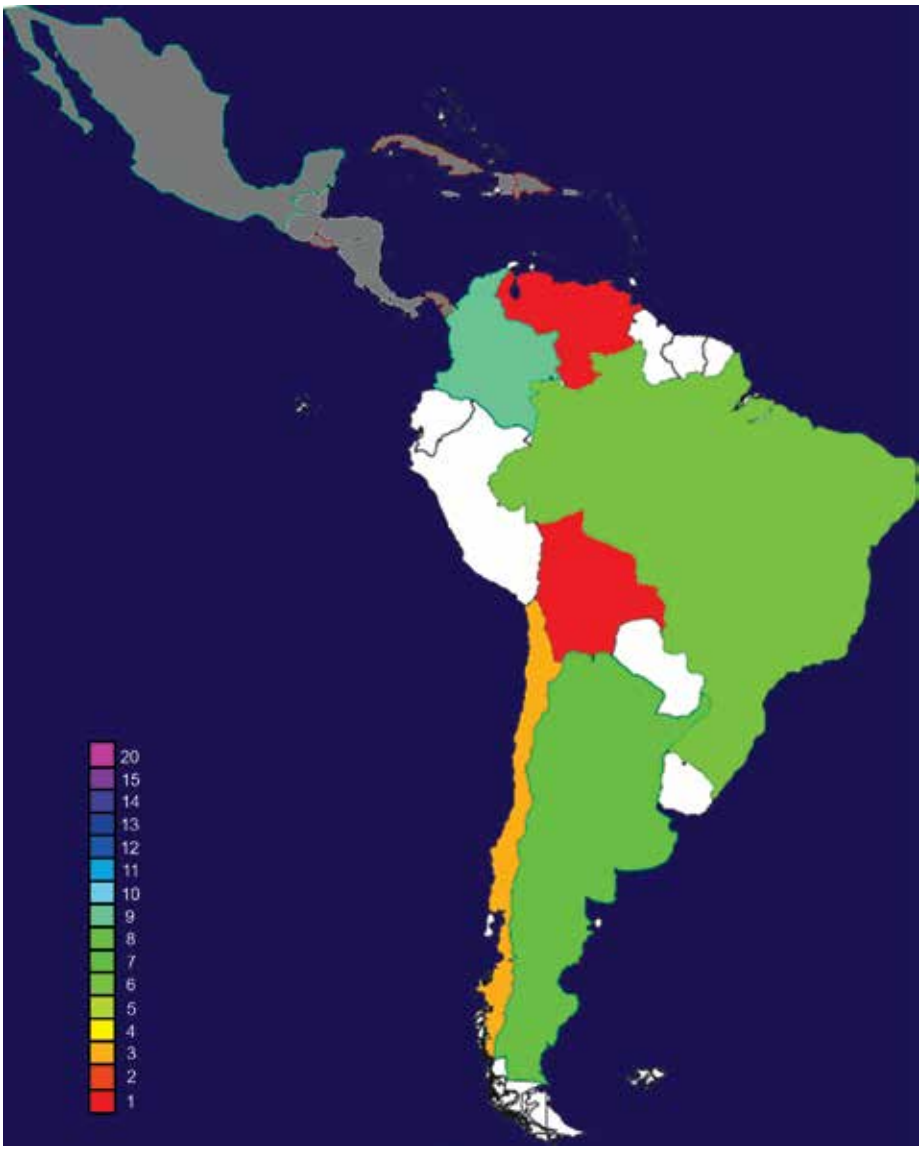

Argentina	9	Brazil	6	Columbia	9	Venezuela	1
Bolivia	1	Chile	3				

Fig. 3f. The mapping of bioengineering/biomedical engineering education in South America.

It is worthwhile mentioning that the above forecast was made before the 2008 World Economic Crisis. Although, to date, no tangible signs have been visible as of the impact of this crisis on bioengineering/biomedical engineering education, yet this matter remains to be appraised.

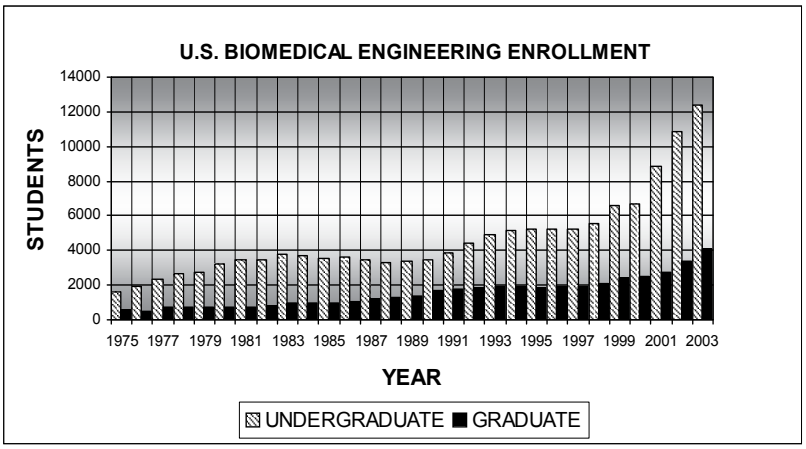

Fig. 4. Undergraduate and graduate student enrollment in biomedical engineering in the United States between 1975 and 2003. (Data was reproduced by digitization from the Whitaker Foundation website (Anonymous, 2006), and extended from Pilkington *et al.* (1989)).

To conclude, the relevance of Project Alexander the Great is multifold:

i. The inception of a web-based 'world map' in bioengineering/biomedical engineering education for the potential international student desiring to pursue a career in this field.
ii. The global networking of bioengineering/biomedical engineering academic and research programs.
iii. The promotion of first-class bioengineering/biomedical engineering education and the catalysis of global proliferation of this field.
iv. The erection of bridges among educational institutions, industry, and professional societies or organizations involved in bioengineering/biomedical engineering.
v. The catalysis in the establishment of framework agreements for cooperation among the identified academic institutions offering curricula in this field.

6. Acknowledgments

This work was supported by funds from the Research Council of the American University of Science & Technology (AUST, Beirut, Lebanon). Professor Ziad Abu-Faraj thanks the following undergraduate students in the Department of Biomedical Engineering at AUST for their invaluable help in acquiring the data for this study: Shadi Barakat, Elie Jabbour, Rawad Saasouh, and Elssy Youssef. He also expresses his gratitude to Mrs. Henriette Skaff in the Department of Languages and Translation at AUST for her valuable help in editing this book chapter.

7. References

Abu-Faraj Z.O. (2008a). Project Alexander the Great: A Study on the World Proliferation of Biomedical Engineering Education, *Proceedings of the 30th Annual International Conference of the IEEE Engineering in Medicine and Biology Society,* pp. 2873-2876, August 20-24, 2008, Vancouver, British Columbia, Canada.

Abu-Faraj Z.O. (2008b). Bioengineering/Biomedical Engineering Education and Career Development: Literature Review, Definitions, and Constructive Recommendations, *International Journal of Engineering Education*, vol. 24, no. 5, pp 990-1011.

Anonymous (2002). Universities with Biomedical Engineering Programs, *IEEE Engineering in Medicine and Biology Society*, Piscataway, NJ, USA. Available online‡: http://embs.gsbme.unsw.edu.au/ColdFusion/indlist.cfm?typ=4

Anonymous (2006). Biomedical Engineering Curriculum Database, *The Whitaker Foundation*, Arlington, VA, USA. Available online†: http://bmes.seas.wustl.edu/Whitaker/

Anonymous (2007a). World Higher Education Database, *International Association of Universities*, UNESCO, Paris, France. Available online‡: http://www.unesco.org/iau/directories/index.html

Anonymous (2007b). Planning a career in biomedical engineering, *Biomedical Engineering Society*, Landover, MD, USA. Available online‡: http://www.bmes.org/careers.asp

Harris T.R., J.D. Bransford, and S.P. Brophy (2002). Roles for learning sciences and learning technologies in biomedical engineering education: a review of recent advances, *Annual Review of Biomedical Engineering*, vol. 4, pp 29-48.

Katona P.G. (2002). The Whitaker Foundation: the end will be just the beginning, *IEEE Transactions on Medical Imaging*, vol. 21, no. 8, pp. 845-849.

Nagel J.H. - Project Editor (2005). Biomedical Engineering Education in Europe – Status Reports, *BIOMEDEA*, International Federation for Medical and Biological Engineering, Zagreb, Croatia, 242 pp.

Nagel J.H., D.W. Slaaf, and J. Barbenel (2007). Medical and biological engineering and science in the European higher education area, *IEEE Engineering in Medicine and Biology Magazine*, vol. 26, no. 3, pp. 18-25.

Pilkington T.C., F.M. Long, R. Plonsey, J.G. Webster, and W. Welkowitz (1989). Status and trends in biomedical engineering education, *IEEE Engineering in Medicine and Biology Magazine*, pp. 9-17.

Potvin A.R., F.M. Long, J.G. Webster, and R.J. Jendrucko (1981). Biomedical engineering education: enrollment, courses, degrees, and employment, *IEEE Transactions on Biomedical Engineering*, vol. BME-28, no. 1, pp. 22-28.

Schwartz M.D. and F.M. Long (1975). A survey analysis of biomedical engineering education, *IEEE Transactions on Biomedical Engineering*, vol. BME-22, no. 2, pp. 119-124.

‡ Uniform Resource Locator (URL) last accessed on March 10, 2008.

† Uniform Resource Locator (URL) last accessed on July 31, 2010.

Edited by Anthony N. Laskovski

Rapid technological developments in the last century have brought the field of biomedical engineering into a totally new realm. Breakthroughs in materials science, imaging, electronics and, more recently, the information age have improved our understanding of the human body. As a result, the field of biomedical engineering is thriving, with innovations that aim to improve the quality and reduce the cost of medical care. This book is the second in a series of three that will present recent trends in biomedical engineering, with a particular focus on materials science in biomedical engineering, including developments in alloys, nanomaterials and polymer technologies.

ISBN 978-953-51-4533-2

Photo by Sybille Yates / Shutterstock

IntechOpen